

DTIC FILE COPY

2

AGARD-CP-428

AGARD-CP-428

AD-A198 665

AGARD

ADVISORY GROUP FOR AEROSPACE RESEARCH & DEVELOPMENT

7 RUE ANCELLE 92000 NEUILLY SUR SEINE FRANCE

AGARD CONFERENCE PROCEEDINGS No.428

Aerodynamics of Hypersonic Lifting Vehicles

DISTRIBUTION STATEMENT A

Approved for public release;
Distribution Unlimited

DTIC
ELECTE
S JAN 21 1988 D
D

NORTH ATLANTIC TREATY ORGANIZATION



DISTRIBUTION AND AVAILABILITY
ON BACK COVER

88 1 12 003

AGARD-CP-428

NORTH ATLANTIC TREATY ORGANIZATION
ADVISORY GROUP FOR AEROSPACE RESEARCH AND DEVELOPMENT
(ORGANISATION DU TRAITE DE L'ATLANTIQUE NORD)

AGARD Conference Proceedings No.428
AERODYNAMICS OF HYPERSONIC LIFTING VEHICLES



Accession For	
NTIS CRA&I	<input checked="checked" type="checkbox"/>
DTIC TAB	<input type="checkbox"/>
Unannounced	<input type="checkbox"/>
Justification	
By	
Distribution/	
Availability Codes	
Dist	Availability for Special
A-1	

Papers presented and Discussions held at the Fluid Dynamics Panel Symposium in
Bristol, United Kingdom, 6-9 April 1987.

THE MISSION OF AGARD

According to its Charter, the mission of AGARD is to bring together the leading personalities of the NATO nations in the fields of science and technology relating to aerospace for the following purposes:

- Recommending effective ways for the member nations to use their research and development capabilities for the common benefit of the NATO community;
- Providing scientific and technical advice and assistance to the Military Committee in the field of aerospace research and development (with particular regard to its military application);
- Continuously stimulating advances in the aerospace sciences relevant to strengthening the common defence posture;
- Improving the co-operation among member nations in aerospace research and development;
- Exchange of scientific and technical information;
- Providing assistance to member nations for the purpose of increasing their scientific and technical potential;
- Rendering scientific and technical assistance, as requested, to other NATO bodies and to member nations in connection with research and development problems in the aerospace field.

The highest authority within AGARD is the National Delegates Board consisting of officially appointed senior representatives from each member nation. The mission of AGARD is carried out through the Panels which are composed of experts appointed by the National Delegates, the Consultant and Exchange Programme and the Aerospace Applications Studies Programme. The results of AGARD work are reported to the member nations and the NATO Authorities through the AGARD series of publications of which this is one.

Participation in AGARD activities is by invitation only and is normally limited to citizens of the NATO nations.

The content of this publication has been reproduced directly from material supplied by AGARD or the authors.

Published November 1987

Copyright © AGARD 1987
All Rights Reserved

ISBN 92-835-0435-6



*Printed by Specialised Printing Services Limited
40 Chigwell Lane, Loughton, Essex IG10 3TZ*

FOREWORD

Through the post-Apollo, reduction of the space effort in the USA and most other western countries the subject of hypersonic aerodynamics has been neglected in favour of more pressing needs in areas like transonic aerodynamics. New developments on both sides of the Atlantic place both the facilities and the qualified personnel in very strong demand again. This is mainly because of renewed strong interest in space applications such as space stations, atmospheric braking, re-entry vehicles, transatmospheric aircraft etc.

The symposium provided a forum for a stocktaking of the still-available and new facilities, a discussion of traditional and newly-developed experimental and numerical techniques for hypersonic applications, as well as for presentations of design techniques and new projects. The meeting was timely, not because of a large body of accumulated good work, but because — at the outset of the presently starting new era of hypersonic aerodynamics — it highlights the directions in which particular effort must be invested in the coming years.

* * *

En raison de la diminution des efforts déployés dans le domaine spatial après le programme Apollo, tant aux Etats Unis que dans la plupart des autres pays occidentaux, la question de l'aérodynamique hypersonique a été négligée au profit de besoins plus pressants dans des domaines tels que l'aérodynamique transsonique. De nouveaux développements réalisés des deux côtés de l'Atlantique font qu'il existe à nouveau une très forte demande en matière d'installations et de personnel qualifié. Ceci est dû principalement à un grand renouveau d'intérêt pour les applications spatiales telles que les stations spatiales, le freinage dans l'atmosphère, les véhicules de rentrée, les avions transatmosphériques, etc.

Ce symposium a été l'occasion d'un forum permettant de faire l'inventaire des installations toujours disponibles et des installations nouvelles, de passer en revue les techniques expérimentales et numériques traditionnelles et nouvellement mises au point, et de présenter des techniques d'étude ainsi que de nouveaux projets. Cette réunion était opportune, non seulement en raison de la grande quantité de bons travaux rassemblés, mais parce qu'elle met en lumière — au début de la nouvelle ère de l'aérodynamique hypersonique qui est en train de s'ouvrir — les directions dans lesquelles un effort particulier doit être consenti dans les années à venir.

AGARD FLUID DYNAMICS PANEL

Chairman: Dip. Ing. P.W.Sacher
Messerschmitt-Bölkow-Blohm-GmbH
LK122
Postfach 80 11 60
D-8000 München 80
Federal Republic of Germany

Deputy Chairman: Mr D.H.Peckham
Superintendent AE1 Division
Royal Aircraft Establishment
R141 Building
Farnborough Hants GU14 6TD
UK

PROGRAMME COMMITTEE

Prof. H.Hornung, Ph.D. (Co-Chairman)
Director, SM-ES
DFVLR — SM-ES
Bunsenstrasse 10
D-3400 Göttingen
Federal Republic of Germany

Dr J.A.Essers
Université de Liège
Institut de Mécanique
Service d'Aérodynamique Appliquée
Rue Ernest Solvay
B-4000 Liège
Belgium

Dr K.J.Orlik-Ruckemann
National Aeronautical Establishment
National Research Council — Montreal Road
Ottawa, Ontario K1A 0R6
Canada

Mr J.Verriere
CEAT
23 avenue Guillaumet
31056 Toulouse Cedex
France

Prof. Dr L.G.Napolitano, Ph.D.
Chair of Aerodynamics
Faculty of Engineering, University of Naples
P. Le Tecchio 80
80125 Napoli
Italy

Dr Ir. J.A.Steketee
Department of Aerospace Engineering
Delft University of Technology
Kluyverweg 1
2629 HS Delft
Netherlands

Dr R.E.Whitehead (Co-Chairman)
Head, Mechanics Division
Code 1132
Office of Naval Research
800 N. Quincy Street
Arlington VA 22217
USA

Prof. Dr T.Ytrehus
Institute of Mechanics
The University of Trondheim
N-7084 Trondheim — NTH
Norway

Mr P.R.Bignell
British Aerospace PLC
Dynamics Group, FPC 067
PO Box 5
Filton, Bristol BS12 7QW
UK

Prof. E.Reshotko
Dept. of Mechanical & Aerospace Eng.
Case Western Reserve University
10900 Euclid Avenue
Cleveland, Ohio 44106
USA

Dr G.K.Richey
Chief Scientist
Air Force Wright Aeronautical Laboratories, FS
Wright-Patterson AFB
Ohio 45433
USA

PANEL EXECUTIVE

From Europe:
Mr M.C.Fischer
AGARD-OTAN
7 rue Ancelle
92200 Neuilly-sur-Seine, France
Tel.(1)4738-5775 — Telex 610 176 (France)

From USA and Canada:
AGARD-NATO
Attn. FDP
APO New York 09777

CONTENTS

	Page
FOREWORD	iii
FLUID DYNAMICS PANEL	iv
	Reference
<u>SESSION I – FACILITIES</u> Session Chairman: P.R.Bignell	
A SURVEY OF EXISTING HYPERSONIC GROUND TEST FACILITIES – NORTH AMERICA by C.E.Wittliff	1
EUROPEAN HYPERSONIC WINDTUNNELS by J.F.Wendt	2
PREPARATION D'ESSAIS PROBATOIRES D'UN GENERATEUR DE PLASMA POUR L'ALIMENTATION D'UNE SOUFFLERIE HYPERSONIQUE par H.Consigny, C.Pacou, O.Papirnyk, Ph.Sagnier et J.P.Chevallier	3
SHOCK TUNNELS FOR REAL GAS HYPERSONICS by R.J.Stalker	4
<u>SESSION II – EXPERIMENTAL INVESTIGATIONS AND TECHNIQUES – PART 1</u> Session Chairman: C.Dujarric	
TURBULENCE MEASUREMENT IN HYPERSONIC FLOW by F.K.Owen and W.Calarese	5
EXPERIMENTAL INVESTIGATIONS ON BLUNT BODIES AND CORNER CONFIGURATIONS IN HYPERSONIC FLOW by D.Hummel	6
DRIVING MECHANISM OF UNSTEADY SEPARATION SHOCK MOTION IN HYPERSONIC INTERACTIVE FLOW by D.S.Dolling and J.C.Nario II	7
THE EFFECTS OF SWEEP AND BLUNTNESS ON A GLANCING SHOCK WAVE TURBULENT BOUNDARY LAYER INTERACTION by N.R.Fomison and J.L.Stollery	8
<u>SESSION III – EXPERIMENTAL INVESTIGATIONS AND TECHNIQUES – PART 2</u> Session Chairman: T.Ytrehus	
UNE METHODE CINEMATOGRAPIQUE ULTRA-RAPIDE POUR L'ETUDE DES SILLAGES EN TUNNEL DE TIR HYPERSONIQUE par A.Köneke, B.C.Jaeggy et G.Koerber	9
THE DRAG OF SLENDER AXISYMMETRIC CONES IN RAREFIED HYPERSONIC FLOW by T.J.Rhys-Jones	10
LOW REYNOLDS NUMBER INFLUENCE ON AERODYNAMIC PERFORMANCE OF HYPERSONIC VEHICLES by G.Koppcnwallner	11
<u>SESSION III – PROPULSION</u> Session Chairman: L.G.Napolitano	
HYPERSONIC AIRBREATHING PROPULSION: EVOLUTION AND OPPORTUNITIES by P.J.Waltrup	12
Paper 13 withdrawn	

	Reference
COMBUSTION RELATED SHEAR-FLOW DYNAMICS IN ELLIPTIC SUPERSONIC JETS by K.C.Schadow, E.Gutmark, S.Koshigoe and K.J.Wilson	14
NUMERICAL ANALYSIS OF FLOW THROUGH SCRAMJET ENGINE INLETS by A.Kumar	15
 <u>SESSION IV – CFD – PART 1 VISCOUS FLOWS</u> Session Chairman: E.Reshotko	
NUMERICAL SIMULATION OF THE HYPERSONIC FLOW AROUND LIFTING VEHICLES by Y.Rizk, D.Chaussee and J.Steger	16
SOLUTION OF SOME 3-D VISCOUS AND INVISCID SUPERSONIC FLOW PROBLEMS BY FINITE-VOLUME SPACE-MARCHING SCHEMES by H.Rieger	17
COUCHE LIMITE LAMINAIRE HYPERSONIQUE, ETUDE PARAMETRIQUE DE LA REPRESENTATION DES EFFETS DE GAZ REEL par B.Aupoix, C.Eldem et J.Cousteix	18
ON THE NUMERICAL SIMULATION OF THREE-DIMENSIONAL HYPERSONIC FLOW by S.Riedelbauch, W.Wetzel, W.Kordulla and H.Oertel Jr.	19
NUMERICAL EXPERIMENTS WITH HYPERSONIC FLOWS BENEATH A CONE-DELTA-WING COMBINATION by N.Qin and B.E.Richards	20
 <u>SESSION IV – CFD – PART 2 – INVISCID FLOWS</u> Session Chairman: J.A.Essers	
A SPATIAL MARCHING TECHNIQUE FOR THE INVISCID BLUNT BODY PROBLEM by R.T.Davis and F.G.Blottner	21
3-D EULER SOLUTION FOR HYPERSONIC MACH NUMBERS by M.Pfützner and C.Weiland	22
COMPUTATION OF FLOW PAST CONICAL HYPERSONIC WINGS USING A SECOND-ORDER GODUNOV METHOD by R.Hillier	23
AEROTHERMODYNAMICS RESEARCH AT NASA AMES by G.S.Deiwert	24
 <u>SESSION V – VEHICLES/DESIGN – PART 1 – WAVE RIDERS AND FLIGHT MECHANICS</u> Session Chairman: K.J.Orlik-Rückemann	
VORTEX FORMATION OVER DELTA, DOUBLE-DELTA AND WAVE RIDER CONFIGURATIONS AT SUPERSONIC SPEEDS by U.Ganzer and J.Szodruch	25
THE OFF-DESIGN PERFORMANCE OF HYPERSONIC WAVERIDERS by L.N.Long	26
NUMERICAL OPTIMIZATION OF CONICAL FLOW WAVERIDERS INCLUDING DETAILED VISCOUS EFFECTS by K.G.Bowcutt, J.D.Anderson Jr and D.Capriotti	27
HYPERSONIC STATIC AND DYNAMIC STABILITY OF AXISYMMETRIC SHAPES – A COMPARISON OF PREDICTION METHODS AND EXPERIMENT by R.A.East and G.R.Hutt	28
DYNAMIC STABILITY OF HYPERSONIC CONICAL LIFTING VEHICLES ACCORDING TO NEWTON-BUSEMANN THEORY by W.H.Hui and H.J.Van Roessel	29

Reference

SESSION VI – VEHICLES/DESIGN – PART 2

Session Chairman: G.K.Richey

LIFTING BODIES – AN ATTRACTIVE AERODYNAMIC CONFIGURATION CHOICE FOR HYPERVELOCITY VEHICLES by A.C.Draper and M.L.Buck	30
EXPERIENCE USING THE MARK IV SUPERSONIC HYPERSONIC ARBITRARY BODY PROGRAM by C.M.E.Fisher	31
THE RAE EXPERIMENTAL DATA-BASE FOR MISSILES AT HIGH MACH NUMBER AND ITS USE IN ASSESSING CFD METHODS by J.Hodges and L.C.Ward	32
CONCEPTS GENERAUX AERODYNAMIQUES-AEROTHERMIQUES D'HERMES par P.Perrier et Ph.Caupenne	33
HYPERSONIC AERODYNAMICS – APPLICATIONS FOR HOTOL by A.J.Wake	34
ROUND TABLE DISCUSSION	RTD

A SURVEY OF EXISTING HYPERSONIC GROUND TEST FACILITIES - NORTH AMERICA

by

C.E. Witliff
Calspan Corporation
P.O. Box 400
Buffalo, NY 14225, USA

ABSTRACT

In the past several years there has been a significant increase in the number of programs involving hypersonic vehicles, resulting in a resurgence of interest in experimental testing in hypersonic wind tunnels. Unfortunately, there are far fewer such facilities operating now than there were 10 or 15 years ago. The primary purpose of this paper is to survey the current status of hypersonic wind tunnels in North America and to describe their performance characteristics. As a part of this survey a comparison is drawn to the number and type of hypersonic wind tunnels that were active in the 1960's and 1970's relative to the current situation. Emphasis is placed on hypersonic aerodynamic and aerothermal testing and related areas. In surveying the hypersonic wind tunnels that are active in North America, all but one are located in the USA. There is a gun tunnel in Canada that will be reactivated this year.

INTRODUCTION

The 1950's and 1960's were a period of concerted effort in hypersonic research and of explosive growth in both the number and variety of hypersonic experimental facilities. The motivation came first from the development of the ballistic missile and then from the early manned space flight programs culminating in the Apollo program to land men on the Moon. During the 1970's the Space Shuttle program and unmanned probes to other planets provided support for hypersonic research. Once the design of the Space Shuttle was finalized and the design of ballistic missile reentry vehicles and planetary probes was well established, interest in hypersonics was greatly diminished. Many hypersonic experimental facilities were "mothballed", placed on indefinite standby status, or scrapped. The number of currently operational facilities is only a fraction of the number that were active in 1971. Now a broad spectrum of new programs

are under development or being considered; including ground-based hypersonic interceptors, advanced ballistic RV's, space-based aeroassisted orbital transfer vehicles, and such advanced manned space vehicles as the National Aero-Space Plane (NASP). Most of these new programs will involve experimental hypersonic research and will strain the present capabilities.

The current number of hypersonic wind tunnels in North America relative to the past is illustrated by comparing the results of surveys published in 1963 (Ref. 1), 1971 (Ref. 2), and 1985 (Ref. 3). The latter survey represents the recent status in as much as no new facilities have been built since then. However, not listed in Reference 3 is a gun tunnel that has been inactive at the National Aeronautical Establishment (NAE), Ottawa. This facility will be moved to the University of Toronto Institute of Aerospace Sciences (UTIAS) and reactivated this year. The following table lists the number of tunnels in each of the categories: continuous; intermittent (blowdown) using air or nitrogen; intermittent helium tunnels; "hotshot" (arc discharge); shock tunnels and other types. Only the facilities that were listed as active in Reference 3 are listed for 1985. Several of the other facilities have been, or are being being reactivated. Thus, the last column for 1987 represents the current status.

Table I
SUMMARY OF HYPERSONIC WIND TUNNELS

	<u>1963</u>	<u>1971</u>	<u>1985</u>	<u>1987</u>
Continuous	14	7	3	2
Intermittent (Air/N ₂)	31	32	10	15
Intermittent (He)	6	4	3	3
Hotshot	14	6	0	0
Shock Tunnel	16	14	2	2
Other	1	12	1	2
TOTAL	82	75	19	24

In 1963, 82 hypersonic facilities were listed in Reference 1 whereas the most recent compilation (Ref. 3) lists only 29 hypersonic wind tunnels in North America (all of them located in the USA). Furthermore, six of these 29 tunnels are described as being inactive or on a standby basis and four are primarily used for propulsion-related research. Since Reference 3 was published, several of the inactive tunnels have been or are in the process of being reactivated and will be included in the present summary. Nevertheless,

the number of wind tunnels available for hypersonic aerodynamic or aerothermal testing is very limited compared to the period from the late 1950's through most of the 1970's. In fact, only one major facility has been built since 1975 -- the Naval Surface Weapon Center (NSWC) Hypervelocity Tunnel 9 (Ref. 4).

There have been some notable changes in the type of hypersonic tunnels in operation as well as in the number of facilities over the period shown in Table I. First it is noted that the number of continuous wind tunnels has decreased from 14 to 2. Although at the time that Reference 3 was published there were three continuous tunnels listed, the NASA Langley Research Center (LaRC) Continuous Flow Hypersonic Tunnel is now operated only in an intermittent blowdown mode and has been renamed the 31-Inch Mach 10 Hypersonic Tunnel. The second notable feature of Table I is the total disappearance of any Hotshot tunnels and the current existence of only two Hypersonic Shock Tunnels. Intermittent (or blowdown) tunnels, which have always been the most numerous type, now dominate.

In this paper the variety and performance of the facilities reported in 1963 and 1971 will be reviewed briefly before discussing the capabilities of the currently active hypersonic tunnels. To meet the constraints of time and space, the discussion will concentrate on wind tunnels for hypersonic aerodynamic and aerothermal testing.

HISTORICAL REVIEW

The ballistic missile programs provided the motivation for significant advances in hypersonic experimental facilities beginning in the mid-1950's. The reentry of vehicles at near-orbital velocities brought to focus a wide range of flow phenomena -- the most publicized being aerothermal heating. Although aero-heating was a problem of major importance, the reentry vehicle also experienced high-altitude low-density hypersonic flows, chemically reacting nonequilibrium and equilibrium flows, and laminar and turbulent boundary layers with mass addition from an ablating surface. Extensive analytical and experimental research was undertaken to study these flow phenomena. Many new ground test facilities were developed in government, industry and university laboratories.

Hypersonic aerodynamic problems were studied in either continuous or intermittent (blowdown) wind tunnels that used a variety of techniques to heat the test gas: conventional heat exchangers, pebble-bed heaters or electrical resistance heaters. Intermittent wind tunnels using helium as the test gas were

built also. These tunnels could produce hypersonic flows without the need to heat the test gas to avoid condensation at the low static temperatures in the hypersonic free-stream. Such facilities were not suited to investigating real-gas effects or the high reentry heating rates. Those problems were best studied in short-duration, high-enthalpy wind tunnels. Shock tubes evolved into hypersonic shock tunnels and the arc-discharge (or "Hotshot") tunnel was developed. Both could provide the flow Mach numbers, total enthalpies and, in some cases, the stagnation pressures of reentry flight. However, their short flow duration precluded the study of surface material and structural response to reentry heating. Long-duration, high enthalpy arc-heated facilities were developed for studying materials for thermal protection systems. Later, the electric-arc heater was applied to intermittent wind tunnels.

Aerodynamic or ballistic ranges also underwent significant improvements in performance during this period and complemented the capabilities of the hypersonic tunnels. At NASA Ames Research Center (ARC) several unique counter-flow facilities were developed that combined a ballistic range with a shock tunnel (Ref. 2). Small models were launched upstream into the flow of a shock tunnel.

The overall performance capabilities of the various hypersonic tunnels in existence or under construction by 1963 are summarized in Figure 1 (taken from Ref. 1). This figure shows Reynolds number per foot as a function of test Mach number. Note that the Reynolds number ranges from 10 to nearly 400 million/foot and that the Mach numbers ranged from 5 to 35. In Reference 1, the facilities reported stagnation temperatures as high as 80,000 degrees R and stagnation pressures up to 100,000 psia. It will be seen in the next section that current capabilities are far more limited.

The development of hypersonic wind tunnels up to 1963 was, of necessity, accompanied by equally extensive instrumentation development programs. This was particularly true of instrumentation for the shock tunnels and hotshot tunnels with their short flow durations. During the decade following 1955, fast-response pressure transducers, heat transfer gauges, and force balances were developed. Yet data recording usually was on oscilloscopes or oscillographs and data reduction was a time-consuming process for the short-duration tunnels.

The number of hypersonic wind tunnels surveyed in 1971 (Ref. 2) is slightly smaller than the number existing in 1963 (Ref. 1); however, in this later survey only hypersonic tunnels having a test section greater than 1 ft. x

1 ft. were listed unless the tunnels were either of special interest or they represented the major wind tunnel capabilities of the reporting organization. By 1971 several new and unique facilities had appeared in addition to the counter-flow ranges at NASA Ames. Notable was the expansion tube/tunnel at NASA LaRC, described in Reference 2, in which an unsteady expansion wave rather than a shock wave was used to accelerate the test gas to hypersonic speeds. Unfortunately, this facility is no longer in operation although there has been some discussion of reactivating it in conjunction with the NASP program.

The overall performance of the hypersonic tunnels reported in 1971 is shown in Figure 2, again as Reynolds number per foot as a function of Mach number. Comparing the 1971 performance with that of 1963 (Fig. 1), it is seen that the maximum Reynolds number capability had decreased only slightly and that the Mach numbers ranged from 5 to 40. In Figure 2, the low Reynolds number scale has been truncated at 1000 because at that time only the General Electric Co. 54" Shock Tunnel (Ref. 2) could produce lower Reynolds numbers. This facility could cover $Re/ft = 100$ Mach numbers from 9 to 18 and could achieve $Re/ft = 10$ at $M = 11$. Also the performance of the NASA ARC Hyper-Velocity Free-Flight Facility (the counter-flow ranges) is not shown in Figure 2 because they are essentially ballistic range facilities rather than wind tunnels. In Reference 2, stagnation temperatures up to 80,000 degrees R and stagnation pressures up to 45,000 psia were reported by facilities that are no longer in operation.

CURRENT CAPABILITIES

In January 1985, NASA published the latest compilation of wind tunnels (Ref. 3) based on a survey that was initiated in late 1983. As mentioned previously (Table I) only 29 hypersonic wind tunnels were reported in the United States and six of them were listed as being inactive or on a standby status. Of the remaining 23, four are devoted primarily to propulsion research. Thus, in 1985 there were only 19 active facilities in the U.S. engaged in hypersonic aerodynamic or aerothermal investigations. Since then several of the six inactive wind tunnels have returned to operational status and there are plans to reactivate the others. However, there is a permanent deletion to the list of hypersonic tunnels contained in Reference 3, the 2-Ft Hypersonic Wind Tunnel of the McDonnell Aircraft Co. has been scrapped. Therefore, Reference 3 reasonably represents the current capability in the USA which amounts to the 23 aerodynamic and aerothermal hypersonic tunnels listed in Table II according to the various categories shown in Table I. The gun tunnel at the NAE, which has been inactive for many years, will be reactivated at the UTIAS this year and is included in

Table II. After some general comments about the current status, these categories will be discussed in greater detail.

Table II

SUMMARY OF CURRENT HYPERSONIC TUNNELS

<u>Designation</u>	<u>Test Section Size</u>	<u>Mach Number</u>	<u>Reynolds No./ft (Millions)</u>	<u>Stagnation*</u>	
				<u>Press (Psia)</u>	<u>Temp. (Deg. R)</u>
<u>CONTINUOUS FLOW</u>					
AEDC Tunnel B	50" Dia.	6,8	0.3-4.7	850	1350
AEDC Tunnel C	50" Dia.	10	0.3-4.7	2000	2250
<u>INTERMITTENT (Air OR N₂)</u>					
NASA LaRC 8' High Temp. #	96" Dia.	5.8-7.2	0.3-2.2	2400	3600
NSWC Tunnel No. 9 (N ₂)	60" Dia.	10, 14	0.06-20	20000	3660
NASA ARC 3.5' Hyper. W.T.	42" Dia.	5, 7, 10	0.3-7.4	1955	3460
Grumman 36" Hyper. W.T.	36" Dia.	8, 10, 14	0.2-4.5	2000	3000
NASA 31" Mach 10 W.T.	31" Square	10	0.4-2.4	1800	1810
Lockheed CA. 30" Hyp. W.T.	30" Dia.	8	0.42.1	550	1400
NSWC Tunnel No. 8A (N ₂)	24" Dia.	18	0.2-0.6	8800	3700
NSWC Tunnel No. 8	17"-11" Dia.	5, 6, 7, 8	0.7-60	2205	1460
NASA LaRC 20" Mach 6 W.T.	20"x20.5"	6	0.5-10.5	550	1018
AFWAL 20" Hyper. W.T.	20" Dia.	12, 14	0.4-1.0	1600	2000
NASA LaRC M=8 Var. Density	18" Dia.	8	0.1-12	3000	1510
Sandia Labs. 18" Hyp. W.T.	18" Dia.	5, 8, 14	0.2-9.7	3000	2500
NASA LaRC Hyper. N ₂ W.T.	16" Dia.	18	0.17-0.40	6000	3500
NASA LaRC Mach 6 High Re.	12" Dia.	6	1.8-50	3200	1060
AFWAL Mach 6 High Re. No.	12" Dia.	6	10-30	2100	1100
<u>INTERMITTENT (Helium)</u>					
NASA LaRC M=20 High Re.	60" Dia.	16.5-18	1.9-15	2000	540
NASA LaRC Aerodyn. Leg	22.5" Dia.	17.6-22.2	1.1-11.3	3000	860
NASA LaRC Fl. Mech. Leg	22"/36" Dia.	20/40	1.3-6	2000	860
<u>INTERMITTENT (CF₄)</u>					
NASA LaRC Hyper. CF ₄ W.T.	20" Dia.	6	0.3-0.5	2500	1260
<u>SHOCK TUNNELS</u>					
Calspan 96" Hyper. S.T.	24"/48"	6.5-24	0.001-75	20000	11500
Calspan 48" Hyper. S.T.	24"/48"	6.5-20	0.006-40	5400	5800
<u>GUN TUNNELS</u>					
UTIAS	12" Dia.	8.3-12.5	12 max.	5200	3800

* Maximum stagnation pressure and temperature

Test gas is combustion product of methane and air

The status of the Northrup Corp. 30-inch and the FluidDyne 20-inch hypersonic tunnels, listed as inactive in Reference 3, is unchanged and they are not included in Table II. The FluidDyne pebble-bed heater is used now as a static test facility.

There are no hotshot tunnels listed in the latest survey and the only shock tunnels listed are those at Calspan Corp. However, the Lockheed California Co., which once had a shock tunnel with a 100" diameter test section (Ref. 2) that was scrapped, is currently working on plans for a new smaller shock tunnel. The NASA Langley expansion tube/tunnel is no longer in operation although there have been proposals recently to reactivate it.

The Reynolds number-Mach number performance map for current facilities, shown in Figure 3, covers a noticeably more restricted range than the performance capabilities that existed in 1963 (Fig. 1) and 1971 (Fig. 2). Because there are far fewer facilities than there were in the earlier surveys, the performance of the individual tunnels are shown rather than an overall envelope. There are such a large number of tunnels in the $M = 6$ to 8 range that no attempt has been made to identify them individually in Figure 3. An exception is the NASA LaRC 8' High Temperature Tunnel because of its large 8-foot exit diameter nozzle. Although the test gas in this facility is the combustion products of methane and air, the tunnel has been used to study detailed flow and heating phenomena on large structures. Several other tunnels are noted in Figure 3 because of their significance. They are the NSWC Tunnels No. 8A and 9, the NASA LaRC Hypersonic Nitrogen Tunnel, the three NASA LaRC Helium Tunnels and the two Calspan Hypersonic Shock Tunnels. The performance of these shock tunnels is represented by an overall envelope because they use three different nozzles each with a number of nozzle throats of varying diameter to obtain the range of Mach number depicted.

In comparing Figure 3 with the previous Figures 1 and 2, two areas of restricted performance are most striking. First, is that fact that the $M = 40$ nozzle of the Fluid Mechanics Leg of the NASA LaRC Hypersonic Helium Tunnel represents the only capability for operating at above $M = 24$, and that facility does not utilize that nozzle on a routine basis. Second, low Reynolds number operation is available only in the two Calspan shock tunnels (Ref. 5). This is primarily a result of the emphasis in recent years on high Reynolds number, turbulent boundary layer research. The NSWC Hypervelocity Tunnel 9 was designed specifically as a high Reynolds number facility (Ref. 4). Recent improvements in that facility were directed at extending the $M = 10$ performance to higher Reynolds numbers (Ref. 6) and the $M = 14$ performance to lower Reynolds numbers (Ref. 7).

The investigation of real-gas effects in air requires high stagnation enthalpies (or stagnation temperatures). The Calspan shock tunnels are the only wind tunnel facilities currently capable of stagnation temperatures of 3800 degrees R and above and flow velocities greater than 7000 ft/sec. An alternative approach to studying real-gas effects is embodied in the NASA LaRC Hypersonic CF_4 Tunnel (Ref. 8), CF_4 or Tetrafluoromethane (Dupont Freon 14) has an effective specific heat ratio of 1.12, and hence the flow fields over models experience large density changes across shock waves typical of high temperature, chemically reacting air flows. Thus, the CF_4 Hypersonic Tunnel ($M = 6$) can be used to simulate high temperature airflows (Ref. 9).

In general all of the current facilities listed in Table II have the capability of measuring aerodynamic forces, pressure distributions, and heat transfer and have some type of flow visualization system. Dynamic stability measurement capability is reported for the AEDC Tunnels B and C and the Sandia Labs. 18" Hypersonic Tunnel.

CONTINUOUS HYPERSONIC TUNNELS

It can be noted in Table II that the Tunnels B and C at AEDC are the only current continuous tunnels. Both have 50-inch diameter test sections, interchangeable contoured axisymmetric nozzles, model injection systems and are variable density tunnels. Although it is not listed in Table II, Tunnel C also has a 24-inch diameter Mach 4 nozzle which provides true temperature capability at that Mach number. Current improvements include adding a 24-inch diameter Mach 8 nozzle for Tunnel C which will give it Mach 8 capability at a higher total temperature than Tunnel B.

INTERMITTENT TUNNELS

The intermittent tunnels listed in Table II have test times ranging from about 1 sec. (NSWC Tunnel 9) to many minutes (NSWC Tunnel 8 and NASA LaRC Hypersonic Nitrogen Tunnel). It has been noted that, although the NASA LaRC 8-foot High Temperature Tunnel has been listed in Table II among the air and nitrogen tunnels, in fact the test medium is the combustion products of burning methane in air. There are plans to add oxygen enrichment so that the tunnel can be used for combustion testing. The addition of Mach 4 and 5 nozzles to this facility is planned also. The NSWC Tunnel 9 is the newest of all hypersonic tunnels and is in wide demand because of its large 60-inch diameter test

section, its Mach 10 and 14 capability, and its high Reynolds numbers. At the time Reference 3 was published, the NASA ARC 3.5-foot Hypersonic Tunnel was on a standby basis, it has since been reactivated and has a heavy test schedule.

The largest number of hypersonic tunnels at any single location is at the NASA Langley Research Center. In addition to the 8-ft High Temperature Tunnel, there are nine other intermittent tunnels listed in Table II. These include four air tunnels, three helium tunnels, one nitrogen tunnel, and the CF₄ (Freon) tunnel. This complex of tunnels is very active and there are plans for upgrading their performance, flow quality, and measurement capability. It is noted in Figure 3 that the NASA LaRC Helium Tunnels provide higher Reynolds numbers than any of the air or nitrogen tunnels at Mach numbers above 15.

SHOCK TUNNELS

The two Calspan Hypersonic Shock Tunnels differ primarily in the size of their test chambers (48" and 96") and their maximum stagnation pressure capability as noted in Table II. Both use the same set of nozzles; 24-inch Mach 8 contoured, 48-inch Mach 16 contoured, and 48-inch conical. Nozzle throats of various diameters are used to cover the Mach number range indicated (Table II and Figure 3). As mentioned previously these are the only current facilities having stagnation temperatures greater than 3800 deg. R. In a shock tunnel the test time is measured in milliseconds rather seconds; however a steady flow of 1 msec can correspond to several body lengths of flow. Thus, only fast response transducers are necessary to obtain valid data. Such instrumentation was developed in the period from 1955 to 1965.

Like many of the other currently active hypersonic wind tunnels, the Calspan facilities are being heavily used and have a backlog of programs extending into 1988.

CURRENT CHALLENGES

In the Introduction it was mentioned that there are a number of new programs involving hypersonic vehicles: ground-based interceptors, advanced ballistic RV's, space-based aeroassisted orbital vehicles (AOTV), and advanced manner space vehicles such as the Aero-Space Plane to mention only a few. An important question is: How adequate are the present hypersonic wind tunnels in relation to the testing needs of these programs? The flight regimes of these vehicles are shown in the Altitude-Velocity map of Figure 4. Also shown for reference is the altitude-velocity duplication capability of the Calspan 96"

Shock Tunnel which is the only currently active tunnel in which flow velocities of 10000 ft/sec or greater can be obtained. This tunnel can fully duplicate velocity and altitude in the region indicated in Figure 4. At velocities above 7000 ft/sec it can duplicate the ambient density to even lower altitudes than it can provide full duplication. This latter capability is significant for flow phenomena governed by the Mach number independence principle. On this basis such a tunnel can cover most of the flight regime of the interceptor vehicle and the lower altitude region of Shuttle-like vehicle. Velocities appropriate to a long-range ballistic RV or an AOTV cannot be achieved in any of the facilities described in this paper. Although they are not treated in this review, ballistic ranges and arc-heater facilities can provide the velocity or the corresponding total enthalpy for 20000 ft/sec. However, such facilities have other shortcomings with regard to aerodynamic testing. Thus, we are faced with the question of what really must be duplicated. What is an acceptable simulation? Rather thorough discussions of similitudes are given in References 10 and 11.

Simulation of inviscid flow phenomena requires duplication of the Mach number, the vehicle geometry, and (strictly speaking) the specific heat ratio (Ref. 10), while Reynolds number duplication is required for boundary layer effects. The Reynolds number/ft. and Mach number for the vehicles shown in Figure 4 are compared with the existing hypersonic tunnels in Figure 5. For the interceptor vehicle and the Ballistic RV, full or nearly full-scale models can be tested in the larger facilities, while models of a Shuttle or an AOTV are more likely to be 1% or 2% scale. In Figure 5, the current wind tunnels can match the Mach and Reynolds numbers for almost all of the interceptor flight regime and for portions of the Ballistic RV and Shuttle trajectories. The Mach number requirements for the AOTV really exceed current capabilities except for the seldom used Mach 40 nozzle of the one NASA LaRC helium tunnel.

In Figure 5 it would appear that simulation for AOTV vehicles is beyond the scope of the hypersonic tunnels described herein. However, the AOTV flight regime is in reality beyond the region of thin boundary layers where only Reynolds number matching is important. The flow fields over such vehicles will be dominated by low density phenomena and viscous interactions. In this region, the viscous interaction parameter \bar{V} (proportional to MA/\sqrt{Re}) may provide the necessary simulation for other than real-gas phenomena. It has been found that this parameter, when modified to include the Chapman-Rubesin viscosity factor C , (i.e. $\bar{V}' = MC/\sqrt{Re}$) provides the best correlation of the aerodynamic coefficients for the Shuttle during hypersonic high altitude flight (Ref. 12). In fact the

high altitude performance aerodynamics of several classes of AOTV's have been predicted in terms of this interaction parameter (Ref. 13).

Assuming a characteristic dimension for an AOTV of 40 feet, the corresponding Reynolds number would range from approximately 20000 to 450000 for the perigee altitudes between 300 Kft and 240 Kft shown in Figure 4 and the viscous interaction parameter would vary from about 0.22 to 0.05. For a 2.5%-scale model (1-foot), this range of values for \bar{V} could be matched at Mach numbers between 10 and 20 with Reynolds numbers/foot ranging from 2000 to about 20,000 as shown in Figure 5. All of these values are within the range of the shock tunnels and partially overlap the capabilities of three other hypersonic tunnels. These simulations would not address the real-gas phenomena however.

Although these new vehicles will undoubtedly make use of the existing hypersonic wind tunnels, there is certainly need for more advanced facilities. A recent review of the requirements of wind tunnels for future aeronautical systems (Ref. 14) defined the need for a large high performance shock tunnel and a shock tube/expansion tube as well as for a facility that could provide the data needed for airframe propulsion integration.

HYPersonic TESTING AND COMPUTATIONAL FLUID DYNAMICS

The role of experiment in the development of Computational Fluid Dynamics (CFD) has been receiving considerable attention in recent years (e.g. Ref. 15). There is no doubt that now and in the future most of the testing in hypersonic facilities will be for the purpose of verifying CFD codes. This type of testing will require facility improvements in the areas of flow quality and instrumentation, particularly important is the development of nonintrusive measurement techniques to obtain flow field data such as density, temperature or species distributions.

SUMMARY

It has been the objective of this paper to provide a survey of existing hypersonic wind tunnels in North America. By comparing the currently active hypersonic tunnels with those reported in 1963 and 1971, the decline in number has been vividly illustrated. While there is a significant capability still in existence and these tunnels are very active in testing some of the new vehicles, there is a definite need for improved capability in two specific areas: high enthalpy facilities to study real-gas effects and high Mach number low-density facilities to better address the flow fields over AOTV-type vehicles.

REFERENCES

1. F.A. Vicente and N.S. Foy, "Hypersonic Wind Tunnel Facilities in the United States," Aerospace Corporation, Rept. No. TOR-169 (3305)-1, Revision 1, October 1963.
2. C.J. Pirrello, et al., "An Inventory of Aeronautical Ground Research Facilities, Vol. 1-Wind Tunnels," McDonnell Aircraft Co., NASA CR-1874, November 1971.
3. F.E. Penaranda and M.S. Freda, "Aeronautical Facilities Catalogue, Vol. 1 - Wind Tunnels," NASA RP-1132, January 1985.
4. J.A.F. Hill, "Hypervelocity Wind Tunnel: Test Planning Guide," Naval Surface Weapons Center Rept. NSWC/WOL/MP 76-2, January 1976.
5. Anon., "Hypersonic Shock Tunnel-Description and Capabilities," Calspan Corp., no no., originally published April 1965.
6. R.A. Kavetsky and J.A.F. Hill, "Mach-10 High Reynolds Number Development in the NSWC Hypervelocity Facility," AIAA Paper 85-0054, January 1985.
7. E.R. Hedlund and W.C. Ragsdale, "Improvements in Low Reynolds Number Testing in the NSWC Hypervelocity Wind Tunnel #9," AIAA Paper 85-0226, January 1985.
8. R.E. Midden and C.G. Miller, "Description and Calibration of the Langley Hypersonic CF₄ Tunnel," NASA TP-2384, March 1985.
9. R.A. Jones and J.L. Hunt, "Use of Tetrafluoromethane to Simulate Real-Gas Effects on the Hypersonic Aerodynamics of Blunt Vehicles," NASA TR R-312, June 1969.
10. W.D. Hayes and R.F. Probstein, Hypersonic Flow Theory, Academic Press, New York, 1959.
11. C.E. Wittliff, et al., "Study of High-Density Hypervelocity Flows and Similitudes," Calspan Corp., AEDC Rept. No. AEDC-TR-67-72, April 1967.
12. W.C. Woods, et al., "A Review of Preflight Estimates of Real-Gas Effects on Space Shuttle Aerodynamic Characteristics," Shuttle Performance: Lessons Learned, NASA CP 2283 Part 1, pg. 309, March 1983.
13. A.W. Wilhite, et al., "Performance Aerodynamics of Aeroassisted Orbital Transfer Vehicles," AIAA Paper 84-0405, January 1984.
14. M.L. Buck and T.R. Sieron, "Future Requirements of Wind Tunnels for Aeronautical Systems Development," AIAA Paper 86-0751, March 1986.
15. J.G. Marvin, "Future Requirements of Wind Tunnels for Computational Fluid Dynamics Code Verification," AIAA Paper 86-0752, March 1986.

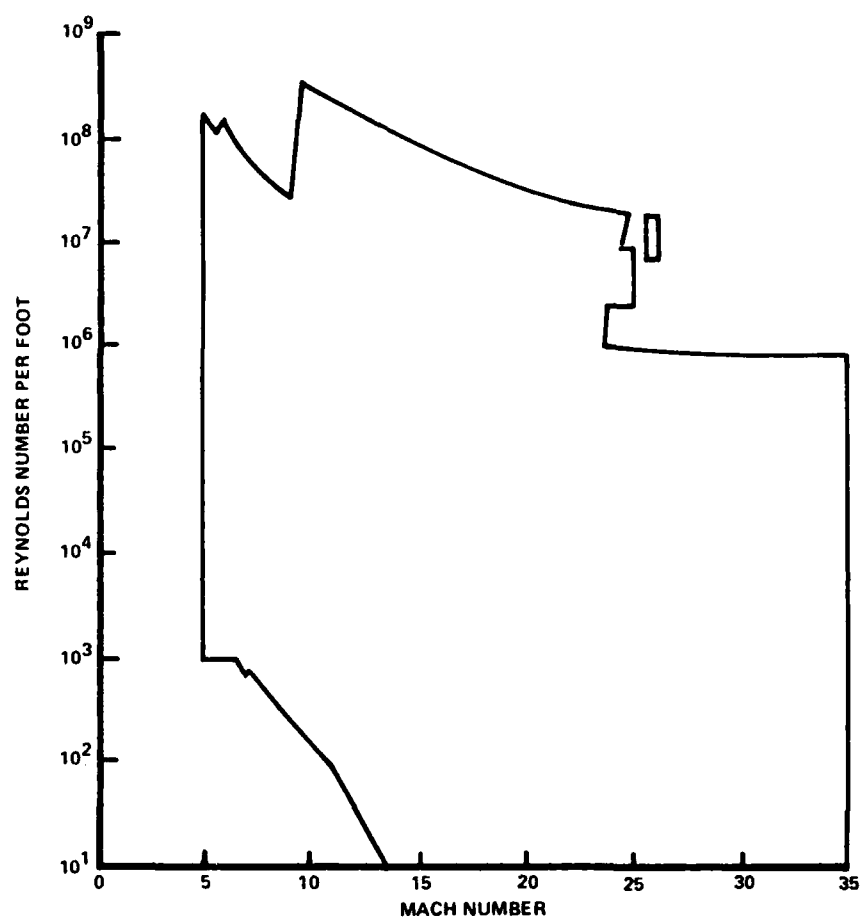


Figure 1 PERFORMANCE MAP OF HYPERSONIC FACILITIES IN 1963

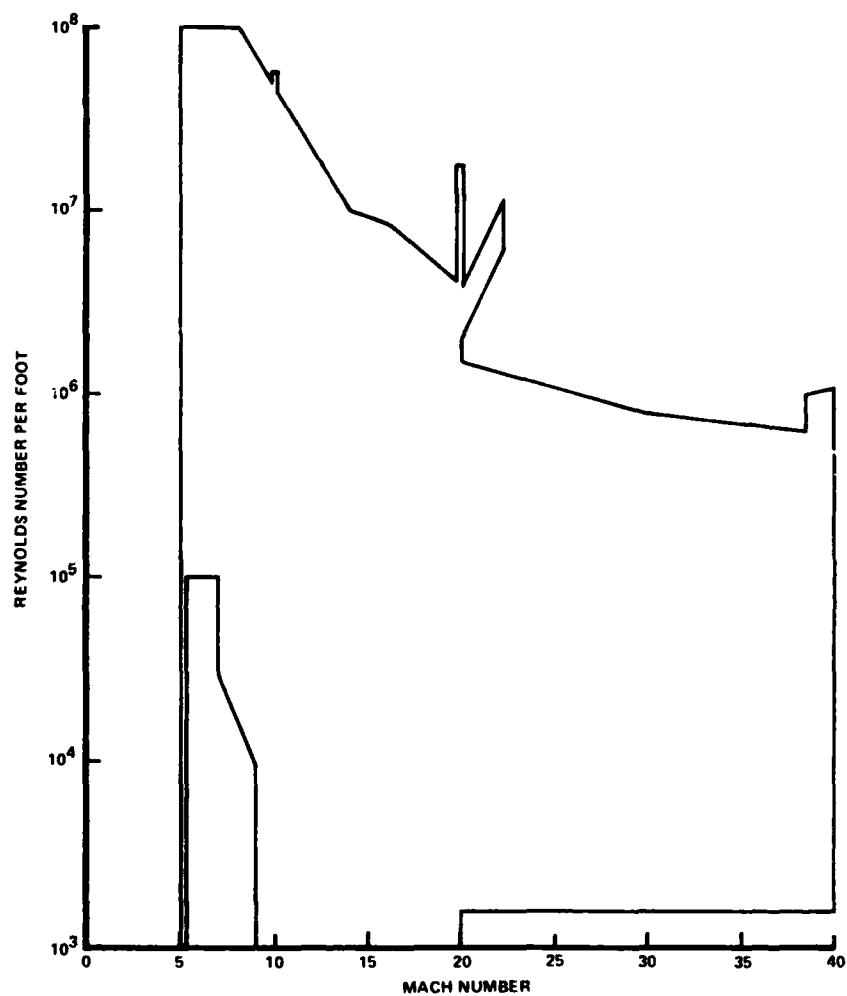


Figure 2 PERFORMANCE MAP OF HYPERSONIC FACILITIES IN 1971

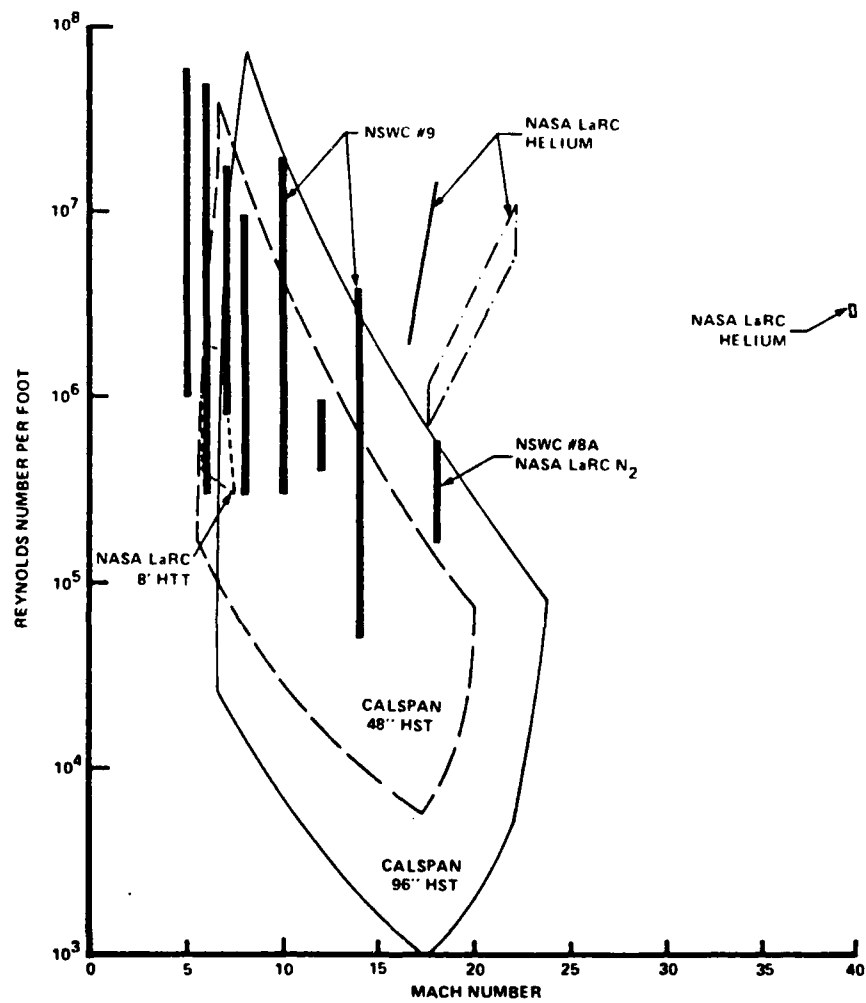


Figure 3 PERFORMANCE MAP OF HYPERSONIC FACILITIES IN 1985

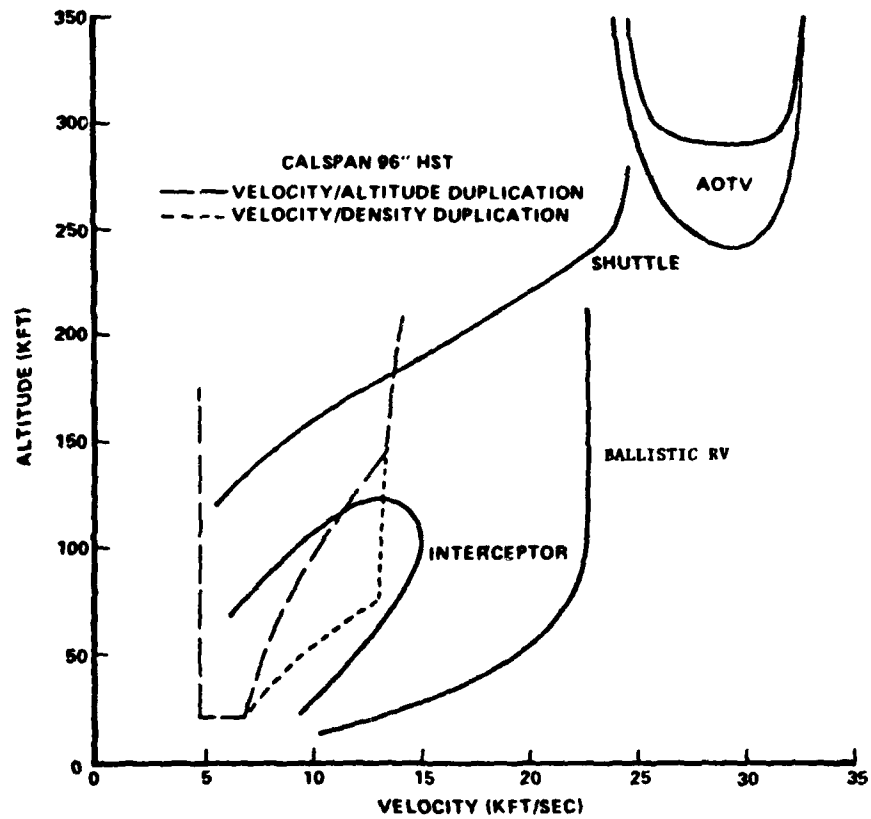


Figure 4 VELOCITY-ALTITUDE COMPARISON OF FLIGHT VEHICLES WITH SHOCK TUNNEL CAPABILITY

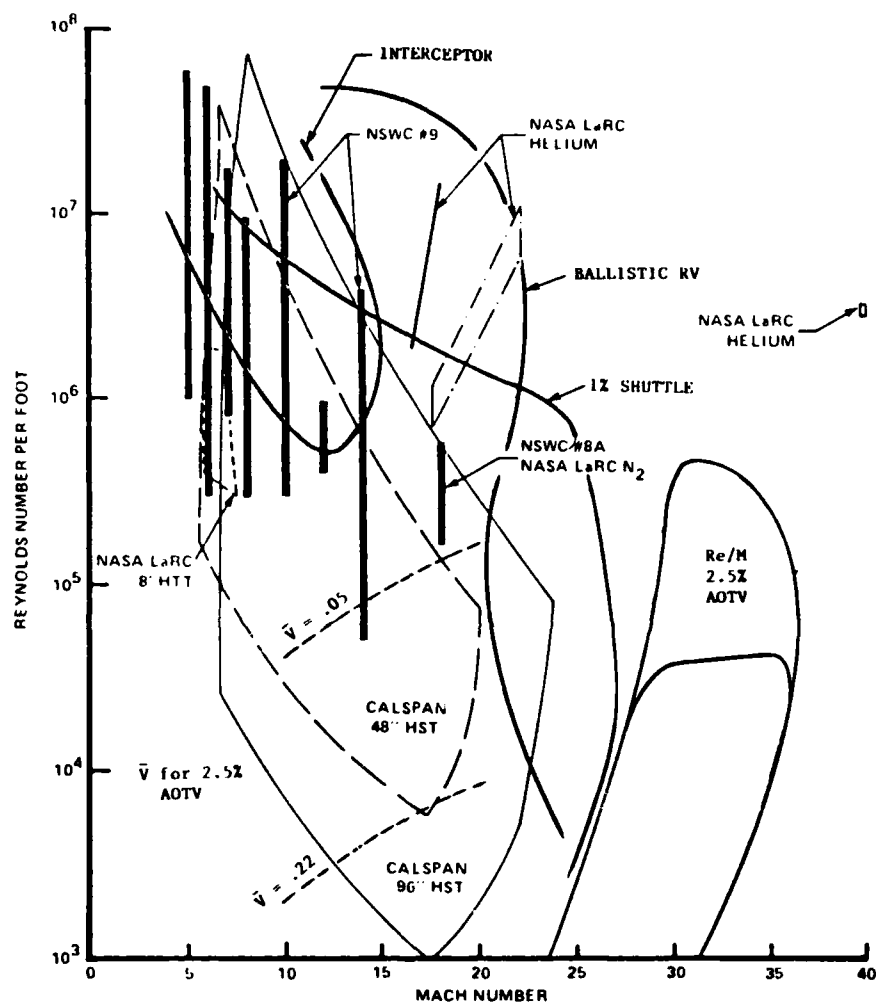


Figure 5 REYNOLDS NUMBER – MACH NUMBER COMPARISON OF FLIGHT VEHICLES WITH CURRENT HYPERSONIC TUNNELS

EUROPEAN HYPERSONIC WIND TUNNELS

J.F. WENDT

VON KARMAN INSTITUTE FOR FLUID DYNAMICS
B - 1640 RHODE SAINT GENÈSE - BELGIUM

1. INTRODUCTION

Although the hypersonic flow regime will probably be the first to be dominated by computational techniques [1] due to serious experimental simulation problems, the next generation of lifting reentry vehicles will still rely on wind tunnels not only for design validation but also to verify computer codes through benchmark test cases. Evidence for this statement is the proposal to utilize European hypersonic tunnels for upwards of 2000 occupancy days from 1986 to 1993 on the HERMES project. Basic research in hypersonics required for the post-HERMES era (e.g. HOTOL, NASP, Sanger, etc.) will also rely heavily on wind tunnels and their associated instrumentation [2]. Thus, it is appropriate to review the present status of hypersonic tunnels. Since a companion paper will deal with the status of facilities in the U.S. [3], this contribution will be restricted to the European scene.

The text briefly discusses the requirements for flow simulation in the hypersonic regime and then summarizes the present situation. Gaps are identified and suggestions for improvements are put forward.

2. FLOW REGIMES IN HYPERSONIC REENTRY

The flow regimes for various hypersonic vehicles are most conveniently illustrated by means of trajectories on the altitude-velocity plot shown in Fig. 1. NASA's STS, ESA's HERMES and Britain's HOTOL provide three examples of reentry from earth orbit. Aero-assisted orbital transfer vehicles would appear in the upper right hand corner of this figure.

Since quantities such as stagnation temperature, unit Reynolds number, stagnation point heat transfer and air dissociation can be expressed as functions of density (and therefore of altitude) and velocity, lines of constant values of these parameters may be superimposed on such a plot. (Lines of constant Mach number could also have been plotted; to a first approximation they would be vertical at $V_\infty = M_\infty(0.3) \text{ km/s.}$) The wide range of flow conditions through which a given orbital reentry vehicle must pass is obvious: from the rarefied regimes characterized by $M_\infty/Re_\infty L > 1$ to the hypersonic turbulent boundary layer regimes for which $Re/m = O(10^6)$. Stagnation temperatures may exceed 5000-6000 K and the air in stagnation regions will be largely dissociated.

3. REQUIREMENTS FOR HYPERSONIC FLOW SIMULATION AND RESEARCH

While the gas dynamic/chemical kinetic equations describing reentry flows can be made non-dimensional to form similarity parameters which can be used in turn to relate the results of tunnel tests to flight predictions, it is well known that not all of the resulting non-dimensional groups can be respected simultaneously. J. Leith Potter, a noted reentry aerodynamicist formerly with AEDC, is quoted as saying "aerodynamic modeling is the art of partial simulation". In other words, the vehicle designer must use engineering judgement to determine which parameters will dominate each part of the hypersonic regime.

A study of the equations of fluid dynamics, combined with considerable fundamental research, has demonstrated that hypersonic aerodynamics can be subdivided into the following regimes:

- the Mach number regime from Mach 6 to Mach 12 or 15 wherein the most important similarity parameters are the Mach number and the Reynolds number;
- the hypervelocity regime wherein real gas effects including chemical reactions such as dissociation are important and for which only duplication of the dimensional variables density times length and velocity is acceptable;
- the rarefied regime, characterized by values of $M/\sqrt{Re} > 0.01$.

The ratio of wall temperature T_w to freestream temperature T_∞ must also be duplicated in wind tunnels to properly simulate both the boundary layer thickness and the state of the boundary layer; i.e., laminar, transitional or turbulent. Here we are somewhat fortunate; T_w/T_∞ in hypersonic flight may vary from 3 to 10. Since most hypersonic wind tunnels expand the working gas to very low values of T_∞ and the model temperature T_w remains of the order of room temperature during the test, the requirement on T_w/T_∞ duplication can be met to first order in many short duration facilities.

The heat loads on structures must also be duplicated in ground test facilities. Because of the difficulty of achieving Mach, Reynolds and heat load (or true total temperature) simulation simultaneously, it is generally accepted that temperature (enthalpy) and pitot pressure are the essential parameters and thus heat loads are studied in high pressure, low Mach number arc or plasma jet facilities.

The requirements on hypersonic test facilities were summarized by Jaarsma and de Wolf [4] more than a decade ago. Their principal conclusions concerning reentry vehicles are just as valid today as they were then:

- for development testing, model lengths should be at least 30 cm to provide ample instrumentation. Final configuration studies may require at least some tests with models (or partial models) of 50 cm in length or more. If high incidence is necessary, and this is likely for $M > 6$, the nozzle diameter may need to be as much as twice the model length to avoid wall or free shear layer interference. Thus, facilities with nozzle diameters of order 0.5 to 1 meter will be essential and of course must operate at the correct Mach and Reynolds numbers. Smaller facilities will still play a vital role in providing, at modest cost, basic research results, "first looks" at new designs, and test conditions for instrumentation developments;
- due to finite flow establishment times, the running time of any facility should be such that its product with model length is of order of 5 milliseconds-meter; thus, using the above factor of two for the ratio of nozzle diameter to model length, it follows that 1 meter facilities should have a running time of at least 10 milliseconds;
- as force measurements will constitute an important aspect of design work, the limitations on internal balances in terms of response times should be considered. While Jaarsma and de Wolf state that test times of order 50 milliseconds or more will be necessary to accurately measure forces on models of lengths in excess

of 50 cm, it is felt by many investigators today that improvements in balance design and compensation techniques may allow this limitation to be reduced to a few milliseconds.

- accurate and detailed dynamic stability measurements with large, complex (moveable flaps, etc.) models will require even longer testing times than those mentioned above, probably some seconds at a minimum;
- the accurate determination of transition location will require "quiet" tunnels.

The above discussion has concentrated on wind tunnel requirements; however, it is obvious that the best wind tunnel will be useless if proper instrumentation is not available. All the classical techniques utilized in commercial transport and combat aircraft design will be required for the hypersonic vehicles: internal strain gauge balances for forces and moments, dynamic stability rigs, multi-port pressure techniques with rapid scan capabilities, surface and flow visualization techniques, etc. The hot flows and/or short running times which characterize most hypersonic facilities pose problems in some of these areas as mentioned above. Heat transfer distributions will be determined with thin film or thin-skin techniques which are now well known. The ability to identify regions on complex shapes which might be susceptible to high local heat transfer (embedded vortices, shock-shock or shock-boundary layer interaction, etc.) will be very important; thermal sensitive paints, liquid crystals, and so forth are proving to be very useful in this regard. Non-intrusive techniques to measure flow temperatures and species concentrations will be essential as a means to validate or correct codes incorporating dissociation/recombination reactions.

A final requirement, which is often overlooked, is the availability of trained personnel - both engineers and technicians. Productive wind tunnels are those in which a team of people have been working together for at least a few years and which is supported by an instrumentation branch. Experience in running facilities; in selecting appropriate measurement techniques compatible with data needs, tunnel characteristics and data handling systems; and in the development of new measurement techniques cannot be purchased; it must be developed in-house and systematically utilized.

4. CHARACTERISTICS OF EUROPEAN HYPERSONIC WIND TUNNELS

The essential characteristics of European hypersonic wind tunnels are noted in the appendix; arbitrarily, only facilities with a nozzle exit diameter greater than 20 cm and a Mach number of five or more have been included. Of course, smaller facilities will continue to play an important role in fundamental research and training.

As Mach and Reynolds number are acknowledged to be important simulation parameters, a selection of the facilities from the appendix has been transposed to Fig. 2 on which are shown the flight regimes of the NASA-ST5, HERMES, HOTOL and MAIA. The characteristic length scale in the Reynolds number for the facilities has been taken as one-half the nozzle exit diameter for the reasons described above. Note that the S4MA M=12 nozzle will only be available in 1988, that some portions of the area identified as "Aachen" for the T.H. Aachen shock tunnel represent predictions, that the RAE shock tunnel and the DFVLR-G Ludwig tube C are currently not in use; etc.

Furthermore, with the renewed interest in hypersonics, some of the facilities are undergoing major renovations and up-dating so that their characteristics are in a state of flux; an example is the VKI Longshot which is being fitted with a contoured Mach 15 nozzle. Finally, a major new facility, the R6 of ONERA is in the detailed planning stage; its predicted performance in the Mach 12-20 range will allow tests at Reynolds numbers which are within a factor of two from the HERMES flight case.

A plot of $\rho u L$ versus velocity in Fig. 3 shows that only two facilities even come close to simulating the expected reacting flows and one of them, R6, as mentioned above, is only in the planning stage. As can easily be deduced as well from Fig. 3, a ρu versus V_∞ plot will show that at best the T.H. Aachen and R6 facilities will provide adequate coverage to about 5 km/s.

5. COMMENTARY ON PRESENT STATUS

While the capabilities of Europe's hypersonic wind tunnels appear adequate on a Mach-Reynolds plot (Fig. 2), many important tunnel characteristics are not made apparent in such a presentation. For example, all the facilities operating at M>12 are characterized by running times measured in milliseconds which results in much poorer measurement accuracies than in low Mach tunnels. Correspondingly, productivity is low and cost per data point is high. Many of these tunnels have conical nozzles and thus strong axial gradients. All intermittent tunnels are, to some degree, "dirty" and the erosive effects on instrumentation may be severe. Finally, flow expansions to high Mach number generally lead to "freezing" of vibration and dissociation, except for the facilities with very high reservoir pressures, and the result is a non-equilibrium freestream whose detailed characteristics often are not well known.

A major deficiency is apparent in velocity duplication, essential for an accurate simulation of chemical effects. T.H. Aachen's shock tunnel seems to come closest to meeting present needs and the predicted performance of R6 Chalais makes it look particularly interesting because of its much longer running time, measured in seconds.

While it is clear that existing (renovated) facilities will play the major role in the HERMES program, it is also clear that time is available to design and construct new facilities for programs with a longer time-scale. It is the author's opinion that emphasis should be placed on:

- a large (≥ 2 m) blowdown facility with Mach numbers to 8-10, reservoir pressures to 200 bar and running times of the order of 10 seconds for detailed configuration testing;
- a high velocity facility, perhaps based on the "Stalker tube" concept as proposed recently by Hornung of the DFVLR-Göttingen;
- a "real gas" facility similar to the CF4 tunnel at NASA Langley to simulate certain blunt body and high incidence effects.

Because of the important need to validate CFD codes for future hypersonic designs, high quality tunnel flows and accurate, non-intrusive instrumentation capabilities will become increasingly important elements in a sound overall program for hypersonic research and development.

Therefore, efforts should continue in the search for "quieter" hypersonic tunnels so as to better duplicate boundary layer transition. The ability to measure local species concentrations and temperatures at high flow speed in short duration facilities is a goal worthy of efforts at a much higher level than currently pursued. Finally, trained personnel - researchers and tunnel engineers - may very well be the most important problem in the whole present-day picture and, if so, its resolution deserves immediate attention.

6. CONCLUSIONS

Europe possesses a large range of hypersonic facilities which, when renovation and modifications currently underway are completed, will constitute a sound basis for Mach-Reynolds simulation. New facilities are needed over the long term to allow refined design studies and to simulate at least some aspects of real gas effects. Non-intrusive instrumentation to aid in code validation and the enhancement of training programs are equally essential elements in a balanced program of hypersonic research and development.

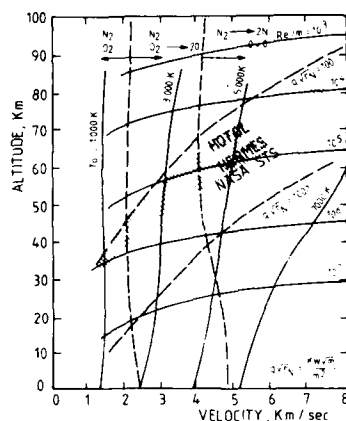
ACKNOWLEDGEMENTS

This paper is based on a report prepared for the European Space Agency under ESA Contract No 5477/83/F/FC(SC) - March 1984 entitled "Aerothermodynamics for Future Launchers : Review of the State of the Art in Europe" and authored by J.F. Wendt and J.A. Essers. The encouragement and assistance of H. Pfeffer of ESA who acted as the contract's technical manager is gratefully acknowledged.

All centers in Europe with an important capability in hypersonics responded to one or more questionnaires concerning facility characteristics and status; their actions are much appreciated.

REFERENCES

1. Influence of computational fluid dynamics upon experimental facilities : a 15 year projection. U.S. National Academy of Sciences, March 1983.
2. Workshop in advanced space transportation technology. Rome, March 16-17, 1987.
3. WITTLIFF, C.E.: A survey of existing hypersonic ground test facilities - North America. AGARD Symposium on Aerodynamics of Hypersonic Lifting Vehicles, Bristol, UK, April 6-9, 1987.
4. JAARSMA, F. & de WOLF, W.B.: Facilities for aerodynamic testing at hypersonic speeds in problems of wind tunnel design and testing. AGARD R 600, December 1973.



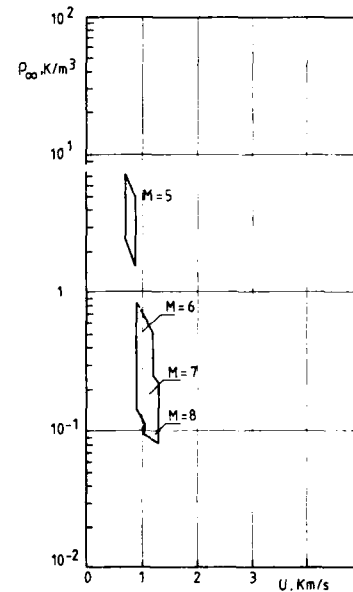
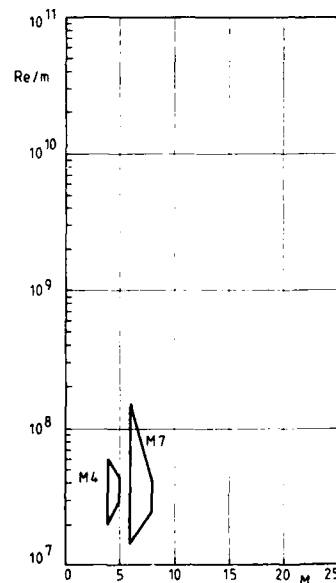
ARA M4 & M7 BLOWDOWN TUNNEL

Organization : Aircraft Research
Association (ARA)
Location : Manton Lane
Bedford MK41 7PF; U.K.

Contact : Mr A.B. Haines
Tel. : (0234) 50681
Telex: 825056
FAX Groups 2 & 3 0234 328584

CHARACTERISTICS

	Blowdown Tunnel M4	Blowdown Tunnel M7
MACH NUMBER	4 to 5 (2D)	7 (contoured)
NOZZLE EXIT DIAMETER, cm	30x40	31
RUNNING TIME	30 s (max)	48 s (max)
SUPPLY PRESSURE, bars	10 to 20	100 to 150
SUPPLY TEMPERATURE, K	380	700
No TESTS/DAY	6 (max)	6 (max), typically 3
PRESENT STATUS	low level	low level
PERSONNEL REQUIRED	2	2
MEASUREMENT TECHNIQUES	force balances, pressures, dynamic measurements (pitch) schlieren	force balances, pressures, dynamic measurements (pitch) schlieren
CHANNELS OF DATA	10 (currently) 16 (near future)	10 (currently) 16 (near future)
COMMENTS		can be adapted with new nozzle pieces to function at M=6 or M=8
CURRENT ACTIVITIES : jet slot blowing ahead of and normal to a surface to develop stand-off shocks ahead of sensitive surfaces; aerodynamic coefficients and in some instances pressure distributions on project shapes		



BAE G.W. TUNNEL

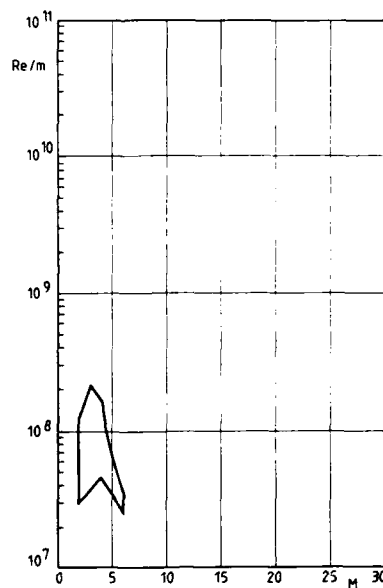
Organization : British Aerospace
 Location : British Aerospace
 The GW Wind Tunnel, W258
 Preston, Lancs PR4 1AX; U.K.

Contact : J.A. Smith
 Tel. : (0772) 63 33 33, Ext. 2831
 Telex: 67627

CHARACTERISTICS

MACH NUMBER	1.7-6.0 (contoured)
NOZZLE EXIT DIAMETER, cm	46x46
RUNNING TIME	10 to 200 s
SUPPLY PRESSURE, bars	35 (max, at M=6)
SUPPLY TEMPERATURE, K	475 (max)
NO TESTS/DAY	4-5
PRESENT STATUS	in regular use
PERSONNEL REQUIRED	6
MEASUREMENT TECHNIQUES	force balances, pressures, heat transfer. Continuous pitch and roll traverses during data acquisition
CHANNELS OF DATA	60 off-line, linked to VAX 11/780

CURRENT ACTIVITIES : aerodynamics of fin-stabilized shells and slender delta planforms;
 behaviour of lateral thrusters; lifting reentry shapes



CEAT H 210 BLOWDOWN TUNNEL

Organization : Centre d'Etudes Aérodynamiques
et Thermiques

Contact : Prof. T. Alziary de
Roquefort

Location : CEAT
route de l'Aérodrome, 43
F-86000 Poitiers, France

Tel. : (49) 58 37 50

MACH NUMBER	7 and 8
REYNOLDS NUMBER	1.3-9.2×10 ⁶ (M=7)
BASED ON EXIT D	1.5-4.2×10 ⁶ (M=8)
NOZZLE EXIT DIAMETER, cm	21
RUNNING TIME	~ 2-3 min
SUPPLY PRESSURE, bars	22-100
SUPPLY TEMPERATURE, K	600-800
No TESTS/DAY	6
PRESENT STATUS	in use
PERSONNEL REQUIRED	2
MEASUREMENT TECHNIQUES	force balances, heat transfer pressure, schlieren
CHANNELS OF DATA	20 on-line

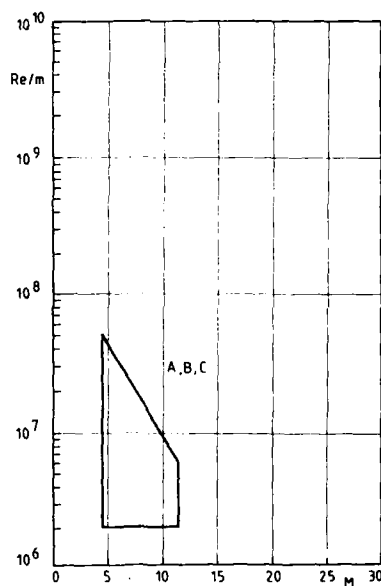
DFVLR-AVA TUBE TUNNELS A, B, C

Organization : Deutsche Forschungs- und
Versuchsanstalt für Luft-
und Raumfahrt, Göttingen
Location : DFVLR-AVA
Bunsenstrasse, 10
D-3400 Göttingen, FR Germany

Contact : Dr G. Koppenwallner
Tel. : (0551) 709 - 2123

CHARACTERISTICS

	Ludwig Tube A	Ludwig Tube B	Ludwig Tube C
MACH NUMBER	2.8, 4.5 (contoured)	5, 6, 7 (contoured)	9, 10, 11 (contoured)
NOZZLE EXIT DIAMETER, cm	50x50 (rect)	50	50
RUNNING TIME	350 ms	300 ms	300 ms
SUPPLY PRESSURE, bars	10 (max)	36 (max)	120 (max)
SUPPLY TEMPERATURE, K	400 (max)	650 (max)	1100 (max)
NO TESTS/DAY	20	20	20
PRESENT STATUS	regular use	regular use	inactive
PERSONNEL REQUIRED	2	2	2
MEASUREMENT TECHNIQUES	force balances, heat transfer using thin skin and liquid crystals schlieren, oil flow		
CHANNELS OF DATA	10 off-line	10 off-line	10 off-line
COMMENTS	design principle means that tunnel noise level is low. Flow establishment times from 10-30 ms		



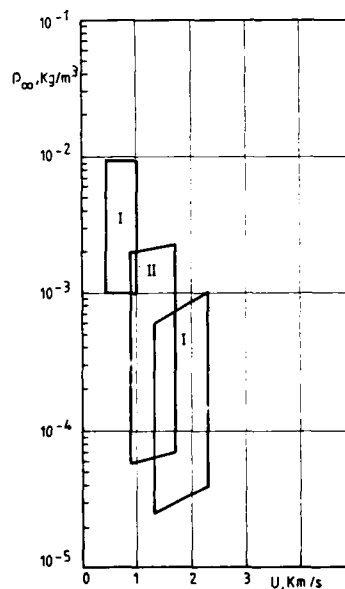
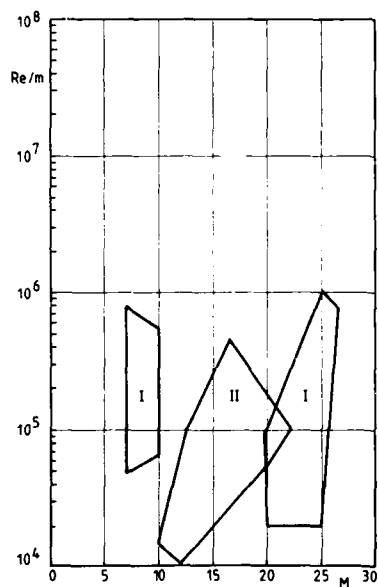
DFVLR-AVA VACUUM TUNNELS I, II, III

Organization : Deutsche Forschungs- und Versuchsanstalt für Luft-
Raumfahrt, Göttingen
Location : DFVLR-AVA
Bunsenstrasse, 10
D-3400 Göttingen, FR Germany

Contact : Dr G. Koppenwallner
Tel. : (0551) 709 - 2123

CHARACTERISTICS

	<u>Vacuum Tunnel I</u>	<u>Vacuum Tunnel II</u>	<u>Vacuum Tunnel III</u>
MACH NUMBER	7-25 (conical)	10-25 (conical)	6-25 (free jet)
NOZZLE EXIT DIAMETER, cm	25 (useful core: 10-20)	40 (useful core: 20-30)	free jet of $\phi \leq 25$
RUNNING TIME	one hour	one hour	continuous
SUPPLY PRESSURE, bars	0.1-500	0.2-50	0.005-15
SUPPLY TEMPERATURE, K	300-2500	300-1800	300-850
NO TESTS/DAY	N.A.	N.A.	N.A.
PRESENT STATUS	not used as wind t.	not used as wind t.	in regular use
PERSONNEL REQUIRED	2	2	2
MEASUREMENT TECHNIQUES	force balances, heat transfer, pressure measurements	heat transfer	force balances, heat transfer
CHANNELS OF DATA	16 on-line	16 on-line	16 on-line
COMMENTS			$Re_p < 1000$, mean free paths to 20 mm



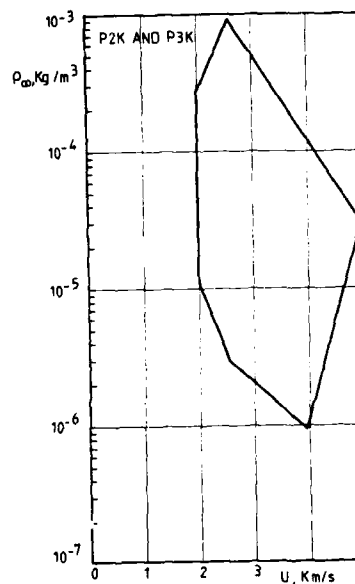
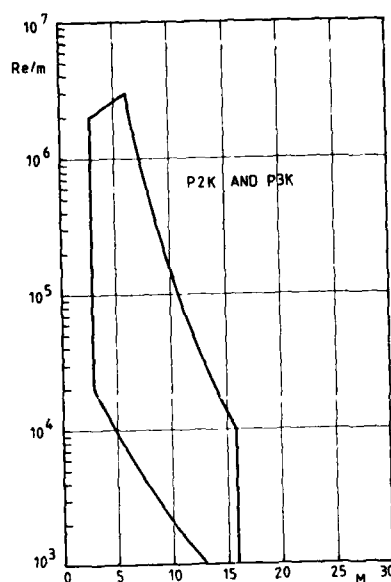
DFVLR HA-KW ARC HEATED TUNNELS PK2 & PK3

Organization : Deutsche Forschungs- und
Versuchsanstalt für Luft-
und Raumfahrt, Köln-Porz
Location : D.F.V.L.R.
Hauptabteilung Windkanäle
Abteilung Köln-Porz
Postfach 90 60 58
D-5000 Köln 90, FR Germany

Contact : Mr H. Esch
Tel. : (02203) 60 11

CHARACTERISTICS

	<u>PK2</u>	<u>PK3</u>
MACH NUMBER	3 - 16 (conical)	3 - 14 (conical)
NOZZLE EXIT DIAMETER, cm	60 (useful core : ~42)	60 (useful core : ~42)
RUNNING TIME	continuous	continuous
SUPPLY PRESSURE, bars	10 (max)	30 (max)
SUPPLY TEMPERATURE, K	6000	7000
GAS	air, N ₂ , A, He	air
PRESENT STATUS	used regularly but for different applications	operational, but not used
PERSONNEL REQUIRED	5	5
MEASUREMENT TECHNIQUES	force balances, pressures, flow visualization with r.f. and electron beam, heat trans- fer, electron beam	pressures, heat transfer, flow field probes
COMMENTS	open jet test section of 2.6 m diameter	open jet test section of 4 m ³



DFVLR HA-KW HYPERSONIC TUNNEL H2K

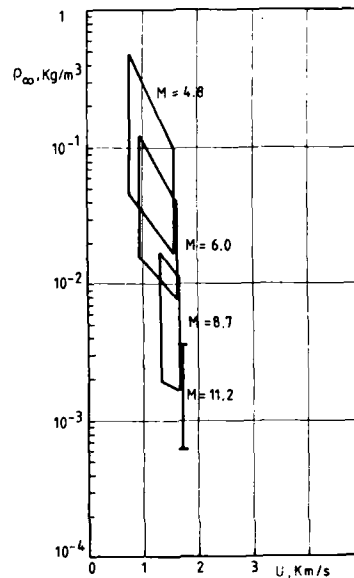
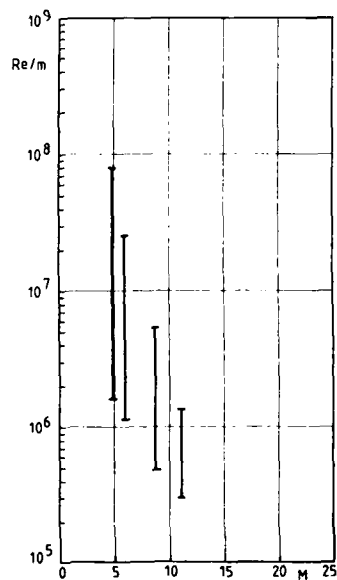
Organization : Deutsche Forschungs- und
Versuchsanstalt für Luft-
und Raumfahrt,

Contact : Mr H. Esch
Tel. : (02203) 60 11

Location : D.F.V.L.R.
Hauptabteilung Windkanäle
Abteilung Köln-Porz
Postfach 90 60 58
D-5000 Köln 90, FR Germany

CHARACTERISTICS

MACH NUMBER	4.8, 6, 8.7, 11.2 (contoured)
NOZZLE EXIT DIAMETER, cm	60 (< 40 useful)
RUNNING TIME	20 s
SUPPLY PRESSURE, bars	3 - 45
SUPPLY TEMPERATURE, K	1400 (max)
GAS	air
PRESENT STATUS	in use
PERSONNEL REQUIRED	4
MEASUREMENT TECHNIQUES	force balances, pressures, schlieren, infrared camera, thermal paints
COMMENTS	open jet test section of 2 m diameter



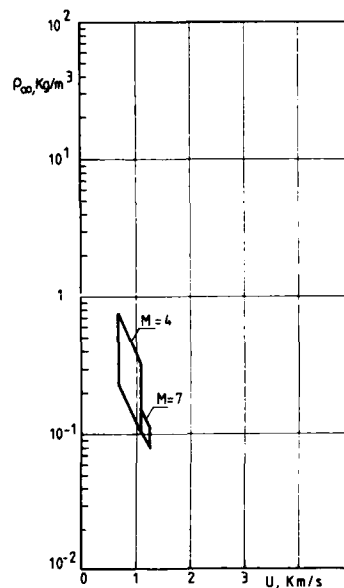
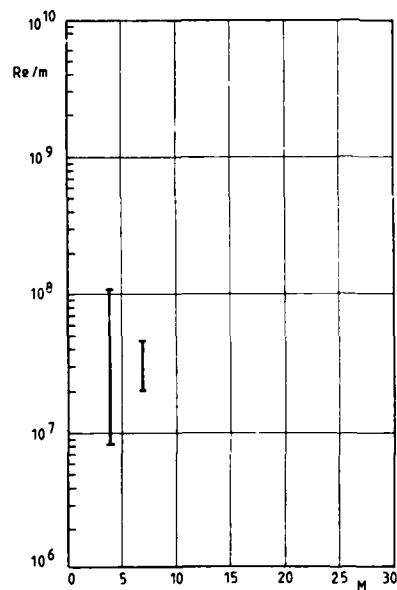
FFA HYP 500 BLOWDOWN TUNNEL

Organization : The Aeronautical Research
Institute of Sweden (FFA)
Location : FFA
Box 11021
S-16111 Bromma, Sweden

Contact : Mr S. Lundgren
Tel. : +46 8 759 10 00
Telex: S-10725

CHARACTERISTICS

MACH NUMBER	4 and 7 (contoured)
NOZZLE EXIT DIAMETER, cm	50
RUNNING TIME	at Re max : 80 s (M=4); 200 s (M=7)
SUPPLY PRESSURE, bars	10-22 (M=4); 110 (M=7)
SUPPLY TEMPERATURE, K	800 design, 600 norm
No TESTS/DAY	8
PRESENT STATUS	operational
PERSONNEL REQUIRED	4-5
MEASUREMENT TECHNIQUES	force balances (α to 35°), $4^\circ/\text{s}$ sweep rate, pressure distribution, heat transfer, schlieren, model injection system
CHANNELS OF DATA	64 on-line (48 low-level; 16 high level)
COMMENT	open jet
CURRENT ACTIVITIES	the tunnel has been restarted and reentry studies are planned. Concurrent numerical analysis is also intended.



I.C. GUN TUNNEL AND N₂ TUNNEL

organization : Imperial College
 Location : Dept. Aeron.-Imperial College
 Prince Consort Road
 London, SW7 2BY; U.K.

Contact : Dr J.K. Harvey
 Tel. : (01) 5895111, Ext. 4011
 Telex: 261503

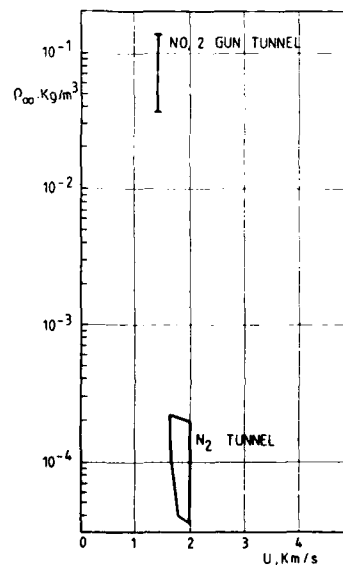
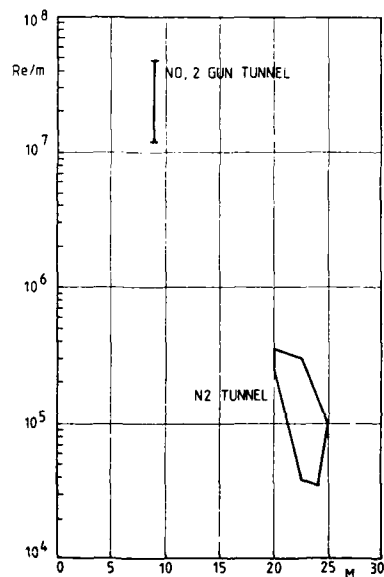
CHARACTERISTICS

	No 2 Gun Tunnel	Heated N ₂ Tunnel
MACH NUMBER	9 (contoured)	20 - 25 (conical)
NOZZLE EXIT DIAMETER, cm	45 (useful core : 25)	20 (useful core : 7.5)
RUNNING TIME	5 ms	continuous
SUPPLY PRESSURE, bars	550 (max)	25 - 500
SUPPLY TEMPERATURE, K	1070	2000 (max)
No TESTS/DAY	4	
PRESENT STATUS	in use	in regular use
PERSONNEL REQUIRED	2	2
MEASUREMENT TECHNIQUES	pressures, heat transfer, schlieren, electron beam	pressures, electron beam (ρ_w, T_{rot}), heat transfer
CHANNELS OF DATA	24 on-line	16 on-line
COMMENTS	1 m ³ open jet test section. Incidence to 25°	a model injection system is available. Model incidence to 45°

CURRENT ACTIVITIES: Research into rarefied flow centres around the Monte-Carlo simulation method. A 3D code has been developed and used to calculate the flow around a blunt-ended cylinder and a spherically blunted cone both at angle of attack at a Knudsen number ≥ 0.06 . Experimental verification has shown that the predictions for the former shape at zero incidence are precise. Experiments are in progress to measure the lift and drag acting on, and the density distribution about, a cone at incidence at $M=25$.

Hypersonic aerodynamics conducted at $M=9$ in the Gun Tunnel is concentrated on a study of the flow in an annular rectangular cavity on a conical body.

Euler codes are being developed with improved shock capturing routines and these are being used to calculate unsteady blast problems and conical hypersonic flows.

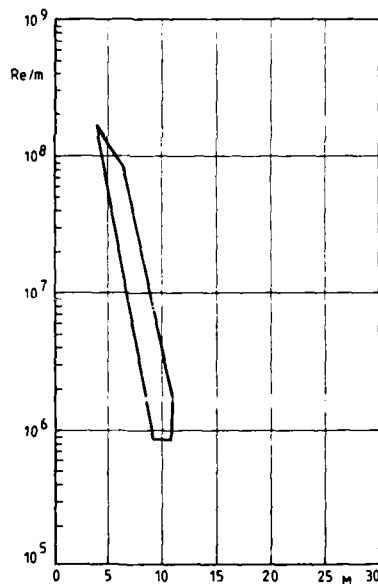


ISL - HYPERSONIC SHOCK TUNNEL

Organization : Institut de Saint-Louis	Contact : G. Smeets
Location : Institut de Saint-Louis	Tel. : 89.69.50.00
12, rue de l'Industrie	Telex: 881386
Boîte Postale No 301	
F-68301 Saint-Louis Cédex, France	

CHARACTERISTICS

MACH NUMBER	4 - 11 (conical)
NOZZLE EXIT DIAMETER, cm	20x20
RUNNING TIME	< 1 ms
SUPPLY PRESSURE, bars	400 (max)
SUPPLY TEMPERATURE, K	7000 (max)
GAS	air
No TESTS/DAY	4
MEASUREMENT TECHNIQUES	interferometry, heat transfer
COMMENTS	the tunnel will be transformed for aeroballistic studies, but the above characteristics will be attainable if desired



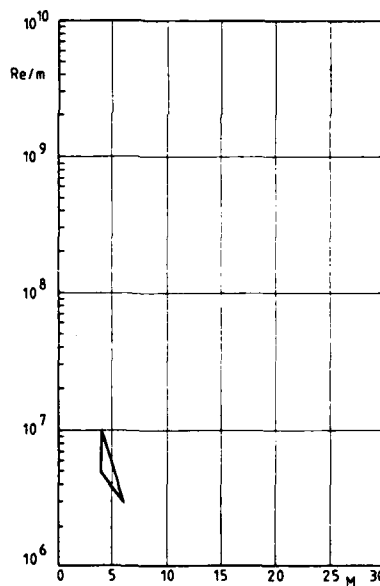
NLR CONTINUOUS SUPERSONIC TUNNEL - CSST

Organization : Nationaal Lucht- en Ruimtevaartlaboratorium
 Location : N.L.R.
 Anthony Fokkerweg, 2
 NL-1059 CM Amsterdam, Netherlands

Contact : Mr S.J. Boersen
 Tel. : (20) 51'5113

CHARACTERISTICS

MACH NUMBER	1.2 - 6.0 (contoured)
NOZZLE EXIT DIAMETER, cm	20x27
RUNNING TIME	continuous (~ 30 min)
SUPPLY PRESSURE, bars	39
SUPPLY TEMPERATURE, K	500
No TESTS/DAY	N.A.
PRESENT STATUS	operational
PERSONNEL REQUIRED	5
MEASUREMENT TECHNIQUES	force balances, pressure distribution, store separation, flutter, mass flow, heat transfer
CHANNELS OF DATA	24 off-line, but results in minutes



Organization : Laboratoire de Recherches Contact : M. Desgardin,
 Balistiques et Aérodynamiques Service Aérodynamique
Location : L.R.B.A. Tel. : 32.21.07.40
 Boîte Postale 914 Telex: LRBA VERN 770817
 F-27207 Vernon Cédex, France

MACH NUMBER	8-16 (conical) 16 (contoured)
REYNOLDS NUMBER	0.26×10^6 /m to 2.9×10^6 /m
NOZZLE EXIT DIAMETER, cm	120 (useful core : 30-60)
RUNNING TIME	10 to 20 ms
SUPPLY PRESSURE, bars	30 to 350
SUPPLY TEMPERATURE, K	1,800 to 2,400
NO TESTS/DAY	3 to 4
PRESENT STATUS	in regular use
PERSONNEL REQUIRED	3
MEASUREMENT TECHNIQUES	force balances, pressure distributions, schlieren
CHANNELS OF DATA	20 analog channels at 50 KHz acquisition with HP 1000 (disc, plotter, ...)
COMMENTS	the C ₂ reflected shock tunnel is normally operated with the Mach 16 contoured nozzle
CURRENT ACTIVITIES :	used intensively for the measurement of the aerodynamic coefficients of reentry shapes

ONERA R2Ch & R3Ch BLOWDOWN TUNNELS

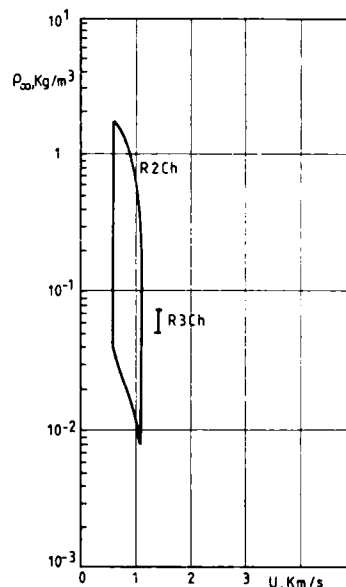
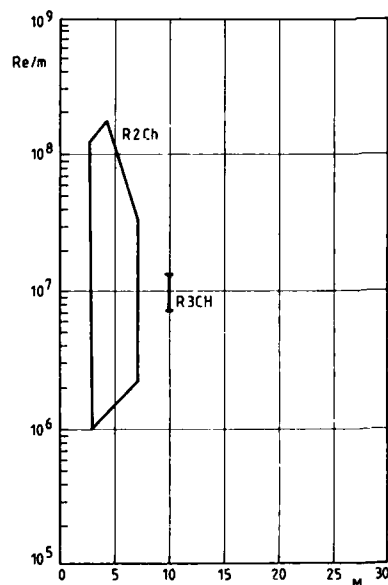
Organization : Office National d'Etudes et de Recherches Aérospatiales
 Location : ONERA-Châtillon
 Boîte Postale 72
 F-92322 Châtillon Cédex, France

Contact : M.C. Capelier
 Tel. : (1) 46.57.11.60
 Telex: ONERA 260907F

CHARACTERISTICS

	R2Ch	R3Ch
MACH NUMBER	3, 4, 5, 6, 7 (contoured)	5, 7, 10 (contoured)
NOZZLE EXIT DIAMETER, cm	19 (M=3, 4) 32.7 (M=5, 6, 7) (useful core : 18 to 29.7)	32.7 (M=5, 7) 34.7 (M=10) (useful core : 22.7 at M=10)
RUNNING TIME	35 s	35 s (10 s at M=10)
SUPPLY PRESSURE, bars	$0.4 < P_1 < 80$	$1.5 < P_1 < 170$
SUPPLY TEMPERATURE, K	$300 < T_1 < 650$	$400 < T_1 < 1100$
No TESTS/DAY	4	4
PRESENT STATUS	regular use	regular use
PERSONNEL REQUIRED	5	5
MEASUREMENT TECHNIQUES	force balances; pressure distributions; heat transfer; local skin friction Visualization : schlieren; wall streamlines; thermosensitive paints	force balances; pressure distributions; heat transfer; local skin friction Visualization : schlieren; wall streamlines; thermosensitive paints
CHANNELS OF DATA	25	25
COMMENTS		starting time : 3 ms sweep rate : $50^\circ/10$ s

CURRENT ACTIVITIES : boundary layer transition with roughness effects, shock boundary layer interactions on a range of two and three dimensional shapes, aerothermodynamic testing on reentry configuration



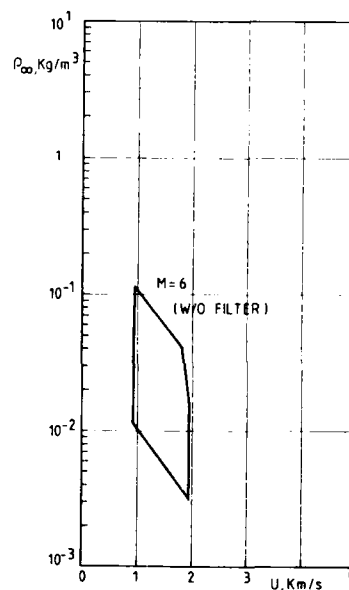
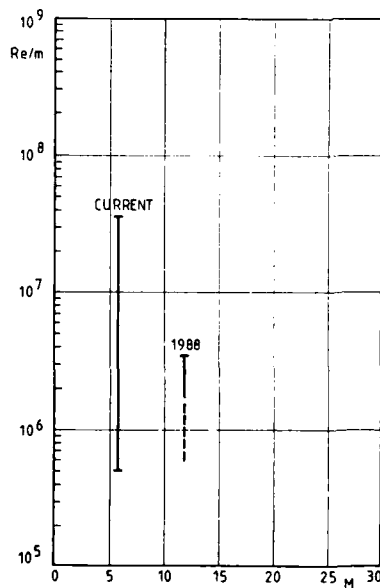
ONERA S4MA BLOWDOWN TUNNEL

Organization : Office National d'Etudes et de Recherches Aéronautiques
 Location : ONERA-Centre de Modane-Avrieux
 Boîte Postale No 25
 F-73500 Modane, France

Contact : M. Laverre
 Tel. : (1) 79 20 30 55
 Telex:

CHARACTERISTICS

	Current S4MA	S4MA Predictions for M 12 nozzle
MACH NUMBER	6 (contoured)	12 (contoured)
NOZZLE EXIT DIAMETER, cm	68 (useful core : 48)	100 (useful core : 60)
RUNNING TIME	50 s - 90 s	30 s
SUPPLY PRESSURE, bars	42 (max)	150 (max)
SUPPLY TEMPERATURE, K	$T_i < 1850$	$T_i < 1850$
GAS	air	air
No TESTS/DAY	2 - 5	2 - 5
PRESENT STATUS	operational for hypersonic tests but possibility of use for airbreathing engines or air intake tests	operational end 1988
PERSONNEL REQUIRED	6	6
MEASUREMENT TECHNIQUES	force balances, pressures, heat transfer, shadowgraph	
CHANNELS OF DATA	48	
COMMENTS	the maximum temperature of the heater is 1850 K. In the case of a filter upstream of the nozzle, the temperature is 1100 K for the Mach 6 nozzle and will be about 1500 K for the Mach 12 nozzle. Currently, S4MA has an open jet test chamber of 2.1 m x 2.8 m cross section and a length of 2.8 m	



OXFORD GUN TUNNEL

Organization : University of Oxford
 Location : Engineering Laboratory
 Parks Road
 Oxford, OX1 3PJ; U.K.

Contact : Prof. D.L. Schultz
 Tel. : (865) 246 561 or 722 274

CHARACTERISTICS

MACH NUMBER	6, 8, 9 (contoured)
REYNOLDS NUMBER based on exit D	12×10^6 (M=6); 6.4×10^6 (M=8); 2.5×10^6 (M=9)
NOZZLE EXIT DIAMETER, cm	16 (M=6); 28 (M=8); 30 (M=9)
RUNNING TIME	50 to 80 ms
SUPPLY PRESSURE, bars	130 (max)
SUPPLY TEMPERATURE, K	720
NO TESTS/DAY	8 (max)
PRESENT STATUS	operational
PERSONNEL REQUIRED	2
MEASUREMENT TECHNIQUES	normal force (with free flight), heat transfer, schlieren
CHANNELS OF DATA	64 on-line
COMMENTS	the tunnel has recently undergone a conversion to the LICH mode (Ludwig tube with Isentropic Compression Heating) yielding M=8.25 and very uniform pressures for 30-40 ms. Conversion to the gun tunnel mode can be made in 1 week.

R A E 3'x4' TUNNEL

Organization : Royal Aircraft Estab.
Location : R.A.E. - 3'x4' Tunnel
Bedford, Beds; U.K.

Contact : Dr L.F. East
Tel. : (0252) 24461; Ext. 2719
Telex: 858134

CHARACTERISTICS

MACH NUMBER	2.5 - 5.0 (contoured)
REYNOLDS NUMBER based on exit D	35×10^6 (max. at M=4.5)
NOZZLE EXIT DIAMETER, cm	91x122
RUNNING TIME	continuous
SUPPLY PRESSURE, bars	0.4 - 12
SUPPLY TEMPERATURE, K	N.A.
No TESTS/DAY	N.A.
PRESENT STATUS	operational
PERSONNEL REQUIRED	N.A.
MEASUREMENTS TECHNIQUES	N.A.
CHANNELS OF DATA	N.A.

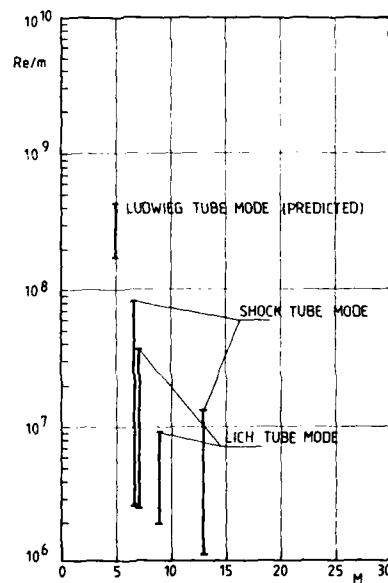
R A E SHOCK TUNNEL

Organization : Royal Aircraft Estab.
 Location : R.A.E. Farnborough
 Hants, GU14 6TD

Contact : Dr L.F. East
 Tel. : (0252) 24461; Ext. 2719
 Telex: 858134

CHARACTERISTICS

	Shock Tube Mode	LICH Tube	Ludwig Tube Mode
MACH NUMBER	7,9,10,13 (conical) 9,13 (contoured)	7,9 (conical)	5 (contoured)
REYNOLDS NUMBER PER METER	$8.7 \times 10^7 - 2.7 \times 10^6$ (M=7) $1.3 \times 10^7 - 1.1 \times 10^6$ (M=13)	$3.7 \times 10^7 - 2.5 \times 10^6$ (M=7) $8.9 \times 10^6 - 1.9 \times 10^6$ (M=9)	$4.3 \times 10^8 - 1.7 \times 10^8$
NOZZLE EXIT DIAMETER, cm	36 (useful core : 20)	36 (useful core : 20 at M=7 15 at M=9)	23 (useful core : 20)
RUNNING TIME	3 to 10 ms (tailored reflected shock)	100 ms	100 ms
NO TESTS/DAY	4	4	4
MEASUREMENT TECHNIQUES	heat transfer, schlieren	heat transfer, pressure, forces, schlieren	heat transfer, pressure, schlieren
CHANNELS OF DATA	17 on-line	17 on-line	17 on-line
PERSONNEL REQUIRED	2	2	2
PRESENT STATUS	not used since 1983	operational	not yet commissioned
COMMENTS	the shock tunnel is currently operating in the LICH mode at M=7 with a 0.38 m by 0.38 m working section. External tube heating to about 250°C maximum is available for LICH and Ludwig tube operation. A larger open-jet working section and model incidence setting equipment will be available by mid-1987. Operating conditions for the Ludwig tube are those projected.		



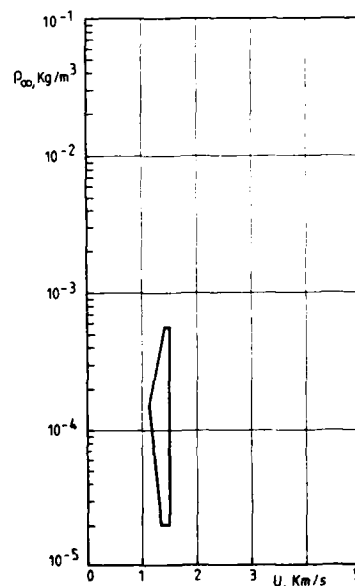
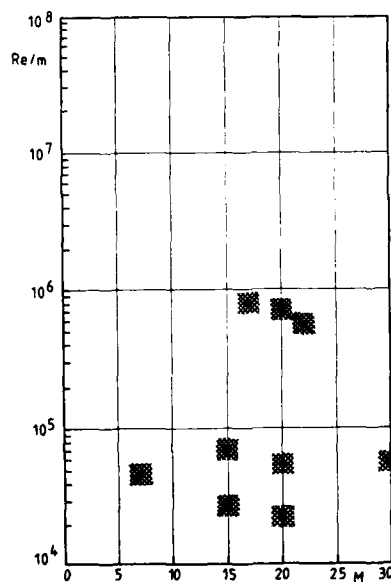
SESSIA/CNRS SR3 TUNNEL

Organization : SESSIA/CNRS
 Location : Laboratoire d'Aérodynamique
 du CNRS
 4ter Route des Gardes
 F-92190 Meudon, France

Contact : Dr J. Allègre
 Tel. : 45 34 75 50

CHARACTERISTICS

MACH NUMBER	2 to 30
NOZZLE EXIT DIAMETER, cm	15 at M=7; 36 at $15 < M < 30$ (useful core : 10-15)
RUNNING TIME	continuous
SUPPLY PRESSURE, bars	up to 120
SUPPLY TEMPERATURE, K	up to 1,500
PRESENT STATUS	in regular use in the supersonic and hypersonic range, mainly at Mach numbers 15 and 20
PERSONNEL REQUIRED	3
MEASUREMENT TECHNIQUES	force balances, heat transfer (thermocouples, infrared system), pressure transducers, electron gun (for local density measurement and visualization)
CHANNELS OF DATA	6 to 20
CURRENT ACTIVITIES :	As flows from continuum to transitional regimes may be produced, high altitude aerodynamics has been emphasized such as stage separation of launchers and satellite direction control. Hypersonic reentry aero- dynamics is now under study.



SOUTHAMPTON ISENTROPIC LIGHT PISTON TUNNEL

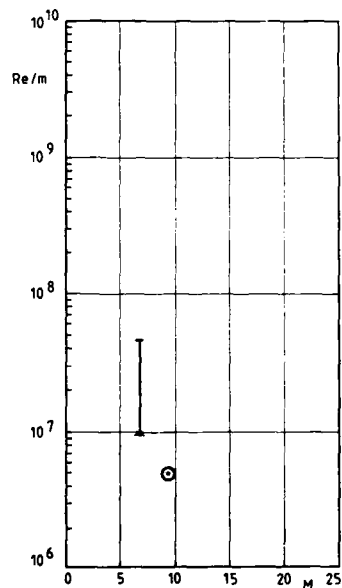
Organization : The University of
Southampton
Location : Department of Aeronautics &
Astronautics
The University
SOUTHAMPTON SO9 5NH, U.K.

Contact : Prof. R.A. East
Tel. : (0703) 559122; Ext. 2324

CHARACTERISTICS

MACH NUMBER	6.85 (contoured)	9.4
NOZZLE EXIT DIAMETER, cm	21 (useful core : 17)	21 (useful core : 17)
RUNNING TIME	1 s	0.28 s (usable)
SUPPLY PRESSURE, bars	90	60
SUPPLY TEMPERATURE, K	600	995
No TESTS/DAY	5	5
PRESENT STATUS	regular use	to date, one calibration condition only
PERSONNEL REQUIRED	3	3
MEASUREMENT TECHNIQUES	dynamic stability, schlieren liquid crystal thermography	dynamic stability, schlieren, liquid crystal thermography
CHANNELS OF DATA	12 on-line	12 on-line

CURRENT ACTIVITIES : Dynamic stability of simple axisymmetric shapes and hyperballistic vehicles - experiments and semi-empirical predictions; free-oscillation experimental techniques for studying large amplitude non-linear effects on hypersonic dynamic stability; dynamic effects of hypersonic separated flow, e.g. a rapidly deployed control surface; development of a continuous recording technique for free flight studies in short duration hypersonic facilities using optical position sensors; aerodynamic characteristics of a range of basic vehicle configurations with lower surface flow containment; development of liquid crystal thermography for heat transfer investigations; a study of interference effects on kinetic heating of slender finned bodies.



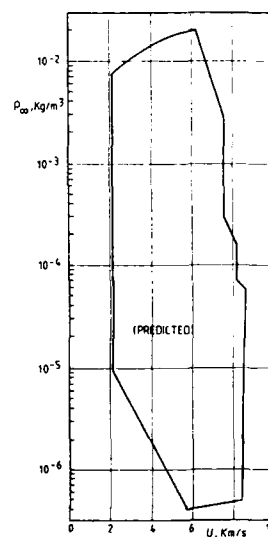
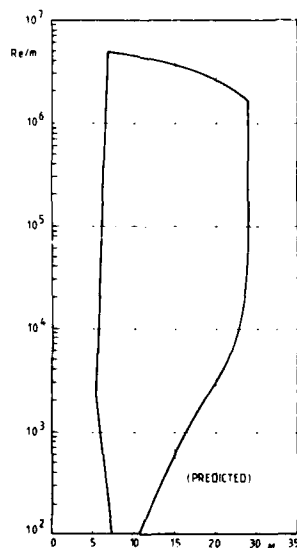
TH AACHEN SHOCK TUNNEL

Organization : Rheinisch-Westfälische
Technische Hochschule
Location : Institut für Luft- und
Raumfahrt
Stosswellenlabor
Templergraben, 55
D-5100 Aachen, F.R. Germany

Contact : Prof. H. Grönig
Tel. : (0241) 80 46 06
Telex: 0832704

CHARACTERISTICS

MACH NUMBER	6 - 24 (conical, 10.5°)
NOZZLE EXIT DIAMETER, cm	three conical nozzles of D=50, 100, 200 cm, each with various throat inserts (useful core for M=24 : $1/3$ D)
RUNNING TIME	10 ms
SUPPLY PRESSURE, bars	1,500 (max)
SUPPLY TEMPERATURE, K	7000-8000 (max)
GAS	N_2 , air
NO TESTS/DAY	1 or 2 (max)
PRESENT STATUS	in preparation for hypersonic reentry experiments with conical nozzle D=50 cm
PERSONNEL REQUIRED	3
MEASUREMENT TECHNIQUES	heat transfer, pressures, schlieren and shadow optics, interferometry
CHANNELS OF DATA	25
COMMENTS	detailed calculations and further tunnel calibration tests are underway predictions shown below are for an initial barrel pressure of 1 bar.



VKI LONGSHOT

Organization : von Karman Institute for
Fluid Dynamics

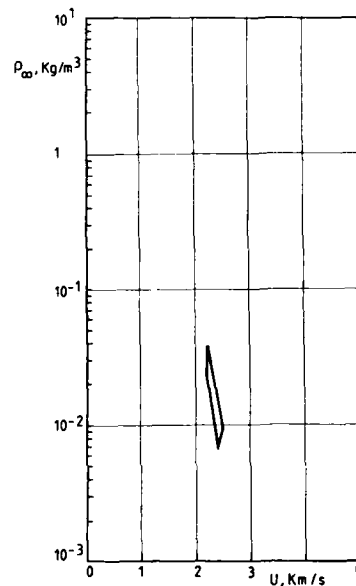
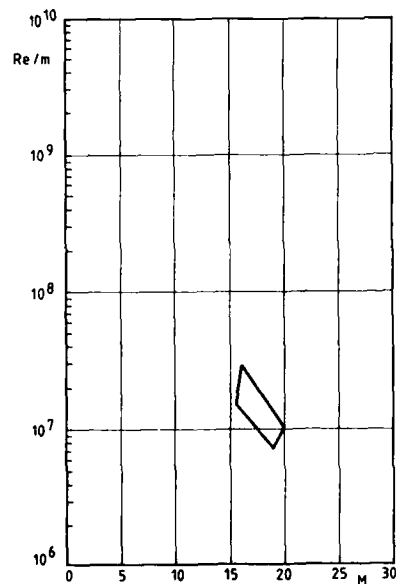
Location : VKIFD
Chaussée de Waterloo, 72
B-1640 Rhode Saint Genèse, Belgium

Contact : Prof. J.F. Wendt

Tel. : (02) 358 19 01
Telefax : (02) 358 77 21

CHARACTERISTICS

MACH NUMBER	15-20 (conical, 6°)
NOZZLE EXIT DIAMETER, cm	36 (useful 23-30)
RUNNING TIME	5-10 ms
SUPPLY PRESSURE, bars	4000 (max)
SUPPLY TEMPERATURE, K	2400 (max)
GAS	N ₂
NO TESTS/DAY	1-2
PRESENT STATUS	in regular use
PERSONNEL REQUIRED	3
MEASUREMENT TECHNIQUES	heat transfer, pressures, schlieren
CHANNELS OF DATA	48 transient recorders, 50 KHz each
COMMENTS	a Mach 15 contoured nozzle of 45 cm diameter is under construction and a conical nozzle of 60 cm diameter for Mach 20+ may be installed. Open jet test section of 10 m ³



**PREPARATION D'ESSAIS PROBATOIRES D'UN GENERATEUR DE PLASMA
POUR L'ALIMENTATION D'UNE SOUFFLERIE HYPERSONIQUE**

M. Consigny, C. Pacou, O. Papirnyk, Ph. Sagnier, J.P. Chevallier
Office National d'Etudes et de Recherches Aérospatiales
Boite Postale N° 72 - 92322 Chatillon CEDEX
R. Leroux (Aérospatiale)

RESUME

L'étude du projet d'avion spatial Hermes fait apparaître la nécessité d'un nouveau moyen d'essais au sol susceptible d'offrir, non seulement des nombres de Mach élevés mais également les enthalpies correspondant aux vitesses de rentrée dans le domaine d'altitude de 70 à 50 km. L'avant projet d'une soufflerie à rafales de quelques secondes a été proposé en envisageant l'utilisation d'éléments existants (sphère à vide, groupe de pompage, tuyères...) avec une alimentation en gaz chauds par un générateur de plasma de l'Aérospatiale Aquitaine. Ce type d'alimentation, soulève des questions sur les qualités requises de l'écoulement :

- permanence, homogénéité, composition, température.

Avant de s'engager dans cette réalisation le CNES a demandé une validation préalable du générateur. L'objet de la présente communication est d'exposer le processus retenu qui comporte les phases suivantes :

- étude et réalisation d'une tuyère se raccordant à des éléments existants et offrant par elle-même les conditions requises pour le sondage,
- étude et réalisation des dispositifs de sondage de cet écoulement (pression dynamique, débit masse local, enthalpie).

1. INTRODUCTION

Le projet d'avion spatial Hermès, confié par le CNES à la société AMD-BA a suscité un examen critique des méthodes et moyens nécessaires à une bonne prévision des caractéristiques aérodynamiques de ce véhicule, en particulier dans sa phase de vol hypersonique.

A la lecture des leçons [1] offertes par le "Space Shuttle", il apparaît que la principale divergence entre prévisions et résultats en vol qui concerne l'équilibrage longitudinal, serait due à une prise en compte insuffisante des effets de gaz réels affectant l'ensemble de l'écoulement [2] ou plus particulièrement les régions d'extrados [3] et d'interaction onde de choc-couche limite. C'est le perfectionnement des méthodes de calcul qui devrait réduire ces marges d'incertitude car l'absence de similitude pour les écoulements de gaz réels ne permet pas l'utilisation directe de résultats obtenus sur modèles réduits.

La validation des codes doit cependant être assurée par des essais probants, c'est-à-dire exécutés dans des installations présentant des caractéristiques suffisantes pour mettre en jeu les phénomènes physiques incriminés. L'analyse de ce besoin, tant pour les études de base que pour des essais à caractère industriel, a conduit à définir un moyen d'essai à rafales de durée moyenne (quelques secondes), propice à toutes sortes de mesures à des niveaux relativement bas de pression et masse volumique. Ce moyen sera brièvement décrit. Il doit utiliser, pour obtenir les enthalpies requises, un générateur de plasma industriel dont il convenait de tester la qualité d'écoulement (permanence, homogénéité, composition, température).

La présente communication a essentiellement pour objet les dispositions adoptées pour ces essais probatoires.

2. PROJET DE SOUFFLERIE R6 CH

Proposé au début de l'année 1985, ce projet résulte de compromis entre impératifs d'ordres divers : coûts, délais, performances. Pour réduire les premiers, il faut, pour son implantation (fig. 1) et sa constitution (fig. 2), appel à des bâtiments et éléments existants ; pour son alimentation à haute enthalpie, il est prévu un générateur de plasma 5 MW de l'Aérospatiale. Sa courbe limite de fonctionnement dans le plan enthalpie-pression (fig. 3) montre que des conditions nominales de 50 b, $H_1/RT_1 = 100$ sont normalement accessibles.

L'étude d'avant projet de cette installation [4] vise à l'obtention, avec des éléments existants ou éprouvés, de rafales de quelques secondes dans des tuyères de dimensions suffisantes pour recevoir des modèles de 0,5 m de longueur environ. Avec une prise en compte approximative (celle-ci sera précisée par l'étude de chaque tuyère) des effets de gaz réels hors équilibre en cours de détente on trouve, pour des nombres de Mach de 12, 16 et 20 les conditions physiques qui figurent dans le tableau suivant.

M	12	16	20
T(K)	240	138	88
ρ_0/ρ_a	$0,16 \cdot 10^{-3}$	$0,17 \cdot 10^{-4}$	$0,37 \cdot 10^{-5}$
P_0/P_a	$0,18 \cdot 10^{-3}$	$0,34 \cdot 10^{-4}$	$0,11 \cdot 10^{-4}$
a(m/s)	311	236	188
Vo(m/s)	3737	3777	3770
Re	$2,5 \cdot 10^3$	$8,6 \cdot 10^3$	$4,5 \cdot 10^3$
M/\sqrt{Re}	0,12	0,17	0,3
Z(km)	63	75	82
$P_1(Pa)$	3083	595	200

On peut remarquer que ces conditions correspondent pour $M = 12$ à une duplication complète des valeurs des pression, densité et température de l'atmosphère standard à 63 km : seule la masse volumique des altitudes de 75 et 82 km est reproduite avec des températures inférieures ; l'énergie figée en cours de détente (dissociation et vibration) est de l'ordre de 10 %. Le domaine de simulation ainsi obtenu dans le plan Mach, Reynolds est donné fig. 4.

Les hypothèses retenues pour calculer les limites en Reynolds de ce domaine doivent être précisées : les valeurs maximales sont obtenues avec un fonctionnement cryogénique limité par la température de condensation hors équilibre [5] soit pour la pression nominale de 50 b, soit pour une pression accrue jusqu'à 150 b (projet de générateur segmenté).

Les valeurs inférieures de Re pourraient évidemment être atteintes en diminuant les pressions génératrices mais c'est au contraire à des pressions maintenues aux maximum, de 50 et 150 b mais aussi à l'enthalpie nominale de 100 que correspondent les valeurs minimales portées sur le diagramme. La couche $p_1 = 50$ b ne constitue pas toute la frontière car aux nombres de Mach les plus élevés la pression d'arrêt à haute enthalpie peut devenir insuffisante pour un amorçage correct de l'écoulement.

Cette figure montre en outre que des valeurs du paramètre de raréfaction M/\sqrt{Re} comparables au vol sont bien reproduites avec, simultanément, des valeurs de l'enthalpie qui, sans égaler le vol, sont cependant suffisantes pour faire apparaître des effets de gaz réels notables.

Ces effets sont illustrés en général par le domaine (vitesse, altitude) simulé (fig. 5) mais peut être plus précisément par la fig. 6 où l'on voit que, à condition d'ajuster la pression génératrice à l'enthalpie selon la courbe $p_1(T_0)$, il est possible de conserver invariants les paramètres de similitude classiques (M , Re , et M/\sqrt{Re}) tout en faisant varier largement le taux de dissociation à l'équilibre (au point d'arrêt).

On peut remarquer que ce taux de dissociation, nettement supérieur à celui qui se situe au cours de la détente dans la tuyère, sera plus facilement atteint dans la couche de choc du fait d'une certaine pré-dissociation amont.

Un autre paramètre important pour les études de couche limite est le rapport entre température de paroi T_p et température statique T_0 ; la fig. 7 montre que, toujours en maintenant constants les paramètres M et Re ($M = 12$; $Re \sqrt{10^4}$ pour une longueur de maquette de 50 cm), grâce à l'ajustage de pression génératrice figuré $p_1(T_0)$, il est possible avec une maquette à température ambiante de faire varier T_p/T_0 dans un large rapport (de 2 à 8) ou au contraire de maintenir T_p/T_0 à la valeur du vol moyennant un refroidissement ou un réchauffage du modèle techniquement concevable. Ce type d'opérations est évidemment plus facile à envisager sur les formes simples propices aux études de base définies dans les programmes de R et D.

La fig. 8 montre que, en maintenant une température juste suffisante pour éviter la liquéfaction (mettant à profit le retard à l'équilibre) une variation indépendante et significative des paramètres M et Re est encore obtenue.

3. ESSAIS PROBATOIRES

Des générateurs de plasma à arc prolongé ont jusqu'ici été plutôt utilisés pour des essais de matériaux [8, 9]. Dans ce dernier cas, les exigences concernant l'homogénéité, la permanence et la pureté de l'écoulement sont moins sévères qu'elles ne doivent l'être pour des essais aérodynamiques. Il a donc été décidé, par les promoteurs du projet R6 Ch brièvement décrit ci-dessus (ONERA, CNES, AMD/BA) de soumettre le générateur prévu (JP50 de l'Aérospatiale) à des essais probatoires permettant de qualifier l'écoulement.

Ces essais ne peuvent se concevoir que sur le site "Aérospatiale" qui comporte l'ensemble coûteux des servitudes nécessaires à l'alimentation du générateur (la transposition de ces éléments pour le projet R6 Ch, fig. 9 en montre l'importance).

Le sondage de l'écoulement implique l'utilisation d'une tuyère de détente représentant une portion amont des tuyères définitives d'un diamètre de sortie suffisant pour un bon contrôle d'homogénéité et assurant, pour des mesures de concentration, un figeage de ces dernières.

Il serait de plus intéressant que cette portion puisse se raccorder à la partie aval d'une tuyère $M = 16$ qui fait partie des éléments existants réutilisables.

Il est enfin nécessaire, compte tenu de l'absence de moyens de pompage et de capacités à vide sur le site Aérospatiale que la tuyère puisse s'amorcer avec une pression de récupération permettant le rejet à l'atmosphère. Pour satisfaire à ces exigences diverses la tuyère, conique et d'ouverture modérée, débouche avec un diamètre de 85 mm dans un petit caisson de mesure (fig. 10) propre à contenir les moyens de sondage et à permettre la visualisation de l'écoulement.

3.1. Tuyère - Calcul de l'écoulement [11]

La forme de tuyère étant déterminée par des considérations purement géométriques de raccord à des éléments existants et de continuité dans l'évolution des courbures, le calcul de l'écoulement est effectué par approximations successives sur le couplage noyau non visqueux-couche limite, en conservant en première approximation l'hypothèse d'un écoulement par tranches. La première région, y compris le col et son voisinage immédiat est calculée pour l'air à l'équilibre (diagramme de Mollier numérisé d'après les tables d'Hilsenrath [10]). A l'aval, le calcul par tranche est poursuivi, hors équilibre thermodynamique et chimique ; le modèle adopté comprend les 9 espèces et 15 réactions dont les vitesses figurent dans le tableau N° 1.

Ce programme [11] résulte d'adaptations successives d'un code établi à l'origine par le CALSPAN [12]. Les principales hypothèses concernant le gaz sont les suivantes :

- fluide parfait, c'est-à-dire sans effets de diffusion des espèces, de viscosité ou de conduction thermique,
- équilibre thermodynamique des énergies de translation et rotation ; relaxation des énergies de vibration des molécules d'azote et d'oxygène (oscillateurs harmoniques) avec des constantes de temps données par les expressions suivantes :

$$\text{pour } O_2 \quad \tau_v = 16,18 \times 10^{-4} e^{101,44/T^{1/2}} \quad \text{dynes s/cm}^2$$

$$N_2 \quad \tau_v = 11,15 \times 10^{-4} T^{1/2} e^{121/T^{1/2}} \quad \text{dynes s/cm}^2$$

- dissociations décrites par le tableau N° 1 et couplage vibration-dissociation par le modèle non préférentiel.

Le système d'équations différentielles ordinaires obtenu est intégré par une méthode de Runge Kutta avec quelques précautions concernant les choix de pas. Les résultats les plus typiques sont présentés en fonction de la distance le long de la tuyère à partir d'une origine située dans le convergent à 33 mm à l'amont du col ; les résultats correspondants au calcul à l'équilibre sont donnés à titre de comparaison ; ils justifient a posteriori le traitement à l'équilibre de la région sonique.

On montre successivement l'évolution le long de la tuyère de la pression (fig. 11), de la masse volumique (fig. 12) des températures (fig. 13) de la vitesse (fig. 14) et du nombre de Mach (fig. 15). Ces résultats suscitent quelques commentaires classiques :

- la zone de non équilibre est relativement courte pour la plupart des réactions et en particulier la figeage des températures de vibration est pratiquement atteint vers 100 ou 150 mm respectivement pour N_2 et O_2 ; la fraction d'énergie figée est faible si on la compare à l'enthalpie totale et en conséquence les vitesses calculées en ou hors équilibre diffèrent peu (fig. 1).

La conservation du débit $\rho V S$ entraîne corrélativement une très faible différence sur les masses volumiques en et hors équilibre à abscisse donc à S donné. L'effet de l'énergie figée est plus évident sur les températures de translation-rotation en fin de détente qui diffèrent de 820 K environ. Hors équilibre, la vitesse du son se trouve donc nettement diminuée et cet effet l'emporte sur la perte de vitesse pour donner des nombres de Mach hors équilibre surpassant de 20 % les nombres de Mach à l'équilibre à l'extrémité de la tuyère.

Un premier calcul de couche limite (laminaire et turbulente) a été effectué pour évaluer les flux de chaleur afin que l'Aérospatiale puisse prévoir le refroidissement de la tuyère tel que décrit ci-après. La prise en compte de l'épaisseur de déplacement dans une seconde itération sur le calcul du noyau non visqueux (code Euler gaz parfait $\gamma = 1,2$) entre 100 et 200 mm montre que l'hypothèse de l'écoulement par tranche est tout à fait justifiée pour la couche limite laminaire et encore acceptable pour une couche limite turbulente (fig. 16).

On peut conclure des résultats précédents que la tuyère répond aux conditions prescrites pour les conditions de sondage : concentrations et températures de vibration figées ; noyau sain de dimension suffisante. Outre les résultats présentés, les calculs de couche limite ont fourni les données de flux thermique nécessaires à l'étude technologique de la tuyère ; en particulier à son refroidissement.

3.2. Tuyère - Réalisation

L'Aérospatiale conçoit et réalise la tuyère. Le dimensionnement de celle-ci est effectué pour les conditions génératrices suivantes :

- pression génératrice : $p_i = 50$ bars,
- enthalpie génératrice réduite : $h_i/RT_0 = 100$,

correspondant à un débit gaz de $0,266$ kg/s et une puissance gaz de $2,09 \cdot 10^6$ W pour le col de section 1 cm².

Le calcul de l'écoulement conduit à des estimations de flux de chaleur de $5 \cdot 10^7$ W/m² au col, décroissant jusqu'à $5 \cdot 10^5$ W/m² environ en sortie. Ces conditions de flux et pressions sont couramment rencontrées dans les générateurs de plasma. La conception retenue est de type classique :

- une enveloppe interne de faible épaisseur en alliage de cuivre est réalisée au profil calculé ;
- un film d'eau à grande vitesse (de l'ordre de 20 m/s) assure le refroidissement d'amont en aval (il permet d'obtenir des coefficients de convection élevés) ;
- des séparateurs assurent la mise en forme de ce film d'eau ;
- l'ensemble est disposé à l'intérieur d'une structure ;
- enfin, à l'aval une couronne maintient l'enveloppe interne et comporte 4 prises de pression pariétales.

Cette tuyère est présentée planche 17. Le refroidissement étudié permet un régime permanent d'écoulement, en l'absence d'usure des pièces. La pressurisation du circuit d'eau de refroidissement est asservie à la pression génératrice dans la limite d'un écart de 20 bars. Le niveau de pression d'eau peut atteindre 100 bars.

3.3. Caisson de mesure et dispositif de sondage

Le caisson de mesure se présente comme une mini soufflerie à jet libre avec une reprise coulissante (fig. 10). Son volume résulte d'un compromis : il doit être assez réduit pour que sa vidange par effet d'induction jusqu'à une pression voisine de $0,04$ atm soit rapide pour assurer un bon amorçage du jet et un fonctionnement correct de la reprise ; il doit contenir l'ensemble du dispositif de sondage, escamoté hors du jet avant et après une traversée assez rapide ($\sim 0,1$ s) pour que les sondes ne subissent qu'un échauffement modéré.

Des hublots doivent assurer un champ d'observation convenable pour des visualisations ombroscopiques. Pour éviter durant la phase transitoire d'amorçage des retours de gaz chaud sur ces hublots, deux précautions sont prises, d'une part la reprise coulissante est amenée au contact de la bride de sortie de tuyère avec une certaine étanchéité pour une éventuelle vidange préalable du caisson, d'autre part une entrée contrôlée d'air frais est ménagée dans le caisson.

Le bras porte-sondes oscillant autour d'un axe parallèle à la veine, actionné par vérin hydraulique avec amortisseurs de fin de course, de même que la reprise coulissante sont commandés par un automate programmable dont la séquence s'insère dans la programmation générale de fonctionnement du générateur.

3.4. Sondes

L'ensemble des sondes utilisées est disposé en arc de cercle à l'extrémité du bras porte-sonde (fig. 18) pour balayer approximativement un diamètre vertical ou horizontal de la tuyère dans un plan très voisin de son extrémité.

- Deux sondes pitot mesurent une pression d'arrêt à l'aval d'un choc normal, l'une pour les valeurs moyennes est équipée d'un capteur Stathans type 731 et donne, compte tenu de sa canalisation (1 mètre) un temps de montée de 7 ms avec dépassement de 8% . L'autre destinée aux mesures de fluctuations contient un capteur Kistler 6001. Son étalonnage dynamique montre (fig. 19) la réponse à un échelon de 150 mb et le spectre de cette réponse qui présente une faible résonnance vers 3 kHz avec atténuation régulière au delà.
- La sonde de débit masse, dans l'axe du mât est tout à fait classique [13, 14] pour un mode de fonctionnement transitoire. Le débit capté par l'entrée d'air de section connue est mesuré grâce au col sonique aval d'après la pression et la température à l'amont de ce dernier. Un échangeur thermique à inertie réduit cette température au voisinage de l'ambiance. Les diamètres de thermocouples et capteur de pression sont choisis pour que les temps de réponse de ces mesures soient du même ordre que le temps de stabilisation de l'écoulement interne dans la sonde (< 1 ms), à condition d'utiliser le thermocouple en régime transitoire [15].
- Sondes d'enthalpie :
Elles sont toutes deux basées sur le même principe : la mesure de flux sur obstacles sphériques. Le flux au point d'arrêt est directement lié à l'enthalpie d'après la formule de Fay et Riddell, mais l'utilisation de deux sondes de diamètre différent permet de vérifier l'absence de pollution solides. Les flux de chaleur liés à l'impact de particules sont indépendants du rayon de courbure alors que les flux aérodynamiques évoluent comme l'inverse de sa racine.
La sonde $\varnothing 10$ mm se prête à l'exploitation de la température superficielle locale au point d'arrêt pour obtenir le flux soit dans l'hypothèse simplificative d'un milieu semi-infini avec correction de courbure, soit avec une méthode de différences finies en admettant une distribution de flux sur la sphère (théorie de Lees).
La sonde $\varnothing 5$ mm est trop petite pour que la localisation de la mesure au point d'arrêt soit assurée ; elle est donc considérée comme un capteur à inertie thermique, pratiquement isotherme et soumis à un

flux moyen résultant de l'intégration de la distribution de Lees. Le dimensionnement des sondes et le choix des matériaux sont dictés par l'utilisation en régime transitoire (traverse du jet en 0,1 s) et conduisent à des échauffements de l'ordre de 400° C, donnant une grande sensibilité de mesure. On s'est assuré du bon fonctionnement de ces sondes à plus faible niveau avec une durée d'exposition accrue (soufflerie R3 Ch).

4. EXPLOITATION DES MESURES

Outre les sondes ci-dessus il est prévu d'exploiter des visualisations strioscopiques ou ombroscopiques qui permettront de s'assurer que le choc sur la sonde de débit masse est bien attaché aux lèvres de l'entrée d'air.

Ces visualisations, à relativement forte densité compte tenu de la détente limitée à $M = 6$ devraient permettre une mesure assez précise de la distance de détachement sur les sondes sphériques. On ne peut en déduire directement la composition du gaz dans la couche de choc. Il semble cependant que cette distance soit assez sensible aux effets de gaz réels [16], sans l'être trop à la conicité de l'écoulement [17] pour qu'il soit ainsi possible de valider les calculs de concentration en cours de détente hors équilibre, ce type de calcul pouvant être poursuivi sur les obstacles [18] et en incluant de préférence effets visqueux diffusion, température et catalycite de paroi.

L'exploitation des mesures de pression d'arrêt ne soulève pas de problèmes particuliers pour évaluer ρV^2 même en présence d'effets de gaz réels. La sonde de débit fournissant ρV on peut en déduire ρ et V et de là $V^2/2$ et l'enthalpie à comparer aux mesures sur les sondes thermiques.

Le but principal des essais probatoires étant de s'assurer de l'homogénéité de l'écoulement, la technique de balayage permet avec les mesures énumérées ci-dessus d'escompter une qualification rapide de l'écoulement.

5. CONCLUSION

Les essais probatoires prévus doivent permettre de vérifier qu'un générateur de plasma peut constituer une alimentation de soufflerie hypersonique fonctionnant en rafales de plusieurs secondes. Pour définir le montage et le système de mesure, il est nécessaire de prendre en compte de nombreux phénomènes physiques et chimiques qui sont aussi analogues que possible à ceux rencontrés en cours de rentrée spatiale. Une fois de plus, il apparaît que la mise au point d'une soufflerie est, en elle-même et avant tout essai sur des maquettes de véhicules, un exercice très fondamental de validation des méthodes de calcul qui serviront à la définition de ces véhicules.

REFERENCES

- [1] - J.P. Arrington, J.J. Jones
Shuttle performance : Lessons Learned. Proc. Conf. Nasa Langley R.C. March, 8-10, 1983.
- [2] - J.R. Maus, B.J. Griffith, R.Y. Szema
Hypersonic Mach Number and real gas effects on space shuttle orbiter aerodynamics. Journ. Spacecraft and Rockets. Vol 21, N° 2, 1984.
- [3] - J.L. Potter
Commentary on the 1985 NASA/Vanderbilt symposium on future hypervelocity flight requirements. NASA CR 176 747, March 1986.
- [4] - C. Pacou
Analyse des moyens d'essais nécessaires à l'étude des problèmes de rentrée. Avant projet d'un moyen d'essais hypersonique à haute enthalpie (soufflerie R6 Ch) pour le programme Hermès. RTS 10/6075 AY, février 1986.
- [5] - F.L. Daum
Condensation de l'air dans une soufflerie hypersonique. AIAA Journ. Vol 1 N° 5, mai 1963 et mars 1968.
- [6] - J. Lukasiewicz
Experimental methods of hypersonics. Ed. M. Dekker New York, 1973.
- [7] - J.P. Chevallier
Rétrospective sur les moyens d'essais et de mesure en hypersonique. 22ème Colloque d'Aérodynamique Appliquée, Lille 1985.
- [8] - AGARDograph
Arc heaters and MHD accelerators for aerodynamic purposes. Agardographie 84. Partics 1, 2 et supplément 1964.
- [9] - J.H. Painter, R.J. Ehsen
Development of a high performance arc heater for ground testing advanced strategic re-entry vehicle components. AIAA Pap. N° 71-259.
- [10] - J. Hilsenrath, M. Klein
Tables of thermodynamic properties of air in chemical equilibrium including second virial corrections from 1500 K to 15000 K; AEDC TR 65-58.

- [11] - Ph. Sagnier
Ecoulement hors équilibre dans la tuyère probatoire R6 pour les conditions nominales de fonctionnement. RT 95/1865 AH, septembre 1986.
- [12] - P.V. Marrone, J.G. Hall
Inviscid, non equilibrium flow behind bow and normal shockwaves. CAL Rep. QM 1626 A 12 (I et II), 1963.
- [13] - R.J. Stalker
A mass flow probe for use in short duration hypersonic flows. NPL AR 1004, March 1962.
- [14] - J.P. Chevallier
Remarques sur les sondes de débit masse dans les souffleries à arc. STA 22ème Réunion Rhodes St Genèse. TP ONERA 169, septembre 1964.
- [15] - J.P. Chevallier
Réponse transitoire de sondes thermiques (1st Int. Congress on instrumentation in Aerospace Simulation Facilities. Paris, 1964).
- [16] - R.K. Lobb
Experimental measurement of shock detachment distance on spheres fired in air at hypervelocities. AGARD Proc. The high temperature aspects of hypersonic flow 3-6 avril 1962, pp. 519-527.
- [17] - Yu. P. Golovachov
Similarity properties in the problem of flow from a supersonic source past a spherical bluntness. Int. J. Heat Mass Transfer Vol 28 N° 6, pp. 1165-1171, 1985.
- [18] - J.G. Hall, A.Q. Eschenroeder, P.V. Marrone
Inviscid hypersonic air flows with coupled non equilibrium process. IAS Pap. 62.67, 1962.

Tableau 1 ESPECES ET REACTIONS CHIMIQUES UTILISEES
DANS LE PROGRAMME "HORS EQUILIBRE"

9 espèces : O, N, e⁻, O₂, N₂, NO, O₂⁺, N₂⁺, NO⁺

15 Réactions :

1	O ₂ + O → 2O	K = 2.110 ¹⁸ T ^{-0.5} e ^($\frac{-59371}{T}$) (Cm ³ mole ⁻¹ s ⁻¹)
2	O ₂ + O ₂ → 2O + O ₂	K = 3.610 ²¹ T ^{-1.5} e ^($\frac{-59371}{T}$) (Cm ³ mole ⁻¹ s ⁻¹)
3	O ₂ + M → 2O + M	K = 1.210 ²¹ T ^{-1.5} e ^($\frac{-59371}{T}$) (Cm ³ mole ⁻¹ s ⁻¹)
4	N ₂ + N ← 2N + N	K = 2.410 ²¹ T ^{-1.5} (Cm ⁶ mole ⁻² s ⁻¹)
5	N ₂ + N ₂ ← 2N + N ₂	K = 2.810 ¹⁶ T ^{-0.5} (Cm ⁶ mole ⁻² s ⁻¹)
6	N ₂ + M ← 2N + M	K = 1.110 ¹⁶ T ^{-0.5} (Cm ⁶ mole ⁻² s ⁻¹)
7	NO + M ← N + O + M	K = 3.210 ¹⁸ T ⁻¹ (" ")
8	N ₂ + O ₂ → 2NO	K = 9.110 ²⁴ T ^{-2.5} e ^($\frac{-65051}{RT}$) (Cm ³ mole ⁻¹ s ⁻¹)
9	O + N ₂ → NO + N	K = 5 10 ¹³ e ^($\frac{-37728}{T}$) (" ")
10	N + O ₂ → NO + O	K = 10 ¹² T ^{0.5} e ^($\frac{3122}{T}$) (" ")
11	N + O ← NO ⁺ + e ⁻	K = 5.410 ²¹ T ^{-1.5} (" ")
12	O + O ← O ₂ ⁺ + e ⁻	K = 10 ²¹ T ^{-1.5} (" ")
13	N + N ← N ₂ ⁺ + e ⁻	K = 10 ²¹ T ^{-1.5} (" ")
14	O ₂ ⁺ + N ₂ → NO ⁺ + NO	K = 10 ¹³ T ^{-0.5} (" ")
15	O ₂ ⁺ + NO → O2 + NO ⁺	K = 10 ¹³ T ^{-0.5} (" ")

M représentant les espèces catalytiques autres que celles concernées à savoir pour les réactions :

3 : N, e, N₂, NO, O₂, N₂, NO⁺

6 : O, e, O₂, NO, O₂, NO⁺

7 : O, N, e, O₂, N₂, NO, O₂, N₂, NO⁺

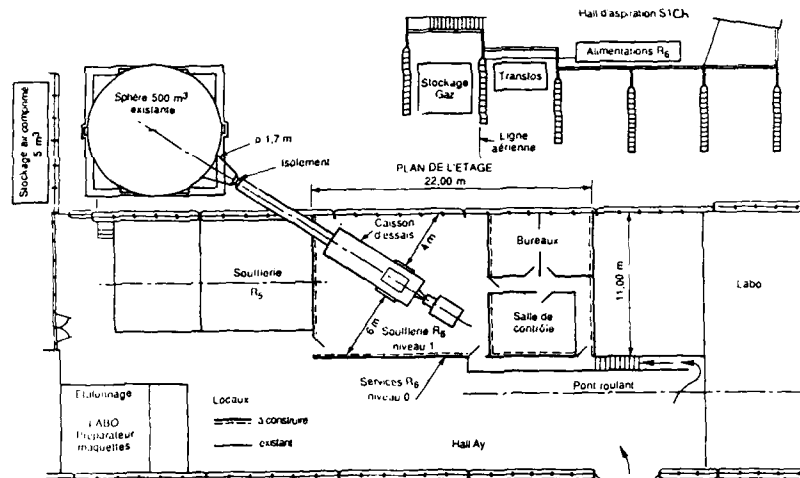


Fig.1- Implantation du projet de soufflerie R6 Ch.

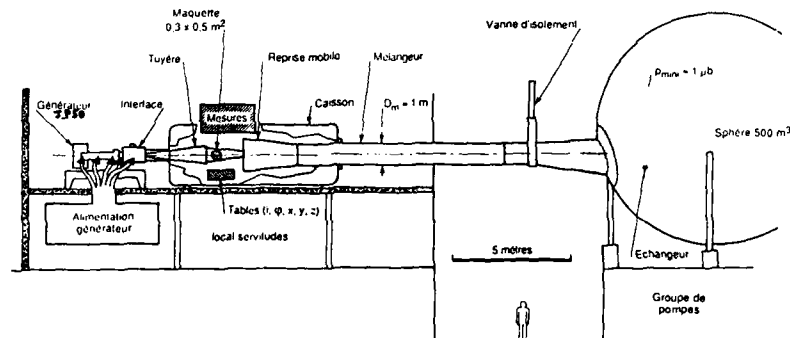


Fig.2- Circuit aérodynamique de la soufflerie R6Ch.

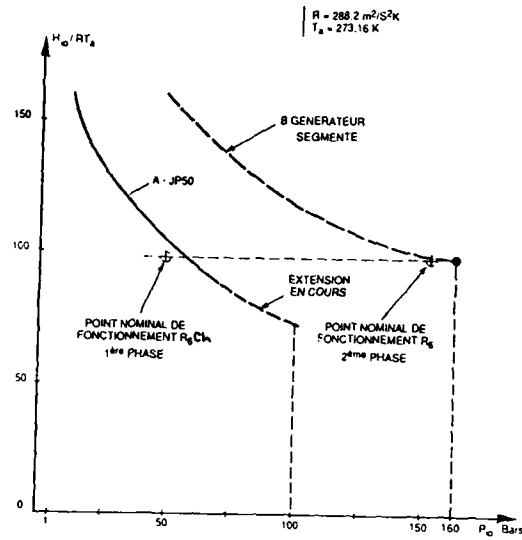


Fig.3. Performances limites du générateur de plasma

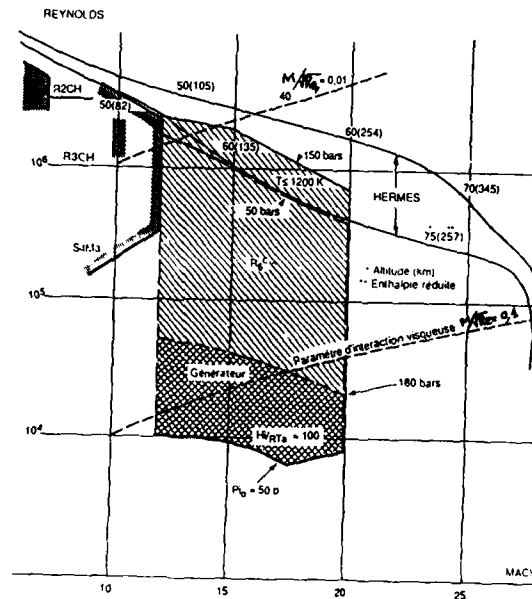


Fig.4. Domaine de simulation Mach, Reynolds

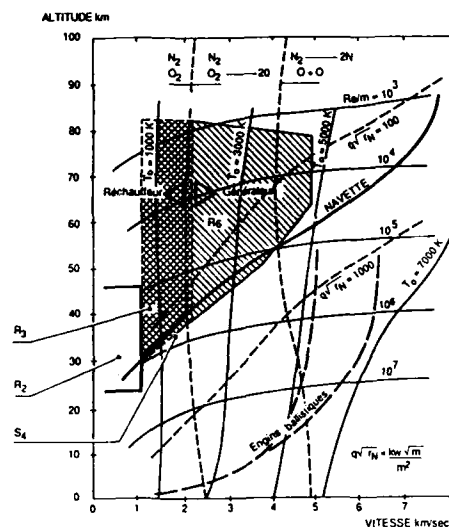
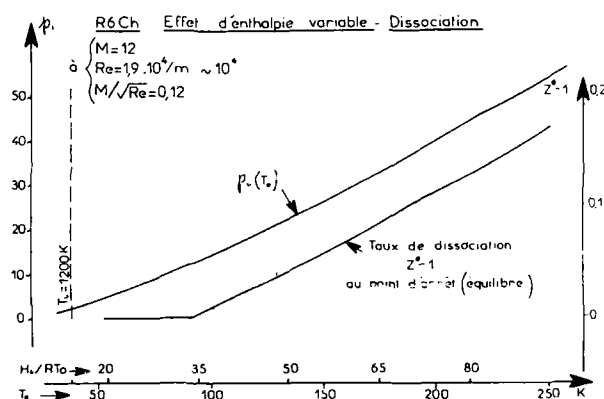
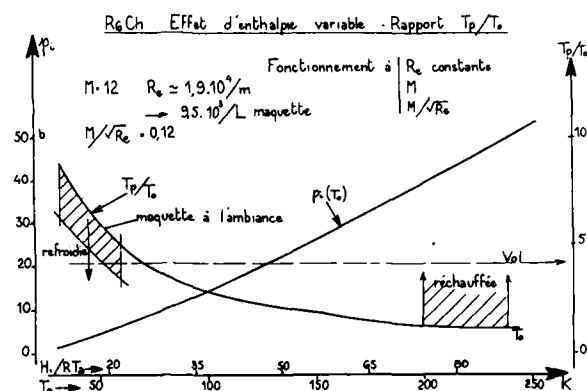


Fig. 5. Domaine de simulation altitude, vitesse

Fig. 6. Taux de dissociation à enthalpie variable ($M = 12$, $Re_4 = 10^4$)Fig. 7. Température de paroi comparée à la température statique à enthalpie variable ($M = 12$, $Re = 10^4$, $M/\sqrt{Re} = 0,12$)

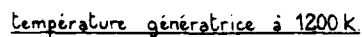


Fig.8- Domaine de variations des paramètres (soufflerie froide)



Fig.9- Circuits de servitudes du générateur JP 50

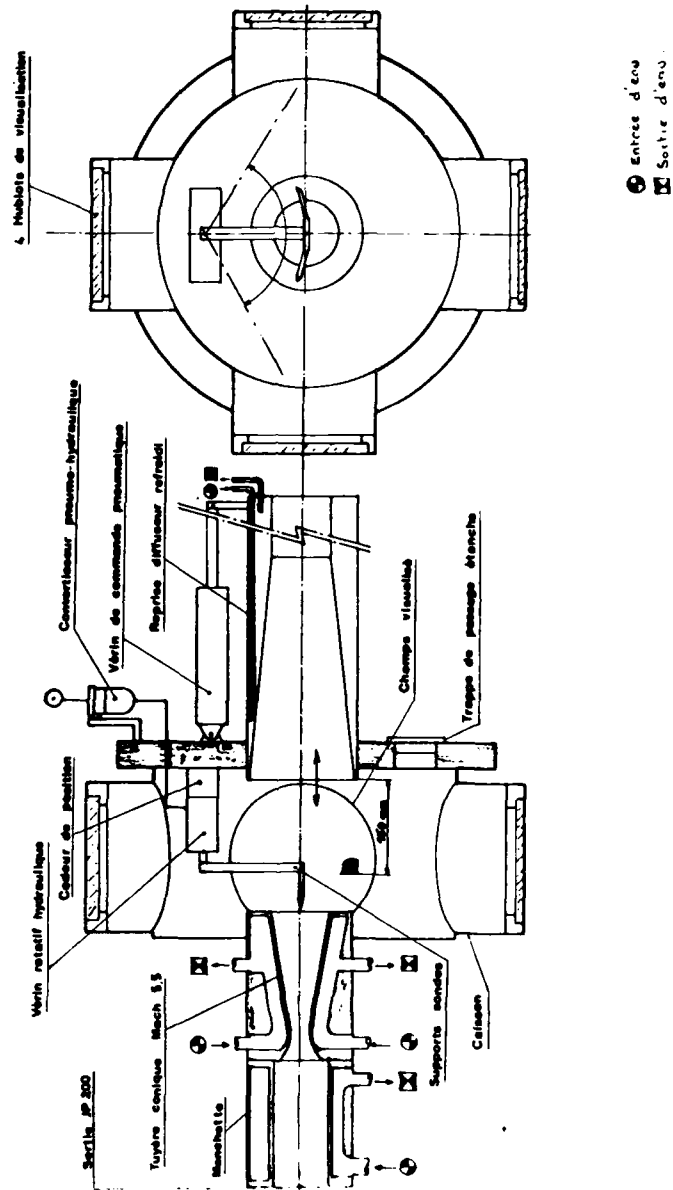


Fig. 10 - Caisson de mesure

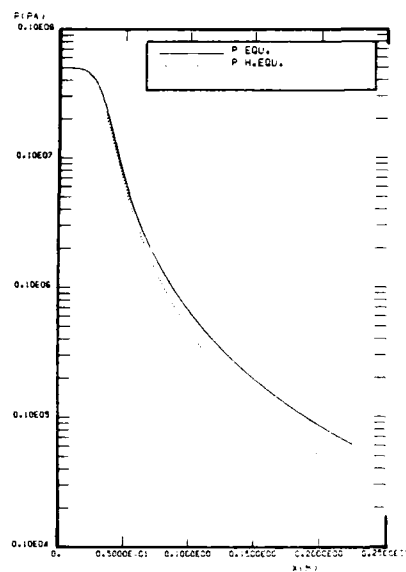


Fig. 11 - Pression en et hors équilibre dans la tuyère.

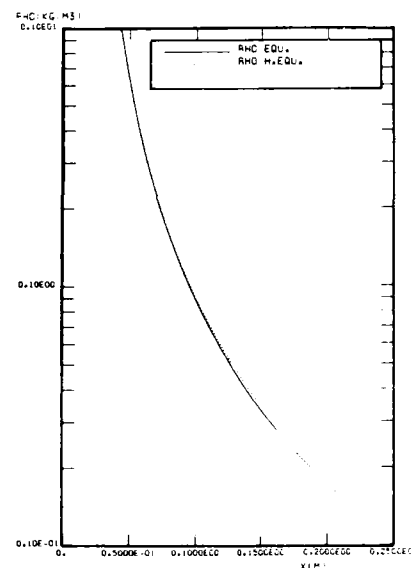


Fig. 12 - Masse volumique en et hors équilibre dans la tuyère.

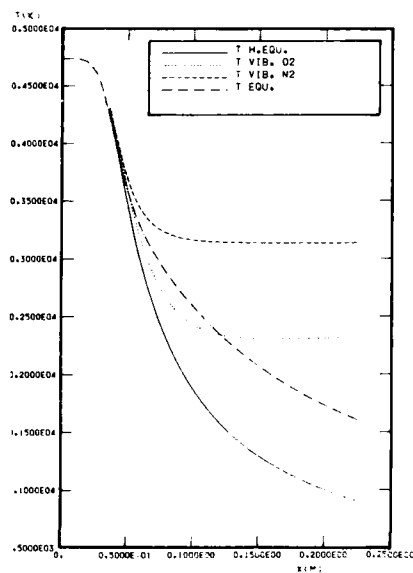


Fig. 13 - Température en et hors équilibre dans la tuyère.

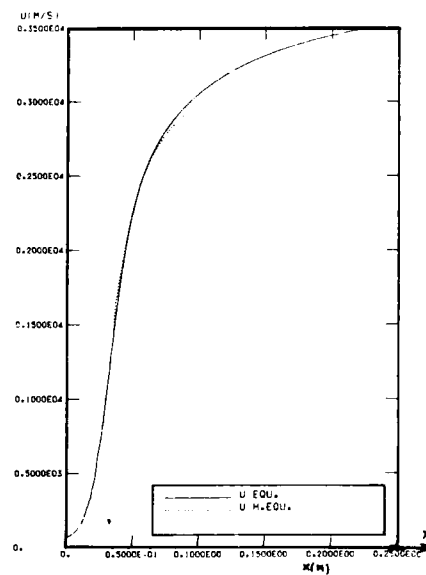


Fig. 14 - Vitesse en et hors équilibre dans la tuyère.

Fig. 15 - Mach en et hors équilibre dans la tuyère.

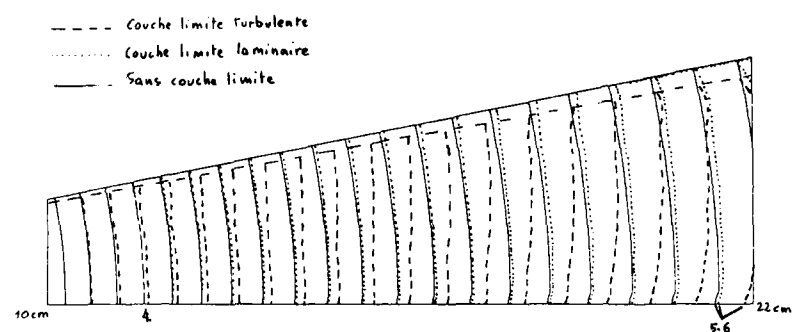
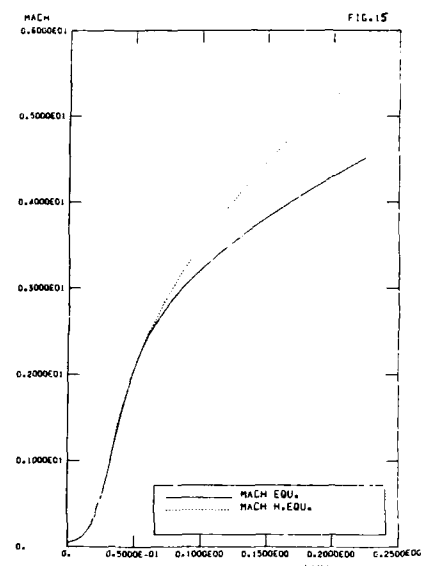


Fig.16 Lignes iso Mach dans la tuyère

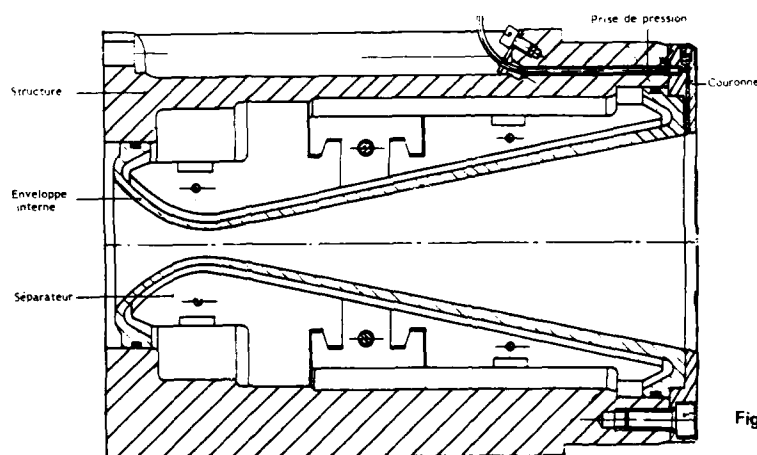


Fig.17 _ Réalisation technologique

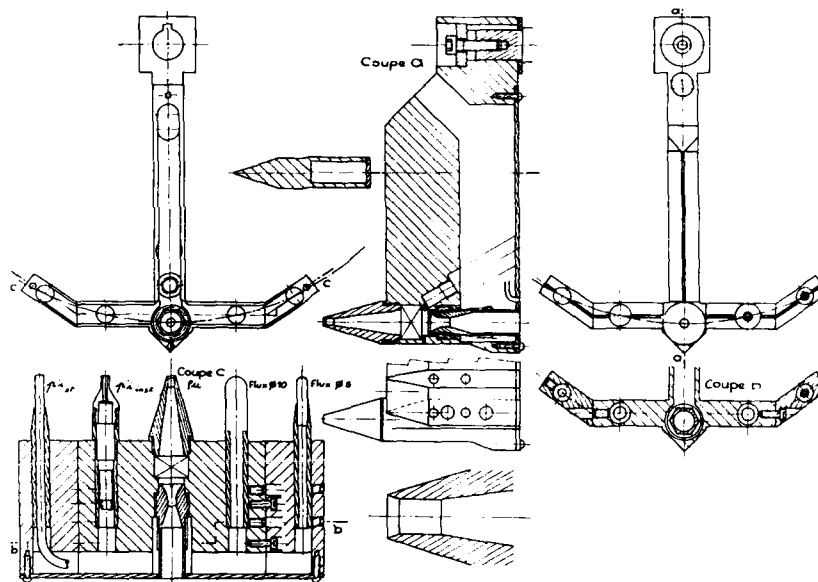


Fig. 18 Ensemble porte-sonde

Capteur : KISTLER 6004 (n° 266495) - $S_e = 14,6 \mu C / bar$
Ampl. de charge : KISTLER 5007 - $S_e = 1 bar / volt$ - $C_g = 1 \mu s$
 (constante de temps : Long)

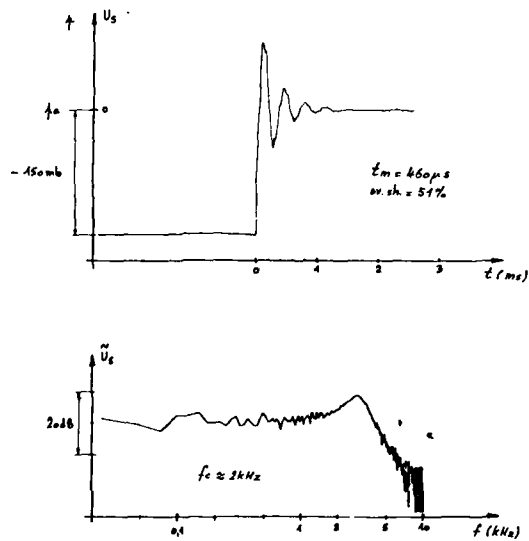


Fig. 19 Etalonnage dynamique d'une sonde d'arrêt

SHOCK TUNNELS FOR REAL GAS HYPERSONICS

by

R.J. Stalker

Department of Mechanical Engineering

University of Queensland

Brisbane Qld 4067

Australia

SUMMARY

The application of free piston shock tunnels to the simulation of real gas effects in hypersonic flight is discussed. It is pointed out that the primary simulation variables for this purpose are the stagnation enthalpy and the binary scaling parameter. The free piston reflected shock tunnel is considered first, and it is shown how test time limitations play a major role in determining the limiting stagnation enthalpy for a given model size. Nevertheless, flight values of the two simulation variables, for vehicles similar to the Space Shuttle Orbiter, can be matched by an existing free piston shock tunnel up to speeds of 7 km.s^{-1} . Experiments performed in this shock tunnel are used to demonstrate real gas effects in model flows.

Radiative energy loss limits the maximum stagnation enthalpy available with reflected shock tunnels. Fortunately, operation in the non-reflected mode circumvents this limitation and, in addition, allows higher values of the binary scaling parameter; although it also leads to greatly reduced test times. The use of the prior steady flow technique to enable high enthalpy non-reflected shock tunnel operation is described, and examples of experiments performed in the facility are used to demonstrate that short test times do not preclude worthwhile experimentation. A variant of the free piston shock tunnel, which is intended for propulsion research at high velocities, also is briefly described.

1. INTRODUCTION - REAL GAS SIMULATION REQUIREMENTS

Real gas effects are a feature of hypersonic flow at high flight speeds. They influence phenomena such as boundary layer heat transfer, shock layer vortex shedding, shock detachment, centre of pressure location, control surface effectiveness and combustion heat release in propulsion systems.

For most problems associated with lifting vehicles, the dominant real gas effects are associated with the dissociation of oxygen and nitrogen. This begins when the gas experiences the sudden temperature rise which occurs when it crosses the bow shock from the vehicle and, because the dissociation reactions take a finite time to come to completion, it continues for some distance downstream with the gas in a non-equilibrium state. An indication of the magnitude of this distance is given in fig.1, where normal shock calculations have been slightly modified to show the streamwise variation of density in a stream tube which crosses a normal shock, and subsequently remains at constant pressure as it passes downstream. The distance downstream is expressed in terms of the binary reaction variable, $\chi = px/u$, where p is the pressure, u is the velocity and x is the distance from the shock. It can be seen that in terms of this variable, two curves at different altitudes (i.e. different densities) and the same flight speed are the same for a considerable distance downstream.

The reason for this is that this part of the non-equilibrium process is dominated by the forward chemical reactions which increase the dissociation levels. All these are reactions which involve only two components⁽²⁾, and therefore the rate at which they proceed is proportional to the density or, at the same temperature and dissociation level, to the pressure. Now, as also may be seen from fig.1, when the gas begins to approach an equilibrium state the curves, which were identical, increasingly diverge. This is because the backward, recombination, reactions play an increasingly important role, and since these involve three components, the direct proportionality between reaction rate and density no longer applies. The binary scaling variable χ then ceases to be effective in correlating flows at different densities.

An indication of the limits to the binary scaling regime for flight vehicles may be obtained by plotting two boundaries on a velocity-altitude diagram, as in fig.2. Here the flow downstream of a shock inclined at an angle of 40° to the oncoming flow is considered, since this is likely to be more representative of the flow field about a re-entry glider than a normal shock. Using curves similar to fig.1, a lower "equilibrium" boundary can be drawn. For altitudes below this boundary, the reactions require a distance of less than 1 metre after the shock to reach equilibrium and, since this may be expected to be an order of magnitude less than the typical dimensions of a flight vehicle, most of the flow about the vehicle can be expected to be in equilibrium. An upper, "frozen", boundary also may be drawn, above which no significant reactions occur for distances less than 1 metre from the shock. Thus, reaction effects will be weak close to this boundary, and will become weaker still at altitudes above the boundary. It may be noted that both boundaries tend to curve steeply to lower altitudes as speeds fall towards 4 km.s^{-1} . This is a manifestation of the fact that real gas effects behind a 40° shock are becoming very weak in approaching this speed, and indicates that wind tunnel facilities must be able to comfortably exceed this speed if they are to produce significant real gas effects in the general flow field about a re-entry glider.

Trajectories for the Space Shuttle Orbiter and possible Aero assisted Orbital Transfer Vehicles also are shown on fig.2. It can be seen that they fall well into the region between the two boundaries, without approaching closely to the equilibrium boundary. This is fortunate, because it implies that

recombination effects are unimportant in the flow field about these vehicles and, in order to simulate real gas effects in a shock tunnel, it generally is necessary only to ensure that the effects of forward reactions are represented, and these are accommodated by matching the values of the binary scaling variable. Similar remarks also apply to an acceleration vehicle because, although its trajectory on fig.2 passes close to the equilibrium boundary, the fact that it may be expected to generate shock angles substantially less than 40° over most of its flow field implies that it also falls into the binary scaling regime.

Thus the primary requirements for real gas simulation in a shock tunnel are:

- (i) Matching tunnel to flight stagnation enthalpies. This ensures that stream energies are sufficient to generate real gas effects of appropriate strength.
- (ii) Matching values of the binary scaling variable at corresponding points in the flight and wind tunnel model flow fields. This can be done by matching tunnel to flight values of the binary scaling parameter $p_\infty D$, where p_∞ is the freestream density, and D is a typical configuration dimension. It is interesting to note that this criterion is the same as that for matching Reynolds' numbers.

This paper discusses existing* shock tunnels which meet these requirements. They are based on the use of a free piston driver, with helium driver gas. the discussion is centred first on the reflected shock tunnel, and then on the non-reflected shock tunnel, showing how the latter extends the capabilities of the former, though with a much reduced test time. A further development of the free piston reflected shock tunnel†, designed to allow propulsion experimentation, is then briefly outlined.

2. THE FREE PISTON REFLECTED SHOCK TUNNEL

The free piston driver employs a simple principle⁽³⁾. It involves filling a compression tube with driver gas at a relatively low pressure. This tube is coupled to the shock tube at one end, and to a reservoir of moderately high pressure air at the other. The air is separated from the driver gas by a piston, which is prevented from moving until the facility is ready to fire. When the piston is released it is driven along the compression tube, accelerating and acquiring energy from the expanding reservoir gas. As the piston approaches the downstream end of the compression tube, its energy is transferred to the driver gas, raising its pressure and temperature to the point at which the shock tube diaphragm ruptures, and the shock tube flow is initiated. The piston is sufficiently massive that the time scale of the driver compression process is roughly two orders of magnitude longer than that of the shock tube flow processes, so that the transient peak driver conditions produced in the compression process can be taken as quasi steady for the purpose of calculating the shock tube flow. Thus, high temperatures and pressures can be generated in the driver gas, without introduction of contaminants, and this permits the high shock speeds which are a feature of the method. For example, a regularly used test condition involves a driver gas compression ratio which raises the temperature of helium driver gas to 4500K, and produces tailored interface operation with air test gas at a primary shock Mach number of 22. The basic layout of a free piston reflected shock tunnel is shown at the top of fig.9, and more details of the layout of such a facility are presented in refs.3 and 4.

(a) Test Time and Simulation

The question of stagnation enthalpy simulation is interwoven with test time considerations, and it is convenient to consider the latter first. It is limited by driver gas contamination arising from the shock boundary layer interaction which occurs as the shock wave reflects from the downstream end of the shock tube. As shown in fig.3(a) the bifurcation of the strong reflected shock as it interacts with the shock tube wall boundary layer causes "jetting" of the driver gas along the walls when the shock reaches the contact surface. The driver gas therefore arrives prematurely at the nozzle entrance, and contaminates the test gas.

Davies and Wilson⁽⁵⁾ have developed an approximate theory which allows test times to be estimated according to this mechanism. This theory has been extended to allow for the effects of high enthalpy operation with a free piston driver⁽⁶⁾, and yields estimates of test times as shown in fig.3(b). The estimates are made for a 75 mm. diameter constant area shock tube but, for shock tube diameters which are within a factor of two of this value, the test time can be taken to be roughly proportional to the diameter. Also, the driver gas pressure and sound speed can be adjusted to take account of the area change at the diaphragm station which is a part of the free piston driver configuration. For the figure, the horizontal axis expresses the stagnation enthalpy in terms of an equivalent flight velocity, and the vertical axis expresses the test time, t , in terms of the approximate length of the slug of test gas which passes through the test section before contamination begins. It can be seen that with given driver gas conditions, the test slug length reduces strongly as the nozzle stagnation enthalpy is increased but, if the driver sound speed is allowed to increase, then the test slug can be maintained roughly constant.

It is worth noting that, in general, this theory errs somewhat on the conservative side, as demonstrated in fig.3(c). This displays measurements of the time of arrival of driver gas contamination at the test section, normalized with respect to the theoretical estimate. Because it generally is difficult to detect the driver gas by aerodynamic methods, mass spectrometry has been employed at the higher enthalpies⁽⁷⁾, and mass capture probes at the lower ones⁽⁸⁾. A substantial scatter exists in the

* In operation at the Australian National University, Canberra, Australia.

† Under construction at the University of Queensland, Brisbane, Australia.

data at the upper end of the enthalpy range for the hydrogen driver results, as the tests approach the tailored interface condition. This is thought to arise from an intermittency in the passage of the gas from the wall jet across the end wall of the shock tube and, if it is ignored, then the general trend is for the measured test times to exceed predictions.

It can be seen that, with a test gas slug length only of the order of metres, the effect of the nozzle flow starting process on the test time becomes important. This is illustrated in fig.4. The figure shows the double shock system which arises from the expansion of the test gas into the shock tunnel nozzle after reflection of the primary shock wave at the end of the shock tube. If the initial gas density in the nozzle is sufficiently low, this shock system passes through the nozzle rapidly enough to ensure that it is always followed by an unsteady expansion. The upstream head of this expansion (the "(u-a) wave") marks the onset of steady flow. Taking the point C on the figure as indicating the arrival of driver gas contaminant at the entrance to the nozzle, it will transmit to the test section along the steady flow particle trajectory from C. It then follows that the difference between the time taken for the (u-a) wave to traverse the nozzle, and that for a flow particle, will be the net loss of the test time associated with the nozzle starting process.

Some estimates of this test time loss lead to the rough rule of thumb that, for a contoured nozzle which begins with an included angle of 30° at the throat, it can be given as

$$\Delta t_s = (2.5 \ell M_s^{-1} + 14r) / \sqrt{2h_s}$$

where ℓ is the overall nozzle length, M_s is the test section Mach number, r is the nozzle throat radius, and h_s is the nozzle stagnation enthalpy. This is plotted in fig 3(b) for an $M_s = 6$ nozzle 1 metre long, with a throat radius of 10 mm. It can be seen that it reduces the useful length of the test gas slug by approximately 0.5 m, and that this is enough to be significant at high enthalpies.

The remaining test slug length provides an indication of the size of models which can be tested in the shock tunnel. For example, for boundary layer studies without separation, the steady flow test slug length must approach three times the model length. Thus, the 4.4 km.s.⁻¹ speed of sound curve in fig.3(b) allows boundary layer studies (including heat transfer measurements) to be made on models which are 0.3 m. long at values of $\sqrt{2h_s}$ up to 7 km.s.⁻¹. Smaller models can be tested at higher stagnation enthalpies. This example shows how the useful stagnation enthalpy limits of a shock tunnel are conditioned by the model size.

The value of the binary scaling parameter, p_D , obtained in a shock tunnel depends on the test section density, as well as the model size. With a given nozzle reservoir pressure (i.e. pressure at the end of the shock tube after the shock reflection process is completed) the density can be increased by reducing the test section Mach number. For a given test section size, this is limited by the allowable nozzle throat size, consistent with avoiding excessive drainage of gas from the shock reflection region. In fact, this requirement is not too demanding and, for the 4.4 km.s.⁻¹ speed of sound curve in fig.3(b), it is possible to operate a nozzle with throat and test section diameter of 25 mm. and 250 mm. respectively to produce test flow Mach numbers ranging from 6.5 to 5.5, depending on the stagnation enthalpy. With this nozzle, a model 0.3 m. long, and a flight to model scale ratio of 100:1, it is possible to establish a simulation boundary on a velocity-altitude diagram. This is shown in fig.5, as the $M = 6$ boundary. Since the flight value of p_D can be simulated for any point above this boundary, by reducing the nozzle reservoir pressure or the throat size, it follows from the figure that much of the high enthalpy portion of the Space Shuttle Orbiter trajectory can be simulated.

3. REAL GAS FLOW EXPERIMENTS IN THE SELECTED SHOCK TUNNEL

A number of basic research studies involving non-equilibrium real gas effects have been performed in the free piston reflected shock tunnel, T3, in Canberra, and some examples are briefly outlined here.

(a) (i) Non-equilibrium Effects in Shock Detachment

Shock detachment is a feature of blunt body flows. It drastically changes the flow field about a body, and can influence the stability characteristics of blunt body flight configurations. An investigation of non-equilibrium real gas effects on shock detachment⁽⁹⁾ has been conducted for two-dimensional wedge configurations, and results are shown in fig.6. First, tests were conducted with argon at low enthalpies in order to confirm the relation between shock detachment and wedge angle in the perfect gas case. This relation then was used to predict the perfect gas shock detachment for nitrogen, and is compared in the figure with measurements taken at $h_s = 22 \text{ MJ.kg}^{-1}$. It can be seen that real gas effects inhibit the development of shock detachment, yielding much less detachment for a given wedge angle than the perfect gas case.

(a) (ii) Constant Temperature Curved Shock

Analysis of the non-equilibrium flow downstream of a curved shock in nitrogen⁽¹⁰⁾ shows that the dissociation reaction is quenched close to the shock, at a temperature which is independent of the shock slope. Thus, the constant density ratio shock wave of perfect gas hypersonic flow is replaced by a constant temperature ratio shock wave. This will, of course, be evident in the shock density ratio and to confirm this effect, Mach Zehnder interferograms were used to measure the density downstream of the curved shock formed by a two-dimensional cylinder model. The results are shown in fig.7., and indicate density ratios consistent with a constant temperature shock.

It is interesting to note that one of the consequences of this effect is a change in the vorticity downstream of the shock.

(a) (iii) Flat Plate Heat Transfer

Thin film gauges were used to study the heat transfer on a flat plate⁽¹¹⁾ 0.5 m. long. The results, shown in fig 8(a), reveal the importance of surface catalysis effects. For the test conditions of the experiments, the oxidized steel surfaces of the shock tunnel models are non-catalytic and the increasing level of frozen atomic species in the freestream as the stagnation enthalpy is increased causes a corresponding increasing reduction in heat transfer level. This is evident in the figure. Also, increasing the tunnel nozzle reservoir pressure at $\sqrt{2h_0} = 5.7 \text{ km.s.}^{-1}$ increases the forward reaction rates in the boundary layer, and produces the further reduction in heat transfer which is evident in the figure.

Using these heat transfer values, combined with available catalytic coefficients for Space Shuttle Orbiter tile materials, it was possible to predict the reduction in heat transfer which is shown to be consistent with flight measurements in fig.8(b).

(b) Tunnel Limitations

These, and other, experiments have established the efficacy of the free piston reflected shock tunnel for real gas flow experiments up to, and perhaps somewhat exceeding, stagnation enthalpies corresponding to Earth orbital velocity. However, to proceed to higher stagnation enthalpies, it is necessary to produce substantial levels of ionization in the test gas at the end of the shock tube after shock reflection and, in experimental studies of this region^{(12),(13)} it was found that radiative energy losses were too high to allow effective reflected shock operation. Thus, a "radiation barrier" prevented the attainment of significantly higher stagnation enthalpies.

Also, some desired experiments called for higher nozzle reservoir pressures than were achieved, either to increase the value of the binary scaling parameter, or to increase the Mach number without reducing the binary scaling parameter.

In order to meet both these requirements, the facility was developed to operate in the non-reflected shock tunnel mode.

4. THE FREE PISTON NON-REFLECTED SHOCK TUNNEL

Non-reflected shock tunnel operation has been employed by previous experimenters (e.g. ref.14). It requires that nozzle flow starting times be minimized, and this has been effected by using a pre-evacuated nozzle, with a light diaphragm near the nozzle entrance. However, this is not possible with the short test times which are available in shock tubes at high stagnation enthalpies, as the diaphragm fragments cannot be removed from the flow sufficiently rapidly. This problem was circumvented by developing the "Prior Steady Flow" technique for starting the nozzle⁽¹⁵⁾.

(a) The Prior Steady Flow Technique

The manner in which the technique operates can be seen by noting that, as shown in fig.4, the starting process in an expanding nozzle normally involves the formation of a secondary shock wave, which tends to propagate upstream into the test gas. Although this shock wave is swept downstream by the motion of the test gas, it can be strong enough to cause a substantial delay in starting the nozzle flow and, if the shock tube test time is short, it may eliminate the steady flow period in the nozzle altogether.

The prior steady flow technique weakens the starting shock by establishing a steady flow of test gas through the nozzle prior to arrival of the primary shock wave at the nozzle entrance. For high shock speeds, the velocity of the prior steady flow is insignificant. However, the associated density distribution in the nozzle is such that the starting shock system is swept through the nozzle without significant decay in velocity, and delays in nozzle starting associated with the starting shock system are eliminated. Steady flow in the test section therefore is established upon passage of the (u-a) wave in fig.4.

Modification of a free piston reflected shock tunnel for non-reflected operation is shown in fig.9. It is effected by removing the nozzle and test section, and replacing them with a new test section, and an extension to the shock tube. The extension is surrounded by a nozzle feed tank, and the test section is vented to the dump tank via the valve assembly. The valve is spring loaded to open. The valve actuating sleeve is rigidly connected to the shock tube and, prior to a test, the dump tank and test section assembly is moved towards the shock tube, allowing the valve actuating sleeve to force the valve to open. The flow of test gas is initiated, passing from the shock tube and feed tank to the pre-evacuated dump tank. The feed tank is large enough to act as a steady state reservoir for this prior steady flow, ensuring that the shock tube pressure does not change significantly as the piston traverses the length of the compression tube. When the piston reaches the end of the compression tube, the shock tube main diaphragm is ruptured and the shock tube flow is initiated.

With the non-reflected modification installed, the overall length of the 75 mm. diameter shock tube, in the T3 facility, is 8.4 m. The entrance to the nozzle is 38 mm. diameter, and the nozzle is contoured to produce parallel flow at the test section. It is a supersonic to hypersonic nozzle, designed for an area ratio of 16.

(b) Test Time and Simulation

The non-reflected shock tunnel avoids the "radiation barrier", because at least half of the stagnation enthalpy takes the form of the flow kinetic energy, and therefore is not subject to radiation loss. However, it achieves this objective at the price of greatly reduced test times. These are displayed in fig.10 in the form of test slug lengths, as in fig.3. They are determined by recording the termination of radiation from the stagnation point of a blunt body in the test section, with the time taken for the nozzle starting process obtained from time resolved Mach Zehnder interferograms. It can be seen that effective test slug lengths are an order of magnitude less than those obtained with the reflected shock tunnel.

The simulation capability of the non-reflected shock tunnel is shown in fig.11. As for fig.5, it is possible to match stagnation enthalpy and the binary scaling parameter for altitudes above the shaded boundary. Because of the higher effective nozzle reservoir pressures associated with non-reflected operation, the simulation boundary lies at a lower altitude than that for the reflected shock tunnel at comparable stagnation enthalpies.

It is worth noting that the high enthalpy capability of the non-reflected shock tunnel affords the interesting possibility of simulating flows associated with entry to the outer planets. The atmospheres of these planets are hydrogen-helium mixtures but, except at very high flow energies, the helium acts only as an inert diluent. In this role, it can be replaced by neon and, with hydrogen-neon test gas mixtures, it is possible to produce effects associated with ionization of hydrogen in the flow. For example, at a stagnation enthalpy of 140 MJ.kg^{-1} , using a 60% H_2 - 40% Ne mixture, it is possible to simulate flow over a blunt cone under conditions corresponding to peak heating in entry to the atmosphere of Saturn.

5. EXPERIMENTS IN THE NON-REFLECTED SHOCK TUNNEL

In order to demonstrate the utility of the non-reflected shock tunnel, two experiments are reported briefly. The first demonstrates the high enthalpy capability of the facility, and the second the high nozzle reservoir pressure capability.

(a) (i) Ionizing Wedge Flows of Hydrogen-Neon Mixtures

Wedge flows of 60% hydrogen 40% neon gas mixtures were studied using Mach Zehnder Interferometry⁽¹⁶⁾. Fig.12 shows a forward fringe shift (towards the leading edge), due to neutral particle density increase across the shock wave, at a wedge incidence of 30° . At 35° , the forward fringe shift is followed by a reverse shift, due to electron production. Close to the surface, a further forward fringe shift marks the presence of the boundary layer. These experiments demonstrated that steady flow over simple models could be established in the short test times available. The results were used to resolve uncertainties in hydrogen ionization rates which existed in the literature at the time of the experiments.

(a) (ii) Non-equilibrium Afterbody Flows

Mach Zehnder interferograms were taken of the two-dimensional flow of nitrogen over a flat plate with a cylindrically blunt nose⁽¹⁷⁾. A typical result is shown in fig.15, and is compared with results of numerical computations. The high effective nozzle stagnation pressures allowed a hypersonic flow to be produced at a pitot pressure level of 13 atm., thus raising the test section density high enough to allow strong real gas effects to occur at the relatively small blunt nose. The Mach Zehnder interferograms allowed the downstream effects of the flow at the nose to be observed. An experimental interferogram is compared with results of numerical computations in fig.13, and the two are seen to be consistent with each other, except near the surface, where the experiments indicate much lower densities than the computations. The reason for this discrepancy had not been resolved at the time of writing.

6. A PROPULSION SHOCK TUNNEL

The search for a means of delivering payloads to Earth orbit which is cheaper than those used at present has directed attention to techniques of airbreathing propulsion at speeds approaching orbital velocity. In order to produce the combustion heat release which is essential to airbreathing propulsion, it is necessary to limit precombustion air temperatures to values around 1500K, even with hydrogen fuel. At the high stagnation enthalpies associated with high velocity flight, this implies that combustion will take place under hypersonic conditions. For vigorous hydrogen combustion to take place within a length scale of, say, 100 mm., experiments similar to those reported in ref.17 have shown that pressures of the order of 0.5 atm. are required and, at a Mach number of 7, this requires nozzle reservoir pressures approaching 2000 atm. Since test times in the non-reflected shock tunnel are considered to be too short for most propulsion experiments, it was necessary to develop the reflected shock tunnel for this purpose.

Now, one of the disappointing features of the free piston shock tunnel T3 has been the pressure losses experienced in passing from the compressed driver gas at diaphragm rupture to the nozzle reservoir region at the downstream end of the shock tube⁽¹⁹⁾, after shock reflection. Whilst the reason for this is not understood at present, model studies have established that the effect can be overcome by ensuring that the face of the piston is well removed from the entrance to the shock tube at diaphragm rupture. To accommodate this, whilst producing the high compressed driver gas temperatures necessary for high enthalpy operation, it is necessary to use a long compression tube.

The construction of a shock tunnel embodying these principles is nearing completion at the University of Queensland. It employs a compression tube 25 m. long and 228 mm. in diameter, driving a shock tube 10 m. long and 75 mm. in diameter. It is designed to produce nozzle reservoir pressures of 2000 atm. and, although it obviously has potential for other applications, it is intended to use it, in the first instance, for studies of hypersonic combustion.

7. CONCLUSION

A discussion of the requirements for simulation of real gas effects in hypersonics leads to the conclusion that, for flows typical of re-entry gliders and acceleration vehicles, only the behaviour of the forward non-equilibrium reactions in air needs to be simulated. This implies that stagnation enthalpy and the binary scaling parameter, $p_{\infty}D$, represent the two primary requirements for simulation.

The coupling of a free piston driver to a reflected shock tunnel has produced a facility which will satisfy both these requirements, for flight vehicles similar to the Space Shuttle Orbiter, at flight speeds up to approximately 7 km.s.⁻¹. The simulation capability is limited by the test time, which is fundamentally determined by the shock boundary layer interaction occurring at shock reflection in the shock tube. Within this limitation, test times are sufficient to allow realistic experimentation on hypersonic real gas effects, and this is confirmed by the results of some typical experiments.

It is worth noting that, although stagnation enthalpy and $p_{\infty}D$ can be matched in the tunnel, the overall simulation will be imperfect, in that freestream composition and Mach number are not matched. However, experience has shown that these imperfections are not a major impediment in many reacting flow situations, largely because conditions downstream of a strong shock tend to be independent of those upstream. If situations occur where they are particularly significant, their effects could be accommodated in numerical real gas simulation models, implying that shock tunnels then could be used to provide the experimental data base for validation of these models.

Because a "radiation barrier" effect limits the maximum stagnation enthalpy available in a reflected shock tunnel, and high nozzle stagnation pressures are sometimes desired for real gas studies, the non-reflected shock tunnel is attractive, notwithstanding its short test times. The prior steady flow technique for nozzle starting makes high enthalpy non-reflected shock tunnel testing a practical proposition. It produces a facility which will allow testing with stagnation enthalpies well in excess of reflected shock tunnel limits, including values which allow simulation of the effects of hydrogen ionization on the gas dynamics of entry into the atmospheres of some of the outer planets. At lower stagnation enthalpies, values of $p_{\infty}D$ appropriate to an acceleration vehicle are possible.

When the established capabilities of the free piston reflected shock tunnel, and the free piston non-reflected shock tunnel, are combined with the designed capabilities of a new high enthalpy propulsion shock tunnel which currently is under construction, it becomes clear that shock tunnel facilities have developed to a point which will allow experimental study of real gas effects in hypersonic flow over the range of flight speeds which are likely to be of foreseeable interest to beyond the turn of the century.

REFERENCES

1. Wittliff, C.E., Sundaram, T.R., Rae, W.J., and Lordi, J.A. Arnold Eng.Devel. Centre, Tenn., "Study of High Density Hypervelocity Flows and Similitudes". 1967, AEDC-TR-67-72.
2. Vincenti, W.G., and Kruger, C.H. "Introduction to Physical Gas Dynamics". New York, Wiley & Sons, Inc., 1965, p.230.
3. Stalker, R.J. "A Study of the Free Piston Shock Tunnel". AIAA Journal, 1967, V5, pp.2160-2165.
4. Stalker, R.J. "Development of a Hypervelocity Wind Tunnel". Aero. J. of Roy. Aero. Soc., 1972, V76, pp.374-384.
5. Davies, L., and Wilson, J.L. "Influence of Reflected Shock and Boundary-Layer Interaction on Shock-Tube Flows". Physics of Fluids. Supplement 1, 1969, V12, pp.1-37 to 1-43.
6. Crane, K.C., and Stalker, R.J. "Driver Gas Contamination in a High-Enthalpy reflected Shock Tunnel". AIAA Journal, 1978, V16, pp.277-278.
7. Crane, K.C., and Stalker, R.J. "Mass Spectrometric Analysis of Hypersonic Flows". J. Phys. D., Appl. Phys., 1977, V10, pp.679-695.

8. Copper, J.A., Miller, H.R., and Hameetman, F.J. "Correlation of Uncontaminated Test Durations in Shock Tunnels". Proc. Fourth Hypervelocity Techniques Symposium, Denver. Res. Inst., Univ. of Denver, 1965, pp.274-310.
9. Hornung, H.G., and Smith, G.H. "The Influence of Relaxation on Shock Detachment". J. Fluid Mech., 1979, V93, pp.225-240.
10. Hornung, H.G. "Non-equilibrium Ideal Gas Dissociation After a Curved Shock Wave". J. Fluid Mech., 1976, V74, pp.143-160.
11. East, R.A., Stalker R.J., and Baird, J.P. "Laminar Flat Plate Heat Transfer Measurements from a Dissociated High Enthalpy Hypersonic Air Flow". J. Fluid Mech., 1980, V94, pp.673-699.
12. Hornung, H.G., and Sandeman, R.J. "Interferometry of Radiating Argon Flow-over Blunt Bodies". J. Phys. D. Appl. Phys., 1974, V7, pp.920-934.
13. Logan, P.F., Stalker, R.J., and McIntosh, M.K. "A Shock Tube Study of Radiative Energy Loss from an Argon Plasma". J. Phys. D. Appl. Phys., 1977, V10, pp.323-337.
14. Oertel, H. "Non-reflected Shock Tunnel Test Times". Proc. 7th Int. shock Tube Symp., Univ. of Toronto Press, Toronto., ed. I.I. Glass, 1970, pp.80-108.
15. Stalker, R.J., and Mudford, N.R. "Starting Process in the Nozzle of a Non-reflected Shock Tunnel". AIAA Journal, 1973, V11, pp.265-266.
16. Stalker, R.J. "Shock Tunnel Measurements of Ionization Rates in hydrogen". AIAA Journal, 1980, V18, pp.478-480.
17. Macrossan, M.N., and Stalker, R.J. "Afterbody Flow of a Dissociating Gas Downstream of a Blunt Nose". American Inst. of Aeronautics & Astronautics, AIAA Paper no. 86-0407, 1987.
18. Stalker, R.J., and Morgan, R.G. "Supersonic Hydrogen Combustion with a Short Thrust Nozzle". Combustion and Flame, 1984, V57, pp.55-70.
19. Stalker, R.J., and Hornung, H.G. "Two Developments with Free Piston Drivers". Proc. 7th Int. Shock Tube Symp., Univ. of Toronto Press, Toronto, ed. I.I. Glass, 1970, pp.242-251.
20. Page, N.W., and Stalker, R.J. "Pressure Losses in Free Piston Driven Shock Tubes". Proc. 14th Int. Symp., on Shock Tubes and Waves, Univ. of N.S.W. Press, Sydney, ed. D. Archer & B. Milson, 1983, pp.118-125.

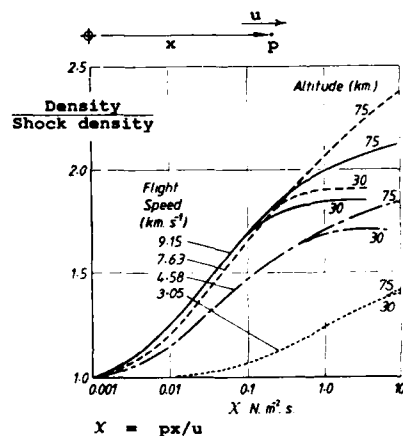


FIG 1. CONSTANT PRESSURE RELAXATION

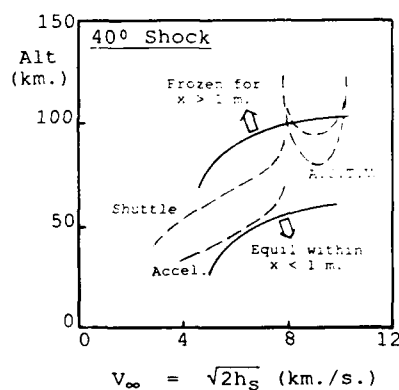


FIG 2. NON-EQUILIBRIUM REAL GAS REGION

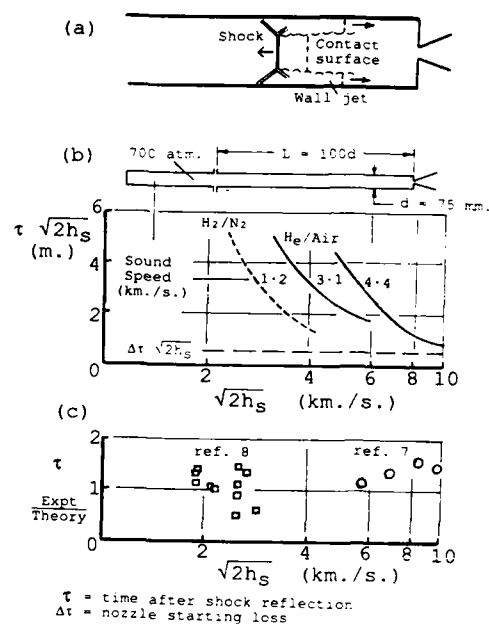


FIG 3. REFLECTED SHOCK TUNNEL TEST TIME

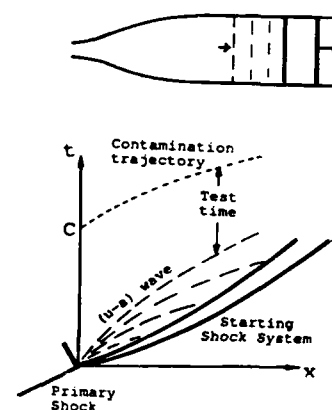


FIG 4. NOZZLE FLOW STARTING

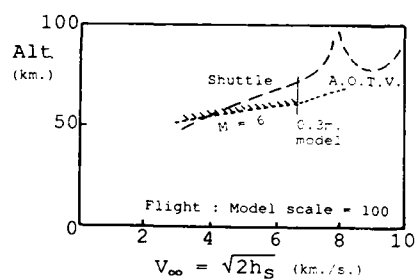


FIG 5. REFLECTED SHOCK TUNNEL FLIGHT SIMULATION BOUNDARY

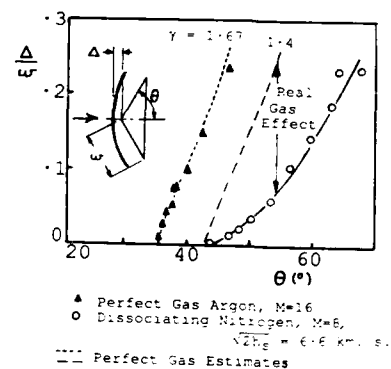


FIG 6. NON-EQUILIBRIUM SHOCK DETACHMENT ON A WEDGE

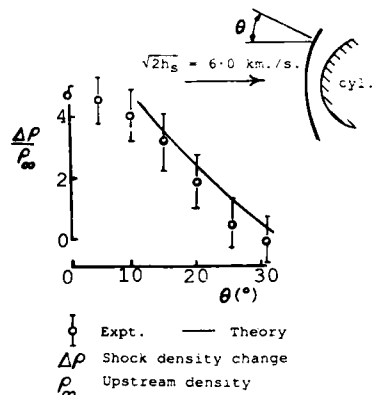
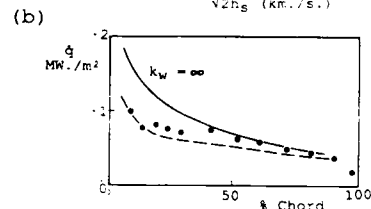
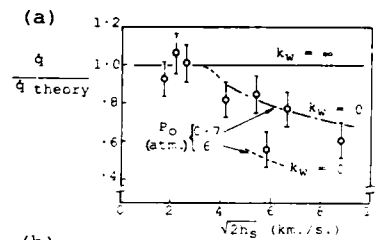


FIG 7. CONSTANT TEMPERATURE CURVED SHOCK WAVE



- (a) T3 flat plate measurements;
 P_0 = test section pitot pressure
 (b) Shuttle flight data,
 • 2nd flight, Alt. 75 km.,
 $V_{\infty} = 7.2 \text{ km./s.}$
 — Preflight prediction, $k_w = \infty$
 - - - Preflight prediction from T3 measurements

FIG 8. NON-EQUILIBRIUM HEAT TRANSFER

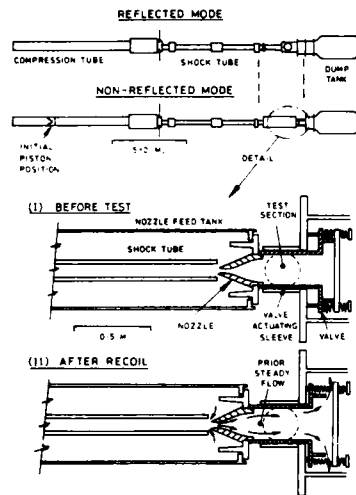


FIG 9. NON-REFLECTED MODIFICATION

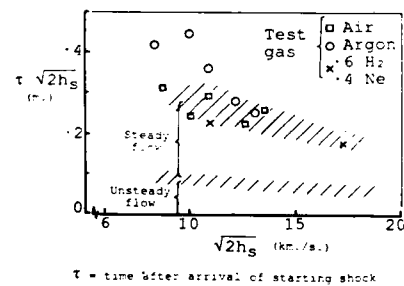


FIG 10. NON-REFLECTED SHOCK TUNNEL TEST TIMES

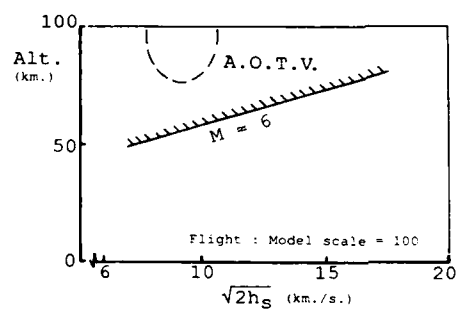
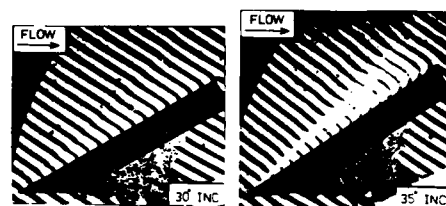
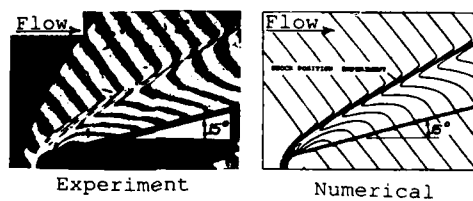


FIG 11. NON-REFLECTED SHOCK TUNNEL
FLIGHT SIMULATION BOUNDARY



0.6 H₂ - 0.4 Ne, $\sqrt{2}h_s = 16.5$ km./s., $M_{\infty} = 6.5$,
Hydrogen 95% dissociated in free stream

FIG 12. IONIZING WEDGE FLOW



Nitrogen test gas, $\sqrt{2}h_s = 7$ km./s.

FIG 13. BLUNT NOSE NON-EQUILIBRIUM
AFTERBODY FLOW

TURBULENCE MEASUREMENT IN HYPERSONIC FLOW

F. K. Owen
Complere Inc.
P.O. Box 1697
Palo Alto, CA 94302

and

W. Calarese
AFWAL/FIMG
Wright-Patterson AFB, OH 45433

SUMMARY

An assessment has been made of the potential for hot wire and laser anemometer measurements of turbulent fluctuations in hypersonic flow fields. The results of experiments conducted in the AFWAL M=6 High Reynolds Number Wind Tunnel are reported and comparisons made with previous hot wire turbulence measurements.

LIST OF SYMBOLS

The following symbols are not defined in the text.			
	Subscripts	Superscripts	
m mass flux	e edge	+	wall variable
M Mach number	f fluid	'	fluctuation
p pressure	m mass flux	—	time average
T temperature	p particle	~, ' rms quantities	
u_t friction velocity	t total		
U, V mean flow velocity	w wire		
Δe_m mass flux sensitivity			
Δe_t total temperature sensitivity			
Δu velocity change			
γ specific heat			
μ viscosity			
ρ density			

1. INTRODUCTION

In the post-Apollo era, a time of reduced space effort in the United States and Europe, the subject of hypersonic aerodynamics has been neglected and many hypersonic simulation facilities have either been scrapped or decommissioned. However, with the resurgence of planned hypersonic research associated with the National Aerospace Plane, for example, facilities and experimental methods for hypersonics are once again in strong demand.

During this period of hypersonic neglect, great strides have been made in our capabilities to compute complex fluid flows. But, reliable flight vehicle designs and modifications still cannot be made without recourse to extensive wind tunnel testing. At present, progress in computational fluid dynamics of hypersonic flows is restricted by the need for reliable experimental data and an improved understanding of both the physics and structure of turbulence in high speed flows which can be used for the development of empirical turbulence models and to validate Navier-Stokes codes. Although some hot wire data have been obtained in previous years, they are of questionable reliability due to the assumptions which must be made to determine velocity fluctuation levels from the measured hot wire variables. Currently, there are few compressible flow measurements which could be used for modelling purposes, and, since additional shear stress terms may be significant at high Mach numbers, models based on incompressible measurements may not be realistic. Experiments designed to aid turbulence modeling of hypersonic flows and verify computer codes will require extensive flow field turbulence measurements.

Experimental methods in lower speed regimes have also made significant advances due primarily to the availability of high power lasers. Their introduction has enabled the field of laser velocimetry to expand from low speed, small scale, closely controlled laboratory applications to the measurement of compressible flows in large scale wind tunnels. (Ref. 1). The advent of the laser velocimeter allows us to measure velocity fluctuations directly in a linear, non-intrusive manner. Of particular value is the capability it offers to measure some of the compressible turbulent shear stresses, since this is an impractical task with hot wires.

The challenge now is to apply these new computational and experimental capabilities to the solution of current and future hypersonic flow problems in a cost effective and timely manner. But, before complex and expensive test plans are made, an assessment of the potential for laser velocimetry in hypersonic flows must be made. To achieve this, fundamental questions of seeding and optical sensitivity must be answered by experimentation. The purpose of this work was to make such a determination for flowfield measurements in the AFWAL M=6 High Reynolds Number Wind Tunnel.

2. BACKGROUND

Current turbulence measurement requirements for hypersonic flow fall into three primary areas, namely: measurements to define wind tunnel flow quality in facilities to be used in future transition experiments, measurements of basic bench-mark flows to support turbulence modeling efforts and measurements to determine the mechanisms and effects of large scale turbulent interactions in flows of immediate practical interest.

At present, the principal research tools for turbulence measurement in low speed flows are hot wire and laser anemometers. In hypersonic flows, hot wires can be used reliably to measure freestream mass flux and total temperature fluctuations but cannot be used in flows which involve high levels of turbulence, separation or time-dependent flow reversal which are often associated with shock/boundary layer interactions (Ref. 2). On the other hand, due to resolution limitations, the laser anemometer is not suitable for low turbulence, freestream measurements. But, with its linear and directional sensitivity it probably represents the instrument of last resort for the non-intrusive measurement of large scale, unsteady turbulent flows. Thus, it is important that the practical problems associated with both hot wire and laser anemometry are addressed and that redundant hot wire and laser velocimeter experiments and comparisons be carried out to determine their reliable ranges of application. Measurements to support turbulence modeling could then be chosen so that the attributes of both techniques could be applied with care.

A hot-wire anemometer senses any changes in the variables which affect the rate of heat-transfer between the wire and the fluid. Variations in heat transfer coefficient can change both wire temperature and resistance. If the wire is made part of a suitable electrical circuit, these changes can be used to generate a signal which is related to the instantaneous heat transfer. Thus, as Morkovin (Ref. 3) points out, for the correct interpretation of the electrical signal we need to know: 1) the identity of possible fluid flow variations (eg. turbulence or sound), 2) the laws of heat transfer between the wire and fluid, 3) the variation of wire resistance with temperature and the effects of conduction to the supports, and 4) the response of the associated electrical system which produces the measured current or voltage variations.

Unfortunately, our knowledge in each of these categories is far from complete and could well be responsible for the current lack of reliable data. A recent review (Ref. 4) of supersonic and hypersonic hot-wire data taken in zero pressure gradient, adiabatic or isothermal wall boundary layers illustrates the problem. Fig. 1, taken from Ref. 4, shows data from several sources for the fluctuating axial velocity component. The scatter is so large that it is impossible to construe that any form of similarity with Reynolds or Mach number exists. The picture is even more confusing when the distributions of the other two normal stresses are reviewed (Ref. 4). The measured shear stress distributions (Fig. 2) once again show that no pattern of similarity can be observed. Indeed, only Klebanoff's incompressible measurements (shown for comparison) approach the anticipated limiting value of unity in the wall region. These results give some indication of the deficiencies in the measurement techniques and data reduction assumptions.

The problem is further compounded by the fact that a significant portion of the available studies were conducted in wind tunnel nozzle wall boundary layers in which unknown upstream influences could have affected the turbulent structure. Also, many measurements have been made with thin film gages which have doubtful validity for quantitative turbulence measurements, since substrate thermal feedback causes probe sensitivities to vary with frequency. It is particularly serious and complex for multiple films mounted on the same substrate which are the type of probes used for shear stress measurement. Even with crossed-wire probes, data interpretation is involved and can be unreliable. For instance, the time-averaged expression for one component of the compressible turbulent shear stress is $(\overline{p v})' u'$ whereas the hot-wire, after questionable assumptions (Ref. 5), measures $(\overline{p u})' v'$ which differs by a first-order term. Thus, it is clear that systematic investigations of fluctuating velocities are still needed, even in zero-pressure gradient compressible boundary layers to establish a reliable data base for turbulence modeling. Clearly, hot wire turbulence measurements in compressible shear flows still present a formidable scientific challenge. Most flows of practical interest can be extremely sensitive to probe interference. Local turbulence levels also normally exceed those for which reliable hot wire measurements can be expected. Directional intermittency can give rise to substantial hot wire errors (Ref. 6).

There are other factors which affect the reliability of hot wire measurements in flows where more than one mode fluctuation is significant. In these flows, a fundamental hot-wire anemometer requirement for meaningful quantitative measurements is one of high-frequency response over a

wide range of wire overheat ratios. This requirement is needed to separate mass flux and total temperature fluctuations in compressible, non-isothermal flows. But it brings out a basic flaw in the most widely used tool for current turbulence research, namely, the constant temperature anemometer (CTA). This weakness is illustrated by the following equation for the CTA frequency response

$$M_{CTA} = M_w / (1 + 2rR_wG) \quad 1$$

where M_{CTA} and M_w are the time constants of the anemometer system and the wire alone, respectively, r is the wire overheat, R is the wire resistance and G is the anemometer transconductance. It can be seen that the CTA frequency response is directly proportional to the wire overheat ratio and at low overheat ratios ($r \rightarrow 0$) the anemometer system time constant approaches the wire time constant. Since M_w can range from 1 to 5 ms (frequency response from 32 to 160 Hz), low-overheat, constant temperature anemometer measurements are clearly open to question.

Unfortunately, low overheat measurements are required to determine the total temperature fluctuations and the mass flux total temperature cross correlations. But, with the use of compensating amplifiers, adequate constant current anemometer response can be maintained even at the lowest overheat ratios. Comparisons of the two basic hot wire systems have been made in Ref. 7. These measurements clearly show that there will be a need for alternate constant current anemometer measurements in many hypersonic flow situations.

Other sources of hot wire turbulence measurement uncertainty are the assumptions involved in reducing the hot wire measurements of mass flux and total temperature fluctuations to terms which appear directly in the momentum and energy equations. For example, to obtain the axial velocity fluctuation levels, we assume that the flow field is isentropic. This permits us to write the energy equation in its differential form as

$$\frac{1}{\alpha} \frac{\partial T_t}{\partial t} = (\gamma - 1) M^2 \frac{\partial u}{\partial t} + \frac{\partial p}{\partial t} - \frac{\partial \rho}{\partial t} \quad 2$$

$$\text{where } \alpha = 1 / (1 + \frac{\gamma - 1}{2} M^2)$$

Then we consider the equation for the mass flow per unit area and time in its differential form

$$\frac{\partial m}{\partial t} = \frac{\partial u}{\partial t} + \frac{\partial \rho}{\partial t} \quad 3$$

Substituting for $\partial p / \partial t$ in equation 2 gives

$$\frac{1}{\alpha} \frac{\partial T_t}{\partial t} = (\gamma - 1) M^2 \frac{\partial u}{\partial t} + \frac{\partial p}{\partial t} - \frac{\partial m}{\partial t} + \frac{\partial u}{\partial t} \quad 4$$

or, collecting terms, we obtain

$$\frac{\partial u}{\partial t} = \frac{1}{\alpha [1 + (\gamma - 1) M^2]} \frac{\partial T_t}{\partial t} - \frac{1}{[1 + (\gamma - 1) M^2]} \left[\frac{\partial p}{\partial t} - \frac{\partial m}{\partial t} \right] \quad 5$$

which, defining $\beta = \alpha(\gamma - 1) M^2$, can be written as

$$\frac{\partial u}{\partial t} = \left(\frac{1}{\alpha + \beta} \right) \frac{\partial T_t}{\partial t} - \left(\frac{\alpha}{\alpha + \beta} \right) \left[\frac{\partial p}{\partial t} - \frac{\partial m}{\partial t} \right] \quad 6$$

In past shear layer studies, the effect of pressure fluctuations has been neglected so that, with $p/p \ll 1.0$, equation 6 may be written as

$$\frac{\partial u}{\partial t} = \left(\frac{1}{\alpha + \beta} \right) \frac{\partial T_t}{\partial t} + \left(\frac{\alpha}{\alpha + \beta} \right) \frac{(\partial u)}{(\partial u)} \quad 7$$

Squaring both sides of this equation leads to an expression for the streamwise turbulence intensity in the form

$$\frac{\overline{u'^2}}{\overline{u}^2} = \left(\frac{1}{\alpha + \beta} \right)^2 \frac{\overline{T_t'^2}}{\overline{T_t}^2} + \frac{2\alpha}{(\alpha + \beta)^2} \frac{(\overline{\rho u})' \overline{T_t}}{(\overline{\rho u} \overline{T_t})} + \left(\frac{\alpha}{\alpha + \beta} \right)^2 \frac{(\overline{\rho u})'^2}{(\overline{\rho u})^2} \quad 8$$

Clearly the measurement accuracy is governed by a pressure fluctuation assumption which is probably not valid in hypersonic flows, and questionable, low-overheat determinations of the first two terms in equation 8. The procedures used to evaluate other terms which appear in the momentum and energy equations are reviewed in Ref. 5. These analyses show that previous hypersonic hot wire measurements could be subject to substantial errors.

However, recent developments in laser velocimetry facilitate the non-intrusive, linear

measurement of complex high speed turbulent flows and the direct measurement of some shear stress terms. But, before laser velocimetry can be extended to hypersonic flow, some basic questions must be addressed. The primary question is that of particle size requirement for reliable response combined with adequate Mie scattering.

The motion of a spherical particle in a fluid flow has been reviewed and summarized by Hinze (Ref. 8). The results show that, given the particle diameter, specific gravity and the local flow conditions, the particle response to sinusoidal velocity fluctuations of the surrounding fluid can be estimated from

$$(d^2\rho_p/18\mu_f)(dV_p/dt) = (V_f - V_p) = 0 \quad 9$$

The analysis, which assumes Stoke's drag with the Cunningham correction, gives the particle response to turbulent fluctuations in the moving frame of reference of the particle. Equation 9 may be transformed to

$$V_p(S)/V_f(S) = 1/(T_p S + 1) \quad 10$$

where S is the Laplace operator and T_p is the time constant defined as

$$T_p = d^2\rho_p/18\mu_f \quad 11$$

By substituting $i\omega$ for S in equation 10, the particle response in the frequency domain may be written as

$$V_p/V_f = 1/(T_p^2\omega^2 + 1)^{0.5} \quad 12$$

where ω is the frequency of the fluid flow fluctuations in radians/sec. However, in the low density and static temperature environments associated with hypersonics, corrections are required to the Stoke's drag coefficient which extend its range of application to flows where the Knudsen number is significant. The form used in Ref. 9 results in a modified time constant which may be written as

$$T_p = (\rho_p d_p^2/18\mu_f)(1 + k L/d_p) \quad 13$$

where k is the Cunningham constant and L is the mean free path. Clearly, the effect of increasing Knudsen number is to degrade particle response. However, when the Knudsen number is large, equation 13 shows that relative seed particle response is proportional to the product of the diameter and specific gravity rather than the square of the diameter. In hypersonic flow, low static density and gas viscosity associated with low static temperature result in relatively large Knudsen numbers. Therefore, the use of large diameter, low specific gravity particles becomes a possibility.

As an example, figure 3 shows some calculated particle response curves for the two operational extremes of the AFWAL 20 inch Hypersonic Wind Tunnel. The curves are for $M=12$ assuming particle densities of 1 gm/cc. Also shown is the response of a 0.1 gm/cc, 5 micron particle of the type used previously in combustion studies (Ref. 10). It can be seen that, when the mean free path is large, Knudsen number effects dominate the seed particle response to such an extent that the lighter 5 micron particle response can exceed that of a 1 micron water droplet. Indeed, when the Knudsen number is large, the lighter seed material can have essentially the same response as that of a 0.5 micron droplet. Since the intensity of the scattered light, and hence signal to noise ratio, is proportional to the square of the particle diameter and, since the number of photons emitted is proportional to the time of flight through the focal volume, the advantages of using large, low density particles in some hypersonic flows is clearly evident.

These initial calculations indicate that final seed particle choice will be governed by the ratio of particle size to mean free path and may well be different in other test facilities. Figure 4 shows the significance of this effect. Clearly, the flow conditions in the 20 inch facility and other hypersonic test facilities will be in the Knudsen number range where careful choice of seed material must be exercised. Mie scattering calculations (Fig. 5) which show the effects of particle size and scattering angle on light collection indicate that the use of larger particles may be mandatory in most back-scatter applications where the scattered light intensity can be reduced by several orders of magnitude.

Although, at first glance, particle response appears to be generally poor in hypersonic flows, we must remember that the seed material is convected in the Lagrangian frame so that frequency response requirements are relaxed by a factor proportional to the difference between the turbulence convection and the local mean velocities. To compare with hot wire turbulence spectra observations, we must convert the frequencies to their equivalent counterparts in a fixed (Eulerian) frame of reference. To do this, we assume that the turbulent fluctuations relative to the moving particle approximate those observed in a frame of reference moving with the local mean velocity. Thus the

turbulent frequencies in the two cases are related by a velocity ratio U_c/U_c where U_c is the turbulence convection velocity. Previous hot wire work in the Ames 3.5 ft. Hypersonic Wind Tunnel (refs. 7 and 11) has shown that the broad-band disturbance convection velocity is close to 0.8 of the freestream value over most of the boundary layer. Thus, the particle response estimates could well be increased by a factor of five. However, close to the wall, where the turbulence levels are highest, filtered space-time cross-correlation measurements (Ref. 7) show that the high frequency, small scale turbulence is convected at velocities within 5 per cent of the local mean. This indicates that the particle response calculations could underestimate the actual response by a factor of twenty. Thus, practical particle response may well be adequate for some, if not all, hypersonic flows.

Particle trajectory calculations also suggest that adequate particle response and recovery across shock waves may be possible in some flow situations. Fig. 6 shows the effect of a normal shock on particle response in the AFWAL 20 inch and $M=6$ facilities. In these calculations, the particles are assumed to be moving with the gas flow ahead of the shock in a nominal, 0.1 ft. thick boundary layer. It can be seen that 3db ($\Delta u_p/\Delta u_t = .707$) response could be achieved in distances comparable to or smaller than those of the model boundary layer thickness in many flow situations. This arises since the density and temperature increases which occur across shock waves dramatically improve particle trackability (see Fig. 7). Clearly, extensive particle research will be required to optimize the seed materials for hypersonic flows.

3. EXPERIMENTAL DETAILS

The hot wire anemometer and laser velocimeter measurements were made in the AFWAL $M=6$ High Reynolds Number Wind Tunnel, which is an open jet, blow down facility. It was designed to produce a maximum free stream unit Reynolds number of 3×10^7 per foot and operates over a stagnation pressure range from 700 to 2100 psia at a fixed stagnation temperature of 1100 R. The supply air is heated in a pebble bed storage heater which allows run times of up to 100 seconds at the maximum mass flow rate of 90 pounds per second. The measurements were obtained in the tunnel empty free stream and on two model configurations namely, on a zero pressure gradient smooth flat plate and in a pressure gradient flow imposed by the introduction of a 30 deg. ramp.

The freestream hot wire measurements were made with two separate anemometer systems. The mass flux fluctuations were determined from high overheat measurements using a constant temperature anemometer and the total temperature fluctuations were measured at low overheat ratios using a constant current system. The hot wire probes which had length to diameter ratios of ≈ 200 were fabricated from 0.0005 inch dia. Platinum-Rhodium wires. Probe fabrication and calibration details are given in Ref. 5.

Two different laser velocimeter configurations were used during the test program. For the initial measurements, a single component forward scatter fringe mode system was fabricated and used to measure the zero pressure gradient velocity profiles. To avoid unknown contamination from upstream flow history, these measurements were made in a fully developed, zero pressure gradient, smooth wall boundary layer. The second system, which was used for the ramp flow measurements, utilized the 4880 and 5145 Angstrom lines of an argon-ion laser and is shown schematically in Fig. 8. One spectral line was used to measure the streamwise velocity component, the other to measure the vertical velocity component. Bragg-cell frequency shifting, a necessity for probing highly turbulent and separated flow regions, was incorporated in both spectral lines. The frequency offsets also facilitated the direct measurement of the vertical velocity component (i.e. ± 45 deg. beam orientations to resolve the vertical velocity were unnecessary). The laser and most of the optical components were fixed on a table where color separation, Bragg-cell frequency shifting and the establishment of the four-beam matrix were accomplished. Only the transmitting optics, collecting lens and photo detectors moved. The traverse system on the opposite side of the test section from the laser held the collecting lens and photo detectors for forward scatter light collection. The traversing system on the laser side of the test section supported the transmitting mirrors and lens.

Seed particle selection was made from theoretical particle response estimates shown in Fig. 9. Bearing in mind the tunnel total temperature requirement, a high flash point fluid (Dow Corning 704) was chosen as the seed material. The fluid was injected through a small atomizer ahead of the throat. The subsequent nozzle flow accelerations and shear were then sufficient to break up the seed material into a fine mist of nominally $0.5 \mu m$ particles. With seed mass flow and injector pressures optimized, data rates of up to 600/sec on both channels were obtained. Signal processing in both cases was accomplished with single particle burst counters. However, since no coincidence requirement was put on the two component arrival times, shear stress calculations could not be made. But, since these measurements were made, we have significantly improved our data acquisition and reduction capabilities. These are described in the Appendix.

4. TEST RESULTS AND DISCUSSION

4.1 Hot Wire Freestream Measurements

One of the largest sources of uncertainty in proposed testing of hypersonic flight vehicles will be consistent documentation of the extent of transitional flow on wind tunnel test models. However, past research has stressed the dominant role that freestream fluctuations have on model boundary layer stability at supersonic speeds. Not only do the external fluctuation amplitudes influence transition, their spectra are also significant. Unfortunately, freestream turbulence intensity and scale vary with facility so that a reliable model transition data base may be difficult to establish. This problem could be alleviated if assessments were made of flow quality in facilities which are likely to be used in future hypersonic flight vehicle development. These documentations would allow judgements to be made as to the meaningful operational range of adequate flow quality in each facility relative to the proposed test program.

With these thoughts in mind, freestream hot wire measurements were made in the M-6 facility and have been compared with data obtained previously in the NASA Ames 3.5 ft. Hypersonic Wind Tunnel and the Langley VDT. The present hot wire data, plotted in mode diagram form, are shown in Fig. 10. Since these mode diagrams are linear, the two hot wire sensing variables namely the mass flux and total temperature fluctuation levels can be determined from the slope and intercept respectively (Ref. 12). The total temperature measurements obtained from the intercept determinations have been confirmed by independent constant current anemometer measurements. Disturbance levels obtained over the entire operating range are shown in Fig. 11. It can be seen that the mass flow fluctuations increase with tunnel total pressure and range from 0.6 to 1.6 per cent. On the other hand, the total temperature fluctuations range between 0.5 and 1.0 per cent. Two sets of data obtained in the Ames 3.5 ft. facility are shown for comparison. The first set was taken in the original test configuration, the latter after the tunnel was converted to a free jet test section. The lower levels in the AFWAL M=6 facility could be due in part to the favorable influence of flow treatment screens installed in the stagnation chamber.

But, if we assume that the disturbances sensed by the hot wire are predominantly sound waves radiated from the turbulent nozzle wall boundary layers, the pressure fluctuation levels can be estimated from hot wire data. Hot wire theory shows this assumption to be consistent with linear mode diagrams which are shown in Fig. 10. The results of these calculations are shown in Fig. 12 and comparison made with the Ames HWT and Langley VDT facilities. These results clearly show the improved flow quality in the M=6 facility. But, sound is not the only disturbance mode, temperature spottiness probably due to non-uniform heating of the supply gas is not negligible (Fig. 11). Thus, the pressure level estimates from the hot wire data should be viewed as upper bounds, the actual levels should be somewhat lower. Direct pressure measurements should confirm this.

Turbulent integral length scales have also been determined from the hot wire time histories. The characteristics of two hot wire signals are shown in Fig. 13. One for a pressure of 930 psia, the other for a pressure of 1860 psia. These traces clearly show the increased high frequency (smaller length scale) contribution at the high tunnel total pressure. Low frequency (large-scale) contributions are also apparent in both hot wire traces. In general, most of the energy is concentrated at low frequencies. Auto-correlation measurements show the turbulent integral length scales to be of the order of the jet exit diameter.

4.2 Laser Velocimeter Measurements

Important methods used to predict compressible turbulent boundary layer flow fields are compressible-incompressible transformation techniques. Their appeal is the desire to employ their simplicity and accuracy for simple flat plate flows. In Ref. 11, three such transformation techniques were used and it was concluded that the Van Driest method was superior when the data were plotted in law-of-the-wall and velocity defect coordinates. Accordingly, such transformations should provide a check on the accuracy of the mean velocity profiles measured with the laser velocimeter.

Mean and fluctuating axial velocity profiles were measured at several stations in the zero pressure gradient flow. Measurements obtained for a momentum thickness Reynolds number of 8000 are shown in Fig. 14, which shows the results of the law-of-the-wall transformation when the data are compared with the incompressible correlation of Coles (Ref. 13). This transformation, made using a wall friction velocity based on the calculated local skin friction, confirms the validity of the mean velocity measurements. In the law-of-the-wall, the data have the correct incompressible slope and show a wake-like region near the outer edge of the boundary layer similar to the incompressible observations. The same data have also been transformed to velocity-defect variables in Fig. 15. The agreement in the outer portion of the boundary-layer is consistent with the wake-like behavior displayed in law-of-the-wall variables. Once again, there is good agreement with the incompressible correlation.

A more stringent test of particle response was also made by perturbing the flow with the

introduction of a 30 deg. ramp. A direct comparison of ramp induced effects on the mean and turbulent flow fields can be seen in Fig. 16 where measurements obtained at the same streamwise station are presented. These measurements obtained at a station 0.3 boundary layer thicknesses ahead of the ramp clearly show retardation of the flow due to the imposed adverse pressure gradient and a significant increase in turbulence level over a wide region. The vertical velocity profile measured at the same location ahead of the interaction is shown in Fig. 17. Local flow angularity profiles across the boundary layer have been calculated from the two component laser measurements. These results (Fig. 18), show that particle response is sufficient to produce local flow angles close to the wedge deflection angle in the shear layer just upstream of the interaction.

The results of the most stringent test of the laser velocimeter measurements are shown in Fig. 19 where the zero pressure gradient turbulence measurements are compared with Klebanoff's incompressible results. There is good agreement between the hypersonic laser velocimeter and incompressible hot wire data when normalized by the wall friction velocity. This is in contrast to previous hot wire compressible flow results, reviewed in Ref. 7, which show a monotonic decrease with increasing Mach number. However, all these past results have been evaluated assuming zero pressure fluctuations which we would expect to become more important with increasing Mach number. It can be seen from equation 8 that this assumption could have a significant influence on the calculated hot wire velocity fluctuations at high Mach numbers.

A comparison of the zero pressure gradient and ramp induced turbulence level profiles shows that the streamwise turbulent kinetic energy for the ramp flow is more than three times that for the flat-plate boundary layer. Turbulent mixing length scales, calculated using local rms levels and mean flow gradients, are an order of magnitude larger, an indication of the large scale, unsteady character of the flow field ahead of the interaction. Turbulence levels based on local mean flow values exceed 30 per cent in the wall region so that significant hot-wire measurement errors and flow interference would arise. At this high intensity, large-scale turbulence results in directional intermittency of up to 15 per cent ahead of the time-averaged recirculation zone. Clearly, hot-wire measurement errors associated with directional intermittency would be considerable (see Ref. 6).

5. CONCLUDING REMARKS

Diagnostic tools are available to attempt the measurement of turbulent hypersonic flows, an area where comprehensive studies are lacking. However, measurement techniques must be used with understanding and care in appropriate test situations. Comparisons of the present laser velocimeter turbulence measurements with previous hot wire results indicates that past data reduction assumptions can result in significant measurement errors in hypersonic flows. Extensive work is needed to establish a reliable data base for turbulence modeling and to define the reliable ranges of hot wire and laser anemometer application.

The laser velocimeter mean flow and turbulence measurements were in good agreement with incompressible results and the ramp induced flow angularity measurements were consistent with the model configuration. Although these results indicate that adequate particle tracking is possible in the M=6 facility, considerable work is still required to optimize seed particle requirements and to define the flow regions in which reliable particle tracking can be expected in other hypersonic test facilities.

REFERENCES

1. Owen, F. K., *Application of Laser Velocimetry to Unsteady Flows in Large Scale, High Speed Wind Tunnels*, ICIASF '83 Record, IEEE Publication 83CH1954-7, 1983.
2. Horstman, C. C. and Owen, F. K., *New Diagnostic Technique for the Study of Turbulent Boundary Layer Separation*, AIAA Journal, Vol. 12, No. 10, 1974.
3. Morkovin, M. V., *Fluctuations and Hot Wire Anemometry in Compressible Flows*, AGARDograph 24, 1956.
4. Fernholtz, H. H. and Finley, P. J., *A Further Compilation of Compressible Boundary Layer Data with a Survey of Turbulence Data*, AGARD-AG-263, 1981.
5. Owen, F. K. and Fiore, A. W., *Turbulent Boundary Layer Measurement Techniques*, AFWAL-TR-86-3031, 1986.
6. Owen, F. K. and Johnson, D. A., *Separated Skin Friction — Source of Error, an Assessment and Elimination*, AIAA-80-1409, 1980.

7. Owen, F. K., Horstman, C. C. and Kussoy, M. I., *Mean and Fluctuating Flow Measurements of a Fully Developed, Non-adiabatic Hypersonic Boundary Layer*, J. Fluid Mech., Vol. 70, pt. 4, p. 393, 1975.
8. Hinze, J. D., *Turbulence, An Introduction to its Mechanism and Theory*, McGraw Hill, 1959.
9. Yanta, W. J. and Gates, D. F., *The Use of a Laser Doppler Velocimeter in Supersonic Flows*, AIAA Paper 71-287, 1971.
10. Owen, F. K., *Laser Velocimeter Measurements of a Confined Turbulent Diffusion Flame Burner*, Progress in Astronautics and Aeronautics, Vol. 53, 1976.
11. Owen, F. K. and Horstman, C. C., *On the Structure of Hypersonic Turbulent Boundary Layers*, J. Fluid Mech., Vol. 53, pt. 4, p. 611, 1972.
12. Kovasznay, L. S. G., *Turbulence in Supersonic Flow*, Journal of the Aeronautical Sciences, Vol. 20, No. 10, p. 657, 1953.
13. Coles, D., *The Problem of the Turbulent Boundary Layer*, Rep. No. 20-69 Jet Propulsion Laboratory, 1953.

APPENDIX

Experience has shown that reliable traverse capability and real time data acquisition and reduction are a requirement for efficient operation in short duration hypersonic blow down facilities. To this end, a computer controlled encoder position indicator system and a data acquisition system and software capable of on-line data reduction and display have been built and tested. Traversing in three dimensions can now be accomplished by microprocessor controlled, stepper motor driven lead screws (Fig. 20). Optical encoders feed back position information to a desk top computer so that immediate corrections for backlash or slippage on any axis can be made. In addition to computer software, the data reduction system consists primarily of two elements: an event synchronizer and a desk top computer as shown in Fig. 21. Each individual realization and essentially simultaneous arrival time is recorded. The coincidence requirement ensures that the velocities are obtained from the same particle. This is a necessary condition for shear stress measurement. Each data point taken by the processor contains the information required to calculate the instantaneous velocities u , v , w . From these determinations, the average velocities \bar{u} , \bar{v} , \bar{w} , turbulence levels u' , v' , w' and the cross correlations $\overline{u'v'}$, $\overline{v'w'}$, $\overline{u'w'}$ are all calculated. Plots of these parameters are displayed on-line as profiles are measured and hard copy is available as required. All the raw and reduced data are stored on flexible disks for permanent storage and retrieval. Real time histograms and probability densities of all three velocity components are displayed during data acquisition.

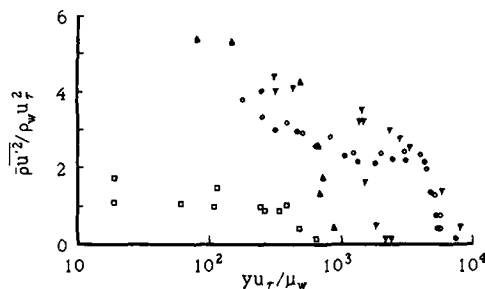


Fig. 1 Reynolds normal stress distribution in compressible turbulent boundary layers (Ref. 4).

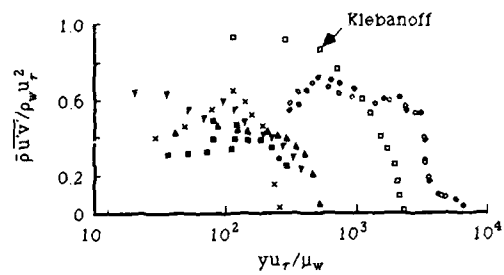


Fig. 2 Reynolds shear stress distribution in compressible turbulent boundary layers (Ref. 4).

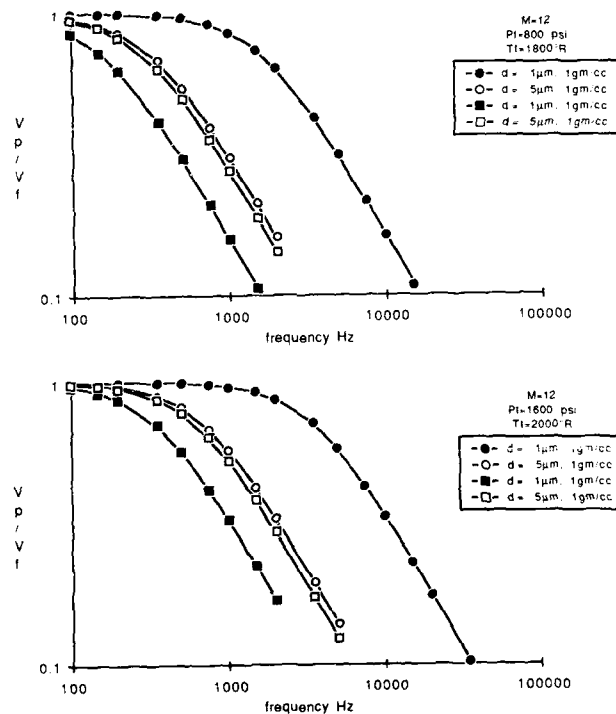


Fig. 3 Particle Trackability in the AFWAL 20 inch Hypersonic Wind Tunnel.

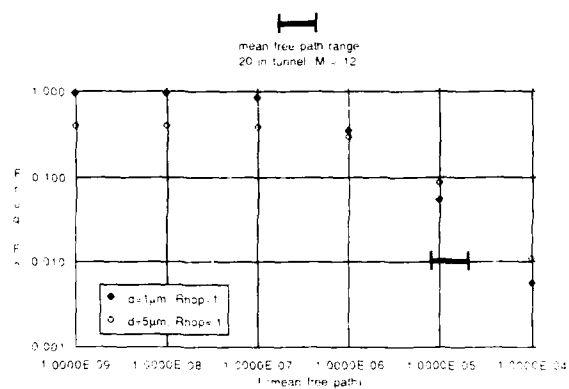


Fig. 4 The Influence of Mean Free Path on Particle Response.

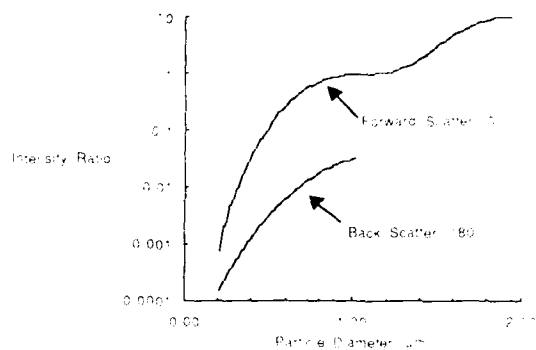


Fig. 5 Light Scattered Relative to Forward Scatter of a 1μm Particle.

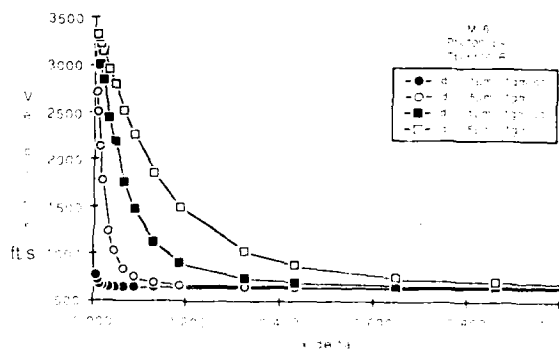


Fig. 6 Particle Trajectory Calculations.

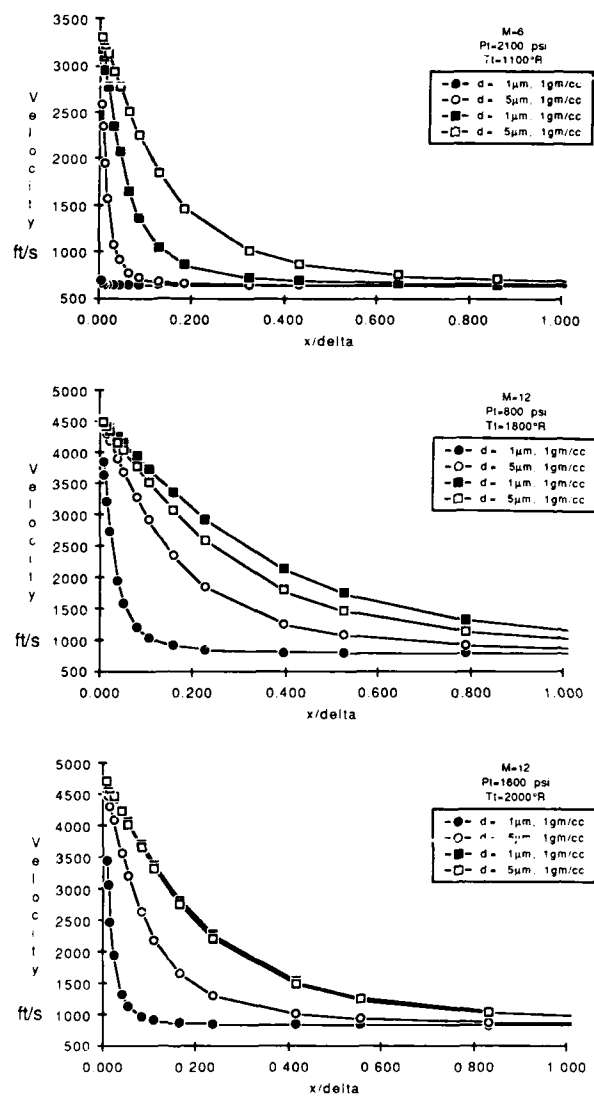


Fig. 6 Particle Trajectory Calculations, continued.

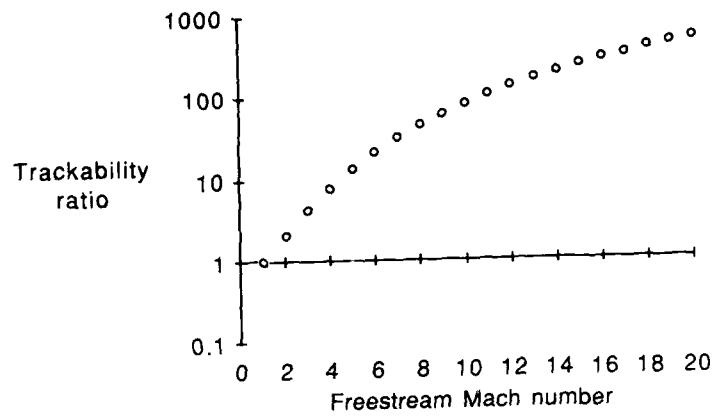


Fig. 7 Particle Trackability Variation.

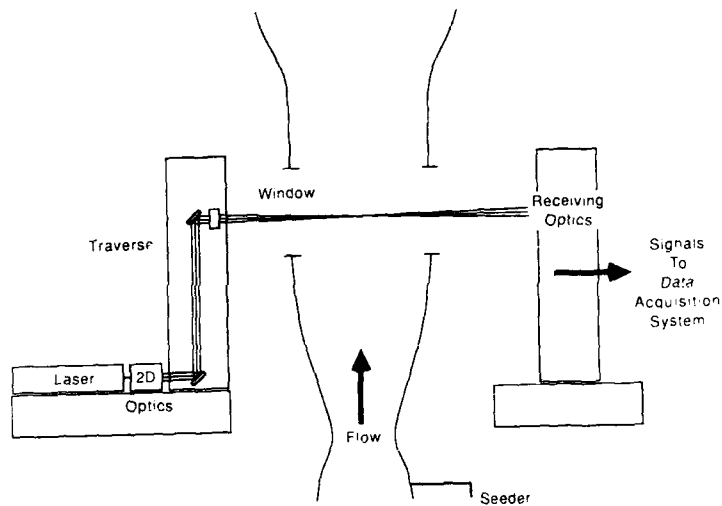


Fig. 8 Schematic of Laser Velocimeter Test Apparatus.

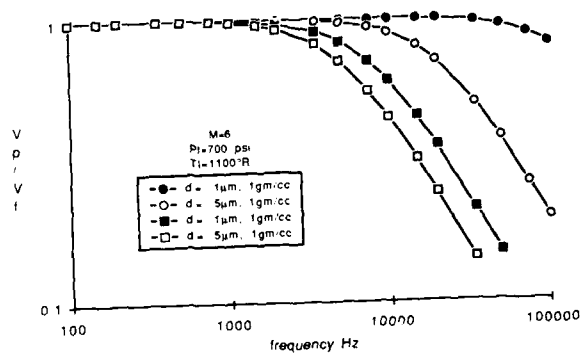
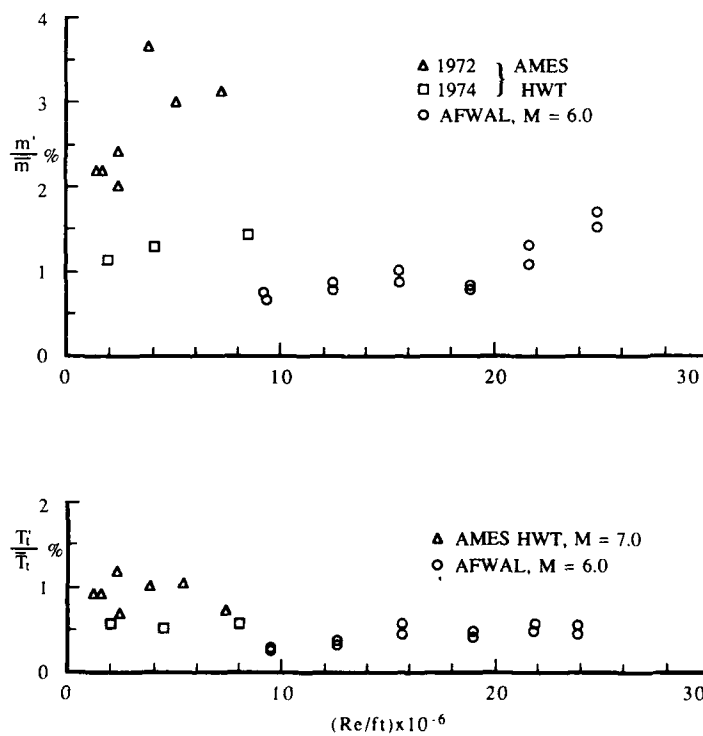
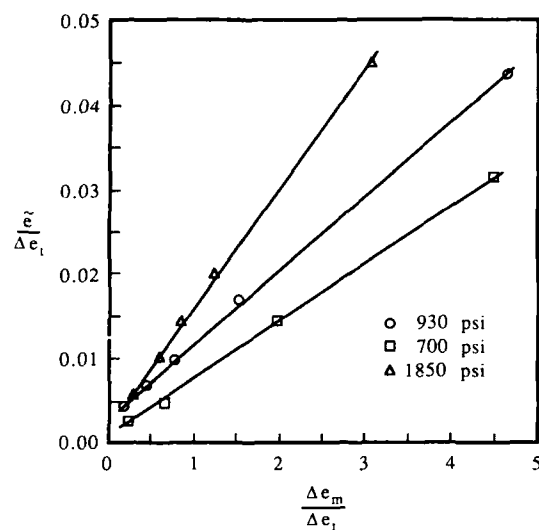


Fig. 9 Particle Response Estimates in the M=6 High Reynolds Number Wind Tunnel.



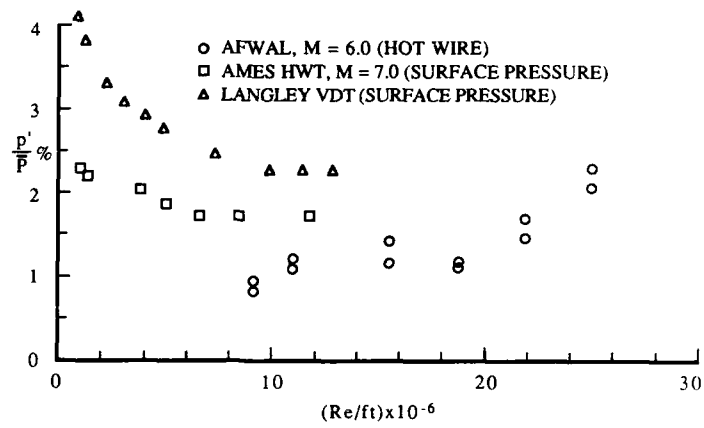
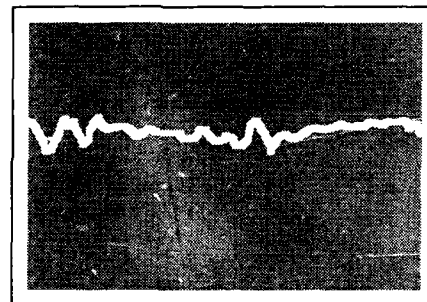
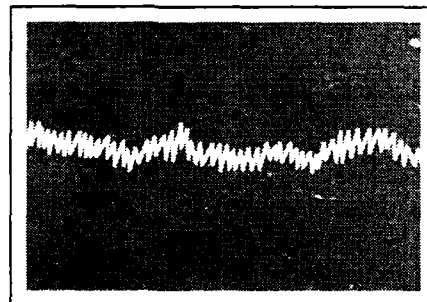


Fig. 12 Freestream Pressure Fluctuations.

 $p_e = 930$  $p_o = 1860$ Fig. 13 Hot Wire Traces, AFWAL, M = 6.0,
Time Scale 1 ms/cm.

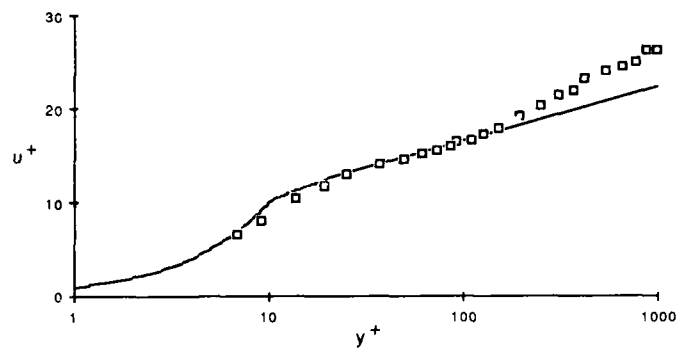


Fig. 14 Law-of-the-wall Correlation in Incompressible Coordinates.

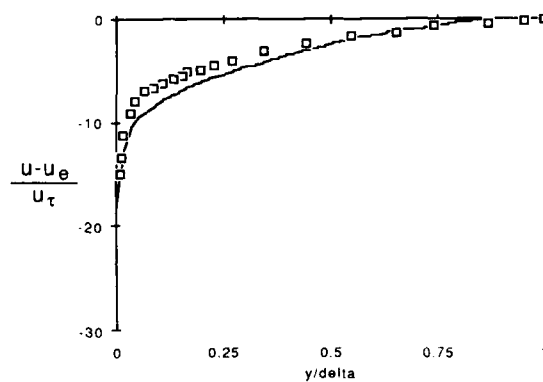


Fig. 15 Velocity-defect Profile in Incompressible Coordinates.

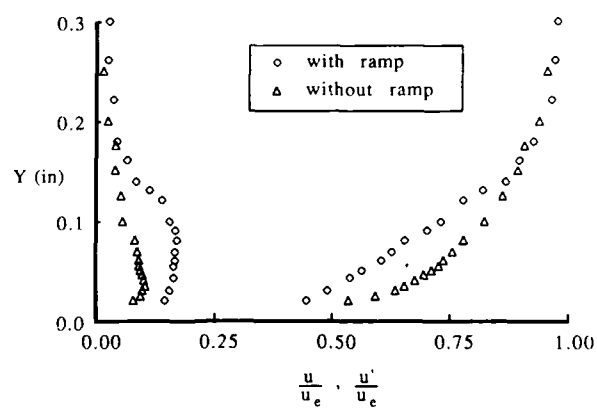


Fig. 16 Mean and Turbulent Velocity Profiles.

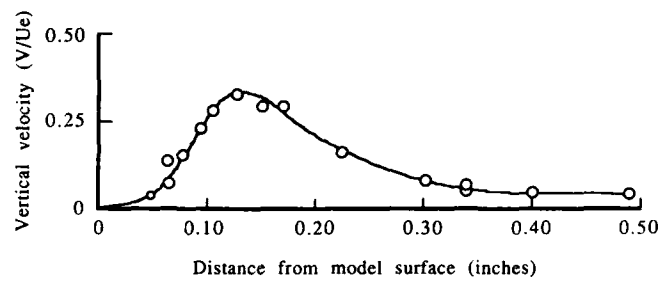


Fig. 17 Vertical Velocity Profile Ahead of Interaction,
 $M_\infty = 6.0$, $p_0 = 700$ psia.

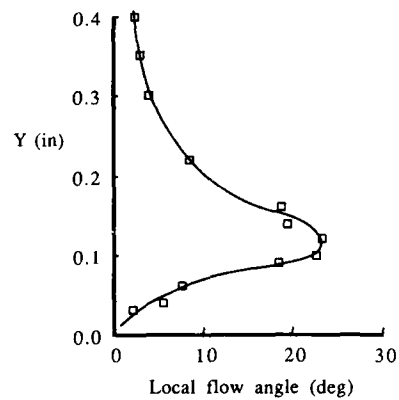


Fig. 18 Flow Angularity Across the Boundary Layer,
 Wedge Angle = 30 deg.

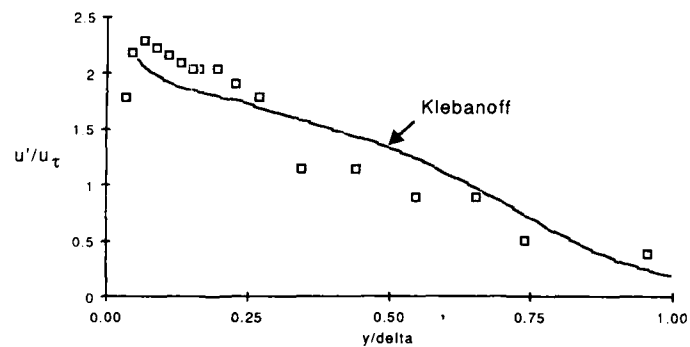


Fig. 19 Velocity Fluctuations Across the
 Zero Pressure Gradient Boundary Layer.

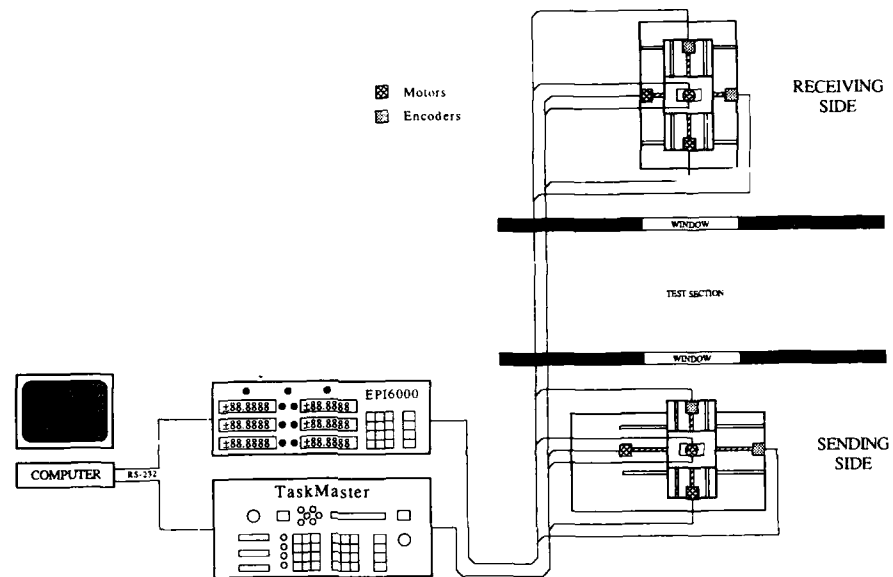


Fig. 20 Six Axis Traverse System with Position Verification and Correction.

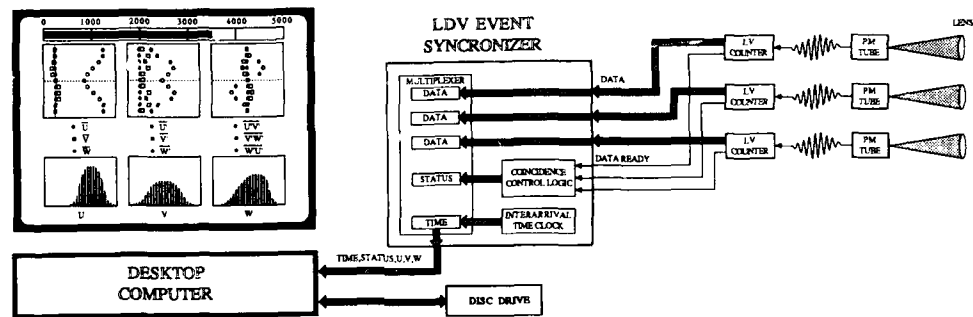


Fig. 21 Data Acquisition System.

EXPERIMENTAL INVESTIGATIONS ON BLUNT BODIES AND CORNER CONFIGURATIONS IN HYPERSONIC FLOW ⁺⁾

by
 Prof. Dr.-Ing. Dietrich Hummel
 Institut für Strömungsmechanik
 Technische Universität Braunschweig
 Bienroder Weg 3
 D-3300 Braunschweig
 Federal Republic of Germany

SUMMARY

Within the framework of some theses hypersonic flows have been investigated theoretically as well as by experiments in the hypersonic facility "Gun Tunnel" of the institute. Some of these activities during the last years are summarized.

The first problem to be treated here is that of a blunt body of revolution with subsonic blowing in the stagnation point region against the hypersonic main flow. Surface pressure and heat transfer measurements have been carried out for two bodies at different free-stream Machnumbers and for various blowing rates. Remarkable agreement has been obtained in comparison with a combination of Newtonian and potential theory.

The second problem discussed in detail is that of the hypersonic flow in corners formed by intersecting swept wedges. The corner angle and the leading-edge sweep angle have been varied systematically. The flow field has been analysed by means of pitot pressure measurements in a characteristic cross-section and the flow structure near the wall has been determined from oilflow pictures as well as from wall pressure and heat transfer measurements. Strong vortical flows have been detected underneath the corner shock system. Starting from a 90° corner of unswept wedges, the heat flux in the corner center can be reduced considerably by increasing the corner angle and by sweeping the leading-edges back.

LIST OF SYMBOLS

A	Cross-section area	γ	Ratio of specific heats
D	Body diameter	δ	Wedge angle normal to the leading-edge
J	Impingement point (Fig. 11)	θ	Corner angle (Fig. 10)
M	Machnumber	ν	Kinematic viscosity
Re	Reynoldsnumber	ρ	Density
R_1, R_2	Reattachment points (Fig. 11)	ϕ	Leading-edge sweep (Fig. 10)
S_1, S_2	Separation points (Fig. 11)	ψ	Angle between the shear stress direction (local flow direction) at the wall and the conical direction, positive towards the corner center
T	Temperature		
Tr	Triple point (Fig. 11)		
U_∞	Free-stream velocity		
Y, Z	Conical coordinates in the measuring plane ($Y=y/x, Z=z/x$), origin at x-axis (Fig. 10)	Subscripts	
\bar{Y}, \bar{Z}	Conical coordinates in the measuring plane, origin at the corner (Fig. 10)	D	Based on body diameter
\bar{Z}	Conical coordinate along the wall of the inclined wedge ($\bar{Z}=\bar{Z}\sin\theta$), (Fig. 15)	T	State at the dividing stream surface
b	Model span	W	State at a swept wedge
c_1	Momentum coefficient ($c_1 = v_j \sqrt{\rho_j} / v_2 \sqrt{\rho_2}$)	W, u	State at an unswept wedge
c_m	Mass flow rate coefficient ($c_m = \dot{m}_j / \rho_\infty U_\infty A_D$)	j	State in the ejection tube
l	Model length	l	Based on model length
\dot{m}_j	Mass flow rate of the ejection ($\dot{m}_j = \rho_j v_j A_j$)	max	Maximum value
p	Pressure	t	Total condition (gas brought to rest isentropically)
\dot{q}	Local heat transfer rate at the wall	2	State behind a normal shock
v	Velocity in axial direction	∞	Free-stream conditions
w	Local velocity	*	Critical conditions
x, y, z	Rectangular coordinate system (Fig. 10)		

⁺⁾ These investigations have been supported by Deutsche Forschungsgemeinschaft under contracts Schl 5/82 and Hu 254/2

1. INTRODUCTION

The hypersonic test facility "Gun Tunnel" of the Deutsche Forschungsanstalt für Luft- und Raumfahrt (DFL) in Braunschweig came into operation in the mid-sixties, see K. Gersten, G. Kausche [1]. Starting from three- and six-component measurements the capability of this tunnel has been developed systematically to include pitot and surface pressure measurements, K. Kipke [2], heat transfer measurements, G. Strömsdörfer [3], as well as flow visualizations by means of an oil-dot technique, W. Möllenstädt [4]. Computer aided control of the facility led to a frequency of about 30 runs (shots) per day, which is a rather high value for this kind of test facility.

During the quiet years of hypersonic research the "Gun Tunnel" in Braunschweig remained in operation. The ownership changed from Deutsche Forschungs- und Versuchsanstalt für Luft- und Raumfahrt (DFVLR) to Technische Universität Braunschweig, and the tunnel is now operated at its original site by the Institut für Strömungsmechanik of TU Braunschweig. When the investigations of K. Kipke [5], [6], [7] on caret wings - which were mainly based on balance measurements - came to a close, new projects have been treated, in which special emphasis was given to the application of pressure distribution and heat transfer measurements. G. Strömsdörfer [8] investigated the problem of subsonic blowing in the stagnation point region of a blunt body against the hypersonic main flow. K. Kipke, D. Hummel [9] initiated a long-term program on hypersonic flow in corner configurations starting with corners between unswept wedges. This program has been continued in the last years by W. Möllenstädt [10], [11], [12], [13], who investigated corners between swept wedges and this program will be continued by an extension to unsymmetric configurations.

Following here some results of the theses of G. Strömsdörfer [8] and W. Möllenstädt [11] will be discussed in some detail in order to summarize the activities of the Institut für Strömungsmechanik of TU Braunschweig within the last years.

2. TEST FACILITY

The experimental investigations have been carried out in the gun tunnel of the institute, which has been described originally by K. Gersten, G. Kausche [1]. The actual data of this tunnel are compiled in Tab. 1. The tunnel is mainly operated at a driver pressure of 150 bar. Test gas is the air within the barrel (length 6 m, inner diameter 50 mm), which usually starts at atmospheric pressure and temperature and which is compressed by the piston to a stagnation pressure of about 150 bar and a stagnation temperature of about 1300 K, see K. Kipke [2]. The flow expands through a conical nozzle the throat part of which can be changed in order to alter the Machnumber. At the beginning of each run the vacuum chamber at the downstream end of the facility starts at a minimum pressure of 0.4 mbar. The total running time at these conditions is about 100 msec.

Within this time margin the measurements of the aerodynamic quantities are taken. For surface pressure and heat transfer measurements 4 channels for the electric signals from the pressure transducers and from the thermo-couples are available. Within the running time of the tunnel on all 4 channels 400 values of the signals are taken and stored in the computer. From the time history of these 400 values the time interval can be determined in which constant aerodynamic parameters and thus steady flow conditions are present at the model. The corresponding measuring time is about 20 msec and the final measuring value for each channel is taken as the arithmetic mean value over the measuring time.

For atmospheric conditions within the barrel the obtainable Reynoldsnumbers depend on the stagnation pressure and the free-stream Machnumber. For a stagnation pressure of 150 bar and a characteristic model length of 100 mm the Reynoldsnumber is $Re_{\infty} = 1.4 \cdot 10^6$ at a Machnumber of $M_{\infty} = 8$ and $Re_{\infty} = 2.0 \cdot 10^5$ at $M_{\infty} = 16$. The corresponding Knudsennumbers are $Kn_{\infty} = 8.5 \cdot 10^{-5}$ and $Kn_{\infty} = 12 \cdot 10^{-5}$ which indicates that continuum flows are present.

Type	Gun Tunnel
Maximum driver pressure	500 bar
Working section (size; type)	$\varnothing = 0.16$ m; open
Machnumber range	8 to 16
Stagnation pressure range	100 to 500 bar
Stagnation temperature range	900 to 1500 K
Typical model length	100 mm
Reynoldsnumber per mm (at maximum conditions)	$1.5 \cdot 10^3$ to $3 \cdot 10^4$
Running time	40 to 300 milliseconds
Usable measuring time	20 milliseconds
Test frequency	30 runs (shots) per day
Balance system	Strain-gauge balances (all six components)
Main use of tunnel	Basic research, force-, pressure- and heat-transfer measurements, flow visualization by oil-dot technique

Tab. 1 : Test parameters of the hypersonic gun tunnel of the Institut für Strömungsmechanik of Technische Universität Braunschweig

3. SUBSONIC BLOWING IN THE STAGNATION REGION OF BLUNT BODIES OF REVOLUTION

3.1 Characteristics of the flow field

One of the important problems of hypersonic flight is to protect the nose region of a blunt body from heating. One of the methods to achieve this is blowing of gas in the stagnation region out of the body against the free-stream flow. Basic research on this topic has been carried out by H.M. McMahon [14] and C.H.E. Warren [15]. In these investigations sonic blowing of small mass flow rates from small orifices in the body surface has been applied. For this type of blowing the overall heat transfer rate from the flow to the body could be reduced, but in some parts of the contour an increase of the local heat transfer rate was found as compared to the stagnation point heat transfer rate. For this reason heat protection by means of sonic blowing has not been applied in hypersonic flight vehicles. Later L.M. Tucker [16] investigated subsonic blowing with larger mass flow rates from contoured nose orifices in supersonic free-stream flow. The measured pressure distributions indicated that for this type of blowing a uniform reduction of heat transfer along the contour might be achieved. Therefore this concept has been investigated experimentally as well as theoretically in the hypersonic flow regime.

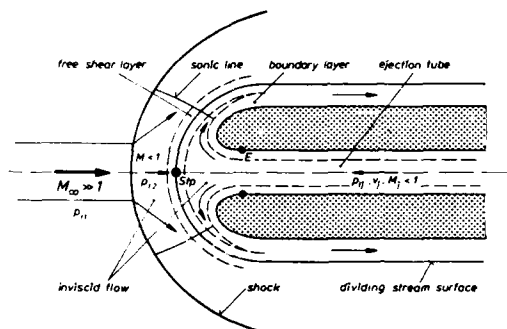


Fig.1: Subsonic blowing from a contoured orifice in the nose region of a blunt body (schematic)
Stp Free stagnation point
E End of the straight tube contour

Subsonic blowing from a contoured orifice in the nose region of a blunt body is sketched in Fig. 1. Between the shock wave and the body a dividing stream surface is formed which separates the hot outer flow from the cool inner flow of the ejected gas. In inviscid flow of the same gas on both sides of the dividing stream surface the stagnation pressure is constant, $p_{2T} = p_{jT}$, but the stagnation temperature may be different, $T_{2T} \neq T_{jT}$. At the dividing stream surface in each point the static pressure is the same on both sides, $p_{2T} = p_{jT}$. This means that

$$\frac{p_{2T}}{p_{t2}} = \frac{p_{jT}}{p_{tj}} \quad (1)$$

$$\text{and} \quad M_{2T} = M_{jT}, \quad (2)$$

which can be written as

$$\frac{w_{2T}}{w_{jT}} = \sqrt{\frac{T_{t2}}{T_{tj}}}. \quad (3)$$

At the dividing stream surface a velocity jump is present in the case of different stagnation temperatures on both sides.

The dimensionless coefficient for the mass flow rate is

$$c_m^* = \frac{\rho_j v_j A_j}{\rho_\infty U_\infty A_D}. \quad (4)$$

If the quantities corresponding to the ejection jet are expressed by the pressure ratio p_j/p_{tj} and if the free-stream quantities are written in terms of the free-stream Machnumber M_∞ , for subsonic blowing with $p_{tj} = p_{t2}$ yields

$$c_m^* = \left(\frac{p_j}{p_{t2}} \right)^{1/\gamma} \left[1 - \left(\frac{p_j}{p_{t2}} \right)^{\frac{\gamma-1}{\gamma}} \right]^{1/2} \left[\frac{2}{\gamma-1} \right]^{1/2} \sqrt{\frac{T_{t2}}{T_{tj}}} \cdot \frac{A_j}{A_D} \cdot f(M_\infty) \quad (5)$$

with

$$f(M_\infty) = \frac{\left[\frac{\gamma+1}{2} M_\infty^2 \right]^{\gamma/\gamma-1} \left[\frac{\gamma+1}{2\gamma M_\infty^2 - \gamma + 1} \right]^{1/\gamma-1}}{\left[1 + \frac{\gamma-1}{2} M_\infty^2 \right]^{1/2} \cdot M_\infty}. \quad (6)$$

For high free-stream Machnumbers $M_\infty > 7$ the function $f(M_\infty)$ becomes independent of M_∞ and in the limit results

$$\lim_{M_\infty \rightarrow \infty} f(M_\infty) = \left[\frac{4\gamma}{(\gamma-1)(\gamma+1)} \right]^{1/(1-\gamma)} \left[\frac{\gamma+1}{\gamma-1} \right]^{\gamma/(\gamma-1)} \left[\frac{\gamma-1}{2} \right]^{1/2} \quad (7)$$

This means that for Machnumbers in the range $10 \leq M_\infty \leq 16$ the flow with subsonic blowing does not depend on the free-stream Machnumber. The principle of Machnumber independence in hypersonic flow therefore applies also for the case of subsonic blowing. Equ. (5) holds for $p_j/p_{t2} \leq p^*/p_{t2}$. Inserting critical conditions into equ. (5) leads to

$$c_m^* = \left(\frac{2}{\gamma+1} \right)^{\frac{1+\gamma}{2(\gamma-1)}} \sqrt{\frac{T_{t2}}{T_{tj}}} \cdot \frac{A_j}{A_D} \cdot f(M_\infty) \quad (8)$$

This is the upper limit of the mass flow rate for which a subsonic flow in the ejection tube is present. In addition equ. (5) and (8) indicate that for a given configuration with the cross-sections of tube A_j and body A_D at constant Machnumber in the ejection tube M_j , which means constant value of p_j/p_{t2} in the case of subsonic blowing, the parameter

$$c_m \sqrt{\frac{T_{tj}}{T_{t2}}}$$

is the relevant one. It can easily be determined in the experiments and it is therefore used subsequently for the presentation of the results.

The preceding considerations were based on the assumption of inviscid flow. In viscous flow, however, the velocity jump across the dividing stream surface leads to the formation of a free shear layer, which is very important for the heat transfer from the hot outer flow towards the body. Shear layers of this kind have been investigated by W. Muest [17]. Underneath the ejected flow a boundary layer develops along the contour of the orifice in the nose region of the body. For rounded contours as indicated in Fig. 1 this boundary layer is unseparated and merges further downstream with the free shear layer. Due to the large mass flow rates at subsonic blowing it is possible to shift the free stagnation point relatively far upstream of the body. In this case a wedge-shaped core of inviscid flow is placed between the free shear layer and the boundary layer in the nose region of the body. This inviscid flow region blocks the heat transfer from the hot outer flow towards the body in the nose region, and this leads to a smooth pressure distribution according to L.M. Tucker [16] and to a considerably reduced distribution of heat transfer rates without peaks. The benefits of the flow field according to Fig. 1 can only be achieved if the ejected flow remains attached at the nose contour. Therefore the orifice has to be contoured in order to avoid flow separations.

3.2 Experimental set-up and test conditions

The experimental investigations have been carried out in the gun tunnel of the Institut für Strömungsmechanik of TU Braunschweig, see chapter 2. All runs of the tunnel have been performed for a stagnation pressure of 150 bar. The free-stream Machnumber M_∞ has been varied between $M_\infty = 10.8$ and $M_\infty = 16.0$ and the corresponding Reynoldsnumbers based on the model diameter were $Re_{D_\infty} = 2.5 \cdot 10^5$ at $M_\infty = 10.8$ and $Re_{D_\infty} = 0.6 \cdot 10^5$ at $M_\infty = 16$.

Fig. 2a shows a sketch of the ejection system which has been used during the tests. The ejection vessel had a volume of $V_K = 10^4 \text{ cm}^3$ and its pressure p_K could be altered continuously. The stagnation temperature in the vessel was $T_K = 300 \text{ K}$ for all tests. In the ejection duct between the vessel and the model a quickly working magnetic valve as well as an orifice plate were installed. As long as sonic conditions were present at the throat a linear dependence between the mass flow rate and the pressure p_K in the vessel resulted as shown in Fig. 2b. For non-critical conditions at the throat the calibration curve is dashed, and for $p_K = p_{t2}$ the flow in the ejection system comes to rest. Before entering the ejection tube of the model the ejected flow passed a settling chamber in which the total pressure p_{tj} has been measured by means of a pitot probe. The operation of the ejection system in relation to the short running time of the gun tunnel has been controlled by the computer which is used to run the tunnel. Details may be taken from G. Strömsdörfer [8]. The measuring time in which a stationary flow in the ejection system has been present was up to 35 msec.

The contours of the nose region of the blunt body of revolution used in the tests are shown in Fig. 3. These shapes have been designed by the method of E. Emdin [18] to produce a constant pressure distribution in two-dimensional flow. These contours have been chosen for the present tests with bodies of revolution in order to get a qualitative extension of the measurements of L.M. Tucker [16] to hypersonic flow.

For the experimental investigations two sets of models were available. One of them was equipped with pressure holes in the contour in order to measure the surface pressure distribution. In the second set of models the contour was manufactured as a thin shell which was equipped by a large number of thermo-couples in order to measure the heat transfer rate by means of the transient thin skin method. Details may be taken from G. Strömsdörfer [3], [8].

3.3 Calculation of the surface pressure distribution for subsonic blowing with small mass flow rates

Theoretical investigations of the flow field for the case of subsonic blowing are due to J.R. Baron, E. Alzner [19]. The dividing stream surface is prescribed and the corresponding body shapes are calculated for different mass flow rates. An extension of this method to include a larger variety of dividing stream

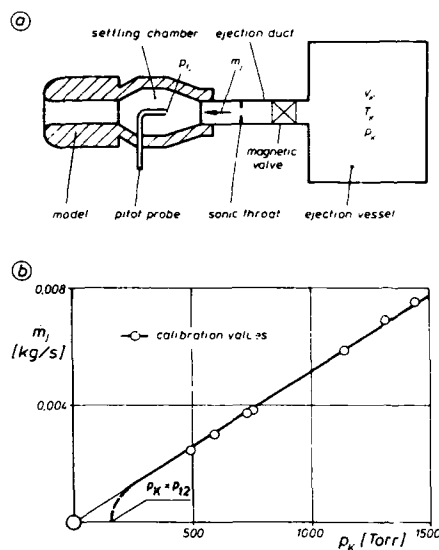


Fig. 2: Ejection system (a) and calibration curve (b) for the determination of the mass flow rate m_j

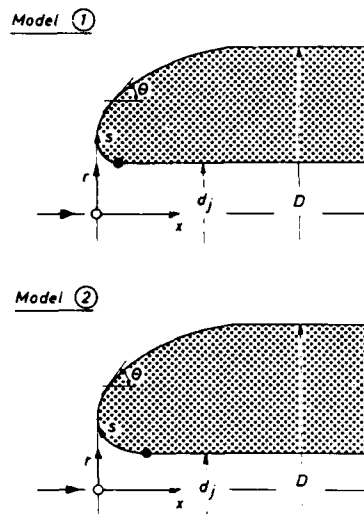


Fig. 3: Shapes of the nose region of the blunt body of revolution
Model 1: $d_j = 9.24$ mm, $D = 30$ mm
Model 2: $d_j = 6.63$ mm, $D = 30$ mm

surfaces with and without angle of attack has been described by Ch. Y. Wang [20], [21]. The papers mentioned so far describe design procedures. A first attempt to calculate a two-dimensional flow with blowing for a given geometry at supersonic free-stream is due to W. Wuest [22]. The flow field is divided into two different parts: The flow within the dividing stream surface is considered to be incompressible and outside the dividing stream surface as compressible. Both solutions are adapted to each other by variations of the shape of the dividing stream surface. This idea seemed to be promising to treat the problem of subsonic blowing against a hypersonic free-stream in the nose region of a blunt body of revolution. The corresponding calculations are due to G. Strömsdörfer [8].

For hypersonic free-stream Machnumbers the local Machnumbers behind the shock wave (see Fig. 1) are small, and therefore as an additional approximation the flow between the shock wave and the dividing stream surface may be regarded as incompressible. If subsonic blowing with very low Machnumbers is considered the flow within the dividing stream surface can also be assumed to be incompressible. Thus the flow in the vicinity of the free stagnation point can be determined from incompressible flow calculations. The following procedure has been applied:

- i) Calculation of the incompressible flow around the given body of revolution with ejection. The free-stream Machnumber for this flow should be the Machnumber M_2 behind the shock wave, but the calculations have been carried out approximately for $M_2 = 0$. Results are the shape of the dividing stream surface as well as the velocity distributions on the body contour and on the dividing stream surface.
- ii) The dividing stream surface is regarded to be a fixed wall for which the pressure distribution can be calculated easily e.g. by means of Newtonian theory.
- iii) Calculation of the final pressure distribution on the body contour starting from the pressure distribution according to ii) under the assumption that the shape of the dividing stream surface remains unchanged.

The calculations of the incompressible flow according to Fig. 4 have been carried out by means of an extension of the method of K. Jacob [23], in which a distribution of vortex rings on the body contour is used. A long tube-like body with the prescribed contoured orifices at both ends has been considered. Due to the different stagnation temperatures on both sides of the dividing stream surface the density of the incompressible flow is $\rho_1 \neq \rho_2$. It has been shown by W. Wuest [22] that in this case the quantity $w\sqrt{\rho}$ is steady at the dividing stream surface. The original method of K. Jacob [23] has been modified by G. Strömsdörfer [8] in such a way that $w\sqrt{\rho}$ is calculated in the flow field rather than w . Instead of v_j/v_2 the momentum coefficient

$$c_1 = \frac{v_j \sqrt{\rho_1}}{v_2 \sqrt{\rho_2}} \quad (9)$$

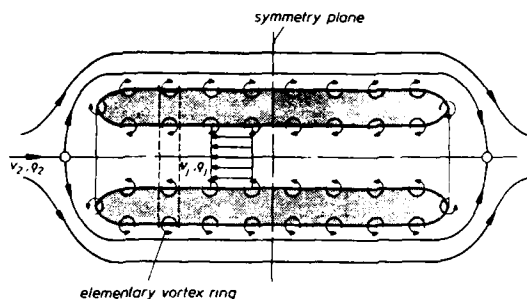


Fig.4: Calculation of the incompressible flow by the method of vortex rings

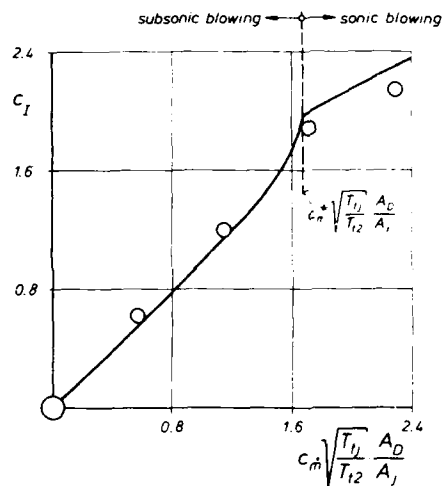


Fig.5: Momentum coefficient c_I as function of the mass flow rate coefficient c_m at high free-stream Mach numbers
 Theory due to G. Strömsdörfer [8]
 ○ Experimental data according to C.H.E. Warren [15] at $M_\infty = 5.8$

is the governing parameter, which determines the strengths of the vortex rings. Between the momentum coefficient c_I used in the theory and the mass flow rate coefficient c_m utilized to order the experimental data exists a relation of the form

$$c_I = c_I \left(c_m \sqrt{\frac{T_{t2}}{T_{t1}}} \cdot \frac{A_D}{A_J} \right) \quad (10)$$

which has been deduced by G. Strömsdörfer [8] for the limit $M_\infty \rightarrow \infty$. The result is shown in Fig. 5 and compared to experimental data of C.H.E. Warren [15].

The shape of the dividing stream surface which turns out from the incompressible flow calculations is assumed to be the final one, which occurs behind the shock wave. This dividing stream surface has been regarded as a fixed wall and the pressure and Machnumber distribution on it has been calculated by Newtonian theory.

For the calculation of the final pressure distribution at the body contour in compressible flow the fact has been used that the system of the lines of constant stream density and constant potential in the flow field is independent of Machnumber if the Machnumbers are low. According to O. David [24] the velocity distribution along a potential-line is given by the differential equation

$$\frac{dw}{w} = \frac{dn}{R(n)} \quad (11)$$

with n as coordinate along the potential line and $R(n)$ as the curvature radius of the streamlines. Under the assumption that the curvature

$$K(n) = \frac{1}{R(n)} \quad (12)$$

is a linear function of n , the integration of equ. (11) can be carried out exactly. For two points (a) and (b) on a potential line, having the distance N (arc length) along the potential line the result is for incompressible flow

$$\left(\frac{w_b}{w_a} \right)_{inc} = \exp \left[- \frac{N}{2} (K_a + K_b) \right] \quad (13)$$

and for compressible flow yields

$$\frac{M_b}{M_a} = \frac{\exp \left[-\frac{h}{2} (K_a + K_b) \right]}{\sqrt{1 + \frac{\gamma-1}{2} M_a^2 \left\{ 1 - \exp \left[-N (K_a + K_b) \right] \right\}}} \quad (14)$$

Under the assumption that the net of streamlines and potential lines is independent of Machnumber, the exponential expression in equ. (14) may be taken from the solution for incompressible flow, equ. (13), which leads to

$$\frac{M_b}{M_a} = \frac{(w_b/w_a)_{inc}}{\sqrt{1 + \frac{\gamma-1}{2} M_a^2 \left[1 - (w_b/w_a)^2 \right]}} \quad (15)$$

To apply equ. (15) one has to locate points of equal potential on the dividing stream surface and on the body contour in incompressible flow. For known values of w_a and w_b from calculation (i) and for the given value M_a in the point at the dividing stream surface according to calculation (ii) the Machnumber M_b and correspondingly the pressure ratio p/p_{t2} can be calculated for the point at the contour. Further details may be taken from G. Strömsdörfer [8].

3.4 Experimental results and comparison with theory

For model (1), see Fig. 3a, the pressure distribution is shown in Fig. 6 for various free-stream Machnumbers M_a and different mass flow rate coefficients c_m . Simple Newtonian theory is the limit of the method according to G. Strömsdörfer [8] for $c_m \rightarrow 0$. In this case within the orifice, $s/D < 0.1$, the agreement between theory and experiments was expected to be poor because of the overall concave shape of the body in this region, but for $s/D > 0.1$ in the outer region of the contour the agreement between theory and experiment is acceptable for this limiting case. For small values of the blowing rate, $c_m \sqrt{T_{t1}/T_{t2}} = 0.059$ and 0.079 , the agreement between theory and experiment is good. For $c_m \sqrt{T_{t1}/T_{t2}} = 0.113$ the differences between theory and experiment increase considerably. In this case the ejection Machnumber is about $M_j = 0.5$ and this means that the assumption of low ejection Machnumbers is no longer fulfilled. The coincidence of the results for different free-stream Machnumbers in the plots of Fig. 6 indicates that $c_m \sqrt{T_{t1}/T_{t2}}$ is the governing parameter which influences the pressure distribution. Similar results are shown in Fig. 7 for model (2). For low values of the parameter $c_m \sqrt{T_{t1}/T_{t2}}$ the agreement between theory and experiments is remarkably good.

The results for the heat transfer measurements on model (1) are shown in Fig. 8. All heat transfer rates q are based on the largest local value q_{max} without blowing. With increasing blowing rate $c_m \sqrt{T_{t1}/T_{t2}}$ the heat transfer is considerably reduced along the whole contour of the blunt body. No local heat transfer maxima occur. At $M_a = 10.8$ a certain increase of the heat transfer rate is

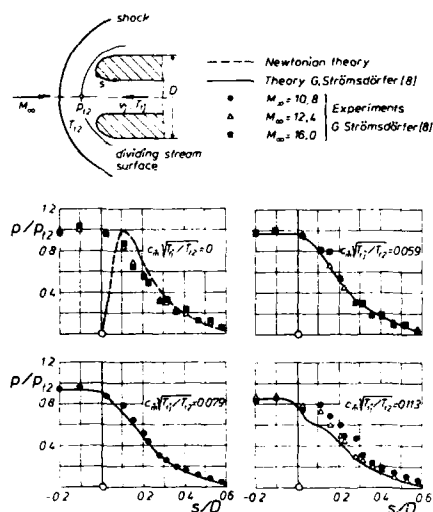


Fig. 6. Pressure distribution on model (1). Comparison between theory and experiment

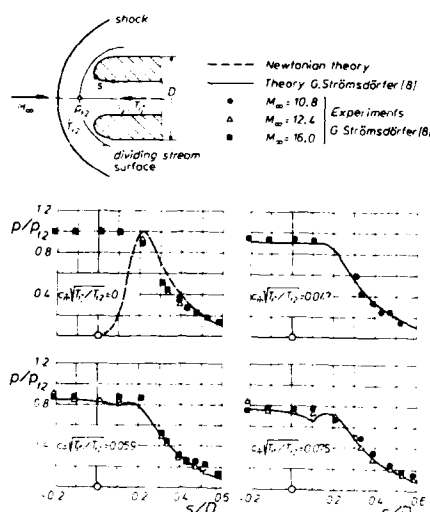


Fig. 7. Pressure distribution on model (2). Comparison between theory and experiment

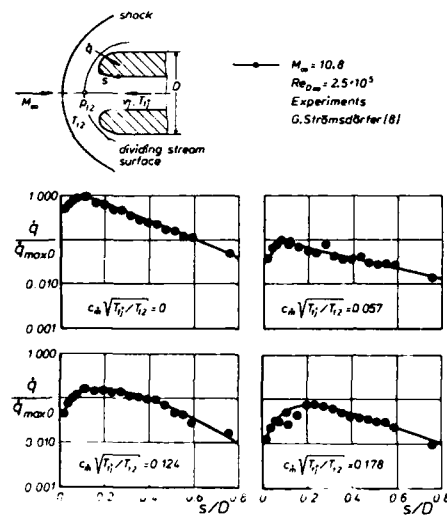


Fig. 8: Distribution of heat transfer rate on model (1)

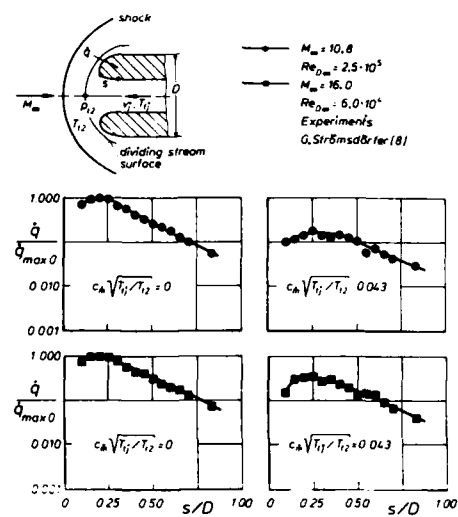


Fig. 9: Distribution of heat transfer rate on model (2)

observed when the blowing rate goes up from $c_b \sqrt{T_{t1}/T_{t2}} = 0.057$ to 0.124. This effect might be due to the fact that the boundary layer becomes turbulent at these relatively high blowing rates. Similar results have been found for model (2) as shown in Fig. 9. The reduction of the heat transfer rate is quite remarkable. Some minor differences exist between $M_\infty = 10.8$ and $M_\infty = 16.0$ since the Reynolds-numbers were also different.

3.5 Conclusions

The experimental results reported here as well as the related theoretical investigations on subsonic blowing from a blunt body of revolution against a hypersonic free-stream led to the following conclusions:

- i) The local and the total heat transfer on a blunt body can be reduced considerably by subsonic blowing of relatively large mass flow rates. This is due to the fact that with increasing blowing rate a wedge-shaped core of inviscid flow is placed between the free shear layer at the dividing stream surface and the boundary layer at the body nose which blocks the heat transfer.
- ii) For high free-stream Mach numbers, $M_\infty \rightarrow \infty$, the pressure distribution depends on the blowing parameter $c_b \sqrt{T_{t1}/T_{t2}}$.
- iii) For the calculation of the pressure distribution a reliable method has been developed by G. Strömsdörfer [8] in which a combination of Newtonian theory and incompressible flow calculations is used.

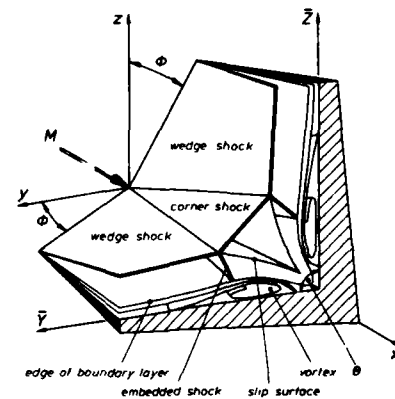


Fig. 10: Schematic view of the hypersonic flow in a swept corner configuration

4. LONGITUDINAL FLOW IN CORNERS OF INTERSECTING WEDGES

4.1 General features of the flow field

Hypersonic flight vehicles are subject to considerable thermal stress due to kinetic heating. High heat transfer rates are not restricted to the nose region and the wing leading-edges as discussed in chapter 3, but they occur similarly also in the junctions between wing and body as well as in rectangular air intakes. The spectacular damages at the X-15 research aircraft are well known.

Measurements of pressure distribution and heat transfer in various corner configurations caused by a hypersonic longitudinal flow have been carried out among others by P.C. Stainback [25], P.C. Stainback, L.M. Weinstein [26] and R.A. Jones [27]. The first investigations on the corresponding structure of the flow field are due to A.F. Charwat, L.G. Redekopp [28] for the supersonic flow in a 90°-corner between two wedges. The general features of this type of flow are shown schematically in Fig. 10 for the case of a swept corner configuration. At supersonic free-stream velocity the flow field can be divided in two parts: In the outer region inviscid flow is predominant. A shock system is formed which consists of the two wedge shocks, the connecting corner shock, two embedded shocks and two slip surfaces. Embedded shocks and slip surfaces are necessary in order to fulfil the shock relations in the vicinity of the two intersecting lines between the wedge shocks and the corner shock. The pressure distribution generated by this shock system has a strong influence on the formation of the viscous layer in the corner region. Due to the embedded shocks flow separations occur in the inward directed viscous flow, which leads to highly non-uniform distributions of static pressure and local heat transfer rate along the walls. In hypersonic flow the shock system is located close to the configuration and a strong interference between the boundary layer flow and the outer shock system takes place.

Further experimental investigations of the flow field in 90°-corners have been carried out at $M_\infty = 19$ and 20 by J.W. Kaye, R.D. Watson [29], R.D. Watson, L.M. Weinstein [30] and R.D. Watson [31], whereas J.E. West, R.H. Korkegi [32] analysed mainly the inviscid outer flow regime at supersonic speeds. Measurements at 60°- and 90°-corners at $M = 11$ are due to R.J. Cresci, S.G. Rubin, C.T. Nardo [33]. An unsymmetric configuration with the combination of a flat plate and a wedge has been investigated at $M = 12.5$ by J.R. Cooper, W.L. Hankey [34]. In this case a shock system without corner shock has been observed. Similar results have been obtained by H.-J. Schepers [35] for a plate/wedge combination at $M = 8.8$. Summaries of the existing knowledge on the three-dimensional flow separations in axial corners are due to R.H. Korkegi [36] and D.J. Peake, M. Tobak, R.H. Korkegi [37].

At the Institut für Strömungsmechanik of TU Braunschweig in 1972 a long-term program on hypersonic flow in axial corners has been started. The first investigations were concerned with symmetric corners between unswept wedges. Wedge angle, corner angle and free-stream Machnumber were varied systematically. The results have been published by K. Kipke, D. Hummel [9]. Later this program has been extended to include also a systematic variation of the sweep angle for symmetric corners of intersecting wedges with different corner angles. These investigations are due to W. Möllenstedt [10-13]. Some of these results are summarized subsequently.

4.2 Experimental program

The measurements have been carried out in the gun tunnel of the Institut für Strömungsmechanik of TU Braunschweig, see chapter 2. All runs of the tunnel have been performed for stagnation pressures of 150 bar. The free-stream Machnumber has been varied between $M_\infty = 12.3$ and $M_\infty = 16.0$ and the corresponding Reynoldnumbers, based on the model length l , were $Re_l = 5 \cdot 10^5$ and $Re_l = 7.7 \cdot 10^5$.

All corner configurations investigated so far were symmetrical with respect to the plane through the apex and the $(\theta/2)$ -line, see Fig. 10. The corner angles were $\theta = 60^\circ, 90^\circ$ and 120° , the wedge angles normal to the leading-edges $\delta = 6.3^\circ, 8.0^\circ$ and 10.0° , and the sweep angles of the leading-edges $\phi = -30^\circ, 0^\circ, 15^\circ, 30^\circ, 45^\circ$ and 60° . In part I of the program corners between unswept wedges have been considered and the varied parameters were the Machnumber as well as the wedge angle and the corner angle. In part II corners between swept wedges were investigated and the varied parameter was the sweep angle at constant wedge angle and constant Machnumber. The dimensions of all models were $l = 100$ mm in free-stream direction and $b = 50$ mm perpendicular to it.

The test program for both parts of the investigations may be taken from Tab.2. Pitot pressure measurements have been carried out in a plane normal to the free-stream close to the model end at $x = 0.9 \cdot l$. In order to check the conicalness of the flow field some measurements have also been performed at $x = 0.4 \cdot l$ and $x = 0.6 \cdot l$. Four pitot probes with an outer diameter of 1 mm have been traversed

Tab.2: Test program for the measurements in corner configurations

Part I: Corners between unswept wedges

(K. Kipke, D. Hummel [9])

M_∞	12.3	16.0
δ	6.3° 8.0°	6.3° 8.0° 10.0°
θ	60° 90° 120°	60° 90° 120°

Part II: Corners between swept wedges (W. Möllenstedt [12])

M_∞	12.3
δ	8.0°
ϕ	-30° 0° 15° 30° 45° 60°
θ	60° 90° 120°

○ heat flux, oil flow pictures

● pitot pressure (flow field), wall pressure, heat flux, oil flow pictures

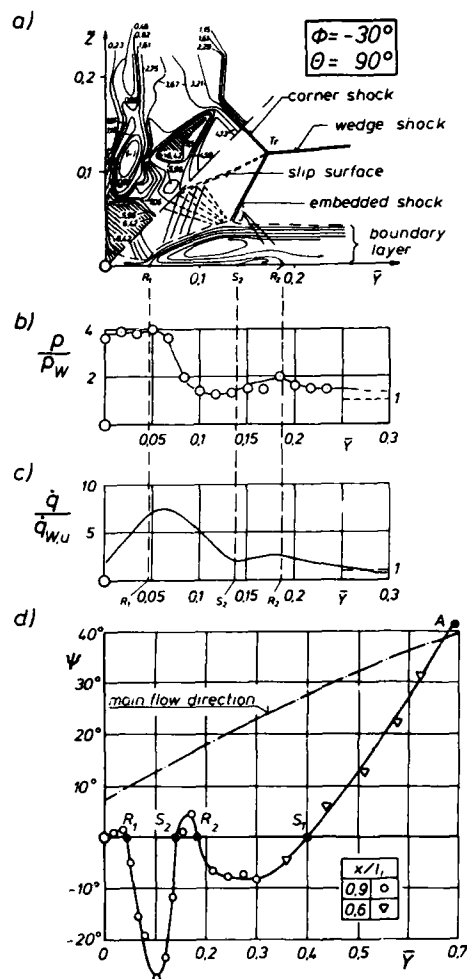


Fig. 11: Experimental results for the -30° swept 90°-corner [12]
 a) Pitot pressure isobars $p_{t2}/p_{t2\infty}$ in the flow field
 b) Wall pressure distribution
 c) Wall heat transfer distribution
 d) Flow direction at the wall (reduced $\bar{\eta}$ -scale)

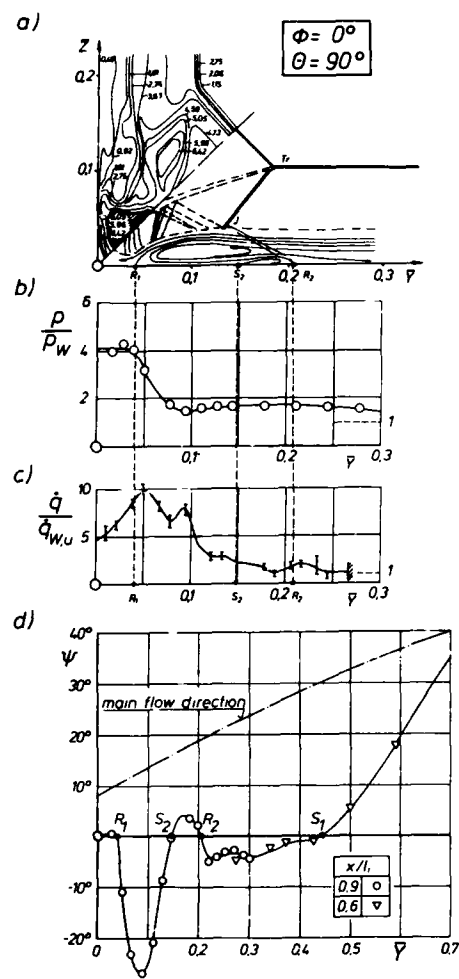


Fig. 12: Experimental results for the unswept 90°-corner [9,12]
 a) Pitot pressure isobars $p_{t2}/p_{t2\infty}$ in the flow field
 b) Wall pressure distribution
 c) Wall heat transfer distribution
 d) Flow direction at the wall (reduced $\bar{\eta}$ -scale)

simultaneously in an area of size 30 mm x 30 mm. About 800 runs of the tunnel were necessary to analyse all details of one flow field. The wall pressure and heat transfer measurements have been carried out in a section at $x = 0.9-1$. The heat transfer rates were determined by means of the transient thin skin technique as described by D. L. Schultz, T. V. Jones [38] and G. Strömsdörfer [3]. The measuring device which contained 11 thermo-couples could be adjusted in different positions in the surface of the corner models in order to achieve a dense distribution of measuring points within the section under consideration.

For the visualization of the flow at the wall an oil-dot technique has been applied. For this purpose a fluid had to be found with relatively low values of viscosity, which does not vaporize under vacuum condition of 0.5 mm Hg pressure and which leads to a distinct displacement of the droplets within the very short running time of 100 msec. Initially vacuum oil was used for this purpose, see K. Kipke, D. Hummel [9]. Later W. Möllenstädt [4] detected a well suited combination of an especially prepared model surface by means of an adhesive film and droplets of dibutylester ($C_4H_9O_2$) supplied with a red-coloured powder of formaldehyd-resin. During the tests the shear stress acts on the droplets and leads to considerable deformations. Local flow directions and qualitative values for the shear stress can easily be evaluated from deformed droplets after the run of the tunnel.

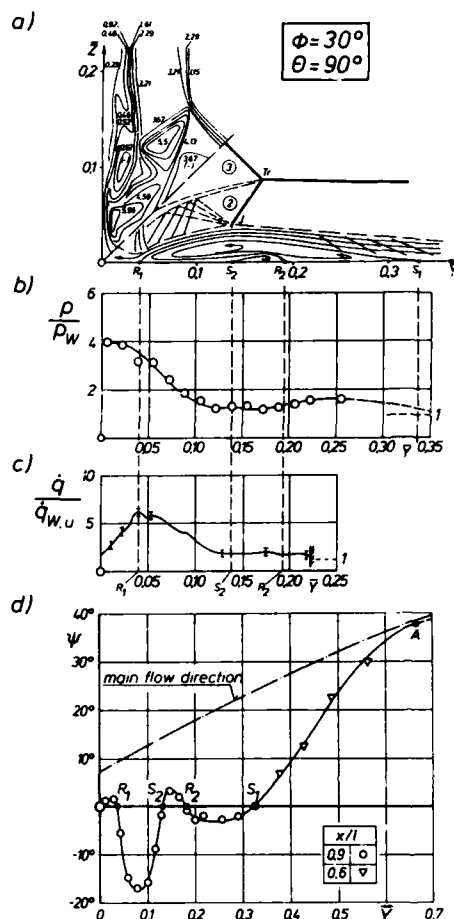


Fig.13: Experimental results for the 30°swept 90°-corner [12]
 a) Pitot pressure isobars $p_{t2}/p_{t2\infty}$ in the flow field
 b) Wall pressure distribution
 c) Wall heat transfer distribution
 d) Flow direction at the wall (reduced η -scale)

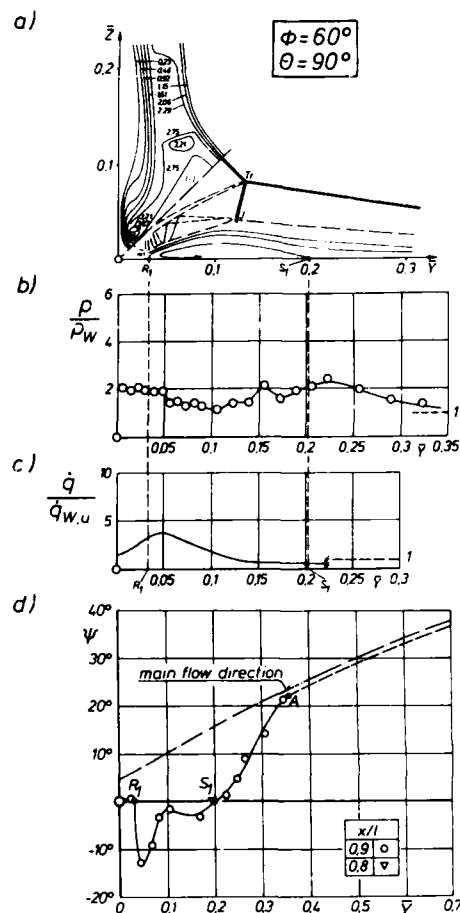


Fig.14: Experimental results for the 60°swept 90°-corner [12]
 a) Pitot pressure isobars $p_{t2}/p_{t2\infty}$ in the flow field
 b) Wall pressure distribution
 c) Wall heat transfer distribution
 d) Flow direction at the wall (reduced η -scale)

4.3 Results

4.3.1 Basic properties of the flow in a 90°-corner

General features of the flow field in a 90°-corner may be taken from Fig. 11, which shows the results for a -30° (forward) swept configuration. The pitot pressure isobars in the measuring plane are drawn in Fig. 11a. Since the flow field is symmetric with respect to the $(\theta/2)$ -line the upper part of the diagram shows the measurements and in the lower part the interpretation is given. In the corner region the system of wedge shock, corner shock, secondary or embedded shock and slip surface can be detected. The shocks are characterized by a steep increase of the pitot pressure, which is strongest for the corner shock. Behind the shocks pitot pressure plateaus at different levels are present. For the measured shock positions the strengths of all shocks can be calculated from the shock relations and the corresponding pitot pressure plateau values are in good agreement with the measured ones. The shocks interfere along the line between the wedge shock and the corner shock which is marked in the measuring plane by the triple point Tr . Due to the different pitot pressure levels on both sides the slip surface is also characterized by a pitot pressure jump. The slip surface divides the flow through the corner shock from that through the wedge shock which crosses also the embedded shock. On both sides of the slip surface the same static pressure is

present, but different velocities tangential to the slip surface as well as different pitot pressures and therefore different values of the entropy exist. According to Crocco's theorem the slip surface is a vortex sheet. The slip surfaces from both sides tend to meet at the plane of symmetry. Therefore the flow through the corner shock does not reach the inner part of the corner flow field. The flow behind the embedded shock and in front of the slip surface is not yet parallel to the wall. The corresponding changes in the flow direction towards the corner center is achieved by passing some expansion and compression regions as indicated in Fig. 11a. Finally in the corner center very high pitot pressures have been found, but the peak values in the hatched regions of the flow field could not be determined due to limitations of the available pressure transducers.

Underneath the wedge shock a decrease of the pitot pressure towards the wall is observed. The onset of the pitot pressure reduction marks the outer edge of the boundary layer. In conical coordinates the flow within the boundary layer is directed inwards. At $Z = 0.1$ oval isobars show a relative pitot pressure minimum, which has been interpreted by K. Kipke, D. Hummel [9] as a total pressure loss due to a vortex in the viscous layer. The corresponding flow separation is caused by the pressure rise due to the embedded shock and it occurs already far upstream at S_1 and the corresponding reattachment line lies at R_1 .

The measured pressure distribution at the wall is shown in Fig. 11b. Its slope is similar to that in two-dimensional flow underneath a shock impinging on a boundary layer as described e.g. by L. Lees, B. L. Reeves [39]. According to [39] the separation takes place at S_1 far upstream of the point of impingement (1. plateau) and increases downstream to the value at reattachment R_1 (2. plateau). In the present situation this scheme is modified by the strong vortex in three-dimensional flow, which produces additional negative static pressures at the wall. Underneath the primary vortex a positive pressure gradient in \bar{y} -direction is present which leads to a secondary separation at S_2 and corresponding reattachment at R_2 .

The positions of separation and reattachment lines have been taken from oil flow pictures. A quantitative evaluation is shown in Fig. 11d. The angle ψ between the wall streamlines and the conical direction is plotted against the coordinate \bar{y} . Positive values of ψ indicate a flow towards the corner center whereas negative values belong to a flow directed outwards. The effect of the second wedge on the flow at the wedge under consideration starts at the conical line A at $\bar{y} = 0.7$ which may be regarded as an influence border, which is located far more outwards than e.g. the second wedge shock. Fig. 11d indicates that the flow in the corner region converges at the separation lines S_1 and S_2 and diverges at the reattachment lines R_1 and R_2 . At these lines the flow follows the conical lines at $\psi = 0$. Between S_1 and R_1 a primary vortex is formed and between S_2 and R_2 a smaller secondary vortex is present also sketched schematically in Fig. 11a. This kind of vortex formation is well known from delta wings with subsonic leading-edges, see e.g. D. Hummel [40]. Due to the strong primary vortex a large portion of the viscous layer finally moves outwards and does not reach the corner center. Correspondingly the viscous layer becomes very thin close to the corner center. This means that in the region of R_1 high energy inviscid flow comes very close to the corner center and causes very high wall pressures and heat transfer rates there.

The measured heat transfer rates are plotted in Fig. 11c. It turns out that in the region of the reattachment line R_1 the heat transfer rate is 7 times as large as on an unswept wedge. A second, relative heat transfer maximum is found in the vicinity of the reattachment line R_2 of the secondary vortex. This correlation between the reattachment lines and the heat transfer maxima has also been observed by R. D. Watson [31], J. R. Cooper, W. L. Hankey [34], J. W. Keyes, R. D. Watson [29] and R. D. Watson, L. M. Weinstein [30].

4.3.2 Effect of leading-edge sweep

The Figs. 11 to 14 show a series of experimental results in which the leading-edge sweep angle ϕ has been varied between $\phi = -30^\circ$ and $\phi = +60^\circ$. With increasing sweep angle ϕ the pitot pressure level in the corner region reduces, all shocks are weakened and the whole shock system moves slightly inboard as indicated by the partial diagrams a) in Figs. 11 to 14. For unswept wedges, Fig. 12a, the wedge shock is parallel to the \bar{y} -axis. However, for swept wedges, Figs. 11a, 13a, 14a, the wedge shock is inclined against the \bar{y} -axis since the distance of the wedge shock from the wedge changes in \bar{y} -direction due to the increased or reduced distance between the leading-edge and the measuring plane depending on the sweep angle. With increasing sweep angle the slip surfaces meet closer to the corner center and the embedded shock impinges more and more normally on the viscous layer.

According to the partial diagrams b) in Figs. 11 to 14 for small sweep angles $|\phi| \leq 30^\circ$ the maximum wall pressure in the corner reaches about 4 times the swept wedge value. The maximum wall pressure decreases considerably with increasing sweep angle ϕ and the width of the corresponding plateau is also reduced.

The partial diagrams c) in Figs. 11 to 14 show that the maximum heat flux in the vicinity of the reattachment line R_1 is highest for unswept corners, for which the maximum heat transfer rate is 10 times as large as for the unswept wedge. With increasing sweep angle ϕ the maximum local heat transfer rate is considerably reduced.

According to the partial diagrams d) in Figs. 11 to 14 the influence border A is located at its outermost position at $\bar{y} > 0.7$ for unswept wedges. The corner shock system is located at $\bar{y} < 0.2$. This means that the interference effects between the two wedges extend through the subsonic boundary layer further outwards than the direct effect of the supersonic shock system. With increasing sweep angle ϕ the corner effect reduces considerably and the influence border moves inwards. Correspondingly the strengths of the primary vortices and of the secondary vortices within the viscous layer are reduced and for large sweep angles, Fig. 14d, the secondary separation disappears. The whole vortex system moves inwards with increasing sweep angle ϕ .

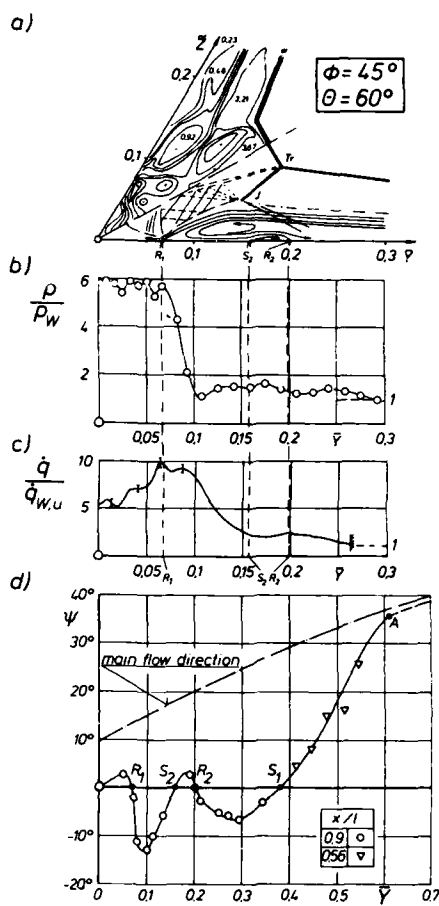


Fig. 15: Experimental results for the 45° swept 60°-corner [12]

- a) Pitot pressure isobars $p_{t2}/p_{t2\infty}$ in the flow field
 b) Wall pressure distribution
 c) Wall heat transfer distribution
 d) Flow direction at the wall (reduced ψ -scale)

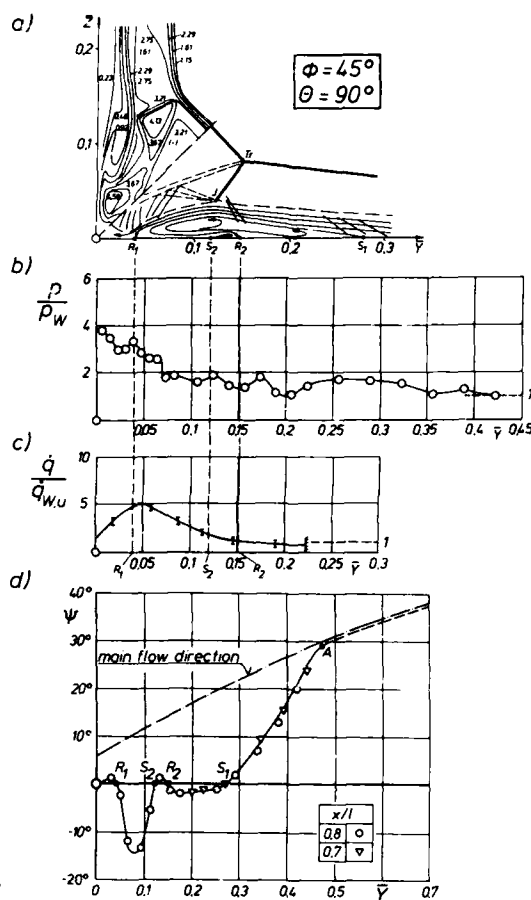


Fig. 16: Experimental results for the 45° swept 90°-corner [12]

- a) Pitot pressure isobars $p_{t2}/p_{t2\infty}$ in the flow field
 b) Wall pressure distribution
 c) Wall heat transfer distribution
 d) Flow direction at the wall (reduced ψ -scale)

4.3.3 Effect of corner angle

In part I of the test program according to Tab. 2 the corner angle θ has been varied systematically between $\theta = 60^\circ$ and $\theta = 120^\circ$ for corners between unswept wedges. The results have been published by K. Kipke, D. Hummel [9]. In the course of the investigations of W. Möllenstädt [12] the corner angle θ has also been varied for corners between swept wedges. Examples of this kind are shown in Figs. 15 to 17 and discussed subsequently.

The partial diagrams a) indicate that the pitot pressure level in the corner region is considerably reduced for increasing corner angle θ . The shock system moves inboard and all shocks weaken. The impingement angle between the embedded shock and the outer edge of the viscous layer is very flat for $\theta = 60^\circ$, but its value increases rapidly with increasing corner angle.

According to the partial diagrams b) in Figs. 15 to 17, at small corner angles a plateau of high wall pressures in the inner part of the corner exists. With increasing corner angle θ this pressure plateau disappears and the maximum wall pressure values are considerably reduced. This means that the pressure gradients are smaller and therefore the flow separations are weakened. The partial diagrams d) in Figs. 15 to 17 indicate weaker flow separations with increasing corner angle, and for $\theta = 120^\circ$ the secondary separation disappears at all. Corresponding to the inboard movement of the shock system with increasing corner angle the corner effects in the viscous layer decrease considerably in width. The influence border A as well as the separation lines S_1 , S_2 and the reattachment lines R_1 , R_2 move inwards with increasing corner angle.

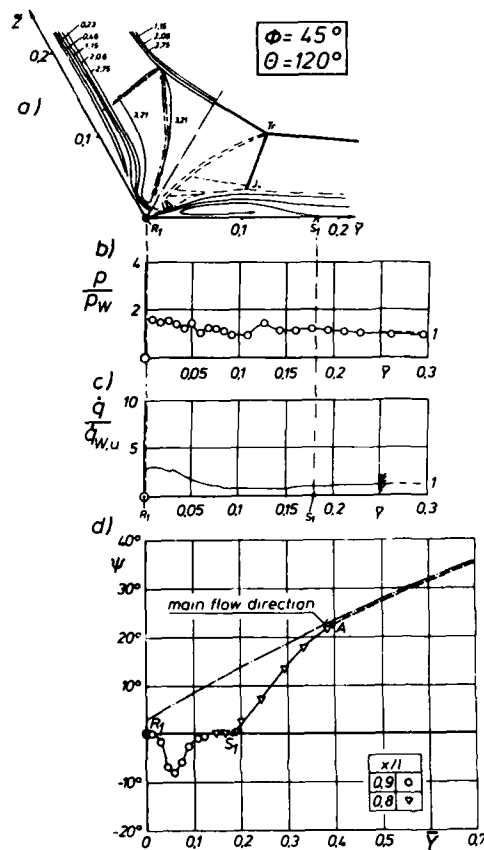


Fig. 17: Experimental results for the 45° swept 120°-corner [12]
 a) Pitot pressure isobars $p_{t2}/p_{t2\infty}$ in the flow field
 b) Wall pressure distribution
 c) Wall heat transfer distribution
 d) Flow direction at the wall (reduced ψ -scale)

The partial diagrams c) in Figs. 15 to 17 show the effect of the corner angle on the heat transfer rates. Since the position of maximum heat flux is correlated with the reattachment line R_1 , the region of maximum heat transfer moves inboard and the maximum values are reduced considerably with increasing corner angle.

4.3.4 Reduction of maximum values for wall pressures and heat transfer

In the course of the experimental investigations of K. Kipke, D. Hummel [9] and W. Möllenstädt [12] reductions of the maximum values for static wall pressure and heat transfer rate due to variations of corner angle θ and of leading-edge sweep ϕ have been found. The possible reductions of these maximum values by variations of the two governing parameters are summarized subsequently.

Fig. 18 shows a schematic diagram of the pressure distribution along the wall in a corner configuration. The maximum value in the corner center is p_{\max} and far away from the corner the undisturbed value for the swept wedge p_w is reached. In the lower part of Fig. 18 the wall pressures are based on the wall pressure of an unswept wedge p_{wu} . In order to be able to show the results in this manner, some additional pressure measurements on swept and unswept wedges far away from the corner have been carried out. The measured pressure ratio p_w/p_{wu} is plotted as a function of the sweep angle ϕ . The well known reduction of p_w with increasing ϕ turns out. The ratio p_w/p_{wu} has also been calculated from the shock relations using the measured shock positions. The agreement with the directly measured data is good. The

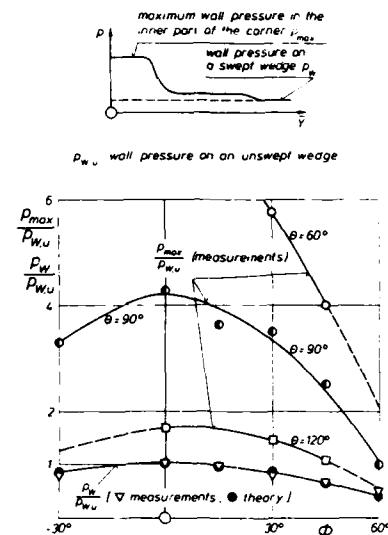


Fig. 18: Maximum wall pressure p_{\max} as function of corner angle θ and sweep angle ϕ

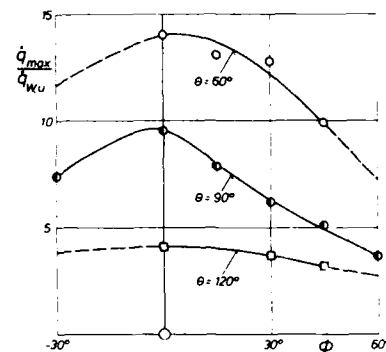


Fig. 19: Maximum heat transfer rate \dot{q}_{\max} as function of corner angle θ and sweep angle ϕ

lower diagram in Fig. 18 shows the maximum wall pressure $p_{w, \max} / p_{\infty}$ as functions of the sweep angle ϕ for different corner angles θ . Both parameters have a big influence. The highest values are found for unswept wedges, $\phi = 0^\circ$, and with increasing sweep angle a considerable reduction is achieved. On the other hand the maximum wall pressure increases very much with decreasing corner angle θ . In an unswept 90° -corner $p_{w, \max}$ is 4 times as high as in a 60° -swept 90° -corner. If the corner angle is reduced from 90° to 60° the wedges have to be 45° -swept to obtain the same maximum wall pressure as in the unswept 90° -corner. Small values of the maximum wall pressure are achieved for combinations of high sweep angles and large corner angles.

Finally Fig. 19 shows the maximum heat transfer rate as functions of the sweep angle ϕ for different corner angles θ . In the diagram the maximum heat transfer rate is based on the value for an unswept wedge. Measurements for swept wedges in the absence of a corner are not available. The maximum heat transfer rate decreases with increasing sweep angle and it increases with decreasing corner angle. In an unswept 60° -corner the maximum heat transfer rate is 14 times as high as for an unswept wedge. For 90° -corners the maximum heat transfer rate can be reduced to about 40% by applying a sweep angle of $\phi = 60^\circ$. If the corner angle is reduced from 90° to 60° the wedges have to be 45° -swept to obtain the same maximum heat transfer rate as in the unswept 90° -corner. Small values of the maximum heat transfer rate are achieved for combinations of high sweep angles and large corner angles.

4.4 Conclusions

The results of a long-term program on the axial flow in corner configurations according to K. Kipke, D. Hummel [9] and W. Möllenstädt [12] have been summarized. The investigations have been carried out in the gun tunnel of the Institut für Strömungsmechanik at TU Braunschweig. The corner models were composed of two intersecting wedges with wedge angles $\delta = 6.3^\circ, 8.0^\circ$ and 10.0° . The corner angles $\theta = 60^\circ, 90^\circ$ and 120° have been investigated in combination with leading-edge sweep angles $\phi = -30^\circ, 0^\circ, 15^\circ, 30^\circ, 45^\circ$ and 60° . The free-stream Mach numbers were $M_\infty = 12.3$ and 16.0 corresponding to Reynolds numbers $Re_{1m} = 5 \cdot 10^5$ and $1.7 \cdot 10^5$.

The conical interference flow has been investigated in one cross-section normal to the free-stream direction on each model. Pitot pressure measurements in the flow field show the position of the shock system, consisting of corner, wedge and embedded shocks and slip surfaces. With increasing leading-edge sweep and increasing corner angle, a displacement of the shock system towards the center of the corner, accompanied by a strong reduction of the pitot pressure level, was found. The flow structure near the wall was determined from oil flow pictures, wall pressures and the pitot pressure measurements. Within the viscous layer strong vortex flows have been observed, which are close to the center of the corner and consist of primary and secondary vortices, whose intensities decrease with increasing corner angle and with increasing leading-edge sweep. The highest static wall pressure occurs in the vicinity of the reattachment line of the primary vortex. Its value decreases with increasing corner angle θ and with increasing sweep angle ϕ . The maximum value of the heat flux at the wall was also found at this reattachment line. For an unswept 90° -corner its value is about 10 times as high as the heat flux on an unswept wedge. This high heat flux can be considerably reduced by increasing the corner angle θ and by sweeping the leading edges back to $\phi = 60^\circ$.

5. LITERATURE

- [1] K. Gersten, G. Kausche: Die Hyperschallversuchsanlage (Gun Tunnel) der Deutschen Forschungsanstalt für Luft- und Raumfahrt. Z. Flugwiss. 14 (1966), 217-229.
- [2] K. Kipke: The data processing system of the hypersonic wind tunnel in Braunschweig. Vortrag EURO-MECH-Colloquium 18, Southampton 1970. Report 70/26 of Inst. f. Strömungsmechanik d. TU Braunschweig, 1970.
- [3] G. Strömsdörfer: Wärmeübergangsmessungen in einem Gun-Tunnel. DLR-Mitt. 75-11 (1975), 91-117.
- [4] W. Möllenstädt: Wand Schubspannungsbilder bei Hyperschallströmung. DGLR-Fachausschuß-Sitzung "Sichtbarmachung von Strömungen", Essen, 1984.
- [5] K. Kipke: Experimentelle Untersuchungen an Wellenreiter-Flügeln im Hyperschallbereich. Abhandlg. Braunschw. Wiss. Ges. 21 (1969), 407-428.
- [6] K. Kipke: Aerodynamische Probleme hypersonischer Wellenreiter. 9. Lehrgang für Raumfahrttechnik, Göttingen 1971, 25-1 bis 25-25.
- [7] K. Kipke: Untersuchungen an schiebenden Wellenreiterflügeln im Hyperschallbereich. Dissertation TU Braunschweig 1972. Z. Flugwiss. 21 (1973), 381-400.
- [8] G. Strömsdörfer: Untersuchungen der Hyperschallströmung um rotationssymmetrische, stumpfe Körper mit Nasenausbläsung. Dissertation TU Braunschweig 1975. Z. Flugwiss. Weltraumforsch. 1 (1977), 161-168.
- [9] K. Kipke, D. Hummel: Untersuchungen an längsangeströmten Eckenkonfigurationen im Hyperschallbereich. Teil I: Ecken zwischen ungepfeilten Keilen. Z. Flugwiss. 23 (1975), 417-429.
- [10] W. Möllenstädt: Experimental investigations of the hypersonic flow in corners of intersecting swept wedges. Vortrag EUROMECH-Colloquium 126, Berlin 1980.
- [11] W. Möllenstädt: Experimentelle Untersuchungen an längsangeströmten Eckenkonfigurationen im Hyperschallbereich. Dissertation TU Braunschweig 1984.
- [12] W. Möllenstädt: Untersuchungen an längsangeströmten Eckenkonfigurationen im Hyperschallbereich. Teil II: Ecken zwischen gepfeilten Keilen. Z. Flugwiss. Weltraumforsch. 8 (1984), 405-414.

- [13] W. Möllenstädt: Experimental investigations on swept corner configurations in hypersonic flow. Vortrag (von D. Hummel) EUROMECH-Colloquium 195, Marseille 1985.
- [14] H.M. McMahon: An experimental study of the effect of mass injection at the stagnation point of a blunt body. GALCIT Hypersonic Research Project Memorandum No. 42 (1958).
- [15] C.H.E. Warren: An experimental investigation of the effect of ejecting a coolant gas at the nose of a blunt body. GALCIT Hypersonic Research Project Memorandum No. 47 (1958).
- [16] L.M. Tucker: An experimental investigation of contoured nose orifices with ejection at free-stream Mach numbers of 1.86 and 4.3. RAE TN Aero 2923 (1963).
- [17] W. Wuest: Zweigaskengrenzschichten in der Umgebung eines freien Staupunktes in inkompressibler Strömung mit Berücksichtigung der thermischen Diffusion. Z. Flugwiss. 14 (1966), 298-305.
- [18] E. Eminton: Orifice shapes for ejecting gas at the nose of a body in two-dimensional flow. RAE TN Aero 2711 (1960).
- [19] J.R. Baron, E. Alzner: An experimental investigation of a two-layer inviscid shock cap due to blunt-body nose injection. J. Fluid Mech. 15 (1963), 442-448.
- [20] Chang-Yi Wang: Contours for stagnation-point mass injection in hypersonic flow. AIAA J. 2 (1964), 178-179.
- [21] Chang-Yi Wang: Mass injection contours for a hypersonic leading edge at an angle of attack. AIAA J. 3 (1965), 184-185.
- [22] W. Wuest: Näherungsweise Ermittlung des Strömungsfeldes an einem Profil mit Nasenausbläsung bei Hyperschallanblasung. Deutsche Luft- und Raumfahrt, FB 66-09 (1966).
- [23] K. Jacob: Berechnung der reibungslosen, inkompressiblen Strömung für rotationssymmetrische Zentral- und Ringkörper mit beliebiger Profilform bei axialer Anströmung. AVA-Bericht 70 R 03 (1970).
- [24] O. David: Die Berechnung der Machzahlverteilung an einem Turbinenprofil. Motortechn. Z. 20 (1959), 92-93.
- [25] P.C. Stainback: Heat-transfer measurements at a Mach number of 8 in the vicinity of a 90° interior corner aligned with the free-stream velocity. NASA TN D-2417 (1964).
- [26] P.C. Stainback, L.M. Weinstein: Aerodynamic heating in the vicinity of corners at hypersonic speeds. NASA TN D-4130 (1967).
- [27] R.A. Jones: Heat transfer and pressure investigation of fin-plate-interference model at a Mach number of 6. NASA TN D-2028 (1964).
- [28] A.F. Charwat, L.G. Redekopp: Supersonic interference flow along the corner of intersecting wedges. AIAA J. 5 (1967), 480-488.
- [29] J.W. Keyes, R.D. Watson: Laminar heating in interior corners at $M = 19$. J. Spacecr. Rock. 7 (1970), 1012-1013.
- [30] R.D. Watson, L.M. Weinstein: A study of hypersonic corner flow interactions. AIAA J. 9 (1971), 1280-1286.
- [31] R.D. Watson: Experimental study of sharp- and blunt-nose streamwise corners at Mach 20. NASA TN D-7398 (1974).
- [32] J.E. West, R.H. Korkegi: Supersonic interaction in the corner of intersecting wedges at high Reynolds numbers. AIAA Paper 72-6 (1972).
- [33] R.J. Cresci, S.G. Rubin, C.T. Nardo: Hypersonic flow in rectangular and non-rectangular corners. AGARD-CP-30 (1968), 18-1 to 18-16.
- [34] J.R. Cooper, W.L. Hankey: Flowfield measurements in an asymmetric axial corner at $M = 12.5$. AIAA J. 12 (1974), 1353-1357.
- [35] H.-J. Schepers: Untersuchungen der wandnahen Strömung und des Wärmeübergangs im Bereich längsangeordneter Ecken bei Hyperschallströmung. Deutsche Luft- und Raumfahrt, FB 76-02 (1976).
- [36] R.H. Korkegi: On the structure of three-dimensional shock-induced separated flow regions. AIAA J. 14 (1976), 597-600.
- [37] D.J. Peake, M. Tobak, R.H. Korkegi: Three-dimensional interactions and vortical flows with emphasis on high speeds. AGARDograph 252 (1980).
- [38] D.L. Schultz, T.V. Jones: Heat-transfer measurements in short-duration hypersonic facilities. AGARDograph 165 (1973).
- [39] L. Lees, B.L. Reeves: Supersonic separated and reattaching laminar flows: I. General theory and application to adiabatic boundary layer-shock wave interaction. AIAA J. 2 (1964), 1907-1920.
- [40] D. Hummel: On the vortex formation over a slender delta wing at large angles of incidence. AGARD-CP-247 (1978), 15-1 to 15-17.

DRIVING MECHANISM OF UNSTEADY SEPARATION SHOCK MOTION IN HYPERSONIC INTERACTIVE FLOW

D. S. Dolling and J. C. Nario II
 Department of Aerospace Engineering and Engineering Mechanics
 The University of Texas at Austin, Austin, Texas 78712

SUMMARY

Wall pressure fluctuations have been measured under the unsteady separation shock wave in Mach 5 turbulent interactions induced by unswept circular cylinders on a flat plate. The wall temperature was adiabatic. A conditional sampling algorithm has been developed to examine the statistics of the shock wave motion. The same algorithm has been used to examine data taken in earlier studies in the Princeton University Mach 3 blowdown tunnel. In these earlier studies, hemicylindrically blunted fins of different leading-edge diameters were tested in boundary layers which developed on the tunnel floor and on a flat plate. A description of the algorithm, the reasons why it was developed and the sensitivity of the results to the threshold settings, are discussed. The results from the algorithm, together with cross correlations and power spectral density estimates suggests that the shock motion is driven by the low-frequency unsteadiness of the downstream separated, vortical flow.

1. INTRODUCTION

Since the early 1950's, it has been known that shock-induced turbulent boundary-layer separation is a highly unsteady process. In early work on step-induced interactions [1], and in later studies employing many different model geometries [2], the unsteadiness was evident from randomly shot sequences of microsecond spark shadow and schlieren photographs, or from high-speed cinema records. Although such optical methods readily reveal unsteadiness, the results are difficult to interpret even for two-dimensional flows. This is because the photograph represents the integration of the light beam across a spanwise rippling shock structure. Consequently, other than providing estimates of the shock motion length scale, little quantitative information has been obtained from them.

Kistler, in 1964, was probably the first to make quantitative measurements and to document the character of the wall pressure signal, $P_w(t)$, near separation [3]. Kistler's tests were made using piezoelectric transducers in forward-facing step flows at Mach numbers of 3 and 4.5. A typical pressure signal, which has all of the features observed by Kistler but from the present study (a separated flow induced by a circular cylinder), is shown in Figure 1. The moving separation shock generates an intermittent wall pressure signal whose level fluctuates between that characteristic of the undisturbed incoming boundary layer and that downstream of the shock wave. Since Kistler's work, pressure signals such as these have been measured in a wide variety of interactive flows at speeds from transonic to hypersonic (i.e., Refs. 4-14). They all show qualitatively similar results. Much of the early work [4-7] was motivated by the need for engineering estimates of the fluctuating pressure field around high-speed vehicles. More recently, the resurgence of interest in the unsteadiness has been motivated largely by the realization that physically accurate interpretations of mean flow data and an understanding of the flow field mechanisms requires a knowledge of the flow dynamics. In most of these more recent studies, the emphasis has been on the separation process [8-14].

One of the most fundamental questions about this unsteadiness is that of the driving mechanism behind it. Andreopoulos and Muck have recently addressed this question [14]. In their experimental study, $P_w(t)$ was measured at several stations in the intermittent region in three, nominally 2-D, compression ramp flows in a high Reynolds number Mach 3 airflow. Of the three flows, two were separated, and the other was in a condition of incipient separation. The pressure signals were analyzed using a conditional sampling algorithm. In this algorithm, the measured pressure signal is converted into a square wave of amplitude unity and varying frequency (Fig. 2). The time T_i between consecutive passages of the shock wave over the transducer can then be determined, and the probability distribution for T_i can be constructed. The distribution is highly skewed with the mean period, T_m , significantly larger than the most probable period, T_p [14].

Andreopoulos and Muck found that T_m was approximately $7.7\delta_0/U_\infty$, where δ_0 and U_∞ are the undisturbed boundary layer thickness and freestream velocity, respectively. Further, T_m was independent of both position in the intermittent region and ramp angle (i.e., independent of shock strength and, hence, apparently independent of downstream flow conditions). The mean shock frequency, f_m , ($=1/T_m$) was equal to $0.13U_\infty/\delta_0$, which Andreopoulos and Muck point out is the same order as the estimated bursting frequency of the incoming turbulent boundary layer. This apparent correlation with the bursting frequency and the independence of f_m on the downstream flow field led these investigators to conclude that the "incoming boundary layer is the most likely cause triggering the shock wave oscillation" [14].

This conclusion does not fully explain certain features of the shock motion. First, with fixed free-stream conditions and fixed δ_0 , it is known that the streamwise length scale of the separation shock motion, L_s , depends on the particular flow field under study. For example, in hemicylindrically blunted fin flows, L_s is of order D , where D is the fin leading-edge diameter [15]. Hence, L_s can vary from a fraction of δ_0 to several δ_0 depending on D . If the shock wave was convected by turbulent bursts, L_s might be expected to remain constant for fixed incoming conditions. Of course, it is possible that different driving mechanisms exist in different flows, but the commonality of rms distributions, amplitude probability densities, power spectral density estimates and many other global and detailed features

suggests a common origin. Second, careful examination of the conditional sampling algorithm of reference 14 by the current authors has suggested that a large number of "false" shocks were counted which significantly increases f_m . This will be elaborated on in sections 3.2 and 3.3.

These observations led to the current investigation, the first results of which are presented in this paper. The study consists of two parts:

- (i) a series of tests has been made of the separation shock-induced pressure fluctuations in interactions induced by circular cylinders in the Mach 5 blowdown tunnel of The University of Texas at Austin. Details of the experiment are given in section 2. The data have been analyzed using a new conditional sampling algorithm designed to avoid the problem mentioned above.
- (ii) wall-pressure fluctuation data taken in hemicylindrically blunt fin-induced interactions at Mach 3 have been re-examined using the new algorithm. These data were taken by the first author in the 20 cm. x 20 cm. (8 in. x 8 in.) Mach 3 blowdown tunnel of the Gas Dynamics Laboratory of Princeton University. Mean wall pressures, distributions of the rms of the fluctuations and some spectral analysis have been reported in Reference 8. A description of the facility and models, the instrumentation, and data acquisition techniques are also given in Reference 8. In summary, fins with $D = 1.27$ cm (0.5 in.) and 2.54 cm (1.0 in.) were tested in incoming turbulent boundary layers with thicknesses ranging from 0.3 cm. to 1.6 cm. The pressure signal was digitized at rates from 20-400 kHz. Up to 72 data records (1024 points per record) were taken at each station.

In this paper, the new experimental study and some of the results from it are described first. The results from applying the same algorithm to the earlier data are then presented and compared with the new findings.

2. EXPERIMENTAL PROGRAM

2.1 Model's and Test Facility

The tests were conducted in the Mach 5 blowdown facility of The University of Texas at Austin. This facility has a 17.8 cm. x 15.2 cm. (7 x 6 inch) test section. All the tests were conducted on a full-span flat plate, 43.7 cm. (18 in.) long, mounted at zero angle-of-attack. Two miniature Kulite pressure transducers were installed upstream of an unswept cylinder which was approximately 33 cm. (13 in.) downstream of the test surface leading edge. The transducers were mounted flush in a 7.6 cm. (3 in.) diameter circular plug which was mounted flush with the surface of the flat plate. The circular plug could be rotated so the transducers could be aligned streamwise or spanwise to the freestream flow.

Cylinders with diameters of 1.27 cm. (0.5 in.) and 1.90 cm. (0.75 in.) with heights of 5.08 cm. (2.0 in.) and 7.62 cm. (3.0 in.), respectively, were used. Based on the criterion of Reference 16, their heights were effectively semi-infinite. The cylinder was moved relative to the transducers. Over the range of travel (at maximum 2.54 cm.), the change in incoming flow conditions had a negligible effect on the interaction properties.

2.2 Instrumentation

The pressure transducers, Kulite model XCQ-062-15A, were 0.29 cm. (0.115) inches center-to-center. This was the closest spacing possible due to physical limitations. The transducers have external diameters of 0.162 cm. (0.064 in.) with a pressure-sensitive diaphragm 0.071 cm. (0.028 in.) in diameter. The natural frequency is quoted as 250 kHz by the manufacturer. Full-scale output is nominally 225 mv for 15 psi giving a sensitivity of 15 mv/psi. The transducers were calibrated statically, since shock tube tests with similar designs have shown that dynamic calibrations are only a few percent lower than those obtained statically[17]. The combined non-linearity and hysteresis are quoted as 0.5% full scale with repeatability of 0.1% full scale.

The output from the transducers was amplified by a PARC, Model 113, amplifier giving a signal in the range 0-10 volts. The signal was then low-pass filtered using an Ithaco filter, Model 4213, with the cut-off set to either one-half the sampling rate or, for sampling rates greater than 100 kHz, it was set at 50 kHz. This was because the dynamic response of the pressure transducers is limited to approximately 50 kHz. The signal was digitized by a 12-bit A/D converter which outputs 0 to 4096 counts for inputs of 0 to 10 volts. Noise on the system was ± 2 counts which resulted in an overall resolution of ± 0.005 psi. Additional details concerning the instrumentation are given in Reference 18.

2.3 Flow Conditions

The freestream and incoming turbulent boundary-layer properties are given in Table 1 and Figure 3 which show the mean velocity profile, plotted in wall coordinates. The boundary layer developed naturally on the upper surface of the flat plate. No trips were used. The measurements match the combined wall-wake law well. The skin friction coefficient deduced from the curve fit is within 10% of that predicted using the van Driest II method.

2.4 Test Technique

First, the intermittent region was mapped out for each cylinder. The sampling rate used was 250 kHz and at each station 70 records were taken on each channel (1 record = 1024 data points). Several stations were then selected for further detailed analysis. At these positions, the number of records taken was increased to 400 (the limit of the data acquisition system) and the sampling rate was reduced to 100 kHz.

TABLE 1. Freestream and Boundary Layer Properties

Freestream Mach Number, M_∞	$4.96 \pm .02$	
Freestream Velocity, U_∞	741 m/s	2430 ft/s
Freestream Reynolds Number, R_{e_∞}	$55 \times 10^6 \text{ m}^{-1}$	$16.8 \times 10^6 \text{ ft}^{-1}$
Stagnation Pressure, P_o	$2.09 \times 10^6 \text{ N/m}^2 \pm 1\%$	303 psia
Stagnation Temperature, T_o	$327 \text{ K} \pm 1\%$	590°R

3. RESULTS AND DISCUSSION

3.1 Conditional Sampling Analysis

The main thrust of the present work was to determine the frequency distribution of the shock wave motion using a conditional sampling technique. This technique transforms the pressure signal into a box-car function which is then analyzed statistically. The technique employs upper and lower thresholds to distinguish between those pressure fluctuations induced by the shock and those characteristic of the turbulent boundary layer both upstream and downstream of the shock. Before the results are presented, the algorithm itself is discussed since understanding its operation is crucial for appraising the results in section 4.

3.2 Upper Threshold Calculation

Transformation of the pressure signal into a box-car function requires careful thought. An obvious requirement is that shock waves in the original signal must also exist in the transformed signal. Since the original signal is that of a turbulent flow, precautions must be taken to ensure that turbulent fluctuations are not inadvertently counted as shock waves.

In earlier work, pressure signals were simply "eyeballed," and a threshold pressure was selected as the level just above the largest pressure fluctuations characteristic of the boundary layer [9,14]. Eyeballing the signal separately at all stations helps avoid problems due to d.c. offsets and drift, but is highly subjective and it is difficult to be consistent from station to station. To avoid such problems, a systematic technique for calculating the threshold level(s) has been developed.

The first step is to calculate the mean pressure, P_m , of that fraction of the signal corresponding to the undisturbed boundary layer for signals in the intermittent region. Only a brief explanation of the method is given below. The detailed programming is given in Reference 18. First, the minimum pressure in each record was determined and the average for N records was calculated to give \bar{P}_{min} . Once \bar{P}_{min} was calculated, a "window" of width 0.01 psi was stepped upwards through the signal in increments of 0.005 psi, starting at \bar{P}_{min} . At each step, the number of data points within the window was counted. The window position at which the greatest number of data points occurs brackets P_m . This is because the boundary-layer pressure fluctuations are distributed normally and the probability is a maximum at the mean value. Figure 4 illustrates this process.

Once P_m was obtained, the standard deviation, σ_p , of the pressure fluctuations in the boundary layer was calculated since this is needed for setting the upper threshold level, T_2 . Since these fluctuations have a Gaussian distribution, the probability of finding points at any chosen values above or below P_m can be defined once σ_p is known. A value of $P_m + 4.5\sigma_p$ was chosen for T_2 , since the probability of finding points greater than $4.5\sigma_p$ above the mean is 0.0000068 (i.e., chances of 1 in 147,000). Hence, pressures above T_2 are characteristic of the flow downstream of the shock wave, and pressures below T_2 are characteristic of the undisturbed boundary layer. This approach sets T_2 consistently just above the largest pressure fluctuations of the boundary layer, and automatically takes care of any small d.c. offsets or drift on the signal from run to run. The process is automated and requires no subjective input from the user.

3.3 Transformation of the signal

Once T_2 is calculated, the signal can be transformed into a box-car function. Two methods were examined. The first was a single threshold method similar to that of Reference 14. Data points are checked sequentially and the passage of a shock over the transducer in the upstream direction is considered to have occurred if the first point is below T_2 and the second is above it. Termination of the shock occurs when this criterion is reversed. The problem with this simple approach is that the resulting box-car does not accurately reflect the original signal.

Close examination of the box-car shows that many "false shock waves" can occur with this algorithm. Figure 5 (resketched from data presented in Ref. 14) shows the inclusion of four shock waves, labeled A, B, C and D, that are not in the original record. The "false shocks" are actually turbulent fluctuations and occur at high frequency. The inclusion of these waves in the box-car drives the mean frequency higher and alters the shape of the probability distribution. Examination of many cases shows that no matter what

threshold level is chosen, turbulent fluctuations such as those labeled A and B will inadvertently create "false shock waves."

The second method used for all of the results presented in this paper uses 2 thresholds. The upper one is given by $T_2 = P_m + 4.5\sigma_p$ and the lower one by $T_1 = P_m$. T_1 is used so that the small amplitude pressure fluctuations present on the signal are not counted as shock waves. The detailed programming is also given in Reference 18. A brief discussion of how it works is as follows. Initially, a "toggle" that determines if a data point has a lower value than T_2 is set to an "off" state. The algorithm then checks successive data points. If the first point is less than T_2 and the second point is greater than T_2 and the "toggle" is "off," this marks the start of the passage of a shock wave. This event initializes the process that determines the time between successive shock waves. The "toggle" is then set "on," and further crossings of T_2 are not counted until a data point has a value below T_1 . Termination of the shock wave occurs when this happens, and the "toggle" is then reset to "off." This process largely eliminates the counting of turbulent fluctuations as shock waves.

However, this algorithm introduces a new problem. If in between two very closely spaced shock passages, $P_w(t)$ does not fall below P_m before increasing again, the toggle is not reset and what is in reality two shock passages is only counted as one. As might be expected, at low intermittency, γ , when significant time spans of undisturbed boundary-layer flow exist between successive shock passages, this is not a problem, but at moderate to large γ it is more severe. To examine this problem, a sensitivity analysis was made in which the effects on f_m of varying T_1 and T_2 were investigated.

The results at low and mid-range γ are shown in Figures 6a and 6b, respectively. The parameter plotted on the horizontal axis is n , where n is given in the expression $T_2 = P_m + n\sigma_p$. Careful examination of the results shows that different problems occur with different pairs of T_1 and T_2 . Because of space constraints, only the more salient results and conclusions are listed below. The reader is referred to Reference 19 for details. For a fixed T_2 , f_m increases as T_1 increases because $P_w(t)$ now has to drop below a progressively higher pressure level for the toggle to be reset. However, when $T_1 = T_2$, the method becomes a single threshold technique and the same problems as discussed earlier occur. With T_1 equal to $P_m + 3\sigma_p$, then $P_w(t)$ must just fall with the range of the boundary-layer fluctuations for the toggle to be reset. However, for this setting of T_1 , T_2 must be set significantly higher to avoid shock-induced turbulent fluctuations (occurring as it moves downstream over the transducer) from being counted as shocks. Setting $T_2 = P_m + 6\sigma_p$ or above provides the necessary discrimination, and f_m is then relatively insensitive to increases in T_2 .

In conclusion, although different combinations of T_1 and T_2 can be justified physically and argued for on rational grounds, any particular pair lacks discrimination with respect to turbulent fluctuations generated either upstream or downstream of the shock wave. This means that the mean shock frequency cannot be pinpointed with precision. However, it can be bracketed within a fairly narrow range. The boundaries of this range are essentially given by the cases $T_1 = P_m$, $T_2 = P_m + 4.5\sigma_p$ (this results in the lower boundary since $P_w(t)$ must fall below P_m to reset the toggle) and $T_1 = P_m + 3\sigma_p$, $T_2 = P_m + 6\sigma_p$ (for which the toggle is reset when P_w falls below the upper pressure level typical of the undisturbed boundary layer). As expected, the variation in f_m between these boundaries is small for low γ . (Figure 6a, for $\gamma \approx 0.2$, shows a variation from 0.55-0.65 kHz.) At higher γ (Fig. 6b), the variation is larger (1.2-1.5 kHz). However, the bounds of this range, as discussed later, do not overlap the ranges of other characteristic flow frequencies such that the lack of precision in specifying f_m does not lead to ambiguities in drawing conclusions.

4. DISCUSSION OF RESULTS

4.1 Incoming Boundary-Layer Properties

In a Mach 5, (740 m/s) 5mm thick, turbulent boundary layer, pressure fluctuations at frequencies as high as several hundreds of kilohertz are to be expected. The transducers used cannot resolve such high frequencies for several reasons. First, the finite size of the transducer limits the resolution of the high-frequency components of the signal. Schewe [20] has studied this problem and, from careful measurements and correlations of incompressible and subsonic data, shown that σ_p normalised by the free-stream dynamic pressure q_∞ is a function of the normalised transducer diameter, $d^+(d^+ \equiv d/\delta)$. The "ideal" transducer has $d^+ \approx 20$. Under the present flow conditions and using the smallest available transducer, the value of d^+ was approximately 770. Extrapolation of Schewe's results suggests that the measured σ_p/q_∞ will be about 40-50% of that of the "ideal" transducer. The current result ($\sigma_p/q_\infty = 7.7 \times 10^{-4}$) is shown correlated with data from other studies in Figure 7. The value is about 60% of that predicted by the semi-empirical correlation of Lawson [21] and about 30% of that predicted by Laganelli et al. [22].

Second, the usable frequency range is limited by the natural frequency of the diaphragm and the effects of the protective screen. Tests have shown that beyond 45-50 kHz the response is no longer flat and resonance effects become significant. The power spectrum in the linear-log form $G(f) \cdot f/\sigma_p^2$ vs f , where $G(f)$ is the power level and f is the frequency, is shown in Figure 8. There are two points worthy of note. First, there is little low-frequency contamination by tunnel noise, so the latter does not

contribute significantly to the overall σ_p . Second, as expected, the energy level increases with increasing f . There is some suggestion of a plateau and subsequent roll-off around 40-50 kHz, but this is probably due to transducer limitations. Future tests with a new transducer with frequency response up to 300 kHz will resolve this.

The cross-correlation $R_{pp}(\xi, \tau)$ of the two signals (transducers streamwise) for $-50\mu s \leq \tau \leq +50\mu s$ is shown in Figure 9. It is evident that, in this boundary layer and with this spacing, a sampling rate of 250 kHz does not adequately resolve R_{ppmax} . The maximum value of the correlation is bracketed between $\tau = 4$ and $8\mu s$. These correspond to broad-band convection velocities of 370 and 730 m/s, respectively. A simple linear extrapolation between adjacent data points, as indicated by the hatched lines gives $R_{ppmax} = 0.84$ at $\tau = 5.9\mu s$, corresponding to a broad-band convection velocity of 496 m/s, approximately $0.67U_\infty$. The average of the phase speeds, summed over the range 0-50 kHz, gives an average phase velocity of 530 m/s, approximately $0.72U_\infty$. These values agree reasonably well with results of other studies (Fig. 10). Similarly, R_{ppmax} of 0.84 (for $\xi/\delta^* = 1.33$) agrees reasonably well with other results (Fig. 11).

4.2 Mach 5 Cylinder Interactions

Distributions of the mean wall pressure, normalised rms level, and intermittency are shown in Figures 12, 13 and 14, respectively. The intermittency is the ratio of the number of data points counted when the toggle is in the "on" state to the total number of data points. The separation locations, obtained from surface flow visualisation, are indicated by 'S.' The trends are identical to those of earlier studies indicating that these particular flows have no features peculiar to this blowdown facility.

Distributions of f_m are shown as a function of γ in Figure 15. In both cases, f_m has a maximum value at $\gamma = .5$. This result differs from the findings of Reference 14 where it was observed that f_m was independent of position within the intermittent region. It is probable that this result is a feature of the single-threshold algorithm as described earlier. The present results show very clearly that f_m changes from station to station. Examination of the pressure signals for different values of γ confirms this qualitatively. From Figure 16, which shows sample time-histories for $\gamma = .25$ and $.75$, it can be seen that the average time between successive passages of the shock wave occurs at different intervals.

The distributions of f_m for both cylinders are similar in shape but have different maxima. The maximum frequency for the 1.27 cm and 1.90 cm cases is approximately 1.6 and 1.2 kHz, respectively. The fact that they differ suggests that the motion is in some way influenced by the downstream separated flow dynamics since the incoming flow conditions are constant, and only the cylinder diameter is changed. Most significant is the observation that the magnitudes of the maximum mean frequencies are more than two orders of magnitude less than a typical large eddy frequency (i.e., $U_\infty/\delta_0 \approx 120$ kHz) and one order of magnitude less than the estimated boundary-layer bursting frequency (of order 10 kHz).

Probability distributions for the shock wave period were constructed at each station. In all cases, the distributions are highly skewed with $T_m \approx T_p$. Results for $\gamma = 0.2$ and 0.5 are shown in Figure 17. The distribution for the smaller-diameter cylinder is more compressed (i.e., higher probability of finding shorter periods and vice-versa). For example, at $\gamma = 0.5$, the probability of finding periods greater than 2 ms is very small for $D = 1.27$ cm, whereas for $D = 1.9$ cm, the maximum period is about 3 ms. An interesting feature is that, although T_m is a function of γ (for a fixed D) and a function of D (for a fixed γ), T_p remains approximately constant (≈ 0.4 - 0.5 ms) at all stations for both cylinders.

Power spectral density estimates provide additional quantitative support for the above findings. Although power spectra calculated using the entire signal present different information than the probability distribution for the shock period alone, they show very clearly that the large amplitude, high-energy fluctuations (i.e., those caused by the shock wave) fall in a fairly narrow low frequency band. Power spectra at the same stations as the probability distributions of Figure 17 are shown in Figure 18. The data are also plotted as $f \cdot G(f)/\sigma_p^2$ vs. f , rather than the more usual log-log form. This method highlights dominant frequency ranges in the signal. The results show that the high-amplitude pressure fluctuations generated by the shock wave motion are distributed in the range of 0.2 to 2-3 kHz. This is the same range of frequencies as indicated in Figure 17. There is very little energy at frequencies of the order of the bursting frequency. In both figures, and all other spectral plots, the effects of changing D are evident. With increasing D , the curves retain their basic shape but are shifted towards a lower range of frequencies.

Initial cross-correlations of the transformed box-cars for the two transducers suggest that the shock wave is not convected by the large-scale structures in the incoming boundary layer. The cross-correlation for two transducers at $X/D = 3.15$ ($\gamma = .65$) and $X/D = 2.92$ ($\gamma = .34$) for the 1.27 cm. case is shown in Figure 19. There are two maxima, one at $\tau = -32\mu s$ and the other at $+28\mu s$, corresponding to the average time delay between the rise and fall in pressure on the two signals as the shock moves upstream and downstream, respectively. From these values of τ and the transducer spacing, the average shock velocity in the upstream and downstream direction was calculated as 91 m/s and 104 m/s, respectively. Without detailed analysis at other stations, and preferably additional tests at higher sampling rates (to improve the resolution of τ), it cannot be stated with any certainty that the downstream velocity is higher than the upstream one or that these velocities are truly representative. However, both are relatively small, of order 20% of the incoming boundary layer broad-band convection velocity. Since the shock velocity in the downstream direction is a small fraction of this convection velocity, it seems unlikely that the incoming turbulence acts as the driving mechanism of the motion. However, before definitive conclusions can be drawn, the probability distribution of the shock velocities must be calculated and examined since the average velocities from the correlation may be misleading.

4.3 Mach 3 Blunt Fin Re-Examination

f_m as a function of intermittency is shown in Figure 20 for fins with $D = 1.27$ cm. and 2.54 cm. The figure includes results for the model on the tunnel floor ($\delta_o = 1.6$ cm.) and on a full span flat plate ($\delta_o = .3$ cm.). In these boundary layers, large eddy frequencies (U_∞/δ_o) are of order 36 kHz and 190 kHz, respectively. Two conclusions can be drawn from the Figure:

- 1) for a given diameter blunt fin, f_m is independent of δ_o , at least over the range tested (5:1 variation in thickness);
- 2) f_m is dependent on D , and decreases with increasing D (i.e., increased interaction and separated flow length scale). This result is the same as that observed using cylinders at Mach 5.

The maximum frequencies in the Mach 3 flow do not differ much from those at Mach 5. For the 1.27 cm. fin at Mach 5 and Mach 3, the maximum frequencies are approximately 1.6 kHz and 1.1 kHz, respectively. The higher frequency corresponds to the higher Mach number and freestream velocity, U_∞ . This observation suggested examining the possibility that a Strouhal number might be formed using U_∞ as the normalising velocity. As a first attempt, the length scale selected for normalization was D . Table 2 shows the pertinent parameters used in the calculation of the Strouhal number.

TABLE 2

Case	Mach #	D(cm)	U_∞	f_m (kHz)	fD/U_∞	fL_{sep}/U_∞
1	4.96	1.27	740	1.6	.027	.071
2	4.96	1.90	740	1.2	.031	.075
3	2.95	1.27	590	1.1	.024	.050
4	2.95	2.54	590	0.7	.030	.063

The reasonably good correlation in terms of such simple parameters suggests that they might play a role in, or be related to, the parameters pertinent to the underlying driving mechanisms. Since D controls the length scale of the separated flow, L_{sep} , (defined as the distance from the fin or cylinder leading edge to the primary separation line as indicated by surface tracers), L_{sep} was also used to calculate a Strouhal number. These values are shown in the right-hand column of Table 2. The scatter is somewhat greater than with D suggesting that the geometric parameter is more important than the overall separated flow length scale. It is highly probable that a more physically appropriate velocity would be some average value characteristic of the upstream flow in the primary vortex, rather than the freestream, but this velocity is not known or easily deduced. However, it is likely that it would depend on the freestream velocity and, hence, U_∞ might be a suitable parameter.

Probability density distributions for the shock wave period and power spectral density estimates were also calculated. The results for $\gamma = 0.25$ and 0.5 are shown in Figures 21 and 22, respectively. Cross-correlations could not be computed since all the tests at Mach 3 were made using a single transducer. Neither the probability distributions nor power spectra are as well-resolved as the Mach 5 data (fewer records were taken), but the shapes of the curves and the trends with D are the same. With decreasing D , the probability distributions show the shift towards larger periods and the power spectra show the shift toward lower frequencies.

5. CONCLUDING REMARKS

Wall pressure fluctuations have been measured under the unsteady separation shock wave in interactions induced by circular cylinders in a Mach 5 airflow. The wall temperature condition was adiabatic. A conditional sampling algorithm has been developed to examine the statistics of the shock wave motion. The same algorithm has been used to examine data taken in earlier studies in the Mach 3 blowdown tunnel at Princeton University. In these earlier studies, hemicylindrically blunted fins with different leading-edge diameters were tested in different incoming boundary layers. Initial analysis show that:

- 1) The mean frequency of the shock wave is a function of position in the intermittent region and reaches a maximum at an intermittency of about 50%. These frequencies calculated using the conditional sampling algorithm are supported quantitatively by independent spectral density calculations.
- 2) Probability distributions for the shock wave period are highly skewed at all stations such that the most probable and mean frequencies are different. Although the mean frequency varies with intermittency and hence position, the most probable frequency does not change significantly from station to station.
- 3) The cylinder and blunt fin-induced flows exhibit the same general trends. The mean shock wave frequency is dependent on the cylinder or fin leading-edge diameter, D , and decreases as D increases. For a fin with fixed D , the mean shock frequency is independent of the incoming boundary-layer thickness over the range tested (5:1 variation).
- 4) The maximum mean frequency generated by different diameter cylinders and fins at the two Mach numbers can be correlated reasonably well by forming a Strouhal number using D and

U_∞ as normalising length and velocity scales, respectively. The Strouhal numbers are in the range 0.024 to 0.031. More data over a wider range of conditions is needed to evaluate the validity of this approach and these parameters.

- 5) Initial cross correlations of the conditionally sampled signals for the Mach 5 cylinder flows show that the average upstream and downstream velocities of the shock wave are relatively small (about 20% of the broad-band convection velocity in the incoming turbulent boundary layer). However, before the motions in either direction can be fully characterised, additional cross correlations at other pairs of stations are required.
- 6) The low, mean shock wave frequencies (relative to either the large eddy frequencies or estimated bursting frequency) and the low shock wave velocities (relative to the broad-band convection velocity of the incoming boundary layer) do not support the view that the motion is triggered by turbulence in the incoming boundary layer. Rather, it suggests that the motion is coupled to the lower frequency motion of the downstream separated flow.

ACKNOWLEDGEMENTS

This study was partly supported by (i) AFOSR Grant 86-0112 monitored by Dr. James Wilson and (ii) the Center of Excellence in Hypersonics Training and Research sponsored by NASA, AFOSR and ONR at The University of Texas at Austin.

REFERENCES

1. Bogdonoff, S. M., "Some Experimental Studies of the Separation of Supersonic Turbulent Boundary Layers," Aeronautical Engrg. Dept., Princeton Univ., Report 336, June 1955.
2. Chapman, D. R., D. M. Kuehn and H. K. Larson, "Investigation of Separated Flows in Supersonic and Subsonic Streams with Emphasis on the Effect of Transition," NACA TN 3869, March 1957.
3. Kistler, A. L., "Fluctuating Wall Pressure Under a Separated Supersonic Flow," J. of the Acoustical Soc. of America, 36, March 1964, pp. 543-550.
4. Robertson, J. E., "Characteristics of the Static and Fluctuating-Pressure Environments Induced by Three Dimensional Protuberances at Transonic Mach Numbers," Wyle Laboratories Research Staff Report WR-69-3, June 1969.
5. Speaker, W. V. and C. M. Ailman, "Spectra and Space-Time Correlations of the Fluctuating Pressures at a Wall Beneath a Supersonic Turbulent Boundary Layer Perturbed by Steps and Shock Waves," NASA CR-486, June 1969.
6. Chyu, W. J. and R. D. Hanly, "Power and Cross Spectra and Space-Time Correlations of Surface Fluctuating Pressures at Mach Numbers Between 1.6 and 2.5," NASA TN-D-5440, Sept. 1969.
7. Coe, C. F., W. J. Chyu and J. B. Dods, "Pressure Fluctuations Underlying Attached and Separated Supersonic Turbulent Boundary Layers and Shock Waves," AIAA Paper 73-996, Oct. 1973.
8. Dolling, D. S. and S. M. Bogdonoff, "An Experimental Investigation of the Unsteady Behavior of Blunt Fin-Induced Shock Wave Turbulent Boundary Layer Interactions," AIAA Paper 81-1287, June 1981.
9. Dolling, D. S. and M. T. Murphy, "Unsteadiness of the Separation Shock Wave Structure in a Supersonic Compression Ramp Flowfield," AIAA J., 21, Dec. 1983, pp. 1628-1634.
10. Tran, T. T., D. K. M. Tan and S. M. Bogdonoff, "Surface Pressure Fluctuations in a Three Dimensional Shock Wave/Turbulent Boundary Layer Interaction at Various Shock Strengths," AIAA Paper 85-1562, July 1985.
11. Tan, D. K. M., T. T. Tran and S. M. Bogdonoff, "Surface Pressure Fluctuations in a Three Dimensional Shock Wave Turbulent Boundary Layer Interaction," AIAA Paper 85-0125, Jan. 1985.
12. Dolling, D. S. and C. T. Orr, "Unsteadiness of the Shock Wave Structure in Attached and Separated Compression Ramp Flowfields," Experiments in Fluids, 3, 1985, pp. 24-32.
13. Muck, K. C., J. P. Dussauge and S. M. Bogdonoff, "Structure of the Wall Pressure Fluctuations in a Shock-Induced Separated Turbulent Flow," AIAA Paper 85-0179, Jan. 1985.
14. Andreopoulos, J. and K. C. Muck, "Some New Aspects of the Shock Wave Boundary Layer Interaction in Compression Ramp Flows," AIAA Paper 86-0342, Jan. 1986.
15. Dolling, D. S., "On Upstream Influence in Shock Wave Turbulent Boundary Layer Interaction," Royal Aero. Soc. Jnl., Oct. 1983, pp. 324-327.
16. Dolling, D. S. and S. M. Bogdonoff, "Scaling of Interactions of Cylinders with Supersonic Turbulent Boundary Layers," AIAA Journal, Vol. 19, No. 5, May 1982, pp. 655-657.
17. Raman, K. R., "A Study of Surface Pressure Fluctuations in Hypersonic Turbulent Boundary Layers," NASA CR 2386, Feb. 1974.
18. Narlo, II, J. C., "Experimental Investigation of the Driving Mechanisms of Separation Shock Wave Motion in Interactive Flows," MS Thesis, Aerospace Engineering and Engineering Mechanics Department, The University of Texas at Austin, Dec. 1986.
19. Dolling, D. S. and L. Brusniak, "Evaluation of the Accuracy of Conditional Sampling Methods for Estimating the Mean Frequency of Unsteady Shock Wave Motion," AIAA Journal (submitted; copies available from senior author).
20. Shewe, G., "On the Structure and Resolution of Wall Pressure Fluctuation Associated with Turbulent Boundary Layer Flow," J. of Fluid Mech., Vol. 134, pp. 311-328.
21. Lowson, M. V., "Prediction of Boundary Layer Pressure Fluctuations," AFFDL-TR-67-167, April 1978.
22. Laganelli, A. L., A. Martelluci and L. L. Shaw, "Wall Pressure Fluctuations in Attached Boundary Layer Flow," AIAA Journal, Vol. 21, No. 4, pp. 495-502, April 1983.

23. Roberts, D. R., "Boundary Layer Pressure Fluctuations at High Reynolds Numbers on a Second Free-Flight Test Vehicle," Aeronautical Research Council, ARC CP No. 1302, 1974.
24. Lewis, T. L., J. B. Dods, Jr., and R. D. Hanly, "Measurements of Surface Pressure Fluctuations on the XB-70 Airplane at Local Mach Numbers Up to 2.45," NASA TN D-7226, March 1973.
25. Richards, E. J., M. K. Bull and J. L. Willis, "Boundary Layer Noise Research in the U.S.A. and Canada - A Critical Review," A.R.C. 21, 766, February 1960.
26. Tran, T. T., "An Experimental Investigation of Unsteadiness in Swept Shock Wave/Turbulent Boundary Layer Interactions," Ph.D. Dissertation, Mech. and Aero. Eng. Dept., Princeton Univ., October 1986.
27. Bull, M. K., "Wall Pressure Fluctuations Associated with Subsonic Turbulent Boundary Layer Flow," *J. of Fluid Mechanics*, Vol. 28, part 4, p. 719.
28. Willmarth, W. W. and C. E. Wooldridge, "Measurements of the Fluctuating Pressure at the Wall Beneath a Thick Turbulent Boundary Layer," *J. of Fluid Mechanics*, Vol. 14, p. 187, 1962.

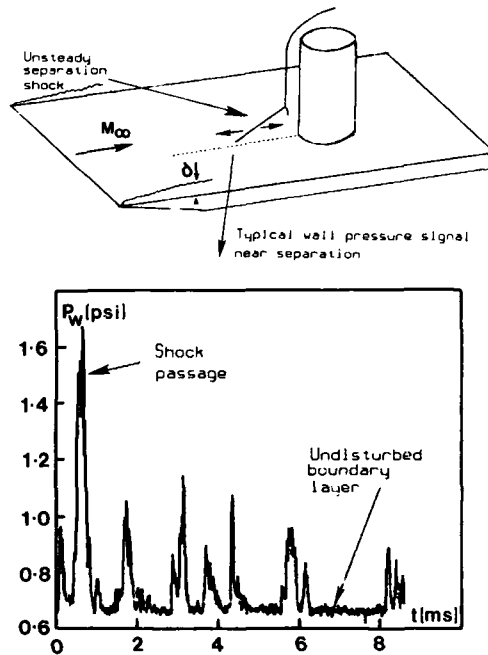


Figure 1 Typical Intermittent Pressure Signal near Separation

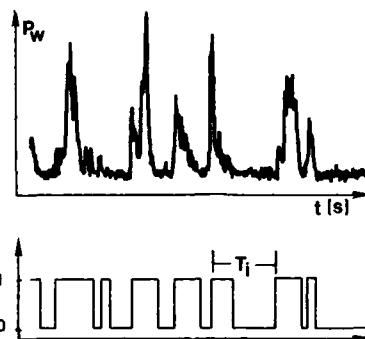


Figure 2 Conversion of Pressure Signal into Box-Car Function

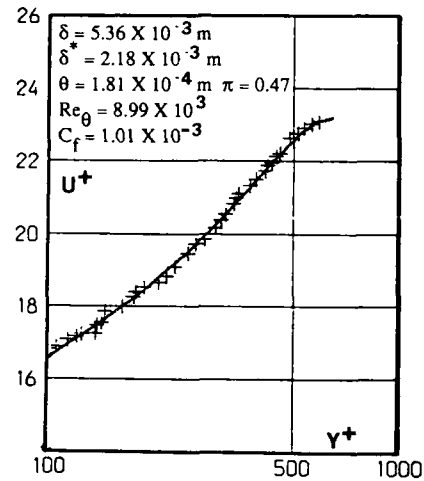


Figure 3 Mean Velocity Profile of Incoming Boundary Layer

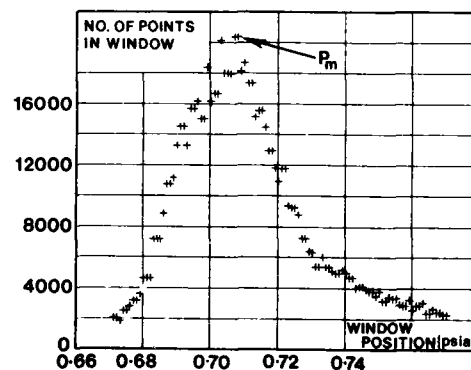


Figure 4 Calculation of Boundary Layer Mean Pressure for Stations in the Intermittent Region

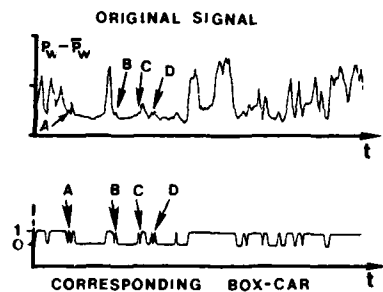


Figure 5 Application of Algorithm of Reference 14 to Pressure Signals

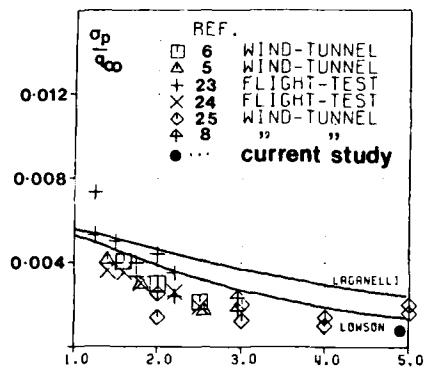


Figure 7 op/q_∞ For Attached Turbulent Boundary Layers as a Function of Mach Number

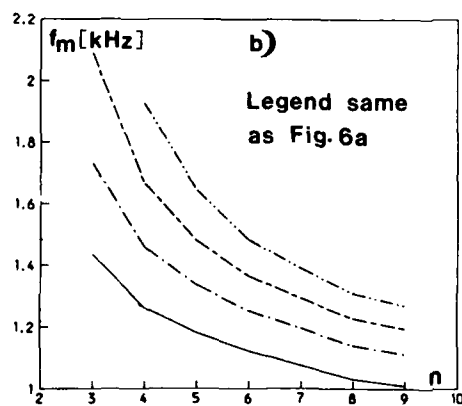
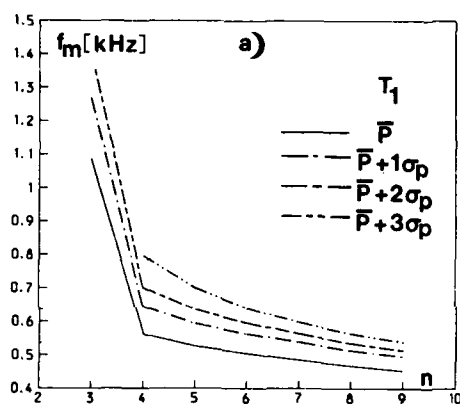


Figure 6 Variation of Shock Wave Mean Frequency with Threshold Settings
a) $\gamma = 0.2$ b) $\gamma = 0.5$

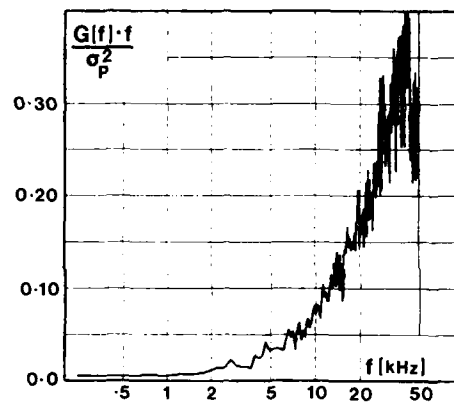


Figure 8 Power Spectrum of Incoming Turbulent Boundary Layer

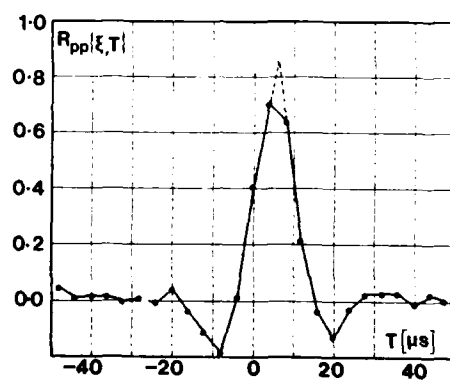


Figure 9 Cross-Correlation of Pressure Signals in Incoming Boundary Layer (transducers streamwise)

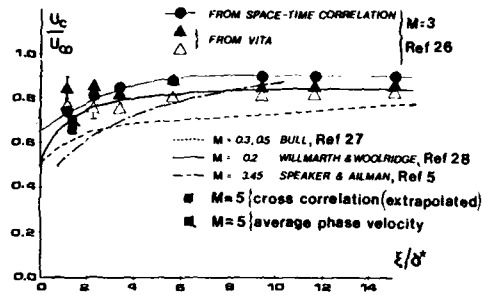


Figure 10 Convection Velocity in Longitudinal Direction (from Ref 26)

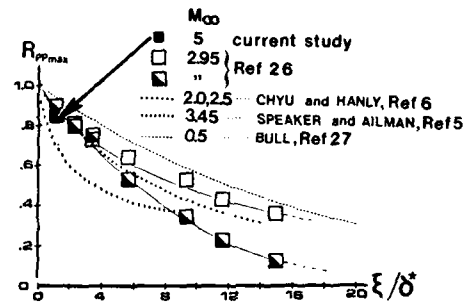


Figure 11 Maximum of Cross Correlation in the Longitudinal Direction (from Ref 26)

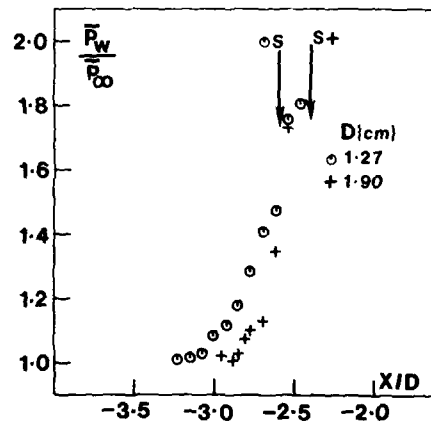


Figure 12 Mean Wall Pressures as a Function of X/D

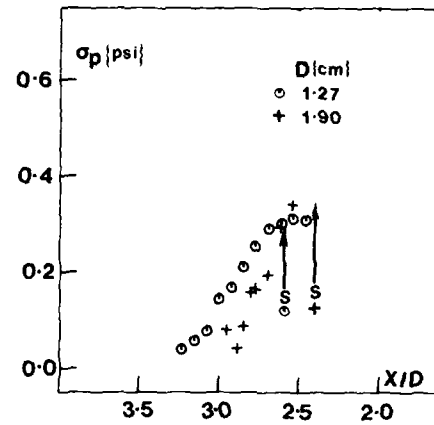


Figure 13 RMS of the Fluctuations as a Function of X/D

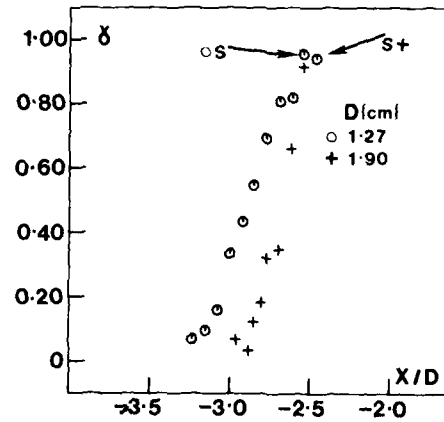


Figure 14 Intermittency as a Function of X/D

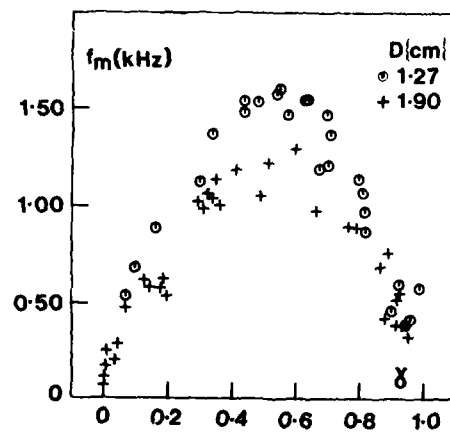


Figure 15 Mean Shock Wave Frequency as a Function of Intermittency (Mach 5)

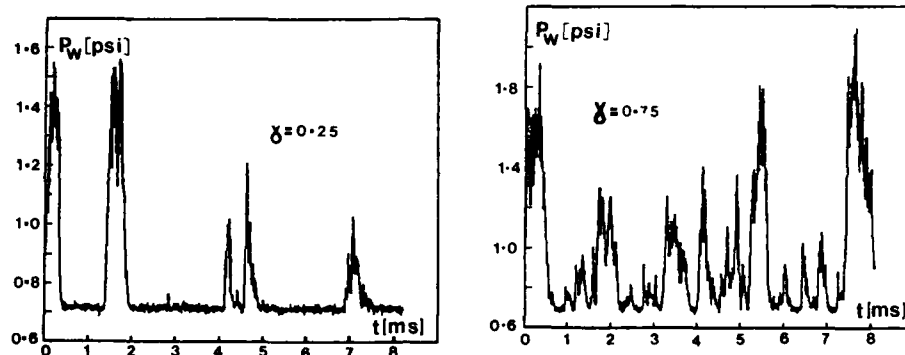


Figure 16 Sample Pressure-Time Histories at $\gamma = 0.25$ and 0.75 (Mach 5)

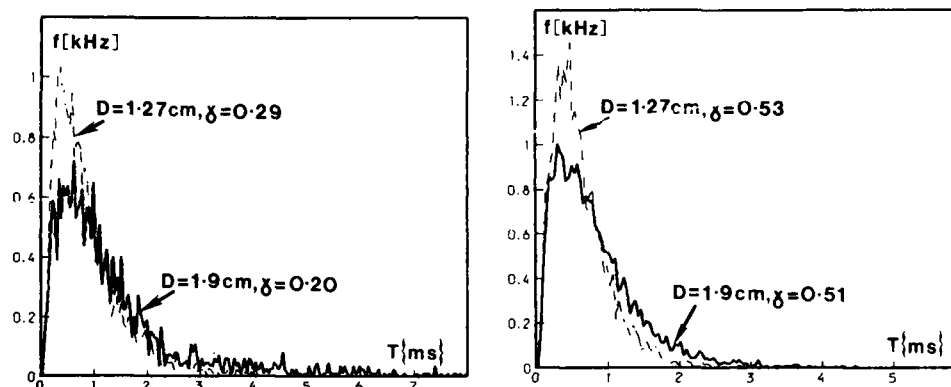


Figure 17 Probability Distribution of Shock Wave Periods (Mach 5)

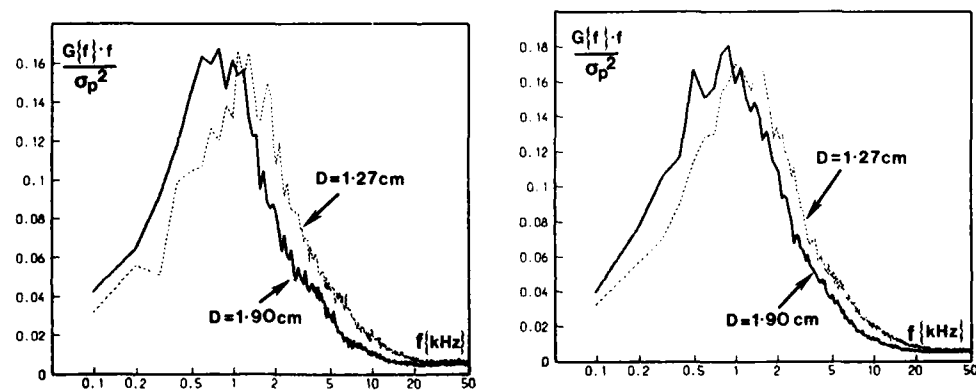


Figure 18 Power Spectral Density of Pressure Signals (Mach 5)

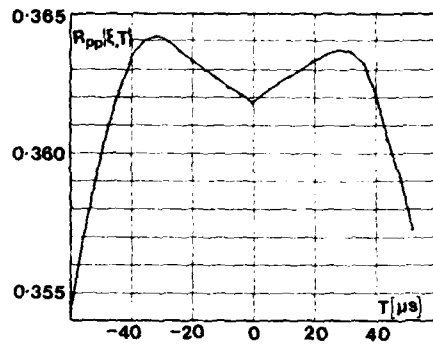


Figure 19 Cross Correlation of Pressure Signals in Intermittent Region (transducer streamwise)

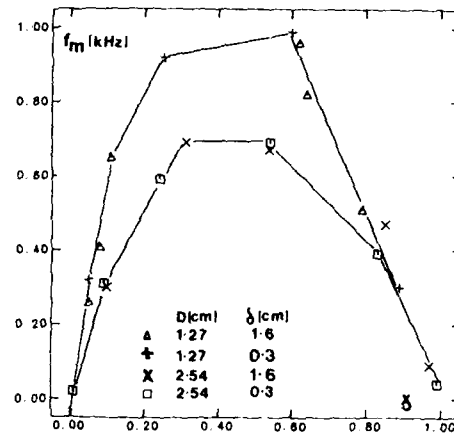


Figure 20 Mean Shock Frequency as a Function of intermittency (Blunt Fins, Mach 3)

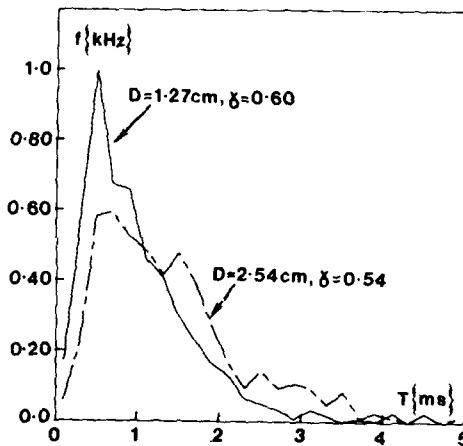
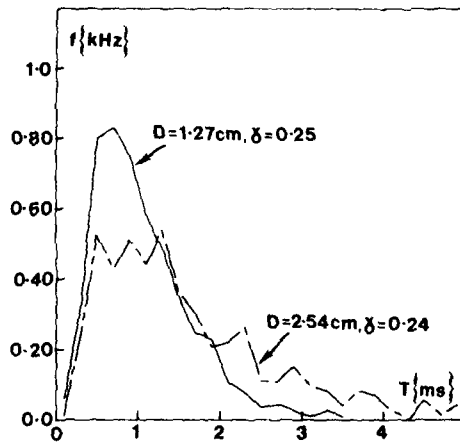


Figure 21 Probability Distributions of Shock Wave Periods (Blunt Fins, Mach 3)

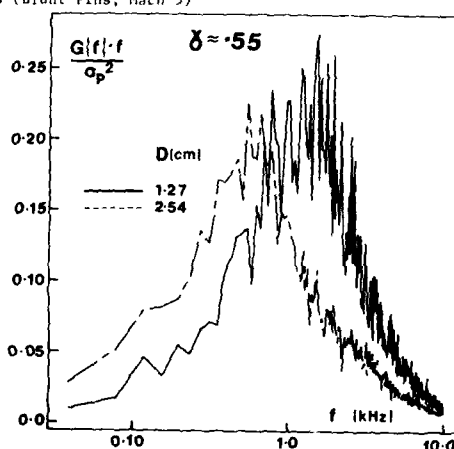
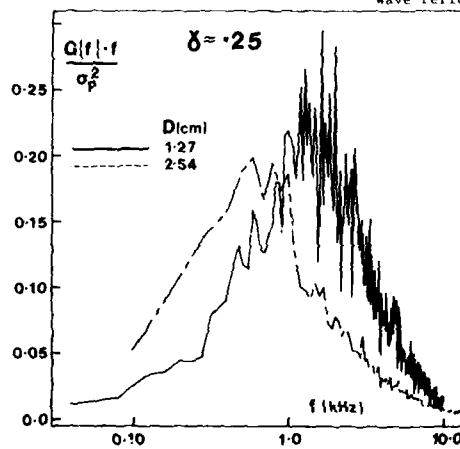


Figure 22 Power Spectral Density of Pressure Signals (Blunt Fins, Mach 3)

THE EFFECTS OF SWEEP AND BLUNTNESS ON A GLANCING SHOCK WAVE TURBULENT BOUNDARY LAYER INTERACTION

by

N.R. Fomison*
College of Aeronautics
Cranfield
Bedford UK
MK43 OAL

J.L. Stollery
College of Aeronautics
Cranfield
Bedford UK
MK43 OAL

SUMMARY

An experimental investigation was conducted into the effects of leading edge sweep and bluntness on the flow characteristics of a glancing shock wave turbulent boundary layer interaction generated by a fin-on-plate configuration. A series of sharp swept fins (covering angles of sweep from 0 to 75°) and a series of blunt unswept fins (ranging in leading edge diameter from 0 to 25.4 mm) were tested at incidences of up to 30° at a Mach number of 2.4 and a freestream Reynolds number of $2.6 \times 10^6 \text{ m}^{-1}$. Observations of the mean flow were made using oil flow visualisation, static pressure measurements, schlieren photography and vapour screen visualisation techniques. In addition, some limited measurements of the unsteady static pressures beneath the interaction were taken. Flow field models are proposed to include the effects of sweep and bluntness and the governing parameters controlling the extent of the disturbed flow and the pressure levels beneath the interaction are examined.

1. INTRODUCTION

Glancing shock wave boundary layer interaction is an important type of three dimensional inviscid/viscous interaction which can frequently have a significant effect on the 'ideal' performance of, for instance, air intakes and control surfaces. It is important for designers of hypersonic vehicles to be able to identify the instances where strong interactions of this type may occur and to determine the region over which the effects associated with the interaction are significant if the vehicle is to be both aerodynamically and structurally efficient. The configurations examined in the present study are illustrated in Figure 1. This investigation represents an extension of the work performed by Kubota¹ on the interaction generated by a sharp unswept fin. Kubota proposed a flow field model to describe the development of the flow with incidence as shown in Figure 2(a). At low incidences, the sidewall flow remains attached and the main features of the flow are a small corner vortex and an induced flow from the fin surface which travels from the high pressure region on the fin towards the low pressure region upstream on the sidewall. These manifest themselves in the surface flow as a separation line on the fin surface and an attachment line on the sidewall surface. For small incidences the induced flow does not present a sufficient obstacle to the oncoming sidewall boundary layer to cause it to separate. However, as the incidence is increased there comes a point at which separation occurs and the flow on the sidewall separates resulting in the flow illustrated in Figure 2(b).

The application of bluntness to the leading edge of an aerodynamic surface as a means of alleviating the stagnation point or attachment line heating rate has been found to have important implications on the magnitude of the interaction generated in the immediate vicinity of the fin or wing root whereas the effect of sweep on the sharp fin interaction has only recently begun to receive attention. It was therefore the aim of the present study to examine the manner in which Kubota's flow field model could be modified to include the effects of sweep and bluntness and to investigate the effects on the overall pressure levels and interaction extent over a broad range of geometric conditions.

2. EXPERIMENTAL ARRANGEMENT

The tests were carried out in the 229 mm x 229 mm working section of the continuous supersonic wind tunnel of the College of Aeronautics. The tunnel is fitted with an interchangeable two-dimensional asymmetric nozzle. Static pressure surveys throughout the test region indicated that the flow Mach number was 2.40 ± 0.05 . The tunnel stagnation pressure is automatically controlled and was maintained at approximately 25.3 kNm^{-2} . Similarly, a watercooling system kept the total temperature at about 293 K resulting in a freestream Reynolds number in the working section of $2.6 \times 10^6 \text{ m}^{-1}$. Under these conditions, the sidewall turbulent boundary layer velocity (99.5%) thickness is 15.2 mm with displacement and momentum thicknesses of 3.8 mm and 1.0 mm respectively. Previous measurements by Kubota have shown that the wall conditions at $M = 2.4$ are very nearly adiabatic.

The two sets of fin models which were employed are shown in Figure 3. (In addition, some tests were also made with the semicones shown.) The models were mounted, with the aid of brackets on their leeward side, to circular inserts on the working section sidewall as illustrated in Figure 4.

* Present address: Hunting Engineering Ltd., Reddings Wood, Amptill, UK

The blunt models were of sufficient height to satisfy the criterion proposed by Dolling and Bogdonoff² for the interaction at the fin root to be unaffected by the finite height of the model. This was confirmed by schlieren photographs of the root flow. For the purpose of the surface oil flow visualisation, the fin and surrounding sidewall were painted matt black to provide high contrast with the mixture of oil and titanium dioxide which was applied. A steady oil flow pattern was produced approximately five minutes after the required working section conditions had been reached. The oil flow studies were used to check that the fin mounting did not influence the flow in the test region.

Static pressure measurements on the sidewall were made using two rotatable pressure tapped sidewall inserts containing up to 220 tappings in a rectangular matrix. Checks made with these inserts failed to show any incidence hysteresis effects in the static pressure footprint of the interactions. The static pressures were measured using a Setra 239 0 - 0.5 psi differential pressure transducer mounted in a Scanivalve Model 9D pressure scanning system. The signal from the transducer, when amplified, was digitised and stored on 5 1/4" floppy discs under the control of a CBM Pet microcomputer.

In order to determine the shape and position of the shock produced by each fin in the absence of any interaction (referred to as the freestream shock location), a conventional single pass schlieren/shadowgraph system was employed together with sting mounted models. In the case of the swept leading edge fins, an appropriate set of delta wing models was constructed and the centreline shock angle determined. The flow field in the neighbourhood of the blunt fin leading edge sidewall junction was also examined using schlieren photography.

3. RESULTS AND DISCUSSION

Effects of Sweep

Firstly the influence of sweep on the interaction surface pressure footprint will be discussed. Figure 5 shows the isobars on the sidewall beneath the interaction for the $\Lambda = 30, 45, 60$ and 75° sweep models at an incidence of 13° . It is apparent that as the sweep is increased so the overall surface pressure level of the interaction falls and the lateral extent of the disturbed flow decreases slightly. The fall in pressure level might be expected because of the reduction in freestream shock angle, as shown in Figure 6, and the reduced compression between the shock and the fin surface. Typical pressure distributions at two stations parallel to the fin are shown in Figure 7(a). In an attempt to collapse these distributions, the asymptotic value which the pressure might be expected to approach at large distances downstream was considered. For any value of Y/b , as defined in Figure 7, as X/b tends to infinity so the pressure approaches the value on the centreline of the corresponding delta wing. These delta wing centreline pressures were estimated using the linearised theories described by Jones³ and Puckett⁴. (It is recognised that linearised theory underestimates the centreline pressures, however its use was justified on the basis of simplicity.) The distributions when nondimensionalised in this way are shown in Figure 7(b). The collapse suggests that the delta wing centreline pressure is a valid scaling parameter for the pressure levels beneath the interaction when the leading edge is swept. It is thought that the use of methods such as thin shock layer theory or that described by Babaev⁵ would result in an even better collapse of the data and a closer prediction of the downstream asymptotic pressures, particularly at higher Mach numbers. (Note however that the overshoot of the limiting value shown in Figure 7(a) at the station close to the fin is due to the influence of the attachment line in this region as shown in Figure 2.) Although more tests are needed to fully confirm this method of scaling, the implication is that if the surface pressure footprint is known for the unswept fin, then the swept fin pressure levels can also be estimated using delta wing theory. Figure 8 shows the alleviating effects of sweep as calculated using the linearised theory. Unfortunately, lack of data prevented the examination of this correlation when applied to peak pressures experienced near the corner attachment line.

Scaling parameters for the extent of the disturbed flow produced by a sharp fin-on-plate configuration have been put forward by Dolling and Bogdonoff⁶ from the tests performed at Princeton University at $M = 2.95$. These are of the form:

$$\frac{L_{UN}}{\delta} \cdot Re_{\delta}^b = f\left(\frac{L_s}{\delta} \cdot Re_{\delta}^b, M_N\right)$$

where	L_{UN}	= upstream influence, see Figure 9
	L_s	= distance along shock, see Figure 9
	Re_{δ}	= Reynolds number based on boundary layer thickness
	M_N	= Mach number normal to shock
	b	= constant, $1/3$
	δ	= boundary layer thickness

The line representing the furthestmost upstream point at which the static pressure is disturbed by the presence of the unswept fin when scaled using the above relationship is shown in Figure 9. Despite the large difference in the freestream Reynolds numbers

of the present tests and those performed by Dolling, the comparison suggests that the expression can be used to scale the interaction on the basis of boundary layer Reynolds number.

The question of the exact manner in which the interaction footprint grows at large distances from the fin has been the subject of much attention. The present experiments tend to suggest that the interaction upstream influence grows in an approximately conical manner with a quasi-two dimensional footprint downstream of the freestream shock location as shown in Figure 10. However the relatively low values, of Y/δ which were attainable probably do not allow the flow to become 'fully developed' (if such a state exists) in the lateral direction. For typical hypersonic vehicles flying at low Reynolds number with consequently very thick boundary layers, this question may, in reality, be of very little consequence.

The method in which the separation of the sidewall flow develops with incidence appears to be qualitatively unaffected by the application of sweep. The development of separation, as observed from the oil flow visualisation, appears to follow a number of stages. These are illustrated in Figure 11 using oil flow photographs of the $\Lambda = 75^\circ$ fin. (In the following description, three-dimensional separation was judged to have occurred if the oil flow streaks on the upstream side of a particular line converge into that line, as discussed by Kubota¹.)

(i) At low incidences a small separated flow region exists around the nose of the fin as shown in Figure 11(a). The ordinary separation line wrapped around the nose of the fin marks a dividing line between the induced flow from the fin surface and the remainder of the sidewall surface flow.

(ii) Further increase in incidence enlarges the lateral extent of the separated region as shown in Figure 11(b). Note, that the separation line is not terminated in a singular point and therefore appears to be an example of an 'open' type separation as discussed by Wang⁷. Ultimately, the separation line extends across the entire test region as illustrated in Figure 11(c). This type of separation growth behaviour demonstrates the complex nature of the flow and indicates the limits of the usefulness of expressions such as that proposed by Korkegi⁸ for the shock pressure ratio necessary to produce incipient separation i.e. even the mean flow separation process must be regarded as a continuous process rather than a single event.

(iii) Also associated with an increase in incidence is the division of the region behind the dividing surface streamline and the fin, into two distinct regions i.e. a region of high surface shear where almost all the applied oil mix has been swept away and a region of relatively low shear sluggish flow immediately downstream of the dividing line. This can be seen in Figure 11(c). The compression region separating the two regions becomes a separation line with an attachment line visible just upstream as the incidence is raised as shown in Figure 11(d). Associated with this development is the appearance of a dip in the static pressure distribution when viewed in the direction normal to the shock as illustrated in Figure 11(d).

The two separation lines present on the sidewall at high incidence can be regarded as being the result of two different processes. The first separation line is produced by the flow induced from the fin surface forcing the sidewall flow off the surface. This induced flow is generated as a consequence of the high pressures recovered in the region of the fin leading edge attachment line and the fin boundary layer induced pressures at zero incidence and at positive incidences by a combination of these and the high pressure on the entire windward surface due to fin deflection.

The second separation line is produced as a result of the difficulty encountered by the secondary flow in passing beneath the shock system in the opposite direction to the freestream flow as shown in Figure 11(c). The location of the secondary separation is very close to the freestream shock location. It is suggested that this might be caused by the higher shear forces experienced by the flow crossing the shock location in the 'reverse' direction once it appears ahead of the main shock structure and encounters flow travelling with almost the freestream flow velocity. This would have the effect of reducing the momentum of the already sluggish reverse flow. Unfortunately, insufficient data was available to determine the necessary conditions for the appearance of the secondary separation line. However it is felt that it would not be wise to attempt to generalise by suggesting that the appearance of the secondary separation line could be linked to certain values of incidence, sweep etc. because of its expected dependence on such factors as boundary layer characteristics (steady and unsteady), shock structure etc. The flow field model proposed for the sharp generator flow field with secondary separation is shown in Figure 12(c). The effect of sweep is to change the rate of development of the flow field shown in Figures 12(a) - 12(c) with incidence i.e. delays each stage of development until a higher incidence. Sweep also has an effect on the flow field in the immediate vicinity of the fin i.e. the introduction of sweep has the effect of moving the attachment line off the fin leading edge. This has a tendency to drive the corner based separation line further into the fin/sidewall junction.

The results of the tests performed with the semicones are shown in Figure 13. These indicate that the semicone which produces the same overall pressure ratio as the sharp unswept fin also produces the surface properties which most closely resemble those of the sharp fin interaction. This tends to support the fact that the overall pressure ratio is the main parameter determining the interaction footprint at any particular Reynolds number rather than purely the shock strength.

Effects of Bluntness

The influence of bluntness on the pressure levels in the zero incidence fin interaction is graphically illustrated by Figure 14 which shows the surface pressures beneath the interaction produced by the $D = 25.4$ mm fin. Note that the disturbance produced by the fin travels approximately $2.5D$ ($\sim 4\delta$) upstream of the leading edge. Clearly the highest static pressures on the sidewall surface (from which highest heating rates can probably be implied based on the work of Winkelmann⁹) occur in the immediate vicinity of the nose. These peak pressures can be associated with flow attachment/reattachment processes inferred from the oil flow studies. A typical oil flow photograph for the $D = 25.4$ mm model is shown in Figure 15. The two separation lines crossing the centreline in front of the fin are easily distinguished. Schlieren photographs taken of the flow on the centreline, such as the one in Figure 16, show that the mean shock structure on the fin centreline is very similar to that found by Kaufman et al.¹⁰ at higher Mach numbers. The origin of the separation shock is very close to the mean position of separation as indicated by the oil flow. The lambda structure is characterised by an Edney Type IV shock/shock interaction (as originally described by Edney¹¹) at the intersection of the bow and separation shocks. Associated with the interaction is a supersonic jet which impinges on the fin leading edge. The cellular shock structure within this jet is visible in Figure 16. The path taken by this jet away from the fin root is an indication of the high pressures in the root region.

The pressure levels experienced on the centreline, as shown in Figure 17, can be approximately estimated using very simple expressions. The semi-empirical two-dimensional analysis of Truitt¹² produces a good estimate of the height of the first peak. This agreement however, must be regarded as rather fortuitous because the theoretical base for Truitt's analysis assumes that the boundary layer remains attached on passing through the front leg of the shock. The second peak pressure is very close to the pressure obtained by stagnating the freestream flow through a single normal shock. Examination of other results suggests that this value represents an upper limit to the steady pressure in this region.

In contrast to the swept fin interaction, the blunt fin interaction in the vicinity of the nose appears to be remarkably insensitive to Mach number and freestream Reynolds number effects as the comparison of the present results with those of Winkelmann⁹ and Saïda and Hattori¹³, demonstrates, Figure 18. This insensitivity, together with the data fitting performed by Truitt, probably explains the close agreement between his prediction and the value of the first peak pressure. A rise in Mach number produces higher pressures along the attachment line A_2 which, by comparison with Winkelmann's results, extends further in the lateral direction at higher Mach numbers. It is thought that this is because the attachment line A_2 is associated with attachment of flow from the freestream rather than flow from the momentum deficient approaching boundary layer. The other major feature of the flow in the region of A_2 is what appears to be a high pressure jet of air, which traces a path from the attachment node on A_2 and into the low pressure region created by the overexpansion of the flow around the fin leading edge. Schlieren photographs, such as Figure 19, of the freestream flow show a compression shock emanating from the fin shoulder, thus providing evidence of this overexpansion.

The use of the leading edge diameter D as a scaling parameter for the vertical and horizontal extent of the interaction has been suggested by several investigators eg: Winkelmann⁹ and Kaufman et al.¹⁰. Figure 20 shows the collapse of the pressure distributions when nondimensionalised in this way. This plot also demonstrates the effect on the pressure footprint of the other characteristic dimensions of the flow i.e. some boundary layer thickness. It seems reasonable to suggest from Figures 18 and 20 that as the parameter D/δ reduces so the pressure levels throughout the interaction decrease and the nondimensional extent of the interaction increases. A similar trend with D/δ is observed at subsonic speeds as shown in the results of Peake and Galway¹⁴. This trend can be explained if it is recognised that as D/δ reduces so the flow approaching a fin of a given diameter exhibits a greater momentum deficit and therefore separates more readily i.e. further upstream. (The present tests at $M = 2.4$ also show an independence of the parameter D/δ for values of $D/\delta \geq 2.0$.)

As was noted to be the case with the sharp fin flow field, the oil flow lines corresponding to the separation lines S_1 and S_2 where they cross the centreline have a limited lateral extent. The extent of the second line S_2 is connected with the disappearance of the pressure dip in the streamwise pressure distribution and occurs typically for $Y/D = 2.5 - 3.5$ (increases with M). This dip can be seen in Figure 14. This suggests that where the mean adverse pressure gradient normal to the separation line necessary for the separation of the reverse flow disappears, then the flow is no longer separated. A flow field model for the flow past the $D = 25.4$ mm model is shown in Figure 21. It is suggested that the fading out of the separation lines S_1 and S_2 is caused by the weakening of the vortices V_1 and V_2 due to viscous diffusion combined with movement of these vortices away from the surface.

For a blunt fin put at incidence, it has been suggested by Dolling¹⁵ that at sufficiently large distances from the fin, the interaction pressure footprint reverts to that produced by a sharp unswept fin at the same incidence. In this respect the interaction flow field behaves in a similar manner to the freestream flow field i.e. the effects of nose bluntness are undetectable at large distances from the fin. Dolling's experiments at $M = 2.95$ suggested that the point at which the footprints match, mirrors very closely the point at which the freestream flows (in particular the shock strength) become indistinguishable. However, the present tests indicate that the influence of the nose bluntness may be felt outboard of this point. A comparison of the sharp fin and the $D = 3.18$ mm fin pressure distributions at an incidence of 13° , Figure 22, shows that even at $Y = 50.8$ mm, where the difference in shock strength (as calculated from the schlieren photographs of the freestream flows) is only approximately 9%, the footprint has not completely reverted to that of the sharp fin. This suggests that at $M = 2.4$, the interaction footprint may not follow the inviscid flow as closely as Dolling found to be the case at $M = 2.95$.

The flow field in the vicinity of the nose i.e. small values of Y/D , changes little as the incidence is raised, as shown in Figure 23. The major change is that the jet on the fin surface shown in Figure 21 becomes weaker. This is probably as a result of the increased pressure levels on the fin surface in relation to the stagnation pressure recovered on A_2 . The development of the oil flow with incidence suggests that the flow field becomes as shown in Figure 24. The secondary separation line S_3 weakens and the flow becomes dominated by the attachment line A_2 . Note, that at low incidence, the nose bluntness is responsible for producing a flow from the sidewall onto the fin surface whereas at higher incidence, this flow is reversed due to the high pressure levels on the fin surface. At incidences outside the present range of study it is expected that a new secondary separation would appear as was observed with the sharp fin, as illustrated in Figure 11(d).

Unsteady Aspects

Measurements of the static pressure fluctuations were made at four locations beneath the interaction generated by a sharp unswept fin at $\alpha = 9^\circ$. These positions are shown in Figure 25(a). Care was taken to mount the Kulite LPS-125-10M differential pressure transducer used for the tests so that its diaphragm was flush (or very slightly below) the surrounding sidewall because of the effect transducer position can have on the RMS level and power spectrum of the measured signal as discussed by Hanly¹⁶. The signal from the transducer was amplified and then recorded on 0.5 ins magnetic tape via a Racal 7M tape recorder. The recorded signals were replayed, digitised and sampled by a Digital Minc minicomputer. Library programs were then used to evaluate the RMS value of the fluctuating signal about the mean as well as the power spectral density of the signal at each location.

The variation of the RMS pressure fluctuation is shown in Figure 25(b). The value at position (I) was unaffected by the presence of the fin and was in reasonable agreement with the estimate obtained using the correlation produced by Laganalli et al¹⁷ for high speed turbulent boundary layers. The highest value occurs in the neighbourhood of the mean position of the separation line and is associated with movement of the separation shock and the unsteady nature of turbulent separation. Although more transducer locations are needed to properly define the peak of this distribution, the maximum measured amplification of 1.5 falls well below the peak values of 12.0 and 8.5 measured by Dolling and Bogdonoff¹⁸ and Dolling and Murphy¹⁹ in blunt fin and two-dimensional swept ramp flows at $M = 2.95$. It is suggested that the sharp fin induced separation is less unsteady than the corresponding separations in blunt fin and ramp flows. In addition, there is also no evidence of intermittency in the pressure-time histories at locations around the mean separation position.

In order to determine whether the increase in the RMS fluctuations around separation could be associated with any particular frequency (i.e. was oscillatory), the power spectra of the pressure signals was obtained. The results indicated that no one dominant frequency is present but that there is an overall increase in the approximate range 3 - 30 kHz.

4. CONCLUSIONS

The flow field model proposed by Kubota¹ has been extended to include higher fin incidences characterised by the appearance of a secondary separation. Associated with the secondary separation is the appearance of a dip in the surface pressure distribution normal to the shock. This model is also applicable to cases where the leading edge is swept back.

The static pressure levels beneath the interaction generated by a sharp swept fin, approximately scale with the pressures experienced on the centreline of the corresponding delta wing at the same incidence. The application of sweep decreases slightly the extent of the disturbed flow field. However, the effect of sweep on the footprint extent when referenced to the freestream shock location, is secondary in comparison to the effect of sweep on the pressure levels. Limited comparisons suggest that existing methods for estimating the effects of Reynolds number (based on boundary layer thickness) on the upstream influence of the interaction produced by an unswept fin, at a particular incidence, are not unreasonable. Fluctuating pressure measurements indicate that the separation induced by a sharp unswept fin is considerably less unsteady than blunt fin induced separation.

A mean flow field model has been put forward for the blunt fin interaction at zero to moderate incidences. Leading edge diameter is found to control the horizontal extent of the flow field even at large distances from the fin. The results indicate that a reduction in the parameter D/δ below approximately 2.0 results in a significant decrease in the interaction surface pressure levels and an increase in the non-dimensionalised (with respect to leading edge diameter) extent of the interaction footprint.

5. ACKNOWLEDGEMENTS

The first author would like to gratefully acknowledge the assistance he received from Hunting Engineering Ltd, Ampthill during the preparation of this paper.

6. REFERENCES

1. Kubota, H. and Stollery, J.L., "An Experimental Study of the Interaction between a Glancing Shock Wave and a Turbulent Boundary Layer" *Journal of Fluid Mechanics*, Vol. 116 p431-458, 1982.
2. Dolling, D.S. and Bogdonoff, S.M., "Scaling of Interactions of Cylinders With Supersonic Turbulent Boundary Layers" *AIAA J.* Vol. 19 p655-657, 1981.
3. Jones, R.T., "Properties of Low Aspect Ratio Pointed Wings at Speeds Below and Above the Speed of Sound" *NASA R-835*, 1946.
4. Puckett, A.E., "Supersonic Wave Drag of Thin Aerofoils" *J. Aero. Sci.* Vol. 13 p475-484, 1946.
5. Babaev, D.A., "Numerical Solution of the Problem of Supersonic Flow Past the Lower Surface of a Delta Wing" *AIAA J.* Vol. 1 p2224-2231, 1963.
6. Dolling, D.S. and Bogdonoff, S.M., "Upstream Influence Scaling of Sharp Fin-induced Shock Wave/Turbulent Boundary Layer Interactions" *AIAA Paper 81-0336*, 1981.
7. Wang, K.C., "Separation Patterns of Boundary Layer Over an Inclined Body of Revolution" *AIAA J.* Vol. 10 p1044-1050, 1972.
8. Korkegi, R.H., "Comparison of Shock Induced Two and Three Dimensional Turbulent Separation" *AIAA J.* Vol. 13 p534, 1975.
9. Winkelmann A.E., "Experimental Investigations of a Fin Protuberance Partially Immersed in a Turbulent Boundary Layer at Mach 5" *NOLTR-72-33*, 1972.
10. Kaufman, L.G. and Korkegi, R.H. and Morton, L.C., "Shock Impingement Caused by Boundary Layer Separation Ahead of Blunt Fins" *AIAA J.* Vol. 11 p1363-1364, 1972.
11. Edney, B., "Anomalous Heat Transfer and Pressure Distributions of Blunt Bodies at Hypersonic Speeds in the Presence of an Impinging Shock" *FFA Report 115*, 1968.
12. Truitt, R.W., "Hypersonic Turbulent Boundary Layer Interference Heat Transfer in Vicinity of Protuberances" *AIAA J.* Vol. 3 p1754-1755, 1965.
13. Saida, N. and Hattori, H., "Shock Wave/Turbulent Boundary Layer Interactions Induced by a Blunt Fin". *Trans. Japan Soc. Aero. Space Sci.*, Vol. 27 p67-77, 1984.
14. Peake, D.T. and Galway, R.D., *NAE Aero, Rept. LR-428*, 1965.
15. Dolling, D.S. and Bogdonoff, S.M., "Blunt Fin-induced Shock Wave/Turbulent Boundary Layer Interaction" *AIAA J.* Vol. 20 p1674-1680, 1982.
16. Hanly, R.D., "Effects of Transducer Flushness On Fluctuating Surface Pressure Measurements" *AIAA Paper 75-534*, 1975.
17. Laganalli, A.L. and Martellucci, A. and Shaw, L., "Prediction of Surface Pressure Fluctuations in Hypersonic Turbulent Boundary Layers" *AIAA Paper 76-409*, 1976.
18. Dolling, D.S. and Bogdonoff, S.M., "An Experimental Investigation of the Unsteady Behaviour of Blunt Fin-induced Shock Wave/Turbulent Boundary Layer Interaction" *AIAA Paper 81-1289*, 1981.
19. Dolling, D.S. and Murphy, M., "Wall Pressure Fluctuations in a Supersonic Separated Compression Ramp Flowfield" *AIAA Paper 82-0986*, 1982.

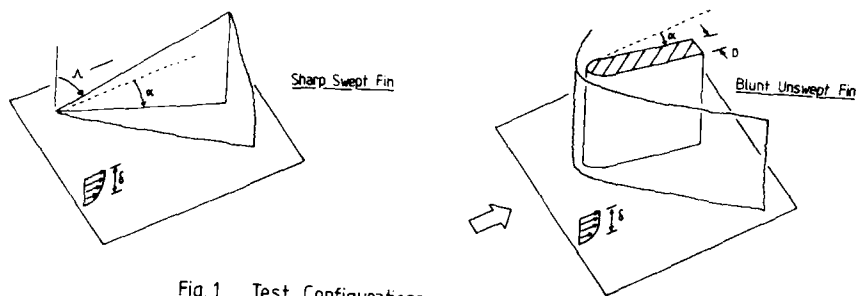


Fig. 1 Test Configurations

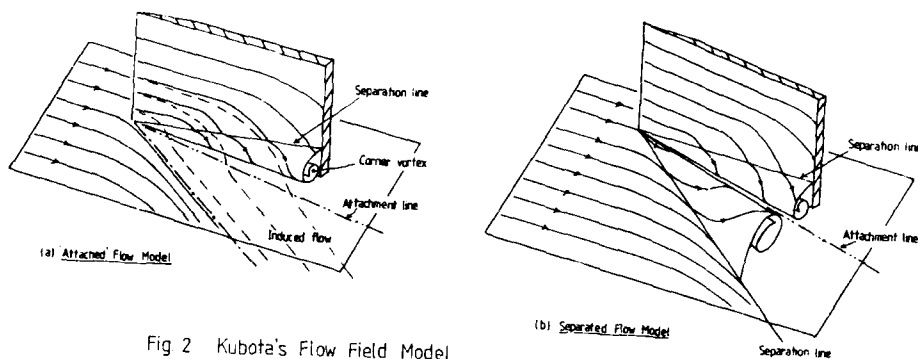
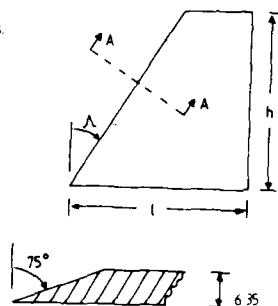


Fig. 2 Kubota's Flow Field Model.

Sidewall Mounted Models.

Λ°	l	h
0	152.4	177.8
30	152.4	177.8
45	152.4	152.4
60	152.4	88.9
75	152.4	42.4

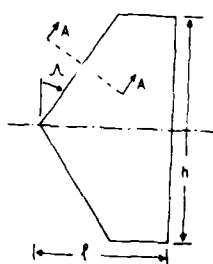
Section A-A
(normal to l.e.)



SHARP LEADING EDGE MODELS.

Sting Mounted Models.

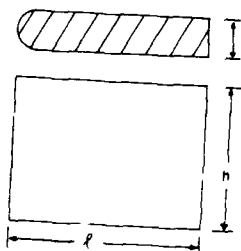
Λ°	l	h
0	152.4	177.8
30	127.0	177.8
45	152.4	152.4
60	152.4	175.3
75	152.4	81.3



Sidewall and Sting Mounted Models.

D	l	h
3.2	152.4	152.4
6.4	152.4	152.4
9.5	152.4	127.0
12.7	152.4	114.3
19.1	127.0	88.9
25.4	127.0	88.9

BLUNT LEADING EDGE MODELS.



Sidewall Mounted Semicone Models.

Λ°	l
11	152.4
17.5	127.0
21	127.0

Section B-B

All dimensions in mm

Fig. 3 Wind Tunnel Models.

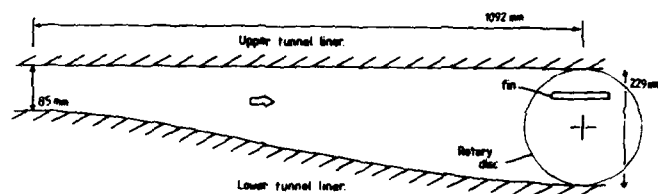
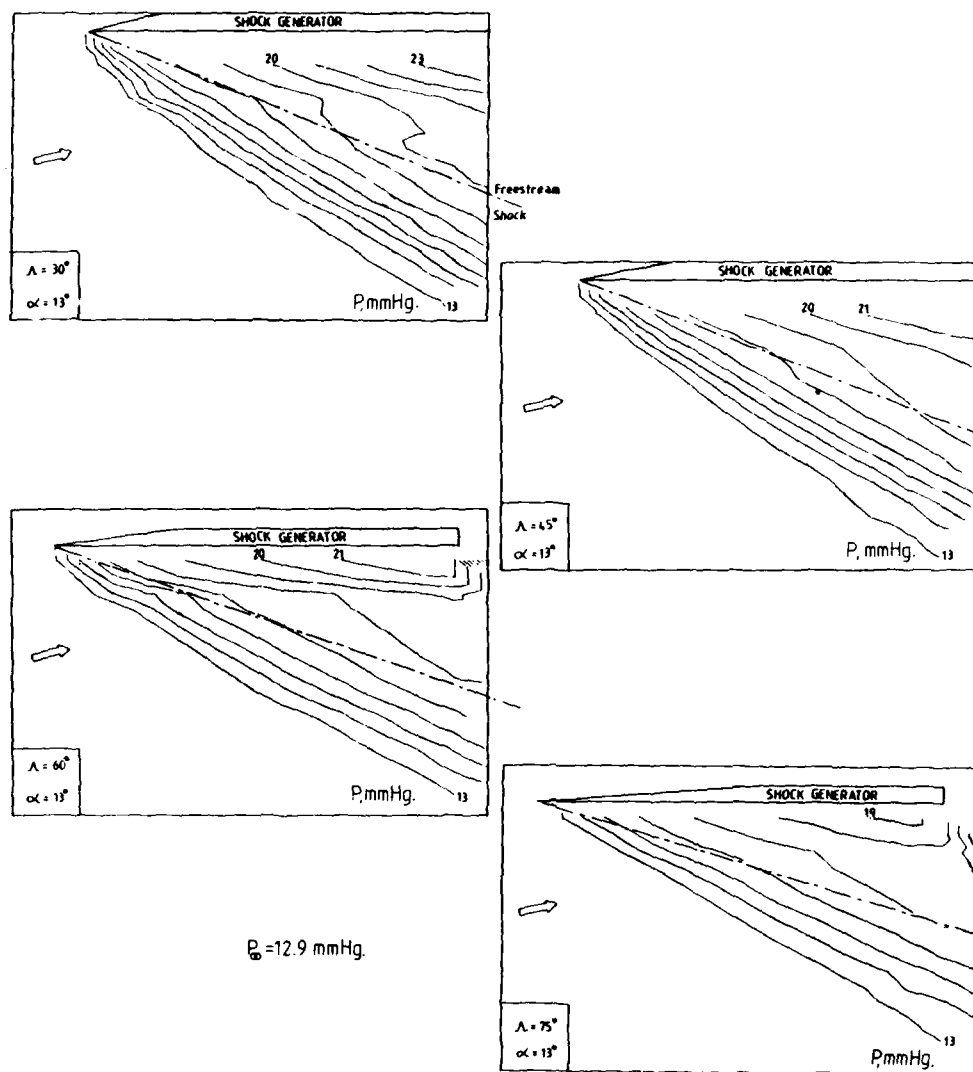


Fig. 4 Test Configuration.

Fig. 5 Sidewall Isobar Plots $\Lambda = 30, 45, 60$ and 75° , $\alpha = 13^\circ$

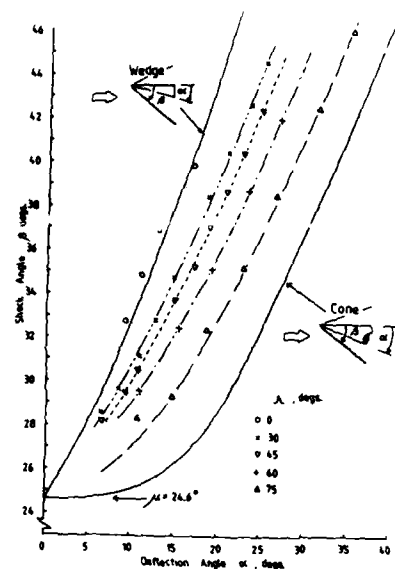
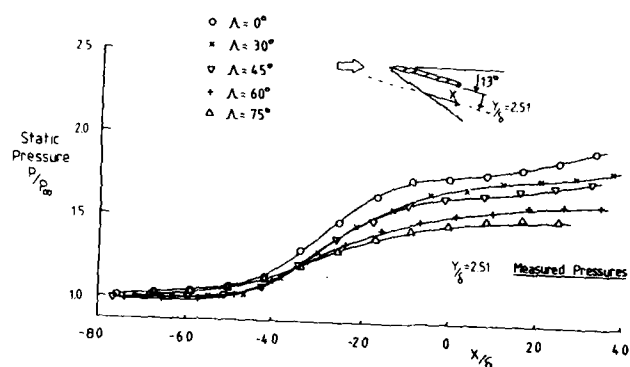
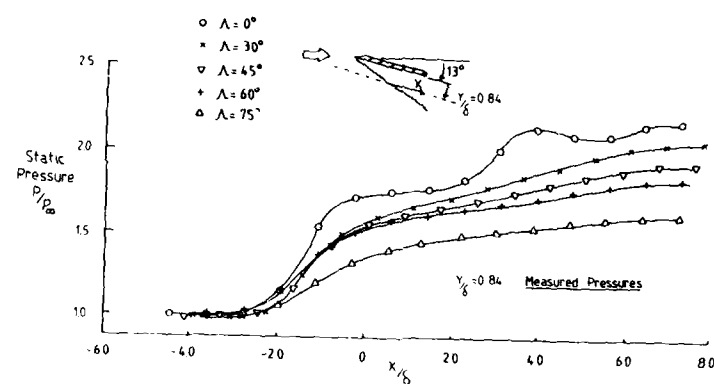
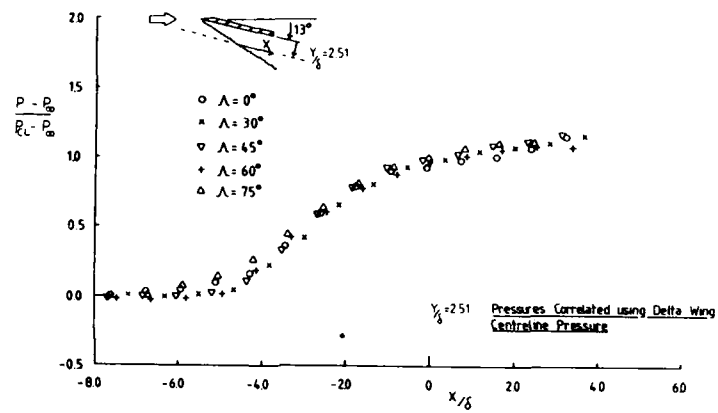
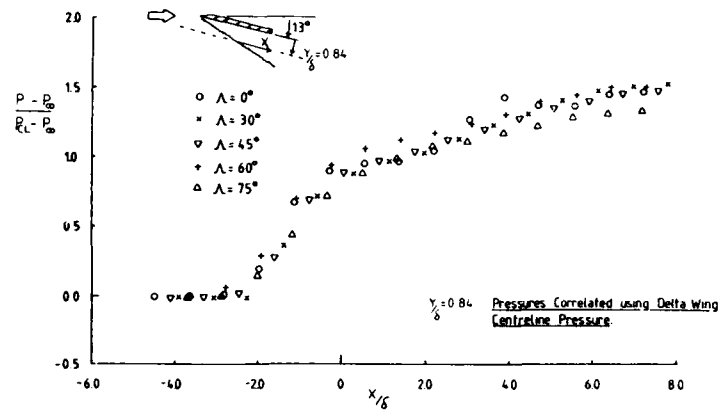


Fig. 6 Delta Wing Centreline Shock Wave Angles



(a)

Fig. 7 Sharp Fin Sidewall Static Pressure Distribution, $\alpha = 13^\circ$



(b)

Fig.7 Cont'd.

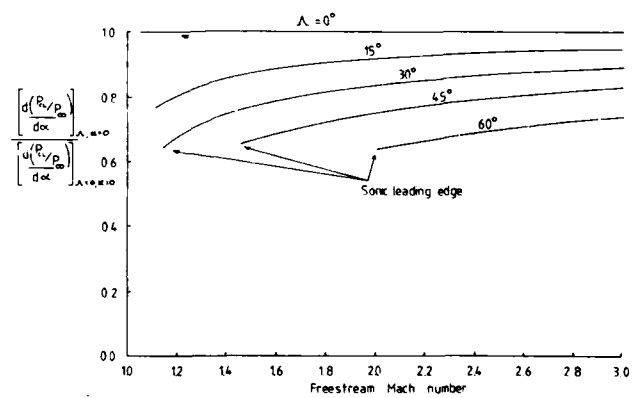


Fig.8 Effect of Sweep on Delta Wing Centreline Pressure.

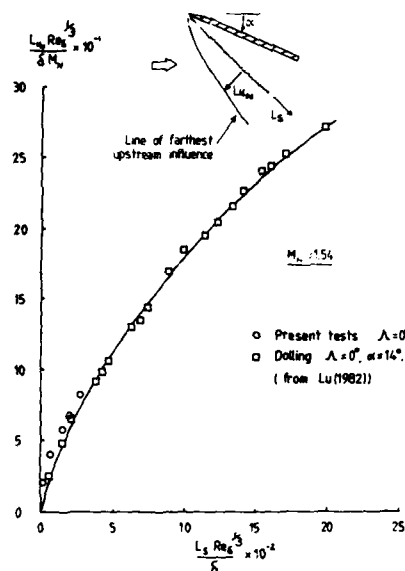


Fig. 9 Reynolds Number Scaling of Upstream Influence.

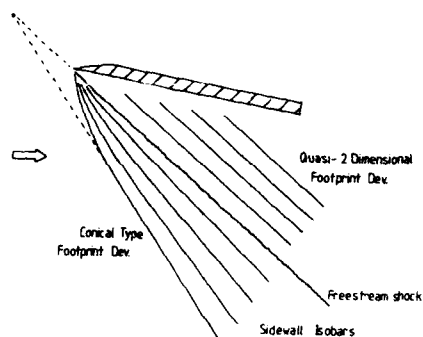
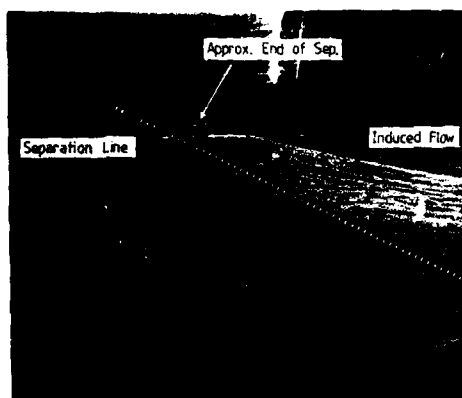
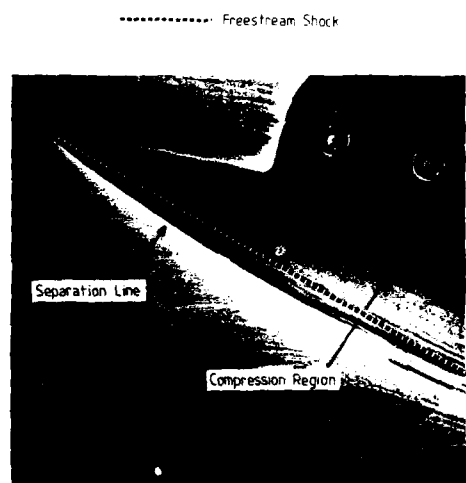


Fig.10 Interaction Footprint Development.

(a) $\alpha = 5^\circ$ (b) $\alpha = 13^\circ$ Fig.11 Oil Flow Visualisation, $\Lambda = 75^\circ$

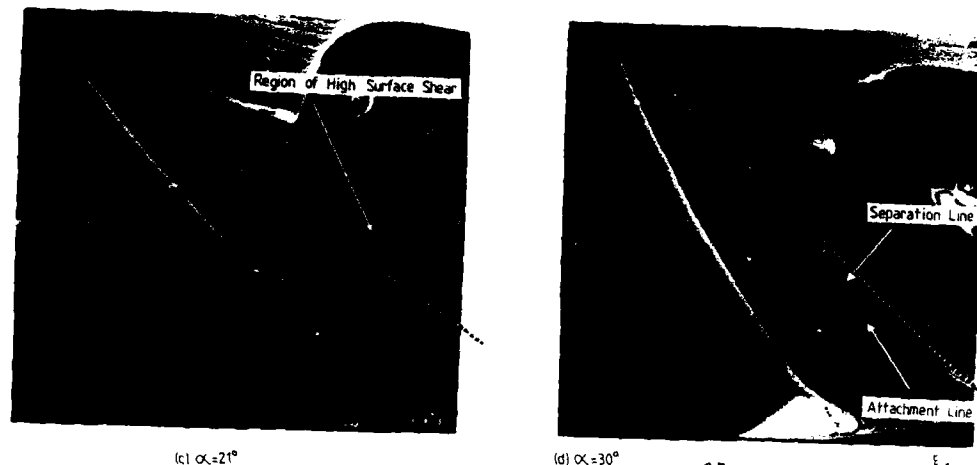
(c) $\alpha = 21^\circ$ (d) $\alpha = 30^\circ$

Fig. 11 Cont'd.

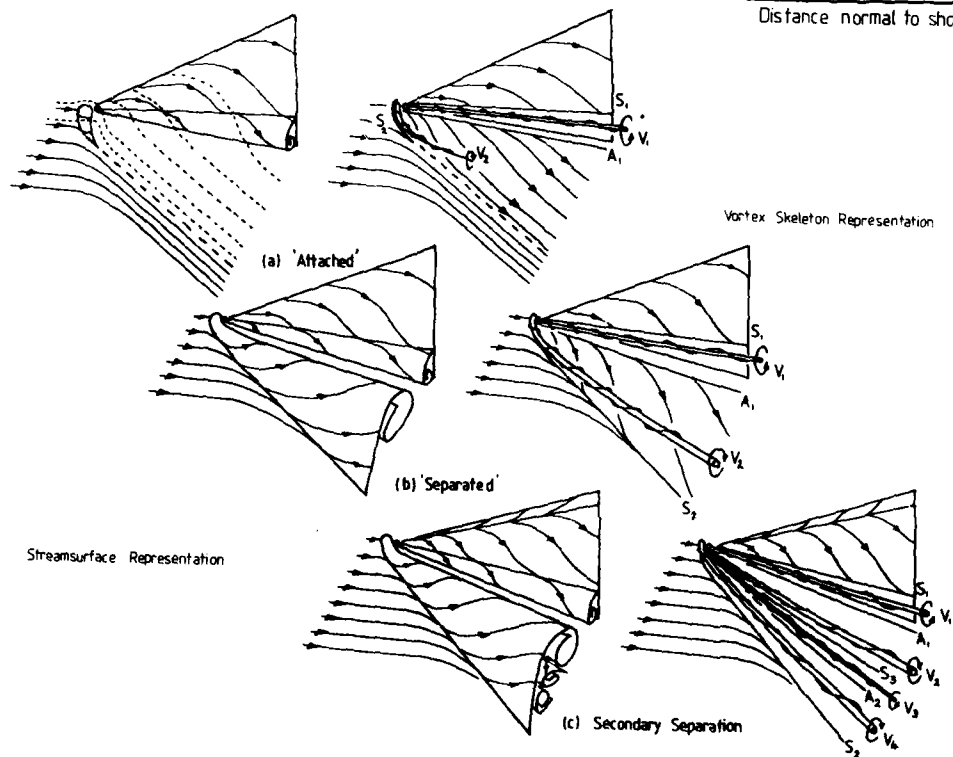
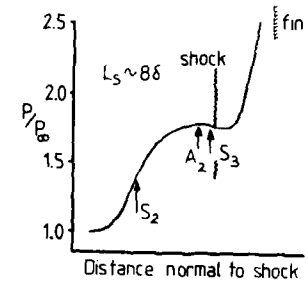


Fig. 12 Sharp Fin Flow Field Model.

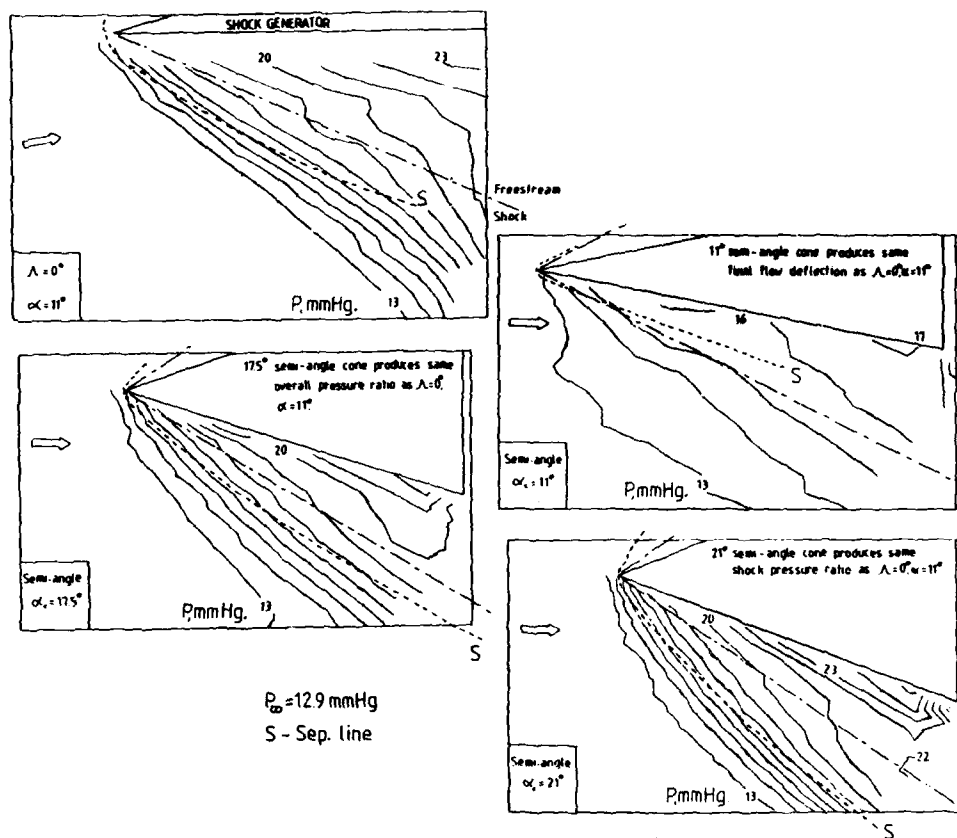


Fig.13 Sidewall Isobar Plots for Semi-cones and Unswept Fin.

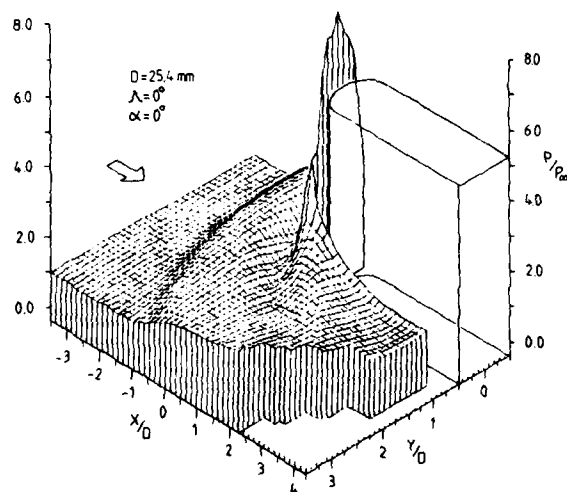


Fig. 14 Static Pressure Distribution on Sidewall.

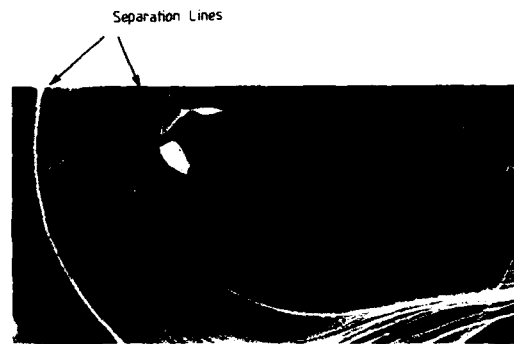


Fig.15 Oil Flow Visualisation,
 $D=25.4\text{ mm}$, $\alpha=2^\circ$

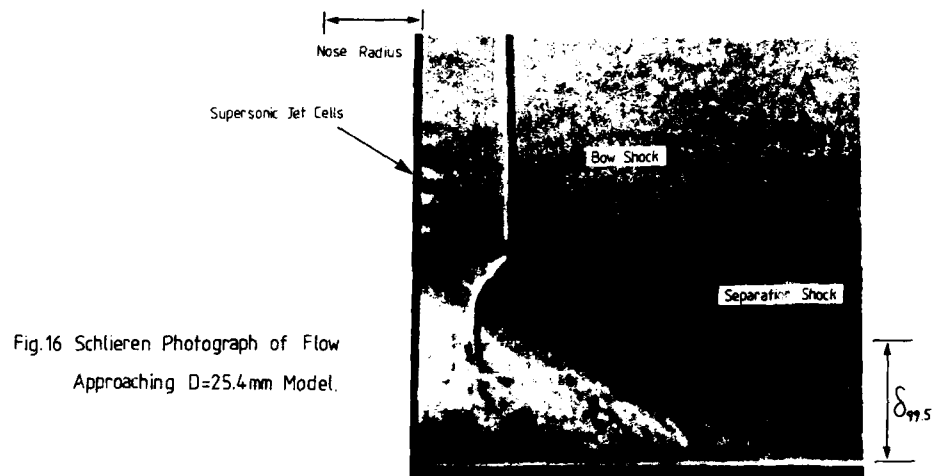


Fig.16 Schlieren Photograph of Flow
 Approaching $D=25.4\text{ mm}$ Model.

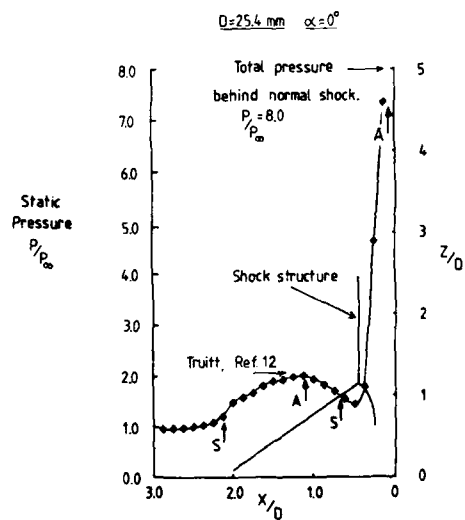


Fig.17 Centreline Pressure Distribution.

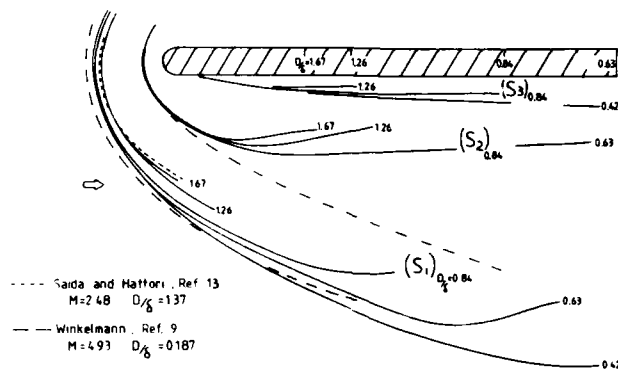
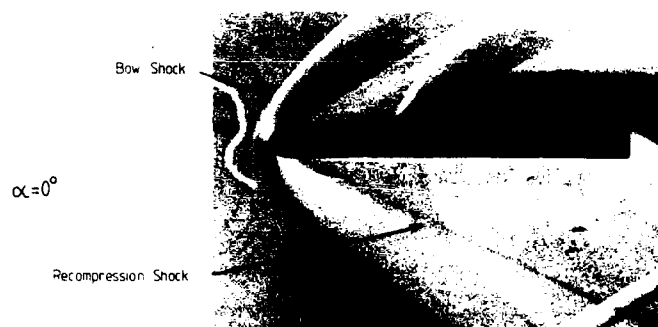
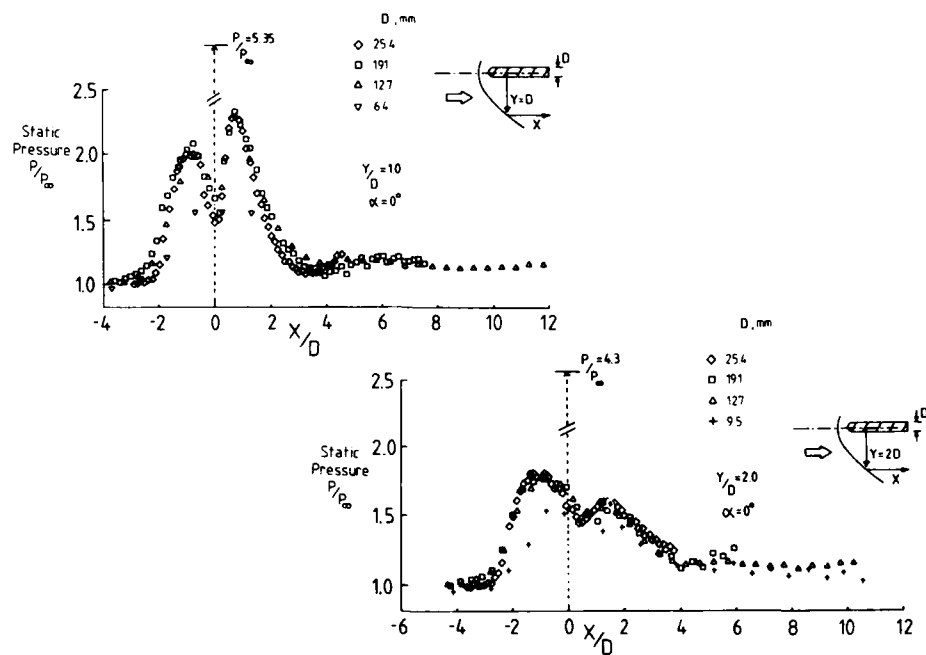
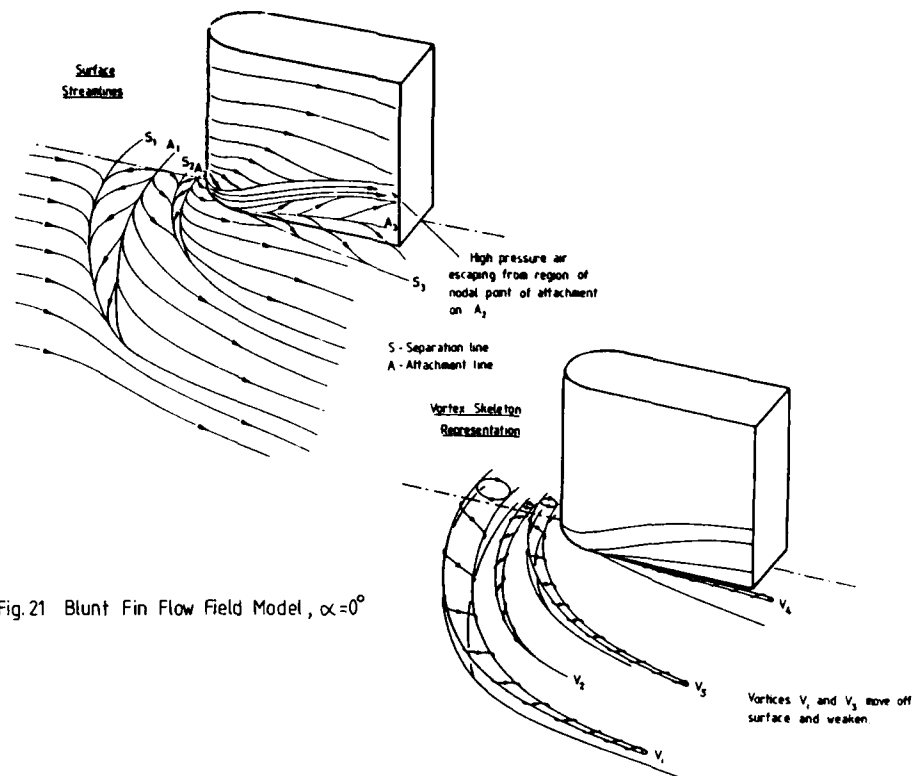
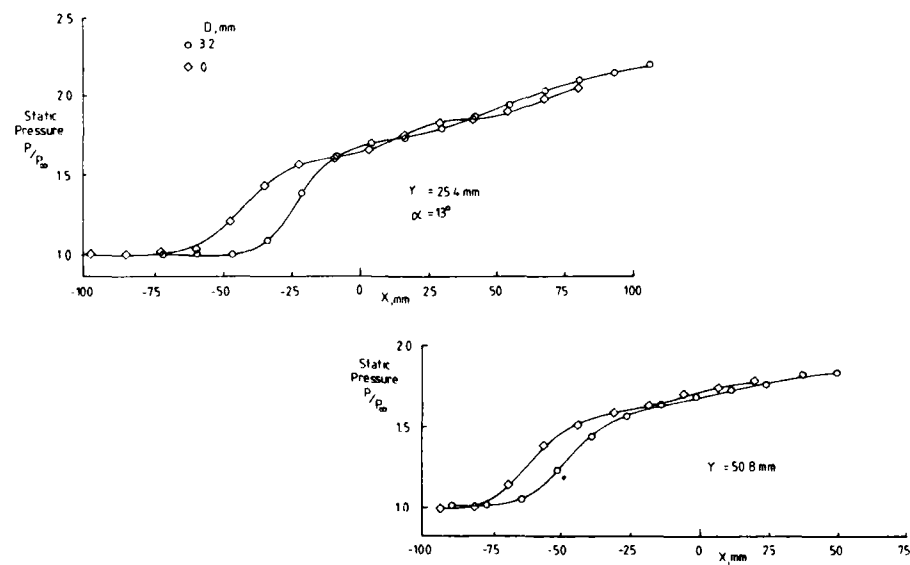
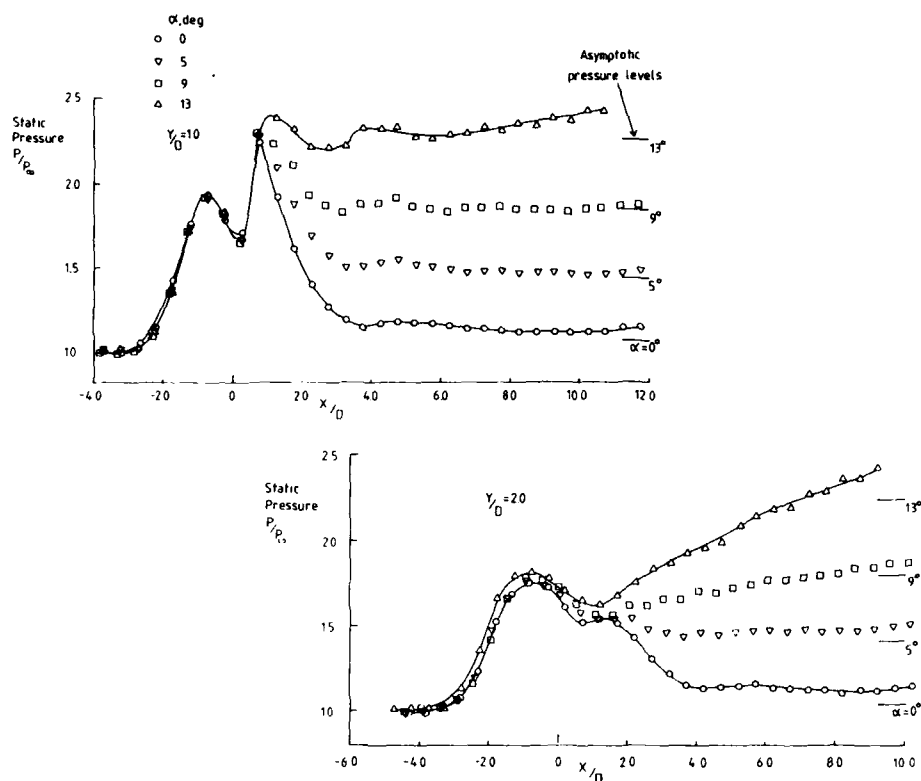
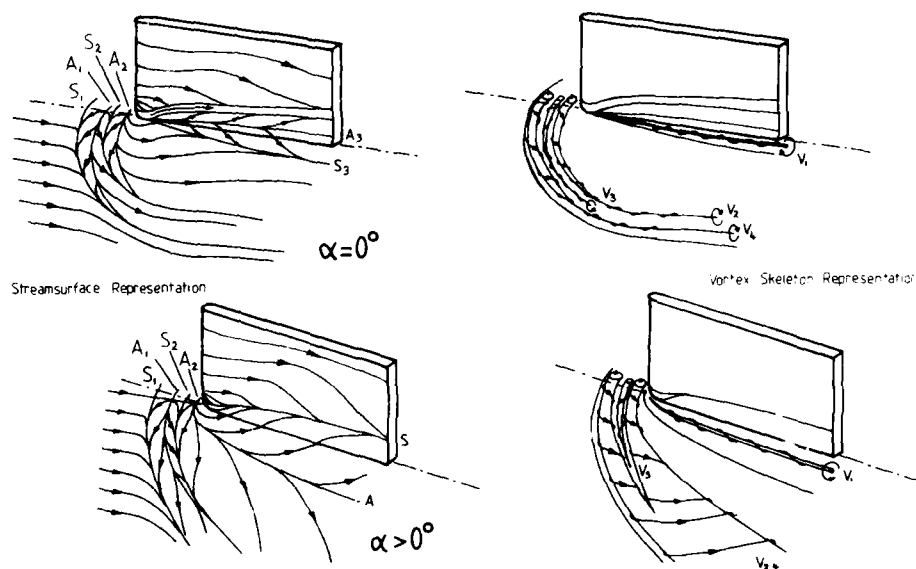


Fig. 18 Position of Separation Lines at Zero Incidence.

Fig. 19 Schlieren Photograph of Flow Past Sting Mounted $D=127\text{mm}$ ModelFig. 20 Collapse of Static Pressure Distributions, $\alpha=0^\circ$

Fig. 21 Blunt Fin Flow Field Model, $\alpha = 0^\circ$ Fig. 22 Comparison of $D=0$ and $D=32$ mm Pressure Distributions.

Fig. 23 Effect of Incidence on $D=12.7 \text{ mm}$ Pressure DistributionFig. 24 Blunt Fin Flow Field Model $\alpha > 0^\circ$

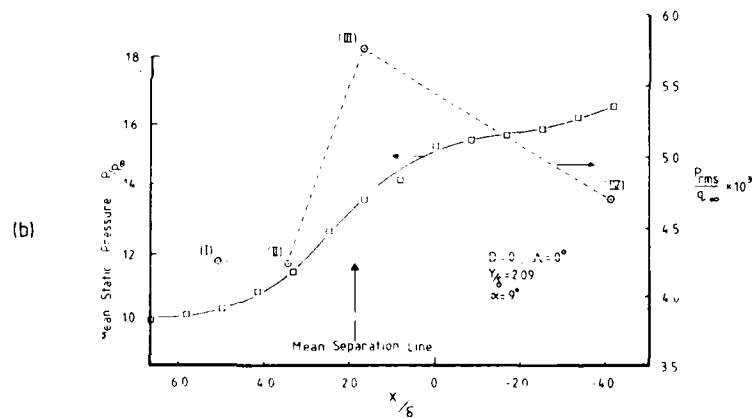
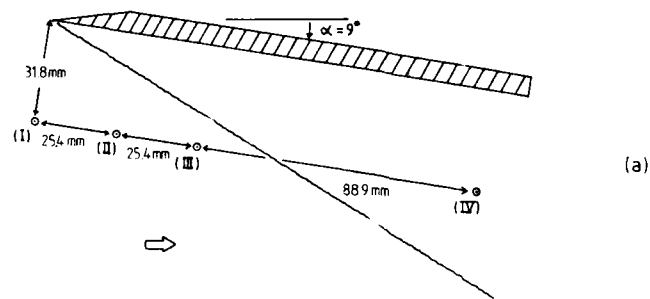


Fig. 24 Transducer Positions and R.M.S. Pressure Fluctuation Distribution.

UNE METHODE CINEMATOGRAFIQUE ULTRA-RAPIDE POUR L'ETUDE
DES SILLAGES EN TUNNEL DE TIR HYPERSONIQUE

by
Axel KÖNEKE, Bernard Charles JAEGGY, Germain KOFRER
Département d'Aérodynamique
INSTITUT FRANCO-ALLEMAND DE RECHERCHES DE SAINT-LOUIS (ISL)
12, rue de l'Industrie
Saint-Louis
68301
France

RESUME

L'utilisation de méthodes optiques est l'une des seules possibilités d'étude des sillages hypersoniques en tunnel de tir. En raison de la vitesse des écoulements, les méthodes utilisées doivent permettre des temps de pose nettement inférieurs à la microseconde. L'ISL utilise depuis longtemps des techniques de visualisation ultra-rapide pour l'étude de la transition dans les sillages hypersoniques, mais les moyens disponibles jusqu'ici ne permettaient pas de suivre dans le temps les instabilités du sillage laminaire.

Nous proposons ici d'utiliser un laser associé à un modulateur acousto-optique comme source de lumière ultra courte, à haute énergie et à grande fréquence de répétition, pour permettre l'enregistrement d'un certain nombre d'images du même phénomène en vue d'étudier l'évolution au cours du temps des instabilités. Les avantages de cette source lumineuse sont une grande énergie, des impulsions de 20 ns seulement, une fréquence de répétition variant indépendamment de la durée des impulsions et une synchronisation aisée avec des événements extérieurs. Le laser constitue une source ponctuelle qui peut être utilisée pour plusieurs montages optiques différents et sa nature cohérente permet d'envisager l'emploi de l'holographie. Le système de réception capable d'enregistrer les images obtenues avec une vitesse suffisante constitue le principal problème de la mise au point de la méthode.

ABSTRACT

Optical methods are among the only possibilities to study hypersonic wakes in ballistic ranges. Because of the flow velocities involved the methods employed must permit exposure times well below one microsecond. The ISL has been using ultra-high-speed visualization techniques for the study of the transition of hypersonic wakes for quite some time, but the means available up to now did not permit to investigate the time-history of the instabilities in the wake.

We are proposing the use of a laser equipped with an acousto-optical modulator as a source of ultra short, highly energetic pulses with high repetition rate to be used to record a certain number of images of the same experiment in order to study the time history of these instabilities. Advantages of the laser as a light source are not only the high energies available together with pulse durations down to 20 nanoseconds, but mostly the free choice of repetition rate independently of exposure time, and the possibility to synchronize the pulses with external events. The laser is a point source and as such can be used in a variety of different optical setups. The coherent nature of the laser light even permits holographic techniques. The reception system capable of recording the images at a sufficient rate is the basic problem in the development and use of the proposed setup.

1. INTRODUCTION

L'aérodynamique hypersonique a été l'un des thèmes majeurs sur lesquels a travaillé l'ISL de 1960 à 1975 et l'établissement s'était doté pour ce faire de moyens d'essais relativement importants, d'une certaine originalité, et pour lesquels a été développé un grand nombre de moyens de mesure d'usage assez peu courant ou même tout à fait nouveaux [1].

Les problèmes qui ont été traités concernaient surtout les problèmes de rentrée dans l'atmosphère de têtes d'engins balistiques et plus particulièrement les deux points suivants :

- l'étude de l'échauffement cinétique et des flux de chaleur, surtout effectuée dans une soufflerie à chocs dont les caractéristiques sont rappelées en [2];
- l'étude des sillages, effectuée au tunnel de tir hypersonique.

Malgré les différences des installations et des sujets traités, un certain nombre de problèmes métrologiques communs ont été rencontrés. En effet, les temps de rafales de la soufflerie à choc sont brefs (de l'ordre de 10^{-4} s), bien que nettement supérieurs aux temps dont on dispose pour les mesures au tunnel de tir hypersonique (au maximum de 10^{-5} s). Mais cela nécessite dans les deux cas l'emploi de méthodes relevant de la physique des temps courts, autre domaine dans lequel l'ISL avait acquis une grande expérience par le moyen d'études relevant de la détonique ou de la propagation des ondes de choc.

Parmi les méthodes qui ont été utilisées figurent évidemment les méthodes de visualisation ultra-rapide. Celles-ci avaient notamment été utilisées pour l'étude de la transition laminaire/turbulent dans un sillage hypersonique, mais cette étude était restée sommaire du fait des limitations des moyens disponibles à l'époque, lesquels ne permettaient pas l'étude du développement des instabilités du sillage laminaire.

Les progrès récents de l'optoélectronique permettent d'aborder aujourd'hui cette étude.

On trouvera successivement dans ce qui suit :

- un rappel des résultats obtenus autrefois, précédé, pour en faciliter la compréhension, par une brève présentation générale et une courte description des moyens d'essais utilisés;

- un examen des possibilités nouvelles offertes par les techniques actuellement disponibles;
- des exemples des premiers résultats obtenus.

2. Etude des sillages hypersoniques

2.1 Motivations de l'étude

Le sillage que laisse derrière lui un engin pénétrant dans l'atmosphère est ionisé et constitue donc un moyen de détection de cet engin. Cette détection peut être soit passive (écoute de l'émission propre du sillage), soit active (écoute du retour d'une onde émise du sol). On peut ainsi suivre la trajectoire d'un engin alors qu'il n'est lui-même pas détectable ou que la communication avec lui n'est pas possible. Théoriquement, la détection est possible dans tout le spectre électromagnétique (radioélectrique, infrarouge, visible, ultraviolet), mais les études de l'ISL ont surtout porté sur la détection active dans la gamme des fréquences radioélectriques ("écho radar") [3]. Dans le cadre de cette étude, l'ISL a mis au point diverses méthodes de mesure de l'ionisation d'un sillage en laboratoire : cavité résonante, interféromètres hyperfréquences, sondes de Langmuir [4]. Du point de vue aérodynamique, l'ionisation du sillage et son évolution en fonction de la distance à l'engin sont gouvernées par différents paramètres liés aux conditions de vol et à la géométrie et aux dimensions de l'objet. Ces paramètres déterminent la nature du sillage qui joue un rôle essentiel. En effet, la décroissance de la densité électronique est bien plus rapide dans un sillage turbulent où il y a mélange avec un écoulement extérieur plus froid que dans un sillage laminaire. L'étude de la transition de l'écoulement laminaire à l'écoulement turbulent dans le sillage a donc constitué un des aspects essentiels de l'ensemble de l'étude et c'est le seul dont il sera question ici. On trouvera en [5] une présentation plus générale de l'ensemble.

2.2 Moyens d'essais

Etant donné le problème posé, l'emploi du tunnel de tir de préférence à la soufflerie s'imposait en raison de :

- la nécessité de faire varier la pression dans les limites rencontrées dans la haute atmosphère (de 1 à 100 mmHg environ) et de réaliser les essais dans un milieu ayant strictement la composition chimique de l'air en équilibre,
- la vitesse à reproduire, de l'ordre de plusieurs km/s, correspondant à des nombres de Mach très élevés (de 10 à 25),
- la nécessité d'éviter tout support de maquette susceptible d'entraîner une perturbation du sillage et du besoin de pouvoir observer le phénomène loin à l'aval de la maquette.

Les essais ont donc été effectués dans le tunnel de tir hypersonique du département d'aérodynamique de l'ISL. Ce tunnel est équipé de deux canons à gaz léger (hydrogène, mais l'hélium a aussi été utilisé) dont la figure 1 précise les caractéristiques*). Les vitesses maximales atteintes ont été de 8,5 km/s pour le canon de 20 mm et de 9,1 km/s pour le canon de 10 mm. La figure 2 donne une photographie de ces canons et la figure 3 une photographie du tunnel de tir proprement dit. Celui-ci comporte une chambre de détente destinée à freiner les gaz de bouche du canon, un diaphragme (pièce métallique percée d'un trou et destinée à arrêter les "sabots" ayant servi à guider les projectiles non cylindriques dans le tube de lancement) et un certain nombre d'éléments variables en fonction des essais à réaliser. La figure 4 donne une configuration typique du tunnel de tir tel qu'il était équipé pour l'étude des sillages hypersoniques. La radiographie-éclair servait à vérifier le bon détachement des sabots. Les deux postes ombroscopiques étaient utilisés pour la mesure de la vitesse du projectile (d'autres postes doivent être ajoutés lorsqu'il faut tenir compte de la décélération du projectile), le spectromètre de masse a servi à une tentative d'étude de la composition chimique du sillage [8] et l'étude des caractéristiques électroniques du sillage était faite dans l'élément terminal de grand diamètre. Les deux postes strioscopiques étaient utilisés pour la visualisation du sillage et l'étude de la transition.

2.3 Visualisations par strioscopies

L'étude de la transition a essentiellement été faite par examen visuel des photographies du sillage obtenues par strioscopies. Cet examen a conduit à l'adoption du critère de transition de Zeiberg [9] pour les sillages de sphères [10] et à celui du critère de transition de Waldbusser [11, 12] pour les sillages de cônes faiblement émoussés [13, 14].

On a également utilisé plusieurs variantes d'un montage dans lequel un faisceau laser traverse l'écoulement avant d'être reçu sur un photomultiplicateur. Le signal reçu dépend des variations de l'indice de réfraction intégré le long du chemin optique et présente un aspect très différent suivant que l'écoulement est laminaire ou turbulent [15, 16].

L'étude a été faite pour des vitesses de 3500 à 6500 m/s, des maquettes de faibles dimensions (ca-libre maximal : 20 mm) et de faibles pressions dans le tunnel de tir (de 2 à 100 mmHg). Dans ces conditions, de très faibles temps de pose (à 5 km/s, le projectile parcourt 5 mm par μ s) et de très fortes intensités lumineuses étaient nécessaires. Pour les obtenir, l'ISL avait construit des flashes ayant les caractéristiques suivantes :

- énergie électrique : 0,7 joule,
- durée d'émission à mi-hauteur : 150 à 200 ns,
- dimensions du canal lumineux : 4 mm \times 1 mm.

Ces flashes équipaient des postes strioscopiques à double passage dont la figure 5 donne le schéma. La plupart des visualisations ont été effectuées en utilisant des miroirs sphériques de rayon de courbure

*) Les caractéristiques données correspondent à l'état actuel de l'installation. Du fait des modifications intervenues depuis la mise en service du petit canon en 1961 [7] et celle du grand canon en 1965 [6], les valeurs indiquées peuvent différer de celles que l'on peut trouver dans les documents ISL plus anciens, qui, pour les mêmes raisons, peuvent donner des valeurs différant entre elles.

égal à 2 m et de diamètre 21 cm [17]. Dans ce cas, deux montages ne différant que par l'orientation des couteaux (l'un à couteaux parallèles à l'axe du tir et l'autre à couteaux perpendiculaires à cet axe) avaient été mis en oeuvre simultanément. Par la suite un montage plus performant avec un miroir sphérique de 5 m de rayon de courbure et de diamètre 50 cm a été utilisé [18]. Son encombrement a nécessité l'emploi d'un miroir de renvoi supplémentaire (figures 6 et 7).

La figure 8 donne un premier exemple de résultat. Il s'agit d'un cône de demi-angle au sommet $12,5^\circ$, d'échouement 0,2, de diamètre au culot 12,4 mm, lancé à 4113 m/s dans de l'air à 100 mmHg. Le sillage laminaire présente d'abord des contours rectilignes jusqu'à 95 mm du nez du projectile. Ensuite apparaissent des ondulations qui induisent dans l'écoulement extérieur du sillage des ondes de choc qui viennent interférer avec l'onde de choc de recompression issue du col du sillage, puis le sillage prend un aspect turbulent caractéristique à partir de 115 mm du nez, avec des "bouffées" plus ou moins importantes.

La figure 9, qui correspond à un projectile identique tiré à vitesse un peu plus élevée (4674 m/s) dans de l'air à la même pression, donc à une transition un peu plus proche du projectile, montre un déroulement analogue : apparition d'ondulations à la frontière du sillage laminaire, mais cette fois dès 70 mm du nez, puis des ondulations du sillage laminaire avant l'apparition de bouffées turbulentes plus ou moins importantes à partir de 92 mm du nez, mais ce n'est guère que dans la partie droite de l'image, c'est-à-dire vers 250 mm du nez, que le sillage turbulent commence à présenter un "grain" à peu près homogène.

La figure 10 montre le sillage d'un cône de même forme mais de dimensions deux fois plus faibles (diamètre de culot 6,2 mm) tiré à 4614 m/s dans de l'air à la pression de 60 mmHg. La transition est alors plus lointaine et le centre de l'image est à 205 mm du culot du projectile. On voit très nettement le développement des instabilités du sillage laminaire et l'apparition progressive de "bouffées" turbulentes de plus en plus importantes. Un examen attentif de l'image montre que les instabilités apparaissent d'abord à la frontière supérieure du sillage laminaire, les instabilités à la frontière inférieure ne deviennent visibles que tout à fait à droite de l'image. Cette figure est une strioscopie à couteaux perpendiculaires à l'axe du tir et visualise donc les gradients de masse volumique dans la direction axiale. La figure 11 donne la strioscopie à couteaux parallèles à l'axe correspondant au même tir. Les deux postes strioscopiques étaient séparés de 75 cm et le déclenchement des éclateurs réglé de manière à ce que le centre de deux images soit à la même distance du projectile. L'examen de la figure 11 permet de retrouver les mêmes structures que sur la figure 10 mais décalées vers la droite. A priori on serait tenté d'attribuer ce décalage à la vitesse de convection de ces structures par l'écoulement et de calculer cette vitesse à partir de ces photographies. Cependant l'influence des incertitudes expérimentales (erreur sur la mesure de la vitesse des projectiles, erreurs sur l'instant du déclenchement des éclateurs) enlèverait toute précision à cette évaluation.

La figure 12 est particulièrement remarquable. Elle correspond à un cône de petit calibre (diamètre au culot 6,2 mm) tiré à 4780 m/s dans de l'air à 20 mmHg. La transition est alors très lointaine et l'éclateur a été réglé de manière à ce que le centre de l'image soit à la distance prévue pour la transition par le critère de Waldbusser (soit à 110 calibres du nez du cône où 68 cm). Mais alors que ce critère est supposé donner la fin de la transition, la photographie montre que l'on est plutôt au début de celle-ci; on y voit nettement se développer une instabilité à la frontière supérieure du sillage laminaire. Cette instabilité contamine progressivement tout le sillage, mais ce qu'il y a de surprenant est son atténuation et sa disparition progressive vers la droite de l'image.

L'intérêt d'une étude détaillée des instabilités que l'on voit sur les figures 8 à 12 (lesquelles sont extraites de [13]) est évident. Il aurait fallu, pour faire cette étude, pouvoir suivre le développement de ces instabilités au cours du temps, ce qui était malheureusement impossible à l'époque où ces photographies ont été obtenues. En effet, chaque éclateur (alimenté par la décharge d'une batterie de condensateurs) ne pouvait être utilisé qu'une seule fois par tir. Une solution théoriquement possible eut été de multiplier le nombre de postes strioscopiques le long de la trajectoire, mais le nombre de postes possibles est limité à quelques unités et leur multiplication ne va pas sans poser des problèmes pratiques. La solution idéale, effectuer plusieurs dizaines de visualisations successives au même endroit, n'était pas possible, faute de source lumineuse appropriée.

3. Cinématographie ultra-rapide

3.1 Considérations générales

Pour visualiser un phénomène instationnaire, il faut que la durée d'observation τ soit nettement inférieure à la durée caractéristique du phénomène. Il est difficile ici d'estimer cette dernière de façon précise, mais on peut en déterminer un ordre de grandeur. En effet, les figures 9 à 12 montrent que les instabilités qui se développent sont à peu près à l'échelle spatiale de l'obstacle. Elles ont donc une taille caractéristique L de l'ordre de 10^{-2} m. Si on prend pour vitesse caractéristique celle du projectile, soit $v \approx 5 \cdot 10^3$ m/s, on obtient un temps caractéristique : $L/v \approx 2 \mu s$, pour la "période" du phénomène à étudier. Il faudrait donc pouvoir faire pendant cette période un certain nombre de photographies avec des temps de poses suffisamment petits. Les éclateurs utilisés ci-dessus ont une durée acceptable (150 ns) mais ne permettent pas la répétition des images.

Il existe un instrument déjà ancien qui permet cette répétition : c'est la chronoloupe de Cranz-Schardin [19], qui consiste en une batterie de 24 éclateurs déclenchés avec des intervalles Δt réglables et, à l'opposé par rapport au phénomène à étudier, une plaque recevant côte à côte les 24 images (figure 13). L'inconvénient du système est qu'il entraîne des erreurs de parallaxe, mais que l'on peut minimiser en éloignant la batterie d'éclateurs et la plaque du phénomène, ce qui entraîne des complications dues à l'emploi de miroirs de renvoi (le laboratoire n'est pas extensible!). Les appareils existant à l'ISL ont une cadence de répétition qui est bonne (Δt minimum égal à 10^{-7} s), mais les temps de pose sont trop longs (au minimum 3 μs) et la puissance lumineuse est assez faible. L'appareil est cependant utilisable pour des sillages de projectiles à faible vitesse, comme le montre l'exemple de la figure 14.

L'idéal serait de pouvoir disposer d'une source lumineuse fournissant des impulsions de l'ordre de 20 ns avec des intervalles entre impulsions de l'ordre de 100 ns.

Remarquons en passant qu'il faudrait aller encore bien plus loin pour accéder aux échelles du mouvement turbulent auxquelles se fait la dissipation par viscosité. En effet, si l'on en croit la théorie [20], ces échelles ont un temps caractéristique de l'ordre de $L/v Re^{-3/4}$, soit ici de l'ordre de 10^{-10} s.

La réalisation de temps d'exposition courts et d'une cadence de répétition élevée peut être obtenue au moyen des trois éléments du montage optique : la source lumineuse, l'optique elle-même et le moyen de réception. Dans la plupart des cas où l'on souhaite effectuer une série de photographies très rapprochées dans le temps, les temps d'exposition et les intervalles entre images successives sont déterminés par le système de réception. C'est le cas des caméras à miroir tournant, des caméras à tambour, ainsi que des systèmes utilisant des obturateurs électroniques. Quel que soit leur mode d'utilisation, le temps d'exposition permis par ces caméras utilisées à grande vitesse est fonction de l'intervalle de temps entre images successives et ne peut être choisi indépendamment. Ces systèmes de réception sont en général utilisés avec des sources lumineuses quasi-continues, qui éclairent l'objet avec une lumière intense pendant la totalité de l'enregistrement.

La chronoloupe mentionnée plus haut est un exemple d'utilisation de la source lumineuse pour fixer la durée d'exposition et la fréquence des images puisqu'elle utilise 24 éclateurs indépendants pouvant être déclenchés par groupes de six. La réception est assurée par 24 appareils photographiques séparés. L'obtention d'enregistrements plus longs comprenant plus de 24 images serait extrêmement difficile pour des raisons pratiques.

3.2 Emission

Des sources lumineuses fournissent des impulsions très courtes et de grande énergie ont été développées récemment sous forme de lasers. Des lasers à rubis, à colorant ou des lasers YAG opérant en mode relaxé fournissent des impulsions de l'ordre de la microseconde. L'utilisation de techniques particulières de modulation intra-cavité du laser permet d'atteindre des durées d'impulsion de l'ordre de la nanoseconde et les impulsions les plus courtes que l'on peut obtenir en combinant la modulation intra-cavité avec des techniques de mise en forme des impulsions extra-cavité atteignent la picoseconde. Mais les énergies de ces impulsions restent limitées et il reste à résoudre le problème de leur répétition et de leur synchronisation avec des événements extérieurs. Un moyen d'obtenir des impulsions courtes, une fréquence de répétition élevée et une énergie suffisante, est d'utiliser un laser YAG à impulsions longues et un dispositif intra-cavité [23], [21] adapté. On obtient ainsi des impulsions d'environ 400 ns ayant une énergie de l'ordre du millijoule et une fréquence de répétition de 100 kHz. L'énergie par impulsion peut être notablement accrue par amplification dans une seconde tête laser. Néanmoins la durée d'impulsion et la cadence de répétition ne sont pas idéales et, surtout, le problème de la synchronisation avec un appareil extérieur demeure.

L'utilisation d'un obturateur acousto-optique pour hacher le faisceau émis par un laser continu en une série d'impulsions brèves permet de résoudre cette dernière difficulté, mais l'énergie de chaque impulsion décroît linéairement avec sa durée, ce qui rend l'enregistrement photographique difficile, voire impossible.

Par contre, l'emploi de techniques de modulation intra-cavité permet d'obtenir des impulsions aussi brèves que 10^{-12} s et des fréquences de répétition jusqu'à 100 MHz. En particulier, la technique dite "cavity dumping" est une bonne solution pour une source lumineuse satisfaisant à toutes les conditions requises :

- énergie d'impulsion élevée,
- impulsions courtes (environ 20 ns),
- fréquence de répétition réglable indépendamment,
- pas d'erreurs de parallaxe d'une impulsion à l'autre,
- nombre d'impulsions non limité,
- synchronisation facile avec des événements extérieurs.

La figure 15 montre le principe du "cavity dumping". Lorsque le miroir M3 est en position basse, la lumière formée dans la cavité est renvoyée par les miroirs hautement réfléchissants M1 et M2 et n'effectue que des aller-retour dans le milieu laser L où elle est amplifiée dans les limites permises par les inévitables pertes dans la cavité et par l'énergie que peut fournir le milieu laser. Si le miroir M3 est alors placé rapidement en position haute, toute l'énergie emmagasinée dans la cavité est réfléchie hors du laser en un temps très court qui ne dépend que de la longueur de la cavité et de la vitesse de la lumière. La vitesse de basculement du miroir est de même déterminée par le temps d'aller-retour des photons dans la cavité. La puissance maximale d'une impulsion ainsi produite est environ 50 fois supérieure à celle fournie en régime continu.

Plusieurs types de modulateurs acousto-optiques ou électro-optiques peuvent être utilisés actuellement. La figure 16 montre le montage que nous avons retenu. Il consiste en un cavité "repliée" par trois miroirs dont deux focalisent le faisceau pour le ramener au diamètre requis pour obtenir une réponse suffisamment rapide du modulateur acousto-optique utilisé ici pour dévier le faisceau hors de la cavité du laser.

Un des avantages de l'utilisation du laser comme source lumineuse est le fait qu'il peut être utilisé aisément pour des montages optiques différents : ombroscopie, interférométrie et même holographie [22]. Les techniques les plus simples sont l'ombroscopie et l'interférométrie différentielle. Toutes deux sont basées sur les variations locales de l'indice de réfraction dans le champ de l'écoulement. Les deux techniques ne nécessitent que des montages simples côté émission et peuvent être utilisées avec différents systèmes de réception. L'holographie fournirait d'avantage d'informations sur la nature tridimensionnelle de l'écoulement, mais demanderait la mise en oeuvre d'un montage plus complexe et d'une technique d'enregistrement spéciale difficiles à utiliser dans l'environnement d'un tunnel de tir hypersonique.

3.3 Réception

Le problème le plus délicat est celui de la caméra utilisée pour la réception. Le déplacement des images successives sur le support d'enregistrement doit avoir lieu très rapidement. Différents types de caméras existants, sont actuellement disponibles à l'Institut et peuvent être utilisés pour la réception des images obtenues.

La première caméra, et la plus lente, est à tambour tournant. Le film est fixé sur un tambour cylindrique de grand diamètre dont le périmètre extérieur se déplace dans le plan focal de l'objectif avec une vitesse tangentielle pouvant atteindre 100 m/s, soit un déplacement de 0,1 mm par microseconde. Si l'on veut enregistrer des images successives ayant une hauteur de 10 mm (ce qui est un minimum raisonnable), un intervalle entre images de 100 μ s est un minimum. Mais la possibilité d'enregistrer 100 images avec une cadence de 10 kHz peut être intéressante pour l'étude d'écoulements plus lents.

Le deuxième type de caméra disponible est à convertisseur d'image électronique. Ses avantages sont une fréquence extrêmement élevée et un gain de lumière dû à un amplificateur de luminance incorporé. Ses inconvénients sont une faible résolution et un nombre d'images (au surplus de petite taille) limité à 8 ou 16. De plus, le laser ne peut être aisément synchronisé image par image avec la caméra en raison de son obturateur électronique interne. Cependant, cette caméra est utilisée pour mettre au point le montage optique et le dispositif de synchronisation avec le passage du projectile.

Les figures 17 et 18 montrent des exemples d'images obtenues avec cette caméra. Les images se succèdent de haut en bas et de gauche à droite. L'intervalle de temps entre deux images est de 5 μ s. Les vitesses du projectile sont respectivement de 3023 m/s et de 3000 m/s. Les deux séries d'images montrent clairement la structure de l'écoulement autour du projectile, mais la frontière du sillage n'est pas visible.

La figure 19 donne des images du sillage longtemps après le passage du projectile. La distance de ces images au projectile n'a pu être déterminée en raison d'un problème de synchronisation, mais on distingue de nombreux détails du sillage. On voit également les réflexions des ondes de chocs sur les parois du tunnel de tir.

La troisième possibilité, et la plus prometteuse, est l'emploi d'une caméra avec un miroir à plusieurs faces mis en mouvement par une turbine à gaz. Avec ce type de caméra le temps d'exposition est une fois de plus proportionnel à la fréquence de répétition des images. Cependant, un signal de synchronisation image par image permet de diminuer nettement le temps d'exposition indépendamment de la fréquence de répétition au moyen du laser utilisé comme source lumineuse. Cette synchronisation est simplifiée si la caméra peut être utilisée en tant que caméra à fente. Alors seulement le laser commande à la fois le temps d'exposition et l'intervalle entre les images. Cette caméra peut enregistrer jusqu'à 80 images successives du même phénomène.

4. Conclusion

Comme on a pu le voir le principal problème réside dans le choix d'un système de réception adéquat et cette question n'est pas tout à fait résolue. Cependant les premiers résultats sont encourageants et le problème devrait trouver une réponse assez rapidement.

On disposera alors d'une méthode permettant l'étude du développement des instabilités dans les écoulements hypersoniques ou l'étude des écoulements hypersoniques instationnaires. En effet, son application n'est pas limitée au tunnel de tir et, contrairement à ce que l'on pourrait croire instinctivement, les ordres de grandeurs à atteindre sont à peu près les mêmes en soufflerie hypersonique qu'en tunnel de tir. En effet, les vitesses de convection des instabilités sont souvent du même ordre que celles de l'écoulement, c'est-à-dire celle du projectile en tunnel de tir.

Bibliographie

- [1] B.C. JAEGER - Les moyens d'essais hypersoniques de l'ISL : description et possibilités. 22ème colloque d'Aérodynamique Appliquée et l'Association Aéronautique et Astronautique de France, Lille, 13-15 novembre 1985. ISL - CO 229/85 (31.10.1985)
- [2] J.F. WENDT - European Hypersonic Wind Tunnels AGARD Fluid Dynamics Panel, Symposium "Aerodynamics of hypersonic lifting vehicles", Bristol, April 6-9, 1987
- [3] M. LAUG - Echo radar d'un sillage ionisé : bases théoriques. ISL - 18/70 (1970)
- [4] M. LAUG, M.J. PIERSON, G. STERN - Les méthodes d'étude au tunnel de tir de l'ionisation dans les sillages. Progress in Aeronautical Sciences, Vol. 10, Pergamon Press, 1970
- [5] G. STERN, B.C. JAEGER - Etude expérimentale et théorique des sillages hypersoniques ionisés. 23ème colloque d'Aérodynamique Appliquée de l'Association Aéronautique et Astronautique de France, Aussois, 12-14 novembre 1986. ISL - CO 240/86 (1986)
- [6] C. LECOMTE - Description et possibilités du canon à gaz léger de 20 mm et du tunnel de tir hyperballistique correspondant. ISL - T 51/65 (31.12.1965)
- [7] C. LECOMTE - Etude d'un canon à gaz léger, ISL - T 5/61 (6.2.1961)
- [8] S. BIHL, R. JOECKLE, A. SONTAG - Mass spectrometric capture and analysis of the ablation products from hypersonic projectiles - 23rd Meeting of the Aeroballistic Range Association, Vernon-sur-Eure, September 19-20, 1972. ISL - 25/72 (8.9.1972)
- [9] S.L. ZEIBERG - Transition correlations for hypersonic wakes - AIAA Journal, Volume 2, No. 3 (March 1964), pages 564-565
- [10] B.C. JAEGER, J. LUNEAU, P. SMIGIELSKI - Etude expérimentale de la transition du sillage d'une sphère en vol hypersonique. ISL - T 57/68 (5.12.1968)

- [11] E. WALDBUSSER - Relationship of laminar wake width to wake transition distance - AIAA Journal, Vol. 3, No. 10 (October 1965), pages 1965-1966
- [12] E. WALDBUSSER - Shape effects on hypersonic slender body wake geometry and transition distance Journal of Spacecraft and Rockets, Vol. 4, No.5 (May 1967), pages 657-662
- [13] B.C. JAEGER, F. ALBE, B. KOCH - Etude expérimentale de la transition du sillage d'un cône émoussé en vol hypersonique. ISL-12/72 (16.5.1972)
- [14] B.C. JAEGER, J.P. HANCY - Etude mécanique du sillage d'un cône émoussé en vol hypersonique ISL - 9/71 (26.4.1971)
- [15] B. KOCH, H.J. PFEIFER - Turbulence diagnostics of supersonic and hypersonic wakes using cw-laser radiation - 14th Meeting of the Aeroballistic Range Association, White Oak, Maryland and Washington, D.C., June 12-14, 1968. ISL - N 13/68 (10.6.1968)
- [16] B. KOCH, M. KÖNIG, A. KOHLMANN, H.J. PFEIFER - Ein kombiniertes Verfahren zur Untersuchung des Nachlaufs von Hyperschallgeschossen mit Hilfe von Mikrowellen- und Laserstrahlung. ISL - T 50/69 (16.12.1969)
- [17] F. ALBE, H. FAGOT, P. SUTTERLIN - Visualisation des sillages de cônes émoussés en vol hypersonique par striescopie. ISL - RT 4/71 (12.3.1971)
- [18] A. STIMPELING, P. SMIGIELSKI, F. ALBE, H. FAGOT, J. SCHWAB - A wide-field schlieren system of high sensitivity for hyperballistic ranges. 23rd Meeting of the Aeroballistic Range Association, Vernon-sur-Eure, September 19-20, 1972. ISL - 24/72 (8.9.1972)
- [19] C. CRANZ, H. SCHARDIN - Kinematographie auf ruhendem Film und mit extrem hoher Bildfrequenz Z. f. Physik, Bd. 56 (1929), S. 147-183
- [20] L.D. LANDAU, E.M. LIFSHITZ - Fluid Mechanics. Pergamon Press, 1959
- [21] A. KÖNEKE, A. HIRTH - Long pulse emission from a frequency doubled neodym YAG-laser. Optics. Com. 34, 2 (1980) p. 245-248
- [22] H. FAGOT, G. SIMON - Visualisation du relief de sillages de projectiles en vol supersonique par holographie ultra-rapide. ISL - N 30/73
- [23] A. HIRTH, A. KÖNEKE - Controlled relaxation oscillations from a neodym YAG-laser. 5th National Quantum Electronics Conference, Hull University, September 23-25, 1981

Remerciements

Les auteurs remercient M. Félix Albe pour la mise à leur disposition des photographies anciennes obtenues par striescopes, MM. Gilbert Kronenberger et Léo Bobin pour le prêt et la mise en oeuvre de la chronoloue, et M. Antoine Hirth pour le prêt du modulateur acousto-optique et ses nombreuses suggestions concernant la mise en oeuvre et les possibilités des lasers.

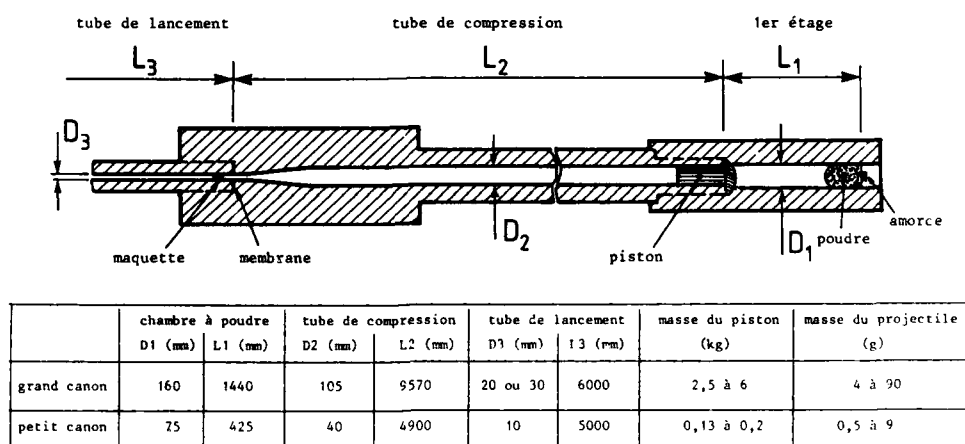


Fig. 1 : Schéma et caractéristiques des canons à gaz léger de l'ISL



Fig. 2 : Canons à gaz léger de 20 (au premier plan) et de 10 mm de l'ISL

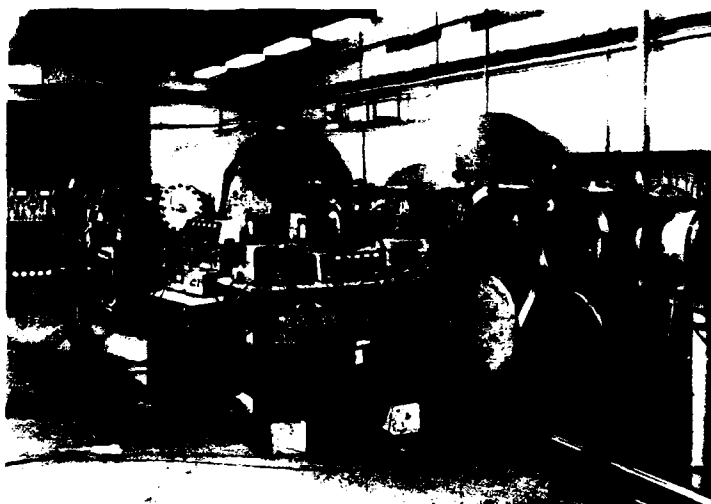


Fig. 3 : Vue du tunnel de tir

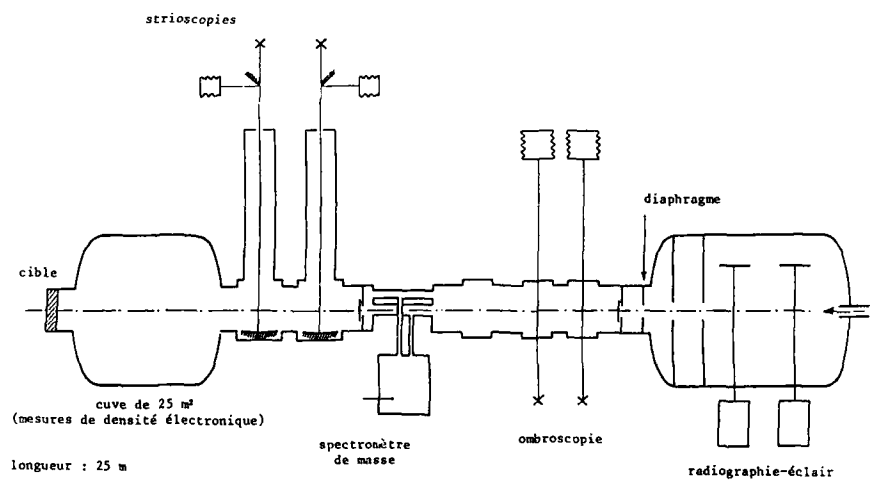


Fig. 4 : Arrangement du tunnel de tir pour l'étude des sillages de cônes émoussés et la récupération des produits d'ablation dans les sillages de sphères

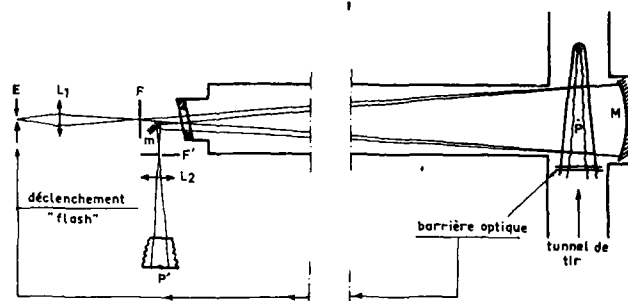


Fig. 5 : Schéma du dispositif strioscopique

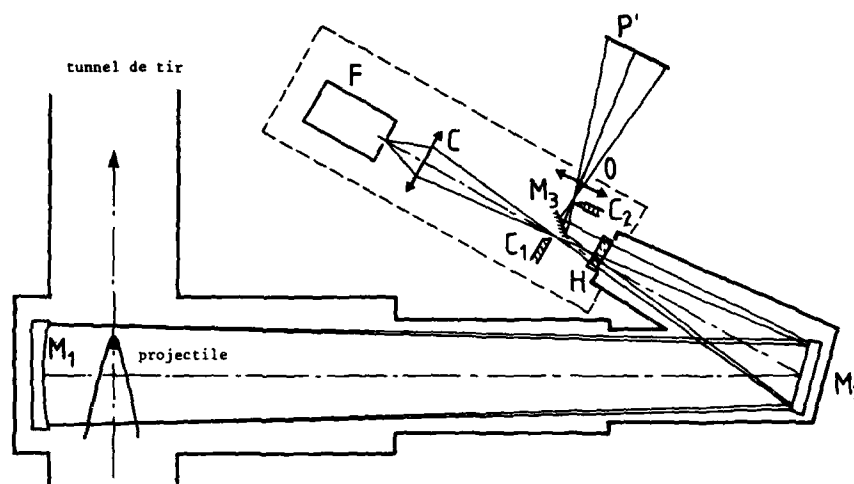


Fig. 6 : Schéma d'un montage stéréoscopique à double passage, en tunnel de tir.
 M_1 : miroir sphérique; M_2, M_3 : miroirs plans; F : dispositif d'éclairage;
 H : hublot de verre; P' : plaque photographique; C_1, C_2 : couteaux



Fig. 7 : Photographie d'une installation stéréoscopique en tunnel de tir
 (schéma de principe fig. 6)

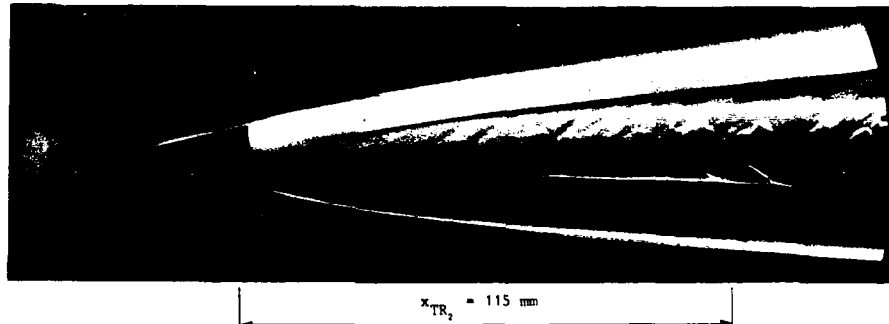


Fig. 8 : Strioscopie à couteaux parallèles à l'axe du tir 469.
Calibre du projectile 12,4 mm. Vitesse 4113 m/s. Pression 100 mmHg

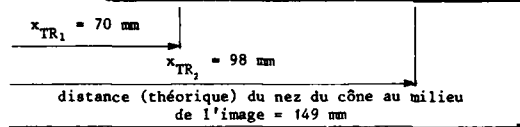


Fig. 9 : Strioscopie à couteaux parallèles à l'axe du tir 462.
Calibre du projectile 12,4 mm. Vitesse 4674 m/s. Pression 100 mmHg

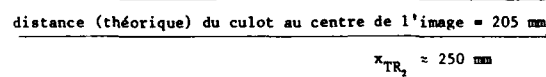
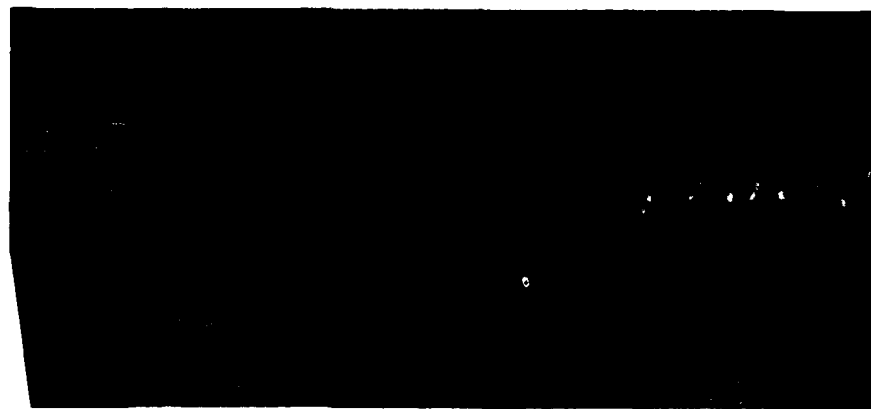


Fig. 10 : Strioscopie à couteaux perpendiculaires à l'axe du tir 1263.
Calibre du projectile 6,2 mm. Vitesse 4614 m/s. Pression 60 mmHg

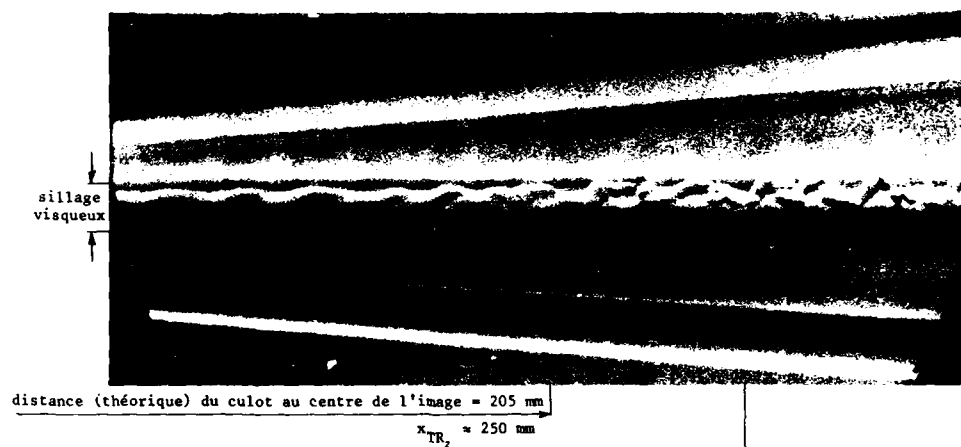


Fig. 11 : Strioscopie à couteaux parallèles à l'axe du tir 1263.
Calibre du projectile 6,2 mm. Vitesse 4614 m/s. Pression 60 mmHg



Fig. 12 : Strioscopie à couteaux parallèles à l'axe du tir 1268.
Vitesse 4780 m/s. Pression 20 mmHg. Calibre du projectile 6,2 mm

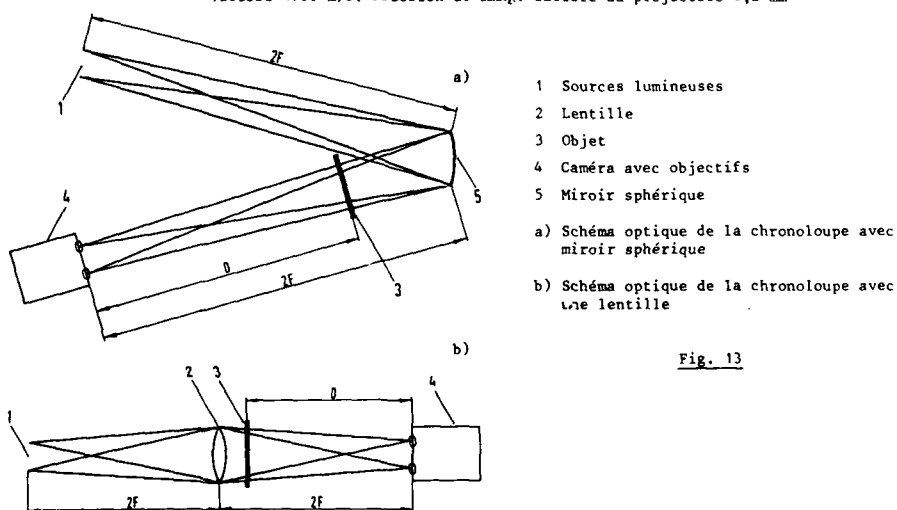


Fig. 13

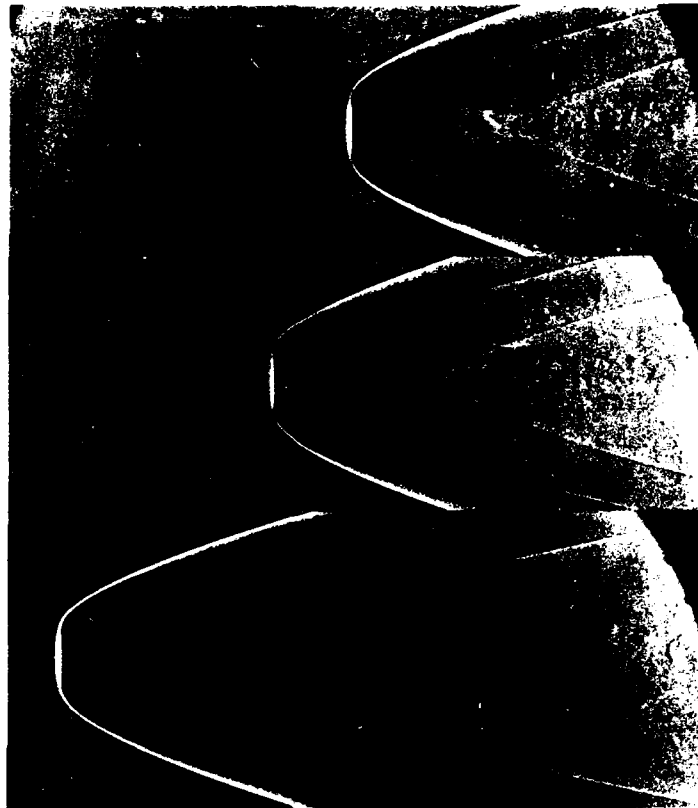


Fig. 14 : Images d'un cylindre en vol hypersonique (chronoloupe)
 $v = 2700 \text{ m/s}$, $\Delta t : 8 \mu s$

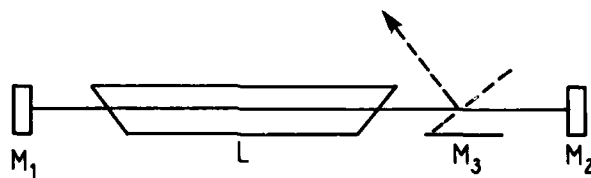


Fig. 15 : Principe du "cavity dumping"

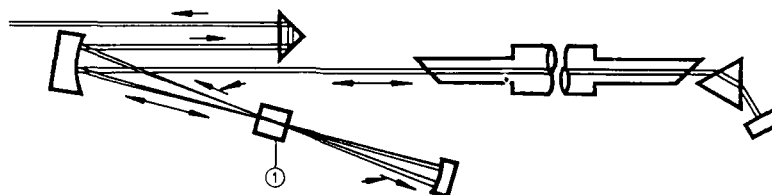


Fig. 16 : Schéma optique du laser avec modulateur acousto-optique ①

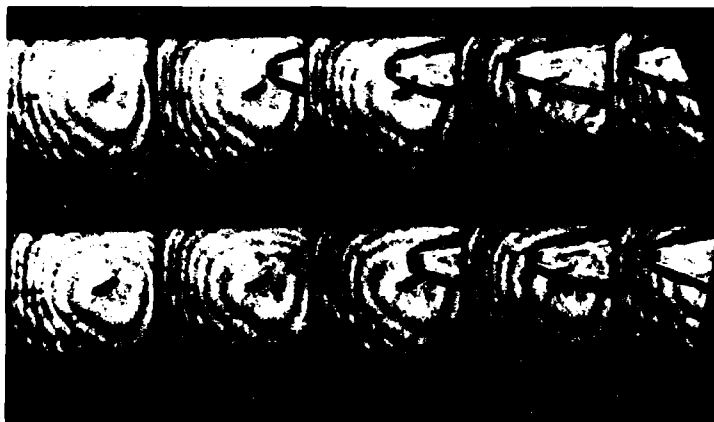


Fig. 17

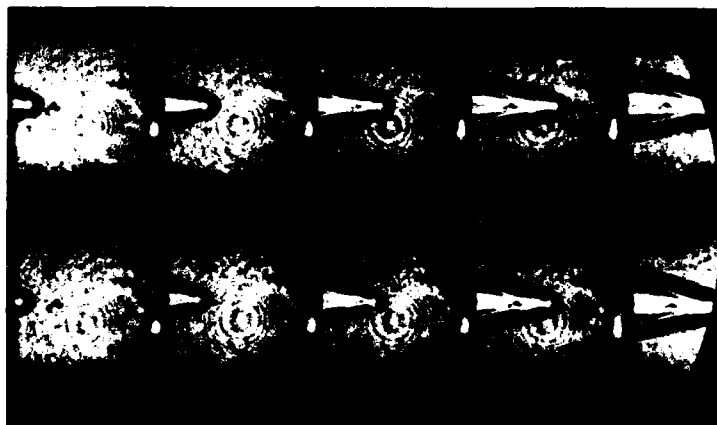


Fig. 18

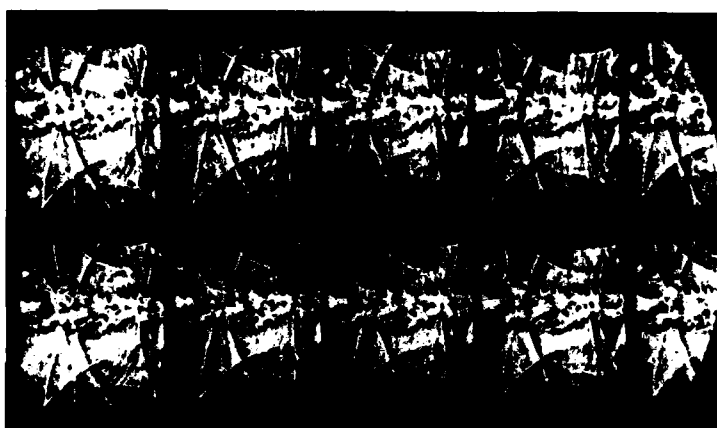


Fig. 19

Fig. 17, 18, 19 : Images obtenues à l'aide de la caméra électronique Δt 5 μs

THE DRAG OF SLENDER AXISYMMETRIC CONES IN RAREFIED HYPERSONIC FLOW

by

T. J. Rhys-Jones

Aerodynamics Department
 Royal Aircraft Establishment
 Farnborough, Hampshire, GU14 6TD, England

SUMMARY

This Paper describes an experimental study performed in the RAE Low Density Tunnel to determine the aerodynamic characteristics of a range of slender axisymmetric bodies in rarefied hypersonic flow. The main purpose of this study was to assess the effects of cone angle, nose bluntness and Reynolds number on the zero incidence drag of cones. In addition, some measurements of axial force, normal force and pitching moment at incidence were made. The bodies were tested at a nominal Mach number of 10 and at flow conditions which correspond to those in the transitional rarefied flow regime. These data have been compared with correlations developed to represent the change in drag coefficient in this flow regime between continuum and free-molecular flow.

LIST OF SYMBOLS

A	base area, πr_b^2
C_∞	Chapman-Rubesin viscosity coefficient, $\mu_w T_\infty / \mu_\infty T_w$
C_A	axial force coefficient
C_D	drag coefficient, $D/q_\infty A$
\bar{C}_D	drag parameter, $C_D / \sin^2 \theta (1 + 0.375 \beta^2)$
C_x	viscosity coefficient, $\mu_x T_\infty / \mu_\infty T_x$
d	base diameter
D	measured drag force
$Kn_{\infty,d}$	Knudsen number, $\lambda_\infty / d (= 1.26 \gamma^{1/2} M_\infty / Re_{\infty,d})$
l	cone length
M	Mach number
\bar{M}	Mach number parameter, $M_\infty \sin \theta (1 + 0.375 \beta^2)^{1/2}$
q_∞	dynamic pressure, $\frac{1}{2} \rho_\infty U_\infty^2$
r_b	base radius of cone
r_n	nose radius of cone
$Re_{\infty,d}$	Reynolds number, $\rho_\infty U_\infty d / \mu_\infty$
S_∞	freestream speed ratio, $U_\infty / (2RT_\infty)^{1/2} (= (\gamma/2)^{1/2} M_\infty)$
T	temperature (absolute)
T_x	temperature parameter, $T_0 [1 + 3(T_w/T_0)]/6$
U	velocity
\bar{U}	velocity parameter, $\frac{(1 + 0.4 T_w/T_0) \cos \theta}{(1 + 0.375 \beta^2) \sin^2 \theta} M_\infty \left(\frac{C_x}{Re_{\infty,d}} \right)^{1/2}$
$\bar{V}_{\infty,d}$	viscous similarity parameter, $M_\infty (C_\infty / Re_{\infty,d})^{1/2}$
α	angle of incidence
β	$\psi / \sin \theta$
γ	ratio of specific heats
θ	cone half angle
λ_∞	ambient mean free path of gas molecules

μ	viscosity
μ_x	viscosity evaluated at T_x
ρ	density
ϕ	$(C_D - C_{D_i}) / (C_{D_{fm}} - C_{D_i})$ or $(C_A - C_{A_i}) / (C_{A_{fm}} - C_{A_i})$
ϕ (Kn)	bridging function
ψ	bluntness ratio, r_n/r_b

Subscripts

c	sharp cone
fm	free molecular value
i	inviscid (continuum) value
o	total or stagnation value
w	wall value
∞	freestream value

1 INTRODUCTION

This Paper describes tests carried out in the RAE Low Density Tunnel to measure the aerodynamic characteristics of a range of slender axisymmetric bodies in rarefied hypersonic flow. The main purpose of the study was to measure the drag of cones at zero incidence. It was intended to assess primarily the effects of cone angle, nose bluntness and Reynolds number on the drag coefficient, however it was necessary to consider also the effects of Mach number and the ratio of wall temperature to freestream temperature. The small variations in Mach number and temperature ratio were due to the conditions and mode of operation of the Low Density Tunnel. As well as some cones, biconic and triconic bodies were tested, and some measurements of axial force, normal force and pitching moment at incidence were made. The purpose of these tests was to provide material for an aerodynamic data base for slender bodies, and data for the development of the so-called 'bridging functions' which define the changes in aerodynamic characteristics through the transitional rarefied flow regime.

The transitional rarefied flow regime is that between continuum and free molecular flow, and is where the viscous effects become increasingly significant. These viscous effects can lead to large changes in the aerodynamic characteristics of bodies. For example, the zero incidence drag coefficient of a slender body changes by an order of magnitude between its continuum value and its value under free molecular conditions. In the transitional rarefied flow regime the theoretical prediction of aerodynamic loads is difficult even for simple axisymmetric bodies under zero incidence conditions. Hence it remains necessary to rely on experimentally-derived data until the most promising of current prediction methods (eg Monte Carlo direct simulation) are fully developed and validated for axisymmetric bodies at incidence.

Over the last 10 years or so, there have been a number of studies in which the zero-incidence drag of slender cones has been measured. However, the results obtained by different experimental investigators do not show good agreement. These differences illustrate the problems of measuring small forces on small models under rarefied flow conditions. The substantial scatter of data tends to obscure any possible effects of such parameters as cone angle, nose bluntness, freestream Mach number and wall temperature. There has been no general agreement about the choice of parameter with which to correlate the drag data, and no completely successful correlation has yet been achieved. The drag data have usually been presented in the form of the coefficient, C_D , or the ratio of the coefficient to the free-molecular drag coefficient, $C_D/C_{D_{fm}}$. However, Potter¹ has suggested that the function $\phi = [C_D - C_{D_i}] / [C_{D_{fm}} - C_{D_i}]$ is used since this removes the geometric effects of similar shapes. (ϕ (Kn) is the 'bridging function' of interest, and C_{D_i} is the inviscid drag coefficient.) The choice of parameter with which the drag is correlated could by any of the traditional rarefaction parameters such as Reynolds number ($Re_{\infty,d} = \rho_{\infty} U_{\infty} d / \mu_{\infty}$), Knudsen number ($Kn_{\infty,d} = 1.26 \sqrt{M_{\infty}} / Re_{\infty,d}$) or the viscous similarity parameter ($\bar{V}_{\infty,d} = M_{\infty} [C_{\infty} / Re_{\infty,d}]^{1/2}$). All of these parameters have been used in the past to try to correlate data, along with others such as $Re_{\infty,d} (T_w/T_{\infty})^{1/2}$, $Kn_{\infty,d} (T_w/T_{\infty})^{1/2}$ and more complicated ones. Geiger² has proposed a correlation which includes terms such as the viscous similarity parameter, the inviscid and free-molecular drag coefficients, the ratio of wall to freestream total enthalpies and an empirical nose-bluntness factor. Taub³ has proposed a correlation involving the viscous similarity parameter, the wall to freestream temperature ratio and a nose-bluntness factor. However, none of these correlations are entirely satisfactory.

The present data will be used for comparison with simple Knudsen number bridging functions, ϕ (Kn). Knudsen number is the ratio of the ambient molecular mean free path to a characteristic body length (usually the base diameter for slender bodies), and is widely accepted as a scaling parameter for low density flows. For $Kn_{\infty,d} < 0.01$ the flow is considered to be continuum and for $Kn_{\infty,d} > 10$ the flow is free-molecular. For these particular tests, the range of $Kn_{\infty,d}$ was 0.0011 to 0.1606. Although these tests fulfil the need for data over part of the Knudsen number range in the transitional flow

regime, there is a definite need for more experimental data over the range $0.1 < Kn_{m,d} < 5$. It is hoped that future enhancements to the Low Density Tunnel may make the coverage of part of this range possible. The present cone drag data will also be compared with the correlation of Taub.

Some additional tests on biconic and triconic axisymmetric bodies at zero and non-zero angles of incidence were made. The zero incidence drag coefficient data for both these bodies and the non-zero incidence axial force data for the triconic body will also be compared with the Knudsen number bridging functions.

2 EXPERIMENTAL DETAILS

2.1 Tunnel operating conditions

Four operating conditions of the RAE Low Density Tunnel were used for these tests. These conditions correspond to two freestream Mach numbers of 8.58 and 9.84. The tunnel uses pure nitrogen as a test gas. The three standard conditions ($M_\infty = 9.84$) are achieved by operating the Mach 10 contoured nozzle at slightly different stagnation conditions. The $M_\infty = 8.58$ condition results from operating the nozzle at off-design conditions. The more rarefied flow at the off-design condition produces a thicker boundary layer along the nozzle wall, and hence a lower Mach number in the free jet outside the nozzle exit. Detailed axial and radial pitot probe traverses were carried out, and these confirmed the uniformity of the nozzle flow at this off-design condition. The four conditions give a range of unit freestream Reynolds number of 11380 per metre to 124023 per metre. The stagnation pressure ranged from $3.12 \times 10^4 \text{ Nm}^{-2}$ to $2.06 \times 10^5 \text{ Nm}^{-2}$ and stagnation temperature from 1170 K to 2110 K.

2.2 Description of models

A large number of models were needed to carry out the parametric study of the effect of various parameters on the zero incidence drag of cones. The parameters varied were cone angle, cone bluntness and Reynolds (or Knudsen) number. The ratio of wall temperature to total temperature varied to a small extent although this was not by choice, but was governed by the tunnel operating conditions and the material of the models. Cones of five different half angles (θ) and six different bluntness ratios (ψ) were tested. This corresponded to a total of 30 different geometries. In addition to this, there were five models of each geometry of different sizes in order to give more variation in Reynolds number than provided just by variation of the four tunnel operating conditions. Hence there was a total of 150 models. The majority of these models were solid and made of mild steel. The exception to this was the largest model for each of the different geometries which were thin-walled models made of a nickel alloy. This was necessary because a solid model of this size would have been too heavy for the sting to support without bending.

These models were fairly slender cones with the half angles ranging from 4° to 10° . The bluntness ranged from $\psi = 0$, a 'nominally' sharp cone, to $\psi = 0.5$, where the nose radius was half the base radius. The range of model lengths was 26.7 mm to 300 mm. Full details of the various parameters are shown in Fig 1. This corresponded to a range of Reynolds numbers based on the cone base diameter ($Re_{m,d}$) of 80 to 13122, or Knudsen numbers ($Kn_{m,d}$) of 0.0011 to 0.1606.

Also shown in Fig 1 are details of the biconic and triconic models. Only one geometry of each of these shapes were tested. The two conic sections of the biconic body had half angles of 11.25° and 4.5° . A single model, of length 150 mm, was tested at one flow condition, corresponding to a Reynolds number ($Re_{m,d}$) of 3324 ($Kn_{m,d} = 0.00442$). The three conic sections of the triconic body had half angles of 7.03° , 3.87° and 7.37° . Four different sized models, of lengths 50 mm to 200 mm, were tested at different flow conditions to give a range of Reynolds number ($Re_{m,d}$) of 157 to 6850 ($Kn_{m,d} = 0.00214$ to 0.0814).

2.3 Force balances and model mounting

The drag forces on the models in the Low Density Tunnel were measured using three externally-mounted force balances of different range. The balances were the Mk 1 one-component balance, and the 100 g and 500 g three-component balances. These three balances can measure maximum axial forces of 0.1, 1.0 and 5.0 Newtons respectively. At zero incidence the axial force is also the drag of the body. All three balances operate on the 'null' principle and use an electromagnetically-derived restoring force to balance the aerodynamic loads. The two three-component balances, which measure axial force, normal force and pitching moment, were used for all tests at non-zero angles of incidence.

All three balances were similarly mounted from rails on the roof of the evacuated working section. The balances were carefully shielded from the high temperature 'free jet' gas flow to prevent any errors due to heating effects. Each force balance was calibrated statically prior to wind-tunnel testing. The repeatability of the measurements from the force balances is $\pm 1\%$ and the accuracy $\pm 1\%$ of full load. It is estimated that the overall accuracy of the drag coefficients is $\pm 4\%$ when uncertainties in the tunnel test flow conditions are taken into account. The results used were those for which the balance was most appropriate to the level of axial force experienced on the model. This would maximise the accuracy of the results. Hence the Mk 1 balance was used for the very small models where the forces were low, and the 500 g balance was used for the larger models where the forces were much higher.

There are two other factors which could affect the measurements. These factors are sting interference and shroud interference effects. The model is mounted on a horizontal sting which is rigidly attached to a vertical sting connected to the balance in the roof of the working section. The vertical sting is protected from the heat of the gas flow by a shroud to prevent any errors due to heating effects. The horizontal sting passes through a hole in the shroud before its attachment to the vertical sting. At no point do the horizontal or vertical stings touch the shroud and great care is taken to make sure this is always so.

Sting interference effects are due to the sting diameter being large in relation to the diameter of the base of the model being tested so as to modify the pressure field (and hence the drag) in the region of the base. For the standard AGARD supersonic/hypersonic calibration models⁴ HB-1 and HB-2, it is stated that the sting diameter must not exceed 30% of the base diameter on an axisymmetric body in order to avoid sting interference effects. For the very smallest models tested in this tunnel programme, the sting diameter was only 23% of the base diameter and for all the other models it was less than 20% of the base diameter. Hence it is concluded that all these measurements are completely free of sting interference effects.

The shroud interference effects will be caused by the shroud being too close to the base of the model (ie the length of the horizontal sting being too short). The shroud, in the same way as a large sting, may modify the pressure field in the region of the base of the model and hence alter the drag. Experiments showed that the shroud interference effects were most severe for the small models when the base diameter is of the order of the shroud width. Stings of differing lengths were used and the pressure close to the base was measured using a tube mounted on the sting. The results showed a considerable variation in base pressure with the separation distance between the base and the shroud. The minimum distance to avoid interference for each case could readily be deduced from these results.

2.4 Estimation of model wall temperature

As the wall temperature ratio, T_w/T_0 , is known to have a large effect on the value of the drag coefficient, C_D (see, for example, Ref 5), it was important to estimate the values of T_w/T_0 which apply to this present data. The estimation of T_w/T_0 was made difficult by the method of operation of the Low Density Tunnel. Firstly, each of the four 'standard' tunnel operating conditions have a different stagnation temperature, and secondly, the 'warming up' of the graphite heater and the establishment of the stable flow condition takes a period of 2-3 minutes. During this time the temperature of the model increases by kinetic heating from the flow and by conduction within the model itself. This results in temperature gradients along the surface of the model, the nose of the model being considerably hotter than the base. The problem is further complicated by the use of both the large thin-walled nickel alloy models and the smaller solid steel models.

In order to measure these temperature gradients, and estimate values of T_w/T_0 for the models as a whole, use was made of the AGA infrared thermal imaging system. This is a non-intrusive technique for measuring the infrared radiation emitted by a surface. The model was viewed by the long-wavelength (8-14 μm) camera through an infrared-transmitting window mounted in the side of the tunnel working-section. The signal from the camera is passed to a microcomputer and is presented as a temperature contour map. Using the software available for the microcomputer the thermal images were processed. The mean surface temperature was calculated for both the solid and thin-wall models at each of the four flow conditions. The accuracy in the measurement of T_w is estimated to be $\pm 5\%$. The range of mean values of T_w/T_0 for the solid models were 0.16 to 0.31 and for the thin-wall models 0.31 to 0.52.

2.5 Values of continuum and free-molecular axial force coefficient

In order to compare the present data in the transitional rarefied-flow regime with its limiting values and to be able to define 'bridging functions', it was necessary to obtain values of continuum and free-molecular axial force coefficient for the geometries used in this study. Although one set of the limiting values of axial force coefficient are referred to in this paper as the continuum limits, the values actually used are inviscid. In the equations for inviscid-flow all shear terms are ignored, and the flow is strictly inertial. In practice, continuum flow corresponds to high Reynolds number flow where the viscous effects are small but not negligible. The values of the zero incidence axial force (ie drag) coefficient and non-zero incidence axial force coefficient for the various geometries were obtained from computational methods.

The values of the inviscid axial force coefficient were obtained from a Report by Morrison et al⁶. These values were calculated using a NSW/WOL⁷ computer code based on a finite-difference solution of the steady inviscid three-dimensional compressible flow equations for a perfect gas with $\gamma = 1.4$. These values are for $M_\infty = 10$ and include the contribution of base drag.

The values of the free-molecular axial force coefficient were obtained from unpublished RAE data. These values are for $M_\infty = 10$ and $T_w/T_\infty = 1.08$, and were calculated using a free-molecular computer code. The usual assumptions of perfect normal momentum accommodation and diffuse reflection were made.

3 DISCUSSION OF CONE RESULTS

3.1 Measured drag of sharp and blunted cones

The measured zero incidence drag forces on the cones were converted to the usual aerodynamic coefficient form, C_D , using the base area as the reference. Some of the data are presented in graphical form in Figs 2 and 3. These graphs show C_D plotted against $Kn_{w,d}$, the Knudsen number with the base diameter as the reference dimension. Fig 2 shows the effect of bluntness ratio, ψ , on C_D for the cone half angle, θ , of 8° . Fig 3 shows the effect of θ on C_D for $\psi = 0.1$.

It can be seen from these graphs that for all the present data, the values of C_D lie between the calculated continuum and free molecular values as would be expected. Also, the expected trend of C_D increasing with increasing $Kn_{w,d}$ (or rarefaction) can be clearly observed. No graphs have been plotted to illustrate specifically the effects of Mach number and wall temperature as these are generally small in the present work. Data for the different Mach numbers of 8.58 and 9.84 can be distinguished on all the figures. Keel et al⁸ state that for Mach number independence, the criteria is $M_\infty \sin \theta > 1$, or, more specifically, $S_\infty \sin \theta > 1$ (where $S_\infty = (\gamma/2) M_\infty$). For the present data the values of $S_\infty \sin \theta$ range from 0.50 (for $\theta = 4^\circ$ and $M_\infty = 8.58$) to 1.43 (for $\theta = 10^\circ$ and $M_\infty = 9.84$). Hence the present data cannot be considered to be Mach number independent.

These Figures indicate that the range of $Kn_{w,d}$ presently covered by the Low Density Tunnel is the one where the most significant changes in C_D characteristics occur. At the lowest values of $Kn_{w,d}$, for which the present data exist, it can be seen that the values of C_D are considerably higher than the continuum limits. This indicates that there is a very significant viscous contribution to the drag at this value of $Kn_{w,d}$ (around 0.001). (The flow is considered to be continuum at around $Re_{w,d} = 10^7$ or $Kn_{w,d} = 10^{-6}$ for $M_\infty = 10$.) At the higher values of $Kn_{w,d}$, the present data is approaching the free molecular limits but is not close enough to be able to ascertain whether it will approach these limits asymptotically, as the lower $Kn_{w,d}$ data does to the continuum limits.

The apparent slight scatter in the data (Figs 2 and 3) is mainly due to the different model materials and flow conditions (ie different values of T_w/T_0). Although these differences in C_D are only about 10% at the most, it is clear that they are greater for the blunter cones. That is to say, the effect of T_w/T_0 increases with increasing ψ . The effect of C_D increasing with increasing T_w/T_0 has been noted by many researchers. In particular, Dahlen⁹ found that the value of C_D for a hot wall ($T_w = T_0$) model was 11% greater than that for a cold wall ($T_w = T_\infty$), whereas Crawford⁵ found that this increase was between 11% and 19%, and was greater for blunt cones than for sharp cones.

Fig 2 shows the effect of bluntness for $\theta = 8^\circ$. It is clear from this Figure that for values of ψ from 0 to 0.2 inclusive, the corresponding values of C_D are very similar. An increase in the values of C_D between each value of ψ from 0.2 to 0.5 is clearly observed. However, the effect of ψ appears to decrease with increasing $Kn_{w,d}$. These trends were also observed for the other values of θ (4° , 6° , 7° and 10°). Unfortunately, there is no data available for higher values of $Kn_{w,d}$, but it would be expected that the effect of ψ decreasing with increasing $Kn_{w,d}$ would continue, as is shown by the free molecular limits.

Fig 3 shows the effect of cone angle, θ , for the bluntness ratio, ψ , of 0.1. It is immediately clear that the effect of θ on C_D is much less than that of ψ for the range of values of θ and ψ used in this study. The graph shows a cross-over of the data as would be expected by looking at the continuum and free molecular limits. At the lower values of $Kn_{w,d}$ the highest value of C_D is for the $\theta = 10^\circ$ case, whereas at higher $Kn_{w,d}$ the highest C_D is for the $\theta = 4^\circ$ case. These trends were also observed for the other values of ψ (0, 0.2, 0.3, 0.4 and 0.5). However, it was observed that this cross-over point occurs at about $Kn_{w,d} = 0.01$ for the $\psi = 0$ case, and at decreasing values of $Kn_{w,d}$ with increasing ψ to about $Kn_{w,d} = 0.005$ for the $\psi = 0.5$ case. Over the region $Kn_{w,d} = 0.001$ to 0.01, there is only a very small effect of θ , whereas for $Kn_{w,d} = 0.01$ to 0.16, the $\theta = 4^\circ$ data are markedly higher than the rest. The data for values of θ between 6° and 10° appear to lie on the same curve. These trends are exactly what would be expected as the data approach the free molecular values.

3.2 Knudsen number correlations

The effects of cone angle, bluntness, wall temperature, Mach number and Reynolds (or Knudsen) number on the drag coefficient of a cone at zero incidence have been described earlier. Any correlation which is derived to define the drag coefficient of a cone in the transitional rarefied flow regime must take into account all of these effects, which may well all be interdependent. The alternative, in the extreme, may be to derive a separate correlation of drag coefficient with Reynolds or Knudsen number for each value of cone angle, bluntness, wall temperature and Mach number. It is expected that, in practice, a compromise between these two extremes will have to be reached. For example, this may be a series of empirical relations defining the effect of each parameter, or perhaps a series of relations, each only applicable to a certain range of geometries and flow conditions.

A logical choice of correlating parameter is Reynolds number or Knudsen number, since both of these have fixed values at which the transitional rarefied flow regime is considered to end. At these limits, the continuum and free molecular flow regimes exist. The value of the drag coefficient for a given geometry is constant within these two regimes. Hence there are fixed values at either end of the transitional rarefied flow regime to which any correlation must asymptote. However, one comes across the first problem when it is realised that the free molecular drag is wall temperature dependent whereas the inviscid drag is not. Also, only the free molecular drag is sensitive to surface roughness and normal momentum accommodation features, which are not discussed at all in this Paper. The effect of Mach number on drag (for $M_\infty > 2$) is the opposite in inviscid flow to that in free molecular flow. The effect of bluntness is much reduced between the continuum and free molecular limits, whereas the effect of cone angle is reversed. To take into account all these changes in the effects will be very difficult.

Dahlen⁹ carried out a study similar to the present one in a low density tunnel, where the effects of cone angle, bluntness and wall temperature were measured. A number of attempts were made to see which were the best parameters to collapse the data. He concluded that the drag was best represented in the form originally suggested by Potter¹, that is $(C_D - C_{D_i})/(C_{D_{fm}} - C_{D_i})$. It was considered that this parameter, also known as ϕ , reduced the effect of bluntness compared with $C_D/C_{D_{fm}}$ or just C_D . Also the relation has limiting values of $\phi = 0$ for continuum flow and $\phi = 1$ for free molecular flow. The drag was plotted against a number of flowfield parameters such as Reynolds and Knudsen numbers, with both the base diameter and cone length as reference lengths, Reynolds and Knudsen numbers multiplied by the wall temperature-ratio, and the viscous similarity parameter. It was concluded that the Knudsen number with base diameter as reference, $Kn_{w,d}$, was the best parameter. A graph of ϕ plotted against $Kn_{w,d}$ will give a curve which can be defined by a function $\phi(Kn)$ - this is known as the 'bridging function'.

Fig 4 is a graph with ϕ plotted against $Kn_{w,d}$ showing all the present data. It can be seen that there is a significant collapse of the data when it is compared with the earlier graphs showing the variation of C_D with $Kn_{w,d}$. A first order Knudsen number relationship (bridging function), $\phi = (Kn_{w,d} + 0.008)/(Kn_{w,d} + 0.09)$ is shown on this graph. This relation is a good fit to the data, and asymptotes to the lower limit of $\phi = 0.089$ rather than $\phi = 0$. (However, the lower limit of $\phi = 0$ is not realistic. In practice, the viscous effects, although small, are not negligible in continuum flow and so the continuum value of C_D will be greater than the inviscid value. Therefore, a lower limit of $\phi > 0$ for continuum flow is better in reality.)

By looking at the effects of the various parameters as shown earlier, it is clear that the drag of the 4° cones is most influenced by wall temperature and Mach number. Since these effects are much more extreme than for other values of ψ , it was decided to exclude the $\theta = 4^\circ$ data from the next graph. Fig 5 shows ϕ plotted against $Kn_{w,d}$ with all the data for $\theta = 6, 7, 8$ and 10° . It is immediately clear that the exclusion of the $\theta = 4^\circ$ data brings about a significantly greater collapse of the data, particularly at the higher values of $Kn_{w,d}$. The removal of the $\psi = 0.5$ data may reduce the spread of the data further. However, it was decided that this would not be greatly beneficial, since much of the spread was due to the effects (although greatly reduced by the use of ϕ) of θ , M_∞ and T_w/T_0 . A second-order Knudsen number relationship is suggested -

$$\phi = \frac{(Kn_{w,d} + 0.008)(Kn_{w,d} + 0.0005)}{(Kn_{w,d} + 0.09)(Kn_{w,d} + 0.0008)}$$

This bridging function is shown on Fig 5. This relation is also a good fit to the data, and asymptotes to the lower limit of $\phi = 0.056$. However, it is considered that the second-order relationship is the better curve and should certainly be adopted for values of $Kn_{w,d} < 0.001$. Further data are needed at values of $Kn_{w,d}$ not covered by this present study to enable a better fit curve to be defined.

3.3 Taub relations

A particular criticism of the $\phi(Kn)$ bridging functions is that they do not make any allowance for wall temperature effects other than in the value chosen for the free molecular drag term. (However, it was decided not to incorporate this in the present study, for simplicity, and so all values of C_{Dfm} were evaluated at the same value of T_w/T_0 , equal to 0.05.) A method which does allow for wall temperature effects more formally (as well as those of Mach number, cone angle, nose bluntness and Reynolds number) is based on correlations by Taub³ of wind tunnel and ballistic range data for sharp and blunted cones at zero incidence in rarefied hypersonic flow. It was found that the results correlated well when plotted in terms of two parameters \bar{C}_D and \bar{U} , which are defined as

$$\bar{C}_D = \frac{C_D}{\sin^2 \theta (1 + 0.3758^2)}$$

and

$$\bar{U} = \frac{(1 + 0.4T_w/T_0) \cos \theta}{(1 + 0.3758^2) \sin^2 \theta} M_\infty \left(\frac{C_x}{Re_{w,d}} \right)^{\frac{1}{2}}$$

where $\beta = \psi / \sin \theta$

and C_x is a coefficient defined as $C_x = \mu_x T_w / \mu_\infty T_\infty$,

with

$$T_x = \frac{T_0}{6} \left(1 + 3 \frac{T_w}{T_0} \right)$$

Taub also estimates a 'hypersonic limit' which all data for $\bar{M} > 4$ reach. This limit is defined by the equation

$$\bar{C}_D = 2 + 1.68\bar{U} + 1.66 \times 10^{-2}\bar{U}^2 + 4.5 \times 10^{-4}\bar{U}^3$$

and the parameter \bar{M} is defined as

$$\bar{M} = M_\infty \sin \theta (1 + 0.3758^2)^{\frac{1}{2}}$$

Some of the present data are plotted on a graph of \bar{C}_D against \bar{U} (Fig 6). Also shown is the estimated 'hypersonic limit'. Taub suggests that curves exist for each value of \bar{M} until the hypersonic limit is reached. Some of the present data are plotted in an attempt to show the effect of \bar{M} . From the $\theta = 7^\circ$ data, it can be seen that the $\psi = 0.2$ cases lie between those for $\psi = 0$ and $\psi = 0.5$. The other data selected for this graph were for $\theta = 4^\circ$ and 10° and $\psi = 0$ and 0.5 . The aim of this was to be able to show the extremes of the various geometric parameters (which corresponded to extremes in values of \bar{M}). It can only be concluded from the effects of the data shown that all the other data will lie

between the limiting values. To plot all the present data would make it impossible to determine the effect of \bar{M} . The correlations produce a reasonable collapse of the data, the worst case, once again, being the $\theta = 4^\circ$ data. However, this value of θ falls outside the range of conditions of the data from which Taub derived the correlations. The data he utilized actually encompassed the ranges: $5^\circ < \theta < 30^\circ$; $0.04 < T_w/T_0 < 1$; $0 < \psi < 0.82$, and $2 < M_\infty < 21.5$. The effects of θ and ψ seem to have been well accounted for in the expression for \bar{M} , although changes in M_∞ are, perhaps, overcompensated for. (This is observed by looking at the data for the same geometry - the $M_\infty = 8.58$ data (lower \bar{M}) lies closer to the hypersonic limit than the $M_\infty = 9.84$ data (higher \bar{M}) for all the geometries shown.) It can only be concluded that this is the reason for the data not lying in ascending order of \bar{M} . However, it may also be an incorrect assessment of the effects of T_w/T_0 in the formulation of the parameters C_p and \bar{U} .

3.4 Comments on correlations

Comparing Figs 5 and 6, it can be seen that with the removal of the $\theta = 4^\circ$ data, the ϕ versus $Kn_{\infty,d}$ graph (Fig 5) produces a better collapse of data than that produced by the correlations of Taub. Although Taub's correlations are some 20 years old and have no physical basis, it can be seen that the present data do not disagree with them. As \bar{M} increases, so the data tends towards the 'hypersonic limit'. There are two criticisms of Taub's correlations. First there is no free molecular limit (value of C_p corresponding to high \bar{U}) as given by kinetic theory, hence the bridging function, ϕ (Kn), is a better physical concept. Secondly, the 'hypersonic limit' ($\bar{M} > 4$) is not realistic, especially for cones with high values of ψ ; for in these cases the criterion is met for M_∞ values < 4 . Although a relation expressing C_p in terms of a power series in \bar{U} , following Taub, could have been derived as a best-fit curve to all the data, it is considered that the ϕ (Kn) relations would be better fits to the present data.

4 DISCUSSION OF BICONIC AND TRICONIC RESULTS

4.1 Measured axial force

The measured axial forces on the triconic body were converted to the usual aerodynamic coefficient form, C_A . The data, for angles of incidence, α , of 0° to 20° , are presented in graphical form in Fig 7. This graph shows C_A plotted against $Kn_{\infty,d}$. It can be seen from this graph that all the measured values of C_A lie between the calculated continuum and free molecular values. The expected trends of C_A increasing with increasing $Kn_{\infty,d}$ and α can clearly be observed. The values of C_A for $\alpha = 5^\circ$ are only slightly greater than those for $\alpha = 0^\circ$, but there are progressively larger increases in these values for $\alpha = 10^\circ$ and 20° . These trends are reflected in the continuum and free molecular values. (The inviscid computational method breaks down at incidences greater than 15° , so C_{A_i} for $\alpha = 20^\circ$ could not be calculated. However, $C_{A_{fm}} = 2.802$ for $\alpha = 20^\circ$.) The magnitude of the changes in C_A with α are comparable to the changes in C_p with ψ for the cones, reported earlier in this paper (over the ranges of α and ψ tested). Again, the $M_\infty = 8.58$ data appear to lie on a lower curve than the $M_\infty = 9.84$ data. This is believed to be due to the effects of Mach number and wall temperature.

4.2 Knudsen number correlations

Since the effects of α (for $0^\circ < \alpha < 20^\circ$) are of the same order as those of ψ (for $0 < \psi < 0.5$), there is no reason why the parameter ϕ should not collapse the C_A data for the triconic body in the same way as it collapses the C_p data for the cones. With ϕ being defined as $\phi = (C_A - C_{A_i}) / (C_{A_{fm}} - C_{A_i})$, changes in the axial force at incidence can be plotted against $Kn_{\infty,d}$. Fig 8 is a graph with ϕ plotted against $Kn_{\infty,d}$ showing the triconic data for $\alpha = 0^\circ$, 5° and 10° , and also the biconic data for $\alpha = 0^\circ$. The effect of α is significantly reduced by the use of the parameter ϕ . In addition, the collapsed data is fitted reasonably well by the bridging function

$$\phi = \frac{(Kn_{\infty,d} + 0.008)(Kn_{\infty,d} + 0.0005)}{(Kn_{\infty,d} + 0.09)(Kn_{\infty,d} + 0.0008)}$$

which was suggested earlier to fit the zero incidence cone data. Hence this shows that the principle of using a bridging function of the form ϕ (Kn) can be extended to cover the axial forces on slender axisymmetric bodies at low angles of incidence.

5 CONCLUSIONS

An experimental investigation has been carried out in the RAE Low Density Tunnel to measure the zero incidence drag of sharp and blunted cones in rarefied hypersonic flow. The effects of a number of geometric and flow parameters on the drag coefficient, C_p , have been determined. The parameters which were varied and their range of values were as follows:

cone half angle, θ	4, 6, 7, 8 and 10°
cone bluntness ratio, ψ	0, 0.1, 0.2, 0.3, 0.4 and 0.5
Mach number, M_∞	8.58 and 9.84
Reynolds number, $Re_{\infty,d}$	80 to 13122
Knudsen number, $Kn_{\infty,d}$	0.0011 to 0.1606
wall to total temperature ratio, T_w/T_0	0.16 to 0.52

The range of $Kn_{\infty,d}$ lies in the transitional rarefied flow regime. The transition referred to is that from continuum to free molecular flow. All measured values of C_D were between the calculated continuum and free molecular limits. As expected, it was found that the effect of increasing $Kn_{\infty,d}$ was to increase C_D . The effect of θ was small, however a cross-over in the C_D traces was observed with the smallest value of θ having the highest value of C_D at the higher values of $Kn_{\infty,d}$. For values of ψ from 0 to 0.2 inclusive the values of C_D were similar, but for $\psi > 0.2$ C_D increased with increasing ψ .

The effects of these various geometric and flow parameters are reduced by plotting the function $\phi = (C_D - C_{D1}) / (C_{D\infty} - C_{D1})$ against $Kn_{\infty,d}$. A second order Knudsen number empirical relationship,

$$\phi = \frac{(Kn_{\infty,d} + 0.008)(Kn_{\infty,d} + 0.0005)}{(Kn_{\infty,d} + 0.09)(Kn_{\infty,d} + 0.0008)}$$

has been suggested to fit the present data. In addition to the zero incidence cone drag, it was found that this relation also fits data for the zero incidence drag of biconic and triconic bodies and the axial force of the triconic body at incidences up to 10° . It is recommended that this relation is used for any calculations related to the zero incidence axial force (ie drag) and low incidence axial force of slender axisymmetric bodies in the transitional rarefied flow regime. The definition of a better bridging function, $\phi(Kn)$, and a greater understanding of the effects of the various parameters requires data at different values of $Kn_{\infty,d}$, M_∞ , α and T_w/T_0 .

In addition to the low incidence axial force there is a need to be able to define changes in other aerodynamic characteristics of slender bodies through the transitional rarefied flow regime. This stems from a requirement to be able to predict the performance of bodies re-entering the Earth's atmosphere. The aerodynamic characteristics required are the axial force coefficient at higher angles of incidence, the normal force coefficient at angles of incidence, the centre of pressure position at angles of incidence, and heat transfer rates at zero and non-zero angles of incidence. The limited data obtained so far from the Low Density Tunnel does not cover a wide enough range of $Kn_{\infty,d}$ to be able to ascertain the effects of the various geometric and flow parameters on these other aerodynamic characteristics. It is hoped to carry out the study of these complementary characteristics over a wider range of $Kn_{\infty,d}$ in the near future.

Copyright ©, Controller HMSO London, 1987

REFERENCES

- 1 J.L. Potter, 'The transitional rarefied-flow regime. Fifth International Symposium on rarefied gas dynamics.' Oxford (1966)
- 2 R.E. Geiger, 'Slender-cone, zero angle of attack drag in continuum and non-continuum flow.' AIAA Paper No.69-711 (1969)
- 3 P.A. Taub, 'Hypersonic, low-density sphere and cone drag correlations.' GASL Technical Report 683 (1967)
- 4 J.D. Gray, 'Summary Report on aerodynamic characteristics of standard models HB-1 and HB-2.' AEDC-TDR-64-137 (1964)
- 5 D.R. Crawford, 'Wall temperature effects on the zero-lift viscous drag of blunted cones in rarefied supersonic flow.' University of California AS-65-15 (1965)
- 6 A.M. Morrison, J.M. Solomon, M. Ciment, R.E. Ferguson, 'Handbook of inviscid sphere-cone flow fields and pressure distributions - Vol II.' NSWC/WOL/Technical Report 75-45 (1975)
- 7 J.M. Solomon, M. Ciment, R.E. Ferguson, J.B. Bell, A.B. Wardlaw, Jr, 'A program for computing steady inviscid three-dimensional supersonic flow on re-entry vehicles.' NSWC/WOL/Technical Report 77-28 (1977)
- 8 A.G. Keel, L.G. Kraige, R.D. Passmore, R.N. Zapata, 'Hypersonic low density cone drag.' AIAA Paper No.71-133 (1971)
- 9 G.A. Dahlen, 'Cone drag in the transition from continuum to free molecular flow.' PhD Thesis, Jesus College, Oxford (1984)

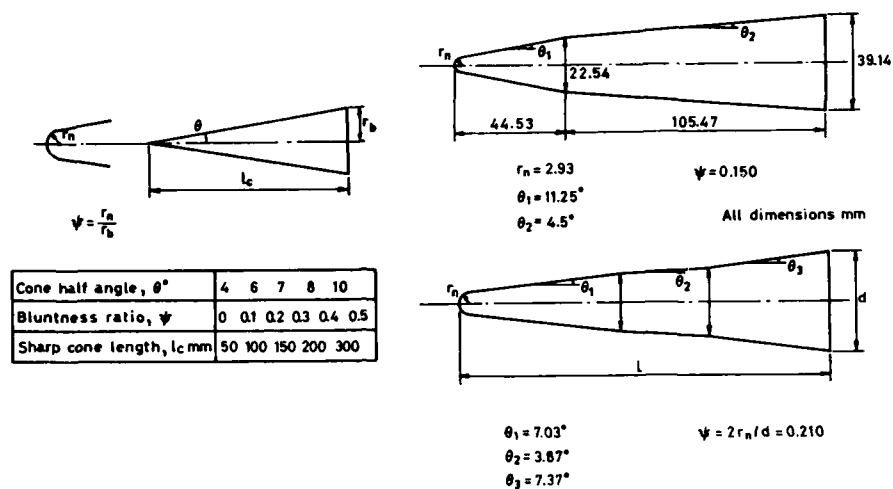
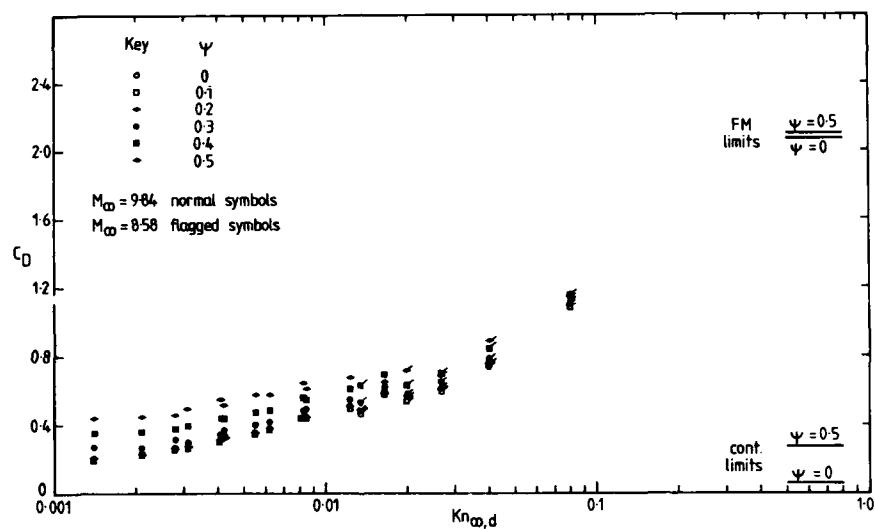


Fig 1 Details of model geometries

Fig 2 Plot of zero incidence drag coefficient against Knudsen number showing data for $\theta = 8^\circ$

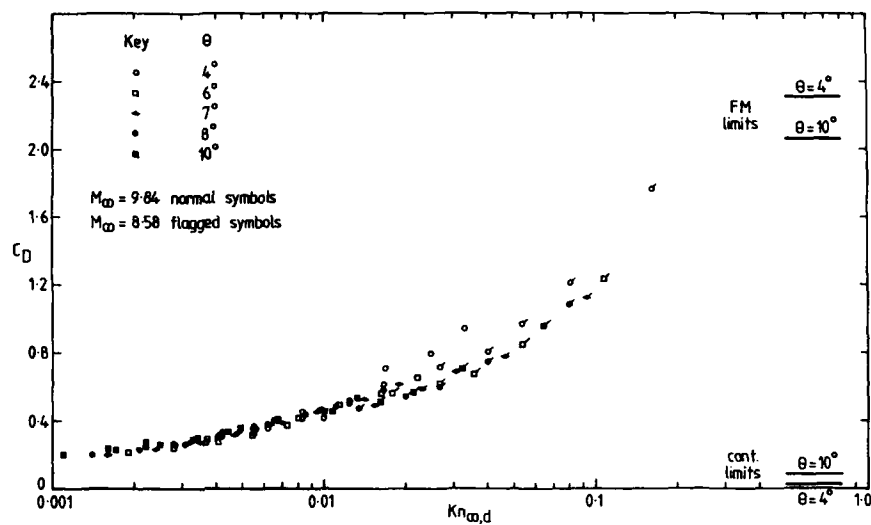


Fig 3 Plot of zero incidence drag coefficient against Knudsen number showing data for $\psi = 0.1$

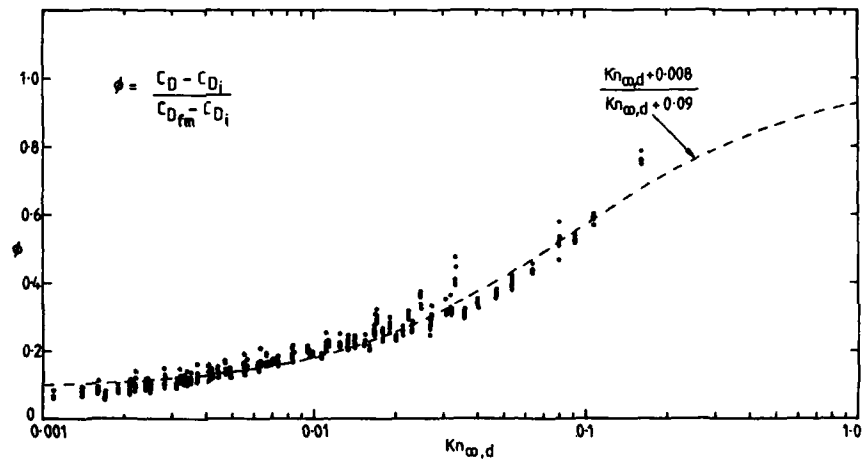
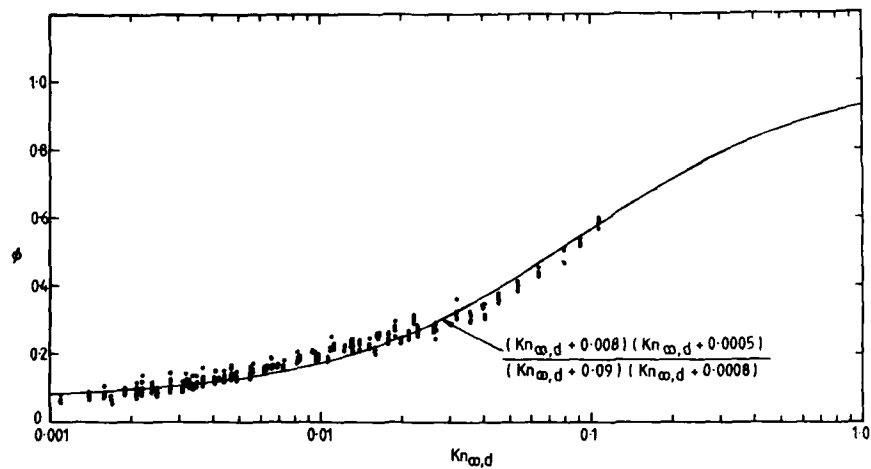
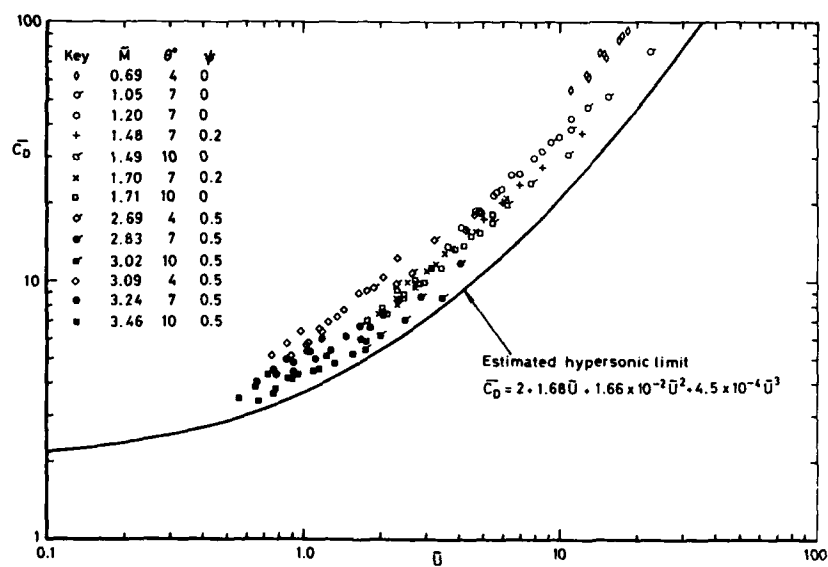


Fig 4 Comparison of all cone data with bridging function

Fig 5 Comparison of cone data (all except $\theta = 4^\circ$) with bridging functionFig 6 \bar{C}_D versus \bar{U} correlation of selected data

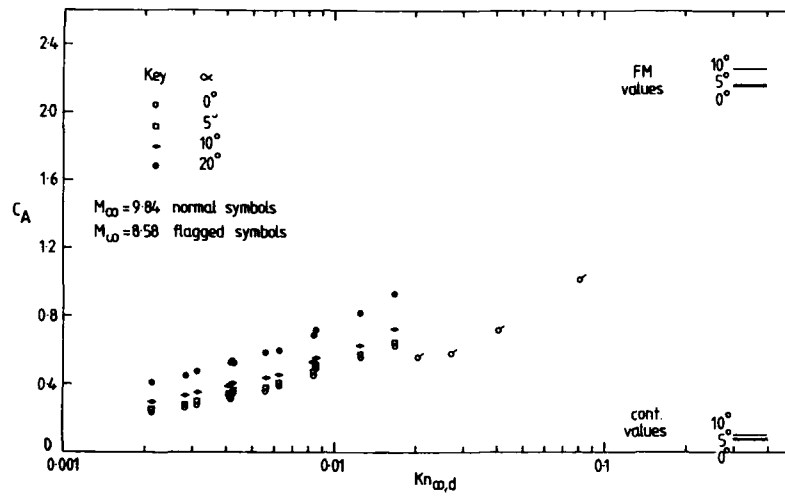


Fig 7 Plot of axial force coefficient against Knudsen number showing triconic data

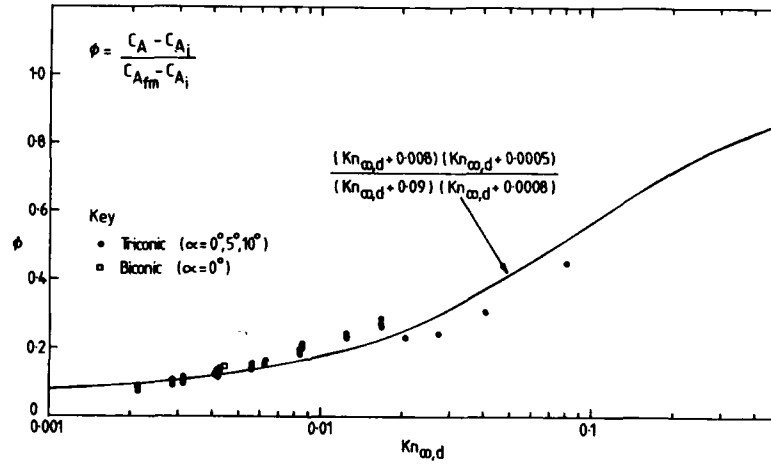


Fig 8 Comparison of biconic and triconic data with bridging function

LOW REYNOLDS NUMBER INFLUENCE ON AERODYNAMIC PERFORMANCE OF HYPERSONIC LIFTING VEHICLES

by

Georg Koppenwallner
Priv.Doiz.Dr.-Ing., Section Head
DFVLR Institute for Experimental Fluid Mechanics
Bunsenstrasse 10, D-3400 Göttingen, F.R.G.

SUMMARY

The aerodynamic performance of lifting reentry vehicles in the high Mach number $Ma > 10$ and high altitude $H > 50$ km regime is analyzed. Due to the high flight velocity chemical reactions and due to the low density viscous and rarefaction effects are of importance. Free flight data of the US-Shuttle and low density wind tunnel data of DFVLR are used. It is found that aerodynamic performance loss and a destabilizing pitching moment change can be explained by viscous-rarefaction effects.

LIST OF SYMBOLS

c_A	axial force coefficient
c_N	normal force coefficient
c_D	drag coefficient
c_L	lift coefficient
c_M	pitching-moment coefficient; $c_M = \frac{M}{c \cdot q_\infty \cdot S}$ or $c_M = \frac{M}{I \cdot q_\infty \cdot S}$
CP	center of pressure
\bar{c}	reference chord length
d	diameter
H	altitude
Kn	Knudsen number; $Kn = \frac{\lambda_\infty}{l}$ or $\frac{\lambda_\infty}{d}$
L_{ch}	chemical relaxation length
l	body length
Ma	Mach number
Re	Reynolds number based on vehicle length l if not otherwise stated
S	plane form area
Sc	scale
v	flight velocity
V, \bar{V}	viscous parameter; $V = \frac{Ma}{\sqrt{Re}}$, $\bar{V} = \sqrt{C} \cdot \frac{Ma}{\sqrt{Re}}$
x	coordinate in length direction
x_p	center of pressure coordinate
x_M	moment reference point coordinate
α	angle of attack
λ	molecular mean free path
δ	boundary layer thickness
η	flap deflection, positive downward

Indices

∞	free stream
l	conditions at body length l

1. INTRODUCTION

The aerodynamic performance of hypersonic reentry vehicles is strongly influenced by viscous and chemical relaxation effects in the high altitude flight regime. Reentry starts with orbital velocity of 7.6 km/s at near free molecular flow conditions. In the initial deceleration phase the aerodynamic forces and moments are small due to the low air density. The aerodynamic lift is also small when compared to the centrifugal force acting on the vehicle. Therefore vehicle stabilization and control must be performed by reaction control jets. In the main deceleration phase from $v = 7$ to 3 km/s the aerodynamic forces, moments, and heating are however most important.

In this part of the trajectory with $v \geq 3$ km/s and $H > 50$ km the flow around the vehicle is dominated by

- Hypersonic high Mach numbers $Ma > 10$
- Laminar viscous and rarefaction effects $V = Ma/\sqrt{Re} > 0.005$
- Chemical reactions and nonequilibrium.

Figure 1 shows for a typical reentry trajectory the lower limits for the regions of

- high Mach number flow
- laminar and rarefied viscous flow
- chemical reactive flow.

It is evident that the three regions overlap each other which means that the aerodynamic behaviour of a vehicle will be determined by all three phenomena and its mutual interaction. This region is sometimes called 'real gas flow' regime.

Unfortunately the present state of wind tunnel technology and theoretical methods does not allow a combined simulation of the three phenomena. Therefore free flight data as obtained from shuttle flights and studies of the single effects with an appropriate synthesis are the only way to obtain more insight and to improve the prediction methods.

In the following contribution we will investigate the influence of laminar viscous and rarefaction effects on the aerodynamics of reentry vehicles. Primary emphasis will be put on the pitching moment because the US-Shuttle flight data showed an unpredicted behaviour. Wind tunnel measurements performed in the DFVLR hypersonic low density tunnels on various reentry configurations will be used to analyse high Mach number viscous and rarefaction effects. The main question to be addressed is: Can the shuttle pitching moment behaviour be attributed to chemical real gas effects as presently stated in the literature or will it be caused by viscous low density effects?

2. SHUTTLE FLIGHT RESULTS AND EXPLANATIONS FROM LITERATURE

After the first flights of the US Shuttle NASA started an extensive study to compare the preflight prediction of aerodynamic characteristics with the inflight measurements.

The preflight aerodynamic predictions are based on 27000 wind tunnel occupancy hours and utilized semi-empirical methods to correct for incomplete simulation in the tunnels. As result of these studies and additional theoretical work the Aerodynamic Design Data Book (ADDB) was established. The ADDB is the basis for shuttle preflight aerodynamic prediction [1]. An excellent review of preflight estimates of real gas effects is given by Woods, Arrington and Hamilton [2].

The complex problem to model the hypersonic flow with viscous, low density, real gas chemistry and relaxation, could not be solved and the following conventional approach was taken.

a) Hypersonic viscous and rarefaction effects

The theoretical approach was to use inviscid hypersonic calculations complemented with viscous laminar boundary layer corrections and the resulting viscous inviscid interactions.

The experimental approach was based on results of conventional hypersonic wind tunnels.

b) Hypersonic real gas and relaxation effects

The theoretical approach was based on inviscid equilibrium air chemistry calculations. Good agreement was found between equilibrium real air chemistry and ideal gas calculations using an effective specific heat ratio of $\gamma = 1.12$. This agreement served as justification for the use of Freon as operating gas in the Langley LaRC CF_4 -hypersonic tunnel.

Relaxation effects of the chemistry were not included in theoretical prediction methods. Besides of the above mentioned Langley facility the CALSPAN Shock Tunnels served as the main tunnels to investigate real gas effects.

2.1 The shuttle flight results

The shuttle prediction, the flight data evaluation, and the post flight comparison is summarized in 'Shuttle Performance: Lessons Learned [3]' and in the following publications [4, 5, 6, 7]. Figure 2 gives the shuttle entry trajectory in a Mach-Reynolds diagram. Also included are the angle of attack α and altitude as function of flight Mach number Ma_∞ . It is important to note that during the deceleration phase the angle of attack is kept constant at $\alpha = 40^\circ$ for $Ma_\infty \geq 12$. Mach-12 is obtained at $H = 53$ km with a viscous parameter of $V_\infty = 0.005$. The hypersonic high altitude region where severe discrepancies between prediction and flight have been found is the flight trajectory with $Ma_\infty \geq 12$ and $V_\infty \geq 0.005$. Only the prediction of the aerodynamic force coefficients agreed well with the flight results, as may be seen from Figure 3 showing L/D, Lift and Drag as function of flight Mach number. A large disagreement was found for the pitching moment c_M behaviour.

Figure 4 shows the trimmed c_M during flight, which must be zero, and the predicted c_M using the flight conditions, i.e. actual flap deflections. It is seen that the difference between prediction and flight is $\Delta c_M = +0.03$ for $Ma_\infty > 15$. Deviation exists for $Ma_\infty \leq 10$. The errorband for prediction becomes very large at Mach numbers above $Ma_\infty = 18$, which is due to the scatter in the wind tunnel tests.

In order to trim the shuttle with the unexpected $\Delta c_M = 0.03$ during the STS 1 flight the body flap had to be deflected by the double of its nominal value, namely 15° instead of 7.5° . This unpredicted moment behaviour is typical for all shuttle flights as shown in 6, where the Space Shuttle flights No. 1 up to No. 8 have been analyzed. The Δc_M error at Mach 20 between data handbook prediction and flight has average values of $\Delta c_M = 60 - 80\%$. The nose up pitching moment in this high Mach number flight regime causes a center of pressure shift to the nose by $\Delta x_p/l = 0.7$. The nominal center of pressure locations is at $x_p/l = 0.668$.

2.2 Review of published explanations for the shuttle pitching moment behaviour

The inability to predict the pitching moment behaviour of the shuttle with the aerodynamic design data book (ADDB) initiated in the US a strong activity to find explanations [3, 5, 7]. It is generally agreed that the Δc_M behaviour must be explained by the high velocity real gas and the low Reynolds number viscous effects, which are not properly included in the ADDB.

Griffith, Maus, and Best published [5, 8] their methodology model for improved prediction. According to this model the actual flight pitching moment c_M is predicted by three additive corrections Δc_{M_i} to a standard hypersonic c_M , which essentially represents the inviscid case at fixed Mach number, namely $Ma_\infty = M_8$.

$$c_{M \text{ Flight}} = (c_M)_{\text{inviscid}} + \sum_1^3 \Delta c_{M_i}$$

$$\Delta c_{M1} = \Delta c_M \text{ (Mach number effects)}$$

$$\Delta c_{M2} = \Delta c_M \text{ (real gas effects)}$$

$$\Delta c_{M3} = \Delta c_M \text{ (viscous effects).}$$

The Δc_M correction terms were obtained in the following way:

Mach number effects, $\Delta c_{M, \text{Mach}}$

Ideal inviscid gas flow calculations for Mach numbers between $Ma = 8$ and 23 using the CM3DT/STEIN computer codes.

Real gas effects, $\Delta c_{M, \text{real gas}}$

Inviscid equilibrium air flow calculations for the actual flight conditions using the CM3DT/STEIN computer codes.

Viscous effects, $\Delta c_{M, \text{viscous}}$

Fully viscous computations for a modified Orbiter geometry using parabolized Navier Stokes codes. In addition a semi-empirical correction as shown in Figure 5 was used. In this semi-empirical approach it is assumed that viscous forces act only on the lower wing surface of the Orbiter.

Using this methodology model Griffith, Maus, and Best recalculated the c_M behaviour of the shuttle for the entry flight conditions, which is shown in Figure 6. According to these calculations Mach number and real gas effects produce nose up Δc_M contributions, whereas viscous effects produce a nose down Δc_M contribution. If all three contributions are summed up a total moment change of $\Delta c_M = 0.03$ results, which agrees with the flight results.

This agreement lead to the conclusion that the methodology model is appropriate and that real gas effects mainly influence the pitching moment. At $\alpha = 40^\circ$ the $\Delta C_M, \text{real gas} \approx 0.025$ as can be seen from Figure 6.

2.3 Critical remarks

At first it shall be remembered that agreement of a prediction method using additive correction terms with free flight data does not necessarily mean that each correction term was calculated right. There exists an infinite number of correction term combinations giving the same answer.

The real gas effect treatment

For shuttle flight conditions with $V_\infty = 0.001$ to 0.03 the treatment of real gas effects with equilibrium chemistry is due to the following argument in adequate. The viscous parameter V_∞ represents a Knudsen number based on the molecular mean free path and the boundary layer thickness δ , namely $V_\infty = Ma/\sqrt{Re} = \lambda_\infty/\delta$. It is well known that chemical reactions need much more molecular collisions to approach equilibrium than a purely gas dynamic change of state. This means that the ratio of chemical relaxation length L_{ch} to boundary layer thickness $L_{ch}/\delta \gg \lambda_\infty/\delta$. If we assume $L_{ch} = 100 \lambda_\infty$ the chemical relaxation length will vary from $L_{ch} = 0.1\delta$ to $L_{ch} = 3\delta$ in the flight regime with $V_\infty = 0.001$ to 0.03 . This means that this viscous flow regime is connected with chemical nonequilibrium effects at high velocities.

The viscous effect treatment

The simplified treatment of these effects as shown in Figure 5 neglects the viscous shear of the cross flow in the nose region. This viscous shear is large due to the small Reynolds number at the nose region and acts also on a large lever arm. The nose region shear shall contribute a nose up pitching moment contrary to the lower surface shear. To neglect the nose region seems therefore questionable.

Figure 7 summarizes the phenomena, which seem improperly modeled in the methodology method.

A definite answer how real gas effects and how the viscous low density effects influence the pitching moment behaviour can only be found by exact calculations or by experiments which simulate these phenomena separately. In the following we will go the experimental way and analyse wind tunnel data obtained at DFVLR Göttingen during the years 1972-74, also in the early shuttle development phase.

3. MODEL SHAPES, WIND TUNNELS AND TEST CONDITIONS AT DFVLR

The ART configurations

These configurations were defined within the German Reentry Technology Program (ART) [9]. The shape ART 04A had external lateral fins whereas the shape 04B had two central fins.

Figure 8 shows the wind tunnel models with a scale of 1:50 tested in the DFVLR Vacuum Wind Tunnels. Models with a scale of 1:41 were tested in the Göttingen Ludwig Tube Tunnels.

The Shuttle-Orbiter models

An early shape of the US Shuttle was also tested. This configuration, the NASA M2 040 A Orbiter, is shown in Figure 9. The canopy and the simple delta shape of the wing have been changed on the final Orbiter configuration.

Wind tunnels and test conditions

The hypersonic low Reynolds number studies were conducted in the DFVLR hypersonic vacuum tunnel V10 [10]. This tunnel allows operation in a Mach 7 and Mach 20 mode. The test conditions covered are summarized in Table 1. The high Reynolds number tests were conducted in the Ludwig Tube Tunnels [11] at Göttingen. For the ART models the viscous parameter V_∞ was varied between 0.0063 and 0.1. Figure 10 shows the test conditions in a Mach-Reynolds diagram with the corresponding trajectory.

For the 040 A Orbiter model only the low Reynolds high Mach number data were obtained at DFVLR. For the high Reynolds number and lower Mach range wind tunnel results from NASA Langley Tunnels LaRC 31'CFHT and LaRC 20'Be served for comparison.

4. TYPICAL AERODYNAMIC PERFORMANCE IN THE HIGH MACH NUMBER VISCOUS AND RAREFIED FLOW REGIME

From drag and pressure distribution measurements on simple shaped blunt bodies [12] it is well known that with decreasing Reynolds number the viscosity and rarefaction tend first to increase the skin friction, and then at Reynolds numbers about one magnitude lower the surface pressure will be affected. It is also known that in this flow regime where primarily skin friction is influenced the appropriate scaling parameter is the viscous parameter V_∞ , which is a Knudsen number based on the boundary layer thickness δ , namely

$$V_{\infty} = Ma_{\infty} / \sqrt{Re_{1\infty}} = \lambda_{\infty} / \delta_1$$

As an illustrative example for this behaviour may serve our pressure- and frictional drag measurements [13] on cylinders shown in Figure 11. This different strong dependence of friction and pressure on the viscous parameter V_{∞} will help to explain the aerodynamic behaviour of lifting reentry vehicles in the high Mach- and low Reynolds number regime.

4.1 The ART-configurations

A synthesis of wind tunnel results on the ART 24B shape is shown in Figures 12 and 13. The data are taken from [14, 15] and cover a range from $V = 0.006$ to $V = 0.1$. At small angles of attack the lift coefficient is quite independent from V_{∞} whereas at higher α a reduction of C_L with increasing V_{∞} is observed. This reduction is mainly due to the viscous forces.

The viscous influence on the drag shows a different behaviour with angle of attack. At $\alpha = 0$ a large increase of the drag with V is observed, whereas at high α this influence is smaller. At high α mainly pressure forces determine the drag, which are in this flow regime not strongly influenced by viscous effects.

The gliding capability, i.e. the L/D ratio is strongly reduced with increasing V (Figure 13). At $V_{\infty} = 0.006$ we have $(L/D)_{\max} = 2.1$, which is approximately the inviscid Newtonian value. At $V_{\infty} = 0.096$ the $(L/D)_{\max}$ is reduced to 1.1. It should be pointed out that at free molecular conditions, which are approached at $V_{\infty} = 8$ for $Ma_{\infty} = 20$ the lift-drag ratio will drop to $L/D = 0$.

This viscous rarefaction effects strongly influence the longitudinal stability as can be seen from Figure 13. With V_{∞} increasing from 0.006 to 0.1 the slope $dc_M/d\alpha$ becomes smaller and a nose up moment contribution $+\Delta c_M$ is observed. At $\alpha = 30^\circ$ the viscous induced change of c_M amounts to $\Delta c_M = 0.03$.

The pitching moment of the configuration 24A, Figure 14, shows the same dependence on the viscous parameter as the shape 24B.

Figure 15 shows for both ART shapes the $(L/D)_{\max}$ reduction and the drag increase in the viscous rarefied regime. It is evident that the viscous parameter V_{∞} scales these integral aerodynamic data quite well.

The very strong influence of the viscous effects on aerodynamic stability and control is shown in Figure 16. Flap effectiveness is reduced by 50 % and a nose up moment of $\Delta c_M = 0.03$ is induced at $Ma/\sqrt{Re} = 0.1$.

4.2 The 040A-Orbiter configuration

The DFVLR test results in the hypersonic vacuum wind tunnels were obtained in September 1983 at a stage when European participation in the shuttle development was still under discussion. The results have until now not been published. The complementary high Reynolds number data from NASA Langley facilities are taken from a US Memo No SSPO E241-696 from 1972.

Tests were conducted on the basic configuration without flap deflection and the external OMS-pods.

In Figures 17, 18, 19 the low Reynolds number DFVLR results are compared with the high Reynolds number US wind tunnel results. Both sets of data cover a $Ma_{\infty}/\sqrt{Re_{\infty}}$ range from 0.01 to 0.12. It is evident that viscous effects reduce the lift and normal force and increase drag and axial force. The viscous $(L/D)_{\max}$ loss amounts to 50 % as can be seen from Figure 19. A very strong nose up influence on the pitching moment is again evident from Figure 19.

An extracted aerodynamic vehicle behaviour at $\alpha = 25^\circ$ is shown in Figure 20 as function of the viscous parameter Ma/\sqrt{Re} . Calculations with Newtonian theory predict the aerodynamic coefficients with exemption of c_M quite well for the high Reynolds number ($Ma_{\infty}/\sqrt{Re_{\infty}} < 0.01$) limit. Viscous effects show with increasing $Ma_{\infty}/\sqrt{Re_{\infty}}$ the same influence as found on the ART configurations, namely L/D loss, increase of axial force and a nose up pitching moment change Δc_M .

4.3 Qualitative explanation of moment and center of pressure shift

All our experiments on reentry vehicles demonstrate that in the viscous slip flow region at $Ma_{\infty}/\sqrt{Re_{\infty}} > 0.01$ and at high angles of attack a nose up pitching moment Δc_M will exist. This nose up pitching moment causes a forward shift of the center-of-pressure.

A simple explanation can be given by following arguments:

In the forebody region of these vehicles the flow is more rarefied and therefore the shear of the cross flow on the lateral surfaces is larger than the shear on the further aft wing. This larger shear acts on a long lever arm and produces a nose up pitching moment.

To quantify these arguments it would be useful to have pitching moment or center of pressure data of simple bodies in the range from continuum to free molecular flow.

Due to the lack of experimental and theoretical simulation no relevant data exist.

In a semi-empirical way we can however analyse the center of pressure behaviour of cones at $\alpha = 90^\circ$. This CP behaviour will approximately be representative for the CP behaviour of a reentry vehicle at high angles of attack.

In inviscid continuum ($Ma/\sqrt{Re} \ll 1$) and in free molecular flow $Ma/\sqrt{Re} > 1$ all flow properties on a cone are constant on rays from the cone apex. Therefore the center of pressure position will be given by the center of the flow projected area, which is at $x_p/l = 2/3$.

To determine the CP position in the transitional flow regime we introduce a local drag coefficient $c_p'(x)$ which we set equal to c_p of a cylinder with diameter equal to the local cone diameter d . In Figure 21 this procedure is explained. During transition from continuum to free molecular flow the local drag coefficient on the cone apex will be higher than on the cone base. Therefore a forward shift of the CP will occur, which shall vanish when free molecular flow on the whole cone exists. Figure 22 shows the result of a CP calculation with the outlined method. Within the rarefied transitional flow regime the center of pressure moves from $x_p/l = 0.666$ forward to $x_p/l = 0.645$ and then back to $x_p/l = 0.666$. The maximum shift is about $\Delta(x_p/l) = -0.02$, which is about three times the value observed during shuttle reentry. This example supports our arguments concerning the viscous influence on the shuttle.

5. CONCLUSIONS

Wind tunnel experiments and qualitative arguments show that the aerodynamic performance of reentry vehicles is strongly influenced by viscous low density effects. It is of importance to note that the nose up pitching moment change of the shuttle at high altitudes can be explained by viscous rarefaction effects. This is in contradiction to other studies which concluded that real gas effects should cause this pitching moment change. These studies however were based on equilibrium chemistry, which is doubtful to exist in the low density flight regime.

To obtain additional understanding studies of the aerodynamic behaviour of some basic shapes with separated influence of viscous low density and chemical nonequilibrium effects would be very useful.

6. REFERENCES

- [1] Aerodynamic Design Data Book, Vol. 1, Orbiter Vehicle. Rockwell International.
- [2] W.C. Woods, J.P. Arrington, H.H. Hamilton, A Review of Preflight Estimates of Real-Gas Effects on Space Shuttle Aerodynamic Characteristics. In Shuttle Performance: Lessons Learned, NASA Conference Publication 2283, 1983, pp.209-246.
- [3] J.D. Arrington, J.J. Jones, Shuttle Performance: Lessons Learned, NASA Conference Publication 2283, Part 1, 1983.
- [4] P.O. Romere, J.C. Young, Space Shuttle Entry Longitudinal Aerodynamic Comparisons of Flight 2 with Preflight Predictions. AIAA J. Spacecraft, Vol. 20, No. 6, 1983, pp.518-523.
- [5] J.R. Maus, B.J. Griffith, K.Y. Szema, J.T. Best, Hypersonic Mach Number and Real Gas Effects on Space Shuttle Orbiter Aerodynamics. AIAA J. Spacecraft, Vol. 21, No. 2, 1984, pp.136-141.
- [6] J.T. Findlay, G.M. Kelly, J.G. McConnell, Shuttle "Challenger" Aerodynamic Performance from Flight Data - Comparisons with Predict Values and "Columbia" Experience. AIAA Paper 84-0485, AIAA 22nd Aerospace Science Meeting, Jan. 1984, Reno/Nevada.
- [7] R.L. Calloway, Real-Gas Simulation for the Shuttle Orbiter and Planetary Entry Configurations Including Flight Results. AIAA Paper 84-0489, AIAA 22nd Aerospace Sciences Meeting, Jan. 1984, Reno/Nevada.
- [8] B.J. Griffith, J.R. Maus, J.T. Best, Explanation of the Hypersonic Longitudinal Stability Problem - Lessons Learned. In Shuttle Performance: Lessons Learned, NASA Conference Publication 2283, 1983, pp.347-380.

- [9] W. Wuest,
Review of German Work on Controlled Reentry Technology.
Progr. Aerospace Sc., Vol. 20, 1983, pp.217-318.
- [10] W. Wuest, G. Koppenwallner, G. Hefer, H. Legge,
Der Hypersonische Vakuumwindkanal der Aerodynamischen Versuchsanstalt Göttingen.
Jahrbuch 1969 der DGLR, pp.38-52.
- [11] H. Ludwig, Th. Hottner, H. Grauer-Carstensen,
Der Rohrwindkanal der Aerodynamischen Versuchsanstalt Göttingen.
Jahrbuch 1969 der DGLR, pp.52-58.
- [12] G. Koppenwallner, H. Legge,
Drag of Bodies in Rarefied Hypersonic Flow.
Thermophysical Aspects of Re-entry Flows. Vol. 103, Progress in Astronautics
and Aeronautics, pp.44-59, AIAA, New York, 1986.
- [13] G. Koppenwallner,
Experimentelle Untersuchung der Druckverteilung und des Widerstands von quer-
angeströmten Kreiszylindern bei hypersonischen Machzahlen im Bereich von
Kontinuums- bis freier Molekularströmung.
Zeitschrift für Flugwissenschaften, 17 (1969), Heft 10. Braunschweig: Vieweg.
- [14] P. Krogmann,
Sechskomponentenmessungen an den Modellen ART 24A und ART 24B bei $Ma_\infty = 6,8$
und $10,3$ im Rohrwindkanal der DFVLR-AVA.
DFVLR Report IB 251-73 C 04, Göttingen, 1973.
- [15] G. Koppenwallner,
Kraftmessungen an den Versionen A und B des Wiedereintrittskörpers ART 24
im hypersonischen Vakuumwindkanal.
DFVLR Report IB 252-74 H 09, Göttingen, 1974.

Table 1. Summary of test conditions

Wind tunnel	Model	Ma_∞	Re_∞	$Ma_\infty / \sqrt{Re_\infty}$
Vacuum V1G	ART 24A	~ 7	$7.8 \cdot 10^3$	0.08
		~ 20	$(42-144.6) \cdot 10^3$	0.1 - 0.05
	ART 24B	~ 7	$(7.8-27.3) \cdot 10^3$	0.08- 0.04
		~ 20	$(40-149) \cdot 10^3$	0.1 - 0.05
	040A Orb.	~ 7 ~ 22	$(34-60) \cdot 10^3$	0.12- 0.089
Ludwig Tube	ART 24A	6.83	$1.2 \cdot 10^6$	0.0063
		10.3	$8.1 \cdot 10^5$	0.011
	ART 24B	6.83	$1.2 \cdot 10^6$	0.0063
		10.3	$8.1 \cdot 10^5$	0.011

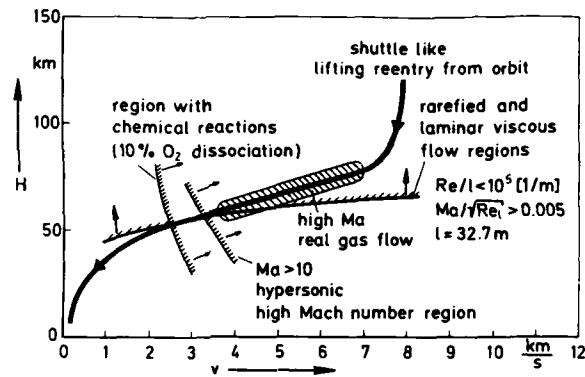


Figure 1. Typical reentry trajectory and the high Mach number real gas flow region.

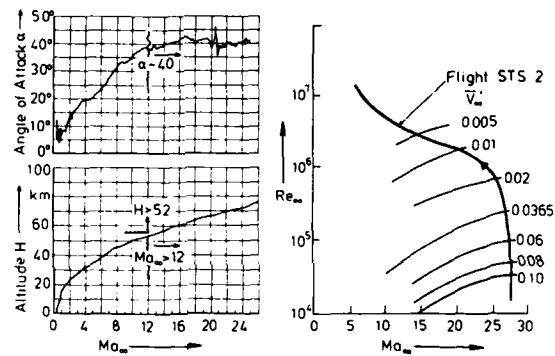


Figure 2. Typical shuttle reentry conditions angle of attack α , altitude H and Reynolds number as function of Mach number Ma .

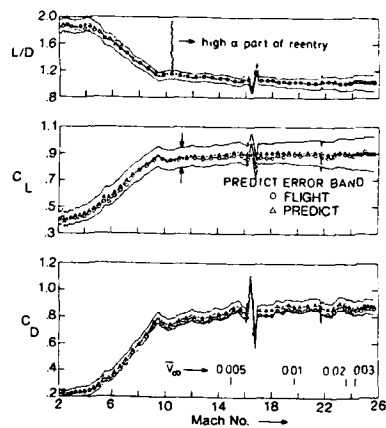


Figure 3. STS 5 aerodynamic performance comparison between prediction and flight.

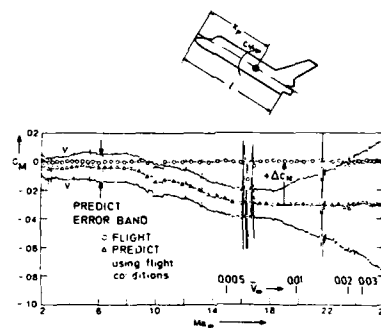


Figure 4. STS 5 pitching moment c_m behaviour comparison between predict and flight. Trimmed flight $c_m = 0$.

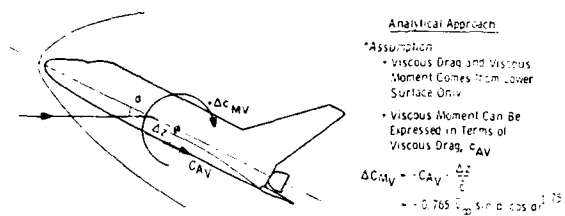


Figure 5. Viscous contribution ΔC_{M_V} to pitching moment according to methodology model of Griffith, Maus, Best. C_{AV} is viscous axial force acting only on the lower surface.

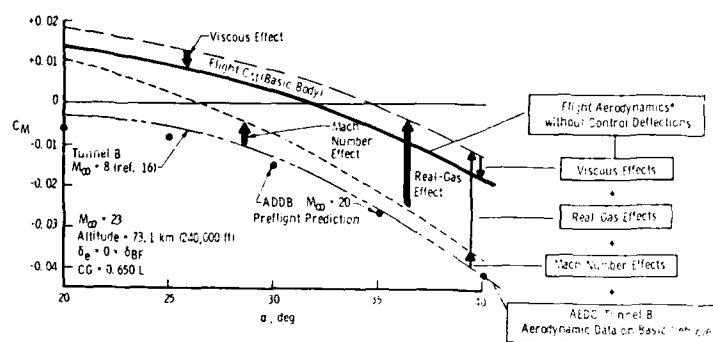


Figure 6. Build up of flight C_M using methodology model, according to Griffith, Maus, Best.

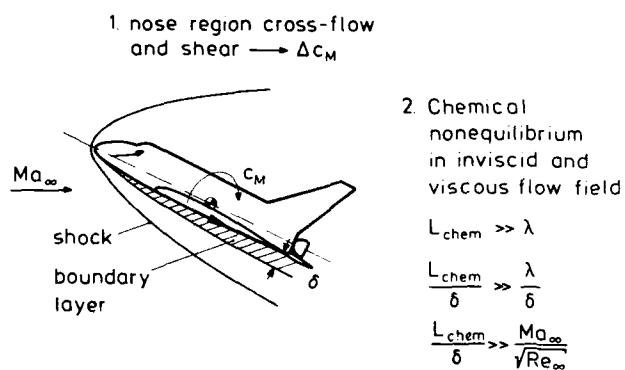


Figure 7. Phenomena improperly modeled in the methodology method.

λ = mean free path

L_{ch} = chemical relaxation length

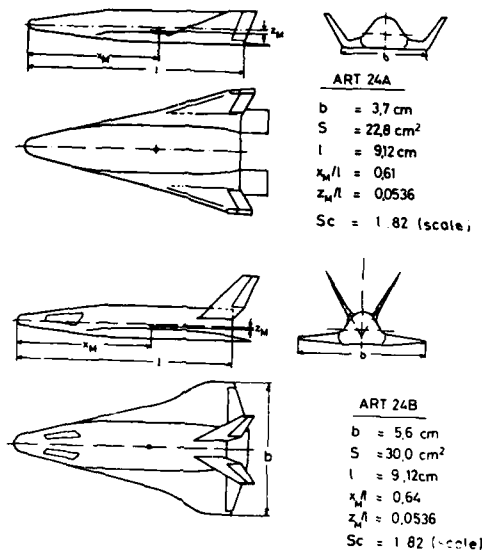


Figure 8. Wind tunnel models of the reentry configurations 24A and 24B.

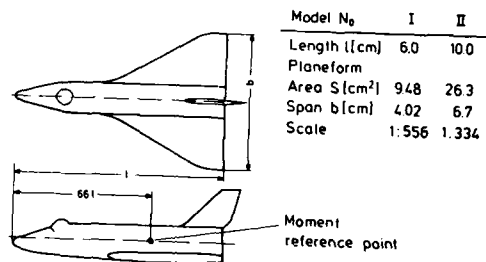


Figure 9. 040A base-line orbiter dimensions of models for DFVLR Vacuum Tunnels.

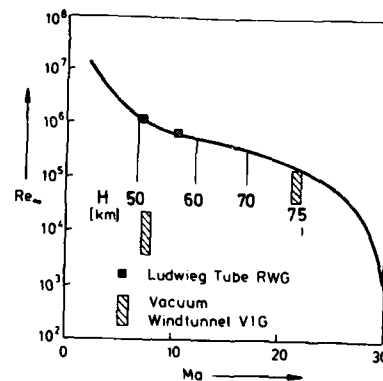


Figure 10. ART 24 reentry trajectory and test conditions.

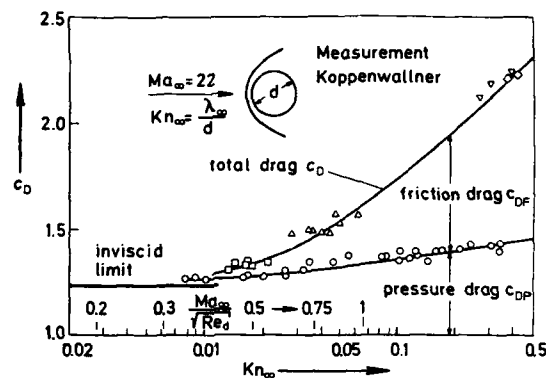


Figure 11. Pressure and friction drag of a cylinder in the rarefied flow regime.

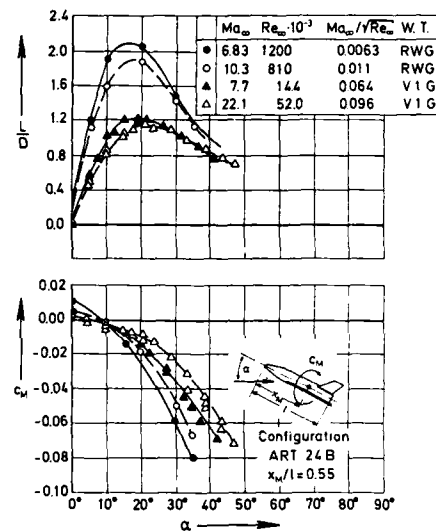
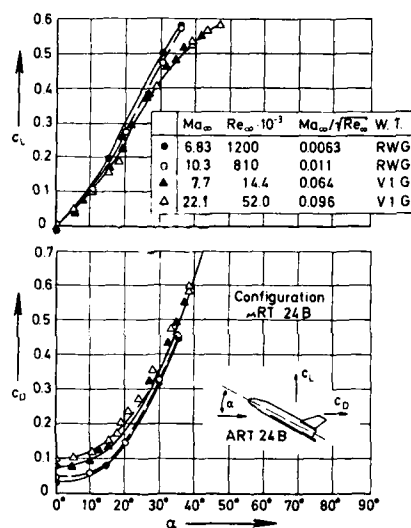


Figure 12. Lift and drag coefficients of ART 24B. Influence of viscous effects.

Figure 13. Lift-drag ratio and pitching moment of ART 24B. Influence of viscous effects.

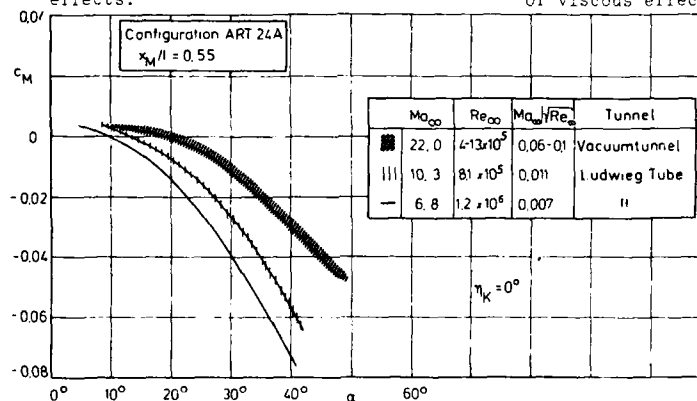


Figure 14. Pitching moment of ART 24A shape at various values of the viscous parameter $V_\infty = Ma_\infty / \sqrt{Re_\infty}$.

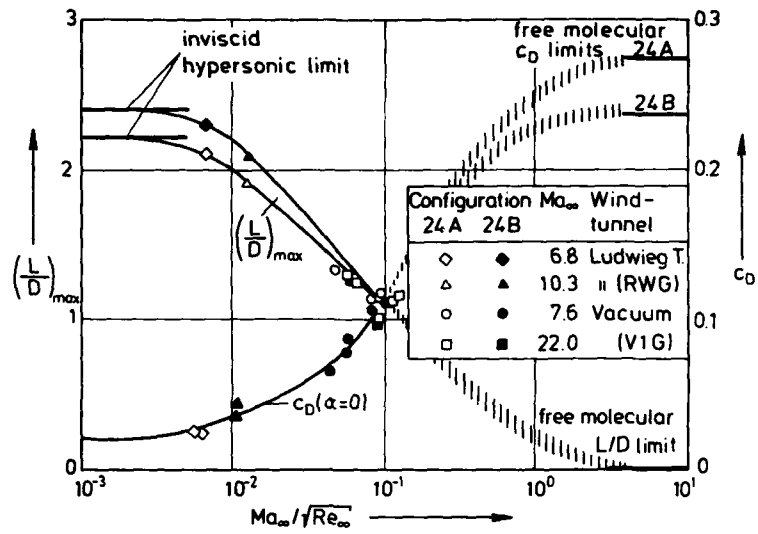


Figure 15. L/D and drag of the ART configurations as function of the viscous parameter.

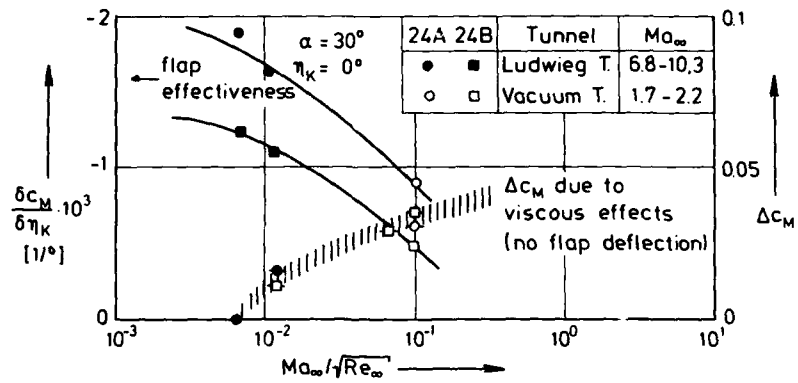


Figure 16. Reduction of flap effectiveness and change of pitching moment ΔC_M due to viscous effects.

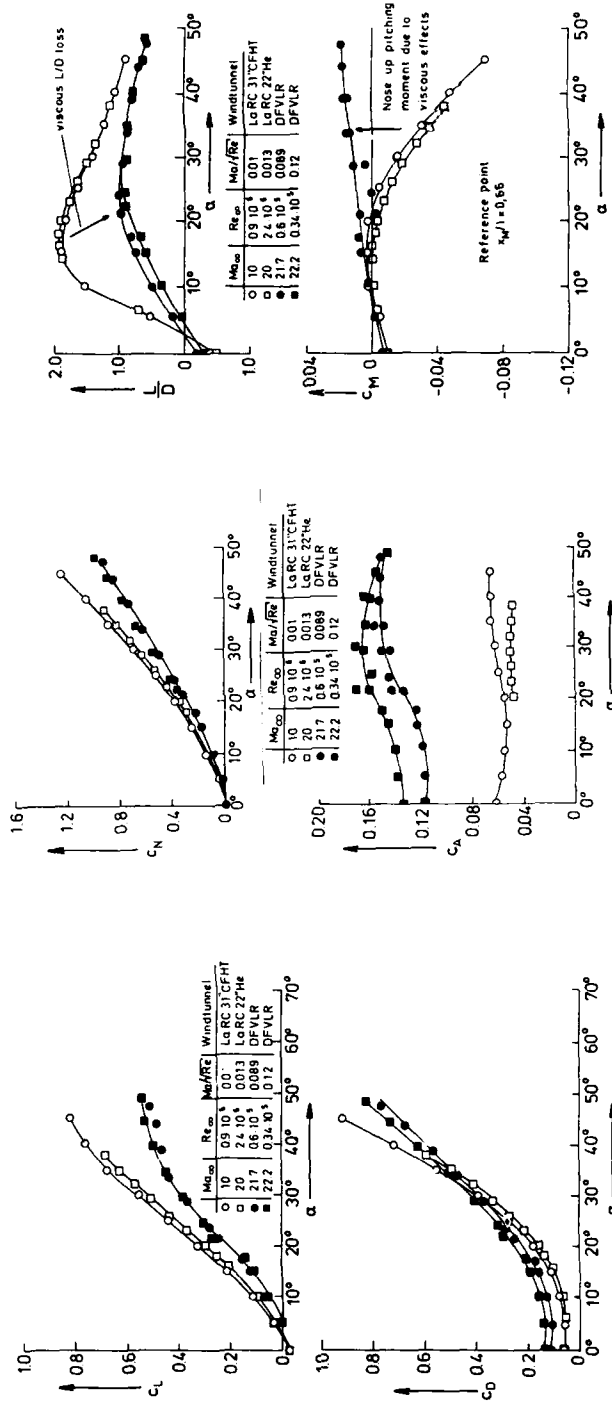


Figure 19. L/D and pitching moment of the 040A Orbiter at different Ma/Re values.

Figure 18. Normal force- and axial force coefficient of the 040A Orbiter at different Ma/Re values.

Figure 17. Lift- and drag coefficient of the 040A Orbiter at different values of Ma/Re .

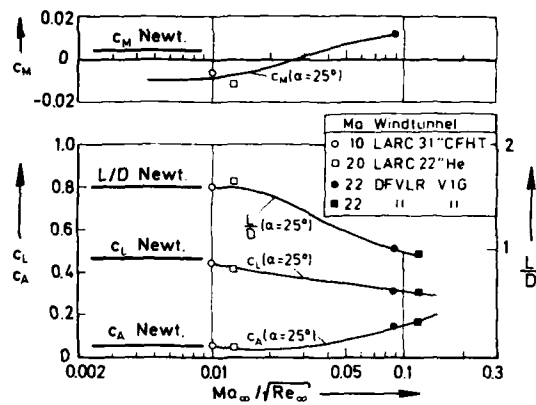
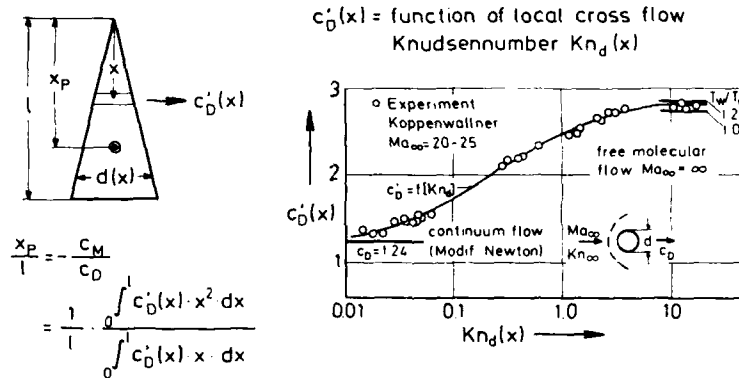
Figure 20. Aerodynamic data of 040A Orbiter as function of $Ma_\infty/\sqrt{Re_\infty}$.

Figure 21. Local cross flow approximation for cone center of pressure analysis.

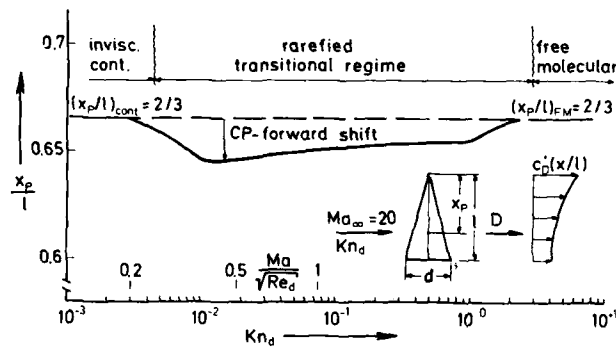


Figure 22. Center of pressure shift of cones due to transition from continuum to free molecular flow.

HYPERSONIC AIRBREATHING PROPULSION: EVOLUTION AND OPPORTUNITIES

by

F. J. Waltrup
The Johns Hopkins University
Applied Physics Laboratory
Johns Hopkins Road
Laurel, Maryland 20707
USA

ABSTRACT

A history of the evolution of airbreathing propulsion, with emphasis on the development of supersonic combustion ramjet (scramjet) engines, is presented. The current status of scramjet engines is discussed and deficiencies in fundamental and applied data and/or knowledge, which comprise opportunities for future work, are noted.

NOMENCLATURE

A - area
 ER_0 - fuel-air equivalence ratio
M - Mach number

Subscripts

0 - free stream
4,5,6 - stations shown in Figs. 1-3, 28
f - fuel

PREFACE

In any historical treatise on a particular technological subject, it is prudent to establish a perspective of events on an evolutionary scale so that those who read it can gain some appreciation for the tremendous advances made in a particular area in recent times. As such, the initial pages of this paper attempt to provide such a perspective on the evolution of powered flight and powerplants which, in this instance, has led to the not-quite-complete understanding and development of airbreathing engines for hypersonic flight.

INTRODUCTION

Man's desire to first fly, and then fly faster and higher, has evolved from the imagination of Greek mythologists to the development of reusable earth-to-orbit vehicles which, in the near future, may well employ airbreathing engines for at least a portion of, if not the entire, flight regime. While notable personages, such as da Vinci (cr. 1490), have devoted extensive efforts throughout history trying to solve the riddle of flight, it was not until the Montgolfier Brothers (Fr) lifted off the ground in their hot air balloon in 1783 that man's first aerial voyage took place. However, it was not for another 120 years that the first heavier-than-air, powered flight would take place. In the interim, powered flight continued in balloons and dirigibles using steam engines (Fr-1852), internal combustion engines (Aus-1872) and electric motors (Fr-1883). In addition, significant advances were to be made in aerodynamics, flight control and aircraft design by such notables as Cayley (GB), Hensen (GB), Lilienthal (Ger), Chanute (Fr, US) and Langley (US). In fact, the thoughts, designs, data and experiences of each of these men were incorporated, to varying degrees, in the Wright Brothers bi-plane design that flew in level flight under power in December of 1903.

Since 1903, the pace and understanding of manned and unmanned powered flight has progressed at an ever increasing rate. For manned flight, it was only another 5 years before the first helicopter flight (Fr-1908) but another 36 years before the turbojet began to replace this piston engine (von Ohain, Ger-1939). Seven years later, the first manned, ramjet-powered aircraft flew (F-80, US-1946). In 1947, the sound barrier was surpassed (Yeager, US), and by the mid-1950's, the U.S. and most European countries had fighter aircraft capable of sustained supersonic flight. By 1961, man had orbited the earth (Gagarin, USSR) and, in 1969, man landed on the moon (Armstrong, Aldrin, US). During the 1970's, manned space exploration in earth orbit became "routine" and by 1981, the U.S. had deployed a reusable Space Shuttle, albeit not without limitations (1986).

On the more practical side, i. e., in general aviation, the fabric covered, wooden or tube framed, biplane designs of the early 1900's were largely replaced by metal structured, single wing designs by the late 1920's. By the mid-1930's, commercial flights became commonplace and, in 1952, the large, long range, propeller-driven aircraft that had evolved were begun to be replaced by turbojet/turbofan-powered aircraft (GB - de Havilland Comet). In 1969, the first jumbo jet service began (US - Boeing 747) and in 1976, the first transport capable of cruising at supersonic speeds (Mach 2+) began commercial flights (Fr, GB - Concorde).

Militarily, the use of aircraft as weapons platforms did not begin until the middle of WWI. By its end, aircraft were used for air superiority, ordinance delivery and forward observations by all nations involved. By 1922, aircraft were being flown from aircraft carriers (USS Langley), expanding their use to sea as well as air control. By 1944, piston-powered aircraft were being replaced by operational turbojets (Ger - ME262, GB - Gloster Meteor, US - P80) and flight speed increased from Mach 0.4-0.6 to Mach 0.8-0.9. Supersonic military aircraft became commonplace in the early 1950's and by 1966, Mach 3+ versions were flying (US - SR71).

Unmanned vehicles, i.e., missiles or projectiles, employing airbreathing engines, by contrast, did not make their appearance in operational systems until 1944 in the form of the V-1 (Ger) powered by a Schmidt designed intermittent or pulse jet. Unlike the subsonic speed V-1, however, most missiles are

required to fly at supersonic or greater speeds (with the exception of current cruise missile designs). In addition, because they are expendable, cost and simplicity are also considered. Consequently, most subsequent airbreathing missile designs were powered by subsonic combustion ramjets because of their efficiency at supersonic speeds, and simplicity and low cost compared to turbojets or fanjets. A limited number were deployed as early as 1955 (see Evolution of Ramjets section). Since that time, any number of ramjet-powered missile and projectile designs have been developed, but very few have made it to the operational stage due primarily to competition from rocket propulsion, long range guidance limitations and politics.

During the course of the 20th century, ramjet and rockets developed along similar paths through the end of WWII and into the mid-to-late 1950's. While bombardment rockets have been around since the 10th century (China)⁴, the technology to convert the principals of rocket propulsion (including the V-2, Ger, 1944) into effective weapons platforms did not really mature until the 1950's with the advent of intercontinental ballistic missiles (ICBM's) as well as launching vehicles for space exploration. Consequently, tandem boosted ramjets with typical cruise speeds of Mach 4⁺, and staged rockets were co-developed for the same applications (other than space launchers) up until the late 1950's, when rockets became, for the most part, the propulsion system of choice for ICBM's and ground-to-air, air-to-ground, air-to-air and ground-to-ground missile applications. Although rockets became the preferred choice for propelling these missiles, it was also recognized that airbreathing ramjets still offered large advantages in range, powered maneuverability and powered intercept compared to rockets in volume and/or weight limited application against nonstationary air or well defended surface targets, resulting in continued development of ramjet-powered systems through the present day.

Two limitations of the subsonic combustion ramjet (compared to a rocket) are its inability to produce thrust at zero or very low speeds and the drastic drop in its performance at flight speeds above about Mach 6. To overcome the former, most ramjets systems use either a tandem rocket or integral rocket (which uses a common combustion chamber for both the rocket and ramjet cycles) to boost the vehicle to a given speed (typically 0.5-0.7 of the cruise speed) before the ramjet begins operation. Alternatively, combined cycle engines have also been investigated which produce static thrust by incorporating either a turbojet embedded with the ramjet (Air Turbo Ramjet)⁷, a rocket-driven turbine and compressor embedded within the ramjet (Air Turbo Rocket), or an ejector system driven by a high pressure gas from either a rocket or fuel and/or oxidizer supply (Ejector Ramjet)⁸. Sometimes the latter is also called an Air-Ducted-Rocket but is not herein to distinguish it from Air-Ducted-Rockets which use a solid monopropellant to supply low pressure fuel to a ramjet combustor which, in turn, is accelerated to its takeover speed by a separate rocket booster^{9,10}.

The upper speed limitation is a result of declining inlet performance and chemical kinetics. As the Mach number increases, so do inlet total pressure losses, especially through the terminal normal shock system. When these losses are coupled with energy losses due to dissociated species at the elevated air total temperatures present, a significant decrease in performance is encountered. Structural and materials problems may also be encountered because of the high static pressures and temperatures in the engine, but can be overcome using innovative, active structural cooling techniques and advanced materials.

To overcome this upper speed limitation, scientists and engineers recognized that if it were possible to inject, ignite and react fuels in a supersonic air stream, then the large total pressure losses associated with the terminal normal shock in a subsonic combustion ramjet could be mitigated and the chemical kinetics losses forestalled to higher flight speeds. Such engines (Supersonic Combustion Ramjets or scramjets), their history, current status and future prospects, are the subject of this paper.

RAMJET AND SCRAMJET ENGINE CONCEPTS

Prior to discussing the evolution of airbreathing engines, and ramjets and scramjets in particular, a brief review of the operation and types of ramjet and scramjet engine concepts previously introduced or those to be discussed in subsequent sections of this paper will be presented for clarity. Conceptual schematics of subsonic combustion ramjets and combined cycle derivatives thereof are shown in Figs. 1 and 2, respectively. Figure 1(a) depicts the traditional can-type, liquid-fueled ramjet (CRJ) with a tandem booster attached. Here, $M_0 > M_1 > 1$ but the air is diffused to a subsonic speed (typically Mach 0.3 to 0.4) through a normal shock system prior to reaching station 4. Fuel is then injected and burned subsonically prior to reaccelerating the flow to a sonic speed at station 5 ($M_5 = 1$) and further accelerating it in the exit nozzle ($M_6 > 1$). A more recent alternative to this concept is to use a common combustion chamber for both the boost and sustain phases of flight, commonly referred to as an integral-rocket-ramjet (IRR). This generally requires a dump-type rather than a can-type combustor, but the cycle operation of the ramjet remains the same. Figure 1(b) schematically illustrates this concept for a liquid-fueled ramjet (LFIRR) and Fig. 1(c) is illustrative of a solid-fueled system (SFIRR). In some applications, SFIRR's are preferable to LFIRR's (or CRJ's) because of the simplicity of the fuel supply, but only when the fuel throttling requirements are low, i.e., when flight altitude and Mach number variations are limited. Another alternative, the Air-Ducted-Rocket (ADR), shown in its IRR form in Fig. 1(d), operates under the same engine cycle principles, but uses a fuel-rich monopropellant to generate a low to moderate pressure gaseous fuel supply for the subsonic combustor. Here, the ADR is a compromise between the fuel supply simplicity of a SFIRR and the throttleability of the LFIRR (or CRJ). It should be noted, however, that the performance of liquid-fueled systems is always superior to any of the others.

While the ramjets shown conceptually in Fig. 1 have been and continue to be viable vehicle propulsion systems, none can produce static thrust. Figure 2 illustrates three types of hybrid ramjet engine cycles that can. The first embeds a turbojet engine within the main ramjet engine and is usually liquid-fueled and called an air-turbo-ramjet (ATRJ-Fig. 2(a)). Here, the turbojet produces the required static and low speed thrust for takeoff (and landing if required) which may or may not be isolated from

the main ramjet flow at supersonic speeds. An alternative to the ATRJ is the air-turbo-rocket (ATR-*Fig. 2(b)*) in which a low to moderate pressure rocket motor is used to drive a turbine and provide a gaseous fuel for the ramjet. The turbine, in turn, drives a compressor, the combination of which will produce static thrust. At supersonic speeds, the compressor, again, may be isolated from the main ramjet flow and the turbine idled so that the vehicle can then operate as an ADR. The final hybrid ramjet cycle capable of producing static thrust is the ejector ramjet (ERJ) shown in *Fig. 2(c)*. Here a rocket motor or gas generator produces a high pressure, generally fuel-rich, supersonic primary or ejector flow which induces secondary air to flow through the engine even at static conditions. The ejector effluent and air then mix and burn (at globally subsonic speeds) and finally expand in the convergent-divergent exit nozzle.

Figure 3 presents schematic illustrations of a generic scramjet engine and two hybrid cycles thereof. In a pure scramjet (*Fig. 3(a)*), air at supersonic speeds is diffused to a lower, albeit still supersonic, speed (typically $0.3-0.5 M_0$) at station 4. Fuel (either liquid or gaseous) is then injected from the walls where it mixes and burns with the air in a generally diverging supersonic combustor. Unlike the subsonic combustion ramjet, however, which always generates a terminal normal shock in the inlet duct with heat addition, the combined effect of heat addition and diverging area in a scramjet combustor generate a shock train at and upstream of the combustor entrance, often called the precombustion shock, which can vary in strength from the equivalent of a normal shock to no shock, depending on M_0 , overall fuel-air equivalence ratio, ER_0 , and combustor area ratio, A_5/A_4 . Also unlike the ramjet, the scramjet has no geometric throat, so that M_5 must always be greater than or equal to unity.

The unique combination of heat addition in a supersonic air stream with a variable strength shock system plus the absence of a geometric throat permit the scramjet to operate efficiently over a wide range of flight conditions, i.e., as a nozzleless subsonic combustion ramjet at low flight Mach numbers, e.g., $M_0 = 3-6$, and as a supersonic combustion ramjet at higher flight Mach numbers, e.g., $M_0 > 5$. At low M_0 and high ER , the combustion process generates the equivalent of a normal shock system and is initially subsonic, similar to that of a conventional subsonic combustion ramjet, but accelerates to a sonic or supersonic speed prior to exiting the diverging area combustor, eliminating the requirement for a geometric throat. As ER decreases at this same M_0 , the strength of the precombustion shock system will also decrease to the equivalent of a weak oblique shock and the combustion process is entirely supersonic. At high M_0 , the strength of the shock system is always equivalent to either a weak oblique shock or no shock, regardless of ER . This is referred to as dual-mode combustion and permits efficient operation of the engine from $M_0 = 3$ to $M_0 = 8$ to 10 for liquid fuels and up to orbital speeds for gaseous (e.g., hydrogen) fuels. The upper limit for the liquid-fueled cycle is, of course, due to energy consumption by dissociating and ionizing species at elevated temperatures which cannot be compensated for by additional fuel as in the case of, for example, a diatomic gas such as hydrogen.

Although the scramjet offers these unique capabilities, it also requires special fuels or fuel preparation in order to operate effectively below $M_0 = 7$ because of "low" static air temperatures and short combustor residence times (< 1 ms). For liquid fuels, this generally means using highly reactive (generally pyrophoric) fuels, fuel blends or fuel/oxidizer pilots which are logistically unsuitable. For gaseous fuels, it requires that the fuel be preheated or combined with a pyrophoric additive. To overcome this deficiency, an alternative to the pure scramjet is the Dual Combustor Ramjet (DCR) shown in *Fig. 3(b)*. The DCR has all of the features of the scramjet except a portion of the captured air is diverted to a small, embedded subsonic dump combustor into which all of the fuel is injected. By maintaining a proper distribution of the fuel, a near stoichiometric flame can be maintained, the heat from which is used to prepare and preheat the remaining fuel so that efficient heat release can be realized in the supersonic combustor. Thus, the dump combustor acts as a hot, fuel-rich gas generator for the main supersonic combustor, similar in principle to the air-ducted rocket previously described in the ramjet cycle section. This cycle, therefore, permits the use of conventional liquid hydrocarbon fuels or gaseous fuels such as hydrogen without resorting to logistically unsuitable additives.

The final supersonic combustion cycle, which is a natural extension of the scramjet and DCR cycles, is the ejector scramjet shown schematically in *Fig. 3(c)*. Unlike the pure scramjet or the DCR, it is capable of producing static thrust using axial fuel injectors fed by a high pressure fuel/fuel-oxidizer supply, yet retains the high speed operating characteristics of the scramjet and/or DCR. These same injectors, perhaps complemented by staged injectors further downstream, can be used for dual-mode scramjet operation, thus making it a viable candidate for a single stage, but multiple cycle, airbreathing engine concept for zero to hypersonic speed flight.

With the ramjet and scramjet cycles thus introduced, let us now return to the evolution of airbreathing engines for powered flight.

EVOLUTION OF AIRBREATHING PROPULSION ENGINES

Concurrent and synergistic with the evolution of vehicles capable of manned and unmanned flight within the atmosphere has been the evolution of the powerplants required to propel them. While these powerplants include devices which produce lift along, e.g., heated air for balloons, and those which produce thrust but carry their own oxidant, e.g., chemical rockets, the following chronology excludes both. It addresses the evolution of airbreathing engines alone with emphasis on subsonic and supersonic combustion ramjets.

Internal Combustion Engines

While the aerodynamic principles required for powered flight were sufficiently well understood one hundred years earlier than the Wright Brothers' first flight (see, e.g., Sir George Cayley's contributions), the requisite high power-to-weight ratio powerplant to achieve powered flight was missing. The steam engine, available even in Cayley's time, was far too heavy because of its indirect

energy supply. The internal combustion engine, which permits a direct energy transfer to the working medium, was developed in the mid-to-late 1800's but was also too heavy in its then available designs. It was not until Langley, Balzar and Manley (USA), and the Wright Brothers (USA) concurrently redesigned and built internal combustion engines in 1903 with the requisite power-to-weight ratios that powered flight could be achieved^{1,4}. For the next 40 years, this engine was to become the premiere powerplant for all heavier-than-air craft with significant improvements in its power-to-weight ratio made both in Europe and the United States. Even today, it continues to play a significant role in the commuter and private aviation industries.

Rotating Machinery Engines

The airbreathing engine which superseded the internal combustion engine was, of course, the gas turbine engine^{2-4,11} with its inherent advantage of converting chemical energy directly into kinetic and, thence, mechanical energy. While the principal of the gas turbine has been around since Hero's Aeolipile (Egypt, cr. 200 B.C.), the first patent (Barber-GB) was not issued until 1791, and it was not until 1939 that a von Ohain (Ger) designed turbojet-powered aircraft flew for the first time. This was followed shortly thereafter by Whittle (GB) and General Electric (USA) designed turbojet-powered flights in 1941 and 1942, respectively²⁻⁴.

The incorporation of a turbine with either a centrifugal or axial flow compressor did not begin until the 1930's²⁻⁴. Although Guillaume (Fr) patented a combined axial flow compressor and multistage turbine concept in 1921, it was not until Whittle (1930) and von Ohain (1935) patented their centrifugal compressor/axial turbine concepts that actual development began. These were preceded by earlier development work using a piston engine in place of the turbine to overcome the problem of static operation. These earlier efforts included designs and patents by Lorin (Fr-1908), Marconnet (Fr-1909), Harris (GB-1917), Miloš (Fr-1920), Fono (Hun-1928) and Campini (It-1932), and a Campini designed engine actually flew in 1940⁵. These turbineless designs, however, proved to be heavy and inefficient for powered flight. Whittle and von Ohain, on the other hand, recognized that an auxiliary power unit could be used to overcome the static starting problem in turbojet engine designs, and the resulting evolution from their initial designs into today's multitude of high thrust-to-weight, efficient turbojet and fanjet designs is history.

The concept of a turboprop²⁻⁴ also appeared during this period. Patents to Ljungström's Angturbin (Sw-1936) and Brown-Boveri (Ger-1939) were issued for multi-stage centrifugal compressor/axial turbine and multi-stage axial compressor/turbine designs, respectively, each attached by a central drive shaft and gear box to a propeller. The latter is a prototype of modern axial flow turbojet engine designs (sans the propeller). Both are forerunners of today's large bypass ratio turbofans.

Ramjet Engines

While many of the inventive minds of the world were focusing on internal combustion engines and derivatives thereof in the early 1900's, Lorin (Fr) and his fellow countrymen, as well as Lake (US), began to look at jet propulsive devices^{2-4,11} which did not contain any instream obstructions (such as pistons or turbomachinery) which they termed compressorless motors (later called Lorin tubes). The first treatise of the potential of ramjet propulsion for low subsonic flight speeds was reported by Lorin in *L'Aerophile* (1913), in which he concluded that its propulsive efficiency would be poor^{4,11} (he did not address high subsonic or supersonic speeds). Others, however, were addressing methods of producing static thrust or augmenting the low speed thrust of rocket motors. Consequently, the first practical ramjet designs were what are currently called ejector ramjets. While Lake was the first to patent this idea (1909)⁶, it was Morize (Fr-1917) and Melot (Fr-1920) who developed and engineered this concept. The Melot concept shown in Fig. 4 was actually tested in France during WWI prior to issuance of the 1920 patent and was tested again in the US in 1927 at what is now the NASA/Langley Research Center⁷. Both demonstrated an increase in static thrust. Interest in this type of device, however, waned until the late 1950's.

The first patent, on the other hand, was not applied for until 1926 when Carter (GB) submitted details of conical nose/annular duct and normal shock inlet, ramjet-like devices for augmenting the range of artillery shells¹². While none of these were built, his application did, for the first time, address the beneficial use of ramjet propulsive devices at supersonic speeds (up to Mach 2) at what was then high altitudes (up to 8500 m (28 kft)), his thinking being influenced perhaps by the early proponents of supersonic flight, e.g., Prandtl and Mach (Ger).

The first clearly recognizable forerunners of today's liquid-fueled ramjet engine designs are those shown in Fig. 5 which were submitted by Fono^{4,11,12} (Hun) in a 1928 German patent application. These clearly show a convergent-divergent inlet to diffuse the flow from supersonic to subsonic speeds, fuel injectors, flameholders, a combustor and a convergent-divergent exit nozzle. These concepts were specifically designed for supersonic, high altitude flight of an aircraft, but never progressed past the design stage.

The first actual construction and ground testing of ramjet engines occurred in the early-to-mid 1930's. In 1933, Leduc (Fr)^{4,11,12} produced designs similar to present day schemes including a ogive/annular diffuser and boundary layer control for efficient inlet operation, especially at supersonic speeds. He was granted a patent on the ramjet-powered aircraft design in 1934, and by 1935, had conducted ground tests on a small scale ramjet engine using liquid fuels at simulated flight speeds up to Mach 0.9. By 1938, work on a full scale, ramjet-powered aircraft had begun and engine component tests at simulated flight Mach numbers up to 2.35 continued into 1939.

All work was halted during WWII but resumed immediately thereafter so that by the end of 1945, an experimental aircraft designated the Leduc-010, was completed. However, it was not until April of 1949 that the first powered flight of this aircraft took place. The interim time was required to develop a separate aircraft to take the Leduc-010 up to its initial flight speed and altitude. These were

followed by tests of refined versions in 1951¹³. These ultimately led to the development of the Nord 1500 Griffon II aircraft (1955) which used a turbojet embedded within the ramjet to produce static thrust, i.e., an air turbo ramjet. In 1957, this aircraft achieved supersonic flight speeds and in 1959, achieved Mach 2.1¹⁴ at an altitude of 15.3 km (50 Kft)¹⁵.

Concurrent with ramjet development in France in the 1930's was an unknown, but parallel effort in the USSR¹⁶. In 1929, Stechkin began publishing theories on ramjet propulsion, and by 1933, he and Pobedonostsev had conducted ground tests at simulated subsonic speeds on a liquid-fueled subscale ramjet engine. In order to conduct tests at supersonic speeds, they switched from liquid-fueled to solid-fueled designs and from 1933-1935, fired a number of 76mm, ramjet-powered projectiles out of artillery pieces at speeds up to Mach 2.0 using phosphorous fuel. While net positive thrust was not achieved, they did increase the range, and through a combination of experimental data and theory, deduced that increasing the size (or diameter) of the ramjet engine, using alternate fuels (Mg/Al) and tailoring the exit nozzle throat-to-inlet area ratio would permit net positive thrust to be achieved.

In order to achieve this increased engine size required a new boosting system. Given the USSR infrastructure, a new team took over ramjet development in 1936, headed by Merkulov and Shcherbakov, with emphasis on tandem rocket-boosted ramjet vehicle designs. While the specific size is not mentioned, they did undertake a development program using pressed Mg/Al solid fuel culminating in successful subsonic flight tests in 1939.

Immediately following these tests, emphasis shifted to using liquid (rather than solid) fueled ramjets to augment the speed of propeller-driven aircraft. Throughout the remainder of 1939, Merkulov and his associates began developing wing-mounted ramjet engine pods, and by the beginning of 1940, aircraft flight tests had begun using 40-50 cm (15.7-19.7 in.) dia ramjet pods. These tests, with a variety of aircraft and ramjet engine designs, continued through 1948 when interest in turbojet engines subverted, at least for a while, the USSR ramjet efforts. None of the tests were very successful in that they all had high installed engine drag and suffered from combustion inefficiencies and instabilities which they were not able to overcome.

Germany also began development of ramjets in the 1930's^{4,15}. In 1935, Trommsdorff¹⁵, initially supported by the faculty at Gottingen and Siemens Ltd. (to be joined later by the faculty at Braunschweig), began developing ramjet-powered artillery shells. By 1938, a number of oxygen deficient, solid-fueled, 8.8-cm (3.5-in.) dia, normal shock inlet units were gun launched at Mach 2.5, but were hampered by a lack of combustion. Efforts then switched to liquid-fueled systems as well as more efficient inlet designs, culminating in a series of multiple-shock conical inlet, liquid-fueled (carbon disulfide), 15-cm (5.9-in.) dia units being successfully fired in the early-to-mid 1940's. Typically, these units left the gun at Mach 2.9 and accelerated to Mach 4.2 in 3.2 s before fuel depletion. In addition to these test units, designs of much larger operational units including a 6000 km, aircraft-launched, ramjet-powered intercontinental guided missile were being considered.

Concomitant with these supersonic speed ramjet development efforts was a parallel effort to develop ramjet engines to power subsonic speed aircraft¹². Initial research began at The Walter Co. in 1936, but it was not until Sanger became involved in 1938 that actual development began. By 1943, he and his co-workers had built and flight tested (on an aircraft) a liquid-fueled ramjet engine and plans were actually made to build an aircraft powered by a ramjet (with rocket assisted takeoff) by 1944¹². Concurrent with these engine development programs were the more fundamental efforts of Oswatitsch and Buseman (high efficiency supersonic inlet designs), Damkolther and Pabst (short-length/high efficiency liquid-fueled combustors), Lippisch and Schwabl (solid fuels for ramjets) and Sanger (metalized slurry fuels), all of which represent foundations upon which today's modern ramjets are based¹.

British interest in ramjets began in the early 1940's as an indirect result of the German efforts. By 1943, Smith had proposed a ramjet powered bombardment missile, with some initial combustor work reported in 1945 and a theory of ramjet propulsion presented in 1946 by Reid and Herbert¹⁷. By 1944, a Guided Aerial Projectiles project was established to oversee rocket and ramjet development, but apparently, was not well supported; most of Britain's efforts being directed towards Whittle's turbojet development.

United States interest in ramjets also began in the early 1940's. By 1941, rudimentary analyses of, and initial experimentation on subsonic speed ramjets had been established by Way, and Becker and Baals¹². These early efforts prompted considerable interest and government support at a number of institutions to study and understand the fundamental physics and chemistry governing ramjet operation at both subsonic and supersonic speeds as well as developing engines applicable to both.

The subsonic flight speed efforts peaked in 1946 when two 51-cm (20-in.) dia M.I.T. designed ramjets were used to augment the thrust of a P-51 aircraft, and when two 76-cm (30-in.) dia liquid-fueled ramjet engines, developed by Marquardt¹⁸, were used to power and accelerate an F-80 aircraft without benefit of any other auxiliary powerplant, the first such demonstration ever recorded. Although some work continued in the subsonic flight speed regime, most notably applying ramjet technology to afterburners in turbojets, emphasis shifted shortly thereafter from subsonic speed aircraft to supersonic speed missiles.

The application of liquid-fueled ramjets to supersonic missiles began in the mid 1940's, principally at the NASA Lewis and Langley Research Centers¹⁹, The Johns Hopkins University Applied Physics Laboratory (JHU/APL)²⁰, and of course, The Marquardt Co.¹⁸ The first successful supersonic flight tests were conducted by JHU/APL in 1945 followed by NASA/Lewis tests in 1947 and NASA/Langley tests in 1950 at speeds in excess of Mach 2. Marquardt's design was not flown until 1955 when it exceeded Mach 4.3 on the Lockheed X-7 test vehicle.

These early successes in the U.S., as well as others in Europe, led very quickly to a series of operational or flight tested systems¹⁸. In the U.S., there were BOMARC (Mach 2.8 at 30 km - 1955),

TALOS (Mach 2.5 at 25 km - 1955) and TYPHON (Mach 4⁺ at 30 km - 1961). In France, there were SIRIUS (Mach 2.7 - late 1950's), VEGA (Mach 4 - early 1960's) and STALTEX (up to Mach 5 - mid-1960's), and in Britain, there were BLOODHOUND (late 1950's) and SEA DART (1960's).

Subsequent to development, demonstration and/or operation of these conventional, tandem-boosted, liquid-fueled ramjets, emphasis shifted to more volumetrically/weight efficient ramjet designs in the late 1960's and early 1970's, an evolution which has continued to the present. Specifically, these are the liquid- and solid-fueled, integral-rocket-ramjets (LFIR, SFIR) and combined cycle systems such as the integral-rocket, Air-Ducted-Rocket (ADR), which typically cruise at about Mach 2-3 at or near sea-level and Mach 4-5 at altitude. Known propulsion systems of these types which have progressed through at least flight tests¹⁸⁻²² include the ALVRJ (LFIR-1973), ASALM (LFIR-1979) and SLAT (LFIR-1987) in the U.S., the ASSM (ADR-1976), ASMP (LFIR-1970's), RUSTIQUE (ADR-1984) and ANS (LFIR-1986) in France, the EPA (ADR) and ANS in Germany, and the SA-4 and SA-6 (ADR's-1970's) in the USSR.

Other combined cycle engines, such as the air-turbo-ramjet and air-turbo-rocket have also been addressed in both the U.S. and Europe, but to the author's knowledge, have not been flight tested at supersonic speeds.

Scramjets

The origins of the concept of employing combustion in supersonic flows can be traced back to interest in burning fuels in external streams to either reduce the base drag of supersonic projectiles or to produce lift and/or thrust on supersonic and hypersonic airfoils in the early 1950's. Actually, these were preceded by some very fundamental theoretical treatments of diabatic flows (1-D flows with heat addition) by Hicks (US) and others beginning in 1945²³⁻²⁶. In 1950, these basic analyses were extended to two-dimensional flows by Pinkel (US)²⁷ and theoretically applied to projectile base drag reduction (Wald, US)²⁸. By 1951, experiments by Baker, et. al. (US)²⁹, had demonstrated base drag reductions in a Mach 1.6 flow of up to 75% using hydrogen fuel and similar results were obtained by Hebrank (US)³⁰ in 1952 using a solid pyrotechnic fuel. These were followed by a successive number of experimental and theoretical investigations continuing through the early 1980's (see, e.g., Refs. 31-34), but are not discussed herein for brevity and because combustion, for the most part, is confined to the subsonic wake region.

Interest in combustion on airfoils in supersonic flows surfaced in 1952 when Pinkel (US)³⁵ and Smith and Davis (US)³⁶ published theoretical predictions of the benefits of external supersonic combustion on both thrust and lift. These were followed by successively more complex and, therefore, realistic treatments of heat addition in external supersonic flows throughout the remainder of the 1950's and into the early 1960's, complemented by experimental investigations. Theoretically, these included U.S. studies by Chu³⁷, Gazley³⁸, McCloy³⁹, Mager⁴⁰, Dugger⁴¹ and Billig⁴² which cover fundamental treatments of the heat addition process as well as vehicle applications and performance.

Experimentally, Smith and Davis³⁶ (1952) were the first to demonstrate the feasibility of supersonic combustion using a flat plate in a Mach 1.7 airstream with hydrogen injected from discrete holes, but found that flameholders and an oxygen pilot were necessary to achieve stable combustion. Krull, et. al. (US, 1958), also ran tests with hydrogen, but used parallel rather than normal injection, demonstrating diffusion-controlled supersonic combustion. Subsequently, Dorsch, Serafini and Fletcher (US) ran a series of discrete hole injection tests from 1955-1960⁴⁴⁻⁴⁶ using a very reactive borohydride fuels, but, while achieving vigorous combustion in a supersonic airstream, were not able to demonstrate net positive thrust. The first demonstration of net positive thrust was by Dugger⁴¹ and Billig⁴² in 1958 on a double wedge model in a Mach 5 airstream using aluminum alkyl fuels. A photograph of this experiment is shown in Fig. 6.

While these initial efforts to understand and demonstrate the concept of supersonic combustion in an external airstream provided valuable insight and understanding of some of the physical and chemical processes which occur as well as some practical engineering experience, it became apparent in the late 1950's that ducting the supersonic flow in an inlet prior to fuel injection and combustion offered large advantages over external burning. These include increased air static pressures and temperatures to enhance ignition and combustion of the more conventional fuels as well as confining the combustion process, resulting in higher static pressures in the combustion zone with its attendant increase in thrust.

The first theoretical studies addressing the concept, i.e., of scramjet as we know it today, were published in 1958 by Weber and MacKay (US)⁴⁷, Roy (Fr)⁴⁸ and Dunlap (US)⁴⁹. These were followed in rapid succession with papers by Sargent and Gross⁵⁰, Dugger⁵¹, Ferri⁵² and McLafferty (US)⁵³ and Mordell and Swithenbank (Can)⁵⁴ in 1960. The papers by Roy, Dunlap, and Sargent and Gross described standing or detonation wave scramjets. In this concept, fuel is mixed with the air upstream of a shock generating obstruction which, in turn, initiates and sustains combustion at that point. While the concept of standing wave combustion in a duct was the first to be pursued, both analytically (Nicholls⁵⁵, US, 1948) and experimentally by Gross⁵⁶ (1959), Nicholls⁵⁷ (1960), Rhodes and Chriss^{58,59} (1961-1962) (US), comparative studies, such as those by Weber and MacKay⁴⁷ and Dugger⁵⁰, demonstrated that the performance of scramjets without the obstruction in which the fuel and air are not premixed, but mix and distributively burn downstream of the fuel injection point, was superior for hypersonic (up to Mach 10) flight. In addition, at the higher flight speeds, i.e., $M_0 > 7$, premixing the fuel and air without combustion would not be possible because of the high air static enthalpy. Consequently, the standing wave scramjet concept was not rigorously pursued, rather emphasis focused on the distributed mixing and combustion concept.

As a result of these initial performance studies and proof-of-concept tests, interest in applying the scramjet engine cycle to both aircraft and missiles rapidly evolved. In the U.S., the Air Force began supporting scramjet research in the late 1950's⁶¹ as did the Navy⁶¹. In late 1959, several major aircraft and engine companies became interested in developing single-stage-to-orbit aircraft using

scramjet propulsion, i.e., the first Aerospaceplane concept (Fig. 7). Principle among them was Republic Aviation⁶² who collaborated with Ferri⁶² and his associates at the General Applied Sciences Lab (GASL) on hydrogen-fueled Scramjet engines for Mach 8 to orbital speeds. This initial impetus led to Air Force interest in evaluating⁶³ and eventually sponsoring an Aerospaceplane program in 1964^{64,65}. In 1962, NASA was asked to participate in a preliminary technology demonstration program⁶⁶ but the program did not materialize. The Navy also expressed some interest, but never progressed beyond supporting some preliminary performance evaluations⁶⁷. Consequently, the Air Force, Navy and NASA pursued separate scramjet development programs until the inception of a new National Aerospace Plane (NASP) program in 1986.

In Europe, interest in supersonic combustion paralleled that in the U.S. throughout the 1960's and into the 1970's. In France, following Roy's initial publication⁴⁸, fundamental work on supersonic combustion resulted in Mestre and Viaud⁶⁸ being the first researchers to present experimental results on supersonic combustion in the open literature. While these initial results were with normal injection of kerosene fuel, emphasis switched to either normal or tangential injection of gaseous fuels such as methane and hydrogen with a number of reports by Leuchter^{69,70}, Ducorneau and Borghi^{71,76} and Bellet, et. al.⁷². A parallel research program on hypersonic inlets was also undertaken during this time with emphasis on axisymmetric designs and tests up to Mach 7^{74,75}. Complementing these basic and applied research efforts were aerodynamic⁷⁶ and application studies for hypersonic missiles and aircraft⁷⁷.

These efforts culminated in a series of connected pipe tests of a 40-cm (15.75-in.) dia scramjet engine (including the exit nozzle) at Modane at simulated Mach 6 flight conditions in the 1972-1973 time period⁷⁸⁻⁸⁰. The engine, a photograph of which is shown in Fig. 8⁷⁸, was axisymmetric in design and used staged, normal injection of hydrogen. Since these tests, interest in scramjet propulsion in France appears to have waned, at least as far as the author can discern. However, a survey paper entitled, "Early Researches in Supersonic Combustion," by Mestre and Barrere (ONERA-FR) is to be given at the 1987 AIAA Propulsion Meeting in June, in San Diego, CA (US), which should clarify this point.

Interest in supersonic combustion and scramjet propulsion in England evolved along several parallel paths in the early 1960's. Initially, three groups pursued combustion in supersonic streams. These included Townend's and Reid's interest in waveriders and base burning⁸¹ at Farnborough, Hawkin's and Fox's interest in scramjets⁸²⁻⁸⁵ at Roll's Royce and the Switwenbank team interest in supersonic diffusion flames at Sheffield University⁸⁶⁻⁸² (after returning to England from McGill University⁹³⁻⁹⁶ Canada). These were to be followed by diffusion flames studies by Cookson, et. al., at Cranfield⁹³⁻⁹⁶ beginning in the late 1960's.

The work at Roll's Royce, begun in 1963, first addressed kerosene-fueled supersonic combustor concepts^{82,83}, for flight speeds in the Mach 6-7 range but switched to hydrogen-fueled concepts, culminating in direct-connect combustor tests at simulated Mach 5 to 7 flight conditions in 1969⁸⁵. At Sheffield, most of the reported supersonic diffusion flame work⁸²⁻⁸⁵ was performed in a shock tunnel at simulated Mach 10 to 11 flight conditions using hydrogen fuel⁸⁷⁻⁸⁹ through the early 1970's, but the last reported work in 1975⁹² was with kerosene. At Cranfield, the first reported work by Cookson⁹³ was on connected-pipe diffusion flame tests at simulated Mach 7 flight conditions with hydrogen. Subsequent tests included methane, kerosene and hydrogen using both axial and transverse injection⁹⁴⁻⁹⁵, the last work being incomplete in 1977⁹⁶. No development tests have been reported in Great Britain in the open literature.

In Germany, most of the reported work on supersonic combustion has been of a more fundamental nature, with the first reported work by Winterfeld in 1966-67⁹⁷. For the next 8-10 years, Winterfeld's group, at Porz-Wahn⁹²⁻¹⁰², including Suttrop and Mauer, along with Kallergis at Braunschweig^{103,104} and Wilhelm's group at Karlsruhe¹⁰⁵⁻¹⁰⁷ directed their efforts at understanding the physical and chemical processes leading to the ignition and combustion of gaseous fuels in supersonic airstreams, Kallergis' work¹⁰⁴ being the exception. These included normal as well as tangential fuel injection, methods of flameholding, and ignition enhancement aids such as preburning a small portion of the fuel⁹⁹. Since the mid-1970's, however, the only reported work has been on application/performance studies^{10,21,22}.

The USSR has also had an extensive program in supersonic combustion and scramjet propulsion since the 1960's, but a review is not presented herein. The reader is referred to Ref. 108 (Bayev and Golovichev) as an initial source for such a review, Ref. 108 being the only textbook known to the author or supersonic combustion.

Three other papers of interest¹⁰⁹⁻¹¹¹ are by Da-Riva, et. al. (Spain)¹⁰⁹, which is an analytical treatment of hydrogen-air supersonic diffusion flames, and Tsuji and Yoshida^{110,111} (Japan) which experimentally investigated normal injection of hydrogen into a vitiated Mach 1.8 airstream.

Returning to the North American continent, interest in Canada in scramjets, as previously noted, began at McGill University in 1960 with Mordell and Switwenbank⁹⁴. Almost simultaneously, Molder and his associates at McGill began parallel efforts in hypersonic inlet aerodynamics¹¹²⁻¹¹⁴ and gun launched scramjet flight testing¹¹⁵⁻¹¹⁷. The inlet work began in the early 1960's and centered around the design of Buseman-type inlets which were inverted to produce modular inlets with very good performance characteristics and low external cowl drag and heating. These novel designs also alleviated starting problems of high area contraction ratio, high design Mach number inlets at low flight Mach numbers. A number were designed and successfully tested over a wide range of Mach numbers (see succeeding discussion of US Navy work).

Gun launching scramjets concepts, a novel idea at the time, began in 1960¹¹⁵, evolved to actual construction in 1966¹¹⁶ (supported by the Canadian Defense Research Board) and a horizontal flight test took place out of a 40.6-cm (16-in.) dia gun in 1968 using triethylaluminum fuel. Unfortunately, the test was unsuccessful, the structure of the engine failing during launch. Another gun launching program, however, was begun in the early 1970's, jointly supported by the National Research Council (Can) and U.S. Army Ballistics Research Lab. In the Spring of 1974, another firing was attempted, this

time at a near vertical (85°) flight angle at a test range on Barbados. This time, the sabot did not fully separate, damaging the control surfaces, resulting in an uncontrolled tumbling flight. Photographs of the engine before and after flight, and of the test range are shown in Fig. 9. While not completely successful, these are the only reported attempts to actually flight test a scramjet.

In the United States, the Air Force, Navy and National Aeronautics and Space Administration (NASA) pursued separate scramjet development programs. Interest within the Air Force focused on a single stage, airbreathing powered Aerospaceplane^{64,65} (Fig. 9) as well as missile applications¹¹⁸. This interest ultimately led to development of two airbreathing propulsion schemes, one being a hybrid subsonic combustion ramjet capable of producing static thrust as well as accelerating a vehicle to low hypersonic speeds, and the other being a scramjet. The former led to the liquid air compression thrust augmentation engine concepts such as those investigated by The Marquardt Corp. (TMC)⁵ in the mid-1960's, a photograph¹¹⁹ of which is shown in Fig. 10.

During this same period, four separate scramjet engine development programs were initiated^{18,120}. These engines, shown in Figs. 11 through 14 respectively, were hydrogen-fueled and achieved performance levels which, in general, substantiated theoretical predictions. Although most of these engines were aerodynamically designed to operate over a wide range of hypersonic speeds and were substantiated by component tests conducted over a wide Mach number range, ground testing of the entire engine was restricted to a narrow Mach number range because of facility limitations.

The United Aircraft Research Laboratory's (UARL) Variable Geometry Scramjet (Fig. 11) was a 45.7-cm (18-in.) dia., variable geometry, water-cooled axisymmetric engine designed for Mach 3 to 12 flight. It was built in the 1965-1968 time period but only free-jet tested at Mach 5^{120,121}. These were, however, preceded by a number of inlet, combustor and nozzle component development tests¹²¹ in the Mach 3.5 to 8.0 flight speed range.

The General Electric scramjet engine, shown in Fig. 12, was also a variable geometry, water-cooled design. In fact, two 22.86-cm (9-in.) dia engines were designed and tested free-jet at $M_0 = 7$ in the 1966-1969 time period. The first engine, CIM-I, provided an evaluation of a combined set of scramjet components designed for operation up to Mach 8¹²⁰. Upon completion of testing in the General Electric Hypersonic Arc Tunnel, CIM-I was subsequently modified by replacing the cowl section with one having a smaller cowl lip angle to reduce external drag, and contouring some of the internal lines to increase performance. Extensive performance tests were conducted on CIM-II to obtain the effects of varying inlet contraction ratio, equivalence ratio, fuel injector location, free stream Reynolds number and total enthalpy^{120,122}. These were also preceded by a number of component development tests¹²³.

The third concept developed (Fig. 13) was a Mach 3-12 engine involving a series of fixed geometry, thermal compression, heat sink engine models of approximately 194 to 226 cm³ (30 to 35 in.³) of capture area, developed and tested by the General Applied Science Laboratories (GASL) under the late Dr. Ferri in the 1964-1968 time period¹²⁴. Engine models demonstrating this concept have been tested at Mach = 2.7, 4 and 7 with inlet component tests covering Mach numbers from 2.7 to 11.3. Modifications to these designs were incorporated into a later engine model shown in Fig. 21 and tested at $M = 7.4$ in the GASL combustion heated, high enthalpy blowdown tunnel using a wide variety of fuel injector patterns and fuel flow schedules^{120,124}.

The final hydrogen-fueled scramjet engine developed and tested under Air Force sponsorship was the TMC Dual Mode Scramjet. The main feature of this concept, as previously discussed, is that the combustor is capable of operating in two modes; one for supersonic combustion and the other for subsonic operation. The engine shown in Fig. 14¹²⁰, which was preceded by extensive component tests of the inlet (from Mach 2 to 10) and combustor (Mach 3 to 6) from 1964 to 1967, was free-jet tested at Mach 3 and 5 in 1967 and 1968^{120,125}.

In the late 1960's, it became apparent that the proponents of the Aerospaceplane had understated the magnitude of the problems to be addressed as well as the time scale needed to resolve them. Consequently, the initial Aerospaceplane program was discontinued^{120,126}. As a result, support for hydrogen-fueled scramjet development was not renewed, rather emphasis was focused on liquid hydrocarbon-fueled scramjets, with TMC and UARL received contracts for component development. The UARL concepts focused on preburning part of fuel to produce a hot pilot to maintain combustion¹²⁷ which the TMC concept used a very reactive pilot oxidizer (ClF_3) to maintain combustion¹²⁸. The Marquardt engine, which is the same as that shown in Fig. 14 but with a longer combustor, was free-jet tested in 1970-1971 at Mach 3 to 6 flight conditions¹²⁹. However, by 1972, the Air Force concluded that scramjets were not appropriate for their mission requirements and support was terminated.

Some interest was expressed by the Air Force in a joint experimental hypersonic aircraft program with NASA in the mid-1970's¹²⁰, but nothing came of it and it was not until the new National Aerospace Plane (NASP) program was initiated in 1986 that the Air Force began, again, to support scramjet research and development.

At the NASA, early interest in scramjet propulsion evolved around both hydrogen-fueled hypersonic transports and an Aerospaceplane. After declining to jointly sponsor an Aerospaceplane program with the Air Force⁶⁶ circa 1962, emphasis was focused on evolving a program to develop the propulsion technology for hypersonic transports³⁰⁻¹³². As a result, in 1965, NASA initiated the Hypersonic Research Engine (HRE) project¹³³ at the Langley Research Center with the goal of flight testing a regeneratively cooled, flight weight scramjet engine on the X-15 research aircraft at speeds up to Mach 8. Garrett Air Research¹³⁴ was selected in 1966 as the contractor to design and develop a flight weight Structural Assembly Model (SAM) for structures, materials and hydrogen regenerative cooling evaluation and a heavyweight, water-cooled Aerothermodynamic Integration Model (AIM) to evaluate engine performance. Although the X-15 program was cancelled in 1968, the HRE program was continued. Consequently, in 1972, the SAM was tested at simulated Mach 7 flight speeds at Langley^{120,135,136} and the AIM engine tested at Plum Brook at Mach 5, 6 and 7 in the 1972-1974 time period^{120,136-138}. Photographs of these engines are

shown in Fig. 15¹³⁶. While not achieving net positive thrust, these tests did provide valuable insight into the design, testing and operation of dual-mode scramjet engines.

Concomitant with the HRE, a parallel, albeit more fundamental, effort to develop hydrogen-fueled scramjet technology was initiated at the Langley Research Center^{132,138,139-143}, including the construction of test facilities^{144,145}. Actually, these were preceded by fundamental studies and tests at the Applied Physics Laboratory under NASA sponsorship¹⁴⁶⁻¹⁵² beginning in 1962 and continuing through the mid-1970's.

With the cancellation of the X-15 program becoming imminent and the recognition that the propulsion integration must play a key role in any vehicle application, Langley personnel began addressing, in 1967^{153,154}, hypersonic hydrogen-fueled scramjet concepts that would be an integral part of a hypersonic transport. This approach evolved to the Airframe Integrated Scramjet concept¹⁵⁵ shown in Fig. 10^{120,136,155} and technology programs addressing this concept continued through 1986¹³⁵ when all NASA efforts were redirected towards technology development for the National AeroSpace Plane. These included additional test facilities and instrumentation; inlet, fuel injector and combustors tests; semi-free-jet engine tests; fundamental mixing, ignition and kinetics studies; and concomitant analyses, including advanced computational fluid dynamics codes^{120,136,156}.

Figures 17 through 20¹³⁶ are photographs of representative test hardware in each of the major areas. Figure 17 illustrates the evolution of inlets, Fig. 18 presents a representative fuel injector/combustor configuration tested, Fig. 19 shows three types of semi-free-jet engines tested at simulated Mach 4, 5.5 and 7 flight conditions and Fig. 20 presents the test facilities used. Excellent reviews of these efforts are given in Refs. 120 and 136.

Navy interest in scramjet propulsion centered around high speed (Mach 6-8) airbreathing missile applications as natural follow-ons to the TALOS and TYPHON ramjet powered missiles, most of which have been carried out by The Johns Hopkins University Applied Physics Laboratory (JHU/APL). Unlike the Air Force's and NASA's programs, which were directed at hydrogen-fueled engine concepts, the work at JHU/APL concentrated on storage liquid-fueled engine designs. As a result of their initial studies, Billig and Dugger applied for the first patent on a Supersonic Combustion Ramjet Missile (SCRAM) in 1961, the details of which are given in Ref. 157 and shown in Fig. 21.

Subsequent to the early feasibility studies, work was directed towards better understanding the physical and chemical processes governing supersonic combustion and developing a technological data base on inlets, fuel injectors, fuels combustors, nozzles and free-jet engines¹²⁰ for the remainder of the 1960's and most of the 1970's. In 1978, work on pure scramjets was terminated in favor of developing the DCR concept.

Examples of scramjet component development efforts are shown in Figs. 22-24. Figure 22 presents photographs of modular inlet designs tested in 1965¹²⁰ from Mach 4 to 10. Figure 23 presents a schematic and photograph of the connected-pipe combustor test apparatus, including a steam calorimeter developed to determine heat release combustion efficiency, used to develop the data base on fuels, fuel injectors, ignition aids and combustors^{120,158-160} for Mach 3 to 8 flight. These culminated in free-jet tests of a 25.4 cm (10-in.) dia engine (Fig. 22) at Mach 5.0, 5.8 and 7.1 from 1968 through 1974¹²⁰ which were the first tests of a scramjet engine in which net positive thrust was measured.

In 1978, emphasis switched to conducting a similar development program on the DCR¹⁶¹ (Fig. 3(b)). To date, tests on multiple inward turning scoop inlets for both the main supersonic combustor and gas generator have been made between Mach 3 and 6. Figure 25 is a photograph of one of the single scoop inlet models tested between Mach 3 and 6 since 1983¹³⁶. Connected-pipe tests of the gas generator alone and in tandem with supersonic combustors have also been made at simulated flight Mach numbers between 3 and 4, and tests at higher simulated flight Mach numbers will be made in the near future. Figure 26 is a photograph and schematic of the DCR connected-pipe combustor test set up. Credit is given here to Mestre and Ducourneau (Fr)¹⁶² who were the first to demonstrate very fuel-rich, stable combustion in subsonic combustors in 1973, a very important step in the evolution of the DCR combustion concept.

Complementing these development efforts have been other, more fundamental, research programs to analytically and experimentally explore and evolve a better understanding of the physics and chemistry governing the operation of the liquid-fueled scramjet and DCR. Analytically, these include components and cycle analyses^{160,163} as well as the application of Computation Fluid Dynamics (CFD) techniques to hypersonic airbreathing propulsion^{156,164}. Experimentally, these include developing new experimental techniques and instrumentation^{159,165} as well as obtaining fundamental process data^{160,166}. These basic efforts have continued through the present day and have been expanded to include fundamental experiments on supersonic free shear layer mixing and combustion and the control of incident shock separation by means of mass addition.

CURRENT STATUS OF SCRAMJETS

Currently, there are two on-going programs within the United States supporting hypersonic propulsion: the Navy's Dual Combustor Ramjet (Fig. 3(b)) and the National AeroSpace Plane (NASP) shown conceptually in Fig. 27. The latter is supported by the Air Force, Defense Advanced Research Projects Agency (DARPA), NASA and Navy. The DCR is a liquid hydrocarbon-fueled engine intended for Naval applications in the Mach 3 to 7 range¹⁶¹ while the NASP program is evolving a single-stage-to-orbit (and back) airbreathing propulsion cycle, the high speed end being a hydrogen-fueled scramjet (as a subset of the NASP, there is considerable interest in developing a Mach 5-6 air transport, i.e., the "Orient Express"). These are complemented by basic research programs supported by the Office of Naval Research, the Air Force Office of Scientific Research, NASA and the Canadian Ministry of Defense and exploratory development work supported the Navy and Air Force. Stalker (Australia) and his associates¹⁶⁷ are also conducting research on supersonic combustion of hydrogen in his shock tunnel. To the author's

knowledge, there are no ongoing programs on scramjets in Western Europe, although Great Britain does have a program to develop a two-stage, Horizontal Take-Off and Landing (HOTEL) space transport. However, while the first stage is an airbreather, it is reported to be a hybrid subsonic combustion ramjet (Fig. 2) with staging at about Mach 6.

The current status or state-of-the-art as applied to the development of scramjet engines, in the author's opinion, is as follows: for liquid- and/or gaseous-fueled scramjet engines, sufficient knowledge and data exist to design, build and fly one or more flight test vehicles over a flight Mach number range of approximately 3 to 7, provided they are boosted to their scramjet takeover speed using a separate propulsion system, e. g., a rocket ^{120,138}. For the DCR, on the other hand, several more years of exploratory inlet and combustor development as well as free-jet engine tests are necessary to achieve this same goal. These statements, however, should not be taken to imply that all of the desired technology is or will be shortly in hand, nor that all of the fundamental physical and chemical processes governing the operation of scramjets or DCR's in this flight regime are well understood or completely predictable. Rather, they are meant to impart the level of current understanding and knowledge ^{120,138,156,160,163,168}.

At speeds above about Mach 7 and on to orbital speeds, there are very little, if any, combustor data ^{120,138,160}. Inlet data, while somewhat more extensive ¹⁶⁸, is also in this category. There are no exit nozzle or engine data. Consequently, engineering design as well as fundamental process data are being rigorously pursued in all of these areas, at least in the U.S., in support of the Navy, Air Force and NASA propulsion development programs. For mixed cycle scramjets, e. g., Fig. 3(c), there is a similar paucity of data, albeit somewhat more extensive than at the high hypersonic speeds ^{8-10,169,170,171}. Mixed cycle ramjet engines, on the other hand, have a much more extensive data base for static and low speed operation.

Potentially, the most revolutionary tool in airbreathing propulsion (and almost all other disciplines) to evolve over the past decade is computational fluid dynamics, made possible by the evolution of supercomputers. In propulsion, CFD codes are currently capable of computing most viscous, non-reacting, albeit with real air thermochemistry, internal flows ^{156,172,173}. They have not, however, evolved to the point where they can predict, with sufficient resolution, three-dimensional, viscous, chemically reacting flows with or without the pressure of shock trains, i. e., typical flowfields with a scramjet combustor ^{156,174,175}. These limitations are due primarily to computational and storage limitations of current Class VI computers and a lack of detailed, fundamental experimental data with which the turbulence, kinetics, etc., models used in these codes can be compared and validated ^{156,160}. CFD, however, even with these limitations, still provides a powerful tool to aid in and provide direction for the design of scramjet engines and concomitant basic and applied experiments.

DEFICIENCIES AND OPPORTUNITIES

For exemplary purposes, the generic, gaseous-fueled, mixed cycle, dual-mode scramjet engine shown schematically in Fig. 28, which has the potential to produce thrust from static-to-orbital speeds, will be used as a point of departure in the succeeding discussions. Also, for convenience, three generic speed regimes, i. e., Mach 0 to 3, Mach 3 to 7 and Mach 7 and above, will be used to identify what, in the author's opinion, are the deficiencies and, therefore, opportunities in basic and applied research, exploratory development and CFD.

Operationally, the engine in Fig. 28 works as follows: static, subsonic and low supersonic speed ($M_0 < 3$) thrust are generated using retractable axial supersonic injectors to pump air through the engine and provide instream fuel injection. Wall injectors may also be used to augment the ejector fuel injection. In addition, the fuel composition (which may contain other than combustible species, especially at subsonic speeds) and distribution, engine equivalence ratio and area distribution between station 1 and 5 are varied such that M_4 and $M_5 \geq 1$, i. e., no geometric exit nozzle throat is required. Recent analyses ¹⁷⁰ and experiments ¹⁷¹ indicate that not only is it desirable to have a nozzleless engine over the entire flight regime to reduce complexity, but eliminating a geometric throat may, in fact, increase low speed engine performance. This operation assumes that the inlet is unstagnated, i. e., that a normal shock sits upstream of the cowl lip plane at supersonic flight speeds.

At flight speeds on the order of Mach 3, the axial injectors would retract, the inlet would start and the engine would operate in the subsonic combustion mode of a dual-mode scramjet with fuel provided by the wall injectors alone or in combination with the axial slot injectors as M_0 increases. The engine would continue to operate in this mode until Mach 6 to 7, when it would begin operating as a conventional scramjet. In this case, the ER and combustor geometry would, again, be modulated such that $M_5 \geq 1$ and the inlet diffusion shock structure would be stabilized between stations 1 and 4.

At about Mach 7, the wall injectors would be turned off so as not to thermally overload the walls in the vicinity of the injectors. In this case, the supersonic axial slot injectors would provide fuel to the combustor and thermal protection for the walls. From Mach 7 to perhaps as high as Mach 15 to 20, fuel alone would be injected from the slots. At speeds above these values, the composition of the injectant may include hot combustion products as well as fuel, i. e., a fuel-rich rocket exhaust, in the event that thrust augmentation is required to achieve orbital speeds.

With the generic engine cycle just described, it is now possible to present, in an orderly fashion, what controls the operation of the engine in the various speed regimes, what the present state-of-knowledge is or is not and what, in the author's opinion, is required to fill in the voids.

At static and subsonic speeds, the primary mechanisms controlling engine operation (including air capture) are the ejector thrust and air entrainment rate and the downstream combustion process. The entrainment rate, in turn, is controlled by the axial position and lateral distribution of the ejectors, the ejectant composition, pressure, velocity and temperature and, ultimately, the entrainment and/or

mixing rate within the compressible free shear layers generated. The combustion process is also controlled by the initial conditions of the ejectant and the diffusion or mixing rate of the free shear as well as equilibrium thermochemistry and the downstream area distribution (to keep M_0 and $M_2 > 1$). At supersonic speeds up to Mach 3 with the inlet unstated, engine operation continues to be dominated by these mechanisms, although the pumping requirements of the ejectors diminishes with speed, especially for $M_0 > 1$, where air capture is dominated by flight speed, internal combustion and area distribution.

Currently, there is a rather extensive design data base on non-reacting ejectors for nozzle and diffuser augmentation^{176,177}. For static and low speed ejector systems with combustion, i.e., ejector ramjets or hybrid rocket-ramjets, the reported data base is substantially smaller^{8,10,171,178,179}. Reference 171 is the only reported data applicable to an ejector scramjet. Analytically, Billig's work¹⁷⁰ is the most recent, and represents the first unified approach to optimizing the performance of combined cycle scramjets. It is evident, therefore, that an exploratory development data base demonstrating and documenting the static to Mach 3 performance of nozzleless ejector scramjet concepts is needed.

On a more fundamental level, the current understanding and predictability of compressible free shear layer mixing and combustion at these speeds is also limited, mainly due to a lack of detailed experimental measurements of turbulence and its influence on mixing and combustion. The experimental data in the literature are generally 10 to 20 years old¹⁶⁰ and only provided limited axial mean flow measurements of shear layer thickness and/or pitot pressure and gaseous species profiles. While these data are useful in specific development programs, they do not document or describe the flow in sufficient detail, nor are they systematic enough to permit an adequate description of the flow structure or the mechanisms controlling it to be made. This deficiency, however, could be overcome by conducting a series of experiments in which the initial and boundary conditions as well as in-stream, normal and axial property profiles are carefully measured using established in-situ measurement techniques, and the latest non-intrusive laser diagnostic techniques¹⁸⁰. Computationally, any number of CFD codes¹⁵⁶ exist which are capable of computing these shear flows with or without equilibrium thermochemistry, but their accuracy is dependent on the turbulence models used which, in turn, is dependent on the existence of a thorough, fundamental, experimental data base.

For the Mach 3 to 7 speed regime (with the inlet started), engine operation and efficiency is governed by the inlet compression process, the normal or axial fuel injection distribution, mixing, ignition and combustion processes, wall skin friction and heat transfer, and nozzle efficiency. Inlet efficiency, in turn, is governed by shock wave and viscous losses, the extent of which is dependent on a particular design, and nozzle efficiency is governed by chemical kinetics, wall friction and non-uniformities in property profiles (including imbedded waves and flow angularity).

The current understanding of engine operation at these speeds is quite good. There exists an extensive inlet design data base^{120,136,168} from which advanced concepts can be evolved with confidence. There is also an adequate semi-empirical data base for designing the length of duct needed to isolate combustion induced compression fields from adversely affecting inlet performance^{136,160}. One possible problem at these speeds, however, is the potential for a large separated zone to exist where the cowl shock intersects the inner body as depicted in Fig. 28. The traditional methods of alleviating this problem are to use shock traps and/or boundary layer bleed. For propulsion systems intended to go to orbital speeds, however, the air mass loss associated with bleed may impose too high an engine performance loss, requiring an alternative approach, such as mass injection to control the extent of the separated zone.

For fuel injector placement and fuel distribution, there are sufficient data to assess the design of combustors with wall injectors^{136,151,160,181} and an adequate data base on combustor wall shear and heat transfer^{120,160}, but not necessarily for the wall slot injectors. While data exist on slot injector placement, fuel distribution, mixing and combustion^{136,151,160}, they are not sufficient to be incorporated into a unified design procedure. This will require a more extensive experimental data base encompassing all of the pertinent parameters, i. e., slot geometry, angle and placement; fuel composition, distribution, temperature, pressure and velocity; and combustor geometry and initial conditions.

Data on nozzle performances alone are non-existent at these speeds, due primarily to test facility limitations. The only data available are wall static pressure distributions and some nozzle exit pitot pressure and species sample surveys obtained in free-jet engine tests^{80,120,136}.

On the more fundamental scientific level, Refs. 136 and 160 gives comprehensive reviews of the state-of-the-art of scramjets in the Mach 3 to 7 speed regimes. Rather than reiterate those discussions, their conclusions, while not always the same, may be summarized as follows: turbulence by itself and its effects on and interaction with chemical reactions is not well understood. Of primary interest are the onset of turbulence (transition) and the influence of turbulence on separation (and control thereof), wall skin friction with and without chemical reactions, and free shear layer mixing with and without combustion. Non-equilibrium thermochemistry in the nozzle is also not well understood. These, then, comprise the opportunities in this speed regime, some of which are currently beginning to be experimentally and analytically addressed, especially in the area of supersonic free shear layer mixing and combustion¹⁸²⁻¹⁸⁴.

Computationally, a large body of CFD codes¹⁵⁶ are available which can compute inlet and nozzle flows in the Mach 3 to 7 speed regimes, but, as previously stated, none exist which can compute, with acceptable resolution, the precombustion shock separated flow in the isolator duct or the 3-D, chemically reacting flows in the combustor. These are being addressed using 2-D¹⁸² or parabolized forms of the Navier-Stokes equations¹⁷⁴. Again, however, the accuracy of these models is only as good as the turbulence and chemistry models and sufficient experimental data do not exist to validate them.

At speeds above Mach 7, the mechanisms governing engine operation are the same as those in the Mach 3 to 7 range with one exception, chemical dissociation because of the elevated static temperatures in the entire engine. While some limited data exist on inlets¹⁶⁸ and forebody shock/boundary layer interaction¹⁶⁹, practically none exist on internally-ducted hypersonic flows, especially with combustion¹⁶⁷. In addition, there are no fundamental process data and, while CFD codes can compute any number of flowfields, there are no data to establish their veracity or accuracy. Consequently, any carefully measured set of data, whether they be basic or applied, would provide a much needed step in confirming the current understanding or evolving a better understanding of scramjet engine operation at very high hypersonic speeds.

CONCLUDING REMARKS

Considerable advances in the state-of-knowledge of scramjet engines and derivatives thereof have been made since the inception of this propulsion cycle approximately 30 years ago. Currently, sufficient knowledge exists to design and build a rocket-boosted scramjet for Mach 3 to 7 flight, but additional development is required to extend the upper bound to orbital speeds and lower bound to static conditions. Computational fluid dynamics, while a powerful tool, is still in its formative stage, being hampered by computer limitations as well as a lack of fundamental process data to validate a number of the physical and chemical models used.

Consequently, opportunities in scramjet research and development abound. On a fundamental level the most pressing need is to understand turbulence, especially at supersonic and hypersonic flight speeds, and to be able to predict its effect on wall shear and heat transfer, boundary layer separation and reattachment, normal-to-axial fuel injection and mixing as well as chemical kinetics. On the more practical side, an extensive effort is required to obtain the requisite engineering design (or development) data base on mixed cycle scramjet engine performance at low speeds, to complement the existing scramjet data base in the Mach 3 to 7 range and to begin to generate a similar data base for flight speeds from Mach 8 to 25.

REFERENCES

1. Anderson, J.D., Introduction to Flight, McGraw-Hill Book Co., USA, 1978.
2. Taylor, C.F., "A Review of the Evolution of Aircraft Powerplants," Annual Report of the Smithsonian Institution, 1962, U.S. Government Printing Office Publication 4518, December 1962, pp. 245-298.
3. Smith, G.G., Gas Turbines and Jet Propulsion, Iliffe and Sons Inc. (London), 1955.
4. Lancaster, O.E. (Editor), Jet Propulsion Engines, Princeton University Press, USA, 1959.
5. Bulstein, R.E., Flight in America (1900-1983), The Johns Hopkins University Press, USA, 1984.
6. Gibbs-Smith, C.H., Aviation: A Historical Survey from its Origins to the End of World War II, Her Majesty's Stationary Office, London, 1970.
7. Briggs, M.M., Campbell, V., Andrus, S.R., and Burger, G.R., "Synthesis and Performance of an Air-Turboramjet-Propelled Supersonic Target Vehicle," AIAA Paper No. AIAA-84-0075, January 1984.
8. Bendot, J.G., "Composite Propulsion Systems for an Advanced Reusable Launch Vehicle Application," Proceedings of the 2nd ISABE, Sheffield, England, March 1972; Also, "Hypermixing Ejectors for Composite Engines," Proceedings of the 3rd ISABE, Munich, Germany, March 1976.
9. History of the Ducted Rocket, 1953-1969, Thiokol Chemical Corp. Brochure, Huntsville, AL, 1970.
10. Benkmann, P., and Kramer, P.A., "Design Considerations and Analytical Comparisons of Different Types of Ramjets and Ramrockets," Ramjets and Ramrockets for Military Applications, AGARD-CP-307, March 1982.
11. Zucrow, M.J., Aircraft and Missile Propulsion, John Wiley & Sons, Inc., 1958, Vol. 2, pp. 348-351.
12. Avery, W.H., "Twenty Five Years of Ramjet Development," Jet Propulsion, Vol. 25, No. 11, November 1955, pp. 604-614.
13. Jane's Pocket Book of Research and Experimental Aircraft, Collier Books, MacMillan Publ. Co., NY, 1976.
14. Hallion, R.P., "Stalin's Stovepipes: The Origins of the Ramjet Engine in the Soviet Union, 1929-1948," National Air and Space Museum Memo, Smithsonian Institution, USA, February 4, 1978.
15. Trommsdorff, W., "High-Velocity Free-Flying Ram-Jet Units (TR-Missiles): Research Work at the German Army Ordnance Office 1936-1945," History of German Guided Missile Development, AGARD 1st Guided Missile Seminar, Munich, Germany, April 1955, pp. 352-374.
16. Herman, G., Jet Pioneers, Duell, Sloan and Pierce, NY, 1963, pp. 195-211.

17. Shortal, J.P., "A New Dimension. Wallops Island Flight Test Range: The First Fifteen years," NASA Reference Publication 1098, USA, December 1978.
18. Curran, E.T., and Stull, F.D., "Ramjet Engines: Highlights of Past Achievements and Future Promise," Proceedings of the 2nd ISABE, Sheffield, England, March 1974.
19. Marguet, R., Ecary, C., and Cazin, P., "Studies and Tests of Rocket Ramjets for Missile Propulsion," Proceedings of the 4th ISABE, Orlando, FL, April 1979, AIAA Paper No. 79-7037, NY, 1979, pp. 297-306.
20. Marguet, R., and Cazin, P., "Ramjet Research in France: Realities and Perspectives," Proceedings of the 7th ISABE, Beijing, China, September 1985, AIAA/ISABE Paper No. 85-7022, NY, 1985, pp. 215-223.
21. Ramjets and Ramrockets for Military Applications, AGARD-CP-307, March 1982.
22. Ramjet and Ramrocket Propulsion Systems for Missiles, AGARD-LS-136, October 1984.
23. Hicks, B.L., "Addition of Heat to a Compressible Fluid in Motion," NACA ACR No. E4A29, 1945.
24. Hicks, B.L., "On the Characterization of Fields of Diabatic Flow," Quarterly of Applied Mathematics, Vol. VI, No. 4, 1949.
25. Hicks, B.L., Herbrank, W.H., and Kravitz, "Comment on Heat Source in a Uniform Flow," Journal of the Aeronautical Sciences, Vol. 17, No. 9, September 1950.
26. Shapiro, A.H., and Hawthorne, W.R., "The Mechanics and Thermodynamics of Steady One-Dimensional Gas Flow," Journal of Applied Mechanics, Vol. 14, No. 4, December 1947. Also, Handbook of Supersonic Aerodynamics, NAVORD Rept. 1488, Vol. I, April 1950; and Shapiro, A.H., The Dynamics and Thermodynamics of Compressible Fluid Flow, Vol. I., The Ronald Press Co., NY, 1953.
27. Pinkel, I.I., and Serafini, J.S., "Graphical Method for Obtaining Flow Field in Two-Dimensional Supersonic Stream to Which Heat is Added," NACA TN 2206, November 1950.
28. Wald, Q., "Reduction of Drag at Supersonic Velocities by Heating the External Air Stream," United Aircraft Corp. Research Dept. M-13362-2, June 1950.
29. Baker, W.T., Davis, T., and Matthews, S.E., "Reduction of Drag of a Projectile in a Supersonic Stream by the Combustion of Hydrogen in the Turbulent Wake," The Johns Hopkins University Applied Physics Laboratory, CM-673, June 1951.
30. Scanland, T.S., and Hebrank, W.H., "Drag Reduction through Heat Addition to the Wake of Supersonic Missiles," Ballistic Research Laboratories, Memo Rep. No. 596, June 1952.
31. Serafini, J.S., Dorsch, R.G., and Fletcher, E.A., "Exploratory Investigation of Static and Base-Pressure Increase Resulting from Combustion of Aluminum Borohydride Adjacent to Body of Revolution in Supersonic Wind Tunnel," NACA RM E57E15, October 1957.
32. Murthy, S.N.B. (Editor), Progress in Astronautics and Aeronautics - Aerodynamics of Base Combustion, Vol. 40, AIAA, NY, 1976.
33. Schetz, J.A., and Billig, F.S., "Simplified Analysis of Supersonic Base Flows Including Injection and Combustion," AIAA Journal, Vol. 14, January 1976, p. 7.
34. Schetz, J.A., Billig, F.S., and Favin, S., "An Approximate Analysis of Axisymmetric Supersonic Base Flows with Injection," AIAA Journal, Vol. 18, No. 8, August 1980, pp. 867-868.
35. Pinkel, I.I., Serafini, J.S., and Gregg, J.L., "Pressure Distribution and Aerodynamic Coefficients Associated with Heat Addition to Supersonic Air Stream Adjacent to Two-Dimensional Supersonic Wing," NACA RM E 51-K26, February 1952.
36. Smith, E.H., and Davis, T., "The Creation of Thrust and Lift by Combustion on External Surfaces of Airfoils," Smith and Davis, Physicists, Silver Spring, MD (BuOrd Contract NOrd 12141) September 1, 1952.
37. Chu, Boa-Teh, "Pressure Waves Generated by Addition of Heat in a Gaseous Medium," NACA TN 3411, June 1955.
38. Gazley, Carl, Jr., "Linearized Solution for Heat Addition at the Surface of a Supersonic Airfoil," Project Rand Rept. RM-1892, ASTIA AD 133025, November 1956.
39. McCloy, R.W., "Propulsion by Supersonic Heat Addition," Report CV-1, "External Heat Addition for Cases Other than Constant-Pressure Heat Addition," Report CV-5, and "Specific Fuel Consumption and Over-all Efficiency for External Heating Processes," Report CV-6, Convair Division of General Dynamics Corporation, March 7, 1958.
40. Mager, A., "Supersonic Airfoil Performance with Small Heat Addition," Journal of the Aero/Space Sciences, Vol. 26, No. 2, February 1959.
41. Dugger, G.L., and Monchick, L., "External Burning Ramjets, Preliminary Feasibility Study," The Johns Hopkins University Applied Physics Laboratory, CM 948, June 1959; also TG-892, March 1967.

42. Dugger, G.L., Deklau, B., Billig, F.S., and Mathews, S., "Summary Report on External Ramjet Program," TC-419, The Johns Hopkins University Applied Physics Laboratory, Laurel, MD, October 1961; Also, Billig, F.S., "External Burning in Supersonic Streams," JHU/APL TC-912, May 1967.
43. Krull, H.G., et.al., "Investigation of Supersonic Burning - Final Summary Report 25002," The Marquardt Co., August 1958.
44. Dorsch, R.G., Serafini, J.S., and Fletcher, E.A., "Exploratory Investigation of the Aerodynamic Effects of External Combustion of Aluminum Borohydride in Airstream Adjacent to Flat Plate in Mach 2.46 Tunnel," NACA RM E57E16, 1957.
45. Dorsch, R.G., Serafini, J.S., Fletcher, E.A., and Pinkel, I.I., "Experimental Investigation of Aerodynamic Effects of External Combustion in Air Stream Below Two-Dimensional Supersonic Wing at Mach 2.5 and 3.0," NASA Memo 1-11-59E, March 1959.
46. Dorsch, R.E., Allen, H., Jr., and Dryer, M., "Investigation of Aerodynamic Effects of External Combustion Below Flat-Plate Model in 10-by-10-foot Wind Tunnel at Mach 2.4," NASA D-282, April 1960.
47. Weber, R.J., and MacKay, J.S., "An Analysis of Ramjet Engines Using Supersonic Combustion," NACA Technical Note 4386, 1958.
48. Roy, P.M., "Propulsion Supersonique par Turboreacteurs et par Statoreacteurs." Paper read at First International Congress in Aeronautical Sciences under the auspices of the International Council of the Aeronautical Sciences, Madrid, Spain, September 8-13, 1958. (Preprint by Pergamon Press, New York, NY)
49. Dunlap, R., Brehm, R.L., and Nicholls, J.A., "A Preliminary Study of the Application of Steady-State Detonative Combustion to a Reaction Engine," Jet Propulsion, Vol. 28, July 1958, p. 451.
50. Sargent, W.H., and Gross, R.A., "Detonation Wave Hypersonic Ramjet," ARS Journal, Vol. 30, 1960, p. 543.
51. Dugger, G.L., "Comparison of Hypersonic Ramjet Engines with Subsonic and Supersonic Combustion," Fourth AGARD Colloquium, Milan, Italy; also Combustion and Propulsion-High Mach Number Air Breathing Engines, Edited by Jaumotte, Rothrock and LeFebvre, Pergamon Press, New York, 1960.
52. Ferri, A., "Possible Directions of Future Research in Airbreathing Engines," Fourth AGARD Colloquium, Milan, Italy; also Combustion and Propulsion-High Mach Number Air Breathing Engines, Edited by Jaumotte, Rothrock and LeFebvre, Pergamon Press, New York, 1960.
53. McLafferty, G.H., "Relative Thermodynamic Efficiency of Supersonic Combustion and Subsonic Combustion Hypersonic Ramjets," ARS Journal, Vol. 30, 1960, p. 1019.
54. Mordell, D.L., and Swithenbank, J., "Hypersonic Ramjets," Second International Council of Aeronautical Sciences, Zurich, Switzerland, September 12-16, 1960.
55. Nicholls, J.A., Dabora, E.K., and Gealer, R.L., "Studies in Connection with Stabilized Gaseous Detonation Waves," Seventh Symposium (International) on Combustion, Butterworth's Scientific Publications, London, 1948, p. 766.
56. Gross, R.A., "Exploratory Studies of Combustion in Supersonic Flow," AFOSR TN 59-587, June 1959; also ARS Journal, Vol. 29, No. 1, January 1959, pp. 63-64.
57. Nicholls, J.A., "Stabilization of Gaseous Detonation Waves with Emphasis on the Ignition Time Delay Zone," AFOSR TN 60-442, June 1960.
58. Rhodes, R.P., and Chriss, D.E., "A Preliminary Study of Stationary Shock-Induced Combustion with Hydrogen Air Mixtures," Arnold Engineering Development Center, AEDC TN 61-36, July 1961.
59. Rhodes, R.P., Rubins, P.M., and Chriss, D.E., "The Effect of Heat Release on the Flow Parameters for Shock-Induced Combustion," Arnold Engineering Development Center, AEDC-TDR-62-78, May 1962.
60. Dugger, G.L., "A Future for Hypersonic Ramjets," Astronautics, Vol. 4, April 1959, pp. 38-39, 114-115.
61. Proceedings, 2nd USAF Symposium on Advanced Propulsion Concepts, October 7-8, 1959, Boston, MA, AFPRD-60-2519, Vol. II.
62. Republic Aviation Corp. Reports related to single-stage-to-orbit studies, 1961-62. RAC 430, 730, and 1306.
63. Jarlett, F.E., "Comparative Study of Aerospaceplanes," 8th Symposium on Ballistic Missiles and Space Technology, Vol. 5, October 16-18, 1963.
64. Republic Aviation Corp., "2-Stage Aerospaceplane Study," RAC1370-20-I, January 28, 1964.
65. Douglas Aircraft Co., "2-Stage Aerospaceplane Study," DAC 47551, 1964.
66. Balch, J.V., and Loftin, L.K., Jr., "Joint USAF/NASA Proposals for Additions to Hypersonic Research Programs Applicable to Airbreathing Vehicles," USAF/NASA Document dated November 9, 1962.

67. Dugger, G.L., Billig, F.S., and Avery, W.H., "Hypersonic Propulsion Studies at The Johns Hopkins University Applied Physics Laboratory," JHU/APL TG-405, June 1961.
68. Mestre, A., and Viaud, L., "Combustion Supersonique dans un Canal Cylindrique," Supersonic Flow, Chemical Processes and Radiative Transfer (Olfe and Zakkay, Ed.), MacMillan Co., NY, 1964; Also ONERA TP-11 (Fr), 1963.
69. Leuchter, O., "Méthode Expérimentale D'Étude de la Combustion Supersonique Air-Hydrogène," ONERA TP-682 (Fr), 1969.
70. Leuchter, O., "Problèmes de Mélange et de Combustion Supersonique D' Hydrogène dans un Statoreacteur Hypersonique," ONERA-TP-973 (Fr), 1971.
71. Borghi, R., and Ducourneau, F., "Etude du Mélange et de la Combustion de deux Flux Supersoniques Paralleles d'Air et de Methane," Proceedings of the European Mechanics Colloquium 19 (Hypersonic Propulsion with Emphasis on Heat Addition to Supersonic Flows), December 1970.
72. Ducourneau, F., and Borghi, R., "Etude Expérimentale du Mélange Avec Combustion de deux Ecoulements Supersoniques Paralleles de Methane et d'Air," Recherche Aerospatiale, Vol. 5, 1971, pp. 310-312.
73. Bellet, J.C., Danzeir, M.P., Soustre, J. and Manson, N., "Influence of Aerodynamic Field on Shock-Induced Combustion of Hydrogen and Ethylene in Supersonic Flow," Laboratoire d' Energetique de l' de l'Université de Portiere Report, 1971.
74. Leynaert, J., "Prise d' Air pour de vol a Mach 7," ONERA-TP-658 (Fr), 1968.
75. Marguet, R., "Ramjets," Propulsion of Hypersonic Vehicles, AGARD-LS-42, Vol. 2, 1972, pp. 96-146.
76. Ceresuela, R., "Aerodynamics Problems," Propulsion of Hypersonic Vehicles, AGARD-LS-42, Vol. 2, 1972, pp. 147-195.
77. Marguet, R., "Choice of Propulsion Mode," Propulsion of Hypersonic Vehicles, AGARD-LS-42, Vol. 2, 1972, pp. 2-29.
78. Soulier, C., and Laverre, J., "Utilisation de la Soufflerie Hypersonique S4MA pour les Essais de Combustion Supersonique de Statoreacteurs," ONERA-TP-924 (Fr), 1971.
79. Contensou, P., Marguet, R., and Huet, C., "Etude Theorique et Experimentale d'un Statoreacteur a Combustion Mixte (domaine de vol Mach 3/7)," ICAS Paper No. 72-74, September 1972.
80. Contensou, P., Marguet, R., and Huet, C., "Etude Theorique et Experimentale d'un Statoreacteur a Combustion Mixte (domaine de vol Mach 3.5/7)," ONERA-TP-1121, 1972; also Recherche Aerospatiale, No. 5, 1973, pp. 259-274.
81. Townsend, L.H., and Reid, J., "Some Effects of Stable Combustion in Wakes Formed in a Supersonic Stream," Royal Aircraft Establishment Technical Note (GB) Aero. 2872, March 1963; also, Supersonic Flow, Chemical Processes and Radiative Transfer (Olfe and Zakkay, Ed.), MacMillan Co., NY, 1964, pp. 137-156.
82. Hawkins, R., and Fox, M.D., "An Investigation of Real Gas Effects Relevant to the Performance of a Kerosene Fueled Hypersonic Ramjet," Supersonic Flow, Chemical Processes and Radiative Transfer (Olfe and Zakkay, Ed.), MacMillan Co., NY, 1964, pp. 113-136.
83. Hawkins, R., "The Feasibility of Supersonic Combustion Ramjets for Low Hypersonic Speeds," B.S.E. A.P.R.G. Report AP-5329 (Rolls Royce, GB), September 1965.
84. Fox, M.D., "Feasibility of an Experimental Study of Supersonic Combustion," B.S.E. A.P.R.G., Report AP-5386 (Rolls Royce, GB), September 1966.
85. Harper, L.R., and Hawkins, R., "Some Tests of a Supersonic/Transonic Combustor," B.S.E. A.P.R.G. Report AP-5618 (Rolls Royce, GB), May 1969.
86. Swithenbank, J., "Hypersonic Airbreathing Propulsion," Progress in the Aero. Sciences, Vol. 8, Pergamon Press, New York, 1966, pp. 229-294 (paper was written in 1964).
87. Ogerby, I.T., "An Investigation of Supersonic Combustion and Heterogeneous Turbulent Jet Mixing Related to the Design/Operation of Scramjets," Ph.D. Thesis, University of Sheffield (GB), October 1965.
88. Swithenbank, J., and Parsons, R.J., "Experimental Techniques for Supersonic Combustion Research in a Shock Tunnel," presented at the AGARD 30th Propulsion and Energetics Panel Meeting, Munich, Ger., September 1967.
89. Swithenbank, J., and Chigier, N.A., "Vortex Mixing for Supersonic Combustion," Twelfth Symposium (International) on Combustion, The Combustion Institute, 1969, pp. 1153-1162.
90. Jacques, M.R., "Mixing and Combustion of Hydrogen in a Supersonic Stream," Final Scientific Report, University of Sheffield (GB), H.I.C. 170, AFEOAR 70-0071, February 1971.

91. Jacques, M.R., Payne, R., and Swithenbank, J., "Studies Leading to the Realization of Supersonic Combustion in Propulsion Applications," University of Sheffield (GB), H.I.C. 174, June 1972.
92. Payne, R., "Supersonic Combustion of Liquid Kerosene," Ph.D. Thesis, University of Sheffield, March 1975.
93. Cookson, R.A., Flannagan, P., and Penny, G.S., "A Study of Free-Jet and Enclosed Supersonic Diffusion Flames," Twelfth Symposium (International) on Combustion, The Combustion Institute, 1969, pp. 1115-1124.
94. Cookson, R.A., "Mixing and Ignition of Enclosed Supersonic Diffusion Flames," U.S. Air Force Report ARL-73-0070, April 1973.
95. Cookson, R.A., and Isaac, J.J., "Factors Affecting Aided Combustion of Liquid and Gaseous Fuels Injected Transversely into a Supersonic Air-Stream," AIAA Paper No. 74-1160, October 1974; Also AIAA Journal, Vol. 14, No. 1, January 1976.
96. Cookson, R.A., and Isaac, J.J., "Combustion Generated Heat Addition to a Ducted Supersonic Stream - I. Theory," Acta Aeronautica, Vol. 6, 1979, pp. 511-530; - "II. Experimental Study," pp. 531-539.
97. Winterfeld, G., "On the Stabilization of Hydrogen Diffusion Flames by Flame Holders in Supersonic Flow at Low Stagnation Temperatures," Proceedings of the Cranfield International Propulsion Symposium, 1967, Oxford: Pergamon Press, 1968, p. 95.
98. Winterfeld, G., "Untersuchungen über den Massenaustausch zwischen Rückstromgebieten hinter rotationsymmetrischen Flammenhalten und der umgebenden Strömung," Deutsche Luft und Raumfahrt Forschungsbericht, DLR-FB-69-07, 1969.
99. Suttrop, F., "On the Effects of Hydrogen Pre-Burning Applied to Supersonic Diffusion Flames," Proceedings of the European Mechanics Colloquium 19 (Hypersonic Propulsion with Emphasis on Heat Addition to Supersonic Flows), December 1970.
100. Kauer, F., Niezgodka, J., and Post, H., "Experimental Investigation of Supersonic Combustion in the Flowfield of Bodies of Revolution and near a Flat Plate," Proceedings of the European Mechanics Colloquium 19 (Hypersonic Propulsion with Emphasis on Heat Addition to Supersonic Flows), December 1970.
101. Suttrop, F., "Ignition of Gaseous Hydrocarbon Fuels in Hypersonic Engines," Proceedings of the 1st ISABE, Marseille, Fr, June 1972.
102. Winterfeld, G., "Investigation of the Stabilization of Hydrogen-Diffusion Flames by Means of Flameholders in Supersonic Flows," Deutsche Luft und Raumfahrt Forschungsbericht, DLR-FB-76-35, 1976, pp. 1-83.
103. Kallergis, M., "Model Investigations on External Supersonic Combustion in the Large Propulsion Windtunnel of DFVLR," Proceedings of the European Mechanics Colloquium 19 (Hypersonic Propulsion with Emphasis on Heat Addition to Supersonic Flows), Dec. 1970.
104. Kallergis, M., and Ahlswede, M., "Theoretische und Experimentelle Untersuchungen über die Wärmezufuhr durch Verbrennung von Triäthylaluminium in Luftströmungen," Deutsche Forschungs- und Versuchsanstalt für Luft- und Raumfahrt, DLR-FB-75-05, 1975.
105. Bier, K., Kappler, G., and Wilhelmi, H., "The Initiation and Propagation of Combustion at Transverse Fuel Injection into Supersonic Air Streams," Proceedings of the European Mechanics Colloquium 19 (Hypersonic Propulsion with Emphasis on Heat Addition to Supersonic Flows), Dec. 1970.
106. Wilhelmi, H., Baselt, J.P., and Bier, K., "Experiments on the Propagation of Mixing and Combustion Injecting Hydrogen Transversely into Hot Supersonic Streams," Fourteenth Symposium (International) on Combustion, The Combustion Institute, 1973, pp. 685-593.
107. Wilhelmi, H., "Experiments on the Ignition Conditions and the combustion Process in Supersonic Diffusion Flames," Archivum Procesow Spalania, Vol. 5, No. 3, 1974, pp. 243-260.
108. Bayev, V.K., and Golovichev, V.I., et.al., Combustion in Supersonic Flow, Nauka Publishing House, Novosibirsk, USSR, 1984.
109. Da-Riva, I., et.al., "Diffusion Flames and Supersonic Combustion," AFEOR Final Report, Grant No. 67-43, June 1969.
110. Tsuji, H., Takeno, T. and Yoshida, A., "A Preliminary Study of Supersonic Combustion in a Vitiated Airstream Using Transverse Injection," University of Tokyo Report No. 510, March 1974.
111. Yoshida, A., Tsuji, H., "Supersonic Combustion of Hydrogen in a Vitiated Airstream using Transverse Injection," AIAA Journal, Vol. 15, No. 4, April 1977.
112. Mölder, S., "Intakes for Hypersonic Ramjets," Canadian Aeronautics and Space Journal, September 1963.
113. Mölder, S., and Romeas, J.M., "Modular Hypersonic Inlets with Conical Flow," AGARD-CP-30, May 1968.

114. D'Souza, N., Mölder, S., and Moretti, G., "Numerical Method for Hypersonic flow over Blunt Leading Edges and Two Blunt Bodies," AIAA Journal, Vol. 10, No. 5, May 1972, pp. 623-629.
115. Mölder, S., and Wu, J., "Air Airbreathing Satellite Booster," IAS Paper No. 60-99, October 1960.
116. Mölder, S., and Raymond, H., "A Proposal for a Research Program to Design, Manufacture and Flight Test a Supersonic Combustion Ramjet Engine (Scramjet)," Aviation Electric Limited and McGill University Proposal No. 9311, April 1965.
117. Amin, M.F., and Mölder, S., "Performance Comparison on Gun Launched Scramjets for Various Fuels," Journal of Spacecraft and Rockets, Vol. 4, No. 8, August 1967.
118. Wilks, W.K., "Scramjet Flights May Begin in 1967," Missiles and Rockets, September 13, 1965, pp. 15.
119. Wise, C.E., and Wood, N., "On to Mach 12," Machine Design, March 2, 1967, pp. 84-89.
120. Waltrup, P.J., Anderson, G.Y., and Stull, F.D., "Supersonic Combustion Ramjet (Scramjet) Engine Development in the United States," Proceedings of the 3rd ISABE, Deutsche Gesellschaft für Luft und Raumfahrt, Cologne, West Germany, A77-17266-05-07, 1976, pp. 835-861.
121. Kepler, C.E., and Karanian, A.J., "Hydrogen-Fueled Variable-Geometry Scramjet," United Aircraft Research Laboratories, AFAPL-TR-67-150, January 1968.
122. Harshman, D.L., "Design and Test of a Mach 7-8 Supersonic Combustion Ramjet Engine," AIAA Propulsion Specialist Meeting, July 1967, Washington, D.C.
123. Colley, W.C., and Harsha, P.T., "Performance Tests of a Supersonic Combustor Having a Wall Step Flameholder," General Electric Report R65FPD18, April 1965.
124. "Investigations of the Low Speed Fixed Geometry Supersonic Combustion Ramjet," General Applied Sciences Laboratories, AFAPL-TR-66-139, March 1967.
125. Burnette, T.D., "Dual Mode Scramjet," The Marquardt Corporation, AFAPL-TR-67-132, June 1968.
126. Roffe, G., Visich, M., Jr., and Ranlet, J., "A Conceptual Design Study for a Low Altitude High Mach Number Vehicle," AFFDL-TR-71-48, September 1971.
127. Kay, I.W., and McVey, J.B., "Hydrocarbon Fueled Scramjet: Vol. XI Combustor Demonstration Program," AFAPL-TR-68-146, May 1972.
128. Heins, Jr., A.E., Reed, G.J., and Woodgrift, K.W., "Hydrocarbon Scramjet Feasibility Program, Part III. Free Jet Engine Design and Performance," AFAPL-TR-70-74, January 1971.
129. Heins, Jr., A.E., Reed, G.J., and Woodgrift, K.W., "Hydrocarbon Scramjet Feasibility Program, Part III. Free Jet Engine Design and Performance," AFAPL-TR-70-74, January 1971.
130. Bickle, P.F., Memo to Langley, "Hypersonic Propulsion Flight Program," February 28, 1963.
131. The Marquardt Company, "Feasibility and Preliminary Design Study of Hypersonic Airbreathing Propulsion Systems for Testing on the X-15 Vehicle," Report 6020, Vol. 1, February 7, 1964.
132. Anderson, G.Y., "Supersonic Combustion Ramjet Performance," NASA TM X-968, February 1964.
133. Source Evaluation Board, HRE Project 76-700-729, Memo to NASA Administrator, "Findings of the Board for Phase I," March 23, 1965.
134. Source Evaluation Board, HRE Project 76-700-729, "Findings of the Board on Results of Phase I and Proposals for Phase II," Langley document, June 2, 1966.
135. Wieting, A.R., "Aerodynamic and Thermal Analysis of Results of Tests of a Hydrogen Cooled Scramjet Engine at Mach 6.3," NASA TM X-2767, May 1973.
136. Northam, G.B., and Anderson, G.Y., "Supersonic Combustion Ramjet Research at Langley," AIAA Paper No. 86-0159, January 1986.
137. "Hypersonic Research Engine Project-Phase II, Aerothermodynamic Integration Model Development - Final Technical Data Report," NASA CR-132654, 1975.
138. Anderson, W.L., and Kado, L., "Hypersonic Research Engine Project-Phase II, Aerothermodynamic Integration Model (AIM) Test Report," NASA CR-132655, 1975.
139. Weidner, J.P., and Trexler, C.A., "Preliminary Investigation of Momentum Diffusion Between Two Supersonic Airstreams in the Presence of Shock Waves," NASA TN D-4974, 1964.
140. Torrence, M.G., "Concentration Measurements of an Injected Gas in a Supersonic Stream," NASA TN D-3860, 1967.
141. Henry, J.R., "Fuel Injection and Mixing in Scramjet Combustors," NASA TM X-1437, 1967.
142. Anderson, G.Y., and Vick, A.R., "An Experimental Study of Flame Propagation in Supersonic Premixed Flows of Hydrogen and Air," NASA TN D-4631, June 1968.

143. Henry, J.R., "Recent Research on Fuel Injection and Mixing and Piloted-Ignition for Scramjet Combustors," Twelfth Symposium (International) on Combustion, The Combustion Inst., 1969, pp. 1175-1182.
144. "Engineering Analyses and Design Calculations of NASA Langley Research Center Hydrogen-Air-Vitiated Heater with Oxygen Replenishment," NASA CR-132381, 1968.
145. Sutton, K., "Descriptions and Operating Parameters of a Mach 2 Nozzle System for the Langley 11-Inch Ceramic-Heated Tunnel," NASA TN D-4750, September 1968.
146. Yates, C.L., Billig, F.S., and Dugger, G.L., "Experimental Results and Data Analysis Techniques of a Hydrogen-Fueled Supersonic Combustor," NASA CR-531, 1966.
147. Morgenthaler, J.H., "Supersonic Mixing of Hydrogen and Air," NASA CR-747, 1967.
148. Orth, R.C., and Funk, J.A., "An Experimental and Comparative Study of Jet Penetration in Supersonic Flow," AIAA Paper No. 67-225, January 1967.
149. Orth, R.C., Schetz, J.A., and Billig, F.S., "The Interaction and Penetration of Gaseous Jets in Supersonic Flow," NASA CR-186, 1969.
150. Billig, F.S., Wagner, J.P., and Cameron, J.M., "Penetration and Spreading of Transverse Jets of Hydrogen in a Mach 2.72 Airstream," NASA CR-1794, March 1971.
151. Orth, R.C., Billig, F.S., and Funk, J.A., "Direct-Connect Tests of a Hydrogen Fueled Supersonic Combustor," NASA CR 1904, August 1971.
152. Anderson, G.Y., Eggers, J.M., Waltrup, P.J., and Orth, R.C., "Investigation of Step Fuel Injectors for an Integrated Modular Scramjet Engine," CPIA Publication 281, Vol. III, 1976, pp. 175-190.
153. Kirkham, F.S., Cabbage, J.M., Vahl, W.A., and Small, W.J., "Studies of Airframe-Propulsion-System Integration for Mach 6 Cruise Vehicles," NASA TN D-4128, 1967.
154. Williams, L.J., and Wilcox, D.E., "Scramjet Vehicle Engine-Airframe Integration Effects," Conference on Hypersonic Aircraft Technology, NASA Ames Research Center, Moffett Field, CA, NASA SP-148, May 1967.
155. Henry, J.R., and Anderson, G.Y., "Design Considerations for the Airframe-Integration Scramjet," 1st International Symposium on Air Breathing Engines, June 19-23, 1972, Marseille, France.
156. White, M.E., Drummond, J.P. and Kumar, A.J., "Evolution and Status of CFD Techniques for Scramjet Applications," AIAA Paper No. 86-0160, January 1986.
157. Dugger, G.L., Avery, W.H., Walker, J.H., Billig, F.S., Rivello, R.M., and Allen, R.W., "A Supersonic Combustion Ramjet Missile (SCRAM) for Naval Air Defense," The Johns Hopkins University Applied Physics Laboratory (USA), TG-449, September 1962.
158. Billig, F.S., Pirkle, J.C., and Dugger, G.L., "Scramjets Fuels Evaluation," AFAPL-TR-72-21, July 1972.
159. Orth, R.C., Billig, F.S., and Grenleski, S.E., "Measurement Techniques for Supersonic Combustion," Progress in Astronautics and Aeronautics, Vol. 34, Instrumentation for Airbreathing Propulsion, MIT Press, January 1974.
160. Waltrup, P.J., "Liquid Fueled Supersonic Combustion Ramjets: A Research Perspective of the Past, Present and Future," AIAA Paper No. 86-0158, January 1986; also Journal of Propulsion and Power, 1987.
161. Billig, F.S., Waltrup, P.J., and Stockbridge, R.D., "The Integral Rocket Dual Combustion Ramjet: A New Propulsion Concept," Journal of Spacecraft and Rockets, Vol. 17, No. 5, pp. 416-424, September-October 1980.
162. Mestre, A., and Ducourneau, P., "Recent Studies on the Spontaneous Ignition of Rich Air-Kerosine Mixtures," Office National d'Etudes et de Recherches Aerospatiales (ONERA) TP 1209, Chatillon, France, 1973.
163. Billig, F.S., "Combustion Processes in Supersonic Flow," Proceedings of the Seventh International Symposium on Air Breathing Engines, Beijing, China, September 1985, AIAA/ISABE Paper No. 85-7026, NY, 1985, pp. 245-256.
164. Billig, F.S., White, M.E., and VanWie, D.M., "Application of CAE and CFD Techniques to a Complete Tactical Missile Design," AIAA Paper No. 84-0387, January 1984.
165. Billig, F.S., Lee, R.E., and Waltrup, P.J., "Instrumentation for Supersonic Combustion Research," CPIA Publication 340, Vol. II, pp. 67-100.
166. Stockbridge, R.D., Schetz, J.A., Waltrup, P.J., and Billig, F.S., "Combustor/Inlet Interactions and Modeling of Hypersonic Dual Combustor Ramjet Engines," AFOSR-TR-84-1261, October 1984.
167. Morgan, R.G., Paull, A., Morris, N., and Stalker, R.J., "Hydrogen Ramjet with Side-Wall Injection," to be presented at the 8th ISABE, Cincinnati, OH, June 1987.

168. Billig, F.S., et.al., "Efficiency Parameters for Inlets Operating at Hypersonic Speeds," to be presented at the 8th ISABE, Cincinnati, OH, June 1987.
169. Saheli, F.P., and Imlay, S.P., "Navier-Stokes Analysis of Thrust Augmentation of a Supersonic Ducted Rocket," AIAA Paper No. 87-0249, January 1987.
170. Billig, F.S., et.al., "A Methodology for Optimization of the Thermally Balanced Variable Equivalence Ratio Rocket-Ramjet," to be presented at the AIAA/SAE/ASME/ASME 23rd Joint Propulsion Conference, San Diego, CA (US), June 29-July 2, 1987.
171. Wu, J.J., "Experiments on High Speed Ejectors," NASA-CR-177419, July, 1986.
172. Agnone, A., "Analytical and Experimental Evaluation of a 3-D Hypersonic Fixed Geometry, Swept, Mixed Compression Inlet," AIAA Paper No. 87-0159, January 1987.
173. Kumar, A., "Numerical Analysis of Flow Through Scramjet Engine Inlets," to be presented at the AGARD Fluid Dynamics Panel Symposium on Aerodynamics of Hypersonic Lifting Vehicles, Bristol, UK, April 6-9, 1987.
174. Dash, S.M., Sinha, H., Wolf, D.E., and York, B.J., "Computational Models for the Analysis and Design of Hypersonic Scramjet Components - Part I: Combustor and Nozzle Models," AIAA Paper No. 86-1595, June 1986.
175. Uenishi, K., and Rodgers, R.C., "Three Dimensional Computations of Transverse Hydrogen Jet Combustion in a Supersonic Airstream," AIAA Paper No. 87-0089, January 1987.
176. German, R.C., Bauer, R.C., and Panesci, J.H., "Methods for Determining the Performance of Ejector-Diffuser Systems," Journal of Spacecraft, Vol. 3, No. 2, February 1966, pp. 193-200.
177. Fage, E., "Apparent Subsonic Choking in Dual Stream Nozzles," AIAA Journal, Vol. 14, No. 5, May 1976, pp. 681-683.
178. Escher, W.J.D., and Flornes, B.J., "A Study of Composite Propulsion Systems for Advanced Launch Vehicle Applications," The Marquardt Company Report 25, 194, September 1966.
179. Bendot, J.G., "Supercharged Ejector Ramjet Engine Technology Program," Vol. I, The Marquardt Company Report 25, 311, July 1970.
180. Hiller, B., and Hanson, R.K., "Simultaneous Measurements of Velocity and Pressure Fields in Subsonic and Supersonic Flows through Intensified Detection of Laser-Induced Florescence," AIAA Paper No. 86-0161, January 1986.
181. Billig, F.S., Orth, R.C., and Lasky, M., "A Unified Analysis of Gaseous Jet Penetration," AIAA Journal, Vol. 9, No. 9, September 1971, pp. 1048-1058.
182. Drummond, J.P., Zang, T.A., Rogers, R.C., and Hussaini, M.Y., "A Detailed Numerical Model of a Supersonic Reacting Mixing Layer," AIAA Paper No. 86-1427, June 1986.
183. Guirguis, R.H., Kailasanath, K., Oran, E.S., Boris, J.P., and Young, T.R., "Mixing Enhancement in supersonic Shear Layers," AIAA Paper No. 87-0373, January 1987.
184. Gutmark, E., Schadow, K.C., and Koshigoe, S., "Non-circular Jet Dynamics in Supersonic Combustion," to be presented at the AIAA/SAE/ASME/ASME 23rd Joint Propulsion Conference, San Diego, CA (US), June 29-July 2, 1987.
185. Holden, M.S., "A Review of Aerothermal Problems Associated with Hypersonic Flight," AIAA Paper No. 86-0267, June 1986.

ACKNOWLEDGEMENTS

This work was supported by the Office of Naval Research, Code 1132P (Dr. R. S. Miller).

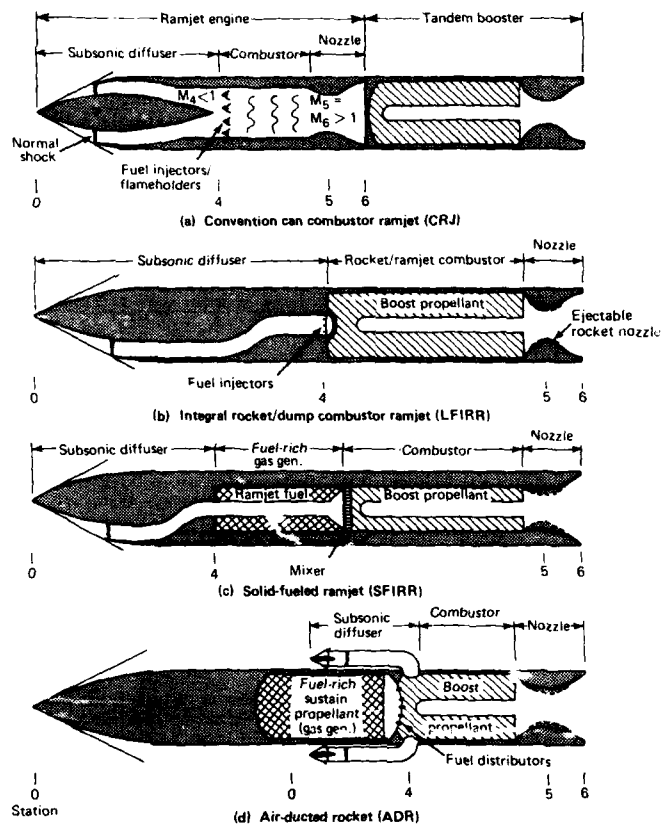


Fig. 1 Schematics of generic ramjet engines.

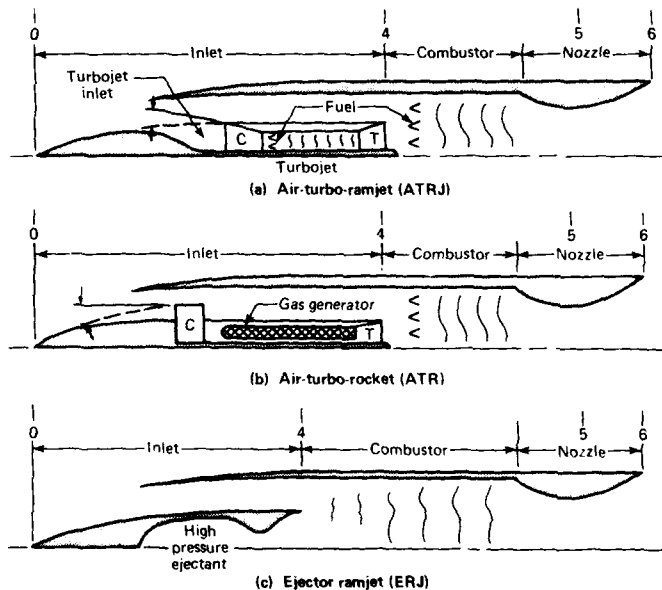


Fig. 2 Schematics of generic hybrid ramjet engines which produce static thrust

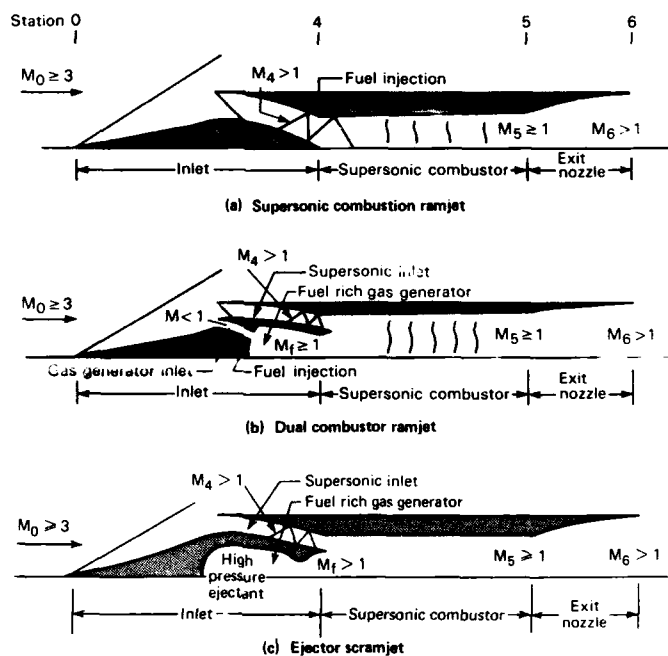


Fig. 3 Schematic of generic supersonic combustion engines.

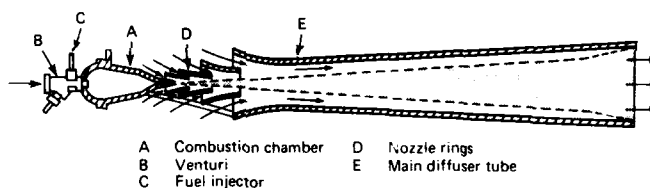


Fig. 4 A Melot multiple-nozzle "thrust augmenter" of the type investigated by the French military authorities in the 1914-1918 war period.

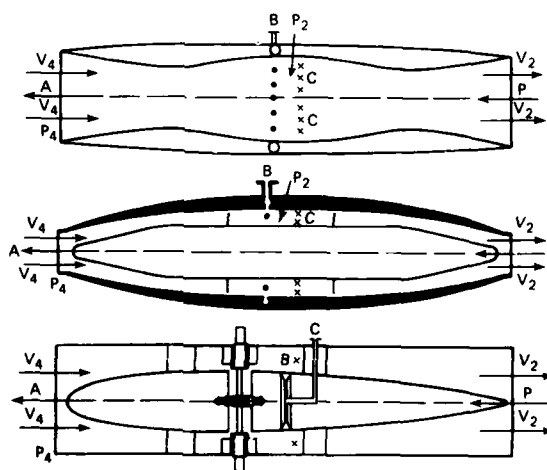


Fig. 5 Reproduction of figure from Fono's 1928 patent. B - fuel injection nozzles; C - flameholders.

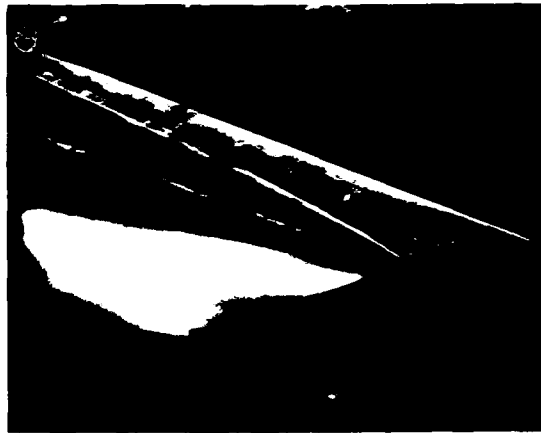
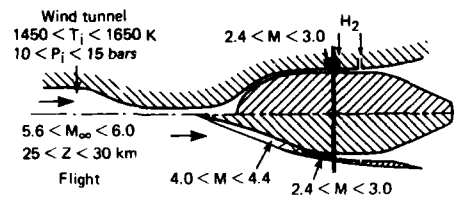


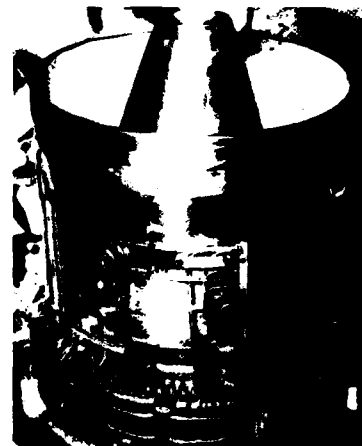
Fig. 6 External burning ramjet, first demonstration of net positive thrust (1968, Billig, USA).



Fig. 7 First aerospace plane concept definition (1968).

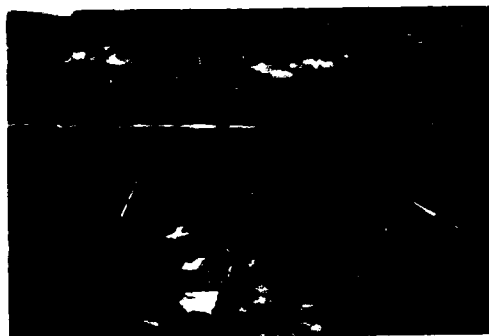


(a) Schematic of semi-direct connect engine tests



(b) Front and rear view of engine

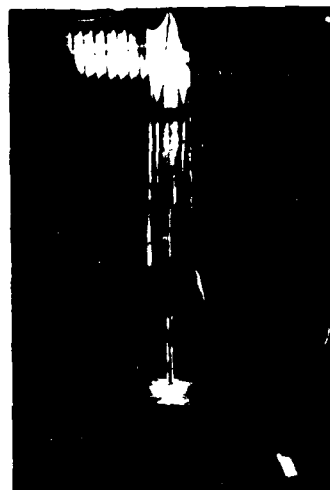
Fig. 8 Semi-connected pipe scramjet engine, Fr. (1971-72).



(b) Test range



(a) Prefiring



(c) Postfiring

Fig. 9 Photographs of gun-launched scramjet tests (Molder, Canada, 1974).



Fig. 10 Hydrogen-fueled ejector ramjet engine (TMC, USA, 1967).

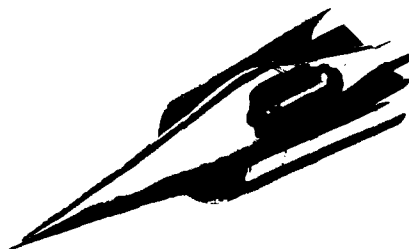


Fig. 11 United Aircraft Research Lab variable geometry hydrogen-fueled scramjet (cir 1968).



Fig. 12 General Electric hydrogen-fueled component integration model scramjet (cr 1969).

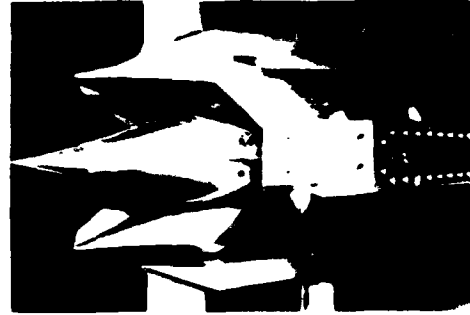


Fig. 13 General Applied Science Lab low-speed, fixed-geometry, hydrogen-fueled scramjet (cr 1968).



Fig. 14 Marquardt hydrogen or liquid hydrocarbon-fueled dual mode scramjet (1968-71).

Structures Assembly Model (SAM)
in Langley 8-ft high temperature structures tunnel



Aerothermodynamic Integration Model (AIM)
in Lewis/Plum Brook hypersonic tunnel facility



Fig. 15 NASA hypersonic research engines (cr 1972).

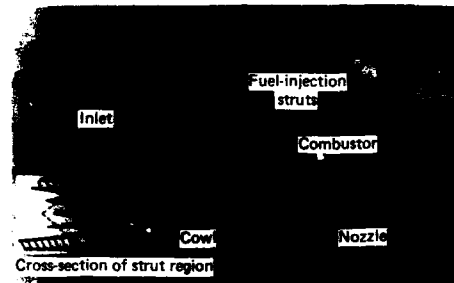


Fig. 16 NASA airframe-integrated supersonic combustion ramjet concept.

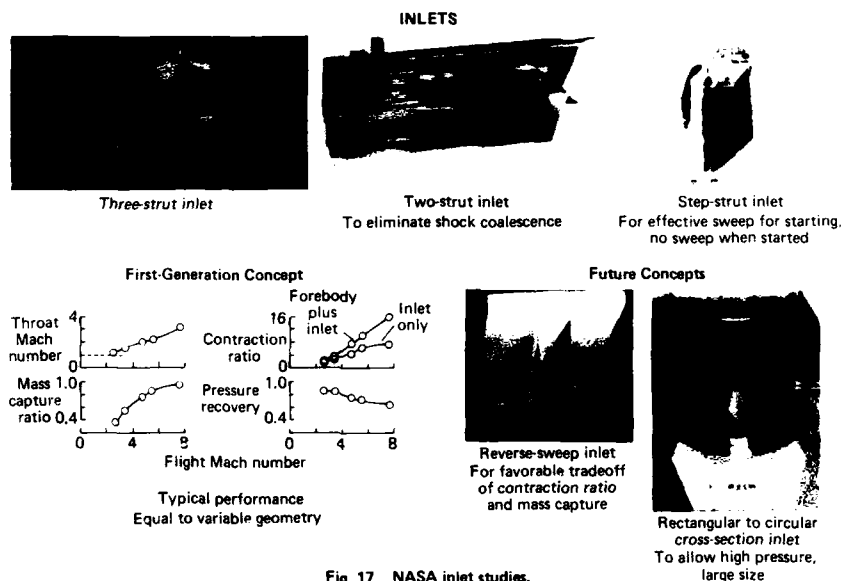


Fig. 17 NASA inlet studies.

Model test conditions
Mach 2.7 (Mach 7 flight at 29 km)
 $T_{t,h} = 2100 \text{ K}$
 $P_{t,h} = 2.9 \text{ MN/m}^2$

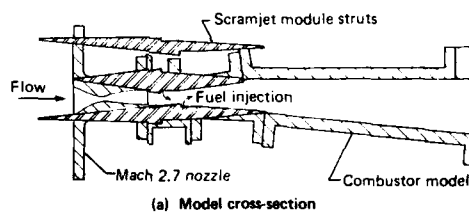


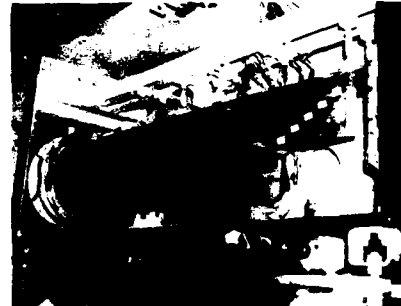
Fig. 18 Representative NASA fuel injector/combustor direct connect test configuration.



(a) Strut engine model



(b) Strutless parametric engine model



(c) Step-strut engine model

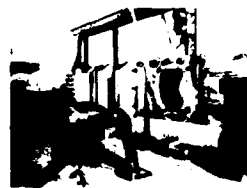
Fig. 19 NASA semifree-jet engine models.



Scramjet test facility
Mach 5.5, 7 engine tests



Test cell No. 1
Mach 4 engine tests



Mach 4 blowdown tunnel
Inlet tests



Component integration
model



Test cell No. 2
Combustor development tests

Fig. 20 NASA/Langley test facilities.

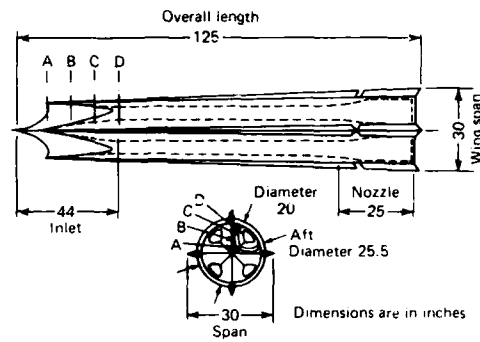


Fig. 21 First scramjet missile patent (Billig and Dugger, 1961).

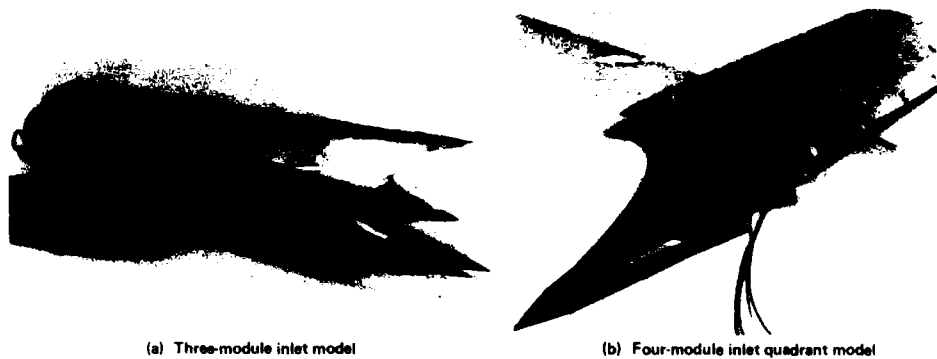
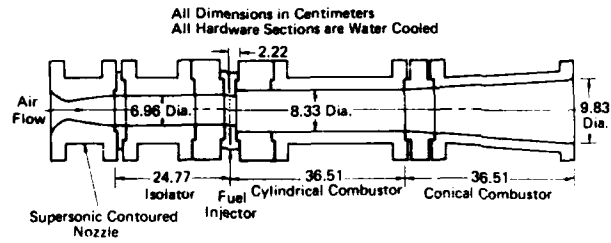


Fig. 22 Photographs of APL scramjet inlets (1965).

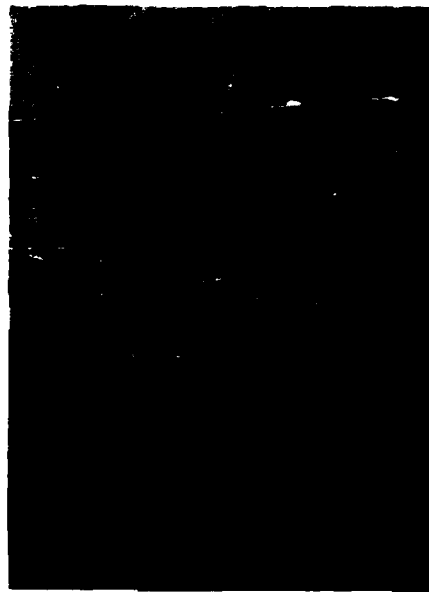


Fig. 23 (a) Photograph

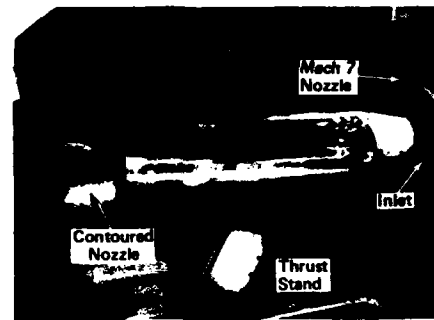


(b) Schematic

Fig. 23 Photograph and schematic of APL direct-connect scramjet combustor hardware.

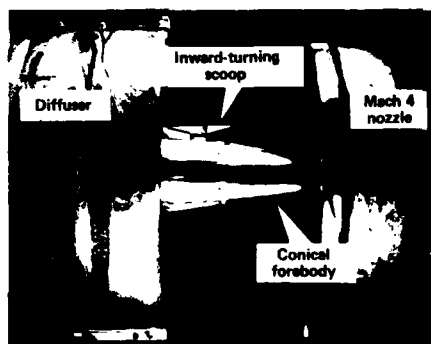


(a) Scram model

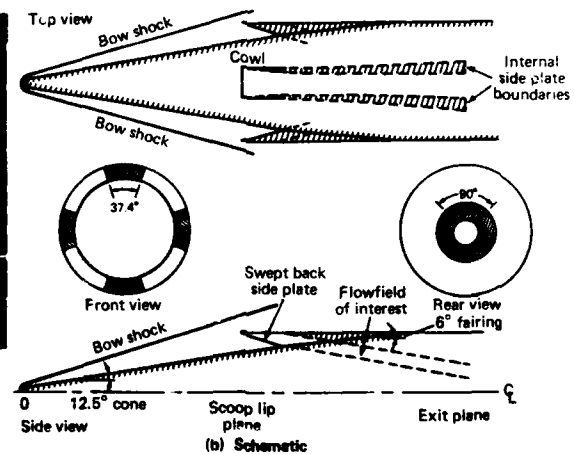


(b) Scram engine with contoured exit nozzle installed on thrust stand in APL free-jet facility with external skin removed

Fig. 24 First scramjet engine to produce net positive thrust (APL, 1968).



(a) Inlet in free-jet test facility



(b) Schematic

Fig. 25 Inward-turning scoop inlet concept (APL, or 1983).

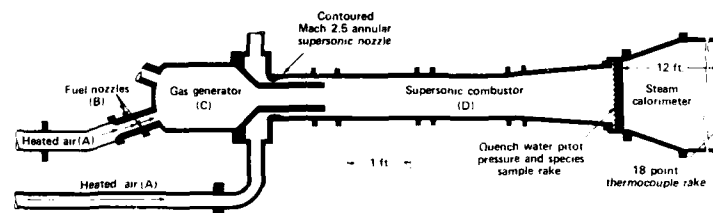


Fig. 26 DCR direct-connect combustor tests (APL, cr 1980).



Fig. 27 National Aerospace plane concept (USA, cr 1986).

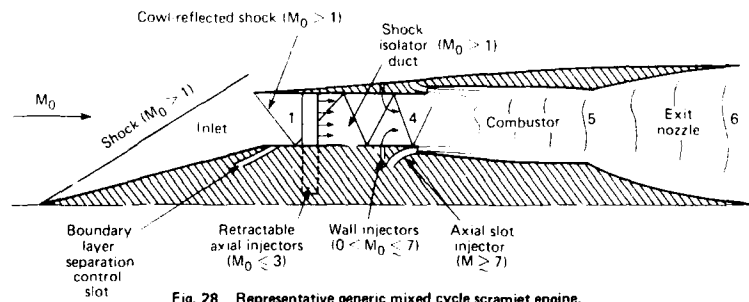


Fig. 28 Representative generic mixed cycle scramjet engine.

COMBUSTION RELATED SHEAR-FLOW DYNAMICS IN ELLIPTIC SUPERSONIC JETS

K. C. Schadow, E. Gutmark, S. Koshigoe, and K. J. Wilson
 Propulsion Research Branch, Code 3892
 Engineering Sciences Division
 Research Department
 Naval Weapons Center
 China Lake, CA 93555-6001

SUMMARY

An elliptic jet having an aspect ratio of 3:1 was studied and compared to a circular jet at three Mach numbers: $M = 0.15$, 1 and 1.3. Hot-wire measurements and Schlieren photography were employed in this study. The superior mixing characteristics of an elliptic jet relative to a circular jet, which were found in previous works in subsonic jets, prevail in the sonic jet and are further augmented by the shock structures of the supersonic underexpanded jet. The major and minor axes switch at a distance of 3 diameters from the nozzle, and the spreading rate of the minor axis side is twice that of a subsonic jet.

The experimental data are supported by results of the linear instability analysis of the supersonic elliptic jet which show that the initial vortices are bending at the major axis side in a similar way to the process which occurs in a subsonic elliptic jet.

INTRODUCTION

In reacting flows, the flame stability and heat release are closely related to the interaction between fluid dynamics and combustion. Specifically in a dump combustor, with a flow field of a ducted jet with dump, the combustion is related to the dynamics of the shear flow originating at the jet exit or the dump.

The evolution of subsonic shear layers, associated with vortex shedding and interaction, has been studied by many investigators both experimentally¹⁻³ and analytically.⁴ These studies, which have recognized the important role of large-scale structures, have opened up the possibility to modify actively or passively the regular breakdown of large-scale vortices into fine-scale turbulence.⁵⁻⁶ One method of passive shear-flow control was obtained using non-circular jet-exit cross sections, which change the initial conditions of the jet. Non-circular jets did not attract interest of researchers and only few studies with triangular and rectangular jets were reported in the literature.⁷⁻⁸

Another non-circular nozzle configuration, which was investigated, is the small aspect ratio elliptic nozzle.⁹ Compared to regular circular jets, the entrainment into the elliptic jet was significantly enhanced in subsonic, nonreacting free-jet and ducted-jet tests at low and high Reynolds numbers.¹⁰⁻¹⁴ Primarily responsible for the mixing enhancement is the phenomenon of axis switching which occurs due to flow self-induction processes associated with the bending of the elliptic vortices.¹⁵

Moreover, the elliptic jet was superior to a circular jet in a subsonic fuel-rich plume combustion process, where, in addition to the entrainment (bulk mixing) of reactants, mixing on the fine-scale (molecular scale) is important.¹⁶ The intense fine-scale activity in the shear layer was due to the generation of azimuthal modes of instability which were excited by the non-circular initial conditions.^{11, 17-18}

Evidence exists that supersonic shear-flow dynamics are also governed by large-scale structures,¹⁹⁻²² a feature which would allow passive shear-flow control in supersonic combustion.

The objective of the present work is to determine whether the special entrainment features of subsonic elliptic jets can also be found in sonic and supersonic free jets. This combined experimental and analytical work provides a basis for future supersonic ducted flow and combustion research.

Experiments were performed with cold and heated free jets in both fully expanded and underexpanded conditions using hot-wire anemometry, thermocouples, and Schlieren photography. The theoretical part includes stability analysis of circular and elliptic jets using an integral-equation formulation of the linear stability analysis which is applicable to arbitrary cross sections.²³

EXPERIMENTAL SET-UP

In the nonreacting tests, air from a blow-down facility was supplied to a free-jet test setup with interchangeable circular and 3:1 aspect ratio elliptic nozzles having a diameter or equivalent diameter of $D = D_e = 1.9$ cm (Figure 1). The measurements were carried out for three conditions: (1) a subsonic jet with exit velocity of $M = 0.15$, (2) a fully expanded jet with sonic velocity at the exit, and (3) an underexpanded jet having a Mach number of $M_j = 1.27$.

Approved for public release; distribution is unlimited.

Paper presented at the Symposium on Aerodynamics of Hypersonic Lifting Vehicles, in Bristol, United Kingdom, 6-9 April 1987.

The mean and turbulent velocity fields of the jets were measured using a constant-temperature hot-wire anemometer with a verified frequency response of 80 kHz. The wire was calibrated up to sonic velocity using a compressibility correction factor.

The hot-wire was mounted on a computer controlled precise traverse mechanism enabling movement in all three axes. A typical measurement included 500 points covering the entire jet from the nozzle to 30 equivalent diameters downstream of the exit.

A 3 mm diameter B&K microphone was used to determine the power spectra of the near field pressure fluctuations at the potential core region. The microphone had a frequency response of up to 140 kHz.

Schlieren photography was used to visualize the shock structures of the circular and elliptic nozzles.

In the reacting tests, the circular and elliptic nozzles were mounted at the exit of a dump combustor burning a lean mixture of air and hydrocarbon fuel at $P = 650$ kPa and $T = 1400^\circ\text{K}$. Color photos were made of the exhaust shock pattern. In addition, mean temperatures in the exhaust jet were measured using a rake of eight tungsten/rhenium-thermocouples.

The hot-wire, thermocouples, and microphone calibration, data acquisition and analysis were done using a VAX-750 minicomputer.

RESULTS AND DISCUSSION

The phenomenon of axis switching in a subsonic three-dimensional jet (elliptic or rectangular) was reported in previous works^{7,8} and is shown in Figure 2 for the present experimental set-up as a reference. The spreading rate of the jet in the minor axis plane was higher than in the major axis plane. The major and minor sides of the initially 3:1 aspect ratio jet became equal at $x/D_e = 23$. This cross-over point was previously shown to be a function of the nozzle aspect ratio and the jet exit velocity. The spreading rate of the elliptic jet is compared to a circular jet. The spreading rate at the minor axis plane of the jet is larger than the circular jet at $x/D_e < 5$ and $x/D_e > 20$. In the other section it is similar in the two jets. This particular behavior of the elliptic jet is a result of the self induction of the asymmetric coherent structures. The coherent structures undergo azimuthal distortion due to the Kelvin-Helmholtz instability and consequently the self induction process is enhanced. The instability process of the subsonic and supersonic jet flows are discussed briefly in the following section to elucidate the basic differences and similarities of the two flows, especially regarding their spreading rates.

Instability Analysis of Elliptic Jets

An integral-equation formulation of the linear stability analysis was developed for jets having arbitrary shapes.^{2,3} Using this method, the stability characteristics of elliptic jets were studied for different aspect ratios and Mach numbers.

Figure 3 describes the dependence of the spatial growth rates ($-\alpha_i$) of disturbances in the initial circular jet shear layer and their phase velocity (C_p) on the frequency of these disturbances, at different Mach numbers. The growth rates diminished with increasing Mach number: for $M = 0$ (subsonic flow), $\alpha_i R_e = -5.6$ (where R_e is the jet equivalent radius) while at supersonic flow ($M = 1.5$), $\alpha_i R_e = -2$. The most amplified frequencies, corresponding to the peak values of the growth rates decreased with increasing Mach number. The nondispersive range of the frequencies, i.e., the range of frequencies which move at the same phase velocity, was wider for higher Mach numbers.

When the jet eccentricity was varied from a circular jet to an elliptic jet with different aspect ratios, the growth rate and the phase velocity of the amplified waves were changed too. The non-circular jet stability characteristics were also associated with various azimuthal modes. These modes represent variation of the disturbances amplitude and phase around the jet circumference. Figure 4 shows the variation of the growth rate and phase velocity as a function of the aspect ratio-- A/B , (where A is the major axis length of the jet nozzle and B is the minor axis length)--for a subsonic flow ($M = 0$). The graph depicts the variation of the two main components of the first azimuthal mode. The insert to the figure shows that the first component, described by the circular symbols, was dominant in the jet section with the large radius of curvature (minor axis plane), while the second component, described by the "plus" symbols, was dominant in the section having the small radius of curvature (major axis plane). When the jet eccentricity was varied from 1 (circular jet) to a 2:1 elliptic jet, the amplification rate of the first component was almost invariable, but its phase velocity was decreased from 0.54 to 0.52. With the same variation of eccentricity, the second component underwent a reduction of its amplification rate accompanied by an increase in the phase velocity from 0.54 to 0.57. The outcome of these changes was that the mode which is dominant at the major axis side moved faster than the one at the minor axis side.

This differential motion caused bending of the jet coherent structures at the major axis side initiating the self induction process and the subsequent accelerated spreading rate of the minor axis section.

When the jet Mach number was increased to 1 (sonic jet), a similar behavior was observed (Figure 5). Although the two components of the azimuthal eigenmode switched the center of their activity between the minor and major axis planes, the phase velocity of the unstable waves at the major axis was still high relative to the minor axis side. The same condition also occurred at supersonic speeds of $M = 1.5$ (Figure 6).

The difference in the phase speed and amplification rates between the major and minor axis sides resulted in a different roll-up location of the vortices at the two sides. The computed streaklines in Figure 7 show that the roll-up was completed in the minor axis sides at $x/R_0 = 1.6$, while at the major axis side it occurred further downstream at $x/R_0 = 2.4$. This pattern of non-symmetric roll-up resulted in the vortex bending which was also observed earlier in water flow visualizations.¹² The self-induction process ensuing from this bending yielded the high spreading rate typical of the elliptic jet. The stability analysis results, which were described above, suggest that the mechanism which was found at subsonic flows prevails also in supersonic flows.

Sonic and Supersonic Axes Switching

The spreading rates of sonic elliptic and circular jets ($M = 1$) are compared in Figure 8. As predicted by the stability analysis, the axes switching can be observed here too. The circular jet's spreading rate was reduced slightly relative to the low subsonic case (Figure 2) but the high spread of the minor axis section resulted in axes switching at $x/D_0 = 20$, which is slightly upstream of the subsonic switching point.

When the jet's chamber pressure was further increased, an underexpanded jet was obtained. The jet Mach number following the initial expansion waves was $M_j = 1.3$. At this condition, the jet initial core was dominated by expansion-compression waves cell structures and its acoustic radiation concentrated in a narrow frequency peak which is called the jet screech frequency. Figure 9 shows the power spectrum of the near field pressure fluctuations of the underexpanded jet with $M_j = 1.3$. The screech frequency is close to 7000 Hz, with a power level of three orders of magnitude above the other broadband frequency components.

The shock structure of the underexpanded jet has a substantial effect on its spreading rate (Figure 10). The spreading rate of the minor axis side was doubled relative to the sonic jet while the width at the major axis side remained unchanged until $x/D_0 = 10$. From this point its growth was similar to the circular jet. Axes switching location was moved far upstream to $x/D_0 = 3$.

The rapid occurrence of the axes switching in the underexpanded jet is also shown in Figure 11 for an elliptic underexpanded reacting jet. The second shock cell has its wider dimension aligned in the minor axis plane and its narrow one in the major axis plane. Temperature measurements done in this elliptic underexpanded jet showed the larger width of the jet at the minor axis plane relative to the other plane at a distance of $x/D_0 = 8$ (Figure 12).

Mean and Turbulent Velocity Field

The mean velocity and turbulent axial velocity contours of the sonic ($M = 1$) and supersonic ($M = 1.3$) jets are shown in Figures 13 and 14, respectively. The region of the supersonic jet core with shock structures was not covered by the hot-wire measurements. The contours in this area are drawn by the computer interpolation procedure. Both figures show that the supersonic jet spreads faster than the sonic jet. The turbulent intensity was higher for the supersonic jet and covered larger sections of the jet.

The mean and turbulent velocity contours on the major and minor axis plans of the underexpanded elliptic jet ($M_j = 1.3$) are shown in Figures 15 and 16, respectively. The high spreading rate on the minor axis plan is evident. The jet width at the major axis plane remains almost constant in the first 10 diameters and its spreading rate further downstream is small. Because of the lack of hot-wire data, the interpolation procedure resulted in a mismatch of the velocity contours at the centerline.

The cells formed by the expansion-compression waves structures inside the jet core, which could not be measured using the hot-wire, were visualized by Schlieren photography. Figure 17 shows these structures in the underexpanded circular and elliptic jets. The non-symmetric shape of the expansion/compression waves in the elliptic jet resulted in a different pattern of flow spread along the two axes of the jet. The intersection of the waves bouncing from the jet boundary were non-symmetric and distorted.

The centerline velocity decay rates of the circular and elliptic jets are compared in Figure 18. For $x/D_0 > 10$ both jets had similar centerline deceleration rates for the three Mach numbers studied. The potential core length of the elliptic jet was very short even for subsonic exit velocity. The core of the subsonic circular jet was 5 diameters long and was decreased at the sonic speed. No measurements were taken for the supersonic jet in this region.

The centerline turbulence intensity of the circular and elliptic jet is shown in Figure 19 for subsonic, sonic, and supersonic speeds. The turbulence intensity is amplified faster in the elliptic jet core than in the circular jet both in subsonic and sonic velocities. Downstream of the core region both jets have nearly the same turbulence intensity for subsonic and supersonic exit Mach numbers. At sonic speed the circular jet has the highest intensity while the elliptic jet has the lowest.

CONCLUSIONS

The high rate of entrainment of the small aspect ratio elliptic jet relative to an axisymmetric or plane jet was attributed to a growth mechanism which does not exist in symmetric jets. This entrainment mechanism is related to self induction of vortices which are being distorted due to the variation of their instability characteristics around their circumference. It was shown here that although the distribution of the various eigenmodes change from subsonic to supersonic jets, the initial vortical structures of the elliptic jet at the major axis plane bend in the streamwise direction relative to the minor axis section. This phenomenon occurs also in subsonic flows. Consequently, the self induction of the jet coherent structures augment the amount of surrounding fluid engulfed by the jet at the minor axis section in the subsonic and sonic elliptic jets.

In a supersonic underexpanded elliptic jet the series of bouncing expansion and compression waves generate a non-symmetric structure of cells. The angle of the oblique shocks and expansion fans are different in the two planes of the jet and the flow changes direction in a non-symmetric pattern. The experimental data which was described in the paper show the large increase of the spreading rate of this jet in the minor axis plane relative to the sonic and subsonic jets. The two axes switch direction at $x/D_e = 3$ instead of $x/D_e = 20$ in the lower velocity jets.

The interaction between the shock cells and the coherent structures of the jet shear layer is being currently studied in our laboratory.

REFERENCES

1. S. C. Crow and F. H. Champagne. "Orderly Structure in Jet Turbulence," *Journal of Fluid Mechanics*, Vol. 48, pp. 547-591, 1971.
2. G. L. Brown and A. Roshko. "On Density Effects and Large Structures in Turbulent Mixing Layers," *Journal of Fluid Mechanics*, Vol. 64, No. 4, pp 775-816, 1974.
3. C. M. Ho and P. Huerre. "Perturbed Free Shear Layers," *Annual Review of Fluid Mechanics*, Vol. 16, pp. 365-424, 1984.
4. A. Michalke. "The Instability of Free Shear Layers," *Progress in Aerospace Science*, 12, Pergamon-Press, pp. 213-239, 1972.
5. A. K. M. F. Hussain. "Coherent Structures and Turbulence," *Journal of Fluid Dynamics*, Vol. 193, 1986.
6. H. E. Fiedler. "Coherent Structures," 1st European Turbulence Conference, Lyon, 1986.
7. P. N. Sforza, M. H. Steiger, and N. Trentacoste. "Studies on Three-Dimensional Viscous Jets," *AIAA Journal* 4, pp. 800-806, 1966.
8. N. Trentacoste and P. N. Sforza. "Further Experimental Results for Three-Dimensional Free Jets," *AIAA Journal* 5, pp. 885-891, 1967.
9. E. Gutmark and C. M. Ho. "Development of an Elliptic Jet," *Bulletin of Physical Society*, Vol. 27, No. 9, p. 1184, 1982.
10. K. C. Schadow, K. J. Wilson, M. J. Lee, and E. Gutmark. "Enhancement of Mixing in Ducted Rockets With Elliptic Gas-Generator Nozzles," *AIAA/SAE/ASME 20th Joint Propulsion Conference*, Cincinnati, Ohio, June 1984, AIAA Paper No. 84-1260. (Also printed in the *Journal of Propulsion and Power*, Vol. 3, No. 2, pp. 145-149, March-April 1987).
11. E. Gutmark, K. C. Schadow, D. M. Parr, C. K. Harris, and K. J. Wilson. "The Mean and Turbulent Structure of Noncircular Jets," *AIAA Shear Flow Control Conference*, Boulder, Colorado, March 1985, AIAA Paper No. 85-0543.
12. C. M. Ho and E. Gutmark. "Vortex Induction and Mass Entrainment in a Small Aspect Ratio Elliptic Jet," *Journal of Fluid Mechanics*, 1987.
13. H. S. Husain and A. K. M. F. Hussain. "Controlled Excitation of Elliptic Jet," *Physics of Fluids* 26, pp. 2763-2766, 1983.
14. K. C. Schadow, K. J. Wilson, D. M. Parr, and E. Gutmark. "Mixing Characteristics of a Ducted, Elliptical Jet With Dump," *AIAA/ASME/SAE/ASME 22nd Joint Propulsion Conference*, Huntsville, Alabama, June 1986, AIAA Paper No. 86-1399.
15. M. R. Dhanak and B. De Bernardinis. "The Evolution of an Elliptic Vortex Ring," *Journal of Fluid Dynamics*, Vol. 109, pp. 189-216, 1981.
16. K. C. Schadow, E. Gutmark, T. P. Parr, D. M. Parr, K. J. Wilson, and G. B. Ferrell. "Enhancement of Fine-Scale Mixing for Fuel-Rich Plume Combustion," *AIAA 25th Aerospace Sciences Meeting*, Reno, Nevada, January 1987, AIAA Paper No. 86-0376.
17. E. Gutmark and K. C. Schadow. "Azimuthal Instabilities and Mixing Characteristics of a Small Aspect Ratio Slot Jet," *AIAA 25th Aerospace Sciences Meeting*, Reno, Nevada, January 1987, AIAA Paper No. 87-0486.

18. J. Cohen. "Instabilities in Turbulent Free Shear Flows," D.Sc. Thesis, University of Arizona, 1986.
19. D. K. McLaughlin, G. L. Morrison, and T. R. Troutt. "Experiments on the Instability Waves in a Supersonic Jet and their Acoustic Radiation," Journal of Fluid Mechanics, Vol. 69, No. 1, pp. 73-95, 1975.
20. G. L. Morrison and D. K. McLaughlin. "Instability Process in Low Reynolds Number Supersonic Jets," AIAA Journal, Vol. 18, No. 7, pp. 793-800, 1980.
21. J. M. Seiner, J. C. Manning, and M. K. Ponton. "The Preferred Spatial Mode of Instability for a Mach 2 Jet," AIAA 10th Aeroacoustics Conference, Seattle, Washington, 1986, AIAA Paper No. 86-1947.
22. J. Lepicovsky, K. K. Ahuja, W. H. Brown, and R. H. Burrin. "Coherent Large Scale Structures in High Reynolds Number Supersonic Jet in Mach Number 1.4," AIAA 10th Aeroacoustics Conference, Seattle, Washington, 1986, AIAA Paper No. 86-1941.
23. S. Koshigoe and A. Tubis. "Wave Structures in Jets of Arbitrary Shape, Physics of Fluids 29, 12, pp. 3982-3992, 1986.

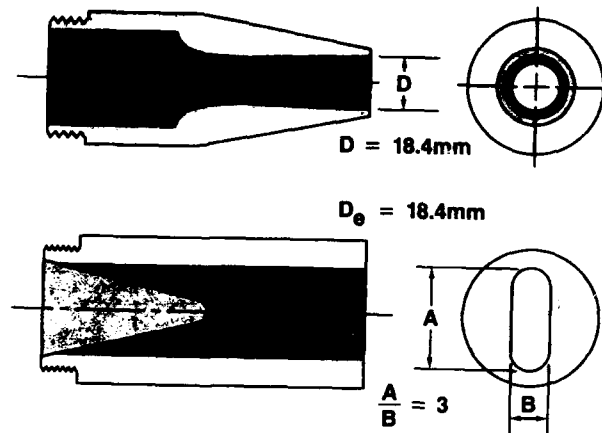


Figure 1. Circular and Elliptic Jet Nozzles.

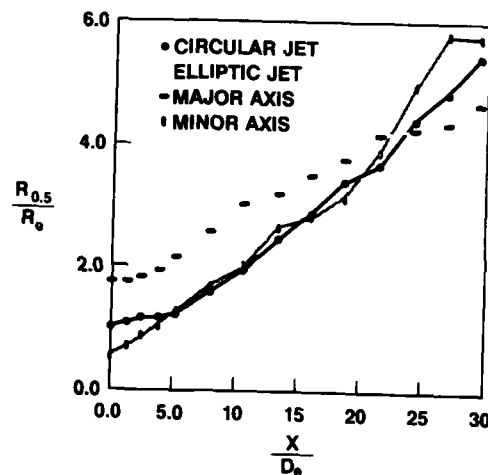


Figure 2. Comparison of Jet Spread Between Circular and Elliptic Jets - Mach 0.15.

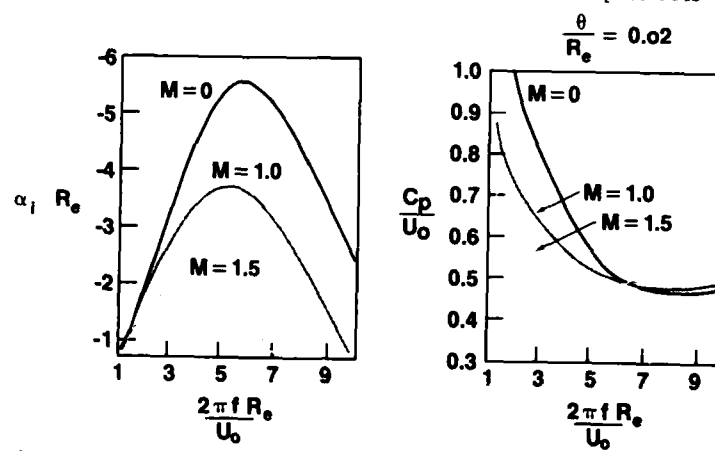


Figure 3. Growth Rate and Phase Velocity as Function of Frequency for Axisymmetric Mode of Circular Jet at Different Mach Numbers.

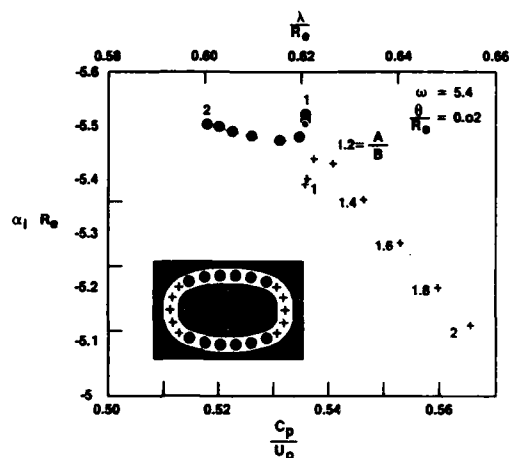


Figure 4. Variation of Growth Rate, Wave Length, and Phase Velocity as Function of Aspect Ratio for the Two Major Components of First Azimuthal Mode at Mach 0.

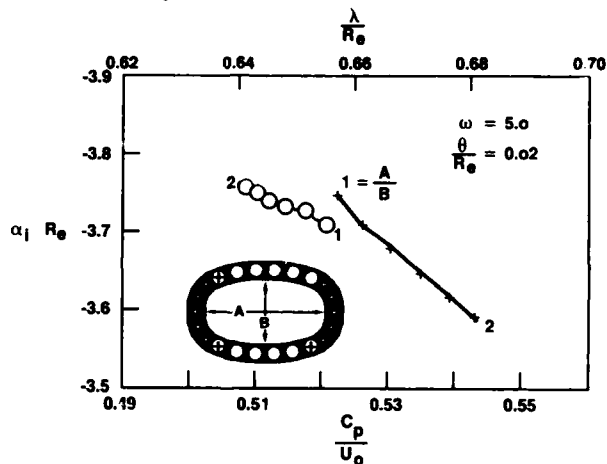


Figure 5. Variation of Growth Rate, Wave Length, and Phase Velocity as Function of Aspect Ratio for the Two Major Components of First Azimuthal Mode at Mach 1.0.

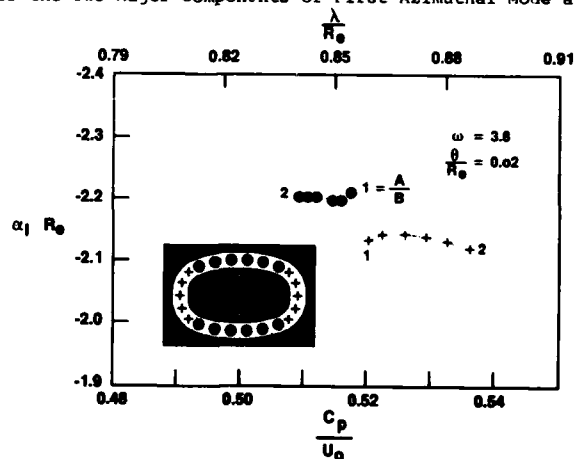


Figure 6. Variation of Growth Rate, Wave Length, and Phase Velocity as Function of Aspect Ratio for the Two Major Components of First Azimuthal Mode at Mach 1.5.

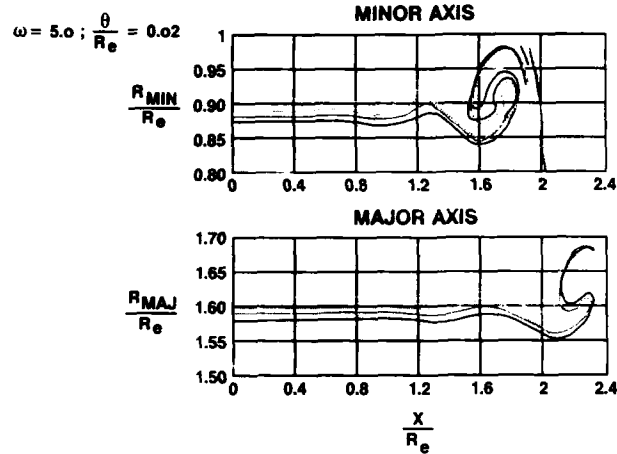


Figure 7. Streaklines for Vortex Roll-Up at Major and Minor Axes for 2:1 Elliptic Jet at Mach 1.0.

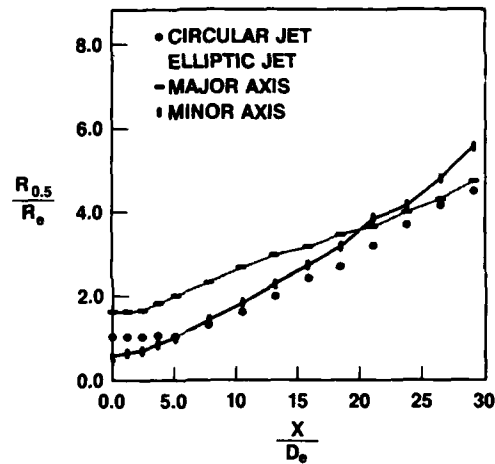


Figure 8. Comparison of Jet Spread Between Circular and Elliptic Jets - Mach 1.0.

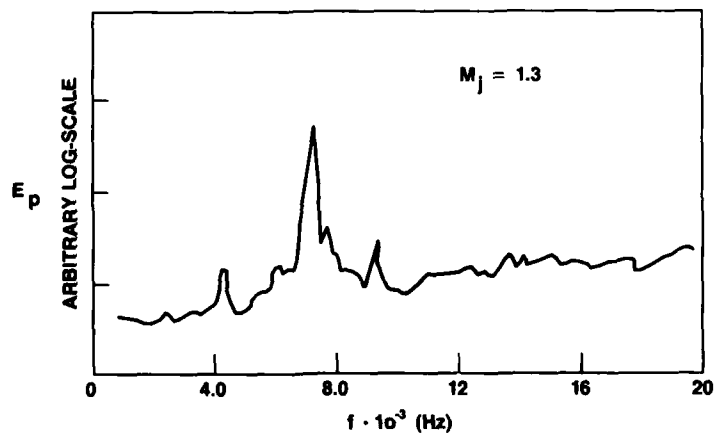


Figure 9. Power Spectrum of the Near-Field Pressure Fluctuations of Underexpanded Circular Jet.

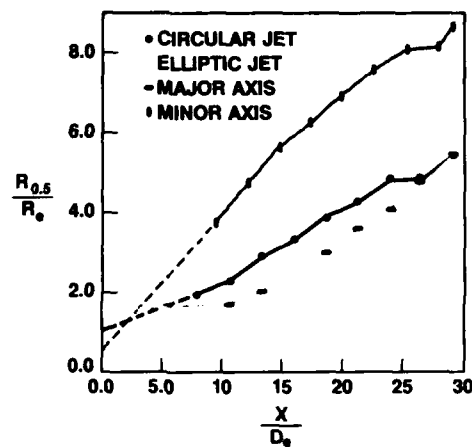
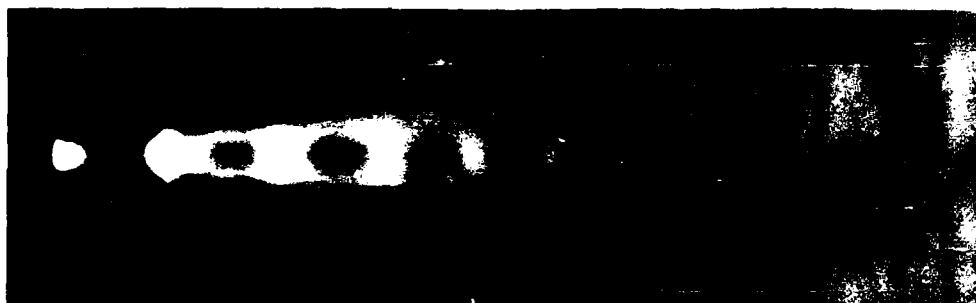
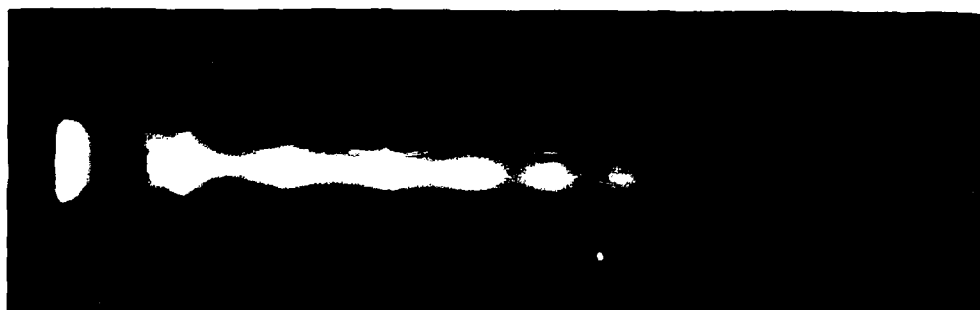


Figure 10. Comparison of Jet Spread Between Circular and Elliptic Jets - Mach 1.3.



(a) Minor Axis.



(b) Major Axis.

Figure 11. Elliptic Underexpanded Reacting Jet.

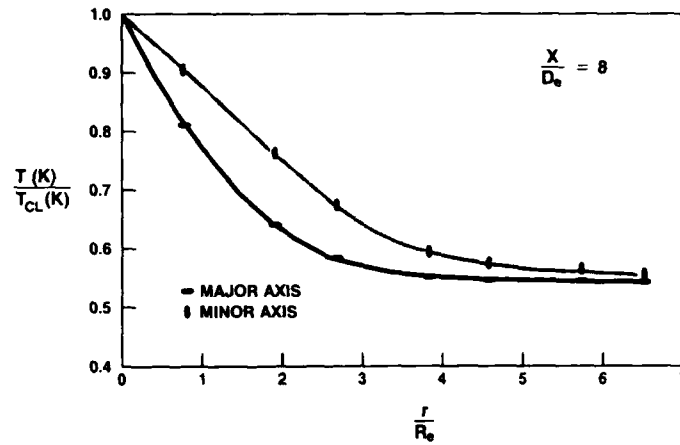


Figure 12. Comparison of Radial Temperature Profiles Between Minor and Major Axes of Elliptic Jet.

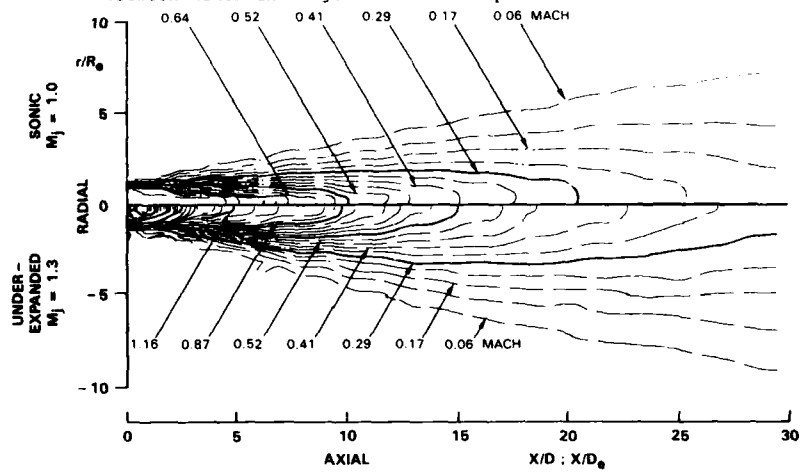


Figure 13. Comparison of Mean Axial Velocity Contours - Circular Jet.

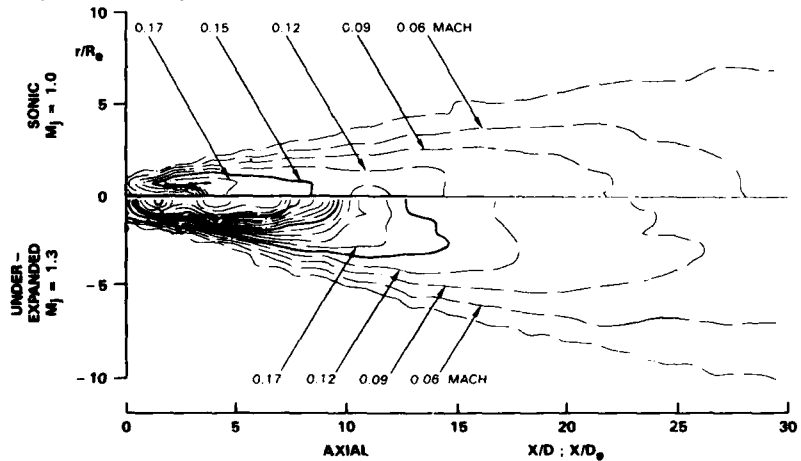


Figure 14. Comparison of Turbulent Axial Velocity Contours - Circular Jet.

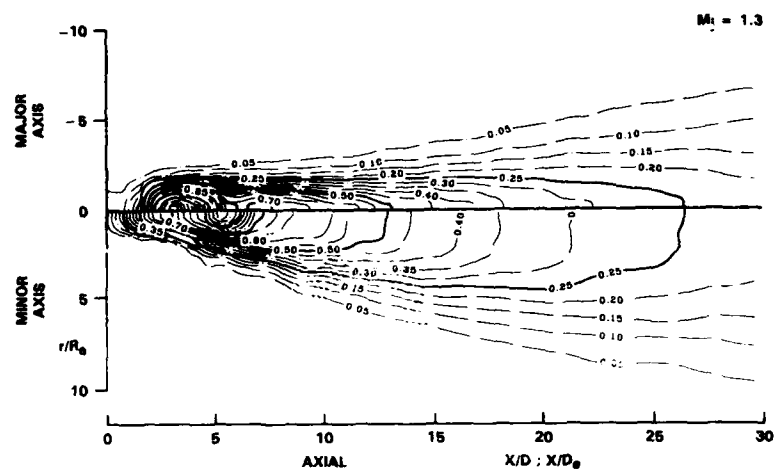


Figure 15. Comparison of Mean Velocity Contours - Elliptic Jet (Underexpanded).

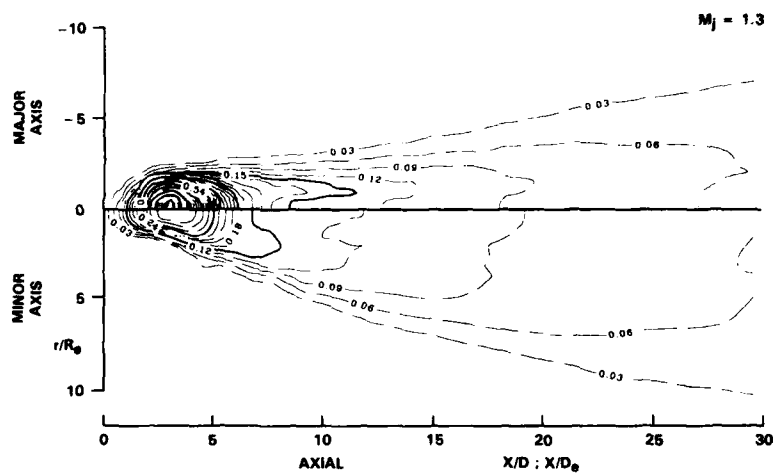


Figure 16. Comparison of Turbulent Axial Velocity Contours - Elliptic Jet (Underexpanded).



(a) Circular jet, 5 msec exposure.



(b) Elliptic jet - major, 5 msec exposure.



(c) Elliptic jet - minor, 5 msec exposure.



(d) Elliptic jet - minor, spark photography (10 nsec exposure).

Figure 17. Schlieren Photographs of the Underexpanded Jets.

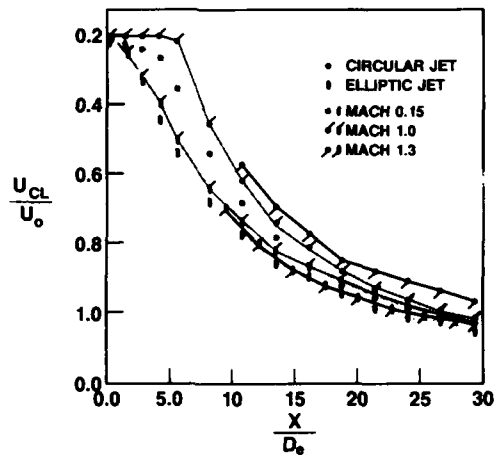


Figure 18. Comparison of Centerline Velocity Decay for Circular and Elliptic Jets at Three Mach Numbers.

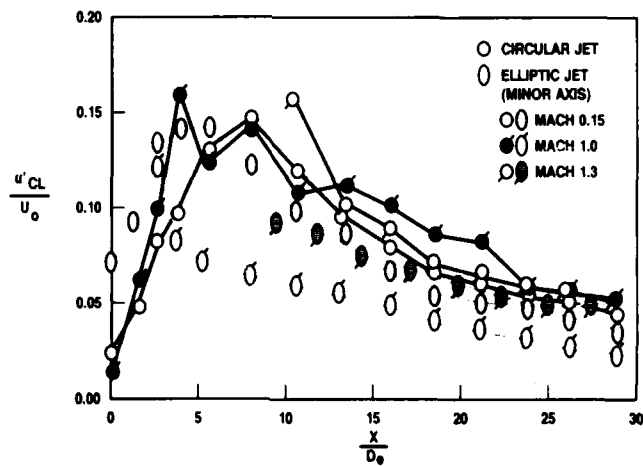


Figure 19. Comparison of Centerline Turbulence for Circular and Elliptic Jets at Three Mach Numbers.

NUMERICAL ANALYSIS OF FLOW THROUGH SCRAMJET ENGINE INLETS

Ajay Kumar*
 NASA Langley Research Center
 Hampton, Virginia
 U.S.A.

Abstract

A set of computer programs has been developed to analyze flow through supersonic combustion ramjet (scramjet) inlets. These programs solve either the two- or three-dimensional Euler/Navier-Stokes equations in full conservation form by MacCormack's explicit or explicit-implicit method. An algebraic two-layer eddy viscosity model is used for turbulent flow calculations. The programs are operational on Control Data CYBER-200 series vector-processing computer system and have been optimized to take maximum advantage of the vector processing capability of the system. Since their development, the programs have been extensively verified and used to analyze a number of very complex inlet configurations. In this paper, results are presented from two-dimensional, quasi-three-dimensional, and three-dimensional analyses of the inlet flow field to illustrate the use of the programs.

Nomenclature

G	throat gap
H	height of inlet
M_1	Mach number at inlet face
$M_{1,N}$	component of M_1 normal to sidewall leading edge
$M_{1,t}$	component of M_1 tangential to sidewall leading edge
M_∞	free-stream Mach number
p	pressure
p_1	pressure at inlet face
T_1	temperature at inlet face
w	width of inlet
x,y,z	Cartesian coordinates
Λ	sweep angle
δ_s	sidewall and strut compression angle

Introduction

The exponential growth of computer speed and storage capacity as well as algorithm sophistication has allowed application of advanced numerical methods to practical design problems in many engineering disciplines such as fluid dynamics. More and more use is being made of numerical methods in analyzing complex flow fields than has been possible in the past. An important example is that of the inlet design of supersonic combustion ramjets (scramjets), where modern computational methods allow the direct numerical simulation of the inlet flow field in a reasonably efficient manner. Intelligent use of such capability can be very helpful in eliminating the poorer designs and in allowing promising design configurations to be developed with less reliance on extensive wind-tunnel testing.

This paper discusses the application of a set of Navier-Stokes codes in the analysis of high-speed inlet flow fields. NASA Langley Research Center has an ongoing research program to define and develop an airbreathing, airframe integrated scramjet engine for hypersonic propulsion.^{1,2} Scramjets become attractive at flight Mach numbers of 4 and above, and they offer the most viable propulsion option at Mach numbers above 6. The scramjet engine concept being developed at Langley uses a fixed-geometry, rectangular module approach that closely integrates with the vehicle. Use of fixed geometry reduces weight and system complexity, whereas vehicle-propulsion system integration takes advantage of forebody compression to reduce inlet size and afterbody expansion to provide a low drag, high area ratio exhaust nozzle. An example of such a module is shown in Figure 1 with a sidewall removed. A cross-sectional view is shown at the bottom of the figure. The module has a fixed-geometry inlet with aft placement of the cowl on the underside of the engine that allows for efficient spillage and good inlet starting characteristics over the operating range with fixed geometry. For this module, the inlet compression is completed by three wedge-shaped struts which also

*Senior Research Scientist, Computational Methods Branch, High-Speed Aerodynamics Division.

provide locations for injection of gaseous fuel. The fuel and air mix and react in the combustor portion of the module. The reacted mixture is then expanded through the nozzle.

Efficient engine design requires a detailed understanding of the internal flow field in various engine components over the range of operating conditions. While the flow field in these components cannot really be separated, each of the components should perform well by itself. Most of the studies in analyzing flow through various engine components have necessarily been experimental in the past due to the complex nature of the flow field which does not lend itself to simple analytical estimates. However, with increasing availability of large storage, high-speed computers and advanced computing techniques, it is becoming more feasible to numerically calculate the flow field in the inlet and nozzle portions of the engine. Analysis of complete combustor flow field still remains beyond the current state of the art.

The effort to provide an inlet analysis tool started with the development of the two-dimensional Euler/Navier-Stokes code described in Reference 3; this was followed by the full three-dimensional Euler/Navier-Stokes code described in Reference 4. This paper briefly describes both the two- and three-dimensional codes. It also describes the application of the two-dimensional code in quasi-three-dimensional form in the analysis of a certain class of inlets. A parametric study in inlet design based on the quasi-three-dimensional application of the two-dimensional code is presented. Results are then presented from a complete three-dimensional analysis of a two-strut scramjet inlet. Comparison with available experimental data is made where possible.

Outline of the Inlet Codes

The codes model the flow field by the two- or three-dimensional Euler or Navier-Stokes equations in conservation form. These equations are transformed from the physical domain to a regular computational domain by using an algebraic numerical coordinate transformation that generates a set of boundary-fitted curvilinear coordinates.⁵ The transformation can accommodate embedded bodies (e.g., struts, cowl) in the flow field. It also allows for concentrating mesh lines in regions of high gradients such as near the solid boundaries. The transformed governing equations are solved by either the explicit or explicit-implicit method due to McCormack.^{6,7} In the case of turbulent flow calculations, an algebraic two-layer eddy viscosity model due to Baldwin and Lomax⁸ is used.

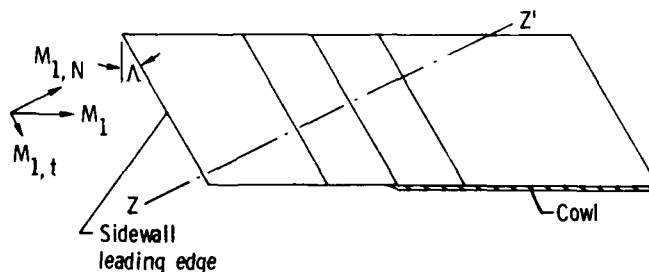
The codes are operational on the Control Data VPS-32 (a specially modified CYBER-200 series computer with a 32 million, 64-bit word primary memory) vector processing computer system at the Langley Research Center and have been optimized to take maximum advantage of the vector processing capability of the computer system.

Results and Discussion

This section describes briefly how the two-dimensional code can be used in quasi-three-dimensional sense to analyze certain class of scramjet inlets. The approach is verified by calculating the flow field in a three-strut inlet shown in Figure 1 and then results from a parametric inlet design study are presented using this approach. Finally, results are presented for a two-strut scramjet inlet as obtained from a full three-dimensional analysis.

Two- and Quasi-Three-Dimensional Analysis

For the type of scramjet inlet configuration shown in the following sketch where all the compression surfaces are swept back at the same angle Λ , it is possible to use the two-dimensional code in a quasi-three-dimensional sense if the shock



waves in the inlet do not detach and if the end effects (i.e., the effects of top surface and cutback cowl of inlet) are neglected. Under these assumptions, the velocity component parallel to the sweep line should remain constant, and the flow disturbances should occur in a plane zz' normal to the sweep line. The flow can, therefore, be solved by using the two-dimensional code in the plane zz' with Mach number $M_{1,N}$. The solution in the zz' plane can be projected to the plane of the cowl, and the velocity distribution in the plane of the cowl can be obtained by superimposing the constant velocity component over the aforementioned solution. In the case of viscous flows, an approximate boundary-layer profile has to be prescribed for the constant tangential velocity component before superimposing it. By knowing the velocity and density distributions, it is possible to estimate the flow spillage from this class of three-dimensional inlets as a function of cowl location.

The preceding approach is verified by analyzing the three-dimensional inlet shown in Figure 1, details of which are given in Reference 9. The inlet sidewalls are swept at an angle of 48° . Figure 2 shows a comparison of the turbulent sidewall pressure distribution with the experimental results of Reference 9. The experimental results are in a plane parallel to the cowl located at mid-inlet height. This particular plane is chosen for comparison so that the cowl shock does not affect the measured sidewall pressure up to the point of comparison in the axial direction. (The present analysis cannot account for the cowl shock disturbances.) It is seen from Figure 2 that the present calculations are in very good agreement with the measured values.

The type of agreement obtained for the three-strut inlet gives credibility to the code in its use as a tool for parametric studies in inlet design. Results of one such parametric study are presented here. In this study, one- and two-strut inlets are analyzed over a range of Mach numbers. The compression surfaces of these inlets are swept back at an angle of 33° . The flow conditions used in the analysis are given in the following table:

M_∞	M_1	$M_{1,N}$	p_1, MPa	T_1, K
4	3.43	2.88	0.00963	322
5	4.29	3.60	0.00648	328
6	5.18	4.34	0.00456	329
7	6.00	5.032	0.00355	335

Figure 3a shows the geometry of a one-strut inlet in a plane normal to the sidewall sweep. Figure 3b shows the pressure contours for the inviscid flow at $M_\infty = 7$. It is seen from the contour plot that the shock waves from the sidewall and strut leading-edge coalesce to form a stronger shock. For the viscous flow, this strong shock caused a large separated region on the sidewall which resulted in aerodynamic choking of the flow at all the Mach numbers considered here except at the highest Mach number with turbulent flow. In the case of inviscid flow, no solution could be obtained at the lowest Mach number for which the shock waves detached in the inlet. The following table summarizes the conditions for which the solutions could or could not be obtained (indicated by "yes" and "no," respectively):

Mach Number M_∞	Type of Flow		
	Inviscid	Laminar	Turbulent
7	yes	no	yes
6	yes	no	no
5	yes	no	no
4	no	no	no

To eliminate the problem of shock wave coalescence in the one-strut inlet, a two-strut inlet is considered in which the strut surface, on which the sidewall shock strikes, is made parallel to the oncoming flow so that no shock is produced by this strut surface. This avoids the possibility of shock-wave coalescence. Figure 4a shows the geometry of the two-strut inlet in a plane normal to the sidewall sweep. The pressure contours and velocity vector field for the laminar flow at $M_\infty = 7$ are shown in figures 4b and 4c.

For this inlet, solutions could be obtained at all the Mach numbers for the inviscid flow and at the highest three Mach numbers for the viscous flow. The following table summarizes the conditions for which the solutions could or could not be obtained (indicated again by "yes" and "no," respectively):

Mach Number M_∞	Type of Flow		
	Inviscid	Laminar	Turbulent
7	yes	yes	yes
6	yes	yes	yes
5	yes	yes	yes
4	yes	no	no

The table clearly shows the improvement in the performance of the two-strut inlet over the one-strut inlet.

The preceding parametric study indicates that the numerical computer code developed herein can be used to modify or eliminate those designs which are not expected to perform well and, thus, can help in reducing the experimental testing required for inlet design.

Three-Dimensional Analysis

Even though the preceding parametric study using the two-dimensional code provides meaningful information, it has only limited applications in the analysis of scramjet inlet flow field because, in most situations, the flow is truly three-dimensional. It is, therefore, necessary to use three-dimensional analysis in order to model all important features of the flow including interaction between the high-pressure internal flow and low-pressure external flow ahead of the cowl caused by the aft location of the cowl. This section presents result from a three-dimensional analysis of the two-strut inlet shown in Figure 5. A line diagram of the inlet is shown in Figure 6. It has a rectangular cross-section with wedge-shaped sidewalls which are swept back at an angle of 30° . Two compression struts are located in the center passage of the inlet which are also swept back at the same angle as the sidewalls. The basic design of the struts is similar to that discussed in the preceding parametric study. Sweep of all compression surfaces ends along line EF and the cowl closure starts at F. The inlet model is parametric and allows adjustments in the overall geometric contraction ratio by moving the sidewalls and the struts in and out. The cowl location can also be adjusted, and it is possible to add top surface compression, if needed.

In order to compare the numerical results with the experimental data, flow calculations for the preceding two-strut configuration are made at the following experimental conditions:

$$M_1 = 4.03$$

$$P_1 = 8724 \text{ N/m}^2$$

$$T_1 = 70 \text{ K}$$

The inlet has a geometric contraction ratio, W/G , of 4.01 and zero top-surface compression. The cowl closure begins at the throat.

Before results of this calculation are presented, it is necessary to discuss how the present analysis includes the end effects in the inlet which arise due to the interaction between the internal flow and the external flow. This interaction occurs due to the aft placement of the cowl which exposes the high-pressure internal flow to the low-pressure external flow in the region ahead of the cowl. The pressure differential causes an expansion wave to run into the inlet flow and a compression wave into the external flow, thus creating an induced flow in the downward direction ahead of the cowl. These end effects can significantly affect the inlet flow field for certain flow conditions, and the induced flow set up by the end effects can result in substantial additional flow spillage other than that due to the sweep of the compression surfaces. In order to account for the end effects in the analysis, a portion of the external flow under the plane of the cowl must be included. Ideally, one should go down and around the sidewalls far enough so that the free-stream conditions can be applied on the free boundaries, but this would greatly increase the computational requirements. In the present analysis, the region is extended as shown in Figure 7 by the dashed line (only half of the inlet flow is calculated due to symmetry). This limited extension of the computational domain is found adequate so far as the inlet flow field is concerned. Extrapolation from interior grid points is used all along the dashed line boundaries except at the inflow boundary where the flow conditions are prescribed.

The calculations presented here are made with a grid of about 271,000 points (77 points in the x-direction, 69 points in the y-direction between the symmetry plane and the sidewall, and 51 points in the z-direction). Out of the 51 planes in the z-direction, 14 planes are located under the cowl plane to account for the end effects. Discretization of this inlet is further complicated by the struts embedded in the flow field. In order to accommodate the strut, the present analysis makes the strut surfaces coincident with two grid planes in the y-direction and further allows 12 more grid planes to go through the strut. This results in slight blunting of the strut leading edge, but this blunting is relatively small due to grid refinement in the neighborhood of the strut surfaces. A typical grid in the symmetry plane and one of the cross-planes is shown in Figure 8. If a particular cross-plane lies above the cowl plane, the grid points lying within the strut are neglected and proper boundary conditions are applied on the strut surfaces, but if the cross-plane lies below the cowl plane, all grid points in the plane are used in the calculations. The preceding simplified approach in discretizing the inlet configuration, although it resulted in waste of some grid points, avoided the need of using more involved grid generation procedures.

Results of the present calculations are shown in Figures 9 through 13. Figure 9 shows the velocity vector field and static pressure contours in a plane located at mid-inlet height. Although the calculations were performed only for half of the inlet,

results are shown here for the full inlet by reflecting to the other half. Slight blunting of strut leading edges and associated small distortions in pressure contours in the immediate neighborhood of the strut leading edges are obvious from this figure. However, the impact of bluntness appears to be local. The velocity vector plot shows several regions of separated flow on the inlet surfaces caused by the shock/boundary-layer interactions and the pressure contour plot clearly shows the complex shock and expansion wave structure present in the inlet.

Figure 10 shows the velocity vector field and static-pressure contours in the symmetry plane of the inlet. The swept shock wave structure caused by the swept compression surfaces is obvious from this figure. The velocity vector plot shows significant flow separation near the top surface of the inlet caused by the shock/boundary-layer interaction. The velocity vector plot further shows a downturn in flow direction ahead of the cowl resulting in some flow spillage from the inlet. This downturn is caused by the swept compression surfaces and the interaction in the cowl plane between the internal and external flow (the so called end effects). Once the inlet flow passes behind the cowl leading edge, it is turned back parallel to the cowl plane; and this turning results in a cowl shock which can be seen clearly in the pressure contour plot of Figure 10.

Figure 11 shows the sidewall pressure distributions at two inlet height locations. Experimental results from reference 10 are also shown. It is seen that the present results compare very well with the experiment at both height locations. Figure 12 shows the pressure distribution on the strut inner surface (i.e., the surface facing the symmetry plane) at the mid-inlet height location. Here again, a comparison with the experimental results of reference 10 shows a very good agreement. The preceding good agreement with the experimental results is significant considering the fact that the flow in the throat region of the inlet is highly complex due to the interactions of sidewall and strut shock and expansion waves, cowl shock, expansion waves due to the end effects, and induced shocks caused by the flow separation; all of which are taking place in relatively small gaps between the sidewalls and struts.

As mentioned earlier, not all the flow approaching the inlet face is captured by the inlet. Some of it is spilled out due to the swept compression surfaces and end effects. The amount of flow captured by the inlet is an important measure of inlet performance. Figure 13 shows a comparison of the predicted inlet capture with the experiment as a function of axial distance from inlet leading edge. It is seen that the predicted capture distribution agrees very well with the experiment.

Preceding good agreement with the experimental results shows that the inlet code has very well simulated the complex flow field of the two-strut inlet configuration. The results also substantiate the adequacy of the procedure used in the analysis to include the end effects and to accommodate the embedded struts in the flow field.

Concluding Remarks

A set of computer programs has been developed to analyze flow through complex scramjet inlet configurations. These programs solve either the two- or three-dimensional Euler/Navier-Stokes equations in full conservation form by McCormack's explicit or explicit-implicit method. An algebraic two-layer eddy viscosity model is used for turbulent flow calculations. The programs are operational on the Control Data CYBER-200 series vector processing computer system at NASA Langley. An important feature of the three-dimensional program is that it allows inclusion of end effects in the inlet flow calculations. These end effects arise as a result of the interactions of the inlet flow with the external flow due to aft placement of the cowl and they affect the inlet flow field very significantly.

Since their development, the programs have been extensively verified and used to analyze a variety of complex inlet configurations. Although the codes were primarily developed for high-speed internal flows, they have also been used for a variety of other problems, including mixed subsonic-supersonic flow, subsonic flow, and external flow.

References

1. Jones, R. A.; and Huber, P. W.: Toward Scramjet Aircraft. *Astronautics and Aeronautics*, vol. 16, no. 2, Feb. 1978, pp. 38-49.
2. Beach, H. L., Jr.: Hypersonic Propulsion. Paper No. XII, NASA CP-2092, May 1979.
3. Kumar, Ajay: Numerical Analysis of the Scramjet Inlet Flow Field Using Two-Dimensional Navier-Stokes Equations. NASA TP-1940, 1981.
4. Kumar, Ajay: Numerical Analysis of a Scramjet Inlet Flow Field Using the Three-Dimensional Navier-Stokes Equations. CPIA Publication 373, Feb. 1983, pp. 25-39.
5. Smith, R. E.: Two-Boundary Grid Generation for the Solution of the Three-Dimensional Compressible Navier-Stokes Equations. NASA TM-83123, 1981.

6. McCormack, R. W.: The Effect of Viscosity in Hypervelocity Impact Cratering. AIAA Paper No. 69-354, May 1969.
7. McCormack, R. W.: A Numerical Method for Solving the Equations of Compressible Viscous Flow. AIAA J., vol. 20, no. 9, Sept. 1982, pp. 1275-1281.
8. Baldwin, B. S.; and Lomax, H.: Thin Layer Approximation and Algebraic Model for Separated Turbulent Flows. AIAA Paper No. 78-257, Jan. 1978.
9. Trexler, C. A.: Design and Performance at a Local Mach Number of 6 of an Inlet for an Integrated Scramjet Concept. NASA TN D-7944, 1975.
10. Trexler, C. A.: The Design and Performance at Mach 4.0 of Two-Strut Hypersonic Inlets for an Integrated Scramjet Concept. Proposed NASA TM.

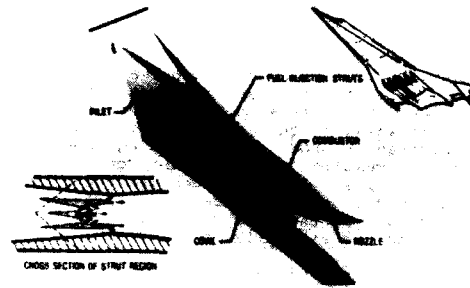


Fig. 1 An example of a scramjet engine module and its cross section.

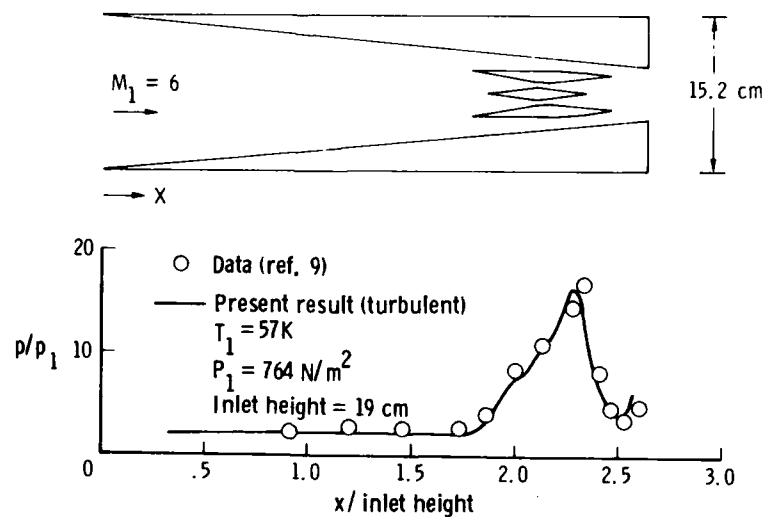


Fig. 2 Comparison of sidewall pressure distribution for three-strut inlet.

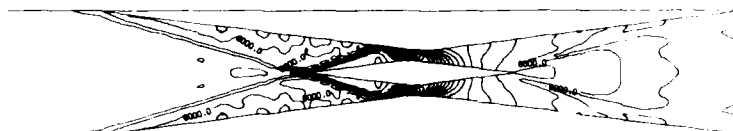
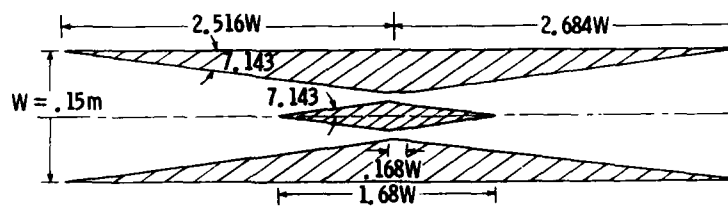


Fig. 3 One-strut inlet: (a) geometry in a plane normal to sidewall sweep; (b) pressure contours for inviscid flow at $M_\infty = 7$.

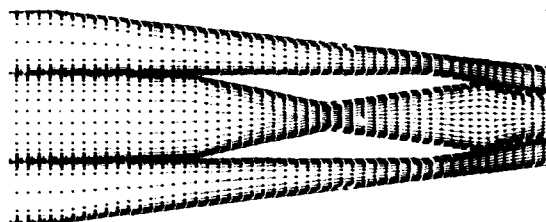
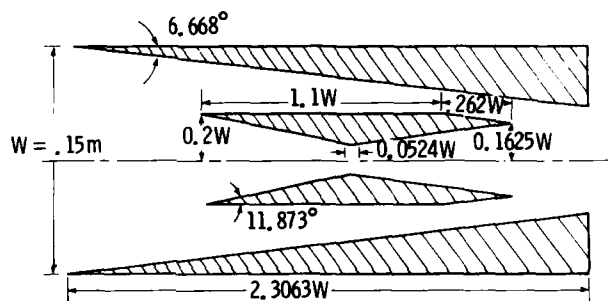


Fig. 4 Two-strut inlet: (a) geometry in a plane normal to sidewall sweep; (b) pressure contours for laminar flow at $M_\infty = 7$; (c) velocity vector field for laminar flow at $M_\infty = 7$.



Fig. 5 Two-strut scramjet inlet configuration.

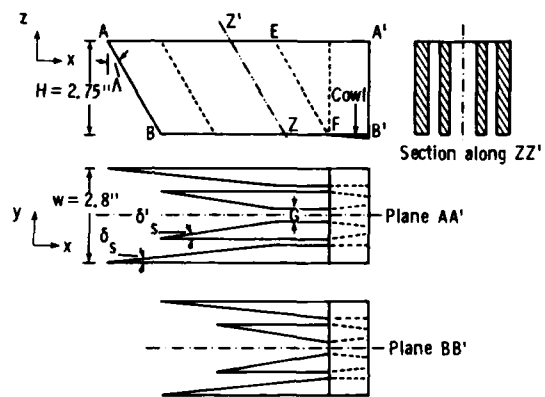


Fig. 6 Line-diagram of the two-strut scramjet inlet configuration.

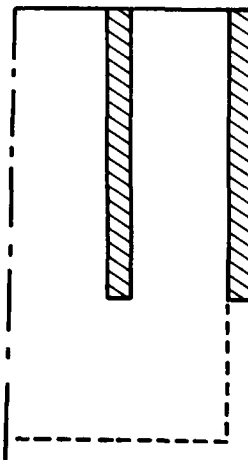


Fig. 7 Physical domain of computation.

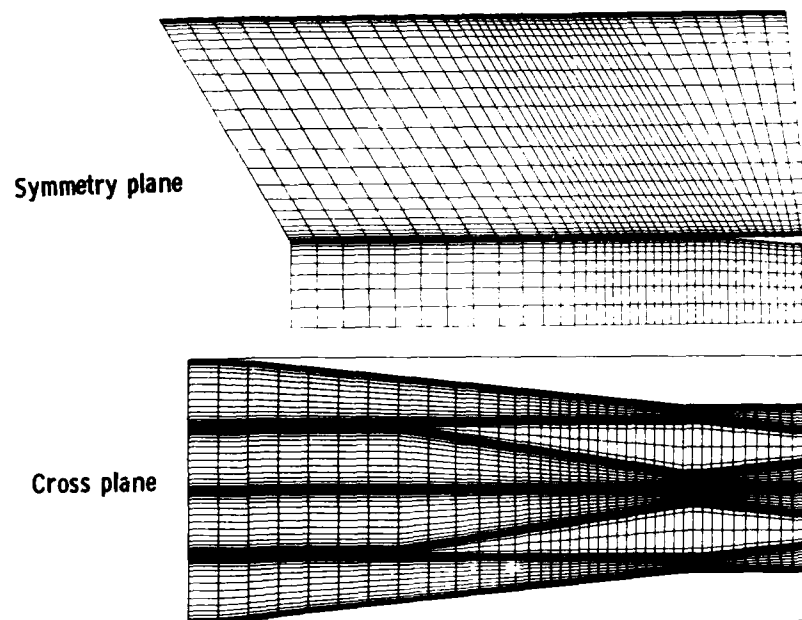


Fig. 8 Computational grid.

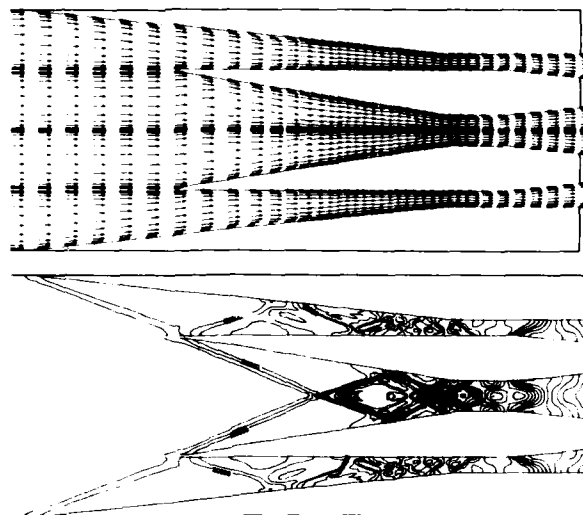


Fig. 9 Velocity vector field and pressure contours in a plane located at mid-inlet height.

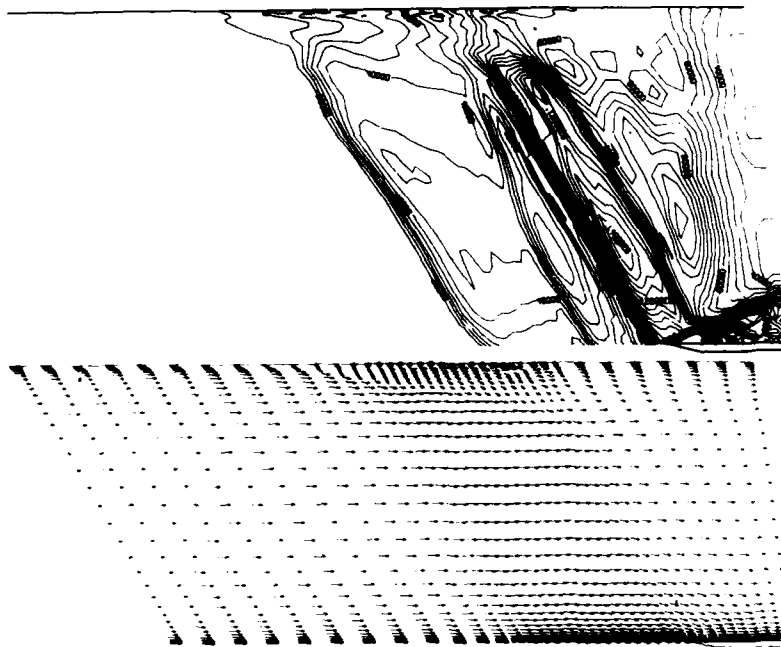


Fig. 10 Velocity vector field and pressure contours in the symmetry plane.

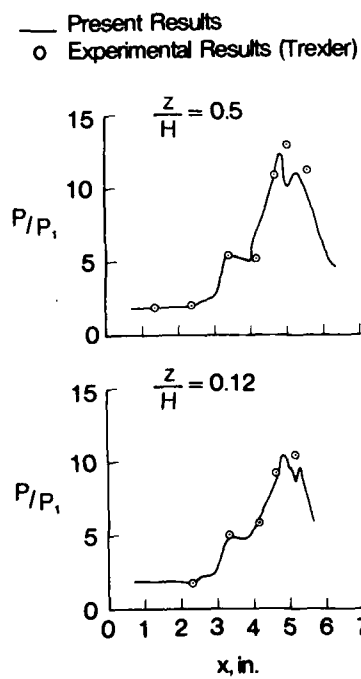


Fig. 11 Pressure distribution on the inlet sidewall.

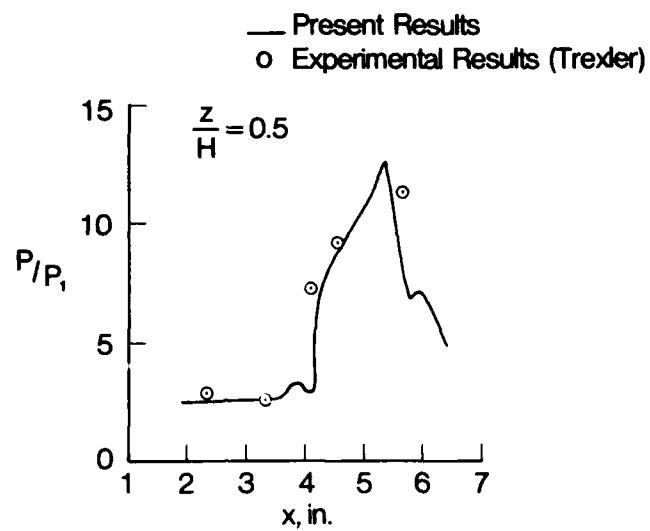


Fig. 12 Pressure distribution on the strut inner surface.

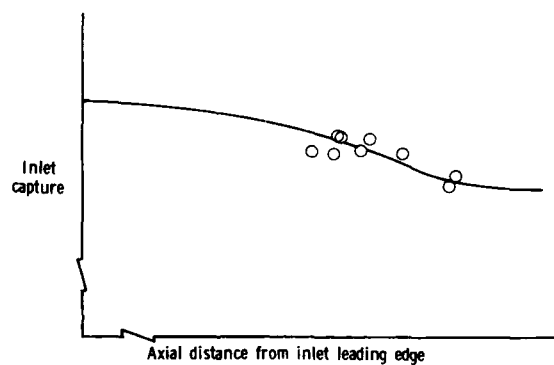


Fig. 13 Axial distribution of inlet capture.

NUMERICAL SIMULATION OF THE HYPERSONIC FLOW AROUND LIFTING VEHICLES

Yehia Rizk

Sterling Federal Systems Inc., Palo Alto, California, 94303.

Denny Chaussee and Joseph Steger

Nasa Ames Research Center, Moffett Field, California, 94035.

SUMMARY

A method for solving the viscous hypersonic flow field around realistic configurations is presented. The numerical procedure for generating the required finite difference grid and the two-factored implicit flow solver are described. Results are presented for the shuttle orbiter and a generic wing-body configuration at hypersonic Mach numbers.

1. INTRODUCTION

With the continuous development of more powerful computers, computational fluid dynamics (CFD) has emerged as a viable tool in understanding complicated three-dimensional fluid dynamics phenomena in subsonic, transonic and supersonic flow regimes. Hence CFD is now being routinely applied to practical problems to supplement wind tunnel experimentation in the design process. The recent renewed international interest in hypersonic transport is partly attributed to the confidence in using CFD solely in design because of the impossibility of simulating the wide range of the actual hypersonic flight conditions in a wind tunnel. This of course necessitates the development of robust hypersonic CFD codes which are reliable for providing important quantities such as the aerodynamic stresses, heat transfer and inlet flow conditions to the engine.

In this paper we describe and apply a numerical technique which is capable of solving the hypersonic flow around three dimensional lifting configurations. In this technique, the computational grid is created using an efficient numerical hyperbolic grid generation procedure (Ref.[1]) and the equations of motion (represented by the Reynolds averaged Navier-Stokes equations) are integrated using the time dependent factored procedure described in Ref.[2].

The present numerical procedure is used to compute the viscous flow around the shuttle orbiter at Mach number of 7.9 and angle of attack of 25 degrees and around a generic wing-body configuration at Mach number 25 and 5 degrees angle of attack. In both cases the fluid was assumed to behave as a perfect gas. The calculations were performed on the CRAY-2 to allow the use of fine grids in order to resolve the details of the complicated flow field associated with the geometries under consideration.

In the following sections, we briefly describe the grid generation procedure, the flow simulation procedure, and the computed results.

2. GRID GENERATION PROCEDURE

In computational fluid dynamics, a three dimensional body fitted mesh is highly desired and can be generated numerically using the elliptic (Refs.[3,4]), hyperbolic(Refs.[1,5]), parabolic or hybrid (Refs.[6,7]) schemes. All these schemes involve solving a set of partial differential equations and they all possess the desirable feature of allowing the user to specify an arbitrary point distribution along the body surface.

In the present study, the hyperbolic scheme was chosen because it automatically creates a body normal grid which is important for viscous flow computations. Also, the hyperbolic grid generation method is efficient in terms of computer time and memory and the resulting grid can be made orthogonal or close to orthogonal everywhere by proper surface grid specification. The major drawback of the hyperbolic scheme is its inability to prescribe an exact location for the outer boundary. However, with a minor modification, the user can specify an approximate location for the outer boundary as will be discussed later. This limited control on the outer boundary shape suffices for a wide range of external flow problems.

The Hyperbolic grid is generated by solving for the cartesian coordinates x, y and z , in terms of the generalized coordinates ξ, η , and ζ where, in general:

$$\xi = \xi(x, y, z)$$

$$\eta = \eta(x, y, z)$$

$$\zeta = \zeta(x, y, z)$$

here ξ is the streamwise coordinate, η is the circumferential coordinate and ζ is the outward coordinate.

A set of three equations are required to solve for the three unknowns x, y and z . Following Ref.[1], the first two equations are obtained by enforcing orthogonality relations between ξ and ζ

lines and between η and ζ lines, whereas the third equation is obtained from the cell volume specification. The following set of partial differential equations result:

$$\bar{r}_\xi \cdot \bar{r}_\xi = 0 \quad (1a)$$

$$\bar{r}_\eta \cdot \bar{r}_\eta = 0 \quad (1b)$$

$$\frac{\partial(x, y, z)}{\partial(\xi, \eta, \zeta)} = J^{-1} = \Delta V \quad (1c)$$

where \bar{r} is defined as $(x, y, z)^T$

The above nonlinear system of equations are locally linearized about the previous step which results in

$$A_i \delta_\xi(\bar{r}_{i+1} - \bar{r}_i) + B_i \delta_\eta(\bar{r}_{i+1} - \bar{r}_i) + C_i \nabla \cdot \bar{r}_{i-1} = \bar{g}_{i-1} \quad (2)$$

where A_i, B_i and C_i are 3×3 coefficient matrices that are formed from the local linearization of Eq. (1). The vector \bar{g}_{i-1} contains the user specified cell volumes

$$\bar{g}_{i-1} = \begin{pmatrix} 0 \\ 0 \\ \Delta V_{i-1} \end{pmatrix}$$

In Eq. (2), δ is the central difference operator used in ξ and η directions whereas ∇ is the backward differencing used in ζ direction. Using approximate factorization, Eq. (2), is reduced to

$$\mathcal{L}_\eta \mathcal{L}_\xi(\bar{r}_{i+1} - \bar{r}_i) = C_i^{-1} \bar{g}_{i-1} \quad (3)$$

where \mathcal{L}_η and \mathcal{L}_ξ are block tridiagonal matrices given by:

$$\mathcal{L}_\eta = (I - C_i^{-1} B_i \delta_\eta)$$

$$\mathcal{L}_\xi = (I - C_i^{-1} A_i \delta_\xi)$$

Therefore, the vector \bar{r}_{i+1} is obtained by solving the following sequence:

$$\mathcal{L}_\eta \bar{g}_{i-1} = C_i^{-1} \bar{g}_{i-1}$$

$$\mathcal{L}_\xi \nabla \cdot \bar{r}_{i+1} = \bar{g}_{i-1}$$

$$\bar{r}_{i+1} = \bar{r}_i + \nabla \cdot \bar{r}_{i+1}$$

Starting from the body surface, the mesh is obtained by marching outward using Eq. (3). In order to improve stability, numerical dissipation terms are added in the ξ and η directions. The dissipation consists of second-order implicit and fourth-order explicit terms which are scaled to the local mesh spacing (Ref. [1]). Additional optional implicit smoothing (Ref. [8]) is used for complicated body shapes to prevent grid line intersection near highly concave sections.

Depending on the boundary conditions specified at the ζ direction, the user can create "C-0" (Fig. 1a) or "H-0" (Fig. 1b) meshes suitable for supersonic external flow problems. The boundary condition procedure developed in Ref. [1] is employed at $\xi = 0$ and $\xi = \xi_{max}$. This procedure takes advantage of the fact that the eigenvalues of either $C_i^{-1} A_i$ or $C_i^{-1} B_i$ are of the form $(\sigma, 0, \sigma)$ where σ is real. The zero eigen value permits the specification of a combination of the dependent variables (e.g. $z = f(x, y)$) or the use of one sided differencing at the boundary. Hence, either one of the following two stable boundary procedure can be used. The first is to specify one combination of the dependent variables and use one sided differencing for the two remaining governing equations at the boundary. This approach is used at a boundary surface (e.g. $\xi = \xi_{max}$ in Figs. 1a, 1b) The second procedure is to specify two combinations of the dependent variables and use one sided differencing for a third governing equation at the boundary. This approach is used at an axis (e.g. $\xi = 0$ in Fig. 1a). In both cases, periodicity is assumed in the η direction.

The surface grid can be arbitrarily specified by the user. For relatively simple body shapes, the user can generate an orthogonal grid along the body surface. This process assures that the resulting grid will be nearly orthogonal in all directions. For complicated configurations, however, the surface grid is generated along cross sections of constant axial distance. Depending on the body shape, the ξ and η lines can be far from being orthogonal. However, this does not introduce any inconsistency because the orthogonality between the ξ and η is not enforced in the grid generation procedure. Experience has shown that the overall quality of the mesh is dependent upon the quality of the surface grid. Therefore, the user should pay extra attention in defining the surface grid to ensure a well behaved grid everywhere.

Since the grid is obtained by marching outward from the body, an exact location for the outer boundary can not be prescribed. Nevertheless, an approximate location for the outer boundary can be specified through proper selection of the cell volumes used in Eq. (1c). The cell volumes are defined by connecting straight lines between the surface boundary and the desired outer boundary shape. A prescribed clustering is then used to define the points along each ζ line. These cell volumes are then used in Eq. (1c) for the marching process. The resulting outer boundary will be close to the desired boundary. If a more exact outer boundary shape is needed, the computed grid points

can be reclustered in the ζ direction to allow that. This is accomplished by calculating the intersection of the computed ζ lines with the desired boundary. The grid points are then obtained by redistributing points between the body and the calculated intersection points along each line using the prescribed clustering. Although, the grid remains body normal, a significant amount of mesh skewness can be introduced especially if the desired outer boundary is relatively close to the body surface. This can be remedied by adding an extra global marching pass to improve the quality of the grid. This is done by computing new cell volumes at the end of the first global marching step and using that as the specified cell volume for the second global step.

3. FLOW SIMULATION PROCEDURE

Although in the current study we are dealing with predominantly supersonic flows, some regions of the flow field may contain pockets of embedded subsonic flow and/or axial separation. In such regions, the flow equations are elliptic, precluding the use of the more efficient space-marching techniques such as the parabolized Navier-Stokes (PNS) codes (e.g. Ref. [9]). Instead, a time-dependent procedure (F3D) is used to find the steady-state solution of the three-dimensional conservation-law form of the Reynolds-averaged Navier-Stokes equations.

3.1 Numerical Procedure

The unsteady Navier-Stokes equations with the thin-layer approximation in a strong conservative form, can be written as:

$$\dot{\vec{Q}} + \vec{E}_\xi + \vec{F}_\eta + \vec{G}_\zeta = Re^{-1} \vec{S} \quad (4)$$

where \vec{Q} is the dependent variables vector, \vec{E} , \vec{F} and \vec{G} are the inviscid-flux vectors, and the \vec{S} is contribution from the viscous terms. These vectors are given in Ref. [2].

A first or second order upwind differencing is used in ξ (streamwise) direction while a second order central differencing is used in η (meridional) and ζ (normal) directions. The implicit non-iterative two-factored scheme developed in Ref. [2] is used to solve Eq. (4). In this scheme, the flow variables at time step $n+1$ are obtained from:

$$\mathcal{L}^+ \mathcal{L}^- (\vec{Q}^{n+1} - \vec{Q}^n) = -\Delta t (\delta_\xi^b (\vec{E}^n)^n + \delta_\xi^f (\vec{E}^n)^n + \delta_\eta^c \vec{F}^n + \delta_\zeta^c \vec{G}^n - Re^{-1} \delta_c \vec{S}^n) \quad (5)$$

where, δ^c is the central operator, δ^b is the backward operator, δ^f is the forward operator and δ is the midpoint central operator. In Eq. (5), \mathcal{L}^+ is a lower block triangular matrix and \mathcal{L}^- is an upper block triangular matrix and they are given by:

$$\mathcal{L}^+ = (I + h \Delta t \delta_\xi^b \hat{A}^+ + \delta_\xi^c \hat{C} - Re^{-1} \delta_c (J^{-1} \hat{M} J))$$

$$\mathcal{L}^- = (I + h \Delta t \delta_\xi^f \hat{A}^- + \delta_\eta^c \hat{B})$$

where the 5×5 matrices \hat{A} , \hat{B} , \hat{C} and \hat{M} are the flux Jacobians of the fluxes \vec{E} , \vec{F} , \vec{G} and \vec{S} respectively.

Equation (5) is solved by a sequence of two one-dimensional like inversions. In practice, smoothing terms are added in the η and ζ directions where central spatial differencing is used. The smoothing consists of second order implicit terms and combination of second and fourth order explicit terms. Also, free stream is subtracted as a base solution to reduce the numerical differencing error.

In the above formulation, upwind differencing is used in the streamwise direction. In hypersonic flows, the bow shock is typically more aligned with ζ lines than with the ξ lines especially near the nose section where the bow shock is the strongest. Therefore, it would be more advantageous to use upwind differencing in the ζ direction and central differencing in the ξ and η directions. Without making significant changes to the code, upwind differencing can be utilized in the outward direction by simply interchanging ξ with ζ and neglecting the implicit portion of the viscous terms in Eq. (5) resulting in:

$$\mathcal{L}^+ \mathcal{L}^- (\vec{Q}^{n+1} - \vec{Q}^n) = -\Delta t (\delta_\xi^b (\vec{G}^n)^n + \delta_\xi^f (\vec{G}^n)^n + \delta_\eta^c \vec{F}^n + \delta_\zeta^c \vec{E}^n - Re^{-1} \delta_c \vec{S}^n) \quad (6)$$

where,

$$\mathcal{L}^+ = (I + h \Delta t \delta_\xi^b \hat{C}^+ + \delta_\xi^c \hat{A})$$

$$\mathcal{L}^- = (I + h \Delta t \delta_\xi^f \hat{C}^- + \delta_\eta^c \hat{B})$$

Here \hat{C}^+ is the flux jacobian of \vec{G} . It must be noted that, while upwind differencing is used for the inviscid flux in the ζ direction, the viscous flux on the right hand side of Eq. (6) is still centrally differenced using the midpoint operator.

The above alternative formulation produces sharper bow shocks as will be shown later. Moreover, by interchanging the algorithm this way, the streamwise axis singularity (at which the grid transformation Jacobian is infinite) is tied to central differencing rather than the most sensitive upwind differencing. The obvious drawback is that the viscous terms are treated explicitly. This proved to reduce the maximum allowable time step increment resulting in slower convergence rates. The possibility of modifying the code in order to retain the implicit viscous terms in Eq. (6) will be addressed in a forthcoming report.

The normal flux split formulation is implemented into the code as an option. An input control parameter activates the calls to the appropriate boundary conditions subroutine. In order to compare

the two formulations, the inviscid flow around the shuttle nose at Mach number of ≈ 7.9 and 25 degrees angle of attack was selected as a test case. The grid in the pitch plane of symmetry is shown in Fig. 2. Figures 3 and 4 show the computed steady state mach number contours in the pitch plane of symmetry obtained using streamwise flux split (Eq.(5)) and normal flux split (Eq.(6)), respectively. It is clearly seen that the normal flux split yields a much sharper bow shock definition near the nose and in the windward region where the shock is roughly aligned with $\zeta = \text{constant}$ surfaces. However, both the streamwise and normal flux split result in shock smearing in the downstream portion of the leeside. This is because the bow shock there is no longer aligned with either the ζ or η surfaces as could be seen from the grid in Fig. 2. It is worth noting that, with the normal flux split, a simple grid adaptation where the grid points are allowed to move on the ζ lines can solve this problem. In general, a formulation in which flux splitting is utilized in both the streamwise and normal directions may be more suitable for general hypersonic flow problems.

3.2 Boundary Conditions

At $\zeta = 0$ (body surface), the viscous no-slip condition is imposed. The normal momentum equation is used to compute the surface pressure. In addition, either an adiabatic wall condition or a prescribed wall temperature are specified. At $\zeta = \zeta_{\text{max}}$ (outer boundary), the bow shock can either be fitted or captured. In the bow-shock-capturing calculations, the boundary values are fixed at its free stream values. With the bow shock fitted, its location as well as the flow variables behind it are determined from the shock fitting procedure of Ref.[10]. The shock is allowed to move along the curved ζ lines. The original clustering is maintained by redistributing points along ζ lines after each time step to adjust for the bow shock movement.

In the present study only cases with bilateral symmetry are considered, and the boundary conditions in the meridional direction η enforces symmetry conditions at the $\eta = 0$ (leeward) and $\eta = \eta_{\text{max}}$ (windward) planes. The symmetry is imposed through the use of reflection points on the opposite sides of the leeward and windward planes.

At $\xi = 0$, either axis ("C-0" mesh) or inflow ("H-0" mesh) boundary conditions are imposed. At the axis the boundary conditions are obtained by extrapolating and then averaging the flow variables from the surrounding points. When upwind differencing is used in the streamwise direction, the flow variables at the first set of grid points away from the axis is obtained by interpolation to avoid integrating the equations of motion at these points. This interpolation step is not needed when central differencing is used in the streamwise direction. At the inflow boundary, all the flow variables are specified. At $\xi = \xi_{\text{max}}$ (outflow boundary) an extrapolation formula consistent with supersonic outflow is used.

All the boundary conditions are implemented explicitly in the code. While the use of explicit boundary conditions with an implicit scheme does cause some degradation of the convergence rates, the use of explicit boundary conditions allows the user to treat different flow problems by merely changing the boundary conditions routines without changing the rest of the code.

4. RESULTS

The current grid generation and flow solution procedures have been used to simulate the hypersonic flow field around the shuttle orbiter and a generic wing-body configuration.

4.1 Shuttle Orbiter

Figure 5a shows an overall view of the mesh generated for the orbiter while Fig. 5b shows the details of the grid near the body surface. The three dimensional mesh is displayed by showing the surface grid ($\zeta = 0$), the grid in the plane of symmetry ($\eta = 0$ and $\eta = \eta_{\text{max}}$) and the grid at the exit plane ($\xi = \xi_{\text{max}}$). It is seen that the grid is well behaved and is body normal. In generating the mesh, an estimate for the bow shock location was made and the appropriate values for the cell volume were chosen to result in an outer boundary location suitable for shock capturing computations. The boundary procedure corresponding to Fig. 1a ("C-0" mesh) is used where the two relations $y = y(x)$ and $z = z(x)$ are employed at the axis. At the outflow boundary the relation $x = \text{constant}$ is employed. The value of the constant is determined from the surface grid. The grid is comprised of 54 points along the body, 61 points in the cross section and 45 points in the outward direction.

The flow conditions are $M_\infty = 7.9$ and $\alpha = 25$ degrees, and a constant wall temperature of 540 degrees. The Reynolds number (based on the orbiter total length) is 1.46×10^6 . The flow was assumed to be laminar. These flow conditions correspond to the wind tunnel experimental data of Ref. [11]. The calculations were performed using the streamwise flux split option. The result of the computations in the region where the wing shock interacts with the bow shock are shown in Figs. 6 and 7. Figure 6 shows the pressure contours at a typical cross section. The pressure and mach number contours in a $\eta = \text{constant}$ plane passing by the wing tip are shown in Fig. 7. The general features of the flow field near the surface is indicated in Fig. 8 which depicts the simulated oilflow pattern. Lines of cross flow separation are clearly visible on the upper wing and on the top part of the orbiter. Also, a line of axial flow separation is observed on the top surface. Fig. 9 show the variation of the surface pressure along the windward plane of symmetry and in a cross plane at $x/l = .796$. The experimental data at $x/l = .8$ is also shown, and it seen that there is a good agreement between the computed results and the data. The steady-state computations required about 7 MW of core memory and took about 8 hours of CRAY 2 time.

4.2 Generic Wing-Body Geometry

The flow about a generic wing body configuration was also computed. The flow conditions for this case are $M_\infty = 25$, $\alpha = 5$ degrees, and a constant wall temperature of 3000 degrees. A specific heat ratio of 1.2 was chosen to simulate the real gas effects at high freestream Mach number.

In order to facilitate the solution at this high Mach number, a segmentation procedure (Ref. [12]) in which the flow field is divided into two regions is used. The boundary between the two adjacent regions is carefully located beyond the rounded nose where the outer inviscid flow is supersonic and the boundary layer is attached. This ensures the absence of any upstream influence between the two regions. This division enables the use of shock fitting in the nose region where the shock is strongest, while shock capturing is used in the downstream section. The use of shock capturing in the second segment avoids the tedious process associated with guessing the initial bow shock shape for the shock fitting procedure.

The grid in the second segment was first created with the outer boundary located far away from the body. Then, the local bow shock slope at the end of first segment was used as guide for determining a more appropriate location for the outer boundary. The grid points were then redistributed in the x direction to reflect this new location as explained earlier. The boundary procedure corresponding to Fig. 1b ("H-O" mesh) is used where the relation $r = \text{constant}$ are employed at the inflow and the outflow boundaries. The surface and resulting computational grid (at the symmetry plane and exit plane) are shown in Fig. 10. The grid consisted of 45 points in the streamwise direction, 92 points in the meridional direction and only 26 points in the outward direction. It is seen that the grid is smooth and body normal everywhere except at $\xi = \xi_{\text{exit}}$ where one of the orthogonality equations was replaced by the relationship $r = \text{constant}$ to ensure stable marching.

The computation was first performed with the original flux split formulation until steady state was reached. Then, the normal flux split option was activated to produce a better definition for the bow shock. The implicit viscous terms on the left hand side of Eq. (5) were neglected as mentioned before. This forced a reduction in the time step by an order of magnitude thus slowing down the convergence considerably. Figure 11 shows the Mach number in a cross plane near the end of the vehicle. The pressure contours on the body surface are shown in Fig. 12. It is seen that there is a pressure rise near the nose and near the wing tip.

CONCLUDING REMARKS

The hyperbolic grid generation scheme allows the generation of a three dimensional body normal mesh suitable for viscous flow computations. The limited outerboundary control is suitable for hypersonic applications. A method for solving the viscous hypersonic flow field around realistic configurations on the CRAY2 computer was presented. Flux splitting was used in the streamwise and normal directions. The normal flux splitting results in a sharper bow shock and avoids the axis singularity problem but requires more iterations because of the explicit treatment of the viscous terms.

REFERENCES

1. Steger, J.L. and Rizk, Y.M., "Generation of Three Dimensional Body Fitted Coordinates Using Hyperbolic Partial Differential Equations.", NASA TM 86753, June, 1985.
2. Ying, S. and Steger, J. and Schiff, L. and Baganoff, D., "Numerical Simulation of Unsteady, Viscous, High Angle of Attack Flows Using a Partially Flux Split Algorithm.", AIAA Paper no. 86-2179.
3. Thompson, J.F., Proceedings of a Symposium on the Numerical Generation of Curvilinear Coordinate Systems and Their Use in the Numerical Solution of Partial Differential Equations. 1982, Nashville, Tennessee.
4. Sorenson, R., "Elliptic Generation of Composite Three-Dimensional Grids about Realistic Aircraft.", NASA TM 88240, March, 1986.
5. Rizk, Y., Steger, J. and Chaussee, D., "Use of Hyperbolic Grid Generation Scheme in Simulating Supersonic Viscous Flow About Three Dimensional Winged Configurations.", International Symposium on Computational Fluid Dynamics, Tokyo, Japan, Sep. 9-12, 1985.
6. Edwards, T., "A Three Dimensional Grid Generation Using a Parabolic Partial Differential Equations.", AIAA Paper No. 85-0485, Reno, Nevada, Jan. 1985.
7. Nakamura, S. and Suzuki, M., "Noniterative Three Dimensional Grid Generation Using a Parabolic Hyperbolic Hybrid Scheme.", AIAA Paper No. 87-0227, Reno, Nevada, Jan., 1987.
8. Kinsey, D.W., and Barth, T.J., "Description of a Hyperbolic Grid Generation Procedure for Arbitrary Two-Dimensional Bodies.", AFWAL Technical Memorandum No. 84-191-FIMM (July, 1984).
9. Schiff, L.B., and Steger, J.L., "Numerical Simulation of Steady Supersonic Viscous Flow.", AIAA Journal, Vol. 18, Dec. 1980, pp 1421-1430.
10. Kutler, P., Pedelty, J.A., and Pulliam, T.H., "Supersonic Flow Over Three-dimensional Ablated Nosetips Using Implicit Numerical Procedure.", AIAA Paper No. 80-0063, Pasadena, Calif., Jan., 1980.

11. Herrera, B. J., "Results of a Flowfield Survey Conducted Using The 0.0175 Scale Orbiter Model 29-0 in AEDC VKF Tunnel B During Test OH52" NASA CR-147, 637, Sep., 1976.
12. Rizk, Y.M., and Ben-shmuel, S., "Computation of the Viscous Flow Around the Shuttle Orbiter at Low Supersonic Speeds." AIAA Paper 85-0168, Reno, Nevada, Jan., 1985.

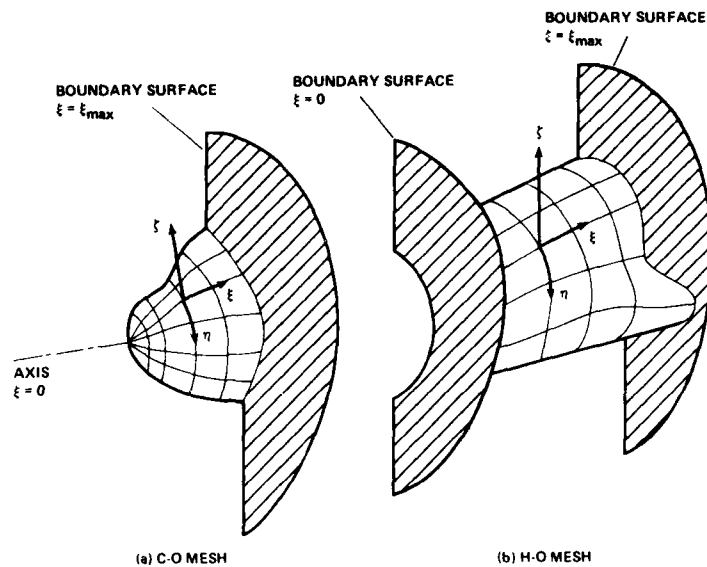


Fig. 1 Mesh topologies for hypersonic flow computations.

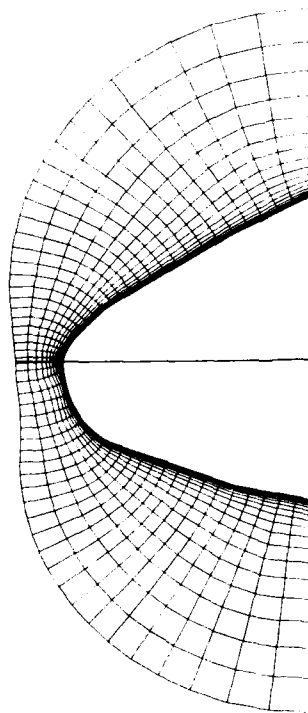


Fig. 2 Computational grid around the shuttle nose.

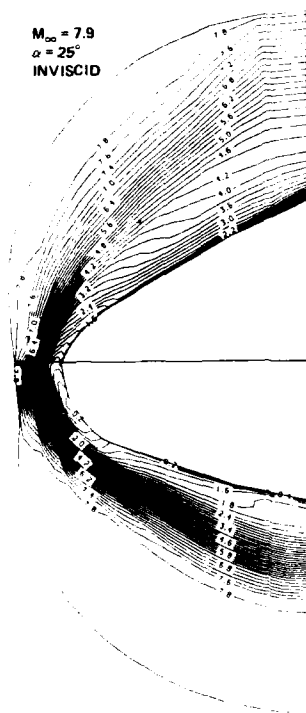


Fig. 3 Mach number contours computed using stream-wise flux splitting.



Fig. 4 Mach number contours computed using normal flux splitting.

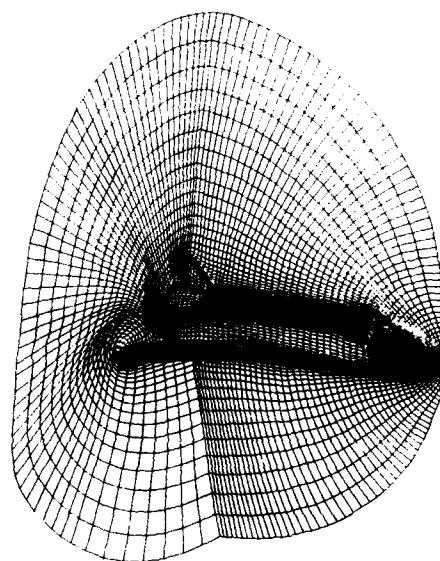


Fig. 5a Overall view of the computational grid for the orbiter.

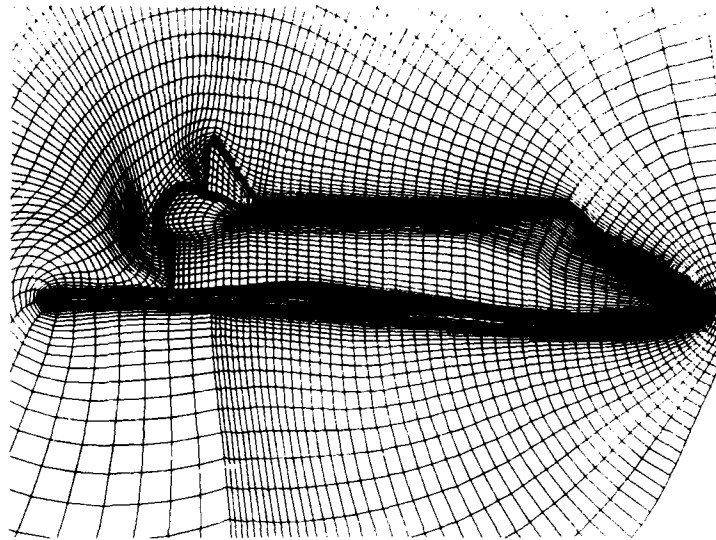


Fig. 5b Details of the computational grid near the orbiter surface.

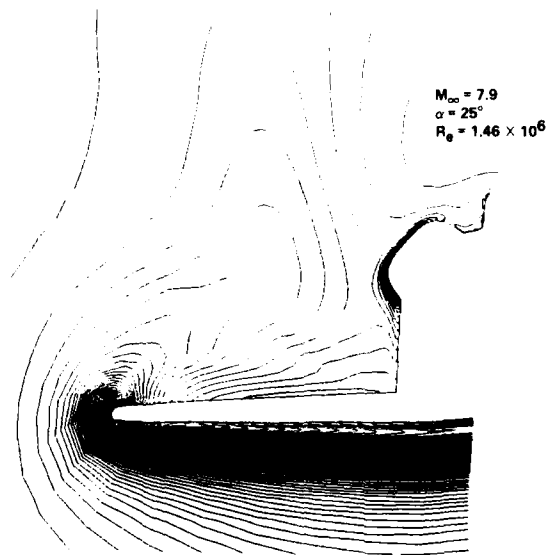


Fig. 6 Pressure contours in a ξ constant plane near the end of the orbiter.

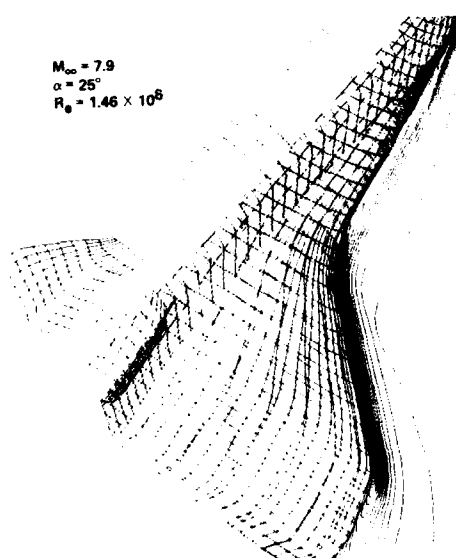


Fig. 7a Pressure contours in an n plane near the wing tip.

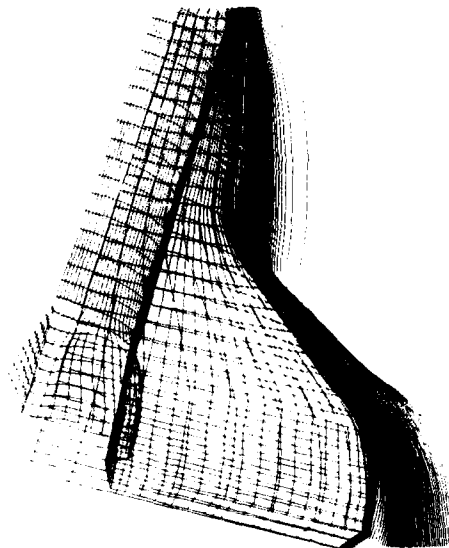


Fig. 7b Mach number contours in an n plane near the wing tip.

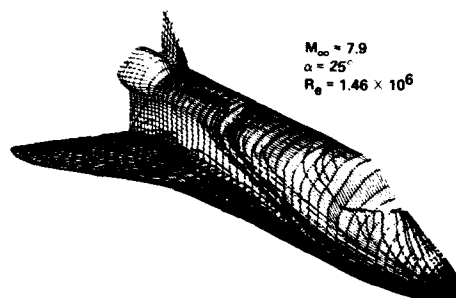


Fig. 8 Computed limiting streamlines on the orbiter surface.

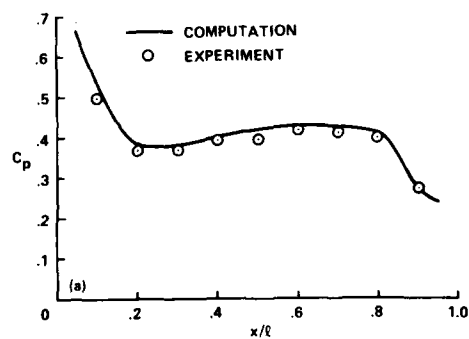


Fig. 9a Comparison between the computed pressure and the experimental data on the windward side.

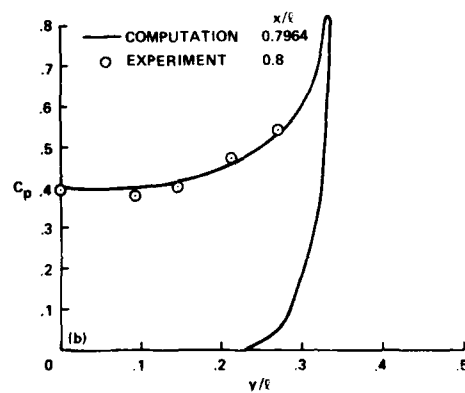


Fig. 9b Comparison between the computed pressure and the experimental data at $x/l = 0.8$.

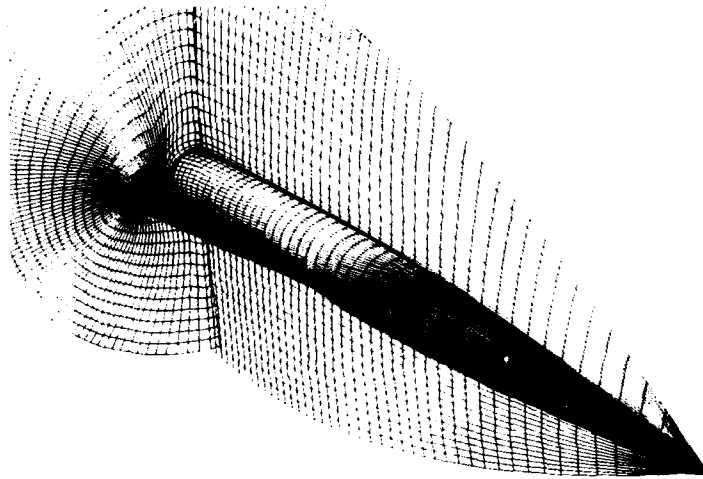


Fig. 10 Computational grid for a generic wing body configuration.



Fig. 11 Mach number contours in a ξ constant plane near the end of the vehicle.

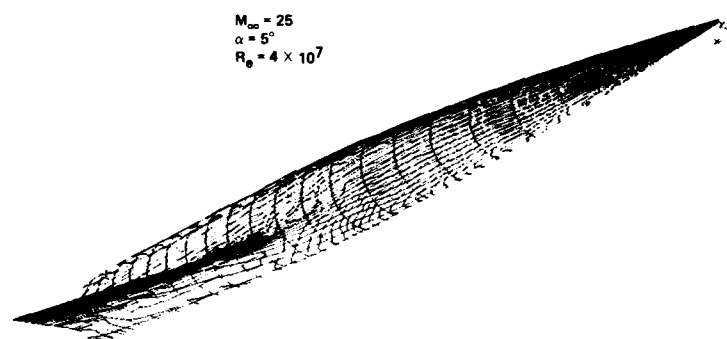


Fig. 12 Pressure contours on the body surface.

Solution of Some 3-D Viscous and Inviscid Supersonic
Flow Problems by Finite-Volume Space-Marching Schemes

4. Rieger

Aerodynamics Department, BF30
Dornier GmbH
D-799 Friedrichshafen 1
Federal Republic of Germany

Summary

For prediction of steady supersonic flow fields two numerical methods for solution of the three-dimensional Euler- and parabolized Navier-Stokes (PNS-) equations are considered. Both are based on a Finite-Volume discretisation (FVD) of the governing conservation laws and because of the special properties of steady supersonic flows cost-effective space-marching integration techniques can be applied. Both methods are described and results for inviscid and viscous flows are presented.

In view of the upcoming European space transportation activities the simulation of hypersonic flows past complex blunted lifting vehicles requires also efficient methods for solution of the full, not-reduced Navier-Stokes equations. These are needed to provide solutions for super- and hypersonic flow fields with large subsonic regions and also to get accurate initial conditions for the space marching codes developed. A relaxation procedure for the steady form of the not-reduced Navier-Stokes and the Euler equations is described and some first results are presented.

1. Introduction

The new strong interest in efficient aerodynamic prediction methods for super- and hypersonic flows has been stimulated by some new European projects and advanced concept studies in the field of high speed missiles and aerospace transportation systems. Basically in the low supersonic flow regime important aerodynamic quantities can be predicted with some success by considering inviscid computational methods. However in the high supersonic or even hypersonic region the flow field is influenced in an increasing manner by viscous and real gas effects as well as by non-equilibrium chemistry phenomena, so that the full conservation laws have to be taken as the starting point for the development of valuable numerical prediction tools. Especially from the theoretical simulation of flow fields around vehicles during reentry extreme reliable results are required concerning thermal and structural loads. On these answers the design of the necessary thermal protection systems and the vehicles payload will critically depend. Also these reentry vehicles will fly for most part of their reentry trajectory with high angle of attack so that strong streamwise vortex systems on the wing leeside will be generated which under some circumstances can interact with existing shock systems resulting in extreme local thermal loads.

To meet these requirements on prediction quality methods based on the parabolisation of the Navier-Stokes equations are offered as a compromise between accuracy and costs. However these methods are built around the assumption of a steady supersonic flow field with the particular property of propagating all waves and disturbances downstreams. Essentially this fact is used as key assumption for construction of any space-marching method. Therefore any physical phenomena acting upstream will be the cause for some problems in a space-marching integration procedure. Some of these upstream effects, like those originated from subsonic regions of supersonic boundary layers can be overcome by special algorithmic treatments. But recirculation regions, if present in the flow field, will effectively be suppressed in a non-iterative, one-sweep space-marching method. What can be simulated with some success, however, are streamwise or vortex separation processes which occur frequently in flows past bodies at high angle of attack.

Even with the restrictions mentioned space-marching methods for integration of the parabolized Navier-Stokes equations are attractive tools in terms of storage and costs. Only data planes perpendicular to the integration direction (which approximately should be parallel to the main flow direction) have to be considered thus the effort to solve three-dimensional problems is reduced to that needed to solve two-dimensional time-dependent problems. Moreover, by space-marching methods the necessary spatial resolution of a three-dimensional flow process can be achieved without running into storage problems.

Most of the successful applications of PNS-methods for more complex geometries follow the solution approach of Vigneron et al [1] and Schiff and Steger [2]. Some notable examples are computations of flows around simple reentry lifting bodies [3], around the US-Space Shuttle assuming ideal gas [4] and real gas behaviour [5,6] as well as flow simulations past a complex fighter configuration [7]. In all these works cited PNS-methods are used which are based on a finite-difference discretisation of the conservation laws. The methods presented in this study are developed as finite-volume schemes.

In the following sections the methods are described in more detail and results for the inviscid and viscous schemes are presented. As test cases for the inviscid code the flows around two different forebodies are considered. Hypersonic flows along a compression ramp, around cones at incidence and around an ogive-cylinder configuration are chosen to demonstrate the capabilities of the PNS-code.

As mentioned previously every space-marching solution depends essentially on the quality of the initial conditions provided. Only for pointed bodies free stream values defined in the cross-plane at the very tip are sufficient as initial conditions. For blunt bodies initial solutions have to be supplied; e.g. by not-reduced Navier-Stokes methods. For computation of steady flows an implicit LU-scheme of Jameson and Yoon [8] seems to be a promising method with some potential. The approach can be viewed as a deferred correction method, where the implicit operator only approximates the corresponding flux jacobians to first order in space. However, the LU-factors have the property of diagonal dominance and therefore are well conditioned allowing a relaxation type solution of the steady equation set. First results are the flow around a hemisphere-cylinder and the flow around a reentry type lifting vehicle.

2. Governing Equations

The proper starting point for development of a Finite-volume space-marching method is the integral form of the steady state conservation laws

$$\int_S (A \underline{v} + B) \cdot \underline{n} dS = 0 \quad (1)$$

There S is the surface bounding a fixed volume in space, where A represents a certain property convected with the mass velocity \underline{v} and B denotes a flux associated with A . From (1) the specific conservation laws for mass, momentum and energy are recovered by substituting A and B by following quantities

$$\begin{aligned} \text{continuity:} \quad A &\equiv \rho & B &= 0 \\ \text{momentum:} \quad A &\equiv \rho \underline{v} & B &= \underline{q} \\ \text{energy:} \quad A &\equiv E_{\text{tot}} = \rho e + \frac{1}{2} \rho (\underline{v} \cdot \underline{v}) & B &= -\underline{q} \cdot \underline{v} + \underline{q} \end{aligned} \quad (2)$$

In usual notation ρ , \underline{v} and \underline{q} are introduced as the mass density, the mass velocity vector and the heat flux vector; whereas \underline{q} denotes the stress tensor, E_{tot} the specific total energy per-unit-volume and e the mass-specific internal energy.

To assure a general applicability of the numerical method it is convenient to express the conservation laws in terms of a generalized curvilinear coordinate system $(x^1, x^2, x^3) = (\xi, \eta, \zeta)$ which is related to the base cartesian coordinate frame $(x^1, x^2, x^3) = (x, y, z)$ by some mapping. The tensor notation applied follows essentially that introduced in [9].

The normal surface vector $\underline{n} dS$ of a surface element belonging to a coordinate surface $x^k = \text{const}$ can be written as

$$d\underline{S}^k = \underline{n}^{(k)} dS^{(k)} = dS_m^k, \underline{a}^m$$

where dS_m^k denotes the cartesian components of the normal surface vector. As an example the continuity equation can then be written in terms of vector components as

$$\int_S \rho v^k dS_m^k = 0$$

To get a direct finite-volume discretisation for a elementary volume dV , bounded by successive surface elements dS_m^k and dS_v^k belonging to the general coordinate surface x^k , the mean value theorem of integral calculus has to be applied, resulting in:

$$\int_S \rho v^k dS_m^k = \sum_{k=1}^3 \Delta_k [\bar{\rho v^k}] \delta S_m^k = 0 \quad (3)$$

Here the delta operator should be understood as $\Delta_k [\bar{\rho v^k}] \delta S_m^k = [\dots]_+ - [\dots]_-$. It should be noted that the relation represents an exact equality and the order of the discretisation error is determined by the definition of the mean value $\bar{\rho v^k}$ and by the accuracy in evaluating the components of the normal surface vector δS_m^k .

The above procedure leading to a finite-volume discretisation of the continuity equation can be repeated in an analogous way for the equations of momentum and energy. Dropping below the bars indicating a mean value one gets, after splitting the stress tensor in a viscous and a pressure contribution $\underline{q} = -p \underline{I} + \underline{\tau}$, the following equations

$$\left(\sum_{k=1}^3 \Delta_k [(\rho v_g^k, v^m + p \delta_m^k - \tau_m^k) \delta S_m^k] \right) \underline{a}^k = 0 \quad (4)$$

$$\sum_{k=1}^3 \Delta_k [(E_{\text{tot}} + p) v^m - \tau_m^k v^k + q^m] \delta S_m^k = 0 \quad (5)$$

The system of equations (3-5) is closed by assuming a perfect gas

$$p = (\kappa - 1) \rho e \quad (6)$$

the validity of Fourier's law of heat conduction, where λ denotes the coefficient of heat conduction and c_v the specific heat at constant volume

$$\underline{q} = -\frac{\lambda}{c_v} \nabla e = -\frac{\lambda}{c_v} e_{,s} g_n^s g^{m'n'} \underline{a}_m \quad (7)$$

and by assuming a Newtonian fluid

$$\begin{aligned} \sigma &= (-p \delta_{21}^{m'} + \bar{\sigma}_{21}^{m'}) g_{m1} \bar{g}_1^{2'} \\ \bar{\sigma}_{21}^{m'} &= -\frac{2}{3} \mu v_{1r}^{m'} \beta_{21}^{r'} \delta_{21}^{m'} + \mu [v_{1r}^{m'} \beta_{21}^{r'} + (v_{21}^{m'})_{,r} \beta_{21}^{r'} g^{n'm'}] \end{aligned} \quad (8)$$

The temperature dependence of the dynamic viscosity μ is taken according to Sutherland's formula.

3. Space-marching schemes

3.1 PNS-Method

The steady state conservation laws (3-6) are valid in the entire flow regime and show mathematically for subsonic flows an elliptic behaviour, meaning, that waves are carried up- and downstreams. However a stable space-marching integration can only be assured for hyperbolic-parabolic systems of equations, which requires the suppression of any elliptical influence acting into the integration direction. To achieve this goal obviously all viscous and diffusive terms affecting the main flow direction have to be neglected.

Assuming that the main flow direction is approximately in parallel to the coordinate $x^1 \equiv \xi$ (along which integration should be performed) and that the coordinate surfaces $x^i = \text{const.}$ are parallel to the cartesian surfaces $x^{i'} \equiv x = \text{const.}$, then some metric simplifications are possible and the conditions for elimination of the viscous terms in (4) and (8) can be expressed as

$$(\Delta_1 [\bar{\sigma}_{21}^{1'}, \delta S_1^{1'}]) \bar{g}_1^{2'} = 0 \quad (9a)$$

$$v_{11}^{i'} \beta_{11}^{1'} = 0 \quad (i' = 1', \dots, 3') \quad (9b)$$

Corresponding conditions for the energy equation (5) and Fourier's law read:

$$\Delta_1 [(-\bar{\sigma}_{21}^{1'} v_{21}^{2'} + q^{1'}) \delta S_1^{1'}] = 0 \quad (9c)$$

$$e_{,1} \beta_{11}^{1'} = 0 \quad (9d)$$

It can be shown [1], that the necessary conditions (9a-d) are not sufficient even in the inviscid limit ($\mu, \lambda \rightarrow 0$), where complex eigenvalues appear for subsonic flow ($Ma < 1$). The reason for that behaviour is the upstream influence of pressure waves in subsonic flow regions. Therefore the success of a space-marching method is crucial dependent upon the modeling and the approximations of the streamwise pressure gradient. A possible remedy for that is the total neglect of the streamwise pressure gradient which from the mathematical point of view fulfills the requirements for a stable space integration procedure. However accurate results can be expected only for some hypersonic flow problems [10].

In first order boundary layer theory one of the basic assumptions is that of a zero normal pressure gradient across the boundary layer. This idea is carried over to a space-marching approach, widely known as 'sublayer approximation' which was refined and extended to implicit, non-iterative schemes by Schiff and Steger [2]. In the development of that technique one argues that a basic assumption of boundary layer theory taken as valid for the whole viscous layer should at least be a very good approximation for only the subsonic portion of a supersonic boundary layer. So the local streamwise pressure gradient from the supersonic side of the subsonic/supersonic boundary is transferred to the subsonic zone and therefore a constant value is taken for the whole subsonic layer. However, this model seems to generate a consistency problem. The flux jacobians indeed possess also for subsonic velocities real eigenvalues but not linearly independent eigenvectors, which should be assured for hyperbolic systems of equations.

Consequently, using the 'sublayer technique' in a space-marching integration procedure some lower bound on the integration step size has to be observed [2,11].

A somewhat other approach is taken by Vigneron et al [1]. They ask for that portion ω of the streamwise pressure gradient which is allowed to be considered in a space-marching procedure with the intent of avoiding any complex eigenvalues which would indicate an elliptic behaviour. Taking the cartesian components of the velocity vector \underline{v} as u, v and w then under the metric simplifications introduced the flux vector \underline{E} corresponding to the x^1 -coordinate can be written as

$$\begin{aligned} \underline{E} &= \underline{\tilde{E}} + \underline{P} \\ \underline{\tilde{E}} &= \delta S_1^{1'} (p u, p u^2 + \omega p, p u v, p u w, (E_{tot} + p) u)^T \\ \underline{P} &= \delta S_1^{1'} (0, (1-\omega)p, 0, 0, 0)^T \end{aligned} \quad (10)$$

In [1] it is shown, that complex eigenvalues for ($Ma_x = u/c < 1$ (c -speed of sound)) are always prevented by the relation.

$$\omega = \frac{\kappa Ma_x^2}{1 + (\kappa - 1) Ma_x^2} \quad (Ma_x < 1) \quad (11)$$

There α is a parameter ($\alpha < 1$) supplied for security. The experience has shown that instabilities in non-iterative space-marching schemes do not occur if β is taken as zero. In comparison to the 'sublayer-approximation' a step size limitation do not exist. This fact is of some importance, because the start of the integration is possible from the very tip of a pointed body by providing only the free stream values as initial data. It is this particular property which has lead to the application of the 'Vigneron-technique' in the space-marching method presented.

3.1.1 Numerical Scheme

For the numerical solution of the PNS-equations (3-5) an implicit Beam-Warming scheme is adopted. The development of the scheme is most easily presented by writing (3-5) with the corresponding parabolisation requirements (9) in symbolic form

$$\Delta_1 \underline{E} + \Delta_2 (\underline{F} - \underline{F}_v) + \Delta_3 (\underline{G} - \underline{G}_v) = 0 \quad (11)$$

There the vectors \underline{E} , \underline{F} and \underline{G} denote the inviscid flux vectors according to the generalized coordinate directions $x^1 \equiv \xi$, $x^2 \equiv \eta$ and $x^3 \equiv \zeta$, whereas the viscous and diffusive fluxes in the cross-plane directions x^2 and x^3 are gathered into the vectors \underline{F}_v and \underline{G}_v . As illustrated in Fig. 1, the space-marching scheme solves for the flow variables in the cross-plane $x^1 \equiv i+1$ and the corresponding finite volume is defined by the coordinate planes $x^1 + (i, i+1)$; $x^2 + (j, j+1)$ and $x^3 + (k, k+1)$. For the flux difference across the cell one may write e.g. $\Delta_1 \underline{E} = \underline{E}_{i+1} - \underline{E}_i$. Then an integration scheme of at most second order ($\beta = 1/2$) in x^1 -direction reads

$$(\underline{E}_{i+1} - \underline{E}_i) + (1-\beta) [\Delta_2 (\underline{F} - \underline{F}_v) + \Delta_3 (\underline{G} - \underline{G}_v)]_i + \beta [\Delta_2 (\underline{F} - \underline{F}_v) + \Delta_3 (\underline{G} - \underline{G}_v)]_{i+1} = 0 \quad (13)$$

By defining the solution vector as $\underline{q} = (\rho, \rho u, \rho v, \rho w, E_{tot})^T$, (13) is linearized with respect to \underline{q} . Taking into account the 'Vigneron-splitting' (10) linearization results in the following relations.

$$\begin{aligned} \underline{p}_{i+1} &= \underline{R}_i^{i+1} \underline{q}_i + O(\delta q) \\ \underline{E}_{i+1} &= \underline{A}_i^{i+1} \underline{q}_{i+1} + O(\delta q^2) \\ \underline{F}_{i+1} &= \underline{B}_i^{i+1/2} \underline{q}_{i+1} + O(\delta q^2) \\ \underline{G}_{i+1} &= \underline{C}_i^{i+1/2} \underline{q}_{i+1} + O(\delta q^2) \\ \underline{F}_{v, i+1} &= \underline{F}_{v, i} + \underline{M}_i^{i+1/2} \underline{q}_{i+1} + O(\delta q^2) \\ \underline{G}_{v, i+1} &= \underline{G}_{v, i} + \underline{N}_i^{i+1/2} \underline{q}_{i+1} + O(\delta q^2) \end{aligned} \quad (14)$$

In (14) it is fact is exploited that the inviscid and viscous flux vectors are homogeneous function to first and zeroth degree (e.g.: $\underline{E}_i = \underline{A}_i^{i+1} \underline{q}_i$, $\underline{M}_i^{i+1/2} \underline{q}_i = 0$), supposing linearization of the viscous flux vectors is done according to [12]. In reading the functional matrices e.g. $\underline{A}_i^{i+1} = (\partial \underline{E} / \partial \underline{q})_i^{i+1}$, it is understood that the upper index indicates the position in x^1 -direction at which the metric is evaluated whereas the lower index points out where the expressions of dependent variables are formed.

Using (14) the scheme (13) reads

$$(\underline{B}_i^{i+1} + \beta [\Delta_2 (\underline{B}_i^{i+1/2} - \underline{M}_i^{i+1/2}) + \Delta_3 (\underline{C}_i^{i+1/2} - \underline{N}_i^{i+1/2})]) \underline{q}_{i+1} + (\underline{B}_i^{i+1} \underline{q}_i - \underline{E}_i) - \beta [\Delta_2 \underline{F} + \Delta_3 \underline{G}]_i + [\Delta_2 (\underline{F} - \underline{F}_v) + \Delta_3 (\underline{G} - \underline{G}_v)]_i = 0 \quad (15)$$

Numerically more suitable is the delta-formulation of (15). By defining $\delta \underline{q} = \underline{q}_{i+1} - \underline{q}_i$ one arrives at

$$\begin{aligned} &(\underline{A}_i^{i+1} + \beta [\Delta_2 (\underline{B}_i^{i+1/2} - \underline{M}_i^{i+1/2}) + \Delta_3 (\underline{C}_i^{i+1/2} - \underline{N}_i^{i+1/2})]) \delta \underline{q} \\ &= -[(\underline{R}_i^{i+1} - \underline{A}_i^{i+1}) \underline{q}_i - \underline{E}_i] - [\Delta_2 (\underline{F} - \underline{F}_v) + \Delta_3 (\underline{G} - \underline{G}_v)]_i \end{aligned} \quad (16)$$

By choosing the values of the solution variables at the cell surfaces by the simple algebraic mean according to $\underline{q}_i = 1/2 (\underline{q}_{i-1/2} + \underline{q}_{i+1/2})$, a finite-volume PNS-space marching scheme is similar to a central difference scheme with the consequence that (16) has to be supported by some artificial dissipation fluxes. The construction of the dissipation-operators \underline{D}_2 and \underline{D}_3 corresponding to the coordinates x^2 and x^3 is essentially that of Jameson et al [13]. There coupled second and fourth order conservative operators are used adaptively.

At shocks the fourth order dissipation is turned off continuously, degrading the numerical method to first order accuracy. However in flow regions with smooth pressure variations and appropriate metrics the finite-volume scheme maintains a leading second order discretisation error. Details about the adjustment of the dissipation operators can be found in [14].

It should be pointed out, that the success of the finite-volume PNS-method is crucially dependent upon the proper treatment of the flux differences in x' -direction. This is especially true for the flux-vector \underline{P} introduced in (10) according to Vigneron [1]. It turns out (15) that the metric variation of the cell faces δS_{i+1} , along the integration direction should not be neglected in considering the vector \underline{P} . Only the portion R_{i+1}^{i+1} of \underline{P}_{i+1} can be assumed to be zero for an implicit, non-iterative finite-volume PNS-method.

The solution of (16) is accomplished using the delta-formulation of the approximate factorization algorithm after Beam and Warming [15]. According to [15] the implicit operator in (16) is approximated by a product of one-dimensional operators.

$$\begin{aligned} [L_2, (\hat{B}_i^{i+1}) L_1] \delta \underline{q} &= \text{RHS}(16) \\ L_2 &= \hat{B}_i^{i+1} + \beta \Delta_2 (\hat{B}_i^{i+1/2} + \hat{B}_i^{i+1/2}) \\ L_1 &= \hat{B}_i^{i+1} + \beta \Delta_1 (\hat{C}_i^{i+1/2} + \hat{C}_i^{i+1/2}) \end{aligned} \quad (17)$$

All necessary boundary conditions are formulated implicitly. To improve the stability of the scheme also the second order dissipation operator is included implicitly. The results presented below are calculated with the choice of $\beta=1$, thus degrading the scheme to first order accuracy into the integration direction.

3.2 Euler-Method

For an inviscid steady supersonic flow the corresponding conservation laws (3-5) are purely hyperbolic in the main flow direction. Because in an inviscid flow steep gradients like those present in viscous shear layers have not to be resolved, explicit integration methods can also be applied cost-effectively. Additionally it is possible to solve directly for the flux vector \underline{E} , which avoids those linearization errors present in any non-iterative one-sweep PNS-method. So the scheme is conservative with respect to the flux vector \underline{E} . A second order 3-stage scheme is applied which can be considered as a fix-point iteration procedure. In symbolic form the Euler-equations can be written analogously to (11) as

$$\begin{aligned} \Delta_i \underline{E} + \underline{S}(q) &= 0 \\ \underline{S}(q) &= \Delta_2 (\underline{F} - \underline{D}_2) + \Delta_1 (\underline{G} - \underline{D}_1) \end{aligned} \quad (18)$$

If the upper index indicates the integration stage the scheme takes the form

$$\begin{aligned} \underline{E}^{(0)} &= \underline{E}_i \\ \underline{E}^{(1)} &= \underline{E}^{(0)} - \underline{S}(q)^{(0)} \\ \underline{E}^{(2)} &= \underline{E}^{(0)} - 1/2 (\underline{S}(q)^{(0)} + \underline{S}(q)^{(1)}) \\ \underline{E}^{(3)} &= \underline{E}^{(0)} - 1/2 (\underline{S}(q)^{(0)} + \underline{S}(q)^{(2)}) \\ \underline{E}_{i+1} &= \underline{E}^{(3)} \end{aligned} \quad (19)$$

Because the flux vector \underline{E} is integrated directly as a dependent variable, at each stage of the scheme the flux vector \underline{E} has to be decoded to get the primitive variables which are needed to form the fluxes representing the operator $\underline{S}(q)$. An explicit scheme like (19) has to observe a stability condition which limits the maximum integration step size. The corresponding CFL-condition reads

$$\lambda_{\max} (\hat{A} : \hat{B}; \hat{A}^{-1} \hat{C}) \leq 2$$

where λ_{\max} denotes the spectral radius of the indicated matrix products.

4. Method for Steady Compressible Flow

Most of the methods for numerical solution of the steady-state compressible conservation laws are based on time-marching integration procedures. In most implicit schemes the time coordinate is used as a means to provide some sort of diagonal dominance in the coefficient matrices which result after discretisation of the implicit operator chosen. In advanced explicit methods time and space discretisation have been separated to allow the application of efficient integration schemes developed for ordinary differential equations [13].

Without using the time coordinate in implicit schemes diagonal dominance can also be assured by suitable implicit operators, which in general however possess a worse discretisation error compared to those for which the method is designed. This feature leads almost automatically to a approximate Newton-iteration method, where the stable implicit operator only approximates the true Jacobians to some order.

An approach belonging to the latter class of deferred-correction relaxation schemes is that of Jameson and Yoon [8, 16], where the implicit operator is inverted by a particular variation of the symmetric over-relaxation algorithm, called LU-SSOR method. Some key features of the scheme are developed below.

Defining the discrete residual of (3-5), resulting from a cell-centered finite volume scheme, analogously to the representation in (11) as

$$\underline{R} = \underline{A}_i (\underline{E} - \underline{E}_v) + (\underline{F} - \underline{F}_v) + (\underline{G} - \underline{G}_v) \quad (20)$$

Then a Newton iteration would read

$$\left(\frac{\partial \underline{R}}{\partial \underline{q}} \right)^n \delta \underline{q}^n + \underline{R}^n = 0 \quad (21)$$

where the upper index indicates the iteration count and $\delta \underline{q}$ is defined as $\delta \underline{q}^n = \underline{q}^{n+1} - \underline{q}^n$. In general the formation and inversion of the functional matrix $\partial \underline{R} / \partial \underline{q}$ is too costly, so that an approximate form has to be found such that the inversion is easy and stable. A choice which has been found beneficial [17] resembles that of flux-vector splitting. Because the particular construction only influences the implicit operator a rather crude choice fulfills the requirements for diagonal dominance of the coefficient matrices. An appropriate approximation to the functional matrix in eq. (21) could be:

$$\left(\frac{\partial \underline{R}}{\partial \underline{q}} \right) = \underline{D}_\xi \underline{A} + \underline{D}_\eta \underline{B} + \underline{D}_\zeta \underline{C} - \underline{L} \underline{D}^{-1} \underline{U} \quad (22)$$

where the difference operators \underline{D}_ξ etc. are defined as:

$$\underline{D}_\xi \underline{A} = \underline{A}_\xi^+ \underline{A}^- + \underline{V}_\xi \underline{A}^+$$

and \underline{A}_ξ and \underline{V}_ξ are the usual forward and backward difference operators, respectively. The experience shows that in principle only the inviscid flux jacobians have to be introduced into the implicit operator, also for viscous calculations. The optimal choice is currently under investigation.

Now the flux jacobians \underline{A}^+ and \underline{A}^- etc. are defined in such a way that they possess only non-negative and non-positive eigenvalues

$$\begin{aligned} \underline{A}^\pm &= \frac{1}{2} (\underline{A} \pm r_A \underline{I}) \\ r_A &\geq \max (|\lambda_A|) \end{aligned} \quad (23)$$

That is achieved by defining r_A as a value which has to be equal or larger than the spectral radius of \underline{A} .

By sweeping forward and backward through the field it turns out that the functional matrix defined in (22) can further be approximated by the factorization $\underline{L} \underline{D}^{-1} \underline{U}$ of strictly lower, diagonal and upper matrices. So the basic scheme can be written as

$$(\underline{L} \underline{D}^{-1} \underline{U}) \delta \underline{q}^n = -\underline{R}^n$$

with

$$\begin{aligned} \underline{L} &= \underline{V}_\xi \underline{A}^+ + \underline{V}_\eta \underline{B}^+ + \underline{V}_\zeta \underline{C}^+ - \underline{A}^- - \underline{B}^- - \underline{C}^- \\ \underline{D} &= (\underline{r}_A + \underline{r}_B + \underline{r}_C) \underline{I} \\ \underline{U} &= \underline{A}_\xi \underline{A}^- + \underline{A}_\eta \underline{B}^- + \underline{A}_\zeta \underline{C}^- + \underline{A}^+ + \underline{B}^+ + \underline{C}^+ \end{aligned} \quad (25)$$

To solve (24) the following cost-effective variation is possible, which avoids the explicit computation of the Jacobian matrices. The particular steps are

$$\begin{aligned} \delta \underline{\tilde{q}}_{i,j,k} &= -\underline{R}_{i,j,k}^n + \delta \underline{\tilde{E}}_{i-1,j,k}^+ + \delta \underline{\tilde{E}}_{i,j-1,k}^+ + \delta \underline{\tilde{q}}_{i,j,k-1}^+ \\ \delta \underline{\tilde{q}}_{i,j,k} &= \underline{D}_{i,j,k}^{-1} \delta \underline{\tilde{q}}_{i,j,k} \\ \delta \underline{q}_{i,j,k}^n &= \underline{D}_{i,j,k}^{-1} (\delta \underline{\tilde{q}}_{i,j,k} - \delta \underline{\tilde{E}}_{i+1,j,k} - \delta \underline{\tilde{E}}_{i,j+1,k} - \delta \underline{\tilde{q}}_{i,j,k+1}) \end{aligned} \quad (26)$$

where

$$\delta \tilde{E}^{\pm} = \tilde{E}^{\pm}(\tilde{q}) - \tilde{E}^{\pm}(q^n)$$

$$\delta E^{\pm} = E^{\pm}(\tilde{q}) - E^{\pm}(q^n)$$

The experience with such a scheme and variations thereof will be reported elsewhere. However it should be noted that full vectorization along planes $i + j + k = \text{const.}$ is possible.

5. Results

5.1 Space-Marching Computations

Inviscid Flow:

As a test case for a typical pointed body the NASA-forebody 4 [18] was chosen, which has the advantage of an analytically defined shape. The flow at $Ma_{\infty} = 1.7$ and an angle of attack $\alpha = -5^\circ$ presents some difficulties for inviscid supersonic space-marching schemes, because a negative angle of attack produces in a region (0.5x50,4) near the nose subsonic values for the velocity components in integration direction. A purely supersonic space-marching scheme fails completely in such situations. For that reason the method described above was modified to allow for so-called marching subsonic regions by including the 'Vigneron-approximation' (10-11), which assures a hyperbolic system of equations. In Fig. 2 the geometry of the forebody, the wall pressures at the upper and lower side in the symmetry plane and the Mach-number distribution in that plane are depicted. In comparison to the experimental data the numerical results show an excellent agreement apart from some small deviations present at the nose region ($0 \leq x \leq 0.2$). As indicated in the Mach-number distribution the finite-volume space-marching scheme presented captures all discontinuities. So problems are avoided in such situations where the outer bow shock is interfered by shock systems produced at a geometrical discontinuity.

As an example for a realistic configuration where such a problem can occur in principle a fighter aircraft forebody is considered (Fig. 3). At $Ma_{\infty} = 1.8$ and $\alpha = 0^\circ$ the Mach-number distribution in the symmetry plane shows beside the outer bow shock a second shock originated by the canopy-fuselage intersection and a strong expansion process in the upper portion of the canopy. A more complete insight is provided by corresponding Mach-number distributions of selected cross-sections. The flow features at stations $x = \text{const.}$ just in front and behind the canopy-fuselage intersection show a distinct horseshoe structure of the canopy shock, which extends below the intersection line. At this point it should be emphasized that all space-marching computations were started from a plane at very nose tip with freestream values as initial data.

Viscous Laminar Flow:

The implicit finite-volume space-marching scheme was tested first at quasi two-dimensional geometries and for laminar flow conditions. For that reason the supersonic flow past a flat plate was considered to get some insight into the performance of the code. The specific parameters chosen are:

$$Ma_{\infty} = 3; Re = 10^6/m, Pr = 0.71; T_{stat_{\infty}} = 293 K; \text{adiabatic wall}$$

For comparison computations were also done using a time-dependent finite-volume Navier-Stokes (TNS) method developed by Haase et al [19]. To simulate two-dimensional conditions in the three-dimensional PNS-code symmetric side conditions were applied. Additionally, in order to guarantee same conditions concerning spatial resolution an identical mesh structure normal to the plate was adopted.

Fig. 4 shows at two different stations $x = \text{const.}$ the resulting velocity and density profiles for both methods. Remarkable deviations can not be identified for the station near the leading edge ($x = 0.05 m$) nor for the station ($x = 0.41 m$) further downstreams. This should be noticed because the PNS-method presented do not need an initial solution provided by a TNS-method.

Considering for that case the pressure and skin friction coefficients c_p and c_f as functions of plate length (Fig. 5) only small differences between the TNS and PNS-method are visible for $x < 0.001 m$. The open symbols representing the result of the TNS-code indicate indirectly the streamwise grid point density of the TNS-mesh at the leading edge. The slight oscillations of the PNS-method at the leading edge are effects of the initial conditions, the insufficient mesh resolution in normal direction at the leading edge as well as strong pressure gradients in normal direction, which appear as a result of the strong viscous-inviscid interaction in that region leading to the formation of an oblique shock wave emerging from the leading edge. An improvement of that behaviour can be achieved by adjusting the free scaling parameters of the dissipation operators.

As a second two-dimensional test case the laminar hypersonic flow past a compression corner is considered. This problem is an interesting case for PNS-methods because for the specific flow parameters

$$Ma_{\infty} = 14.1; Re_L = 1.04 \cdot 10^5, Pr = 0.72, T_{stat_{\infty}} = 72.2 K, T_{wall} = 297 K; \text{corner angle } 15^\circ$$

A recirculation bubble in the corner region was not observed in corresponding experiments performed by Holden and Moselle [20]. Also available for that flow problem are theoretical solutions obtained by a TNS-[21] and a PNS-method [22].

Fig. 6 illustrates the flow topology and the principal flow phenomena together with the pressure distribution predicted by the finite-volume PNS-method. Clearly to recognize are the leading edge shock wave and the formation of the bended corner shock wave as a result of the interaction with the incoming disturbed flow field.

In Fig. 7 the wall pressure coefficient (defined as $c_p = P_w / (\rho U_\infty^2)$) as well as the heat transfer coefficient (defined as $C_H = (-\lambda \frac{\partial T}{\partial n})_w / (\rho C_p U_\infty \Delta T)$, $\Delta T = T_{tot_\infty} - T_w$) are presented as functions of body length. Also depicted are the experimental and theoretical data from [20,21,22]. It is obvious that almost the same pressure variations are obtained for the flat plate region from all theoretical methods available. This differs considerably along the wedge region, where deviations are more pronounced. However the result from the PNS-code of Lawrence et al [22] seems to be the best fit to experimental data. Another impression is obtained by considering the corresponding heat transfer predictions. Obviously the present PNS-method and the TNS-method of Mung and McCormack [21] yield identical results along the flat plate. The PNS-method [22] shows better agreement with experimental data there, but some inconsistencies are noticed for $x/L > 1.5$, which also was pointed out in [22]. In comparison the TNS-method [21] and the present scheme show an similar asymptotic behaviour for $x/L > 1.6$.

However compared to the TNS-result both PNS-codes overpredict considerably heat transfer in the region just behind the corner, which is due to the total suppression of upstream influence being common to all non-iterative one-sweep PNS-methods. The reason for the systematic deviation of all theoretical results from experimental data along the flat plate is up to now not settled.

An important test case for any three-dimensional PNS-code represents the flow around a pointed cone at high angle of attack. Suitable experimental data were provided by Tracy [23], who has investigated cones with 10° half angle for angles of attack $0^\circ \leq \alpha \leq 24^\circ$ and $Ma_\infty \approx 8$. The observed experimental flow topology after Tracy [23] is shown for $\alpha = 12^\circ$ and 24° in Fig. 8. The data are presented in a plane $r = \text{const.}$ of a spherical coordinate system centered at the cone tip. Such conical coordinate systems are beneficial for inviscid cone flow simulations, because these flows show an exact conical behaviour. In contrast the present PNS-computations are performed along cross-planes $x = \text{const.}$ perpendicular to the cone axis, so that corresponding figures show some distortion. Between both geometrical representations exist the simple relation $r_x/r_{xc} = \tan((r_\theta/r_{\theta c}) \cdot \theta_c / \tan \theta_c)$, where r_θ determines the distance of a point in the $r = \text{const.}$ plane to the cone tip and $r_{\theta c}$ the normal distance to the cone axis. With θ_c as the cone half angle the corresponding conditions in the $x = \text{const.}$ plane are obtained.

Fig. 9 shows the coordinate systems in the planes $x = \text{const.}$ for both angles of attack. The half-plane meshes consisted in circumferential direction of 91 equally spaced points and 81 points in normal direction. To achieve a high solution quality concerning shock wave and boundary layer resolution a procedure for generating a solution-adaptive grid [24] was applied. Therefore the global features of the flow process are directly visible in the structure of the grid system. In comparison to the experimental data concerning shock layer thickness the agreement for both cases is excellent.

A look on the static pressure distribution (Fig. 10) illustrates that the use of solution adaptive grid systems produces a solution quality which is essentially equivalent to 'shock-fitting' methods. In Fig. 11 the corresponding Mach-number distributions are presented. For $\alpha = 24^\circ$ as a result of a vortex separation process a large viscous region develops at the leeside which is well captured by the PNS-method presented. Comparing the circumferential wall pressure distributions at the same stations (Fig. 12) an excellent agreement between experimental and theoretical data can be stated. Proceeding to the pitot pressure surveys the same good agreement is recognized (Fig. 13 a,b). It should be noted that the deviations between prediction and experiment for $\alpha = 24^\circ$ and $z = 0.6$ (inch) are the result of a plotting error and in reality the agreement for this particular distance z (z being the normal distance to the cone surface) is comparable to the other curves. The comparison between the results of the present PNS-method and the experimental data of Tracy are completed by Fig. 14, where the heat flux ratio Q/Q_0 (Q_0 = heat flux at corresponding station and $\alpha = 0$) is depicted as a function of the circumferential angle ϕ . More details concerning PNS-results of this test case can be found in [14].

As an example of a more realistic missile configuration an ogive-cylinder geometry was also considered. The flow parameters specified are:

$$Ma_\infty = 4; Re = 3.4 \cdot 10^7/m; Pr = 0.71; T_{stat_\infty} = 223 \text{ K}; T_{wall} = 370 \text{ K}; \alpha = 4^\circ; \text{ laminar flow}$$

Because an appropriate turbulence model was not included at that time the flow was assumed to be laminar, which in reality certainly will not be the case. However concerning vortex separation processes the performance of the code for high-Reynolds-number flow could be tested. The resulting mesh structure in the symmetry plane is depicted in Fig. 15. There the varying strength of the shock wave which is weakened in streamwise direction can directly be observed. An impression of the pressure field in the symmetry plane around the nose is provided by Fig. 16. It shows the high solution quality achievable with adaptive mesh systems, even for the very tip region.

The effects of the leeside vortex separation process on the pressure distribution is illustrated in Fig. 17. Separation starts behind the ogive-cylinder junction $x > 0.3 \text{ m}$ and is well developed for $x > 1.0 \text{ m}$. The pressure peaks arising behind the established pressure plateaus indicate the development of secondary separation. Overall the pressure distributions predicted show some significant features known from turbulent flows around such configurations which is promising for future turbulent simulations. More details concerning this case can be found in [14].

5.2 Steady Compressible Flow Method

The modified LU-SSOR method described in chapter 4 has been validated by considering the three-dimensional flow around a hemisphere-cylinder configuration. In the past this flow problem was investigated experimentally by Hsieh [25], Peake and Tobak [26] and more recently by Lim and Meade as cited in [27]. Theoretical studies have been conducted e.g. by Pulliam and Steger [28], Kordulla and McCormack [29] and also by Ying et al [27], where a more complete list of related works can be found.

The specific flow parameter chosen are:

$$Ma_\infty = 1.2; Re_D = 445000; Pr = 0.71; T_{stat_\infty} = 300 \text{ K}; \alpha = 19^\circ; \text{ adiabatic wall; laminar flow}$$

The spherical type coordinate system used consisted of 49 points in the streamwise direction, 25 points in circumferential direction for the half plane and 49 points normal to the body. In Fig. 18 and Fig. 19 the static pressure and Mach-number distribution in the symmetry plane is shown together with an enlarged map around the nose. There need for a better resolution of the bow and leeside shock wave becomes evident. From the highly structured Mach-number field at the leeside behind the sphere-cylinder junction it can be deduced that a complex interacting flow field establishes which clearly requires a mesh refinement. However the velocity vector fields (not shown here) of successive stations in that region indicate the occurrence of owl eyes immediately behind the junction. Also the primary and secondary separation lines are well captured considering the relative coarse mesh system used. In Fig. 20 the axial pressure distributions along the leeside and the 90°-line are depicted. The present results are close to those of Ying et al [27] for the leeside, however show some remarkable differences along the 90°-line. The reason for these deviations are not clear, because the results of [27] are based on a slightly more refined mesh. However to get more insight into this particular flow problem computations with more optimal grid systems are planned.

In a first effort the code was also applied to hypersonic flow problems around a reentry lifting body. The geometry considered was a late configuration of the HERMES space-shuttle shown in Fig. 21. However up till now only the portion of the vehicle in front of the upward bended outer wing panels which is approximately 70 % of the vehicles length, was considered in the simulations. The particular case presented is an inviscid flow at $Ma_\infty = 8$ and $\alpha = 20^\circ$ assuming ideal gas behaviour. The mesh system used consisted of approximately 300 000 points.

The resulting Mach-number distribution in the symmetry plane is shown in Fig. 22. As can be seen the bow and canopy shock waves are well captured and appear sufficiently sharp represented. Looking at the corresponding distributions in cross-sections near the outer wing panels the development of cross-flow shocks above the wing and the upper fuselage can be observed (Fig. 23). It is obvious that some needs exist for the simulation of the complete vehicle in a broad parameter range to draw the right conclusions concerning these flow phenomena in the context of good aerodynamic design.

6. Conclusions

The development of two space-marching methods for prediction of inviscid and viscous steady supersonic flow fields was described. Both methods rely on a finite-volume discretisation of the corresponding conservation laws and have shown to be stable and robust. It was illustrated that both schemes give accurate results which are in excellent agreement with available experimental data.

Also presented was a new method for solution of the compressible, not-reduced conservation laws for steady inviscid and viscous flows, which appears as a promising method for simulation of super- and hypersonic flows. Further developments will be reported elsewhere.

7. References

- [1] Vigneron, Y.C.; Rakich, J.V. und Tannehill, J.C.
Calculation of Supersonic Viscous Flow over Delta Wings with Sharp Subsonic Leading Edges
AIAA-Paper: 78-1137, 1978
- [2] Schiff, L.B. and Steger, J.L.
Numerical Simulation of Steady Supersonic Viscous Flow
AIAA-Paper: 79-0130, 1979
- [3] Chaussee, D.S.; Patterson, J.L.; Kutler, P., Pulliam, T.H. und Steger, J.L.
A Numerical Simulation of Hypersonic Flows over Arbitrary Geometries at High Angle of Attack
AIAA-Paper: 81-0050, 1981
- [4] Chaussee, D.S.; Rizk, Y.M. und Buning, P.G.
Viscous Computation of a Space Shuttle Flow Field
NASA-TM-85977, 1984
- [5] Prabhu, D.K. und Tannehill, J.C.
Numerical Solution of Space Shuttle Orbiter Flow Field Including Real Gas Effects
AIAA-Paper: 84-1747, 1984
- [6] Balakrishnan, A.
Computation of Viscous Real Gas Flow Field for the Space Shuttle Orbiter
AIAA-Paper: 84-1748, 1984
- [7] Chaussee, D.S.; Blom, G. und Wai, J.C.
Numerical Simulation of Viscous Supersonic Flow over a Generic Fighter Configuration
NASA-TM-86823, 1985
- [8] Jameson, A. and Yoon, S.
LU-Implicit Schemes with Multiple Grids for the Euler Equations
AIAA-Paper: 86-0105
- [9] Flügge, W.
Tensor Analysis and Continuum Mechanics
Springer-Verlag, Berlin, 1972
- [10] Lin, T.C. und Rubin, S.G.
Viscous Flow over a Cone at Moderate Incidence
Computer & Fluids, Vol. 1, 1973, S. 37 - 57

- [11] Kaul, U. und Chaussee, D.S.
A Comparative Study of the Parabolized Navier-Stokes Code Using Various Grid Generation Techniques
AIAA-Paper: 84-0459, 1984
- [12] Steger, J.L.
Implicit Finite Difference Simulation of Flow About Arbitrary Geometries with Application to Airfoils
AIAA-Paper: 77-665, 1977
- [13] Jameson, A.; Schmidt, W. und Turkel, E.
Numerical Solutions of the Euler Equations by Finite Volume Methods Using Runge-Kutta Time-Stepping Schemes
AIAA-Paper: 81-1259, 1981
- [14] Rieger, H.
Thermische Aufheizung von Flugkörpern bei hohen Geschwindigkeiten
DORNIER-Bericht: BF 7/868, 1986
- [15] Beam, R. and Warming, R.F.
An Implicit Factored Scheme for the Compressible Navier-Stokes Equations
AIAA-Journal, Vol. 16, 1978, pp. 393-402
- [16] Yoon, S. and Jameson, A.
An LU-SSOR Scheme for the Euler and Navier-Stokes Equations
AIAA-Paper: 87-0600, 1987
- [17] Jameson, A. and Turkel, E.
Implicit Schemes and LU Decompositions
Math. Comp., Vol. 37, 1981, pp. 385-397
- [18] Townsend, J.C.; Howell, D.T.; Collins, F.K. and Hayes, C.
Surface Pressure Data on a Series of Analytic Forebodies at Mach Numbers from 1.7 to 4.5 and Combined Angles of Attack and Sideslip
NASA-TM-80062, Juni 1979
- [19] Haase, W., Wagner, W. und Jameson, A.
Development of a Navier-Stokes Method Based on Finite Volume Solution Techniques for the Time-Dependent Euler Equation
Proc. of GAMM-Conf. on Numerical Methods in Fluid Mechanics, in Notes on Numerical Fluid Mechanics, Vol. 7, Vieweg-Verlag, 1984
- [20] Holden, M.S. und Moselle, J.R.
Theoretical and Experimental Studies of the Shock Wave-Boundary Layer Interaction on Compression Surfaces in Hypersonic Flow
CALSPAN, Buffalo, N.Y., Rep. AF-2410-A-1, 1969
- [21] Hung, C.M. und McCormack, R.W.
Numerical Solutions of Supersonic and Hypersonic Laminar Compression Corner Flows
AIAA-Journal, Vol. 14, 1976, S. 475-481
- [22] Lawrence, S.L.; Tannehill, J.C. und Chaussee, D.S.
Application of the Implicit McCormack Scheme to the Parabolized Navier-Stokes Equations
AIAA-Journal, Vol. 22, 1984, S. 1755-1763
- [23] Tracy, R.R.
Hypersonic Flow over a Yawed Circular Cone,
Ph.D.-Thesis, California Institute of Technology, Graduate Aeronautical Lab. Memo 69, Aug. 1963
- [24] Haase, W., Misegades, K. und Naar, M.
Adaptive Grids in Numerical Fluid Dynamics
Int. Journal for Numerical Methods in Fluids, Vol. 5, 1985, S. 515-528
- [25] Hsieh, T.
An Investigation of Separated Flows about a Hemisphere-Cylinder at Incidence in the Mach Number range from 0.6 to 1.5
AIAA-Paper: 77-179, 1977
- [26] Peake, D.J. and Tobak, M.
Three-Dimensional Flows About Simple Components at Angle of Attack.
AGARD LS-121, Paper 2, 1982
- [27] Ying, S.X.; Steger, J.L.; Schiff, L.B. and Baganoff, D.
Numerical Simulation of Unsteady, Viscous, High-Angle-of-Attack Flows using a Partially Flux-Split Algorithm
AIAA-Paper: 86-2179, 1986
- [28] Pulliam, T.H. and Steger, J.L.
Implicit Finite-Difference Simulations of Three-Dimensional Compressible Flow
AIAA-Journal, Vol. 18, 1980, pp. 159-167
- [29] Kordulla, W. und McCormack, R.W.
A New Predictor-Corrector Scheme for the Simulation of Three-Dimensional Compressible Flows with Separation
AIAA-Paper: 85-1502-CP, 1985

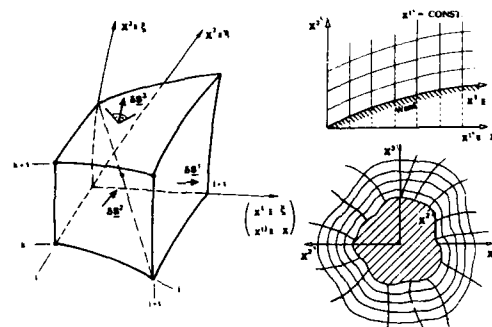


Fig. 1 : Finite-volume element and coordinate systems in physical and computational space

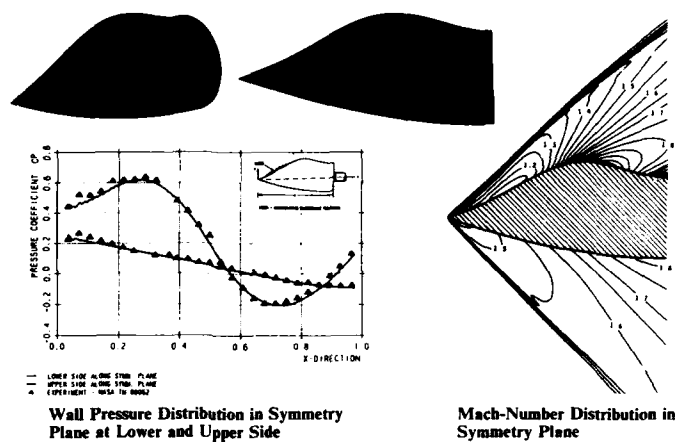


Fig. 2 : Euler space-marching results for NASA-forebody 4 ($Ma = 1.7$, $\alpha = -5^\circ$)

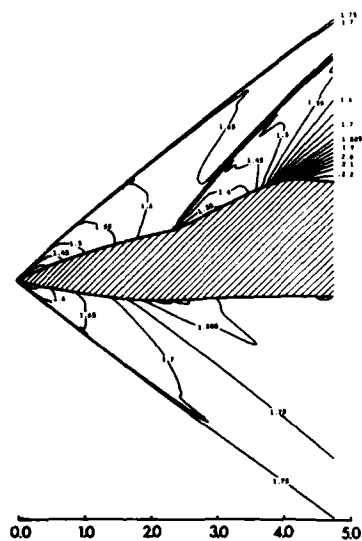


Fig. 3 : Euler space-marching results for fighter forebody
 ($Ma = 1.8$, $\alpha = 0^\circ$)
 above : geometry
 left : Mach-number distribution in symmetry plane

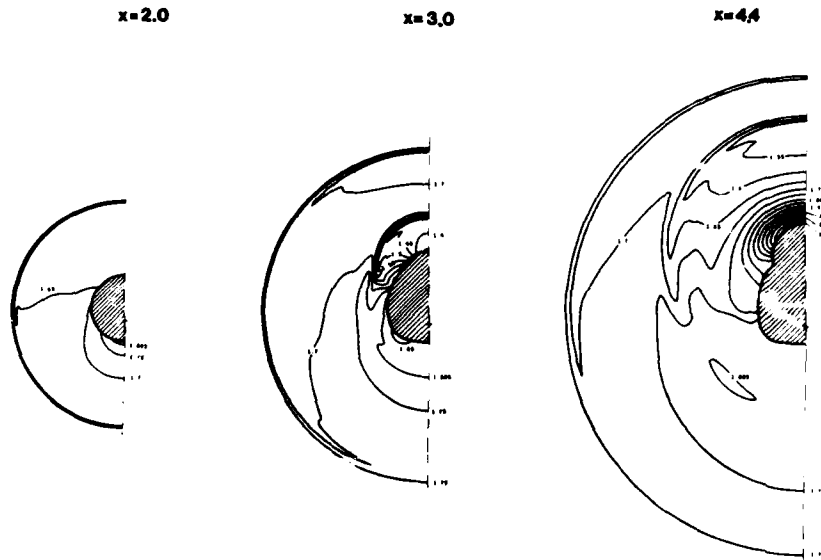


Fig. 3: (cont.) Euler space-marching results for fighter forebody ($Ma = 1.8$, $\alpha = 0^\circ$)
Mach-number distribution in different cross-sections $x = \text{const}$

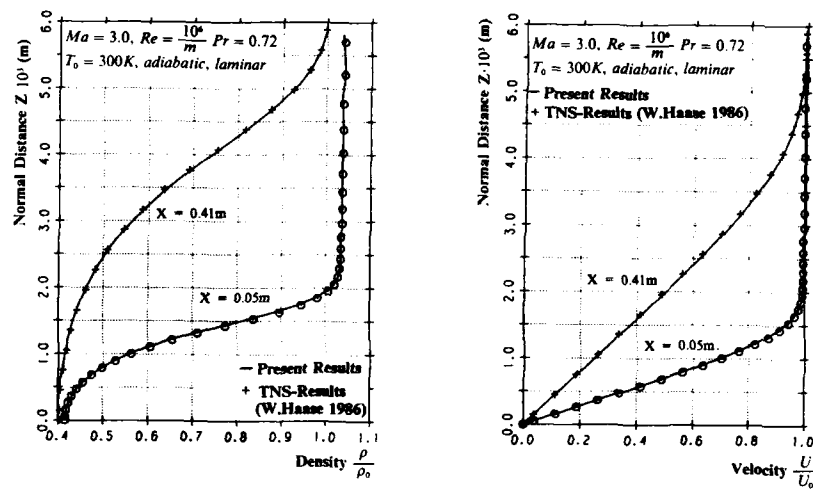


Fig. 4: PNS space-marching results for supersonic flow past a flat plate - density and velocity profiles

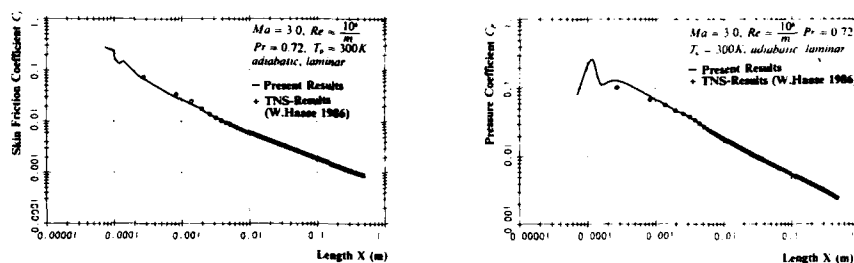


Fig. 5 : PNS space-marching results for supersonic flow past a flat plate
Streamwise skin friction and wall pressure coefficients

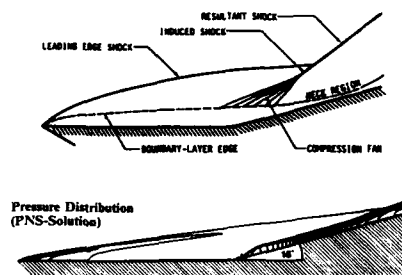


Fig. 6 : Flow topology and PNS-pressure distribution for flow along a 15° hypersonic compression ramp

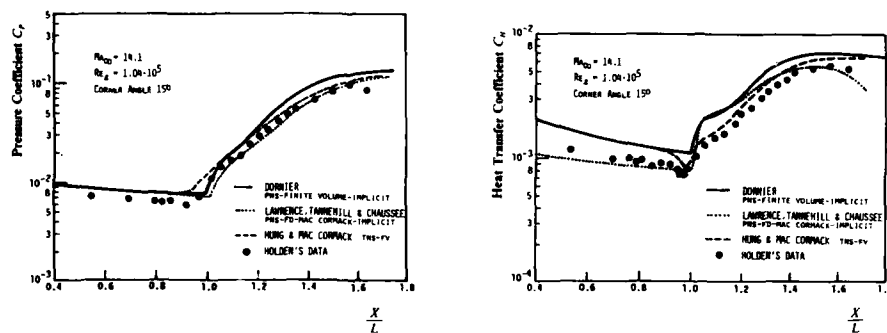


Fig. 7 : Wall pressure coefficient (left) and heat transfer coefficient (right) along compression ramp

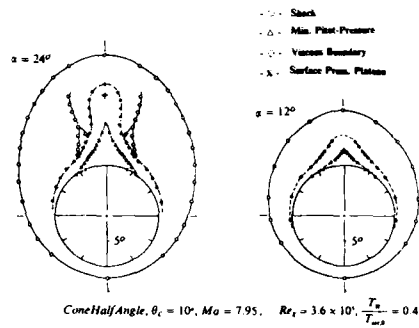


Fig. 8: Flow topology for cones at high angles of attack after Tracy [23]

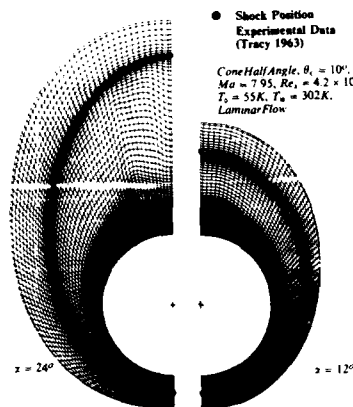


Fig. 9: Solution-adaptive coordinate system for PNS space-marching scheme

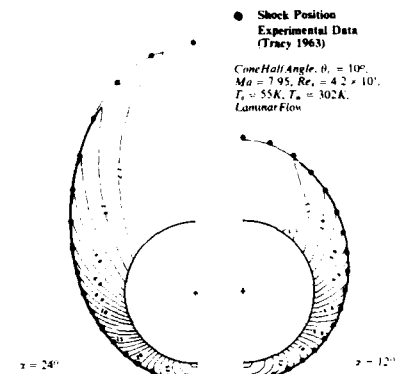


Fig. 10: Static pressure distribution

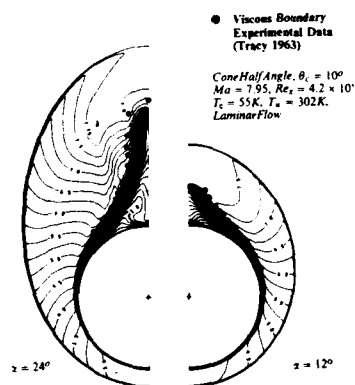


Fig. 11: Mach-number distribution

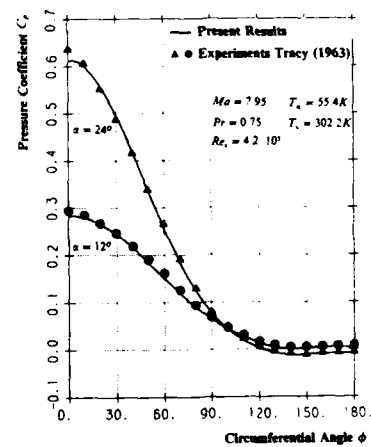


Fig. 12: Circumferential wall pressure distribution

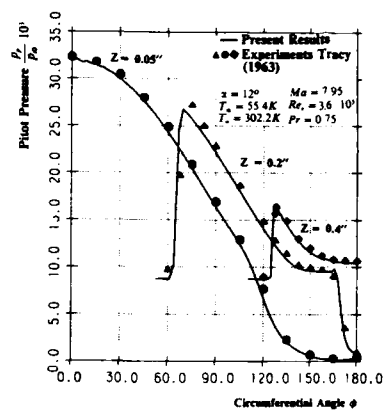
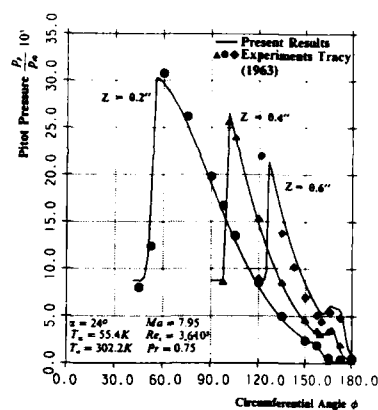
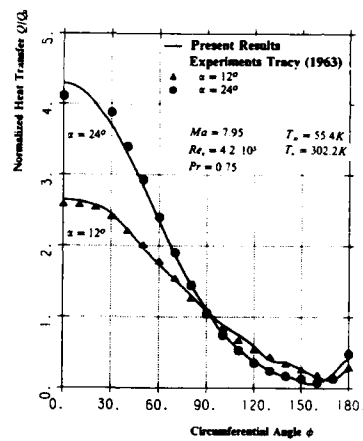
Fig. 13a : Pitot pressure profiles for cone at $\alpha = 12^\circ$ Fig. 13b : Pitot pressure profiles for cone at $\alpha = 24^\circ$ (Q_0 - Heat Flux at 0 Degree Angle of Attack)

Fig. 14 : Circumferential heat flux distribution

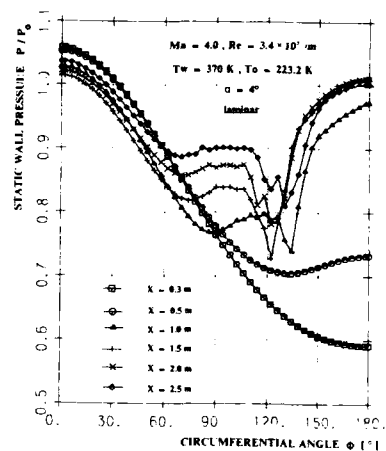
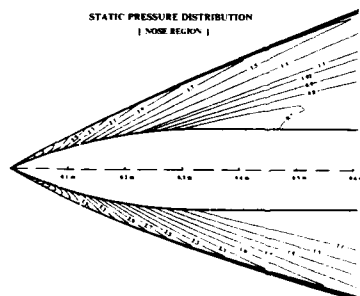


Fig. 17 : Circumferential wall pressure distributions for different axial stations

Fig. 16 : Static pressure distribution around a ogive-cylinder configuration
($Ma = 4$, $Re = 3.7 * 10^5/m$, $\alpha = 4^\circ$)

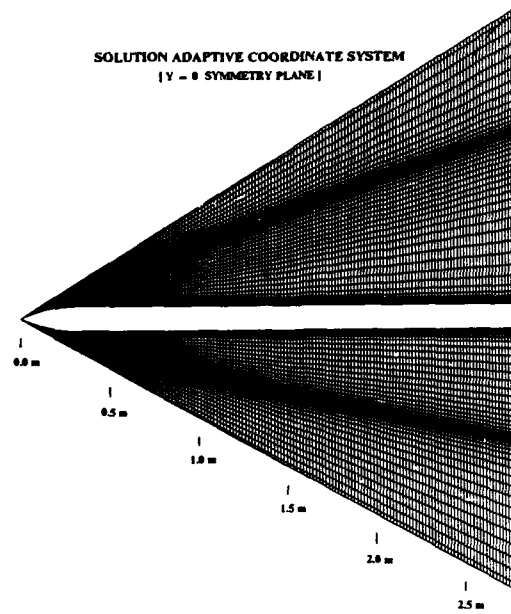


Fig. 15 : Solution-adaptive coordinate system for ogive-cylinder configuration
($Ma = 4$, $Re = 3.7 \cdot 10^6/m$, $\alpha = 4^\circ$)

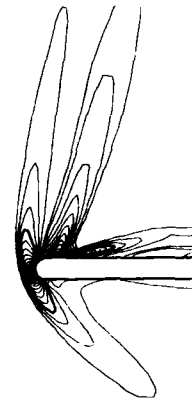
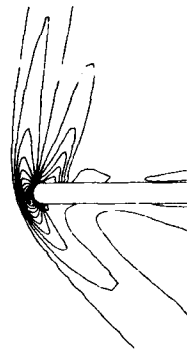


Fig. 18 : Pressure distribution in symmetry plane of hemisphere-cylinder configuration
($Ma = 1.2$, $Re = 4.45 \cdot 10^6/D$, $\alpha = 19^\circ$)

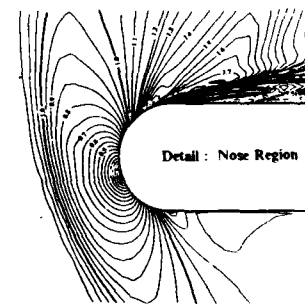


Fig. 19 : Mach-number distribution in symmetry plane of hemisphere-cylinder configuration
($Ma = 1.2$, $Re = 4.45 \cdot 10^6/D$, $\alpha = 19^\circ$)

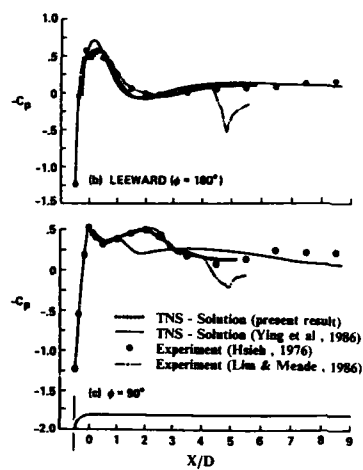


Fig. 20 : Axial wall pressure distribution for hemisphere-cylinder configuration
($Ma = 1.2$, $Re = 4.45 \cdot 10^4$, D , $\alpha = 19^\circ$)

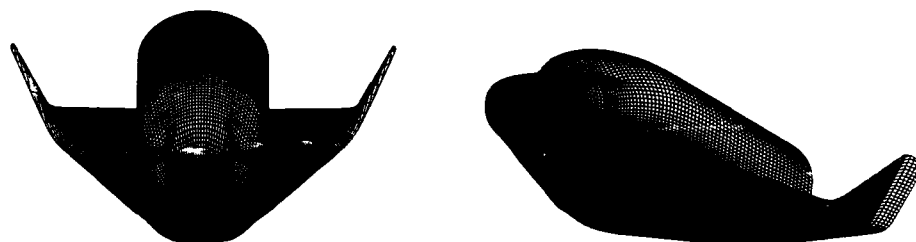


Fig. 21 : Geometry of HERMES space shuttle

Mach Number Distribution
(Symmetry Plane)

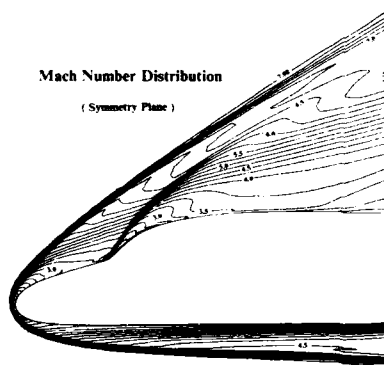


Fig. 22 : Mach-number distribution in symmetry plane around HERMES space shuttle
($Ma = 8$, $\alpha = 20^\circ$, inviscid flow)

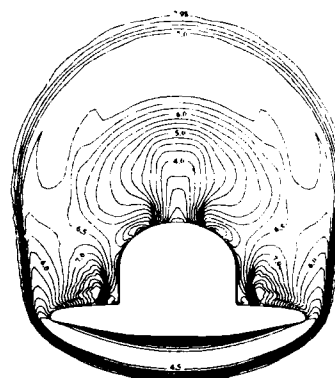


Fig. 23 : Mach-number distribution in cross section at $x = 11.2$ m for HERMES space shuttle
($Ma = 8$, $\alpha = 20^\circ$, inviscid flow)

COUCHE LIMITE LAMINAIRE HYPERSONIQUE ETUDE PARAMETRIQUE DE LA REPRESENTATION DES EFFETS DE GAZ REEL

par

B. Aupoix, C. Eldem et J. Cousteix
ONERA/CERT/DERAT
2 Avenue Edouard Belin
F-31400 Toulouse, France

RÉSUMÉ

L'influence du modèle utilisé pour représenter les effets de gaz réel a été étudiée pour des calculs de couche limite sur un hyperboloïde équivalent à la ligne de symétrie intrados de la navette spatiale, pour le vol SFS 2. Le modèle utilisé est celui de Straub qui ne prend en compte que cinq espèces et suppose l'équilibre thermodynamique. L'étude montre l'importance, non seulement de la catalycité de paroi mais aussi, des vitesses de réactions choisies et de la température de paroi sur le flux de chaleur pariétal et sur l'épaisseur de déplacement. Le coefficient de frottement pariétal est très sensible au modèle de gaz réel. De plus, il est possible de réduire le nombre de réactions chimiques considérées et de simplifier les termes de diffusion, afin de gagner du temps de calcul sans que cela ne détériore trop la prédiction.

ABSTRACT

A sensitivity study of the real gas model has been performed in boundary layer computations on an hyperboloid equivalent to the Space Shuttle windward symmetry plane ; for the SFS 2 reentry. The real gas model is due to Straub and accounts for only five chemical species while assuming thermodynamic equilibrium. The study has brought into evidence the dependance of both wall heat flux and displacement thickness, not only upon the wall catalycity but also upon the selected reaction rates and the wall temperature. The skin friction coefficient is insensitive to the real gas model. Moreover, only a few chemical reactions can be selected and the diffusion model can be simplified to save computational time without drastic changes in the prediction.

I - INTRODUCTION

Les vitesses de rentrée de véhicules tels que les navettes spatiales dans l'atmosphère étant hypersoniques, l'enthalpie d'arrêt est élevée. Dans la couche de choc, entre la paroi du véhicule et l'onde de choc, les vitesses restent modérées. L'énergie cinétique amont est transformée en énergie thermique ; des niveaux de température importants existent dans la couche de choc. D'autre part, du fait de l'altitude, la pression reste faible même en aval du choc. L'air à haute température sous une faible pression a alors tendance à se dissocier et même à s'ioniser. Une partie de l'énergie est ainsi "stockée sous forme chimique". L'étude de l'écoulement doit alors prendre en compte ces effets de gaz réels.

Un des problèmes importants lors de la rentrée d'un véhicule hypersonique est l'échauffement de celui-ci et donc l'évaluation des flux de chaleur pariétaux. Tant que l'interaction visqueuse reste faible, le flux de chaleur peut être calculé par une approche de type couche limite. Du fait des faibles valeurs de la pression à haute altitude, le nombre de Reynolds est modéré ; l'écoulement reste laminaire durant la majeure partie de la rentrée.

Afin de pouvoir prédire l'écoulement autour du véhicule et principalement les flux de chaleurs pariétaux, nous avons donc développé des méthodes de calcul de couche limite laminaire hypersonique, prenant en compte les effets du gaz réel. Nous nous sommes alors intéressés tout particulièrement à l'influence du modèle utilisé pour décrire les effets de gaz réel.

II - COUCHE LIMITE LAMINAIRE HYPERSONIQUE

Rappelons brièvement les équations régissant un écoulement de couche limite d'un mélange de gaz.

Soit ρ_i la masse volumique de l'espèce i , la masse volumique du mélange est $\rho = \sum_i \rho_i$. On définit alors la concentration massique de l'espèce i $C_i = \frac{\rho_i}{\rho}$, telle que $\sum_i C_i = 1$. On note n_i le nombre de moles de l'espèce i par unité de volume et $n = \sum_i n_i$ le nombre total de moles. Le bilan de masse de l'espèce i fait apparaître le taux $\dot{\omega}_i$ de production ou de destruction chimique de l'espèce i et le flux de diffusion Q_i de cette espèce au sein du mélange :

$$\rho \frac{\partial C_I}{\partial t} + \rho u_I \frac{\partial C_I}{\partial x_I} = \dot{\omega}_I - \frac{\partial q_{I,1}}{\partial x_1}$$

La théorie cinétique fournit l'expression du flux de diffusion

$$\begin{aligned} \vec{q}_I &= \sum_{J \neq I} \rho C_I \frac{n_J}{n_I} \frac{M_J}{M} D_{IJ} \left\{ \text{grad} \frac{n_J}{n} + \left(\frac{n_J}{n} - \frac{\rho_J}{\rho} \right) \text{grad} (\ln p) \right\} \\ &\quad - D_I^T \text{grad} (\ln T) \end{aligned}$$

où M_J est la masse molaire de l'espèce J, M la masse molaire moyenne du mélange définie par :

$$\frac{1}{M} = \sum_I \frac{C_I}{M_I}$$

D_{IJ} le coefficient de diffusion polynaire de l'espèce I dans l'espèce J et D_I^T le coefficient de diffusion thermique de l'espèce I. Le rôle de la diffusion polynaire est, grossièrement, d'homogénéiser le mélange tandis que la diffusion thermique entraîne les espèces légères vers les régions chaudes et les espèces lourdes vers les régions froides (effet Soret ou effet de paroi froide). Remarquons enfin que la conservation de la matière impose $\sum_I \dot{\omega}_I = 0$ et $\sum_I \vec{q}_I = \vec{0}$

Dans le cas d'une couche limite bidimensionnelle, stationnaire, l'équation de bilan des espèces devient

$$\begin{aligned} \rho U \frac{\partial C_I}{\partial x} + \rho V \frac{\partial C_I}{\partial y} &= \dot{\omega}_I - \frac{\partial q_{I,y}}{\partial y} \\ q_{I,y} &= \sum_{J \neq I} \rho C_I \frac{n_J}{n_I} \frac{M_J}{M} D_{IJ} \frac{\partial}{\partial y} \left(\frac{n_J}{n} \right) - \frac{1}{T} D_I^T \frac{\partial T}{\partial y} \end{aligned}$$

L'équation de continuité garde sa forme classique pour un écoulement bidimensionnel stationnaire.

$$\frac{\partial}{\partial x} (\rho U R^j) + \frac{\partial}{\partial y} (\rho V R^j) = 0$$

avec $j = 0$ en écoulement plan et $j = 1$ en écoulement de révolution. R étant le rayon du corps. On retrouve aussi les formes classiques des équations de quantité de mouvement

$$\begin{aligned} \rho U \frac{\partial U}{\partial x} + \rho V \frac{\partial U}{\partial y} &= - \frac{\partial p}{\partial x} + \frac{\partial}{\partial y} \left(\mu \frac{\partial U}{\partial y} \right) \\ 0 &= \frac{\partial p}{\partial y} \end{aligned}$$

En ce qui concerne l'équation de l'énergie, on supposera l'équilibre thermodynamique. L'équation pour l'enthalpie a alors la forme classique

$$\rho U \frac{\partial h}{\partial x} + \rho V \frac{\partial h}{\partial y} = - \frac{\partial \phi}{\partial y} + U \frac{\partial p}{\partial x} + \mu \left(\frac{\partial U}{\partial y} \right)^2$$

et la théorie cinétique des gaz donne l'expression du flux de chaleur

$$\phi = - \lambda \frac{\partial T}{\partial y} + \sum_I h_I q_{I,y} + RT \sum_J \frac{n_J}{n} \frac{D_J^T}{M_J} \frac{\partial}{\partial y} \left(\frac{n_J}{n} \right)$$

où h_I est l'enthalpie de l'espèce I. Comme l'inversion de la relation enthalpie-température pour un mélange est malcommode, on préférera travailler avec une équation pour la température

$$\begin{aligned} C_p F \left(\rho U \frac{\partial T}{\partial x} + \rho V \frac{\partial T}{\partial y} \right) &= - \frac{\partial \phi}{\partial y} + U \frac{\partial p}{\partial x} + \mu \left(\frac{\partial U}{\partial y} \right)^2 \\ &\quad - \sum_I h_I \dot{\omega}_I + \sum_I h_I \frac{\partial q_{I,y}}{\partial y} \end{aligned}$$

où $C_p F$ est la chaleur massique figée du mélange.

Enfin, on admet que chaque espèce se comporte comme un gaz parfait.

$$p_i = p_1 \frac{R}{M_i} T \quad \text{où } R \text{ est la constante des gaz parfaits. Compte tenu de}$$
 la loi de Dalton et de la définition de la masse molaire du mélange, on a :

$$p = \rho \frac{R}{M} T$$

III - REPRESENTATION DES EFFETS DE GAZ REELS

III.1. Coefficients de transport

Les équations régissant l'écoulement de couche limite font intervenir divers coefficients de transport (viscosité dynamique μ , conductibilité thermique λ mais aussi diffusion polynaire D_{ij} , diffusion thermique DT_i). La théorie cinétique des gaz permet de calculer ces coefficients de transport au prix de calculs relativement coûteux (réf. 1). De nombreuses formules approchées ont donc été proposées par différents auteurs pour calculer ces coefficients de transport (réf 2-5). Une formulation particulièrement simple a été proposée par Straub (ref 6) dans le cas où l'on ne retient que cinq espèces, à savoir N_2 , O_2 , NO, N et O. Rappelons que les coefficients de transport du mélange se calculent à partir des intégrales de collision entre particules. Straub remarque que toutes les molécules considérées ont des masses molaires voisines et qu'il en est de même pour les atomes. Le calcul des intégrales de collision est ainsi ramené au cas d'un mélange atomes/molécules. Des formules simplifiées sont ensuite proposées pour évaluer la viscosité, la conductibilité thermique et les coefficients de diffusion thermique. En ce qui concerne les diffusions polynaires, des simplifications de type molécule/atome permettent de ne calculer que sept coefficients différents au lieu de vingt. Le défaut de cette simplification est de ne plus vérifier la nullité de la somme des flux de diffusion des espèces.

III.2. Fonctions thermodynamiques

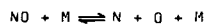
L'équation d'énergie fait intervenir les enthalpies de chaque espèce et le coefficient de chaleur massique figé $C_{pf} = \sum_i C_i C_{pi} = \sum_i C_i \left(\frac{\partial h_i}{\partial T} \right)_p$. Le calcul de ces fonctions thermodynamiques demande la connaissance de la fonction de partition de l'énergie entre les différents modes en fonction de la température pour chaque espèce. Straub et al (ref. 7) proposent d'utiliser la représentation de Schäfer (ref. 8) dans laquelle les différents modes (translation, excitation électronique, rotation, vibration) et les couplages entre ces modes sont pris en compte. Une représentation polynomiale approchée permettant de réduire le temps de calcul, a été proposée par Gordon et Mc Bride (réf. 9).

Rappelons pour finir, qu'en plus des enthalpies de chaque espèce et du coefficient de chaleur massique figé, la connaissance des propriétés thermodynamiques de chaque espèce permet de calculer les constantes d'équilibre des réactions chimiques qui peuvent se produire entre ces espèces.

III.3. Modèle chimique

Si on ne considère que des réactions à deux corps qui sont les plus probables, on peut, avec les cinq espèces considérées, former

- des réactions de dissociation pour les molécules

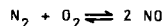


où M représente l'une quelconque des cinq espèces considérées.

- des réactions d'échange

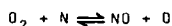


- une réaction de formation directe du monoxyde d'azote

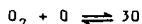
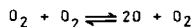


qui est peu probable et donc négligée dans la majorité des modèles.

Parmi ces réactions, il est classique de ne retenir que les trois réactions prépondérantes connues sous le nom de processus de Zeldovich :



Glottz (ref. 10) propose, dans une étude sur l'hyperboloïde AGARD, d'ajouter au processus de Zeldovich les deux réactions suivantes



Les constantes d'équilibre des réactions chimiques, déduites des fonctions thermodynamiques obtenues par spectrométrie, sont connues avec une bonne précision. En revanche, les vitesses de réactions sont difficiles à mesurer, et l'on observe une importante dispersion dans les valeurs proposées dans la littérature. Nous avons utilisé deux jeux de vitesses de réactions ; le premier est celui utilisé par Straub (refs 7, 10) et le second est issu d'un travail de revue récemment édité par Gardiner (ref. 11). La principale différence entre ces deux jeux de constantes porte sur la dissociation de l'oxygène qui est environ mille fois plus rapide dans le modèle utilisé par Straub.

IV - CONDITIONS DE L'ETUDE

IV.1. Cas test

Nous avons étudié l'influence de la représentation des effets de gaz réel dans le cas de la rentrée de la navette spatiale lors du vol STS2. Les points de vol sont documentés dans la référence 12. Ils sont compris entre 92.35 km et 47.67 km d'altitude et correspondent à des nombres de Mach de 27.9 à 9.15. On s'intéresse tout particulièrement à la ligne de symétrie intrados de la navette qui est une des parties de la navette où le flux de chaleur est important. Vu la forme de la navette, cette ligne de symétrie peut être approchée par un arc d'hyperboloïde. Le calcul est donc effectué sur un hyperboloïde de révolution, à incidence nulle, équivalent à la ligne de symétrie intrados. Les caractéristiques sur l'hyperboloïde équivalent pour chaque point de la trajectoire sont données dans la référence 12 et rappelées sur le tableau 1.

IV.2. Conditions initiales

Une condition initiale est nécessaire pour démarrer le calcul de couche limite. Les équations de couche limite sont donc réécrites à l'aide de la transformation de Levy-Lees-Dorodnitsyn. En faisant des hypothèses de similitude sur les profils de concentration de vitesse et d'enthalpie (ou de température), on peut dans le cas du point d'arrêt, transformer les équations de couche limite en un jeu d'équations différentielles ordinaires couplées. La résolution de ces équations par une méthode pseudo-stationnaire, fournit les profils de concentration, vitesse et température au point d'arrêt. Cette solution permet d'initialiser le calcul de couche limite en un point en aval, proche du point d'arrêt, où la vitesse extérieure n'est pas nulle et pour lequel on admet que les profils de similitude obtenus restent valables.

IV.3. Conditions aux limites

A l'extérieur de la couche limite, la seule donnée nécessaire est la pression. Celle-ci est obtenue à l'aide de la formule de Newton modifiée

$$p = p_\infty + (1 - \frac{\epsilon}{2}) \rho_\infty V_\infty^2 \sin^2 \theta_p$$

où p_∞ , ρ_∞ , V_∞ sont les pressions, masse volumique et vitesse à l'infini amont, ϵ le rapport des masses volumiques avant et après choc pris égal à 0.1 et θ_p l'angle entre la vitesse infinie amont et la tangente à la paroi.

La condition pour l'équation d'énergie est de retrouver à l'extérieur de la couche limite l'enthalpie d'arrêt de l'écoulement à l'infini amont. En ce qui concerne les concentrations, on suppose l'équilibre chimique à l'extérieur de la couche limite au point d'arrêt. Les concentrations à l'extérieur de la couche limite en aval du point d'arrêt sont alors obtenues en résolvant à l'extérieur l'équation pour les concentrations dans laquelle on a annulé les termes de diffusion ; on assure ainsi le raccord entre la couche limite et un écoulement extérieur non visqueux.

A la paroi, on a la condition de non-glissement pour les composantes du vecteur vitesse. Pour l'équation de l'énergie, on peut imposer la température à la paroi ou le flux de chaleur pariétal. Toutes les comparaisons présentées ci-dessous seront faites à température de paroi imposée. La condition à la paroi pour les concentrations dépend de la nature chimique du matériau. La surface peut avoir une forte interaction avec le gaz et catalyser les réactions chimiques entre les espèces, par exemple dans le cas d'une paroi métallique. Le cas extrême est la paroi totalement catalytique au contact de laquelle le gaz retourne à l'équilibre chimique. La paroi peut aussi avoir une faible interaction avec le gaz, par exemple dans le cas d'une paroi en silice. Le cas extrême est la paroi non catalytique qui n'interagit pas avec l'écoulement : les espèces adsorbées à la paroi sont ensuite libérées sans modification chimique ; le flux de chaque espèce à la paroi est nul.

IV.4. Schéma numérique

Les équations de couche limite sont intégrées à l'aide d'une méthode de volumes finis selon un schéma hybride (ref. 13). Afin de stabiliser les calculs, les termes sources des équations doivent être traités de façon implicite ; cela conduit à itérer sur le terme de production des espèces pour assurer la conservation de la masse ($\sum \omega_i = 0$).

V - ETUDE PARAMETRIQUE

V.1. Introduction

Nous avons étudié l'influence, sur les caractéristiques de la couche limite, des hypothèses faites sur la représentation des effets de gaz réel. Nous nous sommes intéressés non seulement à l'influence du modèle sur le flux de chaleur pariétal, mais aussi sur l'épaisseur de déplacement qui intervient dans le cas d'un couplage écoulement visqueux/écoulement non visqueux, ainsi que sur le coefficient de frottement pariétal qui contribue à la traînée de l'engin. Comme les nombres de Reynolds restent faibles, le coefficient de frottement reste élevé. On observe qu'il est quasiment insensible au modèle de gaz réel.

Sur les planches donnant l'évolution du flux de chaleur pariétal en fonction de l'abscisse, nous avons porté les flux de chaleur mesurés en vol sur la navette. Il convient de noter que ces flux mesurés ne sont donnés qu'à titre indicatif. En effet, si la forme d'hyperboloïde assure bien la même loi de pression sur l'hyperboloïde que sur la ligne de symétrie intrados de la navette, par contre, la divergence des lignes de courant due à la variation du rayon de l'hyperboloïde de révolution, ne représente pas a priori la divergence des lignes de courant de part et d'autre de la ligne de symétrie intrados de la navette ; or on sait que ces effets tridimensionnels peuvent modifier de façon notable les flux de chaleurs pariétaux. Enfin la méthode de calcul utilisée ne prend pas en compte le phénomène d'avalément d'entropie.

V.2. Influence de la catalycité de paroi

La figure 1 représente les flux au point d'arrêt en fonction du temps lors de la rentrée. La figure 2 montre l'évolution du flux de chaleur le long de l'engin pour un point de la trajectoire proche du maximum de flux de chaleur. En paroi totalement catalytique, la recombinaison des espèces à la paroi étant exothermique, il y a une importante libération d'énergie qui se traduit par une augmentation (en valeur absolue) du flux de chaleur pariétal. Une autre façon simple d'expliquer la différence entre les flux de chaleurs est d'écrire $\phi_p \sim h_p - h_f$ où l'enthalpie de frottement h_f peut être approchée, en hypersonique, par l'enthalpie d'arrêt, soit

$$h_f \approx h_{1e} = C_p T_\infty + \frac{v_\infty^2}{2} \approx \frac{v_\infty^2}{2}$$

L'enthalpie de paroi h_p est égale à $C_p T_p$ dans le cas d'une paroi froide totalement catalytique pour laquelle il y a recombinaison des molécules à la paroi. Dans le cas d'une paroi non catalytique, le gaz étant partiellement dissocié à la paroi, l'enthalpie de paroi est plus importante et donc le flux de chaleur est plus faible. On voit donc l'intérêt d'une paroi non catalytique (ou l'inconvénient d'une paroi métallique) pour diminuer les flux de chaleur pariétaux et l'échauffement de l'engin. Il convient toutefois de noter que cette analyse est très simplifiée car elle suppose que le coefficient de flux de chaleur

$C_h = \frac{\phi_p}{\rho_e U_e (h_p - h_f)}$ ne dépend pas de la catalycité de la paroi. Une telle analyse ne devra donc être considérée que comme une explication qualitative et non un moyen prédictif.

L'influence de la catalycité de paroi sur l'évolution de l'épaisseur de déplacement est plus difficile à interpréter. L'épaisseur de déplacement est définie par $\delta_1 = \int_0^\infty (1 - \frac{\rho U}{\rho_e U_e}) dy$.

Comme le profil de vitesse moyenne est peu affecté par la catalycité de paroi, la variation de l'épaisseur de déplacement dépendra surtout du profil de masse volumique, principalement au voisinage de la paroi. En paroi totalement catalytique, la libération d'énergie due à la recombinaison des espèces à la paroi tend à élever la température dans la région proche de la paroi. D'autre part, la recombinaison des atomes à la paroi et la diffusion des molécules formées à la paroi conduisent à une augmentation de la masse molaire moyenne M . Si l'on se réfère à l'équation d'état

$$p = \rho \frac{R}{M} T$$

on a donc deux effets contradictoires. On ne peut en déduire un effet systématique de la catalycité de paroi sur l'épaisseur de déplacement.

V.3. Influence des vitesses des réactions chimiques

Les vitesses de réactions chimiques étant mal connues, il est important de connaître l'influence de ces vitesses de réaction sur la prédiction de l'écoulement. Nous avons considéré différentes données. Le premier modèle, utilisé par Straub (ref. 7, 10) correspond à l'état des connaissances il y a dix ans. Le second modèle, tiré du livre de Gardiner (ref. 11) est beaucoup plus récent. Enfin un cas limite, correspondant à des vitesses de réactions infinies, est de supposer l'écoulement à l'équilibre chimique. Rappelons que dans le cas d'un calcul à l'équilibre chimique, la catalycité de paroi ne joue pas. Cependant l'écoulement étant à l'équilibre

chimique au voisinage de la paroi, on peut comparer le calcul à l'équilibre chimique à un calcul en paroi totalement catalytique.

La figure 3 représente l'évolution du flux de chaleur au point d'arrêt, en fonction du temps lors de la rentrée, pour les différents modèles chimiques considérés. Les figures 4 à 7 donnent l'évolution du flux de chaleur le long de l'engin pour différents points de la trajectoire.

Dans le cas de la paroi totalement catalytique, le flux de chaleur pariétal est, en majeure partie, dû à la recombinaison des espèces au voisinage de la paroi. On retrouve le même flux de chaleur pour les deux jeux de vitesses de réaction utilisés. Les flux de chaleur obtenus avec l'hypothèse d'écoulement à l'équilibre chimique sont très proches de ceux obtenus en paroi totalement catalytique. La différence provient sans doute du fait que l'hypothèse d'écoulement à l'équilibre chimique supprime tout phénomène de diffusion des espèces et impose un rapport azote/oxygène constant en tout point.

Dans le cas de la paroi non catalytique, on note une forte influence du modèle chimique utilisé. La paroi étant froide par rapport au reste de l'écoulement, à son voisinage, les températures sont faibles et les réactions chimiques au sein de l'écoulement recombinent les atomes. Le modèle de Straub ayant des vitesses de réaction beaucoup plus élevées recombinera mieux les atomes si bien que le niveau de dissociation à la paroi sera plus faible, et donc aussi l'enthalpie de paroi. Si l'on garde l'analyse simple $\phi_p \sim h_p - h_f$, moins le gaz sera dissocié à la paroi, plus le flux sera grand en valeur absolue. On retrouve bien sur les planches 3 à 7 que le modèle de Straub donne beaucoup moins d'effet de catalycité que celui de Gardiner, excepté aux plus hautes altitudes (très faible densité). Avec le modèle de Gardiner on trouve des effets de catalycité sur tout l'engin même aux plus basses altitudes, ce qui n'est pas le cas avec le modèle de Straub.

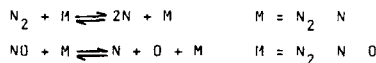
En ce qui concerne la prédiction de l'épaisseur de déplacement, on est toujours ramené au problème d'évolution du profil des masses volumiques. Comme pour les effets de catalycité de paroi, les vitesses de réactions vont jouer de façon antagoniste sur les profils de température et de masse molaire moyenne si bien qu'une tendance générale ne peut être dégagée. La figure 8 peut donner une idée de l'influence, tant du modèle chimique que de la catalycité de paroi, sur la prédiction de l'épaisseur de déplacement.

Le modèle chimique proposé par Gardiner étant le plus crédible, nous ne ferons la suite de cette étude paramétrique, la plupart du temps, qu'avec ce modèle afin d'alléger la présentation des résultats. Les conclusions auxquelles nous aboutirions seraient analogues si l'on utilisait le modèle de Straub.

V.4. Influence du nombre de réactions

Glotz (ref. 10) a montré qu'avec le modèle chimique de Straub, l'on obtenait les mêmes résultats en ne prenant en compte que cinq réactions chimiques prépondérantes. Nous avons vérifié ce résultat dans le cas de la rentrée de la navette (ref. 14).

Dans le cas du modèle chimique de Gardiner, nous avons cherché à réduire le nombre de réactions utiles. Pour cela, nous avons étudié la contribution de chaque réaction chimique au taux de production des différentes espèces pour plusieurs profils de couche limite le long de la trajectoire. Nous avons ainsi pu définir un système de dix réactions chimiques donnant sur toute la trajectoire, une prédiction identique au système complet. Ces dix réactions comprennent les cinq choisies par Glotz plus les réactions de dissociation suivantes :



Le système des cinq réactions proposé par Glotz ou le processus de Zeldovich donnent des résultats identiques et fort proches de ceux obtenus avec le modèle complet ou le modèle à dix réactions comme le montrent les figures 9 et 10. La différence, visible au niveau du point d'arrêt, s'estompe rapidement lorsque l'on progresse le long de l'engin.

V.5. Influence de la température de paroi

Reprenons notre formule simplifiée $\phi_p \sim h_p - h_f$ avec $h_f = h_{fe} = \frac{V_\infty^2}{2}$. Lors de la rentrée, pour les points de vol considérés, la vitesse infini amont décroît de 7500 ms^{-1} à 2960 ms^{-1} ; l'enthalpie d'arrêt de l'écoulement passe de $2,8 \cdot 10^7 \text{ J.kg}^{-1}$ à $4,4 \cdot 10^6 \text{ J.kg}^{-1}$. Dans le cas d'une paroi froide totalement catalytique, les atomes étant totalement recombinés à la paroi, l'enthalpie de paroi est égale à $C_p T_p$ soit $8 \cdot 10^5 \text{ J.kg}^{-1}$ pour une paroi à 800 K ou $1,5 \cdot 10^6 \text{ J.kg}^{-1}$ pour une paroi à 1500 K . L'enthalpie de paroi est faible devant l'enthalpie de frottement aux grandes vitesses tandis qu'en fin de rentrée elles sont du même ordre de grandeur. Une modification de la température de paroi sera donc d'autant plus sensible sur le flux de chaleur que la vitesse infini amont sera faible.

Dans le cas d'une paroi non catalytique, l'écoulement est dissocié à la paroi; l'enthalpie de paroi est plus importante et la différence $h_p - h_f$ plus sensible à une augmentation de la température de paroi. De plus, une élévation de la température de paroi peut entraîner un accroissement du niveau de dissociation à la paroi et donc une sur-augmentation de l'enthalpie de paroi. Le flux de chaleur sera donc plus sensible à la température de paroi en paroi non catalytique qu'en paroi totalement catalytique.

Les figures 11 et 12 confirment ces résultats sur l'influence de la température de paroi. La figure 12 montre que, pour les vitesses les plus faibles, en prenant deux valeurs extrêmes de la température de paroi lors de cette phase de rentrée, l'effet de température de paroi est du même ordre de grandeur que l'effet de catalycité.

En ce qui concerne l'épaisseur de déplacement, l'effet de température de paroi est le même que dans le cas d'un gaz parfait. L'augmentation de la température de paroi entraîne une diminution de la masse volumique et donc une augmentation de l'épaisseur de déplacement.

V.6. Influence du modèle de diffusion

Le modèle de Straub pour le calcul des coefficients de transport a l'avantage de ne calculer que sept coefficients de diffusion polynaire différents. En contrepartie, la somme des *diffusions des espèces* n'est pas nulle avec cette simplification. La formulation proposée par Obermeier et al (ref. 5) permet de calculer les vingt coefficients de diffusion polynaire pour un coût de calcul raisonnable ; la somme des flux de diffusion est alors quasiment nulle. Les calculs effectués avec le modèle d'Obermeier montrent une variation minime du flux de chaleur pariétal au point d'arrêt, les prédictions devenant rapidement identiques en aval du point d'arrêt.

Une autre stratégie est d'essayer de simplifier le calcul des termes de diffusion afin de diminuer le temps de calcul. Une première simplification est de négliger la diffusion thermique. Les flux de chaleur au point d'arrêt augmentent faiblement en paroi totalement catalytique et diminuent faiblement en paroi non catalytique (figure 13). Ces différences disparaissent rapidement en aval.

Une seconde simplification est de représenter le flux de diffusion des espèces à l'aide d'une loi de Fick

$$Q_{i,y} = - \rho D \frac{\partial C_i}{\partial y}$$

où le coefficient de diffusion D est le même pour toutes les espèces afin d'assurer la nullité de la somme des taux de diffusion. On peut alors définir un nombre de Schmidt $S = \frac{\mu}{\rho D}$. Nous avons effectué nos calculs pour un nombre de Schmidt de 0.518. On observe encore une augmentation du flux de chaleur en paroi totalement catalytique et une légère diminution en paroi non catalytique (figure 13). Cette différence s'estompe toujours très rapidement en aval.

Il convient toutefois de noter que l'emploi d'une loi de Fick impose en tout point de l'écoulement un rapport oxygène/azote constant. Les profils de concentration qui étaient peu modifiés par la non-prise en compte de la diffusion thermique sont plus sensibles à cette modification de la diffusion (figure 14). Cependant l'évolution de l'épaisseur de déplacement n'est guère modifiée par ces simplifications.

V.7. Autres simplifications du modèle

L'ensemble des résultats de calcul montre que le nombre de Prandtl $P = \frac{\mu C_p}{\lambda}$ ne varie pratiquement pas au sein de l'écoulement et quelque soit le point de vol considéré. L'hypothèse d'un nombre de Prandtl constant égal à 0.725 permet d'éviter le calcul du coefficient de conductibilité thermique sans affecter les résultats.

Une autre modification possible est l'emploi de polynômes pour représenter les fonctions de partition de l'énergie de chaque espèce. Cette modification permet, elle aussi, d'alléger le temps de calcul sans modifier les résultats.

VI - CONCLUSIONS

Rappelons d'abord l'intérêt de la formulation proposée par Straub pour évaluer les coefficients de transport d'un mélange gazeux de façon simple.

L'étude paramétrique a permis de vérifier l'importance pour la détermination du flux de chaleur pariétal, de la catalycité de paroi, du choix du jeu de vitesses de réactions chimiques dans le cas d'une paroi non catalytique, et de la température de paroi lorsque la vitesse amont est modérée. De plus, nous avons pu montrer que l'on peut obtenir une prédiction satisfaisante en ne prenant en compte qu'un nombre réduit de réactions chimiques, voire, en simplifiant le modèle physique, au prix certes d'erreurs un peu plus importantes. Le tableau 2 résume les différentes simplifications apportées à la description des effets de gaz réel, le flux au point d'arrêt en paroi non catalytique étant le plus sensible aux variations du modèle. La réduction du nombre des réactions chimiques permet de diviser le temps de calcul par quatre, la simplification du modèle physique apporte encore un gain d'un facteur deux. Ces valeurs ne sont bien entendu données qu'à titre indicatif et dépendent de la méthode numérique, du matériel utilisé et du degré de vectorisation.

L'influence du modèle sur la prédiction de l'épaisseur de déplacement ne peut être analysée de façon simple. En revanche, la prédiction du coefficient de frottement pariétal est insensible aux modifications de la représentation des effets de gaz réel.

Les auteurs tiennent à remercier Serge Grunwald pour son travail sur les couches limites à l'équilibre chimique lors de son stage de DEA.

RÉFÉRENCES

- 1 - HIRSCHFELDER J.O., CURTISS C.F., BIRD R.B. "Molecular theory of gases and liquid" - John Wiley & Sons editor, 1954.
- 2 - WILKE C.R. "A viscosity equation for gas mixture" - The Journal of Chemical Physics, vol. 18, n° 4, pp. 517-519, April 1950.
- 3 - ARMALY B.F., SUTTON K. "Viscosity of multicomponent partially ionized gas mixtures" - AIAA Paper 80-1495.
- 4 - MONCHICK L., YUN K.S., MASON E.A. "Formal kinetic theory of transport phenomena in polyatomic gas mixtures" - The Journal of Chemical Physics, vol. 19, n° 3, pp. 654-669, Août 1963.
- 5 - OBERMEIER E., SCHABER A. "A simple formula for multicomponent gaseous diffusion coefficients derived from mean free path theory" - International Journal of Heat and Mass Transfer, vol. 20, pp. 1301-1306, Pergamon Press, 1977.
- 6 - STRAUB D. "Exakte Gleichungen für die Transportkoeffizienten eines Fünfkomponentengemisches als Modellgas dissoziierter Luft" - DLR FB 72-34.
- 7 - STRAUB D., SCHÖNAUER W., SCHABER A., LIN S., ADAMS E. "Stationäre Laminare Hyperschallgrenzschichten um ein Rotationshyperboloid bei thermochemischer Gleichgewicht der Luft" - DLR FB 72-16.
- 8 - SCHÄFER K., "Statistische Theorie der Materie, Bd I" - Göttingen Vandenhoeck, 1960.
- 9 - GORDON S., Mc BRIDE B.J. "Computer program for calculation of complex chemical equilibrium compositions, rocket performance, incident and reflected shocks, and Chapman-Jouguet detonations" - NASA, SP 273.
- 10 - GLOTZ G. "Der einfluß von idealisierungen der Luft und der Randbedingungen an der Wand auf die Lösung der Laminaren Hyperschallgrenzschichtgleichungen" - Universität Karlsruhe - Rechenzentrum Interner Bericht 14/79.
- 11 - GARDINER W.C. Jr "Combustion Chemistry" - Springer Verlag, 1984.
- 12 - SHINN J.L., MOSS J.N., SIMMONDS A.L. "Viscous shock layer heating analysis for the shuttle windward symmetry plane with surface finite catalytic recombination rates" - AIAA Paper 82-0842.
- 13 - PATANKAR S.V. "Numerical Heat Transfer and Fluid Flow" - Hemisphere Publishing Corporation, 1980.
- 14 - AUPOIX B., ELDEM C., COUSTEIX J. "Development of a computational method for hypersonic boundary layer" - Euromech Colloquium 195, Luminy, Juillet 85.

FLUX DE CHALEUR AU POINT D'ARRÊT 0.1 MW/M^2

TP=1500 K MODELE CHIMIQUE DE GARDINER
EFFET DE LA CATALYTIQUE DU PAROI

— TOTALEMENT CATALYTIQUE ——— NON CATALYTIQUE

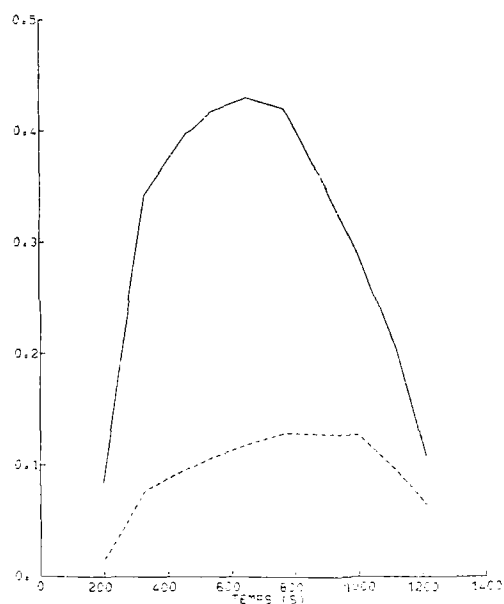


Figure 1

FLUX DE CHALEUR AU POINT D'ARRÊT 0.1 MW/M^2

TP=1500 K
EFFET DES MODELES CHIMIQUES

— EQUILIBRE CHIMIQUE ——— STRAUS TOT CATALYTIQUE
—— GARDINER TOT CATALYTIQUE ——— GARDINER NON CATALYTIQUE

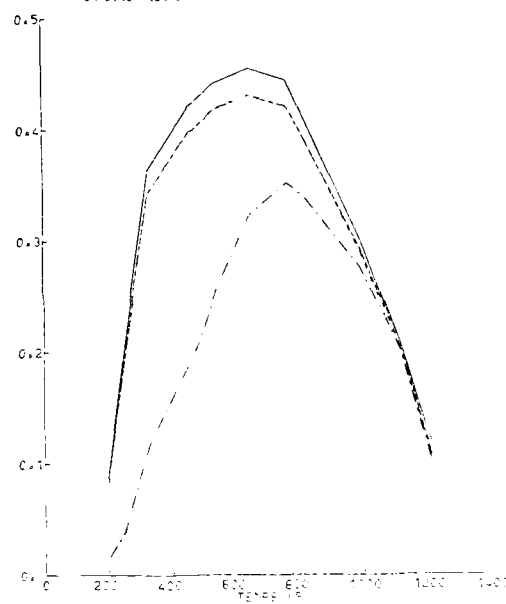


Figure 3

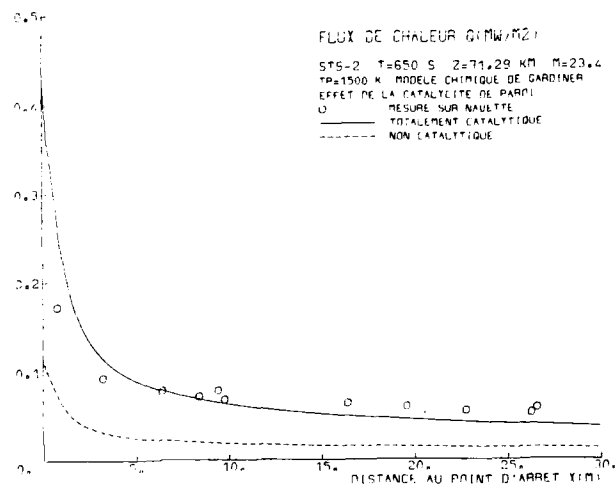


Figure 2

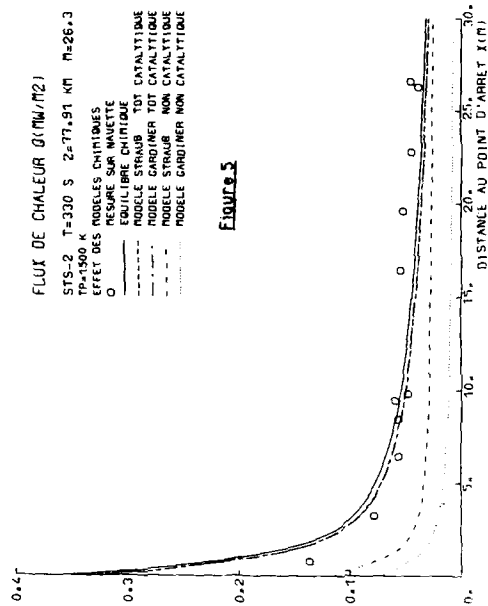


Figure 3

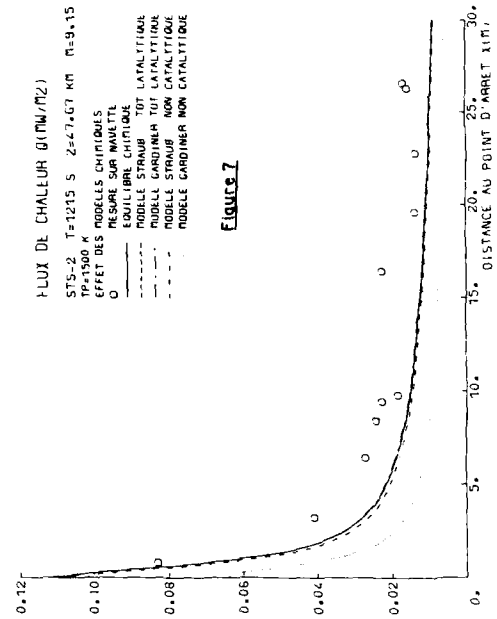


Figure 7

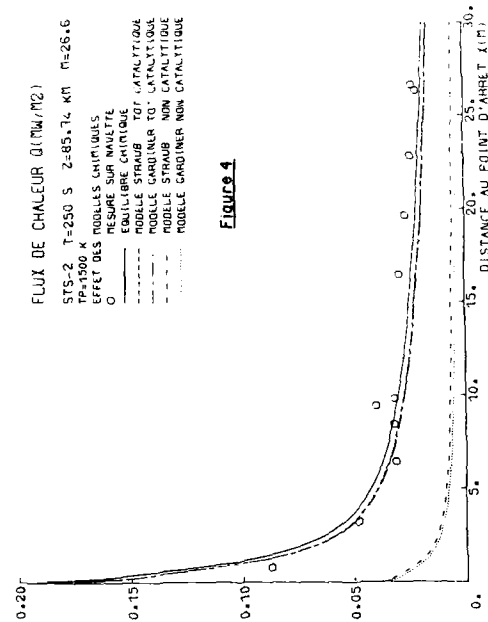


Figure 4

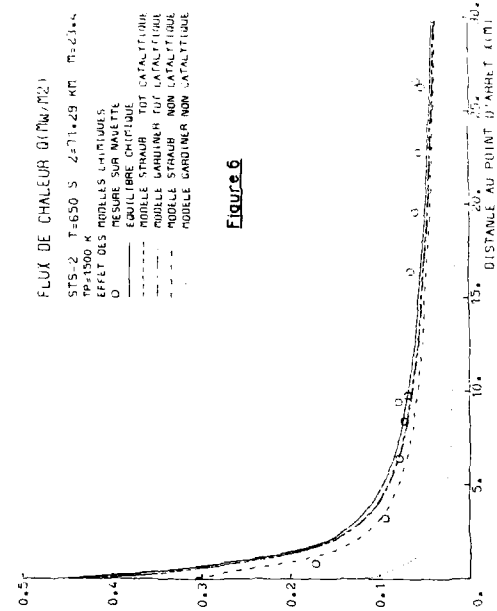


Figure 6

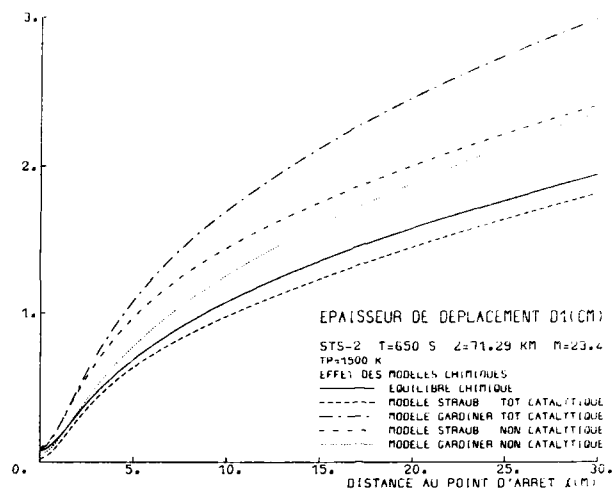


Figure 8

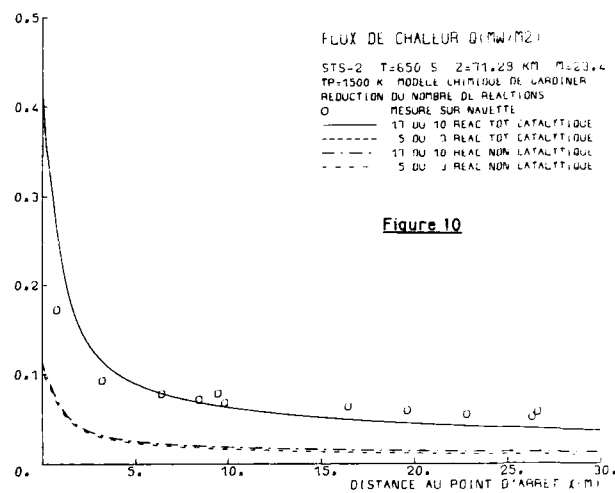


Figure 10

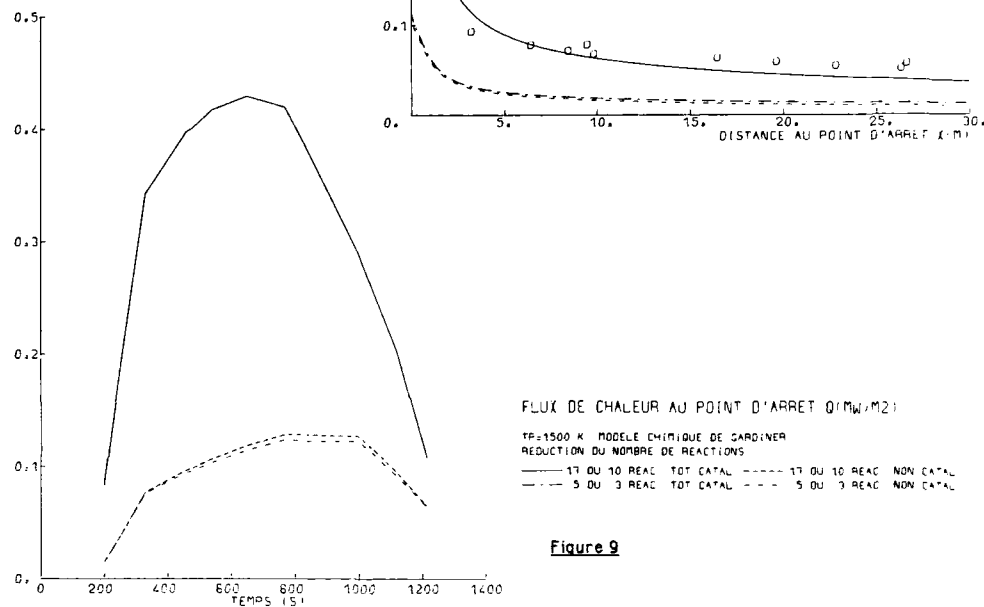


Figure 9

FLUX DE CHALEUR AU POINT D'ARRET Q(MW/M2)

MODELE CHIMIQUE DE GARDINER
EFFET DE LA TEMPERATURE DE PAROI

TP= 800 K TOTAL CATAL TP= 800 K NON CATAL
TP=1500 K TOTAL CATAL TP=1500 K NON CATAL

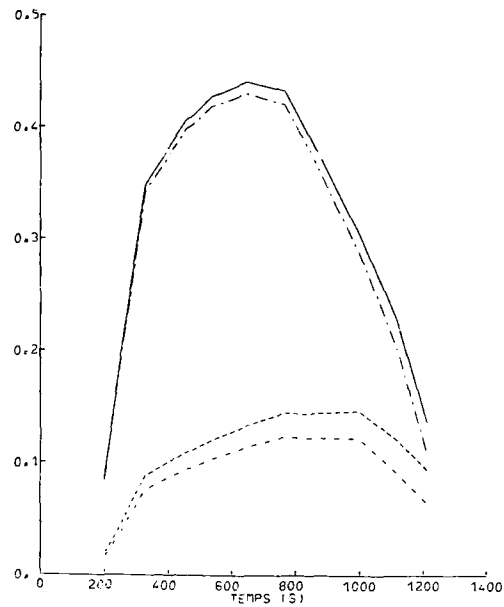


Figure 11

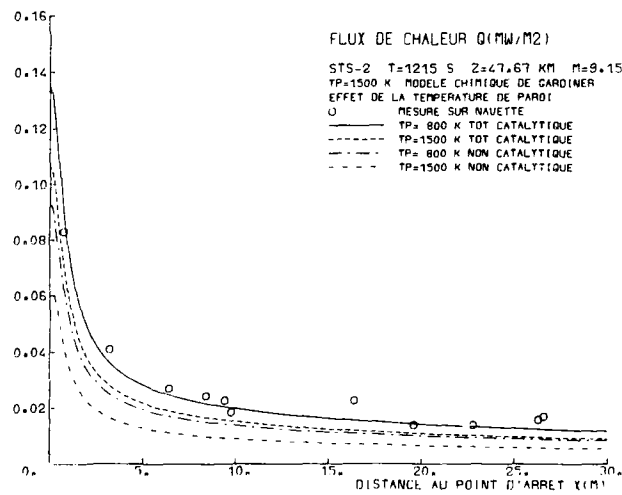


Figure 12

FLUX DE CHALEUR AU POINT D'ARRÊT (MW/M²)

TP=1500 K MODELE CHIMIQUE DE GARDINER
SIMPLIFICATION DU MODELE DE TRANSPORT

— MODELE COMPLET TOTAL CAT ——— MODELE COMPLET NON CATAL
- - - DIFFUS THERMO TOTAL CAT - - - DIFFUS THERMO NON CATAL
- - - SCHMIDT=0.518 TOTAL CAT - - - SCHMIDT=0.518 NON CATAL

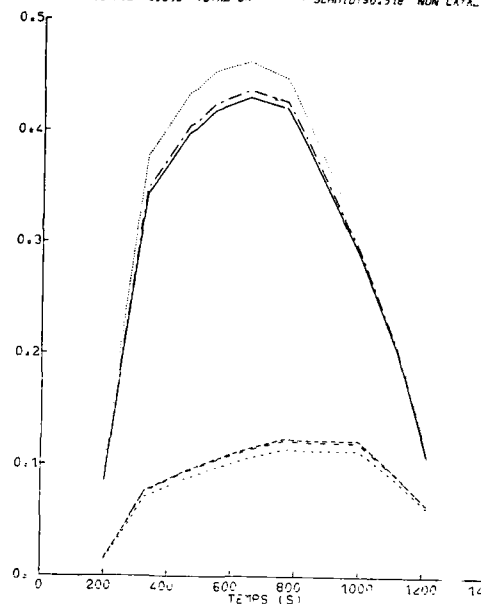


Figure 13

CONCEN. MONOXYDE D'AZOTE A X=20 M

STS-2 T=650 S Z=71.29 KM M=23.4

TP=1500 K TOTAL CATALYTIQUE MODELE DE GARDINER

SIMPLIFICATION DU MODELE DE TRANSPORT

— MODELE COMPLET ——— DIFFUS THERMIQUE NULLE

- - - NOMBRE SCHMIDT = 0.518

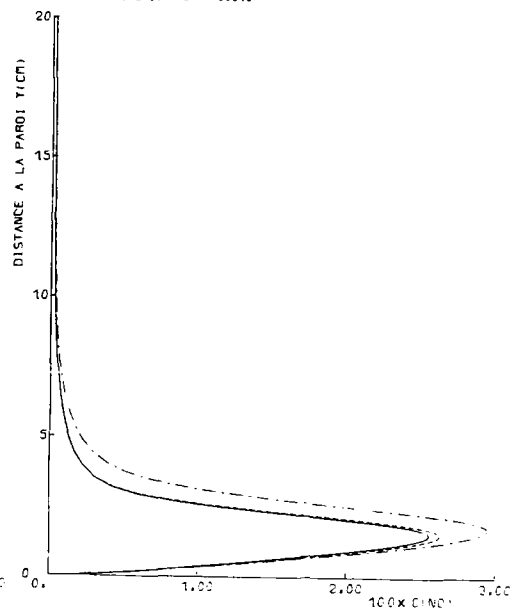


Figure 14a

CONCEN. AZOTE ATOMIQUE A X=20 M

STS-2 T=650 S Z=71.29 KM M=23.4

TP=1500 K TOTAL CATALYTIQUE MODELE DE GARDINER

SIMPLIFICATION DU MODELE DE TRANSPORT

— MODELE COMPLET ——— DIFFUS THERMIQUE NULLE

- - - NOMBRE SCHMIDT = 0.518

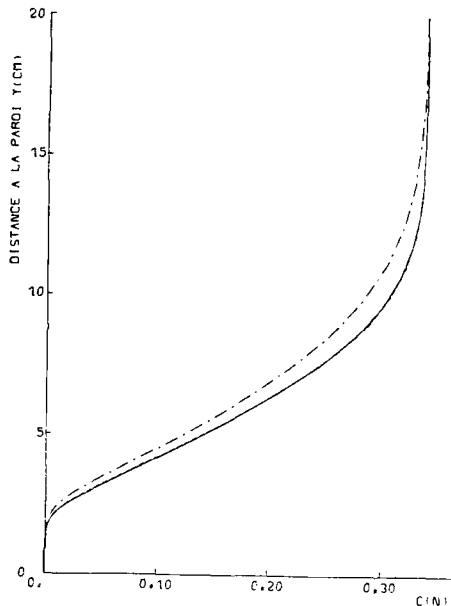


Figure 14b

CONCEN. OXYGENE ATOMIQUE A X=20 M

STS-2 T=650 S Z=71.29 KM M=23.4

TP=1500 K TOTAL CATALYTIQUE MODELE DE GARDINER

SIMPLIFICATION DU MODELE DE TRANSPORT

— MODELE COMPLET ——— DIFFUS THERMIQUE NULLE

- - - NOMBRE SCHMIDT = 0.518

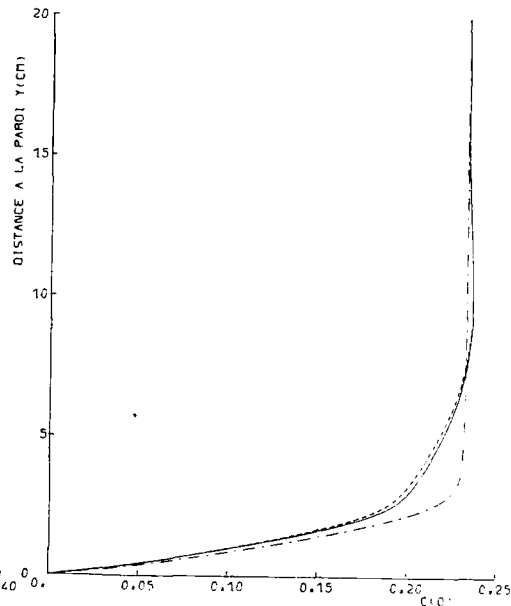


Figure 14c

Tableau 1 - Trajectoire de rentrée STS2 et définition de l'hyperboloïde de révolution à incidence nulle équivalent à la ligne de symétrie intrados (d'après ref. 12).

I S	Altitude Km	U_{∞} km/s	ρ_{∞} kg/m ³	p_{∞} atm	T_{∞} K	Mach	Incidence	$\frac{1}{2}$ angle au sommet des asymptotes deg	Rayon de nez m
200	92.35	7.50	2.184×10^{-6}	1.128×10^{-6}	324	27.90	40.4	41.15	1.296
250	85.74	7.53	6.365×10^{-6}	3.587×10^{-6}	199	26.60	41.0	41.70	1.322
330	77.91	7.42	2.335×10^{-5}	1.316×10^{-5}	199	26.30	40.2	40.80	1.286
460	74.98	7.20	3.815×10^{-5}	2.142×10^{-5}	198	25.50	40.0	40.75	1.276
480	74.62	7.16	4.055×10^{-5}	2.280×10^{-5}	198	25.40	40.3	41.00	1.289
540	73.33	7.03	4.794×10^{-5}	2.831×10^{-5}	200	24.80	40.4	41.10	1.295
650	71.29	6.73	6.824×10^{-5}	3.965×10^{-5}	205	23.40	39.4	40.20	1.253
770	68.67	6.31	9.669×10^{-5}	5.992×10^{-5}	219	21.30	38.5	39.20	1.207
830	66.81	6.05	1.216×10^{-4}	7.925×10^{-5}	230	19.90	41.4	42.20	1.342
1000	60.56	4.99	2.621×10^{-4}	1.877×10^{-4}	253	15.70	42.0	42.75	1.368
1120	52.97	3.87	6.762×10^{-4}	5.025×10^{-4}	262	11.70	38.3	39.00	1.204
1215	47.67	2.96	1.344×10^{-3}	9.900×10^{-4}	260	9.15	34.8	35.50	1.056

Tableau 2 - Comparaison des différentes représentations des effets de gaz réel.

Erreur sur le flux de chaleur au point
d'arrêt en paroi non catalytique.

Modèle	Moyenne	Max	Temps U.C
Complet	0.	0.	1.
10 réactions	0.06 %	0.14 %	0.62
5 réactions	1.7 %	4 %	0.35
3 réactions	2.4 %	4.3 %	0.26
Diffusion thermique négligée	3.3 %	5.8 %	
Nombre de Prandtl $P = 0.725$	4.8 %	7.4 %	0.19
Nombre de Schmidt $S = 0.518$ (Lewis $L = 1.4$)	9 %	11.7 %	0.16
Fonctions thermodynamiques sous forme polynomiale	9 %	11.7 %	0.13

ON THE NUMERICAL SIMULATION OF THREE-DIMENSIONAL HYPERSONIC FLOW

by
S. Riedelbauch, W. Wetzel, W. Kordulla and H. Oertel jr.
DFVLR Institute for Theoretical Fluid Mechanics,
Bunsenstr. 10, D-3400 Göttingen, FRG

SUMMARY

The present paper reports on the first steps towards the numerical simulation of hypersonic flows. Intentionally, the ideal-gas assumption is used to validate the methods by comparing results with experimentally observed or theoretically obtained data in cold hypersonic flows about simple geometries. The approaches cover the continuum as well as the gas-kinetic flow regime. An implicit finite-difference method with bow-shock fitting is employed to integrate the time-dependent Navier-Stokes equations, while the gas-kinetic flow is simulated by approximations to Boltzmann's equation. The Direct-Simulation Monte-Carlo method is preferred to the Molecular-Dynamics approach because of its larger computational efficiency. Results are compared with experimental data for the laminar flow past a blunted cone at $M = 10.6$ and past a hemisphere at $M = 4.15$. The decay of Oseen's vortex at $Kn = 0.1$, and the gas-kinetic flow past a cylinder at $M = 5.48$ with $Kn = 0.1$ and 0.3 have been simulated, and results are shown in comparison with theoretical data. As an application to more realistic configurations the three-dimensional laminar flow past the nose of a typical spacecraft and the gas-kinetic flow in the symmetry plane of the flow past the same configuration is being discussed. The next steps will include real-gas modelling. For hot hypersonic flows experimental data are badly needed for comparison purpose.

1. INTRODUCTION

Because of the development or planing of new spacecrafts such as Hermes [1], Hotol [2] or Sänger [3], or the planning of future supersonic/hypersonic airplanes [4,5,6] there is renewed interest in the understanding of hypersonic flows. It is well known that the development of the US Space Shuttle took mainly place in wind tunnels or by means of other experimental investigations. The experiences gained in free-flight as compared with the experimental and theoretical design are described in [7]. These experiences show that quite a few flow phenomena lack basic understanding, and require further studies. In contrast to the past design of the Space Shuttle, the Hermes vehicle is planned to be designed with the help of advanced numerical methods in order to reduce the expensive and time-consuming experimental investigations. This will provide a major thrust to develop new, more efficient numerical methods, or to apply existing methods to more complicated and realistic configurations. This tendency will be supported by the activities associated with forthcoming super- and hypersonic airplanes, see e.g. [5,6]. Present-day supercomputers such as CRAY-XMP, FUJITSU-VP200 or CYBER-205 enable to simulate viscous three-dimensional flows past fairly complicated configurations based on the assumption of perfect gases, see e.g. [8 to 15]. The numerical simulation of 3-D viscous flows with reactions is more difficult, see e.g. [16 to 20], due to the increased stiffness of the equations, and due to the lack of accurate physical modelling.

The numerical simulation of hypersonic flows in three dimensions is quite a challenge for a variety of reasons, see also [21]. In addition to the well-known difficulties associated with the determination of transition and with the modelling of turbulence in compressible flows at moderate temperatures, one encounters problems associated with real gas effects and with the approximation of dilute gases. In [22,23] experimental devices are discussed which are required in order to better analyze real gas effects at high temperatures, and to provide the necessary physical input or the verification for the numerical simulation. One major task of the numerical simulation is the prediction of integral quantities such as forces and moments acting on the hypersonic vehicle. The analysis of the development of the Space Shuttle Programme seems to indicate that these integral quantities are dominated by Mach number and real gas effects [21]. The other major task in hypersonic flow predictions is to accurately determine the aerothermodynamic load of the vehicle due to heat transfer. Here viscous effects must be considered, in addition. Real gas effects introduce new time scales or length scales into the problems resulting in an increased stiffness of the nonlinear equations. For finite-rate chemistry there is a lack of accurate rate constants at high temperatures.

The range of the hypersonic flow regime can be classified according to the value of the ratio of the mean free path of the particles and the characteristic length of the considered problem, denoted by the Knudsen number Kn . In the continuum flow range at very small Kn , up to $Kn = 0.01 + 0.1$, the Navier-Stokes

equations can generally be used to describe flows, see figure 1, [24,25]. This is true for atmospheric flight in altitudes up to roughly 100 km.

The other limiting case, for very large Kn , corresponds to the free-molecular-flow regime governed by Boltzmann's equation where the collisions of molecules are rare, and can therefore be neglected. The flow regime between the two limiting cases is called transitional, see figure 1. In the transitional-flow regime the mean free path of the molecules is of the order of the characteristic length of the body in question. In order to determine the transitional flow an approximation is required for Boltzmann's equation, see e.g. [25 to 30]. One often and successfully used gas-kinetic approximation for dilute gases is the Direct-Simulation Monte-Carlo approach. When approaching the continuum-flow regime, i.e. with decreasing Knudsen number, the computational effort associated with gas-kinetic flow simulations becomes larger and larger. This happens because the larger density of the gas can only be simulated properly if the number of cells is increased as well because the dimension of such a cell should be of the order of the mean free path of the particles involved. Although the entire regime could be treated by such a technique, current computer capabilities forbid its use for continuum flows. Navier-Stokes solutions may be used, on the other hand, for low-density flows, provided appropriate boundary conditions are employed allowing for slip flow and a jump in temperature.

The present paper discusses work at the DFVLR-Institute for Theoretical Fluid Mechanics done as a first step towards the numerical simulation of hypersonic flows. This first step is based on the assumption that the flow is thermally and calorically perfect. Thus cold hypersonic flows can be treated, and numerical tools can be developed by verification with available experimental data. For the consideration of real-gas effects the corresponding physical models must be developed, and corresponding experiments have to be conducted for validation purpose. The simulation of hypersonic flows is approached from both sides, from the continuum-flow as well as from the gas-kinetic-flow regime, see figure 1. Figure 1 displays a typical flight envelope of a spacecraft such as e.g. Hermes. The flow can be considered continuum throughout most of the flight since it takes place in altitudes less than 90 km. Only for those situations where the speed of more than 7 km/sec is required, the transitional flow regime is entered. Figure 1 also indicates the flow regimes where the perfect-gas assumption, corresponding to cold hypersonic flow, can be made, and where the internal degrees of freedom are excited and reactions start to occur.

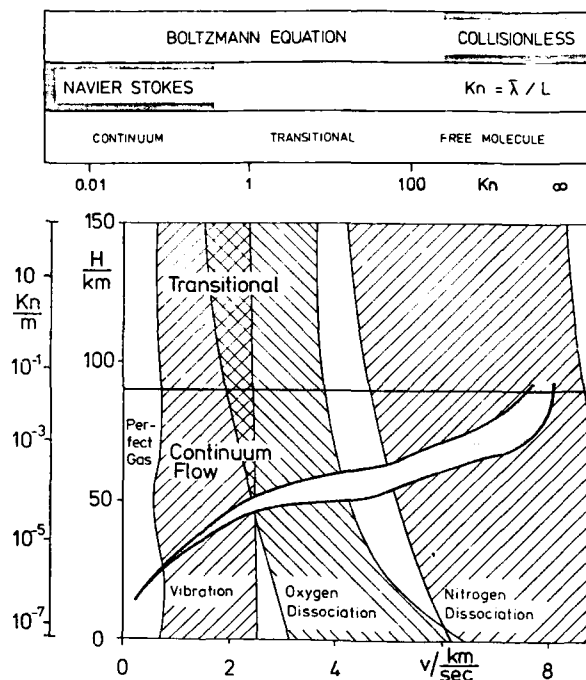


Figure 1: Sketch of the range of hypersonic flow regimes with corresponding speeds, altitudes and Knudsen number ranges, including the flight envelope of a typical spacecraft.

In the following, the integration of the time-dependent Navier-Stokes equations in finite-difference formulation will be discussed first, followed by a presentation of the direct gas-kinetic simulation using the Monte-Carlo technique. As a first application of these methods the results for the computation of the flow in the nose region of a realistic spacecraft are described assuming that the ideal-gas model holds in spite of the chosen realistic free stream flow conditions. The paper is concluded by some remarks pointing out the importance of experimental verification for the development of numerical simulation techniques.

2. SIMULATION OF VISCOUS CONTINUUM FLOW

2.1 GOVERNING EQUATIONS AND ALGORITHM

The governing equations for time-dependent viscous flows are discussed e.g. in [31,32]. The formulation used here is based on the differential formulation in strong conservation-law form which allows to capture flow discontinuities such as shock waves. This property is, however, used only for shock waves embedded in the flow field while the bow shock wave is fitted, thus forming one boundary of the computational domain. A detailed discussion of the equations and the used algorithm is contained in [33], and will therefore only be summarized here.

The equations are based on the assumption of ideal gases using constant specific heats. The flows treated are laminar with the viscosity coefficient being determined with Sutherland's law although this is not accurate over the temperature range encountered in some computations. The heat transfer coefficient is related to the viscosity coefficient via the definition of the laminar Prandtl number which is assumed constant as is usual in supersonic flows. In the case of hypersonic flow at high temperature these assumptions have to be revised completely, and additional equations will have to be added if reactions take place, see e.g. [20].

The time dependent equations have been derived using the thin-layer approximation which is quite common in ideal-gas flow simulations for high Reynolds numbers in order to reduce the computational effort. Owing to this approximation all surface-tangential diffusion terms are neglected based on the argument that only the wall-normal direction can be resolved properly on present-day

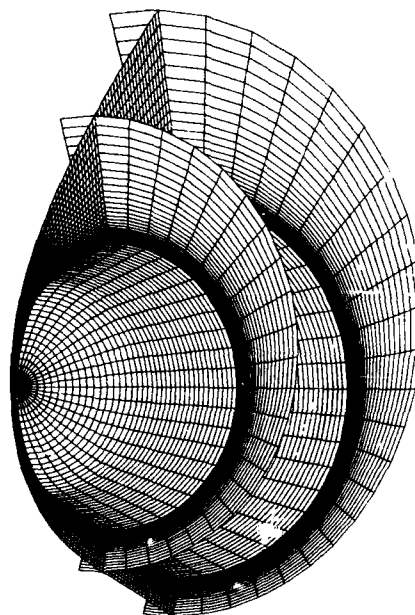


Figure 2: Perspective view of some surfaces of a grid for the simulation of the laminar flow past a blunted cone at $M_\infty = 10.6$, $Re = 110\,000$, $T_0 = 11.1\text{ K}$, $T_w = 300\text{ K}$, $\alpha = 15^\circ$. The grid corresponds to the converged solution with fitted bow shock wave.

supercomputers. Although the thin-layer approximation has been verified for quite complicated flows, see e.g. [34], it needs to be checked for flows with reactions, or if an extremely fine resolution becomes possible in more than the wall-normal direction.

The used solution algorithm is originally based on the implicit Beam-and-Warming scheme as applied in a modified version to axisymmetric supersonic and hypersonic flows past blunt bodies in [35,36]. The extension to three dimensions in [33] takes advantage of the work in [37] which reduces dramatically the computational effort associated with the inversion of the implicit operator in three dimensions. Instead of approximately factoring the multi-dimensional implicit operator into one-dimensional factors, the surface-tangential flux differencing is done in an explicit fashion. Hence only one one-dimensional implicit operator remains to be inverted. This advantage is achieved at the expense of having to reduce the time step considerably if the surface-tangential grid resolution needs to be improved, e.g. near the nose of the body or in regions with embedded shocks. In such cases it may become necessary to take recourse to a more implicit or even fully implicit solution. The hybrid explicit-implicit scheme exhibits another advantage for use on computers with small main memory in that less storage is needed because only one level of the solution vector needs to be stored. A black-and-red pattern relaxation scheme is used for the solution.

The initial conditions used are, in general, post-shock conditions requiring small time steps in the beginning, and increasing these within about 100 steps to the final value. Alternatively, for steady-state problems some artificial viscous layer could be introduced near the body surface to enhance taking large time steps from the very beginning on. Note that constant time steps are being used throughout the entire computational domain. Usually, for solutions at angle of attack the flow field is established gradually, starting with a solution at an angle of attack of 0° . Most crucial is an appropriate initial guess of the shape of the bow shock wave, in particular for more complicated shapes (see below). This may, however, be due to the use of explicit boundary conditions at both the moving bow shock and the surface of the body. Therefore, these conditions are currently being transferred to an implicit treatment which is non-trivial because of the moving grid. The formulation of the boundary conditions at the fitted shock wave uses the Rankine-Hugoniot relations and assumes the pressure behind the shock wave to be known from a calculation based on the values of the previous time step. At the surface no-slip conditions and adiabatic walls or prescribed wall temperatures are currently used. Flow symmetry is assumed to reduce the computational effort because the computations are generally carried out on a CRAY-1S without dedicated input/output device.

2.2 VALIDATION OF THE METHOD

The validation of the code in three dimensions has been carried out in several steps, for cold hypersonic flows as was mentioned earlier. First, it was made sure that the axisymmetric flow is recovered as was obtained previously with the code for axisymmetric flow (without separation). Then, different grids have been used for the same axisymmetric problem [33]. One is based on cylindrical coordinates with a singular axis at the nose, the other avoids the singular axis by wrapping a surface around it. Both solutions give the same answer if the mesh spacings, and the interpolation at the singular axis in the first approach are chosen appropriately [33]. The mesh with singular axis is currently preferred in spite of the difficulties associated with the interpolation because it imposes less restrictive time-step limitations due to the coarser mesh near the nose.

Because the accuracy of the prediction of heat transfer is most important for the design of hypersonic vehicles, experimentally observed heat transfer data for model configurations were sought for comparison purpose. While hot hypersonic flow data are virtually not available at all, those for cold hypersonic flows in well documented form seem to have been established only in the sixties, see e.g. [38 to 40].

The laminar flow past a blunted cone at Mach number 10.6 with Reynolds number 110 000 based on nose radius for the free-stream stagnation temperature 1111 K and prescribed wall temperature of 300 K was chosen as one test case [38,39] because pressure distributions and heat transfer data are given. Figure 2 shows several surfaces of the mesh used for this flow simulation at an angle of attack of 15° in perspective view. The mesh dimensions in longitudinal, circumferential and wall-normal directions are $63 \times 25 \times 41$. Note that the external grid surface corresponds to the fitted bow shock wave as is obtained for the converged solution. Measurements are given only at locations more than about 1.5 nose radii downstream of the nose. Figures 3 and 4 show the excellent agreement of predicted with experimentally observed distributions of pressure coefficients and heat transfer (referenced to the heat transfer at the body nose at zero incidence). The ratio of the heat transfer passes slightly the theoretical value of one at the stagnation point at angle of attack which can be corrected by improving the resolution of the grid near the nose. Figure 5 displays the lines of constant Mach number in the symmetry plane for the same flow conditions. The location of the subsonic flow domain near the stagnation point is indicated as well. The location of the bow shock wave can be estimated well as the external boundary of the domain of the iso-line plot.

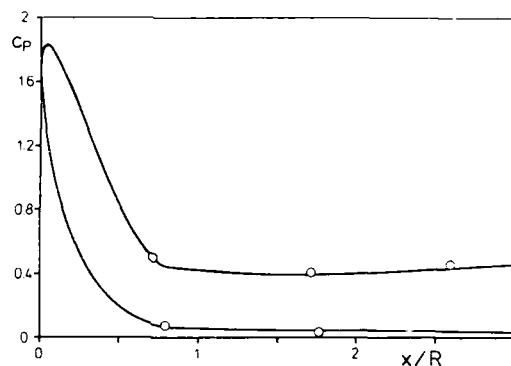


Figure 3: Comparison of predicted and experimentally observed pressure distribution on a blunted cone (o : experiment, Cleary). Legend see fig. 2.

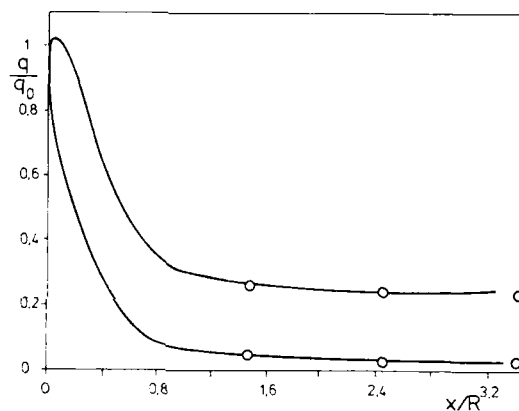


Figure 4: Comparison of predicted and experimentally observed heat transfer data (o : experiment, Cleary). Legend see fig. 2.

It remains to show that the heat transfer is well predicted also in the neighborhood of peak values, near the stagnation point. It is hard to find corresponding experimental data for cold hypersonic flows. Therefore figure 6 shows a comparison for supersonic flow conditions in terms of adiabatic wall temperatures near the nose of a hemisphere. Free-stream conditions are $M_\infty = 4.15$, $Re = 1\,500\,000$ and $T_0 = 389\text{ K}$. The deviation of the experimentally determined stagnation temperature, as referenced to the free-stream stagnation temperature, from the theoretical value of one indicates the error involved. This shows that the predicted values are well within the band width of the experimental error range.

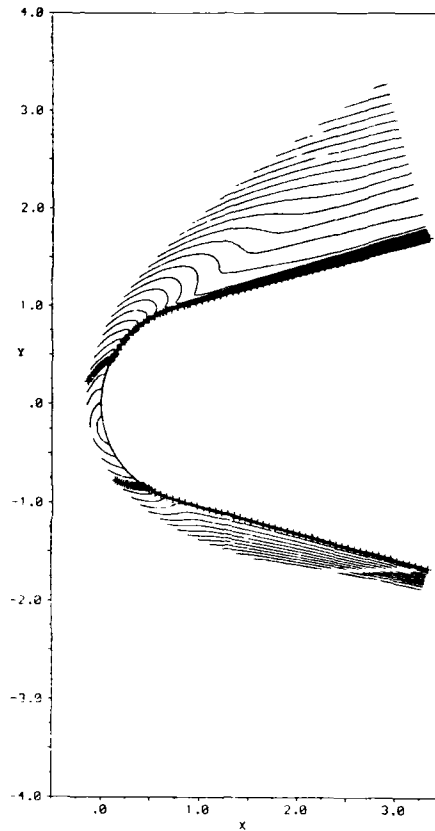


Figure 5: Display of lines of constant Mach number in the symmetry plane of the flow past a blunted cone, see figures 2 to 4 (--- : sonic surface).

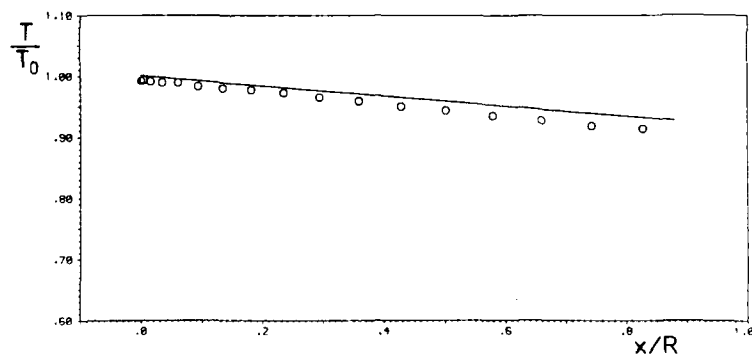


Figure 6: Comparison of predicted and experimentally observed adiabatic wall temperatures near the nose of a hemisphere as referenced to the free-stream stagnation temperature (o : experiment, Beckwith and Gallagher). $M_\infty = 4.15$, $Re = 1\,500\,000$, $T_0 = 389\text{ K}$.

2.3 IDEAL-GAS FLOW PAST A REALISTIC SPACECRAFT NOSE

As an application to more realistic body shapes half of the laminar flow past the nose of a Hermes-like vehicle has been simulated with $\gamma = 1.4$ for a point within the possible flight corridor ($M_\infty = 12.2$, $Re_L = 141\,200$, $L = 1\text{ m}$, $T_\infty = 266.6\text{ K}$), see figure 7. The external grid surface coincides with the bow shock surface for an angle of attack of 10° . The flat windward surface of the body can clearly be seen. Because the desired wall temperature is not known, adiabatic-wall boundary conditions have been employed. Starting with a solution at zero incidence, based on a mesh with $40 \times 41 \times 41$ points, flow fields have been obtained up to an angle of attack of 20° . As indicated earlier, the estimation of the initial shock shape is most difficult, because the solution is rather sensitive with respect to the shock position. Note that the authors are well aware of the discrepancy of the high temperatures near the stagnation point (of the order of 8200 K) and the ideal-gas flow assumption. For an angle of attack of 10° figure 8 shows the lines of constant Mach number in the symmetry plane of the body including the trace of the sonic surface near the stagnation point. Note the flat windward surface which becomes obvious in figure 9 where a cross-sectional plot of the isobars is presented including the cross-sectional shape of the body at the downstream end of the computational domain. The used mesh is indicated in the same figure, with the trace of the bow shock wave indicated by the outmost coordinate lines. The carpet plot of the pressure clearly indicates a typical cross-sectional local maximum of the pressure near the lower "corner" of the body before the flow expands around the shoulder with a fairly small radius of curvature.

The solutions with roughly 67000 grid points could be obtained with an in-core version of the code on the CRAY-1S computer owing to the reduced storage requirements of the hybrid explicit-implicit scheme. Currently the mesh sensitivity of the solution is investigated by running the code on a CRAY-2 computer with the mesh dimensions in the surface tangential directions being doubled. From the cross-sectional view of the mesh in figure 9 it seems that more resolution is needed near the "corners". And actually a flow-adaptive solution would be most appropriate.

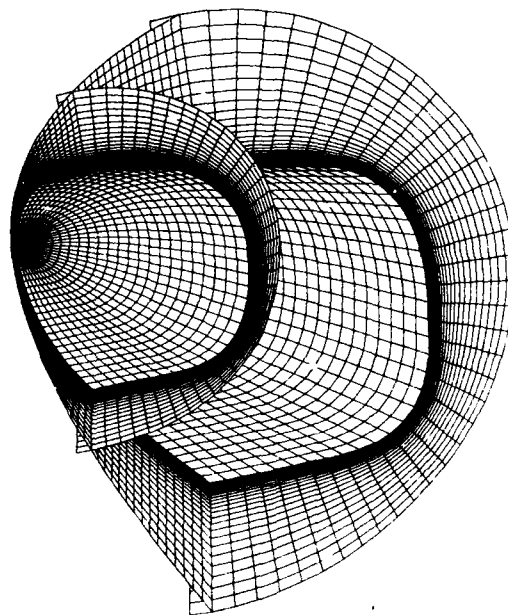


Figure 7: Perspective view of some surfaces of the finite-difference grid used for the flow simulation past a typical spacecraft nose.
 $M_\infty = 12.2$; $\alpha = 10^\circ$; $Re_L = 141\,200$; $L = 1\text{ m}$; $T_\infty = 266.6\text{ K}$; adiabatic;
 $\gamma = 1.4$.

3. GAS-KINETIC FLOW REGIME

3.1 SOLUTION METHODS

For sufficiently dilute gases the fluid is considered to consist of an ensemble of discrete particles. The motion of these particles and the corresponding collisions are described by Boltzmann's equation. There is a single dependent variable, the distribution function, but there are seven independent variables, the time and the coordinates of the position vector and the velocity vector. This explains why it is usually avoided to integrate the equation in three dimensions, even if the collision term in Boltzmann's equation is simple, describing the variation of the distribution function as a consequence of the collisions of the particles.

As an alternative to the numerical integration of Boltzmann's equation two simulation approaches have been investigated. One is the Direct-Simulation Monte-Carlo technique (DSMC), suggested by Bird [41], and the other is the Molecular-Dynamics approach (MD), see e.g. [29,30,42]. In these approaches the distribution function is directly represented by the particles in the phase space where every particle is defined by the position and the velocity vector. The flow simulation is possible with some thousands of model particles which represent the roughly $1E+19$ particles per cubic centimeter existing in reality. This is possible because Boltzmann's equation can be normalized such that it is independent of the number of particles [43], if the product of particle density and cross section of the particle remains constant.

In the MD simulation approach the calculation starts with defining the position and the velocity of the particles within the chosen control volume. Usually statistical assumptions are employed for this purpose. Once the initial conditions have been defined, e.g. based on Maxwell's distribution for the velocities, the motion of the particles is determined completely (deterministic

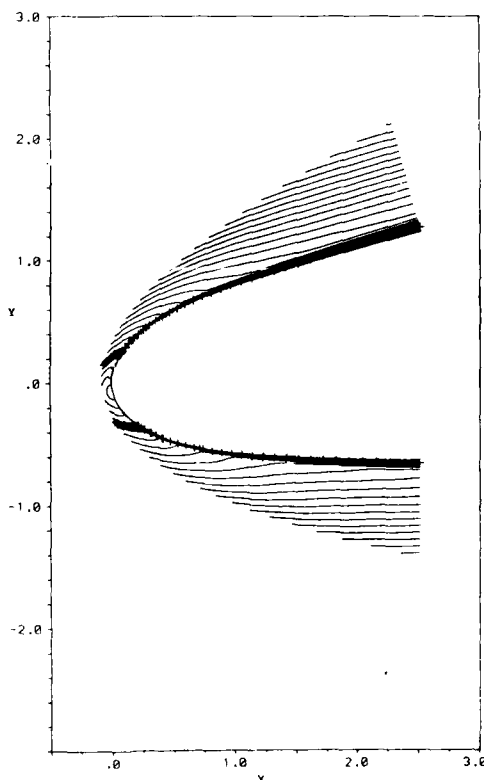


Figure 8: Lines of constant Mach number in the symmetry plane near the nose of a typical spacecraft (+++ : sonic surface). Legend see fig. 7.

approach). This motion is only a function of the chosen particle potential and the conditions at the boundaries of the computational domain. For every time step the impact of the inter-molecular forces on the particles is determined, and the motion of the particles is then considered in a decoupled fashion. Concerning the formulation of the boundary conditions, e.g. specular or diffuse reflection can be used. Specular reflection corresponds to symmetric or inviscid boundary conditions, while diffuse reflection allows to simulate viscous conditions. Macroscopic quantities can be determined at any time by sampling the properties of the particles. For all present MD results a hard-sphere potential has been assumed. This means that there is no interaction between particles unless they collide with each other. Therefore the time step for the calculation must not be chosen larger than the increment between two subsequent collisions. Thus, in principle, any possible collisions need to be checked before the smallest time step is chosen. Then all molecules are moved according to this smallest time step, and just the single collision is then considered based on the governing equations for fully elastic collisions. Although modifications to this approach will speed up the computations considerably [29,30], the accuracy of the MD method is nevertheless achieved at the expense of very time-consuming operations. The advantage of this approach is that the computation itself does not require a grid, and it can therefore be applied to complicated geometries. Also, more complex flow phenomena can be simulated in an accurate manner if the computer resources are large enough.

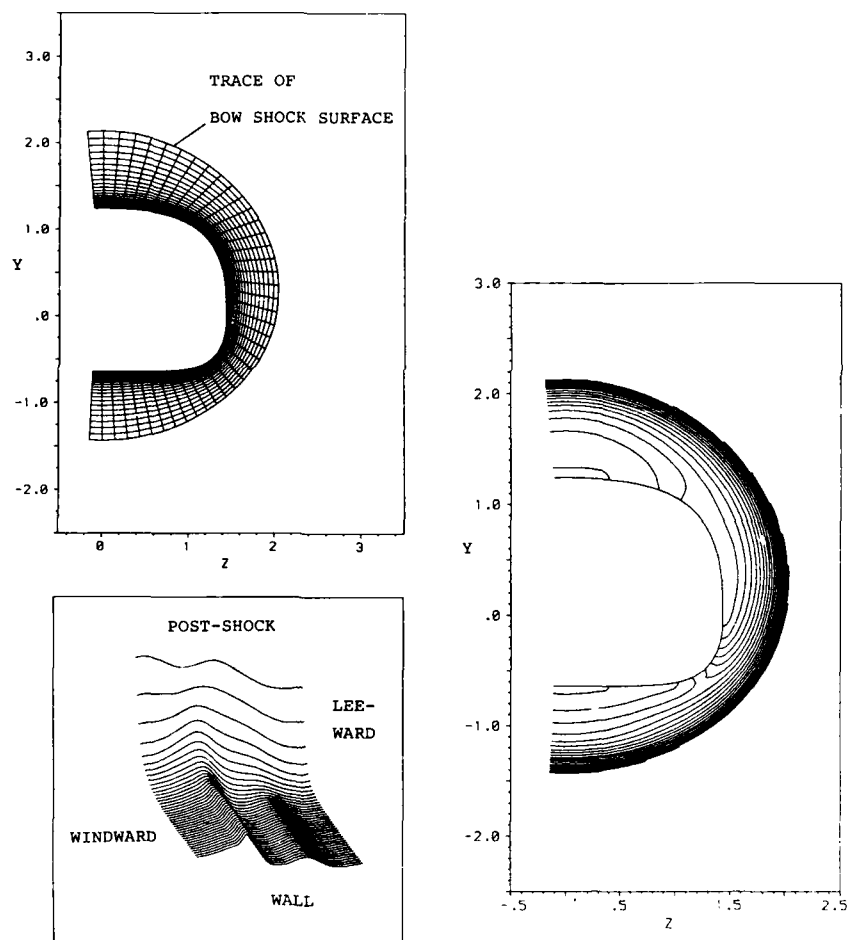


Figure 9: Isobars in a cross-sectional plane near the nose of a typical spacecraft, (right). Corresponding pressure carpet plot in computational space (left, bottom). Cross-sectional mesh (left, top). Legend see fig. 7; $x/L \approx 2.5$ (exit surface).

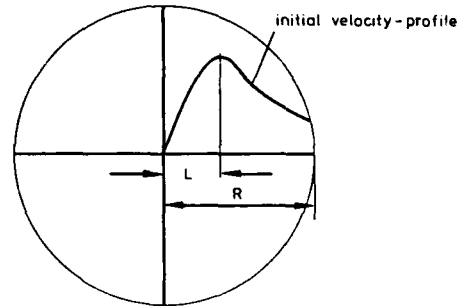


Figure 10: Sketch of the control volume for the simulation of the decay of Oseen's vortex flow, with initial velocity distribution.

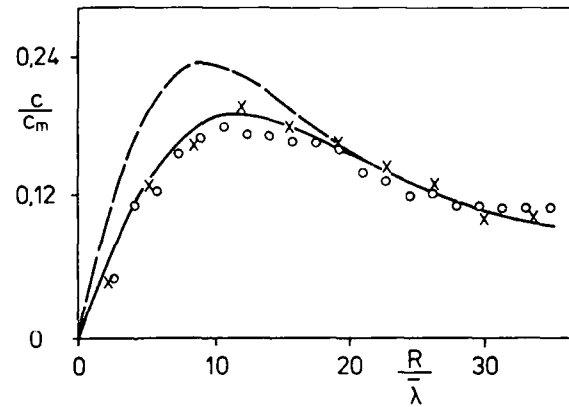


Figure 11: Comparison of predicted and analytical velocity distribution for Oseen's vortex decay for $Kn = 0.1$. --- : initial condition, — : analytic solution, xx : MD result, oo : DSMC result.

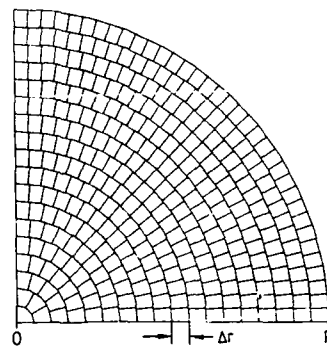


Figure 12: Sketch of the discretization of the flow simulation with the DSMC method.

The DSMC method is similar to the MD approach in so far as the paths of many particles are determined, and the macroscopic quantities are obtained by sampling the microscopic quantities. The difference between both methods originates from the treatment of the collisions where statistical assumptions are employed in the DSMC approach. Because this results in less computational effort, the DSMC method is preferred, in general.

The computational domain in the DSMC approach is first partitioned into discrete cells. The size of a cell has to be chosen such that the variation of the flow properties within that cell are small i.e. of the order of the mean free path. With the initial position and velocity of the particles known, as in the case of the MD method, the DSMC method consists of two steps which are repeated as often as needed. In the first step of the simulation the particles are moved according to their individual velocities for a time step Δt , chosen such that it is small compared with the mean collision time. Thereby the motion is determined without regard of possible interactions with neighboring particles. Collisions with walls are handled in the same way as was indicated for the MD method. The next step then consists of computing for each cell representative collisions between two particles which are chosen in a random manner. These two particles, however, may or may not collide depending on the collision probability which is proportional to the product of relative velocity and cross section. If the two particles collide, the momentum and energy conservation equations are used to determine the new velocity components. This procedure is continued until the time increments Δt , the time between collisions, sum up to the prescribed Δt for all cells. Because the particles do not actually collide in the DSMC method, the impact parameters - for a given interaction potential - are not determined by the geometric consideration as is the case in the MD approach. The Monte-Carlo method makes use of the fact that, in particular for the hard-sphere model, there does not exist a preferred spatial direction for the impact parameters, so that they can be determined in a random way.

Many physical models are available to numerically describe the interaction of particles due to both repulsing and attracting forces. The usefulness of such models have been shown by comparison with experimentally observed data. For engineering purpose it is not necessary to know very well the interaction potential. In [44] an efficient model, the so-called "variable hard sphere (VHS) model" is proposed. This model has the advantage of the hard-sphere model, i.e. the isotropy of the impact parameters. On the other hand the VHS model takes into account the dependence of the cross section upon the relative velocity of the two colliding particles [44].

The kinetic theory for gases consisting of molecules with internal energy is very complex owing to the multi-dimensional phase space, and to the complicated exchange of energy between internal and translatory energy modes of molecules, in the case of inelastic collisions. Therefore it is very difficult to determine exact physical models. As an alternative phenomenological models have been developed: the Borgnakke/Larsen model has proven to represent a valuable tool

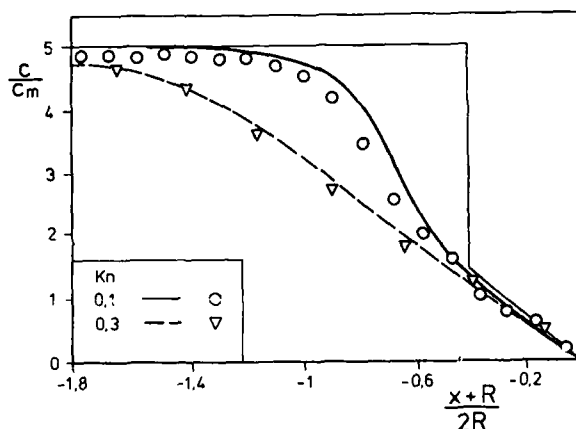


Figure 13: Velocity profiles along the stagnation streamline of the flow past an adiabatic circular cylinder for $Kn = 0.1$ and 0.3 (DSMC). The lines are taken from [46] and the symbols represent present results (the shock location predicted by continuum is included as well).

for engineering applications [45]. The main feature of this statistical model is that part of the collisions is treated completely inelastic. The remaining collisions are considered fully elastic, and are determined as if the considered gas was monatomic. This model will lead to the Maxwell distribution in the case of a gas in equilibrium, where translatory and internal temperature coincide. It is currently being implemented in the DSMC method.

Concerning the gas-kinetic flow simulations, the simulation of the decay of the Oseen vortex and of the hypersonic flow past a cylinder are discussed as part of a validation procedure. Then first results are presented for the flow in the symmetry plane of the nose region of a spacecraft based on simplifying assumptions. Note that the methods are formulated for three dimensions, where the third dimension exhibits in most cases a length of one mean free path because of the lacking computer resources. Hence, all two-dimensional results presented have been obtained in a quasi-three-dimensional fashion.

3.2 VALIDATION OF THE DSMC METHOD

As first test case which is being used to determine the parameters characteristic for both gas-kinetic flow simulation approaches, the decay of Oseen's vortex has been chosen. This flow allows to check the sensitivity of the DSMC method with respect to the conservation of angular momentum which becomes important whenever vortical flows are simulated, see [29,30]. The advantage of this test case is that there is an analytic solution of the Navier-Stokes equations to compare with.

The control volume for the simulation of the vortex decay exhibits a circular shape with radius R , see figure 10. The characteristic length scale L of the problem is chosen to be the distance between vortex core and initial location of the maximum of the velocity. At the boundary of the control volume specular diffusion is imposed which is certainly not consistent with the condition of air at rest (which would rather require diffuse reflection). This way, however, the total amount of angular momentum within the control volume must remain constant. Thus the conservation properties of the considered method can be checked directly. Knowing that the boundary condition is physically incorrect, care is taken that the influence of that condition does not penetrate further in the direction of the vortex core than $R/2$. This is achieved by choosing the simulation time appropriately. The interaction between the particles is modelled with the help of the hard-sphere model.

Figure 11 shows for $Kn = 0.1$, which is close to continuum conditions, a comparison of results for the MD and the DSMC methods with the analytic solution in terms of velocity distribution. The ratio of particle diameter and average distance between particle centers is a measure of the degree of rarefaction. This ratio is 0.4 in the case of the MD method, where 10 000 particles are employed for the simulation. Four independent runs have been made, and the corresponding results have been averaged. In the case of the DSMC method 211 000 particles have been used. The circular computational domain has been partitioned into cells such that the radial extent of each box is roughly 0.8 of the mean free path of the particles, see the sketch in figure 12. This choice of parameters leads to good agreement of the predicted with the analytical solution, see figure 11. As expected, only near the external boundary some systematic disagreement is recognized. The average change in angular momentum per collision of the particles was less than 0.0002 for both gas-kinetic simulation approaches.

After having calibrated the DSMC technique only this one was used in the following because of its superior computational efficiency. As another test case the adiabatic hypersonic flow normal to a cylinder is simulated, the fluid being Argon. The calculations have been performed with the VHS interaction model after Bird for $Kn = 0.1$ and 0.3 and a free-stream Mach number of 5.48. Diffuse reflection with complete thermal accommodation served as boundary conditions. The correlation for the recovery temperature at the surface of a cylinder in dilute gases [46] has been used to determine the wall temperature. Since the outer boundary was far enough away from the cylinder, the total number of particles within the computational domain was kept constant: the number of particles leaving the domain were replaced by the same number entering based on a random distribution. In 1974, a similar investigation was carried out [47]. Therein, however, the inverse 12th-power-law potential was used to simulate the flow of Argon. Figure 13 shows the distribution of the velocity, as referenced to the most probable velocity c_m of molecules in equilibrium, along the stagnation streamline in comparison with the results in [47]. The bow-shock stand-off distance is referenced to the radius R . An additional comparison is the continuum-flow approximation from [47] which has been plotted as well into figure 13. In figure 13 one recognizes the bow-shock wave building up in front of the body with reduced Kn , with the shock thickness decreasing towards the continuum-flow limit. For $Kn = 0.1$, the figures 14 and 15 show lines of constant temperature and constant density for the nearly adiabatic cylinder walls. The curved shock wave, the thickness of which is of the order of the body radius, is clearly seen.

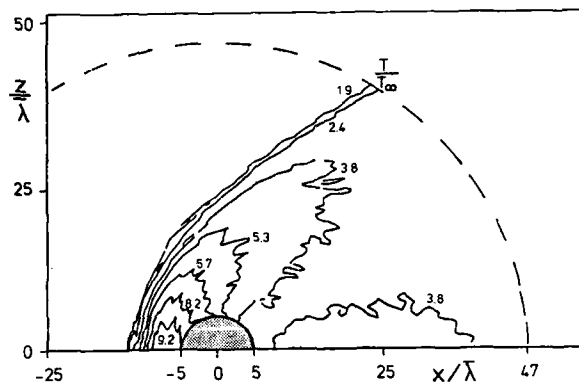


Figure 14: Lines of constant temperature for the flow past a circular cylinder. $M_\infty = 5.48$, adiabatic wall, $Kn = 0.1$.

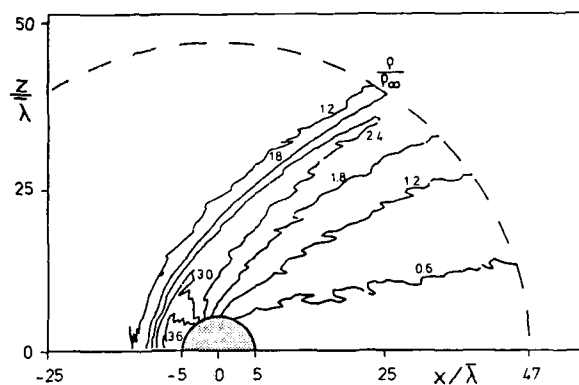


Figure 15: Lines of constant density for the flow past a circular cylinder. $M_\infty = 5.48$, adiabatic wall, $Kn = 0.1$.

3.3 GAS-KINETIC FLOW PAST A REALISTIC SPACECRAFT NOSE

In the following first simulations of the flow past the nose of a realistic spacecraft are discussed. The flow conditions are chosen from realistic reentry parameters. The Knudsen number is roughly 0.08, where the mean free path corresponds to an altitude of 95 km and where the characteristic length is the average nose radius in the symmetry plane. The free-stream Mach number is 25.5 and the prescribed wall temperature is chosen 1043 K. The calculation of the collisions is again based on the hard-sphere model for monatomic gases. The boundary conditions on the vehicle is based on diffuse reflection and complete thermal accommodation. It is obvious that the high free-stream velocity would lead to real gas effects including chemical reactions. These are currently neglected as was mentioned earlier. Figure 16 shows lines of constant Mach number in the symmetry plane of the flow past the typical spacecraft nose. A thick shock layer is seen wrapped around the nose. Note that the solution is rather sensitive to the size of the cells. Also, the same boundary conditions as for the flow past the cylinder has been applied at the external boundary of the computational domain, see figure 16. This assumption will be checked, in future. These calculations are currently being repeated on a CRAY-2 based on the complete three-dimensional shape of the vehicle nose. Future investigations will include real gas effects, and will look into the influence of the boundary conditions on the flow simulation.

4. CONCLUDING REMARKS

The present paper describes results of the first steps made in the direction of numerically simulating realistic hypersonic flow fields past three-dimensional configurations. In order to cover the entire hypersonic flow regime methods are needed for continuum as well as for gas-kinetic flow simulations. The results intentionally concern simple configurations, and are based on ideal-flow assumptions to validate the methods. For such cold hypersonic flows it is not easy to find recent detailed, well documented experiments which allow to check the performance of the methods with respect to e.g. heat transfer which is of major importance in the design of hypersonic vehicles. The experimental situation is even worse in the case of hot hypersonic flows where reactions occur, and of flows where continuum flow prevails but where rarefied flow effects must be considered at solid surfaces, or of flows with recombination taking place at surfaces. Realistic physical modelling is required in these situations, and needs to be incorporated in the existing flow simulation methods and codes. The only way to gain confidence into the usefulness of such modelling is by comparing the computational results with experimentally observed data. To achieve this for hot hypersonic flow, high-enthalpy facilities are badly needed which can simulate properly hypersonic free flight.

Here, ideal-gas assumptions allowed to check the performance of codes in the cold hypersonic flow regime based on fairly simple configurations. In the continuum-flow regime an implicit finite-difference method has been verified by comparing predicted and experimentally observed surface pressure and heat transfer data for the flow past blunted cones and past hemispheres. In the gas-kinetic-flow regime the Direct-Simulation Monte-Carlo (DSMC) approach is preferred to the more accurate Molecular-Dynamics method because of the larger computational efficiency. It is shown that the DSMC is as good as the other approach even with respect to the conservation of angular momentum in vortical flow, if the parameters of the method are chosen appropriately. As further test the flow past a cylinder has been chosen. Finally the flow about the nose of a typical spacecraft has been simulated with realistic free-stream conditions at $M_\infty = 12.2$ (continuum) and 25.5 (gas-kinetic flow). It is noted that due to the limitations with respect to the available computer resources the gas-kinetic flow simulation actually considers only one layer of flow encompassing the symmetry plane of the body. Currently computations are under way on a CRAY-2 computer to perform fully three-dimensional simulations and to study the mesh dependency of the solutions.

The next steps in the development of the simulation codes will concern the modelling of real gas effects and their implementation, including the gas-surface interaction. The modelling of transition and turbulence in hypersonic flows is as important as in the conventional compressible flows. All these features are necessary ingredients for the successful application of prediction methods in the design of hypersonic vehicles. When extending the work to realistic, more complicated configurations, flexible grid generation methods are required.

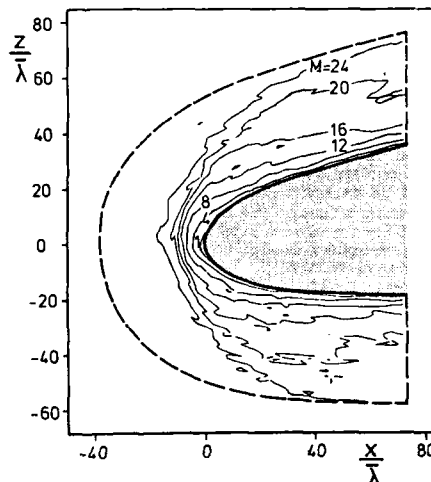


Figure 16: Lines of constant Mach number in the gas-kinetic flow past a typical spacecraft nose. $M_\infty = 25.5$, $T_w = 1043$ K, $Kn = 0.08$, $\alpha = 0^\circ$.

5. REFERENCES

- [1] Langereux, P.: "Europe Aims for Space Independence". Aerospace America, Vol. 10, Special Report, February 1986.
- [2] DeMeis, R.: "HOTOL: the other Aerospaceplane". Aerospace America, pp. 10-12, July 1986.
- [3] Vogels, H.A.: "Von der Mikrosystemtechnik zum Raumtransporter Sänger II". Luft- und Raumfahrt, Jahrg. 7, Heft 4-86, S. 99-108, 1986.
- [4] Högenauer, E.: "Entwicklungstendenzen bei Raumtransportern". Luft- und Raumfahrt, Jahrg. 7, Heft 4-86, S. 109-117, 1986.
- [5] Williams, R.M.: "National Aero-Space Plane - Technology for America's Future". Aerospace America, pp. 18-22, November 1986.
- [6] Dwyer, D.L.; Kumar, A.: "Computational Analysis of Hypersonic Airbreathing Aircraft Flow Fields". AIAA Paper 87-0279, 1987.
- [7] Arrington, J.P.; Jones, J.J. (eds.): "Shuttle Performance: Lessons Learned". NASA CP 2283, 1983.
- [8] Chaussee, D.S.; Rizk, Y.M.; Buning, P.G.: "Viscous Computations of a Space Shuttle Flowfield". Springer Lecture Notes in Physics, Vol. 218, pp. 148-153, 1984.
- [9] Chaussee, D.S.: "High-Speed Viscous Flow Calculation About Complex Configurations". AGARD CP-412, Paper 29, 1986.
- [10] Candler, G.V.; McCormack, R.W.: "Hypersonic Flow Past 3-D Configurations". AIAA Paper 87-0480, 1987.
- [11] Shang, J.S.; Scherr, S.T.: "Navier-Stokes Solution of Flowfield Around a Complete Aircraft". AIAA Paper 85-1509-CP, 1985.
- [12] Srinivasan, G.R.; Nicolet, W.E.; Shanks, S.P.: "Viscous Hypersonic Flow Over Complex Bodies at High Angles of Attack". AIAA Paper 84-0015, 1984.
- [13] Vadyak, J.; Smith, M.J.; Schuster, D.M.; Weed, R.: "Simulation of External Flowfields Using a 3-D Euler/Navier-Stokes Algorithm". AIAA Paper 87-0484, 1987.
- [14] Miyakawa, J.; Takanashi, S.; Fujii, K.; Amano, K.: "Searching the Horizon of Navier-Stokes Simulation of Transonic Aircraft". AIAA Paper 87-0524, 1987.
- [15] Flores, J.; Reznick, S.G.; Holst, T.L.; Gundy, K.: "Transonic Navier-Stokes Solutions for a Fighter-Like Configuration". AIAA Paper 87-0032, 1987.
- [16] Gnoffo, P.A.; McCandless, R.S.; Yee, H.C.: "Enhancements to Program LAURA for Computation of Three-Dimensional Hypersonic Flow". AIAA Paper 87-0280, 1987.
- [17] Li, C.P.: "Chemistry-Split Techniques for Viscous Reactive Blunt Body Flow Computations". AIAA Paper 87-0282, 1987.
- [18] Gnoffo, P.A.; McCandless, R.S.: "Three-Dimensional AOTV Flowfields in Chemical Nonequilibrium". AIAA Paper 86-0230, 1986.
- [19] Chitsomboon, T.; Kumar, A.; Tiwari, S.N.: "Numerical Study of Finite-Rate Supersonic Combustion Using Parabolized Equations". AIAA Paper 87-0088, 1987.
- [20] Bruno, C.: "Non-equilibrium chemically reacting flows". VKI Lecture Series "Computational Fluid Dynamics" 1987-04, Brussels, March 1987.
- [21] Hirschel, E.H.: "Aerothermodynamische Probleme bei Hyperschall-Fluggeräten". Paper presented at the Jahrestagung der DGLR, München, Oct. 9-10, 1986 (see also MBB publication S/PUB/270).
- [22] Hornung, H.: "Laboratory Simulation of the Real Gas Effects of Reentry". ESA SP-265, pp. 13-19, 1986.
- [23] Sharma, S.P.; Park, C.: "A Survey of Simulation and Diagnostic Techniques for Hypersonic Nonequilibrium Flows". AIAA Paper 87-0406, 1987.
- [24] Koppenwallner, G.: "Fundamentals of Hypersonics: Aerodynamics and Heat Transfer". DFVLR-IB 222-84 A 08, Febr. 1984.

- [25] Bird, G.A.: "Low Density Aerothermodynamics". AIAA Paper 85-0994, 1985.
- [26] Moss, J.N.; Cuda Jr., V.; Simmonds, A.L.: "Nonequilibrium Effects for Hypersonic Transitional Flows". AIAA Paper 87-0404, 1987.
- [27] Dogra, V.K.; Moss, J.N.; Simmonds, A.L.: "Direct Simulation of Stagnation Streamline Flow for Hypersonic Reentry". AIAA Paper 87-0405, 1987.
- [28] Moss, J.N.; Bird, G.A.: "Direct Simulation of Transitional Flow for Hypersonic Reentry Conditions". AIAA Paper 84-0223, 1984.
- [29] Meiburg, E.: "Direct Simulation Techniques for the Boltzmann Equation". DFVLR-FB 85-13, 1985.
- [30] Wetzel, W.; Oertel jr., H.: "Gas-Kinetical Simulation of Vortical Flows". To be published in Acta Mechanica, 1987.
- [31] Vinokur, M.: "An Analysis of Finite-Difference and Finite-Volume Formulations of Conservation Laws". NASA CR 177416, 1986.
- [32] Kordulla, W.: "Integration of the Navier-Stokes Equations in Finite-Volume Formulation". VKI Lecture Series "Computational Fluid Dynamics", 1987-04, March 1987.
- [33] Riedelbauch, S.; Müller, B.: "The Simulation of Three-Dimensional Viscous Supersonic Flow Past Blunt Bodies with a Finite-Difference Scheme". DFVLR-FB in preparation, 1987.
- [34] Kordulla, W.; Vollmers, H.; Dallmann, U.: "Simulation of Three-Dimensional Transonic Flow With Separation Past a Hemisphere-Cylinder Configuration". AGARD CP-412, Paper 31, 1986.
- [35] Müller, B.: "Navier-Stokes Solution for Hypersonic Flow Over an Indented Nosetip". AIAA Paper 85-1504-CP, 1985.
- [36] Müller, B.; Rues, D.: "Implicit Finite-Difference Simulation of Separated Hypersonic Flow Over an Indented Nosetip". Notes on Numerical Fluid Mechanics, Vol. 13, Vieweg Verlag, pp. 271-278, 1986.
- [37] Rizk, Y.M.; Chaussee, D.S.: "Three-Dimensional Viscous-Flow Computations Using a Directionally Hybrid Implicit-Explicit Procedure". AIAA Paper 83-1910, 1983.
- [38] Cleary, J.W.: "An Experimental and Theoretical Investigation of the Pressure Distribution and Flow Fields of Blunted Cones at Hypersonic Mach Numbers". NASA TN D-2969, 1965.
- [39] Cleary, J.W.: "Effects of Angle of Attack and Bluntness on Laminar Heating-Rate Distributions of a 15° Cone at a Mach Number of 10.6". NASA TN D-5450, 1969.
- [40] Beckwith, J.E.; Gallagher, J.J.: "Heat Transfer and Recovery Temperatures on a Sphere with Laminar, Transitional, and Turbulent Boundary Layers at Mach Numbers of 2.00 and 4.15". NACA TN 4125, 1957.
- [41] Bird, G.A.: "Molecular Gas Dynamics". Clarendon Press, Oxford, 1976.
- [42] Alder, B.J.; Wainwright, T.: "Molecular Dynamics by Electronic Computers". Proceedings of the Int. Symp. on Transport Processes in Statistical Mechanics, Interscience, New York, 1958.
- [43] Derzko, N.A.: "Review of Monte-Carlo methods in kinetic theory". UTIAS Review 35, 1972.
- [44] Bird, G.A.: "Monte-Carlo Simulation in an Engineering Context". AIAA Progress in Astronautics and Aeronautics: Rarefied Gas Dynamics, Vol. 74, Part 1, 1981.
- [45] Borgnakke, C.; Larsen, P.S.: "Statistical Collision Model for Monte-Carlo Simulation of Polyatomic Gas Mixtures". Journal of Computational Physics, Vol. 18, 1975.
- [46] Dewey, C.F.: "Correlation of Convective Heat Transfer and Recovery Temperature Data for Cylinders in Incompressible Flow". Int. J. Heat Mass Transfer, Vol. 8, 1965.
- [47] Crawford, D.R.; Vogenitz, F.W.: "Monte-Carlo Calculations of the Shock layer Structure on an Adiabatic Cylinder in Rarefied Supersonic Flow". In Rarefied Gas Dynamics, DFVLR Press, Porz-Wahn, 1974.

NUMERICAL EXPERIMENTS WITH HYPERSONIC FLOWS BENEATH A CONE-DELTA-WING COMBINATION

by

N. Qin, Research Student
and
B.E. Richards, Professor and Head of Department
Department of Aeronautics and Fluid Mechanics
University of Glasgow, Glasgow G12 8QQ, UK

SUMMARY

Numerical experiments of hypersonic flows beneath a cone-delta-wing combination have been carried out by solving the compressible Navier-Stokes equations using an assumption of local conicity. An implicit method is combined with a multigrid scheme in the solution procedure to achieve fast convergence to the steady state. Detailed flow field results provide further insight into the complex flow structures due to interaction between the cone shock and the wing shock and the interaction of the resulting flow with the wing or cone boundary layer. Flow field pictures reveal phenomena of value in the design of hypersonic lifting vehicles, such as the interference surface pressure and the high local wall heating. Comparisons with experimental data and conical Euler solution are also made.

LIST OF SYMBOLS

B	state vector
C _p	surface pressure coefficient, $(p_w - p_\infty) / (1/2) \rho_\infty V_\infty^2$, at r
c _p	specific heat at constant pressure
e	total internal energy
F	θ direction flux vector
G	ϕ direction flux vector
H	source term vector
k	thermal conductivity
M	Mach number
n	normal direction
Pr	Prandtl number, $c_p \mu / k$, 0.72
p	pressure
q	heat transfer rate
Re _{w,r}	Reynolds number, $\rho_\infty V_\infty r / \mu_\infty$
r	radial coordinate, measured from cone vertex
S _i	vector in governing equations
St	Stanton number, $ q_w / \rho_\infty V_\infty c_p (T_\infty - T_w)$
T	temperature
t	time
U	conservative vector
u	velocity in r direction
V	resultant velocity, $(u^2 + v^2 + w^2)^{1/2}$
v	velocity in θ direction
w	velocity in ϕ direction
α	angle of attack
γ	ratio of specific heats, 1.4
θ	coordinate, conical angle
μ	viscosity
ρ	density
τ_{ij}	stress tensor
ϕ	coordinate, circumferential angle, measured from windward symmetric surface
Δ, δ	increment
Δ_+, Δ_-	forward and backward finite differencing operator, respectively
Λ	delta wing leading edge sweep angle

Subscripts	
c	cone surface
i, j	value at (r, θ_i, ϕ_j)
t	derivative to time
w	wall value
o	stagnation value
i, j, k	pertaining to r, θ , ϕ , direction
∞	free-stream value
θ, ϕ	derivative to θ , ϕ , respectively

Superscripts	
n	time level
T	transpose

1. INTRODUCTION

A major step towards understanding the flow over general hypersonic vehicle shapes can be made by numerically predicting the flows over a simplified yet representative shape. The cone-delta-wing combination is such a shape in that simplification arises from assuming a locally conical flow, i.e., gradients in a radial direction can be ignored.

In early studies it had been expected that the interference effects on the windward side of a wing-body combination in high speed flows would favour lifting effectiveness. Lack of knowledge of 3-D shock-shock and shock-boundary layer interactions and difficulties in predicting the resultant separation, vortex flow and reattachment, however, did not allow the full exploitation of this benefit. Furthermore undesirable high local heating peaks were generated as a result of these interactions.

Attempts made two decades ago to understand these complicated flows involved surface measurement in supersonic and hypersonic flow beneath such simple geometries[1-3]. The small scale of experiments and the large scatter in the data, however, was so as to make it difficult to predict accurately, especially near the wing-body junction, the details of the surface pressure signature due to the vortex flows generated by the interactions and the resultant high local wall heating rates.

Work has been undertaken by the authors to further the knowledge of this complex flow field using numerical experiments by computer simulation. The unsteady compressible Navier-Stokes equations are solved using a locally conical flow assumption. The efficiency of the McCormack implicit finite difference method[4] was improved by combining it with a multigrid acceleration for steady state solutions[5].

In this paper the numerical method is outlined before giving detailed numerical results for the hypersonic flow beneath a cone-delta-wing combination chosen to have the same shape as that used in the experiment by Meyer and Vail[1]. Comparisons with these experimental results were made where possible. The numerical results for the above cases have been plotted out in detail to allow an understanding of the flow field and its effects on surface parameters. An Euler solution is also given to compare with the Navier-Stokes solution.

2. GOVERNING EQUATIONS AND NUMERICAL METHOD

2.1. The Locally Conical Navier-Stokes Equations and the Conical Euler Equations

The three-dimensional unsteady, compressible Navier-Stokes equations are first written in weak conservation form for a spherical polar coordinate system (r, θ, ϕ) . For supersonic and hypersonic viscous flows around conical bodies, it can be assumed that the gradients in the radial direction are much smaller than those in the crossflow direction. The validity of this "locally conical" approximation downstream from the nose region has been well established through experiment and computation even though a relatively large viscous region exists (e.g. see reference 6 and references therein). Applying this approximation, i.e. $\partial/\partial r = 0$, to all fluid quantities in the above equations, results in the following "locally conical" Navier-Stokes equations.

$$\frac{\partial U}{\partial t} + \frac{\partial F}{\partial \theta} + \frac{\partial G}{\partial \phi} + H = 0 \quad (1)$$

where

$$U = \sin\theta(B), \quad F = \sin\theta(vB - S_2), \quad G = (wB - S_3)$$

$$B^T = (\rho, \rho u, \rho v, \rho w, \rho e)$$

$$S_1^T = (0, \tau_{11}, \tau_{12}, \tau_{13}, -q_1 + u\tau_{11} + v\tau_{12} + w\tau_{13})$$

$$H = \sin\theta \begin{bmatrix} 2\rho u \\ 2\rho u^2 - \rho v^2 - \rho w^2 - (\tau_{11} + p) + (\tau_{22} + p) + (\tau_{33} + p) \\ 3\rho uv - \text{ctg}\theta(\rho w^2 + p) + \text{ctg}\theta(\tau_{33} + p) - 2\tau_{12} \\ 3\rho uw + \text{ctg}\theta\rho v w - \text{ctg}\theta\tau_{23} - 2\tau_{13} \\ 2u(\rho e + p) - u(\tau_{11} + p) - v\tau_{12} - w\tau_{13} \end{bmatrix}$$

$$\tau_{11} = -p - (2/3)(\mu/\text{Re}_{\infty, r})(2u + v_0 + v\text{ctg}\theta + w_0/\sin\theta)$$

$$\tau_{22} = 2(\mu/\text{Re}_{\infty, r})(v_0 + u) + \tau_{11}$$

$$\tau_{33} = 2(\mu/\text{Re}_{\infty, r})(w_0/\sin\theta + u + v\text{ctg}\theta) + \tau_{11}$$

$$\tau_{12} = \tau_{21} = (\mu/\text{Re}_{\infty, r})(-v + u_0)$$

$$\tau_{23} = \tau_{32} = (\mu/\text{Re}_{\infty, r})(w_0 - w\text{ctg}\theta + v_0/\sin\theta)$$

$$\tau_{31} = \tau_{13} = (\mu/\text{Re}_{\infty, r})(u_0/\sin\theta - w)$$

$$q_2 = -(1/2)(\mu/\text{Re}_{\infty, r}\text{Pr})T_0, \quad q_3 = -(1/2\sin\theta)(\mu/\text{Re}_{\infty, r}\text{Pr})T_0$$

The fluid properties, density ρ , velocity components u, v, w , internal energy e , pressure p , temperature T and the viscosity μ , in the above equations have been nondimensionalized with respect to ρ_∞ , V_∞ , V_∞^2 , $\rho_\infty V_\infty^2$, $T_0 - T_\infty$ and μ_∞ . The time t has been nondimensionalized by r/V_∞ correspondingly. Note that, for viscous flow, a length scale dependence remains and is contained in the Reynolds number, $Re_{\infty, r} = \rho_\infty V_\infty r / \mu_\infty$, which determines the location of a crossflow plane, r , in which a solution is computed.

The pressure is given by

$$p = (\gamma - 1) \rho (e - (u^2 + v^2 + w^2)/2)$$

and viscosity is accounted for by the Sutherland formula.

In the above locally conical Navier-Stokes equations if the viscous effects are neglected, i.e. $\mu = 0$, conical Euler equations result with

$$S_1 = \begin{bmatrix} 0 \\ 0 \\ -p \\ 0 \\ -vp \end{bmatrix}, \quad S_2 = \begin{bmatrix} 0 \\ 0 \\ 0 \\ -p \\ -wp \end{bmatrix}, \quad H = \sin \theta \begin{bmatrix} 2pu \\ 2pv^2 - pw^2 \\ 3puv - ctg \theta (\rho w^2 + p) \\ 3puw + ctg \theta \rho vw \\ 2u(\rho e + p) \end{bmatrix}$$

In contrast to the locally conical Navier-Stokes equations no length scale dependence remains in the conical Euler equations, which indicates that for high speed flows around conical shapes conical Euler equations describe strictly conical inviscid flow and the nonconicity is all introduced by the viscous effects.

2.2. An Implicit Scheme with Multigrid Acceleration

The basic integration scheme employed in this work is the two-step implicit method proposed by MacCormack[4]. We apply it to Eq. (1) in the following form.

Predictor:

$$\begin{aligned} \Delta U_{1,j}^n &= -\Delta t (\Delta F_{1,j}^n / \Delta \theta + \Delta G_{1,j}^n / \Delta \phi + H_{1,j}^n) \\ [I - (\Delta t / \Delta \theta) \Delta_+ [A^n]] [I - (\Delta t / \Delta \phi) \Delta_+ [B^n]] \delta U_{1,j}^{n+1} &= \Delta U_{1,j}^n \\ U_{1,j}^{n+1} &= U_{1,j}^n + \delta U_{1,j}^{n+1} \end{aligned} \quad (2)$$

Corrector:

$$\begin{aligned} \Delta U_{1,j}^{n+1} &= -\Delta t (\Delta F_{1,j}^{n+1} / \Delta \theta + \Delta G_{1,j}^{n+1} / \Delta \phi + H_{1,j}^{n+1}) \\ [I + (\Delta t / \Delta \theta) \Delta_- [A^{n+1}]] [I + (\Delta t / \Delta \phi) \Delta_- [B^{n+1}]] \delta U_{1,j}^{n+1} &= \Delta U_{1,j}^{n+1} \\ U_{1,j}^{n+1} &= (1/2)(U_{1,j}^n + U_{1,j}^{n+1} + \delta U_{1,j}^{n+1}) \end{aligned}$$

For further acceleration of the convergence to the steady state, a multigrid scheme is combined with the above implicit method in the solution procedure. Coarser grids are defined by successive deletion of every other line in each coordinate direction. The multigrid strategy used here is by sawtooth cycling. The coarse grid scheme is a one-step Lax-Wendroff explicit scheme expressed as distribution formulae in finite volume integration form by Ni[7]. In this application, the distribution formulae can be written as

$$\begin{aligned} \delta U_{1,j} &= (1/4) [\Delta U + \Delta t (\Delta F / \Delta \theta + \Delta G / \Delta \phi + \Delta H)]_a \\ &+ (1/4) [\Delta U + \Delta t (-\Delta F / \Delta \theta + \Delta G / \Delta \phi + \Delta H)]_b \\ &+ (1/4) [\Delta U + \Delta t (\Delta F / \Delta \theta - \Delta G / \Delta \phi + \Delta H)]_c \\ &+ (1/4) [\Delta U + \Delta t (-\Delta F / \Delta \theta - \Delta G / \Delta \phi + \Delta H)]_d \end{aligned} \quad (3)$$

where a, b, c and d represent the four control volumes surrounding the grid point (1, j).

Based on physical argument[8], the coarse grid scheme involves only inviscid Jacobians, the result of which makes the procedure more efficient. Therefore, in Eq. (3), we have

$$\Delta F = (\partial F_1 / \partial U) \Delta U, \quad \Delta G = (\partial G_1 / \partial U) \Delta U, \quad \Delta H = (\partial H_1 / \partial U) \Delta U$$

For stability a local variable time step, which is determined by the local inviscid stability condition, is used in the coarse grid scheme.

$$\Delta t = CFL \min[(\Delta \theta / (|v| + c)), \sin \theta \Delta \phi / (|w| + c)], \quad CFL \leq 1$$

The restriction and prolongation operators are respectively full-weighting average and bilinear interpolations.

The efficiency of the above numerical procedure was studied in Ref. [5]. Comparison with the corresponding MacCormack explicit method and effect of the multigrid schemes on convergence were investigated there.

3. RESULTS AND DISCUSSION

The cone-delta-wing configuration tested experimentally by Meyer and Vail[1] is chosen. Fig. 1 shows the sketch of the geometry and the solution plane. The conditions are

$$M_\infty = 12.65, Re_{\infty, r} = 3.78 \times 10^5, T_0 = 1800 \text{ K}, T_w/T_0 = 0.16, P_0 = 3.585 \times 10^7 \text{ N/m}^2, \theta_c = 12^\circ, \Lambda = 60^\circ$$

The computation is made at the spherical plane of $r = 3.7 \text{ in}$ corresponding to the experimental measurement. The mesh of 65×65 , illustrated in Fig. 2, is stretched in both θ and ϕ directions in such a way as to ensure sufficient resolution of the viscous effects. A three-level multigrid procedure is used. The initial flow field is set to the flow properties at infinity.

The boundary conditions supplied are:-

- a) on the wall: $u = v = w = 0$; $T = T_w = \text{constant}$ (isothermal wall)
- b) outer boundary: free stream values
- c) symmetric plane: reflection condition

For conical Euler solutions the wall no-slip boundary condition a) is replaced by tangency condition with $v = 0$ on the cone surface and $w = 0$ on the wing surface.

3.1. Angle of attack $\alpha = 0^\circ$

According to inviscid flow theory, flow at zero angle of attack is quite simple. In this case the free stream is aligned with the surface of the wing so no shock wave is generated by the wing. Part of the wing captures the high positive pressure of the cone shock layer and this so-called "inviscid interference pressure" produces an interference lift on the wing.

Unfortunately this is not the case in practice. Viscous effects complicate the flow field. Figs. 3-8 show the numerical results for this case. Fig. 3 presents the crossflow velocity vectors at each grid point and Fig. 4 gives a closer view near the junction. Figs. 5 and 6 show the crossflow Mach number and pressure contours (These contours are plotted in the rectangular computation grid instead of the curved physical grid due to lack of appropriate graphic software). Figs. 7 and 8 compare the surface pressure and heat transfer with the experimental data respectively.

The high pressure field of the cone shock layer interacts with the wing boundary layer, which results in separation on the wing. This is the major feature of the flow interaction, which is clearly shown in Figs. 3-8. The separated flow from the wing forms a very strong vortex, which reattaches first on the cone surface at A_1 and then on the wing surface at A_2 . Flow reattachment creates high local heating rates on the surface as seen in Fig. 8. A secondary vortex between the wing and the primary vortex is easily observed with reattachment at A_2 . The thick viscous layer beneath the wing interacts with the oncoming flow and a weak shock wave forms from the wing leading edge. The outer edge of the viscous layer and the weak shock wave are clearly illustrated in Fig. 5. This weak shock wave again interacts with the cone shock wave and a resulting strong internal shock wave appears clearly outside the primary vortex to decelerate further the high speed flow passing through the weak wing shock and deflecting it into the primary vortex. The internal shock curves inwards because of the influence of the wall as shown in Figs. 5 and 6. A shear layer resulting from the slip surface is seen lying between the shock-shock interaction point and the reattachment point A_1 in Fig. 5, which divides the flow processed by the cone shock from that by the wing shock.

With the flow field pictures in mind, the surface pressure distribution and the heat transfer to the wall become understandable. Comparison with the data of Meyer and Vail's surface pressure measurement is made in Fig. 7. The pressure spike at A_1 predicted by the numerical results aligns qualitatively with measurements at zero angle of attack as reported in [3]. Unfortunately Meyer and Vail[1] failed to give data in this region due to difficulties in measurement near the junction. The peaks in heat transfer corresponds to the reattachment points, A_1 , A_2 and A_3 , while the valleys to the separation points, S_1 , S_2 .

3.2. Angle of attack $\alpha = 5^\circ$

Figs. 9-14 illustrate the results of the numerical simulation of the case at an angle of attack of 5° using the same set of illustrations as for the $\alpha = 0^\circ$ case. At this small angle of attack, a number of its features as described for zero angle of attack are seen, but the effects on the surface parameters on the wing are more accentuated due to the interaction being more directed towards the wing. In the crossflow Mach contour, Fig. 11, the "three-shock configuration" is well represented and instead of a slip surface the shear layer between the shock-shock interaction point and the reattachment point A_1 is clearly seen. The shock resulting from the shock-shock interaction further interacts with the wing boundary layer and another internal shock emerges close to the junction due to influence of the wall. This internal shock directs the strong crossflow to roll through the junction into a strong primary vortex beneath the wing.

Significant is the appearance of a vortex rolling up from the cone surface, which is not seen in the zero angle of attack case. This vortex is seen more prominently in the $\alpha = 15^\circ$ case to be described. It is seen from Fig. 13 that the predictions of the surface

pressure distribution agree well with the measurements of Meyer and Vail[1]. In Fig. 14 the heat transfer distribution agrees qualitatively with the experimental results, which was stated to be laminar, in identifying the peaks and the valleys but the level is obviously lower than the experimental data on the cone surface. At this stage this discrepancy is not understood.

3.4. Angle of attack $\alpha = 15^\circ$

Figs. 15-20 have an equivalent sequence as in the $\alpha = 0^\circ$ and 5° cases. Figs. 15-17 show crossflow features of the flowfield. At this high incidence, the flow structure is clearly different from those at zero and 5° angle of attack cases. From the crossflow velocity vector plot (Figs. 15 and 16), there is observed a narrow separation region beneath the wing and the high energy flow reattaches on the wing first instead of on the cone as in the previous cases. The main stream of this flow passes through the corner then reattaches on the cone surface. It meets the cone boundary layer and rolls up into a vortex. When the high energy flow passes through the corner, a small part of it divides and forms a small vortex near the junction. A secondary separation on the cone surface beneath the primary one can be identified in Figs. 16 and 20.

At this angle of attack, the wing shock wave becomes stronger and the difference in strength and intersection angle between the two shock waves is reduced. The two shock waves appear to merge into each other and the interaction only results in weak compression waves and a shear layer. The compression waves interact with the wing boundary, while the shear layer joins into the process of rolling up of the primary vortex.

The comparison of the wall pressure distribution is given in Fig. 19. The two high pressure peaks near the corner represents the two reattachment points of the high energy stream. Peaks in heat transfer distribution, Fig. 20, exhibit all the four reattachment points, A_1, A_2, A_3, A_4 , on the wall, two on the wing and two on the cone surface, while the valleys in heat transfer distribution are associated with the separation points, S_1, S_2, S_3, S_4 . These peaks and valleys are clearly results of the flow structure shown in Fig. 15-18. The discrepancy with experimental data appears larger in the level of heat transfer distribution at this higher angle of attack.

3.4. Euler solution

To illustrate the importance of viscous effects it is useful to compare the Navier-Stokes solution with the Euler solution. Figs. 21-24 show solution of the conical Euler equations for the 5° angle of attack case. It is not surprising to find that no vortex exists in the inviscid solution. The delta wing shock layer is much thinner than that in the viscous solution. The three shock configuration is clearly shown with a resulting shock reflected on the wing surface. The totally different flow structures produced by Navier-Stokes solutions and Euler solutions indicate the strong viscous effects in this problem.

4. CONCLUSIONS

Numerical simulation of hypersonic flow beneath a cone-delta-wing combination has been generated by solving the compressible Navier-Stokes equations using "locally conical" assumption. Illustrations derived from these solutions and comparisons with surface measurements and conical Euler solutions have resulted in the following conclusions.

- 1) Numerical simulations can provide considerable detail within the flow field and help understanding of the complex flow processes.
- 2) Various types of vortex flows resulting from the shock-shock and shock-boundary layer interactions dominate the flow beneath the combination. The comparison of the results with those from a conical Euler analysis indicates further that the windward flow is governed by viscous effects.
- 3) Surface pressure peaks near the junction are features at low angle of attack cases and very high aerodynamic heating rates are observed in all cases around the strong vortex reattachment points. The flow behaviour appears quite sensitive to the angle of attack, showing large difference between results at 0° and 15° angles of attack.
- 4) Reasonable agreement with surface pressure measurements provides validity of the locally conical assumption and the numerical method, while the discrepancy with the measurement in the level of heat transfer distribution, especially at high angle of attack, needs to be studied further.
- 5) The results give important guidance to design of high speed vehicles of the complex nature of aerodynamic loading and heating on surfaces.

ACKNOWLEDGEMENTS

This work was supported by a Postgraduate Scholarship of Glasgow University and an ORS award to the first author. The Glasgow University Computing Centre has provided the computing time on its ICL 2988 during this research. Excellent service from its staff is greatly acknowledged.

REFERENCES

- [1] Meyer, R.F. and Vail, C.F.: An Experimental Study of the Hypersonic Flow about a Particular Half-Cone-and-Delta-Wing Lifting Configuration.
NRC, NAE Aero Report LR-475, 1967.
- [2] Dunavant, J.C.: Heat Transfer to a Delta Wing-Half-Cone Combination at Mach Number of 7 and 10.
NASA TN D-2199, 1984.
- [3] Scheuing, R.A.: Outer Inviscid Hypersonic Flow with Attached Shock Waves.
ARS Journal, v 31, n 4, 1961, pp486-505.
- [4] McCormack, R.W.: A Numerical Method for Solving the Equations of Compressible Viscous Flow.
AIAA J, v 20, n 9, 1982, pp1275-1281.
- [5] Qin, N. and Richards, B.E.: Simulation of Hypersonic Viscous Flows around a Cone-Delta-Wing Combination by an Implicit Method with Multigrid Acceleration.
Lect Notes in Phys. v 287, 1986, pp528-532.
- [6] MacRae, D.S. and Hussaini, M.Y.: Numerical Simulation of Supersonic Cone Flow at High Angle of Attack.
AGARD-CP-247, High Angle of Attack Aerodynamics, 1979, paper 23.
- [7] Ni, R.H.: A Multiple Grid Scheme for Solving the Euler Equations.
AIAA J, v 20, n 11, 1982, pp1565-1571.
- [8] Johnson, G.M.: Multiple-Grid Convergence Acceleration of Viscous and Inviscid Flow Computations.
Appl Math Comp, v 13, 1983, pp375-398.

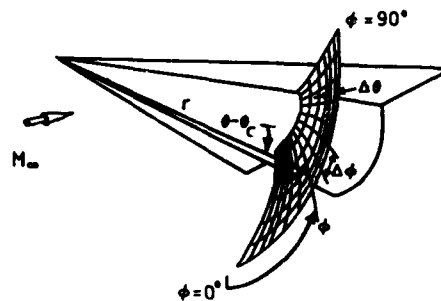


FIG. 1. GEOMETRY AND SOLUTION SURFACE

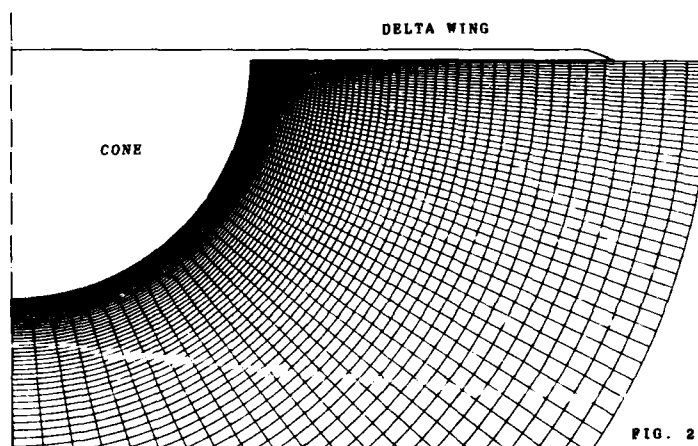


FIG. 2. COMPUTATIONAL MESH

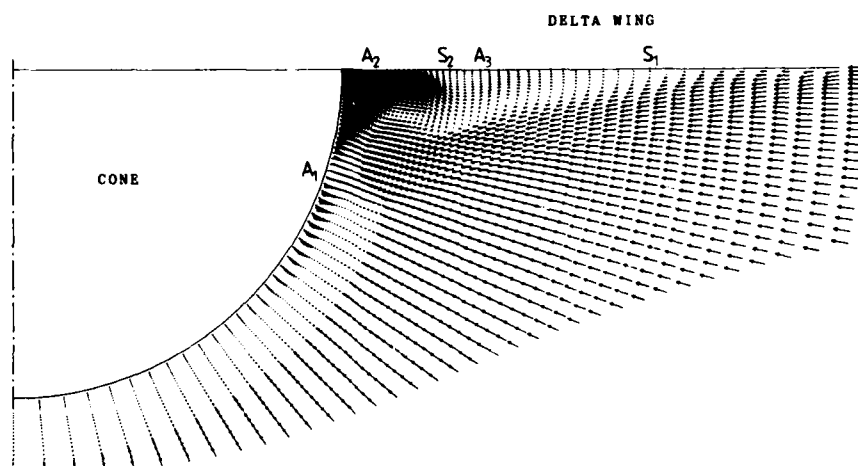


FIG. 3. CROSS FLOW VELOCITY VECTORS
OVERALL VIEW, $\alpha = 0^\circ$, LOCALLY CONICAL NAVIER-STOKES SOLUTION(LCNSS)

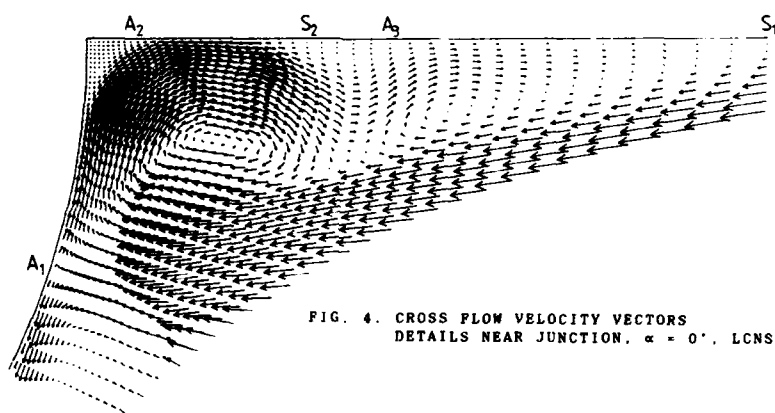


FIG. 4. CROSS FLOW VELOCITY VECTORS
DETAILS NEAR JUNCTION, $\alpha = 0^\circ$, LCNSS

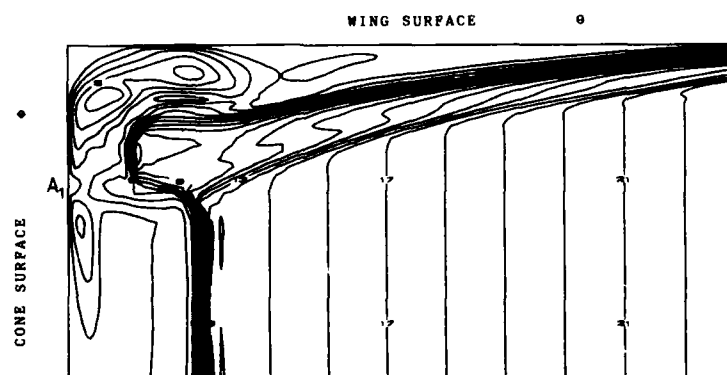
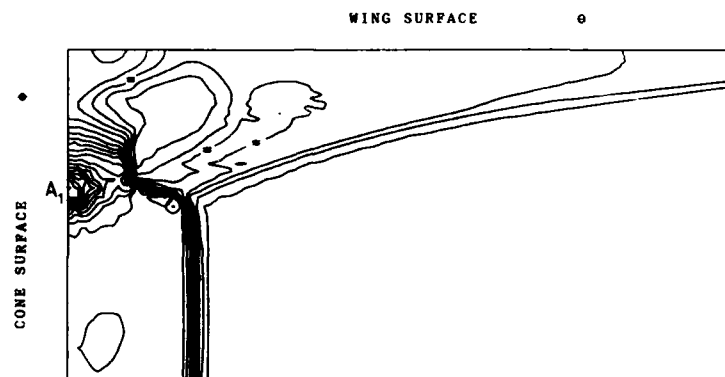
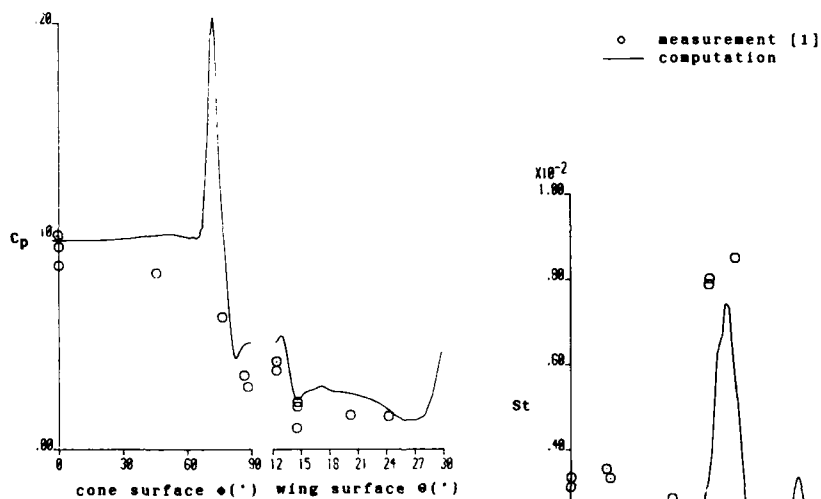
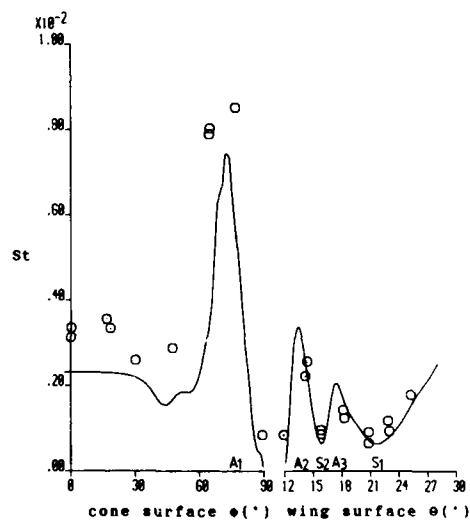


FIG. 5. CROSS FLOW MACH NUMBER CONTOURS, $\alpha = 0^\circ$, LCNSS

FIG. 6. PRESSURE CONTOURS, $\alpha = 0^\circ$, LCNSSFIG. 7. WALL PRESSURE DISTRIBUTION, $\alpha = 0^\circ$, LCNSSFIG. 8. HEAT TRANSFER DISTRIBUTION, $\alpha = 0^\circ$, LCNSS

$M_\infty = 12.65$, $Re_{\infty,r} = 3.78 \times 10^5$, $T_0 = 1800$ K, $T_w/T_0 = 0.16$, $P_0 = 3.585 \times 10^7$ N/m²
 Cone half angle $\theta_c = 12^\circ$, Delta wing leading edge sweep angle $\Lambda = 60^\circ$
 Angle of attack $\alpha = 0^\circ$

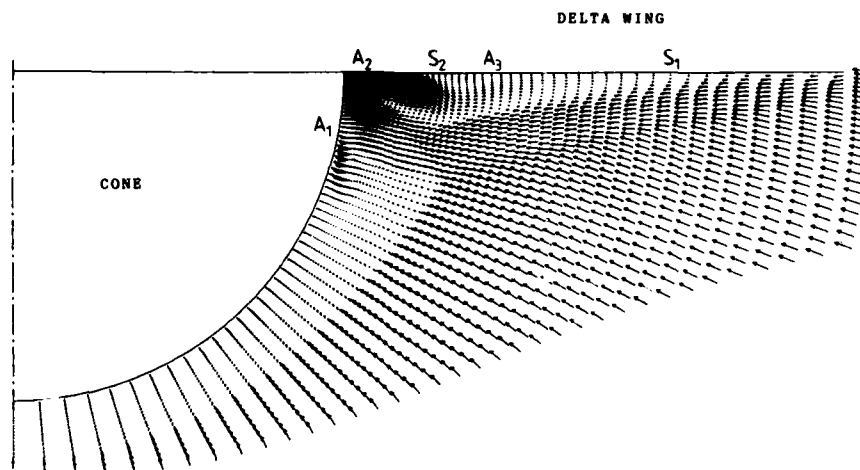


FIG. 9. CROSS FLOW VELOCITY VECTORS
OVERALL VIEW, $\alpha = 5^\circ$, LCNSS

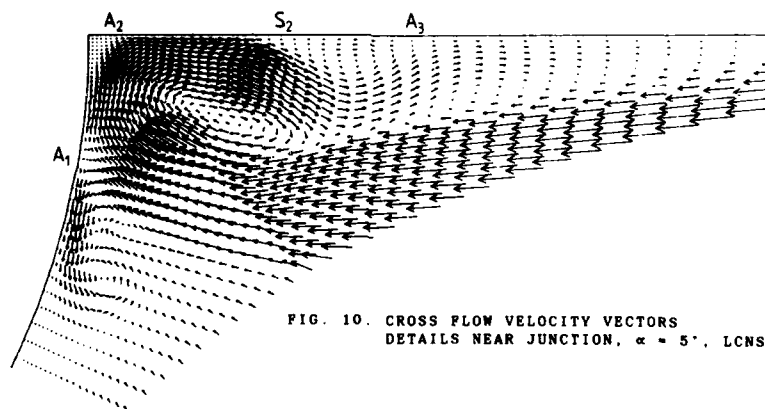


FIG. 10. CROSS FLOW VELOCITY VECTORS
DETAILS NEAR JUNCTION, $\alpha = 5^\circ$, LCNSS

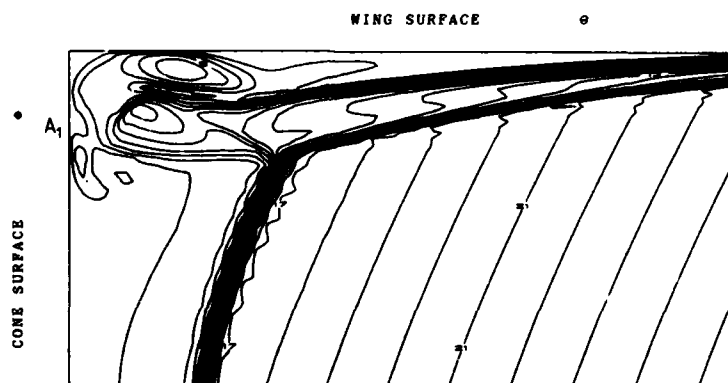
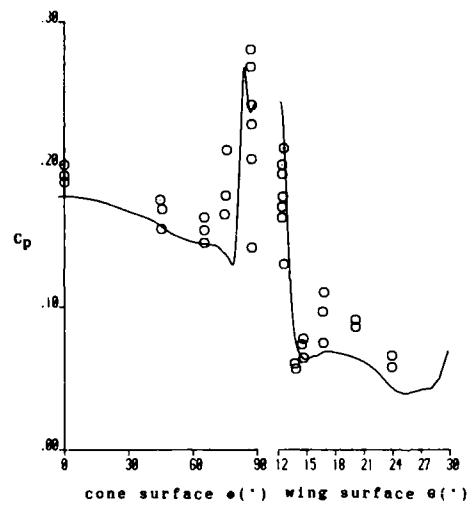
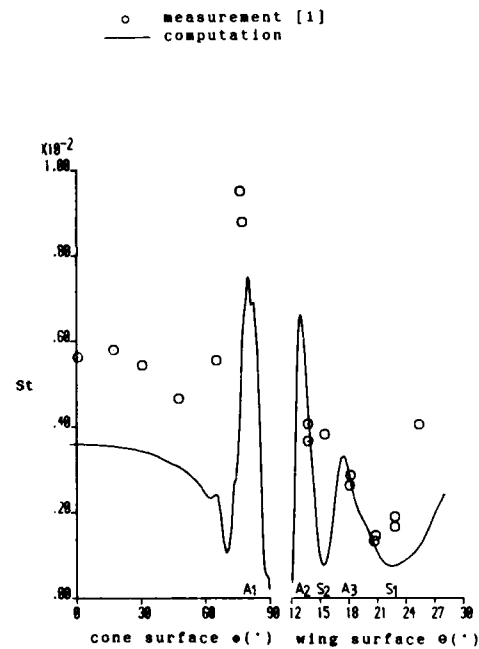


FIG. 11. CROSS FLOW MACH NUMBER CONTOURS, $\alpha = 5^\circ$, LCNSS

FIG. 12. PRESSURE CONTOURS, $\alpha = 5^\circ$, LCNSSFIG. 13. WALL PRESSURE DISTRIBUTION, $\alpha = 5^\circ$, LCNSSFIG. 14. HEAT TRANSFER DISTRIBUTION, $\alpha = 5^\circ$, LCNSS

$M_\infty = 12.65$, $Re_{\infty,r} = 3.78 \times 10^5$, $T_0 = 1800$ K, $T_w/T_0 = 0.16$, $P_0 = 3.585 \times 10^7$ N/m²
 Cone half angle $\theta_c = 12^\circ$, Delta wing leading edge sweep angle $\Lambda = 60^\circ$
 Angle of attack $\alpha = 5^\circ$

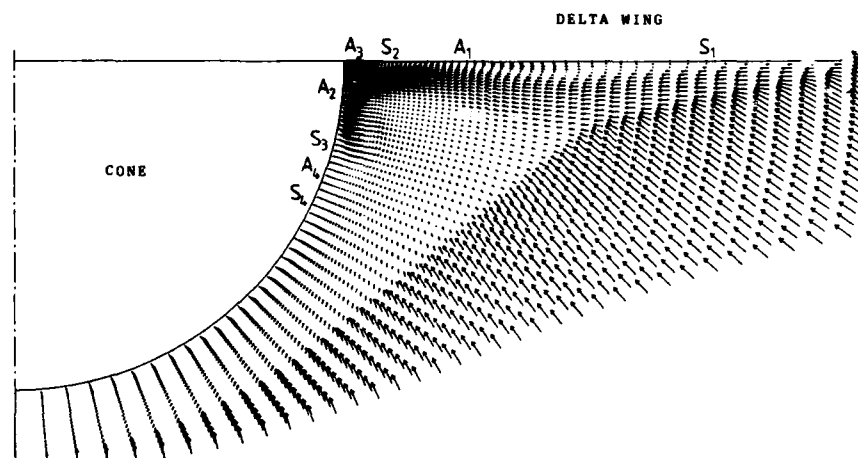


FIG. 15. CROSS FLOW VELOCITY VECTORS
OVERALL VIEW, $\alpha = 15^\circ$, LCNSS

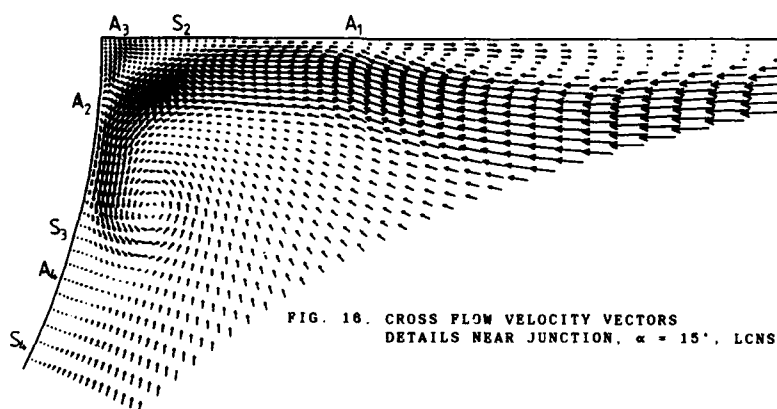


FIG. 16. CROSS FLOW VELOCITY VECTORS
DETAILS NEAR JUNCTION, $\alpha = 15^\circ$, LCNSS

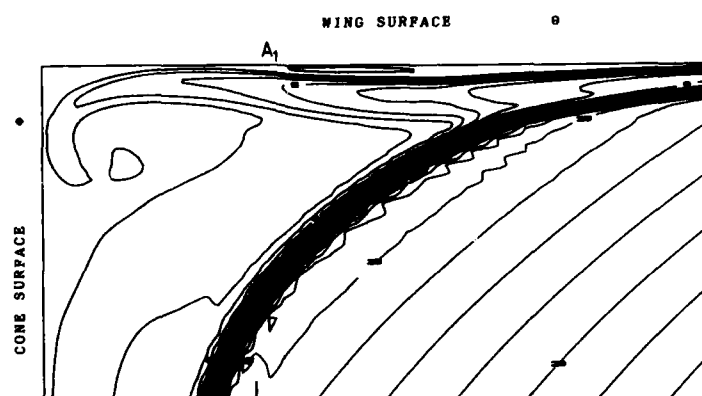
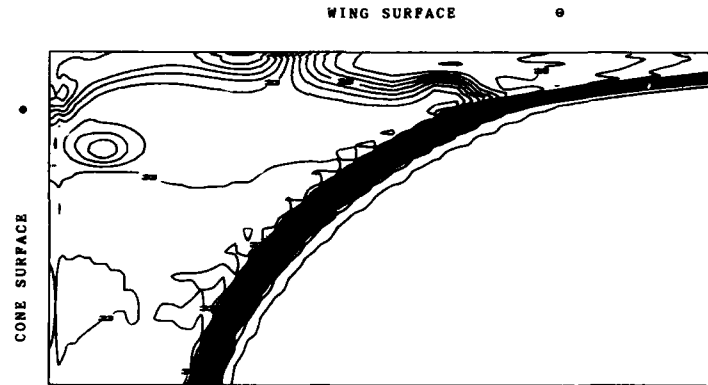
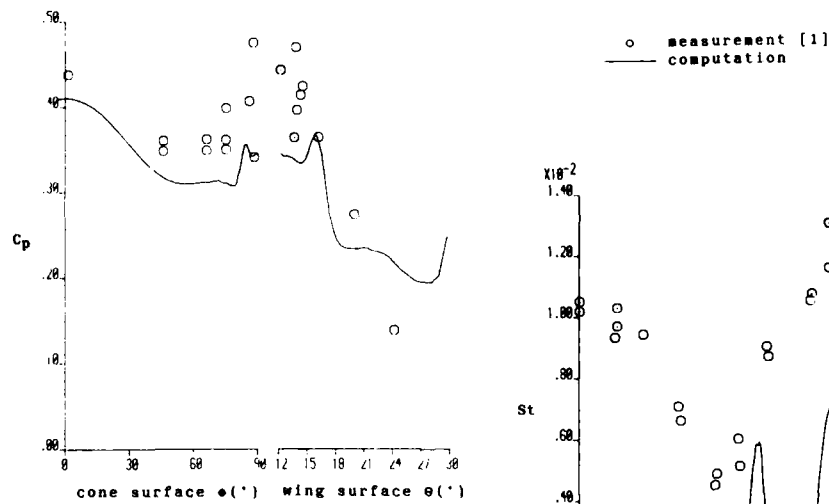
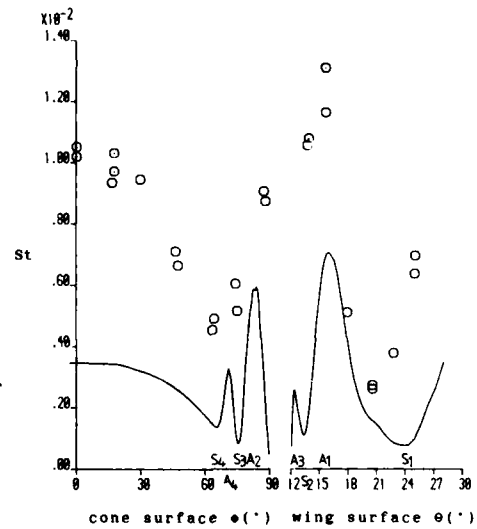


FIG. 17. CROSS FLOW MACH NUMBER CONTOURS, $\alpha = 15^\circ$, LCNSS

FIG. 18. PRESSURE CONTOURS, $\alpha = 15^\circ$, LCNSSFIG. 19. WALL PRESSURE DISTRIBUTION, $\alpha = 15^\circ$, LCNSSFIG. 20. HEAT TRANSFER DISTRIBUTION, $\alpha = 15^\circ$, LCNSS

$M_\infty = 12.65$, $Re_{\infty,r} = 3.78 \times 10^5$, $T_o = 1800$ K, $T_w/T_o = 0.16$, $P_o = 3.585 \times 10^7$ N/m²
 Cone half angle $\theta_c = 12^\circ$, Delta wing leading edge sweep angle $\Lambda = 60^\circ$
 Angle of attack $\alpha = 15^\circ$

DELTA WING

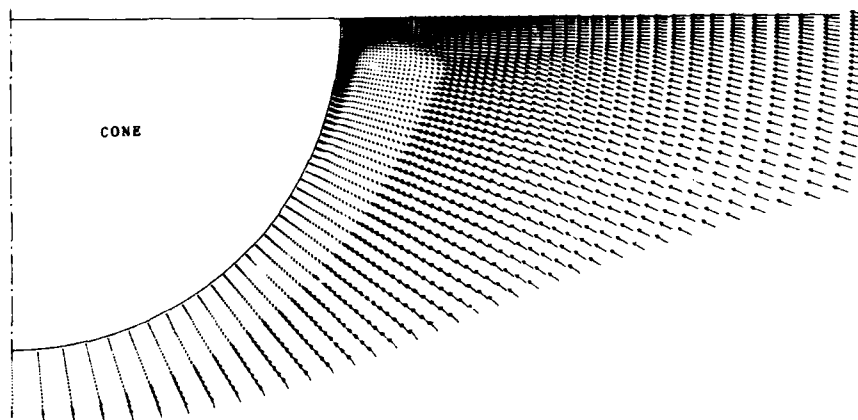


FIG. 21. CROSS FLOW VELOCITY VECTORS
OVER ALL VIEW, $\alpha = 5^\circ$, CONICAL EULER SOLUTION (CES)

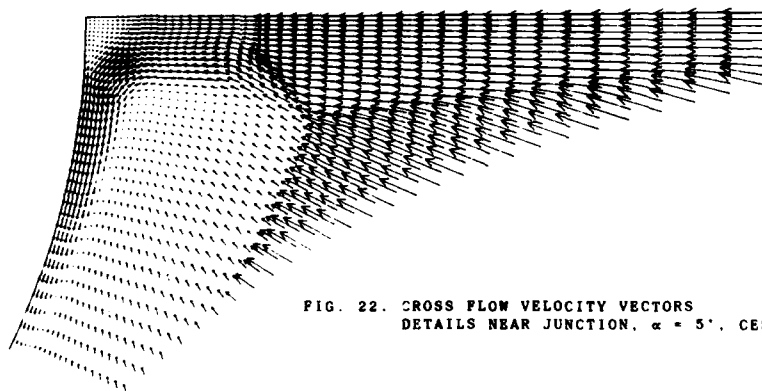


FIG. 22. CROSS FLOW VELOCITY VECTORS
DETAILS NEAR JUNCTION, $\alpha = 5^\circ$, CES

WING SURFACE

9

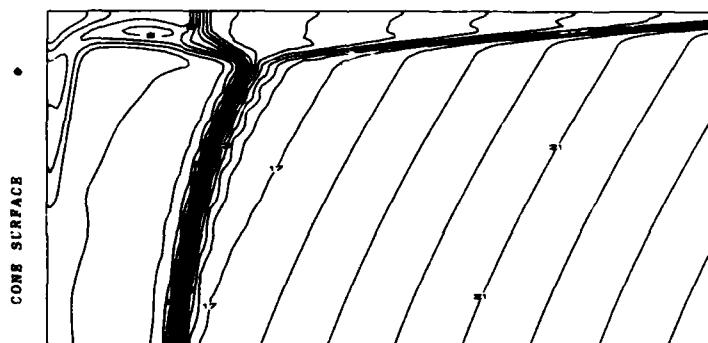


FIG. 23. CROSS FLOW MACH NUMBER CONTOURS, $\alpha = 5^\circ$, CES

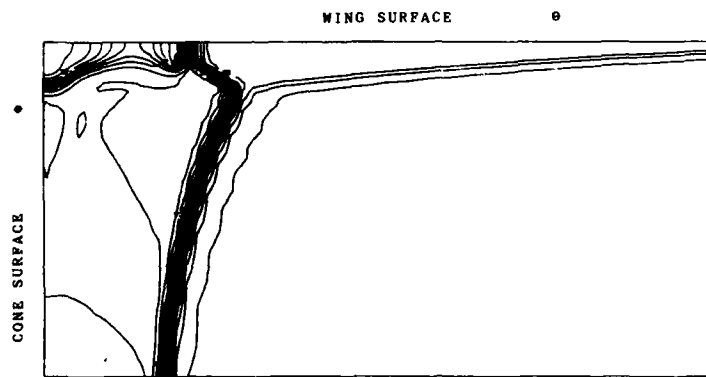


FIG. 24. PRESSURE CONTOURS, $\alpha = 5^\circ$, CES

A SPATIAL MARCHING TECHNIQUE FOR THE INVISCID BLUNT BODY PROBLEM *

R. T. Davis[†]

Professor of Aerospace Engineering
and Engineering Mechanics
University of Cincinnati
Cincinnati, Ohio 45221, USA

Frederick G. Blottner

Computational Aerodynamics Division 1556
Sandia National Laboratories
Albuquerque, New Mexico 87185-5800, USA

Summary

A technique has been developed for obtaining approximate solutions of the inviscid, hypersonic flow on a blunt body with a spatial marching scheme. The scheme introduces the Vigneron pressure gradient approximation into the momentum equation in the direction along the body surface. The resulting governing equations are hyperbolic. With a specified shock wave these equations are solved at the stagnation streamline with an iteration procedure and are solved in the downstream direction with a marching scheme. The complete Euler equations are solved with the numerical scheme when the flow is supersonic. A global iteration procedure is required to obtain the shock wave location. The approximate results from the spatial marching technique are compared with the complete solution of the Euler equations for flow over a sphere. The two results are shown to be in approximate agreement and the spatial marching technique provides useful engineering predictions while requiring considerable less computational time.

1 Introduction

In the nose region of a hypersonic reentry vehicle, the flow behind the shock wave is subsonic and the steady-state Euler equations describing the inviscid flow are elliptic. To avoid solving a system of nonlinear elliptic partial differential equations with a relaxation method, the standard solution method solves a finite-difference form of the time-dependent Euler equations. This approach requires hundreds of time steps to obtain the steady-state solution for the inviscid case but can require thousands of time steps when extended to viscous flows. A faster and more robust technique is needed for engineering design codes, especially when real gas properties are included.

Another technique for solving the blunt body problem is the thin viscous shock layer approach of Davis[1] where the normal momentum equation is simplified in order to allow a marching solution to be used. For an ogive in supersonic flow, Blottner[2] has shown that the thin viscous shock layer approach is not as accurate as a parabolized method where, in the tangential momentum equation, the pressure gradient is held constant across the shock layer and equal to the value at the shock wave. The standard solution technique used downstream on reentry vehicles where the flow is supersonic (except in the boundary layer) has become the parabolized Navier-Stokes approach.

The purpose of this paper is to present a new approach for solving the subsonic nose region with a spatial marching technique. With global iteration on the pressure field, the method can be modified to provide the complete solution of the Euler equations. For supersonic flow regions, the solution is obtained with one spatial marching sweep. The present work considers inviscid flow but the procedure can be extended to viscous flows. When the method is developed further, one code should be able to solve the complete flow field on a hypersonic vehicle. The initial solutions obtained would be approximate but with a reasonable number of global iterations the complete solution of the Navier-Stokes equations should be obtainable.

2 Theoretical Development

2.1 General Solution Procedure

A spatial marching solution technique is obtained by introducing the Vigneron condition for the pressure gradient in the momentum equation in the direction along the body surface. The Vigneron condition requires part of the pressure gradient to be specified depending on the local Mach number. When the Mach number is zero, the complete pressure gradient is specified while for supersonic flow the complete Euler equations are solved without any approximation for the pressure gradient. The Euler equations then become hyperbolic in the subsonic as well as the supersonic flow regions. The elliptic nature of the problem still remains in the boundary conditions at the shock wave and a marching technique requires that a shock shape be specified initially where the flow is subsonic. After each marched solution along the body, an iteration

*This work performed at Sandia National Laboratories supported by the U. S. Department of Energy under Contract No. DE-AC04-76DP00789.

[†]Deceased

on the shock wave location is required until the assumed shock location is the same as the calculated location. Beyond the sonic line where the flow is completely supersonic, the complete Euler equations are solved with a single downstream march. The initial conditions for the marching solution are obtained from the solution of the governing equations along the stagnation streamline where ordinary differential equations result. The elliptic properties of the problem also occur in the solution of these equations as downstream information on the shock shape and pressure field is needed.

The present solution procedure was introduced into a previously developed code for solving inviscid supersonic flow for the case of axisymmetric flow of a perfect gas. Significant changes and improvements have been made in the original code. A surface coordinate system was used in the previous work and is used in the present investigation. This coordinate system is more appropriate when considering viscous flows where the boundary layer terms are more readily included and higher-order terms can be neglected. In addition, with surface coordinates the Vigneron condition for pressure gradient is used only in the momentum equation along the body surface. There are several choices for the dependent variables available. The ones used in this study are the velocity components along and normal to the body surface, the pressure and the gas temperature. The governing partial differential equations are locally linearized and then are written in finite difference form using a box scheme. The difference equations for the governing equations plus the boundary conditions at the wall and shock wave give a system of equations that matches the number of unknown dependent variables. No numerical boundary conditions are required. This system of equations is of block tridiagonal form except the shock layer thickness appears as an additional unknown. This modified form of block tridiagonal equations is also readily solved. The governing equations are reduced to ordinary differential equations at the stagnation streamline and an iteration procedure is used to obtain the solution of the nonlinear governing equations. This solution is used to provide initial conditions for the marching solution along the body. At each marching step along the body, the solution is also iterated until the nonlinear difference equations are satisfied. The solution provides a new value of the shock layer thickness that must match the assumed value for a converged solution.

As a test of the validity and accuracy of the spatial marching technique, the hypersonic inviscid flow over a sphere at Mach number of 8.0 has been obtained. The spatial marching results are compared with the complete solution of the Euler equations to evaluate the present approach.

2.2 Governing Conservation Equations

The inviscid flow equations are written in surface coordinates with s the distance along the surface from the stagnation point and n the normal distance away from the surface. The velocity components are u and v and are in the s and n coordinate directions, respectively. The Euler equations are written in the following form:

s -Momentum

$$u \frac{\partial u}{\partial s} + H v \frac{\partial u}{\partial n} + \kappa u v + (1/\rho) \frac{\partial p}{\partial s} = 0 \quad (2.1)$$

n -Momentum

$$u \frac{\partial v}{\partial s} + H v \frac{\partial v}{\partial n} - \kappa u^2 + (H/\rho) \frac{\partial p}{\partial n} = 0 \quad (2.2)$$

Continuity

$$\frac{\partial(r\rho u)}{\partial s} + \frac{\partial(rH\rho v)}{\partial n} = 0 \quad (2.3)$$

Energy

$$u \frac{\partial H_T}{\partial s} + H v \frac{\partial H_T}{\partial n} = 0 \quad (2.4)$$

where the metric term $H = 1 + \kappa n$ and the radial distance $r = r_b + n \cos \theta_b$. The variable κ is the surface curvature, r_b is the radial distance from the body axis to the surface of the body and θ_b is the angle between the body surface and the body axis. The total enthalpy H_T is written in terms of the pressure p , the density ρ , and the total energy e which gives $H_T = (e + p)/\rho = h + \frac{1}{2}(u^2 + v^2)$ and for a perfect gas the specific enthalpy $h = (\frac{\gamma}{\gamma-1}) p/\rho$.

The variables are nondimensionalized with the freestream velocity V_∞ , freestream density ρ_∞ , and reference length L . The pressure is made nondimensional with $\rho_\infty V_\infty^2$. New coordinates are introduced

$$\xi = s/L \quad \text{and} \quad \eta = (n/L)/F \quad (2.5)$$

where $F = n_{sh}/L$ is the nondimensional distance from the body to the shock along a surface normal. The nondimensional transformed governing equations become

ξ -Momentum

$$F u \frac{\partial u}{\partial \xi} + \frac{F}{\rho} \frac{\partial p}{\partial \xi} + \phi \frac{\partial u}{\partial \eta} - (\eta F \xi / \rho) \frac{\partial p}{\partial \eta} + F u v \kappa = 0 \quad (2.6)$$

η -Momentum

$$F u \frac{\partial v}{\partial \xi} + \phi \frac{\partial v}{\partial \eta} + (H/\rho) \frac{\partial p}{\partial \eta} - \kappa F u^2 = 0 \quad (2.7)$$

Continuity

$$\frac{\partial(F r \rho u)}{\partial \xi} + \frac{\partial(r \rho \phi)}{\partial \eta} = 0 \quad (2.8)$$

Energy

$$F u \frac{\partial H_T}{\partial \xi} + \phi \frac{\partial H_T}{\partial \eta} = 0 \quad (2.9)$$

where $\phi = vH - u\eta F_\xi$ and the metric term $H = 1 + \kappa\eta F$. The foregoing governing equations can be used to solve for four dependent variables and the ones used in this investigation are the u and v velocity components, the pressure p , and the temperature T . The temperature is nondimensionalized with V_∞^2/c_p and for a perfect gas is obtained from $T = h = \left(\frac{\gamma}{\gamma-1}\right) p/\rho$. Therefore, wherever the density ρ appears in the governing equations, it is determined from and replaced with this relation.

The foregoing Euler equations are elliptic when the flow is subsonic and hyperbolic for supersonic flow. There are several techniques to change the properties of these equations so that a marching solution technique can be used when the flow is subsonic. The present approach is to modify the pressure gradient term $(\partial p/\partial \xi)$ in the s -momentum equation with the Vigneron condition which is expressed as

$$\frac{\partial p}{\partial \xi} = p'_\xi = \omega p_\xi + (1-\omega)p_\xi^0 \quad (2.10)$$

The pressure gradient p_ξ^0 is assumed known while the other part of the pressure gradient p_ξ is obtained as part of the solution procedure. It has been shown by Vigneron et al. [3] for the Cartesian form of these equations and by Prabhu and Tannehill [4] for the equations in generalized coordinates that ω can be chosen so that the eigenvalues are real and positive as long as there is no reverse flow. For this situation the equations are hyperbolic and can be solved with a marching technique. For the present set of equations with the Mach number $M_\xi = u/a$ and speed of sound $a^2 = \gamma p/\rho$, the Vigneron condition becomes

$$\omega = \gamma M_\xi^2 / [1 + (\gamma-1)M_\xi^2] \quad \text{where} \quad 0 < M_\xi < 1 \quad (2.11)$$

When the Mach number M_ξ is zero, the pressure gradient is completely specified by p_ξ^0 . When the Mach number $M_\xi \geq 1$, then $\omega = 1$ and the pressure gradient is completely determined from the solution. In the present solutions the part of the pressure gradient that is specified is evaluated at the shock wave since the pressure is known at this location. The specified pressure gradient is assumed to remain constant across the shock layer at constant ξ values. With the Vigneron condition employed, the resulting solution will be an approximate solution to the complete Euler equations. It appears feasible to use a global iteration procedure to include the complete pressure field into the final results. This item has not been considered in this paper. The present paper is concerned with an evaluation of the results obtained from the approximate form of the Euler equations.

2.3 Boundary conditions

At the body surface the velocity normal to the surface, v , is zero. At the shock wave the steady Rankine-Hugoniot relations provide equations to determine the dependent variables. These relations for the present coordinate system and for a perfect gas have been developed in previous work [2] and are given below

$$\begin{aligned} u_{sh} &= u_\infty + (v_\infty - v_{sh})\sigma \\ v_{sh} &= [v_\infty(\sigma^2 + 1/\rho_{sh}) + u_\infty(1 - 1/\rho_{sh})\sigma]/(1 + \sigma^2) \\ p_{sh} &= \frac{2}{\gamma+1} \left(\frac{M_{n\infty}}{M_\infty} \right)^2 \left[1 - \frac{\gamma-1}{2\gamma M_{n\infty}^2} \right] \\ T_{sh} &= \left(\frac{\gamma}{\gamma-1} \right) p_{sh}/\rho_{sh} \\ 1/\rho_{sh} &= \epsilon \left[1 + \frac{2}{(\gamma-1)M_{n\infty}^2} \right] \quad \text{where} \quad \epsilon = (\gamma-1)/(\gamma+1) \end{aligned} \quad (2.12)$$

In the above relations, the freestream velocity components are obtained from

$$u_\infty = \sqrt{1 - (G')^2} = \cos \theta_b \quad \text{and} \quad v_\infty = -G' = -\sin \theta_b \quad (2.13)$$

where the nondimensional body radius is $G = r_b/L$ and G' is the derivative of G with respect to ξ . The velocity component in the freestream that is normal to the shock is written as a normal Mach number and is obtained from the relation

$$M_{n\infty} = M_\infty(v_\infty - \sigma u_\infty)/\sqrt{1 + \sigma^2} \quad (2.14)$$

where $\sigma = \tan(\theta_{sh} - \theta_b) = F_\xi/(1 + \kappa F)$ and θ_{sh} is the shock angle relative to the body axis. If the flow properties γ and M_∞ are specified, the body properties κ and θ_b are given, and the shock shape (F and F_ξ) is assumed; then the dependent variables at the outer boundary can be determined from the foregoing shock relations.

An analytical approximation for the shock wave shape is presently being used and is written as

$$F = F_0 + \frac{1}{2}F_2\xi^2 + \frac{1}{4}F_4\xi^4 + \frac{1}{6}F_6\xi^6 + \dots \quad (2.15)$$

In the solutions that will be presented, the coefficients have been adjusted until the assumed shock layer thickness F obtained from this relation is approximately the same as that obtained from the solution of the governing equations. An automated iteration procedure for the shock layer thickness is not considered in this paper.

2.4 Body Geometry

The body geometrical relations are developed for an arbitrary case and are then specialized for a sphere. It is assumed that the radius of the body r_b is specified as a function of body axial distance z . In the governing equations, $G(\xi) = r_b/L$ is needed as a function of the surface distance $\xi = s/L$. The nondimensional radial distance becomes $r = G + F\eta\sqrt{1 - (G')^2}$. The derivative of the body radius with respect to surface distance is

$$G' = \pm \sqrt{1 - \left(\frac{dz}{ds}\right)^2} = \sin \theta_b \quad \text{where} \quad \frac{dz}{ds} = 1 / \sqrt{1 + \left(\frac{dr_b}{dz}\right)^2} \quad (2.16)$$

The surface curvature is

$$\kappa = -\frac{d\theta_b}{ds} = -\frac{d^2r_b}{dz^2} \left[1 + \left(\frac{dr_b}{dz}\right)^2\right]^{-3/2} \quad (2.17)$$

For a sphere with radius R_N , the axial distance z is related to the distance along the surface ξ by the relation $z = R_N[1 - \cos(\xi/R_N)]$ and the radial distance is $r = G(1 + \eta F/R_N)$. The body radius is

$$G = \sqrt{R_N^2 - (R_N - z)^2} = R_N \sin(\xi/R_N) = R_N \cos \theta_b \quad (2.18)$$

while the derivatives are

$$\frac{dr_b}{dz} = (R_N - z)/G \quad \text{and} \quad \frac{d^2r_b}{dz^2} = -\left[1 + \left(\frac{dr_b}{dz}\right)^2\right] / G \quad (2.19)$$

In the foregoing relations the reference length is taken as the nose diameter which gives $L = 2R_N$ and $R_N = 1/2$ for the nondimensional equations. In addition, the curvature is $\kappa = 1/R_N = 2$.

2.5 Governing Equations at the Stagnation Point

Initial conditions along the stagnation streamline are required to start marching the solution away from the stagnation point. The partial differential equations are reduced to a set of ordinary differential equations along the stagnation streamline. Assumptions are required to obtain a closed set of equations due to the elliptic properties of this problem. The nondimensional distance between the body and the shock wave and the geometrical relations near the stagnation point are expanded as follows:

$$F = F_0 + \frac{1}{2}F_{\xi\xi}\xi^2 + \dots, \quad z = \xi^2 - \dots, \\ G = \xi + \dots, \quad \text{and} \quad G' = 1 - \frac{1}{2}(\xi/R_N)^2 + \dots \quad (2.20)$$

where $F_\xi = 0$ and $F_{\xi\xi}$ is the second derivative of F at the stagnation point. The dependent variables are expanded as follows with $\theta = \xi/R_N$ where R_N is the nondimensional nose radius:

$$\begin{aligned} u &= u_1(\eta) \sin \theta + u_2(\eta) \sin^3 \theta + \dots &= u_1(\xi/R_N) + \dots \\ v &= v_1(\eta) \cos \theta + v_2(\eta) \cos \theta \sin^2 \theta + \dots &= v_1[1 - \frac{1}{2}(\xi/R_N)^2] + \dots \\ p &= p_1(\eta) \cos^2 \theta + p_2(\eta) \sin^2 \theta + \dots &= p_1[1 - (\xi/R_N)^2] + p_2(\xi/R_N)^2 + \dots \\ T &= T_1(\eta) \cos^2 \theta + T_2(\eta) \sin^2 \theta + \dots &= T_1[1 - (\xi/R_N)^2] + \dots \end{aligned} \quad (2.21)$$

The first and second order terms are given in the first form of the expansion. Several forms of the above expansions have been used by various authors as follows:

1. Ho and Prostein[5]: Use the second form of the expansion in Equation (2.21) which is the last column and use the first order terms except second-order pressure term is retained.
2. Kao[6]: Uses $\cos^2 \theta = 1$ in the pressure and temperature expansions. Includes p_2 term in first truncation solution.
3. Conti[7]: Uses above expansions and neglects p_2 in the first truncation.

The radial coordinate becomes $r = \xi H + \dots$ and gives the relations $r_\eta/r = \kappa F/H$ and $\xi r_\xi/r = 1 + \dots$ which are needed. Introduce the above expansions with $u_1 = R_N u_\xi$ into the governing equations (2.6) to (2.9) to obtain the following governing equations at the stagnation point where $v_1 = v$, $p_1 = p$ and $T_1 = T$:

$$Fu_\xi^2 + (F/\rho) \left(\frac{1}{\xi} \frac{\partial p}{\partial \xi} \right) + \phi \frac{\partial u_\xi}{\partial \eta} - (F_\xi/\xi)(\eta/r) \frac{\partial p}{\partial \eta} + Fu_\xi v \kappa = 0 \quad (2.22)$$

$$\phi \frac{\partial v}{\partial \eta} + (H/\rho) \frac{\partial p}{\partial \eta} = 0 \quad (2.23)$$

$$2F\rho u_\xi + \frac{\partial(\rho\phi)}{\partial \eta} + H(r_\eta/r)\rho v = 0 \quad (2.24)$$

$$\phi \frac{\partial H_T}{\partial \eta} = 0 \quad (2.25)$$

where $\phi = vH$. The dependent variable $u = 0$ at the stagnation point and is replaced with the velocity gradient u_ξ as an unknown. In the foregoing equations the elliptic character of the equations and boundary conditions are displayed by the terms

$$\frac{1}{\xi} \frac{\partial p}{\partial \xi} = p_{\xi\xi} \quad \text{and} \quad F_\xi/\xi = F_{\xi\xi} \quad (2.26)$$

in the ξ -momentum equation. These terms require information away from the stagnation point and across the shock layer in order to be evaluated. The second derivative of pressure at $\xi = 0$ from the above expansion gives

$$p_{\xi\xi} = -2[p_1(\eta) - p_2(\eta)]/R_N^2 \quad (2.27)$$

With $R_N = 1/2$, $p_2 = 0$ and $M_\infty = \infty$, the above equation becomes $p_{\xi\xi} = -16/(\gamma + 1)$.

Pressure and velocity behind the shock wave are evaluated by expanding the variables near the stagnation point which gives

$$\begin{aligned} u_\infty &= \xi/R_N + \dots \\ v_\infty &= -1 + \frac{1}{2}(\xi/R_N)^2 + \dots \\ \sigma &= 2\sigma_1\xi + \dots \\ M_{n\infty}^2 &= M_\infty^2 [1 - 4(1 - \sigma_1)^2\xi^2 + \dots] \end{aligned} \quad (2.28)$$

where $\sigma_1 = \frac{1}{2}F_{\xi\xi}/(1 + \kappa F)$. The first-order expansion coefficients in equations (2.21) for the region behind the shock wave become the following from the Rankine-Hugoniot relations (2.12):

$$\begin{aligned} u_1(1) &= 2R_N [1 - (1 + v_1)\sigma_1] \\ v_1(1) &= -[(\gamma - 1)M_\infty^2 + 2] / [(\gamma + 1)M_\infty^2] \\ p_1(1) &= [2\gamma M_\infty^2 - (\gamma - 1)] / [\gamma(\gamma + 1)M_\infty^2] \\ T_1(1) &= -[\gamma/(\gamma - 1)]p_1v_1 \end{aligned} \quad (2.29)$$

At the stagnation point these relations determine the dependent variables behind the shock wave. Once a shock wave is specified, $F_{\xi\xi}$ can be determined and σ_1 and u_ξ can be determined behind the shock wave. The second derivative of the pressure gradient behind the shock becomes $(p_{\xi\xi})_{sh} = -16(1 - \sigma_1)^2/(\gamma + 1)$. The variation of $p_{\xi\xi}$ across the shock layer can be determined by introducing an equation from the second truncation but this approach is not readily handled in the solution procedure. Two procedures have been investigated to approximate $p_{\xi\xi}$ as follows:

1. The second-order truncation term p_2 is neglected and with $p_1 = p$ the value of $p_{\xi\xi}$ is obtained from the expansion expression (2.27).
2. The stagnation solution is obtained by assuming $p_{\xi\xi}$ is the same for all η and equal to shock wave value. This technique is consistent with Vigneron pressure gradient approximation and is the approach that is used.

The boundary conditions for the governing equations at the stagnation point are $v = 0$ at the body surface and the Rankine-Hugoniot conditions (2.29) behind the shock wave. This gives five boundary conditions. Since the governing equations are first-order, four boundary conditions are sufficient to solve this system of equations for the four dependent variables u , v , p , and T across the shock layer. However, the shock layer thickness F appears in the governing equations and is unknown. Therefore, the additional boundary condition gives the necessary relation which allows the value of F to be determined.

3 Numerical Solution Procedure

3.1 Linearization of Steady Shock Wave Relations

Before the governing equations are considered, the shock wave equations (2.12) are linearized such that the unknown variables appear linearly. The shock wave relations are of the form $W = W(u_\infty, v_\infty, \gamma, M_\infty, \sigma, M_{n\infty})$. The freestream velocity components u_∞ and v_∞ are a function of $G' = \sin \theta_b$ and are known from the body geometry. The ratio of specific heats γ and the freestream Mach number M_∞ are also known from the freestream flow conditions. The shock slope relative to the body surface σ is a function of the shock wave shape which is unknown and the surface curvature κ which is known from the body geometry. The shock shape must be determined as part of the solution. This dependence on unknowns is expressed as $\sigma = \sigma(F, F_\xi)$. The normal Mach $M_{n\infty}$ is a function of M_∞ , u_∞ , v_∞ , σ and in terms of unknowns has the form $M_{n\infty} = M_{n\infty}(\sigma)$. Therefore, the shock wave relations are of the form $W = W(\sigma, M_{n\infty}) = W(F, F_\xi)$ and are linearized so that the unknowns F and F_ξ appear linearly.

Rather than using the dependent variables in the solution procedure, the delta form of the dependent variables is used and is expressed in vector notation as $\Delta W = [\Delta u \ \Delta v \ \Delta p \ \Delta T]^T$. The increment or delta form of a variable is defined as follows: $\Delta u = u - \bar{u}$ where u is the new value of the variable and \bar{u} is the initially assumed value of the variable or the value of the variable from a previous iteration. In addition, the shock layer thickness F and shock layer thickness derivative F_ξ are written in delta form which gives $\Delta F = F - \bar{F}$ and $\Delta F_\xi = F_\xi - \bar{F}_\xi$.

As a first step in the linearization of the shock wave relations, consider the linearization of σ and the normal Mach number relation (2.14) which gives

$$\Delta \sigma = a \Delta F_\xi - b \Delta F \quad \text{where} \quad a = 1/(1 + \kappa \bar{F}) \quad \text{and} \quad b = \kappa \bar{\sigma} a$$

$$\Delta M_{\infty} = -\beta \Delta \sigma \quad \text{where} \quad \beta = (\partial \bar{M}_{\infty} / \sqrt{1 + \beta^2} + M_{\infty} u_{\infty}) / \sqrt{1 + \beta^2} \quad (3.1)$$

The next step is linearization of the dependent variables which gives $W_{sh} = \bar{W}_{sh} + A \Delta \sigma + B \Delta M_{\infty}$ where $A = \partial W / \partial \sigma$ and $B = \partial W / \partial M_{\infty}$. With given values of the shock layer thickness \bar{F} and shock wave slope \bar{F}_ξ along with specified flow conditions and body geometry, the shock equations can be used to determine the flow variables behind the shock wave and are denoted as \bar{u}_{sh} , \bar{v}_{sh} , \bar{p}_{sh} , and \bar{T}_{sh} . The dependent variables behind the shock wave may initially have some other values u_{sh}^* , v_{sh}^* , p_{sh}^* , and T_{sh}^* . The new value of the variable can be expressed as $W_{sh} = W_{sh}^* + \Delta W_{sh}$ and the delta form becomes $\Delta W_{sh} = A \Delta \sigma + B \Delta M_{\infty} + (\bar{W} - W^*)$. The foregoing linearizations of σ and M_{∞} are used to obtain the linearized Rankine-Hugoniot shock relations

$$\Delta W_{sh} + d \Delta F + e \Delta F_\xi = S \quad (3.2)$$

where

$$\Delta W_{sh} = \begin{bmatrix} \Delta u_{sh} \\ \Delta v_{sh} \\ \Delta p_{sh} \\ \Delta T_{sh} \end{bmatrix} \quad d = \begin{bmatrix} d_1 \\ d_2 \\ d_3 \\ d_4 \end{bmatrix} \quad e = \begin{bmatrix} e_1 \\ e_2 \\ e_3 \\ e_4 \end{bmatrix} \quad S = \begin{bmatrix} S_1 \\ S_2 \\ S_3 \\ S_4 \end{bmatrix} = \begin{bmatrix} \bar{u}_{sh} - u_{sh}^* \\ \bar{v}_{sh} - v_{sh}^* \\ \bar{p}_{sh} - p_{sh}^* \\ \bar{T}_{sh} - T_{sh}^* \end{bmatrix}$$

For subsonic flow behind the shock wave, the shock layer thickness derivative F_ξ is held fixed and $\Delta F_\xi = 0$. Therefore, equation (3.2) is rewritten as

$$\Delta W_{sh} + D \Delta F = S \quad \text{where} \quad D = d \quad (3.3)$$

Although a new value of the shock layer thickness F is determined as the solution is marched along the body, the shock layer thickness derivative F_ξ is held constant in the shock relations. After the complete solution is obtained in the subsonic flow region, a new shock wave location is determined and the solution is marched again along the body. When the assumed shock thickness F is the same as the calculated shock layer thickness, a solution has been obtained to the Euler equations with the Vigneron pressure gradient approximation.

For supersonic flow behind the shock wave, the shock slope is calculated from

$$\frac{1}{2}(F_{\xi i} + F_{\xi i-1}) = (F_i - F_{i-1}) / \Delta \xi \quad \text{and linearization gives} \quad \Delta F_\xi = (2 / \Delta \xi) \Delta F \quad (3.4)$$

The coefficient D in equation (3.3) becomes $D = d + 2e / \Delta \xi$. In this case the shock wave location is determined as the solution is marched along the body and no global iteration is required. If the subsonic solution does not have a completely converged shock wave location, the supersonic solution will be influenced.

3.2 Difference Equations at Stagnation Point

The governing ordinary differential equations (2.22) to (2.25) are written in difference form with a mid-point scheme which is consistent with the properties of a system of first-order equations. Since the governing equations are nonlinear, the initial step is a local linearization of the equations so that the unknown dependent variables appear in linear form. Rather than solving for the dependent variables, the delta form of the dependent variables ΔW is used. In addition, at the stagnation point the shock standoff distance ΔF is unknown and must be included in the linearization process. The shock wave slope ΔF_ξ is zero and does not enter the problem at the stagnation point. The linearization of a typical term is performed as follows:

$$\phi u_\eta = \bar{\phi} \bar{u}_\eta + \bar{u}_\eta \Delta \phi + \bar{\phi} \Delta u_\eta \quad \text{and} \quad \Delta \phi = H \Delta v + \kappa \eta v \Delta F \quad (3.5)$$

The governing equations are replaced with difference equations at the point $j + 1/2$ where $\Delta \eta_j = \eta_{j+1} - \eta_j$. In the above relation, nondifferentiated variables such as $\bar{\phi}$ and $\bar{\phi}$ are evaluated with the averaging relation

$$w_{j+1/2} = (w_{j+1} + w_j) / 2 \quad (3.6)$$

while the derivatives \bar{u}_η and Δu_η use the mid-point difference relation

$$(w_\eta)_{j+1/2} = (w_{j+1} - w_j) / \Delta \eta_j \quad (3.7)$$

The four governing equations in difference form and using vector notation become

$$\bar{B}_j \Delta W_j + \bar{C}_j \Delta W_{j+1} + d_j \Delta F = S_j \quad j = 1, 2, \dots, J-1 \quad (3.8)$$

where \bar{C}_j and \bar{B}_j are 4×4 matrices and d_j is a column matrix with 4 elements. The dependent variables $W_{j=J}$ at the shock wave are known from the shock conditions while at the body surface the velocity normal to the surface $v_{j=1} = 0$.

The difference equations (3.8) for the governing equations and boundary conditions are rewritten in block tridiagonal form which can be easily solved. In the system of equations below the last equation normally does not occur, but with a slight modification of the usual tridiagonal solver the added equation is readily handled. The system of difference equations requiring solution at the stagnation point are

$$B_1 \Delta W_1 + C_1 \Delta W_2 + D_1 \Delta F = S_1 \quad (3.9)$$

$$A_j \Delta W_{j-1} + B_j \Delta W_j + C_j \Delta W_{j+1} + D_j \Delta F = S_j \quad j = 2, 3, \dots, J-1 \quad (3.10)$$

$$\Delta W_j + D_j \Delta F = S_j \quad (3.11)$$

$$f_{J-1} \Delta W_{J-1} + f_J \Delta W_J + D \Delta F = S \quad (3.12)$$

The four difference equations above each represent four equations as follows:

1. The boundary approximations (3.9) consist of the following:

The boundary condition $v = 0$.

The s-momentum, n-momentum, and energy equations at $j = 3/2$.

2. The difference equations (3.10) consist of the following:

The s-momentum, n-momentum and energy equations at $j + 1/2$.

The continuity equation at $j - 1/2$

3. The boundary approximations (3.11) consist of the linearized Rankine-Hugoniot relations which are given in equation (3.3).

4. The last difference equation is the continuity equation evaluated at $J - 1/2$. The continuity equation coefficients are f_{J-1} = third row of \bar{B}_{J-1} , f_J = third row of \bar{C}_{J-1} , D = third element of d_{J-1} , and S = third element of S_{J-1} .

If a shock wave shape (F_ξ) is assumed, then the above difference equations can be iterated to obtain the solution of the dependent flow variables u , v , p , and T . The shock layer thickness F also appears in the Rankine-Hugoniot relations and is treated as an unknown. In addition, as the solution is iterated the shock layer thickness F in the governing equations is treated as an unknown and is obtained in the solution procedure.

3.3 Difference Form of the Complete Equations

The governing equations (2.6) to (2.9) are replaced with a box difference scheme centered at the point $(i + \frac{1}{2}, j + \frac{1}{2})$ and where $\Delta\xi = \xi_{i+1} - \xi_i$ and $\Delta\eta = \eta_{j+1} - \eta_j$. The dependent variables W and shock wave parameters F and F_ξ are unknown at $i + 1$ and known at i but the shock wave parameters are held fixed where the flow is subsonic. The η -derivative terms are handled in the same manner as previously described for the stagnation point case. The terms must be averaged and this is illustrated as follows:

$$\phi u_\eta = \frac{1}{2} [(\phi u_\eta)_{i+1} + (\phi u_\eta)_i]_{j+\frac{1}{2}}$$

The first term in the bracket is linearized as done previously for the stagnation point problem while the second term is evaluated directly and is known. The ξ -derivative terms are evaluated, for example as

$$F u w_\xi = \frac{1}{2} [(F u w_\xi)_{j+1} + (F u w_\xi)_j]_{i+\frac{1}{2}}$$

The derivative terms are evaluated with mid-point relations which gives

$$(F u w_\xi)_{i+\frac{1}{2}, j} = \left(\frac{F_{i+1} + F_i}{2} \right) \left(\frac{u_{i+1} + u_i}{2} \right)_j \left(\frac{w_{i+1} - w_i}{\Delta\xi} \right)_j$$

The unknowns in this expression are F_{i+1} , u_{i+1} , and w_{i+1} and these variables occur nonlinearly. The resulting linearized relation in delta form is

$$F u w_\xi = (\bar{F} \bar{u})_{i+\frac{1}{2}} \bar{w}_\xi + \frac{1}{2} \bar{F}_{i+\frac{1}{2}} \bar{w}_\xi \Delta u + (\bar{F} \bar{u} / \Delta\xi)_{i+\frac{1}{2}} \Delta w + \frac{1}{2} \bar{u}_{i+\frac{1}{2}} \bar{w}_\xi \Delta F \quad (3.13)$$

The dependent variables that result from the differencing and linearization of the various terms in the governing equations are the flow variables Δu , Δv , Δp , and ΔT at the grid points $j + 1$ and j and the shock shape parameters ΔF and ΔF_ξ and all quantities are at $i + 1$. After further differencing of all the terms in the governing equations and linearizing the resulting difference relations, the difference equations for the governing equations become

$$\bar{B}_j \Delta W_j + \bar{C}_j \Delta W_{j+1} + d_j \Delta F + e_j \Delta F_\xi = S_j \quad j = 1, 2, \dots, J - 1 \quad (3.14)$$

This equation is the same form as that obtained at the stagnation point except ΔF_ξ now appears as an additional unknown. As discussed previously, $\Delta F_\xi = 0$ in the subsonic flow region and $\Delta F_\xi = (2/\Delta\xi) \Delta F$ in the supersonic flow region. With these relations used in the above difference equations (3.14), the resulting equations are combined with the boundary condition $v = 0$ and linearized shock relations to obtain the tridiagonal equations (3.9) to (3.12). At each marching step along the body, the tridiagonal difference equations are iterated several times which reduces the unknown dependent variables in delta form to very small values.

In the nose region where the flow is subsonic, the shock wave parameters F and F_ξ are fixed in the shock relations as the solution proceeds along the body. The shock wave is then moved and new values of F and F_ξ are assumed. This iteration is performed until the assumed shock parameters closely match the values calculated from the marching solution.

4 Numerical Results

The numerical procedure described above has been implemented into a computer code. Numerical predictions have been obtained for hypersonic flow at $M_\infty = 8$ over a sphere to illustrate the present solution technique and accuracy of the approximate solutions to the Euler equations. Presently the shock wave shape is approximated with an even degree polynomial as given by Equation (2.15) where three terms are used and the coefficients are adjusted to give close agreement between the assumed and calculated shock wave location. The assumed and calculated shock layer thickness F as a function of the nondimensional distance along the sphere surface, $s/D = \xi$ and D = sphere diameter, is given in Figure 1. Although

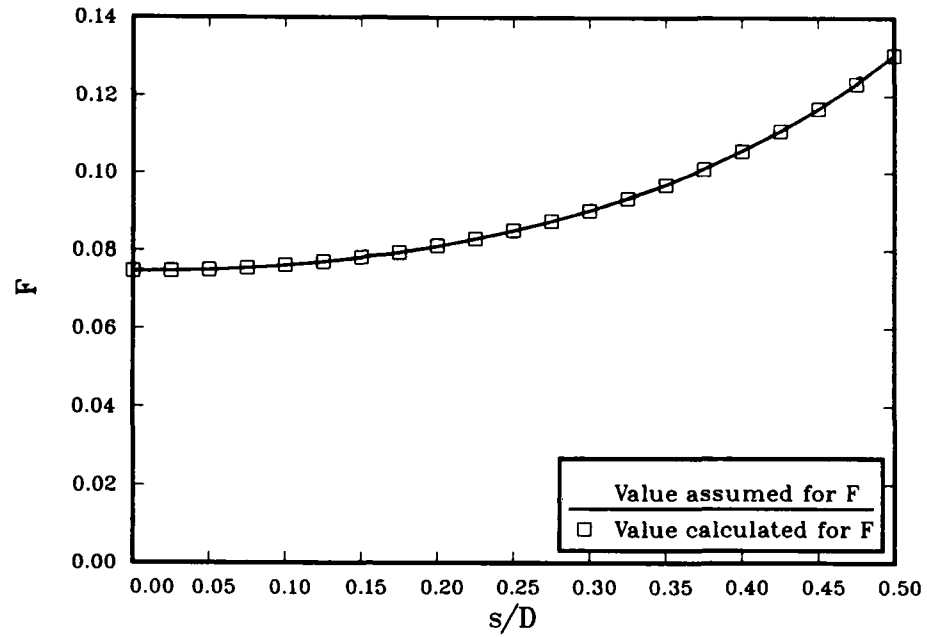


Figure 1: Comparison of assumed and calculated shock layer thickness F along the sphere for $M_\infty = 8$.

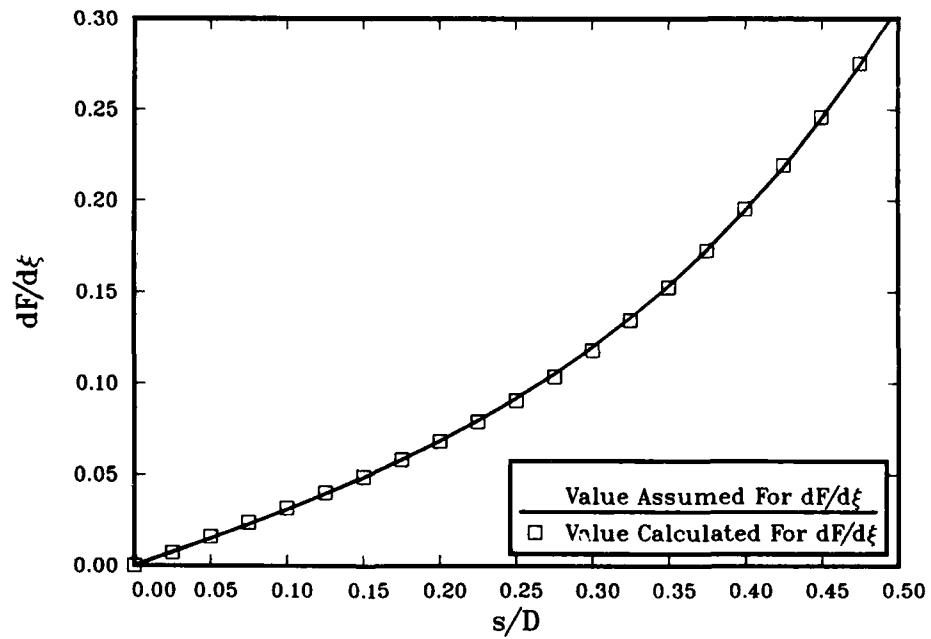


Figure 2: Comparison of assumed and calculated derivative of the shock layer thickness $dF/d\xi$ along the sphere for $M_\infty = 8$.

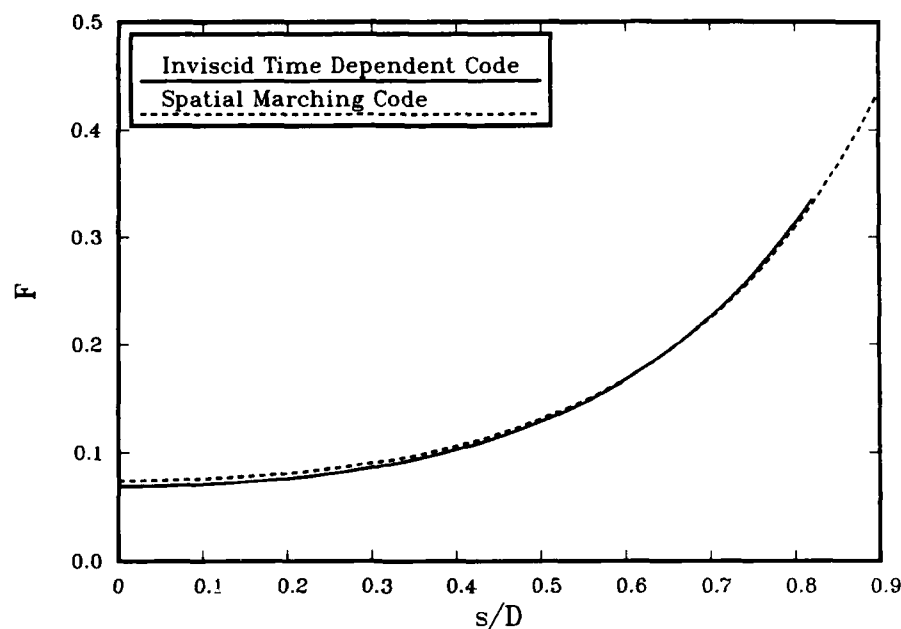


Figure 3: Comparison of the shock layer thickness F obtained from the spatial marching code and from an unsteady Euler code. Flow over a sphere with $M_\infty = 8$.

the curve and symbol appear identical, there are slight differences when the shock slopes $dF/d\xi$ are compared in Figure 2. A converged solution for the approximate governing equations is obtained when the assumed and calculated shock slopes $dF/d\xi$ are identical and the present result is close to a converged solution. For this case the coefficients in the shock wave polynomial are $F_0 = 0.074646$, $F_{\xi\xi} = 0.300$, $F_4 = 1.000$, and $F_6 = 1.000$. This solution was obtained with $\Delta\eta = 0.1$ and $\Delta\xi = 0.025$. For this case the complete Euler equations are solved when $\xi \geq 0.425$ and all of the flow is supersonic.

The present spatial marching code results are compared with steady-state results from an inviscid time dependent code[3] where the complete Euler equations are solved. The time dependent code solution is considered the exact solution for this blunt body problem while the spatial marching code gives an approximate solution due to the Vigneron condition for the pressure gradient. This comparison is made in Figures 3 to 5. As shown in Figure 3, the spatial marching code predicts a slightly thicker shock layer near the stagnation point as a result of the Vigneron condition for the pressure gradient. There is a 7.4 % difference in the two results at the stagnation point and the difference is less at other locations along the body. The derivative of the shock layer thickness is nearly the same from the two solutions as shown in Figure 4. The flow properties near the shock wave for the two cases are also nearly the same since these properties are obtained from the Rankine-Hugoniot relations which are mainly dependent on the value of $dF/d\xi$. The pressure ratio, p_b/p_∞ , along the sphere surface is given in Figure 5 with results from the two codes given.

5 Conclusions and Future Work

The results of this investigation show:

1. A spatial marching technique has been developed to solve the inviscid blunt body problem to obtain approximate solutions. When the complete solution procedure is developed for the Euler equations, it is anticipated that the spatial marching code will be as much as an order of magnitude faster than a time dependent code.
2. The results obtained from the inviscid governing equations with the Vigneron pressure gradient approximation are in reasonable agreement with the complete Euler equation results. This approach provides a good engineering prediction procedure for the hypersonic blunt body problem.
3. Further work is required to improve the iteration procedure used to move the shock wave and to add a global iteration procedure for the pressure so that, if desired, the complete Euler equations can be solved.

6 References

1. R. T. Davis, "Numerical solution of the hypersonic viscous shock-layer equations," AIAA J., vol. 8, May 1970, pp. 843-851.

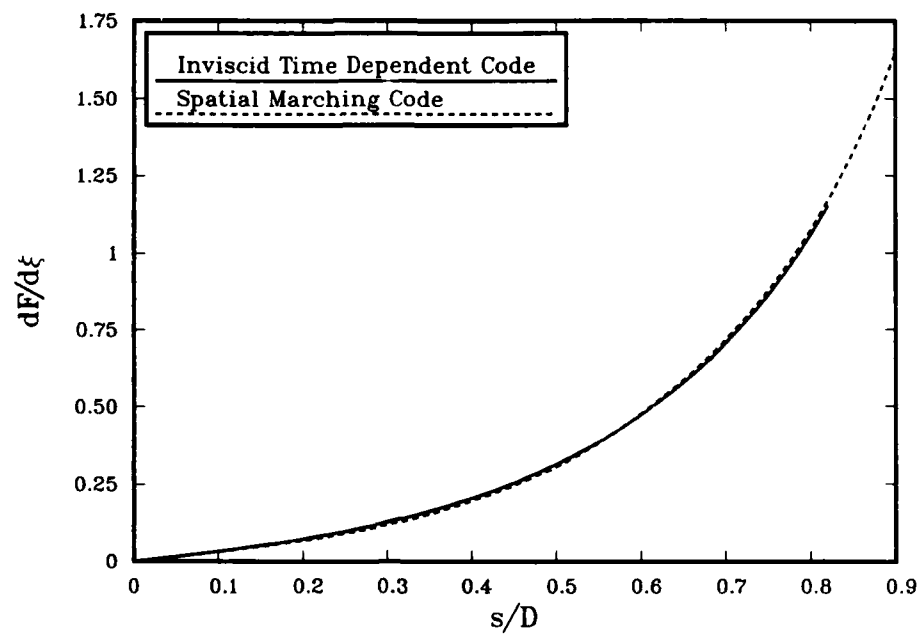


Figure 4: Comparison of the shock layer thickness derivative $dF/d\xi$ obtained from the spatial marching code and from an unsteady Euler code. Flow over a sphere with $M_\infty = 8$.

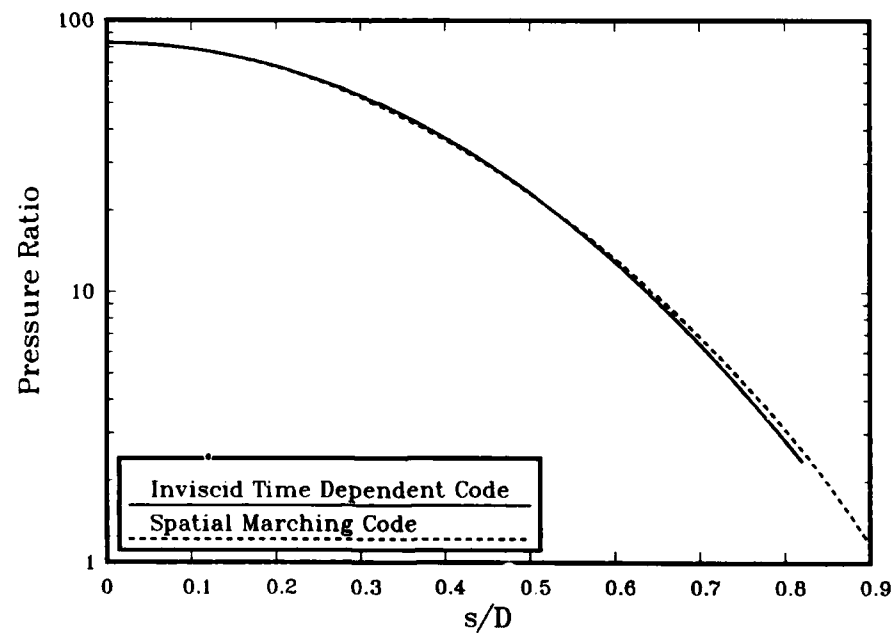


Figure 5: Comparison of surface pressure ratio p_s/p_∞ obtained from the spatial marching code and from an unsteady Euler code. Flow over a sphere with $M_\infty = 8$.

2. F. G. Blottner, "Exact and approximate solutions of the inviscid shock layer flow with an implicit finite-difference scheme," Sandia National Laboratories Report SAND78-0896, June 1978.
3. Y. C. Vigneron, J. V. Rakich, and J. C. Tannehill, "Calculation of supersonic viscous flow over delta wings with sharp subsonic leading edges," AIAA Paper No. 78-1137, July 1978.
4. D. K. Prabhu and J. C. Tannehill, "Numerical solution of space shuttle Orbiter flow field including real gas effects," Paper No. 84-1747, AIAA 19th Thermophysics Conference, June 25-28, 1984.
5. H. C. Kao, "Hypersonic viscous flow near the stagnation streamline of a blunt body: I. A test of local similarity," AIAA J., vol. 2, Nov. 1964, pp. 1892-1897.
6. H.-T. Ho and R. F. Probstein, "The compressible viscous layer in rarefied hypersonic flow," *Rarefied Gas Dynamics*, edited by L. Talbot, Academic Press, New York, 1961, pp. 525-552.
7. R. J. Conti, "A theoretical study of nonequilibrium blunt-body flows," J. Fluid Mech. vol. 24, part 1, 1966, pp. 65-88.
8. J. Daywitt, D. Brant, and F. Bosworth, "Computational technique for three-dimensional inviscid flow fields about reentry vehicles," SAMSO TR-79-5, April 1978.

3-D EULER SOLUTION FOR HYPERSONIC MACH NUMBERS

by

Michael Pfitzner and Claus Weiland
Messerschmitt-Bölkow-Blohm GmbH, Space Systems Group
Postfach 80.11.69
800 München 80, FRG

SUMMARY

The development of reusable re-entry vehicles and hypersonic missiles require the control of aerothermal problems. To that end it is necessary to develop new aerothermal prediction methods and to change and extend existing methods, which have been developed for sub- and supersonic flow problems.

In this paper we discuss the integration of the three-dimensional unsteady and steady Euler equations in the regime of hypersonic flow ($4 \leq M_\infty \leq 30$).

The formulation of the Euler equations in quasi-conservative form and the use of a third order upwind biased discretization formula guarantees an accurate and robust algorithm with good shock capturing capabilities. It is found, that with a procedure, where the strong bow shock is fitted and the imbedded shocks are captured, more accurate flow fields with less grid points can be achieved. Results are shown for flow fields around blunted cones with half-angles between $\delta = 0^\circ$ and 20° and angles of attack between $\alpha = 0^\circ$ and 30° for free stream Mach numbers up to $M_\infty = 30$. Also shown are results for a numerically defined forebody at $M_\infty = 8$ and $\alpha = 30^\circ$. At hypersonic Mach numbers real gas effects become important for $M_\infty \geq 4$. We discuss the generalization of the basic equations and of the upwind algorithm to deal with a general equation of state. For air the equilibrium equation of state can be calculated through existing Mollier - fit routines. The results of ideal gas calculations with isentropic exponent $\gamma = 1.4$ and $\gamma = 1.2$ are compared with real gas calculations using the effective γ approach and the full equations for a blunted cone at $M_\infty = 15$.

1. INTRODUCTION

The construction of reusable re-entry vehicles requires the simulation of hypersonic flow around complex geometries. In this flow regime the numerical simulation is of particular importance since the flow conditions cannot be reproduced fully in existing experimental facilities. The full simulation has to take into account the strong compression of air causing high temperature and real gas effects. In air different phenomena lead to departure from ideal gas behaviour in different temperature regimes [1, 2]:

- a) $T < 500^\circ\text{C}$:
- for low enough pressure air is a calorically perfect gas (constant specific heats)
- at higher pressures van der Waals forces occur and a general equation of state has to be used. This regime is not of particular importance for actual flight conditions.
- b) $500^\circ\text{C} \leq T \leq 2000^\circ\text{C}$:
The excitation of vibronic degrees of freedom causes the specific heats to become temperature dependent. The thermal equation of state is not changed ($Z \approx 1$) (thermally ideal gas)
- c) $2000^\circ\text{C} \leq T \leq 8000^\circ\text{C}$:
Dissociation of oxygen (2000°C - 5000°C) and nitrogen (5000°C - 8000°C) occurs and a general equation of state has to be used.
- d) $T > 8000^\circ\text{C}$:
The different species begin to ionize and a plasma forms. In typical re-entry trajectories the temperature normally does not reach 8000°C and therefore ionisation has not to be taken into account for these calculations.

The typical re-entry trajectory of the space shuttle touches the outer regions of the atmosphere at a height of 100 km [3] reaching a maximum Mach number of about $M_\infty = 30$ (Fig. 1) [3, 28]. With increasing height the Reynolds number decreases, leading to laminar flow above 60 km. In this region the bow shock is smeared out by viscous effects and the boundary layers are rather thick. At the body a slip boundary condition must be imposed as the mean free path of the molecules becomes comparable to the dimensions of the vehicle. The relaxation times for the rotational and translational degrees of freedom are so short that local equilibrium can be assumed for them. The characteristic times for the relaxation of vibration and for chemical reactions are comparable to typical flight times over the shuttle at a height $H > 50$ km. Nonequilibrium effects have to be taken into account in this region.

A complete numerical simulation of the flowfield in the upper atmosphere around a re-entry body requires the solution of the 3-D-Navier-Stokes equations including slip boundary conditions and chemical nonequilibrium effects. In spite of the rapid increase of computer power and memory during the last decades such a simulation would require at least 1-3 orders of magnitude more in speed and memory than exists today [4]. On the other hand, the solution of 3-D-Euler equations around complex geometries is well within reach of today's supercomputer technology and the use of a general equation of state increases the CPU time per step by only 30 % compared to ideal gas. Combination of a 3-D-Euler code with boundary layer codes with inclusion of real gas effects extends the region of applicability up to $M_\infty = 15$ ($H = 60$ km) without increasing the computer requirements beyond current limits.

The shuttle-like configurations, to which the code shall be applied, are rather blunt. For blunt bodies non-equilibrium effects are less important than for sharp-nosed bodies [5]. Therefore the range of applicability of the equilibrium code is greater for shuttle-like than for rocket-like configurations.

In this paper we describe a split-matrix finite difference algorithm to solve the 3-D instationary Euler equations in quasi-conservative form. We discuss the thermodynamic equations necessary for the inclusion of real gas effects. We derive the generalization of the algorithm to deal with a gas in equilibrium with a general equation of state. 2-D and 3-D calculation of hypersonic ideal gas flow around simple blunt forebodies and around a sharp-nosed rocket are presented. We show a comparison of ideal gas flow around a blunted cone at $M_\infty = 15$, $\alpha = 0^\circ$ with real gas calculations, where the real gas effects are approximated on different levels of accuracy (full equilibrium, effective γ , $\gamma = \text{const.} < 1.4$).

2. THERMODYNAMIC FORMULATION

The basic equations governing the inviscid flowfield describe the conservation of mass, momentum and energy. If one chooses the conservative variables

$$Q^T = (\rho, \rho u, \rho v, \rho w, e)^T,$$

these equations can be written as [6]:

$$\begin{aligned} \frac{\partial Q}{\partial t} + \frac{\partial F}{\partial x} + \frac{\partial G}{\partial y} + \frac{\partial H}{\partial z} &= 0 \\ F &= (\rho u, \rho u^2 + p, \rho uv, \rho uw, u(e + p))^T \\ G &= (\rho u, \rho vu, \rho v^2 + p, \rho vw, v(e + p))^T \\ H &= (\rho w, \rho wu, \rho wv, \rho w^2 + p, w(e + p))^T \end{aligned} \quad (1)$$

ρ : density
 u, v, w : cartesian velocity components
 e : total energy per unit of volume
 p : pressure

This system of equations is closed by a relation between the pressure and the dependent variables Q , which has to be derived from the thermodynamic equation of state. In thermodynamic equilibrium there are only two independent variables. Therefore there must be two equations connecting the four variables p (pressure), ρ (density), T (temperature) and e (thermodynamic energy per unit of mass). These equations are the caloric and the thermal equations of state.

The thermal equation of state for real gas can be written as [6].

$$p = \rho RT Z(\rho, T) \quad (2)$$

Z : compressibility factor
 R : gas constant at $T \rightarrow 0$

For non-dissociating and non-ionizing gases we have $Z \approx 1$ if the pressure is low enough that von-der-Waals-effects are not important. In this case the thermal equation of state for thermally ideal gas can be applied:

$$p = \rho RT \quad (3)$$

The caloric equation of state connects the internal energy e to the density and temperature and can be written in general as

$$e = e(\rho, T) \quad (4)$$

In a dilute non-dissociating and non-ionizing gas the energy does not depend on the density and we have

$$e = e(T) \quad (5)$$

$$e(T) = R \int c_v(T) dT$$

$c_v(T)$: specific heat at constant volume

Below 500 °C the specific heat in air is independent of temperature:

$$\begin{aligned} c_v &= 5/2 \\ e &= R c_v T \end{aligned} \quad (6)$$

and air behaves as thermally and calorically ideal gas ("perfect gas"). Above 500 °C molecular vibration can be excited, leading to a temperature dependence of c_v .

The thermal and caloric equations of state can be combined to give the desired expression connecting the pressure with density and energy:

$$p = \rho R T(\rho, e) Z(\rho, e) = p(\rho, e) \quad (7)$$

The internal energy e can be written in the flow variables through

$$e = \frac{\rho}{\rho} - 0.5 (u^2 + v^2 + w^2) \quad (8)$$

For perfect gas eq. (3) and (6) can be combined with the result

$$p = \frac{\rho e}{c_v} = \frac{1}{2} \left(e - \frac{1}{2} \rho (u^2 + v^2 + w^2) \right) \quad (9)$$

If we use the perfect gas relations

$$c_p = c_v + 1 \quad (10)$$

and

$$\gamma = \frac{c_p}{c_v} \quad (11)$$

γ : isentropic exponent

we get the familiar result

$$p = (\gamma - 1) \left(e - \frac{1}{2} \rho (u^2 + v^2 + w^2) \right) = (\gamma - 1) \rho e \quad (12)$$

The velocity of sound for real gases in the variables p, ρ is given by [7]

$$c^2(p, \rho) = \left(\frac{\partial p}{\partial \rho} \right)_s = \frac{(\partial h / \partial \rho)_p}{1/\rho - (\partial h / \partial p)_\rho} \quad (13)$$

$h = e + p/\rho$: specific enthalpy

If we define

$$\gamma_c = [\partial (\ln p) / \partial (\ln \rho)]_s$$

we have

$$c^2 = \gamma_c p / \rho \quad (14)$$

For perfect gases γ_c and $\gamma = c_p/c_v$ are identical, but this is not true for real gases, where γ_c is the more useful quantity. If we use the variables e, ρ , the velocity of sound c becomes

$$c^2(e, \rho) = \frac{p}{\rho^2} \left(\partial p / \partial e \right)_\rho + (\partial p / \partial \rho)_e \quad (15)$$

If the chemical composition of a mixture of diatomic and monatomic gases is frozen, γ_c (and γ) can have values between $9/7 \leq \gamma \leq 3/2$ depending on the ratio of diatomic and monatomic species and on the degree of excitation of molecular vibration.

The implementation of equilibrium gas equation of state in a Euler flow code requires the knowledge of $p(e, \rho)$, and also of $(\partial p / \partial \rho)_e$ and $(\partial p / \partial e)_\rho$ if the velocity of sound is needed by the algorithm. For air the pressure $p(e, \rho)$ can be extracted from tables [8-10] or from (Mollier-)fit routines [11-13]. The derivatives can then be calculated numerically. For application of the code to nozzle flow one can use a program like that in [14] to generate a table of pressures. Chemically frozen flow can be treated as ideal gas if one uses the appropriate value of ρ and subtracts out the frozen amount of internal energy ϵ_f from e .

The implementation of the full equilibrium thermodynamics should be preferable to the use of an effective γ [13] since in the latter case the derivatives of γ are not treated physically correct. The use of a constant effective $\gamma < 1.4$ may be sometimes justified especially if one is interested in pressure only [15, 16] and if execution time is critical. In practice the full equilibrium Euler code with a sophisticated fit routine [13] needs approximately 30 % more execution time than the corresponding ideal gas code.

The real gas effects in hypersonic flow change the pressure only by a small amount. For $M_\infty \rightarrow \infty$ the shock front and the streamlines behind the shock are nearly parallel to the body. In this limit the momentum of the gas normal to the body surface is zero behind the shock and the pressure is given by Newtonian impact theory [17]. Since the argument leading to Newtonian theory does not depend on the equation of state used, it should hold for ideal as well as for real gases. The main effect of the real gas effects is the "swallowing" of compression energy by internal degrees of freedom (vibration, dissociation). This leads to a decrease of the temperature and to an increase of density behind the bow shock in comparison to the ideal gas case.

3. ALGORITHM FOR SOLUTION OF THE 3-D INSTATIONARY EULER EQUATIONS

The basic equations governing the inviscid flow, eq. (1), have to be rewritten in generalized coordinates to be applicable to complex configurations. We introduce the coordinates

$$\begin{aligned} \xi &= \xi(x, y, z, t) \\ \eta &= \eta(x, y, z) \\ \zeta &= \zeta(x, y, z) \\ \tau &= t \end{aligned} \quad (16)$$

If shock fitting is applied, the ξ coordinate is time - dependent and ($\xi = 0, \xi = 1$) corresponds to the body and the shock surfaces, respectively. In a typical grid the coordinate η is roughly along the body axis and ζ represents a polar angle. The dependent variables are not transformed into the new coordinate system, i.e. cartesian velocity components (u, v, w) = (v_x, v_y, v_z) are used. Eq. (1) can then be written in the generalized coordinates:

$$Q_\tau + A Q_\xi + B Q_\eta + C Q_\zeta = 0 \quad (17)$$

with

$$K = a k_x + b k_y + c k_z + k_t$$

$$K = (A, B, C) \text{ für } k = (\xi, \eta, \zeta)$$

and

$$a = \frac{\partial F}{\partial Q}, \quad b = -\frac{\partial G}{\partial Q}, \quad c = -\frac{\partial H}{\partial Q}$$

A quasilinear form (eq. 17) of the Euler equations can be derived for any set of dependent variables Q (e.g. the primitive variables ρ, u, v, w, p). If one uses the conservative variables $Q = (\rho, \rho u, \rho v, \rho w, e)$ the formulation of the equations is called quasiconservative. In this case shock waves can be captured with the correct gain in entropy and with the correct jumps in pressure and density, as is shown later.

The matrices K in eq. (17) for ideal gas can be found in [6] for time independent metrics. If one uses a time dependent grid necessary for shock fitting, the term $k_t I$ (I = identity matrix) has to be added to K from [6]. The eigenvalues of the matrices are given by

$$\lambda_{1/2/3} = U_k$$

$$\lambda_4 = U_k + c |\nabla k|$$

$$\lambda_5 = U_k - c |\nabla k|$$

where

$$U_k = k_x u + k_y v + k_z w + k_t$$

$$|\nabla k| = (k_x^2 + k_y^2 + k_z^2)^{1/2}$$

$$k = (\xi, \eta, \zeta)$$

and

$$c = \left(\frac{\gamma p}{\rho} \right)^{1/2} \text{ (ideal gas)}$$

(Note the term k_t in U_k for time-dependent grid)

We can diagonalize the matrices K :

$$K = T_k A_k T_k^{-1}$$

with

$$A_k = \begin{bmatrix} \lambda_1 & & & 0 \\ & \lambda_2 & & \\ & & \lambda_3 & \\ 0 & & & \lambda_4 \lambda_5 \end{bmatrix}$$

T_k are the righthand eigenvectors and T_k^{-1} are the lefthand eigenvectors of K . Since K has three identical eigenvalues $\lambda_1 = \lambda_2 = \lambda_3$, the eigenvectors corresponding to these eigenvalues are not unique. They can, however, be chosen so that they are linearly independent and one explicit form of the eigenvector matrices T_k and T_k^{-1} can again be found in [6]. The eigenvector matrices are identical for time-dependent and time-independent grids.

The scheme used for the integration of the Euler equations, is based on the split matrix algorithm [18]. The diagonal matrix is split according to the sign of the eigenvalues

$$A_k^+ = \max(A_k, 0)$$

$$A_k^- = \min(A_k, 0)$$

and the corresponding matrices K^\pm are formed

$$K^+ = T_k A_k^+ T_k^{-1}$$

$$K = K^+ + K^-$$

We then write eq. (17) as

$$Q_t + A^+ Q_x^+ + A^- Q_x^- + B^+ Q_y^+ + B^- Q_y^- + C^+ Q_z^+ + C^- Q_z^- = 0$$

Stability of the algorithm (without the addition of damping terms) is achieved if the derivatives Q_x^+ and Q_x^- are discretized such, that the major portion of the stencil is on the upwind side. The discretization we use is an upwind-biased formula [22]

$$Q_x^\pm|_m = \pm \frac{1}{6\Delta\xi} (Q_{m+2} - 6Q_{m+1} + 3Q_m + 2Q_{m-1})$$

which is third order accurate. The formula is unconditionally stable as long as no shocks are present in the flowfield. To avoid oscillations at shocks a non-linear artificial diffusion term d of the MacCormack type [19] is applied

$$d = d_t + d_\eta + d_\zeta \quad (3.18) \quad (28)$$

$$d_k = \alpha_k \Delta k^3 (|U_k| + c) \frac{\partial}{\partial k} \left[\frac{|(\partial^2 p / \partial k^2)|}{4p} - \frac{\partial Q}{\partial k} \right]$$

$$\alpha_k = 0.5$$

This term is small in regions of smooth flow and becomes large near discontinuities. An explicit first order algorithm with local timesteps (except at a fitted shock) is used for the time integration to the steady shock.

At subsonic inflow or outflow boundaries one-dimensional characteristic boundary conditions with the primitive variables are used [6]. At impermeable wall k -boundaries the boundary condition is

$$U_k = 0$$

and the corresponding flux matrix becomes singular. That may cause problems in some cases and therefore the discretization for the flux matrix splitting is done halfway between the boundary point and the first meshpoint above it [21].

Since we want to use this scheme with a general equation of state to include equilibrium real gas effects, we have to rederive the flux matrices K together with their eigenvalues λ and left and right hand eigenvectors T_k , T_k^{-1} . To this end we assume that we have the pressure p as a function of density and internal energy ϵ as it can be calculated for equilibrium air e.g. from Mollier-type fits [11]. To derive the generalized matrices we start from the fluxes eq. (1), which are valid in the real gas case and use the general relation (8) which connects the internal energy ϵ to the total energy e .

The calculation of the matrices K with their eigenvectors and eigenvalues is straightforward, but very tedious when carried out by hand. The derivation was very much facilitated through the use of the REDUCE package [20], which is able to manipulate analytical expressions.

The generalization of the flux matrices K is

$$K = \begin{bmatrix} 0 & k_x & k_y & k_z & 0 \\ k_x \phi_R - u \theta_k & k_x u(1-\bar{p}_r) + \theta_k & k_x u - k_x \bar{p}_r v & k_x u - k_x \bar{p}_r w & k_x \bar{p}_r \\ k_y \phi_R - v \theta_k & k_y v - k_y \bar{p}_r u & k_y v(1-\bar{p}_r) + \theta_k & k_y v - k_y \bar{p}_r w & k_y \bar{p}_r \\ k_z \phi_R - w \theta_k & k_z w - k_z \bar{p}_r u & k_z w - k_z \bar{p}_r v & k_z w(1-\bar{p}_r) + \theta_k & k_z \bar{p}_r \\ (\phi_R - \frac{e+p}{\rho}) \theta_k & k_x (\frac{e+p}{\rho}) - \bar{p}_r u \theta_k & k_x (\frac{e+p}{\rho}) - \bar{p}_r v \theta_k & k_x (\frac{e+p}{\rho}) - \bar{p}_r w \theta_k & \theta_k (\bar{p}_r + 1) \end{bmatrix} + k, 1$$

with

$$\bar{p}_r = \frac{1}{\rho} \left(\frac{\partial p}{\partial \epsilon} \right)_\rho$$

$$c_R^2 = \frac{p}{\rho} \bar{p}_r + \left(\frac{\partial p}{\partial \rho} \right)_\epsilon \quad (30)$$

$$\phi_R = \bar{p}_r (u^2 + v^2 + w^2 - \frac{e+p}{\rho}) + c_R^2$$

$$\theta_k = k_x u + k_y v + k_z w$$

Its eigenvalues are as in the ideal gas case, but with the real gas speed of sound c_R inserted instead of the ideal gas one:

$$\lambda_{1/2/3} = U_k$$

$$\lambda_4 = U_k + c_R |\nabla k| \quad (31)$$

$$\lambda_5 = U_k - c_R |\nabla k|$$

In the ideal gas limit we get

$$\bar{p}_r \rightarrow (\gamma - 1)$$

$$c_R^2 \rightarrow \frac{\gamma p}{\rho} \quad (32)$$

$$\phi_R \rightarrow \frac{(\gamma - 1)}{2} (u^2 + v^2 + w^2)$$

The notation has been chosen to correspond as closely as possible to the one in ref. [6]. Note, however, that the expressions ϕ and γ in [6] cannot be simply replaced by ϕ_R and $(\bar{p}_r + 1)$.

The eigenvectors of K are again degenerate because of three identical eigenvalues. A form of the T_k , T_k^{-1} , which is as close as possible to these in [6] is

$$T_k = \begin{bmatrix} \hat{k}_x & \hat{k}_y & \hat{k}_z & 1 & 1 \\ u\hat{k}_x & u\hat{k}_y - \rho\hat{k}_z & u\hat{k}_z + \rho\hat{k}_x & (u+c_R\hat{k}_x) & (u-c_R\hat{k}_x) \\ v\hat{k}_x + \rho\hat{k}_z & v\hat{k}_y & v\hat{k}_z - \rho\hat{k}_x & (v+c_R\hat{k}_y) & (v-c_R\hat{k}_y) \\ w\hat{k}_x - \rho\hat{k}_z & w\hat{k}_y + \rho\hat{k}_z & w\hat{k}_z & (w+c_R\hat{k}_z) & (w-c_R\hat{k}_z) \\ \hat{k}_xE + \rho(v\hat{k}_z - w\hat{k}_y) & \hat{k}_yE + \rho(w\hat{k}_x - u\hat{k}_z) & \hat{k}_zE + \rho(u\hat{k}_y - v\hat{k}_x) & (\frac{c+p}{\rho} + c_R\hat{\theta}_k) & (\frac{c+p}{\rho} - c_R\hat{\theta}_k) \end{bmatrix}$$

$$T_k^{-1} = \begin{bmatrix} \hat{k}_x(1 - \frac{\phi_R}{c_R}) + \frac{1}{\rho}(w\hat{k}_z - v\hat{k}_y) & \hat{k}_x - \frac{u\hat{p}_x}{c_R} & \frac{\hat{k}_x}{\rho} + \hat{k}_z \frac{v\hat{p}_z}{c_R} & -\frac{\hat{k}_y}{\rho} + \hat{k}_z \frac{w\hat{p}_z}{c_R} & -\hat{k}_x \frac{\hat{p}_x}{c_R} \\ \hat{k}_y(1 - \frac{\phi_R}{c_R}) + \frac{1}{\rho}(u\hat{k}_z - w\hat{k}_x) & -\frac{\hat{k}_x}{\rho} + \hat{k}_y \frac{u\hat{p}_x}{c_R} & \hat{k}_y - \frac{v\hat{p}_z}{c_R} & \frac{\hat{k}_x}{\rho} + \hat{k}_y \frac{w\hat{p}_z}{c_R} & -\hat{k}_y \frac{\hat{p}_y}{c_R} \\ \hat{k}_z(1 - \frac{\phi_R}{c_R}) + \frac{1}{\rho}(v\hat{k}_x - u\hat{k}_y) & \frac{\hat{k}_y}{\rho} + \hat{k}_z \frac{u\hat{p}_x}{c_R} & -\frac{\hat{k}_x}{\rho} + \hat{k}_z \frac{v\hat{p}_z}{c_R} & \hat{k}_z - \frac{w\hat{p}_z}{c_R} & -\hat{k}_z \frac{\hat{p}_z}{c_R} \\ \beta(\phi_R - c_R\hat{\theta}_k) & \beta(c_R\hat{k}_x - u\hat{p}_x) & \beta(c_R\hat{k}_y - v\hat{p}_y) & \beta(c_R\hat{k}_z - w\hat{p}_z) & \beta\hat{p}_x \\ \beta(\phi_R + c_R\hat{\theta}_k) & -\beta(c_R\hat{k}_x + u\hat{p}_x) & -\beta(c_R\hat{k}_y + v\hat{p}_y) & -\beta(c_R\hat{k}_z + w\hat{p}_z) & \beta\hat{p}_y \end{bmatrix}$$

$$\begin{aligned} E &= \frac{(\phi+p)}{\rho} - \left(\frac{c_R^2}{\rho}\right) \\ \hat{k}_i &= k_i/|\nabla k| \\ \hat{\theta}_k &= \theta_k/|\nabla k| \\ \beta &= 1/2c_R^2 \end{aligned} \quad (35)$$

This completes the formulation necessary for calculation of supersonic flow with shock-capturing.

In the hypersonic flow regime the anticipated strength of the bow shock is such, that even in fully conservative schemes errors may occur in the flow variables behind the shock, especially if the shock contour is not aligned with a coordinate line. Therefore and since the anticipated shape of reentry bodies is sufficiently simple, a shock fitting procedure should be applied. Imbedded shocks, which are usually much weaker, can be captured without problems. With shock fitting (where applicable) usually a much smaller number of mesh points is needed to achieve the same level of accuracy, which is very important in 3-D calculations because of the limitation of computer resources.

The Rankine-Hugoniot equations of the shock moving with velocity D are

$$\begin{aligned} \rho(u_n - D) &= \rho_n(u_{n,n} - D) \\ \rho(u_n - D)\vec{u}_t &= \rho_n(u_{n,n} - D)\vec{u}_{t,n} \\ p + \rho(u_n - D)^2 &= p_n + \rho_n(u_{n,n} - D)^2 \\ \epsilon + \frac{p}{\rho} + \frac{1}{2}(u_n - D)^2 &= \epsilon_n + \frac{p_n}{\rho_n} + \frac{1}{2}(u_{n,n} - D)^2 \end{aligned} \quad (36)$$

D : velocity of shock
 u_n : flow velocity normal to shock
 \vec{u}_t : flow velocity tangential to shock

In addition to these 5 equations we need one equation describing the influence from the flowfield behind the shock. This equation depends on the timestepping scheme one uses. To derive this equation one multiplies the discretized eq. (26) by the left eigenvectors T_k^{-1} , picks out the equation corresponding to eigenvalue λ_k and collects all terms belonging to the new time level. We arrive at an equation of the form

$$\sum_{i=1}^5 T_{ki}^{-1} Q_i^{n+1} = R \quad (37)$$

R contains all terms coming from previous time levels and derivatives other than ξ . The components of the flow normal and tangential to the shock surface are

$$\begin{aligned} u_n &= (u\xi_x + v\xi_y + w\xi_z)/|\nabla\xi| \\ \vec{u}_t &= \vec{u} - u_n \nabla\xi/|\nabla\xi| \end{aligned} \quad (38)$$

The 6 equations can be solved so that only one equation containing the function $p(\rho, \epsilon)$ remains to be solved numerically. These equations are

$$\begin{aligned}
 Q &= \rho_\infty (u_\infty - D) \\
 q &= (t^{-1}_{22} \xi_1 + t^{-1}_{23} \xi_2 + t^{-1}_{24} \xi_3) / |\nabla \xi| \\
 R_\infty &= R(Q = Q_\infty) \\
 A &= \frac{1}{t^{-1}_{22}} (\rho q_\infty - R_\infty) + \rho D - p_\infty \\
 B &= \frac{1}{t^{-1}_{22}} (R - \rho q_\infty) - \rho D + p_\infty + \rho^2 / \rho_\infty \\
 C &= -\rho^2 / \rho_\infty \\
 \frac{\rho}{\rho_\infty} &= \frac{1}{2A} (-B \pm \sqrt{B^2 - 4AC}) \\
 c &= c_\infty \frac{\rho}{\rho_\infty} + \frac{1}{t^{-1}_{22}} (R - \frac{\rho}{\rho_\infty} R_\infty - (1 - \frac{\rho}{\rho_\infty}) \rho q_\infty) \\
 \left(\frac{\partial u}{\partial x} \right) &= \frac{\rho}{\rho_\infty} \left(\frac{\partial u}{\partial x} \right)_\infty + \left(\frac{\xi_1}{\xi_2} \right) \left(1 - \frac{\rho}{\rho_\infty} \right) \rho / |\nabla \xi|
 \end{aligned} \tag{39}$$

The equation which has to be solved for D numerically, is

$$p(\rho(D), \epsilon(D)) - p_\infty - \frac{\rho(D)^2}{\rho_\infty} \left(1 - \frac{\rho_\infty}{\rho(D)} \right) = 0 \tag{40}$$

The sign of the square root expression of ρ/ρ_∞ has to be chosen such that $\rho/\rho_\infty > 1$ is satisfied. A Newton algorithm is used to solve eq. (40) very efficiently.

In the implementation of the equilibrium real gas effects a modified version of the subroutine TGAS [11] is used, which calculates $p(\rho, \epsilon)$ and also c_R and \bar{p}_r . The flow variables are normalized such that $\rho_\infty = 1$, $p_\infty = 1$ and for the gas in front of the shock ideal gas with $\gamma = 1.4$ is assumed for simplicity.

For comparison the real gas program can be run in an "effective γ " mode, where the $\hat{\gamma} = h/\epsilon$ from TGAS corresponding to the local density and internal energy is calculated, but ideal gas relations are applied to calculate p , c_R and \bar{p}_r .

In contrast to ideal gas calculations, with real gas the flowfield depends on the (dimensional) values of ρ_∞^* , p_∞^* . For flow around a reentry vehicle, the flight path with the corresponding velocities can be used to find ρ_∞^* , p_∞^* and M_∞ at height H . In this way a one parameter set of flowfields can be calculated along a specified trajectory.

4. RESULTS

The split matrix algorithm with ideal and real gas with the provision of shock fitting and shock capturing has been incorporated in the code EULSPLIT. The 3-D code has also been vectorized on a Fujitsu VP200 resulting in an acceleration factor around 15.

The shock capturing capabilities of the quasiconservative algorithm is demonstrated in fig. 2. Shown are isobars of flow about a sphere at $M_\infty = 4.0$ calculated on an unclustered (32×33) grid. A comparison of the pressure on the surface with the values from Lyubimov and Rusanow [26] is displayed in fig. 2b.

In supersonic flow about rocket-like and shuttle-like bodies at moderate angles of attack a large part of the flowfield is purely supersonic in the direction of the body axis. In these parts of the flowfield we use a space-marching code with shock-fitting [23, 24]. This code applies the prongka process to the quasiconservative formulation of the Euler equations and can capture imbedded shocks correctly [26]. For a sharp-nosed body the space-marching code can be used to generate also a conical solution at the nose. Typical results are shown in Fig. 3.

Displayed are 3-D views of the body and shock contours of flow at $M_\infty = 4.5$, $\alpha = 6^\circ$ about a rocket-like configuration. Streamlines on the body and isobars on the body and in the planes of symmetry are also included. In this case inclusion of real gas effects does not change these results appreciably due to the weakness of the conical shock.

The combination of the (ideal gas) EULSPLIT code with the space marching procedure has been applied to a simplified shuttle-like geometry similar to that used in [27, 28] at freestream conditions $M_\infty = 8.0$, $\alpha = 30^\circ$ (Fig. 4a). The instationary code was applied up to $Z/L = 0.14$ on a $(17 \times 50 \times 19)$ grid. Figs. 4b, c display isolines of pressure and mach number on the surface and in the symmetry planes. The contours reveal clearly the influence of the changes in the curvature of the body geometry and the strong expansion in crossflow direction at $\varphi \sim 130^\circ$ in the front part of the nose. The mach number contours reveal the formation of the entropy layer on the luv side. The subsonic bubble extends to about $Z/L \approx 0.07$. Also shown are the streamlines on the nose calculated from the flowfield [27]. The flowfield around the afterbody $0.14 < Z/L < 0.5$ has been calculated with the space marching code. Figs. 4c, f shows the body and shock contours and pressure isolines on the body. A (17×73) grid was used in the marching planes. The crossflow expansion at $\varphi \sim 130^\circ$ can be resolved much better with this finer grid.

Fig. 5 contains a 3-D view of the mach number isolines of flow about a blunted cone ($\delta = 10^\circ$) at $M_\infty = 15$, $\alpha = 10^\circ$. In the luv symmetry plane and in the outflow plane the layer with high mach number gradients is seen to be forming. Its origin are the regions, where the blunt-body dominated part of the shock merges with the conical-type part.

Fig. 6 displays pressure and mach number isolines of ideal gas flow about a blunted cone ($\delta = 20^\circ$) at $M_\infty = 30$ and $\alpha = 30^\circ$. In this case the flow stays subsonic on the whole luv side symmetry line of the body.

With this analytically defined body geometry the kinks in the isolines at points, where the body curvature is discontinuous, is nicely seen. Note also the strong entropy layer visible on the luv side in the mach number contours. Also shown is the pressure distribution on the body in the symmetry planes. There is a small undershoot on the luv side, whereas on the lee side the pressure monotonously approaches its asymptotic value.

The equilibrium real gas algorithm has been tested with the blunted cone ($\delta = 15^\circ$) at $M_\infty = 15$, $\alpha = 0^\circ$ corresponding to a height of about 60 km on the reentry trajectory. The flowfield has been calculated with ideal gas assumption with $\gamma = 1.4$ and with $\gamma = 1.2$, which is chosen to be consistent with flow about a pointed cone with $\delta = 15^\circ$ [15, 16]. The real gas calculations were done with the full equilibrium code and with the effective γ assumption [13], where the density and energy dependent $\phi = 1 + p(\rho e)$ from the routine TIGAS was used and p , ρ , and c_p have been calculated using ideal gas relations. Fig. 7a shows a comparison of the static pressure on the body in the stagnation point region and in the expansion region for all four models. Around the stagnation point the pressure is virtually unchanged by real gas effects as has been expected since newtonian theory should be applicable. In the aft region of flow again the pressure is similar for the ideal gas ($\gamma = 1.4$ and $\gamma = 1.2$) and the equilibrium calculations. In this region, however, the pressure calculated with the effective γ model, is only $\sim 50\%$ of the correct equilibrium value. Therefore the effective γ approach should not be used, since it leads to physical inconsistencies in regions of flow with strong gradients. Fig. 7b, c show a comparison of isolines of static temperature of ideal gas flow and equilibrium air. From these pictures we can also see, that the shock contour moves towards the body if real gas effects are included. Fig. 7d displays the distribution of static temperature along the body contour. The stagnation temperature is overestimated by 130 % using ideal gas assumption in this case.

5. CONCLUSIONS

In this paper we have presented the thermodynamic equations needed for the simulation of inviscid equilibrium flow with a general equation of state. A quasiconservative split-matrix algorithm capable of capturing shocks correctly has been generalized to include equilibrium real gas consistently. The real gas generalizations of the flux matrices with their eigenvalues and eigenvectors have been derived. The results shown are flowfields about sharp nosed and blunted bodies at freestream mach numbers ranging from $M_\infty = 4.0$ up to $M_\infty = 30$ with ideal gas and equilibrium air assumptions.

REFERENCES

- [1] W. G. Vinceti und C. H. Kruger, Jr.: Introduction to Physical Gas Dynamics, Wiley 1966
- [2] H. W. Liepmann and A. Roshko: Elements of Gasdynamics, Wiley 1965
- [3] G. Koppenwallner: Fundamentals of Hypersonics, Aerodynamics and Heat Transfer, VKI Lecture Series 1984-01 Hypersonic Aerodynamics (1984)
- [4] P. Kutler: A Perspective of Computational Fluid Dynamics, Lecture Notes in Physics 264, pp. 30-48 (1986)
- [5] J. V. Rakich, H. E. Bailey, C. Park: Computation of Nonequilibrium, Supersonic Three-Dimensional Inviscid Flow over Blunt-Nosed Bodies, AIAA Journal 21, 834 (1983)
- [6] D. L. Whitfield and J. M. Janus: Three-Dimensional Unsteady Euler Equations Solution Using Flux Vector Splitting, AIAA-84-1552 (1984)
- [7] E. Becker: Gasdynamik, Teubner 1966
- [8] I. Hilsenrath und M. Klein: Tables of Thermodynamic Properties of Air in Chemical Equilibrium Including Second Virial Corrections from 1500 °K to 15000 °K, AEDC-TR-65-58 (1965)
- [9] R. L. Humphrey und C. A. Neel: Tables of Thermodynamic Properties of Air from 90 °K to 1500 °K, AEDC-TN-61-103 (1961)
- [10] C. H. Lewis und C. A. Neel: Specific Heat and Speed of Sound Data for Imperfect Air, AEDC-TDR-64-36 (1964)
- [11] J. C. Tannehill und P. H. Mugg: Improved Curve Fits for the Thermodynamic Properties of Equilibrium Air suitable for Numerical Computation Using Time-dependent or Shock-capturing Methods, NASA CR-2470 (1974)
- [12] C. H. Lewis und E. G. Burgess, III: Empirical Equations for the Thermodynamic Properties of Air and Nitrogen to 15000 °K, AEDC-TDR-63-138 (1963)
- [13] F. Marconi, M. D. Salas und L. S. Yaeger: Development of a Computer Code for Calculating the Steady Super/Hypersonic Inviscid Flow around Real Configurations, NASA CR-2675 (1976)
- [14] Gordon und McBride: Computer Program for Calculation of Complex Chemical Equilibrium Compositions, Rocket Performances, Incident and Reflected Shocks, and Chapman-Jouguet Detonations, NASA SP-273 (1976)
- [15] K. J. Weilmünster und H. M. Hamilton, II: A Comparison of Computed Space Shuttle Orbiter Surface Pressures with Flight Measurements, AIAA-82-0937 (1982)
- [16] K. J. Weilmünster: High Angle of Attack Inviscid Flow Calculations Over a Shuttle-like Vehicle with Comparisons to Flight Data, AIAA-83-1798 (1983)
- [17] W. D. Hayes und R. F. Probstein: Hypersonic Flow Theory, Volume I, Academic Press 1956

- [18] S. R. Chakravarthy: The Split-Coefficient Method for Hyperbolic Systems of Gas Dynamic Equations, AIAA paper 80-0268 (1980)
- [19] T. H. Pulliam: Artificial Dissipation Models for the Euler Equations, AIAA paper 85-0438 (1985)
- [20] A. C. Hearn (Ed.): REDUCE User's Manual, Version 3.2, Rand Publication CP78 (Rev. 4/85) (1985)
- [21] C. Weiland: A Split Matrix Method for the Integration of the Quasi-Conservative Euler Equations, Notes on Numerical Fluid Dynamics, Vol. 13, Vieweg 1986
- [22] C. Weiland und M. Pfitzner: 3-D and 2-D Solutions of the Quasi-Conservative Euler Equations, Lecture Notes in Physics 264, pp. 654-659 Springer 1986
- [23] C. Weiland: Numerical Integration of the Governing Equations for the Domain of Pure Supersonic Flow, ESA TT-380 (1977)
- [24] C. Weiland: Calculation of Three-Dimensional Stationary Supersonic Flow Fields by Applying the "Progonka" Process to a Conservative Formulation of the Governing Equations, Journal of Computational Physics, Vol. 29, pp. 173-198 (1978)
- [25] C. Weiland und H.-J. Thies: Analysen berechneter dreidimensionaler reibungsfreier Strömungsfelder mit eingebetteten Verdichtungsstößen (Darstellung einer Feldlösung) Teil I, DFVLR-FB 78-09 (1978)
- [26] A. N. Lyubimov and V. V. Rusanov: NASA TT F-714 (1973)
- [27] C. Mundt: Grenzschichtrechnung für ein Wiedereintrittsfluggerät, Diplomarbeit, TU München (1987)
- [28] E. H. Hirschel: Aerothermodynamische Probleme bei Hyperschall-Fluggeräten, MBB-Report S/PUB/270 (1986)

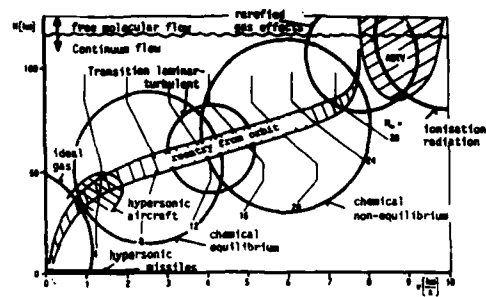


Fig. 1: Re-entry trajectories

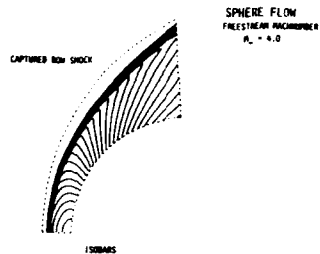
Fig. 2: Sphere - flow with captured bow shock at $M_\infty = 4.0$ 

Fig. 2a: Pressure isolines

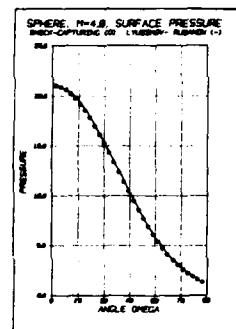


Fig. 2b: Pressure on surface (o) compared to Rusanow (-) [26]

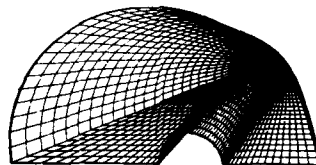
Fig. 3: Flow about a rocket at $M_\infty = 4.5$, $\alpha = 6^\circ$ calculated with space marching technique

Fig. 3a: 3-D view of body and shock contour

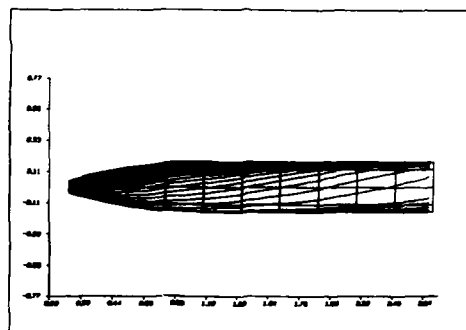


Fig. 3b: Streamlines on body

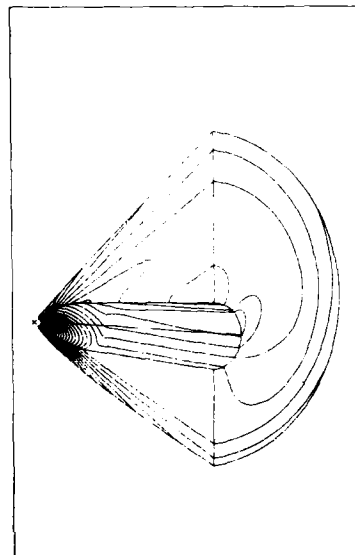


Fig. 3c: Isolines of pressure

Fig. 4: Flow about a simplified shuttle geometry at $M_\infty = 8$, $\alpha = 30^\circ$

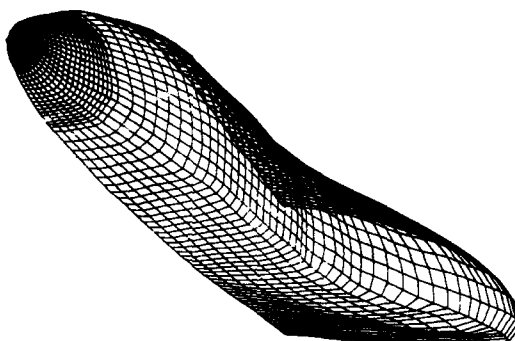


Fig. 4a: Body geometry

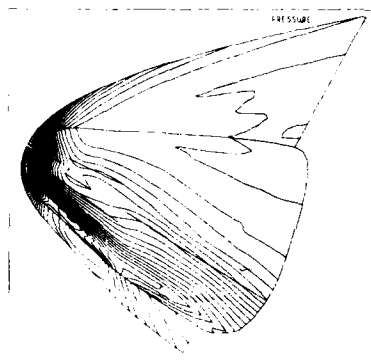


Fig. 4b: Pressure isolines on nose

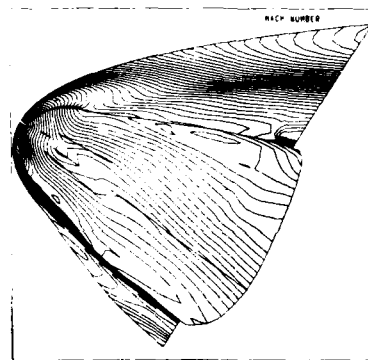


Fig. 4c: Mach number isolines on nose

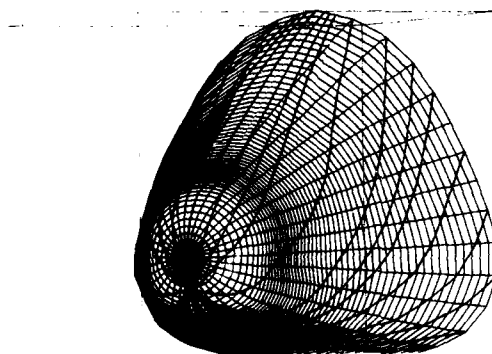


Fig. 4d: Streamlines in nose region

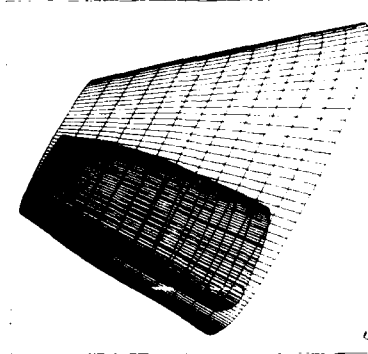


Fig. 4e: Body and shock contour of aft body

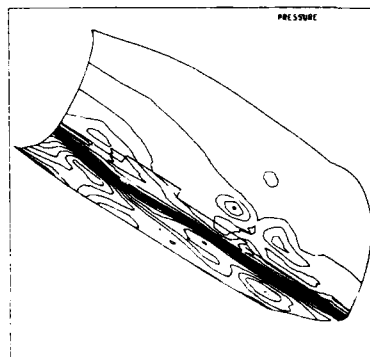


Fig. 4f: Pressure isolines on body

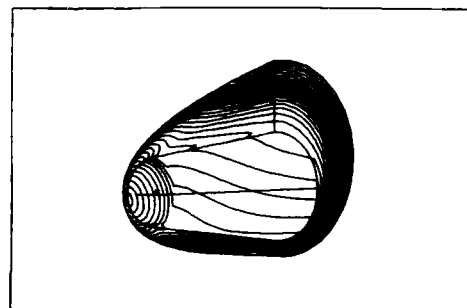
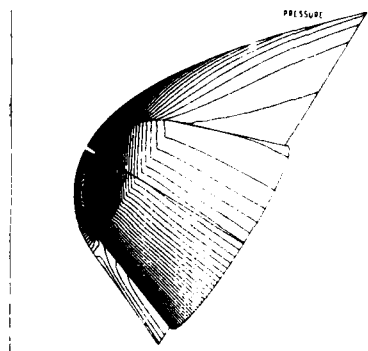
Fig. 5: Mach number isolines of flow about a blunted cone ($\delta = 10^\circ$) at $M_\infty = 15$, $\alpha = 10^\circ$ Fig. 6: Flow about a blunted cone ($\delta = 20^\circ$) at $M_\infty = 30$, $\alpha = 30^\circ$ 

Fig. 6a: Pressure isolines

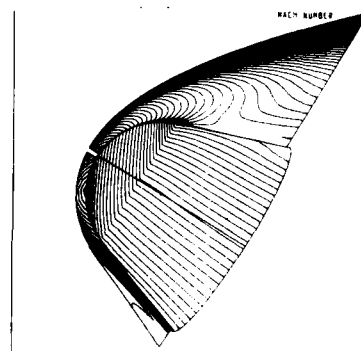


Fig. 6b: Mach number isolines

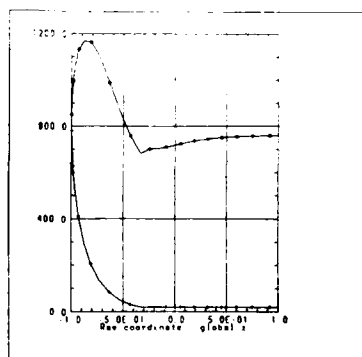


Fig. 6c: Pressure distribution on surface in symmetry planes

Fig. 7: Comparison of perfect gas and equilibrium real gas flow about a blunted cone ($\delta = 15^\circ$) at $M_\infty = 15$, $\alpha = 0^\circ$

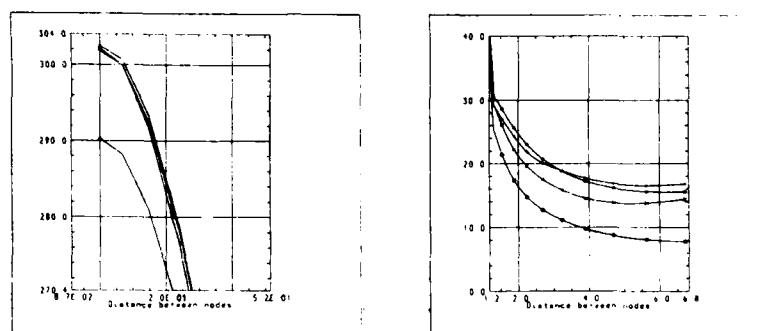


Fig. 7a: Comparison of pressure on surface
 +: ideal gas, $\gamma = 1.4$
 *: equilibrium real gas
 x: ideal gas, $\gamma = 1.2$
 o: effective γ

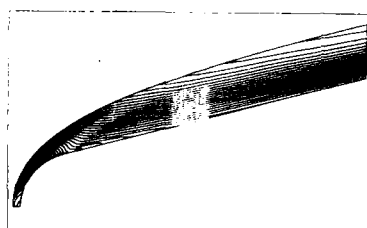


Fig. 7b: Temperature isolines in flowfield
 (ideal gas, $\gamma = 1.4$)

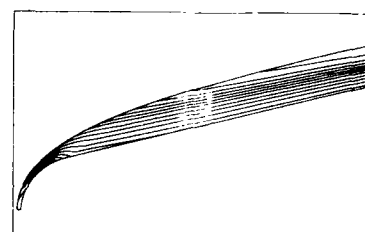


Fig. 7c: Temperature isolines in flowfield (real gas)

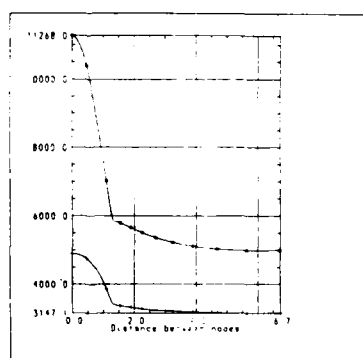


Fig. 7d: Comparison of static temperature on body
 *: ideal gas, $\gamma = 1.4$
 +: equilibrium real gas

COMPUTATION OF FLOW PAST CONICAL HYPERSONIC WINGS
USING A SECOND ORDER GODUNOV METHOD

by

R. Millier

Department of Aeronautics, Imperial College,
London, SW7 2BY,
England

SUMMARY

This paper presents computations of inviscid hypersonic flow past flat plate delta wings using a second order Godunov-type scheme. The governing equations are written in an unsteady conical form and then time-marched to a final conical steady state. The core of the calculation is a generalised Riemann problem which is used to determine the flux transfers at the interfaces between computational cells. Results are presented for wings with shock waves both attached at and detached from the leading edges. The leeward surface flows support embedded shock waves and separated vortex flows and the likely influence of real viscous effects on these is discussed.

1. INTRODUCTION

There is now considerable interest in modelling the flow field past hypersonic wings, operating over a wide range of incidence, sweep and Mach number. Despite advances in prediction methods, the simple delta wing still remains a very challenging problem and is therefore chosen as the subject of study here. For sufficiently low sweep or angle of incidence or high enough Mach number, the shock wave will attach at a sharp leading edge so that the leeward and windward surfaces become independent of each other. When the shock wave detaches from the leading edges the leeward surface flow in particular becomes more complicated. There is then a strong acceleration around the edge, usually from conically subsonic to supersonic so that the compression surface remains independent of the leeward surface flow. The conically supersonic inflow on the leeward surface must eventually turn parallel to the wing axis of symmetry, and the resulting compression generally coalesces to form an embedded shock wave. Stanbrook and Squire (1964) presented a correlation for thin wings, in terms of the Mach number and flow deflection *relative* to the wing leading edge, to distinguish between those leeward surface flows which separated at the leading edge and those where there was a fully attached supersonic inflow at the leading edge, with vortex separation further inboard and, usually, an associated embedded shock. Numerical prediction of these vortex separations is difficult. Squire (1985) and Newsome (1986), amongst others, have shown that although Euler codes may predict leeside separations and vortex flows, the calculated location of separation may not be very reliable. In turn Navier-Stokes codes clearly are dependent upon transition and turbulent models which, at best, are not properly understood for three-dimensional hypersonic flows.

There is a need therefore for further study by both Euler and Navier-Stokes methods together with a careful parallel programme of experimental work. The paper presented here provides inviscid calculations by a Godunov type Euler scheme. Godunov schemes have been used extensively for a wide variety of problems in unsteady gas dynamics, and have produced impressive results for multiple shock flows, shock-vortex-sheet interactions etc. (e.g. Glowacki, Kuhl, Glaz and Ferguson, 1985; Colella and Woodward, 1984). They have been used less extensively in purely aeronautical applications, although results have been presented for blunt bodies (Colella and Woodward, 1984), cascade aerodynamics (Eidelman, Colella and Shreeve, 1984) and slender supersonic missiles using a space-marching variant of the method (Wardlaw and Davis, 1986).

This paper uses a method which is based essentially upon the second-order algorithm developed by Ben-Artzi and Falcovitz (1983, 1984). The purpose is to show how the algorithm is simply extended to deal with conical flow fields, and to present initial results for flat delta wings. Future work is planned both to introduce a general mesh routine, in order to handle non-simple section shapes, and also to introduce a Navier-Stokes (initially laminar) option to the code.

2. METHOD OF SOLUTION

The basic approach, which follows that of Newsome (1986) and Bluford (1979), is to write the equations in an unsteady conical form, which is then time-marched from an impulsive start to a final steady state. The intermediate time-dependent conical flow is not required generally and indeed it has no actual physical counterpart. In the present formulation, the flat delta wing lies in the x - z plane and moves at constant velocity $U_\infty \cos \alpha$ in the direction of negative x as shown in figure 1a. At time $t = 0$ the wing apex lies at the origin of coordinates $x = y = z = 0$. An initial fluid velocity $U_\infty \sin \alpha$ is applied in the y -direction throughout the flow field which simulates an overall incidence of α therefore. The time-dependent Euler equations are then transformed by setting

$$Q(x, y, z, t) \rightarrow Q(\bar{y}, \bar{z}, t) \\ \text{where } z = \bar{z}/(x + t.U_\infty \cos \alpha) \\ y = \bar{y}/(x + t.U_\infty \cos \alpha) \quad (1)$$

and then evaluating them in the reference conical cross plane $x = 0$.

The two-dimensional solution procedure followed here is an "operator-splitting" technique, which employs a sequence of one-dimensional sweeps in the \bar{y} and \bar{z} directions respectively. A single time step Δt is advanced in two-dimensions by the sequence

$$\left(\frac{\Delta t}{2}\right)_{\bar{y}} \left(\frac{\Delta t}{2}\right)_{\bar{z}} \left(\frac{\Delta t}{2}\right)_{\bar{z}} \left(\frac{\Delta t}{2}\right)_{\bar{y}}$$

where $\left(\frac{\Delta t}{2}\right)_{\bar{y}}$, say, represents an advance of the \bar{y} -sweep by $\frac{\Delta t}{2}$.

The resulting \bar{y} -split equations are then written in conservation form as

$$U_\infty \cos \alpha \frac{\partial(Q)}{\partial t} + \frac{\partial E}{\partial \bar{y}} + S = 0 \quad (2)$$

$$\text{where } Q = \begin{bmatrix} \rho \\ \rho u \\ \rho v \\ \rho w \\ \rho e \end{bmatrix} \quad E = \begin{bmatrix} \rho(v - \bar{y}(u + U_\infty \cos \alpha)) \\ \rho uv - \bar{y}((p + \rho u^2) + \rho u U_\infty \cos \alpha) \\ p + \rho v^2 - \bar{y}(\rho uv + \rho v U_\infty \cos \alpha) \\ \rho vw - \bar{y}(\rho uv + \rho w U_\infty \cos \alpha) \\ v(p + e) - \bar{y}(u(p + e) + e U_\infty \cos \alpha) \end{bmatrix}$$

$$S = \begin{bmatrix} \rho u \\ p + \rho u^2 \\ \rho uv \\ \rho uw \\ u(p + e) \end{bmatrix}$$

$$\text{and } e = \frac{p}{(\gamma - 1)} + \frac{1}{2} \rho(u^2 + v^2 + w^2)$$

with a corresponding set for the \bar{z} -sweep.

For convenience during the computations the term $U_\infty \cos \alpha$ was usually set to unity, the Mach number being specified by appropriately setting the ambient speed of sound. It should also be noted that the velocity components u and v in the flux term of equation (2) can be replaced by

$$v^* = (v - \bar{y} u)/(1 + \bar{y}^2)^{1/2} \\ = v \cos \theta - u \sin \theta, \\ \text{and } U^* = (u + \bar{y} v)/(1 + \bar{y}^2)^{1/2} \\ = u \cos \theta + v \sin \theta \quad (3)$$

where θ is the angle between the surface $\bar{y} = \text{constant}$ and the plane of the wing. V^* is then the velocity normal to the surface $\bar{y} = \text{constant}$ and U^* is the component of velocity, in this surface, which is also parallel to the symmetry plane of the flowfield (see Figure 1b).

The flux vector E can therefore be re-written as

$$E = \begin{bmatrix} \rho(V^* \sin \theta)/\cos \theta \\ \rho(U^* - V^* \tan \theta)(V^* \sin \theta) - p \bar{y} \\ p + \rho(U^* \tan \theta + V^*)(V^* \sin \theta) \\ \rho w(V^* \sin \theta)/\cos \theta \\ (e(V^* \sin \theta) + p V^*)/\cos \theta \end{bmatrix}$$

which was the form used, since for an unsteady conical flow it is most appropriate to consider flux velocities resolved normal to, and in the plane of, the surface $\bar{y} = \text{constant}$.

Referring to figure 2, the update of equation (2) from t^n to t^{n+1} for cell j is manipulated to give

$$u_{\infty} \cos \alpha \cdot Q^{n+1} = \frac{u_{\infty} \cos \alpha \cdot Q^n}{(1 + \Delta t / \tau^n)} - \frac{(E_{j+1/2}^{n+1/2} - E_{j-1/2}^{n+1/2})}{(\bar{y}_{j+1/2} - \bar{y}_{j-1/2})} \cdot \frac{\Delta t / \tau^n}{(1 + \Delta t / \tau^n)} - S_j^{n+1/2} \cdot \frac{\Delta t / \tau^n}{(1 + \Delta t / \tau^n)} \quad (4)$$

where Δt is the time step, $n + 1/2$ indicates that a quantity is evaluated at mid-time-step and j and $j \pm 1/2$ respectively represent quantities calculated as cell averages and cell interface values.

The special feature of the Godunov scheme is the use of a Riemann problem to calculate the flux $E_{j+1/2}^{n+1/2}$. Here the method of Ben-Artzi and Falcovitz (1983, 1984) is followed. At the commencement of a time step it is assumed that cell average values are known and also that spatial gradients have been specified. At a cell interface, therefore, there are generally discontinuities in the variables and their space derivatives as shown in figure 3a for density (say). Over the subsequent time step the resulting wave field generates both "left" and "right" facing waves, either of which may be a shock wave or a rarefaction wave, and a contact surface which denotes the trajectory of the fluid particle initially at the interface (figure 3b). The waves may take any position relative to the interface, depending upon whether the general motion is to the left or right and whether it is subsonic or supersonic. At the interface the flow properties change with time (figure 3c). We therefore calculate the Eulerian time derivative at each interface at the commencement of the Riemann

problem, denoted by $\left. \frac{\partial \rho}{\partial t} \right|_i^n$ say, so that

$$\rho_i^{n+1/2} = \rho_i^n + \frac{\Delta t}{2} \left(\frac{\partial \rho}{\partial t} \right)_i^n \quad (5)$$

The term $\rho_i^{n+1/2}$ (say) is the value at the cell interface immediately after the wave interaction commences, and depends only upon the initial values of the variables either side of the interface and not on their spatial gradients. Furthermore since the conical model obviously treats the surface $\bar{y} = \text{constant}$ as the initial surface of discontinuity, this first order Riemann problem must be solved for specified jump conditions in p, ρ and V^* , the velocity normal to the discontinuity. An iterative technique (Chorin, 1976) was used for this, starting with a guess based upon an acoustic solution. Generally this provided convergence after only one iteration, since the specification of initial linear distributions across cells ensures that discontinuities in variables at the interface are usually small. Once this solution has been completed, the interface values of U^* and ω are easily determined, since they are advected as passive scalars; that is their required values are simply the initial values from either left or right of the interface, depending upon whether the contact surface moves to the right or left respectively.

The second order procedure follows closely that of Ben Artzi and Falcovitz (1984, 1985); in this paper we make $O(\Delta t)$ estimates of time derivatives, comprising their so-called E1 scheme. In common with the first order solution, the essential feature of the analysis is the matching of pressure, and normal velocity V^* at the contact surface for both the left and right hand flows, whilst permitting discontinuities across it in ω, U^* and ρ . The characteristics from the \bar{y} -split Euler equations (eqns 2) give

$$\begin{aligned} d\omega = 0, \quad \frac{dU^*}{dt} &= \frac{A}{X} \cdot \frac{V^*}{(1 + \bar{y}^2)} \\ \text{along } \frac{d\bar{y}}{dt} &= \frac{A}{X} \end{aligned} \quad (6)$$

$$\text{and } dp + \rho adV^* + \frac{\rho a U^{*2}}{X(1 + \bar{y}^2)} \left[a + \frac{A}{(1 + \bar{y}^2)} \right] dt$$

$$\text{along } \frac{d\bar{y}}{dt} = \frac{1}{X} \left\{ A + (1 + \bar{y}^2)^{1/2} a \right\} \quad (7)$$

where $X = \tau U_{\infty} \cos \alpha$

and $A = v - \bar{y}(u + U_{\infty} \cos \alpha)$

These characteristic equations are then used to determine the time derivatives at the contact surface, giving

$$a_1 \left(\frac{dB}{dt} \right) + b_1 \left(\frac{dV_c^*}{dt} \right) = c_1 \quad (8a)$$

$$a_2 \left(\frac{dB}{dt} \right) + b_2 \left(\frac{dV_c^*}{dt} \right) = c_2 \quad (8b)$$

$$\left(\frac{dU_c^*}{dt} \right) = \frac{Ac}{X} \cdot \frac{V_c^*}{(1+\gamma^2)} \quad (8c)$$

and

$$\left(\frac{dW_c}{dt} \right) = 0 \quad (8d)$$

where V_c^* is the appropriate normal velocity for the contact surface value deduced from the first order Riemann problem and the coefficients $a_1, b_1, c_1, a_2, b_2, c_2$ are given in Appendix 1. Finally the Eulerian time derivatives at the interface are then obtained from the Lagrangian derivatives of equations 8, again outlined in Appendix 1. These time derivatives depend upon the initial spatial gradients within the computational cell, which itself is deduced here from a simple formulation. First a central difference estimate is made for the gradient. If this results in a cell interface value which is extremum compared with the neighbouring cell average values, the absolute gradient is then reduced until the extremum is just removed. This was sufficient to produce stable solutions for most cases although slight oscillations were noted inboard of the leading edge for the attached shock case so that a further small reduction in gradient in regions of strong compression was then introduced. The gradients for the velocity components were determined by applying the routine above to the Cartesian components u, v and w , which were then appropriately resolved to give the gradients, at cell interfaces, of V^* and U^* .

If both left and right waves of the Riemann problem lie on the same side of the interface (see Figure 3b) we do not need to follow the above procedure. Instead the interface variables and gradients are taken for the upwind side of the interface and simply substituted into the Euler equations to give the interface time derivatives. The source term of equation 4 was evaluated in a like manner, using the cell gradients and cell average values to estimate the values for the half time step.

3. TWO-DIMENSIONAL CONICAL FLOWS

Godunov-type schemes show their best discontinuity resolution when waves are stationary relative to the mesh, which is the case with all the problems studied here, and also when they are aligned with the coordinate surfaces. This is illustrated here by the two-dimensional problem of a flat plate aerofoil shown in Figure 4 for $M_\infty = 4.0$ and $\alpha = 15^\circ$. This shows excellent agreement with exact results, even for a fairly coarse mesh representation, for both the compression surface and expansion surface flows.

4. FLAT PLATE DELTA WING - ATTACHED SHOCK WAVE

For attached shock flows the basic case chosen was a 50° sweep wing with $M_\infty = 4.0, \alpha = 15^\circ$ since this has been used as a test case for a variety of numerical schemes. It was computed using a rectangular mesh with 40 cells to the semi-span, and since the windward and leeward surfaces are aerodynamically independent of each other the data were obtained in two separate runs. Figures 5(a) and 5(b) show cross-plane isobar distributions for the two surfaces respectively; the mesh size is also illustrated on the Figures.

Figures 6 and 7 present the corresponding spanwise pressure distributions. Considering the compression surface first, the constant pressure outer region agrees very closely with the exact oblique shock value shown. There is a slight pressure overshoot (1%) immediately inboard of the leading edge which indicates that the gradient reductions applied to the second order scheme are not quite sufficient. It is easy to modify these further because the reductions were fairly small, but it has to be a matter of numerical experiment to determine the most appropriate formulation. It should be noted that one cause of such overshoots is the operator-split approach to the handling of oblique shock waves, and it may be possible to devise a more refined approach along the lines (say) of Davis (1984).

Further inboard the constant pressure, conically supersonic inflow changes to a non-uniform conically subsonic region at 56.5% span according to exact inviscid theory, which is resolved well by the computations. The pressure distribution in the central, non-uniform region agrees very closely with inviscid computations of South and Klunker (1969) and Voskresenskii (1965). Roe (1972) has produced a theoretical result for the spanwise pressure gradient at the outer limit of the non-uniform zone and this is also included on the Figure. The present computations appear to underestimate this gradient somewhat, as did also the results of South and Voskresenskii. The mismatch doubtless arises because of a combination of numerical smearing in the code (although Figure 4 shows how well gradient discontinuities can be captured) and the local nature of Roe's result. It is intended to explore this point by refined mesh computations.

On the leeward surface Figures 5 and 7 show that the Prandtl-Meyer expansion at the leading edge is smeared over several cells. This mainly arises because the mesh ratio $d\bar{y}/d\bar{x}$ of 0.25 means that the expansion fan does not clear the surface row of cells until the third cell inboard from the leading edge is reached. The asymptotic pressure value then agrees very closely with the exact result of $p/\bar{p}_\infty = 0.146$. Based upon the flow conditions behind the leading edge the Mach cone from the wing apex makes an angle of 4.37° (i.e. $\bar{y}/\bar{z}_{1,e} = 0.091$) to the centreline. The computations show, however, that this Mach cone does not terminate the uniform pressure region; rather an embedded shock wave forms at $\bar{z}/\bar{z}_{1,e} = 0.16$, which abruptly turns the flow parallel to the axis.

5. FLAT PLATE DELTA WING - DETACHED SHOCK WAVE

The case considered here has a 74.6° sweep, operating at $M_\infty = 3.51$, $\alpha = 14.7^\circ$, and has been computed for several mesh densities. Cross plane isobars are shown in Figures 8(a) and (b) for meshes of square cells with 20 and 30 cells (meshes A and B respectively) to the semi-span. In Figure 8(c) mesh C has 40 rectangular cells to the semi-span, but stretched to concentrate them near the surface and close to the leading edge as shown in part by the velocity vector plot of Figure 9. The predicted pressure distributions for the compression surface are shown in Figure 10 and these are compared with experimental data (Hillier, 1973) for a flat compression surface wing with sharp leading edges. Results from all mesh densities agree closely with the experimental data. Meshes A and B show slight oscillation near the leading edge which probably arises because of the close proximity of the shock wave to the edge. This oscillation disappears for the finest mesh C.

Prediction of leeward surface flows is much more difficult because of the wide range of flow regimes which may be encountered. The particular wing incidence, sweep and Mach number chosen here were selected to provide a case where leading edge separation is expected (Squire, 1985; Szodrach, 1978), although no experimental data are available for this case. It is generally recognized that Euler codes can predict separation at sharp edges (see, for example, Rizzi and Eriksson, 1983) although the precise controlling mechanism is unclear. The more difficult case would be when the flow remains attached at the leading edge, conically supersonic, and undergoes an embedded shock-induced separation further inboard. This will always depend upon the leeward surface boundary layer, viscous or numerical, and also on the vorticity convected around the leading edge from the curved shock wave on the compression side.

Figure 9 shows the conical velocity vector plot for mesh C (noting that the vector length is not directly proportional to the velocity magnitude). This shows that a separation commences just inboard of the leading edge at about 91% semi-span. Similar vector plots for meshes A and B gave separation positions at about 80% and 85% semi-span respectively. Thus mesh refinement tends to a leading edge separation, which is indeed the expected result for this case. The flow also remains separated up to the centreline, for all mesh densities, which is consistent with the general data of Szodrach (1978).

Figure 11 shows the corresponding spanwise surface pressure distributions for the three meshes, illustrating the point above that mesh independence has not been achieved near the leading edge. The other, main, prominent feature of the lee surface flow, seen best by the isobar plots of Figure 8, is the cross-flow shock wave located at about 30% semi-span. This extends into the upper region of the separation zone but clearly cannot penetrate down to the surface because of the reversal in cross flow direction. Figure 11, for mesh C say, shows the diffused pressure rise at the surface associated with the shock wave, but now of course it forms the favourable pressure gradient driving the reversed flow near the surface. This figure also shows a relatively large pressure increase just inboard of the leading edge, at about 95% semi-span. This opposes the conical inflow and clearly is associated with the inviscid separation of the flow.

6. CONCLUDING REMARKS

The generalised Riemann problem, as developed initially by Ben-Artzi and Falcovitz, has been extended to conical flows. Computations for both detached and attached shock waves show sharp and stable capture of the main bow shock wave together with leeward surface embedded shocks. The detached shock case predicts separation close to the leading edge. This is consistent with other experimental observations and is unlikely to be affected significantly by real viscous effects.

7. REFERENCES

- Ben-Artzi, M. and Falcovitz, J. 1983 A high resolution upwind scheme for quasi 1-D flows. In Proc. of Euler Equation Workshop, INRIA (edited by F. Angrand and R. Glowinski), SIAM Publ.
- Ben-Artzi, M. and Falcovitz, J. 1984 A second-order Godunov-type scheme for compressible fluid dynamics. J. Comp. Phys. 55, No. 1., 1-32.
- Chorin, A.J. 1976 Random choice solution of hyperbolic systems. J. Comp. Phys. 22, 517-536.
- Colella, P. and Woodward, P. 1984 The piecewise parabolic method (PPM) for gas-dynamical simulations. J. Comp. Phys. 54, No. 1., 174-201.
- Davis, S.F. 1984 A rotationally biased upwind difference scheme for the Euler equations. J. Comp. Phys. 65, 65-92.
- Eidelman, S., Colella, P. and Shreeve, R.P. 1984. Application of the Godunov method and its second-order extension to cascade flow modelling. AIAA J. 22, No. 11, 1609-1615.
- Glowacki, W.J., Kuhl, A.L., Glaz, H.M. and Ferguson, R.E. 1985 Shock wave interaction with high sound speed layers. Proc 15th Int. Symp. on Shock Tubes and Waves.
- Hillier, R. 1972 Pressure distributions at $M = 3.51$ and at high incidences on four wings with delta planform. ARC C.P. No. 1198.
- Newsome, R.W. 1986 Euler and Navier-Stokes solutions for flow over a conical delta wing. AIAA J. 24, No. 4, 552-561.
- Rizzi, A. and Eriksson, L.E. 1983 Numerical simulation of the Euler equations simulating vortex flows around wings. AGARD-CPP-342.
- Roe, P.L. 1972 A result concerning the supersonic flow below a plane delta wing. ARC C.P. No. 1228.
- South, J. and Klunker, E.C. 1969 Methods for calculating non-linear conical flows. NASA SP 228.
- Squire, L.C. 1985 Leading-edge separations and cross-flow shocks on delta wings. AIAA J. 23, No. 3, 321-325.
- Stanbrook, A. and Squire, L.C. 1964 Possible types of flow at swept leading edges. Aero Quart. Vol. 15, 72-82.
- Szodruch, J. 1978 Reynolds number influence on leeside flow fields. AIAA J. 16, No. 12, 1306-1309.
- Voskresenskii, G.P. 1965 Numerical solution of the problem of a supersonic gas flow past an arbitrary surface of a delta wing in the compression region. Mekhanika Zhidkosti i Gaza, 4, 134.
- Wardlaw, A.B. and Davis, S.F. 1986 A Godunov method for supersonic tactical missiles. AGARD Symposium on Application of Computational Fluid Dynamics in Aeronautics, Aix-en-Provence.

APPENDIX 1

The time derivatives of pressure p_c and normal velocity V_c^* along the trajectory of the contact surface are given by

$$a_1 \left(\frac{dp_c}{dt} \right) + b_1 \left(\frac{dV_c^*}{dt} \right) = c_1 \quad (A1)$$

$$\text{and } a_2 \left(\frac{dp_c}{dt} \right) + b_2 \left(\frac{dV_c^*}{dt} \right) = c_2 \quad (A2)$$

where $a_1 = (\rho_L a_L)^{-1}$, $a_2 = (\rho_R a_R)^{-1}$, $b_1 = 1$, $b_2 = -1$.

$$c_1 = -\frac{(1+\bar{y}^2)^{1/2}}{X} \left\{ \frac{1}{\rho_L} \left(\frac{\partial p}{\partial \bar{y}} \right)_L + a_L \left(\frac{\partial V^*}{\partial \bar{y}} \right)_L \right\} - \frac{U_L^*}{X(1+\bar{y}^2)^{1/2}} \{ a_L + \bar{A}_L \}$$

$$c_2 = \frac{(1+\bar{y}^2)^{1/2}}{X} \left\{ \frac{1}{\rho_R} \left(\frac{\partial p}{\partial \bar{y}} \right)_R - a_R \left(\frac{\partial V^*}{\partial \bar{y}} \right)_R \right\} - \frac{U_R^*}{X(1+\bar{y}^2)^{1/2}} \{ a_R - \bar{A}_R \}$$

where $X = t \cdot U_\infty \cos \alpha$ and $\bar{A} = A / (1+\bar{y}^2)^{1/2}$

or $\bar{A} = V^* - \sin \theta$, $U_\infty \cos \alpha$.

The above coefficients are all evaluated using the initial data at the interface immediately before the wave interaction commences. Thus ρ_L, a_L (say) are the initial density and speed of sound on the left of the interface, $\left(\frac{\partial p}{\partial \bar{y}} \right)_L$ is the initial pressure gradient on the left etc. θ and \bar{y} (where $\tan \theta = \bar{y}$) are evaluated at the interface position.

The time derivatives of density at the contact surface is given by

$$\left(\frac{d\rho}{dt} \right)_k = \left(\frac{1}{a_c^2} \right)_k \frac{dp_c}{dt} \quad (A3)$$

where a is the speed of sound at the contact surface evaluated from the first order Riemann problem. Note that the density and speed of sound are discontinuous across the contact surface so that equation A3 must be evaluated on the correct side, that is the left side for a right-moving contact surface and vice versa.

The time derivatives of U and ω at the contact surface result from equations 8c and 8d, that is

$$\frac{d\omega_c}{dt} = 0 \quad (A4)$$

and

$$\frac{dU_c^*}{dt} = \frac{\bar{A}_c V_c^* \cos \theta}{X} \quad (A5)$$

where V_c^* is the normal velocity of the contact surface.

If we consider here a right moving contact surface, the required time derivatives (Eulerian) at the interface are related to the time derivatives along the contact surface by

$$\frac{\partial Q}{\partial t} = \frac{dQ_c}{dt} - \frac{A_c}{X} \cdot \frac{\partial Q}{\partial \bar{y}} \quad (A6)$$

where $Q = (p, \rho, V^*, u, \omega)$.

The Eulerian space and time derivatives of p and V^* are also related by the Euler equations which gives

$$\left(\frac{\partial V^*}{\partial t} \right)_i = \frac{dV_c^*}{dt} + \bar{A}_c \left\{ \frac{1}{\rho_c} \frac{dp_c}{dt} + \frac{U_c^* \cos \theta}{X} \right\} \quad (A7)$$

$$\left(\frac{\partial p}{\partial t}\right)_i = \frac{dp}{dt} + \bar{A}_c \left\{ \rho_c \frac{dV_c^*}{dt} + \frac{\bar{A}_c \rho_c U_c^* \cos \theta}{X} \right\} \quad (A8)$$

To evaluate time derivatives of ρ , U^* and ω at the interface, again for a *right-moving* contact surface, we use the requirement that derivatives in the direction of the *left-facing* (acoustic) wave are continuous as it is crossed, that is

$$\left(\frac{\partial Q}{\partial t}\right)_i + \left\{ \frac{A_L - (1+\bar{g}^2)^{1/2} a_L}{X} \right\} \left(\frac{\partial Q}{\partial y}\right)_L = \left(\frac{\partial Q}{\partial t}\right)_i + \left\{ \frac{A_L - (1+\bar{g}^2)^{1/2} a_L}{X} \right\} \left(\frac{\partial Q}{\partial y}\right)_i \quad (A9)$$

Combined with equation A6 this gives for the required time derivative

$$\begin{aligned} \left(\frac{\partial Q}{\partial t}\right)_i \left\{ 1 - \frac{[A_L - (1+\bar{g}^2)^{1/2} a_L]}{A_c} \right\} = \\ \left(\frac{\partial Q}{\partial t}\right)_L + \frac{[A_L - (1+\bar{g}^2)^{1/2} a_L]}{X} \left\{ \left(\frac{\partial Q}{\partial y}\right)_L - \frac{X}{A_c} \frac{dQ_c}{dt} \right\} \end{aligned} \quad (A10)$$

The time derivative $\left(\frac{\partial Q}{\partial t}\right)_L$ can be expressed in terms of the initial gradients $\left(\frac{\partial Q}{\partial y}\right)_L$ from the Euler equations, to give the final explicit evaluation of $\left(\frac{\partial Q}{\partial t}\right)_i$. Equations for a *left-moving* contact surface follow identically.

This analysis has been presented briefly of necessity, and final results can be written in a fairly compact form. A more detailed version of the derivation is being prepared by the author as an Imperial College Aero. Dept. Report and will be available shortly.

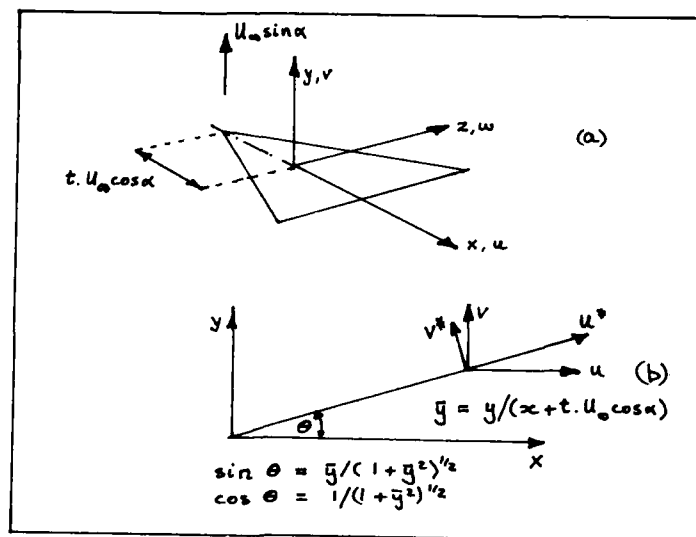


Figure 1. The coordinate system

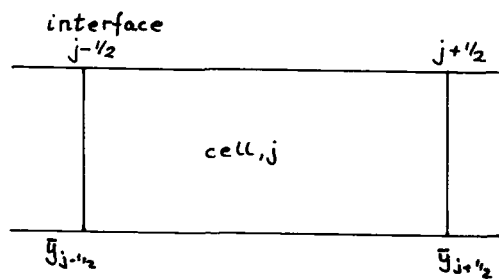


Figure 2. Cell interface notation

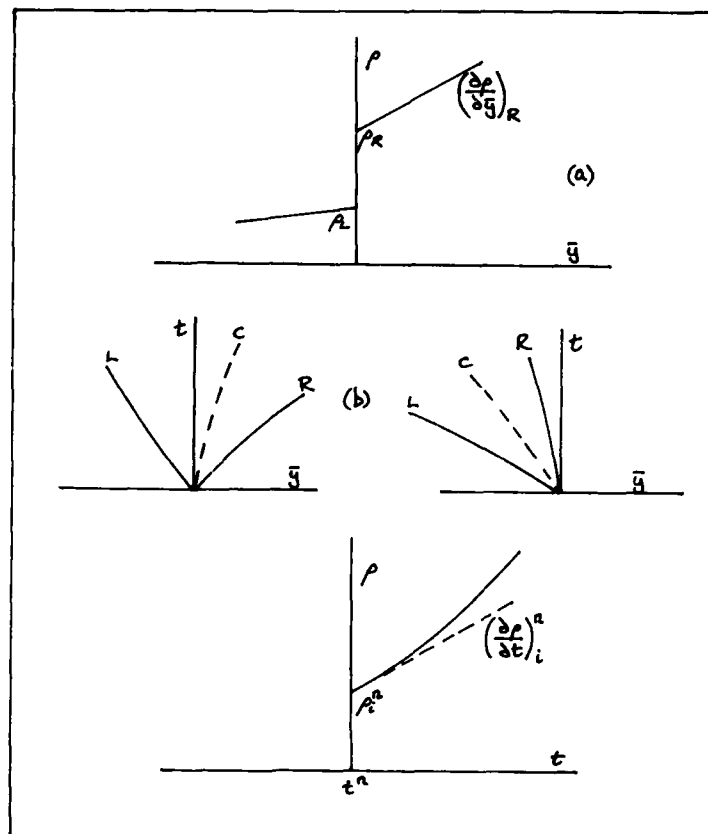
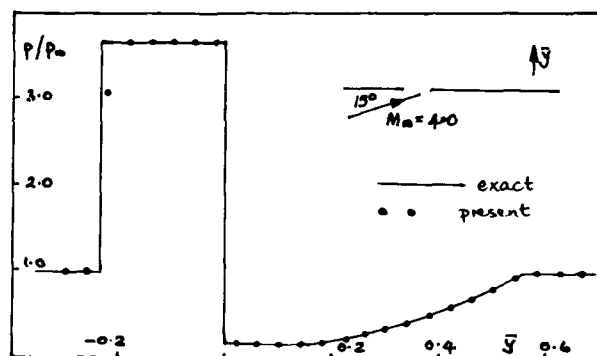


Figure 3. Details of the generalised Riemann problem

Figure 4. Two-dimensional test case. $M_\infty = 4.0$, $\alpha = 15^\circ$, $\gamma = 1.403$.

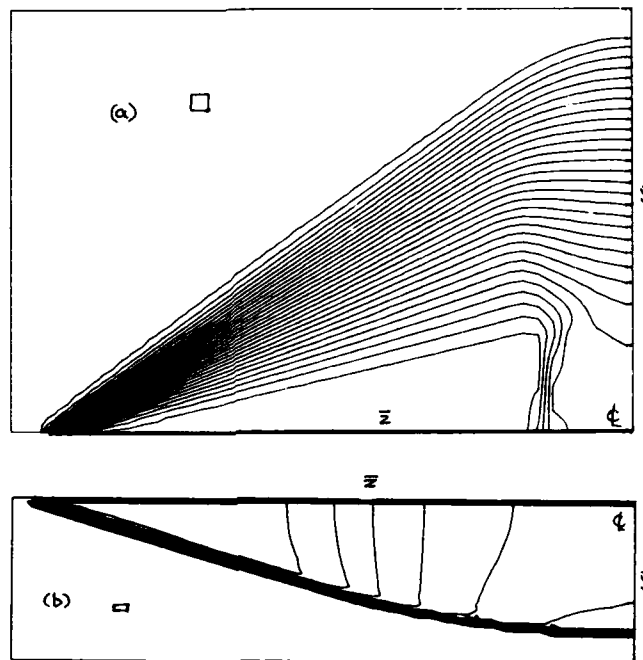


Figure 5. Cross plane isobars for flat delta with attached shock wave. $M_\infty = 4.0$, $\alpha = 15^\circ$, sweep = 50° (a) leeward surface, (b) compression surface.

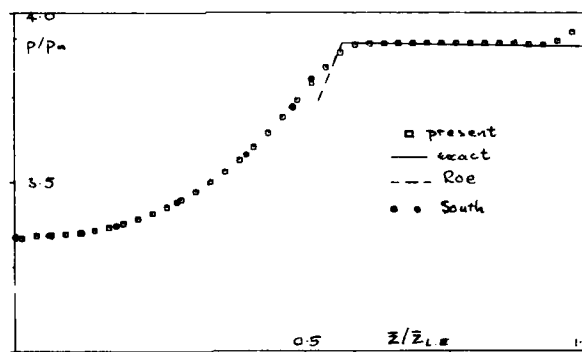


Figure 6. Flat delta with attached shock wave, $\alpha = 15^\circ$, $M_\infty = 4.0$, 50° sweep. Compression surface

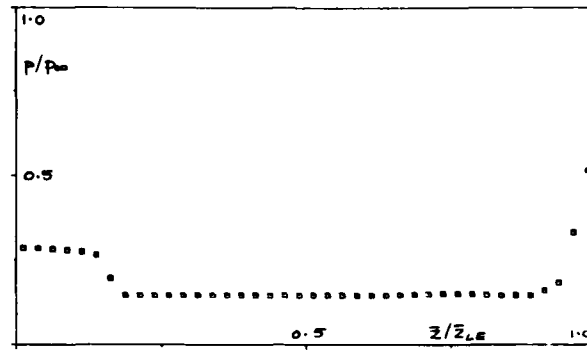
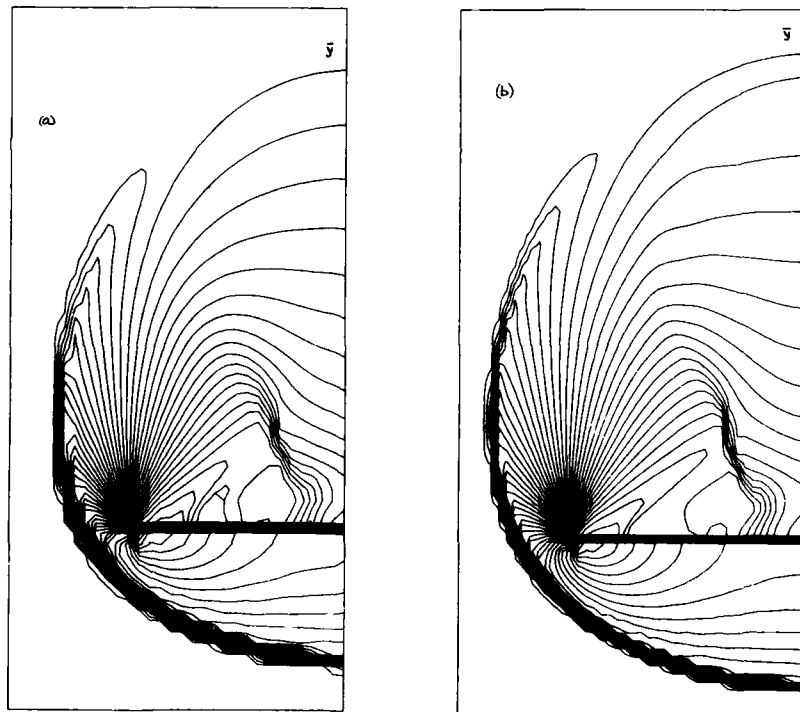


Figure 7. Configuration of Figures 5 and 6. Expansion surface.



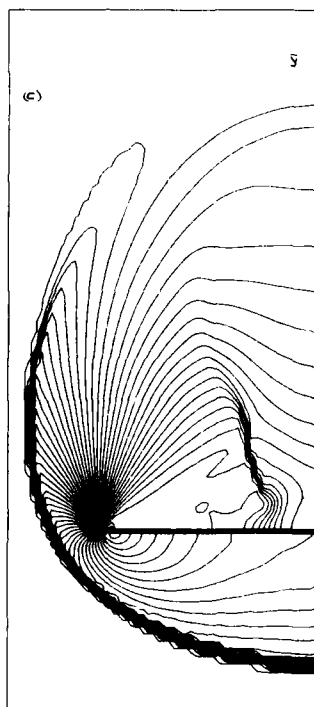


Figure 8. Cross plane isobars for flat delta with detached shock wave. $M_{\infty} = 3.51$, $\alpha = 14.7^\circ$, sweep 74.6° . Stretched rectangular mesh used. Meshes (a), (b) and (c).

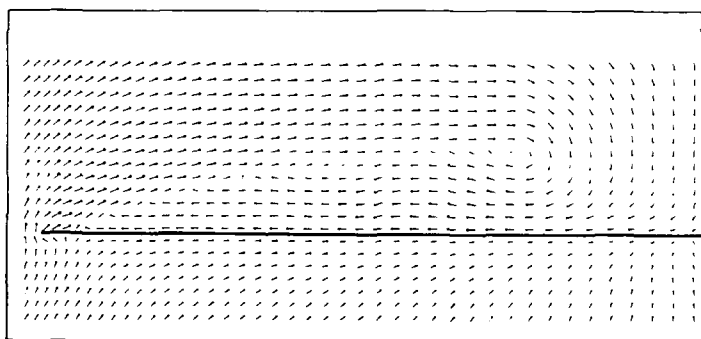


Figure 9. Cross plane 'conical velocity' vector plot, from the configuration of Figure 8, mesh C.

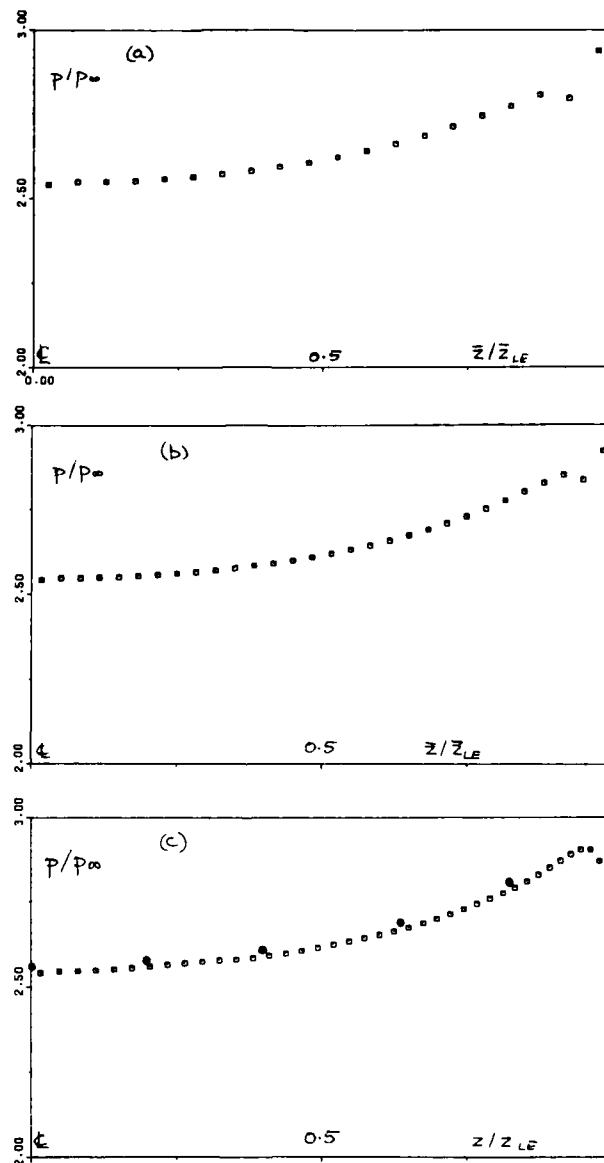


Figure 10. Configuration of Figure 8. Spanwise pressure distribution on compression surface. All meshes. Experimental data (●).

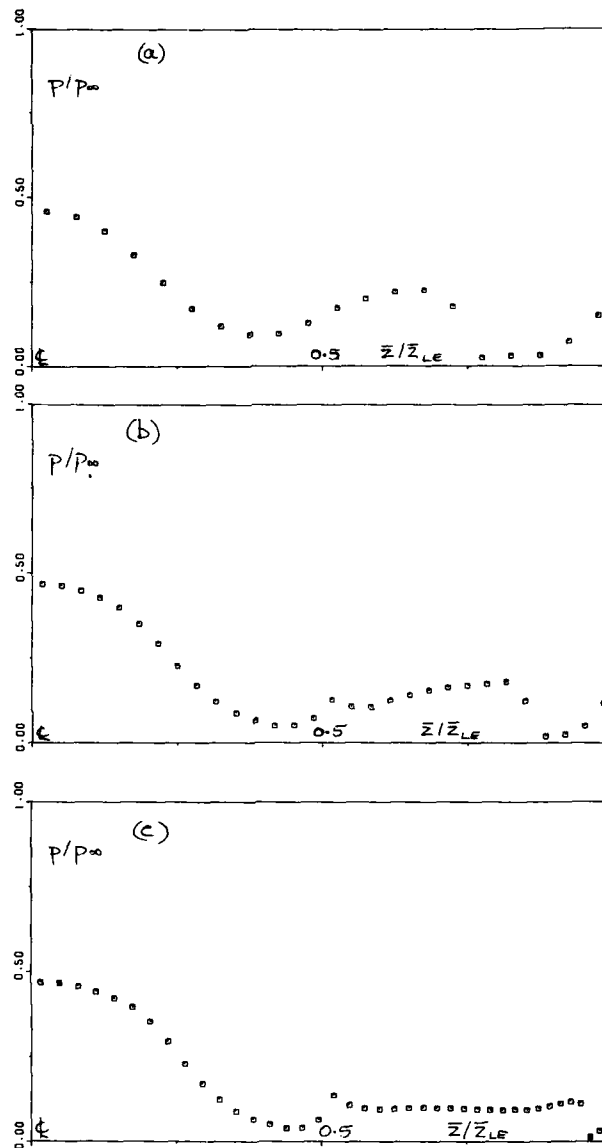


Figure 11. Configuration of Figure 8. Spanwise pressure distribution on leeward surface. All meshes.

AEROTHERMODYNAMICS RESEARCH AT NASA AMES

by

George S. Deiwert
Chief, Aerothermodynamics Branch
NASA Ames Research Center, Moffett Field, California 94035

SUMMARY

Research activity in the aerothermodynamics branch at the NASA Ames Research Center is reviewed. Advanced concepts and mission studies relating to the next generation aerospace transportation systems are summarized and directions for continued research identified. Theoretical and computational studies directed at determining flowfields and radiative and convective heating loads in real gases are described. Included are Navier-Stokes codes for equilibrium and thermo-chemical nonequilibrium air. Experimental studies in the 3.5 foot hypersonic wind tunnel, the ballistic ranges and the electric arc driven shock tube are described. Tested configurations include generic hypersonic aerospace plane configurations, aeroassisted orbital transfer vehicle shapes and Galileo probe models.

INTRODUCTION

Current research activity in the Aerothermodynamics Branch at the NASA Ames Research Center is outlined and described. Focused activity is directed toward orbiting high altitude, high drag aerobraking vehicle configurations such as aeroassisted orbital transfer vehicles (AOTVs), and toward high lift trans-atmospheric vehicles (TAVs), for the purpose of maturing the enabling technology necessary for the design of such vehicles. Research efforts are divided into four distinct areas: 1) advanced mission and concept studies, 2) computational aerothermodynamic flowfield code development, 3) thermo-chemical non-equilibrium reacting gas models and 4) code validation experiments. These four research areas are considered synergistically to extend the state-of-the-art in aerothermodynamic technology.

Advanced mission and concept studies identify the thermal-control requirements for design optimized aeromaneuvering performance for space-based applications and low-Earth orbit sorties involving large multiple plane inclination changes. Heating analyses for hypersonic low density viscous flows including real gas chemistry and surface catalysis are considered. The predicted aerothermodynamic heating characteristics are correlated with thermal-control and flight performance capabilities. Mission payload capability for delivery, retrieval and combined operations is determined for round trip sorties extending to polar orbits. The results help to identify technology issues required to develop prototype operational systems and provide guidance and direction for development of computational aerothermodynamic flow codes.

The design of the next generation aerospace transportation systems will be driven by considerations such as fully reusable systems, maximum payload-to-total-weight ratios and high altitude aeromaneuverability to achieve orbital plane change and cross range capability. These considerations, and others, will be finely tuned to effect designs for economically viable vehicles such as rapid response transatmospheric vehicles (TAVs) and space freighter concepts like the aeroassisted orbital transfer vehicle (AOTV).

In the past heavy reliance was made using ground based test facilities such as shock tubes, arc jets and ballistic ranges, in conjunction with engineering design and analysis codes, to achieve closure on designs of such vehicles as the Apollo, the Space Shuttle, and the Galileo probe. Many of these vehicles were expendable, "one-shot", vehicles that use ablative heat shield materials. The space shuttle, a reusable non-aeromaneuvering vehicle, employs reusable tiles but must undergo considerable refurbishment between missions. To design fully reusable aeromaneuvering vehicles will require design tools significantly improved over those used in the past, and design tolerances will need to be much tighter to avoid unnecessary weight penalties that can drive the cost beyond economic viability.

Ground based test facilities can provide valuable insight for the design and understanding of aerospace vehicles. Such facilities, however, cannot simulate all of the conditions that will be encountered in planned missions of the future. Shown in Fig. 1 is the flight domain for a variety of aerospace vehicles for typical missions in terms of flight Reynolds number and flight Mach number. Superposed are regimes which can be simulated by typical ground based test facilities. The high altitude, high speed regime is the most difficult to simulate, yet it is this regime that will be encountered by vehicles of the future. Flight tests can, and are being planned, such as the aeroassist flight experiment (AFF), to provide data in this regime. But these tests are expensive and can provide only a limited amount of data. To augment this data and to optimize cost effective designs, reliance must be made on advanced computational techniques. Both ground based and flight tests can provide valuable data to validate these computational methods. The computational methods can then, in turn, be used to extrapolate our understanding and analysis in to regimes not covered by existing facilities.

Over the past decade and a half, during the hiatus in hypersonic research, we have seen great advances in three key areas that are now being synthesized to develop advanced computational techniques to a mature technology to enable the design of the next generation aerospace transportation systems. The first of these is the development of inexpensive raw computing power. In the early '70s scientific computers were of the IBM 360 and CDC 6600 class. The IBM 370 series and CDC 7600 machines were just becoming available. Since that time we have seen the Cray 1 and Cray 2 computers, the CDC Cyber 205 and the Fujitsu VP200 and VP400 and Hitachi S 810. Coming along are the ETA 10 and the Cray 3 supercomputers. These computers are faster in terms of computing speed and larger in terms of high speed memory by orders of magnitude and, at the same time, cost orders of magnitude less per unit of computing power than a computer of a decade and a half ago.

During the same period a new and powerful tool in aerodynamics was developed; computational fluid dynamics (CFD). Numerical algorithms have been refined to efficiently solve the Reynolds averaged Navier-Stokes equations for three-dimensional steady and unsteady compressible flows at transonic and supersonic speeds in an ideal gas. Associated with this are sophisticated discretization schemes to describe complex geometries and flowfields. To extend the CFD capability

to the hypersonic flight regime experienced by aerospace vehicles it is necessary to include "real gas" effects. Typically this involves the description of chemical reactions, thermo-chemical nonequilibrium and radiative transport phenomena.

At the very high temperatures associated with high altitude hypervelocity flight there is a paucity of experimental data defining collision cross-sections and transition probabilities necessary to accurately describe the chemical exchange processes involved. To this end recent advances in computational chemistry can be used to fill this critical gap. A recent survey describing the capability of computational chemistry and the impact on the analysis of orbital transfer vehicles is given by Cooper et al¹. The combination of CFD and real gas chemistry, along with modern high-speed computers form the synergistic basis of computational aerothermodynamics (CAT). Three excellent recent review articles on computational aerothermodynamics are given by Anderson², Graves and Hunt³ and Lewis⁴.

The particular phenomena addressed by computational aerothermodynamics is the prediction of aerothermal loads. These include effects such as aerodynamic forces, convective and radiative heating rates, gas/surface interactions and surface catalytic effects, thermal protection systems with active cooling and plasma layers and their effect on communications and power supply. These phenomena are critical to designing vehicles that are to be adequately protected from the very high thermal loads that will be encountered during hypervelocity flight and that are to be aerodynamically stable and maneuverable. Existing ground based test facilities will be used to perform critical experiments designed to provide data for real gas computer code validation.

ADVANCED MISSION AND CONCEPT STUDIES

In conceptual studies extending over the past two decades⁵⁻⁷ the potential of aeroassisted technology for enhancing orbital operations and planetary missions has been widely recognized. This technique calls for using the aerodynamic forces produced by grazing passes through the upper atmosphere to achieve the transition to local orbit by deceleration or directional change; earlier methods relied exclusively on propulsion power. The propellant saved by eliminating the costly propulsive maneuvers not only makes possible missions that are otherwise impractical but also substantially increases payload capability. Exploratory studies⁷ have indicated that two classes of aeroassisted orbital-transfer vehicles (AOTVs) can satisfy a broad range of Earth-centered space transport missions.

Aerobraking AOTVs

One design is useful primarily as a space freighter for transporting large payloads when time is not a constraint in the mission requirements. This "aerobraking" vehicle performs its orbit-change maneuvers by aerodynamic drag in the far-outer extent of the atmosphere to alleviate surface heat fluxes and pressure forces, which minimizes the weight penalties for the aeroassist apparatus. Extensive design and mission-performance analyses for operations encompassing cislunar space have been given by Menees et al^{8,9} and Davies and Park¹⁰ for an AOTV design in this category. A typical near-Earth orbital transfer mission would be between a geosynchronous and an equatorial low earth orbit. The location of a space station at geosynchronous orbit (GEO, 35,841 km altitude) is a future certainty because of its many scientific, commercial, and strategic applications. Consequently, low-cost orbital-change maneuvers between GEO and low Earth or Space Shuttle orbits (LEO, 400 km altitude) for personnel and material transport will be a future requirement of high frequency. The advantages of aerobraking provide substantial savings in propulsion fuel mass for this mission. This is illustrated in Fig. 2 by the schematic of a typical mission profile for a single-pass, aerobraked orbital transfer vehicle (AOTV) maneuvering between GEO and equatorial LEO. Multiple passes are possible and appropriate for unmanned missions for which turnaround time is unimportant, but a single pass in appropriate for manned missions. The constraints on the mission are a re-entry mass of 12 tons (to conform with other studies) and the use of a liquid rocket engine with a specific impulse of 420 s to make the AOTV reusable and refuelable. The mission scenario is as follows: 1) the AOTV with initial mass of 30 tons (the approximate capacity of Space Shuttle cargo bay) is inserted into equatorial LEO; 2) a propulsive thrust of 2395 m/s is required to transfer from the circular LEO to an elliptical orbit with apogee at GEO and perigee at LEO; 3) this consumes a propulsion fuel mass of about 45% of the initial AOTV mass; 4) a propulsive thrust of 1456 m/s is required to achieve the circular GEO from the elliptical transfer orbit; 5) this maneuver consumes an additional 30% of the AOTV mass; 6) a payload of 5.5 tons is picked up for transfer to LEO so that a re-entry mass of 12 tons will be obtained subsequently; 7) a retropropulsive thrust of 1490 m/s is required for transfer to an elliptical orbit with perigee in Earth's atmosphere to take advantage of aerodynamic braking; 8) this maneuver expends 30% of the remaining AOTV mass in fuel and provides the desired re-entry mass of 12 tons; 9) aerodynamic braking occurs with the AOTV, achieving a new elliptical orbit with apogee at LEO; and 10) a final small propulsive thrust of 90 m/s is required for insertion into LEO, which burns a fuel mass of only 2.5%. Thus, aerobraking conserves essentially all of the fuel mass that would be required for return to LEO using all-propulsive maneuvers, which is about 45% of the AOTV mass (the difference between propulsive thrust for steps 2 and 10).

Several design concepts have been considered for orbital transfer vehicles including a conical lifting-brake^{5,11}, a raked elliptic-cone^{12,13}, a raked sphere-cone¹⁴, a lifting body¹⁵, and a ballute. These five concepts have recently been reviewed and critiqued by Park¹⁶. Historical backgrounds, and the geometrical, aerothermal and operational features of the designs are considered as are the technological requirements for the vehicle (namely, navigation, aerodynamic stability and control, afterbody flow impingement, nonequilibrium radiation, convective heat-transfer rates, mission abort and multiple atmospheric passes, transportation and construction, and the payload-to-vehicle weight requirements). These issues are delineated and recent advances that have been made in them are summarized. Each of the five design concepts are critiqued and in Table I are rated on these issues. The highest and the lowest ratings are given to the raked sphere-cone and ballute designs, respectively. A fairly in-depth aeroelastic analysis of the bottom rated ballute concept is given by Park¹⁷ which identifies critical concerns with aerodynamic stability.

The highest rated sphere-cone concept is described in detail by Davies and Park¹⁴ and is illustrated in Fig. 3. To position the thrust line correctly, the two rocket engines must exhaust forward through an opening in the aerobrake as seen in Fig. 3a. The thrust line in each of the two engines passes through the approximate center of gravity (c.g.) at take-off (see Fig. 3c) so that, in case one engine fails, there would be no unduly large yawing moment. The engines have telescopic extensions that serve two purposes: preventing spilling of rocket exhaust gas behind the aerobrake, and increasing nozzle area ratio and thereby thrust. Two hinged hatches must be provided on the aerobrake for the telescopic engines and these

are indicated in Fig. 3c. Similar hatches are already incorporated into the Space Shuttle for its landing gear. Two sets of fuel tanks exist in this design: the main tanks within the heavily armor-protected command/control module, and the auxiliary tanks dispersed behind the aerobrake as seen in Fig. 3b. The fuel in the auxiliary tanks will be used first; the fuel in the main tanks (comprising 5-10% of the total fuel capacity) will be kept as a reserve. The heavy oxygen tanks are located on the central yaw plane to minimize their effect on the trim angle. The tanks for the much lighter liquid hydrogen are located symmetrically on the central pitch plane so that possible imbalance in the amounts of hydrogen in the two tanks would not greatly affect the trim angle of attack. In case one engine fails, oxygen can be shifted from one auxiliary fuel tank to the other to realign (in the yaw plane) the c.g. with the thrust line of the functioning engine. The toroidal-shaped main oxygen tank inside the command/control module has four compartments. Large adjustments in the c.g., if needed during operation of the rocket engines or during atmospheric flight, can be made by shifting liquid oxygen among these four compartments. Fine adjustments in the c.g. during the atmospheric flight can be performed by gimbaling the engines.

On the base side of the aerobrake, the command/control module and the auxiliary fuel tanks are covered by a shroud (see Fig. 3a) made of lightweight heat shield material. The shroud serves three purposes: first, it thermally protects the auxiliary fuel tanks and the command/control module from the hot recirculating flow in the base region; secondly, it protects the tanks from possible meteoroid bombardment; and thirdly, it is used as a radiating surface for the thermal control of the components it encloses. The cargo bay has a two-part shield (seen open in Fig. 3c) which also serves three purposes. First it thermally protects the payload; secondly, it protects the cargo from meteoroid bombardment; and thirdly, in case of failure of one engine, it can serve as a ballast (that is, by opening one shield, the c.g. shifts in the yaw plane which brings the c.g. closer to the thrust line of the functioning engine).

High Lift AOTVs

The other generic AOTV design is a very high-lift "aeromaneuvering" vehicle. This is an essential operational requirement if time-constrained, aeroassisted maneuvers are to be accomplished between low-Earth orbits (LEOs) involving large, multiple plane-inclination changes. Such high-lift vehicles serve as space taxis. They achieve rapid response from one orbital plane to another but have the inherent liability of small payload fraction because of low volumetric efficiency.

Results were given by Menees^{7,9}, Davies and Park^{10,11} and Brown¹⁸ of detailed system design studies for configurations in the high-lift AOTV category. These were the first studies to address the problem of rarefied-hypersonic flow over a lifting surface at incidence with the inclusion of appropriate viscous/inviscid interaction phenomena. A subsequent work by Menees¹⁹ brings together the diverse details of the research activities at NASA Ames Research Center for high-lift AOTVs and is an adjunct to this paper. Special emphasis is given to the problems of hypervelocity, low-density, viscous effects on flow-field dynamics and thermochemical relaxation effects.

The use of high-lift vehicles when returning from low-Earth orbit has many advantages. A primary benefit of lift is the ability to achieve large longitudinal range. Lift also provides the capability to maneuver within the atmosphere. Maneuver ability enhances mission flexibility and increases the choice of landing sites. Lift can also be used to alleviate the deceleration loads and aerodynamic heating accompanying atmospheric entries. The resultant moderation of the entry environment benefits the vehicle's occupants and permits lower structural and thermal protection weights. Skipping flight paths can be used to maximize both longitudinal and cross ranges²⁰ but have associated with them adverse deceleration, structural load factors and aerodynamic heating factors when compared with gliding flight paths²¹. Even for entry angles of less than 10°, the deceleration loads can be an order of magnitude higher for skip flight paths; therefore, the crew of a skipping vehicle experiences severe physiological stress. To withstand the increased structural loads, such major components as the fuselage and wings must be two to three times heavier. Heating rates are 4 to 5 times higher and require heavier thermal protection systems.

Airbreathing TAVs

The developing need for more economical access to space has spurred renewed interest in transatmospheric vehicles (TAV) in both the United States and Europe. Such a transatmospheric vehicle would have responsive, flexible operational characteristics approaching those of aircraft and might eventually replace the Shuttle by providing short launch notice and turnaround times. The TAV would be able to take off and land from ordinary runways and operate in low-Earth orbits. A lower-speed variant of such a vehicle may be used to transport passengers or high-value cargos to any location on the Earth in a small fraction of the flight time of current jet airliners.

The configurations proposed for transatmospheric vehicles would use primarily air-breathing propulsion systems (scramjets) for extended periods of hypervelocity flight to orbital speed. The hypervelocity flight within the atmosphere subjects the vehicle to severe aerodynamic heat fluxes and total heat loads. Therefore, the thermal protection of such vehicles will be major design considerations. A TAV using air breathing propulsion must fly in the denser part of the atmosphere to achieve adequate acceleration to reach orbital speed. The elements of severe aerothermodynamic environment are, therefore, coupled with the requirement of low aerodynamic drag. To achieve low drag, the vehicle must be slender and must have a relatively sharp nose and wing leading edges. Propulsion and aerodynamic performance of typical TAVs were approximated and trajectory and angle of attack histories were derived which allow meaningful computation of the surface heating rates and heat loads^{22,23}. Heating rates, equilibrium wall temperatures and total heat loads at the stagnation point, along a postulated wing leading edge, and on the windward surface centerline of the vehicle are presented.

The combination of high heating rates experienced by surfaces with small curvatures and the long ascent times results in large total heat loads. Therefore, the most severe heating occurs during ascent at the stagnation point and wing leading edges. In contrast, atmospheric entry occurs at large angles of attack, since high drag is desirable to reduce the length of the heating pulse. A comparison of total windward centerline heating loads for typical ascent and entry trajectories²³ are shown in Fig. 4. Temperatures peak around 1300° K during both ascent and entry and radiative cooling should be effective over large areas of the vehicle. Ascent peak stagnation point and wing leading edge wall temperatures are about 3500° K and 2500° K, respectively. Therefore, some form of active cooling may be required for these regions of the vehicle. The corresponding temperatures during entry are 1000° K lower.

COMPUTATIONAL AEROTHERMODYNAMICS

Computational fluid dynamics involves the numerical simulation of the equations of motion for an ideal gas; these equations are the conservation of mass, momentum and energy. In their most general form these equations are the compressible Navier-Stokes (NS) equations. For turbulent flows the range of length scales is too great to feasibly be resolved numerically, and so these equations are time averaged over a scale small with respect to the mean motion time scale yet large with respect to the fine scale turbulent structure. These small scale turbulent transport processes are modelled using eddy viscosity and eddy conductivity concepts. Many flowfields have been well simulated for a variety of shapes and flow conditions where strong viscous/inviscid interactions and/or flow separation are important by solving these equations in a time-like manner until a steady state is asymptotically achieved. When there is no flow reversal and the flow in the streamwise direction is supersonic these equations can be simplified by neglecting the streamwise viscous terms. The solution to these simplified equations, referred to as the parabolized Navier-Stokes (PNS) equations, can be found by efficient streamwise marching techniques. Further simplification can be achieved when viscous/inviscid interactions are weak by decoupling the viscous and inviscid dominated regions from one another and simulating the regions separately in an iterative manner. Here the inviscid Navier-Stokes equations, termed the Euler (E) equations, and are solved in the inviscid region away from body surfaces. Near the body surface the viscous dominated boundary layer (BL) equations are solved. A fourth simplification which can be used for strong viscous/inviscid interactions is the viscous shock layer (VSL) approximation. The VSL equations are obtained from the steady-state NS equations by retaining terms up to second order in the inverse square root of the Reynolds number. In addition, approximations are invoked for the normal pressure gradient and the bow shock location.

These four equation sets, Reynolds averaged NS, PNS, E plus BL, and VSL, are used in computational aerothermodynamics to simulate aerothermo loads for a variety of vehicles and flight conditions. Examples of each will be described later along with the influence of real gas effects.

Real gas effects include thermo-chemical nonequilibrium, where finite rate processes for chemical and energy exchange phenomena occur, and radiative transport. To account for chemical reactions conservation equations for each chemical species must be added to the flow field equation set. There are 5 flow field equations; one continuity, three momentum and one energy equation. For dissociating and ionizing air there are typically 9 species (N_2 , O_2 , N , O , NO , O^+ , N^+ , NO^+ , e^-). The inclusion of conservation equations for each of these species nearly triples the number of equations to be solved. When there are combustion processes or gas/surface interactions or ablation products, the number of species increases dramatically. To account for thermal nonequilibrium and radiative transport there are additional energy equations to describe the energy exchange between the various energy modes (translational, rotational, vibrational, electronic, etc.) To further complicate the analysis the range of time scales involved in thermo-chemical processes is many orders of magnitude wider than the mean flow time scale. This is the single most complicating factor in computational aerothermodynamics. A wide variety of simplifications are used to alleviate problems associated with widely disparate time scales and are discussed briefly next.

Many flows can be adequately approximated by assuming an equilibrium real gas. Here the reaction rates are assumed to all be fast enough that the gas is everywhere in local equilibrium and the thermo-chemical state of the gas can be defined solely by the local temperature and pressure. Reactions are allowed to occur but are completely uncoupled from the flowfield equations. This is a good approximation for lower altitudes and can be used for a major portion of the analysis of such vehicles as transatmospheric vehicles. In the other extreme reactions are sometimes so slow that the gas can be considered frozen in a particular chemical state. This phenomenon typically occurs in regions of rapid expansion such as in jets or base regions of body shapes, but can sometime be used behind compressive shocks as well.

When finite rate chemical reactions are important they can often be considered to be in thermal equilibrium. That is, that the energy modes of the species equilibrate very rapidly compared to the chemical rate processes. Even with this simplification the time scales vary over an extremely wide range, resulting in a "stiff" behavior of the complete equation set and adding to the difficulty in solving the flowfield and species equations in a fully coupled manner. In these cases the species equations are often effectively uncoupled from the flowfield equations and solved separately in a "loosely" coupled manner, often by a different (typically implicit) numerical technique.

VSL Methods

Recent applications using VSL techniques are describe in Refs. 18 and 24 - 27. Green et al^{25,26} obtained VSL solutions for the forebody of the Titan atmosphere entry probe which is planned to make scientific measurements in the organic haze layer of Saturn's largest moon. The flow was assumed to be in local thermo-chemical equilibrium and corresponded to an entry velocity of 12 km/sec. Both radiative and convective heating analyses were performed in order to identify the thermal protection system (TPS) requirements and associated material response necessary to protect the probe. Shown in Fig. 5 is the convective and radiative stagnation point heating histories. The chemical species distribution predicted along the stagnation streamline in the forebody shock layer at a time corresponding to the peak heating pulse are shown in Fig. 6. The heating pulse occurs in the hypersonic, low-Reynolds number region of the trajectory and at the stagnation point the peak flux is 2.5 MW/m². A stagnation-point convective heating correlation was developed from the results of this study which can be employed in approximate heating analyses.

Balakrishnan et al²⁷ solved the radiative VSL equations to analyse the flight data from several experiments including Fire II, Apollo 4 and PAET and compared the computed results with radiometric data from the flight tests. Calculated convective heating rates were found to compare well with experiment, but self-absorption and thermochemical nonequilibrium effects precluded good agreement with the radiative heating rates.

In an attempt to account for thermochemical nonequilibrium, Brown¹⁸ solved the VSL equations for dissociating nitrogen for typical flight speeds of 10 km/sec, altitudes of 80 km and bodies with nose radii from 1 to 50 cm. A two-species, two-temperature nonequilibrium gas model^{28,29} was assumed and comparisons are made with previous theories, experimental data, and results based on the thermodynamic equilibrium assumption. Results shown in Fig. 7, in which heat-transfer rate coefficient C_h is shown as a function of rarefaction parameter K_r , indicate that the inclusion of vibrational relaxation has little effect on the convective heat-transfer rate for a fully catalytic surfaces but can contribute to increased

heating-rates to catalytic surfaces. Preliminary studies^{7,30} indicate that peak heating for a TAV occurs at rarefaction parameter values, K_r^2 , between 8 and 18 for a leading edge radius of 10 cm. If low-catalytic materials are used for thermal protection, vibrational nonequilibrium effects will be critical in the structural design.

The effect of thermochemical nonequilibrium on radiative heating has been addressed by Park^{31,32}. The results of these studies indicate that radiative heating loads for typical AOTV missions are of the same order as the convective heating loads.

Euler Methods

Recent applications using Euler methods are described in Refs. 33-38. A total variational diminishing (TVD) numerical scheme for high Mach number flows in chemical equilibrium with emphasis on improved convergence is discussed in Refs. 33-36. Here TVD numerical dissipation and real-gas properties are added to one dimensional and axisymmetric codes using the Beam and Warming central difference algorithm. Solutions are generated for hemispheres and cylinders at Mach 15 and 20 km altitude. Equilibrium solutions were generated for axisymmetric and 2D spheres and cylinders at Mach numbers up to 15. The altitude (20 km) and velocities were chosen to reflect the flight regime of hypervelocity atmospheric aircraft. The algorithm uses a TVD dissipation operator which allows strong shocks to be captured. Real-gas properties are provided by the Gordon and McBride³⁹ equilibrium chemistry package. Particular attention was devoted to achieving quadratic convergence, which no other equilibrium code has been capable of duplicating. Density and temperature contours show the effect of real-gas chemistry on shock stand-off distance and adiabatic wall temperature. A converged solution gives confidence that the method is stable and correct. In the one-dimensional code³³ fully coupled finite rate chemistry is considered in the simulation of hypersonic flow through a strong normal shock.

Yang³⁷ solved the two-dimensional unsteady Euler equations to simulate the impingement of an oblique blast wave on a two-dimensional AOTV-like configuration. A time accurate hybrid upwind algorithm was used. Shown in Fig. 8 is the geometry and computational grid used for the simulation, and in Fig. 9 are computed Mach number contours for a Mach 30 impinging shock at 15° incidence to the body. These results were computed assuming a frozen gas with $\gamma = 1.1$.

Three-dimensional simulations for equilibrium air are describe by Balakrishnan et al³⁸. Thermodynamic properties are evaluated at each computational grid point using an equilibrium composition method³⁹ and the code has been validated through detailed comparisons with tabulated data of Ref. 40. Results were computed for Mach numbers of 10, 15 and 20 at entry altitudes of 20 and 50 km for a hemispherical blunt body with nose radius corresponding to the Space Shuttle.

PNS Methods

Recent applications using the parabolized Navier-Stokes equations are described in Refs. 41-45. Rakich et al⁴¹ solved the equations in three dimensions for a Space Shuttle configuration in ideal air. Balakrishnan⁴² and Prabhu and Tannehill⁴³ added equilibrium real air properties. Shown in Fig. 10 is a comparison of computed temperature distributions for one cross sectional plane for both ideal and equilibrium air. The real gas temperatures are significantly lower than the ideal gas temperatures at these flight conditions. Prabhu has extended this capability to include chemical nonequilibrium in two dimensions⁴⁴ and three dimensions⁴⁵. The gas dynamic and species concentration equations are solved in a coupled manner using a noniterative, implicit, space-marching finite-difference method. The conditions for well-posedness of the space-marching method have been derived from an eigenvalue analysis of the governing equations. Hypersonic laminar flow of chemically reacting air over cones and wedges has been simulated and the results validated. Shown in Fig. 11 are computed oxygen and nitric oxide species concentrations in the shock layer of a 10° cone for two different altitudes and a speed of 8.1 km/sec. The results compare favorably with reacting boundary layer results⁴⁶.

Navier-Stokes Methods

Recent applications using NS methods are described in Refs. 47-52. These hypersonic applications are based on two well established codes. The first, the ARC2D/ARC3D codes, have been applied and validated for a variety of complex configurations and flow fields. Equilibrium air properties are included to enhance the codes to apply to hypersonic flight. The central difference Beam-Warming algorithm is enhanced by adding TVD (total variational diminishing) modifications so that strong discontinuities can be adequately treated in an upwind-like manner. The second, CSCM (conservative supcharacteristic method), is an upwind scheme developed for hypersonic applications. Equilibrium air properties are included for realistic simulation at flight conditions. Shown in Fig. 12 are computed concentrations of nitrogen for a Mach 20 flow of equilibrium air over a hemisphere forebody⁴⁸. These results compare well with the results of Ref. 40.

Of particular importance in the simulation of complex hypersonic flowfields is the ability to adapt the grid to the solution itself. Two codes, ADAPT2D and ADAPT3D are especially effective as practical and robust methods to define solution adaptive grids (Refs. 53-55). These codes have been used for a variety of flows, both steady and unsteady and in both two and three dimensions. Use of this technique significantly improves the accuracy and efficiency of the Navier-Stokes methods. An application of the CSCM method using the adaptive grid is shown in Figs. 13 and 14 for a two-dimensional hypersonic inlet⁵². The solution adapted grid is shown in Fig. 13 and corresponding computed pressure contours on this grid are shown in Fig. 14. The shock reflection along the lower boundary and the interaction of the expansion waves with the reflected shock are the major features of this flow. The interaction of the expansion fan with the reflected shock results in a curved reflected shock. The predicted pressure recovery behind the reflected shock is critically dependent on accurate resolution of these features. Other applications using solution adaptive grid with Navier-Stokes methods are described in Refs. 56 and 57, and a recent survey of current state-of-the-art in computational aerothermodynamics is given in Ref. 58.

NONEQUILIBRIUM CHEMISTRY

The development and validation of a computer program to calculate the flow of nitrogen and air in thermal and chemical nonequilibrium is a first step toward the longer range goal of predicting multidimensional flowfields in nonequilibrium air and for hydrogen-air combustion processes. This predictive capability is critical to designing the protective heat shield for the AOTV where radiation heating loads are expected to be severe, and to analyzing scramjet engine performance for the air breathing propulsion system of TAVs. Thermo-chemical non-equilibrium reacting gas models have been considered by

Park^{28,29,59}. A computer program identified as "Shock Tube Radiation Program" (STRAP) (Ref. 29) has been developed which computes one dimensional viscous flows of nitrogen and air in a constant-area duct. By improving existing theories and by introducing several new innovations, differences between the translational and rotational temperature and the vibrational and electron-electronic temperature are considered as are chemical reactions whose rates depend on those two temperatures. The computed nonequilibrium thermodynamic properties have been analyzed using the Nonequilibrium Air Radiation (NEQAIR) (Ref. 60) program to determine the spectral radiation characteristics. The resulting radiation characteristics are compared with available experimental data. Shown in Fig. 15 is a comparison of computed and experimental emission intensity spectra for air behind a normal shock at a velocity of 10 km/sec and pressure of 0.1 torr. The computations were performed using a two-temperature gas model in which the translational and rotational temperatures were equal to one another but different from the vibrational and electron temperatures which were assumed equal to one another. The point behind the shock where the comparison is made is nearly halfway between the onset of the shock and the point downstream where the air is once again in thermal equilibrium. Good agreement is observed between the experimental and the present theoretical data, thus validating the computations and the computer code.

Lee⁶¹ derived the basic governing equations for the low-density, high-enthalpy flow regimes expected over the heat shields of proposed AOTVs by combining and extending existing theories. The conservation equations are derived from gas kinetic principles and a four-component ionized gas consisting of neutral molecules, neutral atoms, singly ionized ions, and electrons, assuming a continuum flow. The differences among translational-rotational, vibrational, and electron temperatures are accounted for as well as chemical nonequilibrium and electric-charge separation. Expressions for convective and viscous fluxes, transport properties, and the terms representing interactions among various energy modes are explicitly given. The expressions for the rate of electron-vibration energy transfer, which violates the Landau-Teller relation, are derived by solving the system of master equations accounting for the multiple-level transitions. Subsequently, a theoretical study was made⁶² of the electron-impact vibrational excitation rate processes expected in the AOTV flow fields. Semi-empirical quantum-mechanical treatment was adopted to predict the vibrational excitation cross sections and the rate coefficients. The obtained results for e^- collisions with N_2 showed reasonable agreement with available experimental data. The solution to the $e^- N_2$ vibrational rate equation revealed the unexpectedly slow process to equilibrium which is the result of the diffusion characteristic and multiple-level transitions at high-temperature regions. A modified Landau-Teller-type rate equation and a corresponding relaxation time are suggested which are suitable for numerical calculations relevant to AOTV flow fields.

EXPERIMENTAL PROGRAM

Experimental facilities used for the purpose of code validation include the Ames 3.5 foot hypersonic wind tunnel which is used for testing generic high lift configurations at Mach numbers of 5, 7, 10 and 14, the pressurized ballistic ranges which can produce flight speeds up to 27 km/sec and is used to test AOTVs and planetary probes such as the Galileo probe, and the electric arc driven shock tube which can produce nonequilibrium flows at speeds up to 13 km/sec. Flight experiments for both the drag brake and the high lift configurations are planned for early in the next decade.

Shock Tube

The 24-inch EAST Facility was operated with pressures between 7 and 30 microns of mercury to simulate flight altitudes between 68 to 81 kilometers. Test firings show that: (1) shock velocities in excess of 13 km/sec are achieved at densities equivalent to altitudes of 80 km., (2) the hot driver gas emits radiation in the same pattern as observed in previous higher density, slower shock speed tests, (3) the driver gas does not radiate at unanticipated spectral frequencies, and (4) there is no significant radiation spectra from common impurities such as sodium and iron. This facility will be used to perform basic experiments on thermo-chemical nonequilibrium with particular emphasis on vibrational energy excitation and nonequilibrium. A description of proposed tests and instrumentation is given by Sharma and Park⁶³.

Ballistic Ranges

Two ballistic range facilities at Ames Research Center support hypersonic research⁶⁴, the Hypersonic Free Flight Aerodynamic Facility (HFFAF) and the Pressurized Ballistic Range (PBR). The two facilities compliment each other; each has specific advantages for certain types of tests. Together, they allow testing of a variety of models over a wide range of test conditions. Each facility and associated experiments is described briefly.

Hypersonic Free Flight Aerodynamic Facility

A photograph and schematic of this facility are shown in Fig. 16. The test section is 23 m long and has 16 orthogonal spark shadowgraph stations evenly spaced (1.52 m) over its length. Kerr-cell shutters are used to produce a sharp model and flow-field image on the film. Four deformable-piston, light-gas guns, having bore diameters of 0.71, 1.27, 2.54, and 3.81 cm, are available for launching the model into free flight. Each of these guns can operate to muzzle velocities of about 9 km/sec. A shocktube to provide a countercurrent flow capability is available, but has not been used for recent tests.

Tests in this facility can be conducted from 1 atm to as low as about 20 μ m Hg. And tests can be conducted in nontoxic gases other than air, such as CO_2 , H_2 , He, Kr, and Xe.

Pressurized Ballistic Range

The pressurized ballistic range consists of a large tank that can be pressurized or evacuated and a test section 62 m long. It has 24 orthogonal spark shadowgraph stations irregularly spaced over its length. The station spacing ranges from 2.1 m to 4.2 m. All of the optics are internal to the tank, which imposes a limit on the maximum velocity of the model. Many tests in this facility are conducted with powder gas guns rather than the more sophisticated deformable-piston light-gas guns. The advantages of this facility over HFFAF are threefold: long model trajectory, pressures up to about 6 atm and highly detailed shadowgraphs.

Galileo Tests

The ballistic ranges at Ames have supported all of the United States' probe missions to other planets. These include the 1976 Viking Mission to Mars and the 1978 Pioneer Venus Mission. Currently, tests are being conducted on the Galileo probe. The Galileo spacecraft will be launched in the near future and will arrive at Jupiter two years later. The spacecraft

consists of two major components, an orbiter which is to orbit Jupiter numerous times, concentrating on close encounters with many of Jupiter's moons, and a probe, to enter (and descend through) the atmosphere of Jupiter. The probe will make in situ measurements as it descends through the atmosphere prior to its eventual destruction due to extreme external pressures.

Although the probe aerodynamics were needed initially for design purposes, more accurate aerodynamics are needed in support of the Atmosphere Structure Experiment carried on board the probe. The Atmosphere Structure Experiment is designed to determine the state properties (i.e., density, pressure, temperature) of an unknown planetary atmosphere as functions of altitude from measurements made during the entry and descent of a probe. The experiment consists of a three-axis accelerometer, plus pressure and temperature sensors. During the high-speed portion of the trajectory, from an entry velocity above 47 km/sec to sonic speed, direct measurements are impractical and accelerometers are used to determine the state properties. This requires the precise knowledge of the probe aerodynamics, in particular the vehicle drag and lift coefficients as functions of Mach number and Reynolds number. The aerodynamic characteristics plus the measured decelerations allow the probe attitude to be determined and the atmospheric density to be deduced. Integration of the density gives the pressure, and the temperature is deduced from the equation of state (given the molecular weight, which is measured by another on-board experiment). The ballistic range facilities are well suited for providing the accurate aerodynamic data over a wide range of conditions.

The Galileo probe is a blunt, 45° cone. During the high-speed part of the entry, severe ablation takes place. As much as 40% of the vehicle mass at entry is expected to be ablated away, mostly in the nose and conical regions, and even the maximum diameter will be significantly decreased. Hence, tests must be conducted not only of the entry configuration but of hypothesized ablated configurations as well.

A typical shadowgraph of a Galileo model in flight obtained in HFFAF is shown in Fig. 17. The screw on the model base is for attachment to its sabot prior to launch. The vertical wires are plumb bobs on both sides of the facility for reference purposes and the irregular markings are imperfections in the facility windows caused by past impacts of various sorts.

Low-Reynolds-Number Tests

Ballistic range tests are currently being conducted to precisely define the drag characteristics of the Galileo probe at Reynolds numbers, based on model diameter, of about 500 to 250. The importance of obtaining drag data at these low Reynolds numbers is due to the fact that the drag coefficient is expected to increase markedly as the slip-flow and free-molecule-flow regimes are approached. This dramatic increase in drag coefficient occurs below a Reynolds number of about 1000.

The importance of obtaining drag data at various Reynolds numbers is shown in Fig. 18. Shown are Pioneer Venus data down to a Reynolds number of about 250. The drag coefficient increases continuously below a Reynolds number of 1 million, but the increase becomes most dramatic below 1000.

AOTV Tests

Ballistic range tests have been conducted for two AOTV configurations; a symmetric configuration and raked elliptic cone. These tests were conducted to: 1) Provide experimental aerodynamic data and good flow-field definition against which computational aerodynamicists could validate their computer codes, 2) Define bow shock wave shape and shock standoff distance, 3) Investigate flow impingement on afterbody, 4) Compare the aerodynamics of several configurations, 5) Investigate how minor changes in corner geometry affect the flow field, 6) Determine the trim angle of attack of a trimmed vehicle.

A shadowgraph for the symmetric configuration in Fig. 19 and for the raked elliptic cone in Fig. 20. These flow visualizations plus drag data from these tests are used for computer code validation.

3.5 Ft HWT

The current test program in the 3.5 Ft hypersonic wind tunnel is focused on a generic all-body (elliptic cross section, delta planform) hypersonic aircraft model. This configuration is representative of airbreathing TAVs now being considered. Flow-visualization (shadowgraphs and surface oil-flow patterns), surface pressure, surface heat transfer, and flow-field surveys using probes and non-intrusive lasers will be obtained for this model both with and without control surfaces. Angles of incidence to the free stream will be varied between plus and minus 15° and the free-stream Reynolds number varied between 1.5×10^6 and 25×10^6 . Shown in Fig. 21 is a photograph of the model with all control surfaces attached. The model has a half angle of 75° and is one meter long. There are two nose configurations: a sharp nose and a blunted nose. The simple geometrical configuration is easy to define for computer flow codes and can be readily used to evaluate a wide variety of hypersonic flow codes.

AFE

A forthcoming NASA flight experiment called the Aeroassist Flight Experiment (AFE) is planned for early in the next decade. Ames research center will participate in this experiment by assimilating a large base of radiometric data for high-altitude, high velocity thermochemically nonequilibrium flow conditions. The AFE will be carried to orbit by the Space Shuttle and then deployed for the atmospheric data pass. Accelerated by an 18,000 pound thrust solid rocket motor, the vehicle will enter the atmosphere at nearly 10 km/sec, and then experience approximately 500 seconds of aerodynamic deceleration during which a variety of flight data, including radiative and convective heating rates, will be gathered. The vehicle will exit the atmosphere at orbital speed to be recovered by the Shuttle Orbiter for return to earth for post flight evaluation. As a preliminary to the design of a radiometer for this experiment, an approximate method for predicting both equilibrium and nonequilibrium radiative surface fluxes has been developed⁶⁸. Spectral results for one trajectory state, a velocity of 10 km/sec at an altitude of 85 km, are shown in Fig. 22, where the spectral surface flux at a distance of 20.9 cm behind the shock front is plotted as a function of wavelength in the spectral region from 0.2 to $2.0 \mu\text{m}$. An inspection of the figure reveals that the spectrum appears to be composed of a background continuum with a color temperature in the range of 7,000° K to 8,000° K (based on a flux maximum in the vicinity of $0.4 \mu\text{m}$) on which is superimposed a complex structure of molecular bands and broadened atomic lines. The radiation calculation included nine species (O_2 , N_2 , NO , O , N , N^+ , O^+ , N_2^+ , e^-); some of more apparent band-heads and lines from these species are identified in the figure. These

results, and others like them, are used to develop the instrument parameters for the three different types of radiometers proposed for the experiment.

CONCLUDING REMARKS

Aerothermodynamic research underway at NASA Ames has been described. Four research areas are considered synergistically in an effort to mature the enabling technology necessary for the design of the next generation aerospace transportation systems. These four areas include 1) advanced mission and concept studies, 2) computational aerothermodynamic flowfield code development, 3) thermo-chemical non-equilibrium reacting gas models and 4) code validation experiments. Research in these areas continues in an effort to improve the accuracy and efficiency of predictive methods and our understanding of hypervelocity flows and the effect on aerospace vehicles. A thorough description of the current activity can be found in the references cited in the text of this paper.

REFERENCES

- Cooper, D.M., Jaffe, R.L., and Arnold, J.O., "Computational Chemistry and Aeroassisted Orbital Transfer Vehicles," AIAA Journal of Spacecraft and Rockets, Vol. 22, Jan. - Feb. 1985, pp. 60-67.
- Anderson, J.D., Jr., "A Survey of Modern Research in Hypersonic Aerodynamics," AIAA Paper 84-1578, 1984.
- Graves, R., A., Jr. and Hunt J.L., "NASA's Hypersonic Fluid and Thermal Physics Program (Aerothermodynamics)," AIAA Paper 85-0922, 1985.
- Lewis, C.H., "Current Status of Computational Aerothermodynamics," AIAA Paper 86-0229, 1986.
- Walberg, G.D., "A Survey of Aeroassisted Orbital Transfer," AIAA Journal of Spacecraft and Rockets, Vol. 22, Jan.-Feb. 1985, pp. 3-18.
- Menees, G.P., "Trajectory Analysis of Radiative Heating for Planetary Missions with Aerobraking of Spacecraft," AIAA Journal of Spacecraft and Rockets, 22, 1985, pp. 37-45.
- Menees, G.P., "Thermal Protection Requirements for Near-Earth Aeroassisted Orbital Transfer Vehicle Missions," Progress in Astronautics and Aeronautics, Vol. 96, 1985, pp. 257-285.
- Menees, G.P., Park, C. and Wilson, J.F., "Design and Performance Analysis of a Conical Aerobrake Orbital Transfer Vehicle Concept," Progress in Astronautics and Aeronautics, Vol. 96, 1985, pp. 286-308.
- Menees, G.P., Davies, C.B., Wilson, J.F. and Brown, K.G., "Aerothermodynamic Heating Analysis of Aerobraking and Aeromaneuvering Orbital Transfer Vehicles," Progress in Astronautics and Aeronautics, Vol. 96, 1985, pp. 338-360.
- Davies, C.B. and Park, C., "Aerodynamics of Generalized Bent Biconics for Aero-Assisted, Orbital-Transfer Vehicles," AIAA Journal of Spacecrafts and Rockets, Vol. 22, No. 2, March-April 1985, pp. 104-111.
- Davies, C.B. and Park, C., "Optimum Configuration of High-Lift Aeromaneuvering Orbital Transfer Vehicles in Viscous Flow," AIAA 20th Thermophysics Conference, Paper No. 85-1059, Williamsburg, VA, June 19-21, 1985.
- Scott, C.D., Reid, R.C., Maraia, R.J., Li, C.P., and Derry, S.M., "An AOTV Aeroheating and Thermal Protection Study," Progress in Astronautics and Aeronautics: Thermal Design of Aeroassisted Orbital Transfer Vehicles, Vol. 96, 1985, pp. 309-337.
- Scott, C.D., Roberts, B.B., Nagy, K., Taylor, P., Gamble, B.J.D., Cerimele, C.J., Kroll, K.R., Li, C.P., and Ried, R.C., "Design Study of an integrated Aerobraking Orbital Transfer Vehicle," NASA TM-8264, Mar. 1985.
- Davies, C.B. and Park, C., "Aerodynamic and Thermal Characteristics of Modified Raked-Off Cone," AIAA/ASME 4th Joint Thermophysics and Heat Transfer Conference, Paper No. 86-1309, Boston, MA, June 2-4, 1986.
- Vinopal, T.J., "System Technology Analysis of Aeroassisted Orbital Transfer Vehicles (AOTVs) Low Lift/ Drag (0.0-0.75), Final Report. Vol. 1, Part B-Study Results," F180-29222-1, Boeing Aerospace Company, Seattle, WA, 1985.
- Park, C., "A Survey of Aerobraking Orbital Transfer Vehicle Design Concepts," AIAA 25th Aerospace Sciences Meeting, Paper No. 87-0514, Reno, NV., Jan. 12-15, 1987.
- Park, C., "Theory of Idealized Two-Dimensional Ballute in Newtonian Hypersonic Flow," AIAA 24th Aerospace Sciences Meeting, Paper No. 86-0301, Reno, NV, January 6-9, 1986.
- Brown, K.G., "Chemical and Thermal Nonequilibrium Heat-Transfer Analysis for Hypervelocity, Low Reynolds Number Flow," Progress in Astronautics and Aeronautics, Vol. 103, 1986, pp. 445-477.
- Menees, G.P., "Design and Performance Analysis of an Aeromaneuvering Orbital-Transfer Vehicle Concept," 36th Congress of the International Astronautical Federation, IAF-85-139, Stockholm, Sweden, October 7-12, 1985.
- Menees, G.P., Tauber, M.E., Wilson, J.T. and Adelman, H.G., "Entry Aeromaneuvering Capabilities of Transatmospheric Vehicles," submitted for presentation at the AIAA 22nd Thermophysics Conference, Honolulu, HI, June 8-10, 1987.
- Tauber, M.E. and Yang, L., "Performance Comparisons of Maneuvering Vehicles," submitted to the AIAA Atmospheric Flight Mechanics Conference Monterey, CA., August 1987.
- Tauber, M.E., Menees, G.P. and Adelman, H.G., "Aerothermodynamics of Transatmospheric Vehicles," AIAA/ASME Thermophysics and Heat Transfer Conference, Paper No. 86-1257, Boston, MA, June 1986.
- Tauber, M.E. and Adelman, H.G., "The Thermal Environment of Transatmospheric Vehicles," submitted to the AIAA 22nd Thermophysics Conference, Honolulu, HI, June 8-10, 1987.
- Green, M.J., Budnick, M.P., Yang, L., and Chiasson, "Supporting Flight Data Analysis for Space Shuttle Orbiter Experiments at NASA Ames Research Center," AIAA 18th Thermophysics Conference, Paper No. 83-1532, Montreal, Canada, June 1-3, 1983.
- Green, M.J., Moss, J.N. and Wilson, J.F., "Aerothermodynamic Environment and Thermal Protection for a Titan Aerocapture Vehicle," AIAA 19th Thermophysics Conference, Paper No. 84-1717, Snowmass, CO, June 25-28, 1984.

26. Green, M.J., Balakrishnan, A. and Swenson, B.L., "Aerothermodynamic Environment for a Titan Probe with Deployable Decelerator," AIAA 20th Thermophysics Conference, Paper No. 85-1063, Williamsburg, VA, June 19-21, 1985.
27. Balakrishnan, A., Park, C. and Green, M.J., "Radiative Viscous Shock Layer Analysis of Fire, Apollo, and PAET Flight Data," Progress in Astronautics and Aeronautics, Vol. 103, 1986, pp. 514-540.
28. Park, C., "Convergence of Computation of Chemical Reacting Flows," Progress in Astronautics and Aeronautics, Vol. 103, 1986, pp. 478-513.
29. Park, C., "Assessment of Two-Temperature Kinetic Model for Dissociating and Weakly-Ionizing Nitrogen," AIAA/ASME 4th Joint Thermophysics and Heat Transfer Conference, Paper No. 86-1347, Boston, MA, June 2-4, 1986.
30. Menees, G.P., Brown, K.G., Wilson, J.F. and Davies, C.B., "Aerothermodynamic Heating and Performance Analysis of a High-Lift Aeromaneuvering AOTV Concept," AIAA 20th Thermophysics Conference, Paper No. 85-1060, Williamsburg, VA, June 19-21, 1985.
31. Park, C., "Calculation of Nonequilibrium Radiation in the Flight Regimes of Aeroassisted Orbital Transfer Vehicles," Progress in Astronautics and Aeronautics, Volume 96, 1985, pp. 395-418.
32. Park, C., "Radiation Enhancement by Nonequilibrium in Earth's Atmosphere," AIAA Journal, Vol. 22, No. 1, January-February 1985, pp. 27-36.
33. Eberhardt, S. and Brown, K.G., "A Shock Capturing Technique for Hypersonic, Chemically Relaxing Flows," AIAA 24th Aerospace Sciences Meeting, Paper No. 86-0231, Reno, NV, January 6-9, 1986.
34. Eberhardt, S. and Palmer, G.E., "A Two-Dimensional, TVD Numerical Scheme for Inviscid, High Mach Number Flows in Chemical Equilibrium," AIAA/ASME 4th Joint Thermophysics and Heat Transfer Conference, Paper No. 86-1284, Boston, MA, June 2-4, 1986.
35. Palmer, G.E., "Effective 2-D and Axisymmetric Boundary Conditions for Hypersonic, Inviscid, Blunt Body Flow," NASA TM in publication.
36. Palmer, G.E., "An Implicit Flux-Split Algorithm to Calculate Hypersonic Flowfields in Chemical Equilibrium," submitted for presentation at the AIAA 22nd Thermophysics Conference, Honolulu, HI, June 1987.
37. Yang, J.Y., "A Hybrid Upwind Scheme for the Computation of Shock-On-Shock Interaction Around Blunt Bodies," 10th International Conference on Numerical Methods in Fluid Dynamics, Beijing, China, June 23-27, 1986.
38. Balakrishnan, A., Davy, W.C., and Lombard, C.K., "Real-Gas Flowfields about Three-Dimensional Configurations," Journal of Spacecraft and Rockets, Vol. 22, No. 1, Jan.-Feb. 1985, pp. 46-50.
39. Gordon, S., and McBride, B.J., "Computer Program for Calculation of Complex Chemical Equilibrium Compositions, Rocket Performance," NASA SP-273, 1976.
40. Lyubimov, A.N., and Rusanov, V.V., "Gas Flows Past Blunt Bodies Part I. Calculation Method and Flow Analysis," NASA TT F-714, Feb. 1973.
41. Rakich, J.V., Venkatapathy, E., Tannehill, J. C. and Prabhu, D., "Numerical Solution of Space Shuttle Orbiter Flowfield," AIAA Journal of Spacecraft and Rockets, Vol. 21, No. 1, Jan.-Feb. 1984, pp. 9-15.
42. Balakrishnan, A., "Computation of a Viscous Real Gas Flowfield for the Space Shuttle Orbiter," AIAA 19th Thermophysics Conference, Paper No. 84-1748, Snowmass, CO, June 25-28, 1984.
43. Prabhu, D.K. and Tannehill, J.C., "Numerical Solution of Space Shuttle Orbiter Flowfield Including Real-Gas Effects," AIAA Journal, Vol. 21, No. 1, Jan.-Feb. 1984, pp. 9-15.
44. Prabhu, K.D., Tannehill, J.C. and Marvin, J.G., "A New PNS Code for Chemical Nonequilibrium Flows," submitted for presentation at the AIAA Aerospace Sciences Meeting, Reno, NV., January 12-15, 1987.
45. Prabhu, K.D., Tannehill, J.C. and Marvin, J.G., "A New PNS Code for Three-Dimensional Chemically Reacting Flows," submitted for presentation at the AIAA 22nd Thermophysics Conference, Honolulu, HI., 1987.
46. Blottner, F.G., Johnson, M., and Ellis, M., "Chemically Reacting Viscous Flow Program for Multi-Component Gas Mixtures," Report No. SC-RR-70-754, Sandia Laboratories, Albuquerque, New Mexico, Dec. 1971.
47. Green, M.J., Davy, W.C. and Lombard, C.K., "CAGI2 - A CSCM Based Procedure for Flow of an Equilibrium Chemically Reacting Gas," AIAA 20th Thermophysics Conference, Paper No. 85-0927, Williamsburg, VA, June 19-21, 1985.
48. Green, M.J., "Numerical Simulation of Hypersonic, Axisymmetric Flowfields," AIAA/ASME 4th Joint Thermophysics and Heat Transfer Conference, Paper No. 86-1285, Boston, MA, June 2-4, 1986.
49. Lombard, C.K., Venkatapathy, E. and Bardina, J., "Forebody and Baseflow of a Dragbrake OTV by an Extremely Fast Single Level Implicit Algorithm," AIAA 19th Thermophysics Conference, Paper No. 84-1699, Snowmass, CO, June 1984.
50. Bardina, J., Venkatapathy, E., and Lombard, C.K., "Two Dimensional and Axisymmetric Heat-Transfer Results with the CSCM-S Upwind Implicit Algorithm," Progress in Astronautics and Aeronautics, Vol. 103, 1986, pp. 596-619.
51. Lombard, C.K., Luh, C.-C., Nagaraj, N., Bardina, J. and Venkatapathy, E., "Numerical Simulation of Backward Step and Jet Exhaust Flows," AIAA 24th Aerospace Sciences Meeting, Paper No. 86-0432, Reno, NV, January 6-9, 1986.
52. Venkatapathy, E., Palmer, G.E., Deiwert, G.S. and Lombard, C.K., "An Efficient Adaptive Patched Grid Gas Dynamic Solver for Complex Flows," AIAA/ASME 4th Joint Thermophysics and Heat Transfer Conference, Paper No. 86-1288, Boston, MA, June 2-4, 1986.
53. Nakahashi, K. and Deiwert, G.S., "A Practical Adaptive-Grid Method for Complex Fluid-Flow Problems," NASA TM 85989, June 1984.
54. Nakahashi, K. and Deiwert, G.S., "A Self-Adaptive-Grid Method with Application to Airfoil Flow," AIAA 7th Computational Fluid Dynamics Conference, Paper No. 85-1525, Cincinnati, OH, July 15-17, 1985.
55. Nakahashi, K. and Deiwert, G.S., "Three-Dimensional Adaptive Grid Method," AIAA Journal, Vol. 24, No. 6, June 1986, pp. 948-954.
56. Deiwert, G.S., Andrews, A.E. and Nakahashi, K., "Theoretical Analysis of Aircraft Afterbody Flow," AIAA 17th Fluid Dynamics, Plasma Dynamics, and Lasers Conference, Paper No. 84-1524, Snowmass, Co, June 25-27, 1984.
57. Deiwert, G.S., Rothmund, J.J. and Nakahashi, K., "Simulation of Complex Three-Dimensional Flows," NASA TM 86773, July 1985.

58. Deiwert, G.S. and Green, M.J., "Computational Aerothermodynamics," AAS 33rd Annual Meeting, Paper No. 86-350, Boulder, CO, October 26-29, 1986.
59. Park, C., "Problems of Rate Chemistry in the Flight Regimes of Aeroassisted Orbital Transfer Vehicles," *Progress in Astronautics and Aeronautics*, Vol. 96, 1985, pp. 511-537.
60. Park, C., "Nonequilibrium Air Radiation (NEOAIR) Program: User's Manual," NASA TM 86707, July 1985.
61. Lee, J. H., "Basic Governing Equations for the Flight Regimes of Aeroassisted Orbital Transfer Vehicles," *Progress in Astronautics and Aeronautics*, Vol. 96, 1985, pp. 3-53.
62. Lee, J. H., "Electron-Impact Vibrational Excitation Rates in the Flow Field of Aeroassisted Orbital Transfer Vehicles," AIAA 20th Thermophysics Conference, Paper No. 85-1035, Williamsburg, VA, June 19-21, 1985.
63. Sharma, S. and Park, C., "A Survey of Simulation and Diagnostic Techniques for Hypersonic Nonequilibrium Flows," AIAA 25th Aerospace Sciences Meeting, No. 87-0406, Jan. 12-15, 1987.
64. Intrieri, P.F. and Kirk, D.B., "High-Speed Aerodynamics of Several blunt-Cone Configurations," AIAA 24th Aerospace Sciences Meeting, Paper No. 86-0300, Reno, NV, January 6-9, 1986.
65. Davy, W.C., Park, C., Arnold, J.O., and Balakrishnan, A., "Radiometer Experiment for the Aeroassist Flight Experiment," AIAA 20th Thermophysics Conference, Williamsburg, VA, June 19-21, 1985.

Table I

RATINGS OF FIVE AEROBRAKING ORBITAL TRANSFER VEHICLE DESIGN CONCEPTS

OO - VERY GOOD, O - GOOD, X - BAD, XX - VERY BAD

	BALLUTE	CONICAL LIFTING-BRAKE	RAKED ELLIPTIC-CONE	LIFTING- BODY	RAKED SPHERE-CONE
NAVIGABILITY	XX	O	O	OO	O
STABILITY AND CONTROL	XX	O	XX	OO	OO
BASE FLOW IMPINGEMENT	OO	O	XX	O	O
RADIATIVE HEATING	XX	X	OO	OO	OO
CONVECTIVE HEATING	XX	OO	O	X	O
FRUSTRUM EDGE HEATING	OO	O	X	X	O
ABORT AND MULTIPLE PASS	XX	O	XX	O	O
TRANSPORTATION AND CONSTRUCTION	OO	X	O	O	O
PAYLOAD/WEIGHT RATIO	OO	X	O	?	O
OVERALL RATING	XX	O	X	?	OO

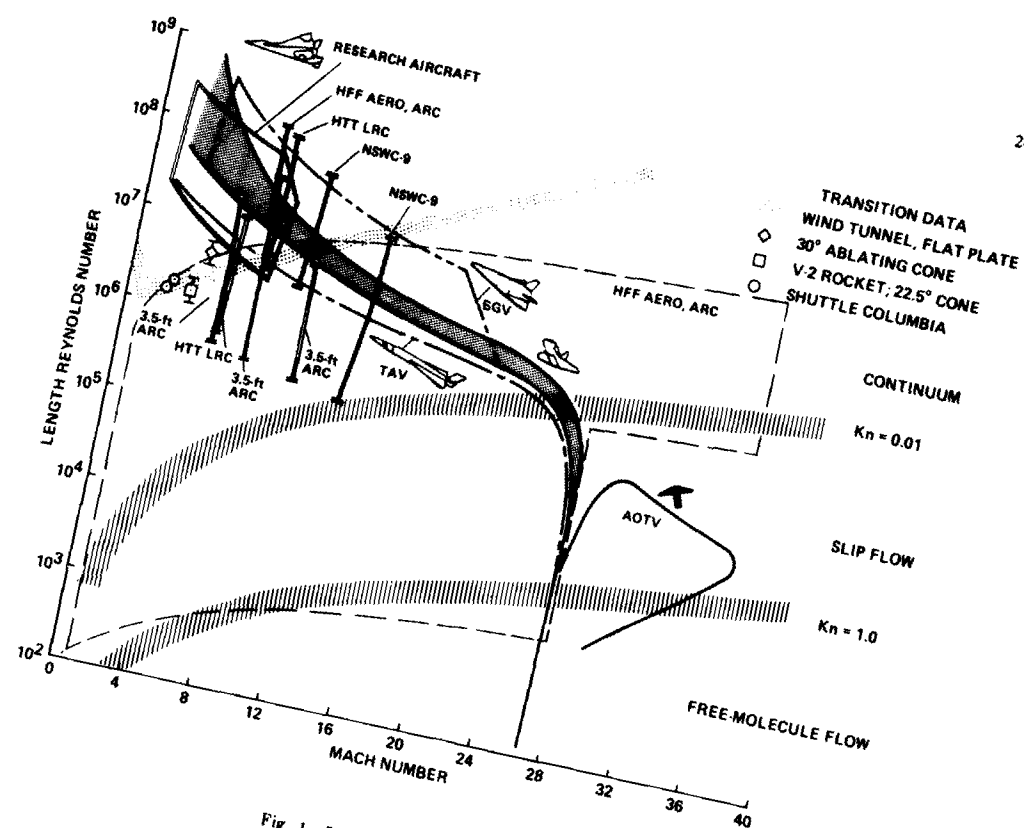


Fig. 1 Flight Domain Simulation Capability.

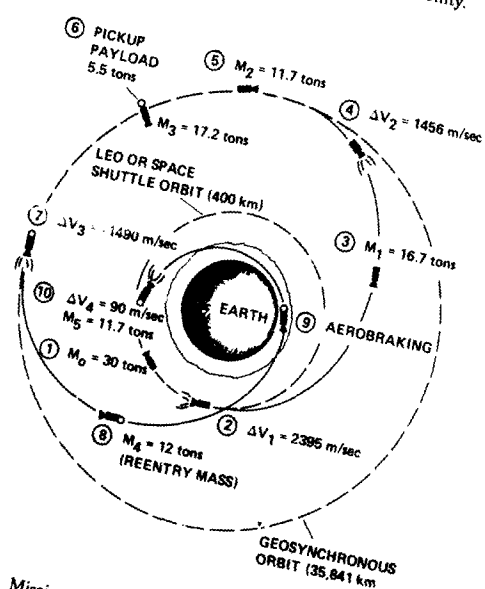


Fig. 2 Mission Schematic for AOTV in Coplanar Maneuver between LEO and GEO. (Masses computed for $i_p = 420$ sec.)

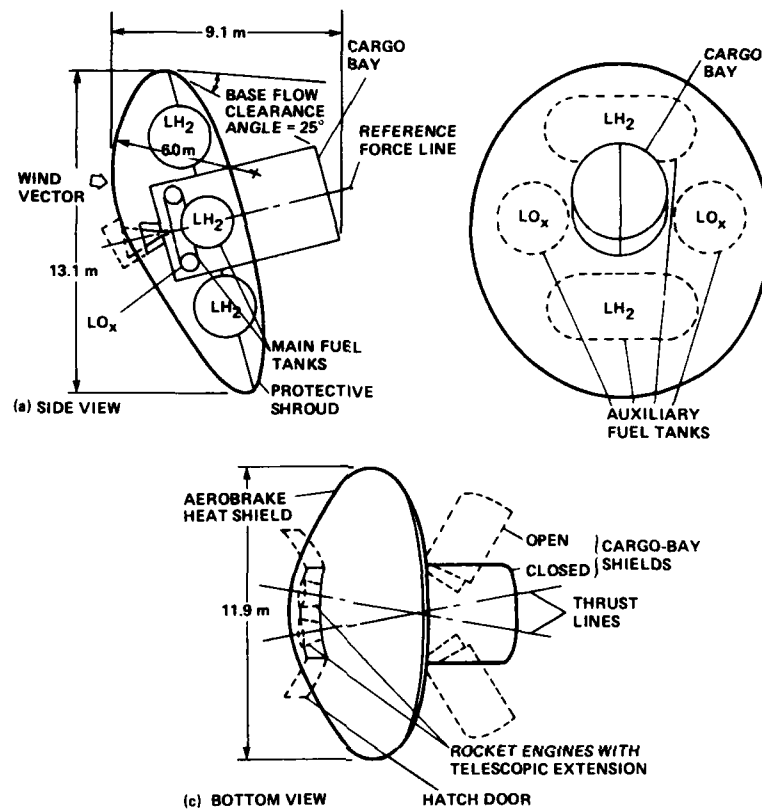


Fig. 3 Overall AOTV Configuration Employing the Sphere-Cone Aerobrake.

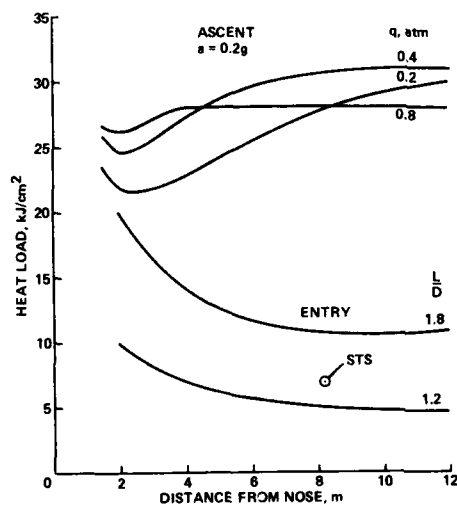
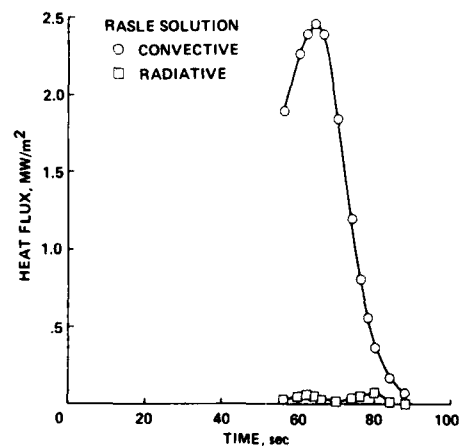


Fig. 4 Total Heat Loads on Generic TAV Windward Centerline.

Fig. 5 Heating Histories at the Stagnation Point ($S/R_n = 0$).

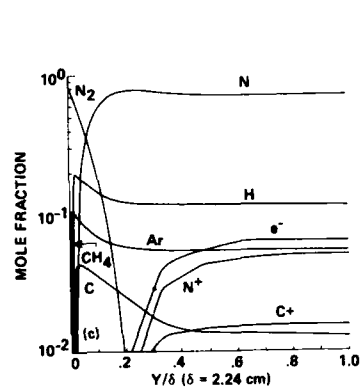


Fig. 6 Shock-layer Structure During Peak Heating along Stagnation Streamline: Chemical Species Profiles.

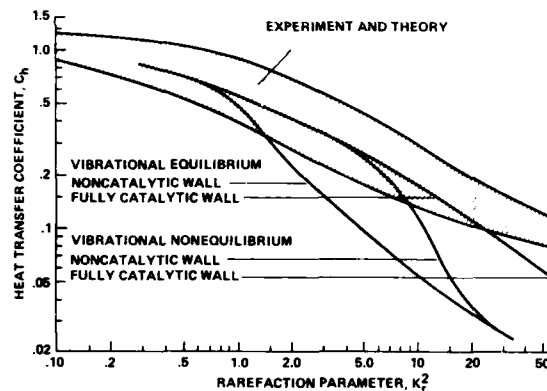


Fig. 7 Convective Heat-transfer Rate Correlation.

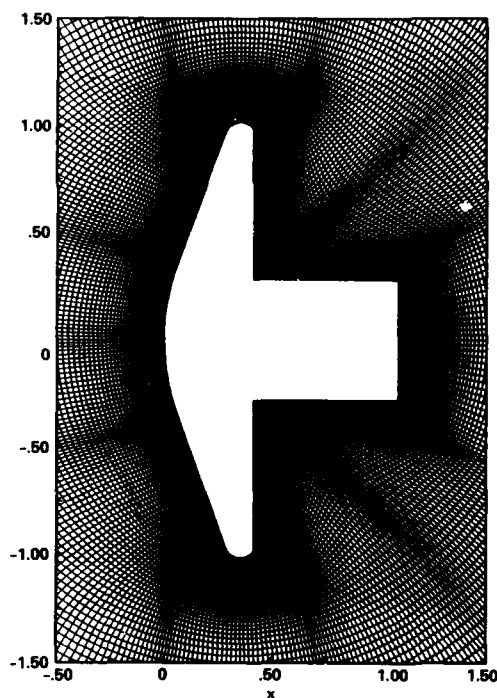


Fig. 8 Geometry and Grid for Two-dimensional AOTV Flowfield Simulation.

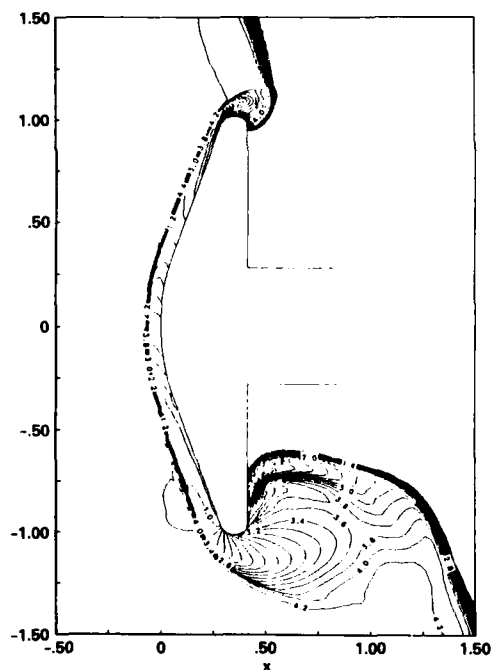


Fig. 9 Computed Mach Contours for Two-dimensional AOTV Shape. $M_{\infty} = 30$, $\alpha = 15^\circ$, $\gamma = 1.1$.

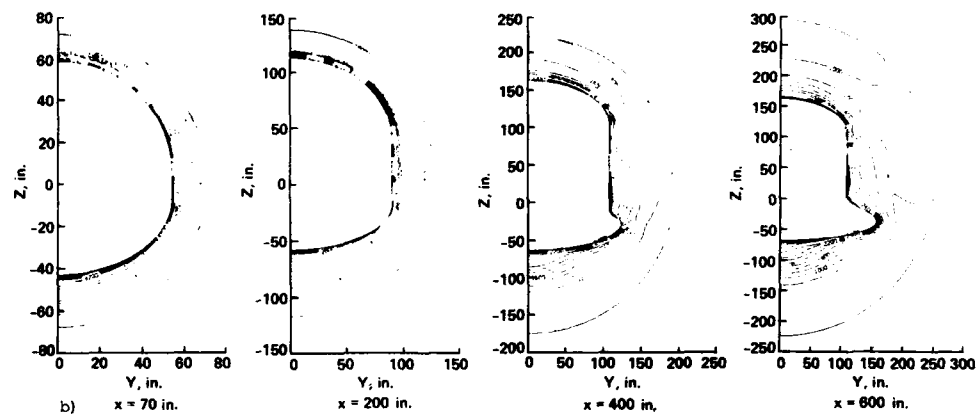
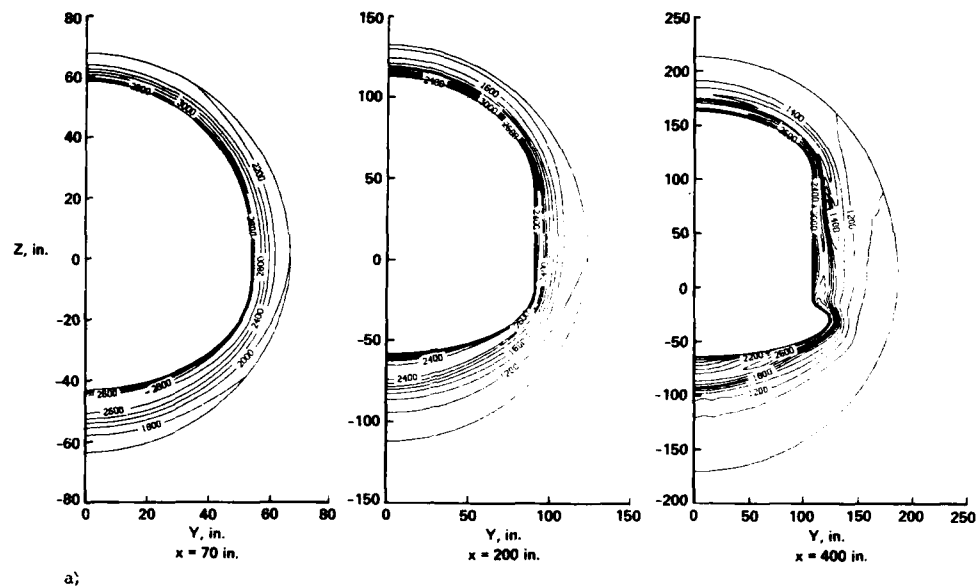


Fig. 10 Comparison of Equilibrium and Ideal Air Temperature Distributions at Several Cross-Sections of the Space Shuttle Orbiter. $M_\infty = 13$, $H = 55.8$ km. a) Equilibrium Air; b) Ideal Air.

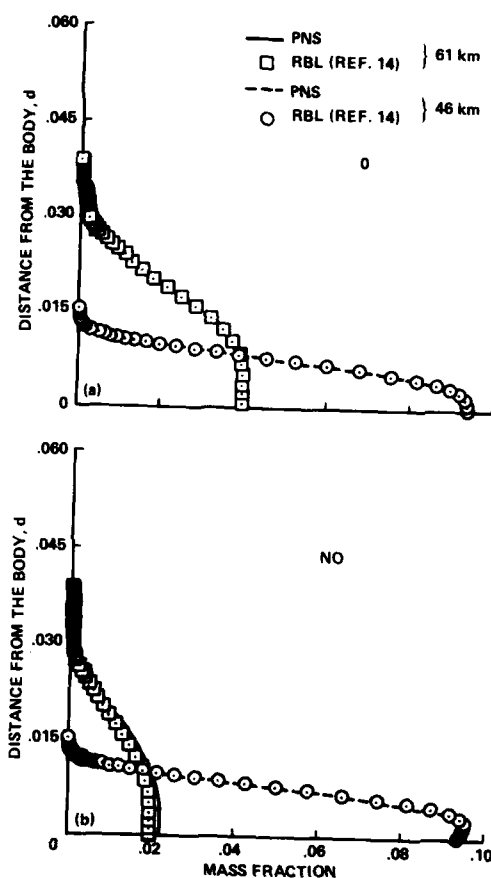


Fig. 11 Computed Species Mass-fraction Profiles in the Shock Layer of a 10° Cone. $V_\infty = 8.1$ km/sec. a) Oxygen Mass Fraction; b) Nitric Oxide Mass Fraction.

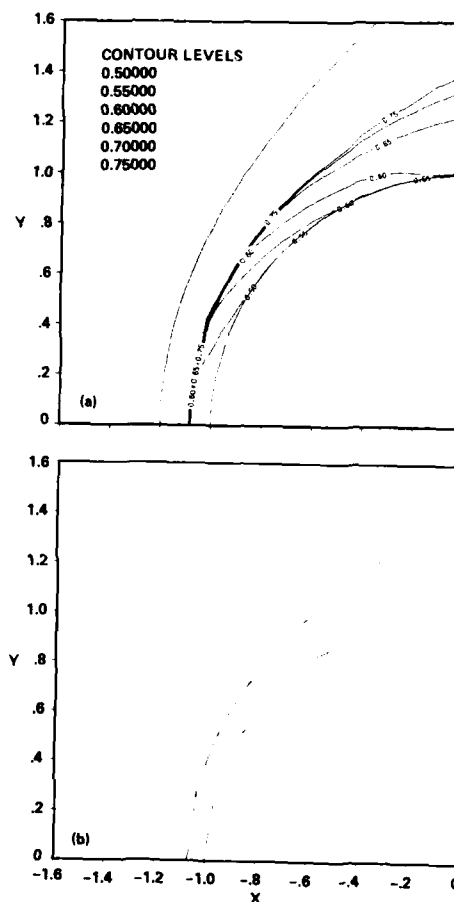


Fig. 12 Comparison of N_2 mole-fraction contours over Hemisphere Nose. $M_\infty = 20$. a) CAGI2 Solution; b) Solution from Ref. 40.

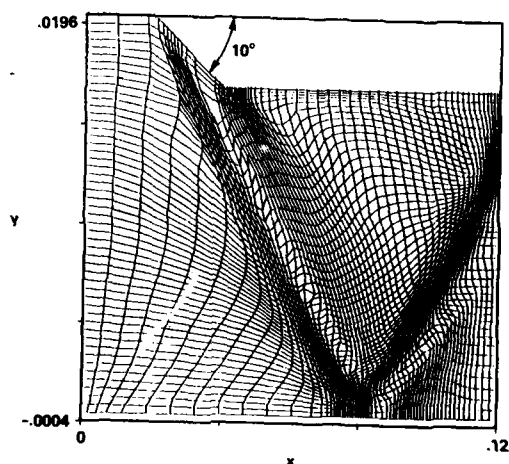


Fig. 14 Computed Isobars for Hypersonic Inlet using Solution Adapted Grid. $M_\infty = 5.0$.

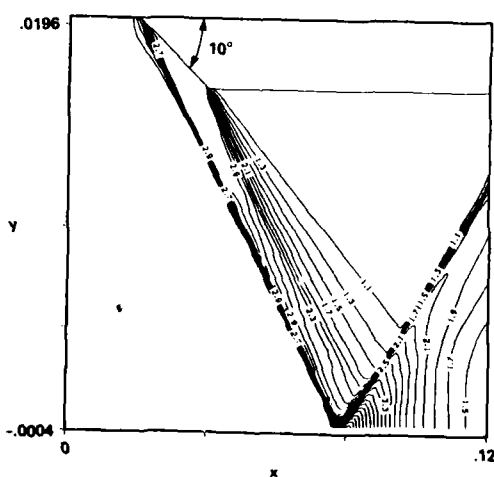


Fig. 13 Solution Adapted Hypersonic Inlet Grid - 10° wedge. (Note unequal scales.)

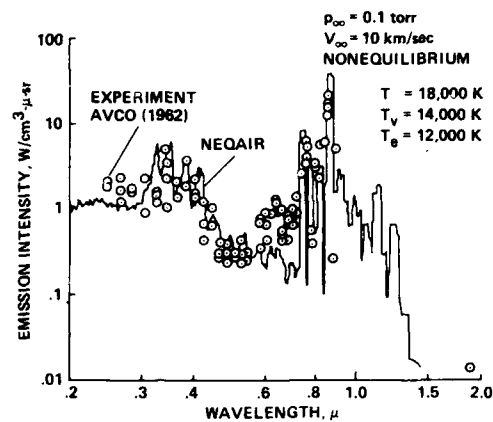


Fig. 15 Comparison between calculated and Measured Spectra behind a Plane Normal Shock Wave.

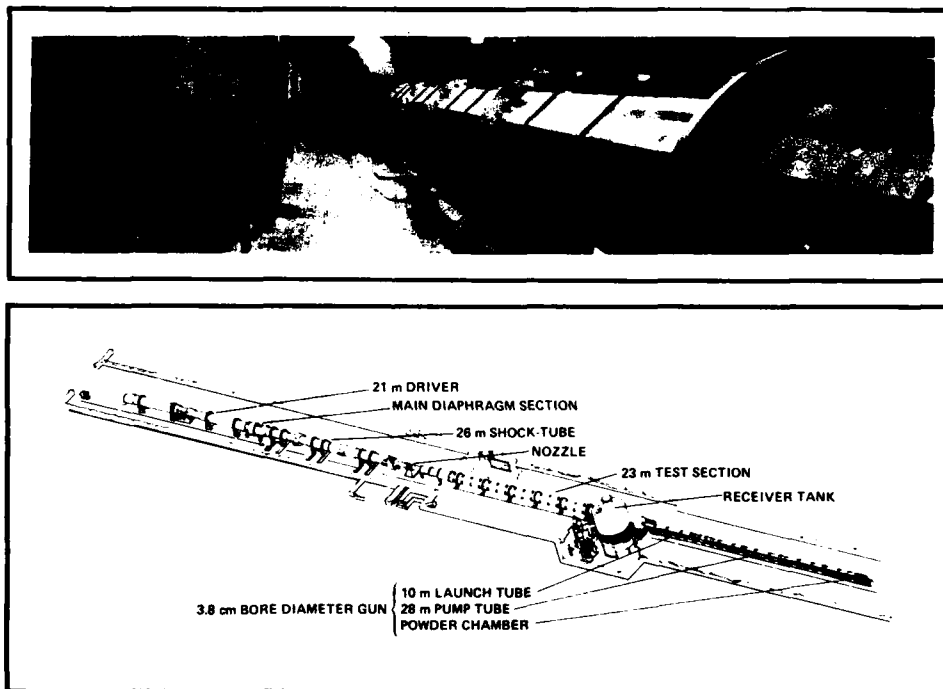


Fig. 16 Hypersonic Free Flight Aerodynamic Facility.



Fig. 17 Shadowgraph of Galileo Probe. $M_\infty = 14$, $Re_d = 100,000$.

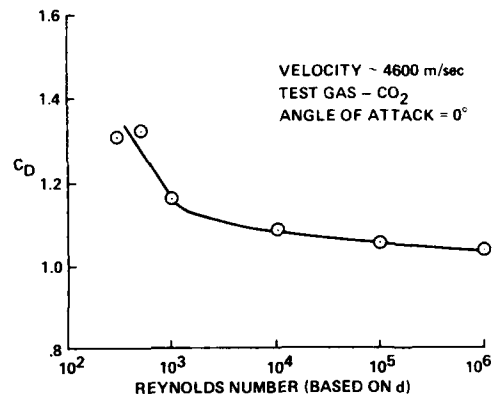


Fig. 18 Effect of Reynolds Number on Drag Character Characteristics of Pioneer Venus.

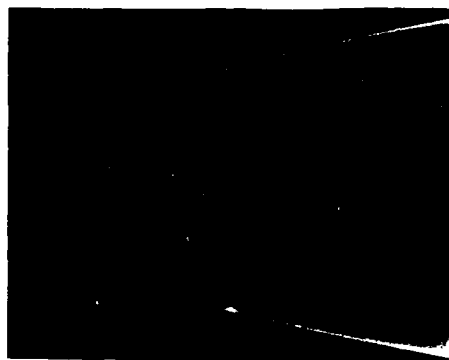


Fig. 19 Shadowgraph of Symmetric AOTV.



Fig. 20 Shadowgraph of AFE Model.



Fig. 21 Generic All-Body Hypersonic Aerospace Plane Model. 75° half-angle delta with elliptic cross section.

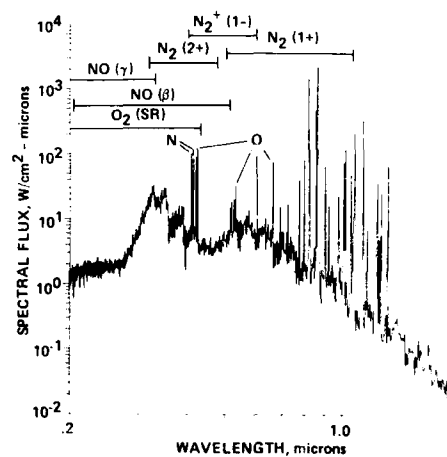


Fig. 22 Nonequilibrium-flow Spectral Flux: Shock-layer Depth = 20.9 cm.

VORTEX FORMATION OVER DELTA, DOUBLE-DELTA AND WAVE RIDER CONFIGURATIONS AT SUPERSONIC SPEEDS

by

Uwe Ganzer and Joachim Szodruch

Messerschmitt-Bölkow-Blohm GmbH

Unternehmensbereich Transport- und Verkehrsflugzeuge
D-2103 Hamburg 95 and D-2800 Bremen 1, FRG

SUMMARY

The flow field of the thick delta wing at high subsonic and at supersonic speeds has been the subject of quite a variety of investigations at the Technical University of Berlin. The research work started as early as in the late 60s and is still going on today. It was triggered off by the initiatives of the late "Dietrich Küchemann-aiming" at a hypersonic transport and it was taken as a contribution to the Eurohyp activities.

The wing configurations investigated at the Technical University of Berlin were of simple shape: Delta wings with straight leading edges and triangular cross sections of different thickness. The interest was focussed on the development of the leeside flow with changes in angle of incidence and main stream Mach number. In addition to that similar delta wings with curved leading edges and also with a jump in leading edge sweep were investigated, as well as two types of wave riders. Besides some theoretical work mainly wind tunnel test were made applying available test techniques: Surface pressure measurements, Pitot measurements in the flow field, flow visualization by Schlieren, vapour and oilfilm technique, skin friction determination using oilfilm interferogram and, finally, laser velocimetry (laser-two-focus-system). The experimental investigations were particularly challenging, because of the small models of generally not more than 6 cm span. This limitation arose from the small size of the transonic and supersonic wind tunnel (15 x 15 cm).

The paper will give a review on the activities and a brief report on some of the findings.

1. INTRODUCTION

About three decades ago - at the end of the 50s - considerable effort started at various West-European research institutions to explore the possibilities of hypersonic transport. Wave rider configurations were found to be the most promising aerodynamics shapes. Such wave riders are in general delta wings featured by a rather thick cross section. At the Technical University of Berlin, the basic aerodynamics of these configurations have been investigated for many years. The investigations comprised simple delta wings with straight leading edges and double delta wings - both with triangular cross sections - as well as wave rider configurations. Vortex-type separations at the leading edges are the main characteristics of these delta wings at subsonic as well as at supersonic speeds.

The origin, location, form and general structure of the vortices depends on many parameters such as Mach number, Reynolds number, sweep angle, angle of attack, form of the leading edge and eventually body shape in general. The effect of these parameters has been experimentally investigated at the supersonic facility of the Technical University of Berlin and various wind tunnels at other research institutes. The experimental tools included surface and flow field pressure measurements, Laser-2-Focus measurements, skin friction measurements, surface and flow field visualization including visualization of skin friction.

The paper will present results obtained for three different configurations:

- 1) The simple delta wing planform with triangular cross section is ideally suited for a description and systemization of the vortical lee side flow fields as they occur for different Mach numbers, angle of attack and leading edge sweep. For these parameters domains of vortical flows can be defined. Additionally the influence of Reynolds number, present only at certain conditions, will be exhibited. Furthermore, the behaviour of free vortices in the wake of delta wings was studied in detail.
- 2) Double-delta planforms, either increasing or decreasing leading edge sweep angle in downstream direction allow detailed insights into the interaction of two or more vortex flow fields emanating from different generators. These studies lead to the conclusion that vortex interference at subsonic and supersonic speeds is different due to Mach number and compressibility effects, and that vortex breakdown is influenced by these interacting vortices.
- 3) Finally wave rider and more sophisticated hypersonic vehicles have been investigated in order to study the configurational influence on vortex formation and eventually on the performance. Details of the flow field studies over a Jones wave rider with vertical stabilizer and representation of a fuselage will be presented.

2. VORTICAL FLOW OVER BASIC DELTA WINGS

The simple delta wing planform with triangular cross-section is ideally suited for a basic description and systemization of the lee-side vortex flow fields as they occur for different Mach numbers,

angle of attack and leading edge sweep angle. For these parameters domains of vertical flow fields can be defined. This classification strictly is valid only for one Reynolds number so that this parameter needs to be included, although for sharp leading edges only at certain flow conditions the vortex behaviour is affected by Reynolds number changes. Important knowledge concerning vortical flows is gained from wake studies downstream of the base of delta wings. Finally the geometry of the cross section of the delta wing can alter strongly the type of vortical flow over the lee-side.

In the following a detailed description on these four topics for simple delta wing configurations at supersonic speeds is given.

2.1 Classification of flow fields

In a first attempt to systemize the compressible lee-side flow field over a delta wing as sketched in Fig. 1, it is assumed that the Reynolds number is fixed and the boundary layer is either fully turbulent or fully laminar. Then there are Mach number, angle of attack and leading edge sweep angles as main variables. For essentially conical flow, the Mach number and angle of attack components normal to the leading edge can be written as

$$M_n = M_\infty \sqrt{1 - \sin^2 \Lambda \cdot \cos^2 (\alpha + \beta)}$$

$$\alpha_n = \tan^{-1} \frac{\tan (\alpha + \beta)}{\cos \Lambda} - \tan^{-1} \frac{\tan \beta}{\tan \Lambda}$$

These relations were derived in [1]. In case of flat topped delta wings ($\beta = 0$), as discussed in this section, these normal components reduce to those originally given by Stanbrook and Squire [2]. Evaluating available experimental results Stanbrook and Squire found mainly two types of flow. When plotting these findings in a diagram with α_n vs M_n , regions of attached and separated flow at the leading edge are divided by the so-called "Stanbrook-Squire Boundary", abbreviated to SSB in the ensuing text, Fig. 2.

Further detailed studies at the Technical University of Berlin with flat topped thick delta wings (thickness-to-chord ratio = 0.25) lead to an extended $\alpha_n - M_n$ diagram. As seen in Fig. 2 especially to the right hand side of the SSB, more details of the vortical flow have been found and thus additional boundaries could be incorporated [3]. These results were supported later by quantitative skin friction measurements and visualization of skin friction [4]. One example for a type of flow to the right of the SSB is shown in Fig. 3.

2.2 Reynolds number influence

In general the Reynolds number influence has to be considered for each individual type of flow left and right of the SSB. This is because for example the vortex at leading edge separation condition is fixed and thus the primary vortical flow is not expected to vary with Reynolds number. In contrast secondary separation may be influenced as well as most of the flow types to the right of the SSB since there attached leading edge flow is prevailing. Details of the flow changes to the left and right of the SSB with Reynolds number variation have been studied in [5]. A summary of these investigations and a comparison to other results is presented in Fig. 4 and 5 [6]. Here at constant α_n and M_n respectively, the influence of Reynolds number on flow types in the $\alpha_n - M_n$ diagram is presented. For the type of flow denominated "separation with shock" we deduce that the effect of transition diminishes until at higher Reynolds numbers this kind of vortical flow field can no longer be ascertained. Here leading edge separation develops directly in the type of flow with shock induced separation.

At high Mach numbers ($M_n \sim 2.5$) and high incidences, Reynolds number variation has the effect of changing the boundary layer thickness developing from the leading edge and thus changing the Prandtl-Meyer expansion around the leading edge. In consequence the shock strength and thereby the primary separation line position is changing. A strong dependence of the boundary between shock induced separation and leading edge separation is supported by the few available experiments used in Fig. 5. Thus, even for the sharp edged delta wing it has been demonstrated that the parameter Reynolds number cannot be neglected.

2.3 Wake flow field of delta wings

It is only fairly recently that the investigation of the delta wing model, shown in Fig. 1, was taken up again. The purpose of the new test campaign was to study the vortex development over the rear part of the model and downstream of its trailing edge. With two models of different thickness, it was a chance to investigate the impact of different base flows on vortex development. The test techniques were laser vapour screening and laser velocimetry. Besides that some Schlieren and oilflow pictures were taken again.

The thick-delta-wing-model may be identified from the Schlieren picture, Fig. 6. The Schlieren-visualization indicates the complex flow structure in the base area of the model. Besides the impact of the expansion at the trailing edge the interaction with the 3-D-base flow structure will determine the flow development of the leading edge vortices downstream of the model.

In the Schlieren-picture it is indicated for which cross sections vapour screen pictures are available [15]. Two examples of vapour screen pictures are shown in Fig. 7. The fotos inherit optical distortions which are been taken out in the drawings. On the leeside of the wing the flow structure is featured by a primary vortex with a feeding layer linking up to the leading edge and a secondary vortex below. On top of the primary vortex the flow is strongly expanded with local velocities being conically supersonic. A shock wave terminates the supersonic region.

The oilflow visualization features a clear dark line which was not found in earlier experiments. Fig. 8. Comparison with vapour screen pictures link this line to the secondary separation caused by the primary vortex. Results of the laser velocimetry measurements for the trailing edge plane ($x/l = 1.0$) are presented in Fig. 9 through 11.

The measurements were handicapped by the fact that no readings were obtained in the vortex region. Obviously no particles entered that area. At its boundary measurements were only obtained by increasing laser power from 0.3 to the max. 1.0 Watt.

Each point did require 3 to 6 measurements of appr. 1 min. Thus the 130 points in one plane of measurement took about 13 hours to measure! The pictures shown are the result of extensive inter- and extrapolation and cross-checking [16].

Fortunately the vapour screen pictures compare very well with the results from laser measurements, so that these pictures may be used to quite an extend for studying the flow field. An example is shown in Fig. 12. It compares the flow structure for the thick and thin delta wing.

In a similar way comparisons were made between the flow structure obtained with a full model and a half model. The comparison revealed that for a half model the flow is strongly influenced by an additional vortex which occurs on the junction between sidewall and model. Thus half models were found not to be useful for this type of study [15, 16].

2.4 Influence of geometry

Two aspects of the geometrical influence on the lee-side flow field shall be discussed in the following. First, it has been pointed out already that there seems to be a different vortical flow development when either thin or thick delta wings are considered, i.e. the angle between upper and lower surface normal to the leading edge ψ is a major geometrical parameter. Secondly it will be shown that the shape of the upper surface can influence the flow types and boundaries as presented in the above classification. Thus, also the angle between the leeward meridian and the X-axis β is considered another important parameter. Therefore it can be expected that at the same α_n and M_n the leeward flow field for a thick ($\psi = 15^\circ$) and thin ($\psi = 40^\circ$) delta wing will differ. The bow shock as well as the flow around the leading edge is different so that the boundary layer development on the upper surface is affected. One example is given in Fig. 13 where the secondary separation line position of the type of flow to the right of the SSB is plotted versus angle of attack.

Also the non-conical regions of a delta wing very close to the tip indicate the influence of ψ . Fig. 14 shows the chordwise starting position of the separation line for two different leading edge angles ψ . The difference between thin and thick wings is evident, however it has to be kept in mind that the reason lies not only in the viscous interaction due to the different geometry but also is caused by imperfections in manufacturing the models. These two examples for the influence of the leading edge angle indicate already that also some of the boundaries in the $\alpha_n - M_n$ diagram are shifted to different positions [6].

The majority of systematic investigations on the lee-side flow over delta wings at supersonic speeds is concerned with flat upper surface as discussed in section 2.1 through 2.3. Based on these results, in [1] the attempt was made to characterize the different types of flow over a wing with a delta shaped upper surface, i.e. the wedge angle is $\beta > 0$. Fig. 15 summarizes the findings in the $\alpha_n - M_n$ diagram, however the normal flow components are now dependent on β as well. While leading edge and shock induced separation is still present, only at different values of α_n and M_n , there are now large regimes of non-conical flow. No apparent correlation between the flat and delta shaped upper surface flow fields of delta wings seem possible.

3. VORTEX INTERFERENCE OVER DOUBLE-DELTA WINGS

In the above sections only delta wings with straight leading edges have been considered. The following discussion concentrates on delta wings having decreasing or increasing leading edge sweep angles. The variation of leading edge sweep can either be gradually or discontinuous, Fig. 16. Then the question arises if the known classification for flow types resulting from straight leading edges is applicable locally for these types of wings.

In any case one must expect that the interaction of vortices emanating from differently swept edges lead to complex vortical flows over these types of double-delta wings. The planform shape of these double-delta wing were designed in such a way that for a given Mach number $M_\infty = 3.0$ a sweep angle at the tip and at the trailing edge of $\Lambda = 80^\circ$ and 69° respectively, will result in experimental trajectories in the $\alpha_n - M_n$ diagram which are positioned left and right to the SSB. An overview of wind tunnel models and the location of the experimental envelope in the $\alpha_n - M_n$ classification is given in Fig. 16. Models with decreasing sweep angles were denominated strake wings, either having a kinked leading edge or a continuously changing sweep angle from tip to trailing edge. The Gothic wings on the other hand are those models with increasing sweep angle in flow direction.

In the following results of investigations on strake and Gothic delta wing configurations immersed in a supersonic flow will be presented.

3.1 Strake wing configuration

Pressure measurements, surface and flow field visualization have been carried out in order to study the vortical flow development. One typical example [9] for a Mach number of $M_\infty = 2.5$ and higher angles of attack is given in Fig. 17.

The visualization in Fig. 17 shows the rather normal vortex development upstream of the leading edge kink, while downstream the complex vortex interaction is hardly detectable from the visualization. One hint in which way the vortex emanating from the upstream leading edge interferes with the vortex shedding downstream of the kink is shown in the water tunnel visualization in Fig. 18.

In general it has been found that for the downstream flow region of the strake wing the classification as used for the basic delta wing with straight leading edge can hardly be utilized. Even the vortex flow upstream of the kink is influenced by the downstream flow field.

These findings are supported by pressure measurements across the rear part of the wing ($x/l = 0.7$) as plotted in Fig. 19 [7]. The interference between tip and kink vortex of the strake wing induces especially for lower Mach numbers high negative pressures as compared with the basic delta wing. Also the vortex intensity in Fig. 20, deduced from wall skin friction lines in oilflow pictures leads to the conclusion of different flow fields of basic delta and strake wing configurations in the downstream part of the flow field.

Thus the interacting vortices in the downstream region of the strake I configuration cannot be classified according to the basic delta wing systemization.

The strake II configuration having a continuously curved leading edge seems to generate one vortex pair only, following the curvature of the leading edge. At higher angles of attack a secondary vortex appears.

The pressure distribution for both strake configurations and the basic delta wing is shown in Fig. 21. At low incidences the similarity of pressure distribution between strake II and basic delta wing is seen, while the strake I configuration clearly indicates the two vortices from the upstream and downstream part of the leading edge. In contrast at high angles of attack the vortex emanating from the tip region of both strake wings seems to dominate the entire downstream flow field so that the pressure distribution shows little differences.

Summarizing the results for the strake II configuration it has been found that as long as the normal Mach number M_n along the entire leading edge is smaller than one, i.e. positions to the left of the SSB, there the leading edge separation type of flow is dominating at all chordwise positions. When the Mach numbers M_n in the downstream part of the strake II wing become larger than one, a different type of flow develops in that region. However, even then the flow is governed by the vortex generated in the tip area.

3.2 Gothic wing configuration

A first impression of the flow field over the Gothic I wing is presented in Fig. 22 [8] with oil-flow and vapour screen pictures at three different incidences. At small angles of attack the leading edge separation occurs according to the local sweep angle. The flow appears to be conical over most parts of the wing. At higher angle of attack again the vortex emanating from the tip region seems to influence the flow field entirely. Separation and attachment lines are mostly conical with respect to the wing tip. Thus it is expected to find similarities to the basic delta wing flow field.

In Fig. 23 the vortex positions above a Gothic and a basic delta wing are compared and up to medium angles of attack a similar vortex behaviour over the two wings is observed. At higher incidences different types of flow between the wings may be encountered: While here the delta wing tends to the flow type "separation with shock" the Gothic wing seems to remain in the flow region with "leading edge separation".

The Gothic II wing with continuously increasing leading edge sweep angle behaves very much like the Strake II wing, i.e. only one vortex system develops and separation and attachment lines follow closely the variation of leading edge sweep. Although from visualization techniques the Gothic II flow field seems to be without major surprises, Fig. 24 shows more details evaluated from Pitot-probe measurements at a chordwise position $x/l = 0.7$. Besides primary and secondary vortex there is apparently a third region above the wing which could be interpreted as a vortex. More detailed measurements are necessary and especially non-intrusive ones are needed to avoid the observed probe influence on the flow field even at these supersonic velocities [14].

4. WAVE RIDER FLOW FIELD AT OFF-DESIGN CONDITIONS

When the possibilities of hypersonic transport have been explored wave rider configurations were found to be the most promising aerodynamic shapes. At the Technical University Berlin two basic wave rider wings were subject of theoretical and experimental investigations, the Nonweiler wave rider and the Jones wave rider respectively. The wave rider design follows the concept of shaping the wing according to a known flow field. Thus the hypersonic flow around a 2-d wedge is the basis for the Nonweiler wing, while the Jones wave rider is based on the flow around a circular cone. Both configurations are characterized by three design parameters as there are the Mach number M_d , the semi-span-to-length ratio s/l and the volume parameter $\tau = V/F$. Both wave riders were designed for $M_d = 7.0$. The Nonweiler wing parameter resulted then in $s/l = 0.3$ and $\tau = 0.08$, while the Jones wave rider was slightly more slender with $s/l = 0.28$ but having more volume at the same time with $\tau = 0.0883$. Thus the Jones concept seems to be closer to application than the Nonweiler wing, not only because of more volume but also since the volume distribution and thereby the payload capabilities are more advantageous.

In the following a summary of these investigations on Nonweiler and Jones wave rider configurations as sketched in Fig. 25 will be presented. The results are confined to off-design conditions in the supersonic speed regime.

4.1 Nonweiler wave rider

The Nonweiler wing is the simplest type of wave rider, having straight leading edges and ridge lines and between these, plane surfaces, Fig. 25. At its design condition this wave rider produces a plane shock wave attached to the leading edges and between this shock and the lower surface the flow is parallel to the lower ridge line. The flow condition corresponds to that of a flow around a two-dimensional wedge of angle θ .

If the Mach number is reduced below the design value (or angle of attack is increased) the shock wave bulges and finally separates from the wing. Thus flow around the leading edges occurs and separations are formed, rolling up into spiral vortex sheets. The vortices account for low pressure on the upper surface of the wing producing a considerable amount of additional lift and thus improving the lift-to-drag ratio, Fig. 26. At subsonic speeds the low pressure due to the leading edge vortices provides roughly half of the total lift in this particular case.

The values for lift and drag have been calculated from measured pressure distributions. The pressure measurements along the surface of the Nonweiler wing revealed remarkable non-conical effects for subsonic and low supersonic free stream conditions. In particular strong upstream influences of base flow are shown to exist especially for the lower surface of the wing. Thus model mounting in the wind-tunnel becomes critical as it effects the surface pressure via the base flow.

If for the Nonweiler wing the free stream Mach number is just slightly below the design value (or angle of attack is just above) the shock wave bulges with a plane portion attached to the leading edges, Fig. 27. Near the leading edges the flow is still parallel with constant pressure. Within the Mach cone the flow direction varies while the flow expands towards the lower ridge line. Such a flow is amenable to an exact but inviscid calculation [13].

The solution for the leading edge region is straight-forward by the use of oblique shock relations. For the central region within the Mach cone a finite-difference solution was necessary. Starting with a zeroth-order solution chosen in such a way that the boundary conditions are satisfied, an iterative process leads to the exact solution. As an example a calculated pressure distribution is shown in Fig. 28. Although the Nonweiler wave rider is of fairly restricted practical importance, such results are of interest for testing approximate solutions.

4.2 Jones wave rider

While the Nonweiler wave rider was designed to produce at the lower surface a flow equivalent to a wedge flow, i.e. a parallel flow following a plane shock, the Jones Wave rider is based on a cone flow, Fig. 29. At the design condition, the shock wave is conical and attached to the leading edges, and the pressure along the curved lower surface is not constant. For practical application of the wave rider concept to a hypersonic cruise configuration the Jones wing is much more realistic, because of reduced dihedral and more favourable volume distribution as compared to the Nonweiler wing. At Messerschmitt-Bölkow-Blohm (MBB) the applicability of the Jones wing to a hypersonic transport configuration has been demonstrated, Fig. 30 [17].

The flow field of the Jones wave rider at off-design condition is more complex, because it is basically non-conical. In particular, when the upper surface is designed to produce an expansion equivalent to a Prandtl-Meyer flow, this surface will also be curved and generally no similarity will exist between cross-section shapes at various chordwise positions. Accordingly the flow structure varies with chordwise position as can be seen from some measured pressure distributions presented in Fig. 31. Such surface pressure measurements have been made for various subsonic and supersonic free stream conditions in order to provide data for comparison with theoretical results.

For subsonic and moderate supersonic speeds an attempt has been made to calculate the flow field for bodies of general shape, such as the Jones wave rider. The assumption was made that the body had to be slender, so that Slender-Body-Theory could be used, but otherwise the body could have sharp leading edges and finite thickness. Following a suggestion of Hummel [18] two-dimensional singularities have been distributed over the surface contour of the body in the cross-sections perpendicular to the main stream direction, Fig. 32. In this way the method is applicable to slender bodies of any cross-sectional and planform shape. For bodies with sharp leading edges, however, leading edge separation occurs even for small angle of attack. Such separations are not accounted for in the theory so that one has to expect that calculated pressure distributions will show considerable discrepancies when compared with experimental results on the upper surface of the wing near the leading edge.

Theoretical results obtained for the Jones wave rider are shown in Fig. 33. They again compare fairly well with experimental results not only for subsonic free stream conditions but also for the supersonic Mach number. The weak point remains the leading edge separation region. As the comparison is made for the cross-section at 60 % chord position, the experimental results are assumed to be free of base-pressure influence.

The chordwise variation of pressure distribution for the Jones wave rider is shown in Fig. 34. While for the Nonweiler wing the pressure level is nearly constant at supersonic free stream conditions, for the Jones wave rider theory predicts variation of pressure level on the lower surface due to the basically non-conical shape to the body.

5. CONCLUSIONS

The variety of mainly experimental results obtained for thick delta wings yields some basic information on the flow structure as it develops at subsonic, transonic and supersonic flow conditions. By comparing the results of different experimental techniques sufficient cross-check is provided to allow fairly reliable conclusions from the tests of comparatively small models. The information given allows first of all a classification of the lee-side flow condition with dominant leading edge separation. Some non-conical features of the flow have been analysed mainly by use of flow visualization methods. They shed some light on the upstream influence of the base flow and the development of the vortex structure downstream of the wing.

6. ACKNOWLEDGEMENT

Most of the work reported in this paper was carried out at the Aerospace Institut (ILR) at the Technical University Berlin. The investigations were supported largely by the German Science Foundation (DFG). Finally, the support of the staff, the various students and researchers over the many years of investigation is greatly acknowledged, especially the contribution of C. Klinger and R. Henke is appreciated.

7. REFERENCES

- [1] Szodruch, J. Zur Systematik der Leeseiten-Strömung bei Deltaflügeln. Z. Flugwiss. Weltraumforsch. 4, 1980, Heft 2.
- [2] Stanbrook, A. Possible types of flow at swept leading edges. Aeron. Quart. 15, 1964, pp. 72 - 82.
- [3] Szodruch, J. Leeseiten-Strömung bei schlanken Deltaflügeln endlicher Dicke. ILR-Bericht 23, 1977, Technical Univ., Berlin.
- [4] Szodruch, J. Messung und Sichtbarmachung von Wandschubspannungen. Z. Flugwiss. Weltraumforsch. 6, 1982, Heft 4.
- [5] Szodruch, J. Reynolds number influence on leeside flowfields. AIAA Journal, Vol. 16, No. 12, 1978, pp. 1306 - 1309.
- [6] Szodruch, J. Leeward flow over delta wings at supersonic speeds. NASA TM 81 187, April 1980.
- [7] Ganzer, U. Leeseitenströmung von Deltaflügeln mit gekrümmter Vorderkante im Überschall. ILR-Mitt. 87, 1981, Techn. Univ., Berlin.
- [8] Henke, R. On the lee-side flow of delta wings with curved leading edges. Euromech-Colloquium 126, April 1980, Berlin.
- [9] Henke, R. Wind tunnel tests of delta wings at $M = 2.5$. CoA Memo 8216, Cranfield Inst. of Techn., 1982.
- [10] Ganzer, U. On the aerodynamics of hypersonic cruise vehicles at off-design conditions. ICAS Proceedings 1978, Vol. 1, A2-03.
- [11] Hoder, H. Über das Strömungsfeld von Wellenreitern im Unterschall und niedrigem Überschall. ILR-Bericht, 1980, Techn. Univ. Berlin.
- [12] Ganzer, U. Experimentelle Ergebnisse zum Nonweiler Wellenreiter im Unter-, Trans- und Überschall. Z. Flugwiss. 21, 1973, Heft 4.
- [13] Ganzer, U. Eine exakte Berechnung des reibungsfreien Strömungsfeldes an der Unterseite von Nonweiler Wellenreitern. Z. Flugwiss. 23, 1975, Heft 4.
- [14] Szodruch, J. Lee-side flow field of delta wings with detached shock waves. Euromech 74 Colloquium, 1976, Cambridge (U.K.).
- [15] Klinger, C. Sichtbarmachung der Leeseiten-Strömung von Deltaflügeln im Überschall. Studienarbeit Inst. f. Luft- und Raumfahrt, TU Berlin, Nov. 1986.
- [16] Klinger, C. Vermessung einer Wirbelströmung mit Hilfe eines Laser-2-Focus-Velozimeters. Diplomarbeit Inst. f. Luft- und Raumfahrt, TU Berlin, Febr. 1987.

- [17] Lifka, H. Prizbilla, H. Untersuchungen an einem Hyperschallflugkörper hoher Gleitzahl (Wellenreiter). MBB-Bericht, Nov. 1971.
- [18] Hummel, D. Berechnung der Druckverteilung an schlanken Flugkörpern mit beliebiger Grundriß- und Querschnittsform in Unter- und Überschallströmung. Inst. f. Strömungsmechanik der TU Braunschweig, Bericht 68/1, 1968.

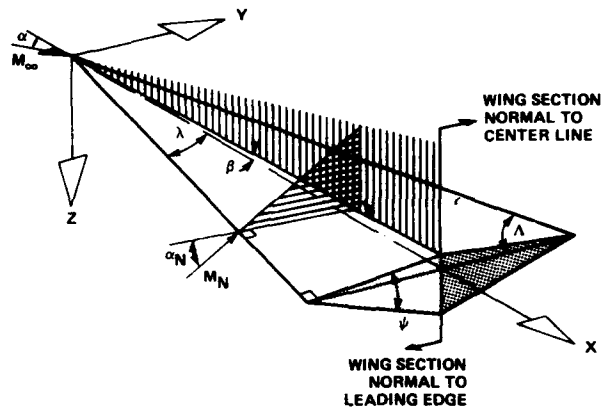
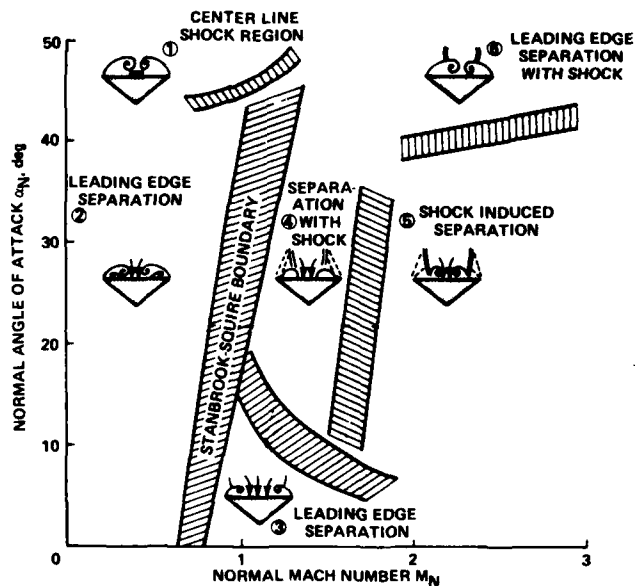


Fig. 1 DELTA WING GEOMETRY AND FLOW COMPONENTS

Fig. 2 LEE SIDE FLOW REGIMES OVER THICK DELTA WINGS AT SUPERSONIC SPEEDS - α_N VS M_N DIAGRAM

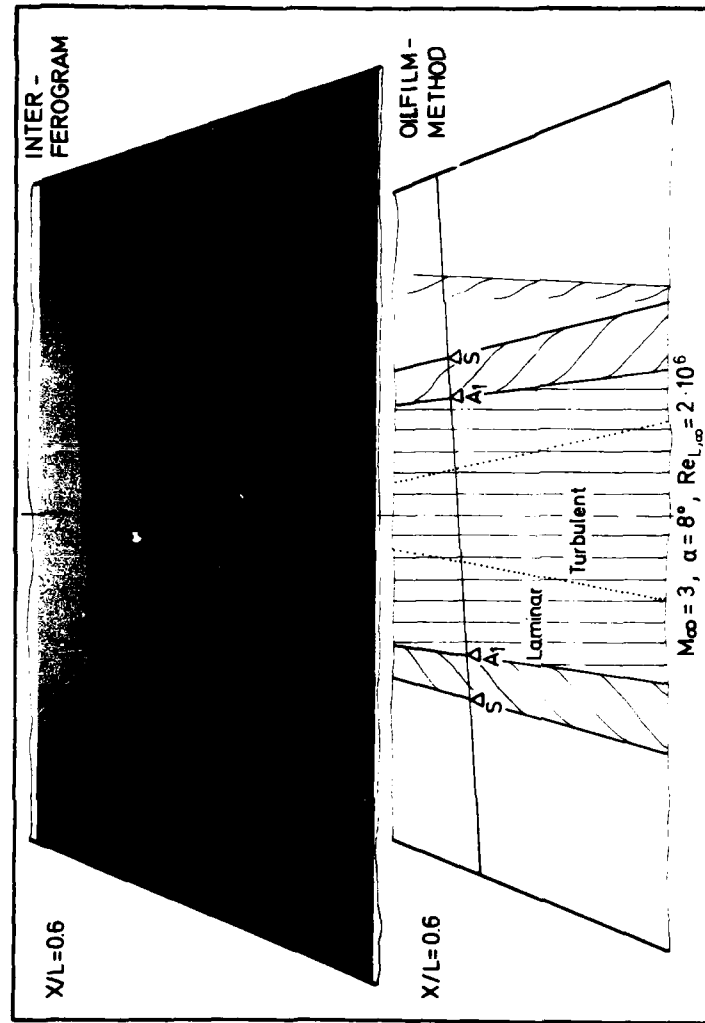


Fig. 3a SKIN FRICTION VISUALIZATION

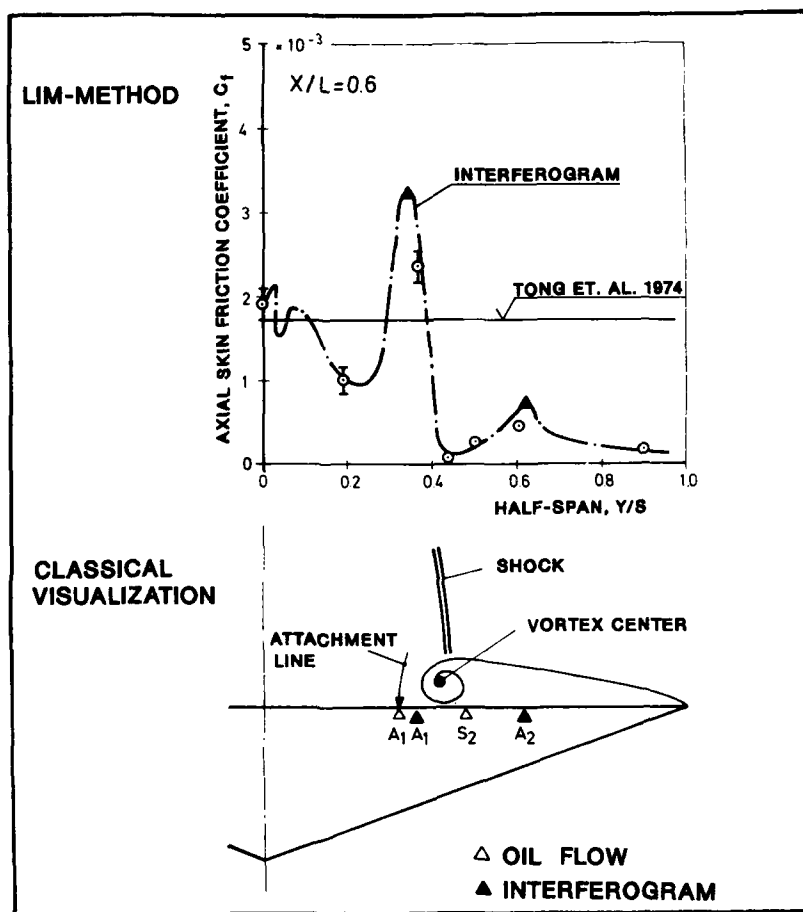
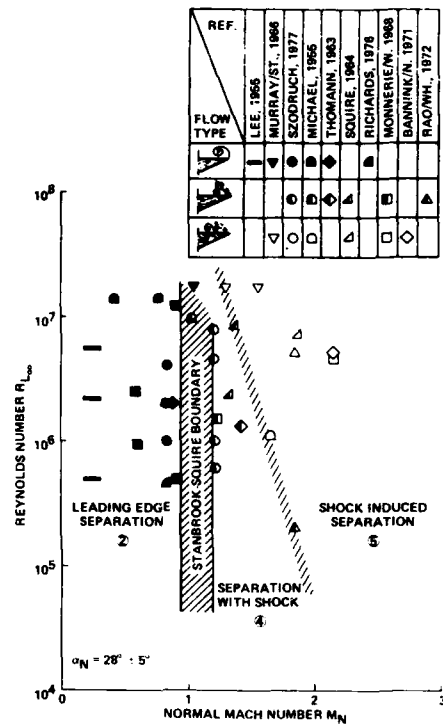
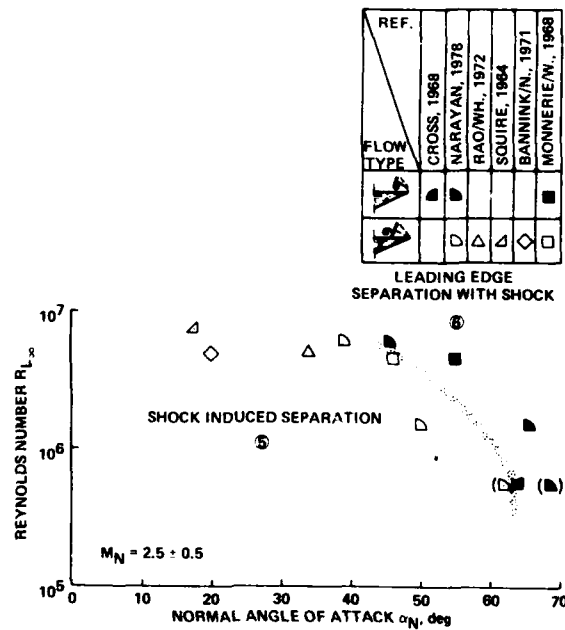


Fig. 3b SKIN FRICTION MEASUREMENT IN COMPARISON WITH VISUALIZATION

Fig. 4 INFLUENCE OF REYNOLDS NUMBER ON FLOW TYPES AND BOUNDARIES AT CONSTANT α_N Fig. 5 INFLUENCE OF REYNOLDS NUMBER ON FLOW TYPES AND BOUNDARIES AT CONSTANT M_N

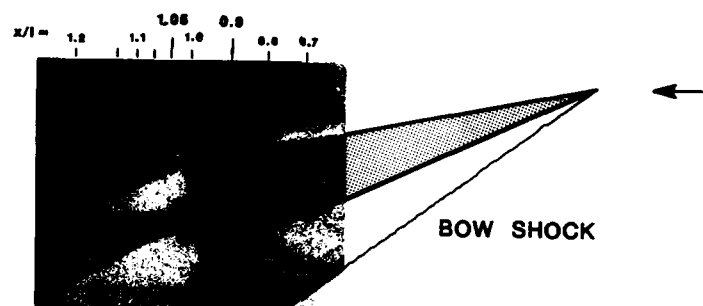


Fig. 6 SCHLIEREN PICTURE THICK DELTA WING
 $M_\infty = 2.0$ $\alpha = 10^\circ$

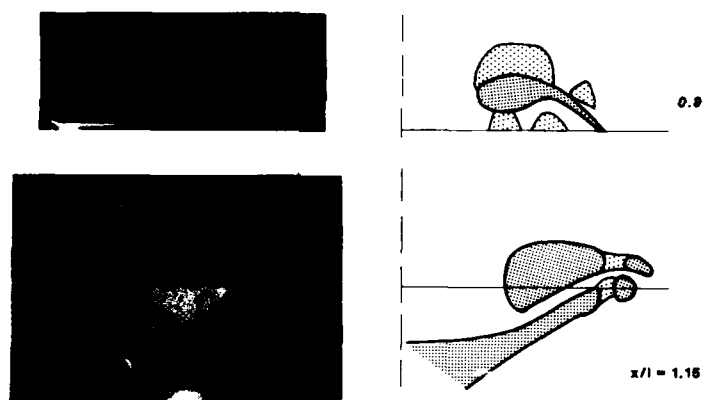


Fig. 7 VAPOUR SCREEN PICTURES THICK DELTA WING
 $M_\infty = 2.0$ $\alpha = 10^\circ$

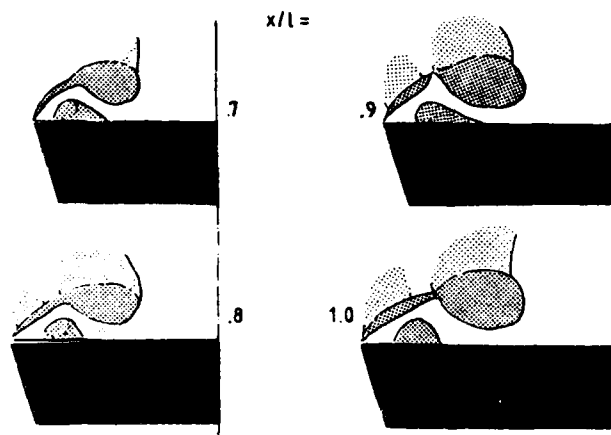


Fig. 8 COMPARISON OF VAPOUR SCREEN AND OTI FLOW VISUALIZATION (THICK DELTA)

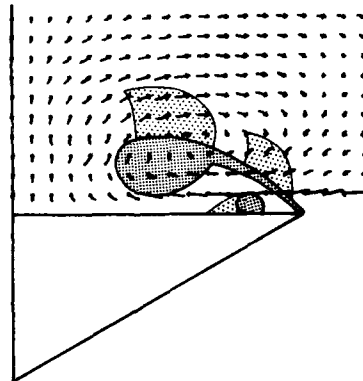
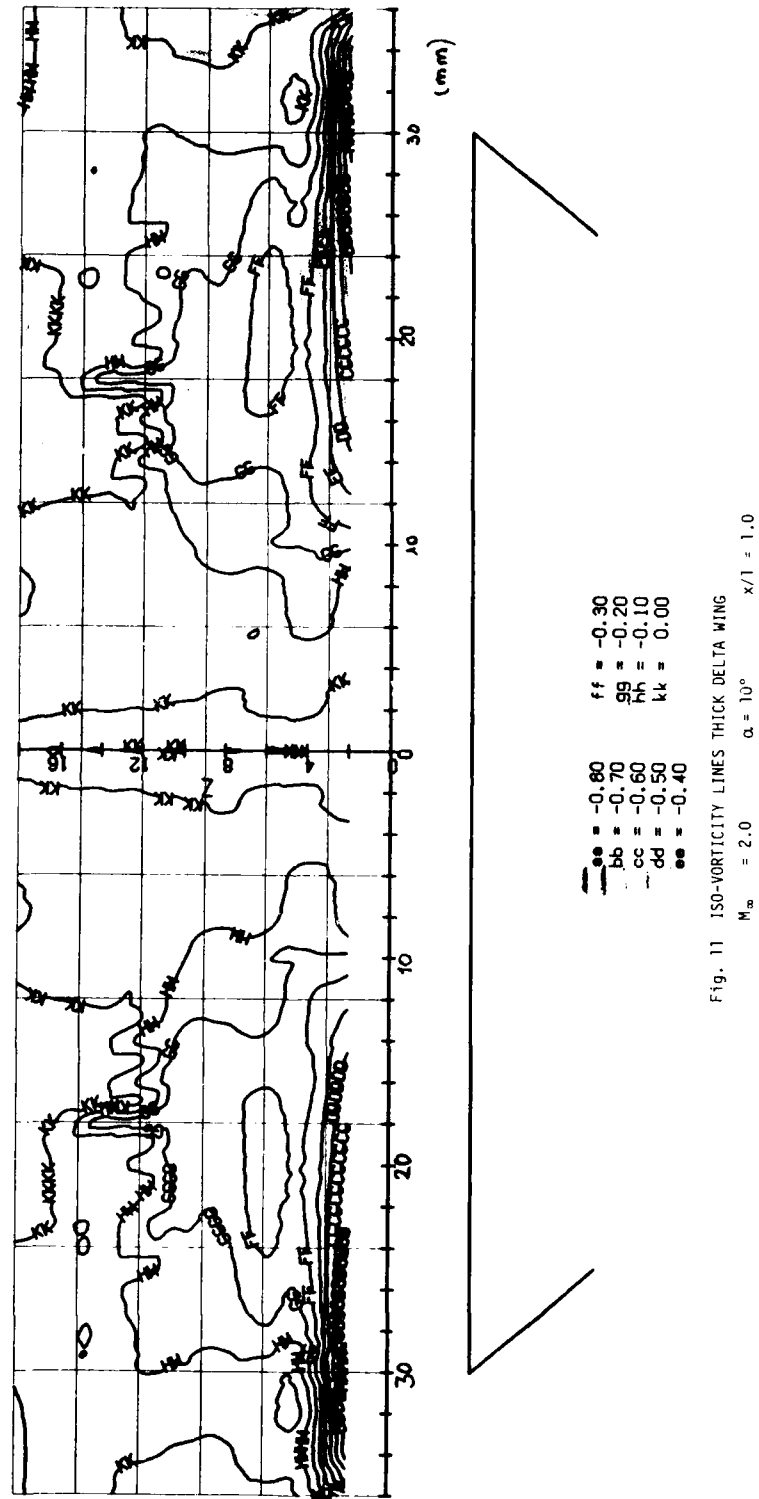


Fig. 9 VAPOUR SCREEN PICTURE & RADIAL MACH NUMBER M_R / M_∞ THICK DELTA WING
 $M_\infty = 2.0$ $\alpha = 10^\circ$ $x/l = 1.0$



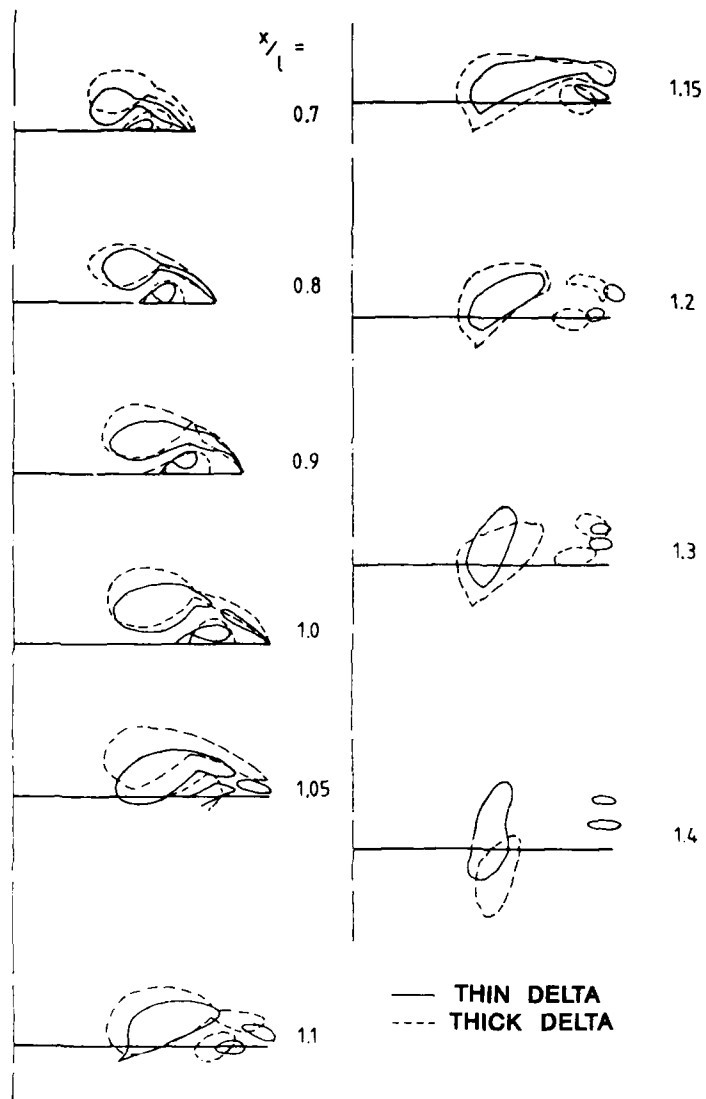


Fig. 12 COMPARISON OF VORTEX POSITIONS OVER THIN AND THICK DELTA WINGS

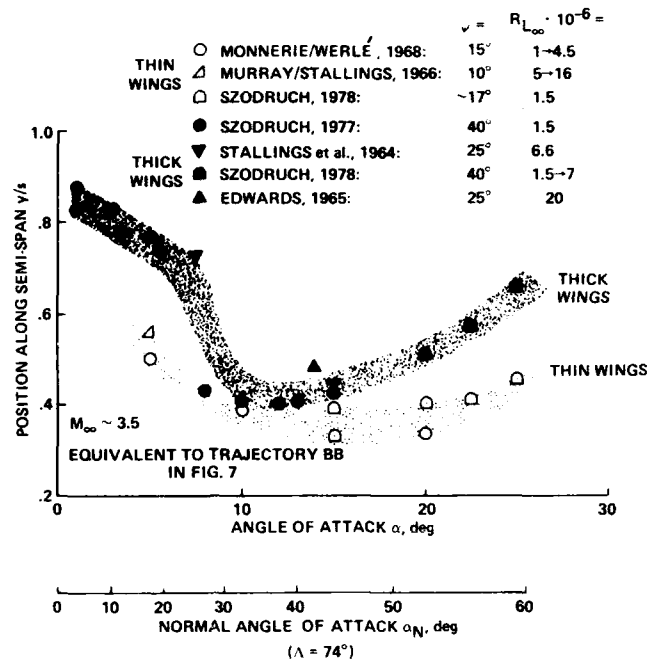
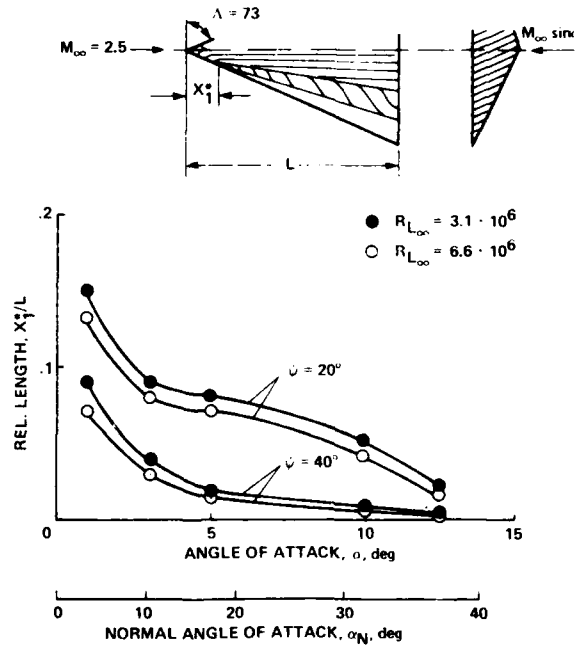


Fig. 13 VORTEX POSITION DEVELOPMENT ON THE RIGHT HAND SIDE OF SSB

Fig. 14 INFLUENCE OF REYNOLDS NUMBER AND LEADING-EDGE ANGLE ψ ON VISUAL START OF LEADING-EDGE SEPARATION LINE

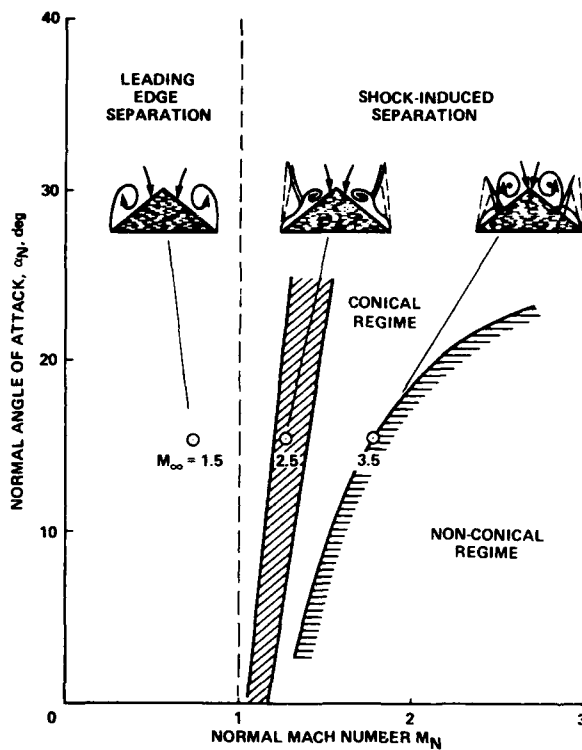


Fig. 15 LEeward FLOW REGIMES OVER THICK DELTA WINGS ($\beta = 14.5^\circ$) WITH FLAT UNDERSIDE

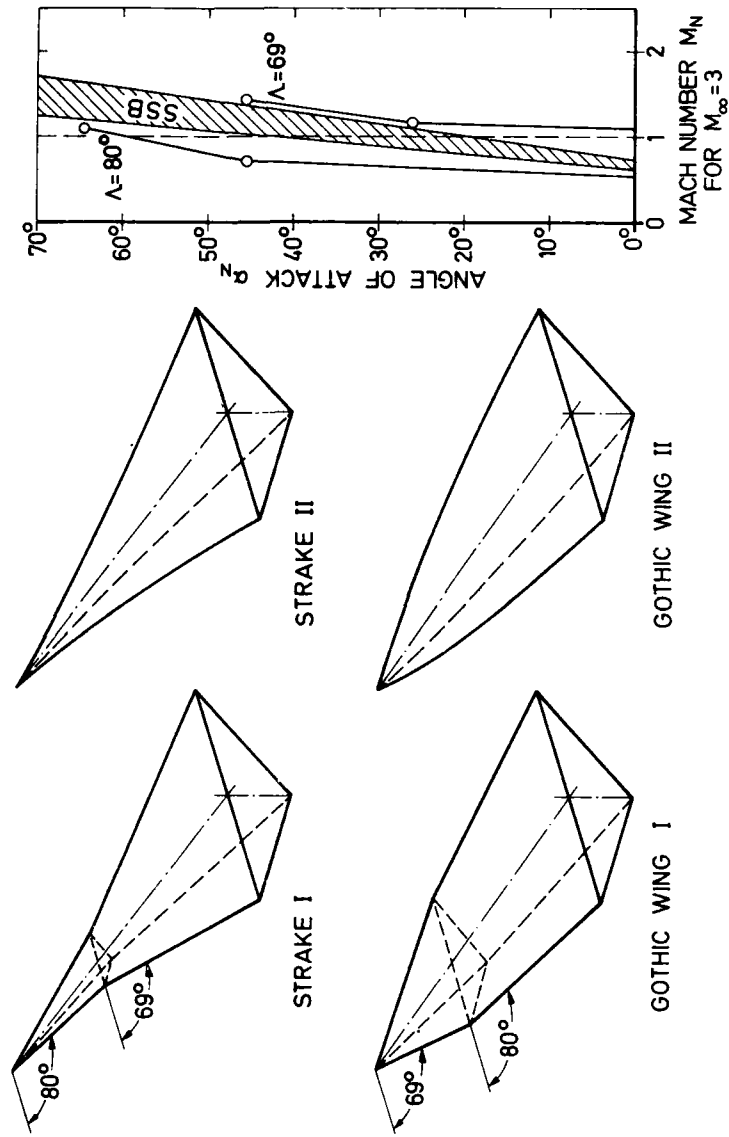
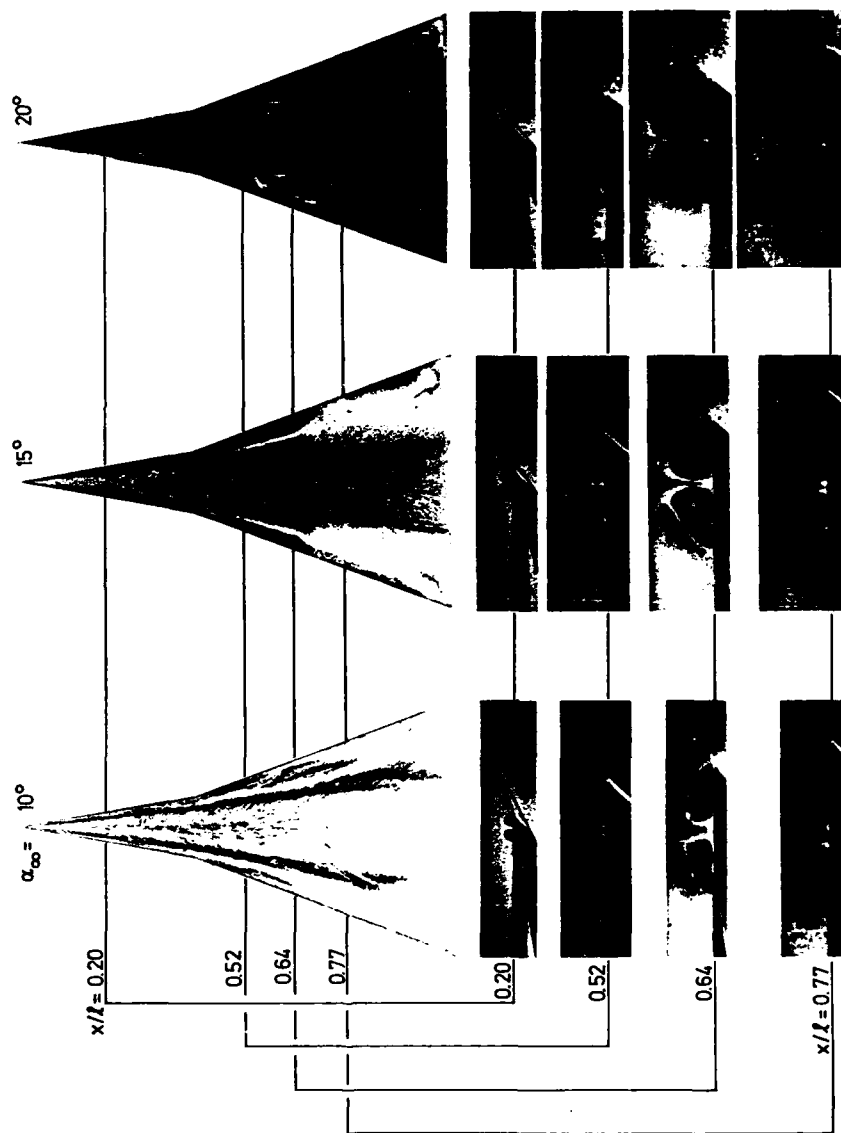


Fig. 16 WIND TUNNEL MODELS

Fig. 17 STRAKE I AT $M_\infty = 2.5$

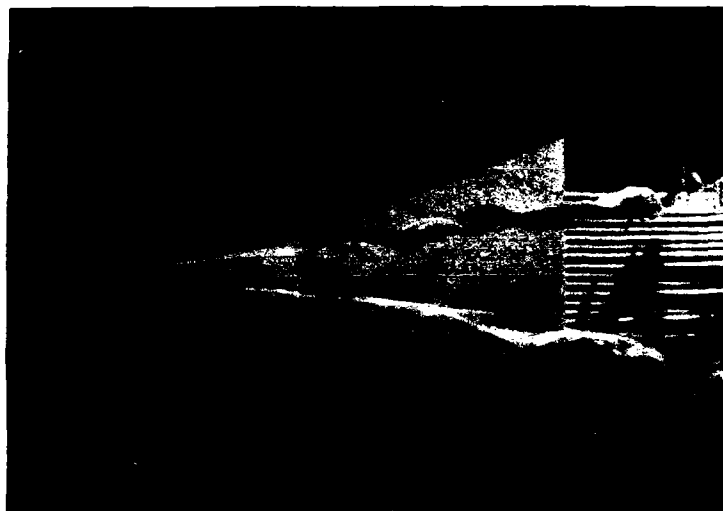


Fig. 18 FLOW VISUALIZATION IN WATER TUNNEL STRAKE I
 $V_W = 30 \text{ cm/s}$ $\alpha = 15^\circ$

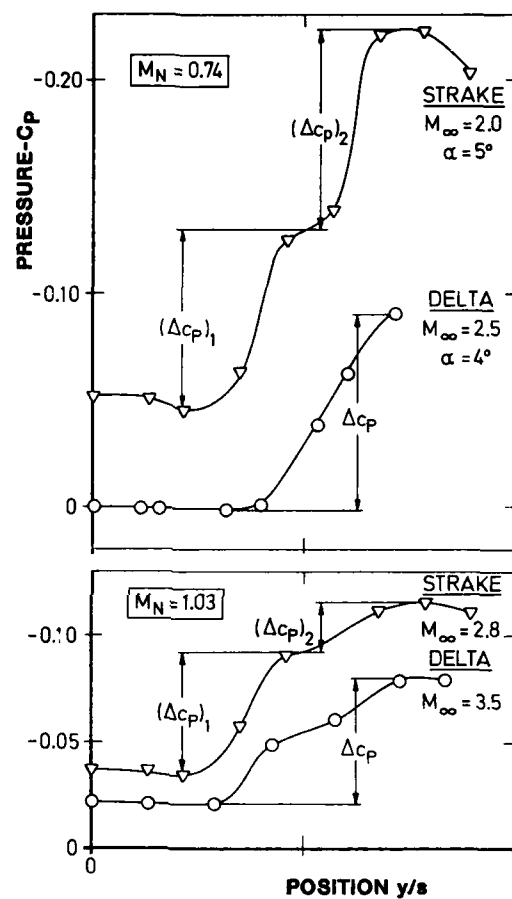


Fig. 19 PRESSURE DISTRIBUTION FOR STRAKE I and DELTA
 $x/l = 0.70$ $\alpha_N = 13.7^\circ$ ($\alpha = 5^\circ$ bzw. 4°)

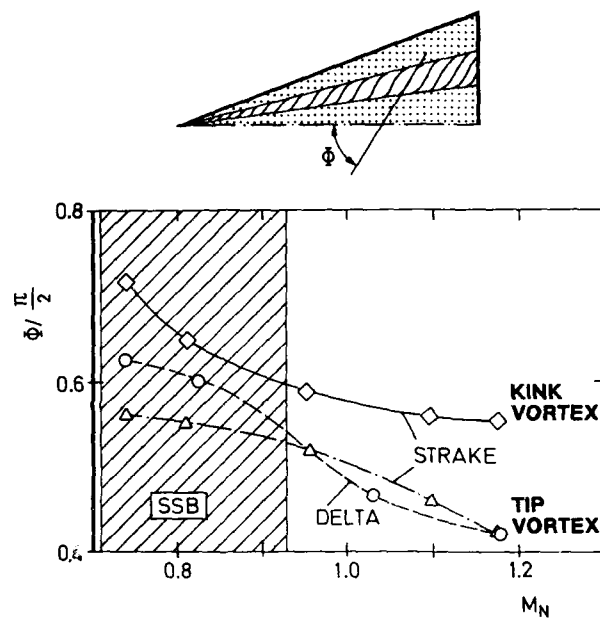


Fig. 20 VORTEX-INTENSITY FOR STRAKE 1 AND DELTA
 $x/l = 0.70$ $\alpha_N = 13.7^\circ$ ($\alpha = 5^\circ$ bzw. 4°)

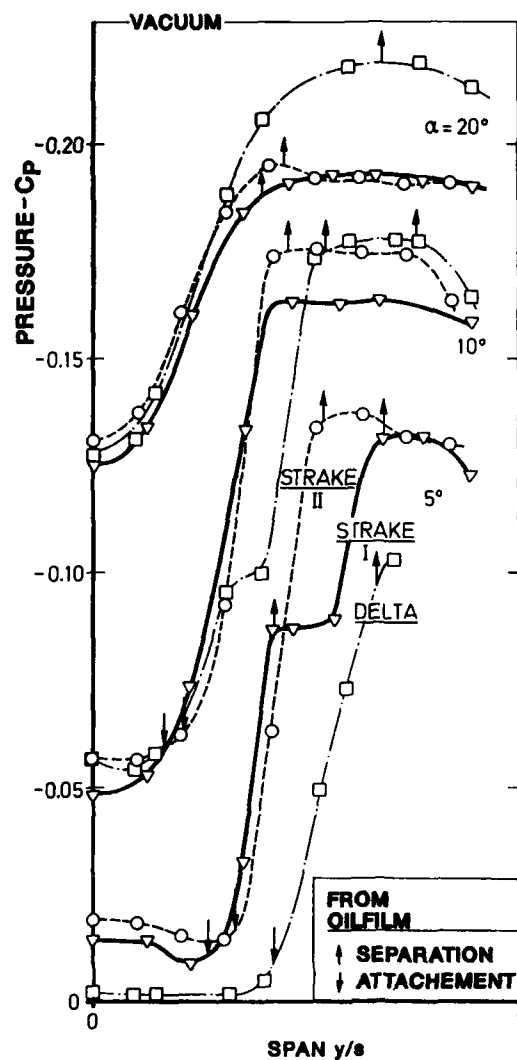
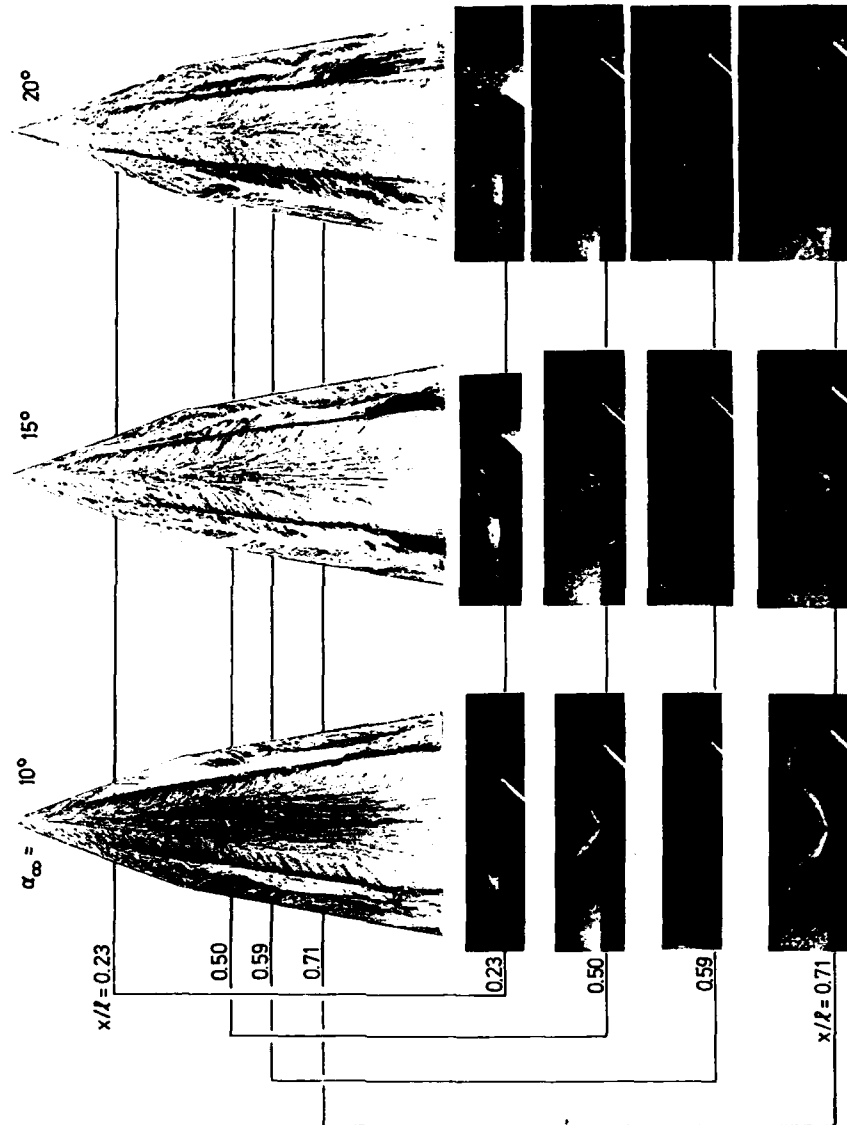


Fig. 21 PRESSURE DISTRIBUTION FOR STRAKE I, STRAKE II AND DELTA
 $x/l = 0.70$ $\alpha_\infty = 2.5^\circ$

Fig. 22 GOTHIC I AT $M_\infty = 2.5$

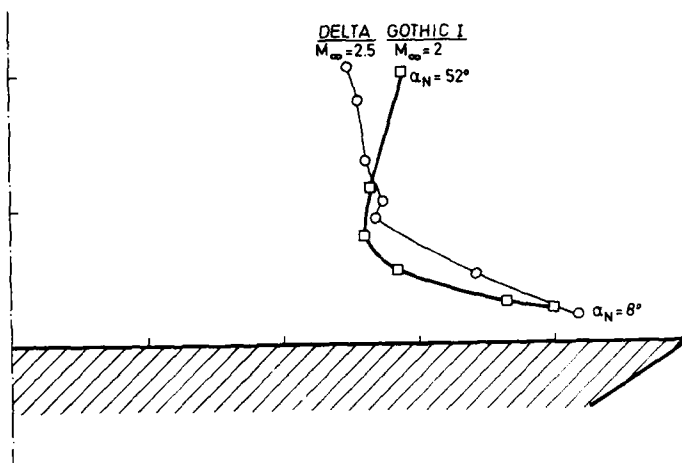
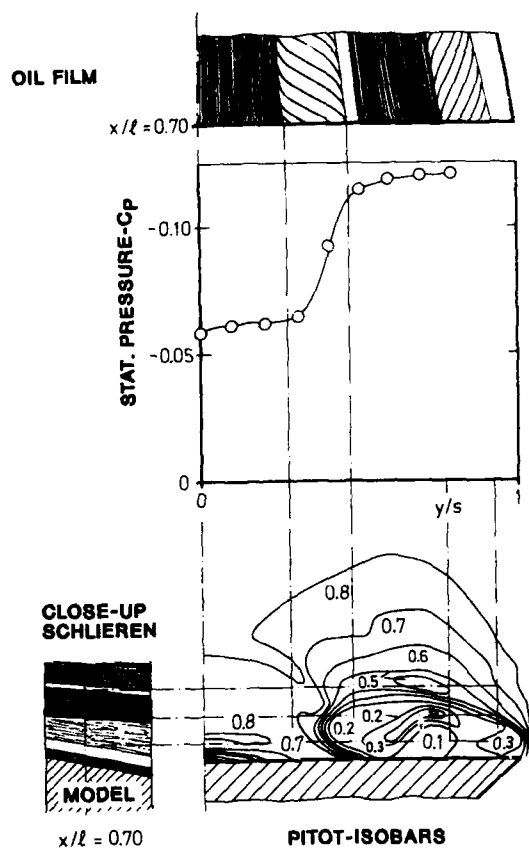
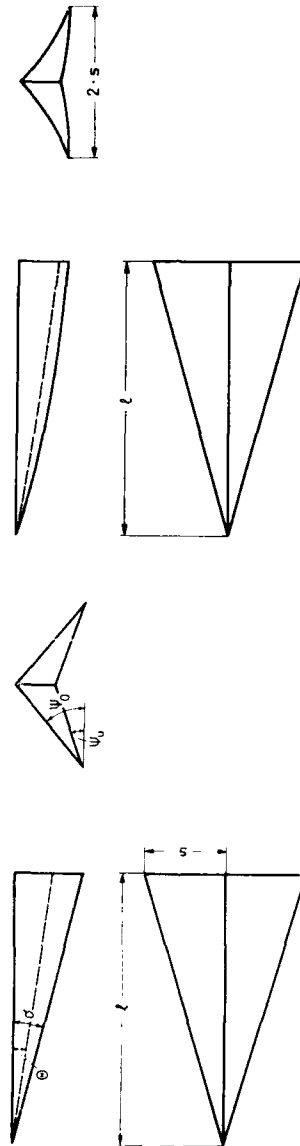


Fig. 23 VORTEX POSITION FOR GOTHIC I AND DELTA

Fig. 24 EXPERIMENTAL RESULTS FOR GOTHIC II
 $x/l = 0.70$ $M_\infty = 3.0$ $\alpha_\infty = 10^\circ$



NONWEILER-WAVERIDER
 $M_E = 7.0 \quad s/l = 0.3 \quad \tau = 0.08$

JONES-WAVERIDER
 $M_E = 7.0 \quad s/l = 0.3 \quad \tau = 0.0883$

Fig. 25 WAVE RIDER DESIGN CONCEPTS

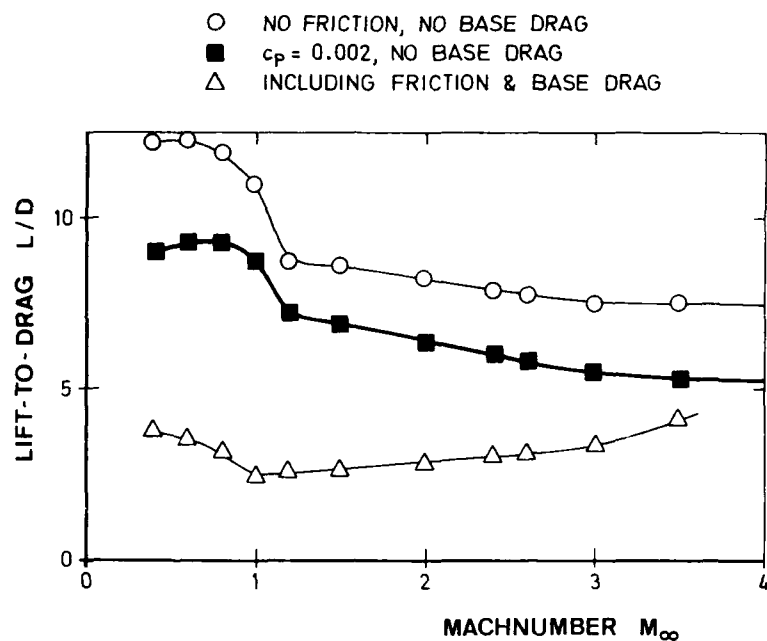


Fig. 26 LIFT-TO-DRAG-RATIO OF A NONWEILER WING
 $M_{\text{DESIGN}} = 7$ $s/l = 0.3$ $\tau = 0.08$ $\alpha = 0^\circ$

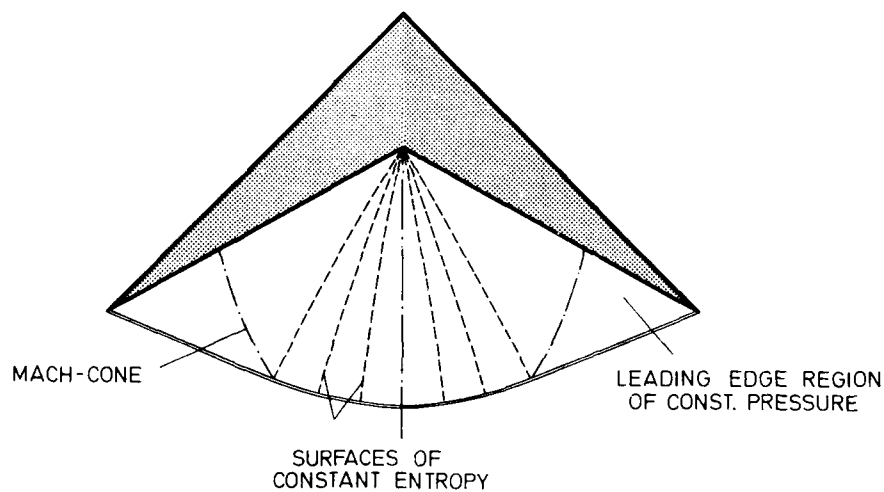


Fig. 27 FLOW-STRUCTURE ON THE BOTTOM SIDE OF A NONWEILER WING
 AT $M_\infty \leq M_{\text{DESIGN}}$

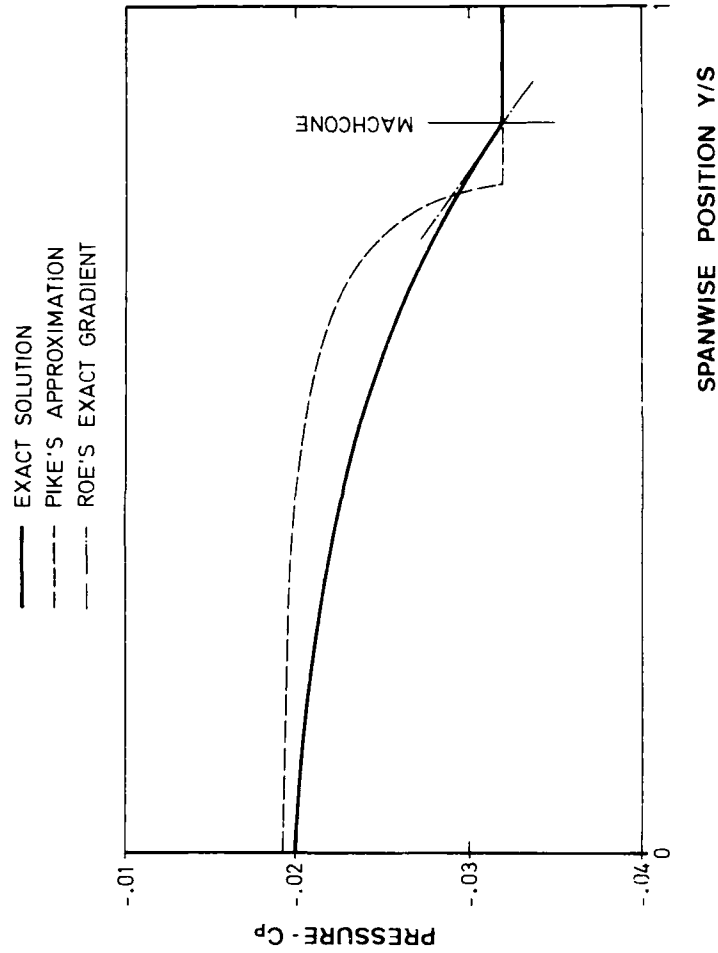


Fig. 28 CALCULATED PRESSURE ON THE LOWER SURFACE OF A NONWEILER WING
 $(M_{DES} = 7.0 \quad s/l = .3 \quad \tau = .08) \quad M_{\infty} = 4.5 \quad \alpha = 2.5^\circ$

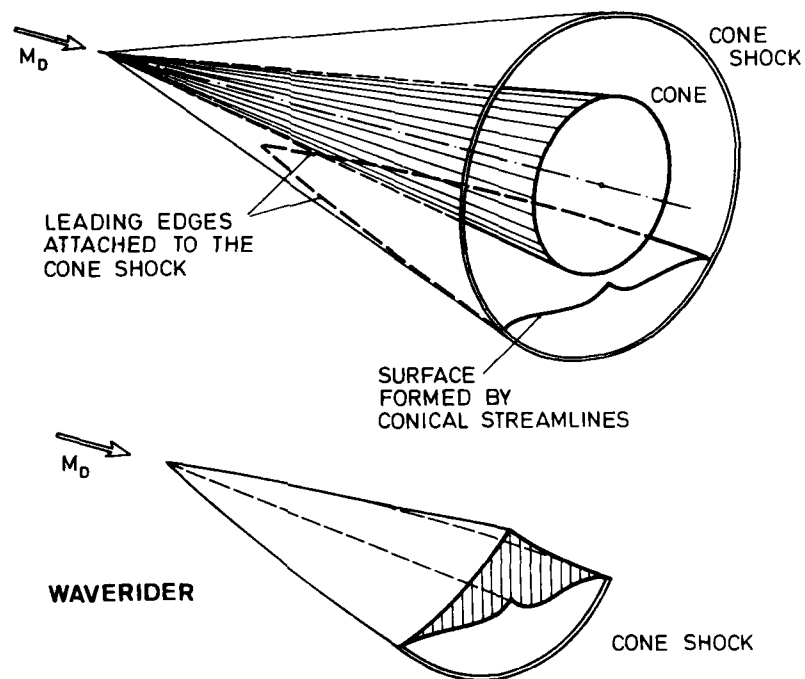


Fig. 29 DESIGN OF A JONES WAVE RIDER

Fig. 30 MODEL OF A HYPERSONIC TRANSPORT
MBB-DESIGN $M_D = 7$

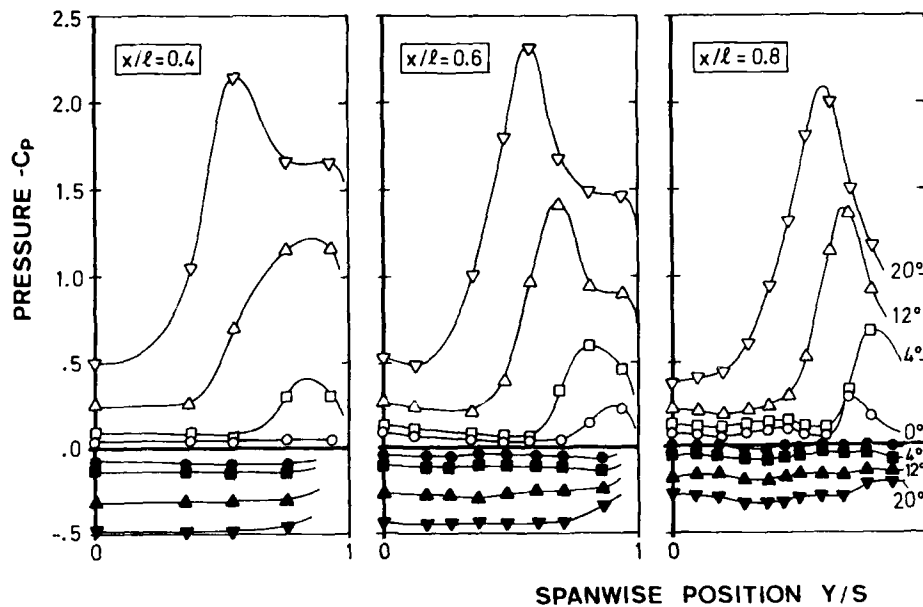


Fig. 31a JONES WAVE RIDER
PRESSURE DISTRIBUTIONS FOR THREE CROSS-SECTIONS x/l
 $M_\infty = .5$

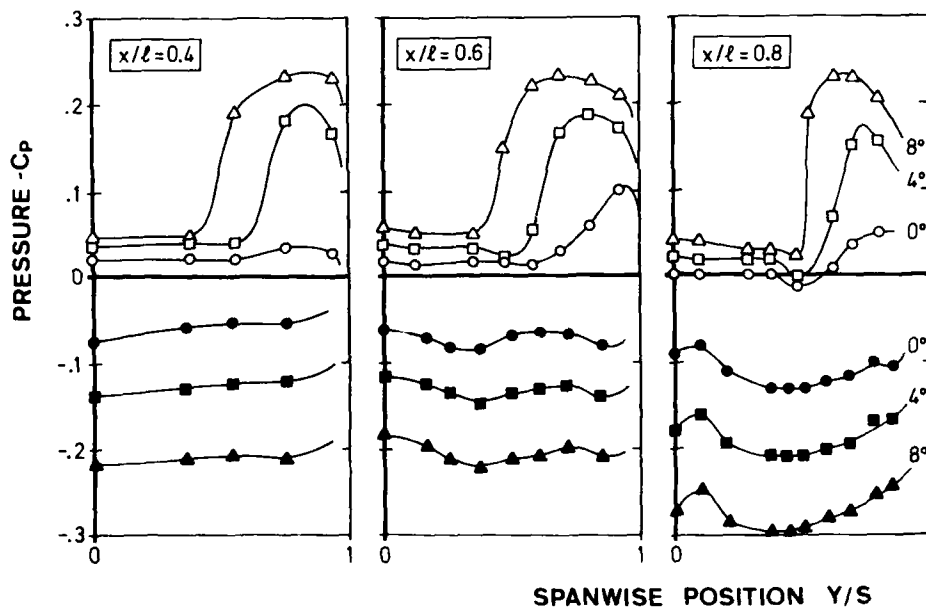


Fig. 31b JONES WAVE RIDER
PRESSURE DISTRIBUTIONS FOR THREE CROSS-SECTIONS x/l

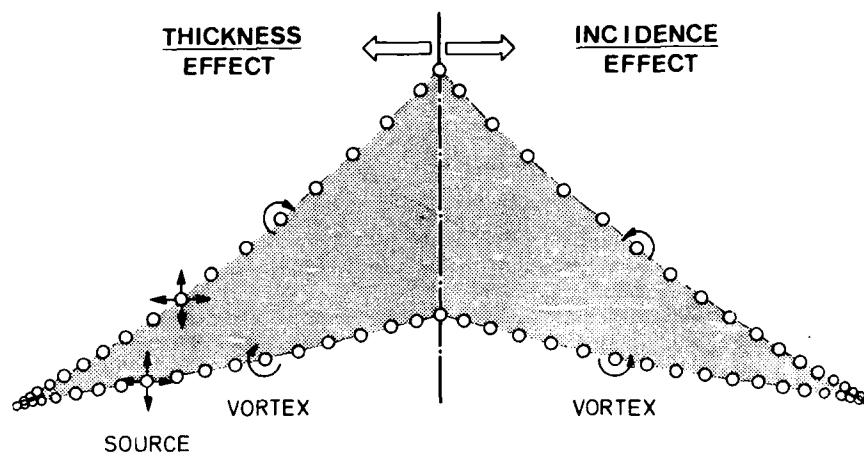


Fig. 32 SINGULARITY DISTRIBUTION ON THE SURFACE OF A SLENDER BODY
IN A CROSS-SECTION $x = \text{CONST.}$

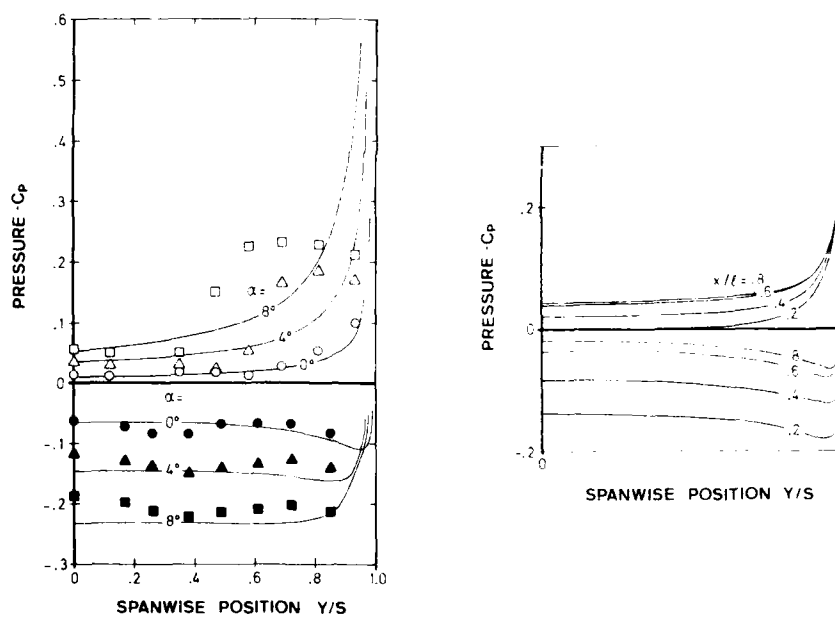


Fig. 33 JONES WAVE RIDER
THEORY & EXPERIMENT EFFECTS OF INCIDENCE
 $M_\infty = 0.5$ $x/l = 0.60$

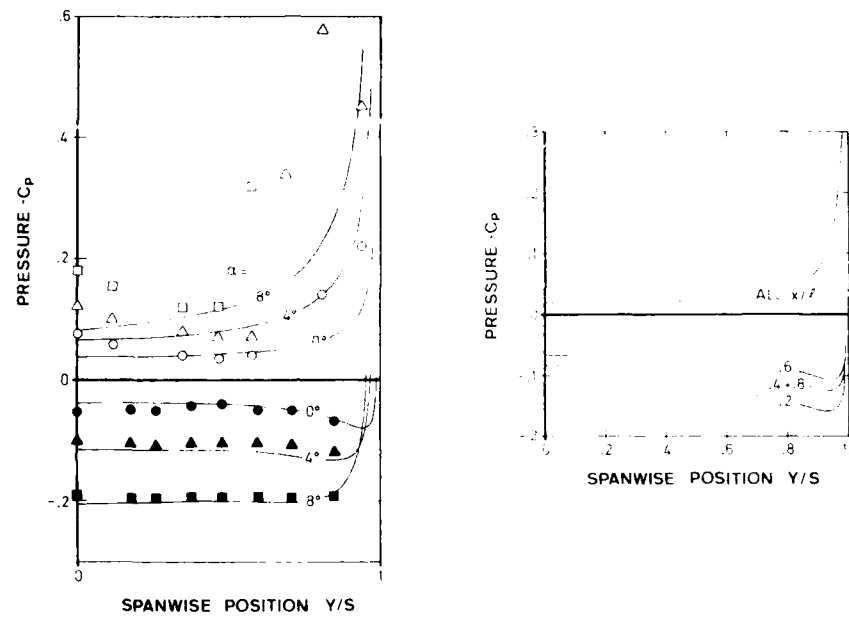


Fig. 34 JONES WAVE RIDER
THEORY & EXPERIMENT EFFECTS OF INCIDENCE
 $M_\infty = 2.0$ $x/l = 0.60$

THE OFF-DESIGN PERFORMANCE OF HYPERSONIC WAVERIDERS

Lyle N. Long
Lockheed - California Company
Post Office Box 551
Burbank, California 91520-7013 USA

ABSTRACT

Waveriders are being considered more and more as potential aerospace vehicles. However there are several questions regarding these configurations that must be answered before they can be considered viable designs. The most significant problems are related to aerothermal heating, propulsion integration, and off-design performance. This paper presents off-design performance predictions for two generic waveriders. The results are from a numerical method based upon the nonlinear, inviscid Euler equations. Comparisons to experimental data are also shown.

INTRODUCTION

The subject of this paper is the off-design performance of hypersonic waveriders. These vehicles are fairly well understood at their design Mach number and angle of attack, but their behavior at other conditions is not well documented. In addition, waveriders that have non-planar or non-conical bow shocks are also not well understood. After a brief discussion of some of the off-design problems encountered on waveriders, some numerical results will be presented. The results will be for two different waveriders, and will be limited to inviscid flows.

With the recent resurgence of interest in aerospace planes, space shuttles, hypersonic missiles, and orbital transfer vehicles, waverider configurations are being proposed as effective hypersonic designs. Waveriders are vehicles which capture a bow shock along their leading edges, this eliminates flow around the leading edges (Ref. 1) and captures the high-pressure air. In effect, the shock wave generated by thickness or volume is also used for lift. The result is a significantly higher lift coefficient (C_L) for a given lift/drag (L/D) ratio than more conventional designs, or a higher L/D for a given C_L . An increase in L/D can usually be equated with an increase in aircraft range or cross-range (Ref. 2).

Kuchemann (Ref. 1) describes how aircraft fall into one of three categories: wing-body (or swept), slender, or waverider. These are schematically shown in Figure 1 in terms of their range and Mach number. An understanding of one class does not necessarily allow one to design an effective vehicle in another. Just as one could not have anticipated the design of the Concorde or the SR-71 in the 1930's, no one can anticipate the ultimate hypersonic cruiser of the next century today.

Figure 2 shows the three types of aircraft in terms of their span/length, design Mach number, and range. Wing-body aircraft are very effective at low speeds, but are not well suited to supersonic flight. Slender configurations have subsonic leading edges at supersonic freestream conditions. As the Mach number is increased, this requirement produces vehicles that are too slender to be practical. If one must use supersonic leading edges, waveriders appear to be very effective, especially if one is interested in global flights in reasonable times (under 2 hours).

Several excellent surveys of waveriders have been published (Ref. 1,3-6), therefore few historical remarks on waveriders will be made. Although these vehicles have been thoroughly studied at their design conditions, off-design they produce very complex flow fields and have not been analyzed in detail. One exception is L.C. Squire's (Cambridge University) work on the off-design performance of waveriders. For example, Reference 6 presents a set of charts for the off-design characteristics of diamond and caret configurations. Off-design behavior is typically determined from wind tunnel tests, many of which are described in References 1,3-6. Off-design performance is critical since many hypersonic configurations will not be "point-design" vehicles. With the recent advances in computational fluid dynamics (CFD) these flows can be analyzed in detail, including real gas and viscous effects. Until realistic waverider configurations are thoroughly studied at off-design conditions, they cannot be seriously considered as practical designs.

Some of the major phenomena that must be addressed before waveriders can be considered viable are:

- Aeropropulsion Integration
- Aerothermal Heating
- Stability and Control
- Non-Conical or Non-Planar Bow Shocks
- Shock Wave Impingement
- Leading-Edge Vortices
- Degradation of Theoretical Performance Due to Viscous Effects
- Effect of Leading-Edge Radii
- Upper Surfaces not Aligned with Free Stream
- Shock Thickening Due to Knudsen number effects

Most of the above effects will only be described briefly here, and then some results for

generic waverider configurations at off-design conditions will be shown.

Viscous effects will be critical to accurately assessing aeropropulsion integration, aerothermal heating, shock/boundary layer interactions, and separated flows. Townsend (Ref. 4) suggests that the heating problems (both the rate and the peak) may be less severe on waveriders than on flat delta wings with the same lower surface deflection angle.

For air-breathing vehicles, the inlets and nozzles may be essentially the entire fore and aft lower sections of the vehicle, respectively. Therefore the aeropropulsion integration problem cannot be separated from the exterior aerodynamics of the vehicle. The hot reacting flows in the base region will be especially difficult to calculate or simulate experimentally due to the interaction of complex chemical kinetic effects and turbulent shear layers. Some of the problems associated with inlets for hypersonic vehicles are discussed by Holder (Ref. 6), Hunt (Ref. 7), and more recently by Hemdan (Ref. 8). Aerodynamic and inlet performance improvements due to fuselage cambering are discussed in Reference 7.

The off-design location of shock waves can seriously impact performance, heat transfer, and propulsion integration. Conventional slender aircraft have leading edges swept inside the bow shock. Waveriders have a bow shock captured on their leading edges. On conventional vehicles, at Mach numbers greater than their design values, the forebody bow shock can impinge upon the wing leading edges. This results in significant increases in local aerothermal heating unless the leading edges are highly swept (Ref. 9). One may not be able to sweep inlet cowl leading edges however, which means they must be actively cooled or incorporate high-temperature thermal protection systems. An excellent review of aerothermal heating is given in Reference 10. Shock wave systems on waveriders are described in Reference 11.

Waveriders at Mach numbers above their design values will encounter a completely different type of shock impingement. Instead of impinging on the leading edges, the shocks may sweep across the upper and lower surfaces. This will cause very complicated shock/boundary layer interactions and possibly high heating rates. Reference 12 presents a very comprehensive review of shock/boundary layer interactions.

Stability and control of waveriders is a concern because of the typically large amounts of anhedral. It may also be difficult to incorporate effective control surfaces without degrading the performance. The stability and control of conventional hypersonic vehicles is discussed in References 13 and 14. Hui has published extensively on hypersonic stability and control (see Ref. 14), including the characteristics of caret wings (Ref. 15).

Few theoretical or numerical studies have included the effects of viscosity on waveriders. Bowcutt (Ref. 16) has included skin friction in his waverider optimization procedure. On slender vehicles such as these it is very important to include viscous effects. Vehicles similar to Bowcutt's will be analyzed experimentally by NASA-Langley in the near future (Ref. 17, 18) in order to further evaluate viscous effects. It would also be of interest to include displacement thickness effects in any analysis procedure, these are not included in Reference 16. Since the boundary layer thickness on a flat plate varies according to :

$$\frac{\delta}{L} \propto \frac{(\gamma-1)^{\frac{1}{2}} M_{\infty}^2}{2 \sqrt{Re_{\infty}}}$$

it can be orders of magnitude larger than at low Mach numbers. At high altitudes it can be of the same order as the thickness of a slender body. In addition, the displacement thickness can be of the same order as the boundary layer thickness.

The configurations in Reference 16 were optimized for L/D and consequently have very small lift coefficients ($CL < .1$). L/D is just one possible parameter that could be optimized. For some vehicles L/D will not be the most important parameter, such as those that go from earth to orbit very rapidly without actually cruising. For these vehicles one might be more interested in maximizing thrust minus drag (T-D) and thus aeropropulsion integration would be the main issue. Configurations that minimized drag or maximized lift may also be of interest.

Classical waveriders are designed using "known" flow fields. The most common are the planar and conical flow fields of wedges and cones, respectively. These are not optimal shapes, even from an aerodynamic standpoint. Optimal hypersonic shapes are described in References 20 and 21. Power law bodies have been shown to have very low drag compared to cones. With advanced computational methods, it should be possible to incorporate these low drag shapes into waveriders. Power law waveriders would have a Gothic-like planform and would consequently have significantly different leading edge vortex flows (Ref. 17) at subsonic and supersonic speeds than a conical waverider with a delta planform. This could significantly alter the aerothermal heating and the low-speed vortex flows off the leading edge. Nonweiler (Ref. 3) showed that rounding the apex of a delta planform would also help reduce the aerothermal heating at the apex. However, the power law bodies will have blunter nose cones, which may increase the total pressure losses to the inlets. Also, optimizing aerodynamic forces will be of little use if the vehicle's performance is governed mainly by aeropropulsion integration. Air-breathing hypersonic vehicles will be characterized as having lift, drag, moments, thrust, and trim all highly coupled.

In addition to being sub-optimal aerodynamically, conical and planar flow fields are not

optimum from a systems standpoint either. These present problems in terms of propulsion integration, control surface location, and landing gear placement. Their tremendous value comes in the guidance they give the designers. However, there has been little to guide the designers as to the effect of deviating from the conical or planar fields. Most studies have shown, however, that minor deviations from the classical shapes do not significantly alter the characteristics. This will be discussed in more detail in the results section.

Since waveriders may be used as aerospace planes that take-off and land horizontally on runways, their low-speed characteristics are also important. As with conventional highly-swept wings, they can be expected to produce significant vortex lift at high angles of attack (subsonically and supersonically). However, the nature of these flow fields may differ significantly from delta wings, due to the differences in thickness and planform.

As mentioned above, the waverider off-design flow field is not amenable to simple analyses. Methods based upon modified Newtonian or other component techniques (such as the Hypersonic Arbitrary Body Program, Ref. 22) are by definition incapable of modeling interference effects. Ideally one would like to use the full Navier-Stokes equations, but this is expensive and not well-validated at hypersonic speeds (particularly turbulence models and boundary layer transition). For many problems, especially as a preliminary analysis, inviscid techniques can be quite useful. They cannot predict the important heat transfer and boundary layer characteristics, but quantities such as surface pressure are often predicted very well with inviscid methods. This is especially true for vehicles that are relatively thick. Figure 3 shows that for relatively thick bodies the skin friction has a negligible effect on the L/D.

However, Figure 3 may not be applicable to higher Mach numbers because it does not show the effect of displacement thickness. The relative importance of the boundary layer on the outer flow can be estimated using the viscous interaction parameter:

$$X = \frac{M^3}{\sqrt{Re}}$$

When this parameter is order unity or larger, the surface pressure distribution may differ significantly from inviscid predictions. For example, at Mach = 10 the interactions may be significant when the Reynolds number is less than 1 million. If a vehicle is designed for high-altitude flight (where the aerothermal heating will be reduced) the Reynolds number will most likely be smaller than these numbers. When these effects are large, the inviscid methods must be abandoned or at least coupled to a boundary layer routine. However at hypersonic speeds the concept of an inner viscous flow and an outer inviscid flow is not always valid.

At high Mach numbers and/or low Reynolds numbers, rarefied gas effects will also become important. These flows are usually characterized by the Knudsen number ($Kn = \lambda/L$, where λ is the mean free path and L is some characteristic length (e.g. $L = \rho / (dp/dx)$). The Euler equations are valid in the limit as $Kn \rightarrow 0$, and the Navier-Stokes for $Kn \ll 1$. Typically when $Kn > .1$, one must resort to kinetic-theory-based methods such as the Direct Simulation Monte Carlo (DSMC) method (Ref. 19). As the Knudsen number is increased, shock waves become thicker and thicker. Therefore at high altitudes the concept of capturing a bow shock on a leading edge becomes somewhat arbitrary. This means that waverider performance will be reduced due to the inability to capture the high pressure air. The performance of waveriders under these circumstances has not been investigated in detail. An important point to make is that although in the freestream $Kn = M/Re$, near stagnation regions $Kn = 1/(M Re)$; therefore surface quantities can often be predicted quite well with continuum theories.

METHOD

In the present study a numerical method based upon the nonlinear Euler equations has been used. These equations accurately model the effects of strong shock waves (not internal shock wave structure however) and vorticity transport. In addition, when the separation point is fixed, such as at a sharp leading edge, they have been shown to predict separated flows reasonably well. Relatively thick bodies will be analyzed here (thickness/chord = .21 and .30), so inviscid methods should be fairly accurate. These types of bodies will be of interest when large amounts of volume are required for payload or fuel. For example, hydrogen-powered vehicles may require relatively thick fuselages due to the low density of liquid hydrogen compared to conventional fuels (Ref. 2).

The results presented below were all obtained using the Lockheed Three-Dimensional Euler Aerodynamic Method (TEAM), the development of which was partially funded by the United States Air Force (Contract Number F33615-84-C-3005). This computer program is based upon the FLO-57 algorithm developed by Jameson, et al (Ref. 23). Lockheed has made various refinements to the method over the past several years (Ref. 24 - 26).

In the TEAM code, the region surrounding a given configuration is subdivided into small cells. In each of the cells, the time-dependent Euler equations (in integral equation form), representing mass, momentum, and energy conservation:

$$\frac{\partial}{\partial t} \iiint Q \, dV = - \iint \left(\mathbf{F} \cdot \mathbf{v} \cdot \mathbf{n} + g \right) \, dS$$

where :

$$Q = \begin{bmatrix} \rho \\ \rho V \\ \rho e \end{bmatrix} \quad F = \begin{bmatrix} p \\ \rho V \\ \rho h \end{bmatrix} \quad G = \begin{bmatrix} 0 \\ p n \\ 0 \end{bmatrix}$$

are integrated in time using a multi-stage Runge-Kutta scheme. The quantities represented by ρ , V , p , e , and h are density, velocity, pressure, internal energy, and enthalpy, respectively. Notice that density, momentum, and energy are all calculated from the time-stepping process; pressure and enthalpy are required for the flux terms. For perfect gases pressure is normally calculated using a form of the energy equation and then enthalpy is calculated from $h = p/\rho + e$. In simulating a real gas in equilibrium, one must calculate pressure, enthalpy, specific heat ratio, and the speed of sound (required for upwind schemes) properly; for example by using the subroutines described in Reference 55. For non-equilibrium chemistry one must add additional equations to the time-stepping procedure that govern the species concentrations. Non-equilibrium effects are not included in the TEAM code at this time.

To accelerate convergence to the steady state, local rather than global time steps are used. This will produce valid steady-state results, when there is a steady-state solution. For unsteady flows one must use the code in a time-accurate mode, which is quite expensive. Implicit residual smoothing (Ref. 27) further reduces the number of time steps required to reach the steady state. Appropriate non-reflecting boundary conditions based on Riemann invariants (Ref. 27) are used at the far-field boundaries and no-normal-flow conditions are used on the solid surface. Upwind differencing based upon a Riemann solver (Ref. 28 and 29) has also been incorporated, and can be used instead of the standard adaptive artificial dissipation. The upwind differencing greatly increases the robustness of the program, but does require slightly more computer time.

On a solid surface, the no-normal-flow boundary condition is imposed by setting all convected flux quantities to zero. Only the pressure on the solid surface contributes to the momentum flux balance. Since pressure is calculated at the cell center, one is forced to estimate its value at the actual surface. This is accomplished by computing the derivative of pressure normal to the surface using the momentum equation:

$$\rho \bar{V} \cdot (\bar{V} \cdot \bar{n}) = n \cdot \bar{V} p$$

where : \bar{V} , \bar{n} , and p are the fluid velocity, surface normal, and pressure; respectively. This derivative and the cell-centered values are then combined to determine the surface pressure. A precise implementation requires that all metric quantities and flow variables occurring in the equation above be evaluated right on the surface. In the original FLO-57 program, the cell-center values were used instead. In the present version of the solver, three additional approaches may be used to obtain the desired flow variables on the actual surface: (1) A Taylor series expansion about the cell center, (2) Lagrange two-point extrapolation along the local normal direction, and (3) Averaging the cell-center values for cells next to the surface in the flow domain and ghost cells outside of the flow domain.

The finite-volume formulation essentially decouples the flow solver from the grid generator. The grids can be constructed in any convenient manner; only the Cartesian coordinates of the nodal points are required by the solver. The present version of the solver can accommodate multiple, patched zonal grids of arbitrary topologies. This is a necessity for analyzing realistic complete aircraft configurations. The original FLO-57 solver was limited to isolated wings having C-H grids, whereas the O-O and C-O types offer improved resolution. The letters C, H, and O refer to the way the grid looks in the spanwise and chordwise directions. A C-H grid wraps around the airfoil section like a C, and has these 2-D grids stacked up in the spanwise direction to form the region around the wing. Thus, from the front, a C-H grid looks like an array of H's. If a C-H mesh is used, adequate resolution near the wing tip can be obtained only by increasing the number of cells in the spanwise direction. It must be noted that none of these topologies is as suitable as the H-H when the detailed flow field is desired about all sections of a wing-body or wing-body-tail configuration.

The finite volume grids used here were all of the C-H type. Several different grids were used, a typical grid had 105 x 29 x 25 cells (76,125) in the chordwise, normal, and spanwise directions, respectively. For the subsonic cases, the far-field boundary was several vehicle lengths away from the body surface, for supersonic flows the far-field boundary was much closer (although still in the free stream). Other than this, no attempt was made to tailor the grid to the particular flow field. Similar grids were used at most Mach numbers, which means they could not have been optimal for all Mach numbers. Ideally one would like to cluster cells near shocks, but shock wave location and strength changes with Mach number. Therefore a new grid would be required at each Mach number; which would have been extremely time consuming. Some type of adaptive grid scheme would have been useful, but is currently not available in the TEAM code. However, the grids used were relatively dense and should yield reasonable results for forces and moments at most Mach numbers.

Depending on which options are used, the TEAM code requires about .00002 CPU seconds/cycle/cell on a Cray XMP-24. For the results presented here 400 - 3000 cycles were required to reduce the residual error by 3-4 orders of magnitude. The convergence rate varied dramatically with Mach number. At the very high Mach numbers, where the shocks are very close to the body and not resolved well, the code converged extremely rapidly. Likewise for coarse meshes, the code converged very rapidly. In principle, this should allow preliminary investigations to be made of configurations very quickly;

with detailed examinations performed afterwards. In some cases the solutions were restarted from previous runs, which did allow some savings in computer time.

RESULTS

Two configurations were investigated here. The first one (referred to here as WR-1) is Rasmussen's elliptical-cone waverider (Ref. 31) shown in Figure 4. This configuration has 20 degrees of anhedral and a leading edge sweep of 65.53 degrees. The second configuration (WR-2) is a flat-bottomed version of Rasmussen's waverider (Figure 5). WR-2 was obtained by simply cutting off the under-side of WR-1. The section removed was cut away by a plane perpendicular to the plane of symmetry and at an angle of -11.95° to the free-stream direction. Whereas the wind tunnel model of WR-1 had a 18.06 cm base height, the base height of WR-2 would be 12.7 centimeters (cm). The length of both of them is 60.0 cm (excluding the fairing at the base).

The shape of WR-2 was chosen because it represents a deviation from the standard conical flow field. Also the flat underside is desirable from a practical standpoint. Both landing gear and inlets may be easier to incorporate into a flat surface. It was also reasoned that the shock wave attached to the leading edge may not be affected too much by relieving the pressure on the very bottom, and thus the flow may still be fairly well contained. If this were true then the bottom portion of WR-1 might contribute more to the drag than to the lift. In addition, WR-2 should have both lower friction drag and base drag, since it has a smaller wetted area and base area than WR-1.

In order to evaluate realistic vehicles, a fairing was added to the aft-end of WR-1 and WR-2. This is shown in Figure 6, which is a typical grid at the plane of symmetry. This fairing is aligned with the free-stream on the upper surface. The lower surface consists of a flat (aligned with upper surface) portion whose length is 10 % of the local chord and then a cosine shaped portion that is an additional 50 % of the local chord. Thus the total length of the fairing is 60 % of the local chord. However, in order to compare to Rasmussen's data directly, the force and moment calculations presented below do not include the forces and moments on the fairing. Since on an actual configuration the aft-end flow would be dominated by jet exhaust entrainment and/or separated wake flow, the inviscid contributions were not added to the forebody forces and moments. In the near future viscous analyses will be performed on these configurations by solving the Reynolds-averaged Navier-Stokes equations and the flow in the base region will be of great interest.

WR-1 was designed for Mach 4 and zero degrees angle-of-attack, where its L/D is a maximum. Experimental and predicted values of L/D (at Mach 4) are shown in Figure 7. The experimental results for WR-1 compare fairly well considering no viscous effects are included, but this should not be a surprise since it is a relatively thick body. The L/D for WR-2 is substantially higher than WR-1, mainly because the parameter $V^{**}(2/3)/S$ is smaller (see Figure 3). Therefore the flattening of the standard Rasmussen waverider would be beneficial from a systems (inlets, landing gear, etc.) viewpoint and the L/D is higher. L/D versus Mach number is shown in Figure 8. The flattened waverider has a higher L/D over the entire Mach number range. Also plotted is Kuchemann's L/D 'limit' of $4(M_\infty+3)/M_\infty$. The performance of both WR-1 and WR-2 is significantly below this limit.

The lift coefficient, C_L , versus angle of attack is shown in Figure 9 for Mach = 4. These results show good agreement between experiment and theory for WR-1. The behavior is virtually linear for both WR-1 and WR-2. Pitching Moment, CM, versus Mach number (including the one experimental data point available) is shown in Figure 10. Figure 11 shows the inviscid drag and lift force (minus base drag). The experimental and predicted values compare well and WR-2 has less drag than WR-1. Note that the reference lengths and areas used here are the same as used in Reference 31, i.e. $L = 60$ cm and $A = 489.22$ cm². The reference area used here is the base area of WR-1 (as in Reference 31) and is not the planform area (which is 1638.16 cm²).

For highly three-dimensional flow fields such as these, it is instructive to use three-dimensional color graphics (reproduced here as contour plots) to interpret the results. Figures 12 and 13 show pressure distributions on front and bottom views of WR-1 and WR-2, respectively, at Mach numbers of 1.1, 2, 4, and 6.0 ($\alpha=0$). The surface has been contoured according to pressure using PATRAN II (Ref. 32), a three-dimensional solid modeling program. All pressures shown here are non-dimensionalized by the free-stream pressure (p/p_∞). For both waveriders, at Mach = 2, 4, and 6, the flow field appears to be quite conical. In addition, the flat bottom waverider (WR-2) shows a very uniform pressure distribution on the underside which would be desirable for modular inlet installation.

The wavy patterns near the edge of the flat underside are due to minor waves in the surface definition. The numerical method is very sensitive to geometry variations, and the grid generation scheme used here (parabolic conformal mapping) is not as effective on these highly swept planforms as one would like. This could be corrected by specifying the body with more points or by using a different type of grid generation scheme. An H-O grid would allow better shock capturing, since the grid could more easily be aligned with the shocks. However the present type of grid is well suited to transonic and subsonic flows.

These configurations were also investigated at angle of attack, only a few results will be shown however. Figure 14 shows the pressure distribution for angles of attack = -10, 0, and 10. This images are for cross-sections of the flow field that are aligned with the free-stream and at the mid-span of WR-2. Figure 15 shows similar views but display

Mach number distributions. One can see the high pressure region near the leading edge, the bow shock, and the expansion in the base. Notice that the shock is smeared over several cells, a consequence of the dissipative nature of the technique. At zero angle of attack there are no disturbances on the upper surface, this is due to the absence of viscosity in this prediction method.

In order to display another aspect of the flow field, lower surface velocity vector plots for WR-1 and WR-2 at Mach = 4 and $\alpha = 0$ are shown in Figures 16 and 17. Both of these figures again show the flow field to be quite conical. In addition, the WR-2 flow field appears to be more nearly two-dimensional (less span-wise flow). Even at angles of attack of -10 and 10 (Figures 18 and 19), there appears to be relatively small amounts of cross-flow on WR-2.

At higher Mach numbers, one simply cannot use a perfect gas model because it predicts pressures and temperatures that are unrealistically high. Figures 20 and 21 show the surface pressure distribution (p/p_∞) on WR-2 at Mach = 15 and $\alpha = 0$ using a perfect gas model and a real gas model (40 Km), respectively. The surface pressures are lower than that predicted by the perfect gas relations, and this causes the forces and moments to differ also:

FOREBODY FORCES AND MOMENTS ($M_\infty = 15$)					
GAS	CL	CD	CM	L/D	
PERFECT	.305	.077	.061	3.96	
REAL	.288	.072	.059	4.00	(@ 40 Km)
% DIFFERENCE	-5.6	-6.5	-3.3	1.0	

Cross-sections of the flow fields around WR-2 at Mach = 15 for perfect and real gases are shown in Figures 22 and 23, respectively.

For many applications, these waveriders will be required to fly through all four speed regimes (subsonic, transonic, supersonic, and hypersonic), therefore it is important to know the behavior of these configurations over the entire range. The only subsonic flow field that will be shown here is Figure 24. As mentioned previously, one can expect significant vortex flows from these configurations at high angles of attack. Figure 24 shows the pressure distribution on the upper surface of WR-1 at Mach = .6 and $\alpha = 20$ degrees. The low pressure region can be attributed to a leading edge vortex. Vortices such as these occur at supersonic speeds also (Ref. 17), and can lead to significant aerothermal heating problems.

CONCLUSIONS

The above results for the waverider are very encouraging because most design methods for hypersonic vehicles are incapable of predicting waverider performance. This is especially true for off-design performance where only a truly nonlinear prediction method is adequate. Because waveriders are based upon favorable interference, methods such as the Hypersonic Arbitrary Body Program (Ref. 22) cannot be used. For lower Reynolds numbers, higher Mach numbers, or more slender vehicles, the viscous effects will become more important and the inviscid CFD methods must be replaced by Navier-Stokes and Boltzmann methods.

The TEAM code has recently been extended to model the Reynolds-Averaged Navier-Stokes equations (Ref. 26), this aspect of the code will be exploited in the near future in order to investigate aerothermal heating, skin friction effects, and displacement thickness effects on realistic waveriders.

REFERENCES

1. Kuchemann, D: The Aerodynamic Design of Aircraft, Pergamon, New York, 1978.
2. Gregory, T.J., Peterson, R.H., and Wyss, J.A.; "Performance Tradeoffs and Research Problems for Hypersonic Transport." J. of Aircraft, Vol. 2, No. 4, July-Aug., 1965, pp.266-271.
3. Schindel, L.H.; Tactical Missile Aerodynamics (Ed.: Hemsch and Nielson), AIAA Prog. in Astro. and Aero., Vol. 104, New York, 1986.
4. Townend, L.H.; "Some Design Aspects of Space Shuttle Orbiters," in Prog. in Aerospace Sciences, Vol. 13, Pergamon, Oxford.
5. Townend, L.H.; "The Waverider," in Hypersonic Aerothermodynamics, Von Karman Institute, Lecture Series 1984-01, Feb., 1984.
6. Bogdonoff, S.M. (Editor); "Hypersonic Boundary Layers and Flow Fields," AGARD Conference Proceedings, CP-30, May, 1968.
7. Hunt, J.L., Johnston, P.J., and Riebe, G.D.; "Flow Fields and Aerodynamic Characteristics for Hypersonic Missiles with Mid-Fuselage Inlets," AIAA Paper 83-0542, Jan., 1983.

8. Hemminger, H.T. and Jischke, M.C.: "Inlets for Waveriders Derived from Elliptic-Cone Stream Surfaces," *Jnl. of Spacecraft and Rockets*, Vol. 24, No. 1, Jan., 1987.
9. Aorkegi, R.H.: "Survey of Viscous Interactions Associated with High Mach Number Flight," *AIAA Jnl.*, Vol. 9, No. 5, May, 1971.
10. Holden, M.H.: "A Review of Aerothermal Problems Associated with Hypersonic Flight," *AIAA Paper No. 86-0267*, Jan., 1986.
11. Venn, J. and Flower, J.W.: "Shock Patterns for Simple Carot Wings," *Aero. Jnl. of the Royal Aero. Soc.*, Vol. 74, April, 1970.
12. Settles, G.S. and Dolling, D.S.: *Swept Shock Wave/Boundary Layer Interactions, Tactical Missile Aerodynamics* (Ed.: Hensch and Nielson), *AIAA Prog. in Astro. and Aero.*, Vol. 104, New York, 1986.
13. Drummond, A.M.: "Performance and Stability of Hypervelocity Aircraft Flying on a Minor Circle," *Prog. in Aero. Sciences*, Vol. 13 (Ed.: D. Kuchemann), Pergamon, Oxford, 1972.
14. East, R.A.: "Hypersonic Static and Dynamic Stability, Part II: Inviscid Prediction Methods for Unsteady Hypersonic Flow," in *Hypersonic Aerothermodynamics*, Von Karman Institute, Lecture Series 1984-01, Feb., 1984.
15. Hui, W.H.: "Stability of Oscillating Wedges and Carot Wings in Hypersonic and Supersonic Flows," *AIAA Jnl.*, Vol. 7, No. 8, 1969.
16. Bowcutt, K.G., Anderson, J.D., and Capriotti, D.: "Viscous Optimized Hypersonic Waveriders," *AIAA Paper No. 87-0272*, Jan., 1987.
17. Johnston, P.J.: NASA-Langley Research Center, Private Communication, 1987.
18. Bauer, S.X.S.: "Application of Hypersonic Waverider Optimization Method," (Abstract Only), *AIAA Paper No. 87-0644*, 1987.
19. Bird, G.A.: *Molecular Gas Dynamics*, Clarendon Press, Oxford, 1976.
20. Spencer, B. and Fox, C.H.: "Experimental Studies of Optimum Body Shapes at Hypersonic Speeds," *Jnl. Astro. Sciences*, Vol. 14, No. 5, 1967.
21. Cole, J.D. and Zien, T.F.: "A Class of Three-Dimensional, Optimum Hypersonic Wings," *AIAA Jnl.*, Vol. 7, No. 2, Feb., 1969.
22. Gentry, A.E.: "Hypersonic Arbitrary Body Aerodynamic Computer Program Mark II, Vol. I-User's Manual," Douglas Aircraft Report DAC 61552, Long Beach, April, 1968.
23. Jameson, A., Schmidt, W., and Turkel, E.: "Numerical Solutions of the Euler Equations by Finite Volume Methods Using Runge-Kutta Time-Stepping Schemes," *AIAA Paper 81-1259*, Jan., 1981.
24. Raj, P. and Long, L.N.: "An Euler Aerodynamic Method for Leading-Edge Vortex Flow Simulation," presented at the USAF/NASA Vortex Flow Aerodynamics Conference, NASA-Langley Research Center, Hampton, Virginia, USA, 1985.
25. Raj, P. and Brennan, J.: "Improvements to an Euler Aerodynamic Method for Transonic Flow Analysis," *AIAA Paper No. 87-0040*, Jan., 1987.
26. Raj, P.: "Applied Computational Aerodynamics: 1986 Year End IRAD Progress Report," Lockheed Report LR-31206, Feb., 1987.
27. Jameson, A. and Baker, T.J.: "Solution of the Euler Equations for Complex Configurations," *AIAA-1929-CP*, 6th Computational Fluid Dynamics Conference, Danvers, Massachusetts, July, 1983.
28. Roe, P.L.: "Approximate Riemann Solvers, Parameter Vector, and Difference Schemes," *Jnl. of Comp. Physics*, Vol. 43, 1981, pp. 357-372.
29. Gnoffo, P.A.: "Application of Program LAURA to Three-Dimensional AOTV Flowfields," *AIAA Paper No. 86-0565*, Jan., 1986.
30. Srinivasan, S., Tannehill, J.C., and Weilmuenster, K.J.: "Simplified Curve Fits for the Thermodynamic Properties of Equilibrium Air," *ISU-ERI-Ames-86401*, Iowa State Univ. Report, Ames, Iowa, June, 1986.
31. Rasmussen, M.L., Jischke, M.C., and Daniel, D.C.: "Experimental Forces and Moments on Cone-Derived Waveriders for $M = 3$ to 5," *Jnl. of Spacecraft and Rockets*, Vol. 19, No. 6, Dec., 1982, pp. 592-598.
32. Anon., PATRAN II, Release Notes, Vers. 2.1, PDA Engineering, Santa Ana, Calif., Sept., 1986.
33. Kim, B.S., Rasmussen, M.L., and Jischke, M.C.: "Optimization of Waverider Configurations Generated from Axisymmetric Conical Flows," *Jnl. Spacecraft and Rockets*, Vol. 20, No. 5, Sept.-Oct., 1983.

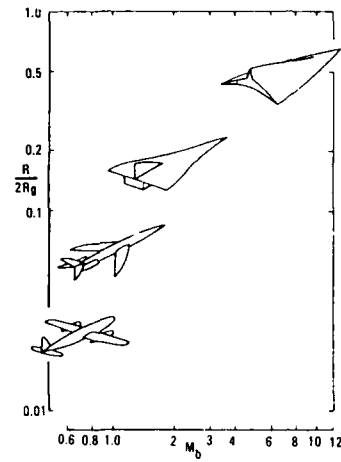


Figure 1. The Evolution of Modern Aircraft (Ref. 1)

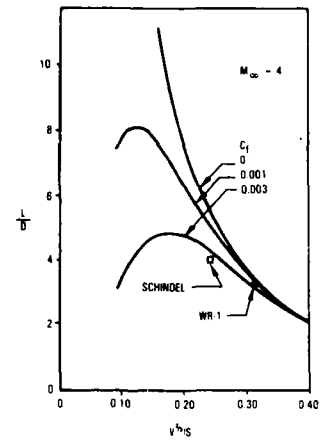


Figure 3. Effect of Skin Friction and Thickness on L/D (Mach = 4, Ref. 33)

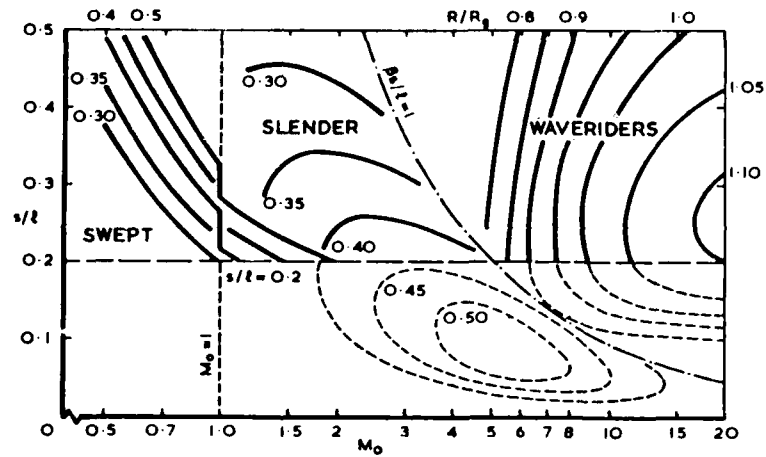


Figure 2. Three Categories of Aircraft: Swept, Slender, and Waverider (Ref. 1)

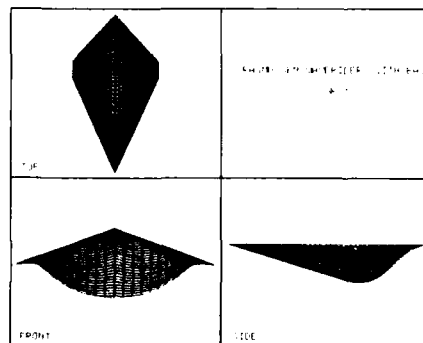


Figure 4. Three-View of Rasmussen's Elliptical Cone Waverider with Base (WR-1)

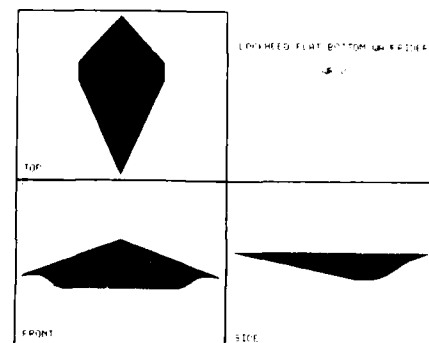


Figure 5. Three-View of Flat-Bottom Waverider with Base (WR-2)

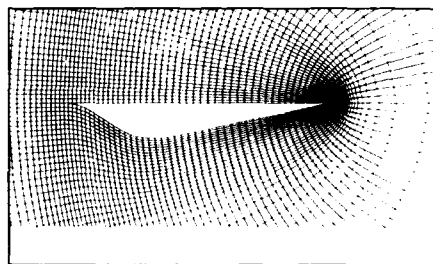


Figure 6. Sample Computational Grid at Plane of Symmetry for WR-2

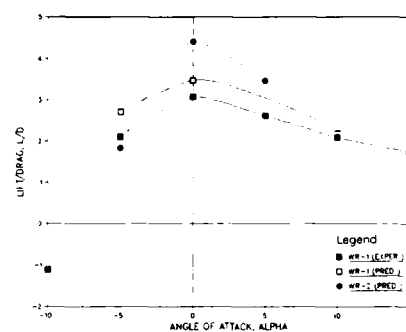


Figure 7. Experimental and Predicted L/D for Various Angles of Attack (Mach = 4)

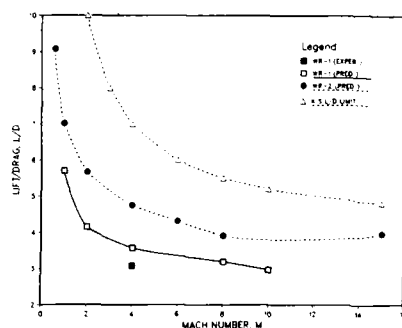


Figure 8. Experimental and Predicted L/D for Various Mach Numbers (Alpha = 0)

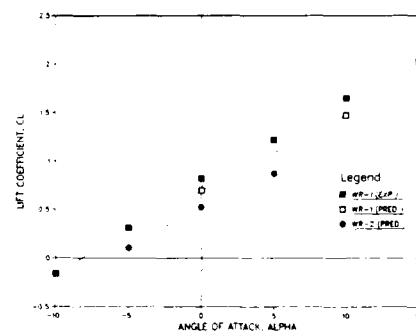


Figure 9. Experimental and Predicted Lift Coefficients for Various Angles of Attack (Mach = 4)

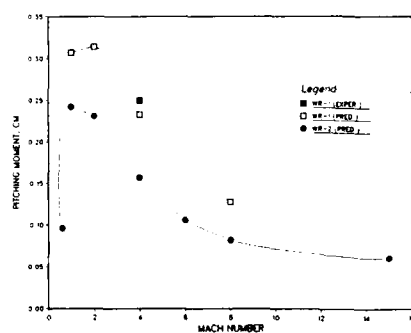


Figure 10. Experimental and Predicted Pitching Moment Coefficients for Various Mach Numbers (Alpha = 0)

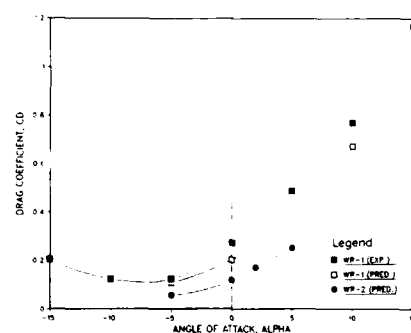


Figure 11. Experimental and Predicted Axial Force Coefficients for Various Angles of Attack (Mach = 4)

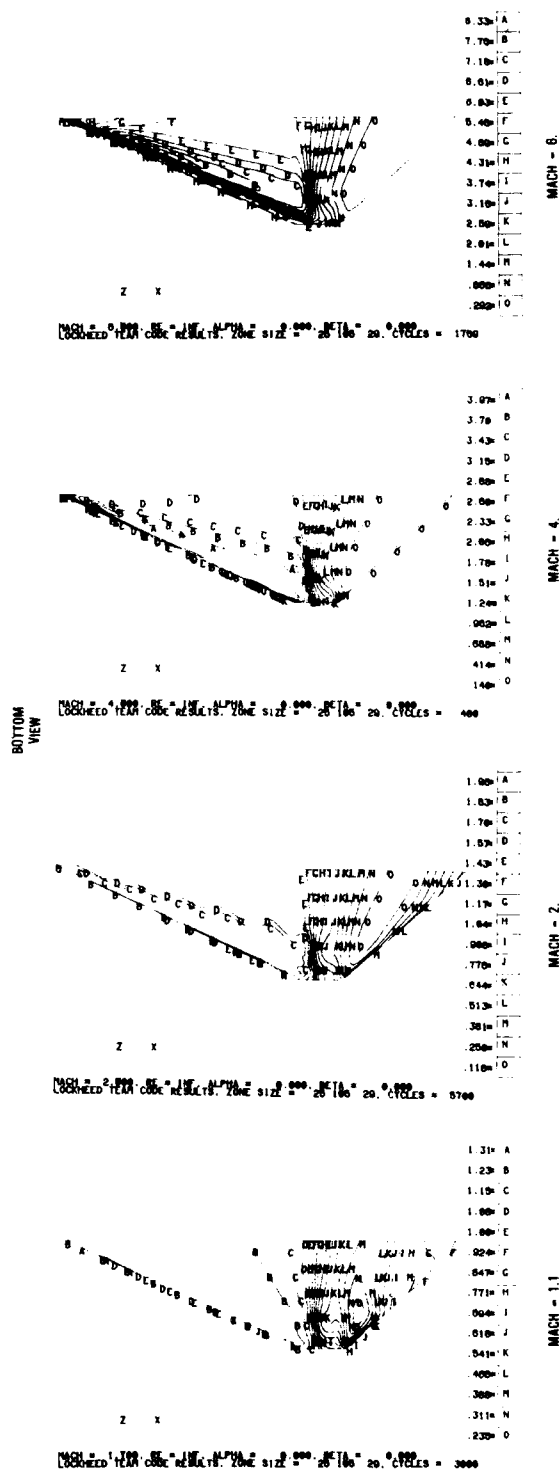
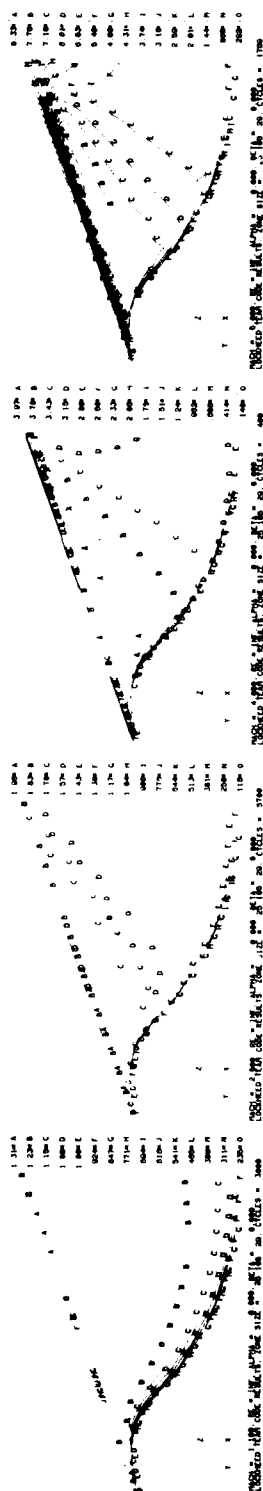


Figure 12. Pressure Distributions (gip/co) over WR.1 at Mach = 1.1, 2, 4, and 6 (Angle of Attack = 0)

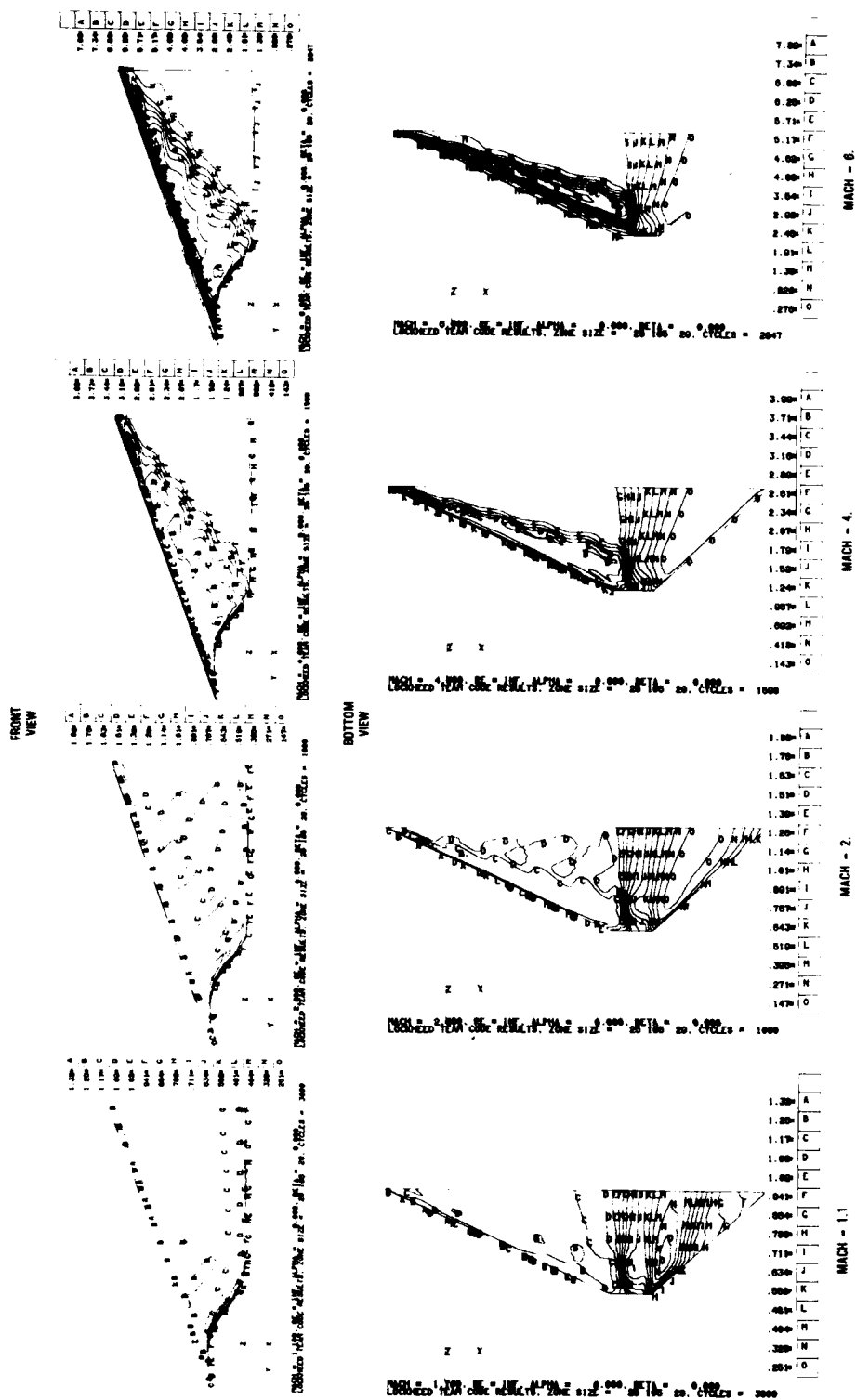


Figure 13. Pressure Distributions (Cp) over W12 at Mach = 1.1, 2, 4, and 6 (Angle of Attack = 0)

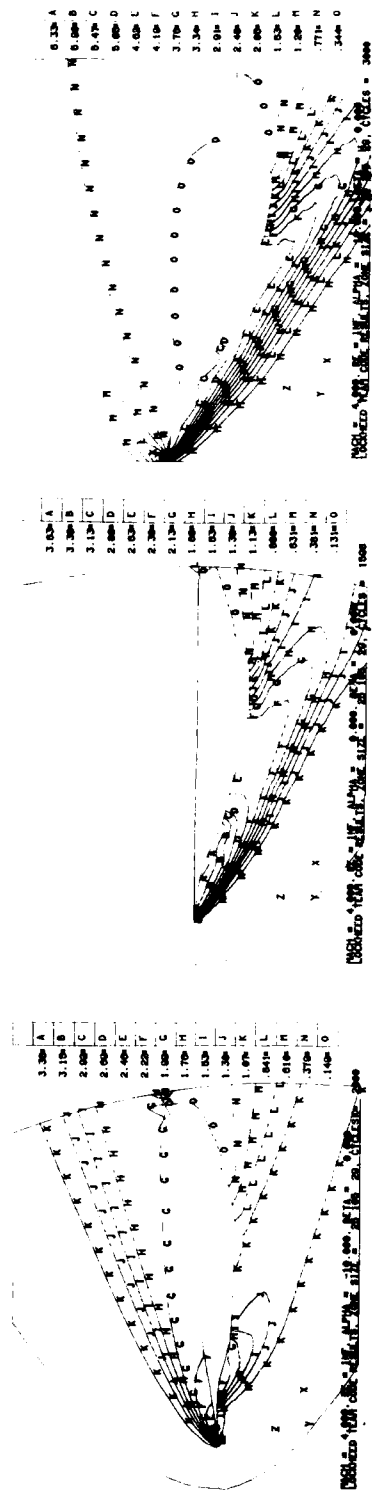


Figure 14. Pressure Distribution (p/p_{∞}) in a Stream-wise Cross-Section of Flow Field at Mid-Span of WR-2 for Angles of Attack -10, 0, and +10 (Mach $\infty = 4$)

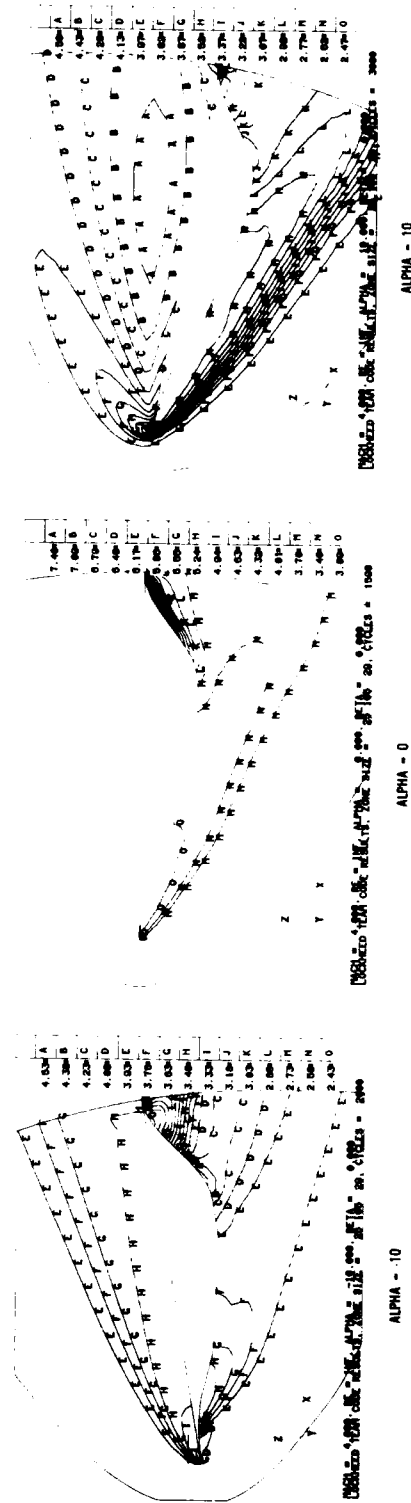


Figure 15. Mesh Number Distribution in a Stream-wise Cross-Section of Flow Field at Mid-Span of WR-2 for Angles of Attack -10, 0, and +10 (Mach $\infty = 4$)

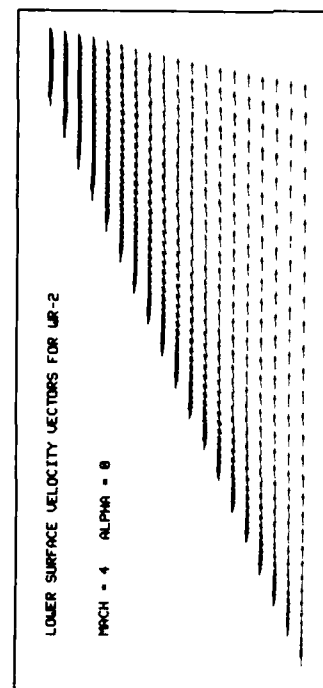


Figure 17. Velocity Vectors on Lower Surface of UR-2 (Mach = 4 and Alpha = 0)

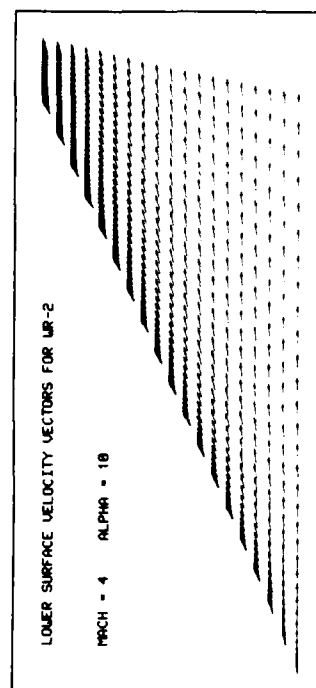


Figure 18. Velocity Vectors on Lower Surface of UR-2 (Mach = 4 and Alpha = +10)

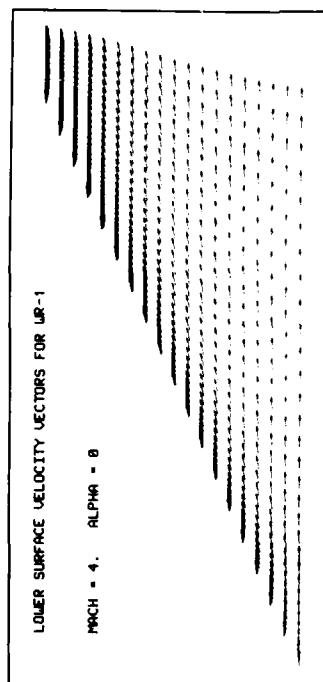


Figure 16. Velocity Vectors on Lower Surface of UR-1 (Mach = 4 and Alpha = 0)

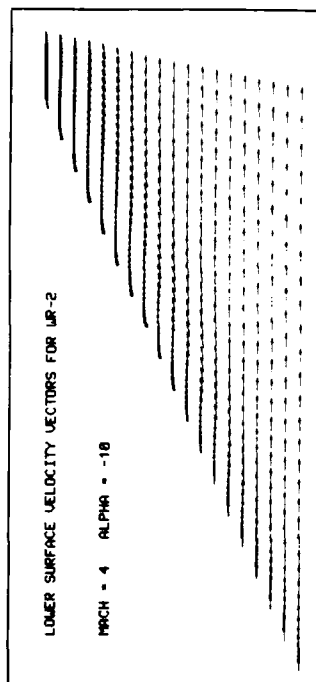


Figure 15. Velocity Vectors on Lower Surface of UR-2 (Mach = 4 and Alpha = -10)

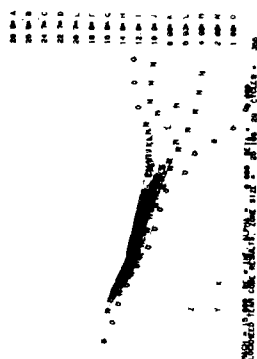


Figure 22. Pressure Distribution in a Stream-wise Cross-Section of Flow Field at Mid-Span of WR-2 for Mach = 15 and a Perfect Gas (Alpha = 0)

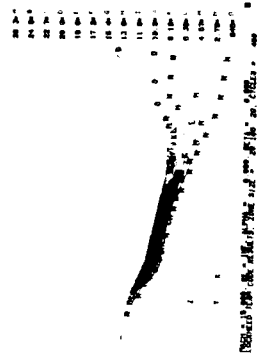


Figure 23. Pressure Distribution in a Stream-wise Cross-Section of Flow Field at Mid-Span of WR-2 for Mach = 15 and a Real Gas (Alpha = 0)

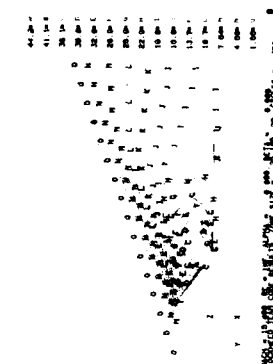


Figure 24. Upper Surface Pressure Distribution due to Leading Edge Vorticity on WR-1, Mach = 8 and Alpha = 20 degrees

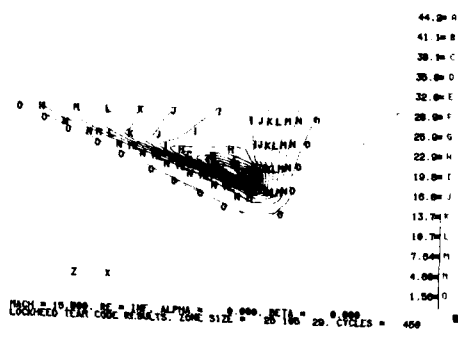


Figure 25. Surface Pressure Distribution (top) on WR-2 Using Real Gas Relations, Mach = 15 and Alpha = 0 degrees (Front and Bottom Views)

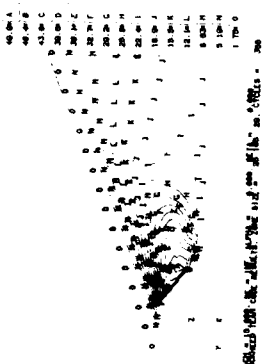


Figure 26. Surface Pressure Distribution (top) on WR-2 Using Perfect Gas Relations, Mach = 15 and Alpha = 0 degrees (Front and Bottom Views)

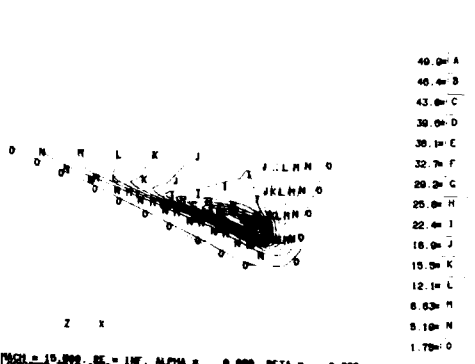


Figure 27. Surface Pressure Distribution (bottom) on WR-2 Using Real Gas Relations, Mach = 15 and Alpha = 0 degrees (Front and Bottom Views)

NUMERICAL OPTIMIZATION OF CONICAL FLOW WAVERIDERS INCLUDING DETAILED VISCOUS EFFECTS

by

Kevin G. Bowcutt,* John D. Anderson, Jr.,** and Diego Capriotti***

Department of Aerospace Engineering
University of Maryland
College Park, Maryland 20742 USA

SUMMARY

This is the second in a series of papers describing some new research on hypersonic waveriders. In particular, a family of optimized hypersonic waveriders is generated and studied wherein detailed viscous effects are included within the optimization process itself. This is in contrast to previous optimized waverider work, wherein purely inviscid flow is used to obtain the waverider shapes. For the present waveriders, the undersurface is a streamsurface of an inviscid conical flowfield, the upper surface is a streamsurface of the inviscid flow over a tapered cylinder (calculated by the axisymmetric method of characteristics), and the viscous effects are treated by integral solutions of the boundary layer equations. Transition from laminar to turbulent flow is included within the viscous calculations. The optimization is carried out using a non-linear simplex method. The resulting family of viscous hypersonic waveriders yields predicted high values of lift/drag, high enough to break the "L/D barrier" based on experience with other hypersonic configurations. Moreover, the numerical optimization process for the viscous waveriders results in distinctly different shapes compared to previous work with inviscid-designed waveriders. Also, the fine details of the viscous solution, such as how the shear stress is distributed over the surface, and the location of transition, are crucial to the details of the resulting waverider geometry. Finally, unique to the present paper is a study of the moment coefficient variations and heat transfer distributions associated with the viscous optimized waveriders.

I. INTRODUCTION

Over the past few years, interest in all aspects of hypersonic flight has grown explosively, driven by new vehicle concepts such as the National Aerospace Plane (NASP), the British spaceplane (HOTOL), aero-assisted orbital transfer vehicles (AOTV's), the hypersonic transport (the "Orient Express"), and hypersonic missiles, to name just a few. An extended discussion of these concepts, as well as a survey of hypersonic aerodynamic research contrasting the "old" with the "new" hypersonics, is given in Ref.1. Hence no further elaboration will be given here.

The present paper deals with a class of advanced hypersonic lifting configurations. It is a sequel to Ref. 2, which describes the generation of a new class of hypersonic waveriders. In the present paper, the work of Ref. 2 is reviewed to some extent in order to provide sufficient understanding of the work. Then, unique to the present paper, results on moment coefficient variations and heat transfer distributions associated with the present waveriders are presented and discussed.

To help understand the motivation for the present work, the following background is given. For a lifting aerodynamic body, it is well-known that high maximum lift-to-drag ratios, $(L/D)_{max}$, are very difficult to obtain at hypersonic speeds, due to the presence of strong shock waves (hence high wave drag) and massive viscous effects. At supersonic and hypersonic speeds, the most efficient lifting surface is the infinitely thin flat plate; the inviscid hypersonic aerodynamic properties of a flat plate are shown as the solid curves in Fig.1, based on the Newtonian limit of free stream Mach number $M_\infty \rightarrow \infty$ and $\gamma = C_p/C_\infty + 1$. Note that L/D theoretically approaches infinity as the angle-of-attack, α , approaches zero. In reality, viscous effects will cause L/D to peak at low values of α , and to go to zero as $\alpha \rightarrow 0$. This is illustrated by the dashed line in Fig.1, which shows the variation of L/D modified by skin friction as predicted by a reference temperature method. Although the infinitely thin flat plate shown in Fig. 1 is the most effective lifting surface aerodynamically, it is the

* Graduate Hypersonic Aerodynamics Fellow, sponsored by the Army Research Office, Dr. Robert Singleton, monitor. Presently, Engineer, Rockwell International, Los Angeles.

** Professor. Currently on sabbatical as the Charles Lindbergh Professor at the National Air and Space Museum, Smithsonian Institution.

*** Graduate Research Assistant

least effective in terms of volume capacity. It goes without saying that all practical flight vehicles must have a finite volume to carry fuel, payload, etc. Hence, the flat plate results, although instructive, are of academic interest only. In contrast, Fig. 2 shows values of $(L/D)_{\max}$ versus the volume parameter $V^{1/3}/S$ for several generic hypersonic configurations, obtained from Ref. 3. Here, V is the body volume and S is the planform area. Note from Fig. 2 that typical hypersonic values of $(L/D)_{\max}$ range from 4 to 6 for such lifting bodies at the conditions shown. These values are also typical of the hypersonic transport configuration studied in Ref. 4. Clearly, values of $(L/D)_{\max}$ for hypersonic vehicles are substantially lower than those for conventional subsonic and low supersonic airplanes. (For example, the maximum L/D values for the World War II Boeing B-29 and the contemporary General Dynamics F-111 are 16.8 and 15.8 respectively, as obtained from Ref. 5). Indeed, as M_∞ increases across the supersonic and hypersonic regimes, there is a general empirical correlation for $(L/D)_{\max}$ based on actual flight vehicle experience, given by Kuchemann⁶:

$$(L/D)_{\max} = \frac{4(M_\infty + 3)}{M_\infty}$$

This variation is shown as the solid curve in Fig. 3. Also shown are a number of data points for various previous hypersonic vehicle configurations at various Reynolds numbers (the open symbols), as well as new results from the present investigation (the solid symbols). Fig. 3 is pivotal to the present paper, and will be discussed at length in subsequent sections. However, at this stage in our discussion, Fig. 3 is used to illustrate only the following aspects:

1. The solid curve represents a type of "L/D barrier" for conventional hypersonic vehicles, which is difficult to break.
2. Data for conventional hypersonic vehicles, shown as the open circles, form an almost random "shotgun" pattern which, for the most part, falls below the solid curve. (The numbers adjacent to these open circles pertain to specific reference numbers itemized in Ref. 7, which should be consulted for details.)
3. The solid symbols pertain to the present study, and represent a new class of hypersonic configurations which break the "L/D barrier." These configurations are conical flow waveriders that are optimized with detailed viscous effects included directly in the optimization process.

To help understand the contribution made by the present work, let us briefly review the general concept of waveriders. In 1959, the design of three-dimensional hypersonic vehicles which support planar attached shock waves was introduced by Nonweiler,⁸ who hypothesized that streamsurfaces from the flow behind a planar oblique shock could be used as supersonic lifting surfaces. This led to a class of vehicles with a caret-shaped transverse cross-section and a delta planform--the so-called caret wing as shown in Fig. 4. Here, the body surface is generated by stream surfaces behind a planar oblique shock wave. The shock wave is attached to the sharp leading edges at the design Mach number, and hence no flow spillage takes place around the leading edge. The lift is high due to the high pressures behind a two-dimensional planar shock wave, exerted on the lower surface of the vehicle. Because the body appears to be riding on top of the attached shock wave, it is called a "waverider". The aerodynamic advantages of such waveriders are listed in Ref. 1, and are discussed in great detail in Refs. 7 and 10. In short, without repeating the details here, at a given lift coefficient, caret waveriders theoretically operate at higher L/D values than other hypersonic configurations.

Expanding on this philosophy, other types of flowfields can be used to generate waveriders. For example, any streamsurface from the supersonic flow over an axisymmetric body can be used to generate a waverider with an attached shock wave along its complete leading edge. Work on such waveriders was first carried out in Britain, as nicely summarized in Ref. 11, where the flow over a right-circular cone at zero degrees angle of attack is used to generate a class of "conical flow" waveriders. Still later, waveriders were generated from inclined circular and elliptic cones, and axisymmetric bodies with longitudinal curvature by Rasmussen et al.^{12,13}, using hypersonic small disturbance theory. This work was further embellished by the search for optimized waverider shapes. For example Cole and Zien¹⁴ found optimized waveriders derived from axisymmetric bodies with longitudinal curvature by using hypersonic small disturbance theory to generate inviscid flow solutions, and then utilizing the calculus of variations to obtain the optimum waverider shapes. Later, Kim et al. used the same¹⁵ philosophy to derive optimum waveriders from flowfields about yawed circular cones¹⁶, and yawed circular and elliptic cones¹⁶. In Refs. 14-16, the advantage of hypersonic small disturbance theory is that analytic expressions are obtained for surface pressure distributions, hence lift and wave drag can be calculated directly, thus enabling the application of the calculus of variations for optimization.

Unfortunately, to date the potential superiority of waveriders as hypersonic high L/D shapes has not been fully demonstrated, either in the wind tunnel or in flight. A basic problem arises because of the tendency for waveriders to have large wetted surface areas, which leads to large friction drag. All previous waverider optimization work (such as Refs. 14-16) has been based on the assumption of inviscid flow, after which an estimate of skin friction for the resulting configuration is sometimes added. As a result, the real aerodynamic performance of the resulting optimum configuration usually falls short of its expectations.

The purpose of the present work is to remove this deficiency. In particular, a series of conical-flow generated waveriders are optimized for maximum L/D wherein detailed viscous effects (including boundary layer transition) are included within the optimization process itself. This leads to a new class of waveriders where the optimization process is trying to reduce the wetted surface area, hence reducing skin friction drag, while at the same time maximizing L/D. Because detailed viscous effects cannot be couched in simple analytical forms, the formal optimization methods based on the calculus of variations cannot be used. Instead, in the present work a numerical optimization technique is used, based on the simplex method by Nelder and Mead¹⁷. By using a numerical optimization technique, other real configuration aspects can be included in the analysis in addition to viscous effects, such as blunted leading edges, and an expansion upper surface (in contrast to the standard assumption of a free stream upper surface, i.e., an upper surface with all generators parallel to the freestream direction). The results of the present study lead to a new class of waveriders, namely "viscous optimized" waveriders. Moreover, these waveriders appear to produce relatively high values of (L/D), as will be discussed in subsequent sections.

II. ANALYSIS

For the present waverider configurations, the following philosophy is followed:

1. The lower (compression) surface is generated by a streamsurface behind a conical shock wave. The inviscid conical flowfield is obtained from the numerical solution of the Taylor-Maccoll equation, derived for example in Ref. 18.
2. The upper surface is treated as an expansion surface, generated in a similar manner from the inviscid flow about a tapered, axisymmetric cylinder at zero angle of attack, and calculated by means of the axisymmetric method of characteristics.
3. The viscous effects are calculated by means of an integral boundary layer analysis following surface streamlines, including transition from laminar to turbulent flow.
4. Blunt leading edges are included to the extent of determining the minimum leading edge radius required to yield acceptable leading edge surface temperatures, and then estimating the leading edge drag by modified Newtonian theory.
5. The final waverider configuration, optimized for maximum L/D at a given Mach number and Reynolds number with body fineness ratio as a constraint, is obtained from the numerical simplex method taking into account all the effects itemized in 1-4 above within the optimization process itself.

The following paragraphs describe each of the above items in more depth; for a highly detailed discussion, see Ref. 7.

A. Inviscid Flow -- Lower Surface

The waverider's lower surface is generated from a streamsurface behind a conical shock wave supported by a hypothetical right circular cone at zero angle of attack. The hypothetical cone and its flowfield is shown in Fig. 5, where θ_c is the cone semi-angle and θ_s is the wave angle. The inviscid conical flow is obtained from the Taylor-Maccoll equation¹⁸

$$\begin{aligned} \frac{\gamma-1}{2} [2h + V^2 - V_r^2 - (\frac{dV}{d\theta} r)^2] [2V_r + \frac{dV}{d\theta} r \cot\theta + \frac{d^2 V}{d\theta^2} r] \\ - \frac{dV}{d\theta} r [V_r \frac{dV}{d\theta} r + \frac{dV}{d\theta} r \frac{d^2 V}{d\theta^2} r] = 0 \end{aligned} \quad (1)$$

solved by a standard Runge-Kutta, forth-order accurate numerical technique, namely the RK45 algorithm obtained from Ref. 19. In Eq.(1), V_r is the component of flow velocity along a conical ray, θ is the angle of the ray referred to the cone axis, h is the flow static enthalpy and γ is the ratio of specific heats.

Any streamsurface from this flowfield can represent the wing undersurface of a waverider, as shown in Fig. 6. (For purposes of illustration, Fig. 6 also shows the waverider upper surface as a freestream surface, but this is only one of many possible choices for the upper surface.) Any particular undersurface is uniquely defined by the intersection of the conical flow streamsurface with the conical shock wave, as shown by the curve labeled "leading edge" in Fig. 7. Let us examine Fig. 7 more closely. It is a front-view of the hypothetical conical flowfield, illustrating the cone apex at the center, and both the cone base and shock base at some arbitrary distance downstream of the apex. Consider a curve in this front-view, lying below the apex (or even including the apex), as shown by the curve labeled "leading edge". Now construe this curve as a

trace on the conical shock wave itself, and visualize streamlines trailing downstream from this trace; the resulting streamsurface is the waverider undersurface sketched in Fig. 6. Indeed, the curve labeled "leading edge" in Fig. 7 is simply the forward projection of the waverider leading edge on the cross-flow (x-y) plane. This curve is treated as completely general, except for the constraints that it be symmetric about the y-z plane, and that it lie entirely below the x-z plane to ensure that the waverider undersurface is a lifting surface. Also in Fig. 7, note the curve labeled "trailing edge". This is the intersection of the particular conical flow streamsurface with the plane of the shock base, and it represents the bottom surface trailing edge of the waverider. This is the shape of the bottom of the waverider base, as sketched in Fig. 6. Returning to Fig. 7, the area between the "leading edge" and "trailing edge" curves is the forward projection of the entire waverider compression surface. Moreover, the dashed line emanating from the cone apex in Fig. 7 is the forward projection of a conical flow streamline; hence, that portion of the dashed line contained between the "leading edge" and "trailing edge" curves is the projection of a particular streamline along the waverider undersurface, from the leading edge to the trailing edge.

B. Inviscid Flow -- Upper Surface

In most previous waverider work, the upper surface is treated as a freestream surface, as illustrated in Fig. 6. Here, the upper surface pressure is freestream pressure, p_∞ . However, if the upper surface is made an expansion surface, where $p < p_\infty$, then a small but meaningful contribution to L/D can be obtained. This approach is taken here. Similar to the philosophy for the lower surface, the upper surface is a streamsurface "carved" from a known expansion flow. The hypothetical expansion body chosen here is a circular cylinder of given radius; the cylinder is aligned parallel to the flow and, at some point, is tapered parabolically to a smaller radius. The result is an axisymmetric expansion flow, where the domain of expansion is bounded by a freestream Mach cone centered on the cylinder axis, as shown in Fig. 8. Parabolic taper was chosen because it is relatively simple, and the resulting expansion body slope is everywhere continuous. Once the expansion body is chosen, it remains only to geometrically position the expansion region relative to the lower surface, choose the initial and final cylinder radii, solve the inviscid expansion flow, then cut a streamsurface from that flow to serve as the waverider upper surface. This basic idea was first developed for two-dimensional expansions by Flower¹⁰, and later for axisymmetric expansions by Moore¹¹.

The axisymmetric flow is calculated from the axisymmetric method of characteristics, using the two-step predictor-corrector iteration scheme of Ferris¹². The details involving the matching of the resulting expansion surface with the conical flow compression surface are straight forward, but lengthy. Considering that the expansion surface contributes only about 10% to the value of (L/D), no further space for its discussion is justified in the present paper; for the complete discussion, see Ref. 7.

C. Leading-Edge Bluntness

Waveriders, by design, have sharp leading edges that support attached shock waves. However, for flight Mach numbers above five, the temperatures for sharp leading edges will exceed the practical limits of most structural materials. This leads to the need for blunt leading edges with sufficiently large radii such that the aerodynamic heat flux is reduced to reasonable levels. However, at the same time the leading edge radius should be as small as possible to reduce the nose drag.

To reduce the required leading edge radius, Nonweiler²³ has proposed adding conducting material aft of the leading edge to transport thermal energy away from the region of high convective heating near the stagnation or attachment line, and conduct it downstream to areas where convective heating is lower, and excess energy can be radiated away from the body. Nonweiler labeled this theoretical concept a "conducting plate", which is somewhat analogous to other passive cooling techniques, such as heat pipes. Using Nonweiler's basic technique, minimum leading edge radii can be ascertained, once flight Mach number, freestream conditions, leading edge sweep, material properties, and maximum allowable temperature are known.

In the present work, Nonweiler's technique was used to determine the leading edge radii for waveriders designed for Mach numbers between 6 and 25. The leading edge material used for the calculations was ATJ graphite, chosen because it is representative of materials with high conductivity and high melting point temperature. Details of this technique as applied to the present work are given in Ref. 7. It is interesting to note that, for conditions associated with the typical flight path of a lifting hypersonic vehicle entering the earth's atmosphere at Mach 25 and decelerating to Mach 6 at lower altitude, the minimum leading edge diameters ranged from 6 to 28 mm --quite small in comparison to a typical overall length of, say 60m. Therefore, the present waveriders are essentially aerodynamically sharp from that point of view. Regardless of the apparently small amount of required leading edge bluntness (from the aerodynamic heating point of view), the present waveriders were geometrically altered to accommodate the blunt edge, and the contribution to aerodynamic forces on the waverider were estimated assuming a modified Newtonian pressure distribution on the leading edge.

D. Viscous Flow Analysis

A major aspect of the present investigation is that optimum waverider shapes are obtained wherein detailed viscous effects are included within the optimization process itself. These viscous effects are calculated by means of two integral boundary layer techniques, described below. In all cases, the boundary layer flow is assumed to be locally two-dimensional, following the inviscid upper surface and lower surface streamlines. Both laminar and turbulent flow are considered, along with a transition region based on empirical correlations.

D.1 Laminar Analysis

The laminar boundary layer calculations were performed using Walz' integral method, as described in Ref. 24. The method requires the solution of a set of coupled first-order ordinary differential equations along the boundary layer edge streamlines. These equations are the boundary layer momentum and mechanical energy equations, given by

$$\text{Momentum: } Z' + \frac{u_e'}{u_e} F_1 Z - F_2 = 0 \quad (2)$$

$$\text{Mechanical Energy: } W' + \frac{u_e'}{u_e} F_3 W - \frac{F_4}{Z} = 0 \quad (3)$$

where

$$Z = \delta_2 \left(\frac{\rho_e u_e \delta_2}{u_w} \right) \quad (4)$$

$$W = \delta_3 / \delta_2 \quad (5)$$

$$\delta_1 \equiv \int_0^\delta \left(1 - \frac{\rho u}{\rho_e u_e} \right) dy \quad (6)$$

$$\delta_2 \equiv \int_0^\delta \frac{\rho u}{\rho_e u_e} \left(1 - \frac{u}{u_e} \right) dy \quad (7)$$

$$\delta_3 \equiv \int_0^\delta \frac{\rho u}{\rho_e u_e} \left(1 - \frac{u^2}{u_e^2} \right) dy \quad (8)$$

and

$$F_1 = 3 + 2H - M_e^2 + n \frac{u_w'}{u_w} \frac{u_e'}{u_e}, \quad n = \begin{cases} 0, & T_w = \text{constant} \\ 1, & T_w \neq \text{constant} \end{cases} \quad (9)$$

$$F_2 = 2a/b \quad (10)$$

$$F_3 = 1 - H + r(\gamma - 1) M_e^2 \left(1 - \frac{\tilde{\theta}}{W} \right) \quad (11)$$

$$F_4 = (2\theta - aW)/b \quad (12)$$

Note that in the above equations, primes denote differentiation with respect to x , here representing the boundary layer coordinate in the streamline direction. The variables in Eqs. (9)-(12) are defined by Walz to be

$$H = \delta_1 / \delta_2 = b H_{12} + r \frac{\gamma - 1}{2} M_e^2 (W - \tilde{\theta}) \quad (13)$$

$$a = 1.7261 (W^* - 1.515)^{0.7158} \quad (14)$$

$$b = \frac{(\delta_2)_u}{\delta_2} = 1 + r \frac{\gamma - 1}{2} M_e^2 (W - \tilde{\theta}) (2 - W) \quad (15)$$

$$r = \sqrt{Pr} \quad (16)$$

$$\tilde{\theta} = \frac{T_{aw}(x) - T_w(x)}{T_{aw}(x) - T_e(x)} \quad (17)$$

and

$$\theta = \theta_u x \quad (18)$$

where

$$H_{12} = 4.0306 - 4.2845 (W^* - 1.515)^{0.3886} \quad (19)$$

$$T_{aw} = T_e + \frac{r u_e^2}{2C_p} \quad (20)$$

$$W^* = (\delta_3)_u / (\delta_2)_u = W/\psi \quad (21)$$

$$\psi = 1 + \frac{(\psi_{12}-1)M_e}{M_e + \frac{\psi_{12}-1}{\psi_0}} \quad (22)$$

$$\psi_{12} = \frac{2-(\delta_1)_u/\delta}{W^*} \tilde{\delta} + \frac{1-(\delta_1)_u/\delta}{W^*g} (1-\tilde{\delta}) \quad (23)$$

$$\psi_0' = 0.0144(2-W^*)(2-\tilde{\delta})^{0.8} \quad (24)$$

$$(\delta_1)_u/\delta = 0.420 - (W^*-1.515)^{0.424W^*} \quad (25)$$

$$g = 0.324 + 0.336(W^*-1.515)^{0.555} \quad (26)$$

$$\delta_u = 0.1564 + 2.1921(W^*-1.515)^{1.70} \quad (27)$$

and

$$x = \{1 + r(\frac{\gamma-1}{2})M_e^2[1.16W^*-1.072-\tilde{\delta}(2W^*-2.581)]\}^{0.7} \\ \cdot [1 + r(\frac{\gamma-1}{2})M_e^2(1-\tilde{\delta})]^{-0.7} \quad (28)$$

Careful inspection of Eq. (21) reveals that it is an implicit equation for W^* , since ψ is a complex function of W^* . Therefore, in practice, a numerical zero-finding routine is used on Eq. (21) to find the value of W^* that yields the known value of W . Walz suggested an approximation that would allow closed form solution of Eq. (21), however, the present authors have found that it caused boundary layer calculations to become unstable when used for a Mach six flat plate test case. Hence, the suggested approximation was discarded in favor of the zero-finding approach. For more details on the numerical solution of these integral boundary layer equations, see Ref. 7.

D.2 Turbulent Analysis

If and when boundary layer transition is predicted, turbulent boundary layer calculations are performed using the inner variable integral method of White and Christopherson. In practice, the method requires solution of one of two first-order ordinary differential equations along the boundary layer edge streamlines, depending upon the value of the parameter λ/λ_{max} , where

$$\lambda = \frac{\sqrt{2}}{C_f} \quad (29)$$

$$\lambda_{max} = 8.75 \log_{10} Re^* \quad (30)$$

$$S = \frac{(T_{aw}/T_e - 1)^{1/2}}{\sin^{-1}A + \sin^{-1}B} \quad (31)$$

$$\text{and } Re^* = \frac{-\rho_e}{\mu_w} \left(\frac{T_e}{T_w} \right)^{1/2} \frac{u_e^2}{u_e} \quad (32)$$

In Eq. (31), the parameters A and B are defined as

$$A = a/c \quad (33)$$

$$B = b/c \quad (34)$$

where

$$a = \frac{T_{aw} + T_w}{T_e} - 2 \quad (35)$$

$$b = \frac{T_{aw} - T_w}{T_e} \quad (36)$$

$$c = \left[\left(\frac{T_{aw} + T_w}{T_e} \right)^2 - 4 \frac{T_w}{T_e} \right]^{1/2} \quad (37)$$

and T_{aw} is defined by Eq. (20), except that now the recovery factor is the turbulent value,

$$r = Pr^{1/3} \quad (38)$$

According to Ref. 25, if $\lambda/\lambda_{max} < 0.36$, or $Re^* < 0$, then the differential equation

$$\lambda' = \frac{1}{8} \frac{\rho_e}{\mu_w} \left(\frac{T_e}{T_w} \right)^{1/2} u_e \exp(-0.48 \frac{\lambda}{S}) - 5.5 \frac{u_e'}{u_e} \quad (39)$$

is valid; however if $\lambda/\lambda_{max} > 0.36$, then the equation

$$\lambda' = \frac{-\frac{u_e'}{u_e} (1 + 9S^{-2} g^* Re^* 0.07)}{0.16f^* S^3} + \frac{\left[\frac{u_e u_e' - 2(u_e')^2}{u_e u_e'} \right] (35^2 g^* Re^* 0.07)}{0.16f^* S^3} \quad (40)$$

applies, where

$$f^* = (2.434z + 1.443z^2) \exp(-44.0z^6) \quad (41)$$

$$g^* = 1 - 2.3z + 1.76z^3 \quad (42)$$

$$z = 1 - \lambda/\lambda_{max} \quad (43)$$

and the primes denote, as in the laminar case, differentiation with respect to the streamline coordinate, x . For more details concerning the numerical solution of these equations, see again Ref. 7.

D. 3 Transition Analysis

The prediction of transition from laminar to turbulent flow at hypersonic speeds is a state-of-the-art research topic. In the present analysis, the correlation used for predicting the onset of transition is based on two sets of data: (1) data for sharp cones at zero angle-of-attack²⁶; and (2) data for wings with blunt, swept supersonic leading edges²⁷. The correlation gives local transition Reynolds number Re_{xt} , as a function of local edge Mach number, M_e , as follows²⁸:

$$\log_{10}(Re_{xt}) = 6.421 \exp(1.209 \times 10^{-4} M_e^{2.641}) \quad (44)$$

In turn, this value of transition Reynolds number is modified for wing leading-edge sweep, as follows:

$$\frac{(Re_{xt})_\Lambda}{(Re_{xt})_{\Lambda=0}} = 0.787 \cos^{4.346 \Lambda - 0.7221e - 0.0991\Lambda + 0.9464} \quad (45)$$

where Λ is the sweep angle, and $(Re_{xt})_{\Lambda=0}$ is obtained from Eq.(44).

Once the onset of transition has been predicted, the extent of the transition region, hence the end of transition, is predicted using a relationship developed by Harris and Blanchard²⁹, as follows:

$$x_{te} = x_{ti} [1 + 5(Re_{xti})^{-0.2}] \quad (46)$$

where x_{te} and x_{ti} are the distances along a streamline from the leading edge to the beginning and end of transition, respectively, and $(Re_x)_{ti}$ is the local Reynolds number at the beginning of transition obtained in the present analysis from Eq.(45).

The variation of local skin friction coefficient within the transitional region (between x_{te} and x_{ti}) is assumed to be a linear combination of the laminar (c_{f_l}) and turbulent (c_{f_t}) values that would have existed if the boundary layer were completely laminar or turbulent, respectively. The transitional friction coefficient, $c_{f_{TR}}$, is thus related to c_{f_l} and c_{f_t} by:

$$c_{f_{TR}} = (1-\xi) c_{f_l} + \xi c_{f_t} \quad (47)$$

where ξ is a weighting factor (a function of x) inspired by Emmons (as discussed in Ref.29). For the present investigation, the following expression for ξ is, as derived in detail in Ref. 7:

$$\xi(x) = 1 - e^{-3 \left\{ \exp \left[\frac{\ln 2}{5x_{ti}} (Re_x)_i^2 (x - x_{ti}) \right] - 1 \right\}^2} \quad (48)$$

It is not possible within the current state-of-the-art to evaluate the accuracy of these transition correlations. After a study of the existing literature, the present authors feel that the above relations form a practical method for simulating transition within the goals of the present study. They provide a mechanism for assessing the effect of transition on optimum waverider shapes; indeed, as discussed in the results, one series of numerical experiments is conducted wherein the transition location is varied as a parameter.

E. Aerodynamic Forces

The lift, drag, and hence L/D is calculated from a detailed integration of the local surface pressures and shear stress over the waverider surface. Consistent with wind tunnel practice as well as other literature, base drag is not included in the present results. (For example, all the data shown in Fig. 3 does not include base drag.) This is done to enable a rational comparison with other data. Moreover, at very high Mach number, the base drag becomes a small quantity in comparison to forebody drag. Details on the pressure and shear stress numerical integration can be found in Ref.7.

F. Waverider Optimization

Once a specific shape for the forward leading edge projection of a waverider is chosen, (such as shown in Fig. 7), the techniques outlined in the previous sections can be used to generate the corresponding waverider and evaluate its lift-to-drag ratio (L/D). Finding the leading edge shape that maximizes L/D, with all other parameters held fixed, then requires an optimization scheme that can systematically change the projected leading edge shape in search of the one that yields maximum L/D. Unfortunately, most existing optimization schemes require that the function of interest have an analytical description -- a requirement not possible in the present work. There is one scheme, however, a non-linear simplex method for function minimization by Nelder and Mead⁷, that requires nothing more than the ability to numerically evaluate the function. This scheme has been used in the present work to find optimum waveriders.

In general, the scheme of Ref.17 minimizes a function of n variables by comparing values of the function at $(n+1)$ vertices of a "simplex", then replacing the vertex with the highest function value by another point determined via the logic of the scheme. As a result of the algorithm logic, "the simplex adapts itself to the local landscape [of the function surface], elongating down long inclined planes, changing direction on encountering a valley at an angle, and contracting in the neighborhood of a minimum", according to Ref.17. In this scheme, three operations -- reflection, contraction and expansion -- are used to modify the current simplex in an attempt to replace the vertex having the highest function value with one having a lower value. Each of three operations replace one or more of the $(n+1)$ points (P_0, P_1, \dots, P_n) that define the current simplex in n -dimensional space with new points that yield progressively smaller function values (f_0, f_1, \dots, f_n) at the new vertex points. A graphic illustration of how the method works is shown in Fig. 9 for a hypothetical function, f , of two variables, C_1 and C_2 . In the figure, a triangle with vertices on the function surface represents a possible simplex. In the optimization process, the triangle (simplex) flip-flops down the function valley, expanding if possible to speed up the process, then contracting when it straddles the minimum.

To use the simplex method for optimizing waverider L/D, the shape of the forward projection of the leading edge must be parameterized in some general way. In the present work, five points in the x - y plane, lying inside of the shock domain, were chosen to represent the forward leading edge projection. A cubic spline-fit through the five points is then used to generate a continuous leading edge. One of the five points, the symmetry plane point, is constrained to lie on the y -axis, hence its x -value is always zero. This leaves nine variables, the remaining x and y values of the leading edge projection points, for the optimization routine to manipulate in search of an optimum waverider. A set of leading edge coordinates thus represent a single vertex point,

$$P_i = (x_2, x_3, x_4, x_5, y_1, y_2, y_3, y_4, y_5)_i \quad (49)$$

of the required simplex, where $x_1 = 0$ as explained, and the function to be minimized is the negative of the lift-to-drag ratio

$$f_i(P_i) = (-L/D)_i \quad (50)$$

Note that the five leading edge points are used to define only half of the projected leading edge shape, since the other half is constrained by vehicle symmetry to be the mirror image of the first half.

With nine variables ($n=9$), ten points (hence ten leading edge shapes) must be chosen to create the initial simplex. In the present work, five polynomials of the form

$$y_{le} = C_1 + C_2 x_{le} + C_3 x_{le}^2 \quad (51)$$

and five cosine curves of the form

$$y_{le} = C_4 + C_5 \cos(\frac{\pi}{2} \frac{x_{le}}{r_s}) \quad (52)$$

were used to describe the initial leading edge shapes; the constants C_1, C_2, \dots, C_6 being varied to generate a set of distinct shapes. An example of a set of initial leading edge shapes is shown in Fig. 10 -- the bold line representing the final shape associated with the optimum waverider for this case. Also note that in the present work, 100 steps of the optimization routine were executed for all cases run, though a convergence criterion could have been implemented as described in Ref. 17. It was found that one-hundred steps provided adequate convergence for engineering accuracy ($\sim 10^{-3}$ to 10^{-4}) without using excessive computer resources to generate an optimized waverider.

For more details on the optimization scheme, see Ref. 7.

III. RESULTS AND DISCUSSION

The present results are divided into six sections, as follows: (1) a presentation of optimum waverider shapes and aerodynamic characteristics at Mach 6 and 25, representing two extremes of the hypersonic flight spectrum; (2) a discussion of two quantities affecting aircraft longitudinal stability, namely moment coefficient and center of pressure, for all optimum waveriders generated for Mach numbers between 4 and 25; (3) an example of the heat transfer distribution and onset of boundary layer transition resulting on an optimized waverider; (4) a numerical experiment to assess the impact of boundary layer transition on the optimized waverider shapes; (5) an assessment of the need to account for detailed surface variations of shear stress in contrast to the use of an average skin friction coefficient during the optimization process; (6) an examination of the question: if the skin friction is deleted from the present analysis, what type of optimized inviscid waverider configuration is produced?

Due to the specialized nature of any waverider generation analysis, including the present one, it is difficult to obtain a direct benchmark comparison with existing data in order to verify the integrity of the current results. However, with the present analysis, it is possible to calculate the aerodynamic properties of a half-cone with a flat delta wing mounted on top; in this case the wing will have a sweep angle corresponding to the shock angle of the cone, and the body will be at zero degrees angle of attack. This specialized case was calculated at Mach 6.8 for a half-cone of $\theta_c = 3.67^\circ$, and the corresponding wing sweep angle of 81° . The result is given as the flagged solid square in Fig. 3. This is to be partly compared with the point labeled P2a, which was obtained from Ref. 3, and which corresponds to a similar flat-top half-cone, delta wing model, but at conditions of maximum L/D, hence at some positive angle of attack. About the only point to be made here is that the calculated L/D at zero angle of attack is lower than the measured (L/D) at some angle-of-attack -- a proper qualitative result. The measured L/D at zero angle-of-attack is not presented in Ref. 3; however, through a personal inquiry to Patrick Johnston at NASA Langley, the present authors have been told that the measured L/D at zero-angle-of-attack was 2.7 -- about eight percent higher than the value of 2.5 calculated with the present analysis. This is a reasonable comparison, and if anything, seems to indicate that the present aerodynamic analysis is conservative. (Please note that the comparisons discussed above are for a given configuration, not an optimized waverider; hence any degree of validation here pertains to the aerodynamic portion of the analysis and not to the present optimization process itself.)

A. Representative Waveriders

In Ref. 7, a series of optimized waveriders is generated, including cases at $M_\infty = 4, 6, 10, 15, 20$ and 25. The conditions correspond to altitude-velocity points along a typical entry flight trajectory of a lifting hypersonic vehicle, such as an aerospace plane. In the present section, only the results at $M_\infty = 6$ and 25 are presented as representative of the two extremes of the flight spectrum. Ref. 7 should be consulted for additional results.

Fig. 11 gives values of (L/D), C_L , and volumetric efficiency, $\eta = V^{2/3}/S_p$, for waveriders optimized at different assumed wave angles for the conical shock. To understand this more fully, consider the conical flow field associated with a given conical shock wave, say $\theta_s = 11^\circ$. For this value of θ_s an optimum waverider shape is obtained (refer again to the bold curve in Fig. 10). The resulting characteristics of this optimized waverider are then plotted on Fig. 11 for $\theta_s = 11^\circ$. This process is repeated for other values of θ_s , say $12^\circ, 13^\circ$, and 14° . For each value of θ_s , an optimized waverider is obtained, and its characteristics plotted in Fig. 11 as the open symbols. (The solid symbols will be discussed later.) Hence, Fig. 11 pertains to an entire series of optimized waveriders. However, note that the (L/D) curve itself has a maximum (in this case for $\theta_s = 12^\circ$). This yields an "optimum of the optimums", and defines the final viscous optimized waverider at $M_\infty = 6$ for the flight conditions shown in Fig. 11. The front views of the optimum shapes at each value of θ_s are shown in Fig. 12, and the corresponding perspective views are shown in Fig. 13. Finally, a summary three-view of the best optimum (the "optimum of the optimum") waverider, which

here corresponds to $\theta_s = 12^\circ$, is given in Fig. 14. Also in Figs. 12-14, the lines on the upper and lower surfaces of the waveriders are inviscid streamlines. Note in these figures that the shape of the optimum waverider changes considerably with θ_s . Moreover, examining (for example) Figure 14, note the rather complex curvature of the leading edge in both the planform and front views; the optimization program is shaping the waverider to adjust both wave drag and skin friction drag so that the overall L/D is a maximum. Indeed, it was observed in all of the present results that the best optimum shape at any given M_∞ results in the magnitudes of wave drag and skin friction drag being approximately the same, never differing by more than a factor of two. For conical shock angles below the best optimum (for example $\theta_s = 11^\circ$ in Figs. 12 and 13), skin friction drag is greater than wave drag; in contrast, for conical shock angles above the best optimum (for example $\theta_s = 13^\circ$ and 14° in Figures 12 and 13), skin friction drag is less than wave drag. (Note: For a hypersonic flat plate, using Newtonian theory and an average skin friction coefficient, it can readily be shown that at maximum L/D, the wave drag is twice the friction drag.)

The results in Figs. 11-14 pertain to $M_\infty = 6$. An analogous set of results for the other extreme of the lifting hypersonic flight spectrum at $M_\infty = 25$ is given in Figs. 15-18. The aerodynamic characteristics of optimum waveriders for $\theta_s = 7^\circ, 8^\circ, 9^\circ$ and 10° are given as the open symbols Fig. 15 (the solid symbols will be discussed later). The respective front views are shown in Fig. 16, and perspective views in Fig. 17. Finally, the best optimum Mach 25 waverider (which occurs at $\theta_s = 9^\circ$) is summarized in Fig. 18. Comparing the optimum configuration at $M_\infty = 6$ (Fig. 14) with the optimum configuration at Mach 25 (Fig. 18), note that the Mach 25 shape has more wing sweep, and pertains to a conical flowfield with a smaller wave angle, both of which are intuitively expected at higher Mach number. However, note from the flight conditions listed in Figs. 11 and 15 that the body slenderness ratio at $M_\infty = 6$ is constrained to be $b/l = 0.06$ (analogous to a supersonic transport such as the Concorde) but that $b/l = 0.09$ is the constraint chosen at $M_\infty = 25$ (analogous to a hydrogen fueled hypersonic aeroplane such as the British HOTOL). The two different slenderness ratios are chosen on the basis of reality for two different aircraft with two different missions at either extreme of the hypersonic flight spectrum. Also note in Figs. 16-18 the optimization program has sculptured a best optimized configuration with a spline down the center of the upper surface--an interesting and curious result, due principally to the competing effects of minimizing pressure and skin friction drag, while meeting the slenderness ratio constraint.

Return to Fig. 15, and note the solid symbols. These pertain to the values of C_L and L/D obtained by setting the ratio of specific heats γ to 1.1 in order to assess possible effects of high temperature chemically reacting flow. The solid symbols pertain to an optimized waverider at $\theta_s = 9^\circ$ with $\gamma = 1.1$. This is not necessarily the best optimum at Mach 25 with $\gamma = 1.1$; rather, it is just a point calculation to indicate that high temperature effects will most likely have a significant impact on optimized waverider generation, and that such effects are worthy of future investigation. The detailed aspects of high temperature effects are beyond the scope of the present paper; additional discussion is given in Ref. 7.

As a final note in this section, return to Fig. 3, and note that the solid symbols pertain to the present investigation. The flagged square has been discussed earlier as the data point for a half-cone with a delta wing at zero angle-of-attack; it is not part of the present waverider family. The un-flagged solid square at $M_\infty = 4$ pertains to a relatively large slenderness ratio of 0.087, used to generate a waverider for wind tunnel testing. The remaining solid symbols, the circles and triangles, pertain to the present discussion. Recall that the circles are for $b/l = 0.06$ (a Concorde-like slenderness ratio for a low Mach number configuration), and that the triangles are for $b/l = 0.09$ (a HOTOL-like slenderness ratio for a high Mach number configuration). In the present section, we have discussed results obtained at Mach 6 and 25; Fig. 3 shows these plus others at intermediate Mach numbers. All of these cases are discussed in detail in Ref. 7. However, in regard to Fig. 3, emphasis is now made that the present viscous optimized waveriders produce values of (L/D) which exceed the "L/D barrier" discussed in Section I, and shown as the solid curve in Fig. 3. Indeed, the present waverider L/D variation is more closely given by

$$(L/D)_{\max} = \frac{6(M+2)}{M}$$

shown as the dashed curve in Fig. 3. Note that the two points given for $M_\infty = 20$ and 25 deviate away from the dashed curve. This is a Reynolds number effect. Recall that all the Mach number-altitude points for the present waveriders are chosen to follow a typical lifting vehicle flight path through the atmosphere. The point at Mach 25 is at very high altitude (250,000 ft.), with a corresponding low Reynolds number ($Re = 1.4 \times 10^6$); the flow is completely laminar. At Mach 20, the Reynolds number is 12 times higher, but based on the transition criterion discussed in Section II the flow is still completely laminar. Hence, the laminar skin-friction coefficient at the Mach 20 point in Fig. 3 is much lower ($c_f \propto 1/Re$) than at the Mach 25 point, with an attendant larger (L/D) at Mach 20. In contrast, the point at Mach 15 is transitional, with regions of both laminar and turbulent flow, and hence with larger skin-friction and a lower (L/D). In any event, the results given in Fig. 3 indicate that the present viscous optimized waveriders produce high values of (L/D), and therefore are worthy of additional consideration for hypersonic vehicle application.

B. Quantities Affecting Longitudinal Stability

Because stability is a crucial aspect of any aircraft design, two quantities affecting longitudinal stability, namely moment coefficient and center of pressure, are presented in Fig. 19 for the best optimum waveriders generated for Mach numbers between 4 and 25. In addition, for comparison, the same quantities are presented for the more conventional Mach 8 design of Ref. 4 at $(L/D)_{\max}$ and a Reynolds number of 156.2 million.

Shown in Fig. 19 are the moment coefficients about the aircraft nose (M_{M_0} =

$M_0/q_\infty A_{ref}$) and the resulting centers of pressure as a fraction of aircraft length for the above mentioned waveriders and Mach 8 design. Fig. 19 is not intended to show trends in moment coefficient or center of pressure with Mach number, but merely to illustrate the values these quantities attain for optimized waveriders, and provide a comparison with a more conventional aircraft design. As is evident in Fig. 19 there is a great deal of scatter in both quantities across the Mach number spectrum. This is due principally to the somewhat irregular pattern of coefficient-of-lift with increasing Mach number that the best optimum waveriders are operating at, which in turn is due to the widely different Reynolds numbers that they are assumed to operate at in keeping with the trajectory of an aerospace plane. Remember that the shock angle, hence C_L that yields the best optimum waverider is a function of Reynolds number, since a sort of balance between skin friction drag and wave drag is achieved by the best optimum waverider.

Looking at Fig. 19 once again, notice that although the moment coefficient of the Mach 8 design is in line with the moment coefficients of the waveriders in the low hypersonic range, the center of pressure of the Mach 8 design (the solid square) is significantly more forward than the waverider centers of pressure. However, it should also be recognized that the center of gravity of the Mach 8 design is probably more forward than that achievable with a waverider. This point is illustrated in Fig. 20 where side views of the Mach 6 and Mach 10 best optimum waveriders, and the Mach 8 design of Ref. 4 are shown. Notice in Fig. 20 the concentration of volume toward the aft portion of both waveriders in comparison to the Mach 8 design. As a final comment, one should also keep in mind that adding nozzles and other devices necessary for flight may have a significant effect on the center of pressure location and moment coefficient of an actual aircraft, especially hypersonic aircraft because of the significant integration of airframe and propulsion system required by them.

C. An Example of Heat Transfer

To illustrate the level of heating to be expected on an optimized waverider, a contour plot of the convective heat flux to an optimum waverider is shown in Fig. 21. Fig. 21 is a planform view of the best optimum waverider generated for Mach 10 conditions at an altitude of 125,000 ft., hence at a Reynolds number of 62.89 million (based on an aircraft length of 60m), and with a skin temperature of 1400K. Shown in Fig. 21 are lines of constant Stanton number (C_h) for both the upper and lower waverider surfaces. The numbers on the contour lines are values of Stanton number multiplied by 100,000, where Stanton number is defined here as

$$C_h = \frac{q_w}{\rho_\infty V_\infty C_p (T_t - T_w)} \quad (53)$$

where q_w is heat flux per second to the wall, ρ_∞ and V_∞ are freestream density and velocity, respectively, C_p is the specific heat of air at constant pressure, T_t is the freestream total temperature and T_w is the wall temperature. Also shown in Fig. 21 are the lines of transition onset for both the upper and lower surface. Note that for the present work, the Reynolds analogy of Adams and Martindale (as reported in Ref. 30) was used to obtain Stanton numbers from skin friction coefficients already calculated using the boundary layer techniques discussed in Section II D.

The most interesting aspects of Fig. 21 are that the heat transfer on the upper expansion surface is significantly less than on the lower surface, and that boundary layer transition occurs further aft on the upper surface -- results to be expected for the conditions of relatively higher Mach number and lower pressure on the upper surface. Also notice that transition on the upper surface occurs further aft at the center line than slightly outboard of the center line, a phenomenon not evident on the lower surface. This behavior is due to a combination of the more complex shape, hence flow characteristics, on the upper surface, and the blunt leading edge effects on transition. Finally, it is interesting to note that the contour line just downstream of the transition line on the lower surface has a value of C_h lower than the values of the contour lines both above and below it, indicating it is in the transition region.

D. Sensitivity to Transition

Because the major thrust of the present work is the inclusion of detailed viscous effects in the waverider optimization, the question naturally arises: How sensitive are the present waveriders to uncertainties in the location of transition from laminar to turbulent flow? To address this question, a numerical experiment is carried out wherein the transition location was varied over a wide latitude, ranging from all lami-

nar flow on one hand, to almost all turbulent flow on the other hand, with various cases inbetween. Specific results at Mach 10 are given in Fig. 22; here values of (L/D) are given for optimized waveriders as a function of assumed transition location. The point corresponding to the transition correlation described in Section 11, D.3, is denoted by "x" in Fig. 22. Other points in Fig. 22 labeled 5x, 10x and 15x correspond to transition locations that are 5, 10 and 15 times the value predicted by the transition correlation. All the data given in Fig. 22 pertain to optimized waveriders for $\theta_s = 9^\circ$, which yields the best optimum at Mach 10 for the usual transition correlation. (Note, however, that $\theta_s = 9^\circ$ may not yield the best optimum for other transition locations; this effect is not investigated here.) The results in Fig. 22 demonstrate a major increase in (L/D) in going from almost all turbulent flow to all laminar flow. However, for the case where transition is changed by a factor of five, only a 2% change in L/D results. Even for the case where transition is changed by a factor of ten, a relatively small change in L/D of 11% results. On the other hand, the shapes of the resulting optimized waveriders are fairly sensitive to the transition location, as illustrated in Figs. 23 and 24. The conclusion to be made here is that waverider optimization is indeed relatively sensitive to transition location, and this underscores the need for reliable predictions of transition at hypersonic speeds.

E. On the Use of Average Skin Friction Coefficients

The present detailed viscous analysis computes the surface shear stress distributions, and integrates over the surface to obtain the total skin friction drag. This requires a substantial amount of computer calculations, and leads to the question: Can an overall average skin friction coefficient be used within the optimization process rather than dealing with the detailed shear stress distributions? To address this question, consider the best optimum Mach six case given in Fig. 11, which was originally calculated with the detailed shear stress distributions. From this result, an average skin friction drag coefficient was calculated for the complete configuration. Then the optimization code was run again for the same Mach six case, now using this average skin friction drag coefficient. The results are given in Fig. 11 as the solid symbols. Only a small difference exists between the two cases; indeed, the resulting waverider shapes are virtually the same, as given in Ref. 7. This implies that if an accurate average skin friction drag coefficient can be obtained, the resulting optimized waveriders would be reasonably valid. However, the problem with this method is that the information needed to obtain the average skin friction drag coefficient is not known a priori. Moreover, if other independent means are used to obtain an approximate average skin friction drag coefficient and this approximate average value is used in the optimization process, the results can be quite different from those obtained from the use of detailed shear stress distributions; see Ref. 7 for more discussion on this aspect. This situation, in combination with the sensitivity to transition demonstrated in the previous section, seems to dictate the necessity of using the detailed shear stress distributions rather than some approximate average value of skin friction drag coefficient for obtaining the proper optimized waveriders.

F. Inviscid Optimized Waveriders

As a final note, it is interesting to pose the question: if the skin friction is deleted from the present analysis, what type of optimized inviscid waverider configuration, with a constraint on slenderness ratio, is produced? To examine this question, the present computer code was run without skin friction as part of the optimization process, covering the range of Mach number from 6 to 25. A typical result for the inviscid optimized configuration is shown in Fig. 25. Here we see essentially a wedge-like caret waverider, such as the classic configuration generated by the two-dimensional flow behind a planar oblique shock wave, as discussed by Nonweiler^{8,9}. This clearly indicates that the optimized inviscid waverider with slenderness ratio as the constraint is indeed a caret wing. The result shown in Fig. 25 is produced by the present conical flow analysis as a "limiting case", wherein the optimum shape is seeking the flattest portion of the conical shock wave. To see this more clearly, return to Fig. 6. The resulting inviscid waveriders are being generated by relatively flat streamsurfaces at the extreme back and bottom of the generating conical flow-field -- where the shock radius of curvature is the largest (relative to the scale of the waverider) and the flow is closest to being two-dimensional. Consequently, the inviscid configurations are tiny shapes compared to the scale of the flowfield in Fig. 6, and they are "squeezed" into a tiny area at the bottom of the shock base. In turn, due to the logic of the existing conical flow code, only a few pressure and shear stress points are calculated on the surface of these tiny waveriders, raising questions about the numerical accuracy of the calculation of their lift and drag. Therefore, no further discussion about the inviscid optimized waveriders will be given here, except to emphasize again that a two-dimensional caret wing seems to be the optimum inviscid shape that is predicted by the present conical flow analysis.

IV CONCLUSIONS

In comparison to previous optimized waverider analyses, the present work is the first to include detailed viscous effects within the optimization process. From this work, the following major conclusions are made:

1. The resulting family of viscous hypersonic waveriders yields predicted high values of (L/D) which break the " L/D barrier" discussed in Section I.

2. The optimization process for the viscous waveriders results in distinctly different shapes compared to previous work with inviscid-designed waveriders.
3. The fine details of the viscous solution, such as how the shear stress is distributed over the surface, and the location of transition, are crucial to the details of the resulting waverider geometry.
4. The center-of-pressure for the present waveriders is located further aft compared to a standard hypersonic transport configuration.
5. The waverider heat transfer distributions exhibit some interesting variations worth further study.

REFERENCES

1. Anderson, John D. Jr., "A Survey of Modern Research in Hypersonic Aerodynamics," AIAA Paper No. 84-1578. Invited paper given at the AIAA 17th Fluid Dynamics, Plasma Dynamics, and Lasers Conference, Snowmass, Colorado, June 25-27, 1984.
2. Bowcutt, Kevin G., Anderson, John D. Jr., and Capriotti, Diego, "Viscous Optimized Hypersonic Waveriders," AIAA Paper No. 87-0272, 1987.
3. Fetterman, D.E., Henderson, A., Jr., Bertram, M.H., and Johnston, P.J., "Studies Related to the Attainment of High Lift-Drag Ratios at Hypersonic Speeds," NASA TN D-2956, August 1965.
4. Penland, J.A., Marcum, D.C., Jr., and Stack, S.H., "Wall-Temperature Effects on the Aerodynamics of a Hydrogen-Fueled Transport Concept in Mach 8 Blowdown and Shock Tunnels," NASA TP 2159, July 1983.
5. Loftin, Laurence, Quest for Performance: The Evolution of Modern Aircraft, Pergamon Press, Oxford, 1978, pp. 448-510.
6. Kuchemann, D., The Aerodynamic Design of Aircraft, Pergamon Press, Oxford, 1978, pp. 448-510.
7. Bowcutt, Kevin G., Optimization of Hypersonic Waveriders Derived from Cone Flows -- Including Viscous Effects, Ph.D. Dissertation, Dept. of Aerospace Engineering, University of Maryland, College Park, Maryland, 1986.
8. Nonweiler, T.R.F., "Aerodynamic Problems of Manned Space Vehicles," Journal of the Royal Aeronautical Society, Vol. 63, 1959, pp. 521-528.
9. Nonweiler, T., "Delta Wings of Shapes Amenable to Exact Shock-Wave Theory," Journal of the Royal Aeronautical Society, Vol. 67, Jan. 1963, pp. 39-40.
10. Townend, L.H., "Research and Design for Lifting Reentry," Progress in Aerospace Sciences, Vol. 18, 1979, pp. 1-80.
11. Jones, J.G., Moore, K.C., Pike, J., and Roe, P.L., "A Method for Designing Lifting Configurations for High Supersonic Speeds, Using Axisymmetric Flow Fields," Ingenieur-Archiv, Vol. 37, 1968, pp. 56-72.
12. Rasmussen, M.L., "Waverider Configurations Derived from Inclined Circular and Elliptic Cones," J. of Spacecraft and Rockets, Vol. 17, No. 6, Nov.-Dec., 1980, pp. 537-545.
13. Rasmussen, M.L., and Clement, L.W., "Cone-Derived Waveriders With Longitudinal Curvature," AIAA Paper No. 84-2100, 1984.
14. Cole, J.D. and Zien, T.F., "A Class of Three-Dimensional, Optimum Hypersonic Wings," AIAA Journal, Vol. 7, No. 2, Feb. 1969, pp. 264-271.
15. Kim, B.S., Rasmussen, M.L. and Jischke, M.C., "Optimization of Waverider Configurations Generated from Axisymmetric Conical Flows," AIAA Paper No. 82-1299, 1982.
16. Kim, B.S., Optimization of Waverider Configurations Generated from Non-Axisymmetric Flows Past a Nearly Circular Cone, Ph.D. Dissertation, School of Aerospace, Mechanical, and Nuclear Engr., Univ. of Oklahoma, 1983.
17. Nelder, J.A. and Mead, R., "A Simplex Method for Function Minimization," Computer Journal, Vol. 7, Jan. 1965, pp. 308-313.
18. Anderson, John D., Jr., Modern Compressible Flow: With Historical Perspective, McGraw-Hill, New York, 1982.
19. Forsythe, G.E., Malcom, M.A. and Moler C.B., Computer Methods for Mathematical Computations, Prentice-Hall, Inc., New Jersey, 1977.
20. Flower, J.W., "Configurations for High Supersonic Speeds Derived from Simple Shock Waves and Expansions," Journal of the Royal Aeronautical Society, Vol. 67, 1963, p. 287.

21. Moore, K.C., "The Application of Known Flow Fields to the Design of Wings with Lifting Upper Surfaces at High Supersonic Speeds," R.A.E. Tech. Rept. No. 65034, ARC 26913, Feb. 1965.
22. Ferri, A., General Theory of High Speed Aerodynamics, Princeton Series, Sears, W.R. (Editor), Vol. 6, 1954, pp.616-623.
23. Norweiler, T., Wong, H.Y., and Aggarwal, S.R., "The Role of Heat Conduction in Leading Edge Heating," Ingenieur-Archiv, Vol. 40, 1971, pp. 107-117.
24. Walz, A., Boundary Layers of Flow and Temperature, M. I. T. Press, Cambridge, Mass., 1969.
25. White, F.M., Viscous Fluid Flow, McGraw-Hill, New York, 1974, pp. 653-657.
26. DiCristina, V., "Three-Dimensional Laminar Boundary-Layer Transition on a Sharp 8° Cone at Mach 10", AIAA Journal, Vol. 8, No. 5, May 1970, p. 855.
27. Pate, S.R., and Groth, E.E., "Boundary-Layer-Transition Measurements on Swept Wings with Supersonic Leading Edges," AIAA Journal, Vol.4, No.4, April 1966, pp. 737-738.
28. Harris, J.E., and Blanchard, D.K., "Computer Program for Solving Laminar, Transitional, and Turbulent Compressible Boundary Layer Equations for Two Dimensional and Axisymmetric Flows," NASA TM 83207, Feb. 1982.
29. Christoph, G. H., "Law-of-the-Wall Analysis Revisited for Reentry Vehicle Design," AIAA Paper 85-0905, June 1985.
30. DeJarnette, F.R. Kania, L.A., Chitty, A., "Aerodynamic Heating and Surface Temperature on Vehicles for Computer- Aided Design Studies," AIAA-83-0411, Jan. 1983.

ACKNOWLEDGEMENT

This work was supported through the Graduate Hypersonic Aerodynamics Fellowship Program, established in 1983 at the University of Maryland by the Army Research Office, with Dr. Robert Singleton as monitor. The authors also acknowledge a close working relationship with the Supersonic/Hypersonic Aerodynamics Branch at the NASA Langley Research Center under a grant monitored by Wallace Sawyer and Patrick Johnston.

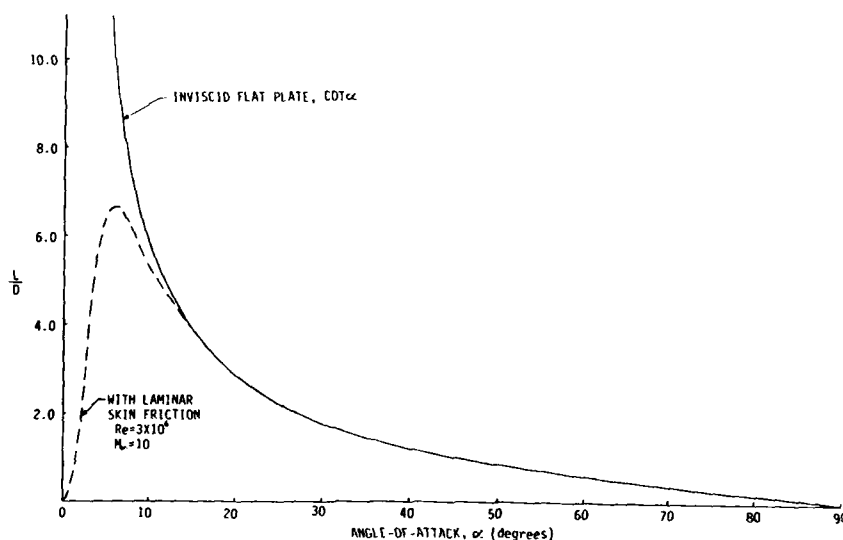


FIG. 1: Newtonian results for a flat plate.

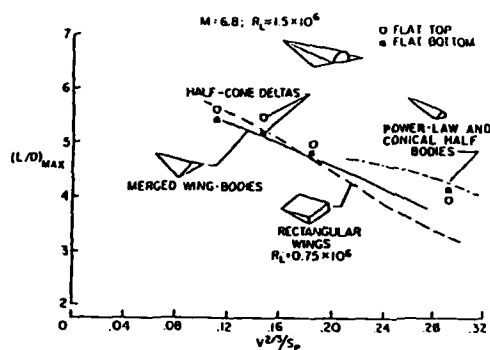


FIG. 2: Performance comparison of various generic hypersonic configurations (from Ref. 3).

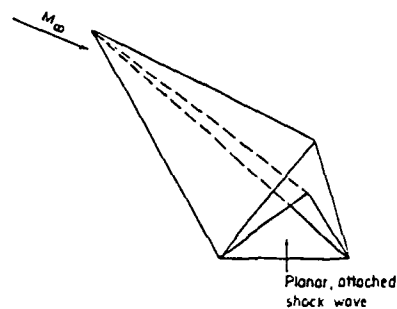


FIG. 4: Schematic of a simple caret wing waverider.

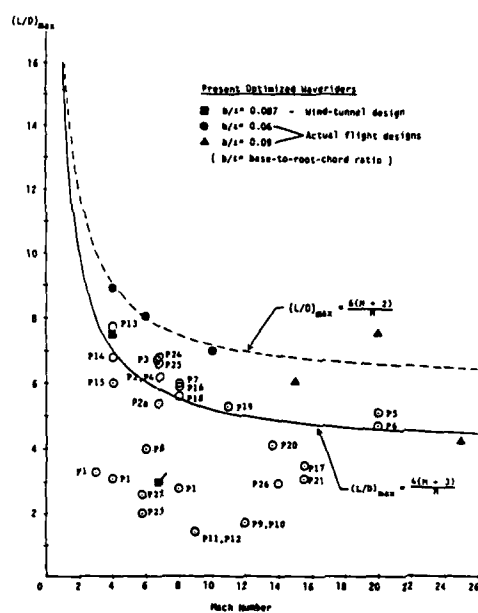


FIG. 3: Maximum lift-to-drag ratio comparison for various hypersonic configurations.

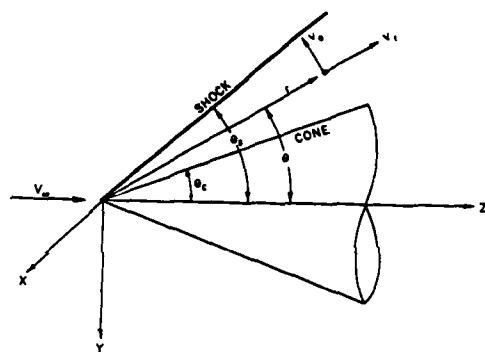


FIG. 5: Spherical coordinate system for cone flow calculations, and cartesian coordinate system for waverider design.

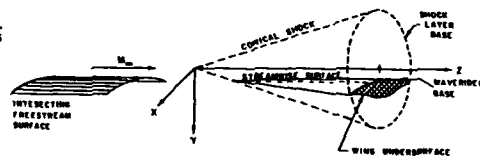


FIG. 6: Perspective view of a conical waverider and generating shock.

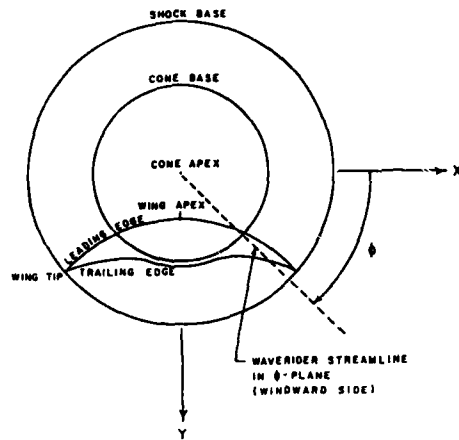


FIG. 7: Front view of a conical waverider with the generating cone and shock.

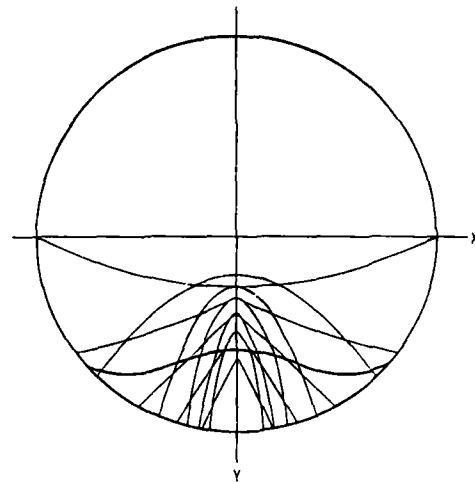


FIG. 10: Example of initial and optimized waverider leading edge shapes.

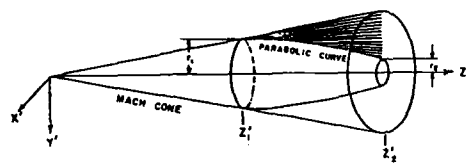


FIG. 8: Expansion cylinder and expansion domain bounded by the Mach cone.

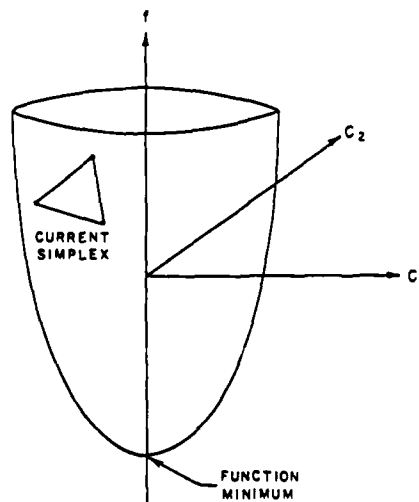


FIG. 9: Example of the optimization process for a function of two variables.

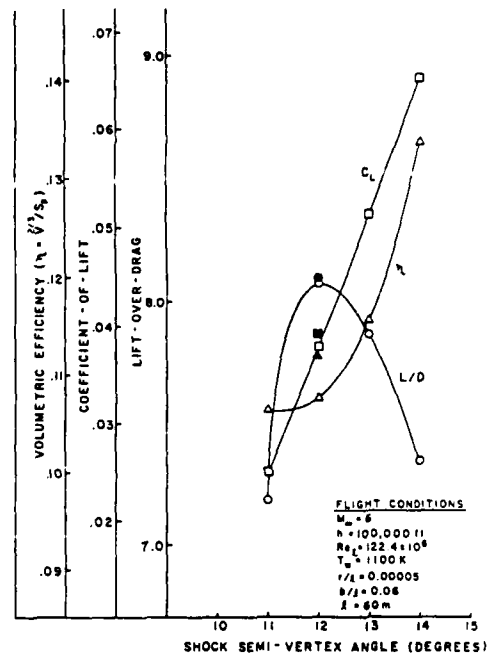


FIG. 11: Results for a series of optimized waveriders at Mach 6.

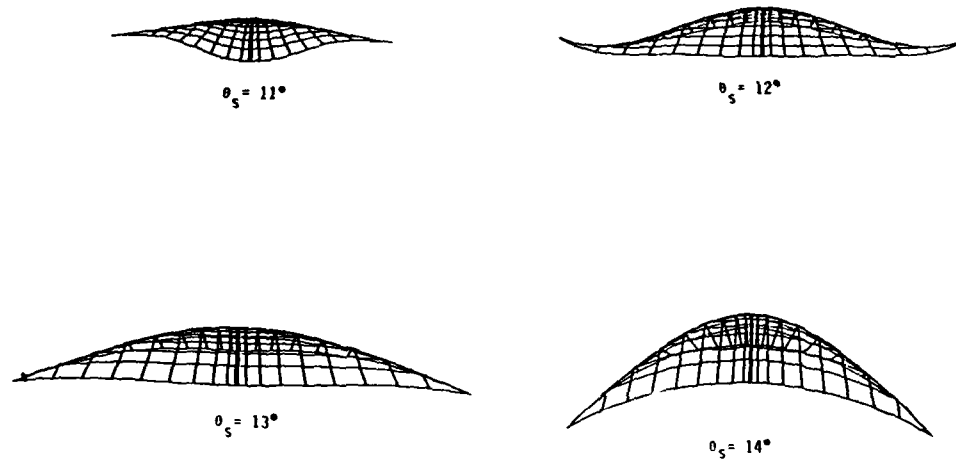


FIG 12: Front views of a series of optimized waveriders at Mach 6.

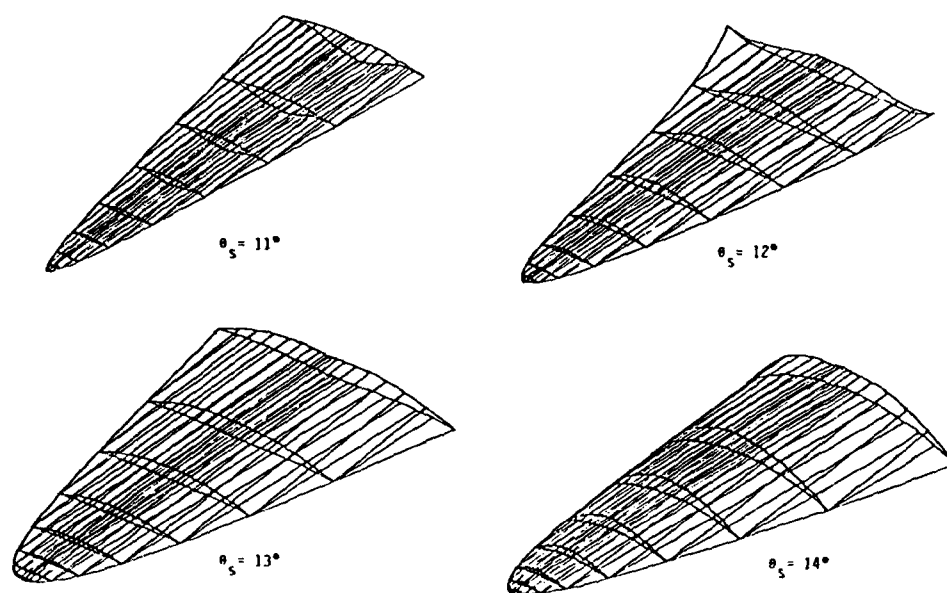


FIG. 13: Perspective views of a series of optimized waveriders at Mach 6.

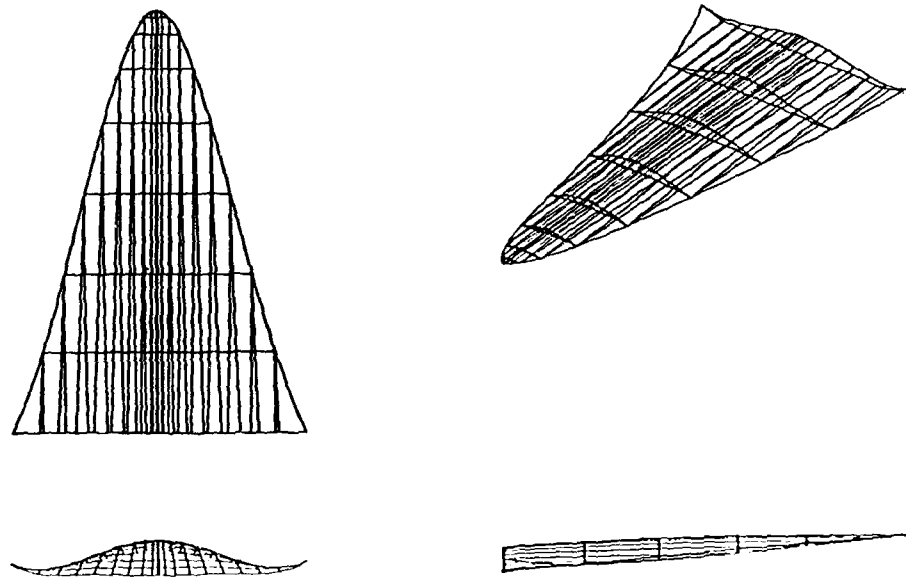


FIG. 14: Three-view of the best optimum waverider at Mach 6. ($\gamma_s = 12$)

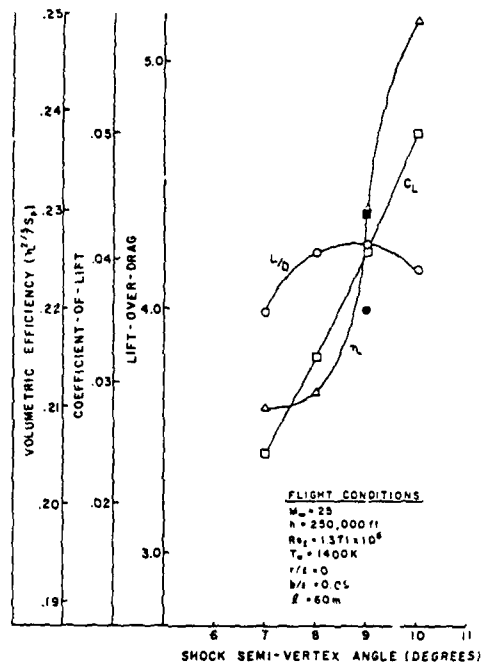


FIG. 15: Results for a series of optimized waveriders at Mach 25.

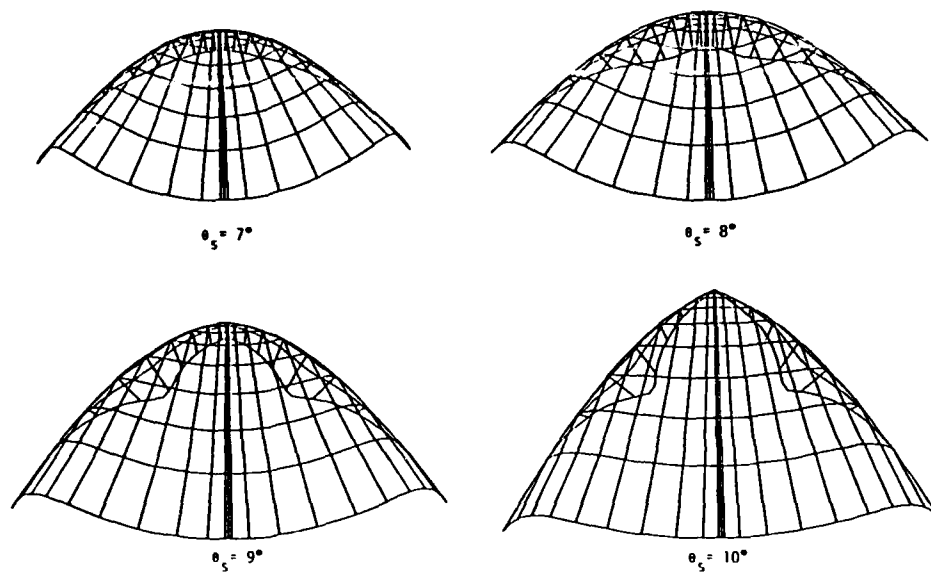


FIG. 16: Front views of a series of optimized waveriders at Mach 25.

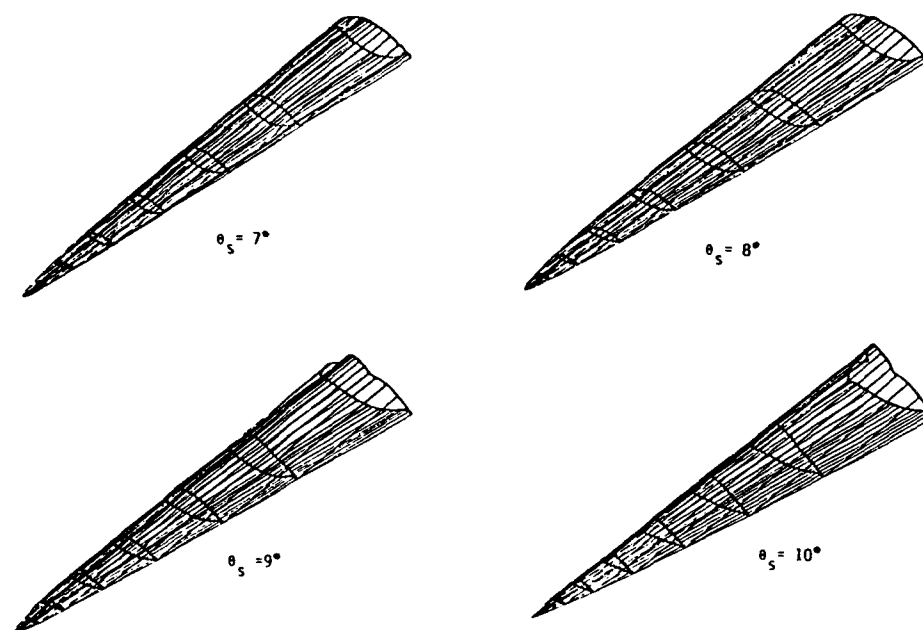


FIG. 17: Perspective views of a series of optimized waveriders at Mach 25.

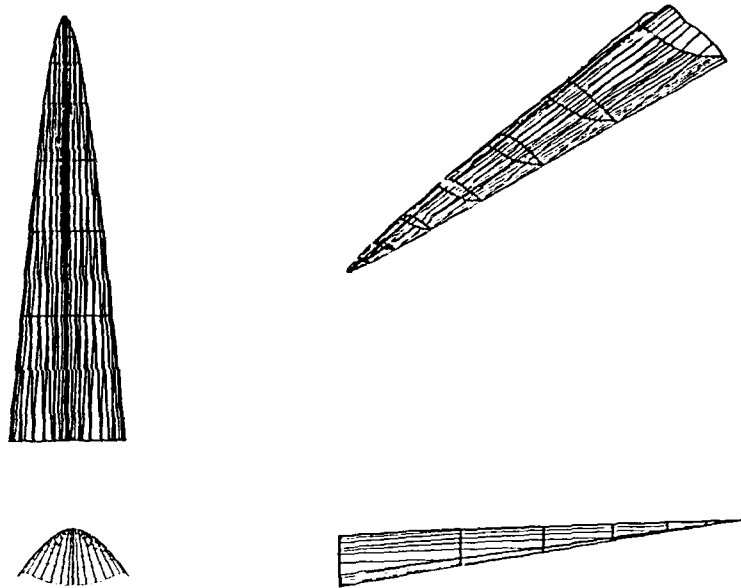


Fig. 18: Three-view of the best optimum waverider at Mach 25. ($\gamma_s = 9$)

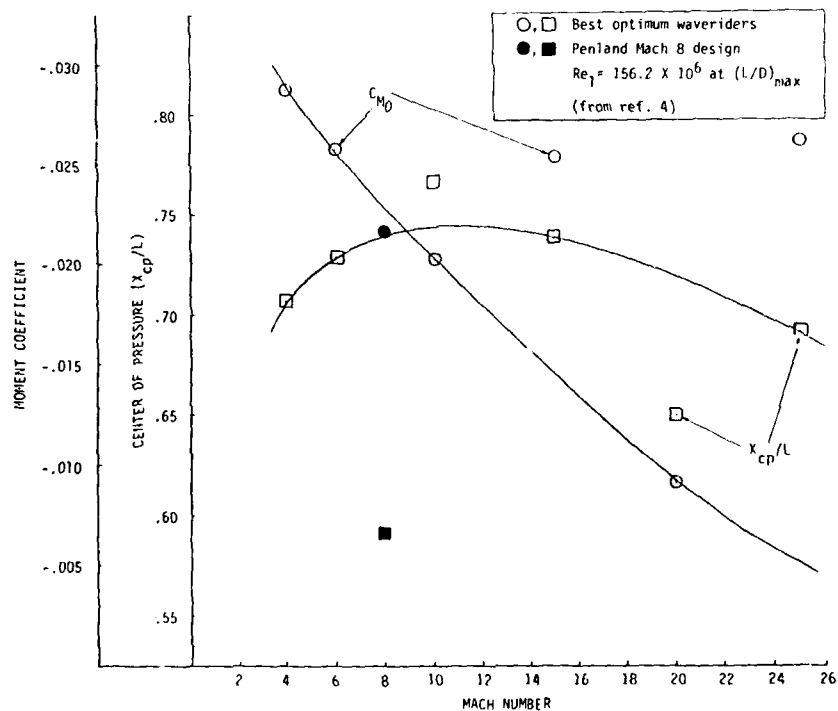


FIG. 19: Quantities that affect the longitudinal stability of a single conventional design and the best optimum waveriders at six different Mach numbers.

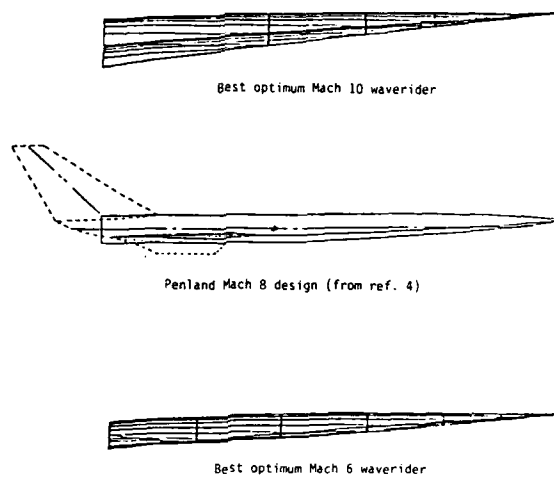


Fig. 20: Side view comparison of two optimized waveriders against a more conventional hypersonic design.

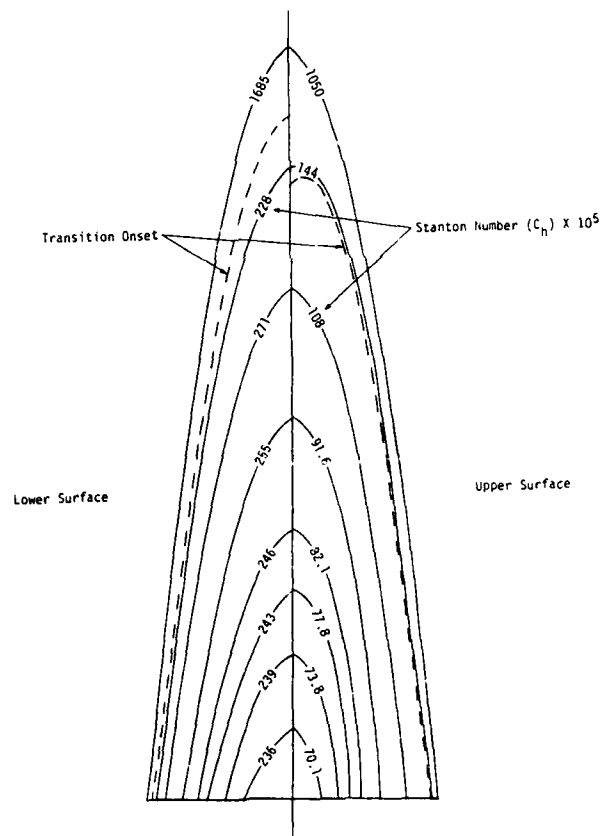


FIG. 21: Upper and lower surface heat transfer contours and transition onset lines.

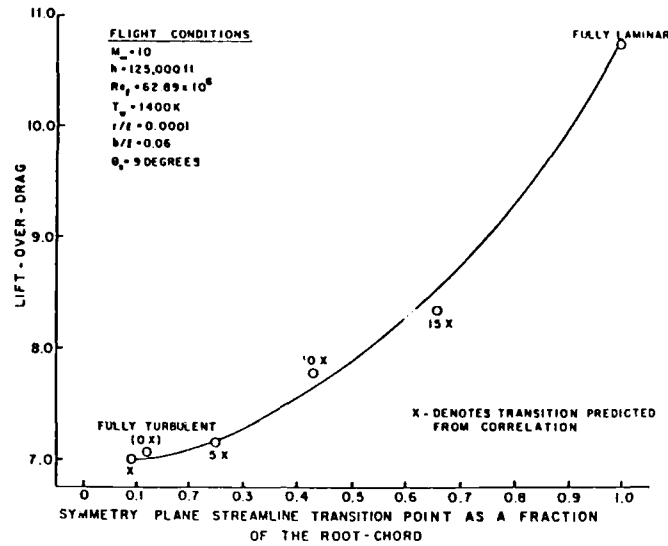


FIG. 22: Lift-to-drag comparison of optimized Mach 10 waveriders designed with various boundary layer transition criteria.

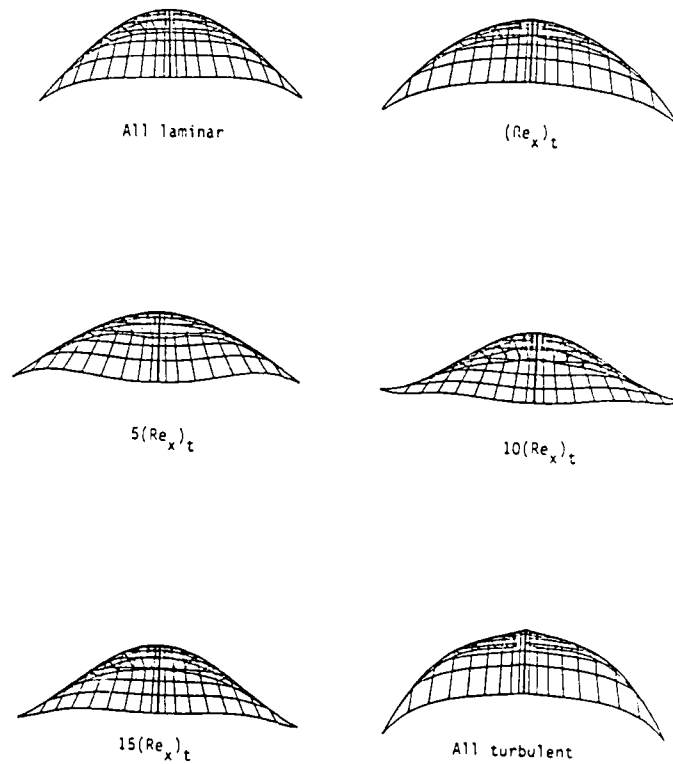


FIG. 23: Front views of optimized Mach 10 waveriders designed with various boundary layer transition criteria.

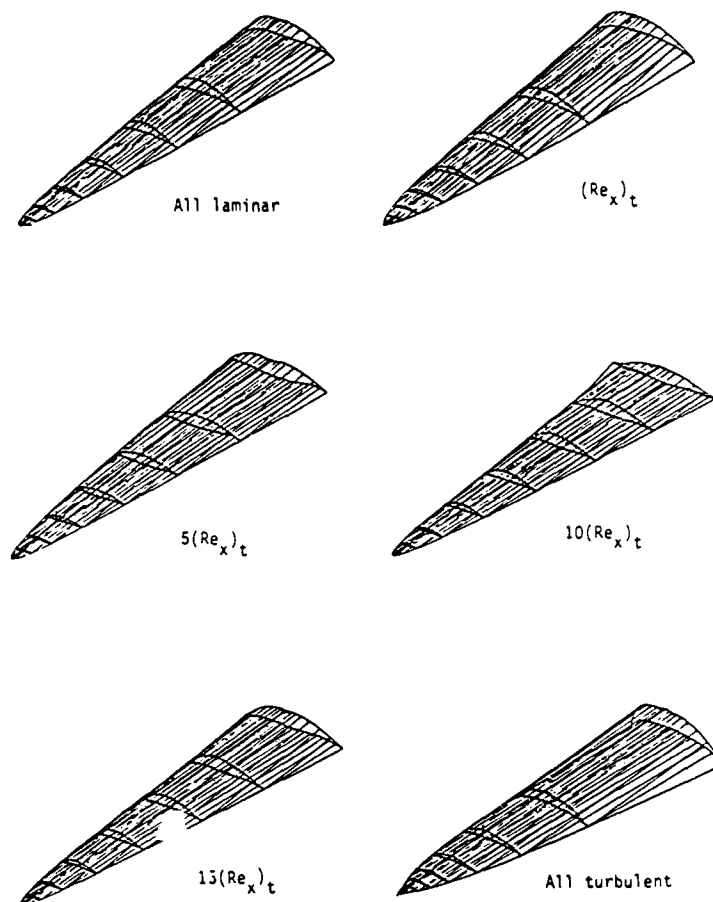


FIG. 24: Perspective views of optimized Mach 10 waveriders designed with various boundary layer transition criteria.

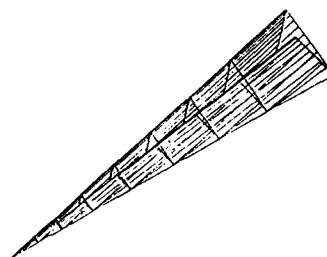


FIG. 25: An optimized inviscid waverider at Mach 10; a caret wing.

HYPERSONIC STATIC AND DYNAMIC STABILITY OF AXISYMMETRIC SHAPES - A COMPARISON OF PREDICTION METHODS AND EXPERIMENT

R. A. EAST and G. R. HUTT

Department of Aeronautics and Astronautics, University of Southampton, United Kingdom

ABSTRACT

The stability of oscillatory motions of vehicles flying at hypersonic Mach numbers is of considerable relevance to their initial design. Methods are needed for quick and accurate predictions of stability and control which are applicable over a wide range of body shapes, angles of attack and flow conditions, without the need to resort to computationally time consuming numerical flow field calculation methods.

The purpose of this paper is to present experimental data, obtained over a range of angles of attack, concerning the static and dynamic pitching stability of a wide range of both pointed and blunted axisymmetric shapes including cones and blunted cylinder flares. These data have been obtained from free oscillation experiments at $M = 6.85$ in a short duration free piston driven hypersonic wind tunnel. Although Newtonian theory gives inadequate accuracy of prediction, inviscid embedded Newtonian theory, which accounts for the reduced dynamic pressure and lower flow velocity in the embedded flow downstream of the strong bow shock, is shown to provide surprisingly good agreement with the experimental data over a wide range of conditions. A particular aspect which is explored is the ability of the inviscid embedded Newtonian theory to predict the effects of nose bluntness, flare geometry, angle of attack and centre of gravity position on single-degree-of-freedom oscillatory motions. Comparisons with experimental results show that the broad flow features and their effect on static and dynamic stability are well described in regimes not containing flow structural change. However, in some cases discrepancies exist between the predictions and experimental observations and these have been attributed to a variety of viscous flow phenomena involving boundary layer transition and flow separation, including complex lee surface vortical flows.

LIST OF SYMBOLS

c	reference length, pointed cone length (L) for cones, cylinder diameter (d_N) for hyperballistic shapes
C_{D_N}	nose drag coefficient, $C_{D_N} = D_N / (\frac{1}{2} \rho_\infty V_\infty^2) (nd_N^2/4)$
C_m	pitching moment coefficient, $C_m = M_p / \frac{1}{2} \rho_\infty V_\infty^2 Sc$
C_{m_α}	aerodynamic stiffness derivative, $C_{m_\alpha} = \partial C_m / \partial \alpha$
$C_{m_\alpha^*}$	pitching moment derivative due to rate of change of angle of attack, $C_{m_\alpha^*} = \partial C_m / \partial (\dot{\alpha} c / 2 V_\infty)$
C_{m_q}	pitching moment derivative due to rate of pitching, $C_{m_q} = \partial C_m / \partial (q c / 2 V_\infty)$
C_N	normal force coefficient, $C_N = N / (\frac{1}{2} \rho_\infty V_\infty^2) (nd_N^2/4)$
C_p	pressure coefficient, $C_p = (p - p_\infty) / (\frac{1}{2} \rho_\infty V_\infty^2)$
C_{p_s}	blast wave pressure coefficient
C_y	empirical coefficient
d_B	base diameter
d_N	diameter of hemispherical nose
f^*	dynamic pressure function, $f^* = \rho V^2 / \rho_\infty V_\infty^2$
g^*	velocity function, $g^* = V / V_\infty$
L	body length, length of equivalent pointed cone for blunt cones
M_∞	free stream Mach number
M_p	pitching moment, positive nose up
N	normal force
p	pressure
p_∞	free stream static pressure
q	pitch rate (rad s^{-1})
r	body cross sectional radius, $r' = r / d_N$
R	radial distance, $R' = R / d_N$
R_s	cross-sectional radius of bow shock, $R'_s = R_s / d_N$
Re	unit Reynolds number

Re_b	Reynolds number based on cone base diameter, d_B
Re_d	Reynolds number based on diameter, $d \approx d_N$ for hyperballistic shapes
S	reference area, base area ($= \pi d_B^2/4$) for cones, cylinder area ($= \pi d_N^2/4$) for hyperballistic shapes
V	velocity in x direction in embedded flow
V_∞	free stream velocity
v_n	velocity component perpendicular to body element
x	axial distance downstream of nose/body junction, $x' = x/d_N$
x_B	x co-ordinate of body base
x_s	x co-ordinate of apex of bow shock, $x_s' = x_s/d_N$
X_{CG}	x co-ordinate of oscillation axis, $\Delta x = x_B - X_{CG}$
z	vertical co-ordinate, $z' = z/d_N$
α	angle of attack
γ	ratio of specific heats
ρ	air density
ϕ	azimuth angle
θ	angle of body surface element
X^*	similarity parameter
ω	angular velocity
ω'	$\omega/2V_\infty$, reduced frequency parameter

Subscripts

B	body base
CG	axis of oscillation
N	body nose
S	shock
$Newton$	Newtonian value
∞	free stream

Superscript

$'$	dimensionless distances e.g. $x' = x/d_N$
-----	---

1. INTRODUCTION

Hypersonic vehicle technology is a subject of increasing importance in a variety of applications. Particular applications include future space transportation systems, aeroassisted orbital transfer vehicles, the hypersonic transport, the transatmospheric aircraft and re entry vehicles. Broad aspects of vehicle performance are determined by the steady aerodynamic characteristics, but the ability to follow a predetermined flight path or re entry trajectory is determined by stability and control considerations. In most projected future applications active control technology and stability augmentation will be used on essentially aerodynamically unstable geometries. The use of these techniques leads to smaller control surfaces, to lower vehicle mass and larger payloads fractions.

In order that these aspects of hypersonic vehicle design may be explored further there is a requirement for both an experimental and theoretical data base. Moreover, there is a need for a rapid means of prediction of vehicle stability data which can be validated with experimental results. Modern computational fluid dynamics, applied to unsteady hypersonic flowfields, can be limited in the range of conditions which can be quickly covered. This paper highlights the surprisingly good agreement between the less time consuming semi empirical inviscid embedded Newtonian technique and experimental data for pitch stability derivatives obtained with a range of axi symmetric models.

The most fundamental approximation of hypersonic pressure coefficients is given by the so called Newtonian impact technique (Refs 1 and 2). However, it was noted by Busemann (Ref. 3) that a centrifugal pressure term must be included with the Newtonian approximation to cater for curved particle trajectories within the shock layer, this was developed into the so called Newton Busemann method. The centrifugal effect is necessary for the ideal Newtonian case of an infinitesimally thin shock layer obtained at the gas dynamic limit of $M = \infty$, $\gamma = 1$. Despite this observation of the requirement of a centrifugal term in the gas dynamic limit, it must be noted that for the majority of hypersonic flight vehicles, infinitesimally thin shock layer and $\gamma \rightarrow 1$ assumptions are not well satisfied. These limitations and the subsequent effect on the prediction of pressure coefficients in realistic hypersonic flight regimes were

considered by Seiff (Ref. 5) and subsequently Ericsson (Ref. 6). The consequences of finite shock layer thickness and bow shock waves determined by nose shape and drag coefficient led to the semi-empirical embedded Newtonian technique. This ignores the centrifugal term, since the theoretical gas dynamic limit is not approached and concentrates on the entropy layer effects downstream of the nose modifying the velocity and dynamic pressure fields in which the downstream body is embedded. For situations in which the ideal limiting Newtonian case is approached Tong and Hui (Ref. 7) have extended the embedded Newtonian method to include the centrifugal correction term in the embedded flow. This paper presents results from all three of the above techniques and draws comparisons with experimental data for pointed and blunted cones and a hyperballistic shape.

A major aerodynamic feature of many of the hypersonic vehicle applications is that the flows are dominated by viscous effects such as viscous interaction, boundary layer transition, separated flows and upper surface vortical flows. These phenomena, which are strongly influenced by vehicle geometry, can exert a large effect on both static and dynamic stability at hypersonic Mach numbers. The effects of these phenomena are exposed by comparing inviscid/viscous hypersonic vehicle pitch stability data obtained over a range of appropriate Reynolds numbers.

2. PREDICTION METHODS FOR THREE-DIMENSIONAL SHAPES

Newton and Newton-Busemann

The simplest technique for establishing the pressure coefficient on a hypersonic flight vehicle is the Newtonian Impact theory. In this flow model, it is assumed that the fluid particles do not interact and that the only change in the velocity of a particle impinging on a body surface takes place normal to the surface. The normal component of momentum is assumed to be transferred to the body and the particles continue to move along the surface with zero tangential acceleration. If the velocity component normal to the surface is written as v_n , the Newtonian surface pressure coefficient becomes

$$C_{p_{Newt.}} = 2 \left(\frac{v_n}{V_\infty} \right)^2 \quad (1)$$

A semi-empirical modification to the above expression replaces the factor 2 by $C_{p_{max}}$, the pressure coefficient at the stagnation point on the body. Examples of the use of the unsteady Newtonian impact theory to calculate the stability derivatives of cones are given in Reference 4.

Busemann (Ref. 3) observed that the expression given in Eq. (1) strictly applies only at the free stream surface of the Newtonian shock layer, since a normal pressure gradient must exist as a consequence of the curved trajectories followed by the fluid particles in this layer. The body surface pressure in the Newton-Busemann theory may therefore be written as

$$P_{surface} = P_{Newt} + P_{cent} \quad (2)$$

where P_{cent} is the centrifugal pressure correction. For steady flow past bodies whose surface geodesics are straight, $P_{cent} = 0$ and Eqn(1) provides the appropriate expression for C_p . For bodies with curved geodesics, Cole (Ref. 8) for slender axis-symmetric bodies, and Hui (Ref. 9) for general two-dimensional and axis-symmetric bodies, showed that the Newton-Busemann expression (Eq. (2)) could be obtained as the limit of gas dynamic theories for $M_\infty \rightarrow \infty$ and $\gamma \rightarrow 1$.

For non steady flow, the particle trajectories do not follow the surface geodesics, although they still move tangentially to the surface. In this case, the curvature of the trajectory is dependent both on the geometric surface curvature and on the curvature of the trajectory induced by the body motion. Mahood and Hui (Ref. 10) have applied the Newton-Busemann method to unsteady flow past oscillating wedges and cones at zero-mean incidence. For both shapes, the steady centrifugal pressure correction term is zero, but the unsteady correction term is significant. They showed that in the double limit $M_\infty \rightarrow \infty$ and $\gamma \rightarrow 1$, the resulting Newton-Busemann unsteady pressure was identical to that deduced from gas dynamic theories by Hui (Ref. 11) for oscillating wedges and Mahood and Hui (Ref. 10) for oscillating cones. This observation was important in explaining the apparent anomaly which had existed in the comparison between the simple unsteady Newtonian model and the limits of theories based on the gas equations of motion for very high Mach numbers as, for example, observed by Scott (Ref. 12) for the case of oscillating cones.

A central assumption in the Newtonian flow model is that the shock layer is thin and the shock wave, therefore, lies close to the body surface. This is often closely satisfied for wedges and cones with modest bluntness, two- and three-dimensional concave shapes and some convex shapes at high angles of attack over a wide range of Mach number. However, for bodies with large bluntness, hyperballistic bodies of revolution, general convex shapes at low and moderate mean angle of attack, the assumption is not well satisfied and Newton-Busemann theory would not be expected to provide a good approximation at conditions far removed from the strict Newtonian limit of $M_\infty \rightarrow \infty$ and $\gamma \rightarrow 1$. As a consequence of the requirement to reduce heat transfer rates and to provide efficient payload packaging, such bodies are of considerable importance at hypersonic Mach numbers and alternative prediction methods for relatively thick shock layers must be sought.

Embedded Newtonian

To remove some of the limitations of Newtonian theory caused by the requirement for an infinitesimal shock layer, Seiff (Ref. 5) proposed the embedded Newtonian method. In this method, which was originally developed for steady flow, a non-uniform rotational inviscid flow is defined downstream of the bow shock wave, whose shape is determined by the nose shape and drag coefficient. The pressures on the afterbody embedded in this flow field are calculated using generalised Newtonian theory. Physically, this method takes account of the large reductions in both dynamic pressure and velocity which arise in the entropy layer caused by the bow shock.

Ericsson (Ref. 6) extended this concept to deal with unsteady flow problems; originally to determine the effects of the entropy gradient induced by the nose bluntness on the static and dynamic stability of an ablating flared body of revolution. Later Ericsson and Scholnick (Ref. 13) and Ericsson (Ref. 14) used the method to determine the effects of moderate hemispherical nose bluntness on the stability of slender cones and Ericsson (Ref. 15) extended the analysis to include large bluntness, moderate angles of attack and finite amplitude of oscillation. A more unified treatment of the unsteady embedded Newtonian method presented by Ericsson (Refs. 16 and 17) removed the hypersonic Mach number restriction on the previous methods, so that the range of application for blunted slender cones could be extended down to $M_\infty = 3$. The earlier methods of predicting the stability of hemisphere-cylinder-flare bodies were extended by Ericsson (Ref. 18) to include other more general hyperballistic shapes with different nose geometries, and to include the effect of Mach number down to moderate supersonic speeds.

Newton-Busemann theory, as described earlier and suitably modified to account for the pressure coefficient at the stagnation point, provides reasonable estimates of pressure coefficients and stability derivatives only when the shock layer is very thin. It is also well known that the Busemann theory overestimates the centrifugal pressure correction term in steady flow with $\gamma = 1.4$ with the result, for example, that the pressure on a sphere is predicted to be zero at a position displaced 60° from the front stagnation point. This is at variance with the predictions of numerical calculations for $\gamma = 1.4$ and with experimental results and suggests that when $\gamma \approx 1$ and the shock layer is not thin, the centrifugal pressure correction term for steady flow is overestimated. Moreover, Van Dyke (Ref. 19) showed that modified Newtonian theory provides reasonable agreement with numerical predictions for cylinder and sphere flows at $M_\infty = \infty$, $\gamma = 1.4$ for angles up to at least 40° from the stagnation point, although this is purely fortuitous in that the effect of different γ appears to cancel with the neglect of the centrifugal correction term. Although conjectural, it is suggested that broadly similar effects occur with regard to the centrifugal term in respect of the streamline curvature resulting from non-steady body motion, and it is possible that the change from $\gamma = 1.0$ in Newton-Busemann theory to $\gamma = 1.4$ for actual flows, provides an effect of opposite sign and of the same order as the centrifugal term. It is therefore argued that for the thick shock layer flows at finite Mach number with $\gamma = 1.4$, characteristic of a large range of hypersonic shapes, the use of the straightforward modified Newtonian impact pressure may, on the same grounds as for steady flows, give a good approximation to the pressure in unsteady embedded Newtonian flow.

For many hypersonic vehicles the region in which the Newton-Busemann assumptions are most closely satisfied is close to the apex. For the remainder of the flow field within the relatively thick shock layer, the assumptions are not well satisfied and the flow field may be considered approximately as a strong curved bow shock, whose shape is determined by nose geometry, together with an inviscid shear flow downstream of the shock in which the pressures are deduced using local generalised Newtonian concepts.

Following Ericsson (Ref. 18) we note that for hemispherical noses, the shock radius R_s at a downstream station x defined in Fig. 1 is given in terms of the nose drag coefficient C_{DN} and diameter d_N by

$$R_s^4 = K' C_{DN}^4 (x' - x'_s)^4$$

where $R_s^4 = R_s^4/d_N^4$, $x' = x/d_N$, $x'_s = x'_s/d_N$ and x_s is the distance of the shock ahead of the x origin. A good approximation for K' at finite Mach number is

$$K' = 1 + 1.57 (x' - x'_s) M_\infty^2 C_{DN}^4$$

where $x'_s = x_N/d_N = x'_s$ if the bow shock stand-off distance is small.

Following Ref. 17 the dimensionless shock distance x'_s for high Mach numbers is given empirically by

$$x'_s = -0.385 \cot \theta_m \cos \theta_m - 0.5 \sin \theta_m$$

where

$$\theta_m = \sin^{-1} \left\{ \frac{1}{\gamma} \left[1 - \frac{1.668}{M_\infty^2} - \frac{1.803}{M_\infty^4} \right] \right\}$$

These expressions show good agreement with shock detachment data for hemispheres (Ref. 20)

The dynamic pressure $\frac{1}{2} \rho V^2$ and local flow velocity V in the flow field downstream of the shock are respectively written in terms of the dimensionless radial distance R' ($= R/d_N$) - see Fig. 1 - using the concept of similar profiles, in the following form

$$\frac{\rho V^2}{\rho_\infty V_\infty^2} = f^* \left(\frac{R'}{R'_s} \right)$$

$$\frac{V}{V_\infty} = g^* \left(\frac{R'}{R'_s} \right)$$

where R'_s is determined from Fig. 1 in terms of the vertical displacement $x' (= z/d_N)$ and angular displacement α . Ref. 18 expresses f^* and g^* in terms of the parameter X^* defined by

$$X^* = \left(\frac{R' - 0.5}{R'_s} \right)^2 \quad (3)$$

for a variety of steady flows past bodies of different nose shapes. The empirical expressions for f^* and g^* are arranged to provide close agreement with flow field calculations based on the Method of Characteristics, for example, over a wide range of Mach numbers. Following Ericsson (Ref. 18) the functions employed for f^* and g^* are:

$$f^*(X^*) = f_0 + 2.75X^* \quad \text{and} \quad (4)$$

$$g^*(X^*) = 1 - 0.362(1 - f_0)^{\frac{1}{2}} + 0.6X^{*0.5}$$

noting that the maximum value of these functions should not exceed unity at the termination of the inviscid shear layer. The term f_0 is of major significance since it is via this term that the finite Mach number dependence of the profiles within the shock shape is determined. For finite Mach number applications

$$f_0 = 0.17 + \left(\frac{9.65}{(M_\infty + 8.7)} \right)^3 \quad (5)$$

The local pressure coefficient on the embedded body in the flow field downstream of the bow shock is given by the local modified Newtonian expression as

$$C_p = C_{p_o} + C_v C_{p_{max}} \left(\frac{v_n}{V} \right)^2 \left(\frac{\rho V^2}{\rho_\infty V_\infty^2} \right) \quad (6)$$

where C_{p_o} is the blast wave pressure coefficient generated downstream of the blunt nose which would exist on an embedded cylinder, and the second term is the additional pressure coefficient due to the local body shape embedded in the inviscid flow field. $C_{p_{max}}$ is the pressure coefficient at the stagnation point which modifies the Newtonian impact pressure and v_n is the velocity component perpendicular to the local surface element. C_v is an empirical coefficient (see Ref.18) which provides an effective Mach number dependence for the Newtonian pressure coefficient.

For a body perturbed in pitch by an angle θ from its mean angle of attack α and pitching at a rate q about an axis distant x_{CG} from the origin an expression for v_n/V is obtained. From thereon the procedure is to substitute for (v_n/V) in Eq (6) and noting that $f^* = (\rho V^2 / \rho_\infty V_\infty^2)$, differentiate Eq.(6) with respect to α and with respect to $(qL/2V_\infty)$ to obtain $(\partial C_p / \partial \alpha)$ and $\partial C_p / \partial (qL/2V_\infty)$. By multiplying by the distance from the oscillation axis and appropriately integrating around the body surface, expressions for the pitching moment stability derivatives are obtained.

Ericsson (Ref.18) has also obtained an expression for the pitching stability derivative $C_{m_q}^*$ due to rate of change of angle of attack which is a consequence of the time lag between the motion of the blastwave generator (the nose) and the resulting motion of the inviscid shear layer at the body element.

These procedures, more complete details of which are given in Ref.18, result in C_{m_α} and $C_{m_q} + C_{m_q}^*$ for the particular embedded body. Additional contributions to each of these derivatives from the nose portion, evaluated from Newtonian methods, are added to give the results for the complete shape.

Unsteady Embedded Newton-Busemann Flow Theory

In view of the success of Hui and Tobak's (Ref.21) unsteady Newton-Busemann flow theory as applied to bodies of revolution in providing results which are in agreement with the appropriate limiting results from gas dynamic theories, Tong and Hui (Ref.7) have applied Newton-Busemann flow theory to the embedded Newtonian flow concept described in the previous section. In essence Tong and Hui have applied the centrifugal correction term to the expression used to calculate the pressure coefficient on embedded flares and compression surfaces within the flow downstream of the bow shock on a hemisphere cylinder basic shape. In their method they have preferred to use the value of 2 for the Newtonian coefficient rather than the value of $C_v C_{p_{max}}$ used in eqn (6), which provides better agreement with experimental results but is empirically based. The expression used by Tong and Hui is therefore

$$C_p = C_{p_o} + 2 \left(\frac{v_n}{V} \right)^2 \left(\frac{\rho V^2}{\rho_\infty V_\infty^2} \right) + C_{p_c}$$

where C_{p_c} is the contribution to the pressure coefficient from the centrifugal term and which has been calculated along similar lines to the method of Hui and Tobak (Ref.21). The method, therefore, seeks to extend Seiff (Ref.5) and Ericsson's (Ref.18) embedded Newtonian concept so that, in the strict Newtonian limit, the pressures on embedded surfaces would be calculated in a manner consistent with gas dynamic theories. For applications to finite Mach number flows, which is the essential purpose of embedded flow methods, empiricism is necessary to describe the similar profiles for the density and velocity variations downstream of the bow shock wave. For these Tong and Hui have used the following empirical fits to Seiff and Whiting's (Ref.22) results for a hemisphere-cylinder in the high Mach number limit for hypersonic flight.

$$\frac{\rho}{\rho_\infty} = \begin{cases} 0.27 + 1.2\bar{X} + 0.15\bar{X}^2 & , \bar{X} \leq 0.65 \\ 1 & , \bar{X} > 0.65 \end{cases}$$

$$\frac{V}{V_\infty} = \begin{cases} 0.7 + 0.3\bar{X}^3 & , \bar{X} \leq 0.65 \\ 1 & , \bar{X} > 0.65 \end{cases}$$

In the above the parameter \bar{X} (see eqn.4, Ref.7) is related to, but slightly different in definition from, X^* defined in eqn.3.

These expressions, which although are Mach number dependent as a consequence of the Mach number dependence of the expressions used for the calculation of the bow shock wave shape in \bar{X} , do not take into account the variations in the shape of the downstream flow profiles with Mach number which have been used by Ericsson (Ref.18) and which are quoted in eqns.(4) and (5). It should be noted that in making subsequent comparisons between prediction methods and experimental results, it is difficult to draw conclusions with regard to the appropriateness of the embedded Newton-Busemann method vis a vis the unmodified embedded Newtonian method since these inherent differences exist.

The inclusion of the centrifugal pressure correction within both steady and non-steady contributions to the pressure coefficient should therefore improve the rigour of the embedded flow concept. However, in steady flow Newton-Busemann theory gives poor comparison with experimental results, principally as a consequence of the finite thickness shock layers which occur on the majority of hypersonic vehicles. It is one of the purposes of the present paper to compare both the uncorrected and the centrifugally corrected embedded Newtonian method with experimental results for stability derivatives in single-degree-of-freedom pitching motions. Such a comparison is difficult to make since the results published by Tong and Hui (Ref.7) incorporate Mach number dependence of the shock shape but do not contain Mach number dependent functions for the downstream velocity and density profiles, whereas, the centrifugally uncorrected embedded Newtonian results of the present paper do. Comparisons between the results of Ref.7 and the embedded Newtonian results to identify the magnitude of the centrifugal term have been facilitated by recalculating the results in the present paper with alternative forms of eqns.(4) and (5) which are appropriate for infinite embedded Mach numbers. However, it is noted that the experiments used for comparison have been performed at the relatively low hypersonic Mach number of 6.85 in which the joint $M \rightarrow \infty$, $\gamma \rightarrow 1$ assumptions are not well satisfied. Not only is the free stream Mach number relatively low but the embedded flow Mach

number is even lower thus rendering Newtonian flow assumptions even more inappropriate for the local Newtonian flow calculations on embedded surfaces.

Unsteady Numerical Techniques

Although the capability of numerical techniques for solutions of the Euler equations for steady flow field calculations on complex body shapes has improved tremendously in the last decade, very few comparable attempts at calculating the unsteady flow past oscillating bodies have been reported. Brong (Ref.23) numerically solved the first order perturbation equations for pitching and plunging cones and Rie et al (Ref.24) carried out a complete non-steady numerical flow field calculation for oscillating blunted slender cones at hypersonic Mach numbers. In spite of the very considerable complexity of this approach, no improvement in agreement with experiment is observed over the semi-empirical predictions of the embedded Newtonian method.

3. EXPERIMENTAL RESULTS AND COMPARISON WITH PREDICTION METHODS

Wind tunnel facility, techniques and models

The experiments were performed in the Isentropic Light Piston Tunnel (ILPT) at the University of Southampton. This is an intermittent wind tunnel facility providing an open jet test section of nozzle exit plane in diameter 0.21m, with a flow Mach number of $M = 6.85$ for durations of typically 0.5s. A more detailed description of this facility is given in Reference 25. The unit Reynolds number test range available is approximately $7.5 \times 10^6 \text{ m}^{-1}$ to $40 \times 10^6 \text{ m}^{-1}$.

The test procedure employed to determine the aerodynamic stiffness and damping derivatives is the small amplitude free oscillation technique. The model under test is held captive in the wind tunnel open jet test section flow on a sting support. The model is mounted on an internally sited rotary flexure pivot which allows the model to oscillate by $\theta \sim \pm 1^\circ$ in the pitch plane. The centre of rotation corresponds to the effective centre of gravity location. The flexure pivot is mounted onto a rigid sting support which is quadrant mounted on the test section floor.

All the experimental stability data were obtained using sting supported models pivoted on cross flexures. Dynamic stability data obtained in such circumstances may be subject to support interference effects, unless certain sting design criteria are met. It is believed that the results presented herein are free from such interference in view of the following experimental features:

- i) The sting geometry is symmetric.
- ii) The test Mach number is relatively low, (Mach number $M = 6.85$) and therefore little affected by sting interference effects detailed by Ericsson (Ref.26) for example.
- iii) The parameter, visible sting length behind the model divided by model base diameter, is large - approximately 3.
- iv) The negligible influence on these tests of base pressure effects has been previously demonstrated by open and closed, model base results reported in Ref.27.
- v) The sting support structure is of sufficient stiffness, that the fundamental mode of vibration has frequencies at least two orders of magnitude higher than the model frequency.

The reduced frequency parameter for these experiments was $0.0018 < \omega^* < 0.0092$.

The measurement of each pair of aerodynamic stiffness and damping derivatives necessitates two experimental tests, the so called 'wind off' and 'wind on' runs. The ensuing model motions, both in vacuum, (wind off) and in the aerodynamic flow (wind on) are monitored via an optical model tracking system (Ref.28), recorded and digitised for microcomputer storage. A subsequent analysis of the two model motion time histories allows the aerodynamic pitch stability derivatives to be deduced.

The analysis adopts the standard U.S. notation, whereby

$$C_m = \frac{M_p}{\frac{1}{2} \rho V_\infty^2 S c}, \quad C_{m_\alpha} = \frac{\partial C_m}{\partial \alpha}, \quad C_{m_q} = \frac{\partial C_m}{\partial q} \left(\frac{c}{2V_\infty} \right), \quad C_{m_{\dot{\alpha}}} = \frac{\partial C_m}{\partial \dot{\alpha}} \left(\frac{c}{2V_\infty} \right)$$

Flow visualisation was achieved by the schlieren flow visualisation technique. Surface flow visualisation was obtained using a sprayed microencapsulated liquid crystal coating to provide a model surface thermographic map.

Experimental pitch stability data have been collected for a range of axisymmetric vehicles shown in Fig.2, which included pointed and blunted 10° semi-angle cones and the hyperballistic shape HBS. These bodies were tested over a range of angles of attack and axis oscillation position which extended to $0 < \alpha < 16^\circ$ and $0.35 < X_{cg}/L < 0.82$ (HBS only).

Results and Discussion

Pointed and Blunted Cone Geometries

A 10° semi-angle pointed cone has been investigated by East et al. (Ref.29). Small amplitude, $\theta = 1^\circ$, oscillatory experiments were performed in the facility described earlier at $M = 6.85$ in the Reynolds number range, $0.4 \times 10^6 < Re_b < 2 \times 10^6$. The zero angle of attack results are shown by Figure 3. This shows how with increasing Reynolds number the stiffness derivative, $-C_{m_\alpha}$, decreases in the range $1.0 \times 10^6 < Re_b < 1.4 \times 10^6$. Further increase in Reynolds number causes the stiffness derivative to rise to a value greater than the low Reynolds value. This minimum of stiffness derivative is accompanied by a maximum in the damping derivative, $(C_{m_q} + C_{m_{\dot{\alpha}}})$. Ward (Ref.30) reported a similar trend in pointed cone results and showed how the maxima and minima in the respective derivatives occurred when there was transitional flow at the base of the model. These observations show that the results given in Figure 4 are subject to transitional flow at the model base, where $Re_b = 1.45 \times 10^6$ and subject to wholly turbulent flow at $Re_b = 2.17 \times 10^6$. Recent surface thermographs have confirmed the transitional nature of the boundary layer at the rear of the pointed cone for these flow conditions. At the greater Reynolds number condition, the inviscid embedded Newtonian technique yields results similar to the experimental trend in that they are generally angle of attack invariant in the range, $0 \leq \alpha \leq 16^\circ$. It is likely that the increase in static stability above the theoretical prediction shown by the experimental data is due to boundary layer displacement thickness effects.

Ericsson (Ref.31) has postulated that the angle of attack dependent trends are associated with aft cone transitional flow. Increasing the angle of attack causes the windward surface transition location to move aft slightly, however, this movement is much less than the associated forward movement of the lee side transition. With increase in angle of attack the crossflow enhanced leeside transition location moves rapidly forward to then remain fixed despite further increase in angle of attack. This asymmetric transition point movement modifies the viscous contribution to stability. This is vividly shown by the comparison between the angle of attack dependent, small amplitude experimental data at $Re_b = 1.45 \times 10^6$ and the inviscid embedded Newtonian theory results shown by Figure 4. In comparison with the inviscid theory the $\alpha = 0^\circ$ experimental stability derivatives are consistent with the effects associated with aft body transition rear of the oscillation axis. The viscous moment contribution acts rear of the oscillation axis at $\alpha = 0^\circ$, but, with increases in angle of attack, the viscous contribution moves forward to then become a statically stabilising effect for $\alpha > 5^\circ$. This conclusion is drawn from a comparison with the inviscid, angle of attack dependent theoretical results. The dominant influence is that of forebody crossflow ($\alpha \approx 0^\circ$) which thickens the lee side boundary layer. Attempts have been made by Ericsson (Ref.26) to predict transition effects by proposing a boundary layer build up modification to an effective body geometry. This was successful for the stiffness derivative but not the dynamic damping derivative. The discrepancy in damping derivative was shown to be due to an 'accelerated flow effect' which affects transition in a similar manner to that by which local pressure gradients affect separated flows. These perturbations are only evident for pointed cones since the favourable pressure gradient present on blunt cones dominates the flowfield.

Ericsson's model was centred on transition *per se* being the dominant viscous influence. However, it is the authors' belief that the viscous influence responsible for the results observed is an interaction between transition and leeside separation, whereby, the prevailing boundary layer state determines the different nature of the lee side flow. Figure 5 shows two sketches of surface flowfields revealed by liquid crystal thermographic methods. Fig 5(a) shows the lee side flow with the model at $\alpha \approx 1^\circ$. It clearly shows the general high temperature region for the aft one third of the body associated with the transitional region. However for the forward portion of the body separate hot and cold regions are shown associated with a generally stream wise vortical structure caused by the viscous crossflow. Results of further experiments show that this structure persists in a modified form at angles of attack up to at least 5° . Fig 5(b) identifies the flowfield at $\alpha \approx 5^\circ$ showing fundamental differences in fore and aft body vortical structure. This suggests that the former transitional flow persists not as a transitional flow *per se* but as an influence on the nature of the aft body lee side separated flow.

Figures 6 to 9 show a comparison between the predictions of embedded Newtonian theory and experimental results for 10° semi-angle cones with hemispherical nose bluntness in the range $0.1 < d_n/d_b < 0.4$. The experimental variations of the derivatives $-C_{m\dot{\alpha}}$ and $(C_{m\dot{\alpha}} + C_{m\ddot{\alpha}})$ with angle of attack are complex and very dependent on nose bluntness. Considerable non-linear effects are demonstrated and significant shifts of centre of pressure (where $-C_{m\dot{\alpha}} = 0$) are evident. Only the pointed cone derivatives are relatively independent of angle of attack up to 20° .

The general trends of the stiffness derivative ($-C_{m\dot{\alpha}}$) for oscillation axis positions of $0.68 < X_{CG}/L < 0.70$ are well predicted by embedded Newtonian theory. For bluntness ratios of 0.1 and 0.2 the stiffness derivative $-C_{m\dot{\alpha}}$ decreases with angle of attack, indicating a forward shift of the centre of pressure. This is accounted for in the theory by the forward movement of the minimum in the typical blunt cone blast wave induced pressure coefficient as angle of attack of the windward surface increases. Since the windward surface plays an increasingly dominant role as angle of attack increases, this forward movement of pressure distribution is reflected in the derivatives. The effect of bluntness on damping is to destabilize as bluntness is increased. This is due to the lower dynamic pressure acting on the conical surface due to the entropy layer resulting from the bow shock.

Data from small amplitude longitudinal stability experiments performed on a 0.2 bluntness ratio 10° cone (Ref.27), at two Reynolds numbers, $Re_b = 1.45 \times 10^6$ and 2.17×10^6 show the results to be independent of Reynolds number within this range and for angles of attack, $0^\circ < \alpha < 16^\circ$. Nose bluntness produces a region of high entropy flow which reduces the local Reynolds number and which has been shown to delay transition. Work by Softley et al (Ref.32) illustrates how blunted cone transition is influenced by the position of the entropy swallowing station at which the entropy layer thins so that the flowfield tends towards that found on the equivalent pointed cone. The distance downstream of the entropy swallowing station at which transition occurs is determined by the freestream Reynolds number, Re_∞ . As the equivalent pointed cone flow is transitional at the rear of the body for the experiments under discussion, the bluntness will serve to move transition off the body into the wake. The above implies that the blunted cone is subject to a purely laminar flow at the Reynolds numbers appropriate to these data.

On the assumption that the differences between the experimental stability results and the predictions from the embedded Newtonian theory shown by Figure 7 are due to viscous effects, it is implied that the viscous contributions at $\alpha = 0^\circ$ are statically destabilising with no change in the dynamic stability. It is postulated that viscous phenomena associated with the nose flowfield effectively increase the nose bluntness. This has been modelled by using the embedded Newtonian technique to prove that a nose bluntness ratio of $d_n/d_b = 0.22$ reduces the stiffness derivative to the experimental value with no effect on the damping derivative.

Having allowed for the increased nose bluntness at $\alpha = 0^\circ$, the trends shown by Figure 7 identify the α dependent viscous contribution to be statically stabilising, but dynamically destabilising for angles of attack, $\alpha < 8^\circ$. This trend reverses for angles of attack, $\alpha > 8^\circ$. The low angle of attack trend is thought to be a crossflow effect which is known to be statically stabilising when the load centre of this effect is ahead of the centre of gravity position. The pointed cone results of Adams (Ref.33) illustrate how this effect subsides with further increase in angle of attack. In this case (Ref.33) the statically stabilising low angle of attack viscous local crossflow effect disappears at $\alpha > 5^\circ$. With increasing angle of attack, ($\alpha > 8^\circ$) the results of the experiments shown here illustrate a reverse trend and the viscous contribution becomes statically destabilising and dynamically stabilising. This effect has been noted on the laminar flow pointed cone, where at large relative angles of attack the local crossflow is dominated by non-linear viscous crossflow. It is suggested that this effect is present on this laminar flow blunted cone. The leeward separated flows, under discussion, are revealed in schlieren flow visualisation by embedded compression waves within the lee side bow shock layer. The presence of the layer on the pointed cone results in an increase in dynamic stability and a decrease in static stability. The flowfields indicate the development of two separating flows. Their axial positions are close to the nose and move forward with increasing angle of attack. This trend is consistent with observations of Stetson (Ref.34) who also showed these flows to be free from subsonic base communication travelling upstream. The high angle of attack embedded flowfield is almost identical to the separated flows identified by Miller and Gnoffo (Ref.35) on the forecone of a blunted biconic geometry in a flow with $M = 6$ and $Re = 29 \times 10^6$ per metre.

The pitch stability derivatives at various angle of attack for nose bluntnesses of 0.3 and 0.4 are shown on Figures 8 and 9. Unlike the 0.2 bluntness ratio cone where the pressure field is composed of both nose and cone influences, the 0.3 and 0.4 bluntness ratio cone flowfield is dominated by the very large nose diameter. This causes a shift in centre of pressure which reduces the $\alpha = 0^\circ$ small amplitude stability derivatives in comparison with the inviscid theory. This comparison implies that the entropy layer effects extend

further downstream than the inviscid results would suggest. It is almost certain that both of these cones are subject to a purely laminar flow at the Reynolds number of the tests, $Re_t = 1.45 \times 10^6$.

At increased angles of attack, the entropy layer present on the dominant windward surface thins. This has the effect of increasing the pressure on the aft region of the body. The resultant change in the moment is reflected by the increase in the stiffness derivative in the angle of attack range, $0^\circ < \alpha < 5^\circ$. Although not shown on these plots, further increase in the angle of attack brings the increased conic pressure component forward and ahead of the oscillation axis and the stiffness consequently decreases. The embedded Newtonian theory overestimates the damping derivatives in the range $\alpha < 10^\circ$, and fails to predict the large rise in damping derivative seen at angles of attack $\alpha > 10^\circ$. This tends to confirm the entropy effects being larger than predicted, since an increase of the nose bluntness would produce decreased stiffness and damping derivatives.

In Fig. 10, absolute values of the damping derivative $-(C_{m\dot{\alpha}} + C_{m\ddot{\alpha}})$ are compared with the results of prediction methods, whereas, in previous papers such comparisons have generally been made with values normalised with respect to the equivalent pointed cone damping predictions. On the previous basis, comparison between experiment and prediction can be obscured if the values taken for the pointed cone differ. The comparison presented in Fig. 10, indicates that for low values of nose bluntness, the centrifugally corrected embedded Newtonian method appears to over predict aerodynamic damping in comparison with simple embedded Newtonian and experimental results.

A detailed comparison between experimental data and various theoretical prediction techniques for the pitch damping derivative of a 10° , 0.3 bluntness ratio cone at Mach number $M = 6.85$ is shown in Figure 11 using results reported by Tong and Hui (Ref. 7). The results of Ref. 7 show that the embedded Newtonian method underpredicts the stability derivative and that inclusion of the centrifugal term, $(C_{m\dot{\alpha}})_{cf}$, is necessary to attain values in keeping with experimental data. However, as indicated earlier it is noted that Tong and Hui's embedded Newton-Busemann method employs infinite Mach number relations for the density and velocity profiles within the bow shock shear layer. If the functions, which have been shown for steady flow to be appropriate for finite Mach numbers, are used in the simple embedded Newtonian method then the prediction is very similar to that with infinite Mach number f^* , g^* functions with centrifugal terms included. Indeed it is arguably superior since the sensitivity to rearward axis position damping increasing is identified. This shows that with the appropriate finite Mach number functions applied to the embedded Newtonian method, the further inclusion of the centrifugal term would overpredict in comparison with experiment. It therefore appears that, at the relatively low hypersonic Mach number at which the comparison has been made, adequate predictions are obtained by the use of embedded Newtonian methods without the Busemann correction. It must be acknowledged that this is a severe test of the Newton-Busemann concept which strictly applies in the $M \rightarrow \infty$, $\gamma \rightarrow 1$ limit, which is not well satisfied at the very low Mach numbers within the embedded flow on a blunt shape at $M = 6.85$.

Hyperballistic Shape HBS

Figure 12 shows the changes in aerodynamic stiffness and damping with increase in angle of attack for the double flared, hemispherically blunted cylinder body. The measured increases in aerodynamic stiffness, corresponding to a rearward centre of pressure movement, are predicted by embedded Newtonian theory, but the magnitude of the predicted increase is less than measured. Also, it is noted that at $\alpha = 14^\circ$ the rearward shift is reversed and a rapid forward shift is predicted.

Values of the damping derivative $-(C_{m\dot{\alpha}} + C_{m\ddot{\alpha}})$ are in excellent agreement with embedded Newtonian theoretical predictions over the complete range of $0 < \alpha < 18^\circ$. The predicted rapid forward shift of the centre of pressure appears as an increase in aerodynamic damping. However, the measured damping for $\alpha = 16^\circ$ for the HBS shape showed a large increase which was experimentally attributed to the impingement of the bow shock on the rearmost flare. This phenomenon occurs similarly in the theory, at which point flare pressures are computed using simple Newtonian theory as the flare has moved out of the influence of the low dynamic pressure entropy layer.

The experimental trends for hyperballistic shapes are, therefore, well predicted by embedded Newtonian theory, aerodynamic damping predictions, in particular, being in excellent agreement with experimental data. The theory takes no account, however, of any cross flows which must occur on these bluff shapes as α increases. Judging from the less rapid rearward movement of the centre of pressure inferred experimentally from the $-C_{m\alpha}$ data, it seems likely that viscous effects, resulting in cross flows, could account for the observed differences.

This is further supported by schlieren flow visualisation and liquid crystal thermographic maps. At near zero degrees angle of attack there are very slight regions of separated flow present at the flow junctions. It is felt these regions offer insignificant viscous contributions to pitch stability in comparison to the dominating flow separation effects associated with the separation induced by the large angle single flare of the AGARD hyperballistic shape HB2 reported in Ref. 18, for example. However, at large angles of attack liquid crystal thermographic maps show that the lee side separated flow increases and this is shown schematically by Figure 13. Whilst it is accepted that the stability derivatives are mainly influenced by the windward surface, it is apparent that the lee side viscous flows will modify the results predicted by inviscid techniques.

The variations of the zero degrees angle of attack values of $-C_{m\alpha}$ and $-(C_{m\dot{\alpha}} + C_{m\ddot{\alpha}})$ with the position of the axis of oscillation are shown in Figure 14. The aerodynamic stiffness plot identifies experimental data and predictions from the inviscid embedded Newtonian technique. The centre of pressure location, where $-C_{m\alpha} = 0$, is predicted to be further aft than that deduced from experimental data, suggesting the theory slightly overestimates the flare effectiveness. The observed difference corresponds to a centre of pressure shift of 5% in the region of the centre of pressure.

The variation of pitch damping derivative with axis position is shown in Fig. 14 together with the results of several prediction methods. The plot includes data associated with experiment, simple Newtonian impact theory, inviscid embedded Newtonian theory as calculated by the present authors and the unsteady embedded Newton-Busemann predictions of Ref. 7. The simple Newtonian impact predictions are clearly in error since there is no allowance for the loss of the flare effectiveness due to the finite Mach number curved bow shock and subsequent entropy layer influence. These deficiencies are redressed fully by the embedded Newtonian predictions of the authors. The embedded Newtonian method predicts a lower value of minimum damping than is observed experimentally, however, it should be noted that a typical experimental error bar for experimental damping derivative is $\pm 20\%$. The predicted locations of the minima with respect to oscillation axis are consistent between the embedded Newtonian and the experimental data.

The final prediction method used is that of Tong and Hui, Ref. 7. This result is a finite Mach number embedded Newtonian prediction but includes the centrifugal term found necessary in the gas dynamic limit of $M = \infty$, $\gamma = 1$. The result predicts a lower damping minimum, but identifies the centre of pressure to be located forward, at $X_{cp/L} = 0.55$. (c.f. experiment and finite Mach number embedded Newtonian damping minima at $X_{cp/L} \approx 0.65$). Strict comparison between the prediction of the embedded Newtonian theory, with and without the centrifugal correction is not possible, since the density and velocity functions used by Tong and Hui (Ref. 7) are for

the infinite Mach number limit, whereas, in the uncorrected model, functions appropriate for finite Mach numbers (see eqn. 4) have been used. Furthermore, it is unclear as to what values have been included in Ref. 7 for the nose contribution to aerodynamic damping. In the present paper, data are presented for infinite Mach number embedded Newtonian f^* and g^* functions, which are effectively Tong and Hui's data without the centrifugal term. This clearly shows how using f^* , g^* functions which are inappropriate for the low embedded flow Mach numbers, leads to underprediction. However, with these provisos, it appears that the embedded Newtonian prediction (without centrifugal correction but with appropriate f^* and g^* functions) gives the best agreement with experimental results, particularly with regard to the axis position at which the damping minima associated with the zero value of $C_{m\alpha}$ occurs. As for the 0.3 bluntness ratio cone, this conclusion should be qualified by the observation that the embedded flow Mach numbers for the extremely blunt HBS shape will be in severe contradiction with the $M \rightarrow \infty$, $\gamma \rightarrow 1$ Newton-Busemann limit, thereby providing an arguably inappropriate test case for the method presented in Ref. 7.

4. CONCLUSIONS

A brief review of three analytical techniques for predicting the stability derivatives of slender axisymmetric hypersonic vehicles is presented. The techniques presented are Newtonian impact, embedded Newtonian and embedded Newton-Busemann. Vehicle geometries considered are pointed and blunted 10° cones and a double flared hyperballistic shape HBS. Comparison of results from these prediction techniques with experimental data demonstrates that the embedded Newtonian technique provides a suitable method for approximate predictions of aerodynamic stiffness and damping over a wide range of conditions.

Although the centrifugal term of the embedded Newton-Busemann method is required for correct predictions in the regime of the gas dynamic limit $M = \infty$, $\gamma = 1$ where shock layers are thin, comparison with experimental results for a range of blunted cones and the hyperballistic shape HBS show that prediction using this method at $M = 6.85$ provides no improvement over the less rigorous method in which the centrifugal correction is omitted.

It is noted that where flow structural change is present, in the form of transition and re-separation, the viscous contributions to the stability derivatives cannot be ignored. The body motion coupling with respect to these viscous flows is an area in need of further research.

REFERENCES

- Hayes, W.D. and Probstein, R.F. 'Hypersonic Flow Theory, I', Academic Press, New York (1960).
- Zartarian, G. 'Unsteady Airloads on Pointed Airfoils and Slender Bodies at High Mach Numbers', Wright Air Development Center, WADC TR-59-583.
- Busemann, A. 'Handwörterbuch der Naturwissenschaften, IV', Flüssigkeits und Gasbewegung, 2nd Ed. Gustav Fisher, Jena, pp 244-279 (1933).
- Tobak, M. and Wehrend, W.R. 'Stability Derivatives of Cones at Supersonic Speeds', NACA TN 3788 (1956).
- Seiff, A. 'Secondary Flow Fields Embedded in Hypersonic Shock Layers', NASA TN D-1304 (1962).
- Ericsson, L.E. 'Unsteady Aerodynamics of an Ablating Flared Body of Revolution Including Effects of Entropy Gradient', AIAA Journal **6**, pp 2395-2401 (1968).
- Tong, B.G. and Hui, W.H. 'Unsteady Embedded Newton-Busemann Flow Theory', J. Spacecraft and Rockets **23**, 2, pp 129-135 (1986).
- Cole, J.D. 'Newtonian Flow for Slender Bodies', J. Aero. Sci., **24**, pp 448-455 (1957).
- Hui, W.H. 'On Axis-Symmetric and Two-Dimensional Flow with Attached Shock Waves', Astronautica Acta, **18**, pp 35-44 (1973).
- Mahood, G.E. and Hui, W.H. 'Remarks on Unsteady Newtonian Flow Theory', Aeronautical Quarterly, **27**, pp 66-74, (1976).
- Hui, W.H. 'Stability of Oscillating Wedges and Carot Wings in Hypersonic and Supersonic Flows', AIAA Journal, **7**, 8, pp 1524-1530, (1969).
- Scott, C.J. 'A Theoretical and Experimental Determination of the Pitching Stability Derivatives of Cones in Hypersonic Flow', AASU Rep. 267, University of Southampton (1967).
- Ericsson, L.E. and Scholnick, I.M. 'Effect of Nose Bluntness on the Hypersonic Unsteady Aerodynamics of Flared and Conical Bodies of Revolution', J. Spacecraft and Rockets, **6**, 3, pp 321-324 (1969).
- Ericsson, L.E. 'Universal Scaling Laws for Hypersonic Nose Bluntness Effects', AIAA Journal, **7**, pp 2222-2227 (1969).
- Ericsson, L.E. 'Effect of Nose Bluntness, Angle of Attack, and Oscillation Amplitude on Hypersonic Unsteady Aerodynamics of Slender Cones', AIAA Journal, **9**, 2, pp 297-304 (1971).
- Ericsson, L.E. 'Unsteady Embedded Newtonian Flow', Astronautica Acta, **18**, pp 309-330 (1973).
- Ericsson, L.E. 'Generalised Unsteady Embedded Newtonian Flow', J. Spacecraft and Rockets, **12**, 12, pp 718-726 (1975).
- Ericsson, L.E. 'Hyper-ballistic Vehicle Dynamics', J. Spacecraft and Rockets, **19**, 3, pp 496-505 (1982).
- van Dyke, M.D. 'A Model of Supersonic Flow Past Blunt Axisymmetric Bodies, with Application to Chester's Solution', J. Fluid Mech, **3**, pp 615-522 (1958).
- Krasnov, N.F. 'Aerodynamics of Bodies of Revolution', Ed. Morria, D.N., American Elsevier Publishing Co. Inc., New York (1970).

21. Hui, W.H. and Tobak, M. 'Unsteady Newton-Busemann Flow Theory Part II - Bodies of Revolution', AIAA J 19, pp1272-1273 (1982).
22. Seiff, A. and Whiting, E.C. 'Calculation of Flow Fields from Bow-wave Profiles for the Downstream Region of Blunt-nosed Circular Cylinders in Axial Hypersonic Flight', NASA TN-D-1147 (1961).
23. Brong, E.A. 'The Flow Field about a Right Circular Cone in Unsteady Flight', AIAA 65-395 (1965).
24. Rie, H., Linkiewicz, E.A. and Bosworth, F.D. 'Hypersonic Dynamic Stability. Part III, Unsteady Flow Field Program', FDL-100T-64-149, Part III (1961).
25. East, R.A. and Qasrawi, A.M.S. 'A Long Stroke Isentropic Free Piston Hypersonic Wind Tunnel', Aeronautical Research Council R&M 3844 (1978).
26. Ericsson, L.E. 'Non-Linear Hypersonic Viscous Crossflow Effects on Slender Vehicle Dynamics', AIAA J 17, 586-593 (1979).
27. East, R.A. 'Non-Linear Hypersonic Static and Dynamic Stability of Axis-Symmetric Shapes', Euromech Colloquium No 126, Berlin (1980).
28. Hutt, G.R. and East, R.A. 'Optical Techniques for Model Position Measurement in Dynamic Wind Tunnel Testing', Measurement and Control 18, 3 pp 99-101 (1985).
29. East, R.A., Qasrawi, A.M.S. and Khalid, M. 'An Experimental Study of the Hypersonic Dynamic Stability of Pitching Blunt Conical and Hyperballistic Shapes in a Short Running Time Facility', AGARD Conference on Dynamic Stability Parameters, AGARD CP-235 (1978).
30. Ward, L.K. 'Influence of Boundary Layer Transition on Dynamic Stability at Hypersonic Speeds', Paper No 6 Transactions of the 2nd Technical Workshop on Dynamic Stability Testing. Arnold Air Force Station, Tenn. (1965).
31. Ericsson, L.E. 'Transition Effects on Slender Vehicle Stability and Trip Characteristics', J. Spacecraft and Rockets 11, pp 3-11.
32. Softley, E.J., Graber, E.C. and Zempel, R.C. 'Experimental Observations of Transition of the Hypersonic Boundary Layer', AIAA J 7, 257-263 (1969).
33. Adams, J.C. Jnr. and Griffith, B.J. 'Hypersonic Viscous Static Stability of a Sharp 5 deg. Cone at Incidence', AIAA Journal 14 pp 1062-1068 (1976).
34. Stetson, K.E. 'Boundary Layer Separation on Slender Cones at Angle of Attack', AIAA J 10, 642-648 (1972).
35. Miller, C.G. and Gnoffo, P.A. 'An Experimental Investigation of Hypersonic Flow over Biconics at Incidence and Comparison to Prediction', AIAA 82-1382 (1982).
36. Khalid, M. 'A Theoretical and Experimental Study of the Hypersonic Dynamic Stability of Blunt Axisymmetric Conical and Power-Law Shaped Bodies', Ph.D. Thesis, Department of Aeronautics and Astronautics, University of Southampton, 1977.

ACKNOWLEDGEMENT

This work has been carried out with the support of the Procurement Executive, Ministry of Defence

The authors wish to express their thanks to Mr D.R.J. Baxter for his contribution to this paper

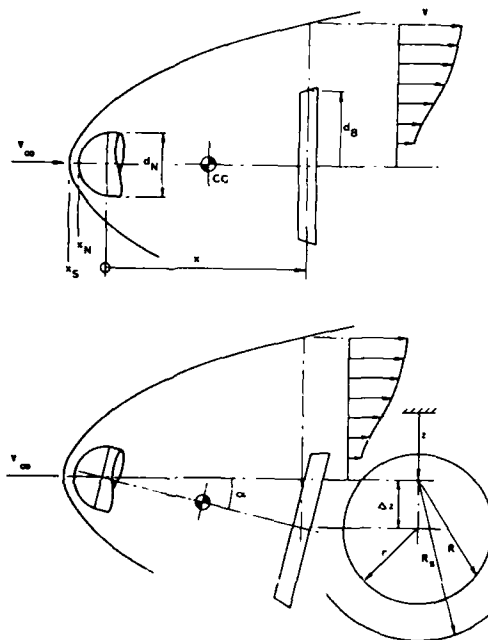


FIGURE 1 Definition of embedded flowfield and body geometry (Ref. 16)

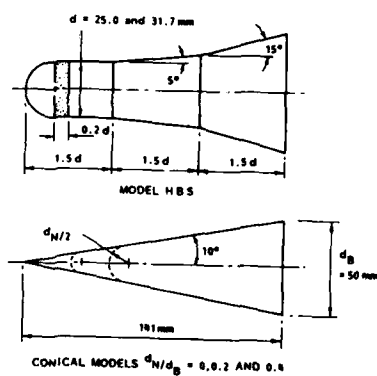


FIGURE 2 Shapes tested for dynamic stability

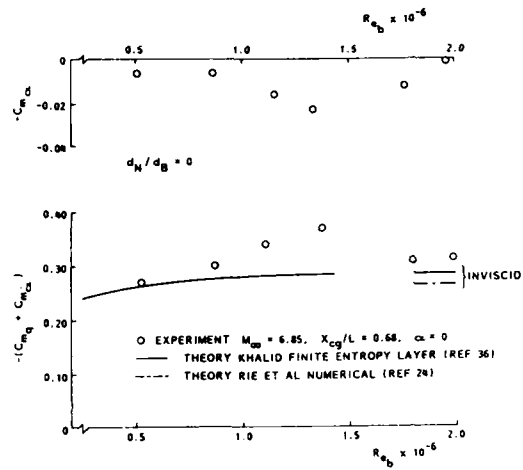


FIGURE 3 Variation of pitch stability with Reynolds number for a 10° semi-angle pointed cone

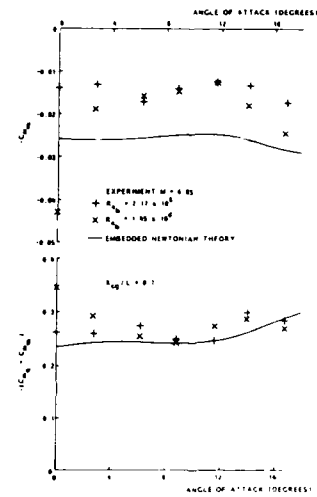


FIGURE 4 Pitch stability derivatives versus angle of attack for a 10° semi-angle pointed cone

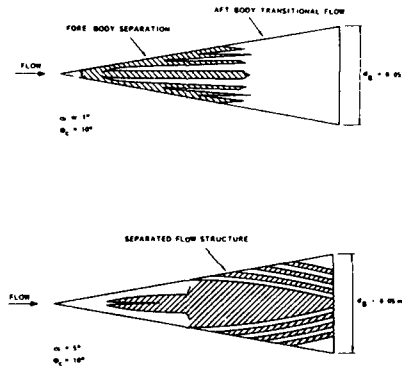


FIGURE 5 Thermographic surface flowfield maps for a pointed cone. $M = 6.85$, $Re_b = 1.45 \times 10^6$

low heat transfer high heat transfer

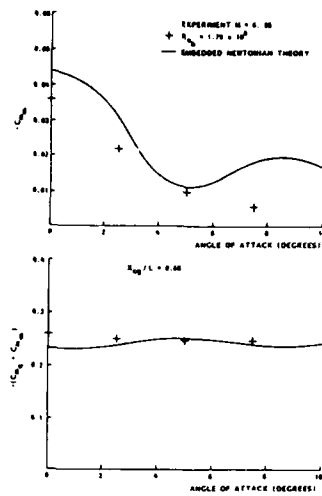


FIGURE 6 Comparison of embedded Newtonian and experimental pitch stability derivatives versus angle of attack for a 0.1 bluntness ratio, 10° semi-angle cone

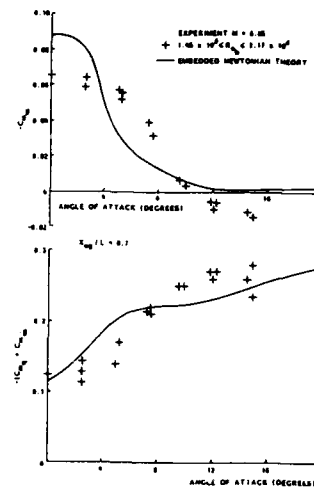


FIGURE 7 Comparison of embedded Newtonian and experimental pitch stability derivatives versus angle of attack for a 0.2 bluntness ratio, 10° semi-angle cone

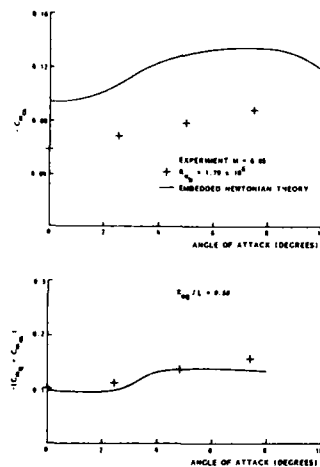


FIGURE 8 Comparison of embedded Newtonian and experimental pitch stability derivatives versus angle of attack for a 0.3 bluntness ratio, 10° semi-angle cone

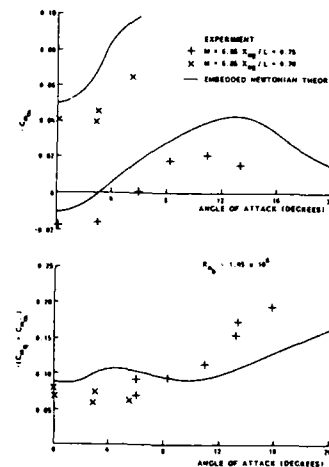


FIGURE 9 Comparison of embedded Newtonian and experimental pitch stability derivatives versus angle of attack for a 0.4 bluntness ratio, 10° semi-angle cone

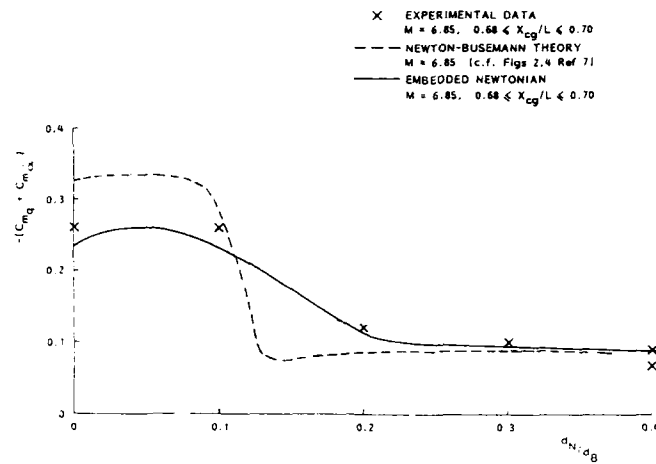


FIGURE 10 Pitch damping derivative results versus bluntness ratio for a family of 10° semi-angle cones - a comparison between experimental data and theoretical prediction

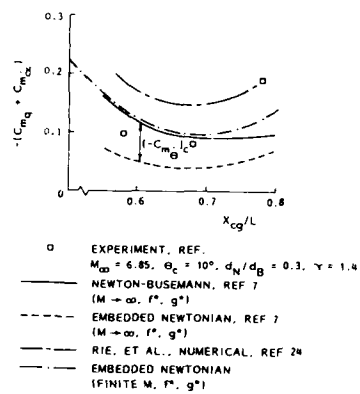


FIGURE 11 Comparison between theoretical and experimental results of the pitch damping stability derivative versus oscillation axis position for a 0.3 bluntness ratio 10° semi-angle cone

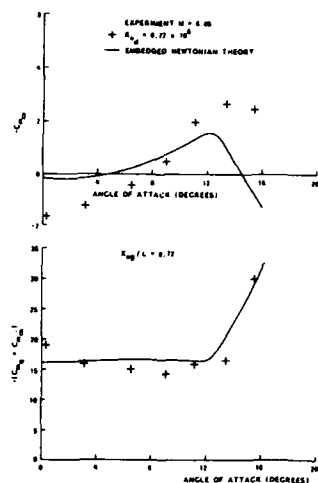


FIGURE 12 Comparison of embedded Newtonian and experimental pitch stability derivatives versus angle of attack for the shape HBS

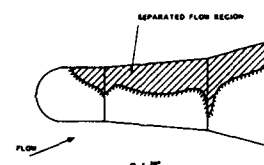


FIGURE 13 Thermographic surface flowfield maps of the shape HBS. $M = 6.85$, $Re_d = 0.95 \times 10^6$

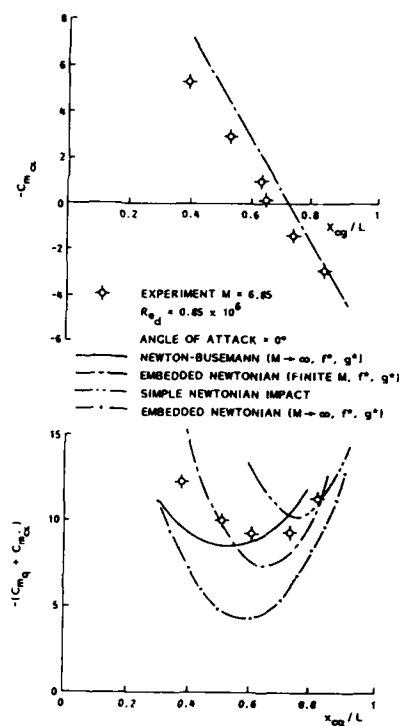


FIGURE 14 Comparison between experimental and theoretical pitch stability derivative results versus oscillation axis position for the shape HBS

DYNAMIC STABILITY OF HYPERSONIC CONICAL LIFTING VEHICLES ACCORDING TO NEWTON-BUSEMANN THEORY

Dr. W.H. Hui
Professor of Applied Mathematics and Mechanical Engineering
University of Waterloo, Waterloo, Ontario, Canada N2L 3G1

Dr. H.J. Van Roesse
Assistant Professor
Dept. of Applied Mathematics, University of Western Ontario, London, Ontario, Canada N6A 5B9

SUMMARY

In this paper a theory is given of the aerodynamic stability of hypersonic conical lifting vehicles performing small amplitude pitching motion about its steady flight by using the Newton-Busemann flow theory, which is the rational limit of gasdynamic theory as the flight Mach number $M_\infty \rightarrow \infty$ and the ratio of specific heats $\gamma \rightarrow 1$. This is done by reformulating the gasdynamic equations using a set of material functions as independent variables which are a generalisation of the stream functions of steady flow. In this formulation, calculations of the steady flow field are reduced to finding the geodesics of the body surface. The unsteady flow field is then calculated by perturbation of the steady flow; in particular for conical shapes it requires only numerical quadrature. The theory is applied to conical wings of parabolic cross-section and the dependence of the stiffness and damping-in-pitch derivative on the angle of attack, the slenderness, concavity and convexity of the wing, and on the pivot axis position is studied systematically.

1. INTRODUCTION

With the recent revival of interests in hypersonic flight information on aerodynamic stability of vehicles at very high Mach number has become wanted, as evidenced in the excellent review papers by Orlik-Rückemann (Ref. 1), Townsend (Ref. 2) and East (Ref. 3).

This paper is devoted to the theoretical prediction of the aerodynamic stability of hypersonic lifting vehicles based on unsteady Newton-Busemann flow theory. The simpler aspects of the latter theory were developed recently by Hui and Tobak (Refs. 4 to 6) and applied to aerofoils and bodies of revolution. In particular, it has been shown that (1) the rational limit of gasdynamic theory, as the flight Mach number $M_\infty \rightarrow \infty$ and the ratio of specific heats $\gamma \rightarrow 1$, is equivalent to the Newtonian impact flow model plus Busemann centrifugal pressure correction; (2) the centrifugal pressure is just as important as the impact pressure and must not be neglected; and (3) with its inclusion the complete unsteady Newton-Busemann flow theory is in good agreement with experiments on sharp-nosed bodies.

Extension to the three-dimensional case was partially given by Hui and Van Roesse (Ref. 7) using a spanwise integration technique to obtain the aerodynamic derivatives. It gives, however, no information of the details of the flow field; in particular, the region of zero pressure, if it exists, was not determined.

In this paper the unsteady Newton-Busemann flow field around a three-dimensional body performing small amplitude pitching motion about steady flight at a trimmed condition is obtained. This is done by reformulating the gasdynamic equations (Ref. 8) using a set of material functions as independent variables, which are a generalisation of the stream functions of steady flow. In this formulation, calculations of the steady flow field are reduced to that of finding the geodesics of the body surface, and the unsteady flow field is then calculated by perturbation of the steady flow.

When applied to conical shapes, the method requires only numerical quadrature. In this way, effects of various factors, such as angle of attack, slenderness, concavity and convexity of a wing, and pivot axis position on the stiffness and damping-in-pitch derivative are investigated systematically.

2. MATHEMATICAL FORMULATION

Consider a rigid vehicle B flying at supersonic/hypersonic speed. In supersonic/hypersonic flight the front of the body is enveloped by a shock wave which extends downstream in the shape of a slightly flared skirt. The flow upstream of the shock wave or shock surface is undisturbed whereas the flow field of interest lies entirely downstream of the shock, between the shock surface and the vehicle surface. In hypersonic flight, with the free stream Mach number $M_\infty \gg 1$, the enveloping shock wave lies very close to the body surface. The region between the shock surface and body surface is termed the shock layer.

We scale the time variable by l/U_∞ , and space variables by l where l is a characteristic length of the body B and U_∞ is the free stream velocity. Scale the dependent variables pressure by $\rho_\infty U_\infty^2$, density by ρ_∞ and velocity by U_∞ , where ρ_∞ is the free stream density. The equations governing the flow field surrounding the vehicle B are the inviscid Navier-Stokes equations or the Euler equations:

$$\frac{\partial \rho}{\partial t} + \vec{v} \cdot (\rho \vec{v}) = 0 ,$$

$$\frac{\partial \vec{v}}{\partial t} + (\vec{v} \cdot \vec{v}) \vec{v} + \frac{1}{\rho} \vec{\nabla} p = \vec{F} , \quad (1)$$

$$\frac{\partial}{\partial t} \left(\frac{p}{\rho} \right) + \vec{v} \cdot \vec{\nabla} \left(\frac{p}{\rho} \right) = 0 ,$$

where p , ρ , \vec{v} are the scaled pressure, density and velocity respectively of the gas, and \vec{F} is the body force per unit mass acting on the vehicle.

The boundary conditions are that the relative velocity of the fluid is tangential to the body at the body surface and that mass, momentum and energy be conserved as the fluid crosses the shock wave. At the body surface this condition is

$$(\vec{v} - \vec{v}_b) \cdot \vec{n} = 0 , \text{ on } B \quad (2)$$

where \vec{v}_b and \vec{n} are the velocity and unit normal of the body surface. The shock wave boundary condition may be expressed in the form

$$\rho \left[\frac{\partial G}{\partial t} + \vec{v} \cdot \vec{\nabla} G \right]_s = 0 ,$$

$$\left\{ \rho \left[\frac{\partial G}{\partial t} + \vec{v} \cdot \vec{\nabla} G \right]^2 + |\vec{\nabla} G|^2 p \right\}_s = 0 , \quad (3)$$

$$[\vec{v} \cdot \vec{t}_\alpha]_s = 0 , \quad \alpha=1,2$$

$$\left\{ \frac{1}{2} \left[\frac{\partial G}{\partial t} + \vec{v} \cdot \vec{\nabla} G \right]^2 + \frac{\gamma}{\gamma-1} |\vec{\nabla} G|^2 \frac{p}{\rho} \right\}_s = 0 ,$$

where \vec{t}_α , $\alpha = 1,2$ are linearly independent tangent vectors to the shock surface $G(t, \vec{r}) = 0$ and $[\cdot]_s$ is defined by

$$[(\cdot)]_s = (\cdot)_s - (\cdot)_\infty , \quad (4)$$

the superscripts s and ∞ denoting that the quantity is evaluated just downstream and just upstream of the shock surface respectively. The shock surface at which Eqns. (3) are to be applied is unknown and must be determined as part of the solution.

Let $(x^i; i=1,2,3)$ be the body-fixed Cartesian coordinates. It is convenient to work within a body-fixed curvilinear coordinate system in which the body surface coincides with one of the coordinate surfaces. Let the body B be defined by the equations

$$x^i = B^i(\xi^1, \xi^2) , \quad i=1,2,3 \quad (5)$$

where the B^i 's are at least three times piecewise continuously differentiable with the Jacobian matrix $\frac{\partial(B^1, B^2, B^3)}{\partial(\xi^1, \xi^2)}$ having rank two almost everywhere. Then $(\xi^\alpha; \alpha=1,2)$ represents a coordinate system on the body surface.

Now define a system of shock layer coordinates $(\xi^i; i=1,2,3)$ as follows:

$$x^i = B^i(\xi^1, \xi^2) + \epsilon \xi^3 n^i(\xi^1, \xi^2) , \quad i=1,2,3 \quad (6)$$

where $\epsilon(>0)$ is a constant, to be chosen in a convenient manner later, and the n^i 's are the components

of the unit normal to the body surface. The equation of the body surface in shock layer coordinates is $\xi^3 = 0$ (or $\xi = 0$). Let the equation of the unknown shock surface be

$$\xi^3 = S(t, \xi^1, \xi^2) \quad (7)$$

In order to apply Newton's law in a non-inertial reference frame we must add those forces due to the relative acceleration of the non-inertial reference frame, namely: $-\ddot{\mathbf{R}}_C$, the translational acceleration; $-2\vec{\omega} \times \vec{v}$, the Coriolis force per unit mass; $-\vec{\omega} \times (\vec{\omega} \times \vec{r})$, the centrifugal force per unit mass; $-\vec{\omega} \times \vec{r}$, the inertial force of rotation per unit mass, where $\vec{\omega}$ is the angular velocity vector of the vehicle. The force \vec{F} in equation (1) is thus

$$\vec{F} = -\ddot{\mathbf{R}}_C - 2\vec{\omega} \times \vec{v} - \vec{\omega} \times (\vec{\omega} \times \vec{r}) - \vec{\omega} \times \vec{r} \quad (8)$$

In component form Equation (1) becomes

$$\begin{aligned} \frac{\partial p}{\partial t} + \frac{1}{\sqrt{g}} \frac{\partial}{\partial \xi^i} (\sqrt{g} \rho v^i) &= 0, \\ \frac{\partial v^i}{\partial t} + v^j \frac{\partial v^i}{\partial \xi^j} + \Gamma_{jk}^i v^j v^k + \frac{1}{\rho} g^{ij} \frac{\partial p}{\partial \xi^j} &= F^i, \\ \frac{\partial}{\partial t} \left(\frac{p}{\rho} \right) + v^i \frac{\partial}{\partial \xi^i} \left(\frac{p}{\rho} \right) &= 0, \end{aligned} \quad (9)$$

where g^{ij} are components of the inverse of the metric tensor, g is the determinant of the metric, and Γ_{jk}^i are the Christoffel symbols of the second kind.

The solution of Equations (9) would represent an Eulerian description of the fluid flow. However, a transformation to Lagrangian coordinates will prove useful. The presence of the $\frac{\partial p}{\partial t}$ term in the continuity equation however, precludes the use of stream functions. But, facilitated by a change of notation, it is possible to introduce a set of new functions to be called material functions.

Letting $\xi^0 = t$, and since the metric is time independent due to the body-fixed frame of reference used, the continuity equation may be written as

$$\frac{\partial}{\partial \xi^I} (\sqrt{g} \rho v^I) = 0, \quad (10)$$

where $v^0 = 1$ and upper case latin indices range from 0 to 3.

Introduce three functions $M^i(\xi^0, \xi^1, \xi^2, \xi^3)$ related to the components of velocity as follows

$$\sqrt{g} \rho v^I = e^{IJKL} \frac{\partial M^1}{\partial \xi^J} \frac{\partial M^2}{\partial \xi^K} \frac{\partial M^3}{\partial \xi^L} \lambda(M^1, M^2, M^3) \quad (11)$$

where e^{IJKL} is the permutation symbol. Substitution into (9a) shows that the continuity equation is identically satisfied. Taking the material derivative of M^i yields

$$\begin{aligned} \frac{DM^1}{Dt} &= \frac{\partial M^1}{\partial t} + v^j \frac{\partial M^1}{\partial \xi^j} = v^I \frac{\partial M^1}{\partial \xi^I} \\ &= \frac{1}{\sqrt{g} \rho} e^{IJKL} \lambda(M^1) \frac{\partial M^1}{\partial \xi^I} \frac{\partial M^1}{\partial \xi^J} \frac{\partial M^2}{\partial \xi^K} \frac{\partial M^3}{\partial \xi^L} = 0 \end{aligned} \quad (12)$$

where λ is an arbitrary function of the M^i 's.

† The notation (ξ, η, ζ) is introduced to replace (ξ^1, ξ^2, ξ^3) whenever the use of indices becomes cumbersome.

This shows that the M^i 's are constant following the fluid and so the name material functions is appropriate. These material functions, analogous to the stream functions for steady flow, are not unique. The existence of these functions was known previously but they have been little utilized. Setting $I = 0$ in (11) results in the following constraint on the material functions:

$$\frac{\partial(M^1, M^2, M^3)}{\partial(\xi^1, \xi^2, \xi^3)} = \frac{\sqrt{g} \rho}{\lambda} . \quad (13)$$

Consider a transformation from the (ξ^I) coordinates to (m^I) coordinates defined by

$$m^I = M^I(\xi^0, \xi^1, \xi^2, \xi^3) , \quad (14)$$

with inverse transformation

$$\xi^I = X^I(m^0, m^1, m^2, m^3) , \quad (15)$$

where M^1, M^2 and M^3 are the material functions of Equation (11) and M^0 is to be chosen by imposing the condition

$$J = \frac{\lambda}{\sqrt{g} \rho} , \quad (16)$$

which results in

$$v^I = \frac{\partial X^I}{\partial m^0} , \quad \frac{\partial X^0}{\partial m^0} = 1 . \quad (17)$$

It is clear that $\xi^i = X^i(m^0, m^1, m^2, m^3)$, considered as a curve parameterized by m^0 with the m^i 's held constant, represents the pathline of the fluid particle identified by (m^1, m^2, m^3) .

The material derivative reduces to

$$\frac{D}{Dt} = v^I \frac{\partial}{\partial \xi^I} = \frac{\partial X^I}{\partial \xi^I} \frac{\partial}{\partial m^0} = \frac{\partial}{\partial m^0} , \quad (18)$$

which shows that m^0 is a measure of time following a fluid particle or Lagrangian time. Therefore, m^0 will be replaced by τ whenever convenient.

Making the transformation (15), the governing equations, (9), become

$$\frac{\partial X^0}{\partial \tau} = 1 , \quad (19a)$$

$$J = \frac{\lambda}{\sqrt{g} \rho} , \quad (19b)$$

$$\begin{aligned} & \frac{\partial^2 X^1}{\partial \tau^2} + \gamma_{jk}^1 \frac{\partial X^j}{\partial \tau} \frac{\partial X^k}{\partial \tau} \\ & - \frac{e}{J \rho} \left(g^{11} \frac{\partial X^2}{\partial m^j} \frac{\partial X^3}{\partial m^k} \frac{\partial X^0}{\partial m^l} - g^{12} \frac{\partial X^3}{\partial m^j} \frac{\partial X^0}{\partial m^k} \frac{\partial X^1}{\partial m^l} \right. \\ & \left. + g^{13} \frac{\partial X^0}{\partial m^j} \frac{\partial X^1}{\partial m^k} \frac{\partial X^2}{\partial m^l} \right) \frac{\partial p}{\partial m^1} = F^1(X^I) , \end{aligned} \quad (19c)$$

$$\frac{\partial}{\partial \tau} \left(\frac{p}{\rho \gamma} \right) = 0 . \quad (19d)$$

Equation (16) only determines M^0 to within an arbitrary function of three independent variables. It is convenient, therefore, to set the shock surface at

$$m^0 = 0 \quad (\text{or } \tau = 0). \quad (20)$$

The body surface will be set at

$$m^3 = 0. \quad (21)$$

This is now a fixed boundary problem.

Equations (19) are six equations for six unknown functions. However, Equation (19a) can be integrated immediately to obtain x^0 and Equation (19b) can be used to eliminate ρ , thus leaving four equations in four unknowns. Furthermore, a first integral can be obtained from (19d). The major difficulty lies with the momentum equations (19c).

It is worth pointing out that while $\{\tau, m^1, m^2, m^3\}$ are Lagrangian variables, they differ from the standard Lagrangian variables in that a distinction is made between Lagrangian time τ and Eulerian time t . This distinction allows for the problem to be rendered a fixed boundary problem. It is shown in Ref. 8 that a further transformation

$$x^i(\tau, m^1, m^2, m^3) = E^i(\tau, \xi_s^1, \xi_s^2), \quad i=1,2,3 \quad (22)$$

where the subscript s denotes evaluation at the shock surface, allows the problem to be formulated as a system integro-differential equation. Taking the Newtonian limit $M_\infty \rightarrow \infty$, $\gamma \rightarrow 1$ and assuming that the unsteady motion is sufficiently slow so that an expansion of the following form

$$\begin{aligned} E^i(\tau, \xi_s^1, \xi_s^2) &= E_0^i(\tau, \xi_s^1, \xi_s^2) + E_\theta^i(\tau, \xi_s^1, \xi_s^2)\theta(t_s) + E_\delta^i(\tau, \xi_s^1, \xi_s^2)\delta(t_s) \\ P(\tau, \xi_s^1, \xi_s^2) &= P_0(\tau, \xi_s^1, \xi_s^2) + P_\theta(\tau, \xi_s^1, \xi_s^2)\theta(t_s) + P_\delta(\tau, \xi_s^1, \xi_s^2)\delta(t_s) \end{aligned} \quad (23)$$

is valid leads to the following partial decoupling of the system of integro-differential equations to the form

$$\begin{aligned} \frac{\partial^2 E_0^a}{\partial \tau^2} + \frac{\partial E_0^3}{\partial \tau} \frac{\partial E_0^a}{\partial \tau} &= 0, \\ E_0^a(0, \xi_s^1, \xi_s^2) &= \xi_s^a, \\ \frac{\partial E_0^a}{\partial \tau}(0, \xi_s^1, \xi_s^2) &= U_0^a(\xi_s^1, \xi_s^2), \\ P_0(\tau, \xi^1, \xi^2) &= \bar{P}_0(\xi^1, \xi^2) + \int_0^\tau \hat{P}_0(\bar{\tau}, \xi^1, \xi^2) d\bar{\tau}, \\ E_0^3(\tau, \xi^1, \xi^2) &= \int_{\tau_0^3(\xi^1, \xi^2)}^\tau \hat{E}_0^3(\bar{\tau}, \xi^1, \xi^2) d\bar{\tau}. \end{aligned} \quad (24)$$

$$\frac{\partial^2 E_\psi^\alpha}{\partial \tau^2} + 2\bar{\Gamma}_\psi^\alpha \frac{\partial E_0^\beta}{\partial \tau} \frac{\partial E_\psi^\gamma}{\partial \tau} + \bar{\Gamma}_{\beta\gamma,\delta}^\alpha \frac{\partial E_0^\beta}{\partial \tau} \frac{\partial E_\psi^\gamma}{\partial \tau} E_\psi^\delta = F_\psi^\alpha ,$$

$$E_\psi^\alpha(0, t_s, \xi_s^1, \xi_s^2) = 0 ,$$

$$\frac{\partial E_\psi^\alpha}{\partial \tau}(0, t_s, \xi_s^1, \xi_s^2) = U_\psi^\alpha(t_s, \xi_s^1, \xi_s^2) , \quad (25)$$

$$P_\psi(\tau, t, \xi^1, \xi^2) = \bar{P}_\psi(t, \xi^1, \xi^2) + \int_0^\tau \hat{P}_\psi(\bar{\tau}, \xi^1, \xi^2) d\bar{\tau} ,$$

$$E_\psi^3(\tau, t, \xi^1, \xi^2) = \int_{\tau_0^*}^\tau \hat{E}_\psi^3(\bar{\tau}, t, \xi^1, \xi^2) d\bar{\tau} - \hat{E}_0^3(\tau_0^*(t, \xi^1, \xi^2), t, \xi^1, \xi^2) \tau_\psi^*(t, \xi^1, \xi^2) , \quad \psi = 0, \delta ,$$

where U_0^α , U_ψ^α , \bar{P}_0 , \bar{P}_ψ are velocity components and pressure at the shock surface and expressions for \hat{E}_0^3 , \hat{E}_ψ^3 , \hat{P}_0 , \hat{P}_ψ , τ_0^* , τ_ψ^* may be found in Ref. 8.

Equations (24a) are to be solved for E_0^1 and E_0^2 . They imply that the particle trajectories in steady flow are just the geodesics of the body surface. Once determined, Equations (25a), being linear o.d.e.'s, may be solved for the corrections E_ψ^α , $\psi = 0, \delta$ to give the particle trajectories:

$$\xi^\alpha = E^\alpha(\tau, t_s, \xi_s^1, \xi_s^2) , \quad \alpha = 1, 2 . \quad (26)$$

Equation (26) is then inverted to obtain

$$\xi_s^\alpha = Z^\alpha(\tau, t, \xi^1, \xi^2) \quad (27)$$

which is then inserted into (24d) and (25d) to obtain, simply by quadrature, the unsteady pressure

$$p = P(\tau, t, \xi, \eta) . \quad (28)$$

Thus the problem of determining the pressure for sufficiently slow unsteady motion in the Newtonian limit is reduced to solving the geodesic equations, a pair of nonlinear ordinary differential equations, for the body B.

3. CONICAL WINGS

We apply the formulation of the previous section to conical lifting vehicles, in particular conical wings with parabolic cross-section. Consider the conical wing (see Fig. 1) given by

$$xy = -\frac{\bar{\lambda} x^2}{2a^2} , \quad \bar{\lambda} = \pm 1 , \quad (29)$$

where a concave wing corresponds to $\bar{\lambda} = +1$ and a convex wing corresponds to $\bar{\lambda} = -1$. The cross-section in the plane $x = \text{const.}$ is a parabola. Surface coordinates $(\xi^1, \xi^2) = (\xi, \eta)$ for the body which are orthogonal may be chosen as follows:

$$\begin{aligned}
 x &= B^1(\xi, \eta) = \frac{\xi}{2} (dn(\eta, m) + \lambda cn(\eta, m)) , \\
 y &= B^2(\xi, \eta) = -\frac{\xi}{2} (dn(\eta, m) - \lambda cn(\eta, m)) , \\
 z &= B^3(\xi, \eta) = c \xi sn(\eta, m) ,
 \end{aligned} \tag{30}$$

where $m = (a^2 - 1)/(a^2 + 1)$, $c = a/(a^2 + 1)^{1/2}$ and sn , cn , dn are the Jacobi elliptic functions of modulus m .

Specifying the sweep back angle Λ and the angle ω from the centre line to the leading edge plane uniquely determines the parabolic conical body yielding

$$a = \frac{\tan(\frac{\pi}{2} - \Lambda)}{\sqrt{\sin 2\omega}} \tag{31}$$

with $\omega > 0$ for concave wings and $\omega < 0$ for convex wings. The surface coordinates are restricted to

$$0 \leq \xi \leq \frac{2}{dn(\eta_L, m) + \lambda cn(\eta_L, m)} , \quad |\eta| \leq \eta_L , \tag{32}$$

where η_L is given by

$$\frac{sn^2(\eta_L, m)}{cn^2(\eta_L, m)} = \frac{\sin 2\omega + \tan^2(\frac{\pi}{2} - \Lambda)}{(\cos \omega - \sin \omega)^2} . \tag{33}$$

For the above body, Equations (24) and (25) are readily solved to obtain the pressure to within quadrature (Ref. 8).

4. STABILITY DERIVATIVES

The pitching moment coefficient C_m , the stiffness derivative $-C_{m_\theta}$, and the damping-in-pitch derivative $-C_{m_{\dot{\theta}}}$ are defined by

$$C_m \equiv \frac{M}{\frac{1}{2} \rho_\infty U_\infty^2 S} = \theta(t)(-C_{m_\theta}) + \dot{\theta}(t)(-C_{m_{\dot{\theta}}}) \tag{34}$$

where the pitching moment

$$M(t) = - \int_B P(t, \xi, \eta) [(\xi Y_1(\eta) - h) n_2(\eta) - \xi Y_2(\eta) n_1(\eta)] \sqrt{g} d\xi d\eta \tag{35}$$

$$Y_1(\eta) = \frac{1}{2} (dn(\eta, m) + \lambda cn(\eta, m))$$

$$Y_2(\eta) = -\frac{1}{2} (dn(\eta, m) - \lambda cn(\eta, m))$$

$$n_1(\eta) = \frac{c}{2v(\eta)} (\lambda dn(\eta, m) - cn(\eta, m)) \tag{36}$$

$$n_2(\eta) = \frac{-c}{2v(\eta)} (cn(\eta, m) + \lambda dn(\eta, m))$$

S = planform area of the wing .

$$v(\eta) = \sqrt{c^2 - m^2 sn^2(\eta, m)}$$

5. RESULTS AND DISCUSSIONS

Systematic computations of the stiffness and damping-in-pitch derivative have been done for various combinations of the defining parameters in the following ranges: $0 < \alpha < 80^\circ$, $-30^\circ < \omega < 30^\circ$, $60^\circ < \Lambda < 80^\circ$ and $0 < h < 2/3$. It has been found profitable to present these results in relative form as $(-C_{m_\theta})/(-C_{m_\theta})_{f\ell}$ and $(-C_{m_\theta})/(-C_{m_\theta})_{f\ell}$, where

$$(-C_{m_\theta})_{f\ell} = 2 \sin 2\alpha \left(\frac{2}{3} - h\right)$$

$$(-C_{m_\theta})_{f\ell} = 4 \sin \alpha \left(\frac{3}{4} - \frac{5}{3}h + h^2\right)$$

are, respectively, the stiffness and damping-in-pitch derivative of the corresponding flat delta wing, i.e. when $\omega = 0$, as given in Ref. 9. We note that they are independent of the sweep-back angle Λ , and that $(-C_{m_\theta})$ is always positive but $(-C_{m_\theta})$ changes sign at $h = 2/3$.

These relative stability derivatives are, strictly, still dependent on the defining parameters α , ω , Λ and h . It turns out, interesting enough, that they are practically independent of the angle of attack α and the pivot axis position h for $20^\circ < \alpha < 75^\circ$ and $0 < h < 2/3$. This is to say that the spanwise concavity or convexity of a conical delta wing does not alter the dependence of the stability derivatives on α and h within the above ranges. Details of the computational results are as follows.

5.1 Λ -dependence

The dependence of the relative stability derivatives on the sweep-back angle Λ is shown in Figs. 2-5. It is observed that increasing Λ (i.e. more slender wings) decreases the damping-in-pitch derivative $(-C_{m_\theta})$ for both concave wings and convex wings. It also decreases the stiffness

derivative $(-C_{m_\theta})$ of convex wings but has little effect for concave wings. These conclusions hold true for any angle of attack α and for $0 < h < \frac{2}{3}$.

5.2 h -dependence

From the comparisons of Figs. 2a-c and 4a-d, which are for different h , we see that relative damping-in-pitch derivative is independent of the pivot axis position h for $0 < h < 2/3$ and for $0 < \alpha < 75^\circ$. The same conclusion holds also for the relative stiffness derivative (Fig. 3a,b and Fig. 5a,b). This near independence of the relative stability derivatives on h for $0 < h < 2/3$ is also shown explicitly in Fig. 6 for the case $\alpha = 20^\circ$ and $\omega = 20^\circ$, from which it is also seen that the relative stability derivatives vary rapidly with h for $h > 2/3$. One possible explanation for this is that in the vicinity of $h = 2/3$, $(-C_{m_\theta})$ changes sign and $(-C_{m_\theta})$ reaches minimum.

5.3 ω -dependence

From Figs. 2 and 3, it is seen that both (spanwise) concavity and convexity of the conical wing tend to decrease the damping-in-pitch and the stiffness derivative for $20^\circ < \alpha < 75^\circ$, and the maximum stability is reached near the flat delta wing. For smaller angles of attack, i.e. $\alpha < 20^\circ$, however, the trend is somewhat different. For these cases (see Figs. 4 and 5) the maxima of the stability derivatives are reached by slightly convex wings.

An explanation of the different trend for smaller angles of attack is that as α becomes small, variation in concavity or convexity of the wing alters significantly the flow around the wing. In contrast, for large $\alpha \gg \omega$, the air flow "sees" mainly the wing as a flat delta wing formed by the leading edge plane.

5.4 α -dependence

The explicit dependence of the relative stability derivatives on the angle of attack α is illustrated in Figs. 7 and 8. The mild dependence on α for $20^\circ < \alpha < 75^\circ$ is noted.

5.5 In most cases calculated, the damping-in-pitch derivative is positive, indicating dynamic stability of the steady flight. However, Fig. 2b shows that for highly concave and very slender wings the damping-in-pitch derivative can become negative, i.e. aerodynamically unstable. This is consistent with an earlier investigation of Hui and Tobak (Ref. 4) on aerofoils where it was found that "the pitching motion of a sharp-nosed aerofoil having (chordwise) concave surfaces will tend toward dynamic instability over a range of axis positions if the curvature of the surfaces is increased beyond a certain value." It was noted (Ref. 4) that this condition of instability arises in part out of a destabilizing contribution from $(-C_{m_q})$, and this unusual circumstance has its origin in the radical rearward displacement experienced by the aerodynamic center of the loading due to angle of attack as the concavity, spanwise or chordwise, of the wing surface is increased.

For application of the present theory to prediction of stability of hypersonic conical lifting wings at finite flight Mach number M_∞ and $\gamma > 1.0$, we remark that the present theory gives the limiting values as $M_\infty \rightarrow \infty$ and $\gamma \rightarrow 1$. It is, however, known that (Refs. 10 and 11) decreasing M_∞ and increasing γ both have the effect of decreasing the damping-in-pitch derivative, possibly rendering it negative under certain circumstances.

Finally, we remark that unsteady Newton-Busemann flow theory as developed above is the rational limit of gasdynamics and applied well to hypersonic flowfields with no stagnation point. These include flow over lifting conical wings, or sharp-nosed or sharp-edged bodies. For blunt bodies, straightforward application of the theory tends to give rather poor results, due to the singularity at the stagnation point inherited in the Newtonian impact model. Some modifications are therefore needed. In this regard, it has recently been shown by Tong and Hui (Ref. 12) that the embedded Newtonian flow concept of Seiff and Whiting (Ref. 13) provides just the needed modifications. Examples of good agreement of the unsteady embedded Newton-Busemann flow theory with experiments are given in Ref. 12.

REFERENCES

1. Orlik-Rückemann, K. J., "Dynamic Stability Testing of Aircraft--Needs Versus Capabilities," Progress in Aerospace Sciences, Vol. 16, No. 4, Pergamon Press, New York, pp. 431-447, 1975.
2. Townsend, L. H., "Research and Design for Lifting Re-entry," Progress in Aerospace Sciences, Vol. 18, No. 1, Pergamon Press, New York, pp. 1-80, 1979.
3. East, R. A., "Hypersonic Static and Dynamic Stability," Parts I-III. Von Karman Institute for Fluid Dynamics, 1984 Lecture Series.
4. Hui, W. H. and Tobak, M., "Unsteady Newton-Busemann Flow Theory, Part I: Airfoils," AIAA J., Vol. 19, No. 3, pp. 311-318, 1981.
5. Hui, W. H. and Tobak, M., "Unsteady Newton-Busemann Flow Theory, Part II: Bodies of Revolution," AIAA J., Vol. 19, pp. 1272-73, 1981.
6. Hui, W. H., "Unsteady Newton-Busemann Flow Theory, Part III: Frequency Dependence and Indicial Response," The Aeronautical Quarterly, Vol. 33, pp. 311-328, 1982.
7. Hui, W. H. and Van Roessel, H. J., "Unsteady Newton-Busemann Flow Theory, Part IV: Three-Dimensional," AIAA J., Vol. 22, pp. 577-578, 1984.
8. Van Roessel, H. J., "Steady and Unsteady Three Dimensional Flow Theory," Ph.D. Thesis, University of Waterloo, Canada, 1985.
9. Hui, W. H., Platzler, M. F., and Youroukos, E., "Stability of Oscillating Supersonic/Hypersonic Wings at Arbitrary Angles of Attack," AIAA J., Vol. 20, pp. 299-304, 1982.
10. Hui, W. H., "Stability of Oscillating Wedges and Caret Wings in Hypersonic and Supersonic Flows," AIAA J., Vol. 7, No. 8, pp. 1524-1530, 1969.
11. Hui, W. H., "An Analytic Theory of Supersonic/Hypersonic Stability at High Angles of Attack," AGARD CP-235, Dynamic Stability Parameters, Paper No. 22, May 1978.
12. Tong, B. G. and Hui, W. H., "Unsteady Embedded Newton-Busemann Flow Theory," J. of Spacecraft and Rockets, Vol. 33, pp. 129-135, 1986; also Vol. 24, p. 96, 1987.
13. Seiff, A. and Whiting, E. E., "Calculation of Flow Fields from Bow-Wave Profiles for the Down Stream Region of Blunt-Nosed Circular Cylinders in Axial Hypersonic Flight," NASA TN D-1147, 1961.

ACKNOWLEDGEMENTS

This work was supported by the Natural Science and Engineering Research Council of Canada.

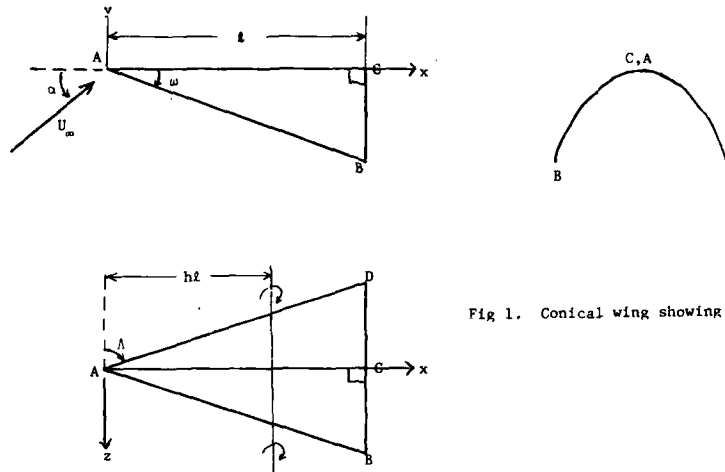


Fig 1. Conical wing showing notation

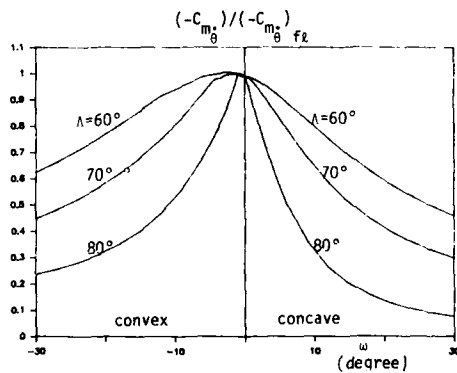


Fig. 2a Relative damping-in-pitch derivative $(-C_{m_g})/(-C_{m_g} f_L)$ vs ω of parabolic conical wing.
 $\alpha = 40^\circ$, $h = 0$

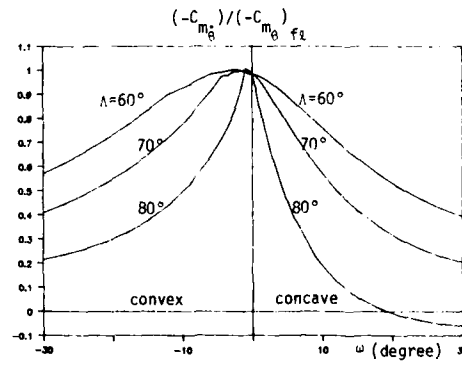


Fig. 2b Relative damping-in-pitch derivative $(-C_{m_g})/(-C_{m_g} f_L)$ vs ω of parabolic conical wing.
 $\alpha = 40^\circ$, $h = l_2$

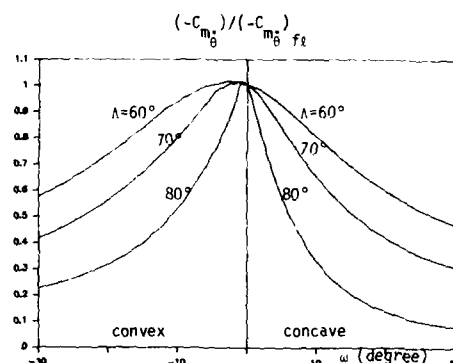


Fig. 2c Relative damping-in-pitch derivative $(-C_{m_{\theta}})/(-C_{m_{\theta}} f_L)$ vs ω of parabolic conical wing. $\alpha = 40^\circ$, $h = 2/3$

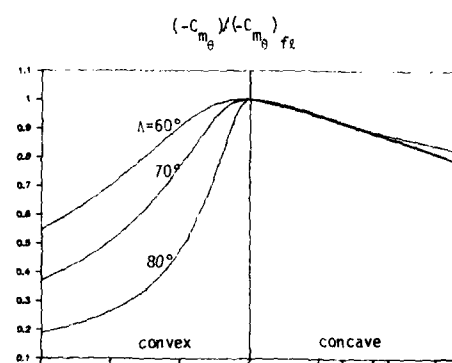


Fig. 3a Relative stiffness derivative $(-C_{m_{\theta}})/(-C_{m_{\theta}} f_L)$ vs ω of parabolic conical wing $\alpha = 40^\circ$, $h = 0$

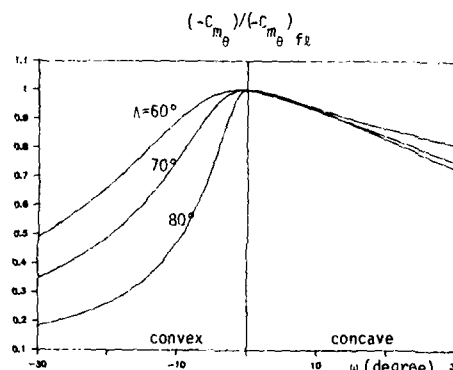


Fig. 3b Relative stiffness derivative $(-C_{m_{\theta}})/(-C_{m_{\theta}} f_L)$ vs ω of parabolic conical wing $\alpha = 40^\circ$, $h = 1/2$

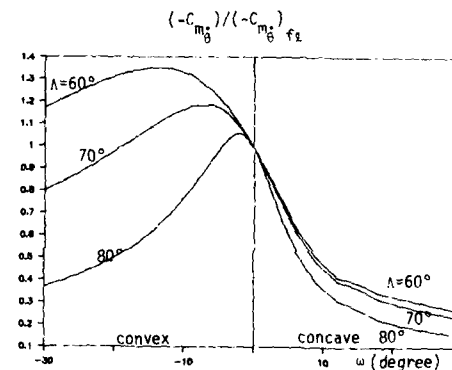


Fig. 4a Relative damping-in-pitch derivative $(-C_{m_{\theta}})/(-C_{m_{\theta}} f_L)$ vs ω of parabolic wing. $\alpha = 5^\circ$, $h = 0$

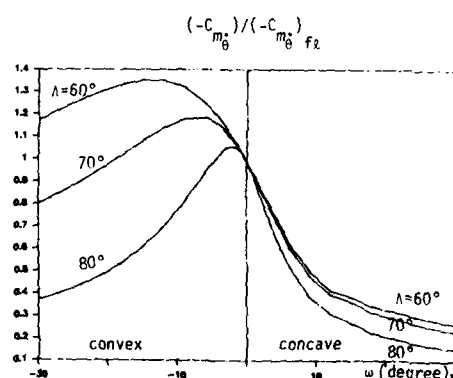


Fig. 4b Relative damping-in-pitch derivative $(-C_{m_{\theta}})/(-C_{m_{\theta}} f_L)$ vs ω of parabolic wing. $\alpha = 5^\circ$, $h = 2/3$

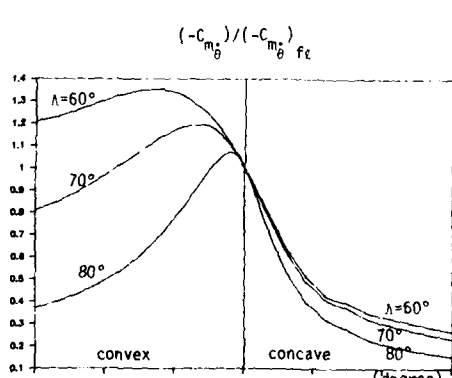


Fig. 4c Relative damping-in-pitch derivative $(-C_{m_{\theta}})/(-C_{m_{\theta}} f_L)$ vs ω of parabolic wing. $\alpha = 15^\circ$, $h = 0$

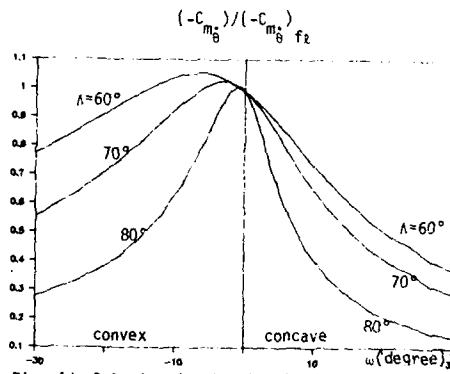


Fig. 4d Relative damping-in-pitch derivative $(-C_{m_\theta})/(-C_{m_\theta} f_L)$ vs ω of parabolic wing. $\alpha = 15^\circ$, $h = \frac{1}{2}$.

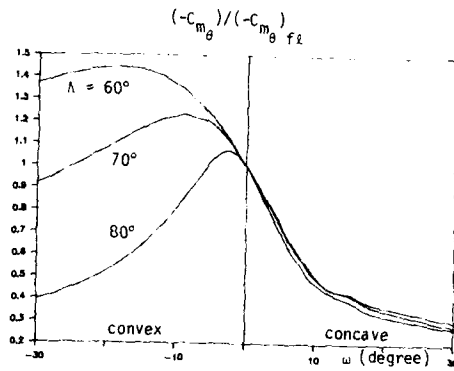


Fig. 5a Relative stiffness derivative $(-C_{m_\theta})/(-C_{m_\theta} f_L)$ vs ω of parabolic conical wing. $\alpha = 5^\circ$, $h = 0$.

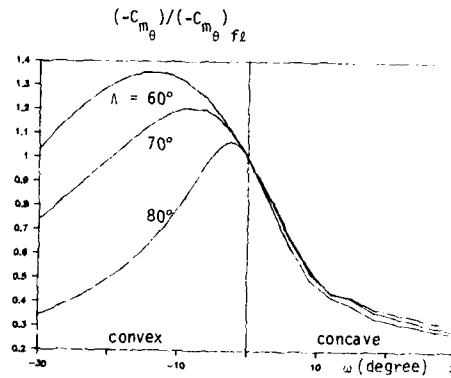


Fig. 5b Relative stiffness derivative $(-C_{m_\theta})/(-C_{m_\theta} f_L)$ vs ω of parabolic conical wing. $\alpha = 5^\circ$, $h = \frac{1}{2}$.

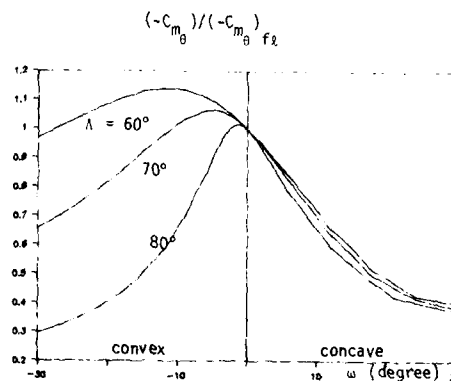


Fig. 5c Relative stiffness derivative $(-C_{m_\theta})/(-C_{m_\theta} f_L)$ vs ω of parabolic conical wing. $\alpha = 10^\circ$, $h = 0$.

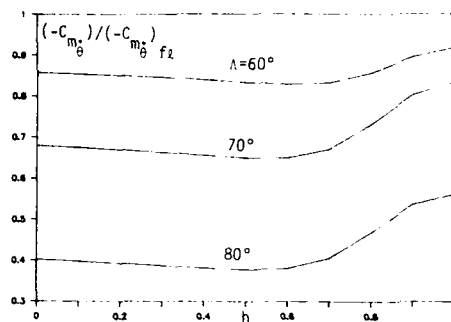


Fig. 6a Relative damping-in-pitch derivative $(-C_{m_{\theta}})/(-C_{m_{\theta}})_{f_L}$ vs h of convex parabolic conical wing. $\alpha = 40^\circ$, $\omega = -15^\circ$

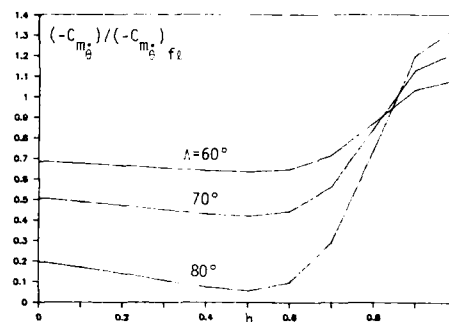


Fig. 6b Relative damping-in-pitch derivative $(-C_{m_{\theta}})/(-C_{m_{\theta}})_{f_L}$ vs h of concave parabolic conical wing. $\alpha = 40^\circ$, $\omega = 15^\circ$

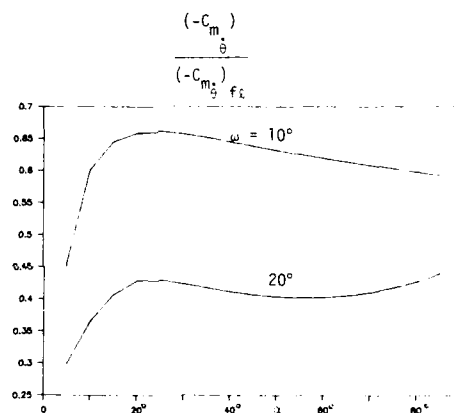


Fig. 7 Relative damping-in-pitch derivative $(-C_{m_{\theta}})/(-C_{m_{\theta}})_{f_L}$ vs α of parabolic conical wing. $\Lambda = 70^\circ$, $h = 0$

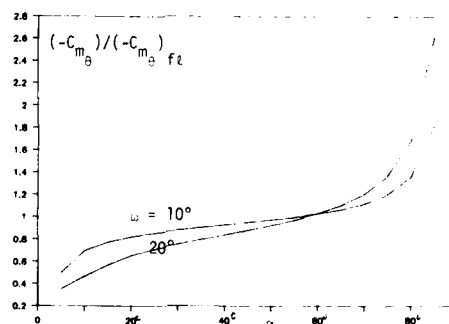


Fig. 8 Relative stiffness derivative $(-C_{m_{\theta}})/(-C_{m_{\theta}})_{f_L}$ vs α of parabolic conical wing. $\Lambda = 70^\circ$, $h = \frac{1}{2}$

LIFTING BODIES - AN ATTRACTIVE AERODYNAMIC CONFIGURATION CHOICE FOR HYPERVELOCITY VEHICLES

Alfred C. Draper and Melvin L. Buck
Aeromechanics Division
Air Force Wright Aeronautical Laboratories
Wright-Patterson AFB, Ohio 45433-6553, USA

SUMMARY

The Flight Dynamics Laboratory has focused activity on Lifting Body aerodynamic research for the development of analytical, experimental, and design methods. Lifting bodies have a set of unique properties which make them particularly attractive for multiple applications. These unique properties including better aerodynamic efficiency at high altitudes and high velocities, reduced TPS weight, and efficient payload packaging are discussed. A brief chronology is given of the Lifting Body Configurations investigated by the Flight Dynamics Laboratory, along with their aeroperformance capabilities including the ASSET, PRIME, the X-24A, and the X-24B. Also included is a brief discussion of lifting body applications at supercircular velocities such as the SORTIE.

A portion of the paper addresses the impact of basic geometric and component effects on aerodynamic performance parameters. These results were then translated into a unique aerodynamic configuration which eliminates the aft vertical fins without degrading the hypersonic lift-to-drag ratio while maintaining directional stability. Additionally, the paper addresses, their benefits and applicability. Specifically, the more significant methods such as the Hypersonic Arbitrary Body Program (HABP), PANAIR, Euler, Parabolized Navier Stokes (PNS), and Navier Stokes (NS) codes are discussed. Experimental capabilities and needs are discussed and finally, long term goals for future lifting body configurations are assessed.

INTRODUCTION

The technology advances that have been made and the availability of that technology has presented the challenge, the opportunity, and the emphasis to accelerate the entry into the era of hypersonic flight. The capability will include operations from point to point on the earth's surface, earth to space, and space to earth. The system designer will continue to search and select vehicle concepts which will provide the desired performance at minimum cost. In any assessment of advanced concepts, it is necessary to emphasize that a broad spectrum of options exists relative to the candidates for lifting vehicles. It is clear that performance considerations suggest that lift will be a primary prerequisite of any future hypersonic vehicles. It is particularly beneficial and useful to give consideration to the general evolution of advanced vehicle concepts as background information. Pragmatic considerations and data availability clearly indicate that reasonable levels of aerodynamic performance are a necessity for hypersonic flight vehicles.

The Advantages of Lift

Classically, drag has been employed to control the level of deceleration of re-entry vehicles and to dissipate the kinetic energy. Lift is also of benefit and enables the vehicle to decelerate at higher altitudes for the same velocity. The range of lift coefficients available effectively defines the re-entry corridor for any configuration. The question of heating is more complex; for the stagnation point heating is reduced at the higher angles-of-attack but other points on the configuration offer special challenges. Lift is employed primarily to obtain maneuverability and the hypersonic lift-to-drag ratio traditionally establishes the down range and cross range capability of re-entry vehicles. This capability can translate in terms of inclination angle changes and recall times from different orbital conditions. Generally speaking, it can be shown that the lifting maneuverable vehicle offers substantial performance benefits; consequently, we will focus on the configuration aspects which offer the most promising potential for a wide spectrum of applications at hypersonic and re-entry speeds. Figure 1 summarizes some of the payoffs of aeroperformance efficiency in terms of cross range, plane change capabilities, and return times.

Configuration Classes

The three most likely candidates for lifting re-entry configurations are the winged/body, the lifting body, and the blended body. Our discussion will generally address the lifting and blended body configurations. The winged/body or winged gliders such as the Dyna Soar have their place if the lower altitudes and velocities are of special interest. The winged vehicles or winged/body configurations are generally characterized with lower sweeps and higher aspect ratios. They further can profit from more "conventional" leading edges and contoured surfaces with reduced base areas in order to improve the low and mid speed performance. Obviously, terminal and landing characteristics can be enhanced as a result. If hypervelocity performance and growth potential are the high value considerations; however, the lifting or blended body configurations appear particularly attractive. In view of the many benefits associated

with the lifting or blended bodies, we will concentrate our discussion on this class of configurations and their utility as candidates for hypervelocity vehicle applications. In any event, the importance of the aeroconfiguration is traced in Figure 2 in terms of a key technology focus and a critical design driver.

The Advantages of Lifting Bodies

It has been shown by many authors that the lifting body offers substantial benefits in terms of its volumetric efficiency which can be viewed as a first order indicator of its payload carrying capability. High volumetric efficiency, $V^2/3/S_w$, also translates itself into reduced wetted area which means reduced skin friction drag hence, a higher hypersonic lift-to-drag ratio which, in turn, results in higher levels of maneuverability both in terms of longitudinal and lateral range. Wetted area also is a first order indicator of the acreage which must be thermally protected; consequently, any reduction means substantial dividends in terms of reduced thermal protection system weight. This, again, can be extended into reduced structural weight and total systems weight. A dual advantage can be experienced here for the lifting body can generally be sized smaller for the same payload and mission requirements largely because of the increased volume. If the limitation is weight rather than volume, the payoffs are still quite measurable in terms of launch or thrust requirements. Figure 2 again shows some of these advantages while Figure 3 indicates the general trend of volumetric efficiency with hypersonic lift-to-drag ratio.

Returning to its aerodynamic properties, the lifting body has a higher angle-of-attack for maximum lift and, further does not experience the rigid clear stall characteristics of winged vehicles. This wide range of angle-of-attack reflects itself in an expanded re-entry corridor. Again, from an aerodynamic heating viewpoint, the lifting/blended body can minimize juncture areas and interference heating. This reduction in juncture points also permits the configuration to be tailored for increased survivability through reduced observability. From a stabilization perspective, the lifting body lends itself to many candidate options for simplified controls. For example, novel stabilization possibilities exist such as the positive compression sharing approach. This approach is the precise contouring of the body in such a manner that directional stabilizing pressures are generated at hypersonic speeds to provide maximum effectiveness with low drag. The compression sharing concept has also demonstrated yaw stability. Lifting body configurations have been developed which have allowed elimination of the aft vertical fins of the vehicles without degrading the hypersonic lift-to-drag ratio and directional stability. Figure 4 displays some of these configuration variations for directional stability including the elimination of the vertical fins.

As previously indicated, the lifting body also can ease some of the propulsion and launch considerations through its reduced weight. Further, most lifting body configurations significantly ease the rocket engine and on-board tankage integration problems. Depending on the mode, the launch stability can be aided by reduced booster fins for stabilization and a potential reduction of launch interference factors.

Perhaps one of the more attractive features of the lifting body is its growth potential from a number of perspectives. We have already mentioned its corridor width potential which enables a wide spectrum of altitude choices. It has an inherent capability for synergetic orbital transfer applications in that significant plane changes can be made resulting in a wide spectrum of orbital inclination angles. This, then, naturally suggests the application to higher energy orbits up to geosynchronous or geostationary along with orbital transfer maneuvers from GEO to LEO to GEO with the resulting capability of performing a successful entry at supercircular velocities along with the attendant thermal management of both the convective and hot gas radiative heat transfer. This capability will be discussed further in the sections addressing maneuverable orbital transfer vehicles and the SORTIE configuration.

Finally, another area which profits from the use of the lifting body is the multi-staged system. For many of the reasons previously cited; the lifting body offers an attractive candidate for both the first and second stage of a two staged system. Through the use of simple geometries, the mating arrangements between the two stages can be greatly facilitated even to the point of employing semi-submerged arrangements. Special attention can be given to improved carriage and separation techniques for the total system for straightforward "drop away" techniques can be used. Integration techniques with different types of propulsion systems can also be accommodated in a minimally disruptive manner. Simply stated, the lifting/blended body is designed not just to survive the hypervelocity environment, but to be at home in it. A representative collection of configurations investigated in considerable depth is displayed in Figure 5.

The Chronology of Lifting Bodies at the Flight Dynamics Laboratory

Serious lifting body configuration programs were being addressed in the early 60's, both at NASA and at the Air Force's Flight Dynamics Laboratory. NASA initiated their activities with the M1 and M2 configurations at Ames, which culminated in the flight testing of the M2F1, M2F2, and M2F3 at Dryden. Langley's early activities were effectively converged with the testing of the HL-10. The Air Force's initial activities centered around the WADD 11, or "Lead Sled" configuration, which was offered as a candidate during the Phase a effort of the Dyna Soar program. The design was analytically and experimentally investigated and proved to be an attractive alternative.

although initially, with far less technical supporting data than that which existed for the winged configuration. Figure 6 shows the WADD II lifting body configuration along with other typical point designs.

In order to develop a comprehensive research program, the Flight Dynamics Laboratory established a process which initially addressed the configuration technology in its most fundamental elements of parametric variations with simple geometries. These parametrics included consistent variations in basic geometric characteristics such as wing sweep, leading edge radii, nose radii, bluntness ratio, thickness, planform, cross-section, body profile angles, and body classification; i.e., conoids, elliptical cones, etc. The procedure has been to compare theoretical and analytical models with experimental data to determine the adequacy of correlation and to postulate techniques to better represent the characteristics of the configuration. The hypersonic lift-to-drag ratio data has, by convention, been defined at 200,000 ft altitude and at a velocity of 20,000 fps. Once a reasonably accurate representation was derived to handle simple geometries, then a consistent approach was employed for configuration "build-up", which involved sizing, location, and configuring of various aerodynamic control surfaces and shaping, which could satisfy the demands of trim, stability, and controllability. After confidence was achieved in our ability to handle generalized configurations, various point designs were developed which enabled the convergence and interaction of the aerodynamic, aerothermodynamic, structural concepts, and control requirements for vehicle concepts synthesized to fulfill specific performance, weight, and payload constraints. Figure 6 further displays this process from parametric variations, configuration build-ups, and point designs.

As previously mentioned, an example of the early work was the design of the WADD II configuration with a hypersonic lift-to-drag ratio of approximately 1.5, quite comparable to the NASA M2F2 configuration. Another generic family of lifting body configurations was developed and designated as the MDF series. The approach was straightforward in that the configurations were designed within the constraints demanded hypersonically and by aerodynamic heating. Nose and leading edge bluntness, sweep, and lower surface geometry were established, but the designs were carefully developed for shaping, contour, and camber of the upper surface to achieve improved terminal performance. A complete family of these configurations employing this dual design approach was addressed and actually employed classical airfoil sections molded into lifting bodies. The hypersonic lift-to-drag ratios generally spanned the range from 1.0 to approximately 1.6, but with substantially improved subsonic L/Ds and characteristics. The MDF-1 configuration, which molded a Clark Y airfoil into the lifting body, can show a lineage relationship with the SV-5 configuration used in both the PRIME and PILOT programs. The MDF-1 configuration is shown in Figure 7 along with the SORTIE configuration now to be discussed.

An additional series investigated was postulated as potential configurations for entry at supercircular velocities. This was essentially a series of modified elliptical cones designated as the SORTIE family of configurations. The lift-to-drag ratios achieved were between 0.75 and 1.2 with near neutral stability to facilitate large modifications in the lift coefficient. This configuration series focused primarily on the technologies which required solution for re-entry from high energy orbits, including GEO. Re-entry velocities of approximately 34,000 fps from orbital altitudes of 20,000 nautical miles were considered. Problems associated with flight at velocities from 25,000 to 34,000 fps can be many, but we will concentrate on the primary problems. The most critical problems are heating and stability. At supercircular re-entry velocities the gas encountered is highly dissociated, partially ionized, and at twice the enthalpy levels as that encountered during low earth orbital re-entry. Hot gas radiation of the shock layer becomes important and significant deficiencies in heating values may occur depending on the prevailing state of equilibrium. The heat transfer rates will be substantially higher than from low earth orbital lifting reentry. Since higher dynamic pressure are encountered, stability problems can become more acute. The lateral, directional, and longitudinal stability characteristics of high energy reentry vehicles at angle-of-attack with associated control also can be demanding problems.

The lifting body configuration class employed, as was previously stated, was a series of asymmetric elliptical cones with various degrees of nose blunting evaluated. Flats were employed on the upper surface and on each side primarily for directional stability. Fineness ratios were also varied. Various control devices were investigated, including canards, elevons, flaps, cambered bodies/nose, and jet spoilers. The delta canards and elevons were evaluated separately, and in combination. Flaps mounted on the trailing edge proved to be quite effective and did not cause trim stability problems and appeared to be the preferred control devices from a minimum heating and interference viewpoint. Despite the fact that a combination of canards and elevons yielded the greatest trim power, center of gravity range, and highest trim L/Ds. Aerodynamic drag devices, to independently modulate the drag relative to the lift, appeared to also offer promise. Two techniques were evaluated; the ejectable drag brake and the slide-trolley drag break which would be used during the initial portions of supercircular re-entry. Some of these control and drag devices are shown in Figure 8 in a composite fashion for economy of illustration. Many were tested as part of a comprehensive configuration/control surface research program.

It became apparent, however, that the prime focus for lifting body designs should initially be for low earth orbits. The Laboratory efforts were consequently shifted toward configurations which could generate high aerodynamic and performance efficiency during re-entry. The high L/D configuration technology, in addition to significant

performance gains, also served as a focus and catalyst for identification of new and challenging research and technology problems. This evolution in configuration research is depicted in Figure 9 which traces the trend as a function of time.

The high lift-to-drag ratio vehicle shapes are generally characterized by highly swept configurations possessing low bluntness ratios and high fineness ratios. These configurations tend to operate at reduced angle-of-attack to achieve their maximum lift-to-drag ratios; e.g., on the order of 3.0. Obviously, the leeward or upper surface, with its expansion pressures, must be treated more accurately with deliberate tailoring to improve aerodynamic efficiency. Viscous effects, as reflected in skin friction force terms, are critical, and wetted area becomes important.

Viscous interaction and boundary layer transition were also identified for more precise treatment. Interaction effects can be masked by blunt leading edges, but will become more important for consideration in the slender designs. Aerodynamic heating, because of the changes in angle-of-attack and sweep back conditions, was also identified for more in-depth assessment. This, of course, was also aggravated by the increase in flight times and could likely necessitate advanced cooling techniques. Further, because of the nature of not only the flight path, but also the generic configurations considered for increased performance efficiency, extensive use of aerodynamic control surfaces appeared to be desirable. This then enabled the focusing of research not only on control effectiveness and design, but also on the aerothermodynamic problems encountered with such deflected surfaces. Increased efficiency in entry design also suggested enhanced research in the area of energy management which could equate to increased sophistication with the addition of more functions and requirements.

The initial efforts with high lift-to-drag ratio configurations were characterized with cautious optimism and approached the feasibility question both analytically and experimentally. Both fixed and variable geometry configurations were investigated with the intent of making the designs amenable to both the high speed and low speed performance characteristics; that is to achieve high aerodynamic efficiency at hypersonic speeds with acceptable terminal performance. Favorable interference configurations were also assessed, but for the most part, were discontinued because of the added complexities associated with localized heating problems, increased TPS, and added weight.

A generic family of configurations evolved which were characterized with large increases in the volumetric efficiency parameter. These configurations minimized the wetted area and employed changes with the profile angles which resulted in volume increases. Simply stated, the designs took full advantage of the lessons previously learned relative to bluntness, sweep, lower surface geometry, length, and fineness ratio. The high L/D configurations were comprehensively assessed from their aerodynamic feasibility, their aerothermodynamic acceptability, performance flexibility, the levels of volumetric efficiency, size and comparative weights, including choice of thermal protection system and structural concepts. The analytical results, experimentally verified, indicated that high L/D vehicle configurations had progressed to the point where a stable vehicle with a high volume could be designed which was controllable and which could sustain the heating environment with feasible TPS structural subsystems and competitive weights. The program in the Flight Dynamics Laboratory essentially was converged into four highly acceptable designs; i.e., the FDL-5, FDL-6, FDL-7, and FDL-8 configurations, the latter of which evolved into the X-24B and X-24C configurations. These configurations are displayed in Figure 10. Comprehensive force moment, pressure and temperature tests were conducted across the complete Mach number range from subsonic through hypersonic Mach numbers of 19.0. The lateral or cross range performance capabilities of these candidate configurations are shown in Figure 11, along with the variation in hypersonic lift-to-drag ratio.

Concurrent with the configuration research investigations and the lessons learned from the information obtained through the ASSET and PRIME flight test programs were being exploited. These are two significant programs that need to be discussed.

The ASSET Program objectives can be summarized as: 1) the correlation of data from hypersonic flight test with ground facility data, 2) the verification of analytical theories and prediction techniques, and 3) the evaluation of structural concepts and materials for hypersonic vehicles. The actual vehicle configuration took advantage of, and evolved from, a research configuration, WLB-1, included within the Laboratory's program. The ASSET configuration, with a L/D 1.25, consisted of a flat bottom, 70 degree swept delta with a planform area of 14 square feet blended with a cone cylinder lifting body. Figure 12 illustrates the relatively simple vehicle configuration and its characteristics which were deliberately selected to simplify analysis, provide a relatively large volume, and allow the maximum use of available wind tunnel data. The vehicles' wing loading was 85 and the angle-of-attack range varied from 20 through 40 degrees. Six vehicles were launched to altitudes ranging from 166,000 to 212,000 ft and at velocities of 13,000 to 19,500 fps. Figure 13 summarizes a typical trajectory flown from the Eastern Test Range. The ASSET flight program provided the first significant hypersonic flight information applicable to lifting re-entry technology. The aerodynamic pressures, temperatures, heat transfer, material, and structural information obtained proved especially beneficial in the evaluation and understanding of the data obtained from subsequent programs, including ground test. The thermal protection employed was metallic and re-radiative with stable shape geometry and has proved to be particularly valuable relative to the understanding of the material capabilities and the evolution of structural concepts.

The PRIME Program

As previously indicated, the MDF-1 configuration can show a lineage relation with the SV-5 lifting body configuration employed in the PRIME and PILOT programs which have been designated the X-23 and X-24A programs, respectively. The programs had a component relationship with the PRIME being the hypersonic unmanned vehicle and the PILOT being its manned trisonic counterpart. The PILOT or X-24A program will be discussed later in this paper. The objectives of the PRIME program can be summarized as: 1) the acquisition of ablative heat shield and aerodynamic data, 2) the demonstration of accurate guidance to the recovery point, 3) the demonstration of cross range maneuvering, 4) vehicle recovery, and 5) a design for performance with minimum weight. The configuration, termed the SV-5, was a lifting body with a sweep back of 77° and a hypersonic lift-to-drag ratio of approximately 1.3. Its lower surface was flat and its wing loading was 67. It operated at angles-of-attack from 21° to 52° and at a maximum velocity of 25,600 fps and a maximum altitude of 400,000 ft. Figure 14 presents a test mission profile for the PRIME. Three flights were flown from the Pacific Missile Range with a primary thermal protection system which was ablative; however, stable shape geometry was maintained since the temperature levels achieved were generally alleviated by the re-radiative properties of the materials used. Pressure, force, temperature, heat transfer, hinge moments, and stability information was obtained from the flight test, as well as the integrity of the thermal protection system and structural concept. Post-flight wind tunnel tests, Figure 15, were conducted with a recovered vehicle in order to assess any effects on the aerodynamic characteristics after the ablative thermal protection system had charred. Based on these tests and data acquired, a simple method was devised to simulate ablative effects on sub-scale wind tunnel models.

Aeromaneuvering Orbital Transfer Vehicles

In order to broaden the spectrum for application of lifting bodies; configurations and performance potential for orbital plane change vehicles were also investigated, not only to identify the benefits, but to also highlight some of the technology problems and areas which could profit from future research.

Orbital transfers, or inclination angle changes, can be made either purely propulsively or by use of aerodynamic forces to change the plane. As the plane change angle increases, the pure impulse propulsive requirements become excessive, even to the point where moderate to large plane changes are not practical. If orbital transfer vehicles are designed to achieve a reasonable value of hypersonic lift-to-drag ratio, then a combination between the propulsive and aerodynamic forces make not only large plane changes practical, but by the use of this synergetic maneuver, moderate plane changes can be effected at substantially reduced velocity. At hypersonic lift-to-drag ratios near 1.0, no significant advantages are apparent at the lower angles, and some penalty may actually be incurred due to the increased weight; but as the lift-to-drag ratio increases to 1.5 through 3.0, performance benefits are clearly evidenced as shown in Figure 16. Further benefits can be achieved with use of the aero-cruise mode if low levels of thrust are maintained to offset the drag during the synergetic maneuvers in that even lower velocities and less propellant are required and the range of change in inclination angle is extended. During calculated maneuvers; optimum bank angle, angle-of-attack, entry angle, thrust alignment, and thrusting procedures were investigated. Steeper optimum bank angles resulted from lower lift-to-weight ratios and high lift-to-drag ratio values. This combination clearly resulted in greater plane change efficiency by reducing drag losses and directing more of the lift force toward plane change and less toward keeping the aerospace vehicle airborne. Since the higher L/D vehicles penetrate deep into the atmosphere, it might be assumed that a greater velocity impulse would be required to exit the atmosphere. This is not the case, for despite the penetration, less impulse and total velocity increments are required for re-establishment of the new orbital mode. The lifting body, with high aerodynamic efficiency, is particularly suited for the synergetic plane change maneuver.

During nominal re-entry, minimum times are spent at high velocities, altitudes, and peak temperatures, for the vehicle simply passes through these conditions. If synergetic maneuvers are made, however, substantial and repetitive flight times may be spent at these conditions thereby making the designs at low densities very important. The vehicle most likely will also have to sustain multi-peak heat pulses and still maintain stable shape geometry, be reliable, and hopefully reusable for orbital plane changes both from Low Earth Orbit (LEO) to LEO, High Earth Orbit (HEO) to LEO and Geocentric Earth Orbit (GEO) to LEO. Simple lifting geometries, or aeromaneuvering core vehicles, have been derived. These configurations can be modified and further augment their lifting area through the use of inflatable chines that result in high sweep and delta planforms. Alternate configurations using different lightweight structures were also investigated. Figure 17 indicates some of the representative configurations assessed, while Figure 18 shows an aeromaneuvering orbital transfer vehicle of the high L/D class. One of the more productive areas for additional research with this class of configuration is associated with the aeropropulsive interfaces if the aerodynamic and propulsive force are blended in an efficient manner such that the total vehicle/configuration concept can be optimized.

If the rocket is pulsed or burned in a throttled condition at a high enough altitude where it can function as an effective propulsion component without dissipating the system, and if the altitude is chosen where the aerodynamic forces are still of consequence; then a most effective performance and operational capability can result.

Obviously, various levels of internal propellant are possible, as well as alternate options for external tankage as shown in Figure 19. A wide variety of tank arrangements are possible, some of which could be effective for repetitive synergetic flights, depending on the flight paths employed.

X-24

The X-24A project was the second flight test project to use the lifting body re-entry configuration. The first project, as previously discussed was titled PRIME (Precision Recovery Including Maneuvering Entry) used three subscale unmanned SV-5s which were boosted to orbital speeds on Atlas boosters. This program provided data, and a feasibility demonstration of the SV-5 configuration in the technical areas of aerodynamics, stability, control, heat protection, and maneuverability covering the speed range from orbital velocity to Mach 2.0.

The purpose of the second project, the X-24A project, called PILOT (Piloted Low Speed Test), was to investigate maneuverable lifting body flight from the low supersonic speed range to touchdown. One of the main X-24A project objectives was to gather data on and to prove that the configuration could be maneuvered to a safe horizontal unpowered landing at a pre-selected landing site. Twenty-eight successful X-24A landings accomplished this objective. The PRIME was mentioned earlier in the paper (Figure 14) and will not be discussed further. A few words, however, will be given on the low speed flight test. The X-24A flight vehicle is shown in Figure 20. The vehicle demonstrated good landing characteristics and achieved a maximum subsonic L/D of 4, a very respectable subsonic L/D for such a low aspect ratio vehicle. Handling qualities were excellent. Figure 21 shows some comparisons between flight and ground test data. Generally the comparisons were very favorable.

As noted earlier our attention was focusing on how to achieve high lift-to-drag ratio at hypersonic speeds in useful vehicles. One of the latter configurations examined was the FDL-8. This was an attempt to develop a flight test vehicle to capture the nature of terminal flight for high hypersonic L/D vehicles. The FDL-8 configuration was translated into the X-24B flight vehicle. This was accomplished by modifying the X-24A. The fineness ratio was increased by extending the body approximately 14 ft and blending the body into aft strakes. The similarity is apparent in Figure 22 where the X-24A and X-24B are shown. Figure 23 shows the X-24A structural modification while Figure 24 points out the design features.

The flat bottom and high sweep angle contributed to the high hypersonic L/D while the three degree nose ramp provided the proper hypersonic trim conditions. The three-inch leading edge radius and 60-degree side body angle were the result of aerodynamic reentry heating considerations. Flared out upper and lower flaps provided stability necessary at high speed. Boattailing these surfaces toward the faired position increased the subsonic L/D for acceptable landing performance. The double delta planform was necessary for the X-24B application in order to move the center of pressure aft. This was required because of the aft center of gravity (cg) resulting from the location of the test aircraft systems - rocket engine, propellant tanks, propellant, existing main landing gear position, etc. Considerable wind tunnel testing in the subsonic regime was conducted to meet the above hypersonic constraints and provide good low speed characteristics. Figure 25 shows development of the configuration using the wind tunnel as an analog. In this case we were concerned about flow separation just forward of the fins at subsonic speed and were contouring the body to avoid the problem.

The flight research program was very successful and consisted of 6 glide flights and 24 powered flights. At the completion of these flights, 6 additional glide flights were flown for checkout of 3 new pilots. The 36 flights were flown between August 1973 and November 1975 gathering data to determine performance, handling qualities and stability and control from subsonic, transonic and supersonic Mach number up to a maximum Mach number of 1.76. Predictions of flight characteristics were based on wind tunnel data; therefore, verification of these data was a primary objective of the program. Figure 26 shows a comparison of flight and wind tunnel. Generally the agreement is good. Subsonically the maximum L/D was 4.5 and the vehicle exhibited good handling qualities over much of the flight envelope. There were some instabilities when the rocket motor was fired but well within the available control power. This program was very successful with a significant number of flights conducted in a short time. This can be attributed to two factors; using the X-24A and the experienced team that continued from the X-24A to the X-24B.

The last configuration in the X-24 series is the X-24C. This investigation did not result in a flight test article, but was the center of extensive investigations which were focused toward a flight test article. This vehicle was to be an experimental test bed as portrayed in Figure 27. Extensive wind tunnel tests were conducted on the configuration including experimental modules and configuration modifications to reduce C_{D0} . Figure 28 is a photo of the oil flow on the wind tunnel model. Some of the regions of flow separation are evident on the upper surface as well as a pair of vortices. Figure 29 shows typical data at Mach 8.

The FDL-5 Concept

This vehicle concept is unique. It was originated as a result of investigations being conducted to achieve high volumetric efficiency while maintaining high aerodynamic efficiency ($L/D \sim 3$). The configuration's uniqueness was the concept of compression

sharing. Although mentioned previously, a more detailed discussion will be given here in view of its importance.

Earlier lifting entry vehicle designs required large aerodynamic fins for stable hypersonic flight. Usually these fins are located in the aft outboard portions of the vehicles. These fins presented a number of challenges and problems including:

- Unpredictable flows
- Regions of high aerodynamic heating
- High structural weight
- Drag contributors

So the concept evolved to attempt to eliminate the fins. This had to be done without degrading stability or subsonic L/D. If this could be done a weight savings and drag reduction were potential gains. The idea was to maintain the cant and dihedral effect of the fins by enclosing the region between the fins and the body. This was accomplished and a number of parametric studies conducted to examine aerodynamic performance and stability, aerodynamic heating, and structural weight. The concept came as a result of a series of lifting body investigations. Figure 30 conceptually shows the parameters that were varied and Table I is the range of the parameters investigated.

TABLE I
SERIES OF AFT BODY PARAMETRIC VARIATIONS

Parameter	Lowest Values	Nominal Values	Highest Values
τ	4°	6°	8°
K	10°	20°	30°
h/H	0.50	0.75	1.00
b/B	0.70	0.85	1.00

An analysis of these parameters was conducted using the Hypersonic Arbitrary Body Program which will be discussed later in the paper. The analyses were conducted at $M = 20$ and an altitude of 200,000 feet at an angle-of-attack of 10 degrees. Viscous effects were included. Figure 31 shows the effect of these parameters on the lift-to-drag ratio. The effect of toe in, roll out, and span parameters is very small. However, the height parameter, h/H, did exhibit a substantial decrease for values above 0.75. This can probably be attributed to the increases in skin friction and pressure drag on that surface at a greater rate than the contribution to lift. Figure 32 is an examination of the longitudinal stability. The variations show a slight increase in pitch stability for increases in the parameter except for the span parameter where no variation is noted. The small change in trim angle-of-attack may be a consideration for configuration development.

The more important considerations in the compression sharing is what happens to the directional stability. The results of the analysis are shown in Figure 33. From the directional stability point of view, the toe-in and roll-out variations tend to show a maximum while variations about that point decrease C_{ng} . There is a substantial increase due to height but that parameter has the greatest adverse impact on L/D (Figure 31). There is a similar increase for increasing shoulder span at low angle-of-attack but that has an adverse effect on the subsonic L/D. In Figure 34 are shown the results for roll stability. The variation in parameters had a very small effect. From this parametric analysis it would appear that the best set of parameters are:

$\tau = 6^\circ$
 $K = 10^\circ$
 $L/H = .75$
 $b/B = .85$

From this analysis a configuration was developed and an experimental program conducted in the Arnold Engineering Development Center (AEDC) facilities. Figure 35 is a picture of the force model of the FDL-5 configuration. The center fin was added to aid directional control and stability especially at low speeds. Figures 36 and 37 are a summary of the wind tunnel data showing the aerodynamic characteristics. Also shown in the figures are comparisons with analysis methods. As can be seen in these data the configuration has good characteristics and there are no real adverse configuration features. Examination of all the data results in the following conclusions:

1. The configuration is stable over the Mach number range 1.5 to 10 at angles-of-attack from 5 to 30 degrees with c.g. location from 62 to 65 percent of the reference length.

2. No elevon deflections into the airstream are required for trim after the range of angle-of-attack from 5 to 30 degrees.
3. Trimmed hypersonic L/D max extrapolated to reference flight condition is 2.84 (see Figure 38).
4. The test data correlates well with analytical methods.

Predictive Analytical and Numerical Methodology for Lifting Body Configurations at Supersonic/Hypersonic Velocities

Configuration development normally proceeds from basic parameters to complex trades. Similarly, the analysis methods need to increase in precision. There are five basic methods or procedures for evaluating the aerodynamic characteristics of lifting body configurations at supersonic and hypersonic flight conditions for design purposes. The five basic predictive procedures are: modified impact or parametric methods, the paneling procedures such as the PANAIR method, the Euler approximation, the parabolized Navier-Stokes approach, and the Navier-Stokes solution. The modified impact or parametric procedures use known theories and approximations, the paneling or PANAIR method and the Euler approximation are based on an inviscid analysis. They are, therefore, incapable of generating independently the drag coefficients and heat transfer distribution. They are, however, relatively easy to use and inexpensive to generate the needed information within certain tolerances. The more recently developed numerical techniques of the parabolized Navier-Stokes equations and the Navier-Stokes equations solver, in principle, can provide all the detailed flow field topology and the key design parameters. The utility, however, for daily applications still requires further research efforts which are currently being pursued in the Laboratory. The detailed descriptions of these predictive procedures are summarized as:

Supersonic/Hypersonic Arbitrary Body Program: The standard model for application of impact methods is the Supersonic/Hypersonic Arbitrary Body Program, often abbreviated S/HABP. The heart of the program is an arbitrary body surface integrator. In this case, pressure and shear stress are integrated to evaluate aerodynamic forces and moments. The shape is described by a set of three-space coordinates, and the smooth surface is reduced to a number of planar facets. The local pressure on each increment is evaluated using Newtonian, tangent cone, tangent wedge, or some similar theory. Shear stress is evaluated using algebraic relations, such as the reference temperature method for laminar and turbulent cases. The S/HABP is a powerful tool for evaluating hypersonic aerodynamic performance. It has been used to develop guidelines for leading edge sweep, nose and leading edge radius, cross section contours, fore and aft ramp angles, pitch and yaw stability, and control effectiveness. Figures 39, 40, and 41 show the type of parametric investigations conducted. The skin friction methods have been verified by wind tunnel data, and the methods are used to extrapolate sub-scale test results to full scale flight. The effect of the vehicle length on this component of drag is seen to be severe at altitudes of 200,000 feet and more, Figure 42. The S/HABP has been used in the development of the Flight Dynamics Laboratory is high lift-to-drag ratio vehicles and in the refinement of these configurations.

PANAIR: The PANAIR procedure is a higher order paneling program and is based on the linearized potential flow approximation. It has many years continuous development within industry. It is a functional approximation of an aerodynamic shape and little computation is needed to get a solution, thus the quick response to timely results is possible. It is based on a small perturbation concept; consequently, it has very limited value for supersonic/hypersonic applications. Potential flow procedures are therefore restricted to applications where the flow is essentially isentropic. The techniques are best suited for slender shapes such as thin wings and high fineness ratio bodies.

Euler Approximation: This method is the most sophisticated inviscid calculation. It can generate the lift and wave drag reasonably well if the body is streamlined. In essence, the lifting body must not produce significant aerodynamic interference, therefore, the designed supersonic/hypersonic configuration is limited. The body shape is a boundary condition, and unless special provisions are made, the flow must not separate from the surface. The skin friction coefficient and heat transfer can also be computed or estimated from the boundary-layer theory based on the Euler flow field solution. For the purpose of preliminary design and for the graduated investigation of the aerodynamic efficiency of the lifting body, this procedure is a cost effective means. The shortcoming of this procedure is that it has not been formed into unified process to be standardized and the procedure is highly problem dependent. The Euler equations themselves can be solved using modern computers and finite-difference mathematical methods. They have been applied to a variety of shapes but are limited by the need to specify the vehicle shape as an analytic surface. Considerable effort is being expended to extend the range of geometries that may be considered.

Aerodynamic heating requires more exacting techniques, but may be approached using a series of simplifying assumptions. Finite difference numeric solutions or momentum-integral solutions are found for simple geometric shapes such as spheres, cones, cylinders and flat plates. Arbitrary geometries may be approximated by the simple geometries and analyzed using rapid solutions of the heat transfer equations. Critical areas that involve shock wave impingement or boundary layer separation/reattachment are not treated with this approach.

The Parabolized Navier-Stokes Methods: Presently, it shows promise for being the backbone design tool for supersonic/hypersonic configurations. For a hypersonic vehicle, this method can and has produced all the essential design information. Figure 43 shows the comparison of the PNS calculations with experimental data. Today, the PNS can generate all the key design parameters at one-fifth of the cost of the Navier-Stokes equations. The only fundamental shortcomings of the PNS procedure are that this procedure cannot simulate the time-dependent phenomenon (transient phase) and the configuration will not permit extensive streamwise flow separations. Due to the relatively small computer core storage needed, this procedure will likely be the first to contain the real gas (high-temperature) capability.

The Navier-Stokes Methods: This procedure is the limit of the macroscopic representation of gas dynamics. The theoretical limitation is that the studied vehicle must operate in the continuum regime where the Knudsen number is less than unity. Beyond this altitude, one must resort to the Boltzman equation for the rarefied gas dynamics. Current applications of the Navier-Stokes equations for vehicle design are limited by the computational efficiency of the system of non-linear partial differential equations and the accurate modeling of turbulence, laminar-turbulent transition, and finite rate chemical reaction. These limitations are common to all the numerical simulations (PNS, Euler) and are an area of current research. In spite of the difficulty encountered at present, this methodology is being used for supersonic/hypersonic vehicle design. At this point in time, no evidence has been indicated, by comparing with experimental observation, that the Navier-Stokes equation fails to duplicate the fluid properties. In 1985, engineering insight and computer power allowed J. Shang to determine the complete flow field about a hypersonic lifting body. Figure 44 presents the code and experimental results for the X-24C configuration.

Experimentation

In the area of lifting bodies and their application to hypersonic flight, a brief discussion is in order relative to the experimental capability to satisfy the needs as they are currently assessed.

Experimental results will be needed as a tool in the development process and as a final verification. The degree may be influenced by our computational capability, but experimental results for final verification will be needed. In addition to that normal process we see a pressing need for experimentation and the facilities to support such experimentation in two critical areas; real gas flows, and Computational Fluid Dynamics (CFD) code validation. Figure 45 is a classic example of how numerics and wind tunnel results can work together to arrive at the correct solution. This is a curve of pitching moment from a Shuttle flight showing the difference between pre-flight estimate and flight data. The procedure used by Griffith and Maus to correct the wind tunnel data is also outlined. One very important element was real gas effects. Another conclusion from this figure might be that for high L/D vehicles which are slender and fly at low angle-of-attack, Mach number effects are very important. Figure 46 is another example of real gas effects on the stability of a cone. In both examples, real gas effects can be significant. At this time our ability to simulate real gas effects in a useful way is very limited. Figure 47 shows the operating envelope in terms of enthalpy and Reynolds number for the most capable facilities. It becomes obvious that for the immediate future it will be necessary to rely heavily on analytical methods to assess real gas effects. This leads us into the other aspect of experimentation; the validation of CFD codes. Code validation is needed for perfect gas case as much as for the real gas case and there are sufficient facilities to do the perfect gas validation. The real gas case; however, is another matter. Our facilities are limited and the unknowns in the flow modelling are significant. One approach is to utilize a small facility which can produce the type of flow needed and use this small scale data to verify and calibrate the CFD methods which can then be used to extrapolate to flight.

It must be kept in mind that hypersonic test facilities are partial simulation facilities which means that there has always been an extrapolation process. So it is necessary to recognize that experimentation for design purposes means that it is required to generate high quality flow fields and surface data which can easily be used in the extrapolation process. For example, it is known that both laminar and turbulent boundary layer data can be extrapolated; however, transitional data cannot be extrapolated to flight.

The bottom line in terms of both numerics and experimentation is that they must go hand-in-hand to develop adequate designs for hypersonic vehicles. They must complement where possible to cover the short comings of each individual approach.

Additional Research Areas, Challenges, and Concluding Remarks

The lifting body offers high potential for multiple applications through its linkage of aerodynamic efficiency, high performance, volumetric efficiency, and payload carrying capability. It further holds promise for reduced TPS, structural, and total weight, and can be designed for compactness which makes it especially attractive for mating with other system components. The possibilities for reduced weight designs and aeropropulsive compatibility is also most attractive. The geometries involved suggest easing of aeroheating and interference problems and simple minimum junctioned configurations lend themselves to increased confidence in analysis, especially at hypersonic speed. A well established data base, both analytical and experimental, contributes to this confidence and can significantly enhance the success of future programs. The

experimental validations are both from ground tests through Mach numbers of 19.0 and from flight tests of lifting body configurations with the demonstration vehicles previously discussed and shown in Figure 48.

Perhaps one of the most serious challenges continues to be associated with the design of an aerodynamic efficient configuration which can develop high performance at peak altitude and velocity conditions while maintaining its effectiveness at interim Mach number and altitude conditions of its flight. It still also must be able to achieve highly effective approach and landing characteristics. This design goal is perhaps more challenging today than previously, for consideration is now being given to sustained time at high Mach numbers and altitudes to perform repetitive synergetic plane changes or to maintain flight conditions with rocket propulsive supplements. If maneuvering is to be achieved at those conditions, considerable attention must be focused on low density effects and rarefied flow analysis, which can severely modify the flows predicted through continuum data bases. Real gas effects become of consequence, for from an aerodynamic viewpoint, pitching moments, control effectiveness, and shock interactions must be reassessed. The aerothermodynamics is also impacted in equilibrium through density variations and out of equilibrium through catalytic/non-catalytic effects. Again, if flight is to be performed at reduced angles-of-attack approaching α optimum (or less) for L/D max, attention must be focused on a better understanding of the upper surface. Lee side aerodynamics and heating become important. A much more comprehensive approach should also be made of the aerodynamic/reaction control blending to assure that the designs can achieve the maximum performance, stability, and control effectiveness.

Boundary layer transition still remains an area which can critically impact the vehicle design through its aerodynamic heating and subsequent choice of thermal protection system and structural concepts. The impact of roughness and sensor penetrations require additional attention and increased thermal protection. As indicated previously, if the flight configuration is to perform maneuvers at high velocity/altitude conditions, then special consideration must be given to multi heat pulse due to its multiple heating exposure.

If increased values of aerodynamic efficiency are desired for maximum performance potential, then reduced nose and leading edge bluntness becomes quite important. A very special challenge exists for imaginative thermal protection, which might take the form of heat pipes or various forms of active cooling. In any event, it is usually desirable to maintain stable shape geometry to assure adequate performance levels.

The analysis or predictive codes have to be developed to the point where they are truly pragmatic engineering methods. The S/HABP has proved to be an effective tool not only for investigation of parametric geometric and configuration effects, but also for the convergence to point designs. The inclusion of empirical data with the analytical codes has proven to be very effective and beneficial. In the final analysis, any predictive code must prove useful and cannot be applicable just to simple geometries at severely reduced flight conditions.

Considerable success has been realized with the PNS code, and has been previously stated, with the Navier-Stokes solution of the X-24C lifting body configuration. More complete and complicated geometries with real gas effects must be accommodated.

It is essential, therefore, to improve the physical realism of the computer codes. The critical examination of the codes against data and the ability to routinely make quality experimental measurements in wind tunnels is an absolute necessity. The validation requires higher quality data than normally produced. Increase data detail is also required, and any reasons for lack of agreement with the codes must be objectively determined. To further address code validation, it will be necessary to define a series of wind tunnel experiments that fully stress the capabilities of the codes. The process will also require precise selection of the wind tunnels and assurance of accurately calibrated data. The mechanism, in its finality, will require careful comparisons of the codes and experiments, including assessments of all errors with a clear and objective display of the validated phenomena.

In summary, we have traced lifting entry vehicle technology in the manner in which it has been pursued in the Flight Dynamics Laboratory and associated organizations. The Flight Dynamics Laboratory's interest has essentially progressed from simple configurations through a rather comprehensive series of lifting bodies investigated for entry from both close proximity and high energy orbits. Our interest has not been restricted to any one given class of vehicles or any specific configuration concept, rather we have directed our attention to many classes of vehicles across the entire spectrum of hypersonic lift-to-drag ratios. Initially, the emphasis was placed on vehicle technology generally in the medium L/D range but has evolved to the higher lift-to-drag ratio configurations. We have also shown that the lessons learned with "research" vehicles such as ASSET, PRIME, X-24A, and X-24B configurations have indeed been quite representative. It has been stressed that our interest in lifting entry vehicle technology has been motivated not only from the viewpoint of achieving practical configuration designs for potential exploitation, but have also outlined the technological reasons for pursuing such research. We have consistently shown that our emphasis has been directed toward developing analysis and design techniques which could be employed for generalized configurations and have emphasized the necessity of assuring not only adequate generality in the techniques and methods developed but also the necessity for encompassing the pragmatic constraints to assure acceptability. We have not only been concerned with potential performance increases, but also the understanding of the required parametric

trade-offs associated with design optimization for multiple applications. In displaying the correlation capability and design methodology which is now available from both ground and flight test for the more moderate lifting entry configurations, we have shown the necessity from the research and technology viewpoint to move into areas which offer more challenging problems and which will, indeed, provide an impetus for new advancements for the entire technology of lifting bodies. As we have mentioned, it is particularly incumbent on the configuration researcher to avoid problems associated with technological plateaus.

BIBLIOGRAPHY

1. Gray, J. D., "Three Component Force Tests of Satellite Reentry at Mach Numbers 2 to 5," Sponsored AEDC Test and Data Report, Aircraft Laboratory, WCLSR-1, Wright Air Development Center, December 1958.
2. Buehl, F. W., Laaksonen, L. E., and Lefterdo, J. M., "X-7A Thermal Data Program Final Report," FDL Sponsored, WADD-TR-60-567.
3. Draper, Alfred C., "Possible Applications of the Aeroballistic Vehicle to Some Advanced System & Research Concepts," FDL, WADD-TM-61-2.
4. Antonatos, Philip P., and Draper, Alfred C., "A Survey of the Trends in Flight Mechanics," Ninth Annual USAF Science and Engineering Symposium, October 9-11, 1962.
5. "Proceedings of the 1962 X-20A (Dyna-Soar) Symposium," ASD-TR-63-148, March 1963.
6. Cosenza, C. J., Alexander, G. L., and Gazerro, W. J., "A Program for Hypersonic Flight Testing in the Areas of Structures, Aerothermodynamics, and Structural Dynamics (ASSET)," FDL-TDR-64-75, July 1964.
7. Hankey, W. L., and Schroeder, L. J., "Optimization of Lifting Re-entry Bodies," Proceedings of 12th Annual Air Force Science & Engineering Symposium, Vol I, 1965.
8. Love, J. E., and Young, W. R., "Component Performance and Flight Operations of the X-15 Research Airplane Program," 1966 Annual Symposium on Reliability, San Francisco, CA, January 25-27, 1966.
9. Landes, P. E., Marks, C. D., et al, "ASSET," Volumes 1-4, AFFDL-TR-65-31, April 1966.
10. Draper, A. C., Benson, B. R., and Neumann, R. D., "Lifting Entry Technology and Advanced Vehicle Concepts," Transactions of the Eleventh Symposium on Space and Ballistic Missile Technology, July 6-8, 1966, Volume I.
11. Quest, R., "The Tip Tank Concept; An Economic Orbital Transportation System," S&E Space Technology Conference, May 1967.
12. Draper, Alfred C., and Buck, Melvin L., "Assessment of the Factors Affecting Advanced Lifting Entry Vehicles," AFFDL-TR-67-137.
13. "SV-5D Prime, Final Flight Test Summary," ER 14465, September 1967.
14. Dahlem, V., and Buck, M. L., "Analysis and Experimental Results of High Lift-to-Drag Configurations," AFFDL-TR-67-138.
15. Draper, Alfred C., and Cosenza, Charles J., "Technological Prospects for High Performance Spacecraft," Proceedings of SAE Space Technology Conference, Washington, DC, May 8-10, 1968.
16. Ehrlich, C., Rising, J., Peyton, R., and Onspaugh, C., "Preliminary Design and Experimental Investigation of the FDL-5A Unmanned High L/D Spacecraft," AFFDL-TR-68-24, March 1968.
17. Draper, Alfred C., and Neumann, Richard D., "Configuration Research and Exploratory Development for Advanced Spacecraft," NASA Space Station Symposium, February 11-16, 1969.
18. Neumann, R., McElderry, E., Gord, P., and Buck, M., "High L/D Vehicle Design," AFFDL-TR-69-82, February 1970.
19. Antonatos, Philip P., Draper, Alfred C., and Neumann, Richard D., "Aerothermodynamic and Configuration Development," AIAA 7th Annual Meeting and Technical Display, Houston, Texas, October 19-22, 1970.
20. Draper, Alfred C., Buck, Melvin L., and Goesch, William H., "A Delta Shuttle Orbiter," Aeronautics and Astronautics, Volume 9, No. 1, January 1971.
21. Selegan, David R., "Parametric Study of Nine Delta Wings on a Modified FDL-8 Vehicle $M = 0.4 - 1.2$," AFFDL-TM-71-26-FXS.

22. Dahlem, Valentine, III, "Summary of Aerodynamic Characteristics of the FDL-6 High L/D Configuration," AFFDL-TR-72-48.
23. Armstrong, J. G., "Flight Planning and Conduct of the X-24A Lifting Body Flight Research Program," AFFTC-TR-71-10, August 1972.
24. Selegan, D. R., Flaherty, J. I., and Norris, R. B., "Effects of Rocket Exhaust on the Aerodynamics of the X-24A and X-24B Lifting Bodies," AFFDL-TM-75-29-FXS.
25. Armstrong, J. G., "Flight Planning and Conduct of the X-24B Research Aircraft Flight Test Program," AFFTC-TR-76-11.
26. Draper, Alfred C., Lane, Paul, and Zima, William P., "A Flight Research Vehicle to Bridge Shuttle and Hypersonic Aircraft Technology," AIAA Atmospheric Flight Mechanics Conference, Hollywood, Florida, August 8-10, 1977.
27. Lane, Paul, Jr., "Flight Research Concepts for Aerodynamic Maneuvering Space Vehicles," Air Power Symposium, Maxwell AFB AL, February 23-25, 1981.
28. Hayes, J. R., and Neumann, R. D., "Trends in the Space Shuttle Aerothermodynamic Data Base," AIAA 19th Aerospace Sciences Meeting, St. Louis MO, January 12-15, 1981.
29. Walberg, Gerald D., "A Review of Aeroassisted Orbit Transfer," AIAA 19th Atmospheric Flight Mechanics Conference, San Diego CA, August 9-11, 1982.
30. Shang, J. S., and Hankey, W. L., "Computation of Flow Past a Hypersonic Cruiser," Proceedings of the 2nd Symposium on the Numerical & Physical Aspects of Aerodynamic Flows, California State University, Long Beach CA, January 16-20, 1983.
31. Allen, H. Julian, "Hypersonic Flight and the Re-entry Problem," Journal of Aeronautical Sciences, Vol 25, Nr 4, April 1958.
32. Eggers, A. J., Jr., and Wong, T. J., "Motion and Heating of Lifting Vehicles During Atmosphere Entry," ARS Journal, Vol 31, Nr 10, October 1961.
33. Bell, Roland V. 1Lt, and Hankey, Wilbur L., "Application of Aerodynamic Lift in Accomplishing Orbital Plane Change," ASD TDR-63-693, September 1965.
34. Draper, Alfred C., Buck, Melvin L., Davis H. Max, and Nicholson, James F., "A Superorbital Design Concept for a Lifting Entry Vehicle," Proceedings of the AIAA Vehicle Design Symposium, November 1963.
35. Kinroth, G. D., Pawlikowski, T. P., et al, "ASSET - Final Aerodynamics and Performance," AFFDL-TR-65-31, December 1965.
36. Lore, Eugene S., "Manned Lifting Entry," Astronautics and Aeronautics, May 1966.
37. Draper, Alfred C., Buck, Melvin L., and Selegan, David R., "Aerospace Technology Demonstrators/Research and Operational Optics," AIAA Aircraft Prototype and Technology Demonstrator Symposium, Dayton OH, March 23-24, 1983.
38. Shang, J. S., and Scheer, S., "Navier Stokes Solution for a Complete Re-entry Configuration," AIAA Journal of Aircraft, April 1986.
39. Neumann, Richard D., "Defining the Aerothermodynamic Methodology II," University of Texas at Austin Short Course on Hypersonics, November 4-7, 1986.

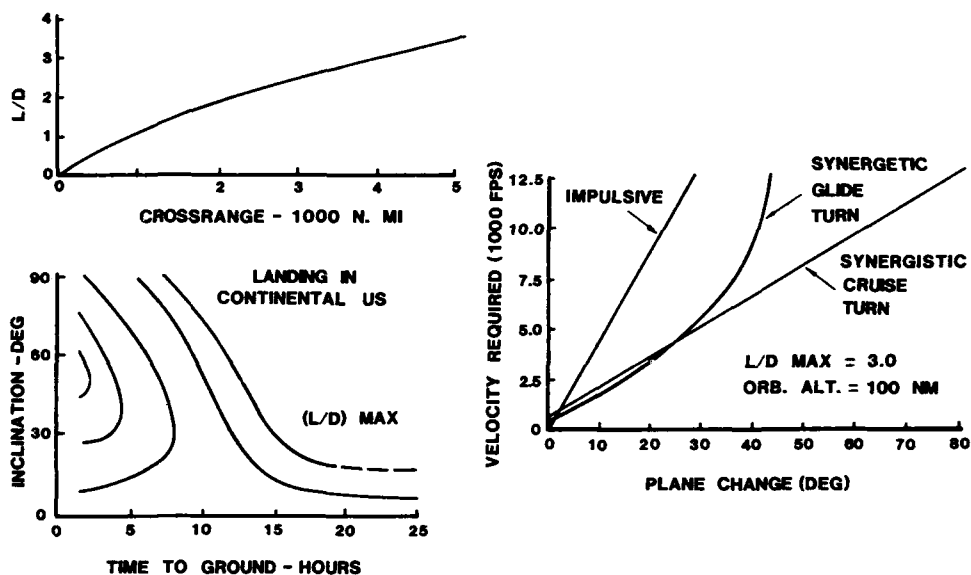
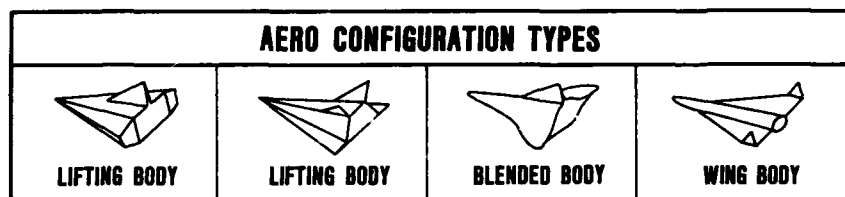


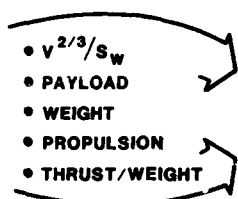
FIGURE 1 PAYOFF OF AEROPERFORMANCE EFFICIENCY



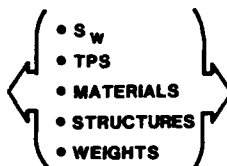
CONFIGURATION SELECTION IS A CRITICAL DRIVER

CHOICE OF CONFIGURATION STABILIZING AND CONTROL SURFACES IS VITAL

VOLUMETRIC EFFICIENCY



AERO HEATING



PERFORMANCE EFFICIENCY

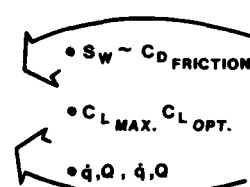


FIGURE 2 KEY TECHNOLOGY FACTORS

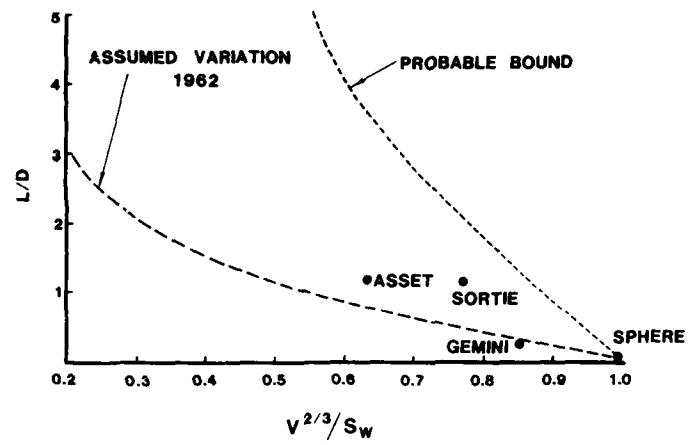


FIGURE 3 HYPersonic LIFT/ DRAG RATIC VS VOLUMETRIC EFFICIENCY

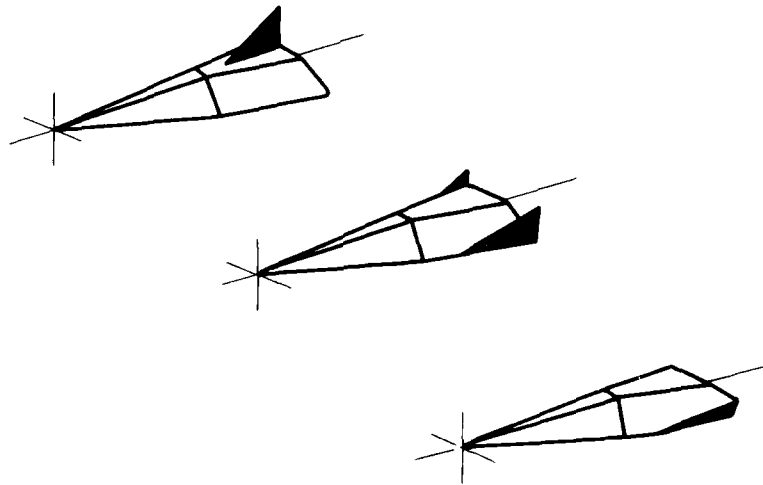


FIGURE 4 CONFIGURATION VARIATIONS FOR DIRECTIONAL STABILITY



FIGURE 5 LIFTING BODY CONFIGURATIONS

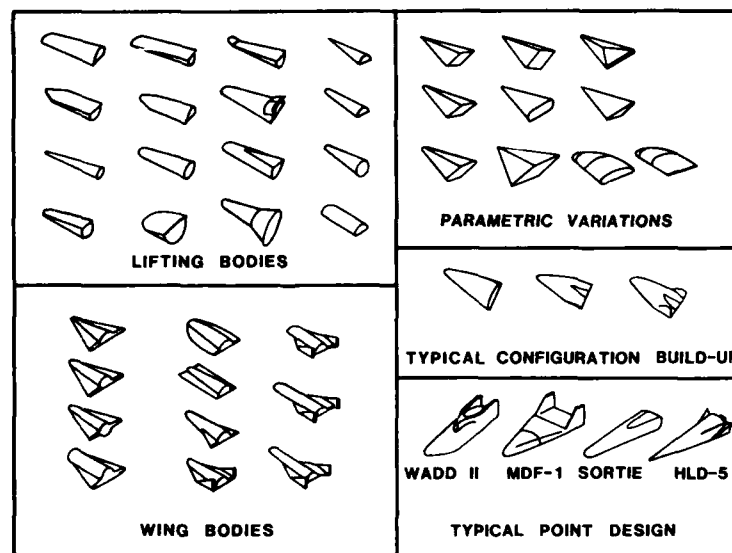


FIGURE 6 CONFIGURATION RESEARCH

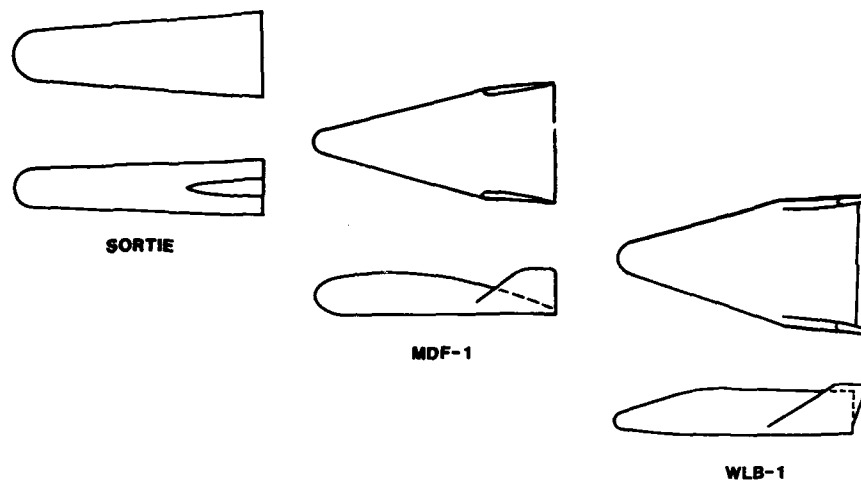


FIGURE 7 HYPERVELOCITY VEHICLE CONFIGURATION RESEARCH

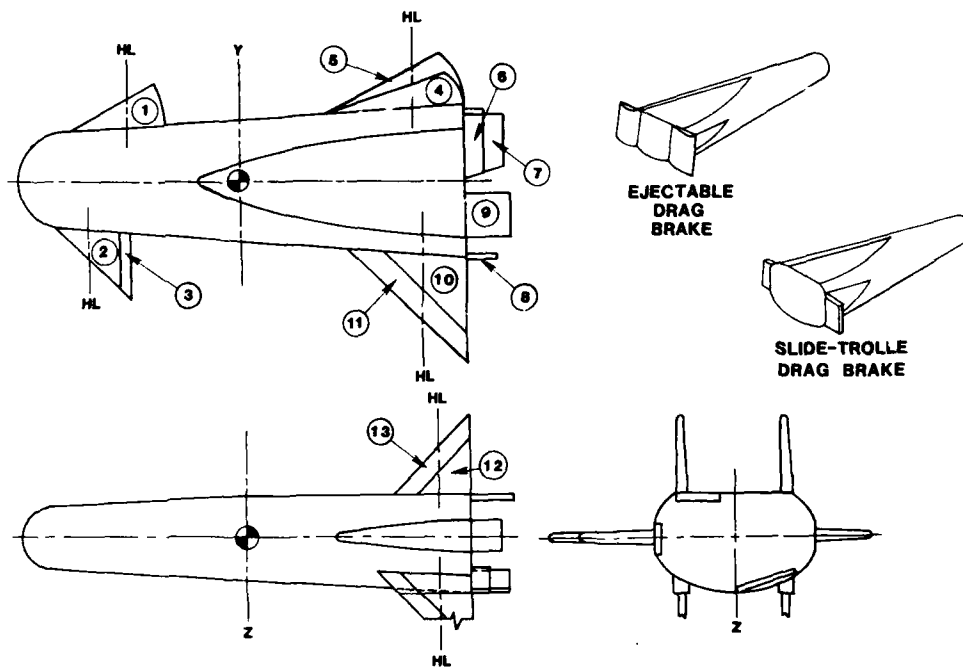


FIGURE 8 AERO CONTROL AND AUXILIARY DRAG DEVICES SUMMARY

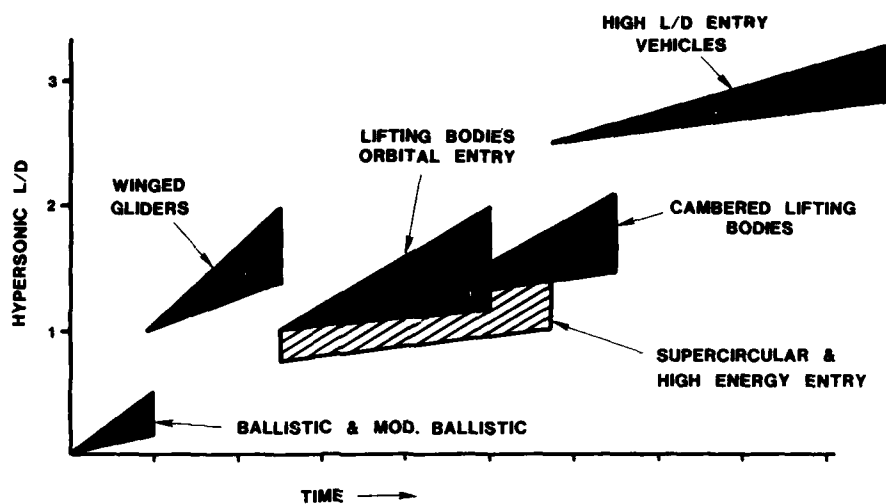


FIGURE 9 THE EVOLUTION OF AERODYNAMIC EFFICIENCY

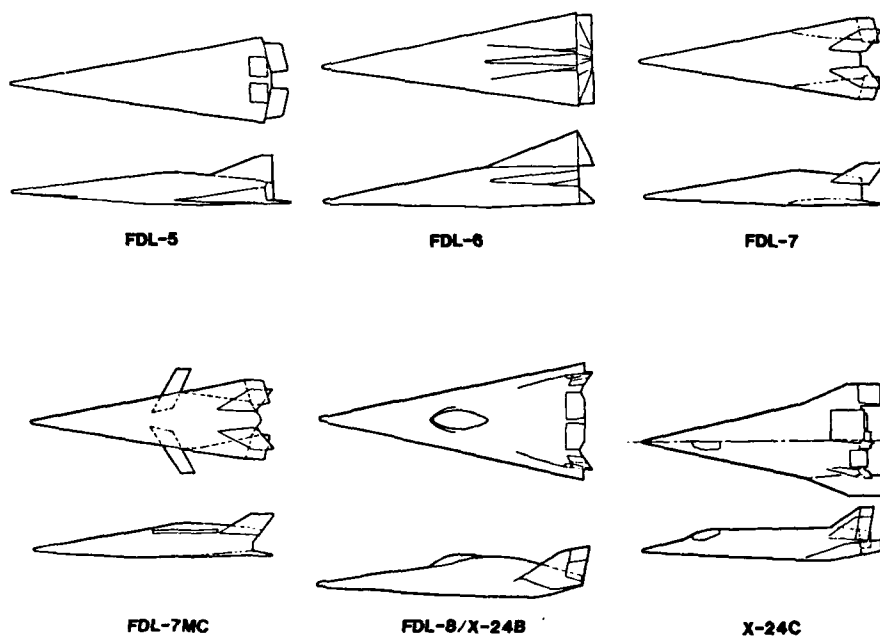


FIGURE 10 CONFIGURATION RESEARCH FOR AERODYNAMIC EFFICIENCY

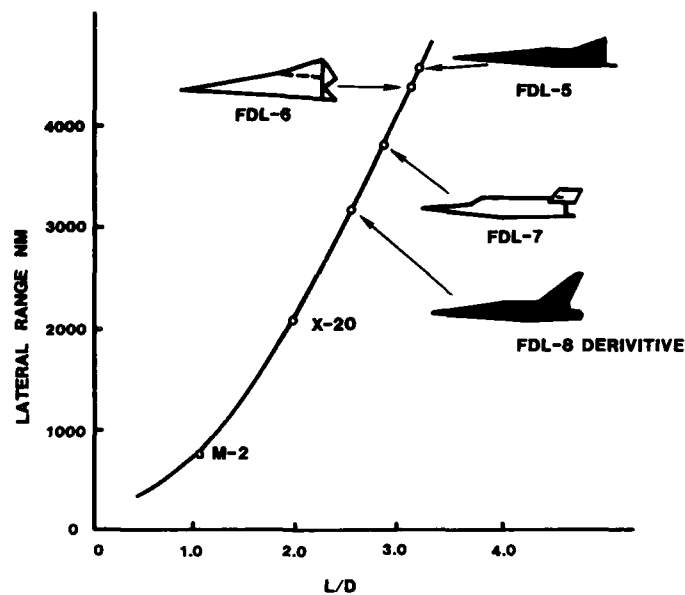


FIGURE 11 L/D FOR TYPICAL CONFIGURATION DESIGNS

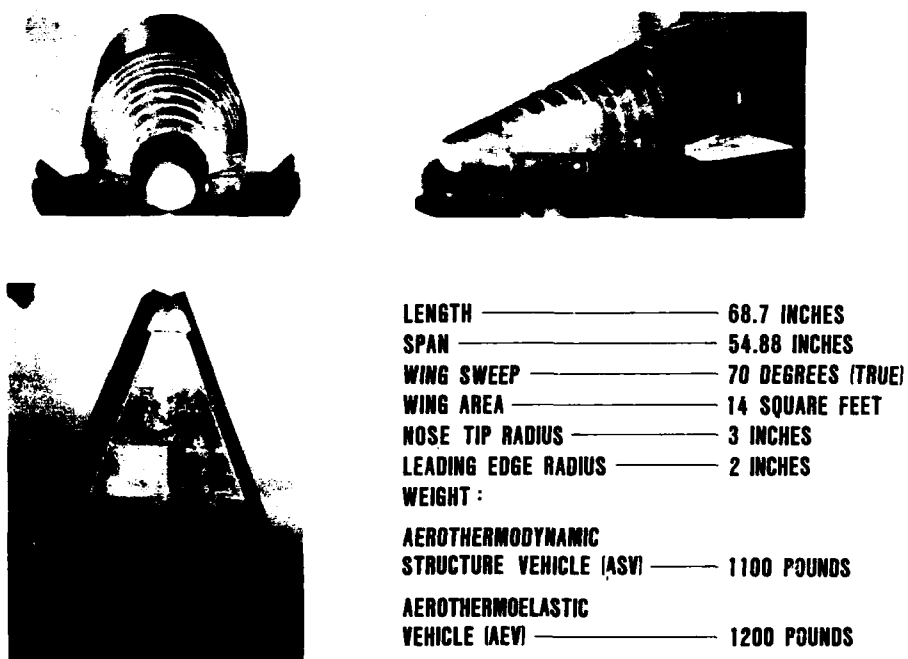


FIGURE 12 ASSET VEHICLE CHARACTERISTIC

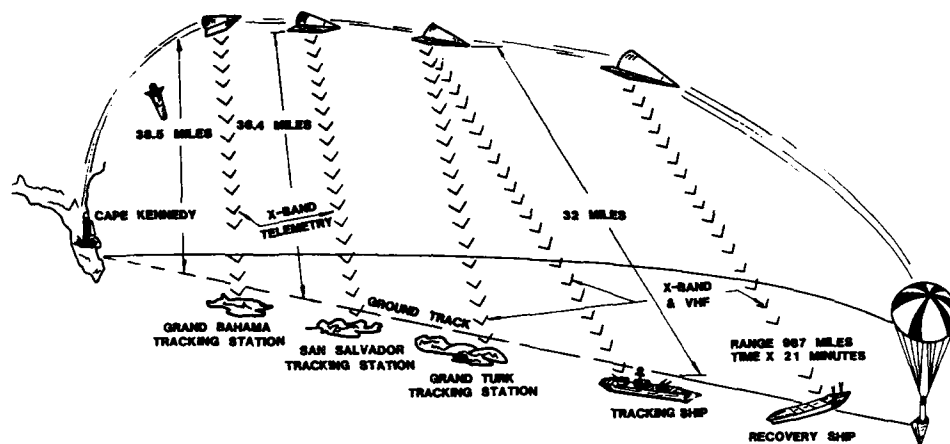


FIGURE 13 TYPICAL ASSET FLIGHT PATH

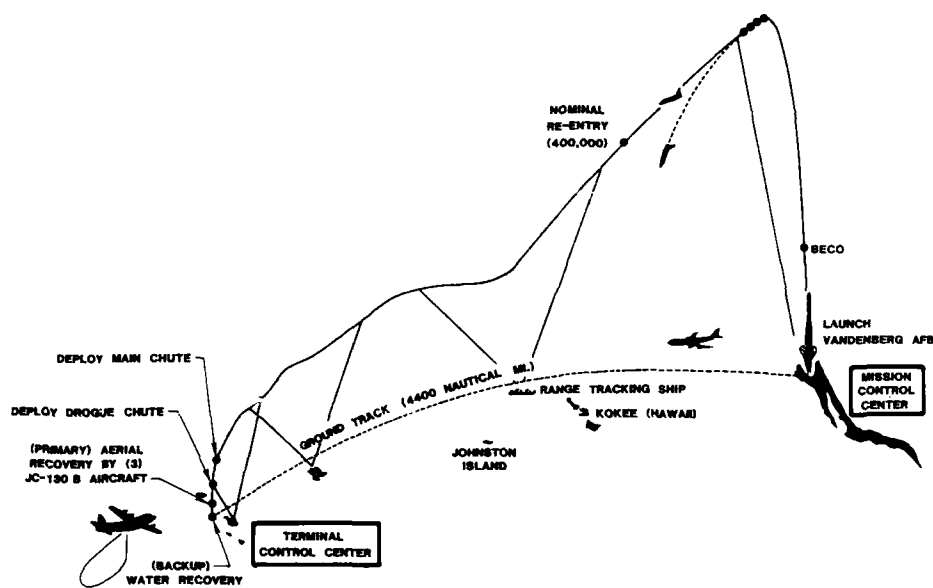


FIGURE 14 PRIME TEST MISSION PROFILE



FIGURE 15 TEST OF RECOVERED PRIME VEHICLE

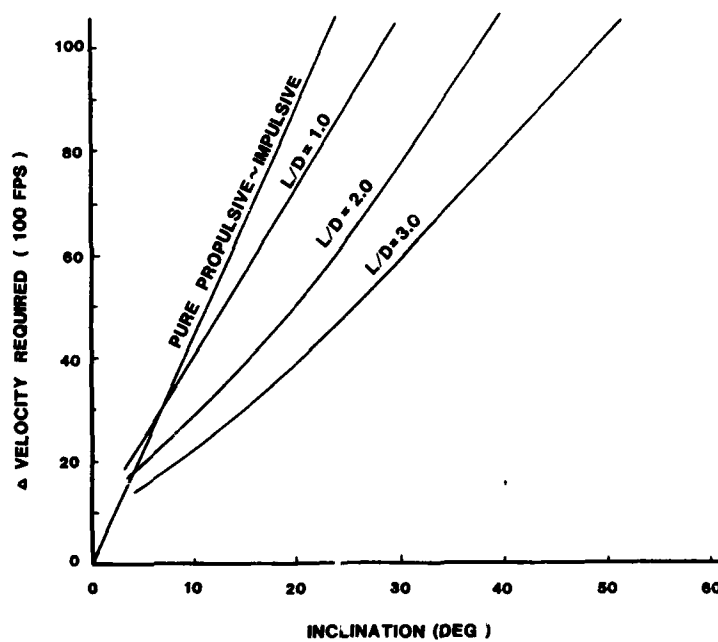


FIGURE 16 SYNERGETIC PLANE CHANGE CAPABILITY

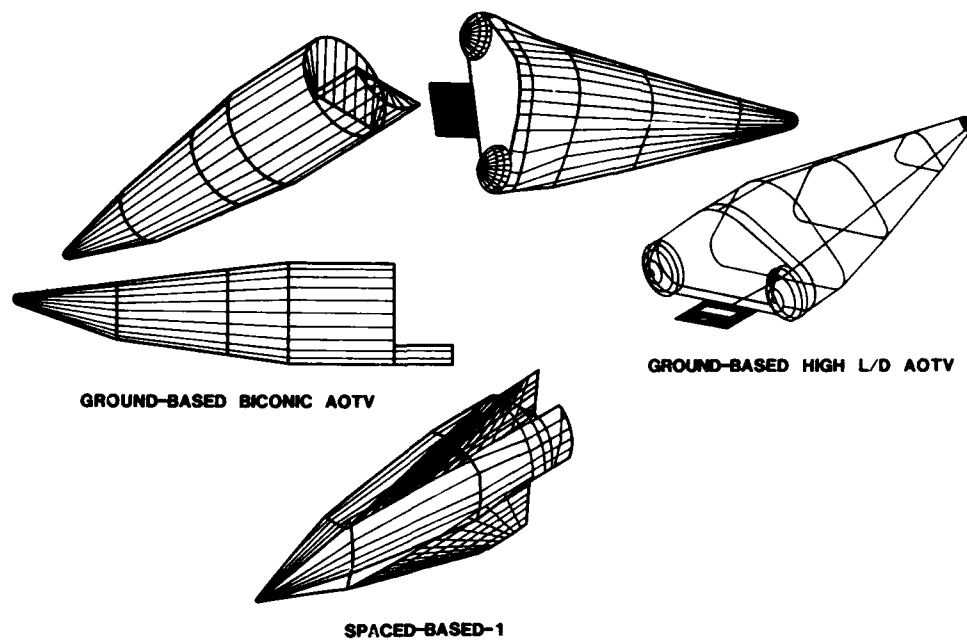


FIGURE 17 AEROCONFIGURED ORBITAL TRANSFER VEHICLES



FIGURE 18 HIGH L/D CONCEPT OF AOTV

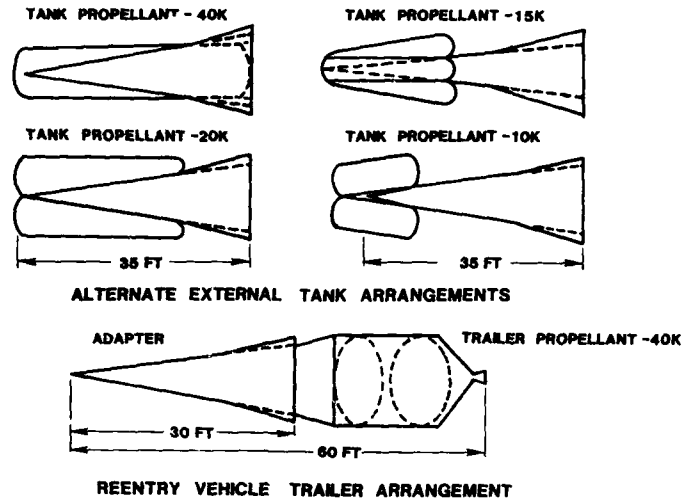


FIGURE 19 PROPELLANT TANK OPTIONS

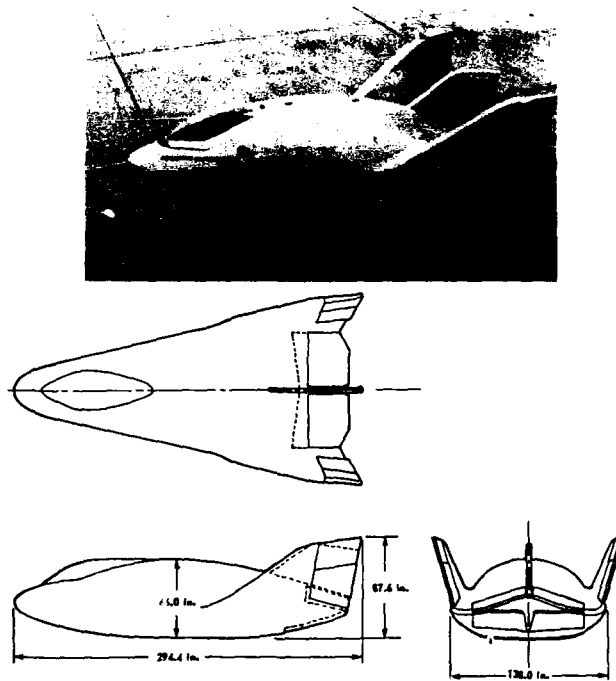


FIGURE 20 X-24A LIFTING BODY VEHICLE

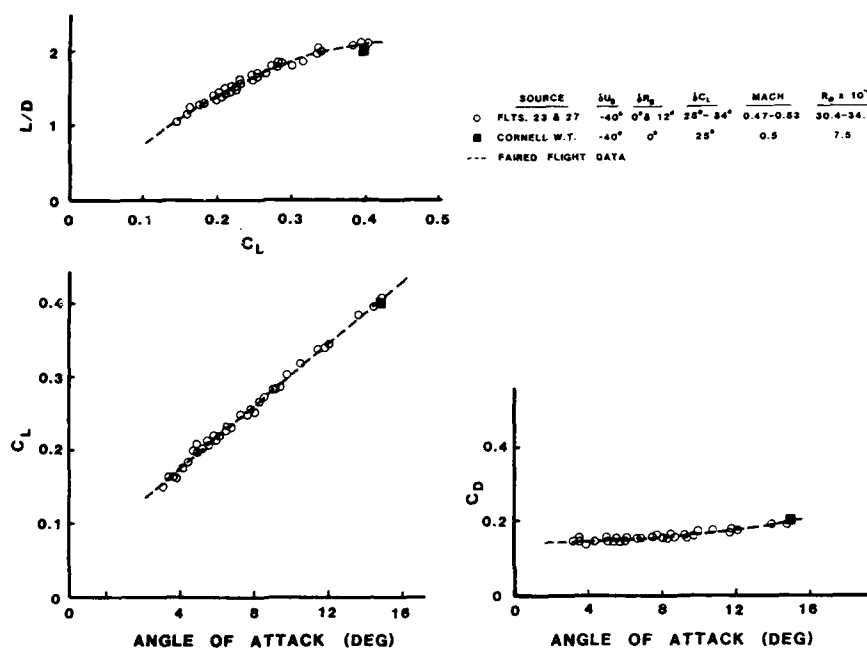


FIGURE 21A TRIM FLIGHT TEST AND WIND TUNNEL PERFORMANCE DATA MACH=0.5

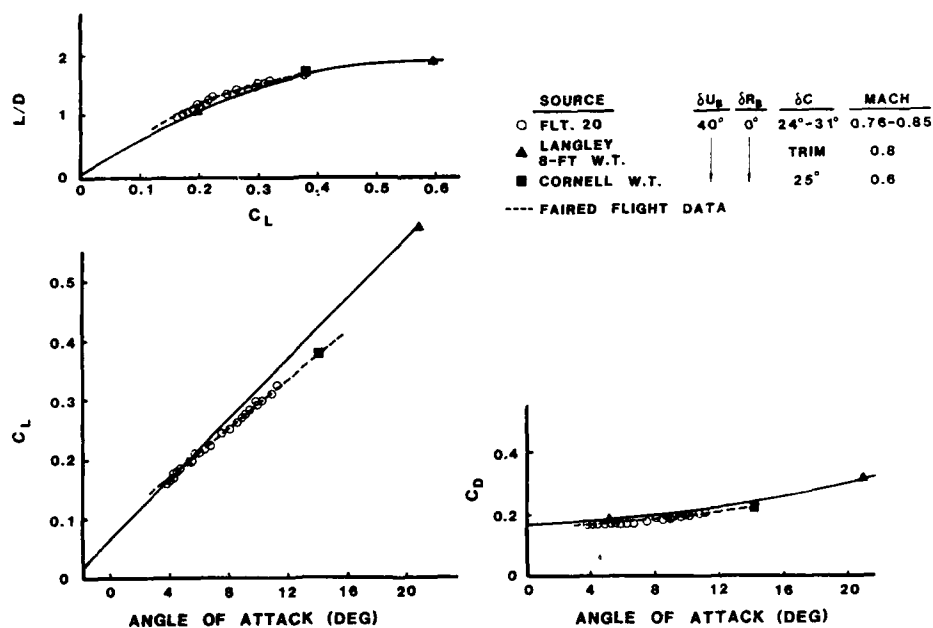


FIGURE 21B TRIM FLIGHT TEST AND WIND TUNNEL PERFORMANCE DATA MACH = 0.8

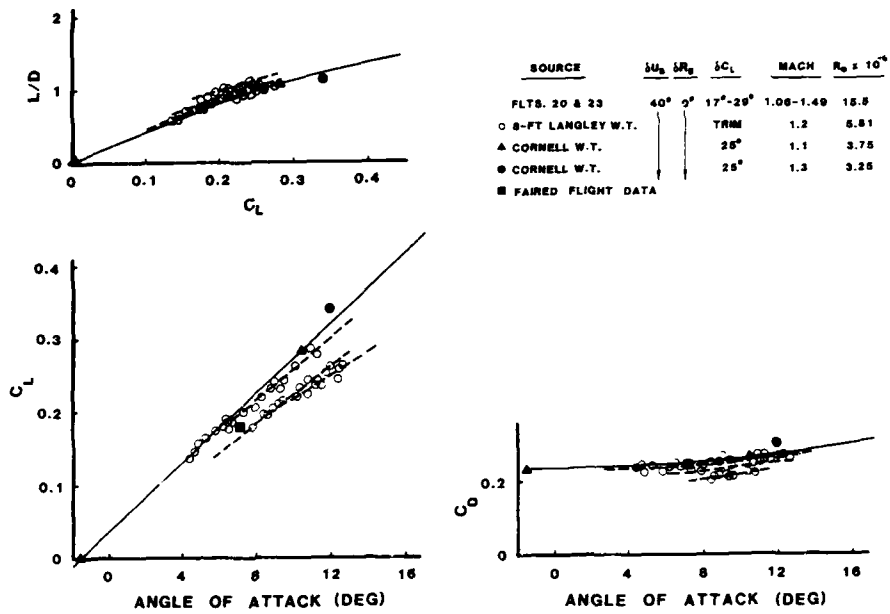


FIGURE 21C TRIM FLIGHT TEST AND WIND TUNNEL PERFORMANCE DATA MACH=1.1

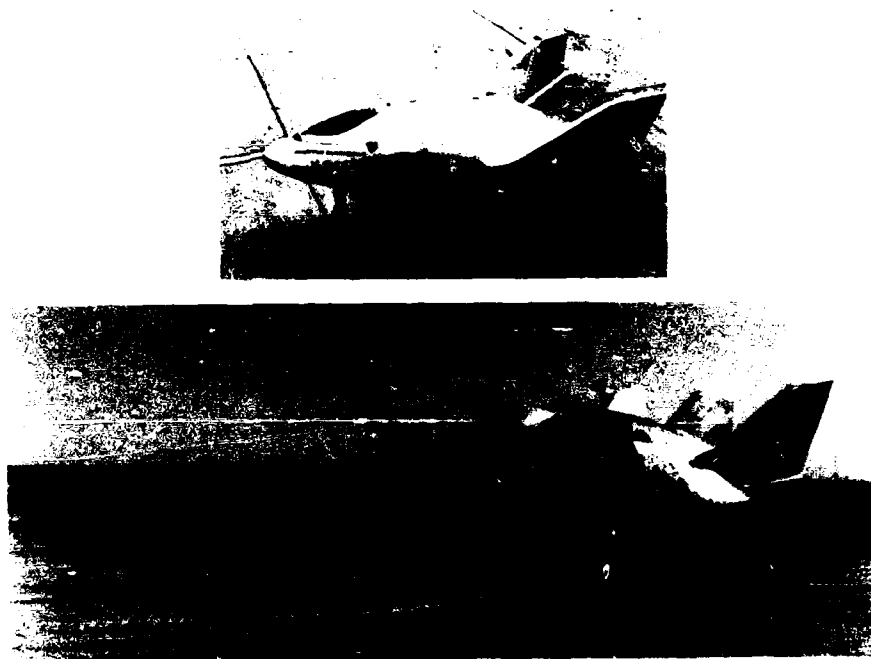


FIGURE 22 COMPARISON OF X-24A AND X-24B



FIGURE 23 PHOTO OF X-24A TO X-24B MODIFICATION

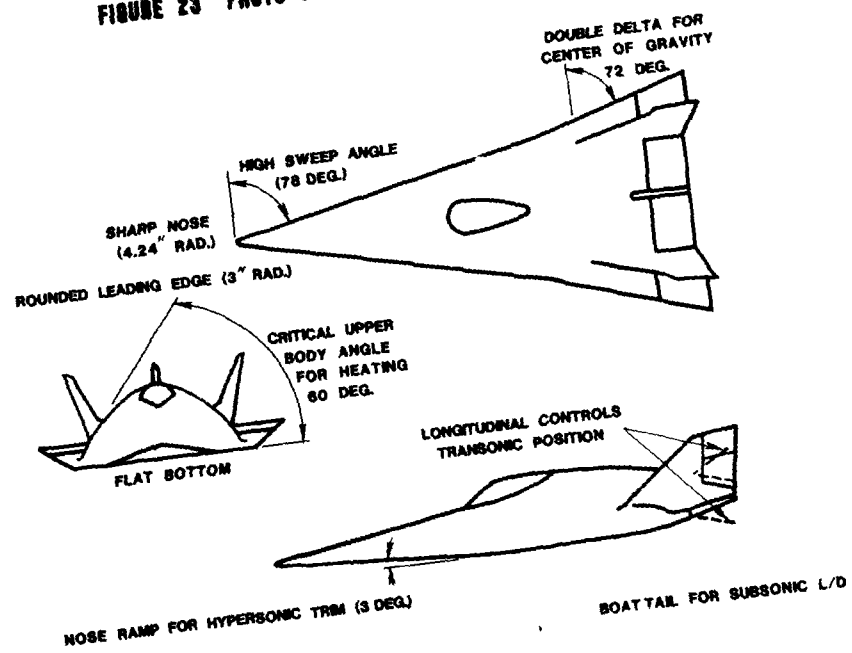


FIGURE 24 X-24B AERODYNAMIC DESIGN FEATURES

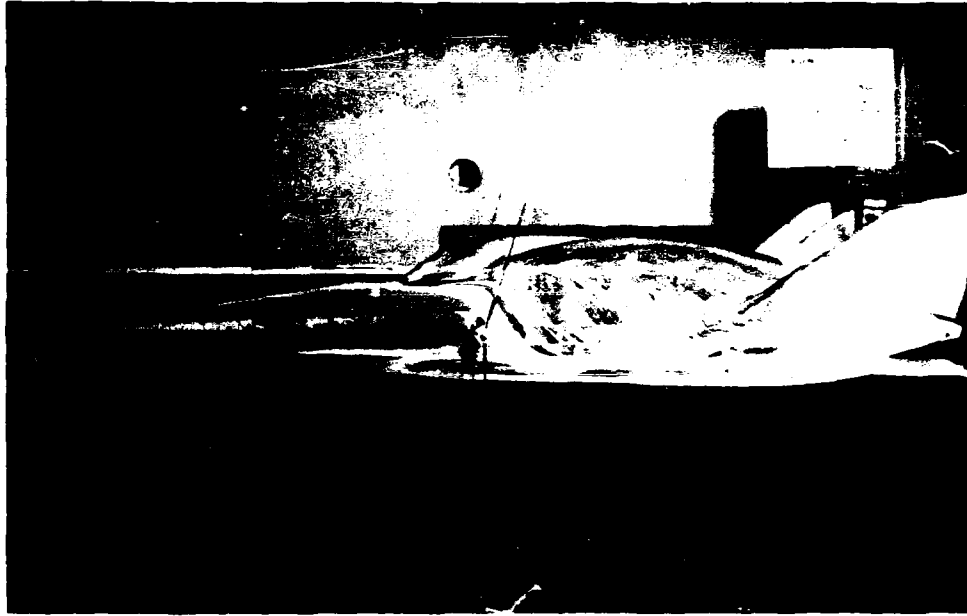
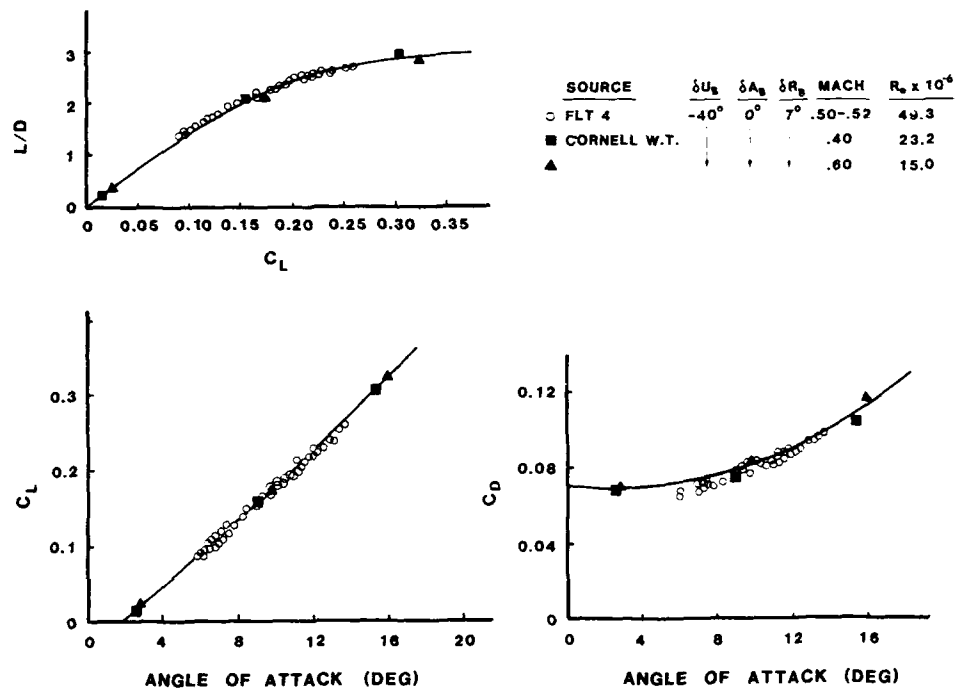
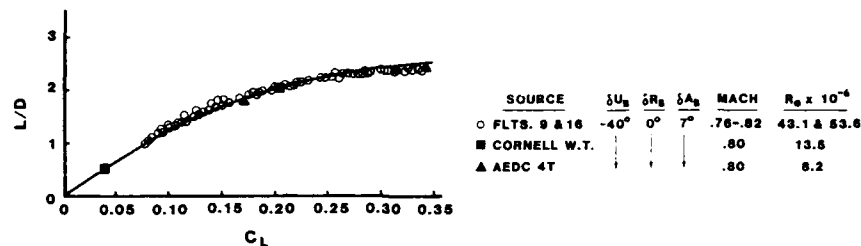
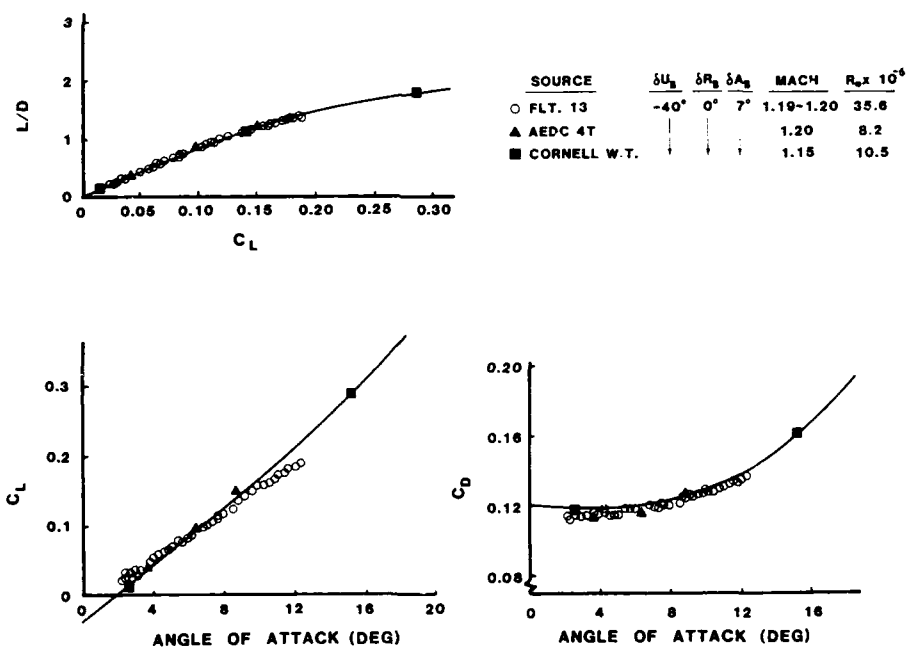


FIGURE 25 FDL-8/X-24B SUBSONIC DEVELOPMENT TEST

FIGURE 26A TRIM PERFORMANCE DATA FOR $M=0.5$

FIGURE 26B TRIM PERFORMANCE DATA FOR $M=0.8$ FIGURE 26C TRIM PERFORMANCE DATA FOR $M=1.2$

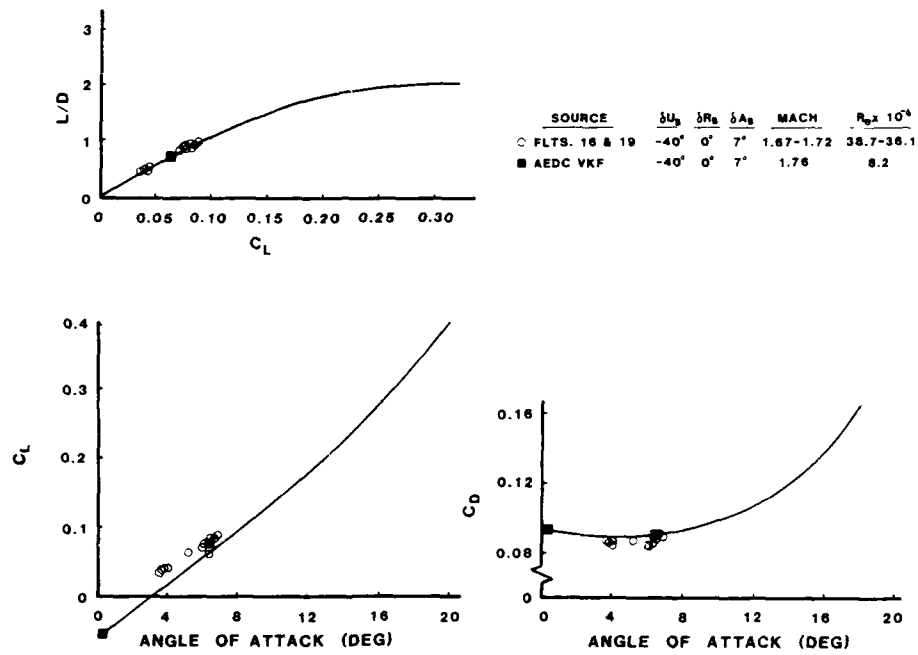
FIGURE 26D TRIM PERFORMANCE DATA FOR $M=1.7$



FIGURE 28 X-24 OIL FLOW

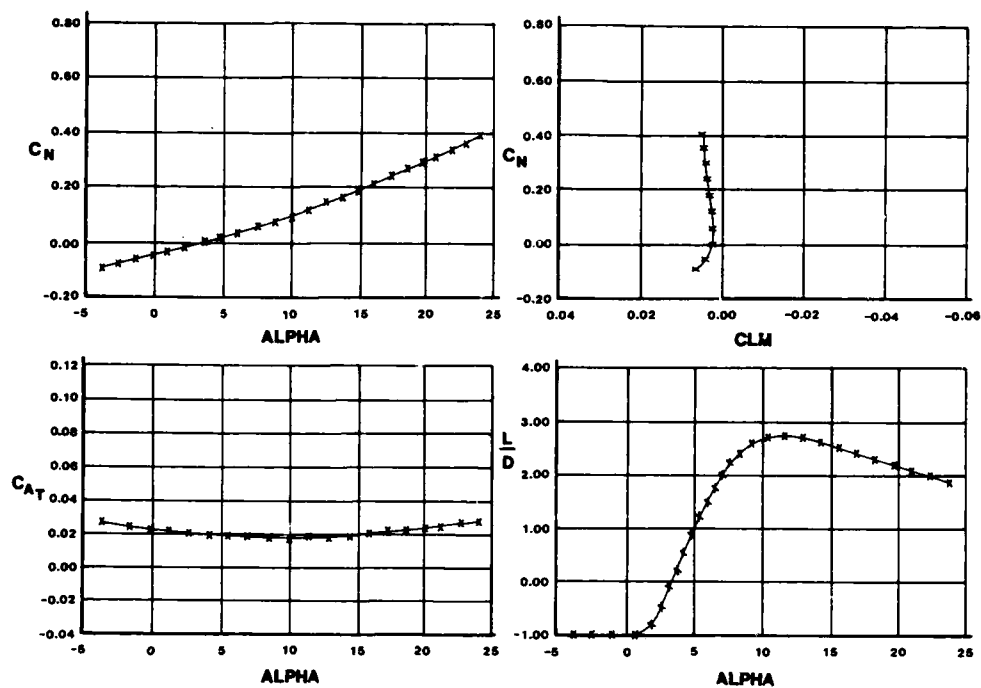


FIGURE 29 X-24C WIND TUNNEL DATA AT M=8.0

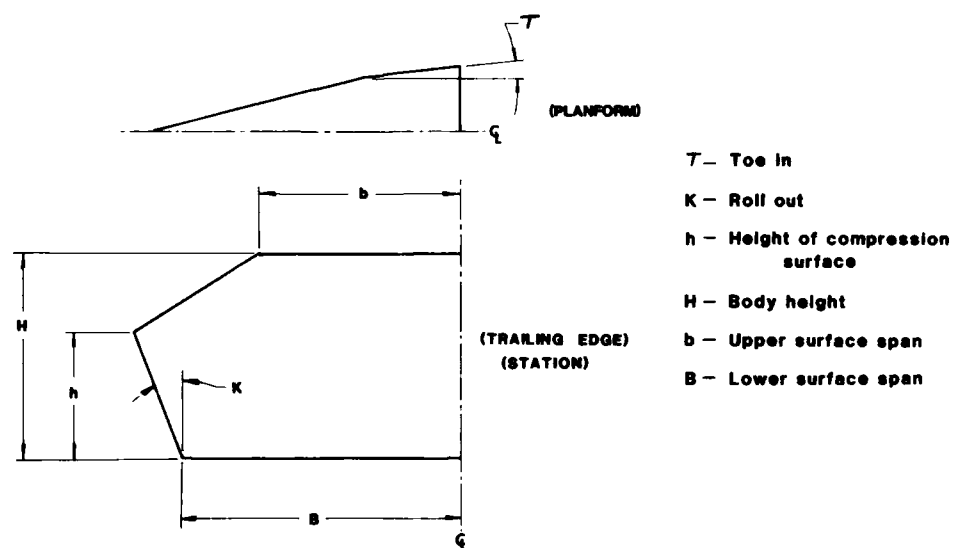
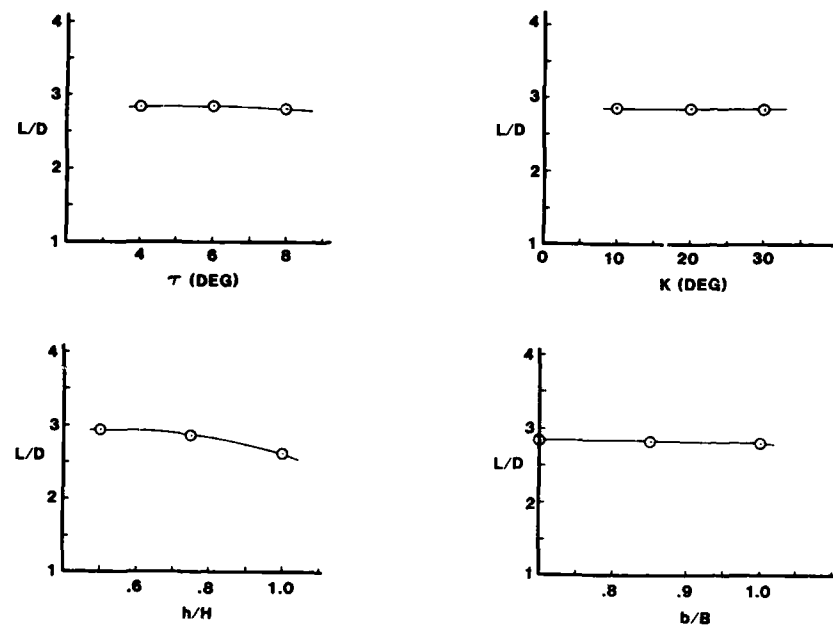
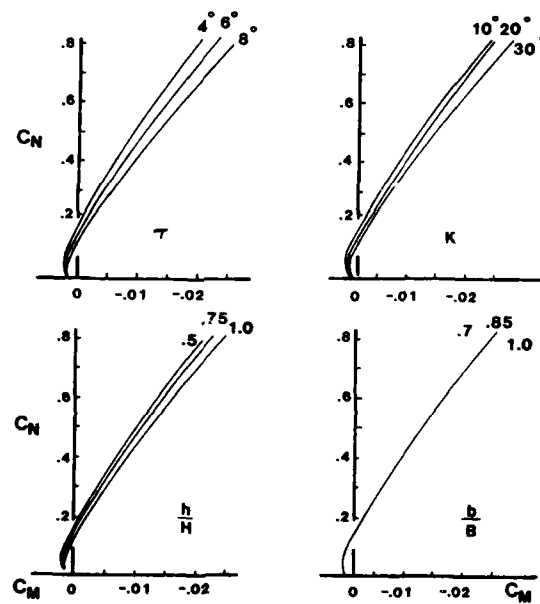


FIGURE 30 DEFINITION OF PARAMETRIC VARIABLES

FIGURE 31 VARIATION OF L/D FOR PARAMETRIC CHANGES

CG = .64L

FIGURE 32 VARIATION OF LONGITUDINAL STABILITY FOR PARAMETRIC CHANGES

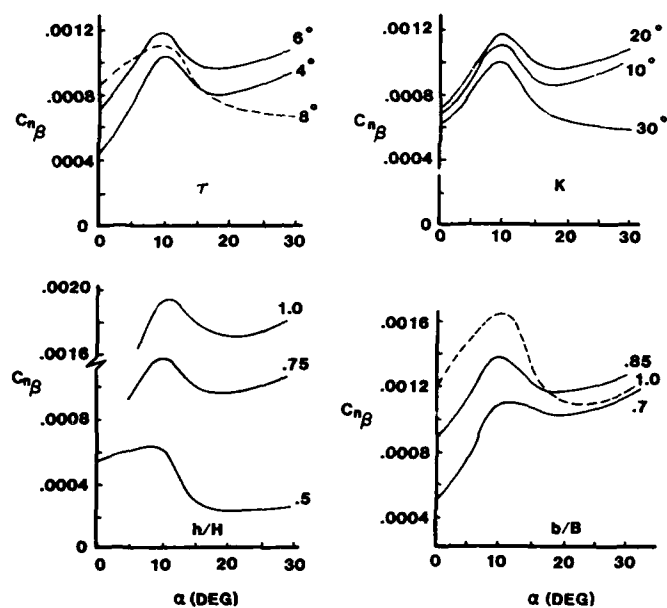


FIGURE 33 VARIATION OF DIRECTIONAL STABILITY FOR PARAMETRIC CHANGES

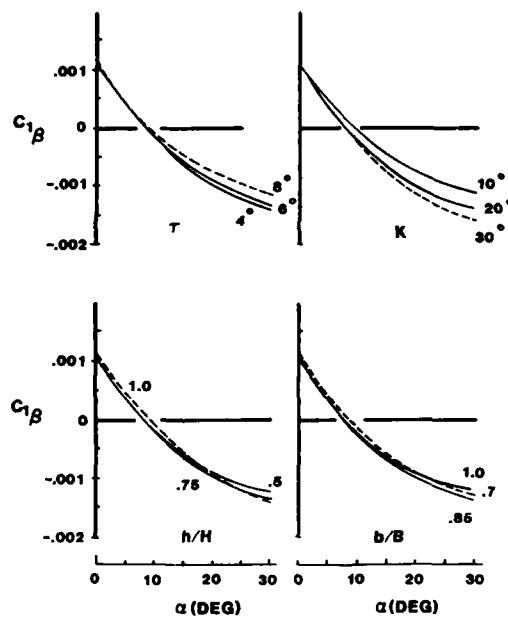


FIGURE 34 VARIATION OF THE ROLL PARAMETER FOR PARAMETRIC CHANGES



FIGURE 35 20-INCH STEEL FORCE MODEL FOR AEDC TUNNELS A, B, AND C

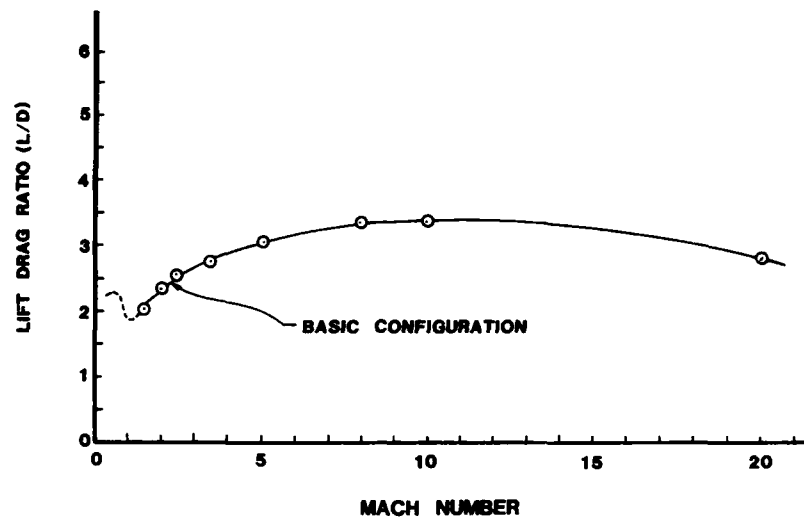


FIGURE 36 FDL-5 VARIATION OF MAXIMUM L/D WITH MACH NUMBER

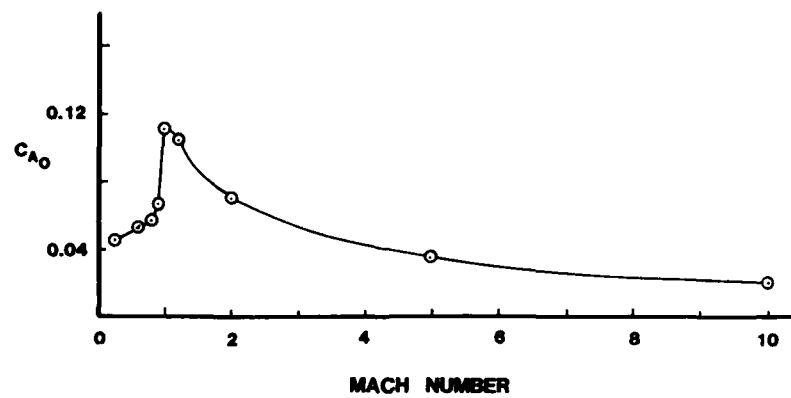


FIGURE 37 FDL-5 WIND TUNNEL RESULTS

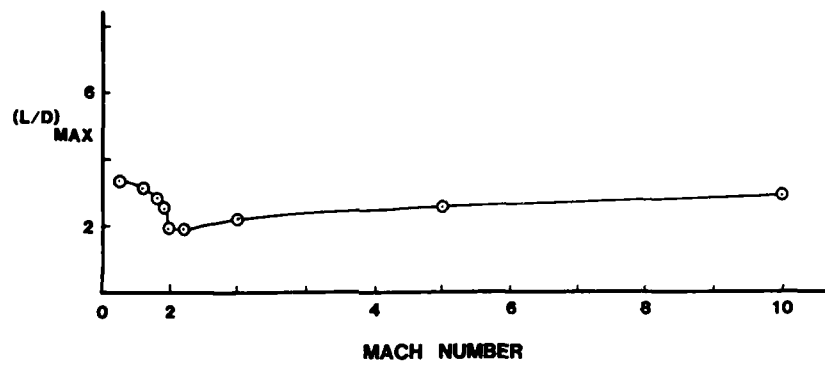


FIGURE 37 FDL-5 WIND TUNNEL RESULTS (CON'T)

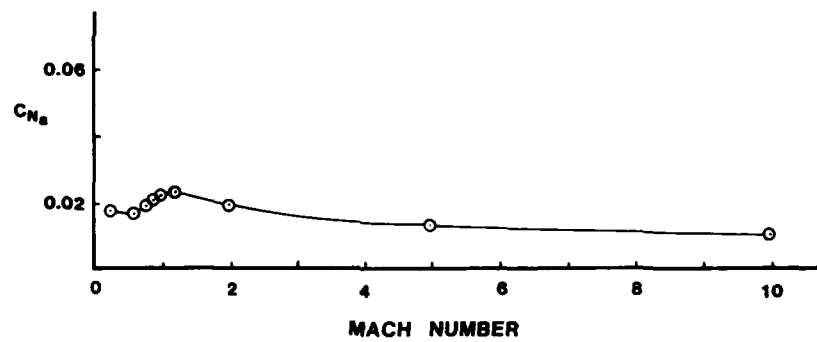


FIGURE 37 FDL-5 WIND TUNNEL RESULTS (CON,T)

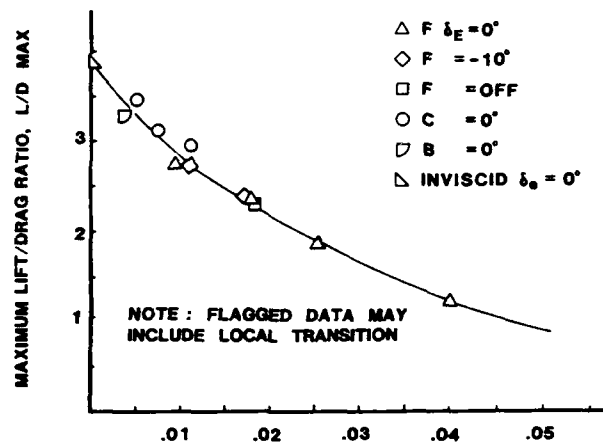


FIGURE 38 RAREFACTION PARAMETER $\bar{V} = M_{\infty} \frac{\sqrt{C_L}}{\sqrt{R C_L}}$

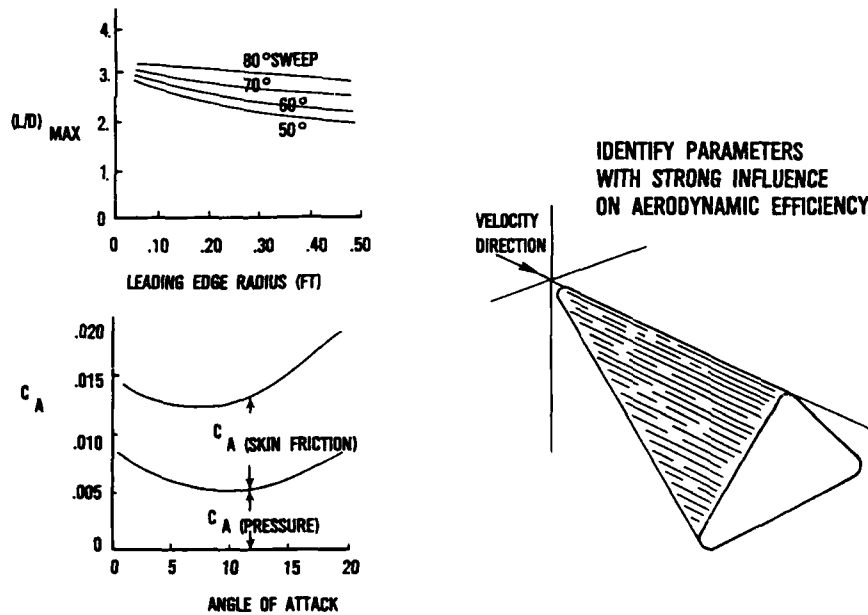


FIGURE 39 CONFIGURATION AERODYNAMICS FOR LIFTING BODIES

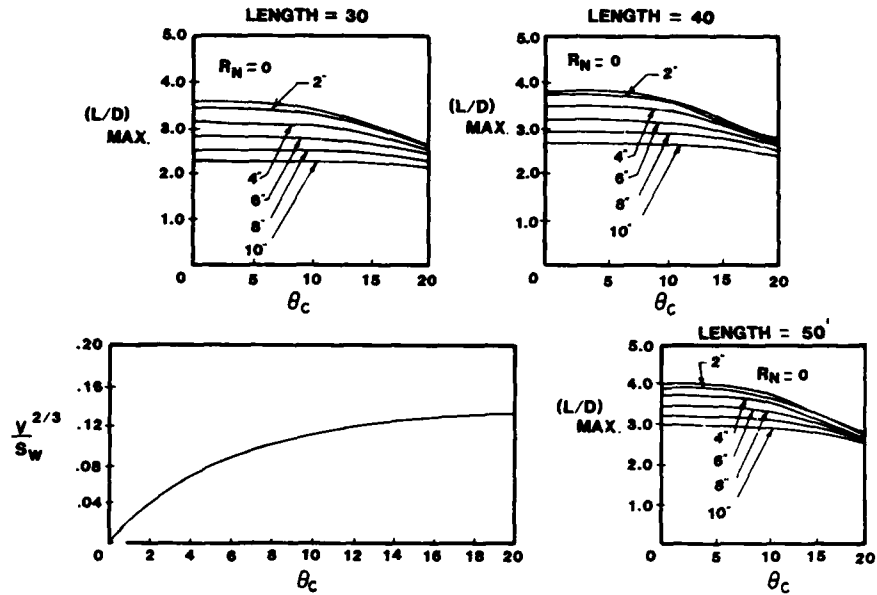


FIGURE 40 GEOMETRY EFFECTS ON L/D

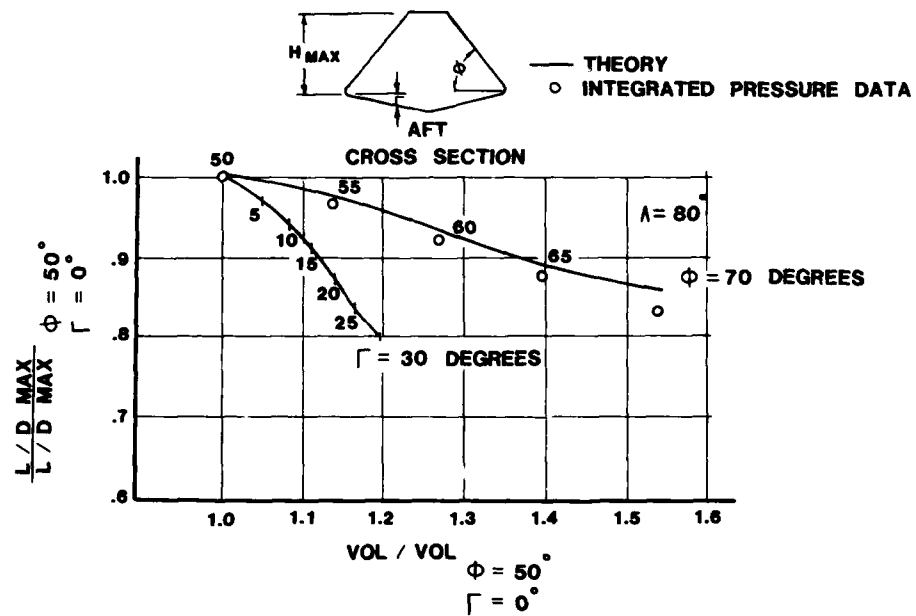


FIGURE 41 VOLUME INCREASE THROUGH CROSS SECTION CHANGES

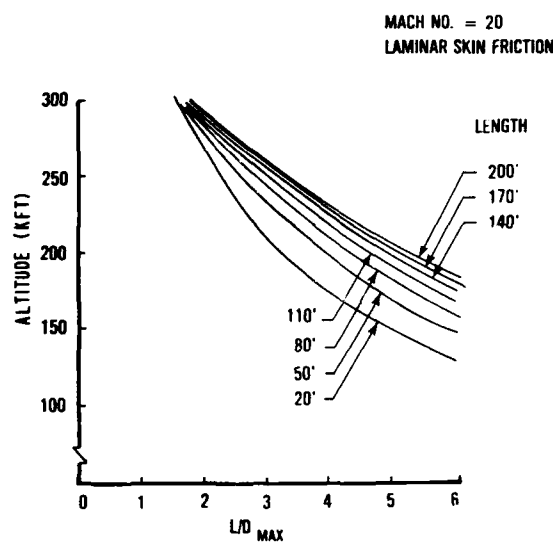


FIGURE 42 OPTIMUM CONFIGURATION EFFICIENCY

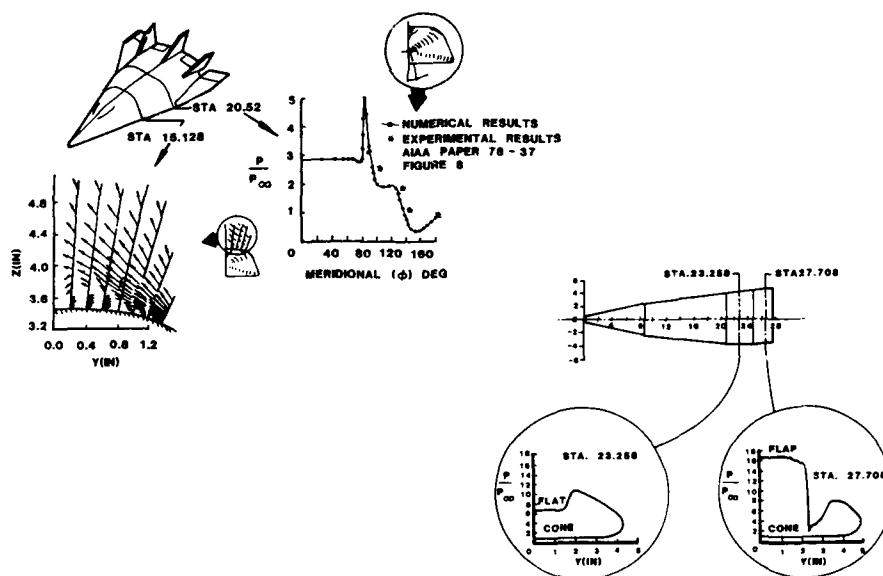


FIGURE 43 FLOW FIELD RESULTS

SURFACE STREAMLINE PATTERN

$M=5.95$
 $REYNOLDS\ NUMBER = 1.64 \times 10^7/m$
 $\alpha = 6\ DEGREES$

	C_L	C_D	L/D
EXPERIMENTAL DATA	3.676×10^{-2}	3.173×10^{-2}	1.158
NUMERICAL RESULT	3.503×10^{-2}	2.960×10^{-2}	1.183
ERROR (%)	4.71	6.71	2.16



FIGURE 44 NAVIER STOKES RESULTS

CONTROL SURFACE PHENOMENA :

- PREFLIGHT PREDICTIONS WERE BASED PRIMARILY ON WIND TUNNEL DATA
- THE ANALYSIS OF GRIFFITH AND MAUS DEMONSTRATED THE VALUE OF COMPUTATIONAL TECHNIQUES TO EXTRAPOLATE WIND TUNNEL DATA TO FLIGHT CONDITIONS.

- AND -

CHANGED FOREVER PAST CONCEPTS OF CONFIGURATION DEVELOPMENT

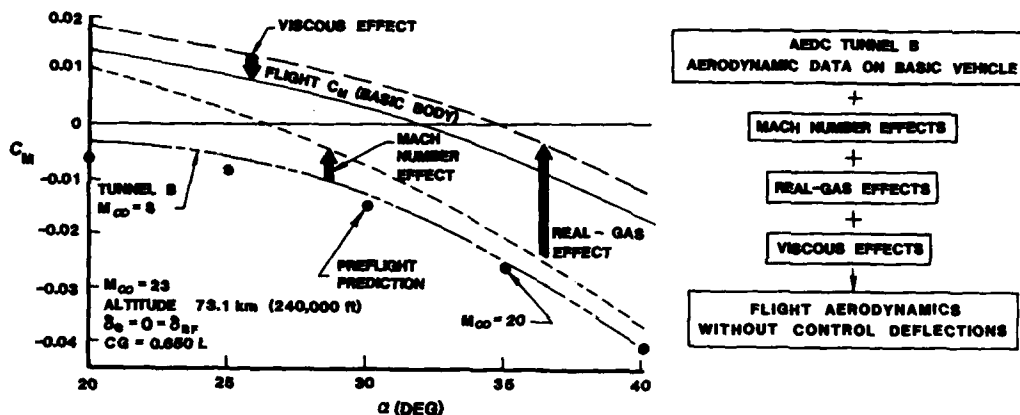


FIGURE 45 CONTROL SURFACE PHENOMENA

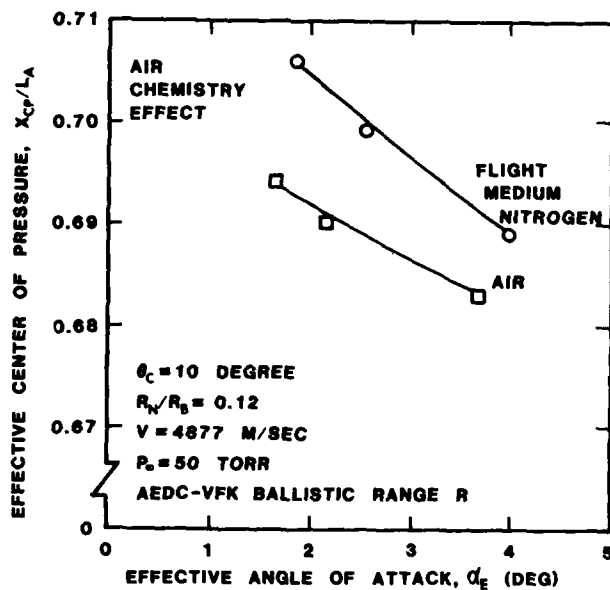


FIGURE 46 FLOWFIELD CHEMISTRY EFFECTS ON STABILITY OF BLUNTED CONES

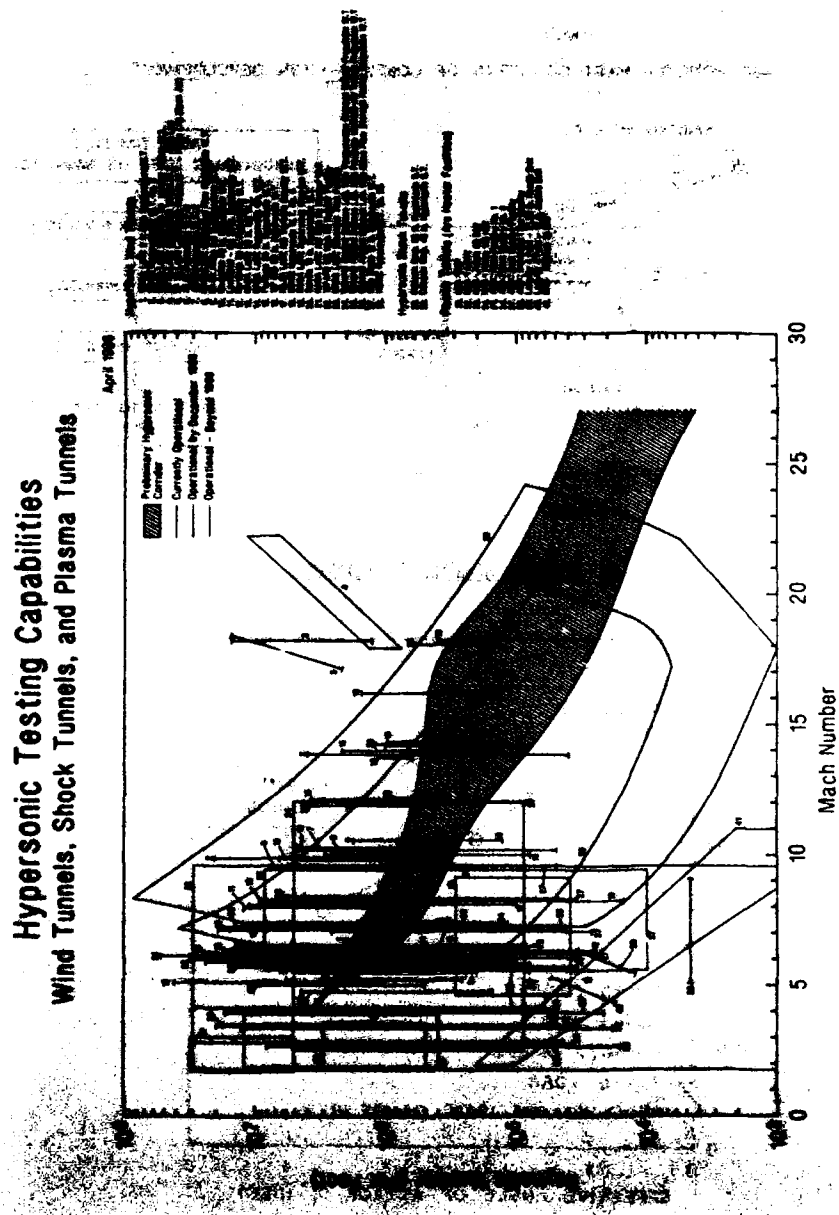


FIGURE 47 GROUND TEST CAPABILITIES

Hypersonic Testing Capabilities Wind Tunnels, Shock Tubes, and Pseudo-Rayonolite

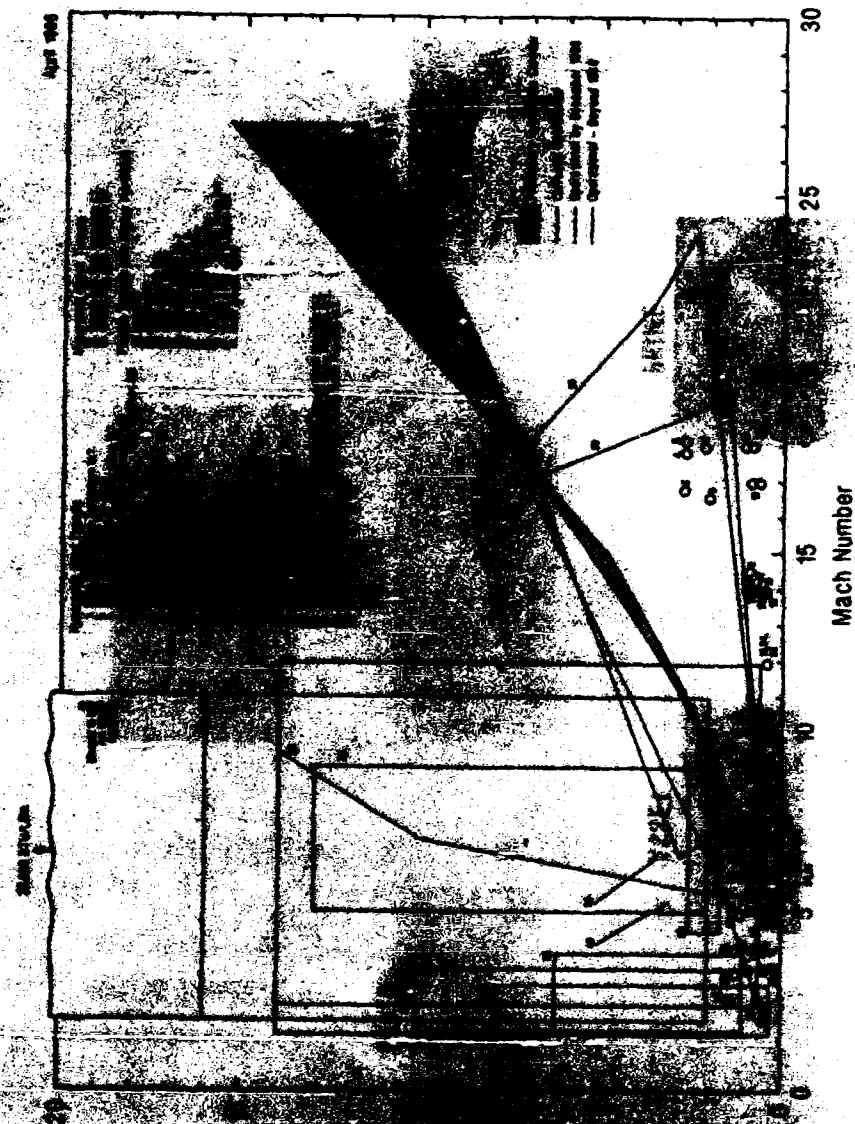


FIGURE 47 GROUND TEST CAPABILITIES

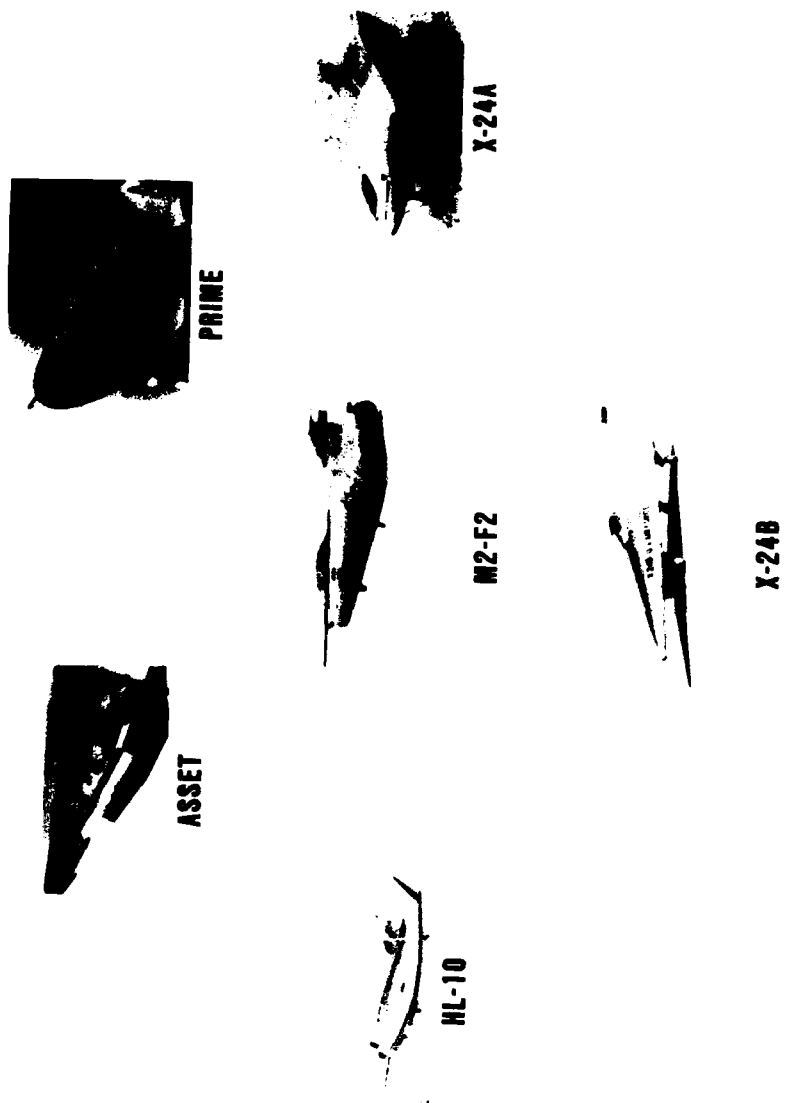


FIGURE 48 PREVIOUS LIFTING BODY RESEARCH VEHICLES

EXPERIENCES USING THE MARK IV SUPERSONIC HYPERSONIC ARBITRARY BODY PROGRAM

by

Miss Carren M.E. Fisher,
Aerodynamics Research Department,
Sowerby Research Centre,
British Aerospace P.L.C.,
P.O. Box 5, FPC 67,
Filton,
Bristol. BS12 7QW
ENGLAND

SUMMARY

This paper describes work done during the last two years in an attempt to gain an understanding of, and to establish a capability for the use of, the Douglas Supersonic/Hypersonic Arbitrary Body Program (S/HABP). The program has a complex structure and offers a large variety of aerodynamic prediction methods to solve many different types of problem.

Most of the features of the program have been used with some success. Aspects of the flowfield routines and viscous options, which could not be utilised correctly, are either under investigation, or updates to the programming are awaited. Some accurate predictions have been made using the inviscid pressure methods, which have been evaluated for a wide range of configurations, for Mach Numbers from 1.7 to 25.0 and from an incidence of -8° to 40° .

The code has been seen to be highly flexible, but the accuracy of the results is user dependent. Relative to computational fluid dynamics codes, S/HABP geometries are easy to prepare and the code is cheap to run.

NOTATION

b	net semispan (wing alone configurations)	MRP	Moment Reference Point
	gross span (body/wing configurations)	Nst	Stanton Number
c	chord	P0	Stagnation Pressure
c ₁	chord at position 1	Pr	Prandtl Number
c ₂	chord at position 2	Re	Reynolds Number
C _f	skin friction coefficient	S	gross semispan (waverider)
C _{f∞}	Chapman-Rubesin viscosity coefficient evaluated in the freestream, based on reference temperature conditions	STS	Space Transportation System
	$C'_\infty = \frac{u_\infty}{u'} \times \frac{T'}{T_\infty}$	T	Temperature
C _A	axial force coefficient	T'	reference temperature
C _D	drag coefficient	T ₀	stagnation temperature
C _L	lift coefficient	T _w	wall temperature
C _m	pitching moment coefficient	V	variation allowed
C _N	normal force coefficient	V'	slip parameter evaluated at freestream conditions
C _p	pressure coefficient		$\frac{V'}{V_\infty} = \frac{M_\infty \sqrt{C'_\infty}}{\sqrt{Re_\infty}}$
C _p ^x	C _p , C _D , C _L , C _m or C _N	x) cartesian co-ordinates, unless
d ^x	length of side of a square section vehicle	y, Y) otherwise defined
D _{max}	maximum body diameter	X _{cp}	centre of pressure
f _m	normal momentum accommodation coefficient	α	incidence angle
f _t	tangential momentum accommodation coefficient	β	sideslip angle
K	Modified Newtonian correction factor	γ	ratio of specific heats
	Modified Newtonian gives:	δ	fin deflection angle
	C _p = K sin δ	λ	configuration roll angle
	where $K = \frac{\gamma + 3}{\gamma + 1} \left[1 - \frac{2}{\gamma + 3} \frac{1}{M_\infty^2} \right]$	μ	dynamic viscosity
	(K = 2.0 for Newtonian flow)	μ'	reference dynamic viscosity
ℓ	reference length	φ	angular polar co-ordinate
L	body length		
L/D	Lift to drag ratio		
M	Mach Number		

Subscripts

x	based on x
∞	based on freestream conditions
ℓ	based on local conditions

A method of identifying inviscid pressure methods is used as follows; e.g. 2,2 (K = 2.0)/9,7 (5/3) is an inviscid pressure method. This consists of two sets of methods separated by a slash. The numbers before the slash apply to the body and the numbers after the slash apply to the controls unless indicated otherwise. The first number (2) applies to the body impact method and the second number (2) applies to the body shadow method. K = 2.0 provides the body K value. A value of K is required if the impact method is 1, 2 or 3.

The numbers after the slash (9,7(5/3)) indicate the impact and shadow methods on the second vehicle component (usually the controls, although it can be a different part of the body). The 9,7 indicates that the shock expansion impact and shadow methods have been used on the second part of the vehicle. The (5/3) is applicable to the shock expansion methods only. The shock expansion method needs starting values for its calculation procedure and these are provided, in this case, by method 5 in the impact region and method 3 in the shadow region. A key to the numbers of the impact and shadow methods is given in Table 1 and further details of the methods are given in References 1 and 2.

If one set of methods alone is used the set applies to the entire configuration. It should be noted that more than two sets of methods can be used.

A key to the Mark III skin friction methods is provided in Table 2.

1. INTRODUCTION

The development of the Douglas Hypersonic Arbitrary Body Aerodynamic Computer Program began in 1964 and was greatly expanded in subsequent years. The Mark IV Supersonic/Hypersonic Arbitrary Body Program (S/HABP, Reference 1) was written in 1973, and updated in 1980, under contract to the Air Force Wright Aeronautical Laboratories (AFWAL). This paper describes some work undertaken during the last two years, to try to gain an understanding of the methods available within S/HABP and to establish a capability for its use. This work has been carried out by the Aerodynamics Research Department of the Sowerby Research Centre (SRC) at British Aerospace, Bristol, with the support of the Procurement Executive of the Ministry of Defence.

The basic methodology, employed by S/HABP, is to consider the vehicle as a conglomeration of many flat plates, called elements, at incidence, which closely resemble the actual model surface. The type of prediction methods employed, on an element-by-element basis, use local slope and freestream Mach Number to calculate pressure. These methods are particularly applicable at high speeds, but an extension to the supersonic speed range is also available in the flowfield option, which uses embedded flowfield concepts to permit first order interference effects to be accounted for. Some of the inviscid pressure prediction methods themselves have also been extended down to supersonic speeds, by the use of empiricism and some purely supersonic inviscid pressure prediction methods have also been added.

Further enhancement of pressure predictions is provided by the shielding analysis, which accounts for the reduction in pressure experienced by those elements hidden from the flow by upstream elements.

The program also performs a viscous analysis in one of two ways. The first is the historically popular flat plate method, which is the same as that used in the Mark III Hypersonic Arbitrary Body Program. The second is an integral boundary layer approach, which involves the solving of the momentum integral equation for laminar flow and the momentum and moment-of-momentum integral equations for turbulent flow.

2. DISCUSSION

2.1 About The Program

S/HABP has a well ordered code structure and each of the basic analysis types is accomplished in a separate program component. The complex structure of the program is illustrated in Figure 1.

The geometry package provides rapid and element-by-element model generation techniques. These consist of quick methods to generate circular and elliptical section vehicles and aircraft components, i.e. wings, fins, stores and arbitrary section fuselages. Additionally, there is a parametric cubic curve fitting technique available to describe configurations. The program converts all geometry input into elements, which are then used by the aerodynamic calculation procedures (or AERO package). A sensitivity test showed that a very large number of elements is not always required when modelling a vehicle, however a high element density is desirable in regions of high rate of change of surface gradient. Generally, elements are input to S/HABP in groups or panels. The user then assembles these panels into components in the AERO package. A component is a major part of the vehicle and is analysed by the AERO package as a unit.

Once the model has been described, it can be viewed by the graphics package, TEKPIC. Graph plotting facilities for the results from the AERO package have also been added. The auxiliary routines enable arbitrary cross-sections sections to be taken through the vehicle, as desired.

The majority of the effort has been expended on the AERO package of the program. The first phase of the work was to ascertain how to use the Inviscid Pressures part of the program. There is a large choice of inviscid pressure methods available and these are listed in Table 1. Further details of each of the methods listed is given in Reference 1. The impact methods are those applied to flow-facing elements and the

shadow methods are applied to those elements facing away from the flow. The methods include the simple Newtonian approach, various purely empirical methods, correlations to exact numerical solutions, small disturbance theory and shock expansion methods. Figure 2 shows how the various methods interrelate, ranging from exact techniques at the top of the figure, to purely empirical methods at the bottom. Some of the exact techniques, such as the Method of Characteristics are not available within the program, but empirical approaches, which are available, approximate these methods. Referring again to Table 1, impact methods 1 to 15 and shadow methods 1 to 9 were those provided in the original version of S/HABP (modification 0) and this study was carried out to evaluate those methods. The remaining methods were provided as updates to eliminate certain deficiencies found in the original choice of methods.

The philosophy behind providing a large selection of pressure methods is that different methods can account for different flow phenomena. The program is therefore applicable to a wide range of vehicle types. A combination of many methods can be used for very complicated 3-D shapes (one impact and one shadow method per component) after which the pressure contributions from each of the vehicle parts can be summed using the data summation option of the special routines.

2.2 The Inviscid Pressure Methods

The Inviscid Pressures part of the code has been evaluated for a wide range of body alone and body/wing configurations, for incidences ranging from -8° to 40° and for Mach Numbers from 1.7 to 25.0. Full details of these results are presented in References 2 and 3.

Table 3 summarises the force and moment predictions made in Reference 2, with sketches of configuration type. The error band shown in the table appears to be large, but averaging includes low incidence predictions, where percentage errors are sometimes large, even for good predictions. Figures 3 to 8 show a sample of the graphical representations of the validation exercises undertaken, with some additional methods to those shown in Table 3. In some cases, an extensive range of methods is presented, since it is desirable to distinguish between methods that give accurate results for a given configuration type and flight condition and those that give poor results. Thus the use of these latter methods can be avoided when necessary.

Figure 3 shows various inviscid pressure method force, moment and centre of pressure predictions for vehicle 3, a tangent ogive cylinder with a boattail at Mach 4.63, together with experimental data. The Newtonian and Dahlem Buck Empirical Methods (1,1 ($K = 2.0$), 1,1 ($K = 1.81$) and 14,1) were not very accurate, but the inclined cone method on the nose, combined with the tangent wedge method on the body (6,4/3,2) gives an accurate C_p prediction. Newtonian predictions on other cylinder-boattail configurations, at different Mach Numbers have also been seen to be inaccurate. C_p is also not well predicted by these methods. This is because the methods used in Figure 3 are mainly of an inviscid nature, and a separate calculation would be required to provide the viscous contribution to C_A , which would be significant.

Figure 4 shows that the Modified Newtonian prediction method (1,1 ($K = 1.794$)) is closer to the experimental data than the Newtonian method (1,1 ($K = 2.0$)), for force, moment and centre of pressure predictions for a blunt nosed cone, vehicle 6, at Mach 4.63.

If a prediction method provides accurate pressure predictions for a configuration, when the results are summed accurate forces and moments are obtained. Thus, in many cases, C_p prediction data was also compared to experimental data. Figure 5 shows predicted and experimental C_p values for a blunted cylinder-conical frustum-flare configuration at Mach 7.0. The Modified Newtonian and Prandtl-Meyer prediction method (2,2 ($K = 1.81$)) is very accurate on the nose and hence needs only to be combined with accurate body predictions for good force and moment predictions to result. None of the methods validated, however, gave sufficiently accurate predictions to be "acceptable" in Table 3; the magnitude of both C_N and C_M were significantly overestimated in all cases. This can be attributed to inaccurate C_p predictions on the conical frustum-flare.

Aerodynamic force and moment predictions for a triangular section body, vehicle 10, at Mach 3.12, are shown in Figure 6. Good C_L and C_D predictions are given by the Modified Newtonian Method (1,1 ($K = 1.75$)) and the C_M trend is reasonable. The C_D prediction is inaccurate though, since no viscous contribution has been included. Many very poor predictions are given for this configuration. It might have been expected that some of the empirical methods would give reasonable C_D predictions, since they are not purely inviscid, but many of the C_D trends are very poor. Validation was also undertaken for bodies alone at Mach 3.12 with the same cross-sectional area distribution and same length as vehicle 10 but having circular (vehicle 4) and elliptic (vehicle 9) cross-sections. The Newtonian Method (1,1 ($K = 2.0$)) gave very good C_L and C_M predictions for these configurations.

Figure 7 shows force and moment predictions for an ellipse section vehicle with monoplane fins, vehicle 16, at a Mach Number of 4.63. Difficulty was encountered when trying to predict C_p accurately. Although some methods approximate the data trend, the magnitude is inaccurate. Perhaps the Modified Newtonian and Prandtl-Meyer method (2,2 ($K = 1.794$)) is a poor choice to apply on the body of this configuration, since this method

should not be applied to a nose impact angle less than that for shock detachment. However, the prediction accuracy is comparable to that of the other methods. C_D is reasonably predicted, and the C_D trend is correct for all the methods shown. C_D magnitude can be improved by adding a viscous contribution.

Figure 8 shows predicted forces and moments for a tangent ogive-cylinder configuration, with two sets of cruciform control surfaces, at Mach 4.6. C_D and C_N predictions are "acceptable" for all the methods shown, though the trends become inaccurate at very high incidences. C_A predictions are again low.

Figure 9 shows pressure predictions and experimental data on the upper surface of a fin alone at several incidences. The three methods presented give similar results; too large a magnitude for C_p is generally predicted. The difference between the zero and 12° incidence predictions is too great, but the difference between the $\alpha = 12^\circ$ and $\alpha = 24^\circ$ predictions is about right.

When attempting to obtain force and moment predictions for body/wing configurations, because of interference flow, larger pressures are expected for windward control surfaces that are not shielded than for controls in isolation. Thus good results can be obtained when particular methods are applied to unshielded, windward control surfaces but the same methods would overpredict pressures if applied to controls in isolation. Conversely, due to shielding, smaller pressures are expected for shielded control surfaces than for controls in isolation. Reasonable predictions have been obtained at SRC for wing/body configurations when the tangent wedge and Prandtl-Meyer methods (3,3) are applied to control surfaces that are not shielded and the tangent cone and Prandtl-Meyer methods (5,3) are applied to those that are. It is also likely that methods 12,3,9,7(3/3) and 13,7 would provide reasonable predictions on shielded control surfaces.

At present S/HABP does not have a suitable method to predict deflected control pressures (as opposed to pressures where the control and body are at the same incidence) since there is no separation model within the program.

Figure 10 shows the predicted and experimental pressure distributions over the lower surface of a triangular section waverider at Mach 8.6. The trend of the data is not followed by the prediction techniques and predictions are particularly disappointing at lower body incidences.

The Blast Wave pressure increments method, impact:15, has also been seen to give some accurate pressure predictions at supersonic Mach Numbers. These have been for hemisphere cylinders and blunted flat plates at zero incidence.

Figure 11 shows the Shuttle Orbiter configuration, as drawn by the graphics package, TEKPIC. The modelling of this configuration involved the use of many geometry options. The model is divided into nine panels. The four body panels were generated using the Aircraft Geometry Arbitrary Cross-Section (uselage) Generation Option and the five nozzles were generated by the Ellipse Generation Method. The tail was modelled by the Aircraft Geometry General Aerofoil Option and the remaining parts were input element by element.

Figure 12 shows the S/HABP Newtonian predictions (1,1 ($K = 2.0$)) to interpolated wind tunnel data and STS-1 data at Mach 13.5. The coefficient trends are mostly good. C_N , C_D , C_D and L/D trends are closer to the STS-1 data than the interpolated wind tunnel data. The C_D and C_L trends are the least accurate, though C_A would be expected to be inaccurate since no viscous contribution is included.

Figure 13 shows STS-5 lift and drag comparisons with preflight predictions from Reference 12. The variation allowed as shown in Reference 12 is also presented. It should be noted that below Mach 10.0 incidence is not constant. Vehicle incidence and Mach Number both vary up to Mach 10.0, incidence starting at 0° at very low Mach Numbers and reaching 40° at Mach 10.0. The curve discontinuities shown are due to shuttle manoeuvres and are not predicted. Various methods and combinations of methods were used, with and without a shielding contribution. On the whole, C_D predictions which included the shielding contribution were poor. The Dahlem Buck Empirical and Prandtl-Meyer Expansion Method (14,3), shown in Figure 13, without shielding gave generally good predictions for all the coefficients, and these were mainly within the allowed variation.

Results from the Free Molecular Flow Method (10,9) produced at Mach 25.0 were poor, however. Predictions from this method depend on the values of normal and tangential momentum accommodation coefficients (f_n and f_t respectively). If both coefficients are set equal to 0.0 Newtonian flow is approximated and both coefficients are set equal to 1.0 for completely diffuse reflection. It was thought that a lengthy calibration process would be required to ensure the right combination of f_t and f_n for the Shuttle configuration at Mach 25.0 and this was not attempted.

It is difficult to identify the best inviscid pressure method for a specific configuration and flow regime. In some cases, a change in Mach Number or incidence angle can considerably alter method accuracy. Table 3 provides one approach to method selection, which can be used if one of the configurations in the table is close to the vehicle shape and flight conditions for which a prediction is required. If pressure coefficient experimental data and prediction comparisons are available for parts of models which resemble parts of the required configuration at, or close to the appropriate Mach Number, then methods can be selected on a part by part basis.

If the general vehicle shape and flight conditions within a parametric study are new to the S/HABP user, then prediction comparisons with experimental data for a similar vehicle and flight condition can be made to aid method selection. Alternatively, S/HABP pressure prediction methods can be compared to results from the appropriate Euler method (e.g. 'SWINT', Reference 13, for a conventional missile shape) for a sample case.

Some improvements to predictions can be made by varying the Modified Newtonian Correction Factor to account for real gas effects. Due to inaccurate circular section body predictions, at supersonic speeds, a new method for use on the leeward side of cylindrical bodies has been recently introduced, this being the ACM Empirical Method. This method has been seen to give considerably improved C_D and X_{CP} predictions, when used in conjunction with the Dahlem Buck Empirical Methods on Blunted Tangent ogive type noses and the inclined cone method on the windward side of the cylindrical body (i.e. when 14,10/6,11 is used).

The program also predicts the various aerodynamic derivatives by the method of small perturbations. The accuracy of this type of prediction depends on how sensitive the aerodynamic force and moment predictions are to varying the parameter concerned. Some reasonable roll damping moment predictions have been gained.

2.3 The Shielding Option

One method provided by S/HABP to enhance inviscid pressure method predictions is the shielding option. This accounts for the reduction in pressure experienced by an elemental panel being hidden or shielded from the flow by another panel by setting C_p on shadow elements and those other elements hidden from the flow to zero. This is widely held to be realistic at hypersonic Mach Numbers, though not at lower supersonic speeds. A low supersonic prediction of vehicle forces and moments, with and without shielding and experimental data are shown in Figure 14. The C_D prediction is marginally improved, but C_L is definitely degraded when shielding is incorporated. Figure 13 also showed considerably degraded C_p predictions for predictions with shielding compared to those without, even at Mach 2.0. The prediction is probably made worse because shadow pressure coefficients which are negative are raised to zero by this method, not decreased. This method has been put to best use when it has been restricted to hidden impact regions only.

2.4 The Flowfield Analysis

The major purpose of the flowfield option is to provide a flowfield around the configuration which can then be used to account for the effects of the interference of one part of the vehicle on another (e.g. the effect of the body flowfield on the forces and moments of a control surface).

The second use of the flowfield option is to provide a surface flowfield, for use in the calculation of surface streamlines.

The flowfield methods of Table 4, can also be converted to pressure methods and the aerodynamic forces and moments of the configuration can then be calculated.

Flowfields can be generated by handloading or by the use of the methods shown in Table 4. An empirical approach is used to calculate the shock wave shape. (For further details of flowfield calculation methods, see Reference 1). A surface flowfield can also be created by transfer of data from the inviscid pressure methods calculation procedure.

Figure 15 shows the Mark IV S/HABP and the method of characteristics shock shape prediction for the minimum drag body of reference 15 at Mach 2.3. Results are good at the nose deviating downstream. Predictions of extent or breadth of the shock field which have been undertaken by S/HABP, have been found to be inaccurate when compared to experimental data.

Figure 16 shows the C_D predictions for the minimum drag configuration with monoplane wings. The tangent wedge prediction with the interference of the body flowfield seems to be the best prediction method, although the interference contribution is small.

As yet, the program cannot be used to interrogate the flow i.e. to output flowfield information between the body and its shock along arbitrary ('interrogation') lines as shown in Figure 17. This facility is currently under investigation by AFWAL and SRC.

2.5 Streamline Calculation

As far as the streamlines are concerned three main problems have been encountered. First, where to start the streamline on the body, second how to ensure sufficient streamline coverage over the entire geometry surface and third streamlines are restricted to continuous parts of the vehicle shape and cannot cross from panel to panel. Logic for these functions has been included in recent program updates, which it is hoped can be incorporated into the program in the near future. The approximations made in the streamline analysis are that the streamlines are two-dimensional and parallel.

2.6 The Viscous Methods

The remaining option is the viscous methods option. This is comprised of two methods: the Mark III Skin Friction Method, which considers the vehicle as a series of flat plates and the Integral Boundary Layer Method, which computes the boundary layer characteristics along streamlines using the Integral Boundary Layer equations.

The Mark III Skin Friction Method calculates the viscous forces on a number of constant property flat plates. Since a coarser model is required here than for the inviscid pressure methods, this requires a second pass into the geometry option. In the Mark III method, incompressible skin friction coefficient is given by Blasius or Sivells and Payne (Reference 16) for laminar or turbulent flow respectively. Correction factors to account for compressibility effects are given by either of the reference temperature or reference enthalpy methods for laminar or turbulent flow, and the Spalding-Chi method can be used instead, if desired, for turbulent flow. Surface wall temperature is also required in the correction factor equations and is either given by a thin skin heat balance, or is input by the user, or the adiabatic wall temperature can be used. The user selects the method and wall temperature combination from Table 2. A real gas viscous option is available, and is used automatically if the laminar reference enthalpy method is selected. Viscous-inviscid interaction, planform effects and flow history are also taken into account in the Mark III Skin Friction Method. (Further details of this method are provided in Reference 1).

In order to assess this part of the code, the accuracy of the Stanton Number prediction was considered. Since this method predicts only skin friction coefficient and not Stanton Number, the following equations were used:

$$N_{St} = \frac{C_f}{2} Pr^{-2/3} \quad \text{for laminar flow}$$

and $N_{St} = C_f/2 \quad \text{for turbulent flow}$

Figure 18 shows the Stanton Number predictions at zero incidence for a sharp nosed 10° cone. A value of $Pr = 0.725$ was used in this case. The S/HABP predictions were lower than the experimental data, and the reference enthalpy and reference temperature methods gave virtually the same result. The laminar, Blasius hand calculation shows the size of the compressibility effect allowed for in S/HABP.

Figures 19 and 20 show the Stanton Number predictions for a blunted 20° cone at zero incidence. A value of $Pr = 0.71$ was used in this case. Close agreement with experimental data is seen for the laminar predictions, while the reference enthalpy and reference temperature calculated wall temperature methods are the best for the turbulent flow regime. At 10° incidence, the accuracy of the turbulent regime reference temperature method, with calculated wall temperature deteriorated considerably, though the laminar prediction remained accurate.

Mark III Skin Friction method predictions for a blunt nosed 50° cone at zero incidence are shown in Figure 21. A value of 0.71 was used for Prandtl Number for this case. Both the laminar and turbulent cases were better predicted by the calculated wall temperature version of the reference temperature laminar flow and Spalding-Chi turbulent flow method than the input wall temperature version.

The Integral Boundary Layer Method can be used to calculate detailed boundary layer characteristics along a streamline. However it cannot be used to calculate the viscous contribution to vehicle forces and moments, since there is no logic to ensure sufficient streamline coverage. The method does not allow for viscous-inviscid interaction or planform effects. Blunt nosed and pointed nosed cones can be analysed, but the input of suitable initial boundary layer thicknesses is required, since there is no logic to find the true starting position of the streamline.

Reasonable Stanton Number predictions for pointed and blunt nosed 50° cones have been achieved with this version of the code. However the prediction is heavily dependent on input boundary layer thicknesses, which are generally not known in advance. It is thought that forthcoming updates will rectify the problems in this version of the method, and correct some errors which have been encountered.

3. CONCLUSIONS

Parts of the original version of S/HABP, namely the flowfield interrogation option, the streamline analysis and the Integral Boundary Layer Method have not been working adequately and updates are awaited.

The remaining options of the program have been used to give some accurate aerodynamic predictions for configurations ranging from a triangular section body alone at Mach 3.1, to the complex Shuttle configuration at Mach 25.0 and including wing/body/control configurations at Mach 5.0. The code is considered to be highly flexible in that it can assess simple and very complicated shapes, but prediction accuracy depends on the user's experience with the code. Very accurate predictions have been gained after calibration of S/HABP results with experimental data or Euler methods predictions.

The ease of setup of vehicle geometries and cheapness of the program make it an ideal tool with which to investigate the aerodynamic potential of a large number of configurations within a parametric study.

REFERENCES

1. Gentry, A.E. et al, The Mark IV Supersonic/Hypersonic Arbitrary Body Program. Vols I - III. AFFDL-TR-73-159, November 1973
2. Fisher, Miss C.M.E., Volume 1 : Assessment and Validation of the S/HABP Inviscid Pressure Methods. BAe SRC JS 10282, March 1985
3. Fisher, Miss C.M.E., Volume 2 : Assessment and Validation of the S/HABP Viscous Options. BAe SRC JS 10282, May 1986
4. Landrum, E.J., Wind Tunnel Force and Flow Visualisation at Mach Numbers from 1.6 to 4.63 for a Series of Bodies of Revolution at Angles of Attack from -4° to 60°. NASA TM-78813, March 1979
5. Jackson, G.M., Determining Surface Pressure on Blunt Bodies of Revolution at Small Angles of Attack in Supersonic Flow. NASA TN-D-4865, November 1968.
6. Unpublished ARA Data
7. Lange, R.H. and Wittliff, C.E., Force and Pressure Distribution at a Mach Number of 3.12 of Slender Bodies Having Circular, Elliptic and Triangular Cross-Sections and the Same Longitudinal Distribution of Cross-Sectional Area. RML56D17, July 1956
8. Shrout, B.L., Warner Robins, A., Longitudinal Aerodynamic Characteristics of an Elliptic Body with a Horizontal Tail at Mach Numbers from 2.3 to 4.63. NASA Technical Paper 2024, June 1982
9. Monta, W.J., Supersonic Aerodynamic Characteristics of an Air to Air Missile Configuration with Cruciform Wings and In Line Tail Controls. NASA-TM-X-2666, December 1972
10. Fellows, Mrs. K.A., Pressure Measurements on a Series of Cruciform and Monoplane Delta and Cropped Delta Wings over the Mach Number Range 0.5 to 2.8 at Comprehensive Incidence and Roll Altitudes. ARA Model Test Note M117/1, April 1980
11. Crabtree, L.F., Treadgold, D.A., Experiments on Hypersonic Lifting Bodies. RAE-TR-67004, January 1967
12. Arrington, J.P., Jones, J.J., (compilers), Shuttle Performance : Lessons Learnt. NASA Conference Publication 2283, Part 1. Conference held at NASA Langley Research Centre, Hampton, Va., March 8-10, 1983
13. Wardlaw, A.B. Jr., Hackerman, L.B., Baltakis, F.P., An inviscid Computational Method for Supersonic Missile Type Bodies - Program Description and Users' Guide. NSWC TR 81-459, December 1981
14. Unpublished RAE Data
15. Jernell, L.S., Comparisons of Theoretical and Experimental Pressure Distributions over a Wing-Body Model at High Supersonic Speeds. NASA-TN-D-6480, September 1971
16. Sivells, J.C., Payne, R.G., A Method of Calculating Turbulent Boundary Layer Growth at Hypersonic Mach Numbers. AEDC-TR-59-3, March 1959
17. Chien, K.Y., Hypersonic, Turbulent Skin-Friction and Heat-Transfer Measurements on a Sharp Cone. AIAA Paper 74-97, Washington DC, 1974.
18. Julius, J.D., Measurements of Pressure and Local Heat Transfer on a 20° Cone at Angles of Attack up to 20° for a Mach Number of 4.95. NASA TN D-179, December 1959
19. Chauvin, L.T., Speegle, K.C., Boundary-Layer-Transition and Heat-Transfer Measurements from Flight Tests of Blunt and Sharp 50° Cones at Mach Numbers from 1.7 to 4.7. NACA RM L57004, April 1957

METHOD NO.	IMPACT METHOD (APPLIED TO WINDWARD SIDE OF VEHICLE)	METHOD NO.	SHADOW METHOD (APPLIED TO LEeward SIDE OF VEHICLE)
1	MODIFIED NEWTONIAN	1	NEWTONIAN (i.e. $C_p = 0$)
2	MODIFIED NEWTONIAN AND PRANDTL-MEYER	2	MODIFIED NEWTONIAN AND PRANDTL-MEYER
3	TANGENT-WEDGE (USING OBLIQUE SHOCK)	3	PRANDTL-MEYER EXPANSION
4	TANGENT-WEDGE EMPIRICAL	4	INCLINED-CONE
5	TANGENT-CONE	5	VAN DYKE UNIFIED
6	INCLINED-CONE	6	HIGH MACH NUMBER BASE PRESSURE ($C_p = -1/M^2$)
7	VAN DYKE UNIFIED	7	SHOCK-EXPANSION (USING STRIP THEORY) - PRANDTL-MEYER EXPANSION FROM FREESTREAM ON FIRST ELEMENT OF EACH STREAMWISE STRIP
8	BLUNT-BODY SKIN-FRICTION SHEAR-FORCE	8	INPUT PRESSURE COEFFICIENT
9	SHOCK-EXPANSION (USING STRIP THEORY)	9	FREE MOLECULAR FLOW
10	FREE-MOLECULAR FLOW	10	MIRROR DAHLEM-BUCK
11	INPUT PRESSURE COEFFICIENT	11	ACH EMPIRICAL DATA
12	HANKEY FLAT-SURFACE EMPIRICAL	12	OSU BLUNT BODY EMPIRICAL
13	DELTA-WING EMPIRICAL		
14	DAHLEM-BUCK EMPIRICAL		
15	BLAST-WAVE PRESSURE INCREMENTS		
16	MODIFIED TANGENT CONE		
17	OSU BLUNT BODY EMPIRICAL		

NOTE: IMPACT METHODS 16 AND 17 AND SHADOW METHODS 10, 11 AND 12 ARE RECENT UPDATES TO S/HABP

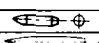
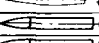

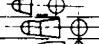




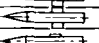


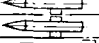
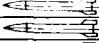





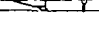
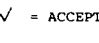
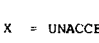
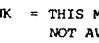
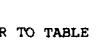
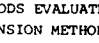

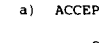

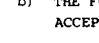
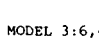
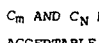
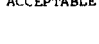
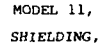










Table 1 : IMPACT AND SHADOW METHODS

METHOD SELECTION		TEMPERATURE SELECTION		
LAMINAR	TURBULENT	CALCULATED WALL TEMPERATURE	ADIABATIC WALL TEMPERATURE	INPUT WALL TEMPERATURE
REFERENCE TEMPERATURE	SPALDING-CHI	0	1	2
REFERENCE ENTHALPY	SPALDING-CHI	3	4	5
REFERENCE TEMPERATURE	REFERENCE TEMPERATURE	6	-	7
REFERENCE ENTHALPY	REFERENCE ENTHALPY	9	-	8

Table 2 : MARK III SKIN FRICTION VISCOUS OPTION METHOD SELECTION AND INTEGRAL BOUNDARY LAYER VISCOUS METHOD TEMPERATURE SELECTION. (NUMBERS SHOWN INDICATE FLAG REQUIRED IN S/HABP.)

FLOWFIELD PREDICTION METHODS	
STARTING CONDITIONS	SHOCK EXPANSION METHODS AVAILABLE
TANGENT WEDGE (IMPACT) PRANDTL-MEYER (SHADOW)	FIRST ORDER ONLY
JONES CONE FLOW (BETTER FOR SHADOW SURFACES)	FIRST OR SECOND ORDER
CP NO. 792 CONE FLOW (BETTER FOR IMPACT SURFACES)	FIRST OR SECOND ORDER

Table 4 : TO SHOW APPROXIMATE ANALYTICAL FLOWFIELD PREDICTION METHODS AVAILABLE WITHIN S/HABP
SEE REFERENCE 1 FOR FURTHER DETAILS OF METHODS AVAILABLE

GEOMETRY	METHOD	C _N	C _m	C _A	METHODS EVALUATED									
					1	2	3	4	5	6	7	8	9	10
	1				X	X	X							
	2				✓	✓	X	X	X	✓	X	X		
	3						X	X	X	X	✓			
	4						X	X	X	X	✓			
	5						X	X	X	X	✓			
	6				✓	X	✓							
	7						X	X						
	8						✓	X	X	✓	X			
	9						✓	X	X	✓	X			
	10				✓	X	X	X	X	X	X			
	11				✓	X	X	X	X	X	X			
	12				X	X			X	X				
	13				X	X	X	✓	X	✓				
	14				X	X	X	X	X	X	X			
	15				X	X	X	X	X	X	X			
	16				X	X	X	X	X	X	X			
	17				X	X	X	X	X	X	X			
	18				X	X	X	X	X	X	X			
	19				X	X	X	X	X	X	X			
	20				X	X	X	X	X	X	X			
	21				X	X	X	X	X	X	X			
	22				X	X	X	X	X	X	X			
	23				X	X	X	X	X	X	X			
	24				X	X	X	X	X	X	X			
	25				X	X	X	X	X	X	X			
	26				X	X	X	X	X	X	X			
	27				X	X	X	X	X	X	X			
	28				X	X	X	X	X	X	X			
	29				X	X	X	X	X	X	X			
	30				X	X	X	X	X	X	X			
	31				X	X	X	X	X	X	X			
	32				X	X	X	X	X	X	X			
	33				X	X	X	X	X	X	X			
	34				X	X	X	X	X	X	X			
	35				X	X	X	X	X	X	X			
	36				X	X	X	X	X	X	X			
	37				X	X	X	X	X	X	X			
	38				X	X	X	X	X	X	X			
	39				X	X	X	X	X	X	X			
	40				X	X	X	X	X	X	X			
	41				X	X	X	X	X	X	X			
	42				X	X	X	X	X	X	X			

KEY

✓ = ACCEPTABLE

X = UNACCEPTABLE

BLANK = THIS METHOD WAS NOT USED OR THIS DATA WAS NOT AVAILABLE

REFER TO TABLE 1 FOR THE KEY TO THE INDIVIDUAL METHODS EVALUATED. METHOD 9,7(5/3) IS THE SHOCK EXPANSION METHOD USED IN THIS TABLE.

NOTES

- a) ACCEPTABILITY CRITERIA FOR C_x :-

$$0.8 \leq \frac{C_x \text{ PREDICTED}}{C_x \text{ EXPERIMENTAL}} \leq 1.25$$
- b) THE FOLLOWING COMBINATIONS ALSO PROVED ACCEPTABLE:
- (i) MODEL 3:6,4 NCSE; 3,2 BODY GAVE ACCEPTABLE C_m AND C_N PREDICTIONS. METHOD 14,1 GAVE AN ACCEPTABLE C_H PREDICTION.
- (ii) MODEL 11, $\lambda = -45^\circ$, METHOD 12,3, WITH SHIELDING, GIVES AN ACCEPTABLE C_m PREDICTION.

(iii) FOR MODEL 13, METHOD 6,4/13,7 GIVES AN 'ACCEPTABLE' C_N PREDICTION AT $M=2.25$ AND AN 'ACCEPTABLE' C_A PREDICTION AT $M=5.0$

(iv) FOR MODEL 14, A: BOTH MACH NUMBERS METHOD 14,5/13,7 GIVES 'ACCEPTABLE' C_N AND C_m PREDICTIONS.

(c) FOR MODEL 15, MANY COMBINATIONS OF METHODS WERE USED. ONLY THE MORE COMMON OR 'ACCEPTABLE' METHODS ARE PRESENTED HERE.

(d) FOR MODEL 16, NO METHOD PREDICTS C_m ACCEPTABLY, BUT EXPERIMENTAL VALUES WERE SMALL AND THEREFORE PERCENTAGE ERRORS WERE LARGE.

Table 3 : TO SHOW 'ACCEPTABLE' C_N , C_m AND C_A PREDICTIONS

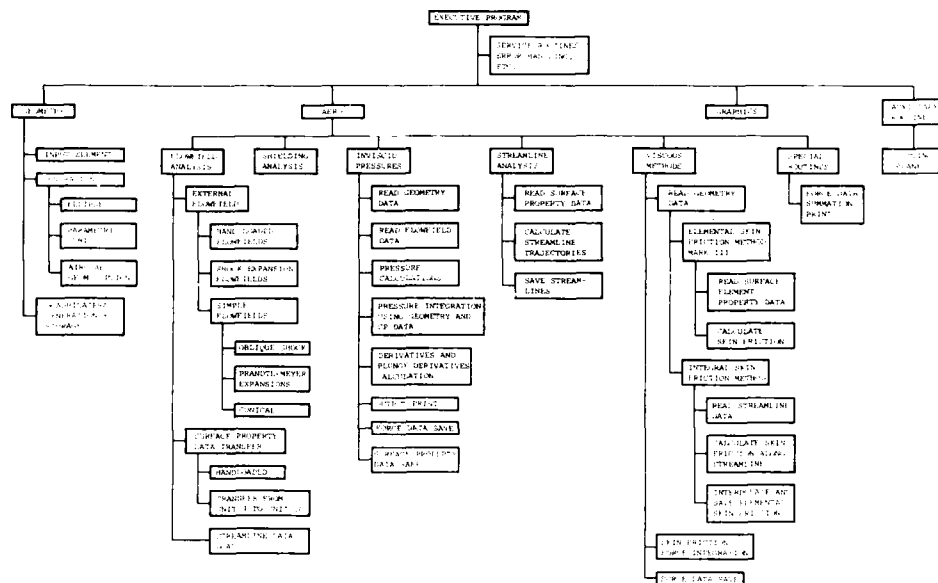


Figure 1 : S/HABP FLOWCHART

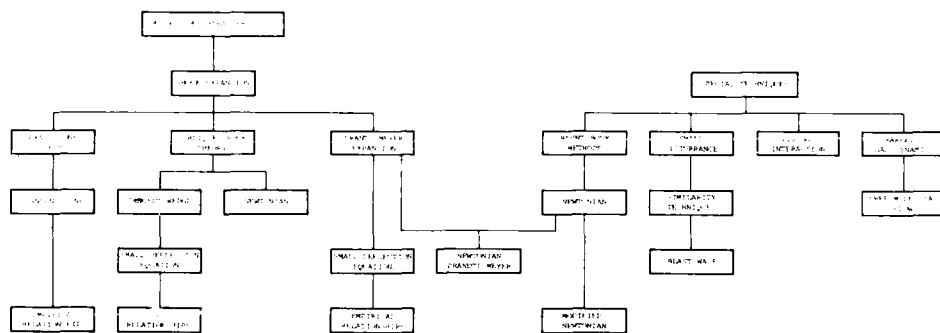


Figure 2 : THE INTERRELATION OF THE PRESSURE CALCULATION METHODS

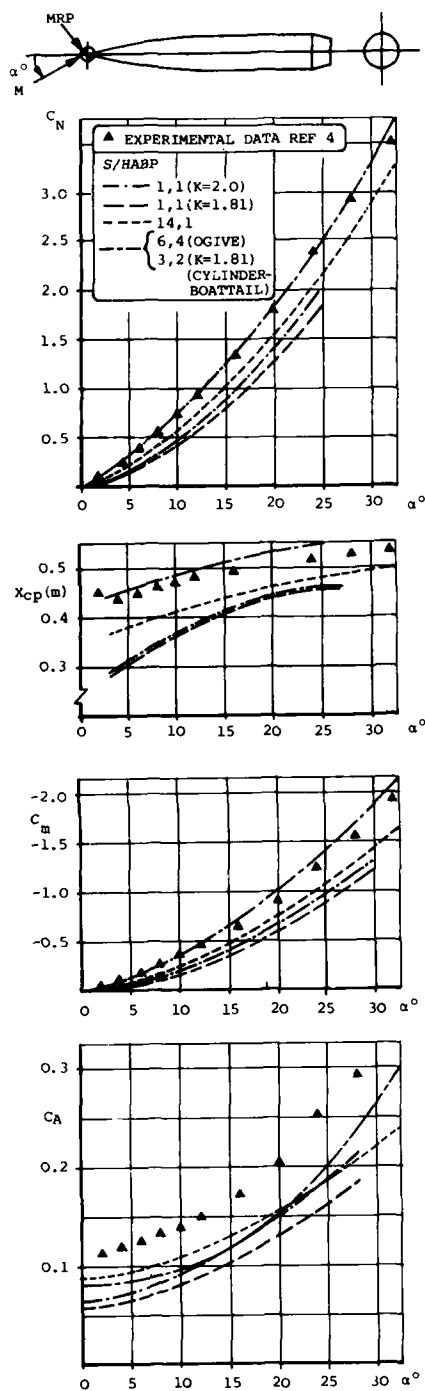


Figure 3 : C_N, C_m, C_A AND x_{cp} VERSUS α ; FOR TANGENT OGIVE-CYLINDER BOATTAIL $M = 4.63$, MRP $x/L = 0.0$ POSITIVE x_{cp} MEASURED AFT OF NOSE

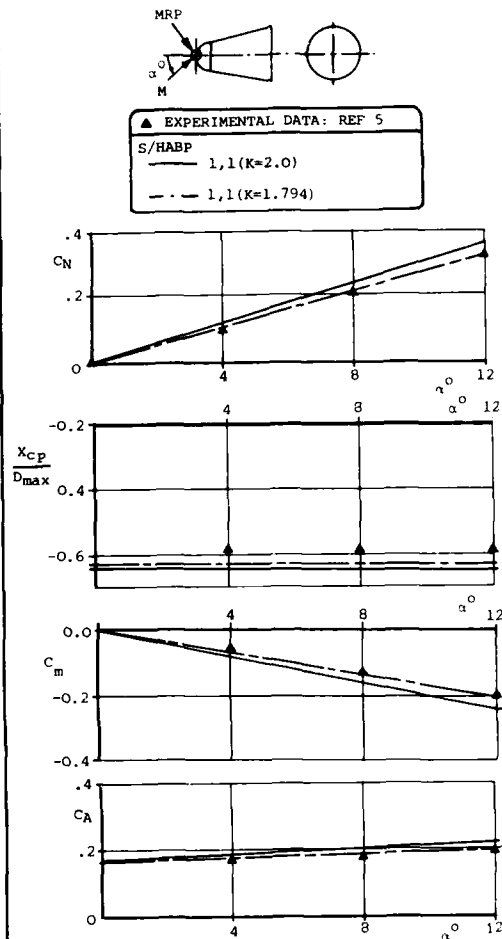


Figure 4 : C_N, x_{cp}, C_m AND C_A VERSUS α . $M = 4.63$, POSITIVE x_{cp} MEASURED FORWARD OF NOSE

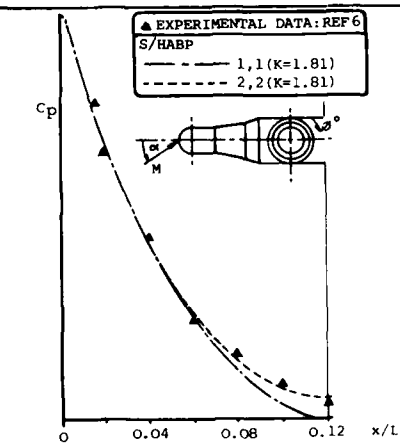
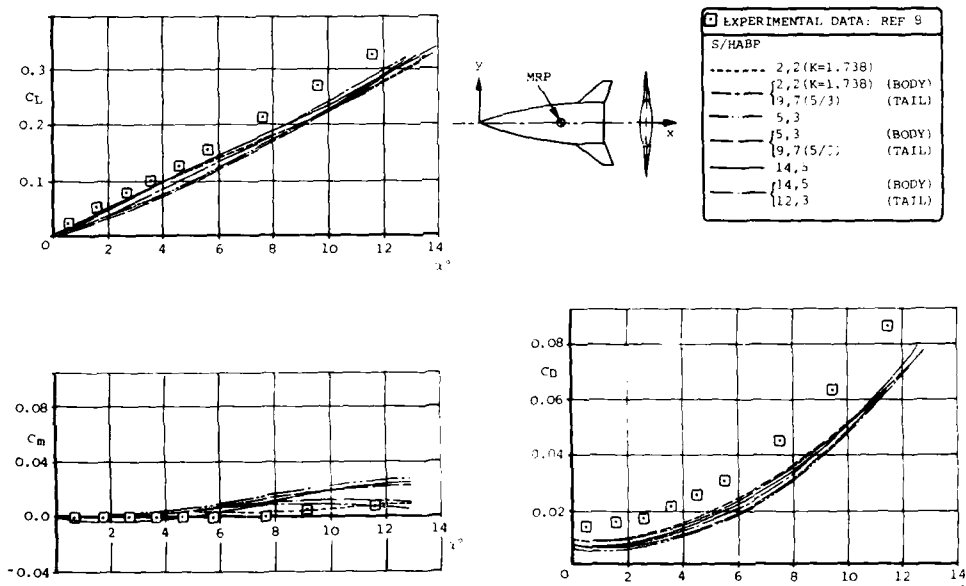
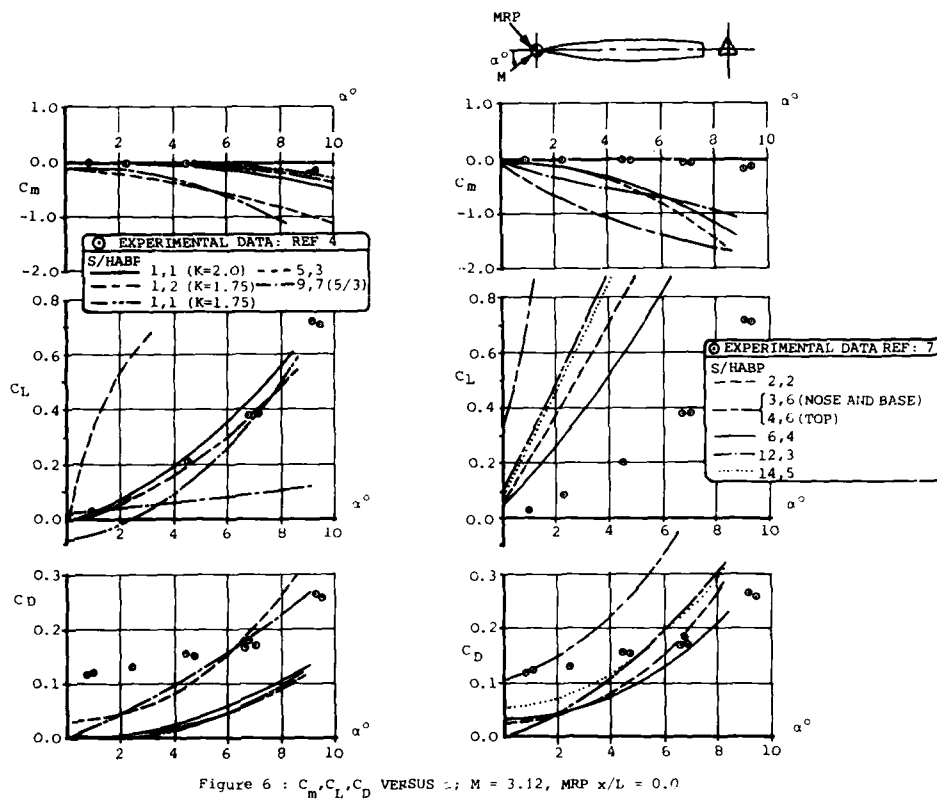


Figure 5 : C_p VERSUS x/L FOR BLUNTED CYLINDER-CONICAL FRUSTUM-FLARE; $\alpha = 0^\circ$, $M = 7.0$: NOSE



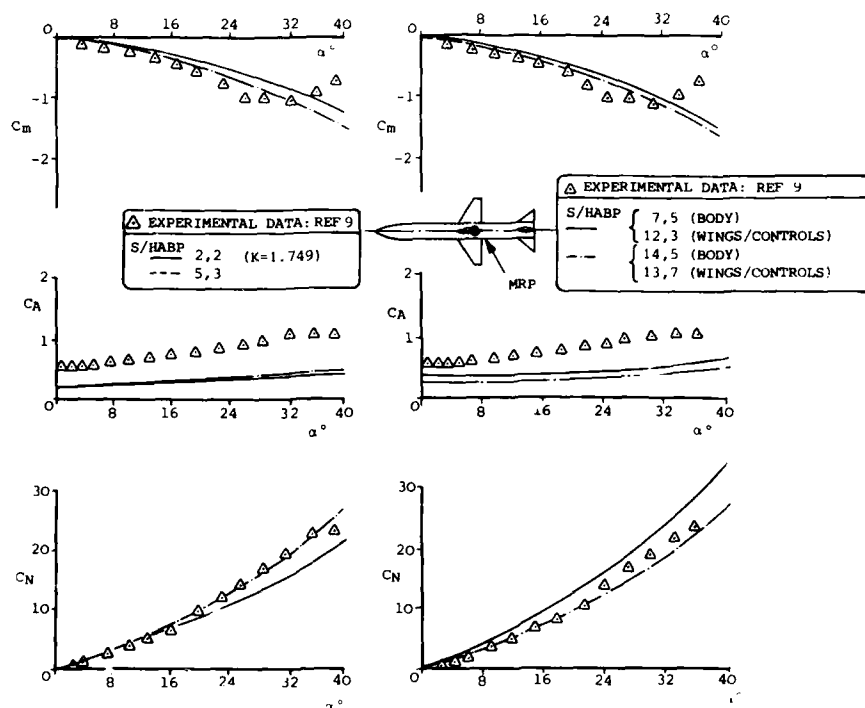


Figure 8 : C_m, C_A, C_N VERSUS α - FOR AN OGIVE CYLINDER BODY WITH CRUCIFORM WING AND CONTROL SURFACES AT $M = 4.6$

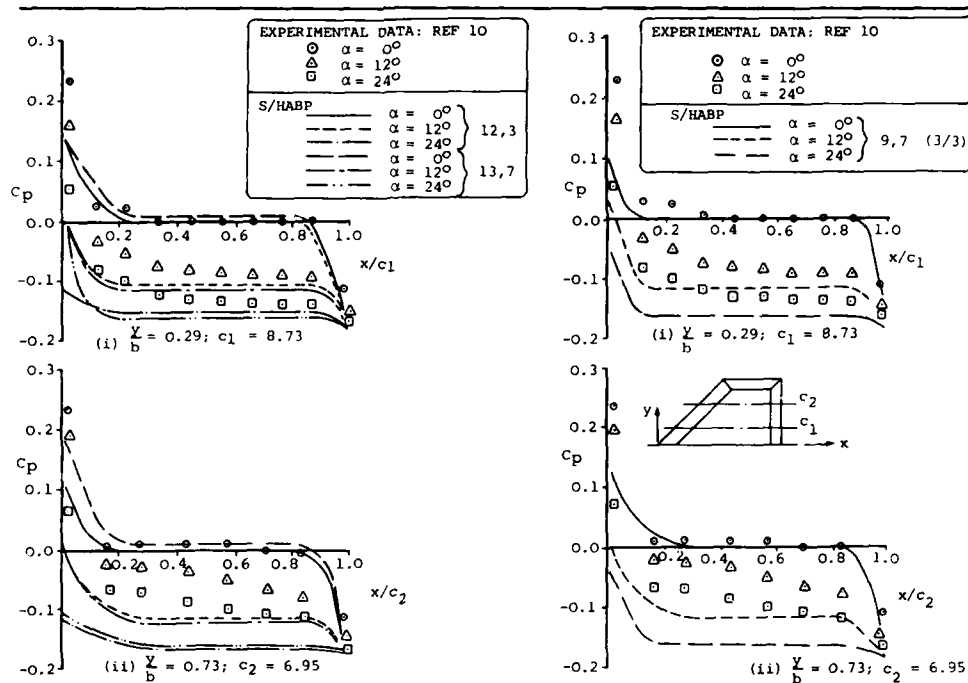


Figure 9 : C_p VERSUS x/c ; $y/b = \text{CONST.}$ $M = 2.8$ - FOR CROPPED DELTA WING ALONE

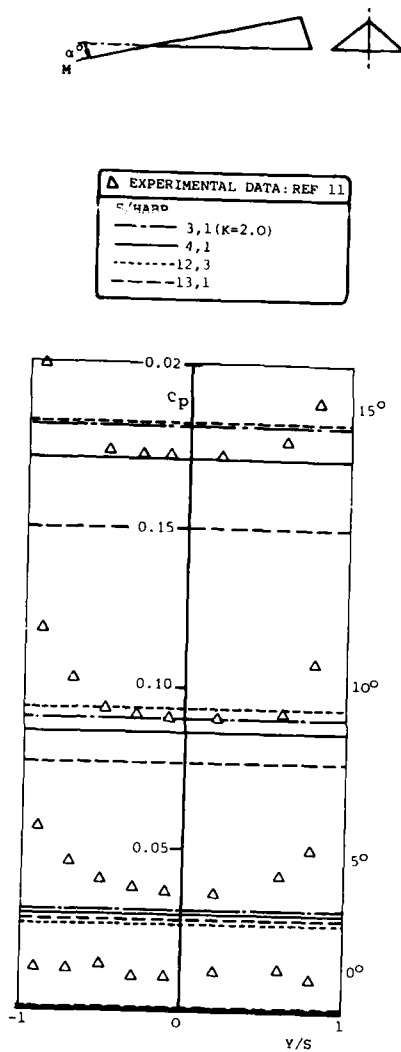


Figure 10 : C_p VERSUS Y/S FOR LOWER SURFACE OF TRIANGULAR CROSS-SECTION WAVERIDER.
 $M = 8.6$, $\alpha = 0^\circ, 5^\circ, 10^\circ$ AND 15° .
 $x/c = 0.62$

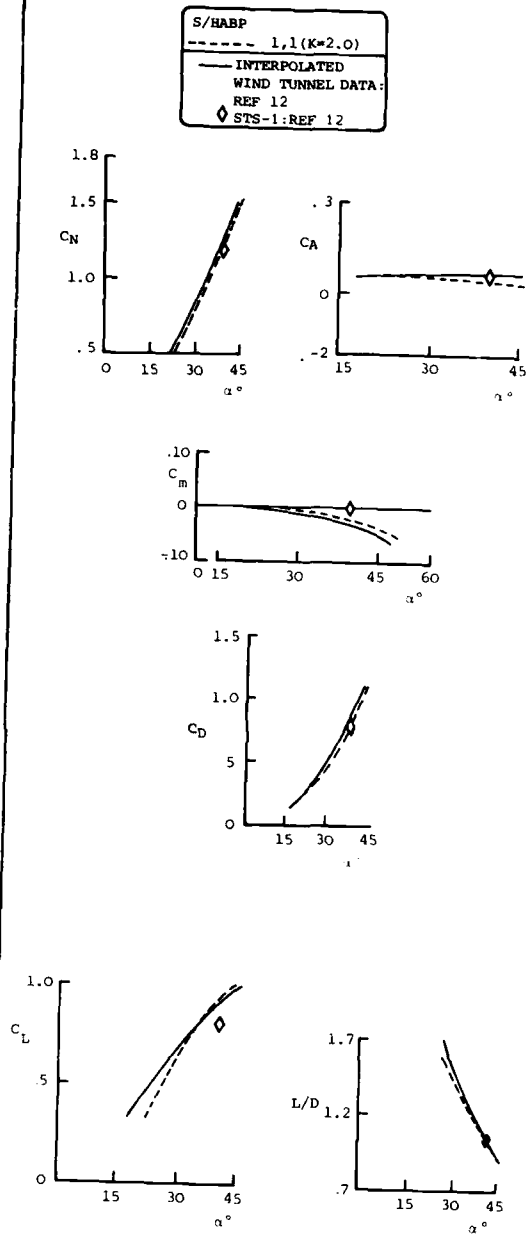


Figure 12 : AERODYNAMIC COEFFICIENT NEWTONIAN PREDICTIONS
 $M = 13.5$, $\gamma = 1.4$
 $\bar{V}_\infty = 0.006$

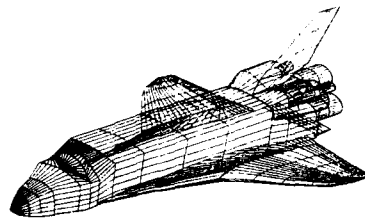


Figure 11 : S/HARP SHUTTLE REPRESENTATION

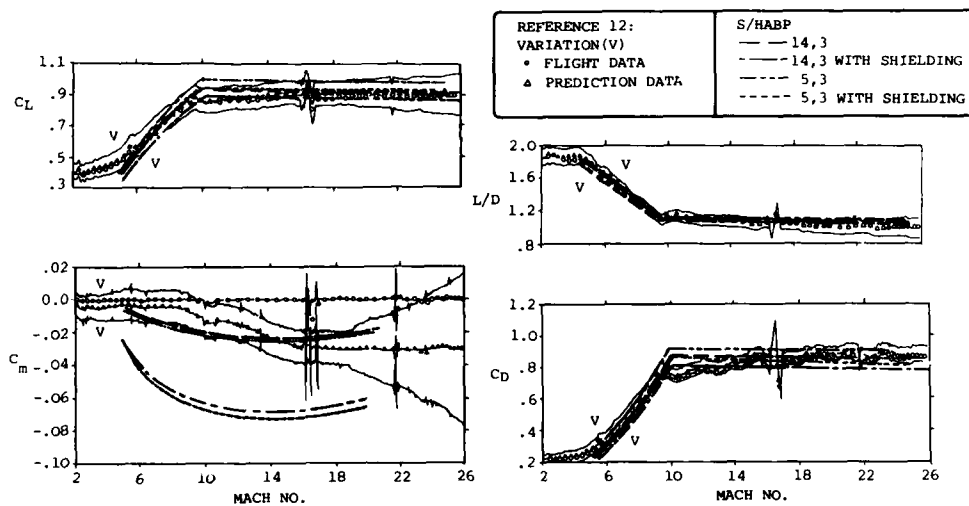
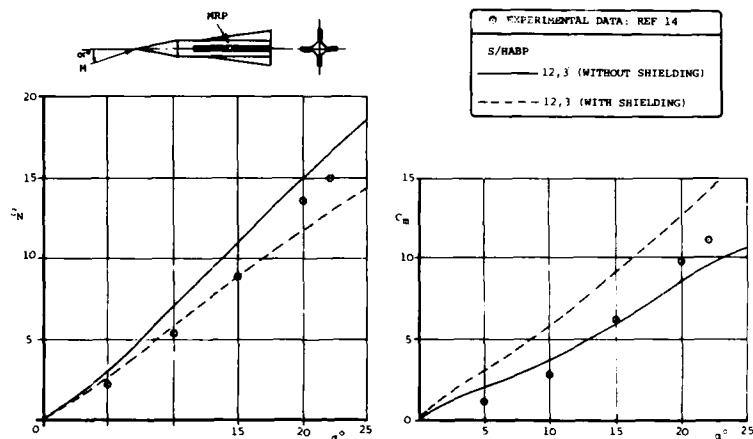


Figure 13 : STS-5 LIFT, DRAG AND MOMENT FLIGHT DATA AND PREFLIGHT PREDICTIONS WITH S/HARP PREDICTIONS. DISCONTINUITIES DUE TO MANOEUVRES. ALTITUDE INCIDENCE DETAILS GIVEN REFERENCE 12

Figure 14 : C_N, C_m VERSUS α FOR SQUARE CROSS-SECTION BODY WITH CRUCIFORM WINGS. $\lambda = 0.0$, $M = 2.0$, MRP = 9.0d AFT OF NOSE

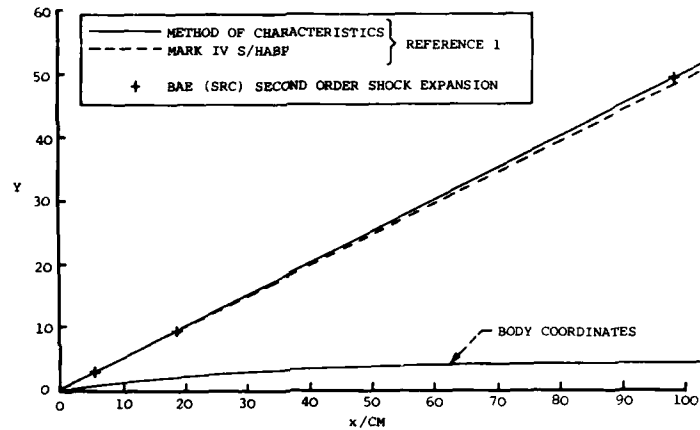


Figure 15 : SHOCK WAVE SHAPE COMPARISON FOR THE MINIMUM WAVE DRAG BODY OF REFERENCE 15. $M_\infty = 2.3$, $\alpha = 0^\circ$

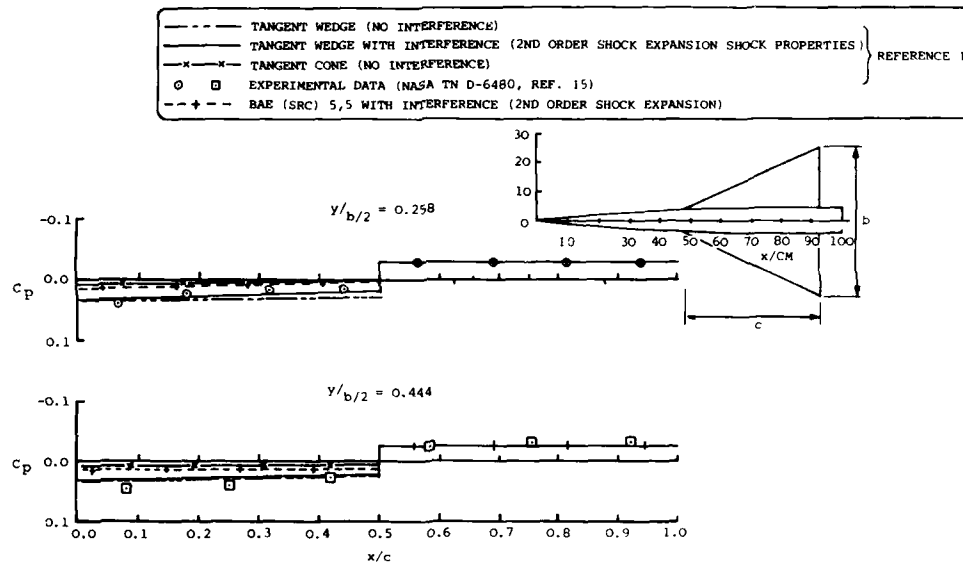


Figure 16 : COMPARISON OF EXPERIMENT AND THEORETICAL CHORDWISE PRESSURE DISTRIBUTION ($y/b/2 = 0.258$ AND 0.444) $M_\infty = 4.63$, $\alpha = 0^\circ$, $\beta = 0^\circ$ (NOTE REVERSE SIGN C_p AXIS)

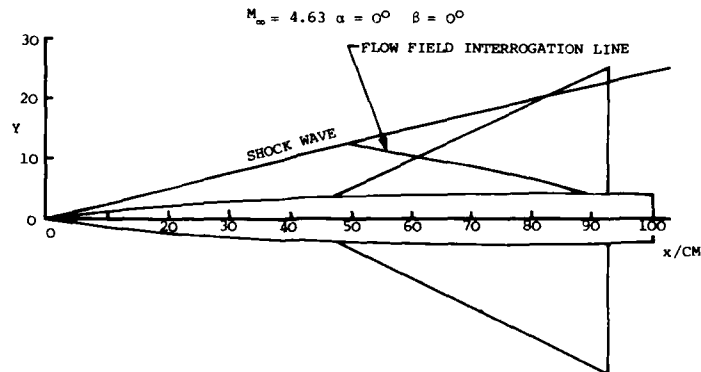


Figure 17 : FLOW FIELD INTERROGATION LINE (MODEL FROM REFERENCE 15)

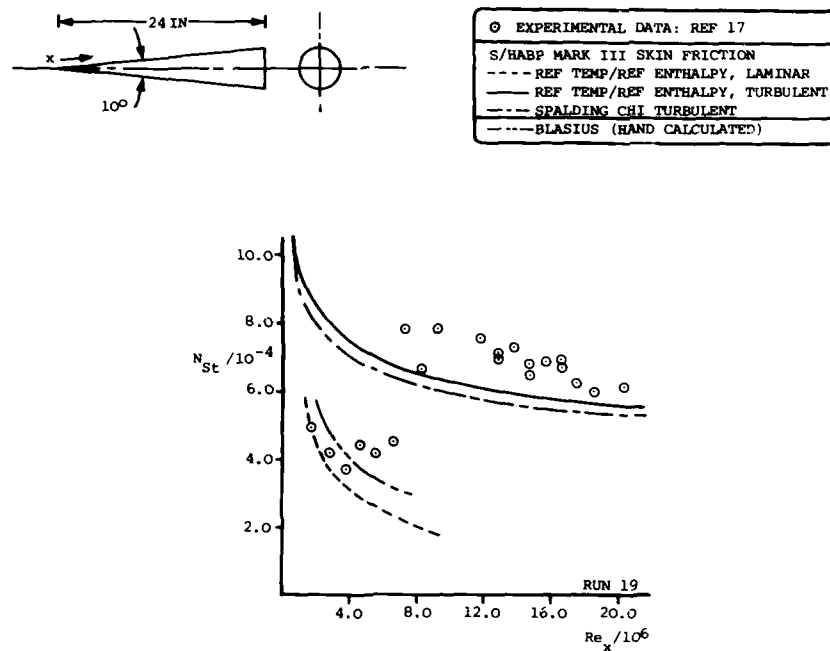


Figure 18 : LAMINAR AND TURBULENT HEAT TRANSFER DISTRIBUTION COMPARISONS FOR A SHARP CONE.

$P_0 = 2.88$ P.S.I., $T_0 = 1437^\circ R$, $M = 7.9$, $T_0/T_w = 0.322$, $\alpha = 0^\circ$

LAMINAR $N_{St} = 0.6196C_f$, TURBULENT $N_{St} = 0.5C_f$

ALL S/HABP PREDICTIONS ARE INPUT T_w METHODS

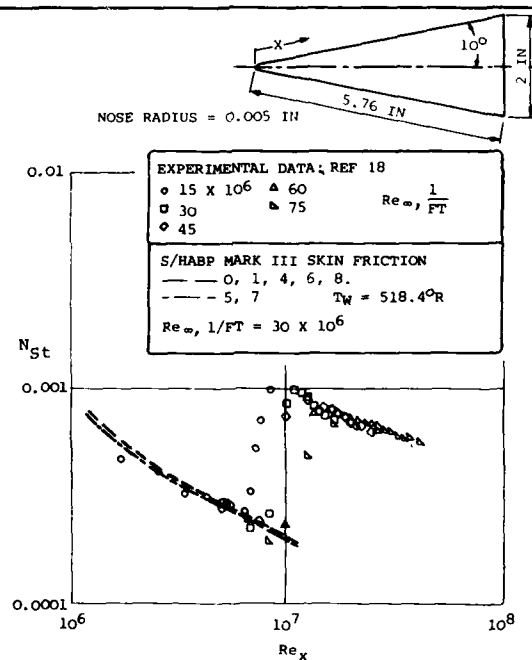


Figure 19 : COMPARISON OF S/HABP LAMINAR BOUNDARY LAYER RESULTS EXPERIMENTAL DATA

$\alpha = 0^\circ$, $\phi = 0^\circ$, $M = 4.95$, $N_{St} = 0.6282C_f$

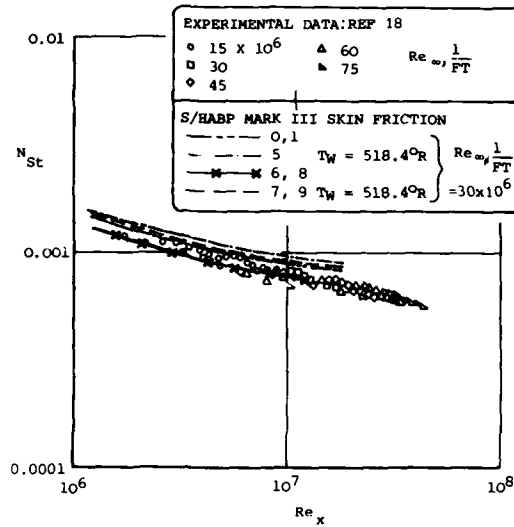
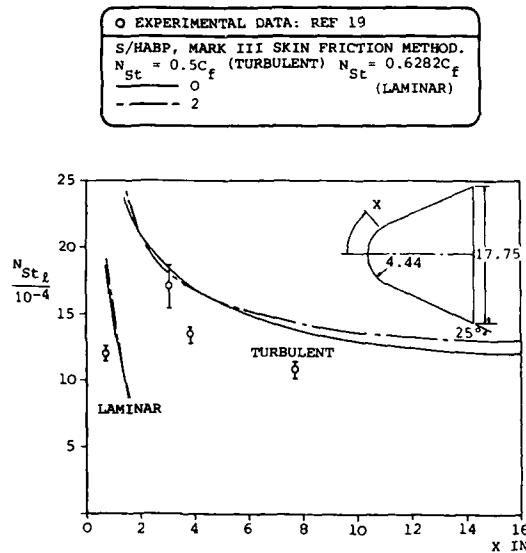


Figure 20 : COMPRISON OF S/HABP TURBULENT BOUNDARY LAYER RESULTS
WITH EXPERIMENTAL DATA $\alpha = 0^\circ$ $\phi = 0^\circ$, $M = 4.95$, $N_{St} = 0.5 C_f$



NOTE: THE MARK III SKIN FRICTION METHOD PROVIDES
LAMINAR AND TURBULENT C_f VALUES AT EACH x STATION.
IN THIS FIGURE THE MOST APPROPRIATE VALUE IS USED.
(EXPERIMENTAL ERROR ALSO INDICATED)

Figure 21 : COMPARISON OF EXPERIMENTAL AND PREDICTED
STATION NUMBER AROUND BLUNT - NOSE CONE
 $M = 2.5$, $\alpha = 0^\circ$ (EXPERIMENTAL ERROR ALSO INDICATED)

THE RAE EXPERIMENTAL DATA-BASE FOR MISSILES AT HIGH MACH NUMBER
AND ITS USE IN ASSESSING CFD METHODS

by

J. Hodges
L.C. Ward
Procurement Executive,
Ministry of Defence
Royal Aircraft Establishment
Aerodynamics Department
BEDFORD MK41 6AE
England

SUMMARY

Wind-tunnel tests are being performed in order to measure overall and panel forces and moments on cruciform body-control and body-wing missile configurations at $M = 2.5$, 3.5 and 4.5 . When completed, the test results will provide a wide-ranging data-base suitable for inclusion into semi-empirical prediction methods. Additionally it can be used to help validate and assess the computational fluid dynamic (CFD) methods that are available.

This Paper gives a detailed description of all the models and the wind-tunnel test conditions, and selected results are presented. Comparisons are shown between the experimental data and results from a space-marching Euler code. An outline is given of the extension of these comparisons to surface pressures.

LIST OF SYMBOLS

C_n overall normal force coefficient; pitches, but does not roll with the model
 C_{np} panel normal force coefficient; sometimes suffixed to denote a particular wing, fin, or control panel; pitches and rolls with both panel, and body, pitch and roll angles
 D maximum body diameter (93.98 mm)
 L overall body length
 M freestream Mach number
 P surface static pressure
 P_∞ freestream static pressure
 X axial location relative to body nose (in calibres positive upstream)
 X_{cp} overall longitudinal centre of pressure location relative to body nose (in calibres)
 ζ rudder angle $\frac{1}{2}(\xi_2 - \xi_4)$
 η elevator angle $\frac{1}{2}(\xi_1 - \xi_3)$
 λ body roll angle; positive clockwise viewed from rear
 ξ panel deflection angle relative to body axis; positive clockwise viewed outwards from body
 σ body angle of attack to freestream
 ϕ angular position on body surface relative to windward generator

Suffixes

1	starboard panel)	control or wing
2	bottom panel)	panel at zero
3	port panel)	roll when viewed
4	top panel)	from the rear

1 INTRODUCTION

A need exists for methods that can be used to predict the aerodynamic behaviour of missiles at high supersonic speeds. For the present and for many years to come, the major source of predictions will be the semi-empirical, or engineering, type methods. These

methods depend upon experimental data as a basic input to a simple theoretical framework. The more comprehensive the experimental data, the wider the ranges of missile configurations and flight envelopes that can be predicted with confidence.

The purely theoretical computational fluid dynamic (CFD) methods that are now being developed and used are not limited by sets of experimental data. With new generations of faster, more powerful computers being introduced, CFD methods (even with longer computing times than semi-empirical methods) are becoming more attractive. In order to validate and assess these methods, much work is required in comparing these predictions with experimental data.

Therefore, for both the semi-empirical and CFD methods, experimental data that cover wide ranges of flow conditions and design configurations are required. The RAE has recently embarked on a series of wind-tunnel tests to provide a high Mach number data-base of forces and moments on body, body-wing, and body-control missile configurations. Additional tests to measure the surface pressures on selected configurations are being planned.

Limitations of computing resources, uncertainties concerning turbulence modelling, and difficulties of use, have, for most computational aerodynamicists, delayed the routine application of codes which solve the Navier-Stokes equations. Codes solving the Euler equations are, however, being applied more extensively. These methods do not model viscosity, but one of its major effects, flow separation and the resultant vorticity, can be modelled if some assumptions regarding separation are employed. This Paper attempts to show, with comparisons between experimental data and results from the space-marching code SWINT¹, that, if used with care, flow separation models can significantly improve predictions.

2 MODELS

2.1 Body plus control configurations

The basic body for use with all the control configurations consists of a sharp axisymmetric 3 calibre long nose having a cubic profile, and a 10 calibre long cylindrical afterbody (see Fig 1).

Three cruciform control sets are available, the planforms consisting of a small delta, a large delta, and a square (see Fig 1). The small and large deltas have 45° leading edge sweep angles, and nominal root-chord and semi-span lengths of 1 and $\sqrt{2}$ calibres. The square planform has nominal root-chord and semi-span lengths of 1 calibre. A small amount of blunting is applied to both leading and trailing edges, so that the actual sizes of all the controls are slightly less than the nominal dimensions.

The control sets are fitted to the body with their rotational axes either 3.5 or 11.5 calibres downstream from the body nose (see Fig 2). Each individual control panel can be deflected in steps of 5° from -25° to +25° (relative to the body axis).

The configuration nomenclature is built up from the body (B1A); the control shape (C1, C2 or C3); and whether the control set is mounted at the forward or rearward (F or R) end of the body. For example, controls C2 mounted at the front end gives B1AC2F, and at the rear end B1AC2R.

2.2 Body plus wing configurations

The bodies consist of axisymmetric noses having cubic profiles, followed by cylindrical afterbodies. The three nose shapes are shown in Fig 3, nose "A" being the same as used for the body-control tests. The equation given for nose "C" is for a sharp nose of fineness ratio 1.5; this shape has then been spherically blunted as shown, giving a final fineness ratio of 1.465. Overall body lengths range from 8 to 19 calibres. Table 1 shows the nomenclature used for describing the overall body lengths and nose profiles.

The cruciform wing sets have nominal root-chord lengths of 9.682, 5.809 and 3.631 calibres as shown in Figs 4 to 6. With the exception of wings W10 and W11, all wing leading, trailing and streamwise edges are slightly blunted as shown in Fig 4. The wing sets can be fixed to the bodies with their trailing edges either in-line with, or 3 calibres forward of the body base.

The configuration nomenclature is built up from 3 components. Firstly the body-nose combination (eg B5A); secondly the wing shape (eg W14); and thirdly the length, in calibres, of the afterbody (if present). Hence wing W14 mounted on body-nose B5A with the wing trailing edge at the body base is designated B5AW14, but if the wing is moved forward 3 calibres the designation changes to B5AW14A3.

3 WIND-TUNNEL, TEST EQUIPMENT AND PROGRAMMES

All the tests are being made at RAE Bedford in the recently recommissioned 3ft x 4ft (0.91m x 1.22m) continuously-running wind-tunnel which has a Mach number range of 2.5 to 5. To avoid condensation shocks at $M = 5$, the stagnation temperature needs to be raised to around 140°C. Neither the control nor wing panel balances would accept this high temperature. Test Mach numbers of 2.5, 3.5 and 4.5 have therefore been chosen. Most of the tests are being performed at a freestream Reynolds number of 13.1×10^6 per metre, with

some data at Reynolds numbers of 6.6×10^6 and 19.7×10^6 per metre. Boundary-layer transition trips are applied to the body nose and the wing and control leading edges. Analysis of the axial force results is consistent with the assumption of a turbulent boundary layer existing over most of the model at all test Mach and Reynolds numbers.

Overall loads on the complete body-wing and body-control configurations are measured using a 6-component strain-gauge balance mounted within the model. An absolute pressure transducer measures the model cavity pressure, this being assumed to act over the whole model base for calculation of the base pressure coefficient. To measure the individual wing loads, two opposing wing planforms are attached to 3-component strain-gauge balances (measuring wing normal force, pitching moment, and rolling moment). All wing planforms stay undeflected relative to the body axis. To measure the individual control loads, two opposing panels are attached to 5-component strain-gauge balances (axial force missing). These balances rotate with the controls, so panel normal force is always normal to the control root-chord.

Data is recorded every 7.5° whilst the model is being continuously rolled from 0° to 360°, a complete roll sweep taking less than 2.5 min. Nominal model incidence angles are -2° to 26°, in steps of 2°.

The body-control test programme is about 70% complete. The body-wing test programme (Fig 7) is about 30% complete.

4 PRESENTATION OF SELECTED RESULTS AT MACH 4.5

4.1 Body plus control configurations

Results presented in this section for the body-control configurations are limited to zero roll angle, ie when the pair of deflected controls are normal to the pitch plane. The variation of the overall normal force coefficient (C_n) with body angle of attack (α) and control elevator angle (δ) for the small delta controls in the rearward and forward positions is shown in Figs 8 and 9 respectively. Body alone results are also presented in each figure. For all values of δ , C_n for the controls in the forward position is always slightly higher than for the rearward position, the greatest difference occurring at an angle of attack around 18°.

The movement of the centre of pressure with changes in the angle of attack, control position, and elevator angle is shown in Fig 10. Body alone results are also plotted. For all angles of attack, the greatest centre of pressure movement occurs with changes in elevator angle when the controls are mounted in the rear position.

4.2 Body plus wing configurations

4.2.1 Effect of forebody length at zero roll

The overall normal force coefficients of bodies B5A and B11A, and with wings W14 added, are shown in Fig 11. For any particular value of α , the effect of increasing the forebody length of B5AW14A3 by 3 calibres to B11AW14A3 is less than the corresponding increase between B5A and B11A (eg at $\alpha = 24^\circ$, 0.92 as opposed to 1.00). However, the opposite is true when wings W13 are added to bodies B5A and B1A, as shown in Fig 12. In this case, the effect of increasing the forebody length of B1AW13 by 3 calibres to B5AW13 is greater than the corresponding increase between B1A and B5A (eg at $\alpha = 24^\circ$, 0.93 as opposed to 0.90).

Analysis of the wing panel loads (Fig 13) indicates that the wing loads are independent of forebody length for the configurations shown, the only effect of forebody length being an increase in C_n due to the additional body length.

4.2.2 Effect of afterbody length at zero roll

The variation of the normal force coefficient with angle of attack for two configurations having the same forebody and wings, but differing in the length of afterbody, is shown in Fig 14, along with the respective body alone coefficients. The difference in C_n between B5AW14A3 and B1AW14 at any particular value of α is around 25% greater than the corresponding difference between B5A and B1A. The wing loads are the same due to the nose and forebody being identical, hence this increase is due to the carry-over of normal force from the wing onto the body being greater for the configuration having the afterbody present. Typically this is between 8% and 11% of the total C_n , the lower value being for configuration B1AW14.

5 FUTURE TEST PROGRAMME

With the growth of CFD prediction methods, a greater need is developing for experimental data to include both surface and flowfield pressure results for direct comparison with prediction. Therefore, the future test programmes for both the body-control and body-wing configurations will not only continue with the force and moment data gathering, but will also include a large pressure data-bank. For the body-control tests, a rig for the 3ft x 4ft wind-tunnel is being built which will accommodate a row of yawmeters for traversing through the flowfield surrounding the model. Of particular interest will be the development of the leeward vortices, and their interactions with the control planforms.

The measurement of surface pressures will be made on selected body-wing configurations which can be fitted with cruciform control surfaces upstream of the wings. Two proposed configurations are shown in Fig 15. Pressure taps will be sited along the body surface and on one wing surface. Additional taps may be added to the nose, and to the control surfaces. The body length between the wings and the controls will be variable, as will be the control deflection angles. Thus many different flowfields over the pressure tapped wing and body areas can be easily achieved.

6 BRIEF DESCRIPTION OF THE SWINT CODE

SWINT is a space-marching Euler code which calculates the supersonic flow between a missile-type configuration and its bow shock, given a starting solution in a crossflow plane near the nose. The computational grid is constructed around the body of the configuration and any controls or wings are assumed to be thin and to lie close to radial grid lines. The grid density can be changed to suit the calculation progressing in the axial direction.

SWINT can be run in either of two modes - a full flowfield (or 360°) calculation, in which the whole of the flowfield between the configuration and the bow shock is computed, and a half flowfield calculation in which symmetry is assumed. The half flowfield mode would be appropriate for a conventional cruciform missile at 0° or 45° roll, but any other roll angle would require a full flowfield calculation.

The missile aerodynamicist is concerned with mainly two types of flow separation: that from a wing or control, and that from a body. For most missile configurations, wing and control edges are sharp, or can be regarded as such, and, in the case of a subsonic leading edge, the location of separation is assumed to be at the leading edge. A missile body at incidence often involves flow separation from a smooth surface, and the location of separation is then more difficult to define. SWINT allows the user to model both these types of flow separation, the location on axisymmetric bodies being determined empirically.

In the original version of SWINT, the option of modelling flow separation from the body was only available for half flowfield calculations. In order to study the effect of roll angle on the interaction between controls and vortices arising from body separation, RAE has extended the body separation option so that it can also be used in full flowfield calculations.

7 COMPARISON OF SWINT RESULTS WITH EXPERIMENT

7.1 Body alone

Calculations were made for body B1A at a Mach number of 3.5 using SWINT with and without employing flow separation from the body. All the calculations were in the half flowfield mode and used a grid of 31 points radially and 19 points circumferentially between the body and the bow shock.

Fig 16 shows the two predicted surface pressure distributions around the body at the base station, significant differences between them being confined to the leeward half of the body. Experimental pressure measurements are not available for comparison and therefore it is not possible at present to judge which curve is more realistic. A comparison between the integrated pressure distributions and experimental values of normal force and centre of pressure position is shown in Figs 17 and 18. Reasonable agreement is demonstrated irrespective of whether flow separation has or has not been modelled.

7.2 Body plus control configuration

7.2.1 Control loads

Calculations were made for configuration B1A1R at Mach 3.5 using SWINT. At 12° angle of attack and a range of roll angles, calculations were made with and without employing the option for flow separation from the body. All these calculations were made in the full flowfield mode, and since the leading edges of the controls were supersonic, attached flow was assumed on these surfaces. A grid of 31 points radially and 36 points circumferentially was used in the region of the controls, and a coarser grid was used upstream. Fig 19 shows the predicted and experimental loads on one control panel as the configuration is rolled through 360°, the panel being in the windward position when the configuration is at zero roll.

The modelling of separation appears to have a negligible effect on the control load while the panel is in the windward half of the flowfield. However, when the control is in the leeward half, the predictions with and without separation modelling show significant differences. The calculations with the flow separation included produce results which are generally in better agreement with experiment. This is probably due to the predicted interaction between the body vortex and the control panels.

The measured loads on the same control panel, but with a 10° rudder deflection applied, are shown in Fig 20, together with the results of SWINT calculations which employed the body separation option. SWINT models the flow over an undeflected control panel by using the actual surface slopes relative to the free stream but applies them through the boundary conditions on a radial plane parallel to the body axis (ie as if the control had zero thickness). For a deflected panel, the same plane is used, and thus the

approximation becomes less realistic as the deflection angle increases. The largest discrepancy is near the 300° position where the panel experiences the largest local angle of attack. Otherwise the predictions are in good agreement with the experimental data.

7.2.2 Overall loads

SWINT calculations for configuration B1AC1R at zero roll were made at a Mach number of 3.5 and over an angle of attack range up to 24°. The half flowfield mode and the options for flow separation from the body and attached flow on the controls were used with a grid of 31 points radially and 19 points circumferentially over the full length of the configuration. Figs 21 and 22 show comparisons between prediction and experiment for the overall normal force and centre of pressure position. The agreement is excellent, normal force being predicted to within 4% of the experimental value, and centre of pressure to within 0.2 of a calibre throughout the angle of attack range.

7.3 Body plus wing configurations

7.3.1 General comments concerning computations

Calculations have been made for two of the body-wing configurations shown in Fig 7, namely B5AW7A3 and B5AW14A3. The Mach number was 3.5 and an angle of attack range between 0° and 20° was attempted, for both the 0° and 45° roll positions. The choice of these roll angles enabled SWINT to be run in the half flowfield mode. In all cases in the region of the wing, calculations were made on a grid consisting of 31 points in the radial direction and 25 points circumferentially. Ahead of the wing a coarser grid was used. The option of modelling flow separation from the body was used throughout the computations unless otherwise stated. Attention is focussed on configuration B5AW14A3 at 45° roll. However, it should be noted that the calculations for zero roll, and for the other body-wing configuration studied (B5AW7A3), support the conclusions drawn herein.

7.3.2 Overall loads

Figs 23 and 24 show comparisons of overall normal force and centre of pressure position respectively. Since the wings have subsonic leading edges at Mach 3.5, the initial SWINT calculations used the leading edge separation option for the leeward side of all lifting surfaces at any non-zero incidence (however small) to the freestream. Thus a step discontinuity occurs in the C_n versus incidence curve at zero angle of attack. Clearly the discontinuity is unrealistic. Physically the leading edge separation will start at a few degrees angle of attack, the actual value being dependent upon the leading edge bluntness and chamfer angle.

Calculations were then made in which no special treatment was applied to the leeward sides of the wings ie attached flow was assumed. The results (also shown on Figs 23 and 24) show a marked improvement in the agreement with experiment. No such computations at angles of attack above 8° were successful due to the prediction of a negative pressure near the leading edge of the lower wing. This suggested that the flow was attempting to turn through too large an angle and the attached flow assumption was invalid. Physically, separation would almost certainly have occurred at well below 8° angle of attack.

It appears that when a leading edge separation is being modelled at low angles of attack, SWINT overestimates the effects of the vortex. There are several possible reasons for this, eg an insufficiently fine grid, lack of viscosity, or a separation model inadequacy. However, it appears that good results can be obtained from SWINT (when calculating the flow past a wing with a subsonic leading edge), by imposing separation from the leading-edge at angles of attack only where an attached flow solution is unobtainable.

Using this procedure, Figs 23 and 24 show that good agreement with experiment can be obtained. The C_n predictions are very close to the experimental values until about 8°, above which the maximum error is approximately 7%. The centre of pressure predictions are excellent, the trend matching the experiment throughout the angle of attack range. The error is less than 0.25 calibres at all points except at 2°, where the centre of pressure is the quotient of two small quantities.

7.3.3 Wing loads

The experimental and predicted normal forces for a lower wing panel are compared in Fig 25. As for the overall loads, the agreement at low angles of attack is improved when attached flow is assumed. However, the trend at higher angles of attack, where wing leading edge separation has to be imposed to obtain a solution, is disappointing.

Similar comments apply to Fig 26 which shows the normal force coefficient for an upper wing panel. The experimental data is substantially non-linear and this feature is reflected in the results of the computations with the leading edge separation imposed.

All the calculations described so far employed the option for modelling flow separation from the body. However, it is probably unrealistic to model such a separation in the region of the wings. The presence of the wings would suppress or at least substantially affect flow separation from the body. Additional calculations were made with the body flow separation option employed ahead of the wings but not in the region of the wings or the afterbody. Fig 26 also shows the results of these computations. As expected, at low angles of attack they merge with the results of the calculations with body flow

separation modelled everywhere. At higher angles of attack, an increase in the predicted wing normal force is seen, giving rise to an improvement in the trend of the results. The improvement in prediction for this upper wing panel is significant. The results for the lower wing and the overall forces were relatively unaffected by these modifications to the body flow separation.

8 CONCLUSIONS

The present comparisons have shown that some useful validation of a CFD code can be made when overall and wing force measurements are available for comparison. Some qualitative knowledge of the aerodynamics of the configuration can allow various options in the code to be critically assessed.

The current work has led to the following conclusions about the space-marching Euler code, SWINT.

- 1 The modelling of body flow separation can significantly affect the predicted pressure distribution on the leeside of a body. However, for the case studied herein, the overall normal force and centre of pressure predictions showed only small changes consequent on whether flow separation was, or was not, modelled.
- 2 Modelling flow separation from the body may provide better predictions of the loads on controls or wings in the leeward half of the flowfield. Further improvements to these predictions may be obtained by modelling flow separation ahead of the wings or controls, but not in the region of the wings or controls themselves.
- 3 Modelling of wing leading edge separation appears to overestimate the effect of leading edge vortices at low angles of attack. Better results are obtained for the cases considered here if attached flow on the wings is assumed until the angle of attack is too high to permit an attached flow solution.
- 4 Some qualitative knowledge of the aerodynamics of a missile, together with careful use of the separation options in SWINT, has enabled excellent predictions of loads and moments to be made for the configurations studied so far.
- 5 When validating and assessing CFD codes, measured surface pressures or flowfield data should ideally be available in addition to force and moment data. Discrepancies between predictions and experimental results can then be pinpointed.

Future work will include the following items.

- 1 Calculations will be made for other configurations in the experimental data-base in order to assess further the SWINT code.
- 2 The data-base will be used for comparison with calculations made using other CFD codes.
- 3 Experimental body and wing surface pressure measurements will be made at Mach numbers from 2.5 to 4.5 for more detailed comparisons with the results from CFD codes.

TABLE 1
BODY LENGTHS AND NOMENCLATURE

Body	B9A	B10A	B4A	B1A	B1B	B1C	B5A	B5B	B11A	B11B
L/D	8	10	11	13	13	12.965	16	16	19	19

REFERENCE

- 1 A.B. Wardlaw et al. An inviscid computational method for tactical missile configurations. NSWC TR 81-457 (1982)

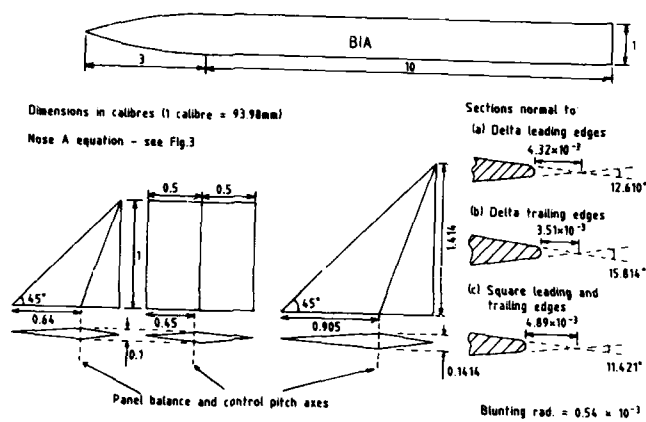


Fig 1 Details of body and controls

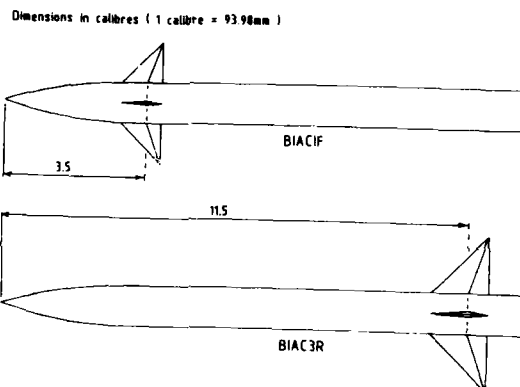


Fig 2 Typical configurations showing forward and rearward control locations

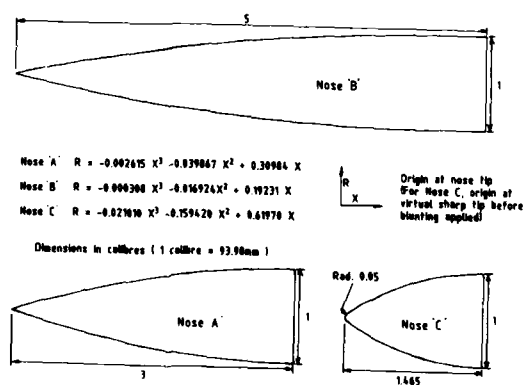
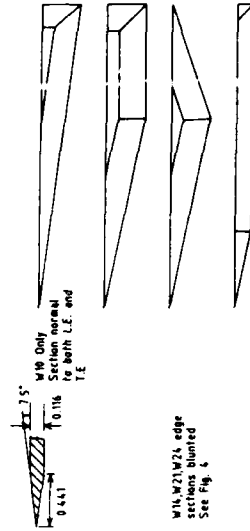


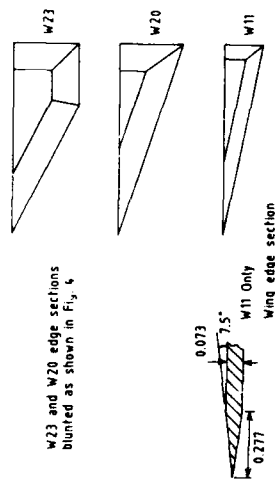
Fig 3 Nose sizes and profiles



Wing	Semi-span	L.E. sweep	Taper ratio	Aspect ratio
W7	1.35	82.444°	0	0.556
W8	0.75	85.511°	0	0.390
W13	0.75	78.328°	0.425	0.991
W9	0.555	88.799°	0	0.229
W22	0.3	78.328°	0.85	0.007

Dimensions in calibers (1 caliber = 93.88mm)

Fig. 4 Wings of root-chord length 1.403 calibers



Wing	Semi-span	L.E. sweep	Taper ratio	Aspect ratio
W23	1.224	63.435°	0.326	1.017
W20	1.210	71.565°	0	1.333
W11	0.75	78.328°	0	0.826

Fig. 5 Wings of root-chord length 5.809 calibers

Wing	Semi-span	L.E. sweep	Taper ratio	Aspect ratio
W11	0.75	82.444°	0	0.516
W21	0.75	78.328°	0.375	0.376
W24	0.3	78.328°	0.75	0.516
W24	0.3	78.328°	0.75	0.710

Dimensions in calibers (1 caliber = 93.88mm)

Fig. 6 Wings of root-chord length 5.809 calibers

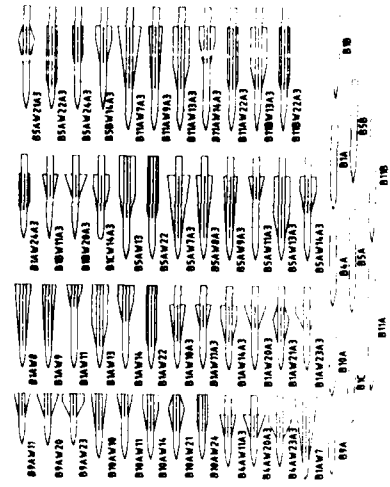


Fig. 7 Poly and poly-wing configurations

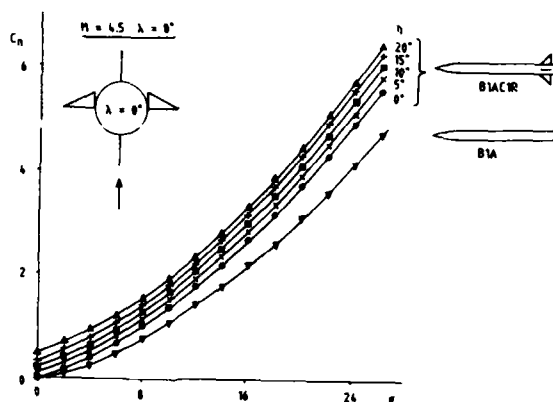


Fig 8 Overall normal force for B1A and B1AC1R

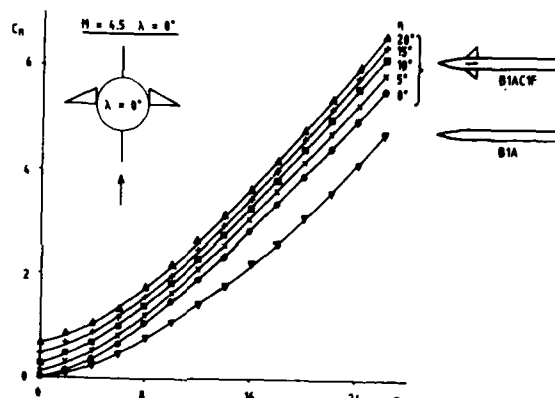


Fig 9 Overall normal force for B1A and B1AC1F

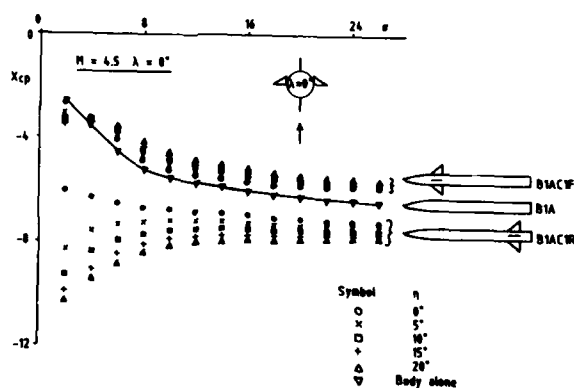


Fig 10 Centre of pressure movement due to control position

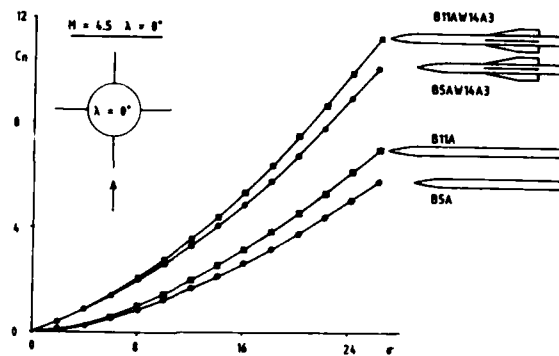


Fig 11 Effect of forebody length on overall normal force; wing W14

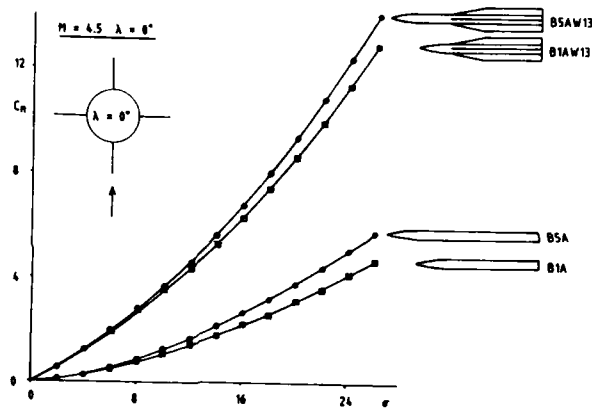


Fig 12 Effect of forebody length on overall normal force; wing W13

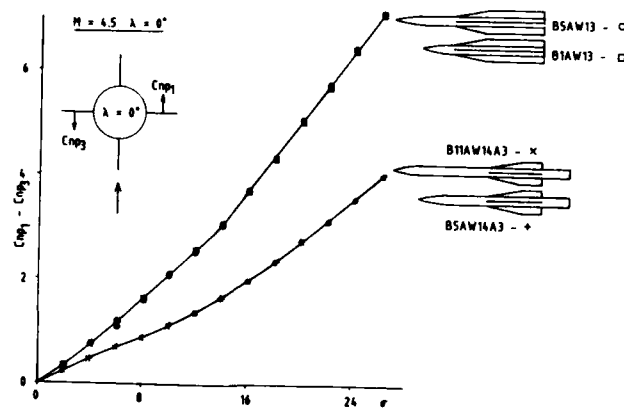


Fig 13 Effect of forebody length on wing normal force; wings W13 and W14

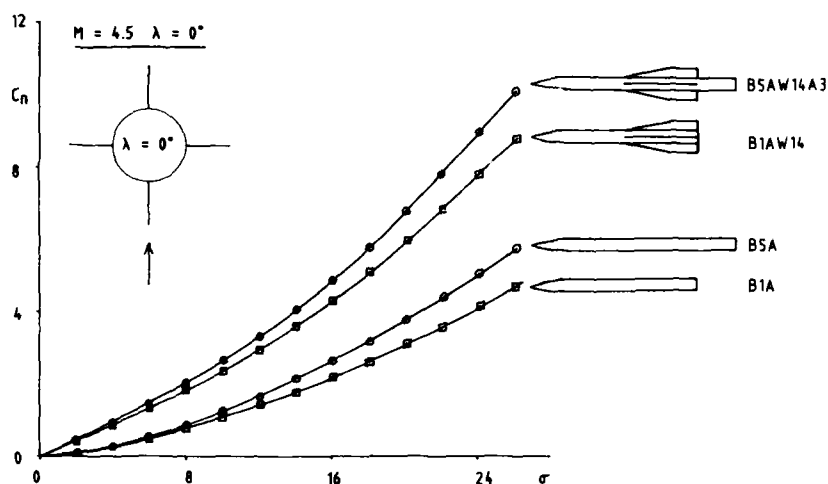


Fig 14 Effect of afterbody length on overall normal force; wing W14

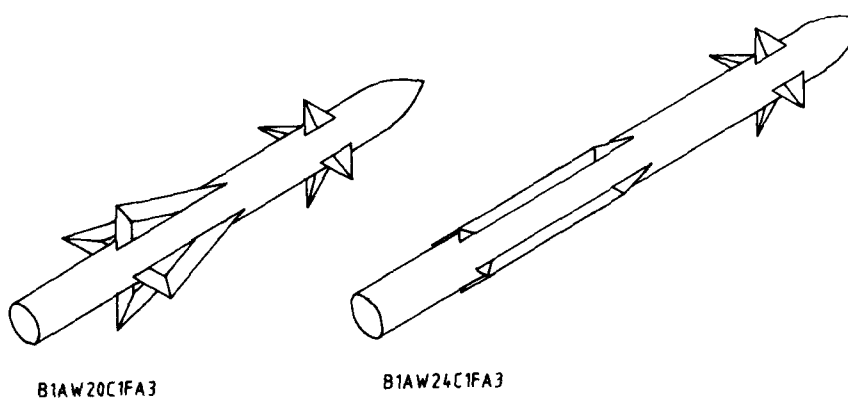
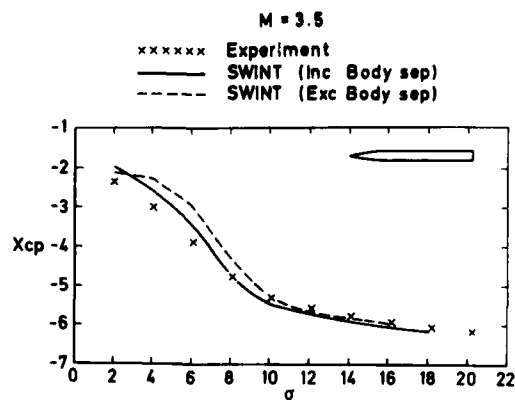
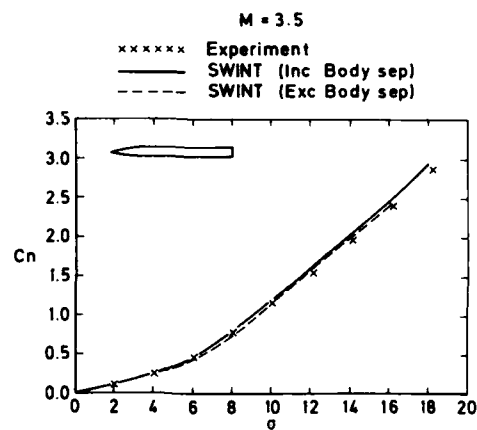
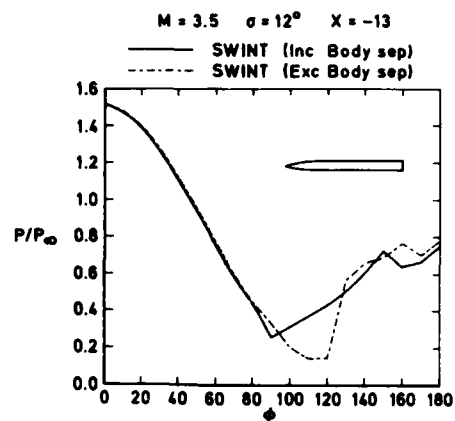


Fig 15 Two planned configurations for the measurement of surface pressures



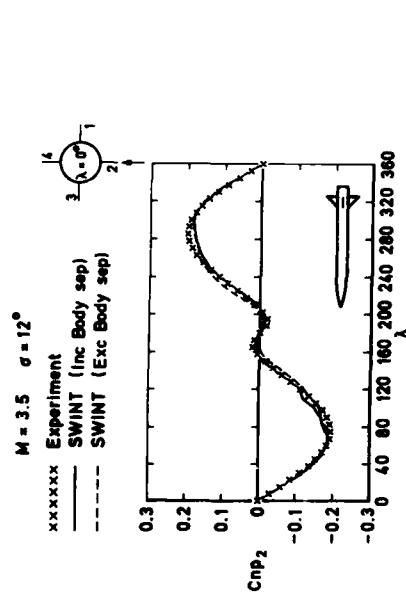


Fig 19 B1AC1R: effect of roll on panel normal force, predictions and experiment

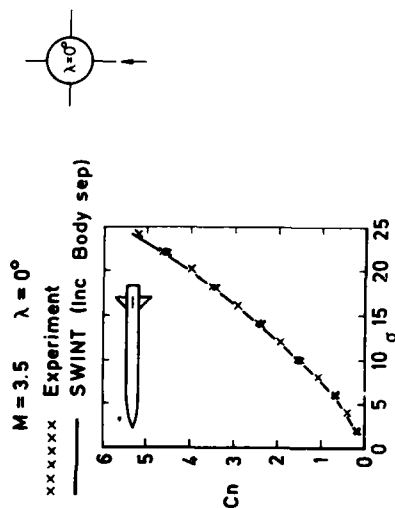


Fig 21 B1AC1R: overall normal force, prediction and experiment

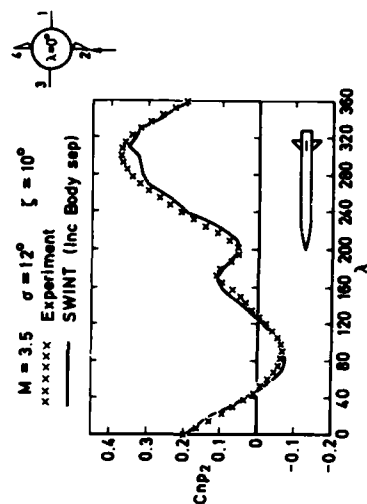


Fig 20 B1AC1R: normal force on deflected panel, prediction and experiment

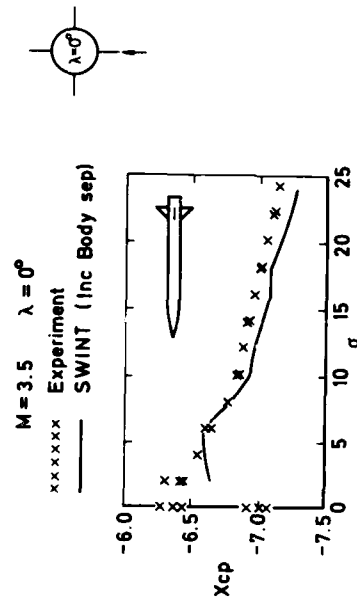


Fig 22 B1AC1R: centre of pressure, prediction and experiment

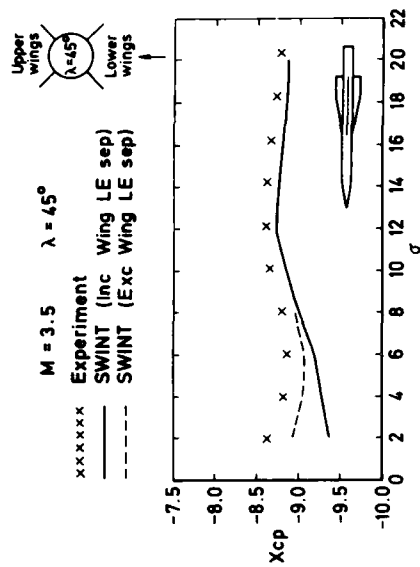


Fig 24 B5AW14A3: centre of pressure, predictions and experiment

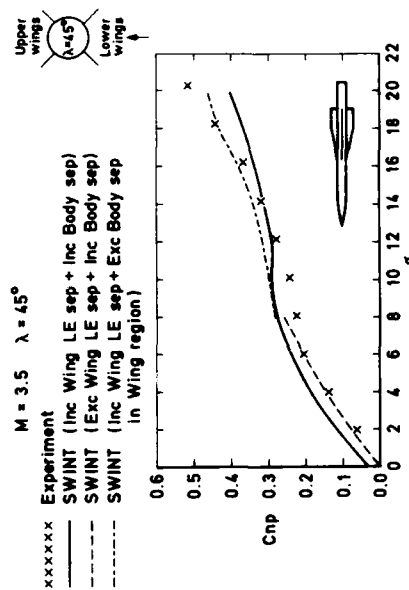


Fig 26 B5AW14A3: upper wing normal force, predictions and experiment

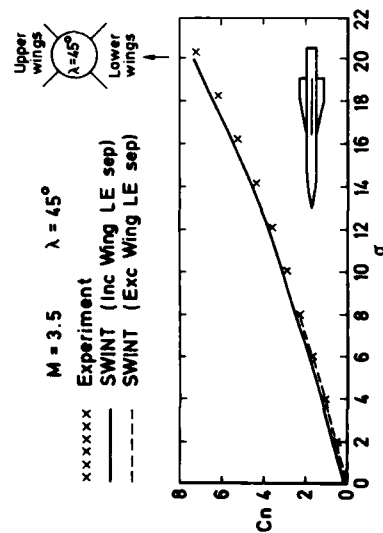


Fig 23 B5AW14A3: overall normal force, predictions and experiment

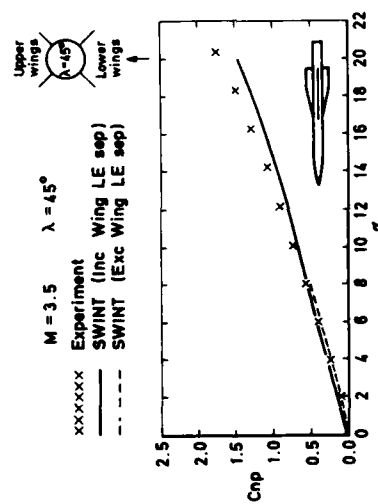


Fig 25 B5AW14A3: lower wing normal force, predictions and experiment

CONCEPTS GENERAUX AERODYNAMIQUES-AEROTHERMIQUES D'HERMES

par

P. Perrier et Ph. Caupenne
Avions Marcel Dassault - Breguet Aviation
78, Quai Carnot - 92214 Saint Cloud
France

- O. L'avion spatial Hermès a fait l'objet, pour l'année 1987, d'un financement de l'Agence Spatiale Européenne dans le cadre d'un programme préliminaire. Ce programme est financé maintenant par l'ensemble des états membres après avoir été limité à la France et à quelques pays en relation bilatérale. Au cours de la phase initiale, des études détaillées de la forme aérodynamique et des flux nominaux ont été poursuivies pour acquérir une première définition à étudier expérimentalement par les Avions Marcel Dassault-Breguet Aviation ceux-ci avant été chargés de la responsabilité d'Hermès en tant que véhicule volant.

Nous passerons successivement en revue les concepts généraux retenus pour les études du dessin d'Hermès, nous donnerons quelques exemples de leurs applications et justifierons la méthodologie générale retenue pour cet ambitieux programme européen.

1. CONCEPTS GENERAUX DE DESSIN

1.1 - Concepts de dessin aérodynamique

L'objectif d'Hermès est le transport d'hommes en orbite avec une charge utile limitée. Hermès doit ainsi être satellisé grâce à un lanceur commercial Ariane V et récupérer hommes et charges ou permettre des opérations en orbite en connexion vers le module de station orbitale Colombus.

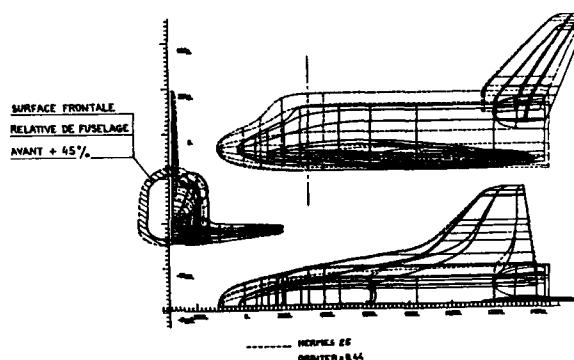
Ariane V impose à l'avion spatial une taille relativement beaucoup plus faible que l'Orbiter mais avec des performances demandées supérieures :

- utiliser des pistes européennes pour le retour d'orbite, c'est-à-dire des pistes usuelles avec un déport latéral permettant de rattraper un décalage d'orbite,
- avoir un équipage à deux, ce qui induit une taille relative de fuselage beaucoup plus grande que l'Orbiter,
- avoir des frais de remise en état limités.

Pour s'adapter à ces exigences, l'étude a montré que le dessin aérodynamique était bien plus critique que sur l'Orbiter et que des progrès sur la réalisation de la protection thermique étaient également nécessaires par suite des accroissements de flux liés à la diminution des dimensions.

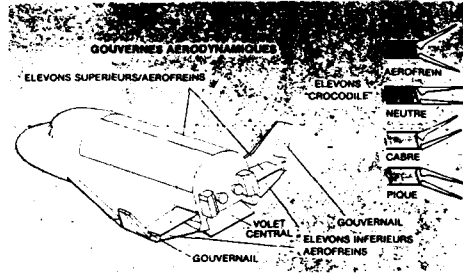
On voit sur la figure 1 que les tailles comparées des fuselages qui créent la déstabilisation en longitudinal et latéral sont relativement 40 % plus grandes.

Fig:1



L'utilisation de pistes plus courantes conduit à viser l'emploi de charges alaires réduites permettant, pour une incidence donnée à l'impact, une réduction de 20 kts à l'approche. Pour réaliser ce gain en SCZ, sachant que l'on ne peut guère espérer augmenter notablement l'envergure relative, il a semblé nécessaire de centrer au mieux l'avion à l'impact, ce qui permet de limiter la diminution de la charge alaire à environ 20 %. Pour réduire la masse, on utilise complètement le concept CAG sur les 3 axes afin de minimiser les surfaces stabilisatrices nécessaires. Ceci a conduit à l'implantation de dérives d'extrémité de voilure induisant des efforts et moments bien situés par rapport au centre de gravité et permettant de passer en gouvernes aérodynamiques sur les 3 axes dès que la densité est suffisante et ainsi de minimiser la masse. Enfin le contrôle de la vitesse sur trajectoire en finale s'effectue par variation de traînée, ce qui est possible par une configuration en crocodile des gouvernes, figure 2. Ainsi les différentes fonctions présentes sur un démonstrateur militaire Rafale sont présentes avec cependant une complexité réduite par l'absence de modes supérieurs comme l'antirafale.

Fig:2



Les principaux choix aérodynamiques sont bien clairement liés à l'objectif d'un pilotage sain durant toute la réentrée et l'approche et l'atterrissage, demandant dans toutes ces phases de vol des efficacités suffisantes sur tous les axes et des courbes aérodynamiques raisonnablement linéaires. Ceci conduit à retenir des flèches de bord d'attaque assez élevées et des cambrures de voilure suffisantes pour permettre une bonne marge de linéarité de fonctionnement en incidence et dérapage.

1.2 - Objectifs de dessin aérothermique

La diminution de taille par rapport à l'Orbiter induit des problèmes de plus grande difficulté liés à l'augmentation corrélative des flux : les matériaux de l'Orbiter sont déjà assez proches de leurs limites sans les marges importantes qu'il semble nécessaire d'admettre dans le cas d'emploi régulier de l'avion spatial. Ainsi la marge d'altitude entre la trajectoire au plafond de rentrée et la trajectoire à échauffement critique sur le nez ou les points les plus chauds est fortement réduite voire inexistante si l'on ne décroît pas la charge alaire (cette décroissance est donc doublement nécessaire car compatible avec les objectifs basse vitesse). Enfin, puisque l'on n'admet pas de surchauffes locales, on en déduit que l'on doit éviter les dessins présentant des risques de telles surchauffes locales. A ce point de vue, les stabilisateurs en extrémité d'aile sont éventuellement cause de surchauffe si leur rayon de bord d'attaque et leur dessin lui-même n'est pas très progressif. De plus, il semble évidemment nécessaire d'éviter les surchauffes dues aux croisements de chocs en évitant des formes en plan à cassure de bord d'attaque comme l'Orbiter. Les formes retenues pour Hermès mettent toutes les formes aérodynamiques dans l'enveloppe des chocs attachés à l'intrados, de même que les problèmes de protection des transparents conduisent à garder une marge suffisante du nez par emploi d'un fuselage avant assez développé et protégeant les transparents de cabine. Enfin l'échauffement des surfaces mobiles étant limité grâce au rerayonnement des parois, nous avons retenu la configuration en crocodile ouverte pour le vol hypersonique de façon à permettre ces reradiations, tout en mettant un accent particulier sur l'évaluation des échauffements de gouverne : c'est une des limites majeures de leur efficacité à cause des limitations de braquages maximaux qu'ils supposent. On donne sur la planche 3 ci-dessous un résultat typique de calcul au cours d'une réentrée sur laquelle on remarque bien les zones critiques de nez et gouverne ainsi que de bord d'attaque.

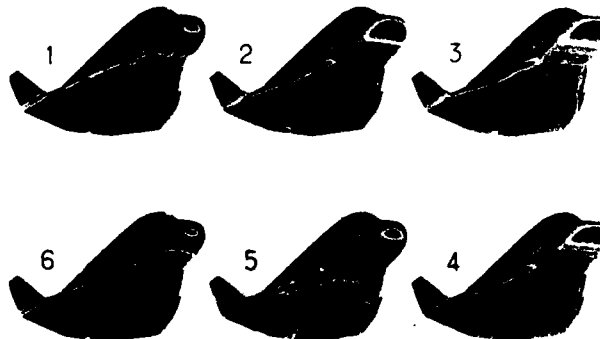
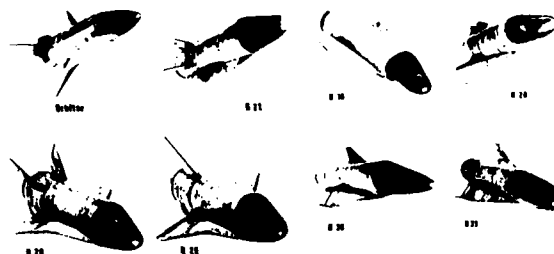


Fig:3

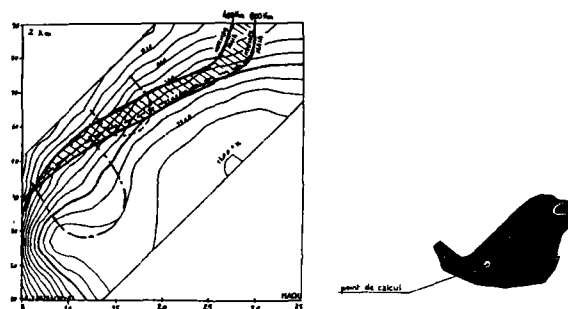
1.3 - A partir de ces éléments de calculs puis d'essais, il est possible d'évaluer différentes formules et de les comparer afin de sélectionner au mieux leurs caractéristiques. On voit sur la planche 4 ci-dessous qu'un grand nombre de configurations ont été calculées et un certain nombre envoyées en soufflerie pour s'assurer que le dessin général était raisonnablement proche d'un dessin présentant une sensibilité point trop exagérée aux variations de formes ou de dimensions, variations qui seront probables au cours de la finalisation du projet.

Fig:4



En particulier, on vérifie constamment que les marges d'échauffement max. restent réalistes pour les matériaux disponibles.

Fig:5



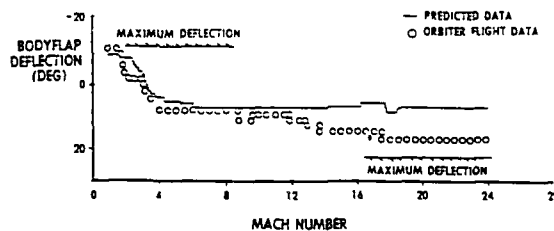
La prise en compte récente de critères de sécurité renforcés à la suite de l'accident de l'Orbiter conduit également à revoir le dessin avec des masses à vide augmentées et rend particulièrement critiques les pertes de masse qui seraient créées par des formes extérieures inadéquates à même volume interne.

2. EXEMPLES DE PRISE EN COMPTE D'OBJECTIFS

2.1 - Equilibre longitudinal aérodynamique

On sait que les marges prises sur l'Orbiter pour couvrir des erreurs sur l'évaluation des braquages de gouverne nécessaires étaient particulièrement faibles et ont posé quelques problèmes de validation des performances nominales :

Fig:6



L'étude détaillée par le calcul et sur recouplement en essais de soufflerie a déjà montré que des calculs simplifiés ne sauraient suffire à l'évaluation des efficacités de gouverne et des moments déstabilisateurs du véhicule. Il a été proposé au CNES de calculer avec les meilleurs outils disponibles (calculs Euler) les différents dessins d'Hermès malgré l'augmentation du coût en calcul correspondant. On voit sur la figure 7 ci-dessous que l'écart le plus critique des braquages se fait entre $M = 1,5$ et $M = 10$ ou plus et que cet écart est sensible à la méthode de calcul : a priori les méthodes les plus simples sont exclues de la panoplie de calcul nécessaire.

On peut voir sur cette même planche que même la correction aux modèles linéarisés supersoniques ne permet pas d'envisager de calculs rapides ; l'analyse des résultats montre que ceux-ci sont dus à la forme très arrondie et aux grandes incidences caractéristiques des trajectoires d'Hermès.

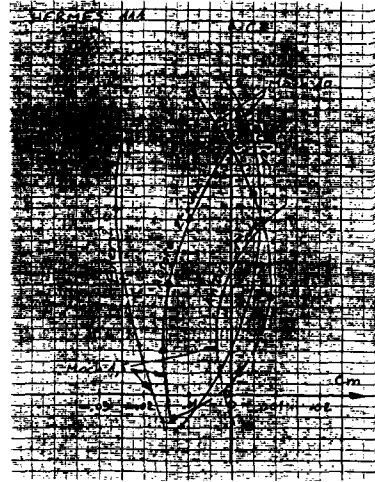


Fig:7

On voit sur la planche 8 relative à un calcul d'AOTV qui exagère l'effet de gaz réel que l'approximation du local peut conduire à des écarts très importants des caractéristiques en moment, écarts qu'il importe de prévoir sur les formes complexes d'Hermès.

Cependant l'expérience de l'Orbiter (fig. 6 ci-dessus) montre des erreurs maximales à fort Mach, soit par effet de dissociation, soit par effet de gaz raréfiés et l'on ne peut pas actuellement le vérifier par le calcul car les codes de calcul n'ont pas la précision requise excepté pour des dessins très simples comme l'AOTV pour lesquels on a pu faire des comparaisons assez précises.

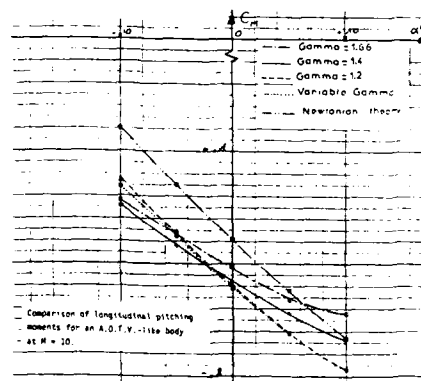


Fig:8

2.2 - Un exemple en aérothermique

De la même façon, il importe d'optimiser par le calcul les échauffements des différentes parties en essayant de régler les courbures locales du nez, des bords d'attaque, etc... de façon à minimiser les surchauffes et l'emploi de matériau carbone à haute température. Mais par ailleurs, il importe de ne pas oublier que l'on doit couvrir, comme sur un avion, la combinaison de paramètres la plus désastreuse en prenant en compte les variations de l'atmosphère mais aussi et surtout les variations de sensibilité à la transition et les effets de catalycité.

On donne ci-dessous les cas déterminant-enveloppe qui ont été déterminés de cette façon. On pourra remarquer que, par rapport au cas présenté pl. 3, il y a des contraintes beaucoup plus élevées (pl. 9).

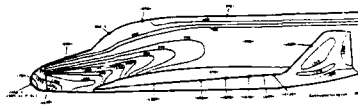
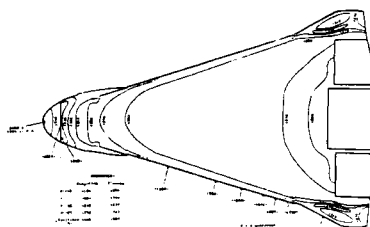


Fig:9



L'élément principal dans ce cas est la variation de la position de la transition en présence de l'effet des rainures entre pavés.

On peut voir sur la planche 10 que l'on peut espérer, quoique sur des cas pratiques assez restreints, une détermination assez précise de la transition en hypersonique. Mais il reste des problèmes de surchauffe locale que l'on ne sait probablement pas atteindre dans la simulation expérimentale et qui induisent une grande imprécision sur les flux réels.

Fig:10

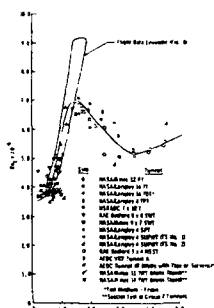


Fig:11

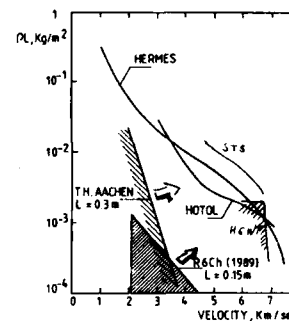
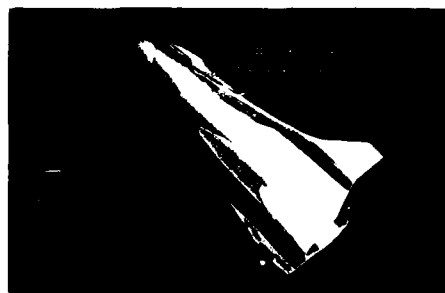


Fig:12



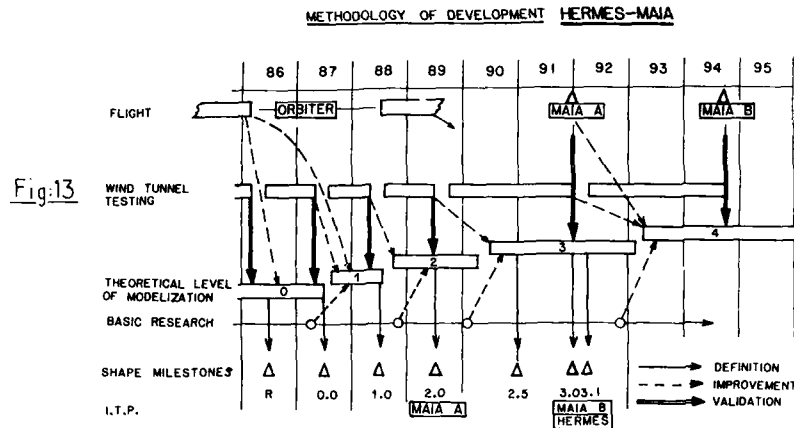
Thermocolor - Calcul.



3. METHODOLOGIE GENERALE

On a vu qu'il y avait des risques importants d'ignorance de problèmes mal connus au cours de l'estimation des efforts et flux dans un projet aussi complexe que l'Hermès. Ce non contrôle des aléas est principalement technique voire scientifique par suite de la très grande difficulté des problèmes posés.

Par conséquent, il a été mis en place un support de recherche couvrant environ 50 axes de recherche dont la moitié en analyse numérique et l'autre en mécanique des fluides. C'est d'ailleurs celle-ci qui est la plus critique par suite de l'absence d'équipes qualifiées suffisantes et de moyens expérimentaux, spécialement de mesure, adéquats. Le support de recherche est donc essentiel et sera assez exhaustif grâce aux meilleurs spécialistes européens.



Pour valider mieux ces résultats complets, il est proposé d'employer un démonstrateur lancé également par Ariane et qui permettrait de faire avancer la technique en validant assez tôt et les calculs et les expériences transposés par le calcul. La commission de l'ESA chargée d'évaluer la méthodologie avec démonstrateur a également recommandé que les premiers lancements soient faits avec des Hermès inhabités.

La méthodologie générale couvre donc trois efforts parallèles, l'un relatif à la recherche de base de compréhension et vérification de la modélisation des phénomènes de base, le second relatif aux essais et calculs des formes industrielles, le troisième à la vérification globale en vol qui s'appuiera sur l'expérience de l'Orbiter puis sur des expériences européennes.

Ainsi l'amélioration de la technologie européenne en hypersonique fera d'Hermès un démonstrateur technologique et une étape essentielle vers les lanceurs futurs complètement récupérables qui donnent des moyens économiques à l'homme pour travailler dans l'Espace.

REFERENCES

- J.P. CHEVALLIER Rétrospective sur les moyens d'essais et de mesure en hypersonique AAFF
22ème Colloque Aérodynamique appliquée - Lille 1985
- P. PERRIER Programme de recherche aérodynamique-aérothermique
22ème Colloque Aérodynamique Appliquée AAFF - Lille 1985
et Euromech colloquium 195 - Marseille 1985
- J.F. WENDT European Hypersonic Wind tunnel AGARD 1987 - 17/AR
- Shuttle Performance : Lessons Learned NASA C.P. 2283 - March 83
- J.G. MARVIN Future requirements of wind tunnels for Aeronautical Systems development
AIAA Paper 86-0751
- D.S. DCLLING et S.M. BOGDONOFF : Scaling of interactions of cylinders with supersonic
turbulent boundary layers AIAA Journal vol 19405 - 1982
- Mc CORMACK R.W. : a numerical method for solving the equations of compressible
viscous flow - AIAA Journal vol 20 n° 9 - 1982
- M.S. HOLDEN A review of Aerothermal problems associated with hypersonic flight
AIAA Paper n° 86 - 0267 - 1986
- B. STOUFFLET, J. PERIAUX, F. FEZOUJ, A. DERVIEUX : Numerical simulation of 3-D hypersonic
Euler flows around space vehicles using adapted finite elements
- P. VANCAMBERG Experimental and Theoretical Tests for the prediction of Aerodynamic
moments of Hermes in hypersonic flight ICAS 86.210.1
- B. AUPOIX, C. ELDEN, J. COUSTEIX : Development of a computational method for hypersonic
boundary layer - Euromech colloquium 195 Luning 1985
- P. PERRIER Aerodynamic and Aerothermal design : from Hermes to ASTS
ESA Workshop on advanced transportation technology
Rome March 1987, ICAS May 87

HYPERSONIC AERODYNAMICS - APPLICATIONS FOR HOTOL

by

Mrs. Alison J. Wake
HOTOL Study Team
British Aerospace PLC
Military Aircraft Division
Warton Aerodrome
Preston PR4 1AX
United Kingdom

Summary

HOTOL has emerged from studies between BAe and Rolls-Royce as a totally reusable airframe with a hybrid air-breathing propulsion system. It is aimed at placing payloads into low earth orbit for 20% of the cost of the U.S. Space Shuttle.

As part of the current Proof-of-Concept Study an assessment is being made of the aerodynamic characteristics of the vehicle including those in the hypersonic regime. This assessment will also identify areas of high risk and where current methods are deficient.

This report details some of the results obtained, the areas so far identified as requiring further work and proposes a five year programme to investigate these areas.

Introduction

BAe have identified the need for a new launch vehicle to supplement and eventually supersede existing launch vehicles by the end of this century. Forecasts of the potential market show that the currently available launch capacity will be exceeded by then.

Studies of the economics of existing satellite launch and recovery systems show that the high costs are largely attributable to throw away components, such as external tanks, retrieval and refurbishment of solid rocket boosters and the large number of support staff required for vertical take-off operations.

HOTOL, Figure 1, has emerged from studies between BAe and Rolls-Royce as a totally reusable airframe with a hybrid air-breathing propulsion system, with horizontal take-off and landing to simplify turn-around operations. It is aimed at placing payloads into low earth orbit for 20% of the cost of Shuttle.

A Proof-of-Concept Study, lasting two years, was begun in Autumn 1985 with BAe Military Aircraft Division, Warton as lead Division. The objectives of the study are:-

- to demonstrate that there are no insuperable problems to the development of the engine.
- to show that the vehicle can be engineered at a reasonable cost.
- to identify areas of high risk and to propose programmes to investigate these areas.
- to detail test and support facilities to fulfil these programmes and
- to identify what the cost will be.

The HOTOL aerodynamic design is driven by a trade-off between the best aerodynamic performance and minimum structural weight. The hypersonic region is perhaps the most challenging aspect of the aerodynamic design, especially for re-entry into the atmosphere which is a critical phase of reusable spacecraft operations.

Re-entry

Re-entry into the atmosphere is initiated by a deorbit manoeuvre. Firstly the reaction control thrusters are used to turn the HOTOL tail first. Then the orbital manoeuvring engines are used to slow the vehicle down. The thrusters are used to turn the vehicle round again and to set up the correct attitude for re-entry.

Because of HOTOL's low planform loading, deceleration can begin at high altitude to minimise peak velocity and minimise aerodynamic heating. Figure 2 shows a comparison between the HOTOL and Shuttle re-entry trajectories. You will notice that HOTOL is intended to travel more slowly than Shuttle at altitudes between 60 and 80 km where maximum heating rates are expected.

To maintain minimum velocity HOTOL must have adequate lift which means it must be possible to trim and control the vehicle at high angles of attack. Although reaction control thrusters may be used to augment control the additional fuel required penalises the payload or results in vehicle growth.

As the vehicle enters the atmosphere the high incidence gives a large force normal to the trajectory. If this force is allowed to act entirely in the orbit plane it will cause the vehicle to skip out of the atmosphere. Therefore the in-plane component of lift must be controlled by rolling the vehicle out of the trajectory plane. The out-of-plane component can be used to realign the landing track by maintaining the roll angle or to extend the down-range capability by periodically reversing the roll angle.

Once peak heating has been passed the vehicle is slowly pitched down to maximum L/D to maximise cross - or down - range performance.

In optimising the trajectory, to give maximum range performance within structure and internal temperature constraints, it is necessary to resolve the "infernal triangle".

The "Infernal Triangle"

This is the close interaction of trim/control, cross-range and heating rate, see Figure 3. The required incidence must be able to be trimmed with an adequate control margin. Viscous and real gas effects must be taken into account when determining if trim is possible. A high incidence gives a lower speed which reduces the kinetic heating rate, \dot{Q} . However, a lower incidence, giving a high lift to drag ratio, is required to maximise cross-range performance. A low lift to drag ratio shortens the duration of the re-entry and hence the heat soak being the integral of heating rate and total exposure time.

Accurate knowledge of heating and heating rates is essential in deciding what materials are used to build the structure and what insulation is required. Because of uncertainties in this knowledge tolerances must be applied to control and heating estimates requiring additional control power and insulation with consequent mass penalties. Let us consider each of these three aspects in turn:-

- (i) trim
- (ii) cross-range
- (iii) heating
- (i) Trim

Good correlation of Newtonian predictions with wind tunnel and flight measurements have been seen in published reports for overall forces and moments. However reference 1 indicates that wing trailing edge flaps can be more effective than Newtonian theory would predict. An investigation into this "hyper-effectiveness" has been carried out and is reported in reference 2. This proposes that Newtonian theory does not perform well in estimating pressures, for the concave shape that occurs when trailing edge flaps are deflected, because of the low Mach number of the flow in the shock-layer. Newtonian theory is based on the assumption that the high freestream Mach numbers are also typical of the local flow behaviour. Figure 4 shows the effect of deflecting a trailing edge flap on a flat plate at incidence in a flow which is inviscid. Once the shock-layer properties are known the control force can be deduced from simple oblique-shock theory.

If the flap is deflected through a sufficiently large angle an attached oblique shock will not be possible and the effectiveness of the flap will be considerably reduced. The existence of viscous effects introduces additional constraints on the performance of the flap. A sufficiently large increase in pressure across the hinge line will cause the boundary layer to separate. Figure 5, taken from reference 3, shows the shock systems with the associated pressure distributions for laminar and turbulent flow. For laminar flow the inviscid and viscous pressure rises are approximately equal although the point of action of the flap force is further upstream for the viscous case.

For turbulent flow the inviscid pressure rise is greater than the viscous. Again the point of action of the force is further upstream for the viscous case than the inviscid. The variation of flap pressure with control deflection is shown in Figure 6. This shows the compatible inviscid and viscous values up to turbulent separation and the low level of the Newtonian estimate.

Note that real gas effects are such that the flap angle before shock detachment occurs is increased. Therefore for this case it is pessimistic not to take account of them.

Now consider the pitching moment due to flap deflection shown in Figure 7. Note that the inviscid and viscous solutions are no longer the same below turbulent separation; this is because of the differences in the points of action of the flap force.

The effect of incidence on control power is illustrated in Figure 8. As incidence increases turbulent separation occurs at lower control deflections. This means that the maximum control moment and consequently the trimmable c.g. range reduces with incidence. Figure 9 shows the expected trimmable c.g. range for the current configuration using wing and body flaps. For the re-entry case there is adequate trim for low incidence where maximum L/D occurs. However, at high incidence, required for the initial stages of re-entry, the range of acceptable c.g. position becomes progressively smaller so that 45° is the maximum incidence that can be trimmed. Although higher incidence capability is desirable, the currently predicted performance is quite satisfactory.

(ii) Cross-range

Figure 10 shows the achievable cross-range with a maximum allowable surface temperature of 1200 K. The variation of cross-range with L/D - effectively vehicle shape, and planform loading - a measure of vehicle mass and size, are shown.

Maximum cross-range is obtained for a vehicle with high L/D ratio and low planform loading. For the current HOTOL configuration the expected cross-range is about 25° latitude.

If however the maximum allowable temperature could be increased by only 50K this would result in a significant increase in cross-range capability as shown in Figure 11, about 25% for the current vehicle. However, this would result in an increase of insulation mass, to protect internal structure and systems, of 30% resulting in an increase in GLOW (Gross Lift Off Weight) of 9 tonnes. This emphasises that accurate prediction is essential because a small tolerance is significant.

(iii) Heating

Maximum heating rates, and consequently temperatures, are expected to occur at the stagnation point and along attachment lines. A procedure for estimating this attachment line heating is reported in reference 4 for both laminar and turbulent conditions. It is concluded that, for laminar heating rates, the effects of realgas are of second order importance - being always less than 20%. Therefore reasonably accurate estimates may be obtained by assuming that air is thermally perfect. However, for turbulent flow real gas effects on heating rates are much more important. Since transition to turbulence occurs at relatively low altitudes, the assumption of a thermally perfect gas may still be acceptable but further work is necessary to quantify these effects.

The onset of transition is critical as heating rates in turbulent boundary layers are significantly higher than in laminar flow. At the start of re-entry, where Reynolds number is low, the flow is laminar. As the vehicle comes lower into the atmosphere Reynolds number increases and transition to turbulent flow occurs. The criterion for transition is based on an allowable reference Reynolds number, reference 5. The reference Reynolds number is a function of speed (= altitude for a given trajectory) and local geometry so transition does not occur on all parts of the vehicle at the same point in the trajectory. Figure 12 shows the variation of Reynolds number with altitude for various X stations on the vehicle. This shows that turbulent flow first occurs over the intake at about 70 km. Figure 13 shows the expected equilibrium wall temperatures on the HOTOL centreline at a position 25 m aft of the nose.

Several areas have been identified as requiring further investigation:-

- the location of attachment lines
- the variation of critical step size with reference Reynolds number
- the optimisation of the re-entry trajectory to minimise the critical heating
- the behaviour of complex flows in the region of the intake (including shocks, expansion fans).

In addition to the attachment line heating, regions of local superheating are likely to occur as the result of shock interaction. Shock-shock, shock-boundary layer, shock-surface and shock-shear layer interactions all have an effect. Reference 6 shows that the local hot spots generated undergo heating rates up to an order of magnitude higher than other parts of the structure.

see Figure 14. This increase in heating rate depends on the strength of the shock and can be alleviated by sweep. The precise location of these local hot spots is difficult to determine and more work, both experimental and computational, needs to be done before these effects can be determined with any degree of confidence.

Experience gained from wind tunnel and flight tests of the Shuttle has indicated that there is significant heat transfer taking place on the leeward side of the vehicle due to flow reattachment. This also occurs on the vehicle sides due to embedded vortices developing in unstable boundary layers and due to scrubbing by the vortices generated at the wing-body junction. Again estimation of these effects is difficult and further work is necessary.

The Way Forward

A possible HOTOL development programme is shown in Figure 15. This would lead to first flight in 1998, development of the engine proceeding in parallel with the airframe with the intention to demonstrate the engine cycle at an early stage. In parallel with both the initial phases of the airframe and the engine programmes there is a proposed Enabling Technology research and development programme. This activity is aimed at verifying the design assumptions and minimising the risks at entry into the full development programme. Proposed activities come under the following major headings:

- Materials and structures
- Aerodynamics including heating effects
- Vehicle systems
- Command and control, including ground infrastructure
- Unmanned flight

A significant part of these technology programmes would be relevant to any European launch vehicle.

Aspects of hypersonic aerodynamics which would be included in this work are summarised as:-

- Accurate estimates of temperature and heating rates to minimise insulation mass and maximise cross-range, including location of attachment lines on windward and leeward sides of the vehicle and real gas effects.

- Prediction of the position and magnitude of local hot spots caused by shock intersections in order to provide adequate protection for the structure.

- Prediction of accurate forces and moments during re-entry is necessary to ensure:-

- adequate lift during the early stages of re-entry to minimise speed and hence aerodynamic heating
- adequate L/D to meet cross-range requirements
- adequate aerodynamically trimmable c.g. range due to the large fuel/weight penalty for trimming with reaction control thrusters.

These are areas which the UK and Europe now need to mobilise their resources, both experimental and computational, in order to bring the aerospaceplane to reality.

References

1. Wilhite, A.W. 1983
"Optimum wing sizing of a single-stage-to-orbit vehicle".
Journal of Spacecraft and Rockets, 20, 115-121
2. Clarke, J.F. et al April 1986
"Forces and Moments on HOTOL at $M = 25$ at an altitude of 75 km".
Cranfield College of Aeronautics Report NFP86/19
3. Popinski, Z. and Ehrlich, C.F. 1966
"Development design methods for predicting hypersonic aerodynamic control characteristics."
Air Force Flight Dynamics Laboratory Technical Report, AFDL-TR-66-85
4. Poll, D.I.A. November 1986
"A preliminary assessment of the kinetic heating loads experienced by the HOTOL vehicle".
DIACON - Fluid Mechanic and Thermodynamic Consultants.

5. Poll, D.I.A. June 1985
"Boundary layer transition on the windward face of space shuttle during re-entry"
AIAA-85-0899
6. Hiers, R.S. and Loubsky, W.J. February 1967.
"Effects of shock-wave impingement on the heat transfer on a cylindrical leading edge"
NASA TN D-3859

Acknowledgement

The assistance of Cranfield Institute of Technology, in particular the work done by Dr. D.I.A. Poll, is gratefully acknowledged.

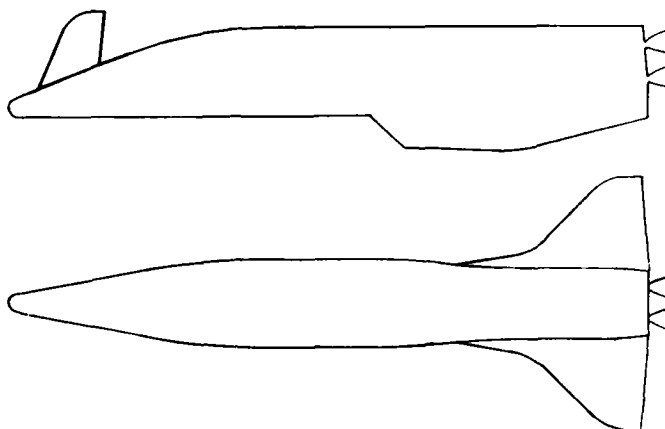


FIGURE 1 HOTOL - side and plan view

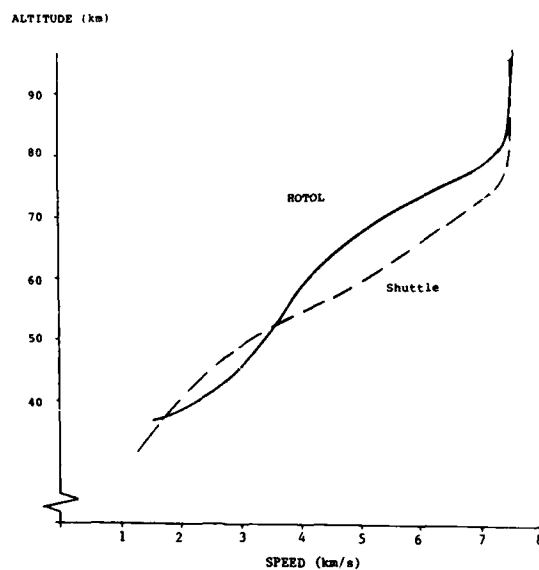


FIGURE 2 Re-entry trajectories

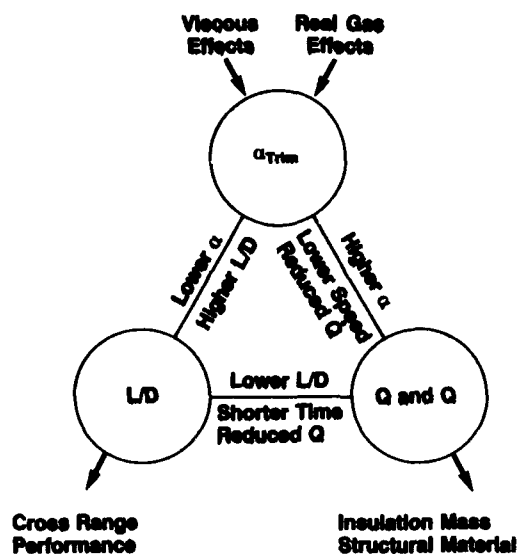


FIGURE 3 The "infernal triangle"

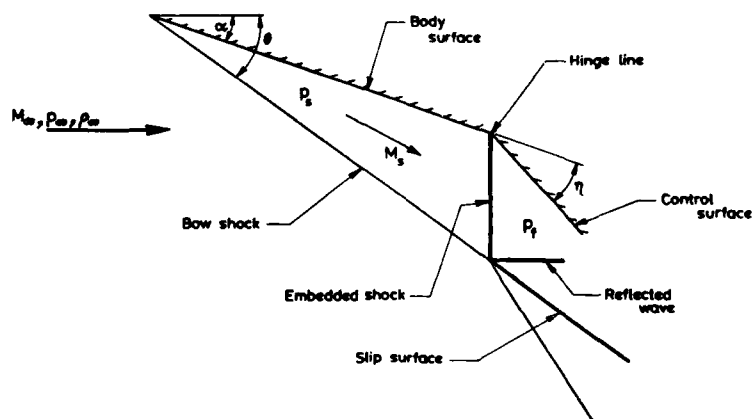


FIGURE 4 Inviscid flow past an inclined flat plate

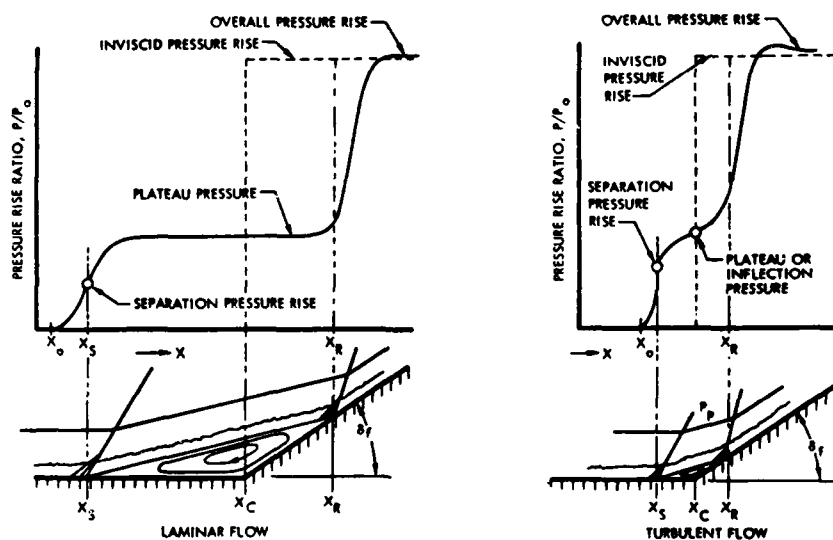


FIGURE 5 Pressure distributions in a concave corner

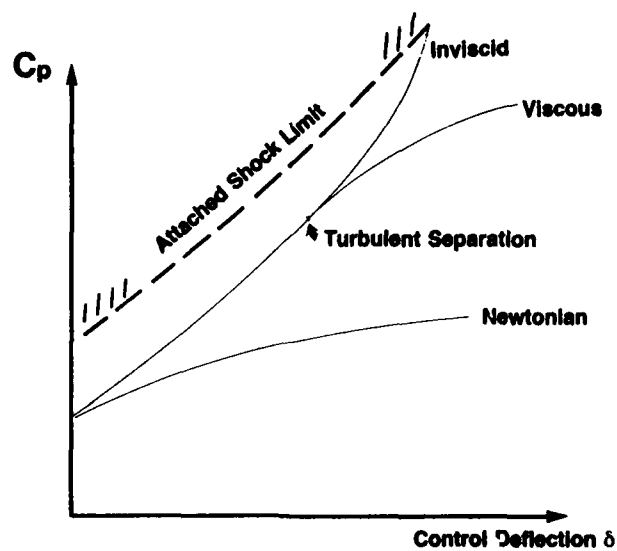


FIGURE 6 Wing trailing edge control pressures

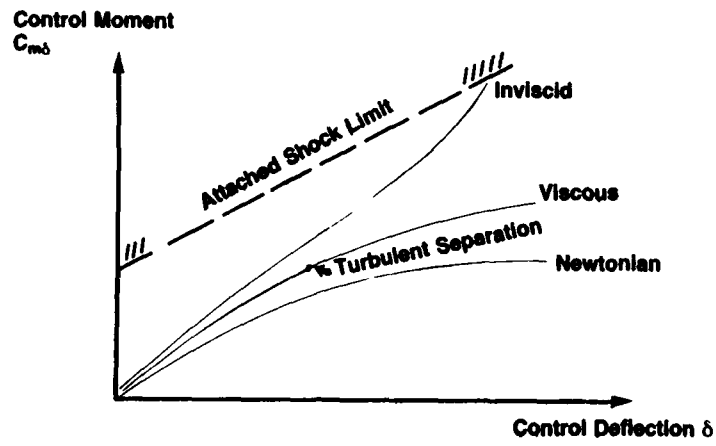


FIGURE 7 Control power

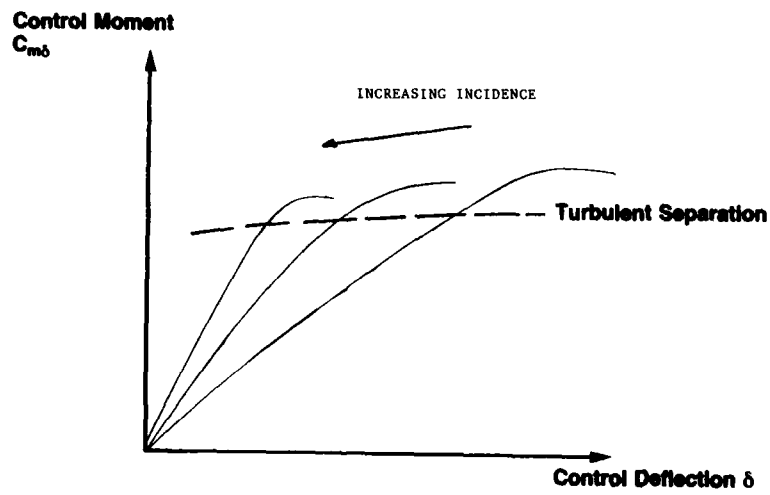


FIGURE 8 Variation of control power with incidence

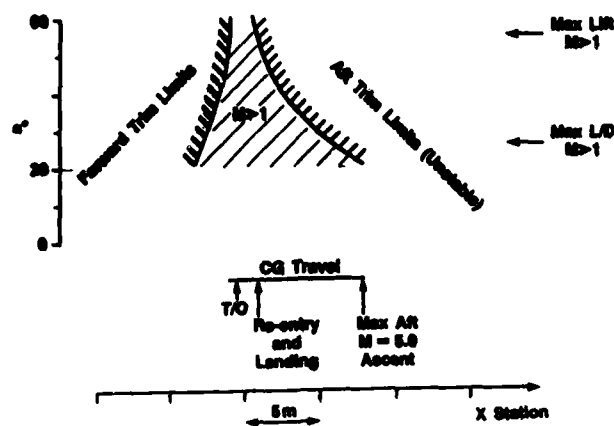


FIGURE 9 Centre of gravity limits

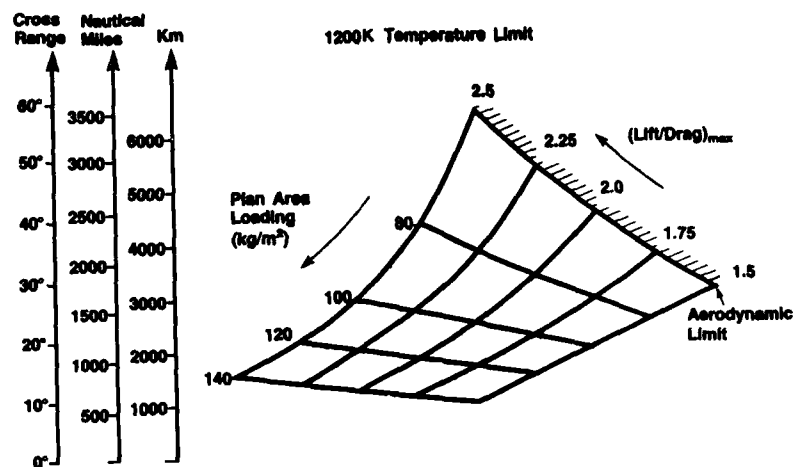


FIGURE 10 Cross-range capability

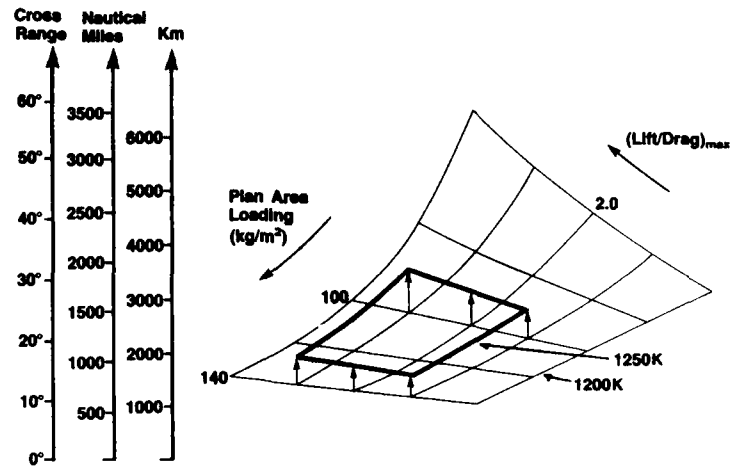


FIGURE 11 Effect of temperature on cross-range

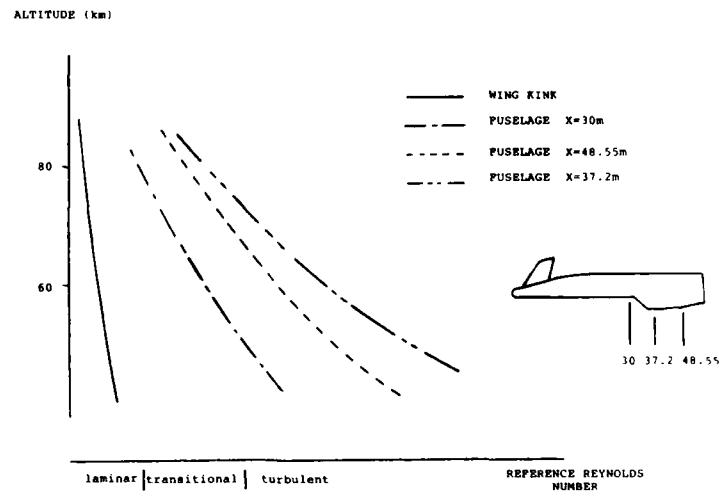


FIGURE 12 Variation of transition occurrence

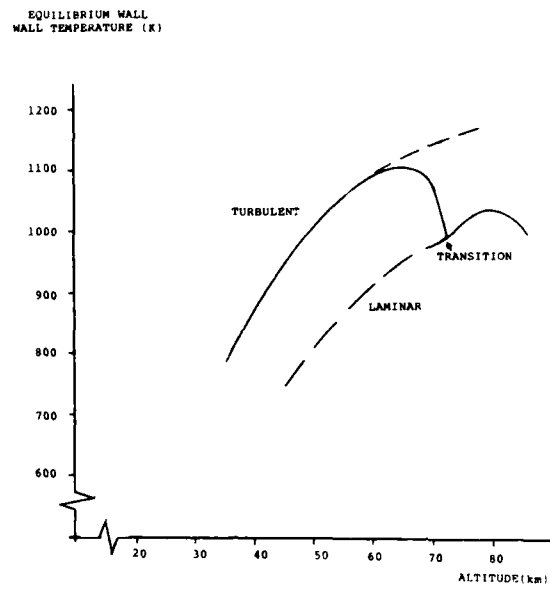


FIGURE 13 HOTOL fuselage centreline equilibrium wall temperature

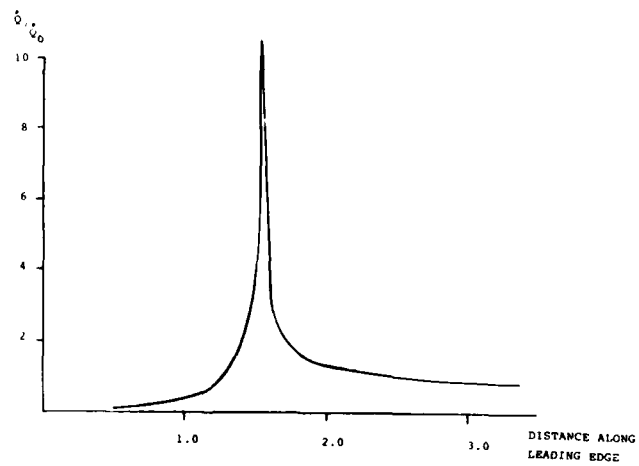


FIGURE 14 Spanwise heat transfer distribution

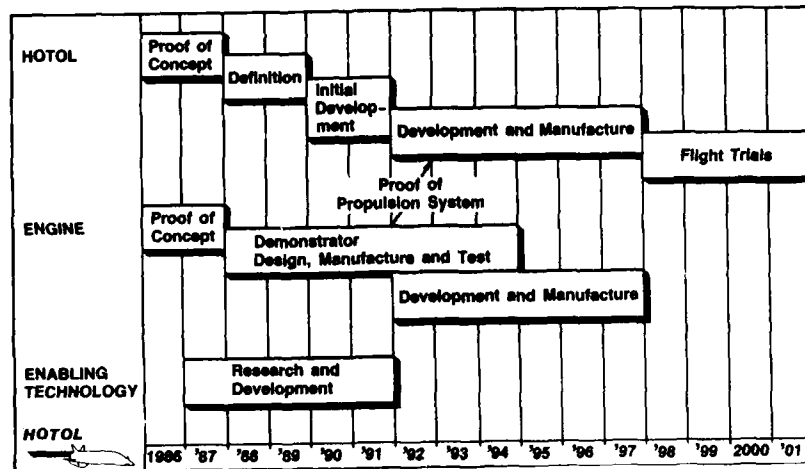


FIGURE 15 Development programme

ROUND TABLE DISCUSSION

AEROTHERMODYNAMICS OF HYPERSONIC LIFTING VEHICLES
April 9, 1957S. Bogdonoff, Princeton

Ladies and Gentlemen,

Let me say first how pleased I was to be asked to be technical evaluator for this meeting. Hans Hornung and Bob Whitehead are two old friends, and I didn't realize quite when I said yes many months ago, how enjoyable this was going to be. Although I tried to listen to every paper with great detachment, I am afraid I got swept away every now and then. The job of the technical evaluator is one which I have taken in a very wide view. There were many excellent papers presented, and I will make no attempt to talk specifically about each paper here. What I would like to do, instead, is to share with you a general impression of what was covered, what was not covered, and make some comments which I hope might be helpful for some of you, individually, or for AGARD, with regard to the continuation of efforts like this in the future.

The meeting was entitled "Hypersonics", but it really wasn't in the full sense. Many of the papers were on high speed fluid mechanics which, in many cases, has some relevance to Hypersonics.

I was particularly interested in the mix of people who were at this meeting. I want to congratulate the group who proposed this meeting some years ago. Although Hans Hornung said that it was luck, I think that it was great foresight. One of the things that I think is important in the evaluation of the meeting is the audience. I categorize the audience in three groups: there are "grey hairs and no hairs" who worked in this field well over a decade ago. There are a small group of people who connect the past with the present. They have been working on hypersonic problems over many years. Then there are many young people who clearly are working in hypersonics for the first time, who don't know about all the mistakes that were made, and are prepared to make their own mistakes all over again! Part of the difficulty I had in evaluating the papers individually is that the papers were written for and presented by different segments of the audience.

One thing that I think was missing was an overview of the field, as an introduction to bring these three groups together in some sort of a framework. As the meeting went on, some comments came up which did part of that job. An overview might be helpful when there is a very diverse audience and things which are well known to some of the people are totally unknown to others.

The discussions, in particular, and the coffee and tea breaks helped to solve some of this. It would be helpful if we had a chance to define the key issues for hypersonics, and then it would be easier to say, "what have we done", "what haven't we done" and "what are those issues that are yet to be resolved". The last point I want to make is the question of "where does hypersonics start?". An old answer is that it is "wherever you are when you say you are working in hypersonics". I think that applies very well to some of the papers in this meeting. There were some excellent papers in high speed aerodynamics, but I question whether they are key issues to be faced in hypersonics; whether they are the key elements that designers need to know for hypersonic designs. I want to give you a possible frame of reference so that you will understand the basis of my remarks. Hypersonics is not just an extension of high speed aerodynamics. High Mach numbers brings into play a whole group of new phenomena. One way to put it is that, if you are flying at 5, and you compare it to flying at 15, you are talking about an order of magnitude difference in energy. If you go into orbit from the ground, about one-half of the energy goes in above Mach 15. Working at Mach numbers of 5 and 10, which may sound like hypersonics, is not attacking the crucial parts of the problem, which occur at high mach number. It is important to work on high speed aerodynamics, but, there is a good reason to think about hypersonics in different ways. I divide hypersonics into "low speed" and "high speed". Low speed, to me, is under Mach 10. I make that division because I believe that it is possible to take what we know about supersonics and get pretty close to 10 by extensions and extrapolations. It's primarily aerodynamics. We have some facilities, and we have the ability to compute. But when you get above Mach 10, you enter a different region where there are very significant new phenomena. They are there at lower mach number, but they are not critical. When you work in hypersonics, you have to take into account new phenomena, which we don't ordinarily consider in high speed aerodynamics. We design airplanes in the supersonic range and "low" hypersonic range primarily for aerodynamic efficiency. When you consider "high" speed hypersonics, strong interactions, heat transfer, materials, ionized gases, real gases, are important. It is from this point of view that I say that "hypersonics" is different. You can't design a hypersonic vehicle from aerodynamics alone. It may not be the optimum aerodynamics vehicle because you can't handle the heat transfer or the control or the materials and structures. Hypersonics is an integrated field, a lot different than what we are used to in high speed aerodynamics. It is particularly important in propulsion, which I will comment on further in my evaluation report.

What I would like to do is to go over each of the sessions (without going through individual papers) and give you a "overall" view. First, let me say that the organization of the meeting was very good. It went from fundamentals to real applications. The idea of putting the integrated design problems at the end gave everybody some perspective of where their own little world of research or computation fit'ed in to the real problem. It also highlighted the needs of the people who have the responsibility to figure out how to make one of these things fly.

RTD-2

Session I. Facilities

I was disappointed in the discussion about facilities. In many cases there has been a struggle in the last few years to resurrect the facilities that we had buried, or threw away or neglected. There are very few people who have had the luxury of having facilities operating for the past 10-15 years, improving them all the time, and doing better instrumentation, and so on. Most of the facilities that we are talking about were designed 20-30 years ago, when we knew much less about hypersonics than we know now. I suggest that the world has changed significantly, our ability to do things has changed, and surely our ability to measure has changed radically. I would suggest that, when we discuss facilities, we ought to first determine what is really needed. What kind of information are we looking for? You can approach this in many ways, but I think that most people who work in the field would end up giving a list which is similar. The question is how do you get that information, how do you get that data. Although many of us were brought up on wind tunnels, ranges, or shock tubes, I believe that hypersonics demands a broader look than that. I don't think that we are going to be able to generate all of the information that we need for hypersonics in ground facilities. There may be some new concepts, but so far I haven't heard of them. When you speak of facilities for hypersonics, you should start from what you need, and figure out every way that you can possibly get that data. Hypersonic testing, without considering flight instruments, is not very realistic. Many things that we can do on the ground are extraordinarily useful, and must be done. But, there are some phenomena which will be very difficult to simulate. I will come back to that later when I discuss CFD. There is a problem with flight tests. It is extraordinarily expensive, and it is very difficult to get the quality of data that we are going to need to make progress in hypersonics. I suggest that this is part of what the cost is going to be. Part of the responsibility of a group in this field is to work on such a program, not being tied to in the past, what conventional aerodynamicists have been tied to the wind tunnel. Hypersonics needs more than that! After being so negative, let me say that ground facilities, with modern instrumentation, can supply a lot of information that hasn't been supplied yet, and it will be very useful information. In many cases it will be crucial to the continued development of hypersonics. But, we are going to need more!

Session 2. Experimental Investigations and Techniques

I was quite interested in this session because it contained many excellent papers in high speed fluid mechanics. However, most were not aimed at the critical problems of hypersonics per se. There are significant differences between phenomena that are important at Mach numbers of 3, 5 and 7 and those that happen at 15, 17 and 19. We know so little about what happens at very high mach numbers that, it seems to me, most of our resources (if we have the ability to move our resources) should be focussed on the critical areas that we don't know very much about: turbulence, transition, boundary layers under very cold wall conditions, real gas effects, catalysis. All of these are very important items if we are going to try to do something for a hypersonic vehicle. To tackle these questions is very difficult, but that is the crucial part of hypersonics. I suggest that we might gain a lot in our future progress if we could focus on these areas, perhaps at the detriment of some other things that we are in love with, that we have worked with, and which have supported us for years. The future is going to require an attack on new difficult problems.

There were some interesting papers about low density flows. Most aerodynamicists work with continuum flows. Hypersonics is, as I have commented, an extension of high speed aerodynamics to new phenomena. One I didn't mention is the non-continuum area. As an aerodynamicist or a fluid mechanician working in hypersonics, you have to be very well aware of what is going on in free molecular flow. In addition, there is the wonderful region, totally unknown, in between free molecular and continuum. We simply don't know, at the moment, how to get from continuum to free molecular. George Koppenwallner's paper demonstrated that two end points doesn't describe the phenomena in between. That is the sort of surprise that we may find in other phenomena in this transition region, simply because we haven't been there! Outside of the kinetic theory part of it, it is all non-equilibrium, a phenomena which is usually not considered in aerodynamics.

Session III. Propulsion

Propulsion got short shrift in this discussion. I believe I understand why. When you talk about hypersonics, there is again another division. If you consider propulsion using rockets, you only worry about external aerodynamics. The rockets are mounted at the back, and have little influence on the vehicle shape. But there is another group that considers "air breathers". For this group, it is impossible to talk about the aerodynamics of the vehicle without talking about the power plant at the same time. A hypersonic air breather is the most integrated vehicle that we have ever conceived. You can't separate the engine from the airframe. The integration that is involved is several steps more complex than a vehicle which uses a rocket. The propulsion system may tell you what is the optimum airframe. Let me point out though that there is only a part of the hypersonic world that considers air breathers. Rocket propulsion has a great advantage in the design of a hypersonic vehicle in that it may be much simpler. However, when you use a rocket, it has a big, blunt, back end, which is a problem if you want to fly at lower speeds or when the rocket is not operating.

Session IV. Computational Fluid Dynamics

Let me comment about one of my favorite subjects, CFD. There is a major difference, in my mind, between the role that CFD plays in the subsonic and supersonic field, as compared to the hypersonic field. In the subsonic and supersonic field there is enough experience and data around so that, when you compute something wrong, you know that it is wrong right away. In hypersonics, there is a serious problem. The CFD community has developed an extraordinary talent for the techniques, and the computer industry has developed great tools; the difficulty is that we don't know what is real and what is not. The design people kept bringing that up. They need some tools to tell them things that they can't measure at conditions which they have not experienced. I suggest that hypersonic CFD, at the moment, has not taken on the important job of determining what specific codes can and can't do. If it can do it, what sort of error band is realistic? It is very important that the CFD people, who have been having so much fun so far, get down to business and try to provide tools for industry. This requires the definition of what you

can and what you can't do. What has become so critical in the hypersonic field is that CFD is the glue that is going to put all of the hypersonic elements together. We are going to have test data simulating different phenomena of CFD. There are only two ways of putting it all together. One is you put everything together on a vehicle and see what happens. The other way is to have CFD tools available which will permit you to put things together, with some reasonable confidence, that they are going to give you the right answer. CFD validation is critical. I suggest that you should make no computations unless there is data available (of the right sort) to check against, or it is associated with a test which is going to be made which will tell you something about the comparisons. That is an extreme statement, but I think that we are going to have to face that.

Session V. Vehicle Design

I personally want to thank the design group who talked about trying to design vehicles. The problems about trade-offs, parametric studies, and validated CFD codes are what these people need to put a vehicle together. They have to design vehicles that go from Mach 0 to 25, they have to work at altitudes from sea level to space. What they have to work with is the data that you can get out of wind tunnels, the data that you can put together with CFD, and the data that you get out of flight experiences. People who do basic or applied research ought to listen carefully to those people. It was clear to me that they dropped back orders of magnitude in the kind of sophistication which we were talking about during the rest of this meeting. Whatever they use, they have to believe in well enough to invest money in it. Most of us just invest papers and some reputation.

I will try, in the final written report, to make some comments of a more technical nature, but thank you again for giving me the opportunity to be involved in this group. I have learned a great deal, and I hope that all of you will go onward and upwards with hypersonics.

H. Hornung, DFVLR

We now come to a ritual which is common to AGARD meetings. We will have a discussion session in which there is a peculiarity which distinguishes it from the other discussions, namely that everything is recorded. This means that if you make a contribution to the discussion, we must insist that you wait until the mike is switched on and say your name and your affiliation clearly because what you say will be sent to you for editing. So, if you don't like what you said, you still have a chance to modify it, slightly.

To make the most of this discussion and to make it useful, ask short questions and make short comments. Don't give quarter hour talks, we only have two quarter-hours. The floor is open for discussions.

F. Myaliwetz, MBB

In my mind, and I think many of you will agree, efficient hypersonic flight will be a reality in the future. There is a long way to go to reach this end. I think that we are presently at the stage which is comparable to the late '40's or early '50's with respect to supersonic flight. We can visualize that there is a lot to be done. We need more resources, money, methods, experimental facilities and what we need above all is young, gifted people. The average age of us here is about 50. In ten years when Hermes is flying the average age will be about 60. This means that we have to try to inspire young people to come to this field and devote their time to it.

H. Hornung, DFVLR

Thank you for that comment. Do I see any other hands up?

M. Ahmet, British Aerospace

One thing that I personally was a little bit disappointed in was the exclusion of the experimental uncertainty in the examples which have been shown when validating theoretical methods which covers the computational as well as the semi-empirical and other types.

S. Bogdonoff, Princeton

I would suggest that people who make computations should also include error bands. Practically everybody who presents the results of a computation, present it as a thin black line. We have done some analysis of some of these computations and that "thin line" should be drawn with a big black brush. It would be very helpful for the experimentalist, because it would show the need for a measurement of a specific accuracy, if you are going to check a computation. I think that the discussion, of error bands applies to both computation and experiments.

H. Hornung, DFVLR

Yes, this is currently a problem that we all are aware of, but I would like to say that hypersonics is, more than anything else, a field where now after all we have got to get these experimenters and CFD people closer together. We mustn't fight against each other; we must work together.

A. Roshko, Cal Tech

This was an excellent symposium. I enjoyed it hugely. I think that I am in a category of those who are weighting the average towards 60 or higher by now. One of the things that struck me, and it is certainly no fault of the organizers, is the lack of what I might call analysis in all the proceedings. It is not only true here, but at most conferences these days. By analysis I mean the search for the simplifying and unifying concepts that have been so common to aeronautics in the past. In trying to figure out why that is so, one possibility is that all the simple problems are gone, that they were skimmed off thirty or so

RTD-4

years ago in the last round, but I really don't believe that. Another possibility is that all the analysts are gone. If you ask where they are gone, I suspect that a lot of them are gone into computation. If so, I guess this problem should correct itself in another 10 or 20 years once computation becomes a tool like experimentation is, at present, because I believe that the end product of computation is the same as the end product physical experimentation, except, of course, that you have more measurements accessible from computation. However, all the data that will eventually come out of computations still needs the kind of unifying treatment that was provided in the past by analysts. I am a little puzzled as to the present situation; it may be that analysts are not obtaining the support or the welcome that they did in the past.

R. Graves, NASA

I want to address the question of attracting young people back into the field. In the United States, the Office of Naval Research, the Air Force Office of Scientific Research and NASA Headquarters have entered into a program to fund training and research in hypersonics with six universities with the specific purpose of attracting new young people into the field to work on Master's and Doctoral degrees and providing them adequate support for training as well as support in terms of research. This is our first step in hopefully reinstituting hypersonics into the university community in the U.S. It could serve as a model for other countries in terms of reinitiating hypersonic training into the university community.

H. Hornung, DFVLR

Thank you for that comment which is also very welcome to me. Will someone say something about CFD?

W. Schmidt, Dornier

I don't want to say something about CFD now, I would just like to give a small comment to what you said previously. Since I belong to those who did some work in hypersonics more than 10 years ago, starting as a very young person, I must also tell you that by that time I was somewhat disappointed because we were very enthusiastic and started things and then there was a decision that there was no use. So now we restart again working in this field, but we should be well aware of the fact that this makes no sense if we have to stop again in some years.

H. Hornung, DFVLR

In other words you would like to see something that really flies.

P. Perrier, Avions Marcel Dassault

As the person responsible for the aerodynamics and aerothermodynamics of Hermes, I have two general remarks on that session. First, it seems to me that there is not sufficient emphasis on the accuracy and on the problem of measurement in the wind tunnel or any hypersonic facility. The great difference actually between the measurement in a current wind tunnel and use of true hypersonic facilities, not facilities at Mach number 8, but facilities with problems typical of hypersonics is that you change your scale. When you use for designing an aircraft a wind tunnel result, you use a scale such that you can see one count in pitching moment, one count in lift or one count in drag. When you use currently that sort of terrific ground installation, you change the scale many times by a factor of 10. So it is not realistic at all for the design and we have to go from something that is more an experimental level to an industrial level. This can be seen by the fact that all the equipment for the measurements are not at the level of quality that is necessary. For example, if you wish to have heat fluxes or something as simple as a pressure it is not useful to use the current aerospace industry scale, otherwise the scatter is too large. My second remark is on the CFD side. It seems to me the people have not done sufficient emphasis on the fact CFD effort is increasing in hypersonics, not only by the fact that it increases everywhere, but because it is necessary for solving the problems of hypersonics. It is the only way to put together all the different influences that are important in hypersonics. Typical figures 10 years ago in the percentage of CFD in the design of an aircraft was at the order of 10% or lower. Currently, on the Rafale demonstrator, that is our last prototype, we have put the figure at the order of 50%. It seems to me that it was necessary for having sufficient manoeuvrability on the general design in transonic and supersonic. It seems to me that when I have to fight with CNES or European Space Agency for having a percentage of CFD in Hermes that is larger than 50%, it is perhaps too soon, but I had no large success because I have not many experiences of that sort of design behind me. But it is quite evident that it is the only way for the future of the design. Otherwise, if you use the scatter we have in experimental research, what will be the result of that? Either we have to be extremely conservative or to choose a very risky design.

J. Slooff, NLR

This is not a comment to M. Perrier's remarks, but rather it should be put in the context of answering your invitation for remarks on CFD a minute ago. I have one which can probably be put in the category of kicking against open doors, but I will give it anyway. Professor Bogdonoff stressed the point when he talked about facilities. I think that development of new facilities in particular should be addressed from the standpoint of what the needs are; what sort of information precisely do we want out of it. The type of facility should be determined by the answers to those kind of questions. I think that he did not stress the point that the situation is exactly or should be exactly the same in CFD. We have had a lot of fun in the CFD community in the past 10 years or so, to speak with Professor Bogdonoff's words, and it has led to a tremendous amount of codes of varying sophistication that have filled lots of symposia, etc.. However only a very small number of these codes have been developed. Most just have developed, I think. As far as CFD is concerned, we are going to enter an era, several people have already done so, in which you start with designing a code from the viewpoint of what we need it for and what sort of information we want to get out of it, with what accuracy, etc., and then start the development. That is what I wanted to say.

W. Schmidt, Dornier

Now I think that I have to say something about CFD. From my opinion there is kind of a mix between two things. One is physics of flow fields and one is computational methods. When people are talking here about CFD they are more or less blaming the non-understanding of the physics rather than the method itself. If we state a physical problem which we understand in all the details, if we have a very clear physical model, and if we have the corresponding differential equations or finite difference equation, I think that we are capable of solving this equation to any accuracy you like, at least in a large amount of cases. What we are lacking especially in hypersonics, but also in most speed regimes is the right physical understanding, the right understanding of length scales and thus also the right modelling, for instance with meshes to resolve certain areas of flow fields. We have to get much better physical understanding and this is something that we don't get by CFD in itself. We have to play back the ball to the experimentalists. What we need is much better experiments with much more quality in the details because we have to get the physics from the experiments, the methods won't give the physics.

R. Bradley, General Dynamics

I have a comment I would like to make on Wolfgang's comment. I agree wholeheartedly that instrumentation and measurement accuracy to a much higher degree are necessary. However, I would like to reinforce what Professor Bogdonoff said earlier, I am convinced that we do not understand the numerical physics that are in many codes that we use routinely. I feel that we need a much higher degree of understanding of the effects of grid densities, convergence and artificial viscosities because many times the physics can be totally obscured by the numerics.

H. Hornung, DFVLR

Eli, I would like to change the subject.

E. Reshotko, Case Western Reserve University

I'll try. First I will answer Wolfgang Schmidt by emphasizing one of Anatol Roshko's remarks, namely, that when you don't understand the physics, experiment is not the only alternative, there is also analysis. In this whole symposium, I did not once hear the expression hypersonic similarity nor about the hypersonic similarity laws, which were once the backbone of hypersonic flow relationships. In fact sometimes when I am asked what is hypersonics, I say that a hypersonic flow is one that obeys hypersonic similarity laws. For blunt body flows that may be at Mach numbers as low as 2. For slender body flows it might be at Mach 15 or higher. The fundamental understanding of the physics is all important, and there must be an appreciation of the need for getting good physics out of computation. I am disappointed that in the computation of laminar flows there isn't a clear solution. We went through an exercise recently in the United States where the same problem was solved using five different PNS codes for laminar flow, and we obtained five different answers. Now, there are not five different laminar flows, there is only one, so we don't know which one is right. There has to be some attention given to making sure that the computation codes are responsive to the flow physics. That is what Professor Bogdonoff meant when he said that there must be redundancy in the flow calculation procedures because they are not reliable until so proven.

In changing the topic I want to get to some of the technical elements now as well. I was disappointed generally in the lack of sophistication in the methods presented at this meeting for the consideration of viscous flows. We have a long past history of being able to deal successfully with two-dimensional integral methods for boundary layer and for estimation of aerodynamic heating. I grew up in aerodynamic heating, and I am on the higher side of the average age as estimated in this room. I don't understand why the established three-dimensional finite difference methods and three-dimensional integral methods for boundary layer and for estimation of aerodynamic heating are not in use. It would seem to me that if it was done 20 years ago, it could be done now. Also I would expect hypersonic viscous interactions to play a more prominent role in the phenomenology than showed up at this meeting. There were papers presented covering dynamic stability considerations that ignored the boundary layer, and yet for sharp cones or wedges, there are interactions near the leading edge that can introduce, not only additional pressures but pressures that are out of phase with the motion because of the character of the unsteady boundary layer. The dynamic stability characteristics can depend on frequency and should not be represented only by their zero frequency limit. These are issues that I feel should have been raised at this meeting but were missing. I hope in the future to see some of the old sophistication returning.

H. Hornung, DFVLR

I think the leading edge of intakes are particularly relevant problems.

L. Ericsson, Lockheed

I want to follow up on Eli's comment in regard to viscous flow. Often in meetings you will find that people will be very concerned about turbulence closure without ever mentioning the word boundary layer transition. You don't have to go into the "tickling" of the boundary layer, using Morkovin's nomenclature. That is not needed to describe the coupling between boundary layer transition and vehicle motion. All you need is to describe the slowly varying environment, the slowly varying coefficients, if you will, that determine the effect of boundary layer transition on the vehicle dynamics. I think that the CFD people should be eminently capable of including that at the present time.

RTD-6

S. Molder, Ryerson Polytechnic Institute

I would like to address my remarks to the code-smiths and be a bit critical about their presentations, the type of presentations which start with Navier Stokes equations and end up with vector plots of the results without all that much in between; without much explanation of the steps that have been taken or the methods that have been followed. This makes us admire their efforts; however, it's not very useful because we cannot objectively judge the accuracy, or even the gross validity in some cases, or the results. We cannot use the presentation or the accompanying papers to write programs of our own; and in very many cases the authors or their agencies are not willing to supply more detailed information or the computer programs themselves. What I would suggest to the organizers in the next CFD sessions is to extract from all the CFD authors a promise to supply their codes if they are asked for them.

H. Hornung, DFVLR

I don't know if you have much experience with promises from number crunchers.

G. Koppenwallner, DFVLR

I would like to make a comment concerning wind tunnels and code validation. We need two kinds of wind tunnels, one kind which is essentially used for industrial testing and then we need another kind of wind tunnels which we use for code validation. These wind tunnels must work at very well defined conditions. For instance, I think that in wind tunnels where we make only Mach-Reynolds simulation we must exactly know our gas conditions. Therefore, we use only a single component gas and avoid dissociation. Then wind tunnels where we study only rarefaction effects, again with a well-defined gas. Then wind tunnels for real gas do this. This is one point where we don't want to mix everything up. That is one point which I want to make. The next point concerns the comparison between theory and experiment. Here one must be very careful because in hypersonics we have, for instance, a large change of temperature and also viscosity. For an appropriate comparison the viscosity law and temperatures of the theoretical calculations shall match the experimental conditions. Literature data is usually insufficient to do this. This is one point which is very important. Also, if you are going to compare pressure data which are on the lee side of a body in hypersonic flow. These pressures are very small and you cannot compare on a linear scale. You must go on a logarithmic scale in order to see the details. These are some points I find important for the comparison of codes with experiments.

A. Young, Queen Mary College

One of the areas of which one heard relatively little in detail during the discussions is that of real gas effects. We saw how important real gas effects could be from the trajectories that were shown of vehicles. This is an area where I think that there may well be an accumulation of information which is not being properly tapped. There was work done on real gas effects 10 or 15 years ago when the subject was alive and popular, and I have no doubt that there must be material in various physics laboratories which would be relevant to some of the problems of real gas effects. I think that this is an area that would repay a lot more attention than is being given at the moment.

H. Hornung, DFVLR

I should make use of the general interest in accuracy in wind tunnels that has been voiced to make a plug here for the next AGARD meeting which is on Wind Tunnel Accuracy, Quality Requirements and Achievements. This addresses precisely the point that has been discussed here, though of course, in transonic flow.

If there are no more questions, then we come marvelously on time to the end of the discussion. I would like to say one word which is appropriate here in Bristol. I don't know if you have noticed, but we keep talking about heat transfer and heating here, and just between this theater and the other side of this wall is a picture of the second Professor of Engineering in this University, who was Stanton. He was the second Professor, the first one was Hele-Shaw. I think that at this point I will hand over to Peter Sacher who is going to go through the final ritual of this meeting.

P. Sacher, MBB

At the end of this busy week, it is up to me to find some closing remarks. Following the discussions, the presentations, especially these last discussions, one may say that there are many more questions left open than answered. But I think that is not a characteristic of a bad meeting; on the contrary, I think this may follow the purpose of a symposium: to stimulate new work, to improve contacts and cooperation and we have had, I think we all agree, a very complete state-of-the-art review. If somebody says that most of the material being presented here is 10 years old, then it may lead to a kickoff stage of new investigations in this field. Then, at least in my opinion, we will have fulfilled our purpose.

Now let me say some words of acknowledgement. First of all, I wish to thank all of our speakers for their outstanding presentations, delivery of papers, and of course, the audience here for their enthusiastic and active participation in the discussions.

I hope that we all agree to congratulate and very much thank our Program Committee for arranging this successful meeting. We acknowledge the tremendous effort by the two co-chairmen of this meeting, namely, Prof. Hans Hornung from the DFVLR Göttingen, and Dr. Robert Whitehead from the U.S. Navy. In addition we have to thank our excellent session chairmen for leading us through the program and through the discussions. I would like to express once more our appreciation to the National Delegates of the U.K. for having invited us, especially Mr. Scott-Wilson and Professor Lawson for the warm welcome on Monday morning and the opening address they have given to us, and of course, Alderman Williams and the city of Bristol for the outstanding hospitality at the reception Monday evening. In addition, I thank the University of Bristol for providing the local arrangements for the meeting and the two coordinators of the University, Dr. Roger Moses and Dr. John Flower. In addition, our two local FDP points of contact, Bob Bignell, who

is a resident here in Bristol and Derek Peckham, our Deputy Chairman who has arranged many things throughout this week.

Really outstanding work in organizing and preparing the meeting has been done by the National Coordinator throughout the whole week, namely, Captain Ray Hillary and his secretary, Diana Halliday.

Now I would like to thank our Executive, Mike Fischer and the FDP Secretary, Anne Marie Rivault, for providing excellent support and service throughout the whole week from the administrative side.

Concluding, I have to address our appreciation and acknowledgement to the technical staff. We thank our interpreters, Miss Rita Day and James Sneckman. Thank you very much for doing a hard job speaking and translating. I have to thank especially our technicians for the projections and the help in our microphone service, John Bracy and John Henriette. The latter had a bad car accident and I want to thank him very much for being here and helping us throughout the whole week.

To conclude, I would like to make some commercials for the FDP program. I will come back to our program in 1987. We have just had our first symposium on Aerodynamics of Hypersonic Lifting Vehicles. Hans Hornung has announced already our second which will take place in September/October in Naples. We are running two special courses; Modern Theoretical and Experimental Approaches to Turbulent Flow and Missile Aerodynamics. We have currently three working groups: one on Boundary Layer Control, one on Three-Dimensional Viscous Flow Boundary Limits and the third one on Rotary Balances.

Let me introduce to you our program for 1988. In spring we will have a symposium on Validation of Computational Fluid Dynamics in Portugal. As you can see one point of this emphasis will be the validation and the use of experimental data bases. This concerns also high speed hypersonic flow. We try to establish limits of applicability of CFD codes for engineering work. The second symposium in 1988 will deal with Fluid Dynamics of Three Dimensional Turbulent Shear Flows and Transition and we try to fulfill a secondary requirement which was part of our previous discussion; the understanding and the prediction of the physics of three-dimensional turbulent shear flows. You are all invited to participate in our future programs. In summary we have in addition in 1988 two special courses; one on Boundary Layer Simulation Methodology and the other on Aerodynamics of Hypersonic Vehicles. We will have also two new working groups; one on Adaptive Wind Tunnel Walls and a second on Air Intakes for High Speed Vehicles. This concludes my final remarks. Thank you all for attending our present symposium and I hope to see many of you at one of our next activities.

REPORT DOCUMENTATION PAGE			
1. Recipient's Reference	2. Originator's Reference	3. Further Reference	4. Security Classification of Document
	AGARD-CP-428	ISBN 92-835-0435-6	UNCLASSIFIED
5. Originator	Advisory Group for Aerospace Research and Development North Atlantic Treaty Organization 7 rue Ancelle, 92200 Neuilly sur Seine, France		
6. Title	AERODYNAMICS OF HYPERSONIC LIFTING VEHICLES		
7. Presented at	Fluid Dynamics Pnael Symposium in Bristol, United Kingdom, 6—9 April 1987.		
8. Author(s)/Editor(s)	Various		9. Date November 1987
10. Author's/Editor's Address	Various		11. Pages 572
12. Distribution Statement	This document is distributed in accordance with AGARD policies and regulations, which are outlined on the Outside Back Covers of all AGARD publications.		
13. Keywords/Descriptors	<div style="display: flex; justify-content: space-between;"> <div> Lifting bodies Hypersonic characteristics Test facilities </div> <div> Fluid dynamics Computation Design </div> </div>		
14. Abstract	<p>The Symposium was conducted at the outset of a new era in hypersonic aerodynamics. The Proceedings therefore present a valuable stock taking of the status of the field after a comparative lull in the last decade. A particular gap exists in the field of experimental facilities. At the same time, new developments in computational fluid dynamics and experimental techniques provide possibilities that did not exist 10 years before.</p> <p>The papers presented were grouped in the fields: experimental facilities; experimental techniques and results; computational techniques; design methods; and new projects. The most significant result of the symposium was a perspective of the needs for special effort in the near future.</p>		

<p>AGARD Conference Proceedings No.428 Advisory Group for Aerospace Research and Development, NATO AERODYNAMICS OF HYPERSONIC LIFTING VEHICLES Published November 1987 572 pages</p> <p>The Symposium was conducted at the outset of a new era in hypersonic aerodynamics. The Proceedings therefore present a valuable stock taking of the status of the field after a comparative lull in the last decade. A particular gap exists in the field of experimental facilities. At the same time, new developments in computational fluid dynamics and experimental techniques provide possibilities that did not exist 10 years before.</p> <p>P.T.O.</p>	<p>AGARD-CP-428</p> <p>Lifting bodies Hypersonic characteristics Test facilities Fluid dynamics Computation Design</p>	<p>AGARD Conference Proceedings No.428 Advisory Group for Aerospace Research and Development, NATO AERODYNAMICS OF HYPERSONIC LIFTING VEHICLES Published November 1987 572 pages</p> <p>The Symposium was conducted at the outset of a new era in hypersonic aerodynamics. The Proceedings therefore present a valuable stock taking of the status of the field after a comparative lull in the last decade. A particular gap exists in the field of experimental facilities. At the same time, new developments in computational fluid dynamics and experimental techniques provide possibilities that did not exist 10 years before.</p> <p>P.T.O.</p>	<p>AGARD-CP-428</p> <p>Lifting bodies Hypersonic characteristics Test facilities Fluid dynamics Computation Design</p>	<p>AGARD-CP-428</p> <p>Lifting bodies Hypersonic characteristics Test facilities Fluid dynamics Computation Design</p>
<p>AGARD Conference Proceedings No.428 Advisory Group for Aerospace Research and Development, NATO AERODYNAMICS OF HYPERSONIC LIFTING VEHICLES Published November 1987 572 pages</p> <p>The Symposium was conducted at the outset of a new era in hypersonic aerodynamics. The Proceedings therefore present a valuable stock taking of the status of the field after a comparative lull in the last decade. A particular gap exists in the field of experimental facilities. At the same time, new developments in computational fluid dynamics and experimental techniques provide possibilities that did not exist 10 years before.</p> <p>P.T.O.</p>	<p>AGARD-CP-428</p> <p>Lifting bodies Hypersonic characteristics Test facilities Fluid dynamics Computation Design</p>	<p>AGARD Conference Proceedings No.428 Advisory Group for Aerospace Research and Development, NATO AERODYNAMICS OF HYPERSONIC LIFTING VEHICLES Published November 1987 572 pages</p> <p>The Symposium was conducted at the outset of a new era in hypersonic aerodynamics. The Proceedings therefore present a valuable stock taking of the status of the field after a comparative lull in the last decade. A particular gap exists in the field of experimental facilities. At the same time, new developments in computational fluid dynamics and experimental techniques provide possibilities that did not exist 10 years before.</p> <p>P.T.O.</p>	<p>AGARD-CP-428</p> <p>Lifting bodies Hypersonic characteristics Test facilities Fluid dynamics Computation Design</p>	<p>AGARD-CP-428</p> <p>Lifting bodies Hypersonic characteristics Test facilities Fluid dynamics Computation Design</p>

<p>The papers presented were grouped in the fields: experimental facilities; experimental techniques and results; computational techniques; design methods; and new projects. The most significant result of the symposium was a perspective of the needs for special effort in the near future.</p> <p>Papers presented and Discussions held at the Fluid Dynamics Panel Symposium in Bristol, United Kingdom, 6—9 April 1987.</p> <p>ISBN 92-835-0435-6</p>	<p>The papers presented were grouped in the fields: experimental facilities; experimental techniques and results; computational techniques; design methods; and new projects. The most significant result of the symposium was a perspective of the needs for special effort in the near future.</p> <p>Papers presented and Discussions held at the Fluid Dynamics Panel Symposium in Bristol, United Kingdom, 6—9 April 1987.</p> <p>ISBN 92-835-0435-6</p>
<p>The papers presented were grouped in the fields: experimental facilities; experimental techniques and results; computational techniques; design methods; and new projects. The most significant result of the symposium was a perspective of the needs for special effort in the near future.</p> <p>Papers presented and Discussions held at the Fluid Dynamics Panel Symposium in Bristol, United Kingdom, 6—9 April 1987.</p> <p>ISBN 92-835-0435-6</p>	<p>The papers presented were grouped in the fields: experimental facilities; experimental techniques and results; computational techniques; design methods; and new projects. The most significant result of the symposium was a perspective of the needs for special effort in the near future.</p> <p>Papers presented and Discussions held at the Fluid Dynamics Panel Symposium in Bristol, United Kingdom, 6—9 April 1987.</p> <p>ISBN 92-835-0435-6</p>